7th MASHCON

International Conference on Ship Manoeuvring in Shallow and Confined Water

with non-exclusive focus on clean power in shallow water

Conference program and proceedings

18 - 21 May 2025, Bruges, Belgium

Flanders Hydraulics

Flanders State of the Art

GHENT UNIVERSITY

7th MASHCON

International Conference on Ship Manoeuvring in Shallow and Confined Water

with non-exclusive focus on clean power in shallow water

Conference program and proceedings

18 - 21 May 2025, Bruges, Belgium

Editors
Katrien Eloot, Jeroen Verwilligen, Steve Claes
Flanders Hydraulics, Belgium

Guillaume Delefortrie, Evert Lataire
Ships and Marine Technology Division, Ghent University, Belgium

Although all care is taken to ensure the integrity and quality of this publication and the information herein, no responsibility is assumed by the publisher nor the authors for any damage to property or persons as a result of operation or use of this publication and/or the information contained herein.

Published by
Flanders Hydraulics and Knowledge Centre Manoeuvring in Shallow and Confined Water
Ships and Marine Technology Division, Ghent University.

D/2025/3241/136 https://dx.doi.org/10.48607/316

This work is licensed under a Creative Commons Attribution 4.0 International License.

Cover photo: © MDK & Port of Antwerp-Bruges

Organisation

Members of the International Scientific Committee

Prof. Moustafa Abdel-Maksoud	Hamburg University of Technology, Germany m.abdel-maksoud@tu-harburg.de
Dr. Carl-Uwe Böttner	Federal Waterways Engineering and Research Institute (BAW), Germany carl-uwe.boettner@baw.de
Prof. Guillaume Delefortrie	Ships and Marine Technology Division, Ghent University, Belgium guillaume.delefortrie@ugent.be
Dr. Jonathan Duffy	Australian Maritime College, National Centre for Maritime Engineering and Hydrodynamics, University of Tasmania, Australia j.duffy@utas.edu.au
Dr. Katrien Eloot	Flanders Hydraulics, Belgium katrien.eloot@mow.vlaanderen.be
Prof. Yoshitaka Furukawa	Department of Marine Systems Engineering, Kyushu University, Japan furukawa@nams.kyushu-u.ac.jp
Dr. Tim Gourlay	Perth Hydro Pty Ltd, Australia tim@perthhydro.com
Prof. Nikolai Kornev	Faculty of Mechanical Engineering and Marine Technology, University of Rostock, Germany nikolai.kornev@uni-rostock.de
Prof. Evert Lataire	Ships and Marine Technology Division, Ghent University, Belgium evert.lataire@ugent.be
Dr. Jialun Liu	Wuhan University of Technology, China jialunliu@whut.edu.cn
Raul Redondo	Siport21, Spain raul.redondo@siport21.es
Dr. Weichao Shi	Net Zero Maritime Systems (Marine renewable energy and marine propulsion) , Marine, Offshore and Subsea Technology Group, Mechanical Engineering and Marine Technology, Newcastle University, UK weichao.shi@ncl.ac.uk
Prof. Eduardo Aoun Tannuri	Departamento de Engenharia Mecatronica e Sistemas Mecanicos, Escola Politecnica da Universidade de Sao Paulo, Brazil eduat@usp.br
Dr. Tahsin Tezdogan	Naval Architecture, Ocean and Marine Engineering, University of Strathclyde, UK t.tezdogan@soton.ac.uk
Em. Prof. Marc Vantorre	Ships and Marine Technology Division, Ghent University, Belgium marc.vantorre@ugent.be
Prof. Hironori Yasukawa	Department of Transportation and Environmental Systems, Hiroshima University, Japan yasukawa@naoe.hiroshima-u.ac.jp

Dr. Dong Jin Yeo	Korea Research Institute of Ships and Ocean Engineering, Republic of Korea lonepier@kriso.re.kr
Dr. Zhiming Yuan	Naval Architecture, Ocean and Marine Engineering, University of Strathclyde, UK zhiming.yuan@strath.ac.uk
Dr. Lu Zou	School of Naval Architecture, Ocean and Civil Engineering, Shanghai Jiao Tong University, China luzou@sjtu.edu.cn
Prof. Zao-Jian Zou	School of Naval Architecture, Ocean and Civil Engineering, Shanghai Jiao Tong University, China zjzou@sjtu.edu.cn

Review Coordination

Steve Claes	Flanders Hydraulics, Belgium

Organising Committee

Dr. Katrien Eloot	Flanders Hydraulics, Belgium
Jeroen Verwilligen	Flanders Hydraulics, Belgium
Prof. Guillaume Delefortrie	Ships and Marine Technology Division, Ghent University, Belgium
Prof. Evert Lataire	Ships and Marine Technology Division, Ghent University, Belgium

Lay-out

David Rutten	Flanders Hydraulics, Belgium

Table of Contents

Organisation IV
Table of Contents VI
Preface XII
Sponsorship XIII
Conference program XV
18 MAY 2025 XVI
19 MAY 2025 XVI
20 MAY 2025 XVIII
21 MAY 2025 XX
22 MAY 2025 XXII
SHALLOW WATER SPEED/POWER TRIALS WITH CRUISE LINER FOR BENCHMARKING 1
Gijs Struijk, MARIN, The Netherlands 1
Guillaume Delefortrie, Ships and Marine Technology, Ghent University, Belgium 1
Dmitriy Ponkratov, Siemens, UK 1
Jeroen Verwilligen, Flanders Hydraulics, Belgium 1
Evert Lataire, Ships and Marine Technology, Ghent University 1
ON THE RESISTANCE ESTIMATION OF AN INLAND VESSEL IN SHALLOW AND CONFINED WATER 17
José Villagómez, Flanders Hydraulics, Belgium 17
Wim Van Hoydonck, Flanders Hydraulics, Belgium 17
Thibaut Van Zwijnsvoorde, Flanders Hydraulics, Belgium 17
Maxim Candries, Ships and Marine Technology, Ghent University, Belgium 17
APPLICATION OF CFD FOR THE PREDICTION OF HYDRODYNAMIC FORCES ACTING ON AN INLAND WATERWAY SHIP IN SHALLOW WATERS. LESSONS LEARNED FROM THE SHINING WORKSHOP 33
Lahbib Zentari, Federal Waterways Engineering and Research Institute, Germany 33
Antoine Bedos, Maritime Research Institute Netherlands, the Netherlands 33
Wim Van Hoydonck, Flanders Hydraulics, Belgium 33
Jens Ley, Development Centre for Ship Technology and Transport Systems, Germany 33
Guillermo Chillcce, University of Duisburg-Essen, Germany 33
COMBINING NUMERICAL AND EXPERIMENTAL METHODS TO EXPLAIN SHIP-BANK INTERACTIONS 43
Bedos, Antoine, MARIN, The Netherlands 43
Gornicz, Tomasz, MARIN, The Netherlands 43
Tonelli, Roberto, MARIN, The Netherlands 43
UNSTEADY HYDRODYNAMICS OF A BOX WHEN ENTERING A LOCK 60
Zhi-Ming Yuan, University of Strathclyde, UK 60
Yihan Liu, China Classification Society, CN 60
Momchil Terziev, University of Strathclyde, UK 60

SIMULATION AND APPLICATION OF MODEL-BASED AND MODEL- FREE TRACK CONTROLLERS FOR SHIP MANOEUVRING IN SHALLOW AND CONFINED WATER 77
Eloot Katrien, Flanders Hydraulics, Belgium 77
Cisneros Matteo, University Antwerp, Belgium 77
Verwilligen Jeroen, Flanders Hydraulics, Belgium 77
Donatini Luca, Ghent University, Belgium 77
Mansuy Marc, Ghent University, Belgium 77
Daems Walter J.F., University Antwerp, Belgium 77
Massobrio Renzo, University Antwerp, Belgium 77
Hellinckx Peter, University Antwerp, Belgium 77
ENHANCED FREE-RUNNING MANOEUVRING TESTS OF INLAND VESSELS IN MODEL SCALE 96
Matthias Tenzer, DST - Development Centre for Ship Technology and Transport Systems, Germany 96
Felix Roettig, DST - Development Centre for Ship Technology and Transport Systems, Germany 96
Rainer Kaiser, DST - Development Centre for Ship Technology and Transport Systems, Germany 96
Justin Jasa, DST - Development Centre for Ship Technology and Transport Systems, Germany 96
Benjamin Friedhoff, DST - Development Centre for Ship Technology and Transport Systems, Germany 96
COURSE-KEEPING SIMULATIONS OF A SHIP IN CONFINED WATERWAYS BASED ON INTEGRATED CFD METHOD AND CONTROL ALGORITHM 109
Zi-Qiang Zheng, School of Ocean and Civil Engineering, Shanghai Jiao Tong University, China 109
Yu He, School of Ocean and Civil Engineering, Shanghai Jiao Tong University, China 109
Lu Zou, School of Ocean and Civil Engineering, Shanghai Jiao Tong University, China 109
Zao-Jian Zou, School of Ocean and Civil Engineering, Shanghai Jiao Tong University, China 109
VALIDATION OF SLENDERFLOW IN SHIP - SHIP INTERACTION SCENARIOS 124
Andreas VERBEKE, Ships and Marine Technology, Ghent University, Belgium 124
Tim GOURLAY, Perth Hydro, Australia 124
Guillaume DELEFORTRIE, Ships and Marine Technology, Ghent University, Belgium 124
Maxim CANDRIES, Ships and Marine Technology, Ghent University, Belgium 124
Wim VAN HOYDONCK, Flanders Hydraulics, Belgium 124
Evert LATAIRE, Ships and Marine Technology, Ghent University, Belgium 124
A SYSTEMATIC STUDY ON ROPES MODELLING OF THE INTERAC- TION FORCES BETWEEN A SAILING SHIP AND A SHIP MOORED AT A QUAY WALL WITH A COMPLEX GEOMETRY 141
Sara Sanz Sáenz, IMDC, Belgium 141
Wojciech Misiag, IMDC, Belgium 141
EXPLORING THE HYDRODYNAMIC EFFECTS AT HIGH RUDDER ANGLES ON INLAND VESSELS 165
Justin Jasa, DST - Development Centre for Ship Technology and Transport Systems, Germany 165
Matthias Tenzer, DST - Development Centre for Ship technology and Transport Systems, Germany 165
Benjamin Friedhoff, DST - Development Centre for Ship technology and Transport Systems, Germany 165

NUMERICAL STUDY ON THE RUDDER INFLOW BEHIND THE HULL AND THE PROPELLER IN FOUR QUADRANTS 175

Suli Lu, Ships and Marine Technology, Ghent University, Belgium, Suli.Lu@UGent.be 175

Wim Van Hoydonck, Flanders Hydraulics, Belgium 175

Santiago Lopez Castaño, Flanders Hydraulics, Belgium 175

Evert Lataire, Ships and Marine Technology, Ghent University, Belgium 175

Guillaume Delefortrie, Ships and Marine Technology, Ghent University, Belgium 175

HYDRODYNAMIC PERFORMANCE OF A NEWLY DESIGNED RHINE VESSEL INTEGRATED WITH VARIOUS PROPULSION IMPROVEMENT DEVICES FOR SHALLOW WATER OPERATIONS 186

Nathalie Reinach, Development Centre for Ship Technology and Transport Systems (DST), Germany 186

Ravindu Us Gamaralalage, Development Centre for Ship Technology and Transport Systems (DST), Germany 186

Jens Ley, Development Centre for Ship Technology and Transport Systems (DST), Germany 186

COMPUTATIONAL MODELLING OF SQUAT AND RESISTANCE OPTIMISATION IN FULLY CONFINED WATER 202

Momchil Terziev - Department of Naval Architecture, Ocean and Marine Engineering, University of Strathclyde, Glasgow, UK 202

Muhammad Iqbal - Department of Naval Architecture, Faculty of Engineering, Universitas Diponegoro, Indonesia. 202

Yujia Wei - School of Aerospace, Transport and Manufacturing, University of Cranfield, UK. 202

Atilla Incecik - Department of Naval Architecture, Ocean and Marine Engineering, University of Strathclyde, Glasgow, UK. 202

A ONE DIMENSIONAL HYDRAULIC MODEL FOR CONFINED NAVIGATION WITH A LONGITUDINAL VARIATION OF THE HULL 213

Julien Dambrine, Laboratoire de Mathématiques et Applications (UMR 7348), CNRS, University of Poitiers, France. 213

Valentin Jules, Institut Pprime (CNRS UPR 3346), CNRS, University of Poitiers, ISAE-ENSMA, France. 213

Pierre-Jean Pompée, Voies Navigables de France, France. 213

Morgan Pierre, Laboratoire de Mathématiques et Applications, (UMR 7348) University of Poitiers, France. 213

Germain Rousseaux, Institut Pprime (CNRS UPR 3346), CNRS, University of Poitiers, ISAE-ENSMA, France. 213

INTEGRATING POTENTIAL FLOW CODE FOR SHIP BANK INTERACTION AT REAL TIME SIMULATIONS229

Ibarrondo, Marta, MARIN, The Netherlands 229

Gornicz, Tomasz, MARIN, The Netherlands 229

Kleermaker, Wim, MARIN, The Netherlands 229

LOCAL HYDRODYNAMICS EFFECTS IN NARROW AND SHALLOW CHANNELS. ITS IMPORTANCE IN DESIGN AND TRAINING 247

Rafael Ros, Siport21, Spain 247

Raul Redondo, Siport21, Spain 247

Lourdes Pecharroman, Siport21, Spain 247

HYDRODYNAMIC INFLUENCE OF WAVY SEABED ON SHIP-SEABED INTERACTION 267

Yunxin Xu, School of Engineering, Newcastle University, UK 267

Weichao Shi, School of Engineering, Newcastle University, UK 267

MANEUVERING OF A MODEL SCALE SHIP IN NATURAL FLUID MUD 280
Jan Mense, Federal Waterways Engineering and Research Institute, Germany 280
Carl-Uwe Böttner, Federal Waterways Engineering and Research Institute, Germany 280
FULL SCALE MANOEUVRING TESTS WITH A SMALL, FLEXIBLE AUTOMATED, ZERO-EMISSION (SFAZ) VESSEL 295
Mansuy, M., Delefortrie, G., Candries, M., Ships and Marine Technology, Ghent University, Belgium 295
Alliot, A., Mesnil, L., Alliot, I., NEAC-INDUSTRY, France 295
EVALUATING THE IMPACT OF WIND-ASSISTED SHIP PROPULSION ON THE MANEUVERABILITY OF A SUEZMAX TANKER 314
Gustavo L. de O. Santana, Ferdinando R. Freire, Maria E. F. Chame, Claudio M. Sampaio, Eduardo A. Tannuri, ... 314
Lucia B. F. Logsdon, Nathalie Sanghikian 314
TPN-USP (Numerical Offshore Tank - University of São Paulo), Brazil 314
Petrobras Petróleo Brasileiro S.A., Brazil 314
APPLICATION OF THE MMG-METHOD TO PREDICT THE PROPULSIVE PERFORMANCE OF A BULK CARRIER WITH FLETTNER ROTORS 335
Hironori Yasukawa, Hiroshima University, Japan 335
DEVELOPMENT OF A PUSH BOAT BARGE UNIT 349
Benjamin Kossmann, Ould el Moctar, Thomas E. Schellin, University of Duisburg-Essen, Germany 349
A METHOD TO ESTIMATE EMISSIONS OF AN INLAND WATERWAY SHIP MANEUVERING IN RESTRICTED WATERS 361
Jakob Rzeszutko, University of Duisburg-Essen (UDE), Germany 361
Daniel Weber, Federal Waterways Engineering and Research Institute (BAW), Germany 361
Lahbib Zentari, Federal Waterways Engineering and Research Institute (BAW), Germany 361
Christian Noss, Federal Waterways Engineering and Research Institute (BAW), Germany 361
Ould el Moctar, University of Duisburg-Essen (UDE), Germany 361
APPROACH TO ELIMINATE TANK WALL EFFECTS FROM OPEN WATER MANOEUVRING MODELS 377
Guillaume Delefortrie, Ships and Marine Technology, Ghent University, Belgium 377
Arghya Kamol Roy, Ships and Marine Technology, Ghent University, Belgium 377
Katrien Eloot, Flanders Hydraulics, Belgium 377
Evert Lataire, Ships and Marine Technology, Ghent University, Belgium 377
INFLUENCE OF THE RETURN CURRENT AND THE PRIMARY WAVE OF A PASSING SHIP ON HARBOUR HYDRODYNAMICS 392
Ina Teutsch, Federal Waterways Engineering and Research Institute (BAW), Germany 392
Marko Kastens, Federal Waterways Engineering and Research Institute (BAW), Germany 392
SHIP-GENERATED WAVES IN CONFINED 402
Pablo Nieutin, Institut Pprime, CNRS - Université de Poitiers - ISAE-ENSMA, HYDÉE team, France 402
Clément Maubant, Institut Pprime, CNRS - Université de Poitiers - ISAE-ENSMA, HYDÉE team, France 402
Gérard Pineau, Institut Pprime, CNRS - Université de Poitiers - ISAE-ENSMA, HYDÉE team, France 402
Damien Calluaud, Institut Pprime, CNRS - Université de Poitiers - ISAE-ENSMA, HYDÉE team, France 402

NUMERICAL PMM TEST IN FINITE DEPTH AND APPLICATION TO MMG MODEL OF SHIP MANOEUVERING 412

Junhoi Choi, Department of Naval Architecture and Ocean Engineering, Seoul National University, Korea 412

Shuguang Wang, Department of Naval Architecture and Ocean Engineering, Seoul National University, Korea 412

Yonghwan Kim, Department of Naval Architecture and Ocean Engineering, Seoul National University, Korea 412

VISCOUS CFD SIMULATION OF PMM TESTS IN SHALLOW WATER AND IN A CANAL 425

Takuya Ohmori, National Maritime Research Institute, Japan 425

Kunihide Ohashi, National Maritime Research Institute, Japan 425

Yoshitaka Furukawa, Kyushu University, Japan 425

Hiroshi Ibaragi, Kyushu University, Japan Yuya Matsunaga, JAPAN MARINE UNITED CORPORATION, Japan. 425

HYDRODYNAMIC FORCES ACTING ON SHIP RUNNING IN CURVED WATERWAY WITH CONSTANT RADII 434

Yoshitaka Furukawa, Kyushu University, Japan Hiroshi Ibaragi, Kyushu University, Japan 434

Takuya Ohmori, National Maritime Research Institute, Japan 434

Kunihide Ohashi, National Maritime Research Institute, Japan 434

Yuya Matsunaga, Japan Marine United Corporation, Japan 434

PATH FOLLOWING OF AN UNDERACTUATED SHIP IN RESTRICTED WATERS USING CLOS AND COMPENSATED LQR METHODS 445

Yu He, School of Ocean and Civil Engineering, Shanghai Jiao Tong University, Shanghai, China 445

Lu Zou, 1. School of Ocean and Civil Engineering, Shanghai Jiao Tong University, Shanghai, China; 2. State Key Laboratory of Ocean Engineering, Shanghai Jiao Tong University, Shanghai, China 445

Wei-Min Chen, Shanghai Ship and Shipping Research Institute Co., Ltd., Shanghai, China 445

Zao-Jian Zou, 1. School of Ocean and Civil Engineering, Shanghai Jiao Tong University, Shanghai, China; 2. State Key Laboratory of Ocean Engineering, Shanghai Jiao Tong University, Shanghai, China 445

Jin-Lan Li, School of Ocean and Civil Engineering, Shanghai Jiao Tong University, Shanghai, China 445

BAYESIAN-SVR MODEL FOR PREDICTING SHIP MANEUVERING TRAJECTORIES IN DEEP AND SHALLOW WATER CONDITION 462

Donghyeong Ko, HD Hyundai Heavy Industries Co., Ltd; Department of Naval Architecture and Ocean Engineering, Seoul National University, Republic of Korea 462

Seong Ho Moon, HD Hyundai Heavy Industries Co., Ltd, Republic of Korea 462

Bo Woo Nam, Department of Naval Architecture and Ocean Engineering, Seoul National University, Republic of Korea 462

(Corresponding Author: bwnam@sun.ac.kr) 462

UNBERTHING SIMULATIONS OF A SHIP USING A FIRST-ORDER LAG MODEL TO TAKE THE HYDRODYNAMIC MEMORY EFFECT INTO ACCOUNT 474

Ryusuke Okuda, National Maritime Research Institute, Japan 474

Hironori Yasukawa, Hiroshima University, Japan 474

COMPUTATION OF VESSEL MOTIONS IN WAVES USING FORWARD-SPEED FREE-SURFACE GREEN FUNCTION 490

Wim van der Molen, Baird, Australia 490

COMPARISON OF WAMIT WITH MEASURED WAVE-INDUCED MOTIONS OF CONTAINER 505
Tim Gourlay, Perth Hydro, Australia 505
PREDICTIVE SIMULATION OF ONSHORE POWER SUPPLY REQUIREMENTS FOR PORTS 519
Lourdes Pecharromán, Siport21. Spain 519
Raul Redondo, Siport21. Spain 519
Raul Atienza, Siport21. Spain 519
Arturo Medio, Technical University of Madrid, Spain 519
Luis Ulla, Technical University of Madrid, Spain 519

Preface

It is our pleasure as organisers, Flanders Hydraulics and Ghent University, to welcome you to the 7th edition of the MASHCON conference – a conference that has grown into a valued tradition within our specialist community focused on ship manoeuvring in shallow and confined water.

Our journey began modestly in 2009 in Antwerp, and since then, MASHCON has found a rhythm of convening every two or three years, alternating between venues in Belgium (Antwerp, Ghent, Ostend and now Bruges) and abroad, locally organised by our international peers in Trondheim, Hamburg and Glasgow. Each edition has brought together experts from around the world in a setting that created both scientific discussions as well as personal connection.

While never a large-scale event, the MASHCON conferences remain a focused and close-knit forum. Its strength lies precisely in this: the opportunity for specialists to meet in a collegial atmosphere, to discuss the state of the art, share recent developments, and explore emerging challenges and solutions in our specific field.

As in every edition, this time we have chosen a non-exclusive theme to highlight a timely and pressing issue. For MASHCON 2025, we focus on *Clean Power in Shallow Water* – a subject so relevant in today's rapidly changing maritime landscape. Alongside this theme, all aspects of ship manoeuvring in shallow and confined water remain central to the programme, ensuring continuity and relevance to the diverse interests of you, participants.

For those attending in person, we also hope you will take the opportunity to enjoy the unique charm of Bruges – a beautifully preserved medieval city that offers a rich historical, cultural and gastronomic experience.

We look forward to fruitful discussions, renewed collaborations, and continued progress while our ships remain safe and sound in shallow and confined water.

Welcome to MASHCON 2025, welcome to Bruges.

We have ships, we have beer and chocolate.

Prof. Evert LATAIRE

Sponsorship

HR Wallingford is a world leader in computer and laboratory physical modelling of water. Whether this is inland, coastal, or offshore. Our expertise range from climate resilience, coastal management, energy, flood management, waterway and port design, masterplanning, port operations with real-time ship simulations, water resources, dams and reservoirs as well as the design and supply laboratory equipment for use in laboratory and industrial test facilities. We are both supplier of these physical modelling facilities and measurement systems but also major user of these systems for our own commercial and research activities.

Established in 1947, HR Wallingford is a centre of excellence for maritime, coastal and fluvial engineering based at our headquarters in Wallingford, UK. The company also has regional offices in Manchester, UK; Perth, Australia; Mumbai; Kuala Lumpur; Abu Dhabi; Houston; and Shanghai.

A high proportion of the work, undertaken for our clients uses physical scaled models. Through this work, HR Wallingford has gained a wealth of experience in both building wave generating systems that realistically simulate sea conditions, and developing the associated instrumentation, including data acquisition equipment required to capture and analyse the results. HR Wallingford is also recognised as a world leading supplier of hydrological and hydrodynamic research test facilities and measuring instrumentation. These include Cavitation Tunnels, Towing Tank and Sea-keeping and Manoeuvring Basins multi-motion carriages that combine with our Wave Generation Systems.

In addition to this, HR Wallingford have an extensive range of measuring instrumentation and dynamometry for use within physical model test facilities. In December 2019, HR Wallingford extended its portfolio within the Equipment, Technology and Innovation (ET&I) group with the acquisition and integration of The Marine Hydrodynamics division of Manchester-based Cussons Technology. This included the experienced Manchester based team that design and fabricate this equipment, together with the guardianship of Kempf & Remmers equipment and facilities designs recognised and used throughout the world.

HR Wallingford Howbery Park, Wallingford, Oxfordshire, OX10 8BA, United Kingdom
Shaun Ross - s.ross@hrwallingford.com
Living and working sustainably with water | HR Wallingford

Hertzberger Propelling Technology

Rijswijk, NL

Gideon Hertzberger - gideon@propellingtechnology.nl

Hertzberger Propelling Technology

Voka - Alfaport

Markgravestraat 12, 2000 Antwerpen BE

Sofie Coppens - sofie.coppens@voka.be

Antwerpen-Waasland | Voka

Belgische Scheepvaartvereniging BSV

Brouwersvliet 33/6, 2000 Antwerpen, BE

Saskia Evenepoel - saskia.evenepoel@bsv-bsf.be

asv.be

Department of Mobility & Public Works

Marie-Elisabeth Belpairegebouw

Simon Bolivarlaan 17, 1000 Brussel, BE

Mobiliteit en Openbare Werken | Vlaanderen.be

De Vlaamse Waterweg

Havenstraat 44 3500 Hasselt, BE

Erik Schrooyen - erik.schrooyen@vlaamsewaterweg.be

De Vlaamse Waterweg

7th MASHCON

International Conference on Ship Manoeuvring in Shallow and Confined Water

with non-exclusive focus on clean power in shallow water

Conference program

18 - 21 May 2025, Grand Hotel Casselbergh, Bruges, Belgium

18 MAY 2025 (SUNDAY)

17:30 – 19:30	**Registration + Welcome Reception at Hotel Casselbergh**

19 MAY 2025 (MONDAY)

08:45 – 09:00	**Registration**
09:00 – 09:15	**Opening address by the Knowledge Centre**
09:15 – 10:00	**Keynote by Florent Maes from CLdN**
SESSION 1: Resistance Chair: Zhiming Yuan	
10:00 – 10:25	SHALLOW WATER SPEED/POWER TRIALS WITH CRUISE LINER FOR BENCHMARKING **Gijs Struijk**, MARIN, The Netherlands; Guillaume Delefortrie, Evert Lataire, Ships and Marine Technology, Ghent University, Belgium; Dmitriy Ponkratov, Siemens, UK; Jeroen Verwilligen, Flanders Hydraulics, Belgium
10:25 – 10:50	ON THE RESISTANCE ESTIMATION OF AN INLAND VESSEL IN SHALLOW AND CONFINED WATER **José Villagómez**, Wim Van Hoydonck, Thibaut Van Zwijnsvoorde, Flanders Hydraulics, Belgium; Maxim Candries, Ships and Marine Technology, Ghent University, Belgium
10:50 – 11:15	**Refreshment Break**
SESSION 2: Inland vessel Chair: Lu Zou	
11:15 – 11:40	APPLICATION OF CFD FOR THE PREDICTION OF HYDRODYNAMIC FORCES ACTING ON AN INLAND WATERWAY SHIP IN SHALLOW WATERS. LESSONS LEARNED FROM THE SHINING WORKSHOP **Lahbib Zentari**, Federal Waterways Engineering and Research Institute, Germany; Antoine Bedos, Maritime Research Institute Netherlands, the Netherlands; Wim Van Hoydonck, Flanders Hydraulics, Belgium; Jens Ley, Development Centre for Ship Technology and Transport Systems, Germany; Guillermo Chillcce, University of Duisburg-Essen, Germany
11:40 – 12:05	COMBINING NUMERICAL AND EXPERIMENTAL METHODS TO EXPLAIN SHIP-BANK INTERACTIONS **Bedos Antoine**, Gornicz Tomasz, Tonelli Roberto, MARIN, The Netherlands
12:05 – 12:30	UNSTEADY HYDRODYNAMICS OF A BOX WHEN ENTERING A LOCK **Zhi-Ming Yuan**, Momchil Terziev, University of Strathclyde, UK; Yihan Liu, China Classification Society, CN
12:30 – 13:30	**Lunch**

SESSION 3: Track control Chair: Eduardo Aoun Tannuri	
13:30 – 13:55	SIMULATION AND APPLICATION OF MODEL-BASED AND MODEL- FREE TRACK CONTROLLERS FOR SHIP MANOEUVRING IN SHALLOW AND CONFINED WATER **Eloot Katrien**, Verwilligen Jeroen, Flanders Hydraulics, Belgium; Donatini Luca, Mansuy Marc, Ghent University, Belgium; Cisneros Matteo, Daems Walter J.F., Massobrio Renzo, Hellinckx Peter, University Antwerp, Belgium
13:55 – 14:20	ENHANCED FREE-RUNNING MANOEUVRING TESTS OF INLAND VESSELS IN MODEL SCALE **Matthias Tenzer**, Felix Roettig, Rainer Kaiser, Justin Jasa, Benjamin Friedhoff, DST - Development Centre for Ship Technology and Transport Systems, Germany
14:20 – 14:45	COURSE-KEEPING SIMULATIONS OF A SHIP IN CONFINED WATERWAYS BASED ON INTEGRATED CFD METHOD AND CONTROL ALGORITHM **Zi-Qiang Zheng**, Yu He, Lu Zou, Zao-Jian Zou, School of Ocean and Civil Engineering, Shanghai Jiao Tong University, China
14:45 – 15:15	**Refreshment Break**
SESSION 4: Hydrodynamic effects Chair: Yoshitaka Furukawa	
15:15 – 15:40	VALIDATION OF SLENDERFLOW IN SHIP - SHIP INTERACTION SCENARIOS **Andreas VERBEKE**, Guillaume DELEFORTRIE, Maxim CANDRIES, Evert LATAIRE, Ships and Marine Technology, Ghent University, Belgium; Tim GOURLAY, Perth Hydro, Australia; Wim VAN HOYDONCK, Flanders Hydraulics, Belgium
15:40 – 16:05	A SYSTEMATIC STUDY ON ROPES MODELLING OF THE INTERAC- TION FORCES BETWEEN A SAILING SHIP AND A SHIP MOORED AT A QUAY WALL WITH A COMPLEX GEOMETRY **Sara Sanz Sáenz**, Wojciech Misiag, IMDC, Belgium
16:05 – 16:30	EXPLORING THE HYDRODYNAMIC EFFECTS AT HIGH RUDDER ANGLES ON INLAND VESSELS **Justin Jasa**, Matthias Tenzer, Benjamin Friedhoff, DST - Development Centre for Ship technology and Transport Systems, Germany
16:30 – 16:55	NUMERICAL STUDY ON THE RUDDER INFLOW BEHIND THE HULL AND THE PROPELLER IN FOUR QUADRANTS **Suli Lu**, Evert Lataire, Guillaume Delefortrie, Ships and Marine Technology, Ghent University, Belgium; Wim Van Hoydonck, Santiago Lopez Castaño, Flanders Hydraulics, Belgium
17:20 – 18:20	**City tour**

20 MAY 2025 (TUESDAY)

09:00 – 09:15	**Opening address**
09:15 – 10:00	**Keynote by Marcel Cleijsen from Wärtsilä**
SESSION 5 – Shallow water Chair: Katrien Eloot	
10:00 – 10:25	HYDRODYNAMIC PERFORMANCE OF A NEWLY DESIGNED RHINE VESSEL INTEGRATED WITH VARIOUS PROPULSION IMPROVEMENT DEVICES FOR SHALLOW WATER OPERATIONS **Nathalie Reinach**, Ravindu Us Gamaralalage, Jens Ley, Development Centre for Ship Technology and Transport Systems (DST), Germany
10:25 – 10:50	COMPUTATIONAL MODELLING OF SQUAT AND RESISTANCE OPTIMISATION IN FULLY CONFINED WATER **Momchil Terziev**, Atilla Incecik - Department of Naval Architecture, Ocean and Marine Engineering, University of Strathclyde, Glasgow, UK.; Muhammad Iqbal - Department of Naval Architecture, Faculty of Engineering, Universitas Diponegoro, Indonesia.; Yujia Wei - School of Aerospace, Transport and Manufacturing, University of Cranfield, UK.
10:50 – 11:15	**Refreshment Break**
SESSION 6 – Confined water Chair: Evert Lataire	
11:15 – 11:40	A ONE DIMENSIONAL HYDRAULIC MODEL FOR CONFINED NAVIGATION WITH A LONGITUDINAL VARIATION OF THE HULL **Julien Dambrine**, Morgan Pierre, Laboratoire de Mathématiques et Applications, (UMR 7348) University of Poitiers, France.; Valentin Jules, Germain Rousseaux, Institut Pprime (CNRS UPR 3346), CNRS, University of Poitiers, ISAE-ENSMA, France.; Pierre-Jean Pompée, Voies Navigables de France, France.
11:40 – 12:05	INTEGRATING POTENTIAL FLOW CODE FOR SHIP BANK INTERACTION AT REAL TIME SIMULATIONS **Ibarrondo Marta**, Gornicz Tomasz, Kleermaker Wim, MARIN, The Netherlands
12:05 – 12:30	LOCAL HYDRODYNAMICS EFFECTS IN NARROW AND SHALLOW CHANNELS. ITS IMPORTANCE IN DESIGN AND TRAINING **Rafael Ros**, Raul Redondo, Lourdes Pecharroman, Siport21, Spain
12:30 - 13:30	**Lunch**

SESSION 7 – Ship bottom interaction Chair: Marc Vantorre	
13:30 – 13:55	HYDRODYNAMIC INFLUENCE OF WAVY SEABED ON SHIP-SEABED INTERACTION **Yunxin Xu**, Weichao Shi, School of Engineering, Newcastle University, UK
13:55 – 14:20	MANEUVERING OF A MODEL SCALE SHIP IN NATURAL FLUID MUD **Jan Mense**, Carl-Uwe Böttner, Federal Waterways Engineering and Research Institute, Germany
14:20 – 14:45	FULL SCALE MANOEUVRING TESTS WITH A SMALL, FLEXIBLE AUTOMATED, ZERO-EMISSION (SFAZ) VESSEL **Mansuy, M.**, Delefortrie, G., Candries, M., Ships and Marine Technology – Ghent University, Belgium; Alliot, A., Mesnil, L., Alliot, I., NEAC-INDUSTRY, France
14:45 – 15:15	**Refreshment Break**
SESSION 8 – Clean energy in Shallow Water Chair: Weichao Shi	
15:15 – 15:40	EVALUATING THE IMPACT OF WIND-ASSISTED SHIP PROPULSION ON THE MANEUVERABILITY OF A SUEZMAX TANKER **Eduardo A. Tannuri**, Gustavo L. de O. Santana, Ferdinando R. Freire, Maria E. F. Chame, Claudio M. Sampaio, TPN-USP (Numerical Offshore Tank - University of São Paulo), Brazil; Lucia B. F. Logsdon, Nathalie Sanghikian, Petrobras Petróleo Brasileiro S.A., Brazil.
15:40 – 16:05	APPLICATION OF THE MMG-METHOD TO PREDICT THE PROPULSIVE PERFORMANCE OF A BULK CARRIER WITH FLETTNER ROTORS **Hironori Yasukawa**, Hiroshima University, Japan
16:05 – 16:30	DEVELOPMENT OF A PUSH BOAT BARGE UNIT WITH AN AUXILLARY SHALLOW WATER PROPULSION SYSTEM **Benjamin Kossmann**, Ould el Moctar, Thomas E. Schellin, University of Duisburg-Essen, Germany
16:30 – 16:55	A METHOD TO ESTIMATE EMISSIONS OF AN INLAND WATERWAY SHIP MANEUVERING IN RESTRICTED WATERS **Jakob Rzeszutko**, Ould el Moctar, University of Duisburg-Essen (UDE), Germany; Daniel Weber, Lahbib Zentari, Christian Noss, Federal Waterways Engineering and Research Institute (BAW), Germany
18:15 – 19:30	**Guided Tour & Beer Masterclass at Brewery The Halve Maan**
19:30 – 23:00	**Conference Dinner**

21 MAY 2025 (WEDNESDAY)

09:30 – 09:35	**Opening address**
SESSION 9 – Waves in confined water Chair: Tim Gourlay	
09:35 – 10:00	APPROACH TO ELIMINATE TANK WALL EFFECTS FROM OPEN WATER MANOEUVRING MODELS **Guillaume Delefortrie,** Arghya Kamol Roy, Evert Lataire, Ships and Marine Technology, Ghent University, Belgium; Katrien Eloot, Flanders Hydraulics, Belgium
10:00 – 10:25	INFLUENCE OF THE RETURN CURRENT AND THE PRIMARY WAVE OF A PASSING SHIP ON HARBOUR HYDRODYNAMICS **Ina Teutsch**, Marko Kastens, Federal Waterways Engineering and Research Institute (BAW), Germany
10:25 – 10:50	SHIP-GENERATED WAVES IN CONFINED WATERWAYS: LABORATORY AND NUMERICAL STUDY OF FLOW FEATURES NEAR SLOPING BANKS WITH DIFFERENT ANGLES **Clément Maubant**, Pablo Nieutin, Gérard Pineau, Damien Calluaud, Institut Pprime, CNRS - Université de Poitiers - ISAE-ENSMA, HYDÉE team, France
10:50 – 11:15	**Refreshment Break**
SESSION 10 – Experimental Fluid dynamics Chair: Guillaume Delefortrie	
11:15 – 11:40	NUMERICAL PMM TEST IN FINITE DEPTH AND APPLICATION TO MMG MODEL OF SHIP MANOEUVERING **Junhoi Choi**, Shuguang Wang, Yonghwan Kim, Department of Naval Architecture and Ocean Engineering, Seoul National University, Korea
11:40 – 12:05	VISCOUS CFD SIMULATION OF PMM TESTS IN SHALLOW WATER AND IN A CANAL **Takuya Ohmori**, Kunihide Ohashi, National Maritime Research Institute, Japan; Yoshitaka Furukawa, Hiroshi Ibaragi, Kyushu University, Japan; Yuya Matsunaga, JAPAN MARINE UNITED CORPORATION, Japan
12:05 – 12:30	HYDRODYNAMIC FORCES ACTING ON SHIP RUNNING IN CURVED WATERWAY WITH CONSTANT RADII **Yoshitaka Furukawa**, Hiroshi Ibaragi, Kyushu University, Japan; Takuya Ohmori, Kunihide Ohashi, National Maritime Research Institute, Japan; Yuya Matsunaga, JAPAN MARINE UNITED CORPORATION, Japan
12:30 - 13:30	**Lunch**

SESSION 11 - Ship manoeuvring Chair: Zao-Jian Zou	
13:30 – 13:55	PATH FOLLOWING OF AN UNDERACTUATED SHIP IN RESTRICTED WATERS USING CLOS AND COMPENSATED LQR METHODS **Yu He**, Jin-Lan Li, School of Ocean and Civil Engineering, Shanghai Jiao Tong University, Shanghai, China; Lu Zou*, Zao-Jian Zou ; 1. School of Ocean and Civil Engineering, Shanghai Jiao Tong University, Shanghai, China; 2. State Key Laboratory of Ocean Engineering, Shanghai Jiao Tong University, Shanghai, China; Wei-Min Chen, Shanghai Ship and Shipping Research Institute Co., Ltd., Shanghai, China
13:55 – 14:20	BAYESIAN-SVR MODEL FOR PREDICTING SHIP MANEUVERING TRAJECTORIES IN DEEP AND SHALLOW WATER CONDITION **Donghyeong Ko**, HD Hyundai Heavy Industries Co., Ltd; Department of Naval Architecture and Ocean Engineering, Seoul National University, Republic of Korea; Seong Ho Moon, HD Hyundai Heavy Industries Co., Ltd, Republic of Korea; Bo Woo Nam, Department of Naval Architecture and Ocean Engineering, Seoul National University, Republic of Korea
14:20 – 14:45	UNBERTHING SIMULATIONS OF A SHIP USING A FIRST-ORDER LAG MODEL TO TAKE THE HYDRODYNAMIC MEMORY EFFECT INTO ACCOUNT **Ryusuke Okuda**, National Maritime Research Institute, Japan; Hironori Yasukawa, Hiroshima University, Japan
14:45 – 15:00	**Refreshment Break**
SESSION 12 – Wave induced motions Chair: Hironori Yasukawa	
15:00 – 15:25	COMPUTATION OF VESSEL MOTIONS IN WAVES USING FORWARD-SPEED FREE-SURFACE GREEN FUNCTION **Wim van der Molen**, Baird, Australia
15:25 – 15:50	COMPARISON OF WAMIT WITH MEASURED WAVE-INDUCED MOTIONS OF CONTAINER SHIPS AND BULK CARRIERS, USING AN ADJUSTMENT FOR SHIP SPEED **Tim Gourlay**, Perth Hydro, Australia
15:50 – 16:15	PREDICTIVE SIMULATION OF ONSHORE POWER SUPPLY REQUIREMENTS FOR PORTS **Lourdes Pecharromán**, Raul Redondo, Raul Atienza, Siport21. Spain; Arturo Medio, Luis Ulla, Technical University of Madrid, Spain
16:15 – 16:25	**Closing Words**

22 MAY 2025 (THURSDAY)

09:00 – 13:00	**Optional excursion: Flanders Maritime Laboratory**

SHALLOW WATER SPEED/POWER TRIALS WITH CRUISE LINER FOR BENCHMARKING

Gijs Struijk, MARIN, The Netherlands

Guillaume Delefortrie, Ships and Marine Technology, Ghent University, Belgium

Dmitriy Ponkratov, Siemens, UK

Jeroen Verwilligen, Flanders Hydraulics, Belgium

Evert Lataire, Ships and Marine Technology, Ghent University

SHALLOW WATER SPEED/POWER TRIALS WITH CRUISE LINER FOR BENCHMARKING

GIJS STRUIJK, MARIN, THE NETHERLANDS
GUILLAUME DELEFORTRIE, SHIPS AND MARINE TECHNOLOGY, GHENT UNIVERSITY, BELGIUM
DMITRIY PONKRATOV, SIEMENS, UK
JEROEN VERWILLIGEN, FLANDERS HYDRAULICS, BELGIUM
EVERT LATAIRE, SHIPS AND MARINE TECHNOLOGY, GHENT UNIVERSITY

SUMMARY

Within the frame of the Joint Industry Project JoRes, multiple full scale measurements were carried out to quantify the resistance and propulsion behaviour of seven selected vessels. One of these vessels was a 252 m long cruise ship, known as the JoRes3 Cruise Liner, for which speed/power trials and zigzag tests were performed in two water depths, but also in (not purposely) different weather conditions. In the frame of the MASHCON conference, the results of the speed/power trials are opened, together with a comprehensive post-processing assessment.

NOMENCLATURE

Variable	Unit	Name
A_{E}/A_0	-	Propeller blade area ratio
A_{WL}	m²	Waterplane area
A_X	m²	Transverse wind area
B_{WL}	m	Beam at waterline
C_{B}	-	Block coefficient
C_X	-	Longitudinal wind coefficient
D_{P}	m	Propeller diameter
h/T	-	Water depth to draught ratio
k	-	Coverage factor
k_s	µm	Equivalent sand grain roughness
L_{PP}	m	Length between perpendiculars
L_{WL}	m	Length at waterline
N_{AVG}	1/min	Shaft speed
P/D	-	Propeller pitch diameter ratio
$P_{\mathrm{S(C)}}$	kW	(Corrected) shaft power
Q_{ms}	kNm	Measured shaft torque
Q_{SC}	kNm	Corrected shaft torque
R_{AA}	N	Added resistance due to wind
S	m²	Wetted surface area
T_{A}	m	Draught aft
T_{F}	m	Draught forward
T_{M}	m	Draught amidships
U	-	Expanded uncertainty
$u_c(y)$	-	Uncertainty of quantity y
V_{S}	kn	(Average) ship speed
V_{SC}	kn	Corrected ship speed
V_W	m/s	Relative wind velocity
Z	-	Number of propeller blades
Z_P	m³	Polar section modulus of shaft
β	deg	Drift angle
Δ, ∇	m³	Displacement volume

Variable	Unit	Name
ϵ_{ms}	rad	Measured strain at shaft
ν	m²/s	Kinematic viscosity
$\rho_{(A)}$	kg/m³	Density of water (air)
ψ_W	deg	Relative wind direction

1 INTRODUCTION

1.1 PROBLEM STATEMENT

The MASHCON conference series have set a tradition to share benchmark data prior to the conferences, so that papers discussing and using these benchmark data could be presented at the conference. At the successive conferences benchmark data on ship-bank interaction (2009), ship-ship interaction (2011), ship-lock interaction (2013), ship-bottom interaction (2016), ship-wave interaction (2019) and port manoeuvres (2022) were made available. This tradition was only partially followed at the 7th MASHCON. Given the topic of the conference, clean power in shallow water, an effort was made to prepare full scale data. However, more time was needed than anticipated, and the benchmark data could not be shared beforehand, but only at the conference itself.

Full scale measurements come indeed with their own set of risks, such as the difficulty to control the weather or to convince a captain to navigate his or her ship into sufficiently shallow water. These examples are more than illustrative as will be explained in this paper. On top of that, conducting trials with a cruise liner also implies having thousands of passengers on board who should rather be unaffected of the science that is happening on their voyage.

For the post-processing of the data the appropriate ISO standard has been followed, namely the 'Preparation, Conduct and Analysis of Speed/Power Trials' (2024), co-authored by one of the co-authors of this paper; ISO15016:2015. The trials were performed in 2023 on the North Sea, close to Scotland for the deep water and in Dutch EEZ for the shallow water case. The shallow and deep water trials were conducted in 24 m and 80 m water depth respectively. Given the draft of the vessel, which did not exceed 7 m, this corresponds to a h/T of around 3.5 and 11.5 respectively. In both areas the following trials were performed, all with both propellers running at 79 rpm:

- two double runs for speed/power trials
- one double run for 10/10 zigzag tests
- one double run for 20/20 zigzag tests

where a double run denotes two runs in opposite direction. Normally, this follows the dominant wave directions (head and following waves), however for the shallow water runs, this was not achieved as priority was given to obtain a run along a constant water depth.

Moreover as the vessels called a port on a river continuous monitoring was performed during the transit on the river as well. The topic of the benchmark data in this paper are the speed/power trials, which will be explained with detail, including a post-processing and uncertainty assessment. It is the authors' intention to publish about the zig zag tests as well as the continuous monitoring in the future.

1.2 DATA FORMAT

The benchmark data discussed in this paper is made available in h5-file format and in csv-file format. The former can be transformed to csv format by following coding example in Python:

```
import pandas as pd

runs = range(1, 4)

for i in runs:
    filename = "dfrun_" + str(i)
    df = pd.read_hdf('hdf5/' + filename + '.h5')
    df.to_csv('csv/' + filename + '.csv')
```

The data is ordered according to the headers mentioned in Table 1.

The data is ordered according to the headers mentioned in Table 1.

Table 1. Explanation of the headers of the benchmark data.

Channel name	unit	Description	source
index	time	datetime64[ns] in UTC	MARIN DAQ
Lat	deg	latitude, WGS84	MARIN DGPS at bridge
Lon	deg	longitude, WGS84	MARIN DGPS at bridge
HDG	deg	heading	MARIN DGPS at bridge
SOG	kn	speed over ground	MARIN DGPS at bridge
COG	deg	course over ground	MARIN DGPS at bridge
Lat_aft	deg	latitude, WGS84	MARIN DGPS at stern
Lon_aft	deg	longitude, WGS84	MARIN DGPS at stern
HDG_aft	deg	heading	MARIN DGPS at stern
SOG_aft	kn	speed over ground	MARIN DGPS at stern
COG_aft	deg	course over ground	MARIN DGPS at stern
MTi_AccX	m/s^2	MRU on bridge	MARIN MRU: MTi
MTi_AccY	m/s^2		MARIN MRU: MTi
MTi_AccZ	m/s^2		MARIN MRU: MTi
MTi_Roll_spd	deg/s		MARIN MRU: MTi
MTi_Pitch_spd	deg/s		MARIN MRU: MTi
MTi_Yaw_spd	deg/s		MARIN MRU: MTi
MTi_Pitch	Deg		MARIN MRU: MTi
MTi_Roll	Deg		MARIN MRU: MTi
MTi_Yaw	Deg		MARIN MRU: MTi
SMC_AccX	m/s^2	MRU at the aft mooring deck (for sync check)	MARIN MRU: SMC
SMC_AccY	m/s^2		MARIN MRU: SMC
SMC_AccZ	m/s^2		MARIN MRU: SMC
SMC_Pitch	deg		MARIN MRU: SMC
SMC_Pitch_spd	deg/s		MARIN MRU: SMC
SMC_Roll	deg		MARIN MRU: SMC
SMC_Roll_spd	deg/s		MARIN MRU: SMC
SMC_Yaw	deg		MARIN MRU: SMC
SMC_Yaw_spd	deg/s		MARIN MRU: SMC
RPM_PS	1/min	shaft speed PS	MARIN PMS
RPM_SB	1/min	shaft speed SB	MARIN PMS
TRQ_PS	kNm	shaft torque PS	MARIN PMS
TRQ_SB	kNm	shaft torque SB	MARIN PMS
PWR_PS	kW	shaft power PS	MARIN PMS
PWR_SB	kW	shaft power SB	MARIN PMS
Rudd_PS	deg	rudder angle PS	MARIN wire sensor
Rudd_SB	deg	rudder angle SB	MARIN wire sensor
COG_ship	deg	course over ground	Ship system
UKC	m	under keel clearance	Ship system
TF	m	draught fwd	Ship system
TA	m	draught aft	Ship system
Lat_ship	deg	latitude, WGS84	Ship system
Lon_ship	deg	longitude, WGS84	Ship system
STW	kn	speed through water	Ship system

Channel name	unit	Description	source
SOG_ship	kn	speed over ground	Ship system
AWS	kn	apparent wind speed	calculated
AWA	deg	apparent wind angle (relative to ship)	calculated
TWS	kn	true wind speed	Ship system
TWD	deg	true wind direction (earth-fixed compass direction)	Ship system
TWA	deg	true wind angle (relative to ship)	calculated
TWS_10m	kn	true wind speed, corrected to 10 m ref. height	calculated

1.3 UNCERTAINTY ASSESSMENT PROCEDURE

The objective of the performed speed/power trials is to determine the speed/power relation of the vessel in ideal trial conditions for both deep and shallow water. To minimize uncertainty, high fidelity speed/power trials were performed using state-of-the-art correction methods.

The uncertainty in the results can be considered as originating from two distinct sources:

- the measurement chain
- the analysis steps

The components within these sources have an effect on either speed or power. The contributing components will be discussed: the nature of their contribution, the magnitude of the standard uncertainty $u_c(y)$ for each component y, as well as their propagation into the end result. The expanded uncertainty U is calculated as $U = ku_c(y)$, with k the coverage factor, taken as 2 assuming normal distribution, to arrive at a 95% confidence interval. Assuming uncorrelated contributions, the components are combined through Root of Sum of Squares (RSS) to build up the total uncertainty.

2 THE SHIP JORES3 LINER

2.1 SHIP DIMENSIONS

2.1 (a) Main dimensions

The trials were performed with a 252 m cruise vessel, the main dimensions of which are listed in Table 2 the full and detailed 3D geometry is available via the JoRes website (www.jores.net). The loading conditions at the two trials were different. Draughts observations have been performed two times in confidential Port A (after arrival and before departure) and also in confidential Port B after arrival. At the same time the water density was measured and the draughts have been recorded by a GoPro camera. The video files were subsequently analysed independently by two experts, which allowed to find the ship's draughts at the time of measurement. At the time of trials the moulded draughts at the perpendiculars have been calculated for the trial conditions, including changes in fuel consumption and weight of a number of tenders not present at one of the draught readings. The entire calculation procedure is elaborated in a separate report, available at the JoRes website (Ponkratov et al., 2024a). For this case, the uncertainty on the draught readings was determined to be 20 mm, taking into account differences between observers. Using the waterplane area it is determined that the propagation of uncertainty is 0.4% on the displacement volume.

Table 2. Main dimensions of the JoRes3 Liner

	Deep water trials	Shallow water trials	All trials	
L_{PP} (m)	225.840	225.840	D_{P} (m²) (2x)	5.200
L_{WL} (m)	236.677	238.051	Z (-)	5
B_{WL} (m)	32.200	32.200	A_{E}/A_0 (-)	0.709
T_{F} (m)	6.953	6.608	P/D (-)	1.277
T_{M} (m)	6.964	6.722		
T_{A} (m)	6.974	6.835		
∇ (m³)	34227	32792		
ρ (kg/m³)	1.025	1.023		

	Deep water trials	Shallow water trials	All trials	
S (m²)	8807	8639		
A_{WL} (m²)	6245	6184		
C_{B} (-)	0.676	0.671		
A_X (m²)	1185.6	1193.4		

2.1 (b) Geometry information

Although the name of the vessel is confidential, the full geometry information (592 MB) is made available to perform CFD computations. The geometry includes hull, propellers, rudders, shafts with brackets, simplified geometries of bow and stern thrusters and bilge keels. The active fin stabilisers were not engaged during the trials, so they were not modelled in the geometry. This information contains the following:

- 3D CAD geometry. Including all the geometry parts exported from 3D CAD (Rhinoceros) in the following formats
    - IGS SolidWorks solid, with iges tolerance: 0.001 mm
    - STP AP203ConfgControlDesign scheme
    - X_T
- CFD geometry, which contains all the geometry parts exported from STAR-CCM+ in stl format
- ANSYS, which contains the geometries saved in the mesher file format (fcdoc)
    - SpaceClaim file version 2022
    - SpaceClaim file version
- STAR-CCM+, which contains the geometries saved in the mesher file format (sim)
    - Sim geometry file version 15.06.007
    - Sim geometry file version 17.02.008

2.1 (c) Roughness condition

Before the trials the hull roughness was measured with following values:

- The measured value of Average Hull Roughness (based on Rt50 measurements) for the vessel is 109 µm.
- The measured value of Average Rudders Roughness (based on Rt50 measurements) is 528 µm.
- The suggested equivalent sand grain roughness k_{s} for the hull is 15 µm based on 120 locations (230 µm for the rudder based on 12 locations).

More information is available in Ponkratov et al. (2023), available at the JoRes website.

Roughness measurements were also performed for the propeller: the average roughness (Ra) is 5.68 µm, while the suggested sand grain roughness (k_{s}) is 3.86 µm. More information is available in Ponkratov et al. (2024b), available at the JoRes website.

3 TEST INSTRUMENTATION

3.1 POSITION AND SPEED

A GNSS system (CSI Wireless Vector Pro) was installed on the top of the portside bridge wing to measure the ship's position (Latitude and Longitude), as well as heading and course over ground. The speed over ground was derived from the ship's position.

3.2 SHAFT TORQUE AND PROPELLER RATE

The benchmark data are delivered with MARIN's Power Measurement System (PMS) which measures torsional strain and speed of the shafts to arrive at shaft power. The system uses strain gauges glued to the shafts and an optical pickup to register shaft speed using a reflective tape (Figure 1).

The ship was also permanently equipped with VAF TT-sense systems on both shafts, delivering shaft torque, thrust and speed.

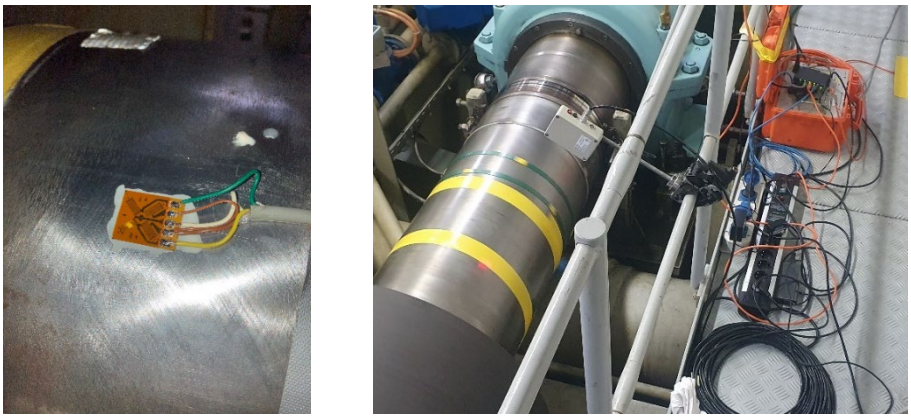

Figure 1. Shaft measurements - strain gauge (left) and setup with conditioner/transmitter, receiver and optical pickup (right)

3.3 SEA STATE AND WIND

Prior to the trial, a Sofar Ocean Spotter wave buoy was deployed in the shallow water trial area. From this buoy, directional wave spectra were obtained for all shallow water runs. A dedicated down looking wave radar was also installed on the bow. For the deep water trials no dedicated wave buoy was available, so hindcast data was used. The hindcast model was validated for the shallow water conditions where wave buoy data was available.

The ship's own anemometer was used to register the apparent (relative) wind speed and direction.

Figure 2. Wave buoy deployed from vessel (left), down looking wave radar mounted on the bow (right)

3.4 MANUAL MEASUREMENTS

Water samples were taken before and after the trials, from which the water temperature and density were measured. The air temperature, pressure and humidity was noted every run (Table 4). Furthermore, the sea water temperature and density was sampled in both trial areas.

4 TRIAL CONDUCT

4.1 PERFORMED RUNS

Per water depth double-double runs (four single runs) were performed at the same propeller speed.

Table 3. Overview of performed speed runs

	Run no.	Run set	propulsion setting	Run start time (LT)	Run dir.	Heading	SOG (made good)	Water depth (h)	h/T_M
	[-]	[-]	[rpm]	[HH:MM]	[F/R]	[deg]	[kn]	[m]	[-]
Shallow	1	1	79	11:09	F	274.0	10.97	23.9	3.6
	2	1	79	11:49	R	84.9	13.52	24.2	3.6
	3	1	79	12:21	F	272.4	10.97	24.4	3.6
	4	1	79	13:04	R	81.5	13.36	24.2	3.6
				(+2 days)					
Deep	11	2	79	14:20	F	7.9	13.50	80.1	11.5
	12	2	79	15:19	R	182.5	12.44	80.2	11.5
	13	2	79	16:10	F	7.2	13.51	80.4	11.6
	14	2	79	16:54	R	182.0	12.43	79.9	11.5

4.2 ENVIRONMENTAL CONDITIONS

The environmental conditions for the shallow water runs were unfavourable, with a true wind speed of 21 knots from the NW and a significant wave height of 2.7 m at a peak period of 8.5 s. Nevertheless, these conditions are still within the ISO limits (respectively 26.8 kn and 3.4 m for wind speed and significant wave height). During the deep water runs, the conditions were a bit more benign, with a true wind speed of 13 knots from the SE and a significant wave height of 1.2 m at a peak period of 8.3 s.

During the shallow water runs, the wave buoy was deployed and its measured values are used in further analysis (SPAWAVE wave correction). During the deep water runs, use was made of the down looking wave radar data at the bow as no wave buoy was available. Consistency was checked against hindcast models and the buoy data during the shallow runs. The EWAM model, made for European waters, showed best match to the wave buoy and wave radar measurements. As the wave radar does not measure wave direction, the wave direction for the deep water runs was taken from this hindcast model.

The average air and water properties during the shallow and deep water runs are given in Table 4, the wave data per trial run in Table 5.

Table 4. Air and water properties

	Air		Water	
	Temperature [deg C]	Pressure [mbar]	Temperature [deg C]	Density [kg/m3]
Shallow	13.0	1017.5	7.5	1023.0
Deep	12.5	1024.0	7.9	1025.0

Table 5. Wave statistics per run, used for SPAWAVE wave correction

	Sign. wave height	Mean period	Peak period	Mean direction	rel. wave direction (0 = head waves)
	m	s	s	deg	deg
Shallow	2.66	6.7	7.9	333.7	59.6
	2.59	6.7	8.5	343.4	258.5
	2.74	6.9	9.3	342.3	69.9
	2.78	7.2	10.2	343.3	261.8
Deep	1.19	6.6	8.1	347.0	339.1
	1.16	6.7	8.4	347.0	164.5
	1.21	6.8	7.8	348.0	340.8
	1.27	6.2	8.4	350.0	168.0

5 SPEED/POWER ANALYSIS

5.1 SPEED OVER GROUND

The speed/power trial results are analysed in accordance with the ISO15016:2015 standard. The analysis process was performed using STAIMO v2.6.0 (STAIMO, 2024). A description of the steps and applied corrections is given in this and following sections.

The ship's speed made good over ground during a run is determined by taking the distance from start (COMEX) to finish (FINEX) of a run, divided by elapsed time and correcting for sideways drift due to current. The headway distance L_2 is then taken to compute the speed over ground, by correcting the distance L_1 with the difference between heading and course over ground (COG), see Figure 3.

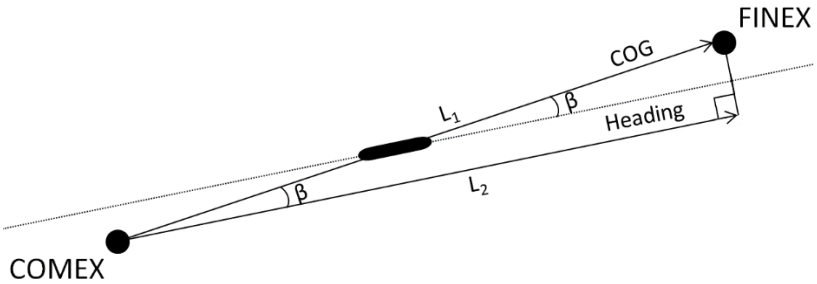

Figure 3. Determination of ship's speed made good over ground

5.2 CORRECTIONS ON POWER

5.2 (a) Overview

The corrections made to the measured shaft power to arrive at ideal conditions are for the effects of wind and waves. Other correction methods that are available in the method, but not used in the current case are:

- Correction for sea water properties (temperature and density). For this case, the results are presented as valid for the respective trial's sea water properties (see Table 4), so no correction on those properties is required.
- Displacement correction. For this case, the results are presented for the respective trial draughts and displacement (see Table 2).
- It is noted that the shallow water correction is <u>not</u> used, as to deliver corrected trial averages uncorrected for water depth influences, such that the results can be used for validating any correction model going forward. Section 5.7 offers a comparison with the Raven method for shallow water corrections.

5.2 (b) Wind correction

As ideal condition, zero true wind speed is defined. To correct for the added resistance due to the observed wind speed the ISO15016:2015 method is used. This method uses predefined drag coefficients for specific ship types applied to the vessel's transverse projected wind area in trial condition. For this case, a coefficient set for a generic cruise liner is used, see Table 6.

Table 6. Wind induced drag for a generic cruise liner

Incidence angle*	deg	0	10	20	30	40	50	60	70	80	90
C_X	-	- 0.684	- 0.719	- 0.753	- 0.676	- 0.544	- 0.403	- 0.367	- 0.211	- 0.177	- 0.113

Incidence angle*	deg	100	110	120	130	140	150	160	170	180
C_X	-	-0.260	-0.179	-0.101	0.033	0.320	0.552	0.708	0.675	0.568

**0 deg = on the bow*

The added resistance due to wind is determined by $R_{\mathrm{AA}} = \frac{1}{2}\rho_{\mathrm{A}} C_X(\Psi_{\mathrm{W}}) A_X V_{\mathrm{W}}^2 - \frac{1}{2}\rho_{\mathrm{A}} C_X(0) A_X V_{\mathrm{S}}^2$. Within the wind correction, the following uncertainty components are identified:

- The used wind resistance coefficient C_X from the ISO standard is one for a generic ferry/cruise vessel, not the specific vessel. Review of literature and MARIN's internal database shows a spread in C_X values of around 0.1 for

different cruise liners. This is about 14% of the used C_X values, which is taken as the expanded uncertainty propagating linearly into the wind correction.

- The measurement uncertainty within wind speed V_W is stated by the manufacturer of the used anemometer (Gill WindSonic) as 2%. This is taken as the expanded uncertainty propagating quadratically into the wind correction.
- The frontal wind area A_X is determined from drawings at an estimated accuracy of 4%, taken as the expanded uncertainty propagating linearly into the wind correction.
- Placement of the anemometer - in practical use of an anemometer in a ship's mast, it is unavoidable to be in a region of disturbed flow. Taking from the research by Moat (2003), and looking at the consistency of true wind calculations for all runs (averaged per double run versus non-average) as well as reviewing hindcast wind data, the estimated uncertainty on wind speed is 5%, propagating quadratically into the wind correction.
- Similarly, the work by Moat states the wind angle can be disturbed by about 10 degrees, leading to a different C_X value being used for that different angle of about 10% and 8%, for shallow and deep water runs respectively, propagating linearly into the wind correction.

With the above, the total uncertainty on the wind correction is 21.4% and 20.1% for shallow and deep water runs respectively. The propagation is proportional to the magnitude of the wind correction, which in the presented case is around up to -14% of measured power in head waves and around 3% in tailwind. This leads to propagated expanded uncertainty level of 1.8% and 1.6% of measured power for the trial average for shallow and deep water runs respectively.

5.2 (c) Wave correction

As ideal condition is defined at zero wave height, the influence of the waves present during the trials must be corrected. Normally, either STAWAVE 1 or 2 is used for sea trials. The present trials, and especially the shallow water runs, however needed to be performed in beam waves, a direction for which those methods are unsuitable. To not neglect the (significant) influence of the sea state, the SPAWAVE method (Grin, 2022) was applied, allowing corrections for all wave directions.

Within the wave correction, the following contributions can be identified:

- Measured wave height - the uncertainty of measured wave height by wave buoy was determined by Van Essen (2018) to be 2%. This propagates quadratically into the wave correction to an expanded uncertainty level of 4%.
- For this trial, discrepancies between the wave buoy and wave radar values and the hindcast model were observed, with differences of about 10 cm in wave height between them, or about 4 - 8% of measured value, propagating quadratically into the wave correction to an expanded uncertainty level of 8% and 17% for shallow and deep water runs respectively.
- The wave added resistance method - the estimated uncertainty of the used method (SPAWAVE) is 31%.

The total uncertainty of the wave correction is 32% and 35% for shallow and deep water runs respectively. Analogous to the wind correction, the propagation is proportional to the magnitude of the correction made, which in the presented case is 13 - 20% and 3 - 4% of measured power for the shallow and deep water runs respectively. This leads to a propagated uncertainty level of 5.5% and 1.2% of measured power respectively.

5.3 CORRECTION ON SPEED

5.3 (a) Measurement: GNSS uncertainty

The GNSS system used (CSI Wireless Vector PRO) has a documented standard uncertainty u(GNSS) = 0.5 m for horizontal position in DGPS mode. However, this could be on the optimistic side with perfect constellation coverage. Conservatively the estimate is doubled to u(GNSS) = 1.0 m. As prescribed in the ISO15016:2015 standard, the speed over ground is determined from the distance between start and end positions of the run, divided by the time. If both the start and end positions have a standard uncertainty of 1 m, the standard uncertainty on the distance d is $u_c(d) = \sqrt{(1^2 + 1^2)}$ = 1.4 m. Dividing that to the distance yields the relative uncertainty for speed over ground. The resulting expanded uncertainty $U(V_S)$ is around 0.08% for the average ship speed.

5.3 (b) Speed through water determination: current correction

The speed through water is calculated for a run set by a current correction. ISO15016:2015 offers the choice of using either of two methods: the mean of means (MoM) method and the iterative method. For this trial, with only one run set, only the

MoM method is available. There is no general statement on the accuracy of these methods, making the evaluation difficult. As a measure of uncertainty, the difference between using the MoM method and a hindcast current from the ERA-5 model (which will have its own uncertainty) is taken as a (be it crude) measure of the overall uncertainty on speed through water (see Figure 4). The difference between using the methods is 0.15 kn for the shallow water runs and 0.04 kn for the deep water runs, which is taken as the expanded uncertainty of speed through water obtained from the run sets (3.7% and 1.4% of the average ship speed, respectively).

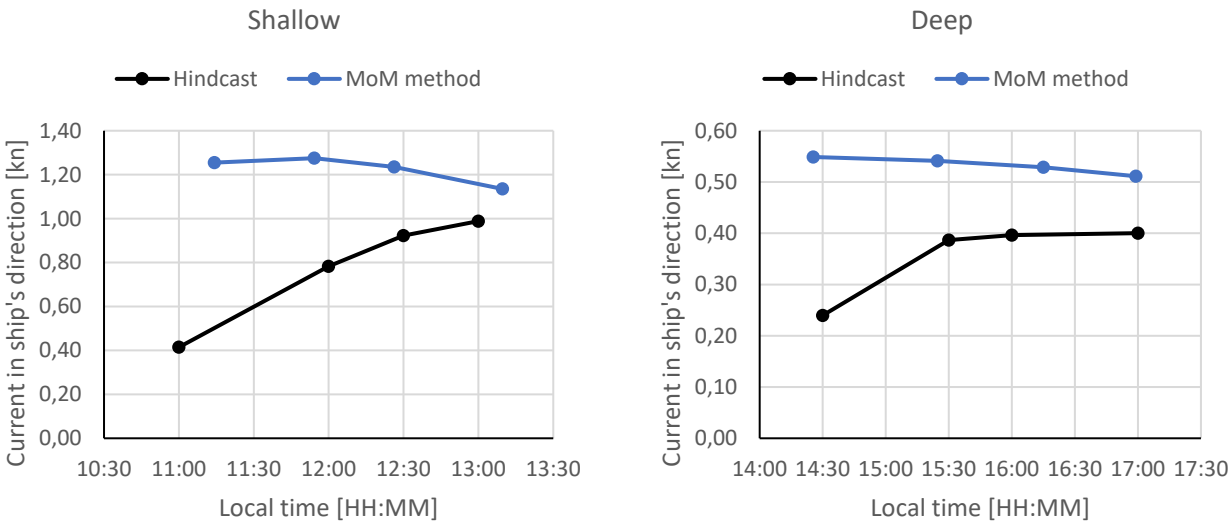

Figure 4. Current estimates from a hindcast model and the trial results (using mean of means method), shallow runs (left) and deep runs (right).

5.4 CORRECTED TRIAL RESULTS

After the above corrections on speed and power are made, the corrected averages are obtained per run set and presented in Table 7. These corrected trial averages are then used for curve fitting, see Figure 5. The tabulated results are given in Table 11.

Table 7. Trial averages (corrected for wind, wave and current, <u>not</u> for shallow water or displacement), totals both PS and SB shafts

	V_{SC} [kn]	N_{AVG} [1/min]	Q_{SC} [kNm]	P_{SC} [kW]
Shallow	12.24	77.6	575.0	4671
Deep	12.97	77.9	633.5	5166

5.5 UNCERTAINTIES PROPAGATING TO POWER

The contribution of the uncertainties within the measurement chain of shaft power and the different correction methods used is detailed below.

5.5 (a) Shaft power: measurement uncertainty

The shaft power is determined from measured shaft torque Q_{ms} and shaft speed n_{ms} by:

$$P_{ms} = Q_{ms} n_{ms} \frac{2\pi}{60} \qquad (1)$$

5.5 (a) 1 Shaft speed uncertainty

The shaft speed is measured by an optical pickup aimed at a reflective tape on the shaft, passing once per revolution. If the pickup fails to register up to one cycle per run, the associated uncertainty in shaft speed amounts to U_n = 0.1%.

5.5 (a) 2 Shaft torque uncertainty

The determination of shaft torque Q_{ms} is done by measurement of shaft strain by a strain gauge glued to the shaft. From the strain ϵ_{ms}, shaft torque is calculated by $Q_{\mathrm{ms}} = \epsilon_{\mathrm{ms}} \frac{2}{k} G Z_P$. Table 8 lists the associated uncertainty components.

- As sensor uncertainty, for measuring the shaft's torsional strain ϵ_{ms} three sources of uncertainty are considered: the strain gauge's uncertainty, the installation and the zero calibration.
  - The uncertainty of the strain gauge is listed by the manufacturer as expanded uncertainty $U = 1.0\%$.
  - The installation uncertainty was taken as the average difference between the MARIN and torque readings by an alternative method, resulting in an uncertainty of 1.0%.
  - The zero calibration was done both before and after the trials, with a difference of 0.3%.
- The shaft diameter was determined by measuring circumference of shaft, which is estimated to be within 1 mm accurate. The diameter is therefore within 0.3 mm accurate. It propagates into the shaft torque via the polar section modulus to 0.2%.
- The actual G-modulus for a specific shaft is not often tested, so the standard value of 82,400 N/mm^2 is taken. This value was chosen as a mean value during the STA-JIP. From that work, the spread was judged to be 2.5%, which is taken as expanded uncertainty propagating linearly into the shaft torque.

The above components for torque and the uncertainty in shaft speed combined result in an uncertainty on the measured shaft power of 2.9% for both trials.

Table 8. Uncertainty components in Q_{ms}

Component	U	Propagation to Q_{ms}	Propagated
Sensor: strain gauge	1.0%	Linear	1.0%
Installation error	1.0%	Linear	1.0%
Zero calibration	0.3%	Linear	0.3%
Shaft diameter	0.1%	Via polar section modulus: $Z_P = \frac{\pi}{16} D^3 \sim D^3$	0.2%
G-Modulus	2.5%	Linear	2.5%
Total			**2.9%**

5.5 (b) Effect of displacement uncertainty on power

The displacement uncertainty (see 2.1 (a)) propagates via the ISO standard ($P_{\mathrm{ref}} = P_{\mathrm{act}} \left(\frac{\nabla_{\mathrm{ref}}}{\nabla_{\mathrm{act}}}\right)^{2/3}$) to a 0.3% uncertainty on power.

5.6 TOTAL UNCERTAINTY ON SPEED AND POWER

Table 9 gives a summary of all the uncertainty components discussed so far, and their propagation to speed and power.

- For the shallow water runs, the uncertainty on corrected power (P_{SC}) is 8.6%, while the uncertainty on corrected ship speed (V_{SC}) is 3.7%
- For the deep water runs, the uncertainty on corrected power (P_{SC}) is 3.9%, while the uncertainty on corrected ship speed (V_{SC}) is 1.4%

Table 9. Summary of the total propagated uncertainties, uncertainties in power depicted relative to both measured shaft power (P_{SM}) and corrected shaft power (P_{SC})

	Shallow	Deep	
GNSS	0.1%	0.1%	
STW (current correction)	3.7%	1.4%	
Total propagated to speed	**3.7%**	**1.4%**	**[%V_{SC}]**
Shaft power measurement	2.9%	2.9%	

	Shallow	Deep	
Displacement	0.5%	0.4%	
Wind correction	1.8%	1.6%	
Wave correction	5.5%	1.2%	
Total propagated to power	**6.4%**	**3.5%**	**[%P_{SM}]**
	8.6%	**3.9%**	**[%P_{SC}]**

5.7 RAVEN SHALLOW WATER CORRECTION METHOD – VALIDATION

The trial results from Table 7 are used to validate the Raven Shallow Water Correction Method (Raven, 2016). To be able to compare the two trials, a correction is applied for the displacement difference (deep water trial was performed at 4.4% higher displacement volume). Using the admiralty coefficient (ISO15016:2015) to correct the deep water results to the displacement of the shallow water trials, the results are as given in Table 10.

Table 10. Trial averages (corrected for wind, wave, current and displacement, not for shallow water), totals both PS and SB shafts

	V_{SC} [kn]	N_{AVG} [1/min]	Q_{SC} [kNm]	P_{SC} [kW]
Shallow	12.24	77.6	575.0	4671
Deep	12.97	77.9	615.6	5021

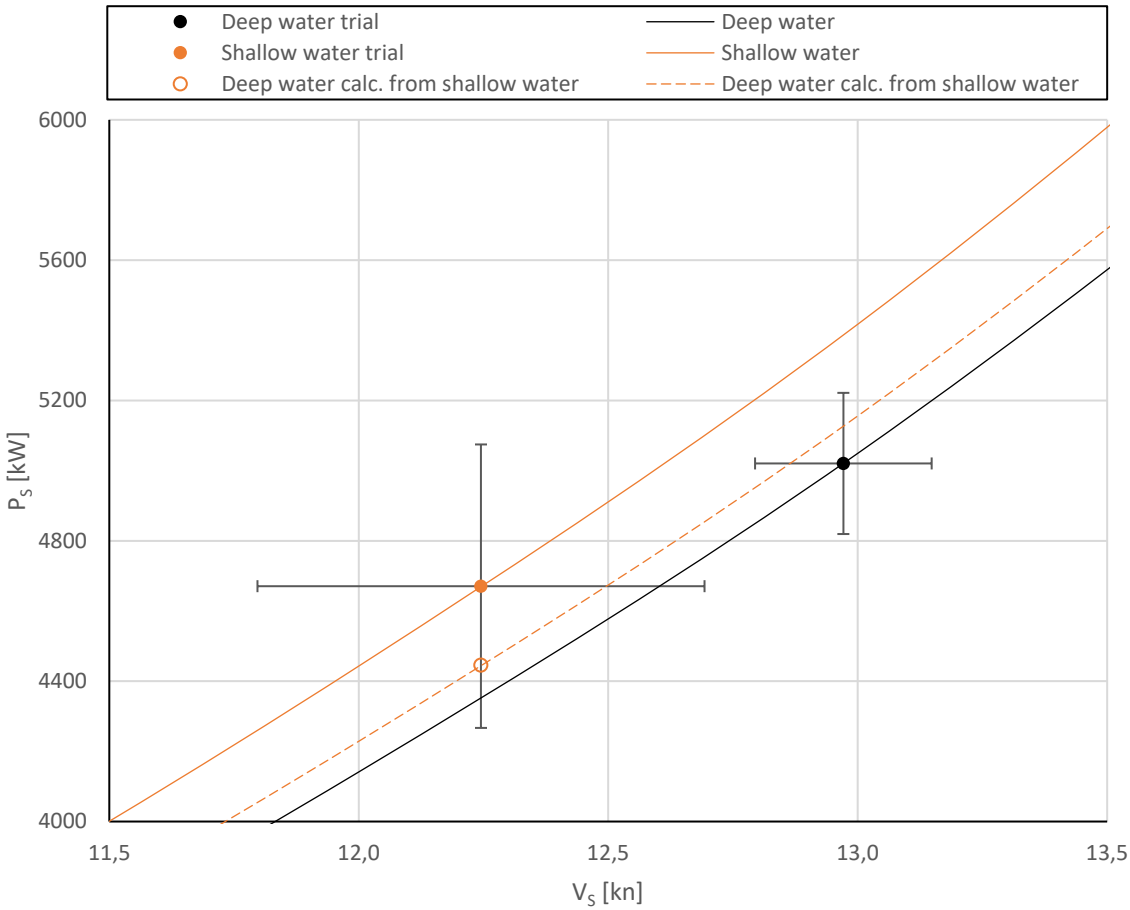

Figure 5. Trial averages, corrected to equal displacement, with fitted curves, including correction of shallow water result to deep water by Raven method (dashed orange curve)

Using Raven's method a deep water estimate is derived from the shallow water result. The speed/power curve from (confidential) model test is fitted to all results to enable comparison at the shallow water trial speed. Also the uncertainty intervals from Table 9 have been added. Raven's method predicts a deep water power 2.1% above the deep water trial results (evaluated at equal displacement), see Figure 5. A fair result, considering all uncertainties and differing conditions between the two trials.

Table 11. Curves fitted to trial averages (data from Figure 5)

	Shallow water	Deep water	Deep (calc from shallow)
Vs	Ps	Ps	Ps
kn	kW	kW	kW
11.0	3588	3344	3415
12.0	4443	4141	4229
13.0	5417	5049	5156
14.0	6582	6135	6264

6 CONCLUSIONS

This article introduced new benchmark data for the 7th MASHCON conference on clean power in shallow water. These data were created as part of the JoRes project. Speed/power trials were conducted on board the JoRes3 Cruise Liner in both deep water (h = 80.2 m) and shallow water (h = 24.2 m), following the ISO15016:2015 standard. Measurements were taken of the ship's speed over ground, shaft power, shaft speed and apparent wind. The wave conditions were recorded by a wave buoy during the shallow water runs, and a wave radar during the deep water runs.

The following conclusions summarise the findings from the speed/power measurements and analysis:

- The trials were conducted in 2023 on the North Sea. The environmental conditions were unfavourable for the shallow water runs (true wind speed of 21 kn from NW, significant wave height 2.7 m), and moderate for the deep water runs (true wind speed of 13 kn from SE, significant wave height 1.3 m).
- The speed/power data is analysed following ISO15016:2015, using STAIMO software. Corrections were made for the effects of wind, waves and current. The following corrected averages were obtained from the trial (totals both PS and SB shafts, corrections applied for wind, waves, current), and are valid for the stated trial draughts and displacements:

	T_F m	T_A m	Disp. Vol. m3	V_{SC} [kn]	N_{AVG} [1/min]	Q_{SC} [kNm]	P_{SC} [kW]
Shallow	6.608	6.835	32792	12.24	77.6	575.0	4671
Deep	6.953	6.974	34227	12.97	77.9	633.5	5166

- While sensor uncertainties are low for shaft strain in torque direction (about 1%), and speed over ground (0.1%), dominant factors in the total propagated uncertainties in speed, power in ideal conditions are the corrections for wind and waves, shaft G-modulus and current corrections. The total propagated uncertainty levels on speed, power corrected to ideal weather (no wind, no waves, no current) are as follows:
    - For the shallow water runs, the uncertainty on corrected power (P_{SC}) is 8.6% and on corrected ship speed (V_{SC}) 3.7%
    - For the deep water runs, the uncertainty on corrected power (P_{SC}) is 3.9% and on corrected ship speed (V_{SC}) 1.4%
- After correcting the above values for displacement differences between the shallow and deep runs and curve fitting, the Raven shallow water correction method could be validated. Raven's method predicts a deep water power 2.1% above the deep water trial results (evaluated at equal displacement). A fair result, considering all uncertainties and differing conditions between the two trials.
- Data is available in digital format upon simple request to info@shallowwater.be

7 ACKNOWLEDGEMENTS

Even though the vessel is anonymous, and the shipowner cannot be disclosed, it is important to acknowledge the significant support and collaboration from the owner. It is not common to perform such comprehensive full scale measurements on a cruise liner during normal commercial operation with passengers on board.

8 REFERENCES

Eloot, K., Vantorre, M., Delefortrie, G., Lataire, E., 2016. Running Sinkage and Trim of the DTC Container Carrier inHarmonic Sway and Yaw Motion: Open Model Test Data for Validation Purposes, in: 4th MASHCON-International Conference on Ship Manoeuvring in Shallow and Confined Water with Special Focus on Ship Bottom Interaction. pp. 251–261. https://doi.org/10.18451/978-3-939230-38-0_29

Grin, R., 2022. SPAWAVE, An Empirical Method to Predict Wave Added Resistance in all Wave Directions, 14th SNAME, Vancouver, Canada, June 2022.

Lataire, E., Vantorre, M., Eloot, K., 2009. Systematic Model Tests on Ship-Bank Interaction Effects, in: Proceedings of the 1st MASHCON, 2009, Antwerp, Belgium. pp. 9–22.

Lataire, E., Vantorre, M., Delefortrie, G., 2009. Captive Model Testing for Ship-to-Ship Operations, in: Proceedings of the International Conference on Marine Simulation and Ship Manoeuvrability (MARSIM), 17-20 August 2009, Panama City, Panama. International Marine Simulator Forum (IMSF), pp. M-14–1/10.

Ponkratov, D., Candries, M., Belaja, A., 2023. JoRes 3 cruise liner hull roughness assessment, Jores project report, 2023-06-15, Ref. 2023-024.

Ponkratov, D., Delefortrie, G., Struijk, G.D., Belaja, A., Tugay, D., 2024a. JoRes3 Liner Vessel Draughts Observations, JoRes project report, 2024-06-18, Ref. 2024-48.

Ponkratov, D., Hamblett, P. 2024b. JoRes3 Cruise Liner Propeller roughness assessment before sea trials, JoRes project, 2024-02-24, Ref. 2024-001.
RAVEN, H.C., A correction method for shallow-water effects on ship speed/power trials, MARIN report 98800-1-RD, accessible at https://www.marin.nl/en/publications/a-correction-method-for-shallow-water-effects-on-ship-speed-trials

STAIMO, 2025. Software package developed by the STA-Group for the analysis for Speed/Power Trials according to the ITTC 7.5-04-01-01 “Recommended Procedures and Guidelines for Speed and Power Trials, https://staimo.com/, last accessed January 13, 2025.

Van Essen, S.; Ewans, J.; McConochie, J. (2018), Wave Buoy Performance in Short and Long Waves, Evaluated Using Tests on a Hexapod, 37th OMAE Conf., Madrid

Vantorre, M., Delefortrie, G., 2013. Behaviour of ships approaching and leaving locks: open model test data for validation purposes, in: Proceedings of the 3rd MASHCON, 2013, Ghent, Belgium. pp. 337–352.

Van Zwijnsvoorde, T., Ruiz, M.T., Lataire, E., 2019. Sailing in Shallow Water Waves With the DTC Container Carrier: Open Model Test Data for Validation Purposes, in: Proceedings of 5th MASHCON, 2019, Ostend, Belgium. pp. 1–20.

Van Zwijnsvoorde, T., Delefortrie, G., Lataire, E., 2022. Passing ship effects in shallow and confined water: open model test data for validation purposes, in: 6th MASHCON - International Conference on Ship Manoeuvring in Shallow and Confined Water with Special Focus on Port Manoeuvres, 22 - 26 May 2022, Glasgow, UK. Flanders Hydraulics Research, pp. 254–283.

9 AUTHORS BIOGRAPHY

Gijs Struijk is a naval architect and Senior Project Manager at the Maritime Research Institute Netherlands (MARIN), specialising in ship hydromechanics and full-scale experiments on ships and offshore structures. Working within MARIN's Performance at Sea department, he is involved in various full-scale ship performance projects, including the development of the 'FlowPike' device, which had enabled detailed full-scale propeller inflow measurements. His expertise encompasses areas like speed/power trials, seakeeping validation, noise and vibrations, propeller cavitation observations, wind propulsion, and in-service performance monitoring.

Guillaume Delefortrie: naval architect (MSc, Ghent University 2001, PhD, Ghent University, 2007), associate professor at the Ships and Marine Technology Division of Ghent University, lecturer in charge of courses in marine hydrodynamics. Experienced in EFD based research, with focus point on ship manoeuvring in shallow and confined water. He has been a member of the 27*th*-29*th* ITTC Manoeuvring Committee. Member of the organization and scientific committees of MASHCON conferences since their creation (2009).

Dmitriy Ponkratov is a Marine Director at Siemens Digital Industries Software. With over 20 years of international experience, he has held academic and industry roles in China, Norway and the UK. Dr. Ponkratov leads the Joint Research Project (JoRes), which developed benchmarks for full scale numerical simulations.

Jeroen Verwilligen holds the current position of senior expert in nautical research at Flanders Hydraulics Research. He is experienced with simulation studies, nautical accessibility studies and full scale measurements.

Evert Lataire is head of the Ships and Marine Technology Division at Ghent University. His research focuses on the behaviour of ships in shallow and confined waters and is often based on model tests. In recent years his division diversified to other floating devices subject to waves and current such as aquaculture in open sea and floating PV-panels in an offshore environment. Member of the organization and scientific committees of all MASHCON conferences .

ON THE RESISTANCE ESTIMATION OF AN INLAND VESSEL IN SHALLOW AND CONFINED WATER

José Villagómez, Flanders Hydraulics, Belgium
Wim Van Hoydonck, Flanders Hydraulics, Belgium
Thibaut Van Zwijnsvoorde, Flanders Hydraulics, Belgium
Maxim Candries, Ships and Marine Technology, Ghent University, Belgium

ON THE RESISTANCE ESTIMATION OF AN INLAND VESSEL IN SHALLOW AND CONFINED WATER

JOSÉ VILLAGÓMEZ, FLANDERS HYDRAULICS, BELGIUM
WIM VAN HOYDONCK, FLANDERS HYDRAULICS, BELGIUM
THIBAUT VAN ZWIJNSVOORDE, FLANDERS HYDRAULICS, BELGIUM
MAXIM CANDRIES, SHIPS AND MARINE TECHNOLOGY, GHENT UNIVERSITY, BELGIUM

SUMMARY

This paper investigates the resistance prediction of an inland vessel in confined water based on experimental tests performed in the Towing Tank for Manoeuvres in Confined Water at Flanders Hydraulics and CFD (Computational Fluid Dynamics) computations executed at five different scales in deep water, shallow water and confined water.

The measured resistance of a 1/20 scale model towed in different channel sections is used to investigate different extrapolation approaches to consider the effect of co nfinement. The contributions of viscous and pressure components to the resistance, their variation at different scales and the interactions with channel boundaries is investigated using CFD calculations at five different sca les. The accuracy and limitations of different extrapolation methods are discussed for different levels of confinement. This paper is the first part of ongoing research to predict the full-scale resistance of a ship sailing in confined water using model scale towing tank tests and a limited number of numerical computations.

NOMENCLATURE

CFD	Computational Fluid Dynamics	
EASM	Explicit Algebraic Stress Model	
EFD	Experimental Fluid Dynamics	
ITTC	International Towing Tank Conference	
RANS	Reynolds-Averaged Navier Stokes	
UKC	Under Keel Clearance	
VOF	Volume of Fluids	
A	Waterway cross sectional area	m²
A_s	Ship cross-sectional area	m²
B	Breadth	m
B_s	Breath of channel section	m
C_A	Correlation allowance	-
C_B	Block coefficient	-
C_F	Frictional resistance coefficient, ITTC (1957)	-
C_R	Residual resistance coefficient	-
C_T	Total resistance coefficient	-
C_{TM}	Total resistance coefficient, model scale	-
C_{TS}	Total resistance coefficient, full scale	-
Fr_h	Depth-based Froude number	-
h	Water depth	m
L_{OA}	Length over all	m
L_{PP}	Length between perpendiculars	m
L_{ref}	Reference length	m
m	Blockage (= A_s/A)	-
R_T	Total resistance	N
R^*_{TM}	Normalized total resistance, model scale	-
R^*_{TS}	Normalized total resistance, full scale	-
S	Wetted surface	m²
T	Draft	m
T_1	Design draft	m
T_2	Scantling draft	m

V	Speed	m s⁻¹
V_{crit}	Critical speed	m s⁻¹
V_{ref}	Reference speed	m s⁻¹
x_G	Longitudinal position of centre of gravity (w.r.t. midship)	m
z_G	Vertical position of centre of gravity (w.r.t. free surface)	m
z_M^*	Normalized mean sinkage, model scale	-
∇	Displacement	m³
γ	Overspeed ratio	-
θ_M^*	Normalized trim angle, model scale	-
λ	Scale	-
ρ	Density	kg m⁻³

1 INTRODUCTION

The prediction of resistance for inland vessels involves environments with shallow and confined waters, where the bathymetry of the fairway changes along the transportation route. Therefore, a preliminary estimate of energy consumption during the design stage must consider the variations in resistance due to different confinement levels.

Although resistance prediction in shallow water has received more attention in recent years, the specific issue of resistance in confined waters is often only marginally discussed as an extension of the shallow water problem. However, confinement has stronger effects on the pressure field and flow around the hull. Additionally, the semi-empirical approximations used to estimate the effects of confinement have significant limitations.

Raven et al. (2008) discuss the simplifications of the *extrapolation procedure*, which relies on assumptions that are not always appropriate and are no longer necessary with the use of CFD calculations. However, the empirical modifications to the extrapolation methods over time make it challenging to achieve better results with a CFD approach. In a subsequent study, Raven (2012), the importance of selecting an appropriate extrapolation method for shallow water is emphasized. It is stated that the viscous component can be incorrectly estimated if a depth-dependent form factor is not considered. The scale effect (the different relative proportions of viscous resistance at model and ship scale) in extrapolation is not significant until $h/T = 0.6$. For more shallow water, this proportion is inconsistent, and a numerical calculation of viscous resistance could be used.

Zeng (2019) highlighted the physical changes due to limited water depth in both the velocity and pressure fields around a ship hull. Additionally, in shallow water, the boundary layer of a ship cannot develop freely, which influences shear stress and leads to a water depth-dependent frictional resistance. Thus, an adaptation for each of the three components of the extrapolation method is proposed, as none of them remains the same at model scale and full scale. The method includes a numerical friction line and other correction parameters derived from numerical experiments performed on different ship types (e.g., inland vessels).

Terzief, Tezdogan, and Incecik (2019) studied scale effects on ship bare hull resistance. Several hypotheses were tested with a geosim analysis using CFD. Wave resistance is shown to depend on the scale at which the computation is executed. In addition, free surface effects on frictional resistance are shown to depend on the Reynolds number. These findings contradict with the basic assumptions on which the ITTC (International Towing Tank Conference) extrapolation procedure to estimate full scale ship resistance relies.

Korkmaz et al. (2021) investigated the possibility to improve ship power prediction by introducing a combined EFD (Experimental Fluid Dynamics)/CFD method where the experimental determination of the form factor $(1+k)$ is replaced with double body RANS (Reynolds-Averaged Navier Stokes) computations for KVLCC2 and KCS. A comparison of full-scale viscous resistance predictions obtained by extrapolation of model scale results and direct full-scale computations show that the combined method results in less scatter and may be preferred.

According to ITTC (2021a), the total resistance coefficient C_T is defined as:

$$C_T = \frac{R_T}{\frac{1}{2}\rho S V^2} \tag{1}$$

whenever referred to the model, C_{TM} or the full scale ship, C_{TS} and where ρ is the water density and V, the speed. C_T can be decomposed into:

$$C_T = (1+k)C_F + C_W, \tag{2}$$

where $(1+k)$ is the form factor, C_F the frictional and C_W the wave-making resistance.

When the free surface is replaced with a rigid symmetry plane, $C_W = 0$ and Eq. 2 reduces to (Terzief, Tezdogan, and Incecik 2019),

$$C_T = (1+k)C_F = C_{VP} + C_F, \tag{3}$$

where the frictional resistance coefficient, C_F is defined by:

$$C_F = \frac{0.075}{(\log_{10} Re - 2)^2} \tag{4}$$

and C_{VP} is the viscous pressure resistance. Combining Eqs. 2 and 3, the wave resistance is computed from the difference between the total resistance computed with a free surface approach and the total resistance computed with a double body approach,

$$C_W = C_{T_{FS}} - C_{T_{DB}}. \tag{5}$$

The form factor is computed from the double body resistance (Terzief, Tezdogan, and Incecik 2019),

$$(1+k) = \frac{C_{T_{DB}}}{C_{F_{DB}}}, \tag{6}$$

or using a suitable friction line (Korkmaz et al. 2021),

$$(1+k) = \frac{C_F + C_{VP}}{C_{F0}} = \frac{C_{T_{DB}}}{C_{F0}}, \tag{7}$$

where C_{F0} is the equivalent flat plate resistance in two dimensional flow obtained at the same Reynolds number as the computations.

2 EXPERIMENTAL RESEARCH

Resistance model tests have been carried out in the Towing Tank for Manoeuvres in Confined Water (Flanders Hydraulics). The towing tank has a total length of 87.5 m, of which 68 m is useful for experiments, and a width of 7 m. More information on this facility can be found in Delefortrie, Geerts, and Vantorre (2016). Tests were carried out with a 4.25 m long inland ship model, with a scale of 1:20. The main characteristics of the scaled model and the full scale ship are provided in Table 1. The experimental program included two loading conditions and multiple environmental configurations corresponding to deep, shallow, and confined water conditions, with different channel sections physically constructed in the tank (see Fig. 2). Table 2 presents an overview of the tested environments. Note that all sections are rectangular banks, except for Section 4, which has a slope with a vertical-to-horizontal ratio of 1:2, corresponding to an angle whose tangent is 0.5. The towing tank carriage setup allows the model to sink and trim freely.

The model resistance curves were generated across a wide range of speeds, from very low speeds (0.05 m/s) to either the critical speed or the sinkage limit (due to the risk of contact with the bottom in shallow and confined waters). The critical speed V_{crit}, is determined using Schijf's formula (Schijf 1949),

$$V_{crit} = 3.6 \left(2 \sin \frac{\arcsin(1-m)}{3} \right)^{3/2} \sqrt{gh} \tag{8}$$

where m is the blockage factor, g is the gravitational acceleration and h is the average water depth. Eq. 8 gives V_{crit} in km/h, which is common practice for inland navigation vessels.

All model resistance tests were conducted following the procedures of the ITTC (ITTC 2021b). Sand strips were added to the bow of the hull at 4.032 m (leading edge) from the transom stern, with a width of 0.01 m and a grain size of 0.5 mm, to minimize the influence of natural laminar-to-turbulent boundary layer transition on the measured resistance ITTC (2024) . Note that for shallow water conditions, the resistance-increasing effect due to the tank walls is considered (see Section 3.1).

From an experimental perspective, tests in confined water present additional challenges: the critical speed is reached at lower speeds than in shallow water, and sinkage increases rapidly with speed, raising the risk of bottom contact. Therefore, the data required to compute the confined water form factor is limited, and the range of available speeds must be carefully selected, adding uncertainty to the extrapolation.

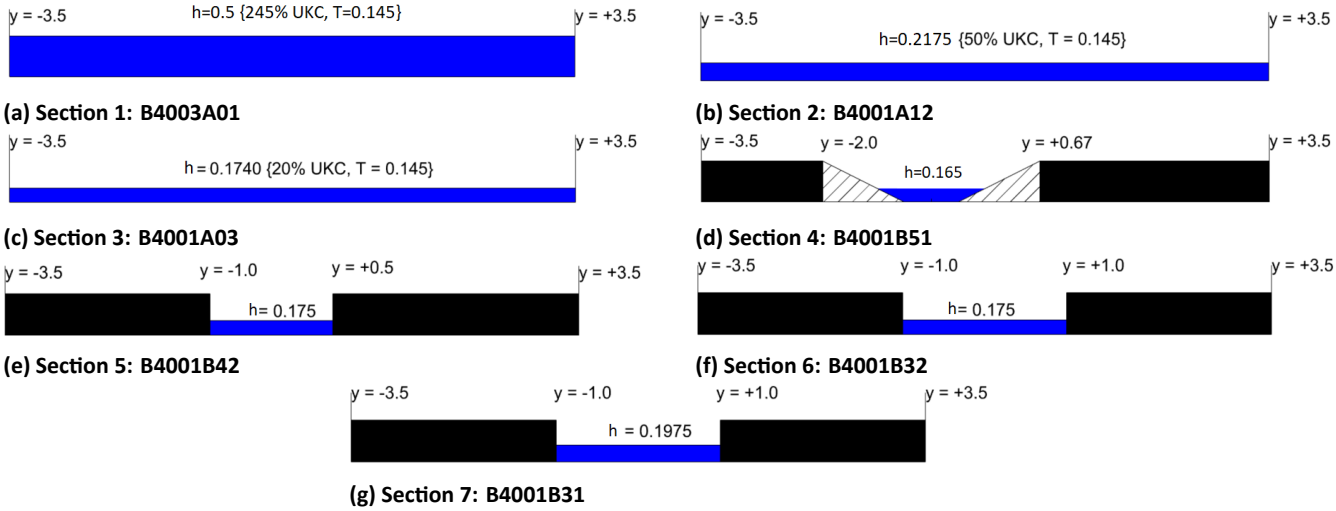

Figure 1: Transversal section of the towing tank for the tested environment conditions for $T_2 = 0.145$ m. Sloped bank (Section 4) only tested with $T_1 = 0.125$ m. All dimensions in meters.

3 EXPERIMENTAL RESULTS

3.1 RESISTANCE

Since all resistance measurements were conducted in the towing tank — which has neither infinite depth nor width — the results will be treated as resistance with different confinement levels in this section. Tests performed with the maximum water depth possible in the towing tank, also "feel" the effect of the tank walls and bottom. This effect will be estimated in Section 5.

The measured resistance for both drafts and all the investigated environments are presented in Fig. 3a and Fig. 3b which show that at a given speed, the resistance increases significantly as the level of confinement rises. In the graphs, the resistance values have been normalized with respect to the measured resistance at the design speed and design draft under deep-water condition. For the maximum draft $T_2 = 0.145$ m at 0.6 m/s, the resistance with the maximum water depth in the towing tank, h = 0.5 m (Section 1), is R^*_{TM} = 0.382 (Fig. 3b). When the water depth is reduced to h = 0.175 m (20% UKC - Section 3), the resistance rises to 0.677. If the channel width is reduced — while maintaining the same water level — from 7.0 m to 2.0 m (Section 6), the resistance increases to 1.069. This represents an increase of 77 % and 180 % for the shallower and more confined water environments, respectively, compared to the resistance in deep water. As the speed increases, the resistance diverge further, indicating that the increasing effect is even more pronounced as the speed grows. The asymptotic behaviour of the resistance occurs near the estimated critical speed. This is evident in the curve for $T_1 = 0.125$ m, where the calculated critical speed was V_{crit} = 0.391 m/s, and the asymptotic jump occurs at 0.4 m/s.

3.2 SINKAGE

The sinkage increases dramatically as the level of confinement transitions from deep water to shallow and confined water, as shown in Fig. 3c and Fig. 3d. These figures present the normalized sinkage, z^*_M, with respect to the measured sinkage at

Table 1: Ship model and full-scale characteristics

	Loading condition 1		Loading condition 2	
λ	20	1	20	1
L_{OA}	4.259	85.12	4.259	85.12
L_{PP}	4.245	84.9	4.245	84.9
B	0.48	9.6	0.48	9.6
T	0.125	2.5	0.145	2.9
C_B	0.845	0.845	0.855	0.855
∇	0.215	1720	0.253	2024
x_G	-0.0657	-1.314	-0.0778	-1.556
z_G	0.030	0.6	0.032	0.64

Table 2: Environment definition for resistance tests (model scale)

Code	Section	B_s	T	h	UKC (Under Keel Clearance)	m	Fr_{crit}	V_{crit}	$1+k$
B4001A12	Section 2	7.00	0.145	0.2175	50	0.046	0.742	1.083	1.2716
B4001A03	Section 3	7.00	0.145	0.1740	20	0.057	0.713	0.932	1.3845
B4001B42	Section 5	1.50	0.145	0.1750	21	0.265	0.401	0.525	3.3104
B4001B32	Section 6	2.00	0.145	0.1750	21	0.199	0.476	0.623	2.3885
B4002B32	Section 6	2.00	0.125	0.1750	40	0.171	0.512	0.671	1.8104
B4002B31	Section 7	2.00	0.125	0.1975	58	0.152	0.539	0.750	1.8406
B4002B42	Section 5	1.50	0.125	0.1750	40	0.229	0.440	0.577	2.5106
B4002A02	Section 2	7.00	0.125	0.1875	50	0.046	0.742	1.006	1.2506
B4002A03	Section 3	7.00	0.125	0.1500	20	0.057	0.713	0.865	1.4736
B4002B51	Section 4	1.00	0.125	0.1650	32	0.364	0.307	0.391	4.6222
B4002A01	Section 1	7.00	0.125	0.5000	300	0.017	0.842	1.864	1.1007
B4003A01	Section 1	7.00	0.145	0.5000	245	0.020	0.829	1.835	1.1249
B4003B31	Section 7	2.03	0.145	0.1975	36	0.174	0.508	0.707	1.9564

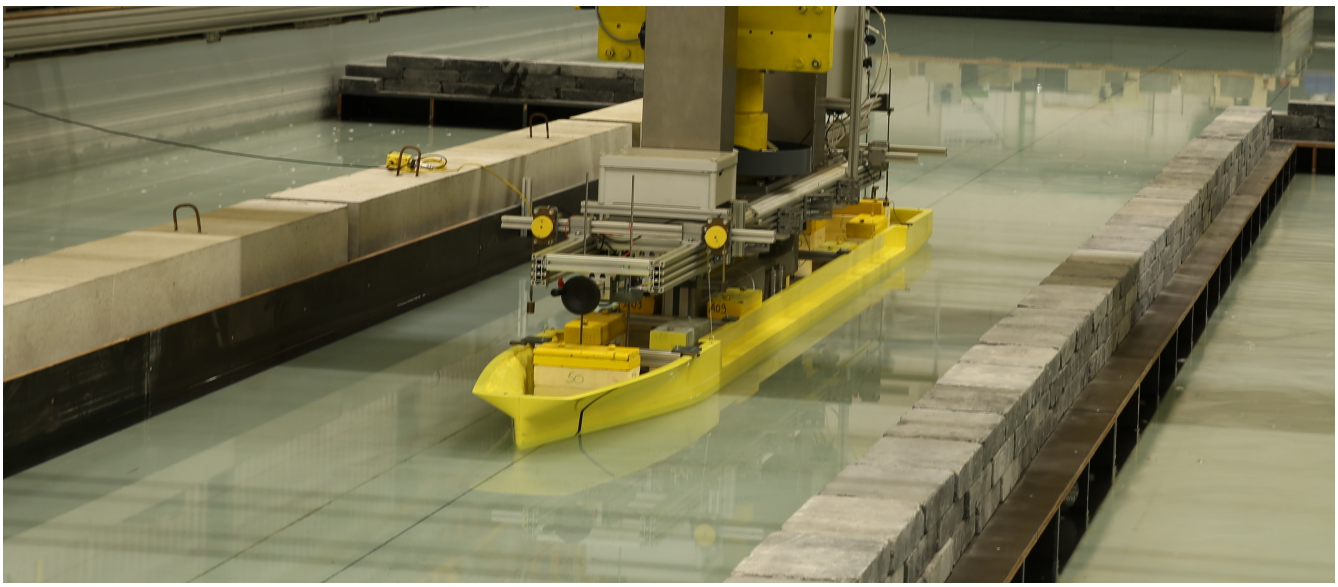

Figure 2: Resistance tests in confined water at the Flanders Hydraulics towing tank - Inland ship model at T =0.125 m during tests in Section 7.

the design speed and design draft at deep water. The measured sinkage curves exhibit a similar behavior to the resistance curves, rapidly increasing with speed as the critical speed is approached. This can be observed by comparing the sinkage curve behaviour of Section 5 (more confined environment) and Section 1 (maximum water depth) for the smallest draft, $T_1 =$ 0.125 m in Fig. 3c.

3.3 TRIM

Figures 3e and 3f present the normalized trim, θ^*_M, for both drafts. Although the measured absolute values are small for all the executed tests (less than 0.5°), they are consistently negative (bow down) in the less confined environments, increasing with speed. For more shallow conditions, the trim starts negative (bow down), but becomes positive (bow up) as it approaches the critical speed. In more confined environments, the trim remains positive even at lower speeds.

4 NUMERICAL COMPUTATIONS

4.1 INTRODUCTION

For the current research, CFD is used to investigate scale invariance of resistance components, sinkage and trim in deep water, shallow water and confined water. Computations are executed at five different scale factors from full scale (1) to model scale (20) that are almost uniformly distributed on a logarithmic scale: 1, 2.5, 5, 10 and 20. To determine the wave

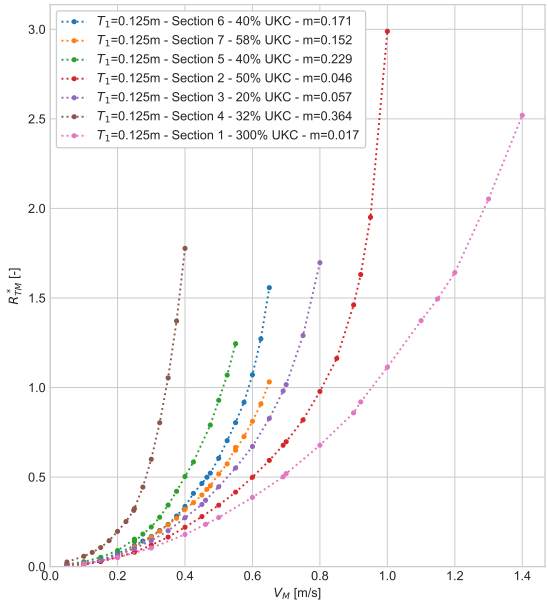

(a) Measured resistance — $T_1 = 0.125$ m.

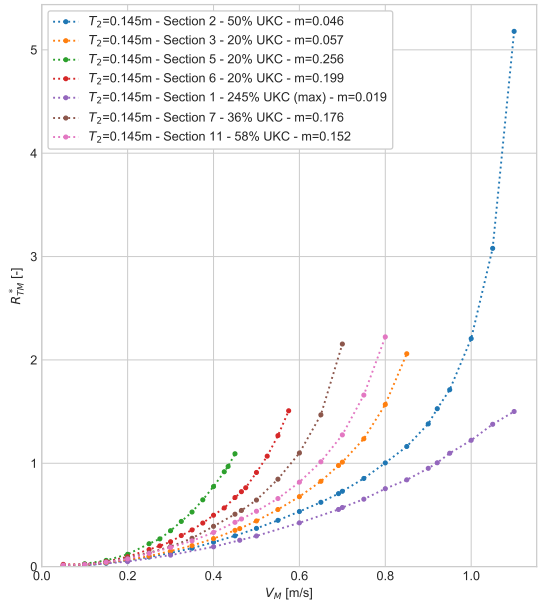

(b) Measured resistance — $T_2 = 0.145$ m.

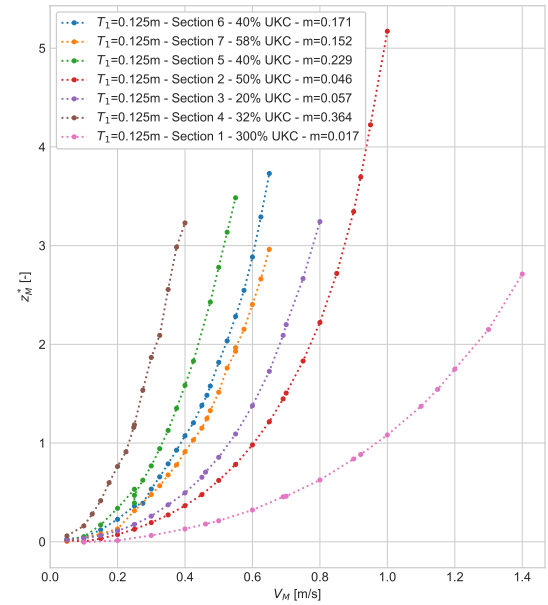

(c) Measured mean sinkage — $T_1 = 0.125$ m.

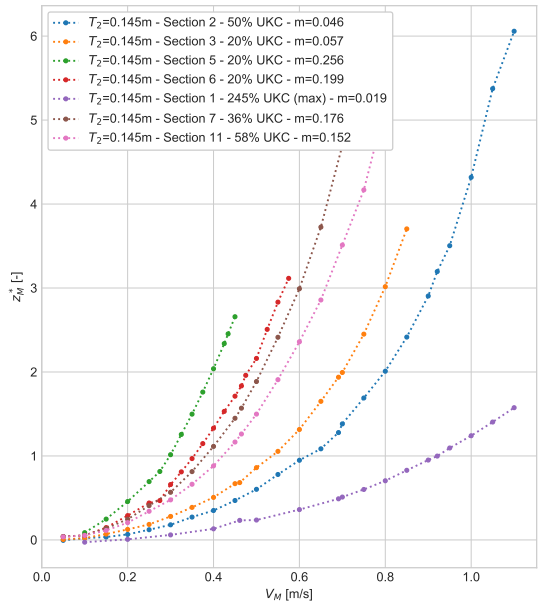

(d) Measured mean sinkage — $T_2 = 0.125$ m.

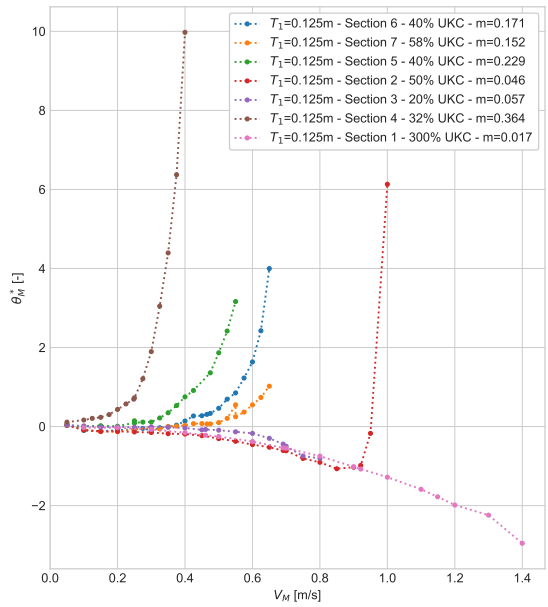

(e) Measured trim — $T_1 = 0.125$ m.

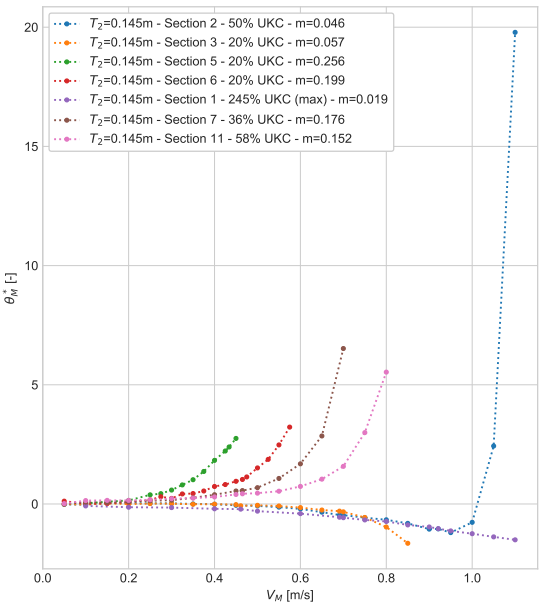

(f) Measured trim — $T_2 = 0.145$ m.

Figure 3: Normalized model resistance, mean sinkage, and trim angle for $T_1 = 0.125$ m (left) and $T_2 = 0.145$ m (right) in all tested environments.

making resistance C_W, two computations are executed for each condition, one including the free surface and a second one using a double-body approach (rigid lid).

A summary of the conditions that are investigated is presented in Table 3. Note that the under keel clearance in the confined section was exactly the same as the shallow water condition[1]. As such, the effect of lateral blockage (in addition to vertical blockage) on the results can be determined separately. The ship velocity that was used in the deep and shallow water condition was however too high to get converging results in confined water, and hence it was reduced (to 7.5 km/h or 2.083 m/s at full scale). CFD computations are executed at a draft of T = 2.9 m. Domains are geometrically scaled with the scale factors mentioned before, Froude scaling is used to scale the reference velocity and time (such as the time to accelerate to the target velocity). Due to the large difference in Reynolds number at full and model scale, the grids are not simply scaled geometrically with the domain, but the parameters for the viscous layers inserted on the hull and the domain bottom (when in shallow or confined water) are recomputed to ensure similar values of Y+ are used at all scales. As a consequence, at model scale, the first layer thickness is larger and fewer layers are inserted as compared to full scale.

Table 3: CFD conditions of the computations at full scale.

condition	section	UKC	speed
deep	1	-	6 kts
shallow	3	20%	6 kts
confined	6	20%	4.05 kts

4.2 COMPUTATIONAL SETUP

The bare hull in free surface computations is free to sink and trim but otherwise constrained (similar to the setup used in the towing tank experiments). In shallow and confined water, sinkage will be significantly larger than in deep water conditions due to increased blockage. As a consequence, the sinkage values obtained in the free surface computations are used to increase the hull draft in the double body computations. For deep water conditions, the small sinkages obtained with the free surface computations are not compensated for in the double body computations.

The computational setup and some results are discussed only briefly in this paper, a full description with analysis of all results (including grid convergence study) is left for a future publication.

4.2 (a) Domain sizes

To reduce grid sizes, only the port side of the hull is included in the domain. As a reference length for sizing the domain, the value of L_{OA} (see Table 1) is rounded to an integer: $L_{ref} = 85$ m. In deep water (including the free surface), the domain length equals 8 L_{ref}, the inlet is located 3 L_{ref} ahead of the bow and there is 4 L_{ref} between the stern and the outlet. The domain width is 3 L_{ref} and its height equals 4 L_{ref}, with 2.5 L_{ref} below the keel and 1.5 L_{ref} from the keel to the domain top. For shallow water free surface computations, the domain height is reduced to 2 L_{ref}. Finally, in confined water, the domain width of the shallow water computations is reduced to 20 m (at full scale) while the other dimensions remain unchanged.

Using results of the free surface computations, the domains for their respective double body computations are constructed. For the shallow and confined water double body computations, the hull is moved vertically to compensate for the sinkage. The hull is cut at the free surface and only the submerged part is retained.

The CFD computations use a right-handed axes system where the X-axis points towards the bow, the Y-axis points to port and the Z-axis points upward.

4.2 (b) Grids

For the current investigation, the unstructured hexahedral grid generator HEXPRESS™(available as part of the FINE/Marine™CFD software package) is used. To capture the deformation of the free surface with sufficient detail, anisotropic refined is applied to cells near the free surface ($z = 2.9$ m) in the complete domain. In addition, a refinement sector is added to capture the Kelvin wake with sufficient detail that extends 0.8 L_{ref} aft of the hull. Areas of the hull with a small curvature radius (such as the bow and chines) are given extra refinement. In the shallow and confined cases, the grid below the hull bottom is refined more than in the deep water case to ensure a sufficient number of cells in the gap. Viscous layers are added to the hull and bottom, where a target Y+ of 1 is used for the hull. At full scale, more layers will be inserted than at model scale and as a consequence, grid sizes reduce with increasing scale factor. For deep water computations with free surface, grid sizes vary

[1]In the experiments, the water depth at 20% UKC differs 1 mm (or 0.02 m at full scale) from the water depth in sections 5 and 6 as shown in Fig. 1.

between 7.7 × 10^6 and 5.7 × 10^6 cells, while for the corresponding double body computations, they vary between 4.8 × 10^6 and 3 × 10^6 cells. All grids for the shallow water cases have sizes between 10.3 × 10^6 and 7.2 × 10^6 cells while for the confined water cases, the cell count varies between 8.8 × 10^6 and 4.0 × 10^6.

A view of the resulting grids at the midship location for deep and confined water are shown in Fig. 4.

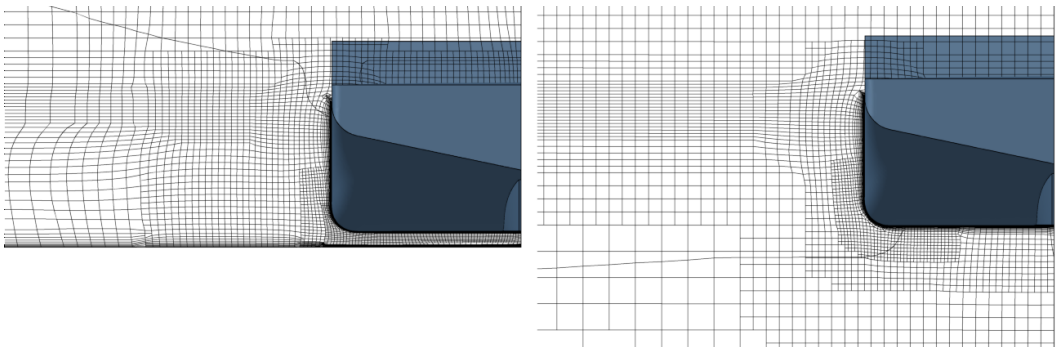

Figure 4: View of the grids at the midship location for confined water (left) and deep water (right) at full scale. Note that for the confined water computation (left), the hull is meshed below the hydrostatic position.

4.2 (c) Solver settings

FINE/Marine™12.1 is used to configure all computations. The ISIS-CFD solver uses a VOF (Volume of Fluids) approach to model the interface between fluid fractions. For all simulations, the flow is assumed to be fully turbulent, even at model scale. This is a reasonable approximation, as in the experimental campaign, turbulence stimulation was applied at the bow of the hull (see Fig. 2).

A time stepping approach is used for all computations, even for the double body computations. The time step depends on the transit time of the setup, $\Delta t = a\frac{L_{ref}}{V_{ref}}$ where a is a scaling factor equal to $1/200$ and $1/100$ for free surface and double body computations, respectively and L_{ref} and V_{ref} are the scaled values of the reference length and reference velocity.

For the free surface computations, a quasi-steady approach is used to solve the sinkage and trim to reduced the number of time steps to reach sufficiently converged results.

For turbulence closure, the EASM (Explicit Algebraic Stress Model) turbulence model is used. For resistance prediction applications, this model gives slightly better results than standard k-omega SST turbulence closure models, while computing times do not increase noticeably (Deng and Visonneau 1999).

4.2 (d) Boundary conditions

For all cases, a mirror condition is use at the symmetry plane of the hull. For the computations including the free surface, the boundary condition at the domain top is *Prescribed pressure - updated hydrostatic pressure*. The double body computations use an additional mirror condition at the location of the free surface. At the inlet a *far field* boundary conditions is applied where velocity equals 0. For the double body computations, the boundary condition at the outlet is *prescribed pressure - frozen pressure*, while for the free surface computations, the outlet is also a *far field* boundary condition with velocity equal to 0.

Solid walls that are not part of the ship hull are assigned *wall function* (i.e., the domain bottom in shallow water computations and both the domain bottom and domain side for confined water computations). For all hull patches except for the deck, the boundary layers are resolved ($Y+ < 1$) and a slip condition is applied to the deck surfaces.

4.3 RESULTS

Fig. 5 shows the non-dimensional wave elevation (computed as the wave elevation divided by the draft) at the five different scales for the water (a) and confined water (b) computations[2]. It is noted that the confined water computations were executed at a lower Froude number than the deep and shallow water computations; the deformation range is therefore also smaller. For the three environments, the wave elevation patterns show slight variations with scale, especially at the stern. For example, the stern wave in shallow water gets progressively more washed out at smaller scales. The visualisations show that although the differences due to scale effects are small, simply assuming that wave making resistance is completely scale-independent without further investigation, may not hold true.

[2]The deep water wave elevations are not shown in Fig 5 but they are discussed in the text.

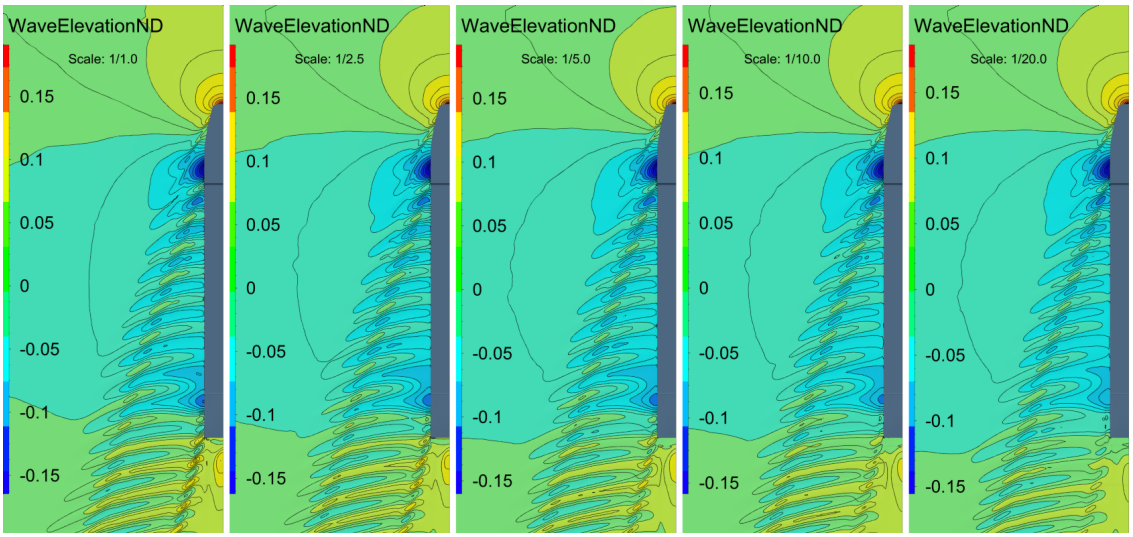

(a) Shallow water.

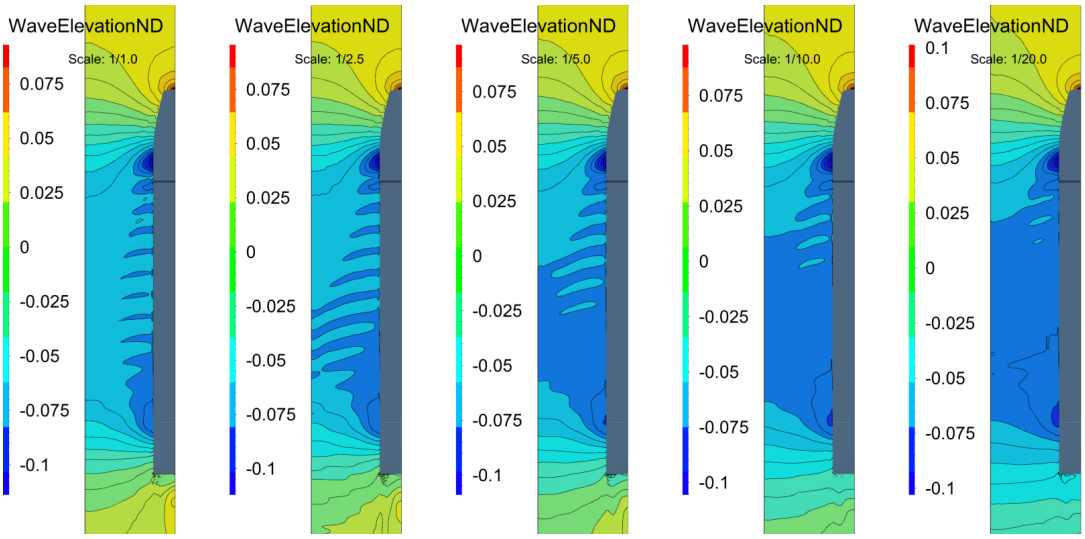

(b) Confined water.

Figure 5: Comparison of non-dimensional wave elevation in shallow and confined water at five different scales.

Fig. 6a shows the dimensionless vertical displacement[3] and trim values of the hull for the free surface computations. In deep water, the scale does not affect the sinkage, while for shallow and confined water, there is a deviation at smaller scales: sinkages at model scale are slightly underestimated as compared to the full scale values. At model scale, the boundary layer between the hull and domain bottom is thicker than at full scale, which reduces the relative speed of water below the hull, as a consequence the hydrodynamic pressure is higher and the sinkage reduces. The trim is hardly affected in deep water by the computation scale, while in shallow and confined water, there are visible differences. In deep and shallow water, the computations predict a positive trim (bow down) while in shallow water, a negative trim is predicted. Note that all values are smaller than $|0.01°|$ at full scale. Compared to the sinkage of the centre of gravity, these values are less important.

In Figs. 6b to 6d, the friction, pressure and total resistance of the hull are shown for deep, shallow and confined water conditions, both for the free surface and double body computations. In deep water, the pressure resistance of the hull is very close to scale-independent, with only slightly larger values at full scale. Pressure resistance values are also significantly lower than frictional resistance values in deep water, while in shallow water, pressure resistance approaches frictional resistance. In confined water, pressure resistance is higher than friction resistance both for the double body and free surface computations. Both components show a decreasing trend with increasing scale, hence are Reynolds-dependent.

Finally, the wave making resistance and the form factor (computed using Eq. 6) are determined for deep water, shallow water and confined water (Fig. 7). Except for C_W in deep water, all results show a significant dependence on the scale factor.

[3]Vertical displacement is made dimensionless by dividing it with the draft T.

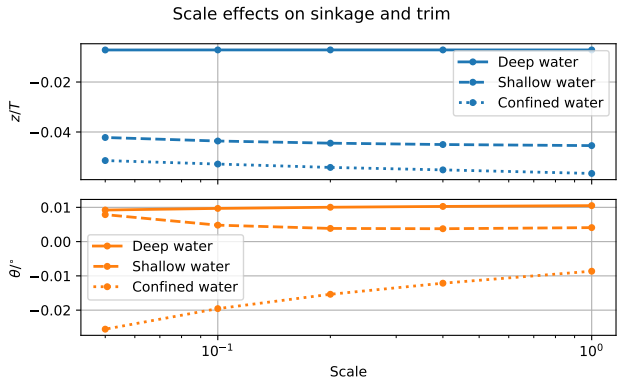

(a) Scale effects on sinkage and trim.

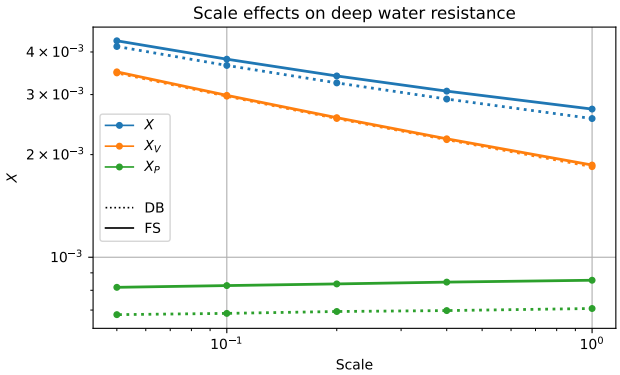

(b) Scale effects on resistance: deep water.

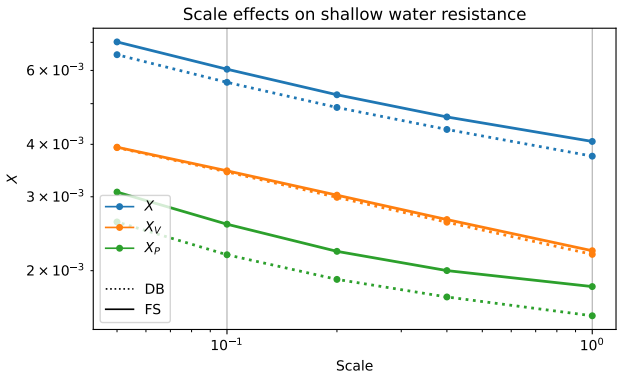

(c) Scale effects on resistance: shallow water.

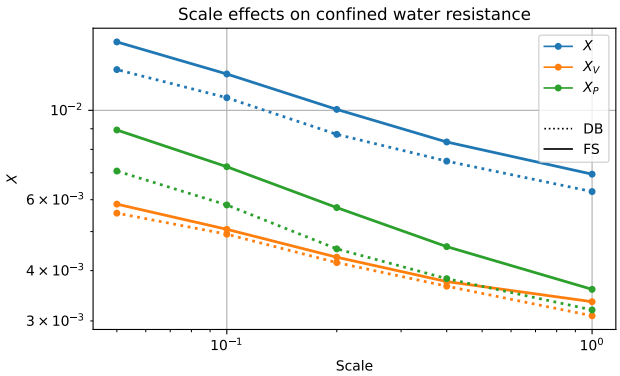

(d) Scale effects on resistance: confined water.

Figure 6: Influence of scale on sinkage and trim, pressure (X_P), friction (X_V) and total resistance (X) in deep, shallow and confined water for double body (DB) and free surface (FS) computations.

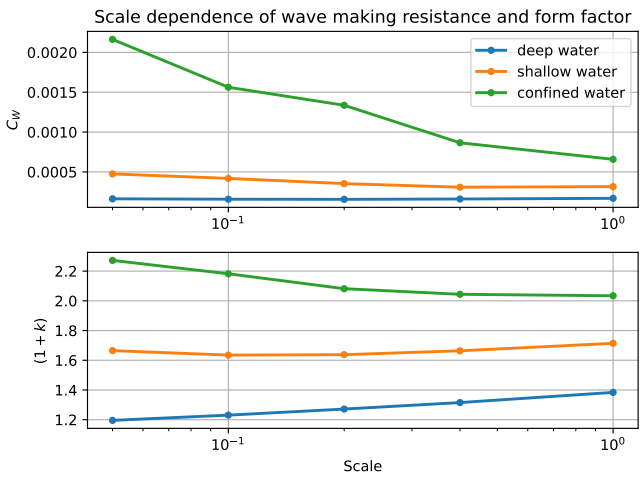

Figure 7: Wave making resistance (C_W) and form factor $(1 + k)$ for deep, shallow and confined water conditions as function of scale factor.

5 ANALYSIS OF RESULTS

The numerical calculations at different scales are used as reference to evaluate the extrapolated results of the three investigated cases in Table 3: deep, shallow and confined water condition. Initially, the resistance results obtained both numerically and experimentally at the model scale are compared to assess the degree of agreement. In order to perform the comparison, the model resistance has been corrected to account for the effect of the tank walls. It is important to note that the numerical calculations for both deep and shallow water conditions were performed with a wide domain to mitigate any influence from the tank walls. In contrast, for confined environments, the numerical domain precisely represents the channel geometry to capture its hydrodynamic influence on the resistance, so no correction is necessary for the experimental measurements at the model scale.

The model resistance has been corrected by calculating the return flow speed using the method proposed by Kreitner (1934). Assuming a constant flow over the midships and estimating the sinkage due to the pressure drop near the hull, an expression is derived as a function of the depth-based Froude number Fr_h and the blockage m:

$$\gamma\left(1 - m + \frac{1}{2}{Fr_h}^2(1-\gamma^2)\right) = 1, \tag{9}$$

where the overspeed ratio is defined as $\gamma = u/V_M$, with u being the longitudinal component of the flow velocity next to the ship and V_M the measured model speed. The corrected values are used to calculate the form factor using Prohaska's method (Prohaska 1966) based on the experimental tests for deep, shallow, and confined water, as presented in Figure 8 and Table 2. Both the slope of the linear fit and the intersection with the vertical axis (which corresponds to the obtained form factor) increase with the level of confinement. The form factor for deep water is $(1+k) = 1.112$, and it gradually increases for shallow water to 1.384, and to 3.31 in the confined water case.

Fig. 9a presents the obtained resistance curves at model scale along with the numerical calculations for deep, shallow, and confined water for the analyzed cases. To evaluate the variation due to the tank wall correction (Eq. 9), the resistance values without this correction are also plotted. The variation in the resistance corresponds to a decrease relative to the uncorrected values. As expected, this difference becomes more significant in the shallow water condition as the speed increases, due to the local flow velocity next to the model. The relative differences between the corrected measurements and the numerical results at model scale are on the order of 3%, -5%, and -8% for the deep, shallow, and confined cases, respectively. This difference seems to increase with the level of confinement and may be related to the uncertainty of the numerical method, which will be addressed in a separate publication. Note that the differences would be 8%, 18%, and -8%, respectively, if the tank wall correction were not considered.

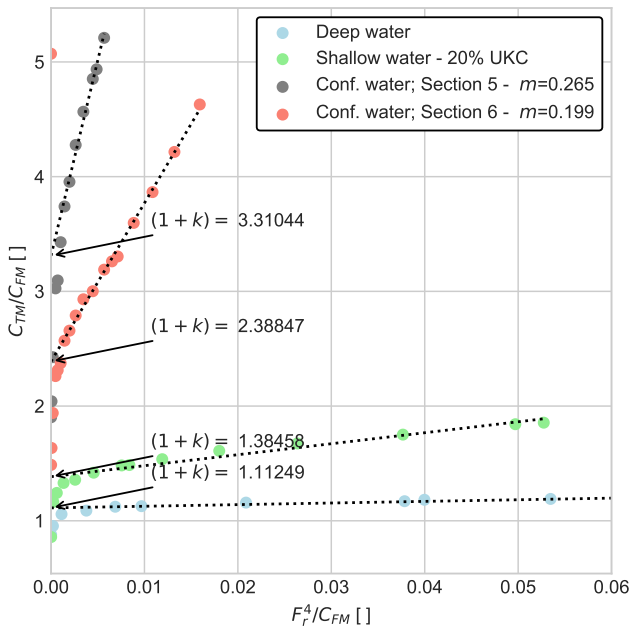

Figure 8: Form factor calculation based on EFD for deep, shallow and confined water case using (Prohaska 1966).

Based on the corrected model resistance measurements, different extrapolation approaches and variations have been tested:

Method I Froude extrapolation

Method II Extrapolation using form factor (calculated from model tests at deep water)

Method III Extrapolation using form factor depending on the environment condition.

Method IV Extrapolation using form factor depending on the environment condition and C_A=0.0004

Method V CFD calculation

Method I corresponds to Froude's method, which assumes that total resistance can be decomposed into frictional resistance and residual resistance. The ITTC friction line is typically used to estimate the frictional component, while the residual resistance is extrapolated from model tests conducted at the same Froude number as the full-scale ship. Method II involves extrapolation by calculating the form factor using Prohaska's method based on deep-water resistance tests. Method III incorporates an environment-dependent form factor and Method IV investigates the effect on the extrapolated resistance when assuming a typical correlation allowance value of C_A = 0.0004. Finally, Method V corresponds to the CFD calculations, which are used as the baseline for comparison.

The extrapolation methods that produced the closest results to the numerical resistance calculations at full scale (Methods III, IV and V) are presented in Figure 9b where resistance is normalized in relation with the full scale resistance at the design speed and design draft at full scale, R^*_{TS}. For the deep water condition, the best extrapolation result was obtained by Method IV (form factor depending on the environment and C_A=0.0004) with a difference of −1 % compared to the numerical results. Method IV (C_A=0) shows a difference of −16 %. Table 4 presents the extrapolation coefficients and the obtained differences for all the calculated methods. From the numerical results, it is verified that the wave resistance coefficients at model and full scale are equivalent, $C_{WM} = C_{WS}$ in deep water. Although C_{WM} is overestimated by 37 % using the form factor approach (in Methods III, and IV), the C_W is small compared to the total value of C_T (only 4 % at model scale and 6 % at full scale). Thus, the most significant component is related to C_{VS} (94 % of C_{TS}), which is underestimated by −19 %. This is the reason why C_A=0.0004 is needed to compensate for this difference. The source of this discrepancy may have two related origins: the friction line or the form factor calculation.

In the shallow water case, the two best approaches were Methods III and IV, which yielded relative differences of −3 % and 6 % compared to the numerical estimation, respectively (Figure 9b). Table 5 also contains the extrapolation coefficients, showing that the computed C_{WS} is 34 % smaller than C_{WM} ($C_{WM} \neq C_{WS}$), and that C_W gradually increases in relation to C_T compared to the deep water case (7 % and 8 % at model and full scale).

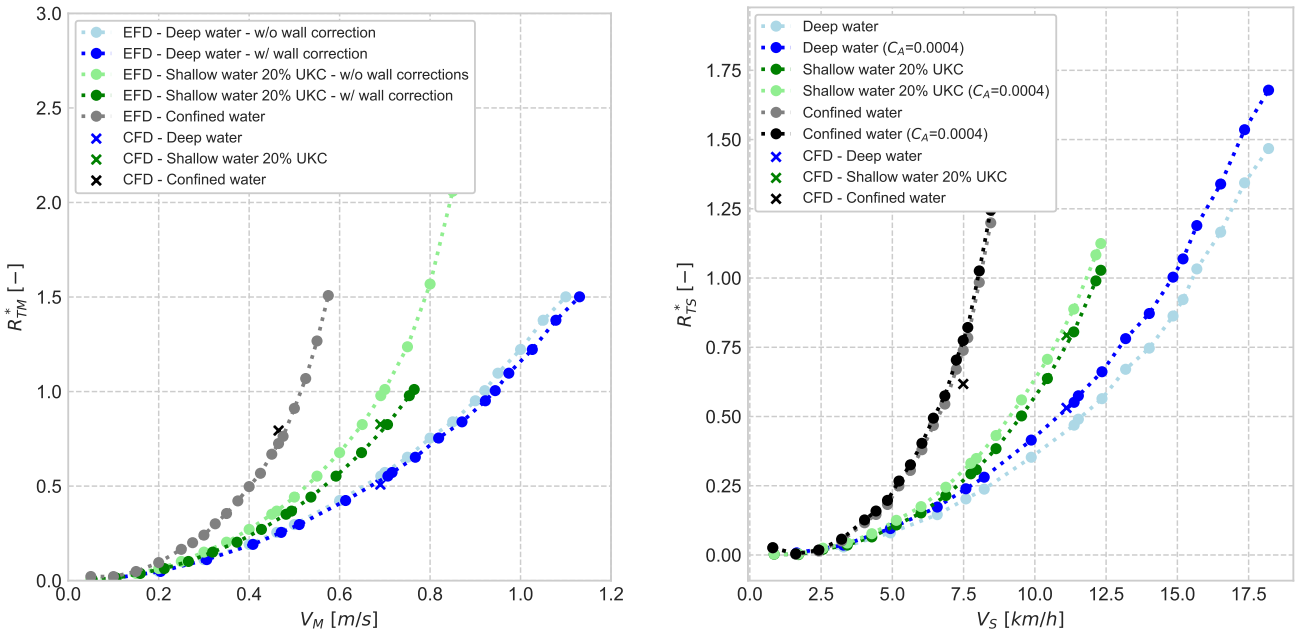

(a) Resistance comparison at model scale: EFD vs CFD calculation. (b) Resistance comparison at full scale: Extrap. vs CFD calculation.

Figure 9: Normalized resistance for deep, shallow and confined water compared with numerical calculations.

In the confined water case, the closest result, although overestimated with a relative difference of 19 % compared to the

numerical calculation, was obtained by Method III (Figure 9b). Table 6 shows that the computed C_{WS} is 70 % smaller than C_{WM} ($C_{WM} \ll C_{WS}$), and that C_W becomes more significant in relation to C_T than in the deep and shallow water cases (14 % and 10 % at model and full scale, respectively). The viscous component nearly doubles compared to the shallow water case and triples the viscous component in deep water (even with a lower speed of 7.48 km/h in confined water at full scale, versus 11.1 km/h in shallow and deep water).

Figure 10 shows the full-scale sinkage and trim compared with the numerical calculations for deep, shallow, and confined water. A very small maximum sinkage deviation (in absolute value approximately 2 cm) was observed in the deep water case. For the other cases (shallow and confined water), the prediction closely matches the scaled sinkage. The trim values are very low in both the numerical estimation and the measured angles (less than 0.8° in absolute value). However, the positive trim angle (bow-up) in confined water is captured by the simulation, whereas the negative angle (bow-down) is observed in the deep and shallow water cases.

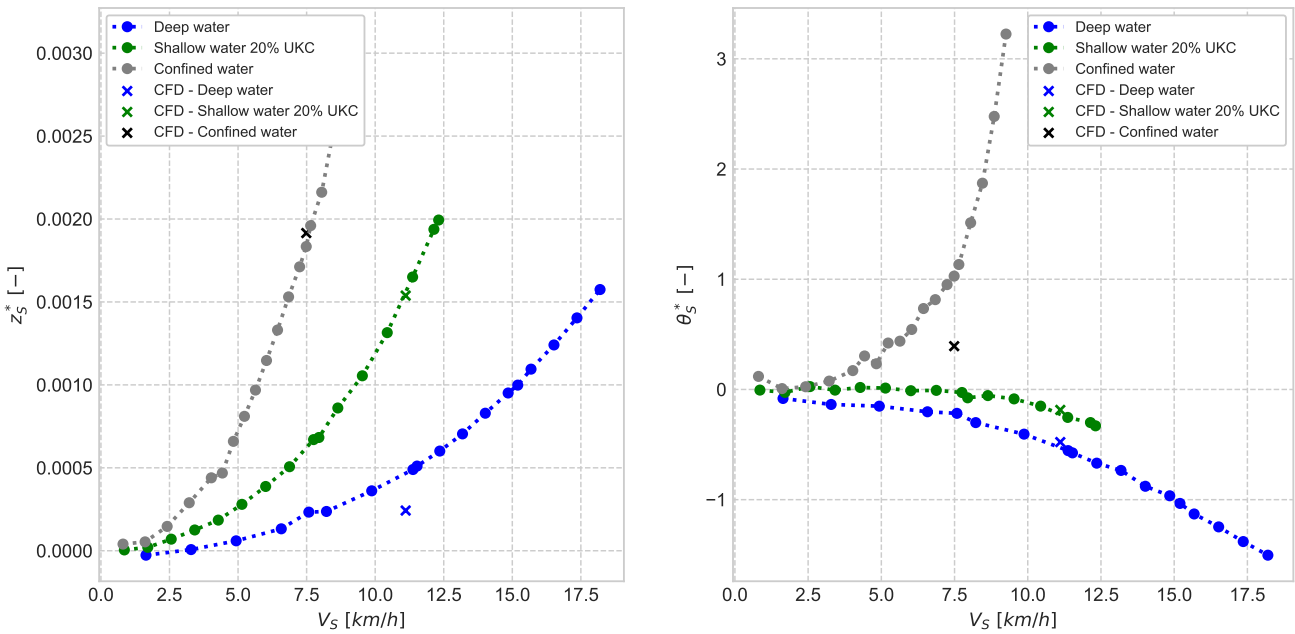

Figure 10: Left: Normalized mean sinkage at full scale for deep, shallow and confined water compared with computed sinkage. Right: Normalized trim at full scale compared with numeric calculations.

Note that in Tables 4, 5 and 6, C_V corresponds to C_F and C_W to C_R in the Froude extrapolation (Method I).

Table 4: Deep water case: T=2.9m, full tank width sailing at 6 knots (11.1km/h). (CFD: Deep water, EFD: Test B4003A01 at 0.69m/s)

Method	$C_{TM} \times 10^5$	$C_{VM} \times 10^5$	$C_{WM} \times 10^5$	$C_{VS} \times 10^5$	$C_{WS} \times 10^5$	$C_{TS} \times 10^5$
I	444	380	64	184	64	249
II	444	422	22	205	22	227
III	444	422	22	205	22	227
IV	444	422	22	205	22	267
V	431	415	16	255	16	272

6 CONCLUSIONS AND FUTURE WORK

An extensive experimental test campaign has been conducted to evaluate the accuracy of the resistance extrapolation method under different confinement levels, ranging from deep to shallow and fully confined water. The scale effect under these conditions has been analyzed by performing free-surface and double-body numerical calculations to assess the variation in the viscous and wave resistance components across five different scales.

The relative differences between the resistance measurements (corrected for tank wall effects) and the numerical predictions at model scale are approximately 3%, -5%, and -8% for the deep, shallow, and confined cases, respectively. The correction for

Table 5: Shallow water case: T=2.9 m, Section 3 sailing at 6 knots (11.1 km/h). (CFD: Deep and shallow water, EFD: Test B4001A03 at 0.69m/s)

Method	$C_{TM}\times10^5$	$C_{VM}\times10^5$	$C_{WM}\times10^5$	$C_{VS}\times10^5$	$C_{WS}\times10^5$	$C_{TS}\times10^5$
I	665	380	285	184	285	470
II	665	422	242	205	242	448
III	665	532	133	258	133	391
IV	665	532	133	258	133	431
V	701	654	47	374	31	406

Table 6: Confined water case: T=2.9m, Section 6 sailing at 4.04 knots (7.48 km/h). (EFD: Test B4001B32 at 0.465m/s

Method	$C_{TM}\times10^5$	$C_{VM}\times10^5$	$C_{WM}\times10^5$	$C_{VS}\times10^5$	$C_{WS}\times10^5$	$C_{TS}\times10^5$
I	1347	413	934	195	934	1130
II	1347	459	888	217	888	1105
III	1347	986	360	467	360	828
IV	1347	986	360	467	360	868
V	1478	1262	216	628	65	694

tank wall effects improved the resistance agreement by 13%, demonstrating that it cannot be neglected in resistance analysis.

In terms of extrapolation, the limitations of the method using the environment-dependent form factor have been confirmed. In the case of shallow water, a depth-dependent form factor can partially compensate for differences in the viscous component, still providing an acceptable approximation (with a difference of approximately 6% compared to the computed full-scale resistance). However, in the case of confined water, the increase in the viscous component is so significant that it cannot be compensated for by a confinement-dependent form factor, leading to an overestimation of around 19% compared to the computed full-scale resistance. Therefore, the viscous contribution should be numerically estimated. On the other hand, the wave resistance coefficient can no longer be assumed constant; in fact, in the studied case, it shows a reduction of about 70% relative to the model scale.

There is no general consensus on the methodology for resistance extrapolation in confined waters. In the literature, generic references can be found for computing the difference in viscous resistance between the ship and the model. However, if the goal is to extrapolate a complete resistance curve with limited numerical effort, additional assumptions may be required. To the best of the author's knowledge, there is no detailed procedure available for performing such a complete extrapolation by combining experimental and numerical approaches. Therefore, this paper serves as a preliminary step toward achieving this goal.

7 ACKNOWLEDGEMENTS

The authors would like to acknowledge ZULU ASSOCIATES for providing the experimental data, which was essential for this publication. Their support and collaboration have significantly contributed to the completion of this research.

8 REFERENCES

Delefortrie, G., Geerts, S., and Vantorre, M., 2016. The towing tank for manoeuvres in shallow water. In: Proceedings of the 4th International Conference on Ship Manoeuvring in Shallow and Confined Water with Special Focus on Ship Bottom Interaction, Bundesanstalt für Wasserbau (Federal Waterways Engineering and Research Institute).

Deng, G. and Visonneau, M., 1999. Comparison of explicit algebraic stress models and second-order turbulence closures for steady flow around ships. In: 7th Symposium on Numerical Ship Hydrodynamics. Vol. 10. 1.534, p. 5953.

ITTC, 2021a. Recommended Procedures 1987 ITTC Performance Prediction Method. 7.5-02-03-01.4. Version Revision 05.

ITTC, 2021b. Recommended Procedures and Guidelines – Resistance Test. 7.5-02-02-01. Version Revision 05.

ITTC, 2024. Recommended Procedures and Guidelines – Ship Models. 7.5-01-01-01. Version Revision 05.

Korkmaz, K. B., Werner, S., Sakamoto, N., Quetey, P., Deng, G., Yuling, G., Guoxiang, D., Maki, K., Ye, H., Akinturk, A., Sayeed, T., Hino, T., Zhao, F., Tezdogan, T., Demirel, Y. G., and Bensow, R., 2021. CFD based form factor determination method. In: Ocean Engineering 220.108451. DOI: https://doi.org/10.1016/j.oceaneng.2020.108451.

Kreitner, J., 1934. Über den Schiffswiderstand auf beschränktem Wasser. In: Werft, Reederei und Hafen 15.7.

Prohaska, C. W., 1966. A Simple Method for the Evaulation of the Form Factor and Low Speed Wave Resistance. In: Proceedings of the 11th ITTC (Tokyo). ITTC.

Raven, H. C., 2012. A computational study of shallow-water effects on ship viscous resistance. In: Proceedings of the 29th Symposium on Naval Hydrodynamics (Gothenburg, Sweden, Aug. 26, 2012–Aug. 31, 2021).

Raven, H. C., Van der Ploeg, A., Starke, A. R., and Eça, L., 2008. Towards a CFD-based prediction of ship performance: Progress in predicting full-scale resistance and scale effects. In: International Journal of Maritime Engineering 150.

Schijf, J. B., 1949. Protection of embankments and bed in inland and maritime waters, and in overflows or weirs. In: XVIIth International Navigation Congress, Section I: Inland Navigation (Lisbon). PIANC.

Terziev, M., Tezdogan, T., and Incecik, A., Nov. 2019. A geosim analysis of ship resistance decomposition and scale effects with the aid of CFD. In: Applied Ocean Research 92.101930. DOI: https://doi.org/10.1016/j.apor.2019.101930.

Zeng, Q., 2019. A Method to Improve the Prediction of Ship Resistance in Shallow Water. PhD Thesis. Delft, the Netherlands: Delft University of Technology.

9 AUTHORS BIOGRAPHY

José Villagómez M.Sc, naval architect, is nautical researcher at Flanders Hydraulics Research with experience in numerical and experimental manoeuvring and seakeeping models. He is involved with research on generation and validation of manoeuvring models through fast-time and real time simulations. Member of the Manoeuvring Committee of the 31st International Towing Tank Conference (ITTC).

Wim Van Hoydonck obtained his PhD at Delft University of Technology and is nautical researcher at Flanders Hydraulics. His research interests include the application of numerical methods to ship hydrodynamics and aerodynamics.

Thibaut Van Zwijnsvoorde PhD, is a nautical researcher at Flanders Hydraulics. He oversees the physical model testing in the two shallow water towing tanks.

Maxim Candries is a postdoctoral researcher at the Ships and Marine Technology Division of Thent University. A substantial part of his research involves inland navigation.

APPLICATION OF CFD FOR THE PREDICTION OF HYDRODYNAMIC FORCES ACTING ON AN INLAND WATERWAY SHIP IN SHALLOW WATERS. LESSONS LEARNED FROM THE SHINING WORKSHOP

Lahbib Zentari, Federal Waterways Engineering and Research Institute, Germany
Antoine Bedos, Maritime Research Institute Netherlands, the Netherlands
Wim Van Hoydonck, Flanders Hydraulics, Belgium
Jens Ley, Development Centre for Ship Technology and Transport Systems, Germany
Guillermo Chillcce, University of Duisburg-Essen, Germany

APPLICATION OF CFD FOR THE PREDICTION OF HYDRODYNAMIC FORCES ACTING ON AN INLAND WATERWAY SHIP IN SHALLOW WATERS. LESSONS LEARNED FROM THE SHINING WORKSHOP

LAHBIB ZENTARI, FEDERAL WATERWAYS ENGINEERING AND RESEARCH INSTITUTE, GERMANY
ANTOINE BEDOS, MARITIME RESEARCH INSTITUTE NETHERLANDS, THE NETHERLANDS
WIM VAN HOYDONCK, FLANDERS HYDRAULICS, BELGIUM
JENS LEY, DEVELOPMENT CENTRE FOR SHIP TECHNOLOGY AND TRANSPORT SYSTEMS, GERMANY
GUILLERMO CHILLCCE, UNIVERSITY OF DUISBURG-ESSEN, GERMANY

SUMMARY

The main objective of the SHINING research group is to establish a benchmark and best practices for the use of Computational Fluid Dynamics (CFD) methods to predict hydrodynamic forces acting on inland waterway ships. This paper presents selected results from the first three workshops to highlight the effect of shallow water on the hydrodynamic forces and moments acting on inland waterway ships. It emphasizes the ability of different CFD methods to capture the main flow features passing by inland waterway vessels in shallow water, considering computational accuracy and efficiency.

1 INTRODUCTION

Inland navigation in Europe faces several challenges, primarily due to climate change. Prolonged periods of low water levels severely affect the manoeuvrability of inland waterways vessels, leading to a shift toward comparatively more polluting modes of transport. To address this issue, a combined effort of policymakers, ship designers, and researchers is required to develop new guidelines and design inland waterway vessels better adapted to such c onditions. Achieving this goal first requires a comprehensive understanding of the hydrodynamics of inland vessels manoeuvring in extreme shallow waters, which will enable the development of suitable mathematical models for navigability analyses.

Given the widespread use of Computational Fluid Dynamics (CFD) methods in maritime research today, it is clear that these powerful tools can be leveraged to achieve this objective. However, computational studies on the manoeuvrability and self-propulsion of inland vessels in restricted waters remain scarce, particularly in terms of robust validation data and best CFD practices. Notable exceptions include studies such as Bedos and Tonelli (2022), Mucha, el Moctar, et al. (2017), Chillcce (2023), Zentari et al. (2022), and Lyu et al. (2024).

Manoeuvrability studies of seagoing vessels using computational and experimental methods have long been a focus of the maritime community. The renowned *SIMMAN2020* Workshop has established itself as a reliable source of high-quality validation data and best practices for CFD applied to manoeuvring problems (Quadvlieg, Flensborg Otzen, et al. 2023).

The SHallow water INland ships manoeuvrING (SHINING) research group aims to advance the common knowledge of six leading European institutions on extreme shallow water manoeuvring through a collaborative approach, inspired by the SIMMAN initiative. These institutions are, in alphabetical order, the German Federal Waterways Engineering and Research Institute (BAW), the Development Center for Ship Technology and Transport Systems (DST), Flanders Hydraulics (FH), the Maritime Research Institute Netherlands (MARIN), the University of Duisburg-Essen (UDE), and Rijkswaterstaat (RWS).

To systematically address the issue, the SHINING workshops were structured around the validation of virtual captive manoeuvring tests in deep and shallow water using state-of-the-art CFD methods. All institutions considered a representative inland waterway vessel, described in detail by Mucha, el Moctar, et al. (2017). To date, three workshops have been held, each focusing on the computational analysis of a specific captive planar motion.

The first workshop, held in May 2022 in Karlsruhe, Germany, was dedicated to predicting hydrodynamic forces and moments acting on a bare hull inland waterway vessel in quasi-steady drift te sts. The second workshop, held in March 2023 in Wageningen, the Netherlands, dealt with predicting hydrodynamic forces acting on the same bare hull inland waterway ship in quasi-steady circular tests. In the third workshop, held in February 2024 in Antwerp, Belgium, participants expanded on their results from the first two workshops by analysing hydrodynamic forces and moments acting on the inland ship in combined quasi-steady drift and circular m otion. The fourth workshop, scheduled for 2025 in Duisburg, Germany, will represent the culmination of these joint efforts, focusing on the effects of different computational setups on the manoeuvring predictions for a typical $135\,\mathrm{m}$ inland ship.

In this paper, our aim is to disseminate selected results of the first three workshops and summarise the main findings of the SHINING research group. This paper is structured as follows. First, the considered test cases are briefly presented, including the ship geometry and the test matrix for the first three workshops. This is followed by a summary of the main computational approaches of each participant. Finally, a presentation and discussion of key results from selected cases of the first three workshops is given, highlighting the main findings.

2 DESCRIPTION OF TEST CASE

The ship geometry used in the SHINING workshops is representative of a CEMT[1] class Vb inland waterway ship, typically operating on the Rhine. This test case, first designed and described in Mucha, el Moctar, et al. (2017), was further analysed in Mucha, el Moctar, et al. (2018) and Mucha, Dettmann, et al. (2019). Unlike seagoing test cases (e.g. KCS[2], DTC[3], KVLCC2[4], JBC[5]), this geometry is one of the few public inland waterway test cases, often referred to as the reference ship. The geometry is available upon request.

The design represents a typical inland vessel, suitable for various types of cargo, with two ducted propellers and four Schilling rudders. For our study, calculations were performed on the bare hull at a scale of 1:16, including a horizontal plate at the stern which aims to prevent propeller ventilation. The design draught of 3.5 m is typical for the lower Rhine area. The main ship's particulars, according to ITTC standards, are listed in Table 1 and the lines plan is shown in Figure 1.

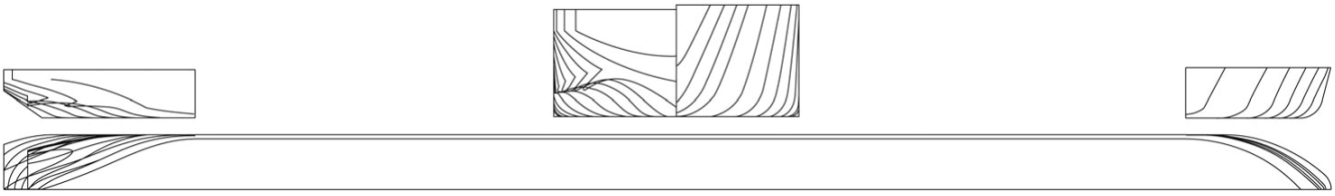

Figure 1: Reference ship bare hull lines.

Table 1: Main particulars of the reference ship (Mucha, el Moctar, et al. 2018).

Principal particulars	Symbol	Units	Full scale	Model scale
Scale	λ	-	1	16
Length at waterline	L_{WL}	m	134.42	8.4013
Length between perpendiculars	L_{PP}	m	135.0	8.4375
Length over All	L_{oA}	m	135.0	8.4375
Breadth at waterline	B	m	11.45	0.7150
Draught	T	m	3.50	0.2188
Wetted surface	S	m^2	2376.1	9.2817
Block coefficient	C_{B}	-	0.92	0.92
Displacement	∇	m^3	4992	1.2187
Mass	Δ_{m}	ton	4984.6	1.2169
Longitudinal centre of gravity (LCG)	X_{CG}	m	-0.1718	-0.01074

In this workshop, the participants relied on a common coordinate system. All hydrodynamic forces acting on the hull and ship motions are defined in a yawed-only direct coordinate system $R1$ (O, x, y, z). This system is nearly ship-fixed but does not rotate in roll and pitch, ensuring that the x- and y-axes remain in the horizontal plane. The coordinate system is defined as follows:

- The origin is ship-fixed and located at the intersection of the midship section (midway between APP and FPP), the centreline, and the waterline at rest.
- The x-axis is aligned with the ship's centreline and waterline at rest, pointing from stern to bow.
- The y-axis is defined by the intersection of the midship section and the waterline at rest, pointing to portside.

[1]Conférence Européenne des Ministres des Transports
[2]KRISO Container Ship
[3]Duisburg Test Case
[4]KRISO Very Large Crude Carrier
[5]Japan Bulk Carrier

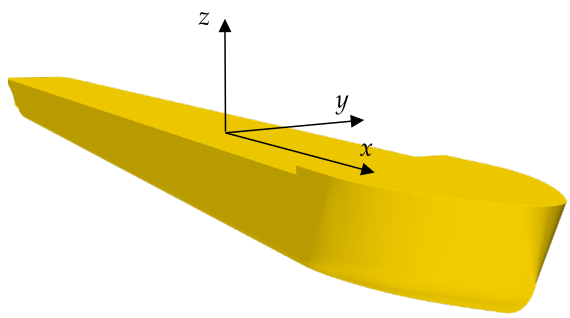

Figure 2: Body-fixed frame used in the workshops, defined at the intersection of amidship, water plane and ship's symmetry plane.

- The z-axis is in the earth-fixed vertical direction, pointing upward.

Figure 2 illustrates the yawed-only coordinate system used throughout the workshops.

Ship motion kinematic parameters such as drift angle β, non-dimensional yaw rate r' and ship reference velocity U_0 are defined as follows

$$U_0 = \sqrt{u^2 + v^2}, \qquad \beta = \text{arctan}\left(\frac{v}{u}\right), \qquad r' = \frac{r\,L_{PP}}{U_0}, \tag{1}$$

with u and v the velocity components in ship-fixed x- and y-axis, respectively. Hydrodynamic forces and moments acting on the bare hull of the inland waterway ship are the longitudinal force X', the lateral force Y', vertical force Z', roll moment K', pitch moment M' and yaw moment N'. These hydrodynamic forces and moments are non-dimensionalised using:

$$X' = \frac{X}{0.5\rho L_{\text{PP}} T U_0^2}, \qquad Y' = \frac{Y}{0.5\rho L_{\text{PP}} T U_0^2}, \qquad Z' = \frac{Z}{0.5\rho L_{\text{PP}} T U_0^2}, \tag{2}$$

$$K' = \frac{K}{0.5\rho L_{\text{PP}} T^2 U_0^2}, \qquad M' = \frac{M}{0.5\rho L_{\text{PP}} T^2 U_0^2}, \qquad N' = \frac{N}{0.5\rho L_{\text{PP}}^2 T U_0^2}. \tag{3}$$

In this paper, we examine selected cases from the three workshops, each addressing a specific captive manoeuvring test mode. Across all workshops, participants provided results for water depths ranging from $h/T = 3.0$ (deep water) to $h/T = 1.2$ (very shallow water). The first workshop focused on the ship in a quasi-steady drift condition. The second explored quasi-steady circular tests, and the third combined quasi-steady drift and circular motions. For clarity, Table 2 presents the test matrix, detailing the workshop, water depth-to-draught ratio h/T, ship velocity U_0, drift angle β, and non-dimensional yaw rate r'.

Table 2: Test matrix of all conditions investigated in SHINING WP1, WP2 and WP3.

Workshop	h/T	U_0 (m/s)	β (deg)	r'
WP1	3.0	0.556	0, 2, 4, 8, 12	0.0
WP1	1.5	0.556	0, 2, 4, 8, 12	0.0
WP1	1.2	0.556	0, 2, 4, 8, 12	0.0
WP2	3.0	0.556	0	0.1, 0.2, 0.3, 0.4, 0.5
WP2	1.5	0.556	0	0.1, 0.2, 0.3, 0.4, 0.5
WP2	1.2	0.556	0	0.1, 0.2, 0.3, 0.4, 0.5
WP3	3.0	0.556	-4	0.2, 0.4, 0.6, 0.8
WP3	1.5	0.556	-4	0.2, 0.4, 0.6, 0.8
WP3	1.2	0.556	-4	0.2, 0.4, 0.5
WP3	3.0	0.556	-12	0.4, 0.6, 0.8
WP3	1.5	0.556	-12	0.4, 0.6, 0.8

In parallel to the numerical investigation carried out as part of the SHINING workshop, MARIN performed model tests in shallow water with the reference ship in their offshore basin in fall 2023. The ship model was used in a captive set-up, restrained in surge, sway, roll and yaw, but free in heave and pitch. This set-up is further described in Hallmann and Quadvlieg 2015. The wooden model was built at the same model scale as for the CFD calculations ($\lambda = 1 : 16$), and was tested in a large range of conditions, including those indicated in Table 2. A subset of the results is shown in this article to provide an element of comparison to the numerical submissions. An extensive description of the experimental set-up and results will be part of an upcoming article.

3 NUMERICAL SETUPS

In this section, we present an overview of the numerical setups used by the participants to calculate the hydrodynamic forces and moments acting on the inland waterway ship in WP1, WP2, and WP3. Considering the wide range of numerical techniques used, this section focuses on highlighting the key lessons learned by all participants. In particular, solvers, turbulence models, meshing strategies, free surface treatment, and body motion methods are discussed briefly.

3.1 SOLVERS

Participants used four primary solvers to address the flow problem in each workshop, as detailed in Table 3, along with the corresponding institutions. Additionally, the table outlines the depth-to-draught ratios (h/T) investigated and the turbulence models used. All participants relied on RANS-based methods, with most using the classical two-equation k-ω SST model of Menter (1994) for turbulence closure. Exceptions include FH and UDE-2, which used a type of Reynolds stress turbulence model implemented in the FINE/Marine and STAR-CCM+ software packages, respectively.

Depending on the work package, participants tackled the problem using either an inertial or a body-fixed reference frame. In the inertial frame, the motion of the ship is modelled directly, while in the body-fixed frame, the flow is modelled as moving around a stationary ship. Each method offered its own advantages and disadvantages in terms of accuracy and computational time, but produced comparable results. Further details of these approaches can be found in Chillcce et al. (2025).

Table 3: Institutions and numerical procedures used through WP1, WP2 and WP3.

Institution	Solver	Frame	h/T	Turbulence model
BAW	STAR-CCM+	Inertial / Body-fixed	1.2, 1.5, 3.0	k-ω SST
DST	FINE/Marine	Inertial / Body-fixed	1.2, 1.5, 3.0	k-ω SST
FH	FINE/Marine	Inertial / Body-fixed	1.2, 1.5, 3.0	EASM
MARIN	ReFRESCO	Body-fixed	1.2, 1.5, 3.0	k-ω SST
UDE-1	OpenFOAM	Body-fixed	1.2, 1.5, 3.0	k-ω SST
UDE-2	STAR-CCM+	Body-fixed	1.2, 1.5, 3.0	RSM

3.2 MESHING STRATEGY

The flow around inland waterway ships manoeuvring in restricted waters is highly complex. Inland waterway vessels are comparatively bulkier and less optimised than their sea-going counterparts. Consequently, the flow is characterised by separations, recirculation zones, and significant vortex shedding. Accurate prediction of the hydrodynamic forces and moments acting on the hull therefore requires capturing the main flow features with high fidelity. This, in turn, necessitates well-adapted meshing strategies.

The workshop participants used similar meshing strategies, so this section focuses on their main features. First, it is crucial to capture the flow in the under-keel region. This requires sufficient vertical cell distribution, which consequently increases the total number of cells. Second, in order to resolve the high velocity and pressure gradients in the immediate vicinity of the ship, fine refinement zones were created around the ship. Particular attention was paid to the stern and bow regions, where sharp geometric edges required more refined meshing. Third, with few exceptions, participants relied on y^+ values below unity on the hull to fully resolve the flow in the boundary layer. In particular, at larger drift angles and rotation rates, a significant portion of the flow passing the ships may be separated, for which wall functions are less suitable.

To illustrate these strategies, Figures 3 and 4 present two mesh representations from different institutions. Figure 3 shows a transverse view of the numerical mesh at section $x = -0.45L_{pp}$, located at the stern of the inland waterway ship. This mesh was used in WP1 using the double-body method by the UDE partner. In this case, fine refinement zones were arranged uniformly around the hull to avoid hanging nodes. The total cell count for this mesh reached approximately $9 \cdot 10^6$ cells. Figure 4 presents a side view of the numerical grid around the inland ship for the calculation of forces in WP2 using the

rotating mesh approach. In this case, the BAW partner employed the overset grid technique, incorporating the free surface. As shown, particular emphasis was placed on refining the under-keel region, as well as the bow and stern areas. Due to the requirements of the overset grid approach, the cell count was comparatively higher, reaching approximately $13 \cdot 10^6$ cells.

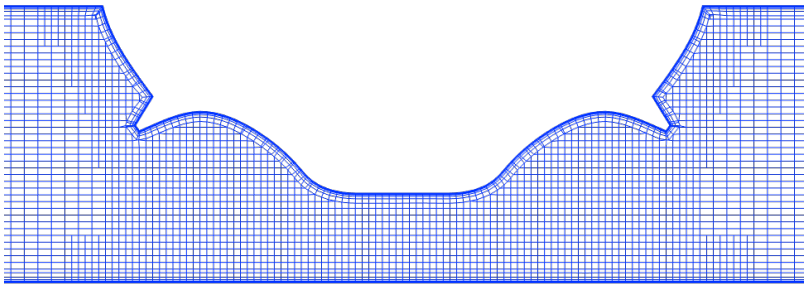

Figure 3: **Transverse view of the numerical mesh topology at section $x = -0.45L_{pp}$ used by UDE-2 in the WP1. The aim of the meshing strategy for this particular case was to produce a boundary layer with y^+ below one for the hull and the numerical domain bottom, and to have at least 20 control volumes between the numerical domain bottom and the ship bottom. The mesh was coarsened for visualization purposes.**

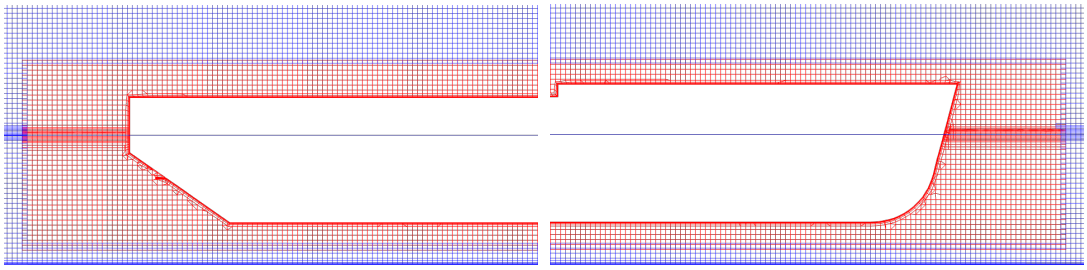

Figure 4: **Side view of the numerical grid around the inland waterway ship for the calculation of forces in WP2 using the overset-grid method, reproduced from Chillcce et al. (2025). Here, the red grid indicates the overset mesh, which moves with the ship; the blue grid indicates the background mesh. Also, the refinement of the free surface is visible on both overset and background meshes.**

3.3 FREE SURFACE AND BODY MOTION TREATMENT

According to ITTC recommendations (ITTC 2011), wave-making resistance becomes significant starting from a Froude Number F_n higher than approximately 0.12. It is thus acceptable to neglect the free surface for the simulation of ships advancing below this threshold value. However, the water-depth restriction has a significant impact on the trim and sinkage (squat) of a ship sailing in shallow and/or confined water, making accurate prediction of these values essential. However, due to high block coefficient of the vessel, values of trim for velocities below $F_n = 0.12$ are negligible. The robustness of numerical squat predictions depends on both the body-motion algorithm and the quality of the computational mesh around the floating body.

Within the SHINING workshop, participants used two main methods. The first, commonly integrated into the flow solvers used in this study, couples the flow solver with a body-motion solver. Here, a floating object dynamically reacts to fluid forces, necessitating the solution of a two-phase flow problem and a robust algorithm to manage mesh deformations caused by the ship's motion. For example, the solver *Simcenter STAR-CCM+* utilizes the Dynamic Fluid-Body Interaction (DFBI) solver (see Simcenter STAR-CCM+ CFD software 2023), which dynamically adjusts the floating position based on body constraints. This algorithm has demonstrated accuracy and robustness for squat predictions in restricted waters, as highlighted by Bechthold and Kastens 2020. A similar approach is implemented in the flow solver *ISIS-CFD*. Because of the static type of the test cases, a quasi-static simulation approach can be used to identify the hydrodynamic equilibrium to increase computational efficiency. The body's position is updated over a predefined period of time followed by an evolution interval in which the body is fixed to reach numerical convergence. This approach was used by DST and FH, for example.

When body-motion is considered, these algorithms require proper handling of the free surface. The Workshop participants predominantly relied on the Volume of Fluid (VoF) scheme, as implemented in their solvers. A precise refinement of the free-surface was necessary to obtain physical results, presenting thus a common bottleneck in the process. This refinement demanded careful grid adjustments at the interface, smaller time steps, and consequently, longer computational times. However, at the ship speed $U_0 = 0.556\,\mathrm{m/s}$, corresponding to a Froude number of $F_n = 0.061$, the inclusion of the free surface did not significantly influence the final results but was crucial for resolving body motion and predicting squat.

The second approach, introduced by Chillcce 2023, overcame this issue by resolving the body motion problem in a double-body, single-phase setup. Utilizing a Newton-Raphson algorithm, this method iteratively corrects the ship's motion based on the balance of vertical (hydrodynamic and gravity) forces acting on the ship. Although this technique is not extended to include trim, the predicted sinkage values closely correlate with the measured towing tank data. At higher ship speeds ($F_n > 0.12$), the inclusion of the free surface becomes indispensable, as wave-making resistance increases with higher Froude numbers. In contrast, in shallow water, most ships operate at lower speeds, primarily driven by safety considerations.

The SHINING group limited the scope to vertical water-depth restrictions. In narrow channels, the inclusion of the free surface may be necessary, even at lower speeds.

4 RESULTS AND DISCUSSION

To provide a snapshot of the findings from the investigations in WP1, WP2 and WP3, we focus on the shallowest water depth analysed, $h/T = 1.2$. In WP1, we performed steady drift tests with the ship model at drift angles β ranging from 0 to $12°$. WP2 involved steady rotation tests for non-dimensional yaw rates r', spanning values from 0.1 to 0.5. For a comprehensive overview of the test parameters, refer to Table 3.

This section compares the computed values of non-dimensional longitudinal force X', lateral force Y', and yaw moment N' from all participants. Figure 5 presents these forces for the quasi-steady drift scenario, while Figure 6 illustrates the corresponding results for the quasi-steady rotation tests and Figure 7 shows these results for the combined drift and rotation. The individual results of the participants are not shown in these figures. Instead, for each condition the average and standard deviation of all contributions are displayed. For comparison, for a small subset of the conditions, experimental results are added as well.

For the quasi-steady drift case (Figure 5), the results are remarkably consistent, especially at lower drift angles up to $8°$. Beyond this range, some discrepancies emerge, likely due to variations in the computational setups employed in WP1. For instance, the BAW results exhibit a broader spread at higher drift angles. This divergence is attributed to the partner's use of a narrow computational domain, designed to replicate the size of the physical test facility of DST. Such lateral confinement introduces increased forces due to blockage effects. The highest standard deviation in the CFD-results was observed for the non-dimensional longitudinal force X'. Nevertheless, the variety of setups — both with and without free-surface modeling — had a minimal impact on the computed forces at the velocity under consideration. At $\beta = 4°$, the experimental results differ very little from the numerical results. The difference increases somewhat for $\beta = 8°$, especially for the yawing moment.

The same comparison exercise yields different results when analysing the quasi-steady rotating arm test (Figure 6). In this case, the scatter of the forces is notably more significant. For instance, the difference between the highest and lowest computed X' force approaches $15\,\%$. A similar trend is observed for the Y' force, particularly at higher rotation rates. However, the key driving quantity in rotating arm tests, the yaw moment N', remains remarkably consistent across all contributions (numerical and experimental).

Examining the results for the rotating arm cases with drift (Figure 7), similar observations can be made as for the pure rotating arm cases with the difference that for the yawing moment N', the standard deviation of the numerical results reduces with increasing r'. This is caused by differences in the slope of the results and the change in sign of N' at intermediate values of r'.

The observed differences in X' may be attributed to the sensitivity of this quantity to turbulence modeling approaches. For example, the UDE method employed the Reynolds-Stress Model (RSM) for turbulence closure, which accounts for the anisotropy of turbulence by resolving all components of the Reynolds stress tensor. This approach resulted in higher longitudinal force predictions. Despite these variations, a clear conclusion emerges: the scatter in longitudinal force values is largely independent of the non-dimensional rotation rate r', whereas the scatter in sway forces (Y') and yaw moments (N') exhibits a dependency on r'. Specifically, the scatter in Y' and N' increases as r' grows.

In summary, computations of drift forces demonstrated relatively low sensitivity to variations in the computational setup. In contrast, rotating arm simulations were significantly more sensitive, particularly at higher rotation rates for the Y' force.

The specific pressure distributions on the hull caused by pure drift and pure rotation are shown exemplarily in Figure 8 for the highest drift angle $\beta = 12°$ and for the largest turning rate $r' = 0.5$ at $h/T = 1.2$. In these figures, dark red around the bow marks high pressure, with adjacent blue zones indicating lower pressure. This pattern aligns with typical flow behaviour, where high pressure corresponds to low velocity, and blue zones signify accelerating flow.

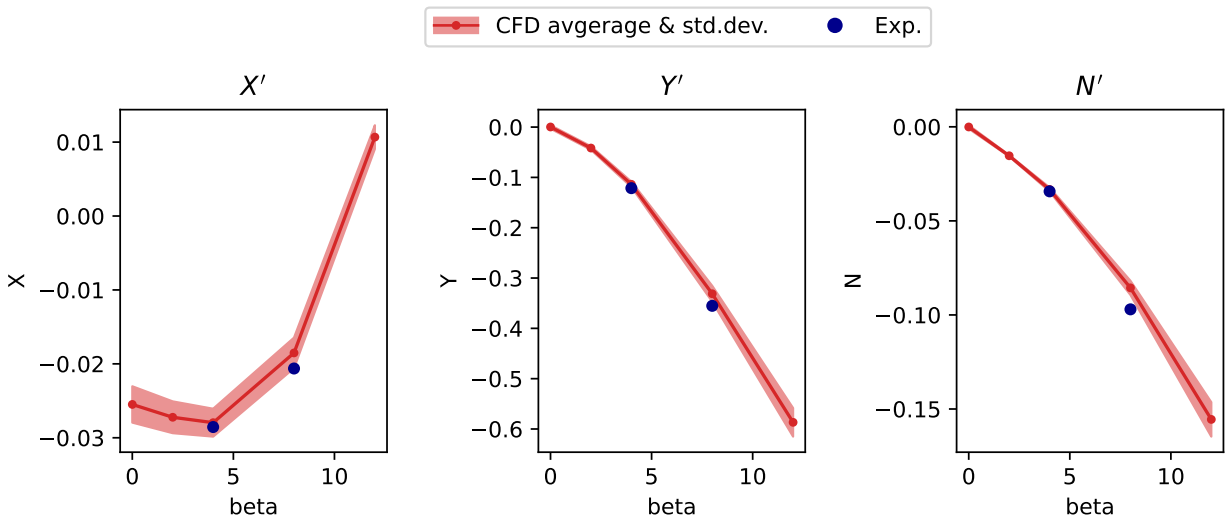

Figure 5: **Average hydrodynamic forces and moments acting on the hull at $h/T = 1.2$ during pure drift (WP1).**

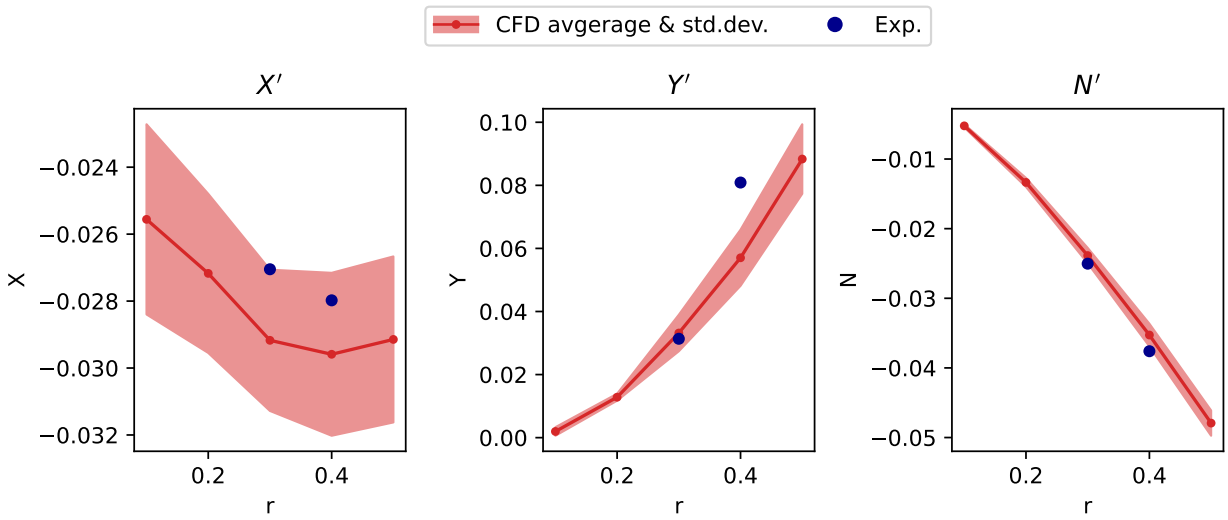

Figure 6: **Average hydrodynamic forces and moments acting on the hull at $h/T = 1.2$ during pure rotation (WP2).**

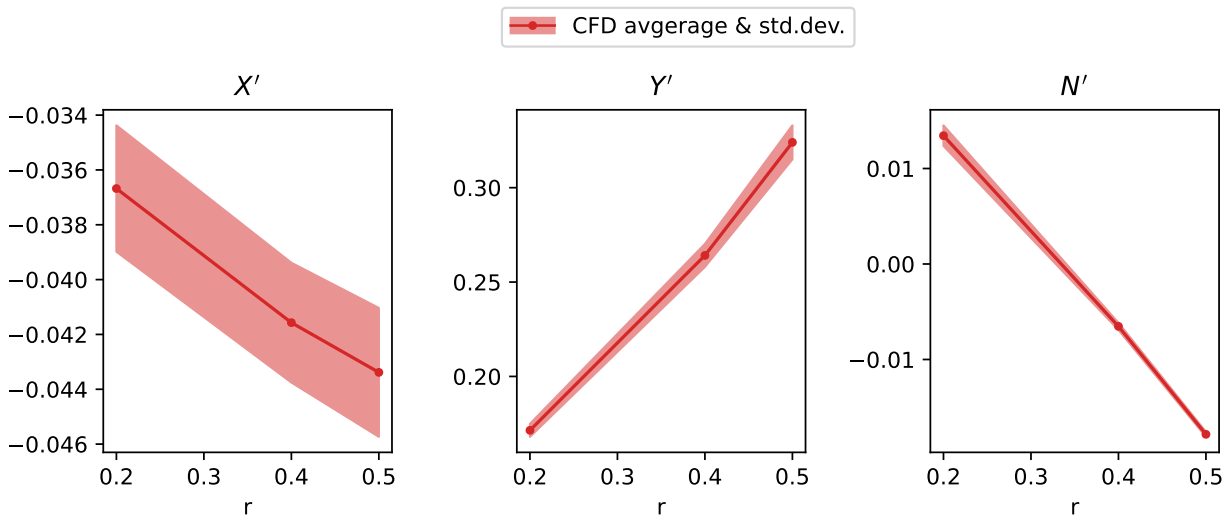

Figure 7: **Average hydrodynamic forces and moments acting on the hull at $h/T = 1.2$ and $\beta = -4°$ during combined drift and rotation (WP3).**

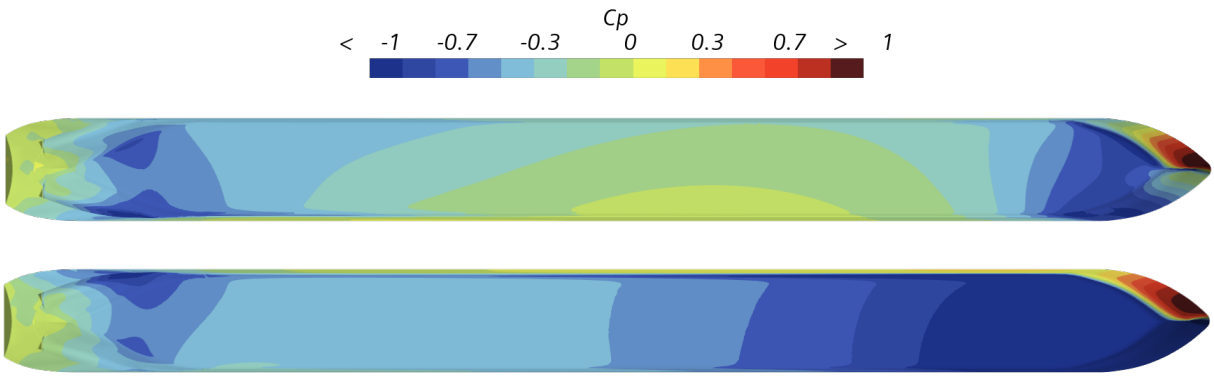

Figure 8: Distribution of pressure coefficient on the hull for the cases pure rotation at $r' = 0.5$ (top) and pure drift at $\beta = 12°$ (bottom). Both cases computed for $h/T = 1.2$ using the same method.

5 FUTURE WORK AND OUTLOOK

The first three work packages of the SHINING workshop focused on the capabilities of numerical methods to predict hydrodynamic loads of an inland waterway ship hull operating in shallow and extreme shallow water. The immediate next step is to propose an extensive comparison of these results against experimental data and offer a validation study of these techniques. The integration of the propulsion and steering effects, and their contribution to hydrodynamic loads, will be a future point of attention. In parallel, the gap between predicted hydrodynamic loads and simplified manoeuvring models required for ship-handling simulators will be bridged. The objective of the next work package is to investigate how the shallow-water effects identified by the CFD results presented above can be implemented in manoeuvring models in a reliable way, and how sensitive simulated sailing trajectories are to the predicted hydrodynamic loads. The knowledge gained can be used to formulate future requirements for calculation methods and to improve the dynamic behaviour of inland vessels in ship handling simulators for operations on very low water levels.

From a wider perspective, the inland waterway transport faces major challenges to remain safe and climate resilient. The different actors of the sector must work hand in hand to develop new navigation guidelines and design the ships of tomorrow. The SHINING research group shows a good example of the benefits of cooperating at a national and international level to tackle these challenges.

6 ACKNOWLEDGEMENTS

The authors would like to thank Roberto Tonelli (MARIN), Frans Quadvlieg (MARIN) and Jan Kaufmann (DST) for their detailed suggestions and the fruitful discussions during the workshops. The research by MARIN was partly funded by the Dutch Ministry of Economic Affairs. The research by UDE was partly supported by the Federal Ministry for Economic Affairs and Energy (Bundesministerium für Wirtschaft und Energie) of Germany through the project FernBin (project number 03SX506F).

7 REFERENCES

Bechthold, J. and Kastens, M., Feb. 2020. Robustness and quality of squat predictions in extreme shallow water conditions based on RANS-calculations. In: Ocean Engineering 197, p. 106780. DOI: 10.1016/j.oceaneng.2019.106780.

Bedos, A. and Tonelli, R., 2022. An Extensive Experimental Investigation of Shallow- and Confined-Water Effects on the Manoeuvring Forces of a 110m Inland Ship. In: MASHCON conference, pp. 1–9.

Chillcce, G., 2023. Mathematical Models for Manoeuvring under Realistic Environmental Conditions. en. PhD thesis. University of Duisburg-Essen. DOI: 10.17185/duepublico/81271.

Chillcce, G., Zentari, L., Van Hoydonck, W., Bedos, A., Ley, J., Gornicz, T., Yang, Y., Oud, G., Tenzer, M., Rzeszutko, J., and el Moctar, O., Feb. 2025. Numerical calculation of hydrodynamic forces on inland waterway vessels during circular motion in shallow and extreme shallow waters. In: Ocean Engineering 318, p. 120095. DOI: 10.1016/J.OCEANENG.2024.120095.

Hallmann, R. and Quadvlieg, F., 2015. Instationary captive model tests. In: International Conference on Ship Manoeuvrability and Maritime Simulation (MARSIM), Newcastle, UK.

ITTC, 2011. Practical guidelines for ship CFD applications. In: Proceedings of the 26th International Towing Tank Conference. International Towing Tank Conference.

Lyu, W., Kaufmann, J., Ley, J., Tenzer, M., and Schellin, T. E., 2024. An efficient method to simulate ship self-propulsion in shallow waters and its application to optimize hull lines. In: Ocean Engineering 312, p. 119238. DOI: https://doi.org/10.1016/j.oceaneng.2024.119238.

Menter, F., Aug. 1994. Two-equation eddy-viscosity turbulence models for engineering applications. In: AIAA Journal 32.8, pp. 1598–1605. DOI: 10.2514/3.12149.

Mucha, P., Dettmann, T., Ferrari, V., and el Moctar, O., Feb. 2019. Experimental investigation of free-running ship manoeuvers under extreme shallow water conditions. In: Applied Ocean Research 83, pp. 155–162. DOI: 10.1016/j.apor.2018.09.008.

Mucha, P., el Moctar, O., Dettmann, T., and Tenzer, M., May 2017. Inland waterway ship test case for resistance and propulsion prediction in shallow water. In: Ship Technology Research 64.2, pp. 106–113. DOI: 10.1080/09377255.2017.1349723.

Mucha, P., el Moctar, O., Dettmann, T., and Tenzer, M., Nov. 2018. An experimental study on the effect of confined water on resistance and propulsion of an inland waterway ship. In: Ocean Engineering 167, pp. 11–22. DOI: 10.1016/j.oceaneng.2018.08.009.

Quadvlieg, F., Flensborg Otzen, J., Stern, F., Yasukawa, H., Kim, Y.-G., Wentao, W., and Yang, H., 2023. Analysis of submissions for forces and moments in captive conditions. In: Workshop on Verification and Validation of Ship Manoeuvring Simulation Methods, pp. 37–66, 93–112.

Quadvlieg, F., Stern, F., Kim, Y.-G., Flensborg Otzen, J., Yasukawa, H., Wang, W., and Han, Y., eds., 2024. SIMMAN2020. Workshop on Verification and Validation of Ship Manoeuvring Simulation Methods (July 17–19, 2023).

Simcenter STAR-CCM+ CFD software, 2023. https://www.plm.automation.siemens.com/global/en/products/simcenter/STAR-CCM.html. Siemens Digital Industries Software.

Zentari, L., el Moctar, O., Lassen, J., Hallmann, R., and Schellin, T., Apr. 2022. Experimental and numerical investigation of shallow water effects on resistance and propulsion of coupled pusher-barge convoys. In: Applied Ocean Research 121. DOI: 10.1016/j.apor.2022.103048.

8 AUTHORS BIOGRAPHY

Lahbib Zentari is a research engineer at the federal waterways engineering and research institute (BAW) in Karlsruhe. His research interests are CFD methods applied to shallow water manoeuvring problems, ship-waterway interaction and ship-handling simulators.

Antoine Bedos holds the position of Senior Project Manager at MARIN in the Netherlands. He is conducting experimental and numerical research for the maritime industry, with a focus on shallow-water and manoeuvring applications.

Wim Van Hoydonck obtained his PhD at Delft University of Technology and is nautical researcher at Flanders Hydraulics. His research interests include the application of numerical methods to ship aerodynamics and shallow water hydrodynamics problems.

Jens Ley graduated in 2009 in Naval Architecture at the University of Duisburg-Essen (UDE). His research activities covered ship motions and loads in waves, hydroelasticity effects and wave induced added resistance. Since 2018 he is heading the department for ship design and simulations at DST. His current research is related to hydrodynamics of inland waterway ships and shallow water effects. He is assistant lecturer at UDE.

Guillermo Chillcce is a research scientist at the Institute for Autonomous and Sustainable Maritime Systems (INAM) of the University of Duisburg-Essen (UDE). His expertise covers numerical methods applied to manoeuvring under realistic environmental conditions.

COMBINING NUMERICAL AND EXPERIMENTAL METHODS TO EXPLAIN SHIP-BANK INTERACTIONS

Bedos, Antoine, MARIN, The Netherlands

Gornicz, Tomasz, MARIN, The Netherlands

Tonelli, Roberto, MARIN, The Netherlands

COMBINING NUMERICAL AND EXPERIMENTAL METHODS TO EXPLAIN SHIP-BANK INTERACTIONS

BEDOS, ANTOINE, MARIN, THE NETHERLANDS
GORNICZ, TOMASZ, MARIN, THE NETHERLANDS
TONELLI, ROBERTO, MARIN, THE NETHERLANDS

SUMMARY

Bank effects refer to the suction and repulsion forces a ship experiences when sailing near a bank. Recently, various factors have driven the maritime community to gain a deeper understanding of this phenomenon. In inland waterways, increasing traffic and repeated low-water episodes result in ships operating in increasingly confined environment, leading to stronger interactions with banks and other ships. This paper compares experimental and numerical methods in a straightforward test case involving a representative 135m inland waterway ship sailing along a vertical bank. The study examines the total loads and squat of the ship at various distances to the bank and under-keel clearances, ranging from 300% to 20%. It also verifies several new functionalities in the MARIN in-house CFD package ReFRESCO, which can be used for calculations of complex scenarios involving ships navigating in confined and shallow water.

NOMENCLATURE

δ	Rudder angle (deg)
λ	Linear scale ratio (-)
ρ	Fresh-water density (1,000 kg/m^3)
θ	Pitch angle (deg)
A_C	Cross-sectional area of the waterway (m^2)
A_S	Ship's underwater midship cross-sectional area (m^2)
B	Ship breadth (m)
C_P	Dynamic pressure coefficient (-)
d	Distance between the ship side and the bank (m)
d/B	Non-dimensional distance to bank (-)
F_r	Froude number (-)
F_{rh}	Depth Froude number (-)
F'_X	Ship surge force (-)
F'_Y	Ship sway force (-)
h	Water depth (m)
h/T	Water depth-to-draught ratio (-)
L_{PP}	Ship length between perpendiculars (m)
M'_Z	Ship yaw moment (-)
T	Ship draught at rest (m)
RPM	Propeller revolution rate (1/min)
S	Blockage factor A_S/A_C (-)
V_{cr}	Critical canal speed (km/h or m/s)
V_s	Ship speed (km/h or m/s)
y+	Thickness of the first viscous layer cell (-)
BAW	German Federal Waterways Engineering and Research Institute
CFD	Computational Fluid Dynamics
CFD FS	CFD calculations at full scale
CFD MS	CFD calculations at model scale
EXP	Experiments
MARIN	Maritime Research Institute Netherlands
DST	Development Centre for Ship Technology and Transport Systems
SHINING	Shallow Water Inland Ships Manoeuvring working group
VoF	Volume of Fluid

1 INTRODUCTION

Bank effects (or ship-bank interactions) describe the hydrodynamic interaction between a sailing ship and a nearby boundary of the sailing area, typically a quay in ports or a bank on inland waterways. The restricted space influences the flow and pressure fields around the ship, altering its navigation behaviour compared to a fully unrestricted environment.

Research on bank effects was initiated in the mid-20th century, but regained interest in the last few years following recent events. In 2021, the 20,000 TEU container vessel Ever Given collided with a bank of the Suez Canal and obstructed it for several days, illustrating the race for ever larger ships sailing through very confined channels and locks. In inland waterways, the increasing traffic and repeated low-water episodes result in ships sailing in increasingly confined environment and experiencing stronger interactions with banks. A large share of the research consists in predicting the increase in resistance and squat when sailing near a bank (Lataire et al., 2015, Raven, 2019;), or in deriving reduced-order models to quantify the suction and repulsion forces resulting from the ship-bank interaction (Norrbin, 1985; Delefortrie et al., 2024).

These models aim to be implemented in ship-handling simulators for crew training, design of ports and waterways, accident investigations, and definition of guidelines and regulations. Navigation models must be reliable for comprehensive and complex scenarios, including shallow and confined waterways with dense and potentially dangerous traffic situations. The prediction of ship-bank interactions within these models needs to be accurate enough to result in a realistic behaviour, and fast enough to calculate the hydrodynamic loads in real time. These tools are essential to ensure safe and efficient navigation of vessels in confined environment. As an example, Bedos et al. (2019) investigated the impact of an irregular bank on the sailed trajectory of an inland ship in a river and the risk of collision with a nearby bridge. Mai et al. (2021) assessed the effects of manoeuvring near a bank and in shallow water for an autonomous ship by means of simulations. Verwilligen et al. (2022) studied the accessibility of the Ghent-Terneuzen canal for the widest allowed ship, in a very restricted and irregular area.

Model tests have been and remain a favoured way to study this complex physical interaction. However, they require significant resources, especially when investigating a large range of ship types and bank geometries. The progress of Computational Fluid Dynamics (CFD) capabilities and its affordability has made numerical predictions a promising complement to model-scale experiments. To build up confidence in the numerical set-ups for such applications and learn more about the underlying physics, it is crucial to benchmark the performance of CFD techniques. This was done for example in Van Hoydonck et al. (2019), which compares a large range of prediction methods to experiments for the KRISO Very Large Crude Carrier (KVLCC2). This need for benchmarking is particularly critical for applications on inland waterways, as they are facing tremendous challenges with the higher seasonal variations of water level and widths of sailable corridors.

This paper compares experimental and numerical results of a test case considering a reference inland waterway vessel sailing along a vertical bank. It documents the experimental and numerical set-ups, and shows ship-bank interaction forces applied to the ship for various water depths and distances to the bank. It also presents a detailed analysis of the predicted flow fields, to understand better the underlying physics and the challenges for prediction techniques in extreme conditions. Finally, the study investigates potential scale effects for such application.

2 TEST CASE

The ship investigated in this study is a representative 135m inland ship of CEMT-class Vb, typically travelling on the river Rhine. This benchmark ship was designed in 2014 by the Federal Waterways Engineering and Research Institute (BAW) and the Development Centre for Ship Technology and Transport Systems (DST). This public hull is the test case of experimental studies focusing on the resistance, propulsion and manoeuvring performance of inland ships in shallow water (Mucha et al., 2017, 2018, 2019). More recently, this reference ship was selected in the SHINING workshop to investigate CFD techniques to predict manoeuvring forces and moments in shallow water (Chilcee et al., 2025).

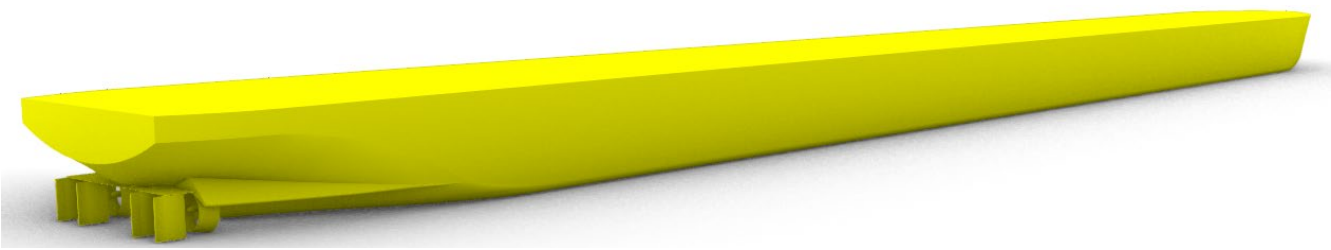

Figure 1. Isometric view of the ship geometry.

Figure 1 shows the ship geometry. The main particulars of the inland waterway ship and its appendages are detailed in Table 1. Characteristics are given for the full scale and at a linear scale ratio of λ = 1:16, since the investigation was mostly conducted at model scale. The ship is equipped with a conventional twin-shaft arrangement with two ducted propellers and four fishtail-type rudders with an endplate. The propellers have a diameter 1.6 m and rotate inward over the top. The duct geometry is similar to the 19A type, but is trimmed horizontally at the bottom at the height of the baseline. The projected lateral area of the rudders is about 4 x 2.36 m^2, which corresponds to 4 x 0.50%·L_{PP}·T. Mucha et al. (2017) provide further information about the aft-ship arrangement.

This study compares numerical and experimental methods to determine ship-bank interactions for the reference ship in shallow water. To ensure a fair comparison, both methods aim at using the same set-up. The ship sails along a regular bank that consists of a vertical wall located on the port side of the ship. A parallel vertical wall is located on the starboard side, further away from the ship. The distance between the two side walls is about 22.1 times the ship width, mimicking a waterway with straight vertical walls. The ship is towed in a semi-captive condition where the surge, sway, roll and yaw motions are imposed, while the heave and pitch are free. This ensures a more realistic equilibrium of forces, as the squat may be large in shallow and confined water and has a strong sensitivity to the hydrodynamic loads, even at low speeds.

Table 1. Main particulars of the inland waterway ship and its appendages.

Designation	Symbol	Full scale	Model scale
Linear scale ratio (-)	λ	1	16
Length between perpendiculars (m)	L_{PP}	135.0	8.438
Breadth moulded on waterline (m)	B	11.44	0.715
Draught at rest, even keel (m)	T	3.50	0.219
Displacement volume (m^3)	∇	4,991.5	1.219
Propeller diameter (m)	D	1.6	0.100
Pitch ratio at 70% radius (-)	P/D	1.000	1.000
Expanded blade area ratio (-)	A_E/A_0	0.679	0.679
Number of blades (-)	Z	4	4
Rudder height (m)	b	1.726	0.108
Rudder chord (m)	c	1.370	0.086

The ship is sailing straight at a constant speed V_s with zero drift and roll. The investigation includes various distances between the portside bank and the closest ship side *d*, and various water depths *h*. They are expressed in a non-dimensional way, as a ratio of the ship breadth (*d/B*) and ship draught at rest (*h/T*). The propellers are rotating at a fixed revolution rate (*RPM*), that is close to the model-scale self-propulsion point at the given water depth but in horizontally-unrestricted water. The rudders are fixed to their neutral angle. Table 2 lists the stationary conditions that are presented in this article.

Table 2. Matrix of stationary conditions (quantities are indicated at model scale).

Configuration	h/T (-)	Vs (m/s)	d/B (-)	RPM (1/min)	δ (deg)	F_{rh} (-)	V_s/V_{cr} (-)	EXP (-)	CFD MS (-)	CFD FS (-)
Appended	3.0	0.972	1.5	303	0	0.38	0.45	✓	✓	✓
Appended	1.5	0.972	1.5	322	0	0.54	0.69	✓	✓	✓
Appended	1.2	0.972	1.5	341	0	0.61	0.79	✓	✓	✓
Appended	1.5	0.972	2.5	322	0	0.54	0.69	✓		
Appended	1.5	0.972	2.0	322	0	0.54	0.69	✓	✓	
Appended	1.5	0.972	1.0	322	0	0.54	0.69	✓	✓	
Appended	1.5	0.972	0.5	322	0	0.54	0.69		✓	

EXP: experiments, CFD MS: CFD calculations at model scale, CFD FS: CFD calculations at full scale

All conditions are performed at the model-scale speed of 0.972 m/s, which corresponds to 14 km/h at full scale and a Froude number of F_r = 0.107. The depth Froude F_{rh} number ranges between 0.38 and 0.61. The cross-section of the waterway results in a horizontal restriction and potential confinement effects. The lowest water depth results in a blockage factor of S = 4.5%. The critical canal speed (or Schijf-limiting speed) V_{cr} is the speed that ships cannot exceed due to the energy balance between the continuity equation and Bernoulli's Law (Schijf, 1949). The most extreme condition is performed at a relatively high-speed corresponding to $V_s = 0.79 \cdot V_{cr}$, which is an interesting stress test both for the experimental and numerical set-ups.

3 EXPERIMENTAL AND NUMERICAL SET-UPS

The experimental campaign was held at MARIN in 2024. The model tests were carried out in the Shallow-Water Basin, which measures 220m x 15.8m in length and width. Its bottom is a fixed concrete floor. The water level can be adjusted between 0 and 1.1 m by pumping water in or out.

The testing facility features a towing carriage that travels in the longitudinal direction. The ship model is fixed to the carriage by means of 2 cardan joints. Both cardan joints have a heave and pitch freedom, and the backward joint have an additional surge freedom. In that way, the ship model is free to heave and pitch, but is restricted in all other directions. Each cardan joint is mounted on a force measurement frame, from which the hydrodynamic loads on the ship model are recorded. Figure 3 shows the basin carriage and the test set-up. More information on the basin can be found in Tonelli et al., 2015, including a study on the roughness of the basin bottom and its compliance with the ITTC shallow water guidelines.

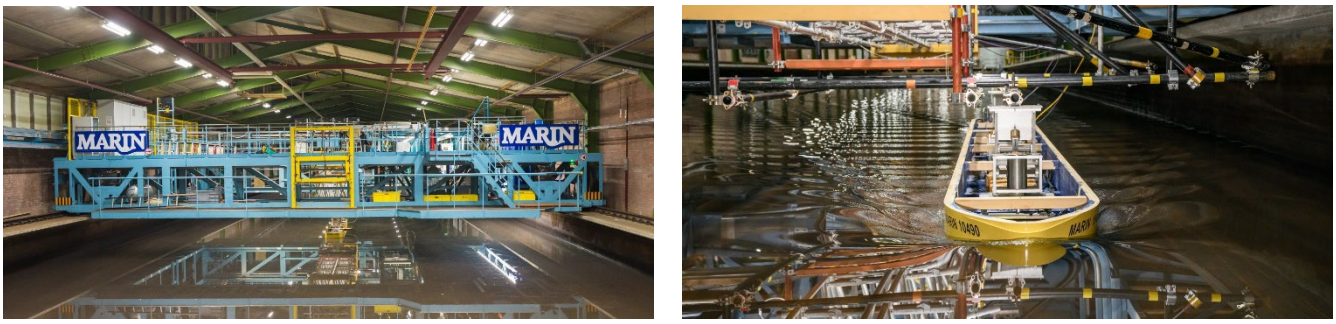

Figure 3. MARIN's Shallow-Water Basin and test set-up.

The calculations are performed with MARIN's CFD package ReFRESCO, which solves multiphase steady and unsteady incompressible viscous flows using the Navier-Stokes equations, complemented with turbulence models. The reliability, robustness and accuracy of the code have been tested for a large range of applications, such as in Bhushan et al. (2019). The ship domain is discretised with unstructured hexahedral elements generated with the commercial software Hexpress. The height of the first cell near the wall $y+$ is kept under 0.1 to resolve the boundary layer and guarantee the turbulence model's stability. Table 3 summarises the main particulars of the numerical domain and mesh.

Table 3. Numerical domain and mesh.

Parameter name	Values
Computational domain size (m)	93 x 15.8 x 26
Type of grid (-)	Unstructured, hexahedral
Number of grid cells (-)	30-50 million
Thickness first viscous layer cell (-)	$y+$ ~ 0.08

Figure 4 shows a 3D view of the domain as well as some details of the grid at the ship stern. The width of the domain is equivalent to the width of the towing tank where the experiments are conducted. In the calculations, the ship is free to heave and pitch by means of a quasi-static method. The computed squat is modelled through local grid deformation using radial basis functions. All vertical side boundaries are modelled as inflow boundaries with a fixed velocity condition. The top of the domain is implemented as a pressure boundary with homogeneous condition for the pressure. The bottom is modelled as a no-slip wall. The k-ω SST (2003) model from Menter (1994) is used in the URANS turbulence equations. This turbulence model offers good robustness and accuracy for this type of application, and was successfully used in numerous ship hydrodynamic-related CFD computations, such as in Bhushan et al. (2019).

A second-order (limited) scheme is employed for the spatial discretisation of the momentum equations, while the turbulence equations are solved using a first-order upwind discretisation. The linear systems from both of these equations are solved using a GMRES solver with a block Jacobi preconditioner. The pressure system is solved using a preconditioned Conjugate Gradient method (Klaij and Vuik, 2013). The resulting set of equations is solved in a segregated manner. A two-phase flow (water and air) is simulated using the Volume of Fluid (VoF) approach.

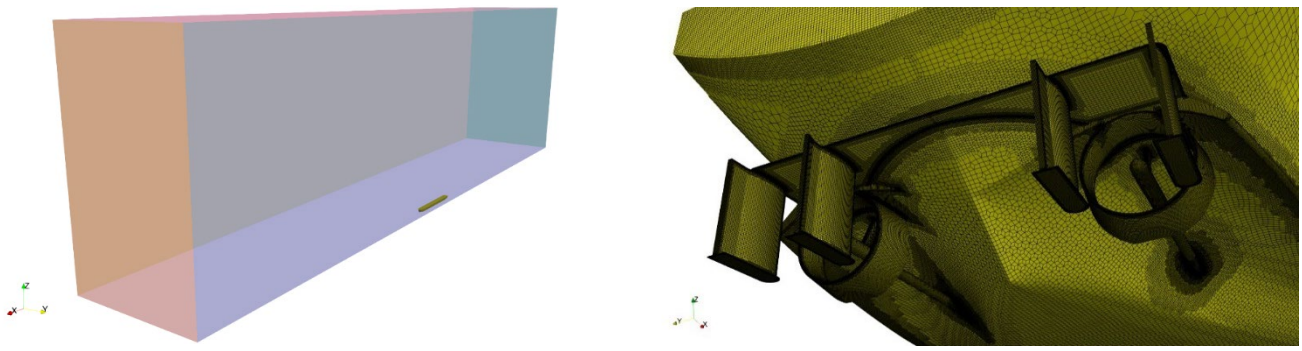

Figure 4. Computational domain (left) and details of the grid at the ship stern (right).

The time-dependent simulations are solved with a first-order (implicit Euler) time integration method. The time step is chosen to 2% of the characteristic time L_{PP}/V_s. The equation governing the free-surface transport uses three sub-cycling steps within each outer-loop iteration.

New ReFRESCO features are verified in these simulations. These improvements include a better correction for grid non-orthogonality, helping to achieve a higher order of discretisation. The grid deformation enabling trim and sinkage, which uses radial-based functions, is also revised to maintain a higher grid quality after deformation. Besides, free-surface sub-cycling is optimised, allowing different time steps to solve momentum and free-surface equations, therefore drastically reducing calculation costs. Finally, the latest version of adaptive grid refinement is implemented to increase grid density in the relevant regions, such as vortices or flow separations.

4 RESULTS AND DISCUSSION

This section presents and discusses the main findings of the study. It is divided into three aspects: the effect of the under-keel clearance, the effect of the distance to the bank, and the scale effects. To refer to the different configurations, figures use the following labels:

- **EXP**: experimental results.
- **CFD MS**: CFD calculations at model scale.
- **CFD FS**: CFD calculations at full scale.

Ship forces and moments are expressed in a ship-fixed coordinate system R_0. The origin is located at the intersection between the midship section (station 10), the centreline, and the waterline at rest. The x-, y-, and z-axes point forward, to portside, and upward respectively.

The ship sway force and yaw moment are given in a non-dimensional form, using the ship speed V_s, fresh-water density ρ and draught at rest T. These non-dimensional loads are defined as follows:

$$F_Y' = \frac{F_Y}{0.5\,\rho\,L_{PP}\,T\,V_s^2} \qquad M_Z' = \frac{M_Z}{0.5\,\rho\,L_{PP}^2\,T\,V_s^2} \tag{1}$$

With F_Y and M_Z the sway force and yaw moment respectively. The effect of confinement on the surge force has been studied in detail in numerous earlier publications, therefore it is not the point of attention of this paper. The dynamic sinkage z' is expressed as a ratio of the ship draught:

$$z' = -\frac{z}{T} \tag{2}$$

4.1 EFFECT OF UNDER-KEEL CLEARANCE

This section presents the results at an intermediate distance to bank of d/B = 1.5 for various water depths. Figure 5 shows the sway force and yaw moment acting on the ship at water depth-to-draught ratios of h/T = 3.0, 1.5, and 1.2. In all conditions, the ship experiences a transversal suction force (positive F_Y') towards the vertical bank. The centre of application of this force is located aft of midship, as illustrated by the bow-out yaw moment (negative M_Z'). The intensity of the bank effect increases as the under-keel clearance decreases. These first observations are consistent with the experience of shippers and other research studies on bank effects (Lataire et al., 2009, Delefortrie et al., 2024).

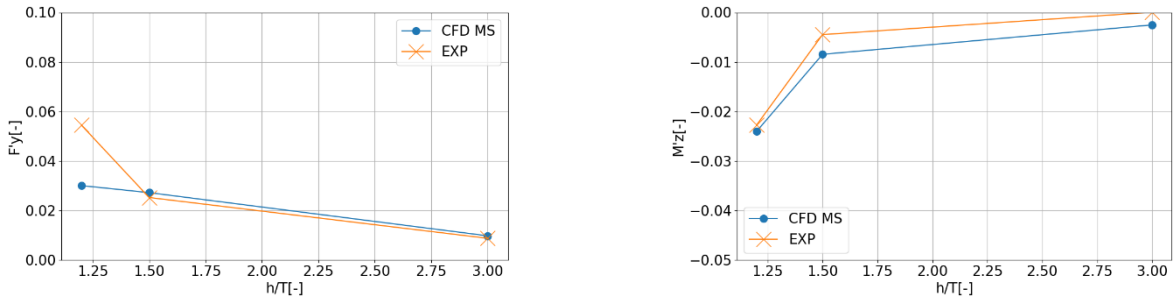

Figure 5. Ship sway force and yaw moment at various water depths (*d/B* = 1.5, F_r = 0.107).

The model tests and numerical predictions show a good qualitative agreement, with the exception of the transverse force in the shallowest condition (*h/T* = 1.2). In this case, the CFD calculation predicts a similar F'_Y compared to a slightly deeper case (*h/T* = 1.5), while the experiments show an increase of more than 100% between these two under-keel. The complexity of predicting accurately the transverse component of the bank suction in such extreme shallow water was also identified in previous investigations, such as a comprehensive study considering the sea-going crude carrier KVLCC2 (Van Hoydonck et al., 2019). The source of the discrepancy is not entirely known. However, the experimental F'_Y results in the shallowest condition were very sensitive to propeller rotation rate. In the cases with the water-milling propeller, no sudden increase in the F'_Y was found. This indicates that an accurate modelling of the flow around the propellers in the shallowest case is critical. In the CFD calculations, the propellers were simulated using the actuator disk model, which could be too simple to mimic the behaviour of the propellers in cases with the smallest under-keel clearance. Indeed, at low under-keel clearance the propeller inflow velocity reduces due to the hull blockage effect, characterised by an increase in wake fraction. In severe conditions, flow separation in front of the propeller can even occur. The increase in propeller loading substantially affects the dynamic pressure and hydrodynamic force distributions, but is not captured by the actuator disc model.

Figure 6 presents the results of the squat. The dynamic sinkage increases as the under-keel clearance decreases, going from around 0.03 in the deepest case (*h/T* = 3.0) to more than 0.10 in the shallowest condition (*h/T* = 1.2) based on experimental results. The trim angle remains however very small and never exceeds -0.06 deg (stern down).

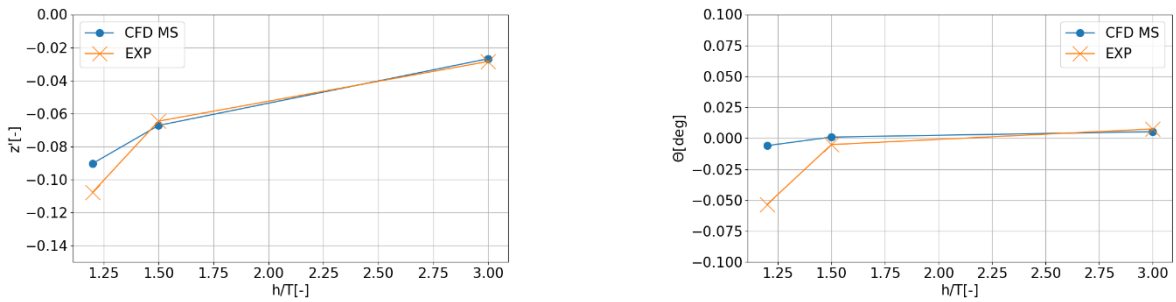

Figure 6. Dynamic trim and sinkage at various water depths (*d/B* = 1.5, F_r = 0.107).

The numerical predictions share the same trends as the model tests and have an excellent agreement up to *h/T* = 1.5. In lowest under-keel clearance, CFD results slightly underpredicts the dynamic sinkage and trim (stern down) compared to the model tests. This may partially explain the underprediction in F'_Y for this condition.

CFD allows to look more in-depth at the underlying physical phenomena, for instance by looking at the force distribution along the hull, the dynamic pressure coefficient on the appended ships and on the waterway bottom and side wall, and the longitudinal velocity fields. Figure 7 presents the distribution of the transverse bank-suction force F'_Y at each station (i.e. a ship cross-section). Integrating this force along the complete hull results in the same total F'_Y indicated in Figure 5. Similarly, integrating this force while multiplying by the distance to midship results in the total yaw moment M'_Z.
The ship bow experiences a repulsion force from the bank between stations 16 and 20, which is slightly behind the fore-shoulder. The transverse force reverses from this point and until the beginning of the tunnel, approximately at station 3. In this range where the ship cross-section is constant, the force is directed towards the bank. The forces vary more in the aft ship, but a small suction force can be observed between stations 0 and 1, at the location of the rudders and ducts.

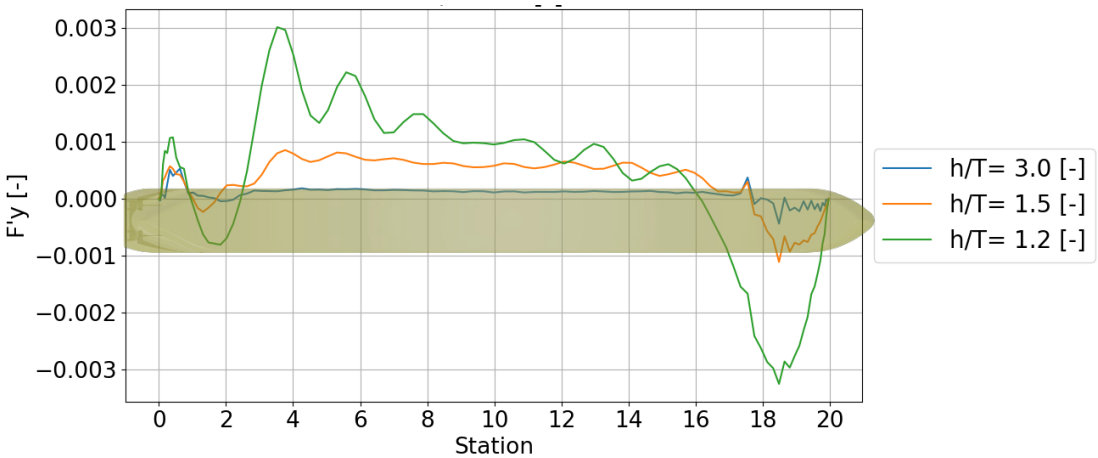

Figure 7. Distribution of sway force along the hull at various water depths (*d/B* = 1.5, F_r = 0.107).

The under-keel clearance has a very strong effect on the intensity of the local transverse force. The integrated repulsion force at the bow varies with more than a factor 5 between *h/T* = 1.5 and *h/T* = 1.2. The suction force along the midship cross-section increases also to the same extent. However, the total F_Y' predicted by the CFD calculations has the same intensity, as pointed out in Figure 5. This evidences that the transverse bank force is a force of low intensity, resulting from the difference between two large forces of opposite directions. Therefore, a minor prediction error of either of these forces will result in a large error of the total bank suction force. This may partly explain the challenges to reliably and accurately predict such force with numerical methods for extreme shallow-water conditions such as *h/T* = 1.2. On the other hand, both these forces result in yaw moments of the same sign. Therefore, the numerical prediction of the yaw moment may then be less sensitive to the CFD modelling.

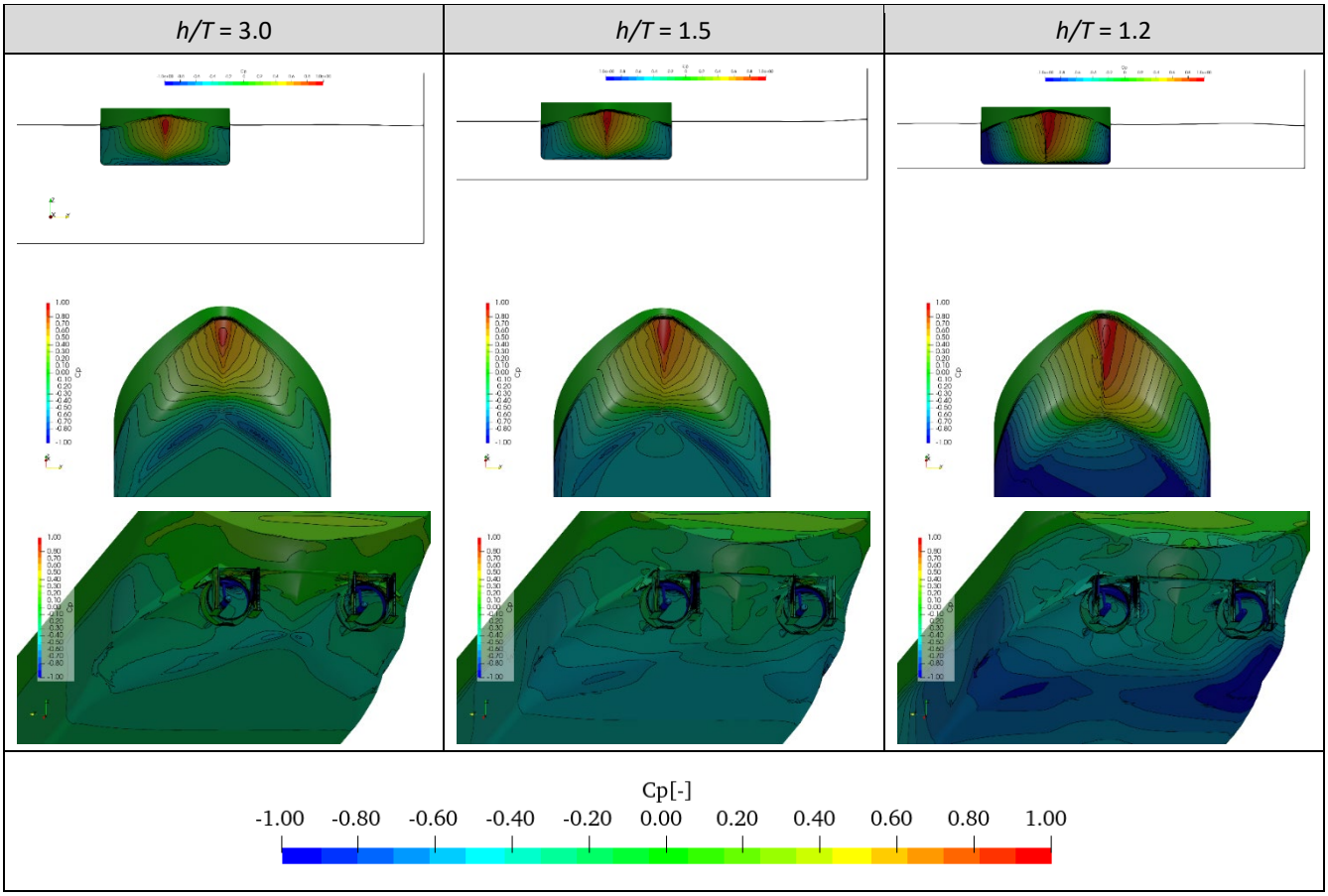

Figure 8. Dynamic pressure coefficient on the appended ship at various water depths (*d/B* = 1.5, F_r = 0.107).

Figure 8 plots the dynamic pressure coefficient on the bow and stern of the appended ship. The same high-pressure and low-pressure regions can be observed at all water depths, but with an increasing intensity as the under-keel clearance decreases. At *h/T* = 1.2, the strong low-pressure area on the ship bottom illustrates the accelerated flow travelling under the ship keel and explains the increased squat. At the same time, the asymmetry in the pressure field becomes more marked between the portside and starboard side of the hull, in particular at the bow.

Similarly, Figure 9 shows the dynamic pressure coefficient on the waterway bottom and bank surrounding the ship. It can be seen that the zone of influence of the ship grows in shallower water, both in the longitudinal and transverse directions. At *h/T* = 1.5 and lower, this zone extends to the opposite bank of the waterway. This emphasizes the confinement effect on the ship, which then interacts with both vertical walls.

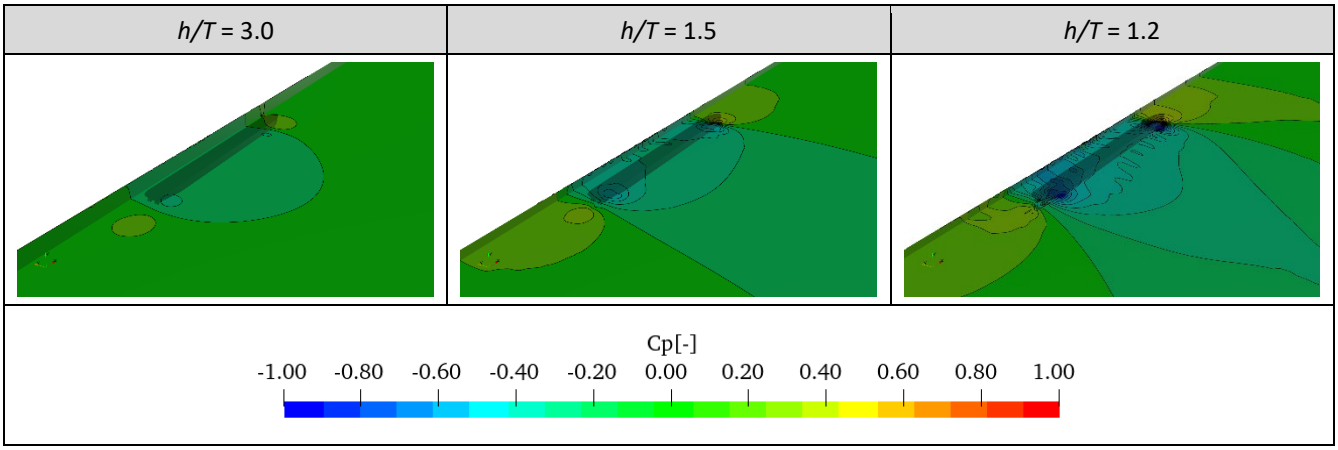

Figure 9. Dynamic pressure coefficient on waterway bottom and side wall at various water depths (*d/B* = 1.5, F_r = 0.107).

Figure 10 displays the flow longitudinal velocity between the ship and the bank for cross-sections located at ship stations 0, 10 and 17. The blue colour in the flow field indicates where the water is still. The red colour shows the regions where the flow velocity is opposite to the direction of the ship, evidencing a return flow. The purple colour represents the boundary layer, indicating the regions where the flow travels in the same direction as the ship.

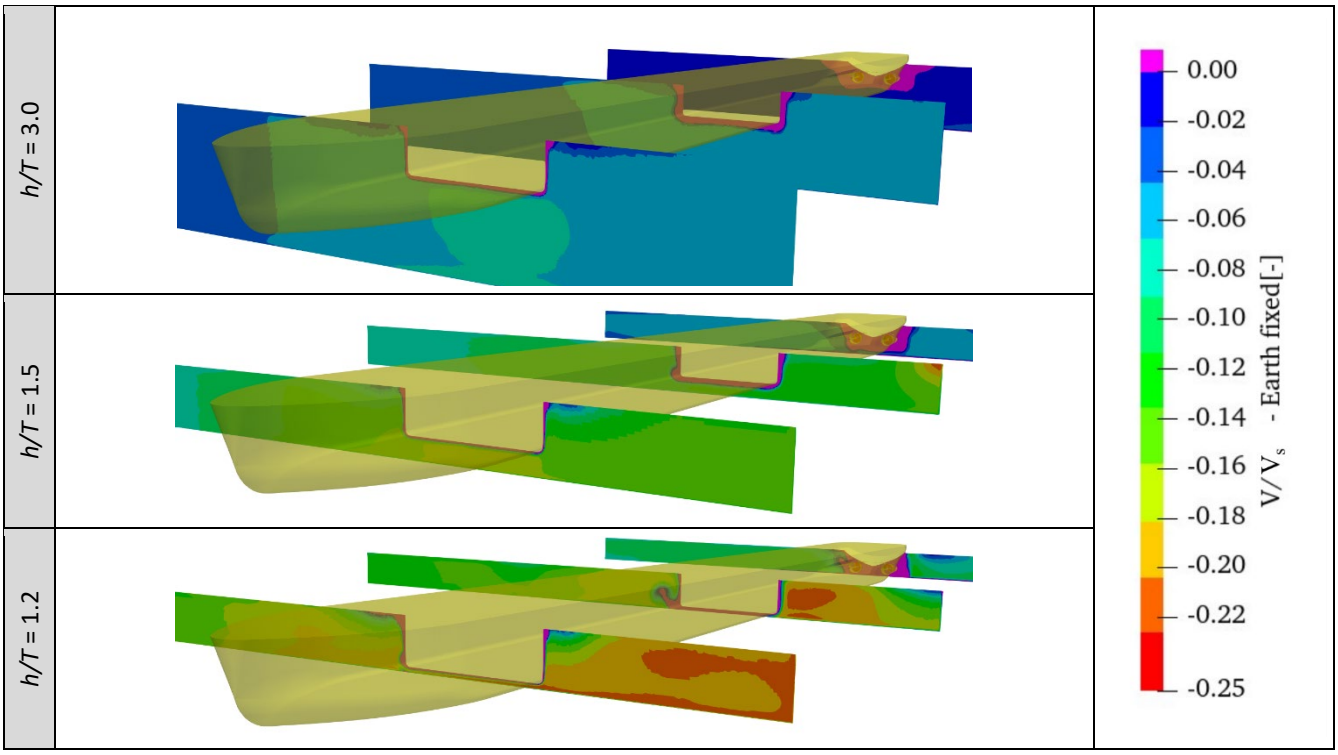

Figure 10. Longitudinal velocity fields at stations 0, 10 and 17 between the ship and vertical bank at various water depths (*d/B* = 1.5, F_r = 0.107).

Figure 10 shows that the under-keel clearance strongly influences the intensity of the return flow under the ship, between the ship and the closest bank, but also on the open side (here starboard side). The deep-water case evidences little disturbance of the flow field between the ship and the side wall. The water displaced by the ship travels under the ship, where the return flow is in the range of -0.08V_s. As the water level decreases, less water can travel under the hull. It is instead displaced laterally, and in particular between the hull and the closest wall. In the case *h/T* = 1.2, the magnitude of the return flow velocity is up to 25% of the ship speed in the region near the side wall. It can also be seen that the return flow is more pronounced in the bow than near the stern. The lower cross-section area at the stern and the suction of the propellers contribute to this phenomenon.

As a summary of the previous observations, the results show a high sensitivity of the ship-bank interactions to the under-keel clearance. Even at a distance to the closest bank as far as *d/B* = 1.5 (more than 17 m at full scale), the magnitude of the repulsion force at the bow and the suction force on the rest of the ship increase by at least a factor two between *h/T* = 1.5 and *h/T* = 1.2. Sudden variations in water depth may result in unexpected bank effects, demanding immediate correction from the captain to limit the change in trajectory.

4.2 EFFECT OF DISTANCE TO BANK

This section explores the sensitivity of the bank effects to the distance between the ship and the bank, indicated as *d/B*. Figure 11 shows the sway force and yaw moment acting on the ship at a distance to the bank *d/B* between 2.5 and 0.5, for a sailing speed V_s of 0.972 m/s and an intermediate water depth-to-draught ratio of *h/T* = 1.5. This speed and confinement can typically be encountered in rivers and canals, with a blockage factor *S* of 3%, a depth Froude number F_{rh} of 0.54, and a speed corresponding to 76% of the critical canal speed V_{cr}. Nevertheless, the narrowest distance between the ship and the bank is *d/B* = 0.5, which is about 5.7 m at full scale and is considered as an extreme condition.

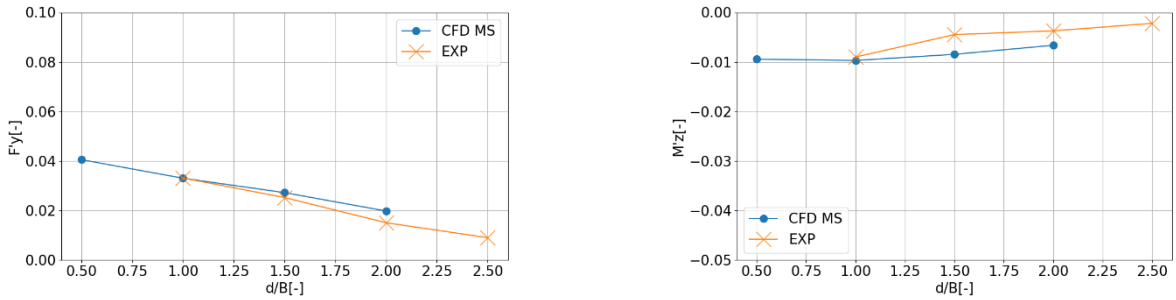

Figure 11. Ship sway force and yaw moment at various distances to the bank (*h/T* = 1.5, F_r = 0.107).

As expected from literature, the ship experiences a transversal suction force (positive F'_Y) towards the vertical bank. The centre of application of this force is located behind midship, as illustrated by the bow-out yaw moment (negative M'_Z). The intensity of the bank effect increases as the distance to the bank reduces. The results show a roughly linear trend for this range of *d/B* and more modest compared to the trend observed with respect to the water depth. Figure 12 shows that the squat is only mildly impacted by the distance to the bank, with only minor differences between *d/B* = 2.5 and 0.5. Experiments and numerical predictions show comparable trends.

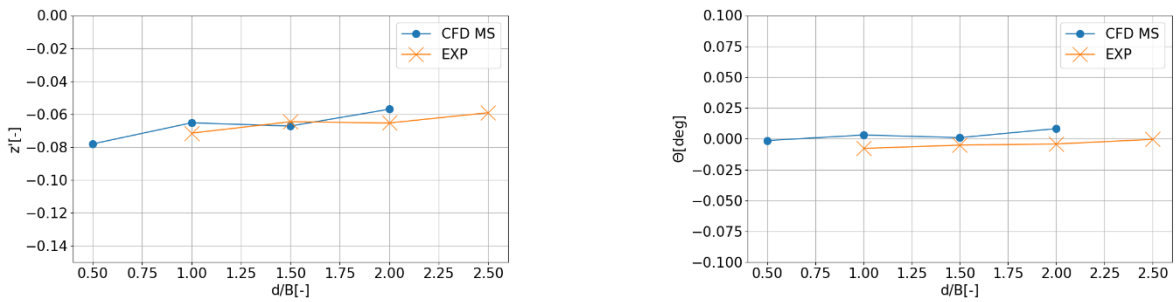

Figure 12. Dynamic trim and sinkage at various distances to the bank (*h/T* = 1.5, F_r = 0.107).

Figure 13 presents the distribution of the transverse bank-suction force F'_Y at each station. All distances to bank show a magnitude of the repulsion force at the bow of a comparable order, slightly increasing as the ship gets closer to the bank. A similar observation can be made about the suction force spread over the midship cross-section.

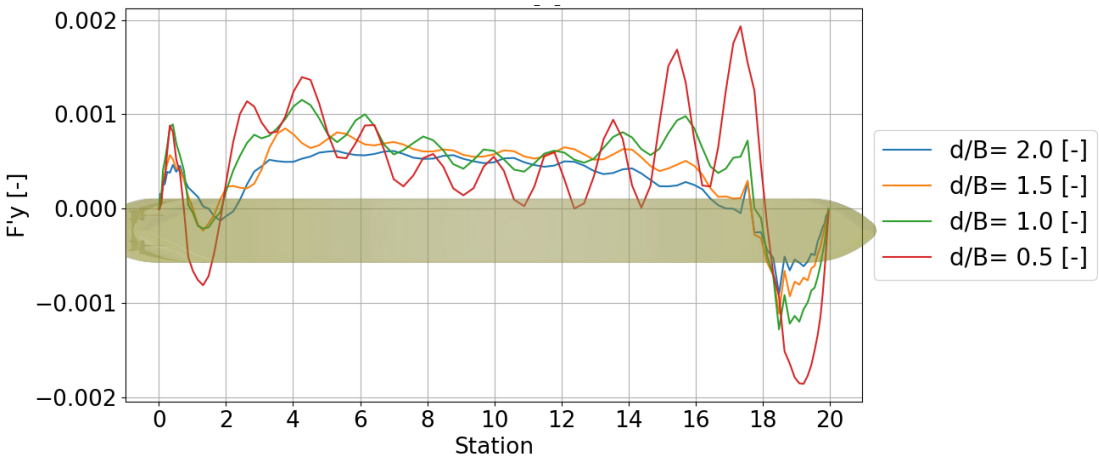

Figure 13. Distribution of sway force along the hull at various distances to the bank (*h/T* = 1.5, F_r = 0.107).

This can also be seen in Figure 14, which displays the dynamic pressure coefficient on the bow and stern of the appended ship. The pressure gradients are qualitatively similar at all distances to bank, with slightly more pronounced asymmetry at *d/B* = 0.5. This can be seen in the low-pressure peak on the port side of the ship bottom near the fore shoulder.

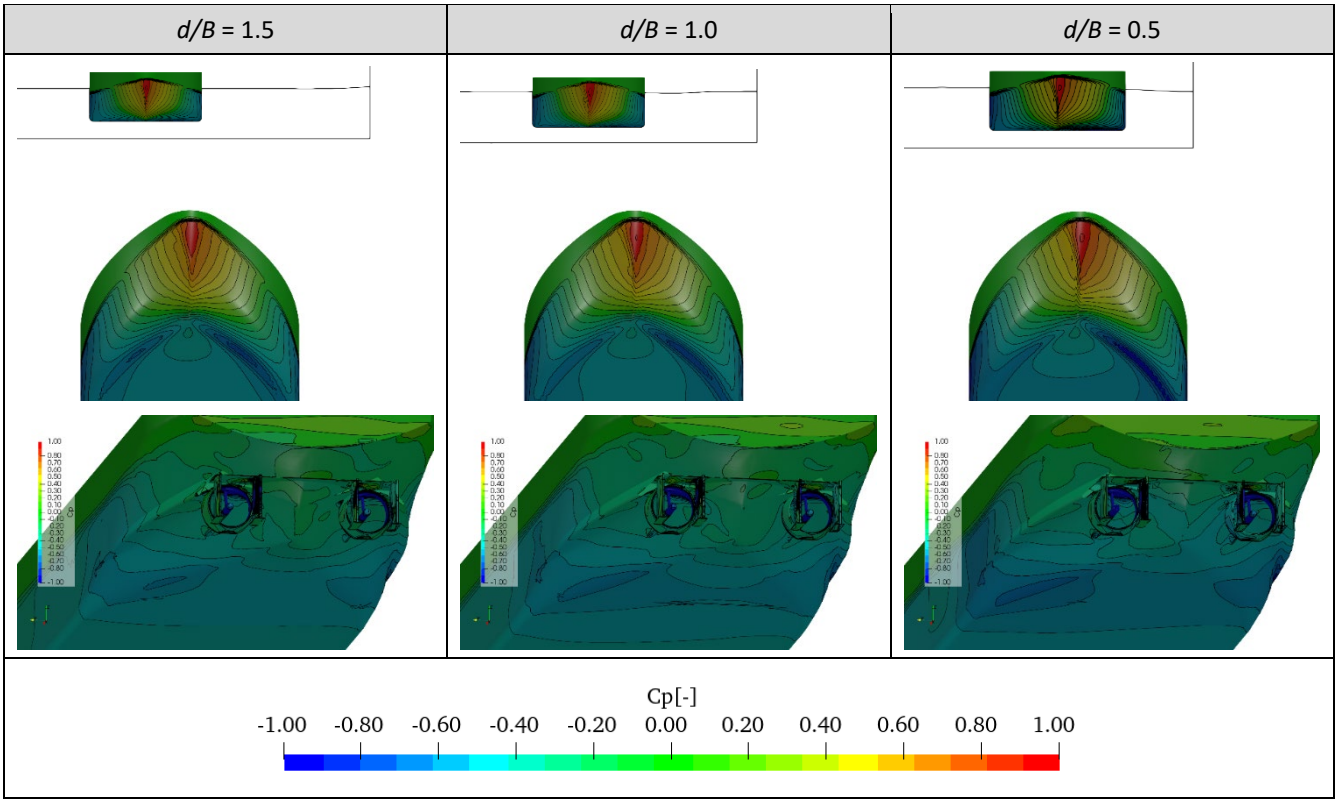

Figure 14. Dynamic pressure coefficient on the appended ship at various distances to the bank (*h/T* = 1.5, F_r = 0.107).

Figure 15 shows the dynamic pressure coefficient on the waterway bottom and bank surrounding the ship. It can be seen that the zone of influence of the ship is similar for all three cases, since they all correspond to the same blockage coefficient. Nevertheless, the intensity of the pressure on the wall is greater when the ship is closer, as expected. This illustrates the risks of degradation of natural banks, which are under more stress when ships sail too close.

Figure 16 displays the flow longitudinal velocity between the ship and the bank for cross-sections located at ship stations 0, 10 and 17. The variation in *d/B* shows similar trends as the variation in *h/T* on the velocity field near the ship. The return flow speed between the ship and the bank, in particular at the bow (station 17), is particularly sensitive to *d/B*. At this water depth, only a limited amount of water can flow under the keel and must therefore travel to the sides. When the area between the ship and the bank is too small, for example in the case *d/B* = 0.5, the return flow near the bank is sucked under

the hull, not only moving backwards but also from portside to starboard. This can be seen by the eddy on the starboard side of the hull on station 10 slice.

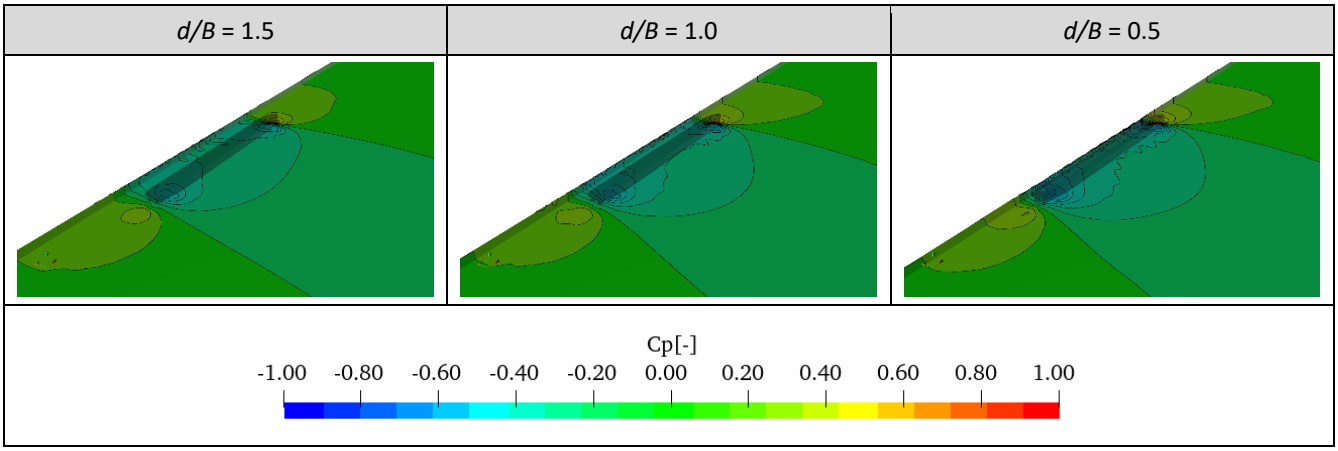

Figure 15. Dynamic pressure coefficient on waterway bottom and side wall at various distances to the bank (*h/T* = 1.5, F_r = 0.107).

As a summary, the test case illustrates the sensitivity of the ship-bank interactions to the distance between the ship and the bank. The hydrodynamic loads seem to increase linearly as the ship is closer to the bank, but keeping the same order of magnitude for the range of distances investigated in this study. Experiments and numerical predictions show comparable results.

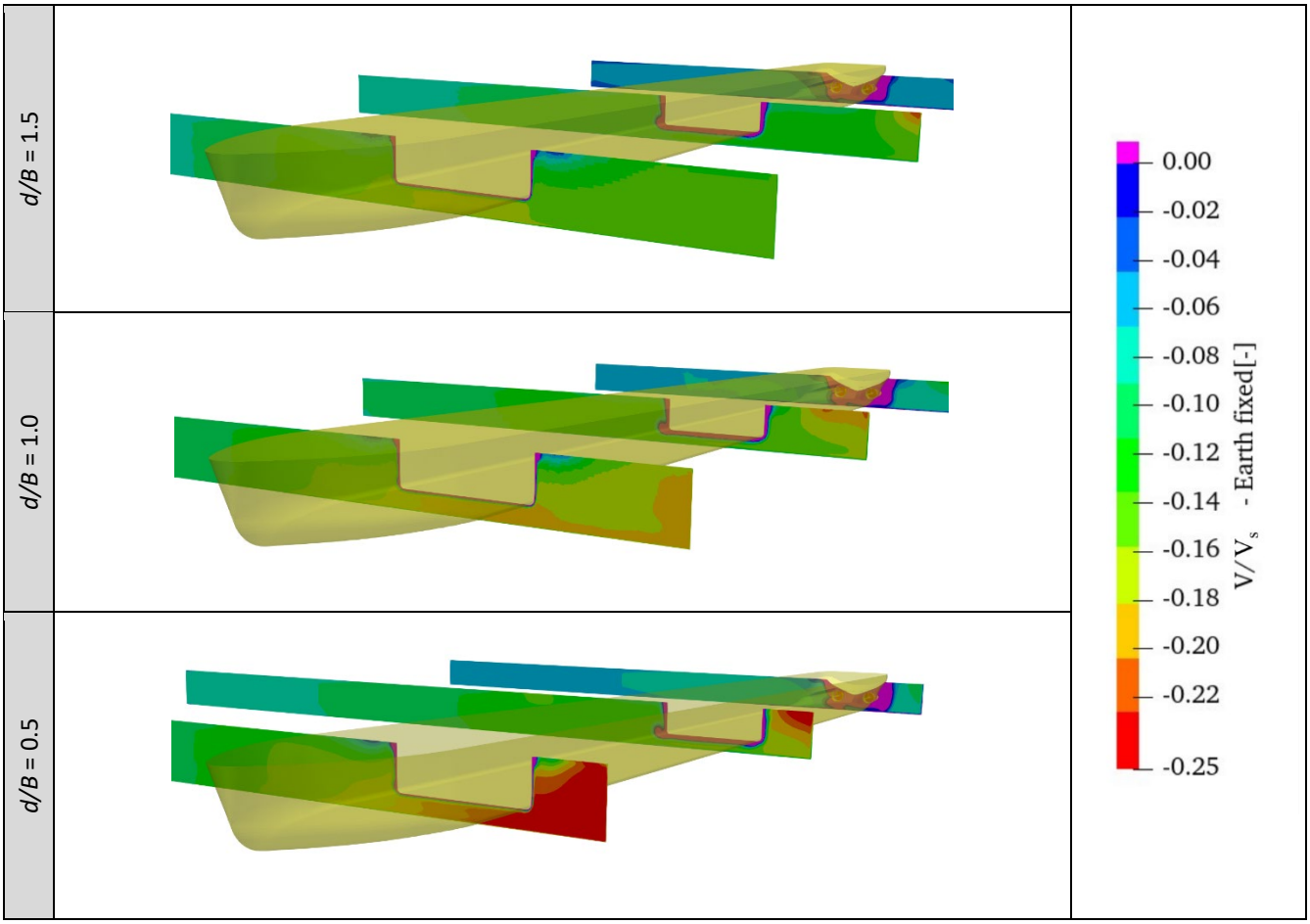

Figure 16. Longitudinal velocity fields at stations 3, 10 and 17 between the ship and vertical bank at various distances to the bank (*h/T* = 1.5, F_r = 0.107).

4.3 SCALE EFFECTS

To investigate scale effects related to bank effects, additional full-scale CFD calculations were carried out and are presented in this section. Figure 17 shows the sway force and yaw moment acting on the ship at a distance to the bank *d/B* of 1.5 and water depth-to-draught ratios *h/T* of 3.0, 1.5, and 1.2. The most tangible difference between model-scale and full-scale predictions is observed in the shallowest case. However, this is known to be a challenging condition resulting from the difference between two large forces of opposite directions, as observed earlier.

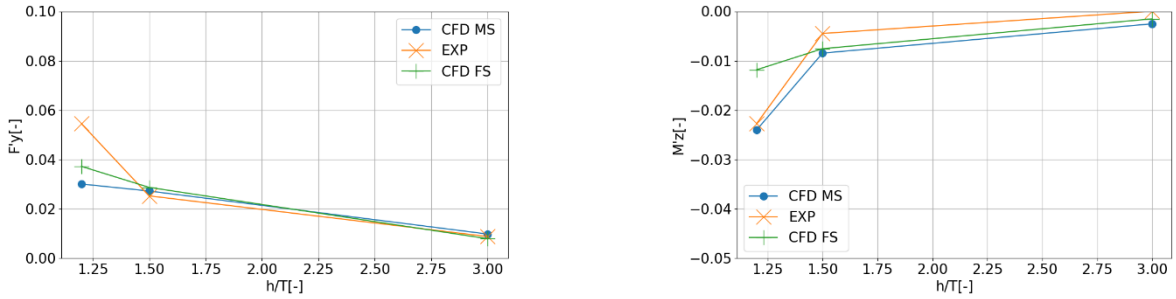

Figure 17. Ship sway force and yaw moment at various water depths, model and full scale (*d/B* = 1.5, F_r = 0.107).

Figure 18 displays the dynamic pressure coefficient at the stern of the appended ship. The pressure gradients are qualitatively the same, with some more marked differences in the shallowest condition.

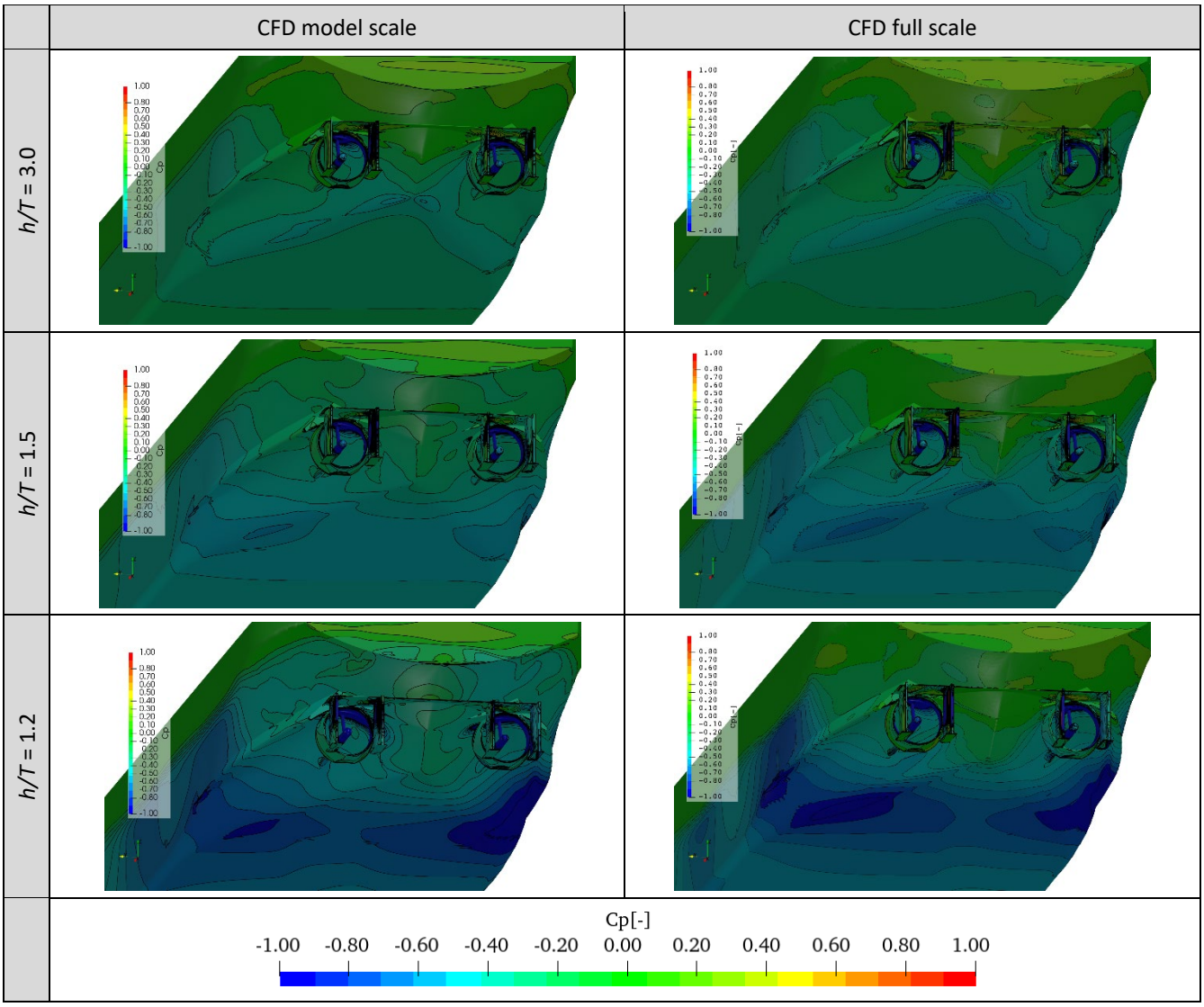

Figure 18. Dynamic pressure coefficient on ship stern at various water depths, model and full scale (*d/B* = 1.5, F_r = 0.107).

Figure 19 displays the flow longitudinal velocity between the ship and the bank for the cross-section located at ship station 10. Here more qualitatively differences are visible. As expected, the boundary layer is larger at model scale. The pattern of the flow fields is quite close between model and full scale, but with some increasing differences in magnitude as the water depth decreases. The return flow speed between model and full scale is basically the same at *h/T* = 3.0. At *h/T* = 1.5, the full-scale CFD calculation predicts more return flow close to the bank. At *h/T* = 1.2, the largest differences between model and full scale are observed close to the ship, with a return flow speed exceeding 25% at model, and only up to 20% at full scale. One of the reasons may be the difference in boundary layer thickness. Since less water is able to travel under the ship in the full-scale computation, due to a thicker boundary layer, the return flow can almost only be on the sides of the ship.

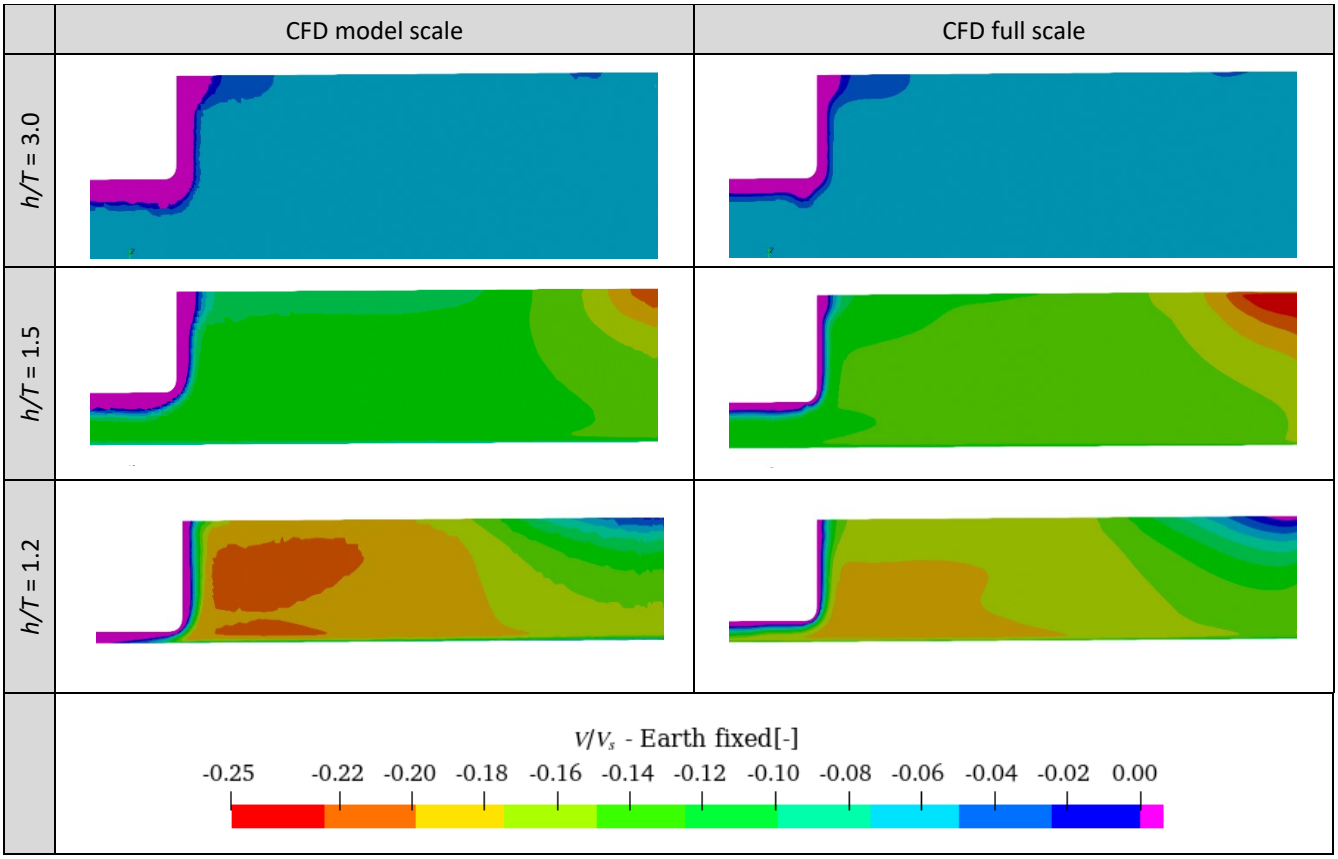

Figure 19. Longitudinal velocity fields at station 10 between the ship and vertical bank at various water depths, model and full scale (*d/B* = 1.5, F_r = 0.107).

This difference is also clearly visible in the force distribution as depicted in Figure 20, showing how larger the force is at model scale. This is particularly noticeable at the bow and around station 3.

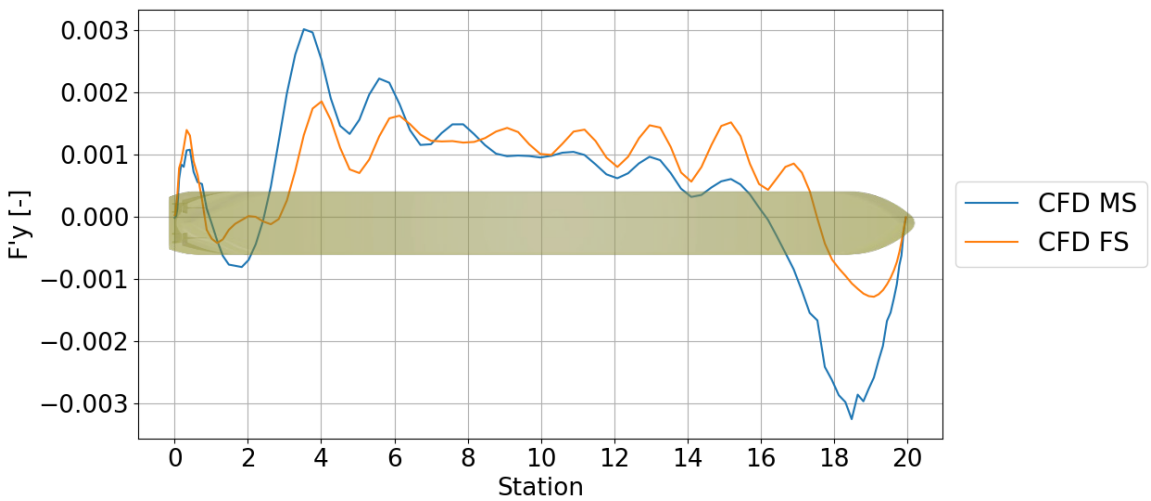

Figure 20. Distribution of sway force along the hull (*h/T* = 1.2, *d/B* = 1.5, F_r = 0.107).

As a summary, the test case illustrates the sensitivity of the ship-bank interactions to the scale effects. Up to *h/T* = 1.5, the hydrodynamic loads seem to be marginally affected by the scale. Discrepancies become larger at a water depth-to-draught ratio *h/T* of 1.2.

5 CONCLUSIONS

This paper presents experimental and numerical methods to identify the bank effects experienced by a representative 135m inland waterway ship sailing along a vertical bank. It compares the total loads acting on the ship as well as the squat, as a function of distances to the bank and under-keel clearances, ranging from 300% to 20%. The numerical predictions share the same trends as the model tests and are consistent with the experience of shippers and other research studies on bank effects. The two methods show an excellent agreement up to medium shallow water (*h/T* = 1.5). In the lowest under-keel clearance (*h/T* = 1.2), CFD results deviate from the experiments by underpredicting the transversal force and the squat motions.

CFD allows a deeper analysis of the underlying physical phenomena by looking at force distributions, but also pressure and velocity fields. The force distribution along the hull evidences that the transverse bank force is a force of low intensity, but resulting from the difference between two large forces of opposite directions. This may partly explain the challenges to reliably and accurately predict such force with numerical methods for extreme shallow water conditions (*h/T* = 1.2). Pressure distributions on the bank also illustrate also the risks of degradation of natural banks when ships are sailing too close.

The paper demonstrates the high sensitivity of ship-bank interactions to the under-keel clearance. Even at a distance to the closest bank as far as *d/B* = 1.5 (more than 17 m at full scale), the magnitude of the repulsion force at the bow and the suction force on the rest of the ship increase by at least a factor two between *h/T* = 1.5 and 1.2. Sudden variations in water depth may result in unexpected bank effects, even for vertical banks. This would require immediate correction from the captain to limit the change in trajectory. This underlines the importance of monitoring the bathymetry of rivers and accurately modelling bank effects in navigation simulators for training and research purposes.

Scale effects, such as a thicker boundary layer at model scale, were also identified. Results show that up to medium-shallow water depth (*h/T* = 1.5), the hydrodynamic loads seem to be marginally affected by the scale. Discrepancies become larger at a water depth-to-draught ratio *h/T* of 1.2.

Numerical predictions and experiments provide complementary insights on ship-bank interactions. Together, they provide reliable validation material for simulator models, but also a detailed outlook of the underlying physical phenomena.

6 REFERENCES

Bedos, A., Oud, G., De Boer, W., 2019. Impact of an Irregular Bank on the Sailed Trajectory of an Inland Ship. In: Proceedings of the Smart Rivers 2019 Conference. Lyon, France.

Bhushan, S., Yoon, H., Stern F., Guilmineau, E., Visonneau, M., Toxopeus, S.L., Simonsen, C., Aram, S., Kim, S.E., Grigoropoulos, G., 2019. Assessment of Computational Fluid Dynamic for Surface Combatant 5415 at Straight Ahead and Static drift 20 deg. Journal of Fluids Engineering. https://doi.org/10.1115/1.4041229.

Chillcce, G., Zentari, L., Van Hoydonck, W., Bedos, A., Ley, J., Gornicz, T., Yang, Y., Oud, G., Tenzer, M., Rzeszutko, J., el Moctar, O., 2025. Numerical Calculation of Hydrodynamic Forces on Inland Waterway Vessels During Circular Motion in Shallow and Extreme Shallow Waters. Ocean Engineering. Vol. 318. https://doi.org/10.1016/j.oceaneng.2024.120095.

Delefortrie, G., Verwilligen, J., Eloot, K., Lataire, E., 2024. Bank Interaction Effects on Ships in 6 DOF. Ocean Engineering. Vol. 310, Part 1. https://doi.org/10.1016/j.oceaneng.2024.118614.

Klaij, C.M., Vuik, C., 2013. Simple-Type Preconditioners for Cell-Centered, Collocated Finite Volume Discretization of Incompressible Reynolds-Averaged Navier–Stokes Equations. International Journal for Numerical Methods in Fluids. Vol. 71, pp. 830-849.

Lataire, E., Vantorre, M., Eloot, K., 2009. Systematic Model Tests on Ship – Bank Interaction Effects. In: Proceedings of the 1st International Conference on Ship Manoeuvring in Shallow and Confined Water: Bank Effects (MASHCON). Antwerp, Belgium, pp. 9-22.

Lataire, E., Vantorre, M., Delefortrie, G., 2015. Longitudinally Directed Bank Effects. In: Proceedings of the International Conference on Ship Manoeuvrability and Maritime Simulation (MARSIM). Newcastle, UK, pp. 1-14.

Mai, T.L., Jeon, M., Vo, A.K., Yoon, H.K., 2023. A Numerical Study on the Ship–Bank Interaction at Various Water Depths of a Surface Ship. Science Progress. Vol. 106(1). https://doi.org/10.1177/00368504221149624.

Menter, F., 1994. Two-Equation Eddy-Viscosity Turbulence Models for Engineering Applications. AIAA Journal. Vol. 32, pp. 1598-1605. https://doi.org/10.2514/3.12149.

Mucha, P., el Moctar, O., Dettmann, T., Tenzer, M., 2017. Inland Waterway Ship Testcase for Resistance and Propulsion Prediction in Shallow Water. Ship Technology Research. Vol. 64 (2), pp.106-113. https://doi.org/10.1080/09377255.2017.1349723.

Mucha, P., el Moctar, O., Dettmann, T., Tenzer, M., 2018. An Experimental Study on the Effect of Confined Water on Resistance and Propulsion of an Inland Waterway Ship. Ocean Engineering. Vol. 167, pp.11-22. https://doi.org/10.1016/j.oceaneng.2018.08.009.

Mucha, P., Dettmann, T., Ferrari, V., el Moctar, O., 2019. Experimental Investigation of Free-Running Ship Manoeuvres Under Extreme Shallow Water Conditions. Applied Ocean Research. Vol. 83, pp.155-162. https://doi.org/10.1016/j.apor.2018.09.008.

Norrbin, N., 1985. Bank Clearance and Optimal Section Shape for Ship Canals. In: Proceedings of the 26th PIANC International Navigation Congress. Brussels, Belgium, pp. 167-178.

Raven, H., 2019. Shallow-Water Effects in Ship Model Testing and at Full Scale. Ocean Engineering. Vol. 189. https://doi.org/10.1016/j.oceaneng.2019.106343.

Schijf, J. B., 1949. Influence on the Form and Dimensions of the Cross-Section of the Canal, of the Form, of the Speed and the Propulsion System of Vessels. In: Proceedings of the 17th PIANC International Navigation Congress, section 1, Inland Navigation. Lisbon, Portugal, pp.61-78.

Tonelli, R., Quadvlieg, F., 2015. New Benchmark Data for Manoeuvring in Shallow Water Based on Free Running Manoeuvring Tests Including Uncertainty of the Results. In Proceedings of the ASME 2015 34th International Conference on Ocean, Offshore and Arctic Engineering. St. John's, Newfoundland, Canada, Vol. 11. https://doi.org/10.1115/OMAE2015-42254.

Van Hoydonck, W., Toxopeus, S., Eloot, K., Bhawsinka, K., Queutey, P., Visonneau, M., 2019. Bank effects for KVLCC2. Journal of Marine Science and Technology. Vol. 24, pp. 174-199. https://doi.org/10.1007/s00773-018-0545-3.

Verwilligen, J., Lataire, E., Tello Ruiz, M., Eloot, K., 2022. Evaluation of Bank Effects on a Bulk Carrier in a Confined Channel Cased on Towing Tank Tests and Full-Scale Measurement. In: Proceedings of the 6th International Conference on Ship Manoeuvring in Shallow and Confined Water: Port Manoeuvres (MASHCON). Glasgow, UK, pp.285-298.

7 AUTHORS BIOGRAPHY

Antoine Bedos holds the position of Senior Project Manager at the Maritime Research Institute Netherlands (MARIN). He conducts experimental and numerical research for the maritime industry, and has a particular interest for shallow-water and manoeuvring applications. Over the past few years, he has focused on the inland shipping sector. He is also expert in mathematical manoeuvring models and time-domain simulations.

Tomasz Gornicz holds the position of CFD Specialist at the Maritime Research Institute Netherlands (MARIN). He graduated from a technical university in Poland, where his professor, Jan Kulczyk, introduced him to the fascinating world of inland shipping hydrodynamics. For more than 10 years, he has been conducting numerical studies in ship manoeuvring and non-conventional propulsion systems.

Roberto Tonelli holds the position of Senior Researcher at the Maritime Research Institute Netherlands (MARIN). He is also the coordinator of the Manoeuvring research programme within the organisation. He has conducted experimental and numerical research for the maritime industry for more than 10 years. Over the past few years, he has deepened his knowledge and expertise on mathematical manoeuvring models and time-domain simulations.

UNSTEADY HYDRODYNAMICS OF A BOX WHEN ENTERING A LOCK

Zhi-Ming Yuan, University of Strathclyde, UK
Yihan Liu, China Classification Society, CN
Momchil Terziev, University of Strathclyde, UK

UNSTEADY HYDRODYNAMICS OF A BOX WHEN ENTERING A LOCK

Yihan Liu, China Classification Society, CN
Momchil Terziev, University of Strathclyde, UK
Zhi-Ming Yuan, University of Strathclyde, UK

SUMMARY

The hydrodynamics of ships entering a lock are exceedingly complex. During this process, ships inevitably encounter a sudden narrowing of the channel and continuous or abrupt variations in water depth. The fluid is displaced and accelerates as it flows through the gaps between the ship, the lock walls, and the bottom, significantly increasing the risk of collision or grounding. As a result, the manoeuvrability of ships during lock entry has long been a topic of interest among researchers. However, beyond this focus, the intricate hydrodynamic phenomena associated with the free surface within the lock during ship entry have received relatively little attention. This paper aims to explore the causes of these phenomena and analyse their impacts on ship hydrodynamics, thereby providing further theoretical support for addressing manoeuvrability issues of ships during lock entry.

NOMENCLATURE

C_T	Total resistance coefficient
C_w	Wave making resistance coefficient
F	Force (N)
g	Density of water (kg/m^3)
L	Length (m)
B	Breadth (m)
D	Depth (m)
T	Draft (m)
P	Pressure (N/m^2)
R_w	Wave making resistance (N)
S	Area (m^2)
A_s	Cross section area (m^2)
t	Time (s)
U	Ship velocity (m/s)
v	Return flow velocity (m/s)
V	Volume(m^3)
ν	Kinematic viscosity (m^2/s)
ρ	Density of water (kg/m^3)
φ	Velocity potential
ζ	Velocity potential
δ	Blockage ratio
κ	Acceleration coefficient

1 INTRODUCTION

The dynamic behaviour of ships during lock entry remains an intricate and challenging topic, largely due to the complex interplay of hydrodynamic factors. Variations in channel design, depth changes, flow interactions, and the effects of confined spaces contribute to significant alterations in a ship's hydrodynamic environment. These changes are especially pronounced as vessels encounter restricted channel dimensions and reduced water depths when entering locks. The resulting compression of flow around the hull leads to increased velocity and reduced pressure, with potential consequences such as enhanced sinkage and trim. Additionally, differential pressure distributions can induce wave resistance and pitching moments, while lateral asymmetries in the waterway may cause unbalanced forces, raising the risk of unintended bank contact, grounding, or collision.

Real-world incidents, including the well-known Suez Canal blockage in 2021, highlight the operational challenges associated with navigating constrained waterways. To address these risks, significant research has been conducted on ship behaviour in

confined settings. Investigations into shallow-water effects, bank proximity, and vessel interactions have been led by institutions such as the David Taylor Model Basin (1960), with experimental studies in locations like the Panama Canal. Other noteworthy contributions include analytical and experimental studies by Norrbin (1976) on bank effects, as well as model tests conducted by Flanders Hydraulics Research and Ghent University, exploring ship-bank (Lataire, et al., 2009; Lataire, et al., 2016), ship-bottom (Lataire, et al., 2012; Lataire, et al., 2016), ship-lock (Lataire, et al., 2012) and ship-to-ship interactions (Vantorre, et al., 2002). These efforts underscore the influence of boundary conditions on ship performance in narrow passages.

Wave phenomena associated with lock entry have also received some attention. Studies by Vrijburcht (1988) focused on calculating ship speeds and wave heights, while simulations by Meng and Wan (2016) analysed flow patterns during lock entry, highlighting water accumulation in front of the ship. More recent research by Wan et al. (2022) examined water-level fluctuations in specific lock configurations, linking these to operational parameters such as discharge rates and emptying sequences. Despite these contributions, there has been limited exploration of the wave fields generated as ships enter locks, particularly regarding their impact on hydrodynamic forces and ship responses.

This paper seeks to fill this gap by enhancing the capabilities of the potential flow solver MHydro, which employs a three-dimensional boundary element method with Rankine source functions. By refining the solver, this study aims to capture the unsteady wave phenomena occurring during lock entry and evaluate their implications for ship hydrodynamics in restricted waterways. The methodology is detailed in Section II, followed by an analysis of wave dynamics for simplified geometric cases in Section III. Key findings and their broader implications are discussed in Section IV.

2 MATHEMATICAL MODELLING

2.1 BOUNDARY VALUE PROBLEM

As depicted in Figure 1, this study employs two distinct right-hand coordinate systems: a global coordinate system *O–XYZ*, fixed to the midpoint of the lock entrance, and a local coordinate system o_0-$x_0y_0z_0$, positioned at the geometric center of the ship.

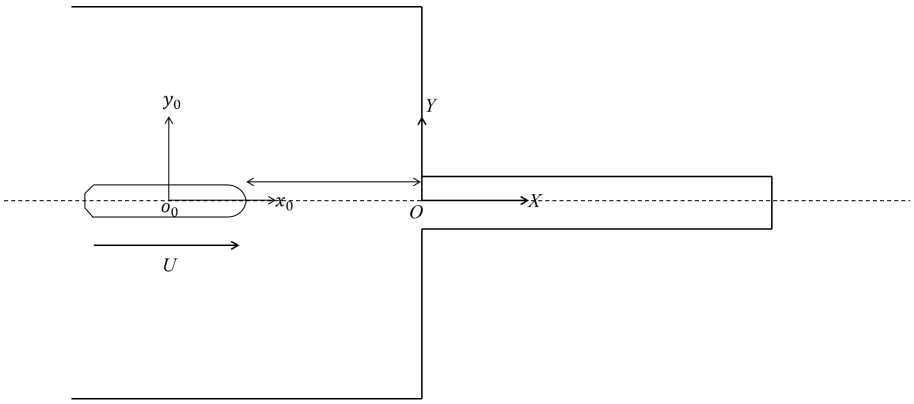

Figure 1 Sketch of the problem

In the global coordinate system, the *x*-axis points from the lock entrance toward the lock gate. Meanwhile, in the local coordinate system, the *x*-axis runs from the stern to the bow of the ship, with both *z*-axes pointing upward as the positive direction. The ship advances at a constant speed *U* along the positive *x*-axis while gradually entering the lock. This study assumes an ideal fluid based on potential flow theory, meaning the fluid is considered inviscid, irrotational, and incompressible. The flow is characterized by the velocity potential $\varphi(x, y, z, t)$ and the free surface is described by the wave elevation $\zeta(x, y, t)$.

The velocity potential $\varphi(x, y, z, t)$ satisfies the Laplace equation:

$$\frac{\partial^2\varphi}{\partial x^2}+\frac{\partial^2\varphi}{\partial y^2}+\frac{\partial^2\varphi}{\partial z^2}=0, \tag{1}$$

The free surface is expressed by the kinematics and dynamics free surface conditions,

$$\frac{\partial\zeta}{\partial t}-U\frac{\partial\zeta}{\partial x}+\frac{\partial\varphi}{\partial x}\frac{\partial\zeta}{\partial x}+\frac{\partial\varphi}{\partial y}\frac{\partial\zeta}{\partial y}-\frac{\partial\varphi}{\partial z}=0, at\ z=\zeta \tag{2}$$

$$\frac{\partial\varphi}{\partial t}-U\frac{\partial\varphi}{\partial x}+g\zeta+\frac{1}{2}\nabla\varphi\cdot\nabla\varphi+\frac{P}{\rho}=0, at\ z=\zeta \tag{3}$$

where φ_t and ζ_t are the time derivative of φ and ζ. φ_x, φ_y, and φ_z are the x, y, and z-direction derivatives of φ, respectively.
In this study, it is crucial to acknowledge that the omission of nonlinear terms in free surface conditions results in an inability to evaluate the impact of nonlinear effects on unsteady phenomena comprehensively. Nevertheless, by referencing established research, certain relevant conclusions can still be drawn. Specifically, when a ship undergoes prolonged acceleration in shallow water, its wave resistance can be effectively predicted using both the linear and unsteady potential flow solver, MHydro, and computational fluid dynamics (CFD) methods. Importantly, predictions from these approaches align closely, with only slight discrepancies observed near critical speeds (Terziev, et al., 2024). This finding highlights the predominant role of unsteady effects in wave-making resistance at low speeds in shallow water, where the influence of nonlinear effects is comparatively minor.
Then, the free surface conditions are discretized by inducing and extending the numerical program MHydro (Yuan, 2019; Li, et al., 2020). Specifically, a kind of three-level scheme is used to obtain the derivatives of φ and ζ in the time and location scale,

$$(\varphi_t)_{i,j}^{m+1} = \frac{1}{\Delta t}\left(\frac{3}{2}\varphi_{i,j}^{m+1} - 2\varphi_{i,j}^{m} + \frac{1}{2}\varphi_{i,j}^{m-1}\right) \tag{4}$$

$$(\zeta_t)_{i,j}^{m+1} = \frac{1}{\Delta t}\left(\frac{3}{2}\zeta_{i,j}^{m+1} - 2\zeta_{i,j}^{m} + \frac{1}{2}\zeta_{i,j}^{m-1}\right) \tag{5}$$

$$(\varphi_x)_{i,j}^{m+1} = \frac{1}{\Delta x}\left(\frac{3}{2}\varphi_{i,j}^{m+1} - 2\varphi_{i,j+1}^{m+1} + \frac{1}{2}\varphi_{i,j+2}^{m+1}\right) \tag{6}$$

$$(\zeta_x)_{i,j}^{m+1} = \frac{1}{\Delta x}\left(\frac{3}{2}\zeta_{i,j}^{m+1} - 2\zeta_{i,j+1}^{m+1} + \frac{1}{2}\zeta_{i,j+2}^{m+1}\right) \tag{7}$$

where m represents the mth time step and i and j indicate that the element is located on the ith row and j^{th} column on the free surface. As a result, the kinematic free surface condition can be discretized first at iterative step k as

$$\frac{1}{\Delta t}\left(\frac{3}{2}\zeta_{i,j}^{(m+1,k)} - 2\zeta_{i,j}^{(m,k)} + \frac{1}{2}\zeta_{i,j}^{(m-1,k)}\right) - \frac{U}{\Delta x}\left(\frac{3}{2}\zeta_{i,j}^{(m+1,k)} - 2\zeta_{i,j+1}^{(m+1,k)} + \frac{1}{2}\zeta_{i,j+2}^{(m+1,k)}\right) - \frac{\partial\varphi_{i,j}^{(m+1,k)}}{\partial z} = 0, \tag{8}$$

Then, the value of $\zeta_{i,j}^{m+1}$ is obtained accordingly, and updating the value of unknown potential φ at t^{m+1} also becomes feasible now,

$$\frac{1}{\Delta t}\left(\frac{3}{2}\varphi_{i,j}^{(m+1,k)} - 2\varphi_{i,j}^{(m,k)} + \frac{1}{2}\varphi_{i,j}^{(m-1,k)}\right) - U\frac{\partial\varphi_{i,j}^{(m+1,k)}}{\partial x} + g\zeta_{i,j}^{(m+1,k)} = 0, \tag{9}$$

The calculation mentioned in above Eq. 8 and Eq. 9 pertains to the results obtained during the current k_{th} iteration. These results must undergo verification against pre-defined accuracy criteria $|\varphi_{i,j}^{(m,k)} - |\varphi_{i,j}^{(m,k-1)}| < \varepsilon$ and $|\zeta_{i,j}^{(m,k)} - \zeta_{i,j}^{(m,k-1)}| < \varepsilon$ where ε equals to 0.00001. Only when all specified conditions are satisfied can the computation proceed to the iteration of the next time step.
Apart from the free surface conditions, the boundary conditions on body should reflect the body surface is impenetrable and the value of the flow's normal velocity should be the same as the ship velocity U,

$$\frac{\partial\varphi}{\partial\boldsymbol{n}} = Un_1, \tag{10}$$

where $\boldsymbol{n}=(n_1, n_2, n_3)$ is the unit normal vector on body surface. On the sea bottom and side walls, the same boundary condition with the body surface is applied, but the normal velocity of flow here should equal to zero,

$$\frac{\partial\varphi}{\partial\boldsymbol{n}} = 0, \tag{11}$$

After the unknown velocity potential φ has been solved, the forces/moments can be obtained from the Bernoulli's equation,

$$F_i = \iint_S Pn_i dS, \qquad i = 1,2,\ldots,6 \tag{12}$$

where i represents the degree of freedom, and

$$P = -\rho\left[\frac{\partial\varphi}{\partial t} - U\frac{\partial\varphi}{\partial x} + \frac{1}{2}(\nabla\varphi)^2\right], \tag{13}$$

Similarly, the free surface elevation can be expressed as

$$\zeta(x,y,t) = -\frac{1}{g}\left[\frac{\partial\varphi}{\partial t} - U\frac{\partial\varphi}{\partial x} + \frac{1}{2}(\nabla\varphi)^2\right], \tag{14}$$

2.2 RETURN FLOW COEFFICIENT

Although the box sails along the positive x-direction with a constant speed U, once it reaches the entrance of the lock, the water volume will increase due to the sudden narrowing of the waterway. This increase in volume elevates the free surface height within the lock and induces significant return flow inside the lock. This return flow has a substantial impact on the results. In the present study, the effect of return flow will be incorporated into the body surface boundary condition. The increased volume can be expressed as

$$\Delta V = UA_{\mathrm{s}}(t)\cdot\Delta t, \tag{15}$$

where A_s is the cross section area of the box's wetted surface at moment t. This means a return flow will follow and the same volume of water will flow through the clearance between the ship and the lock bank. As the box keeps entering the lock, the distance between the bow of the box and the lock gate will continue to decrease, which results in an increase in the return flow velocity $v(x, t)$ (Yuan, 2019). Considering the return flow as a uniform flow, the effect of the return flow can be treated as an additional time-dependent velocity term on body surface boundary condition $v(t)$,

$$\frac{\partial\varphi}{\partial n} = [U + v(t)]n_1, \tag{16}$$

where $v(t)$ can be obtained by

$$v(t) = \begin{cases} 0, & \text{while } t < t_{\mathrm{e}} \\ \kappa\dfrac{\delta}{l}(t - t_{\mathrm{e}})U^2, & \text{while } t_{\mathrm{e}} < t \le t_{\mathrm{c}} \end{cases} \tag{17}$$

where δ is the blockage ratio, which equals the ratio of the cross section area of the box to that of the lock, l is the lock length, t_e represents the moment when the box arrives at the entrance of the lock, and t_c represents the moment when the ship is totally in the lock.

As the existence of the return flow, the box will receive an acceleration and κ is the acceleration coefficient. After the moment t_c, the return flow will persist. Nevertheless, the acceleration coefficient will be reduced to a value smaller than κ. This is because, at this stage, the total water volume within the lock remains constant, and the return flow primarily results from variations in the displaced water volume. In this case, an empirical iteration method is introduced to estimate the return flow velocity,

$$v(t_{\mathrm{n}}) = v(t_{\mathrm{n-1}}) + \kappa\frac{\delta}{l}(U\Delta t)[v(t_{\mathrm{n-1}}) - v(t_{\mathrm{c}}) + U], \qquad \text{while } t > t_{\mathrm{c}} \tag{18}$$

where $v(t)= v(t_c)$ is the initial condition of Eq. 18.

2.3 NUMERICAL SIMULATION SETUP

In the numerical modelling process, panels are exclusively arranged on the body surface, free surface, and bank surface. To optimise computational efficiency, the bottom surface was not explicitly represented in the simulation. Instead, mirroring techniques were applied, treating the bottom surface as a reflective boundary to account for its effect on the computational outcomes. Likewise, this study utilises the symmetry of the computational domain, modelling only half of it.

Additionally, based on testing, the computational domain was truncated at a distance equivalent to four ship lengths aft of the stern. At this boundary, no influence on the simulation results was observed. Furthermore, as previously stated, the free surface remains continuous within the time domain, advancing alongside the ship. This ensures that the panels on the free surface maintain a constant distance from the ship's hull throughout the simulation.

The wave making resistance in this study has been non-dimensionalized and denoted as the wave making resistance coefficient,

$$C_{\mathrm{w}} = \frac{R_{\mathrm{w}}}{(1/2)\rho U^2 S}, \tag{19}$$

where S is the area of the wet body surface and R_{w} denotes the wave making resistance, which equals F_1 in Eq. 12.

A convergence analysis is also included in this study to ensure the stability of the numerical simulation results, as shown in Figure 2,

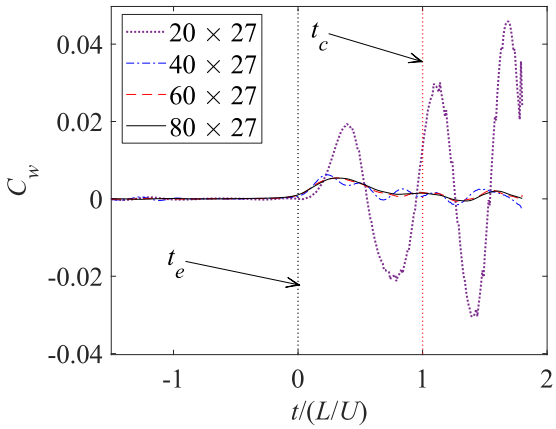

Figure 2 Convergence study on the numerical model, where C_w is the wave making resistance coefficient and $t/(L/U)$ is the dimensionless over time t.

The convergence study of the number of panels on the free surface includes four sets of grids, i.e., 40×27, 60×27, and 80×27 panels in the x and y directions within each ship length. It is observable that when the density of mesh is relatively sparse, the predicted wave making resistance exhibits considerable volatility, with the resistance curve not being smooth. However, as the density increases, these issues are noticeably ameliorated. After considering both the accuracy of the computational results and computational efficiency, this study uses the third set of grids to construct the numerical model.
Simultaneously, the fully unsteady approach adopted in this study necessitates that all results remain interconnected across each time step. This method imposes stringent requirements on the selection of the time step to ensure accuracy and stability. Consequently, the time step for this simulation was determined to be 0.0139s.

3 RESULTS AND DISCUSSION

This study delves into the hydrodynamic phenomena encountered by objects navigating through confined waterways. To ensure the research results align more closely with practical conditions, the study involves a box entering a lock at a low velocity within a confined channel. The selection of the dimensions for both the box and the lock will be explained later in this chapter

3.1 EXPERIMENTAL SETUP

The experiment was conducted in the towing tank of the Kelvin Hydrodynamics Laboratory (KHL), which boasts dimensions of 76 m in length, 4.6 m in width, and a maximum depth of 2.5 m, as illustrated in Figure 3. Further comprehensive details regarding this facility can be accessed via KHL's official website.

Figure 3 The towing tank of KHL.

The third set of lock chambers of the Panama Canal, which have a length varying between 427 and 488 m and a width of 55 m (Delefortrie, et al., 2009), was chosen as the lock model.
To simplify model construction and enable effective benchmarking against experimental data, this study selected a bulk carrier with a block coefficient (CB) close to 1. This choice facilitated the approximation of the ship's hull as a box-like structure for experimentation, with a scale model constructed at a 1:115 ratio. The detailed dimensions of the model box and the lock are provided in Table 1.

Table 1 Model Information.

	Lock(MS)	Box(MS)
L(m)	3.5	2.4
B(m)	0.5	0.4
T(m)	0.225	0.15
D(m)	0.3	0.2

In the test setup, water level fluctuations were monitored using wave gauges placed at five distinct locations, as illustrated in Fig. 19(c). An ultrasonic wave probe, moving synchronously with the box, recorded the wave elevations at the bow. Meanwhile, four fixed resistance wave gauges were used to measure the wave patterns within the lock.

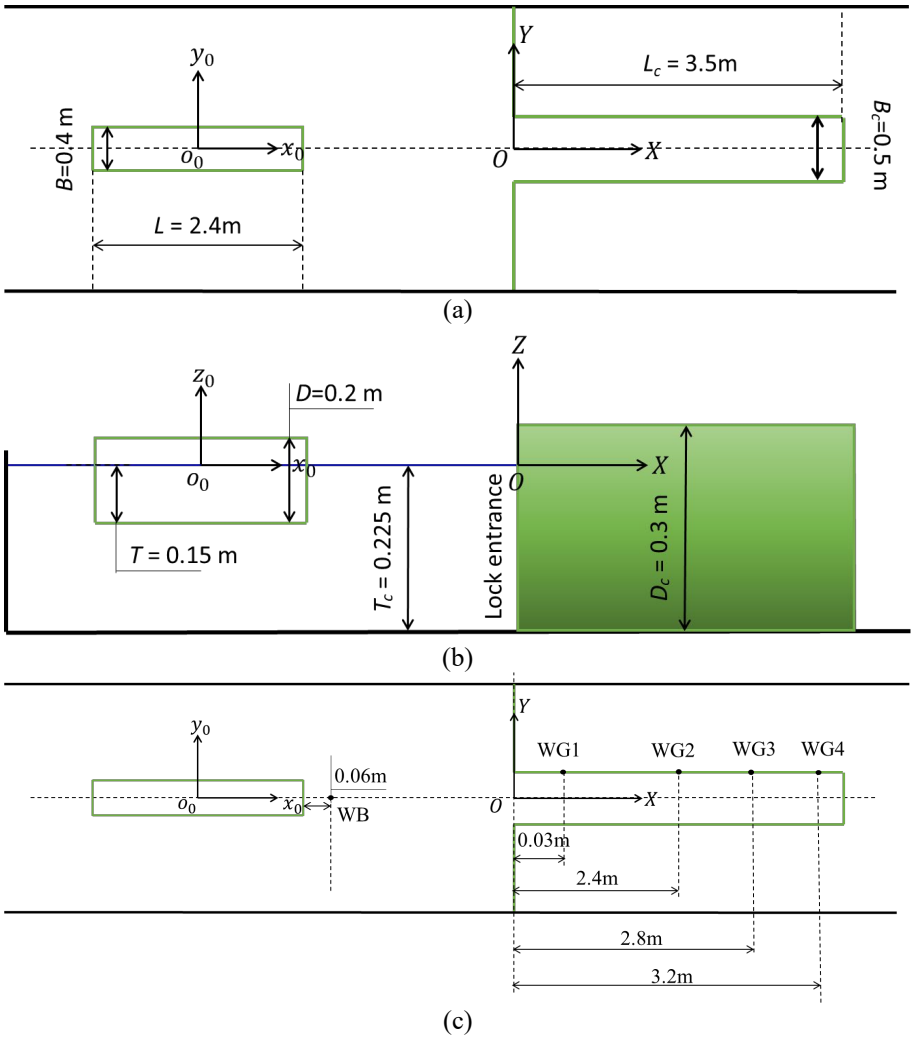

Figure 4 General layout of the towing tank for a box entering a lock and the positions of wave gauges: (a) top view of the tank; (b) side view of the tank; and (c) the positions of wave gauges.

In the experiments, marine plywood was used to construct both the ship and lock models. The ship model was carefully ballasted to ensure it remained watertight. To stabilise the lock model at its location, external L-shaped wooden supports were added, allowing weights to be applied for additional stability (refer to Figure 5). The box model was pulled by a carriage

featuring a computer-controlled digital drive, offering precise and repeatable speed control. All six degrees of freedom of the box were constrained, meaning sinkage and trim were determined with the applied force divided by the hydrostatic restoring force. A Kistler piezoelectric multicomponent dynamometer was positioned at the connection between the box and the carriage to accurately measure the resistance encountered by the box during its lock entry process. This apparatus provided measurements of sway force and yawing moment around the box's origin.

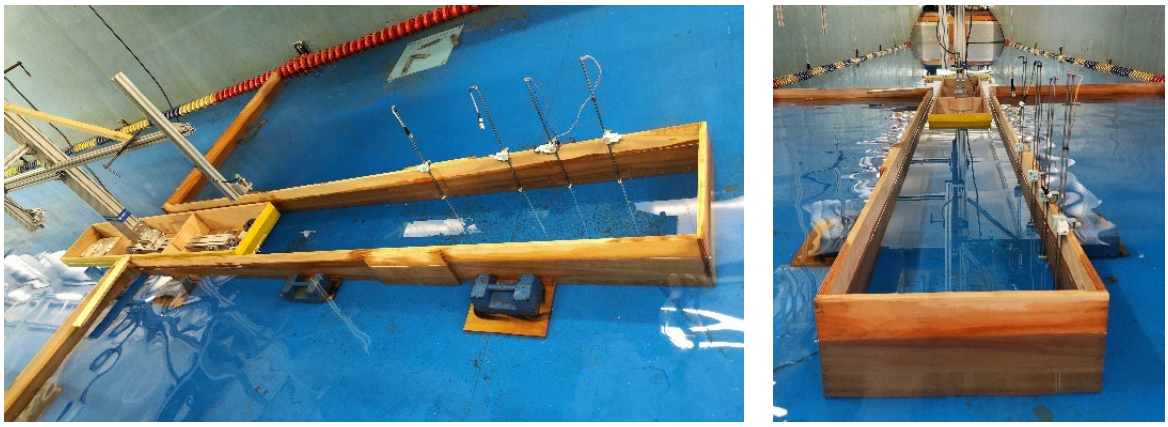

Figure 5 Floating box entering the lock.

Given the unsteady conditions of the tests, the reproducibility of the results is strongly influenced by the acceleration phase of the box and the abrupt narrowing of the channel. This effect is particularly pronounced when the box begins accelerating too close to the lock entrance, leading to noticeable disturbances in the measured wave heights inside the lock, especially near the entrance. To mitigate this issue, the tests were initiated in calm water, with the starting point of acceleration positioned 12 m away from the lock entrance. This arrangement ensures that the box has sufficient distance to reach its desired speed before approaching the entrance, thereby reducing the influence of acceleration-induced waves.

3.2 VALIDATIONS AND DISCUSSION OF THE NUMERICAL SIMULATION

The panel distribution of this case in the simulation is shown in Figure 6. It can be seen, the computational domain is truncated at 3.5L upstream, 1L sideways, and 3.5L downstream. This study ultimately arranged 520 panels on the body surface, 2746 panels distributed across the free surface, and 1510 panels on the bank surface.

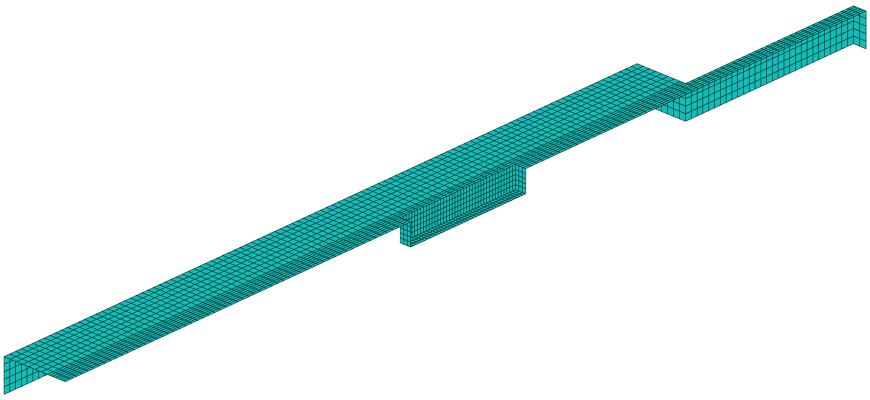

Figure 6 Panel distribution on the computation domain of a box entering a lock Model.

The experiment was conducted under five distinct velocity conditions, represented by U values of 0.1, 0.15, 0.2, 0.25, and 0.3 m/s. For comparative analysis, results from three experimental cases with velocities of $U = 0.1$ m/s ($Fr = 0.02$), $U = 0.2$ m/s ($Fr = 0.04$), and $U = 0.3$ m/s ($Fr = 0.06$) were specifically examined.

In addition to the experimental results, simulation results from CFD are also introduced in this paper to increase the confirmation of the reliability of the MHydro results. The CFD solutions are produced using the commercially available solver Star - CCM+. The developed model makes use of the Wilcox k - ω turbulence model with second order convective accuracy following previous experience, which indicates computational efficiency and accuracy with this model. The near-wall mesh is determined a priori using the approach detailed in with a $y^+ < 1$ in all cases. The free surface is resolved using the volume of fluid method, and since the time is discretized using a second order accurate scheme, the Courant number is limited to 0.5.

This determines the time step, which is set to ensure the Courant number is 0.3 to accommodate local flow acceleration. The body is encased in an overset mesh and translated in the x direction only. The results simultaneously include both pressure resistance and frictional resistance.

The computational boundaries are arranged to mirror the towing tank experiment as much as possible: the domain sides and bottom are no-slip walls. The domain top is placed one body length vertically from the undisturbed free surface, which is assigned a symmetry boundary condition, in addition to the plane coincident with the domain and body midplane. A pressure outlet boundary is placed approximately to match the experiment. The mesh on the free surface is progressively refined until 15 cells per transverse wavelength ($\lambda = 2\pi U^2 / g$) are achieved.
As shown in Figure 7, the total resistance experienced by the box exhibits a clear stepwise increase with rising velocity. This pattern is largely a result of unsteady effects. Higher velocities cause a larger volume of water to enter the lock within the same timeframe, intensifying the constriction effect of the channel. This, in turn, amplifies the unsteady behaviour.

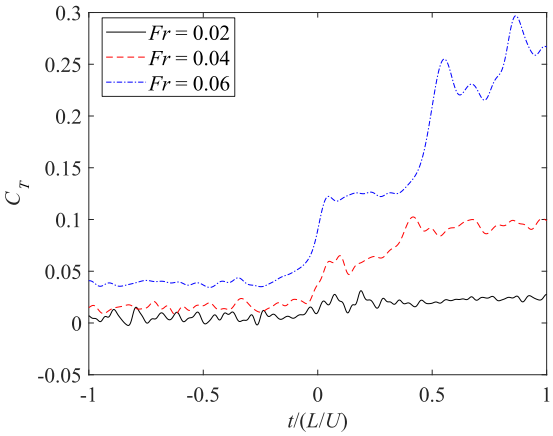

Figure 7 Results of the model experiments at different Froude numbers, where C_T is the dimensionless coefficient of the total resistance applied on the box: the x-axis represents both the dimensionless time and, simultaneously, the position of the bow of the box throughout the process of it entering the lock. When $t/(L/U)$= 0, the bow of the box has just reached the entrance of the lock.

Before commencing this study, it was observed that during a ship's entry into a lock, the water surface within the lock exhibited simultaneous rising and falling motion. This phenomenon was also replicated in model experiments involving an ellipsoid entering a lock (Liu, et al., 2024). In this paper, such movement of the free water surface is referred to as "piston motion." To ensure that the experimental results more closely align with real-world conditions, model experiments involving a box entering a lock were designed, as described in this study.
However, as illustrated in Figure 8, a comparison of the waves generated by the box within the lock at varying velocities reveals that the expected piston effect is barely noticeable at a velocity of 0.1 m/s due to the influence of fluid viscosity. This limitation is alleviated as the box's velocity increases, with a distinct upward displacement of the free surface within the lock being observed, followed by persistent oscillations at an elevated level. Unfortunately, the anticipated simultaneous downward displacement of the free surface remains absent in the experimental results. This absence is likely attributable to the limited space between the box and the lock walls, which restricts the fluid's ability to flow outward from the lock on both sides. It is anticipated that further increases in velocity would mitigate this constraint. Therefore, the model experiment conducted at a velocity of 0.3 m/s has been specifically chosen as a focal point for our case study. This deliberate selection is due to the fact that at this particular velocity, the elevation of the free surface within the lock becomes more prominent.

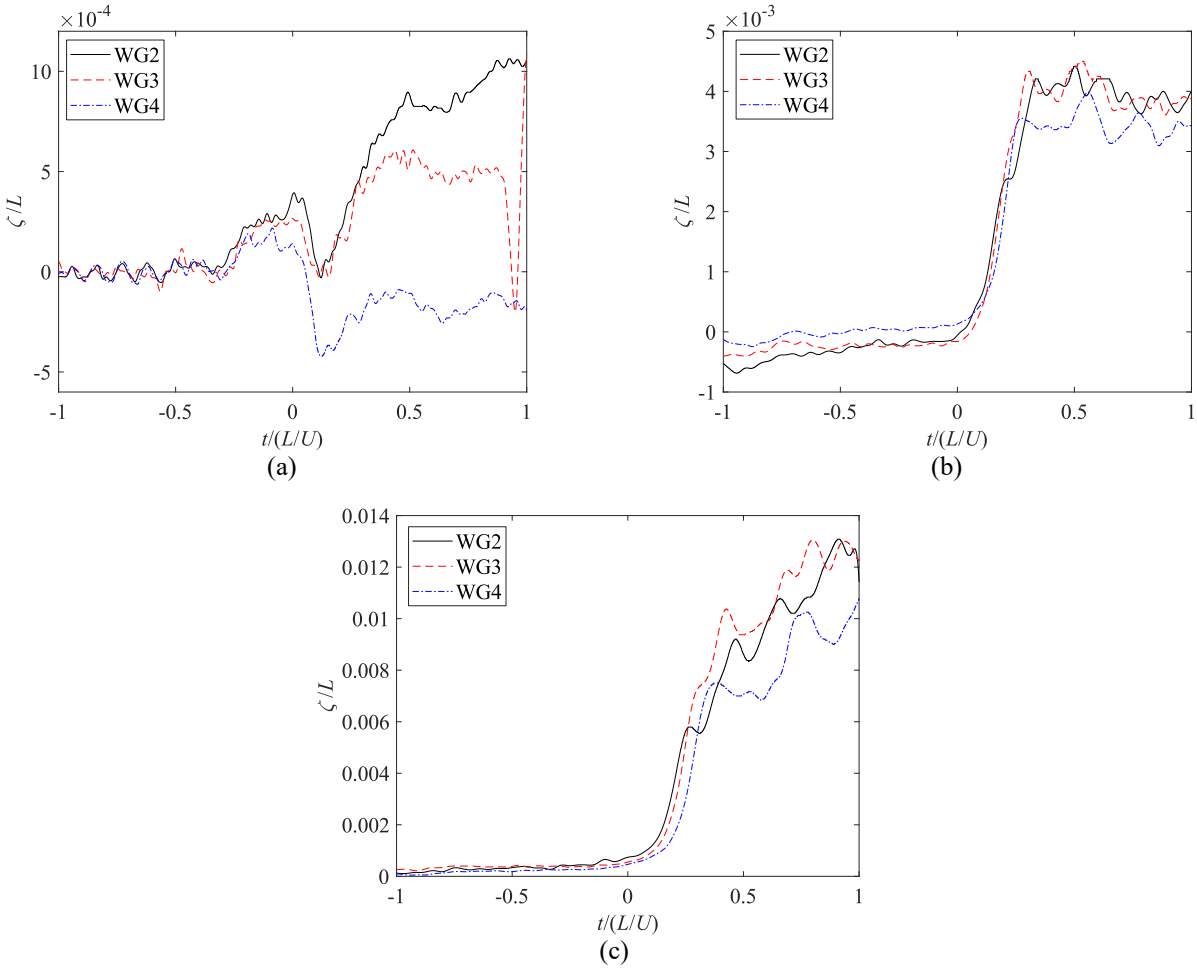

Figure 8 Wave elevations in the lock at different Froude numbers: (a) *Fr* = 0.002; (b) *Fr* = 0.004; and (c) *Fr* = 0.006.

3.2 (a) Validation of the numerical simulation

Firstly, a preliminary validation of the simulation results will be conducted in this section. The model experiment with a velocity of 0.3 m/s has been selected as a case study, not only because at this velocity, the elevation of the free surface inside the lock is more pronounced, but also because the data from this set of experiments has been validated through five repeated trials, as shown Figure 9.

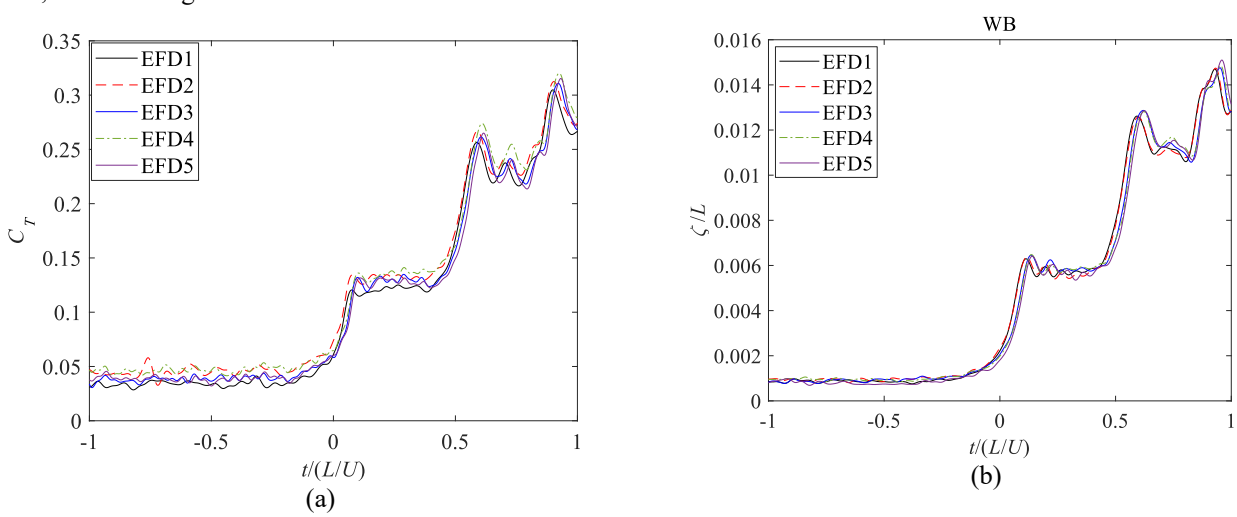

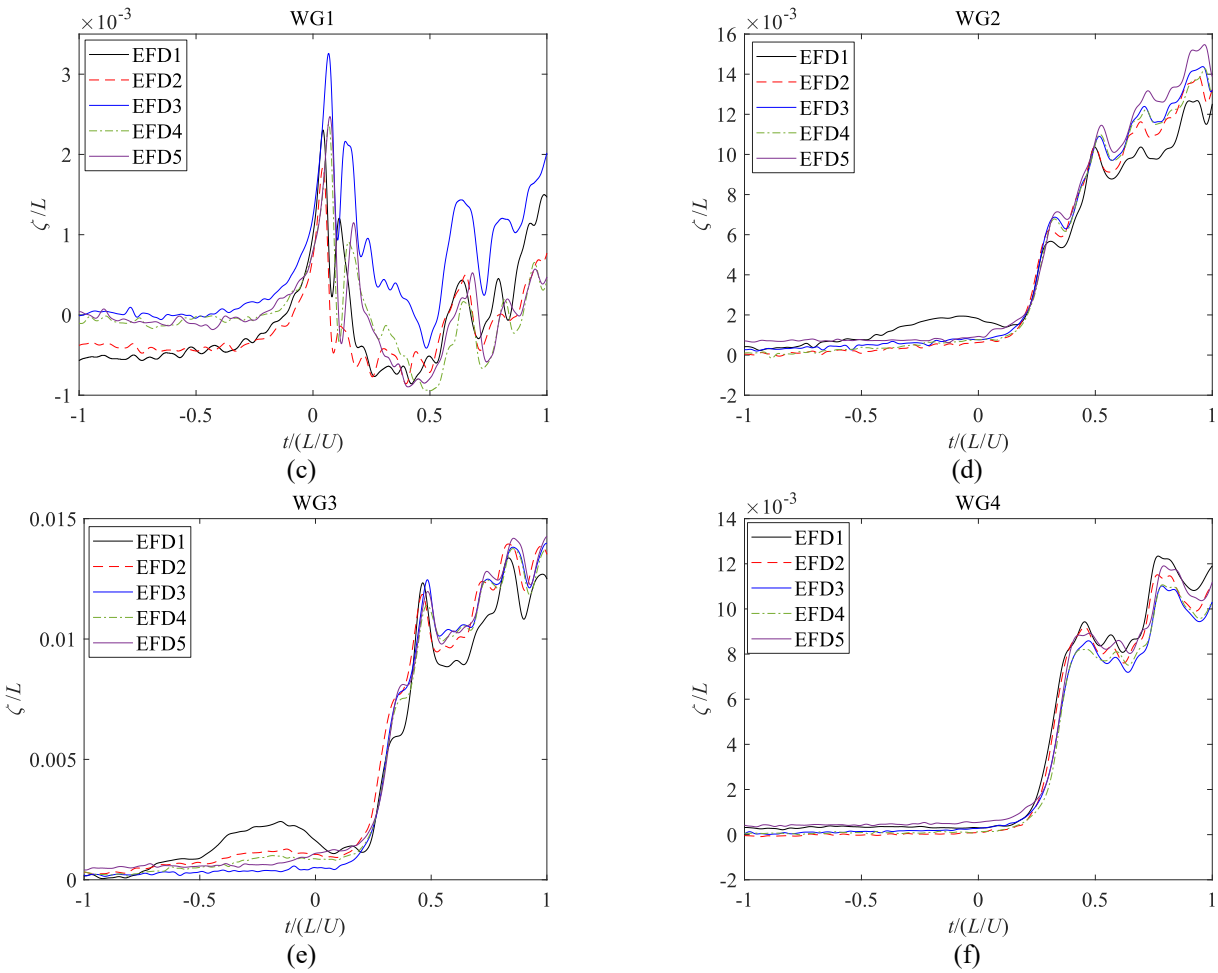

Figure 9 Repetitions of the Model Experiment when *U* = 0.3 m/s.

After verifying the accuracy of the experimental results, this paper began to test the simulation results. Figure 10 (a) demonstrates that MHydro effectively predicts the general trend of surge force variation as the box enters the lock, though some finer details are missing. At the initial stage, discrepancies between MHydro and experimental results are evident. These differences stem from MHydro accounting only for wave-making resistance during the box's forward motion, whereas the experimental data reflect total resistance, including frictional forces. With a low Froude number (Fr = 0.06) indicative of a very low velocity, frictional resistance becomes a dominant factor in the total resistance, which MHydro does not fully capture. Further evidence supporting this observation is provided in Figure 10 (b), which shows that MHydro effectively captures the wave elevation at the box's bow during its entry into the lock. The experimental results reveal three distinct steps at $t/(L/U)$ values of 0.2, 0.5, and 0.75. The numerical simulation similarly reflects this trend, albeit with slight variations in the step positions.

Figure 11 presents the wave field within the lock during the box's entry. It is evident that the elevation of the bow waves undergoes three distinct transitions, occurring at approximately $t/(L/U)$ values of 0.1, 0.6, and 0.9.

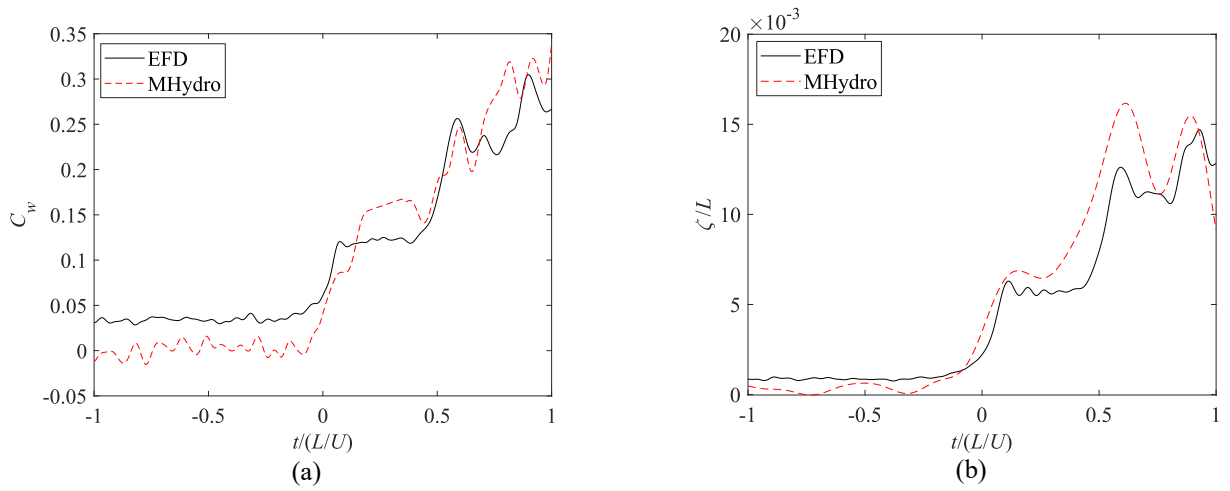

Figure 10 Comparison of the surge force applied on the box and the wave elevation at the bow while *Fr* = 0.06 where the result from EFD is the total resistance and MHydro's result is wave making resistance: (a) surge force and (b) waves at the bow.

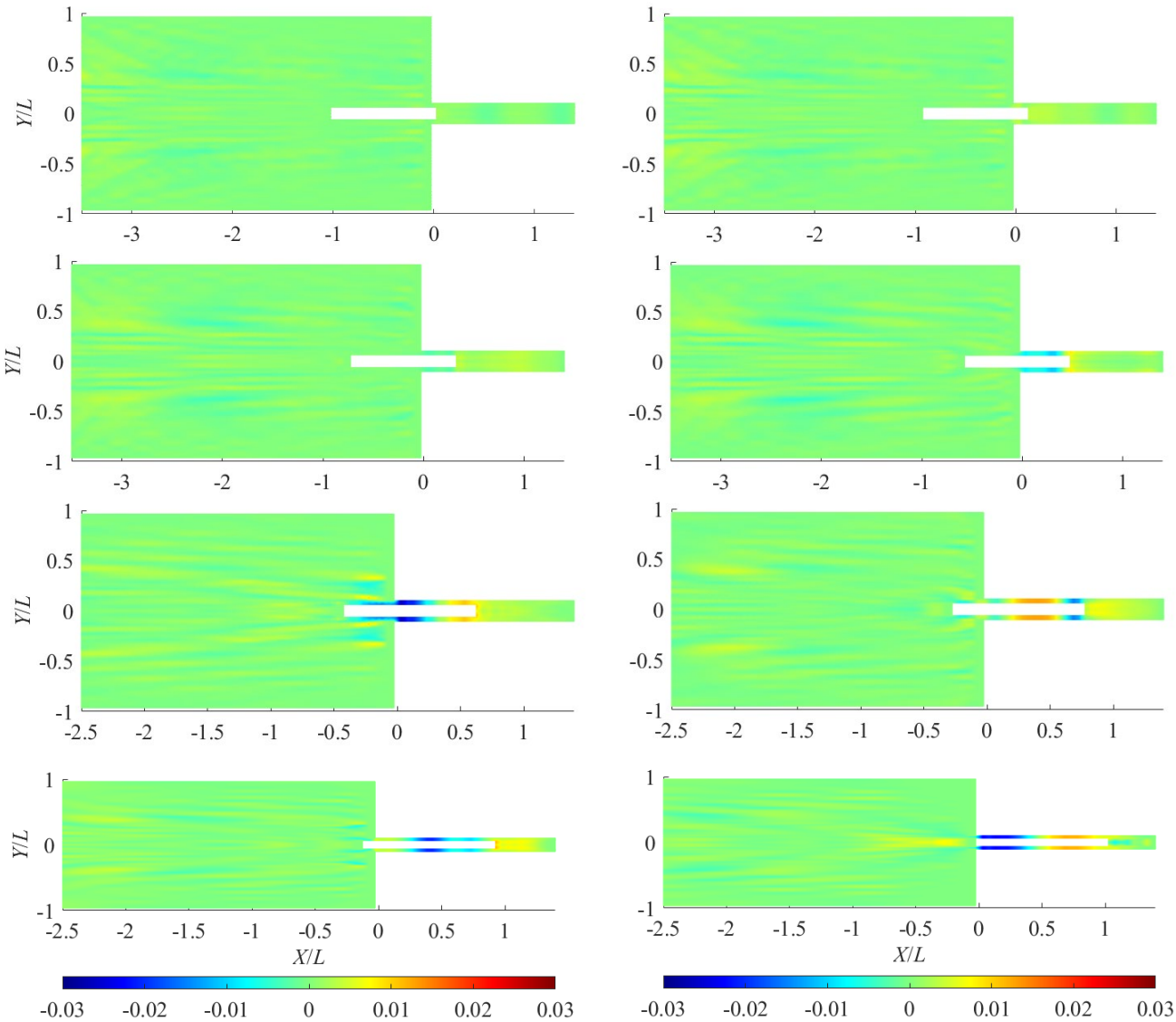

Figure 11 The wave field in the lock when the box is entering the lock, where the color bar represents *ζ/L*

Figure 12 validates the predicted wave heights within the lock, with wave gauge locations shown in Figure 12 (e). The MHydro simulation results generally align well with the experimental fluid dynamics (EFD) data. The wave elevation oscillations are well captured, although some finer details are not fully represented. In contrast, the computational fluid dynamics (CFD) results exhibit excellent agreement up to $t/(L/U)\leqslant 0.6$. Beyond this point, while the experimental results stabilise, the CFD predictions continue to increase. It can also be observed, initially, as the box begins to enter the lock ($t/(L/U)\leqslant 0.2$), the volume of fluid within the lock changes only slightly, resulting in minimal variation in the free surface. As the box progresses further, its kinetic energy is converted into gravitational potential energy, leading to a rapid rise in the free surface. Theoretically, after reaching the peak level, the gravitational potential energy should be transformed back into kinetic energy, causing fluid to flow out of the lock and a subsequent decrease in the free surface. However, this phenomenon was not observed in this case. At $t/(L/U)$=0.45, the free surface reaches its maximum level and continues to oscillate at that point, indicating that the kinetic energy absorbed and lost by the fluid has reached equilibrium, and the free surface height remains relatively constant.

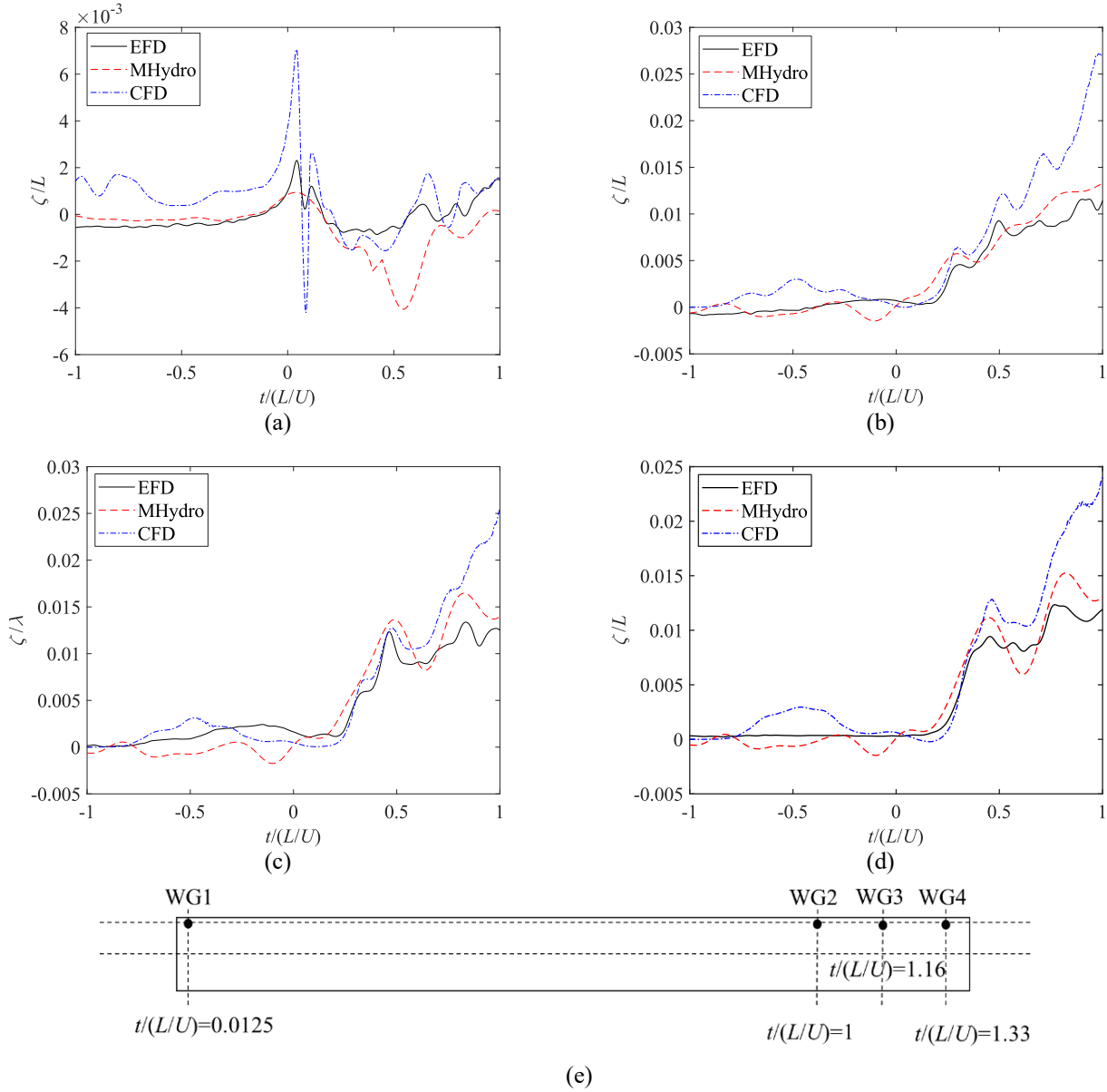

Figure 12 Comparison of the wave elevations in the lock while *Fr*= 0.06: (a) waves at WG1; (b) waves at WG2; (c) waves at WG3; (d) waves at WG4; and (e) positions of wave gauges.

3.2 (b) Return flow phenomenon

As illustrated in Figure 13, the majority of the hydrodynamic phenomena observed within the lock are predominantly caused by the return flow. When the return flow is excluded from the simulation ($\kappa = 0$), changes in the free surface within the lock are negligible. However, wave resistance is strongly influenced by wave elevations, leading to a significant distortion in the predicted wave-making resistance under such conditions. By comparing simulation outcomes with experimental results, it

was determined that using $\kappa = 15$ produces results that closely match the experimental data. This value represents a balanced compromise, as the coefficient's selection is highly dependent on specific parameters, such as the hull shape.
Furthermore, this study identified that the return flow within the lock is inherently non-uniform. Fluid near the bow of the box is more significantly affected by the return flow compared to areas nearer the lock walls. This discrepancy arises due to the initiation of return flow caused by the box entering the lock. As a result, the flow field surrounding the bow, which moves along with the box, demonstrates a stronger interaction with the return flow than fixed regions farther from the box.

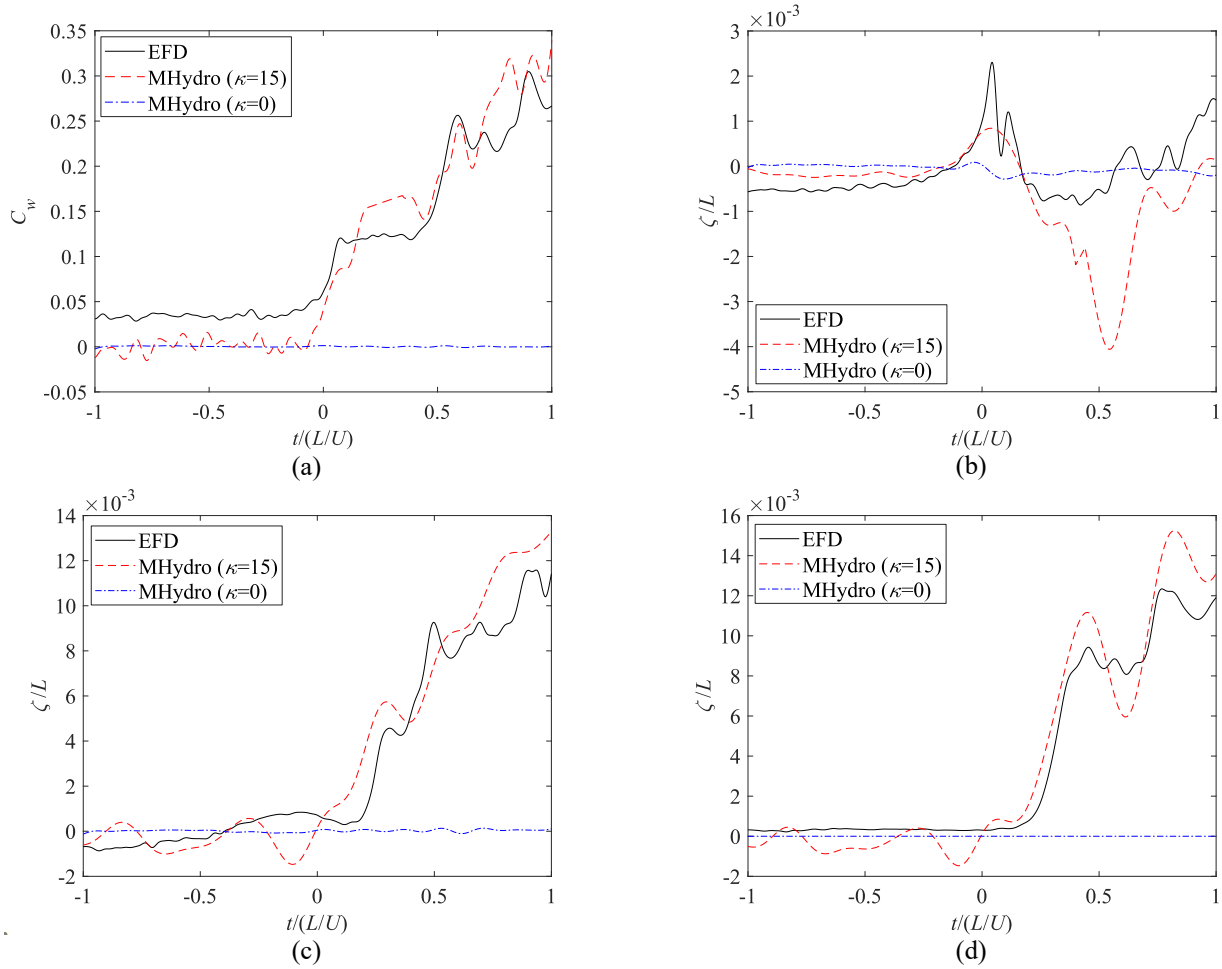

Figure 13 Comparison of the numerical simulation results with different acceleration coefficients j while *Fr*=0.06: (a) wave making resistance; (b) waves at WG1; (c) waves at WG2; and (d) waves at WG4.

3.2 (c) Free surface effect and piston phenomenon

Figure 14 compares total resistance and wave-making resistance obtained through different methods. The experimental results from EFD provide the total resistance coefficient C_T, while the MHydro simulations yield only the wave-making resistance coefficient C_w. The numerical simulation results show progressive convergence toward the experimental data as the free surface establishing approach evolves: first treating the free surface as a rigid wall, then introducing a linear quasi-steady free surface, and finally incorporating unsteady effects. Notably, the step phenomena observed in the experimental data are reproduced only when unsteady effects are fully included in the simulations, highlighting their critical role. This explains why the step phenomena become increasingly pronounced with higher box velocities, as greater entry speeds intensify unsteady free surface effects within the lock. Figure 15 further emphasises the importance of employing a 3D free surface model and accounting for its unsteady behaviour to address this problem accurately.
This study also demonstrates that unsteady free surface effects are essential for replicating the piston phenomenon within the lock. If free surface effects are entirely neglected, the water level inside the lock rises sequentially, driven solely by the high-pressure field ahead of the ship's bow. When a linear quasi-steady free surface is incorporated, the water level rises simultaneously across the lock but follows a smooth curve rather than the abrupt elevation observed experimentally. Only the fully unsteady MHydro method successfully reproduces the step-like rise seen in experiments, as depicted in Figure 16.
However, no clear simultaneous decrease in the free surface level was observed in this case. Even so, some trends resembling such behaviour can be identified in the wave profiles at WG3 and WG4. As shown in Figure 16 (a) and Figure 16 (d), during the interval $t/(L/U)$ equals to 0.5 to 0.8, the wave elevations at both locations initially decrease before increasing again, with

the changes occurring simultaneously. This phenomenon arises from the energy dynamics explained earlier and, from an external perspective, is influenced by the larger flow space at these points. Being farther from the lock entrance, these locations allow for a temporary lowering of the free surface.

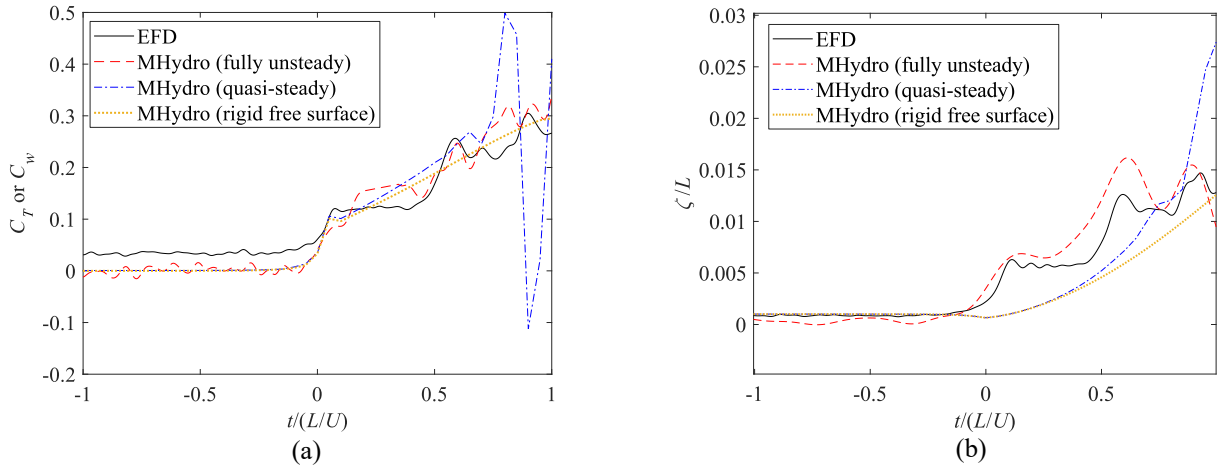

Figure 14 Resistance applied on the box obtained by different methods: (a) surge force and (b) waves at the bow.

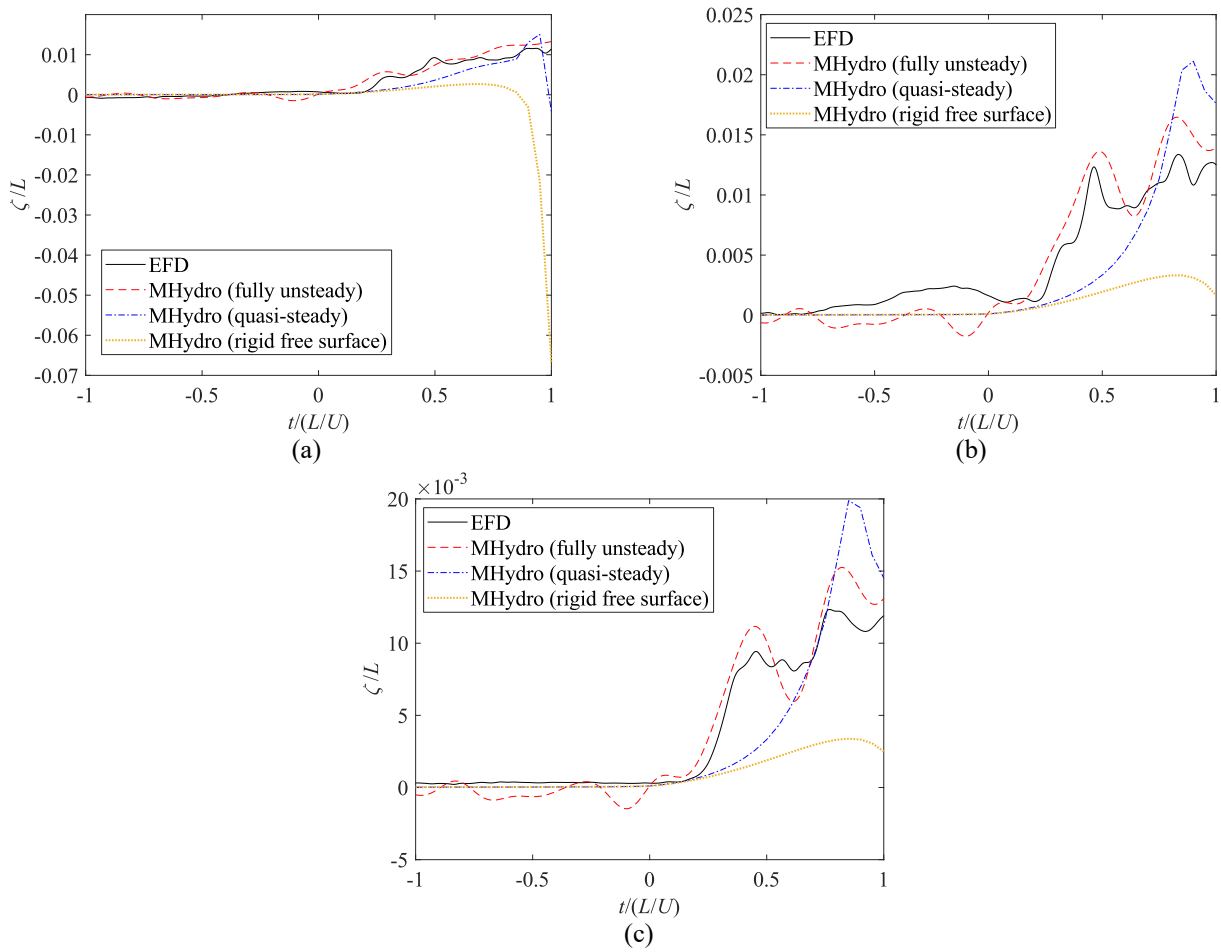

Figure 15 Wave elevations inside the lock: (a) waves at WG2; (b) waves at WG3; and (c) waves at WG4.

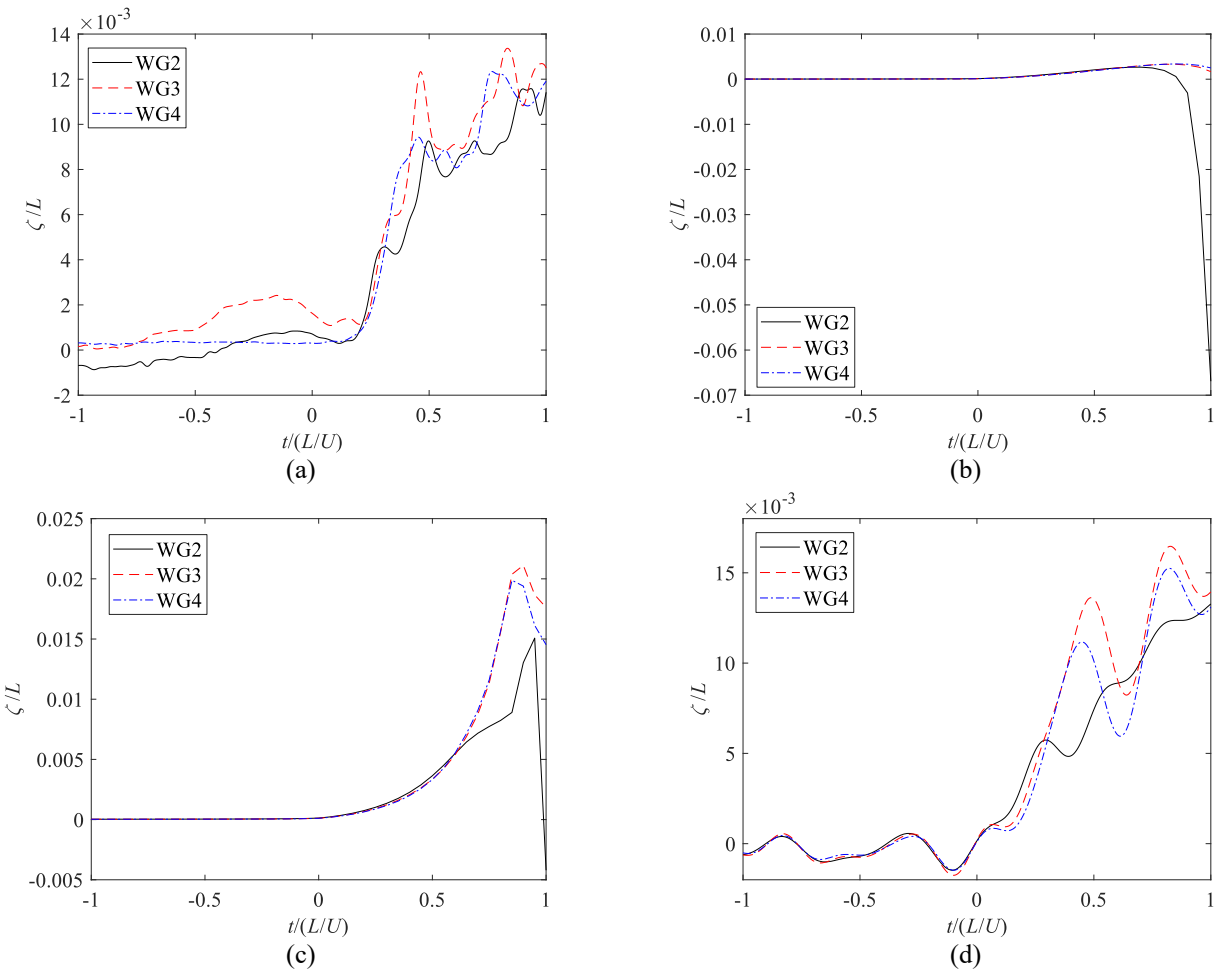

Figure 16 Wave elevations at WG2, WG3, and WG4: (a) EFD results; (b) results with a rigid free surface; (c) results with a quasi-steady free surface; and (d) results with a fully unsteady free surface.

4 CONCLUSION

Through the simulation and analysis of a box entering a lock at low speeds, this study demonstrates that the potential flow solver MHydro effectively captures the forces acting on the box and the general trends of wave generation during lock entry. Nevertheless, it recognises certain limitations in fully resolving the complexities of flow dynamics, attributing these issues to the simplifications inherent in the return flow model employed. The non-uniform distribution of return flow within the lock contributes to inaccuracies in the simulation results, highlighting the need for future advancements in predictive modelling. Furthermore, while a significant piston effect was not observed during the box's entry into the lock—primarily due to the constrained clearance between the box, lock walls, and lock bottom—the study underlines that its absence in this scenario does not preclude its occurrence in other ship-lock interactions. The presence and intensity of the piston effect are strongly influenced by factors such as the ratio of the ship's cross-sectional area to that of the lock and the entry velocity, necessitating further investigation to thoroughly understand its role and implications.

5 REFERENCE

Delefortrie, G., Willems, M., Vantorre, M. & Laforce, E., 2009. *Behavior of post panamax vessels in the third set of panama locks.*

Lataire, E., Delefortrie, G. & Vantorre, M., 2016. *Impact of banks on ship squat.*

Lataire, E., Vantorre, M. & Delefortrie, G., 2009. *Captive model testing for ship to ship operations.*

Lataire, E., Vantorre, M. & Delefortrie, G., 2012. A prediction method for squat in restricted and unrestricted rectangular fairways. Volume 55, pp. 71-80.

Lataire, E., Vantorre, M., Delefortrie, G. & Candries, M., 2012. Mathematical modelling of forces acting on ships during lightering operations. *Ocean Engineering,* Volume 55, pp. 101-115.

Li, M., Yuan, Z. M. & Yeung, R. W., 2020. *Unsteady wave-making resistance of an accelerating ship.*

Liu, Y. et al., 2024. Unsteady hydrodynamics of a surface piercing and fully submerged body when entering a lock. *Physics of Fluids*, 36(6).

Meng, Q. & Wan, D., 2016. URANS simulations of complex flows around a ship entering a lock with different speeds. *International Journal of Offshore and Polar Engineering,* 26(2), pp. 161-168.

Norrbin, N. H., 1976. *Bank effects on a ship moving through a short dredged channel.*

Schoenherr, K., 1960. *Data for estimating bank suction effects in restricted water and on merchant ship hulls.*

Terziev, M., Liu, Y., Yuan, Z. M. & Incecik, A., 2024. The resistance of a trans-critically accelerating ship in shallow water. *Ship Technology Research,* 71(1), pp. 14-32.

Vantorre, M., Verzhbitskaya, E. & Laforce, E., 2002. Model test based formulations of ship-ship interaction forces. *Ship Technology Research,* Volume 49, pp. 124-141.

Vrijburcht, A., 1988. *Calculations of wave height and ship speed when entering a lock,* Report No. PUB-391.

Wan, Z. et al., 2022. Effect of ship-lock induced surges on navigation safety in a branched lower approach channel system. *Journal of Hydrodynamics,* 24(2), pp. 481-496.

Yuan, Z. M., 2019. Ship hydrodynamics in confined waterways. *Journal of Ship Research,* 63(1), pp. 16-29.

6 AUTHORS BIOGRAPHY

Yihan Liu holds the current position of surveyor at China Classification Society. He is responsible for ship inspection, classification and certification. His previous experience includes study unsteady hydrodynamics as a PhD student in University of Strathclyde.

Momchil Terziev is currently a lecturer/assistant professor at the University of Strathclyde. He specialises in Computational Fluid Dynamics modelling for shallow water ship hydrodynamics and scale effects.

Zhi-Ming Yuan holds the current position of Reader at the University of Strathclyde, UK. His research activity is mainly focused on the Marine Hydrodynamics and Offshore Renewable Energy. He has been a member of the 29th-31st ITTC Manoeuvring Committee. Member of the organization and scientific committees of MASHCON conferences since 2022.

SIMULATION AND APPLICATION OF MODEL-BASED AND MODEL- FREE TRACK CONTROLLERS FOR SHIP MANOEUVRING IN SHALLOW AND CONFINED WATER

Eloot Katrien, Flanders Hydraulics, Belgium

Cisneros Matteo, University Antwerp, Belgium

Verwilligen Jeroen, Flanders Hydraulics, Belgium

Donatini Luca, Ghent University, Belgium

Mansuy Marc, Ghent University, Belgium

Daems Walter J.F., University Antwerp, Belgium

Massobrio Renzo, University Antwerp, Belgium

Hellinckx Peter, University Antwerp, Belgium

SIMULATION AND APPLICATION OF MODEL-BASED AND MODEL-FREE TRACK CONTROLLERS FOR SHIP MANOEUVRING IN SHALLOW AND CONFINED WATER

ELOOT KATRIEN, FLANDERS HYDRAULICS, BELGIUM
CISNEROS MATTEO, UNIVERSITY ANTWERP, BELGIUM
VERWILLIGEN JEROEN, FLANDERS HYDRAULICS, BELGIUM
DONATINI LUCA, GHENT UNIVERSITY, BELGIUM
MANSUY MARC, GHENT UNIVERSITY, BELGIUM
DAEMS WALTER J.F., UNIVERSITY ANTWERP, BELGIUM
MASSOBRIO RENZO, UNIVERSITY ANTWERP, BELGIUM
HELLINCKX PETER, UNIVERSITY ANTWERP, BELGIUM

SUMMARY

If autonomous navigation in dense harbours and waterways will be made possible, knowledge on different domains will have to be incorporated. The paper presents a short background on model-based and model-free track controllers that are used for systematic research on the accessibility of ships in shallow and confined water. Both control methods were evaluated based on a simulation of a 110 m inland vessel at different loading conditions when navigating on the river Seine in Paris at different water levels, discharges and wind conditions. The model-based controller gives far more precise control in comparison with human controlled tracks on the same simulator platform than model-free controllers. Therefore, an investigation started on the use of multi-paradigm simulation methods that combine different training and validation platforms for model predictive reinforcement learning in, for example, path following. The principle of this methodology is shown in a simulation on the Western Scheldt and will be further investigated in the DDSHIP, Data-driven smart shipping, project.

NOMENCLATURE

c	Weights of cost function aft, mid or fore (-)
e	(Cross track) Error (depending on parameter)
K	Proportional, integral and derivative gains of PID controller
mTEI	Mean track error integral (m)
MTE	Maximum track error (m)
mRI	Mean rudder integral (deg)
mRTV	Mean rudder total variation (deg)
mHEI	Mean heading error integral (deg)
T	Propeller thrust (N)
u	Longitudinal velocity (m/s)
v	Lateral velocity (m/s)
r	Yaw rate (deg/s or rad/s)
ξ	Look-ahead distance (time cycles in calculation)
η	Lateral deviation for cost function aft, mid or fore (-)
ψ	Heading (d = desired) (deg)
δ	Rudder angle (deg)

ABBREVIATIONS

AI	Artificial Intelligence
DOF	Degrees of freedom
FHSM	Flanders Hydraulics Simulator Matlab
LOS	Line of sight
MDP	Markov Decision Process
MPRL	Model Predictive Reinforcement Learning
NN	Neural Network
PMTC	Pre-science Model based Track Controller
RL	Reinforcement Learning

1 INTRODUCTION

Although, in Europe, not all waterways are yet open for remotely (human) controlled (inland) ships, research institutions and companies are joining efforts to investigate the challenges and possibilities for reliable path planning and path following by (model predictive) controllers. These controllers or autopilots can support different levels of autonomy as stated by CCNR (2022). Research is presently focusing on level 1 for steering automation, level 2 Partial automation for steering and propulsion control, and also level 3 systems with conditional automation to succeed in collision avoidance. High automation (level 4 with fallback performance without intervention of a boatmaster/skipper) and Autonomous or full automation (level 5 with unconditional performance without intervention) are not tackled yet.
Det Norske Veritas (DNV, 2025) presented during a webinar on January 14 2025 what "autonomy" should look like with systems in a two-dimensional field graded by the axes of "Level of automation" and "Degree of uncrewed operation" (Figure 1). The solutions on automation and crew reduction become larger so that depending on the economical and logistic operation of a ship and the available technologies a design can be chosen. In Flanders, conventional ships are upgraded with autonomous functions and decision support. Through the remote operations centres (ROC) (e.g. Shore control center from Seafar) inland and sea-going ships (FAST SIM from FastLines) are remotely controlled from the ROC with backup from the crew onboard. New ship designs are under investigation to combine the autonomy challenge with the zero-emission goals (X barge). With the timeline of the Japanese automation of ships set to 2040 (NIPPON Foundation), a more realistic time frame for developing trustworthy technologies for fully autonomous ships is introduced.

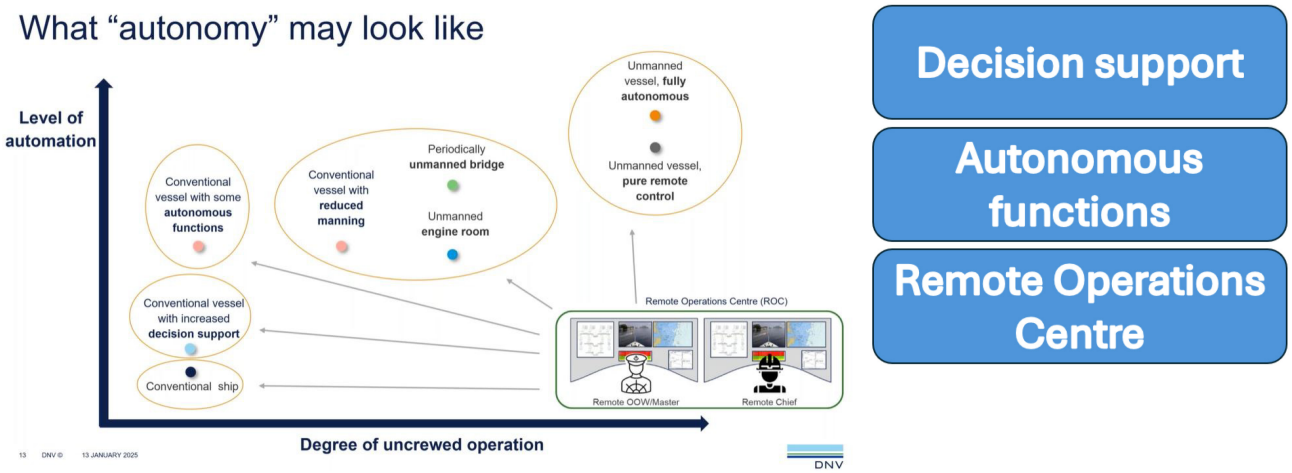

Figure 1 What "autonomy" looks like according to DNV (2025) (left) and the key elements in autonomous navigation (right).

The conditions in which ships operate differ, and in shallow and confined waterways with dense traffic the systems should be capable of interacting with the weather and waterway, other ships and constructions. An automated ship should set a preferred and continuously optimized path (planning) that considers the navigational parameters from the ship in the environment and follow that path (following) as accurately as possible with the propulsion and steering system.
Path planning and path following are closely connected because setting a path that a ship afterwards cannot follow, should be avoided by all means as controllers will not be capable of following the path.
The main focus of the paper is on path following with a predefined path based on knowledge of registered AIS tracks or human strategy. In open sea, the restrictions are due to the environmental constraints (wind, current, waves) and the closeness of ships towards each other in the waterway lanes, so that COLREGS (IMO) define the regulations to avoid collisions.
In shallow and confined water, restrictions in under keel clearance and lateral deviations occur due to the combination of bottom, banks and other shipping traffic in free-flowing or canalized rivers or canals, in open and sheltered wind areas. The use of predefined tracks is growing in inland navigation but these tracks are as smart as they represent a mean path of registered real ship tracks in very diverse circumstances (Potgraven, 2024). No local dynamic changes are automatically taken into account, so without observing the real situation a skipper, trusting the predefined track and the controller, can bring the ship in dangerous situations. The variability of tracks depends largely on the specific waterway dimensions in relation with the ship dimensions, the density of traffic and environmental conditions. Two examples are given based on profound AIS-analysis executed by Flanders Hydraulics in the framework of accessibility studies for the Flemish and Dutch Government (Verwilligen *et al.*, 2024a) and the Service Public de Wallonie (Verwilligen *et al.*, 2024b). In confined inland

waterways the ships are mainly sailing close to the centerline of the navigable section in both inbound and outbound directions and only for meetings or overtakings a two lane passage is organized. In Figure 2, this is shown based on an extensive AIS-analysis to investigate the traffic along the Walloon waterway network, with the red/orange (outbound) and greenish (inbound) tracks on the same path width at Péruwelz on the canal Nimy-Blaton-Péronnes.

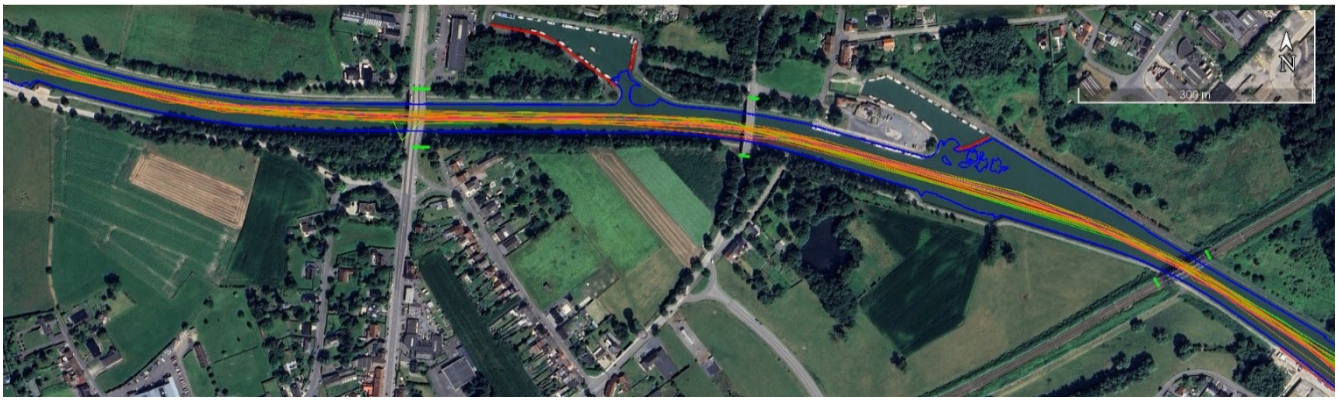

Figure 2 **Canal Nimy-Blaton-Péronnes at Péruwelz with inbound (greenish colour) and outbound (reddish colour) tracks of inland vessels (15-23/08/2022).**

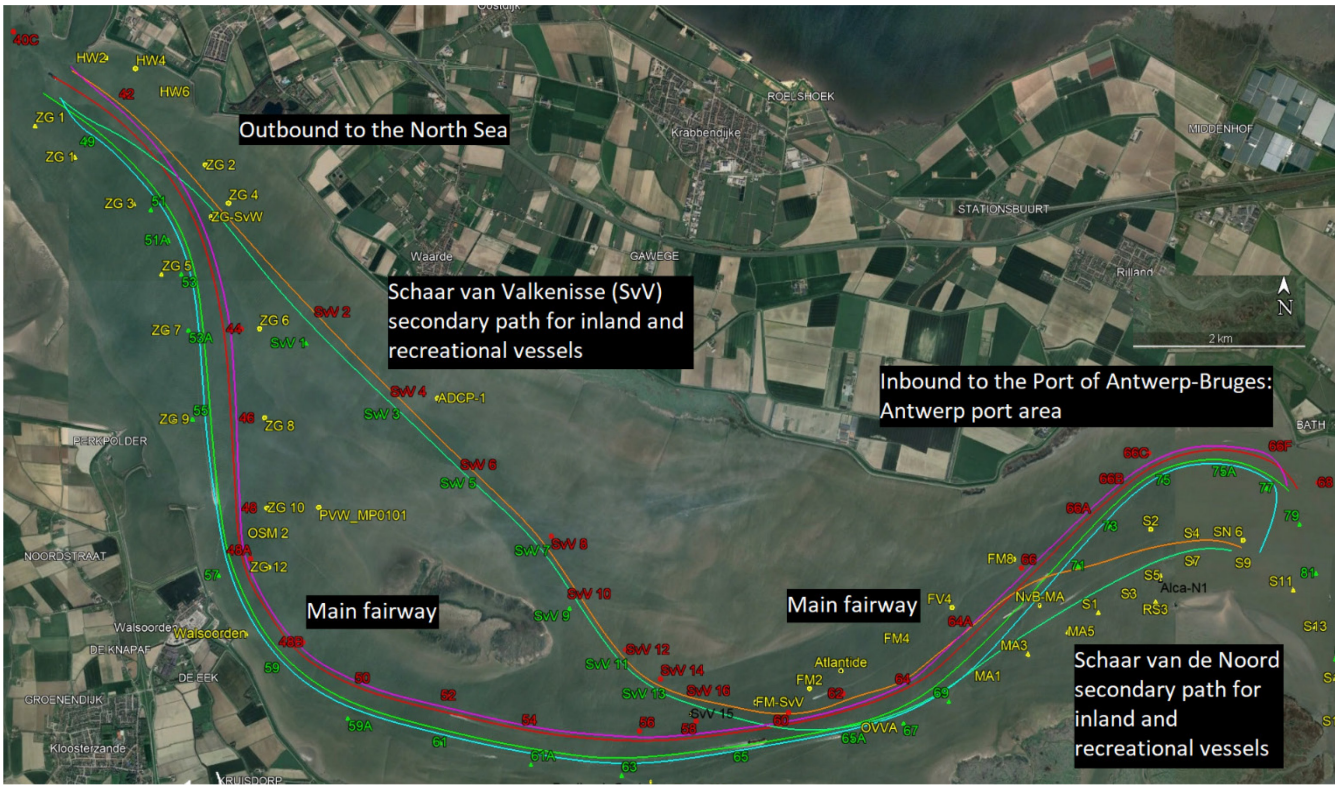

Figure 3 **Mean paths of sea-going (green = inbound, red = outbound) and inland (main fairway: blue = inbound, purple = outbound; secondary path: light green = inbound, orange = outbound) vessels on the Western Scheldt main fairway and secondary paths based on AIS-analysis (December 2013).**

On the Western Scheldt both sea-going and inland ships are operating. When both ship types are present in the main fairway, then ship waves of sea-going ships may hinder inland ships. On the other hand dedicated secondary paths (by-passes) for inland ships induce additional crossings of the main fairway with corresponding increased risk of collision. In Figure 3 the mean paths are shown for outbound (red=sea-going, purple=inland) and inbound (green=sea-going, blue=inland) vessels in the main fairway, and outbound (orange) and inbound (lighter green) inland vessels on the secondary paths of Schaar van Valkenisse and Schaar van de Noord. Two clearly distinctive lanes occur as the fairways with dense traffic require separate paths. The mean paths of the inland vessels in the main fairway are closer to the buoy lines than the sea-going (larger) vessels. Predefined tracks, designed based on these mean paths on two-way fairways or a centerline path (less ship-bank interaction) on inland waterways, require different design parameters for collision avoidance path planning and path following.

The research in this paper belongs partially to the joined project Data-driven Smart Shipping (DDSHIP) with the aim of setting a methodology for the development of model predictive reinforcement learned (MPRL) path planning and following (Flanders Hydraulics, University of Antwerp and Ghent University). For the training, simulation software of different institutes is interfaced so that a digital platform is developed which should not only serve research institutes but also companies willing to test their technologies like autopilots in virtual, representative environments.

2 CONTROLLERS IN SIMULATION

Flanders Hydraulics has a long experience in using a pre-science model based track controller (PMTC) for steering the design ship in diverse environmental conditions through manoeuvring simulations for port or waterway design. High-fidelity models are then available (derived from hundreds to thousands of model tests in a towing tank) that can accurately predict the ship behaviour in the confined waterway.
Nevertheless, for the majority of the vessels sailing worldwide and passing confined waterways, such advanced prediction models are lacking and only data (positional, kinematical and control) monitored while sailing can support the prediction. A demonstration of the use of different controllers from the PMTC to a fuzzy autopilot and thus model-based or model-free controllers was previously done for sea-going vessels in Chen *et al.* (2021) for the Western Scheldt and is now given for passages of the river Seine in Paris, a very confined river with nearby banks and more than 35 bridges of which 20 historical arch bridges. Considering the advantages of the fuzzy autopilot compared to the PMTC for the Western Scheldt, the question arises if model-free controllers suffice for confined inland waterways.

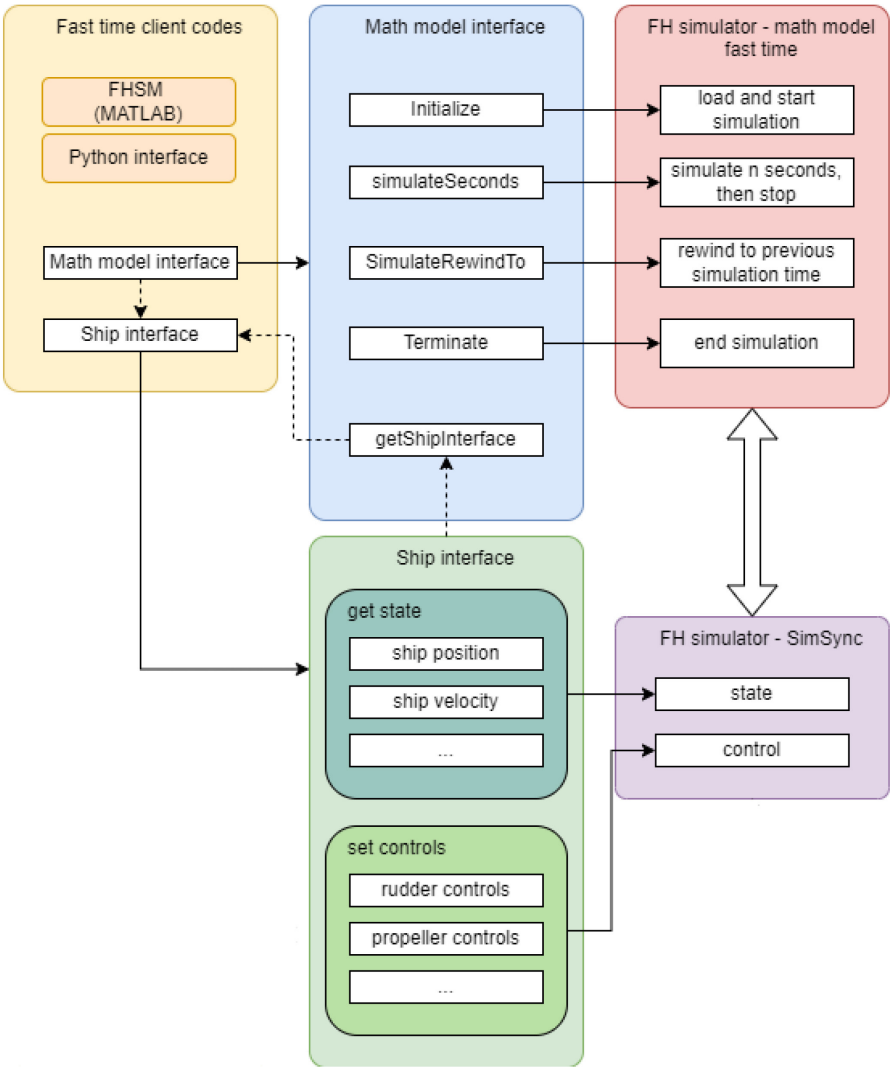

Figure 4 **Interfacing between the external client codes and the simulator at Flanders Hydraulics.**

2.1 INTERFACING SHIP MANOEUVRING MODELS AND CONTROL FOR SIMULATION

Flanders Hydraulics (FH) has several full mission bridge simulators specifically devoted to ship manoeuvring in shallow and confined water. At the heart of the simulators, mathematical manoeuvring models account for the forces related to shallow water, banks, ship - ship interactions, locks, waves, wind and current and nautical bottom. The simulators can now also serve as a virtual test bed for autonomous navigation by interfacing (third-party) controllers via newly developed software interfaces (Figure 4). The new interfaces, written in native C++ with a .NET wrapper to expose their functionality to a wider range of programming languages, provide control over the simulation (starting, pausing, rewinding, stopping), as well as the possibility to interact with SimSync, the communication layer of FH simulators. The interaction with SimSync provided by the new interfaces allows any client code to read ship state variables (e.g. the ship's position and velocity in 6DOF) and to change control values (e.g. propeller rate and rudder angle), thus making it possible to gain full control over a simulated ship. The new interfaces provide a reliable and practical way for client code to interact with both fast time and real time simulations, also decoupling the logic of the interface functionality from the implementation details of FH simulators.

2.2 MODEL-BASED TRACK CONTROLLERS

2.2 (a) Description

Model-based controllers are used in a wide range of disciplines. The models which are mathematical or data-driven, should describe the (physical) behaviour of the system that has to be controlled. In ship manoeuvring, model-based controllers are introduced to give more realistic control within the constraints of the ship in the environment. Mathematical models that are used at Flanders Hydraulics are at least 3 degrees-of-freedom (DOF) which describe the physical behaviour of the ship in the horizontal plane (surge, sway and yaw). But in control by non-nautical researchers, often lower DOF models are used. In the DDSHIP project researchers from different backgrounds are working together, which translates in the use of simplified 1 DOF (yaw) models up to 6 DOF complex modular models with all degrees of manoeuvring and sea-keeping (surge, sway, heave, roll, pitch, yaw) and separate modules to take into account the effects of hull, propulsion and steering but also the interactions between these modules.

2.2 (b) Pre-science model-based track controller or PMTC

The PMTC, which is a prescience model-based track controller developed at Flanders Hydraulics (Vantorre *et al.*, 1997), (Changyuan Chen *et al.*, 2021), is a model predictive controller (MPC) which uses high-fidelity mathematical models (Figure 5) not only for open water but also for other external hydrodynamic effects (e.g. ship-bank, ship-ship). The controller was first introduced in the 1990s to control ships under strong bank effects at the Canal Ghent-Terneuzen. The advantage is the accurate prediction rate but the drawback is that such models are not available for all ship types in all loading conditions and environmental circumstances, met in real life. The principle of adding different prediction models in a decision support system based on a cost function as Eq. (1) that minimizes the deviations (cross track errors) at fore, mid and aft of the ship contour compared to the reference track, can be used in simpler model-based controllers. The propulsion and steering system parameters (propeller rate and rudder angle for a conventional ship) are evaluated in the pre-science prediction phase so that the settings are chosen that minimizes the error from the reference track. The parameters that can be tuned, are the weights of the cost function c_F, c_M and c_A and the look-ahead distance ξ (Figure 5), together with the frequency and steps in which the propeller rate and rudder angle are changed to mimic the interval based settings by humans. This PMTC in prediction can be made as complex as necessary taken the ship and the waterway where the model-based control has to be executed. An investigation of the availability of different models in the prediction with some related accuracy has been conducted in Eloot & Mansuy, (2024). The exercise was made on the Seine in Paris and showed that some hydrodynamics (wind or ship-bank interaction) are more important than others for a specific control path.

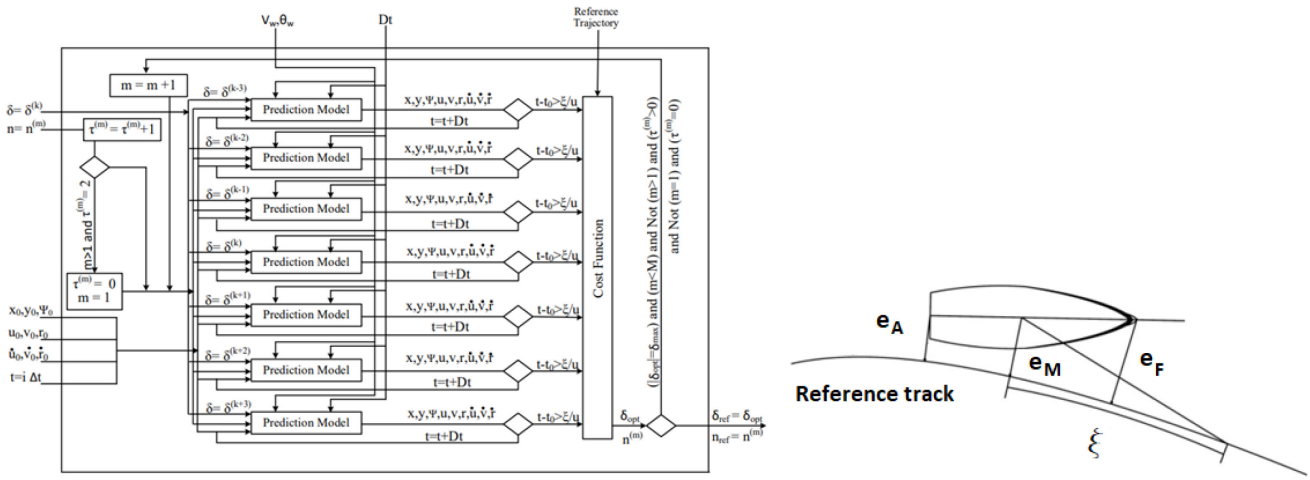

Figure 5 Description of principle and cost function of pre-science model-based track controller or PMTC.

$$C = c_F e_F^2 + c_M e_M^2 + c_A e_A^2 \quad (1)$$

2.2 (c) Model predictive reinforcement learning or MPRL

The DDSHIP research project, current state-of-the-art reinforcement learning (RL) algorithms are enhanced by incorporating model predictive control with domain-specific knowledge for collision avoidance and complex manoeuvring. This approach considers both data-driven and simplified manoeuvring models and is presented in Figure 6. In traditional RL, a deep neural network predicts the expected reward for each possible action given the current state, and the Markov Decision Process (MDP) selects actions based on a probability distribution of these expected rewards. The proposed enhancement combines this reward prediction with simulation-based validation. The key innovation is a two-stage process. First, a subset of actions with the highest predicted rewards are defined. Then, these actions are simulated over a predefined timeframe to recalculate their actual rewards. The MDP uses both the initial predictions and the simulation results to make final action selections, accounting for any discrepancy between predicted and simulated outcomes. This hybrid approach aims to leverage the strengths of both neural network predictions and physics-based simulations. Through this methodology, more reliable and safer decision-making in complex manoeuvring scenarios is expected to be achieved, while maintaining computational efficiency by limiting detailed simulations to the most promising actions.

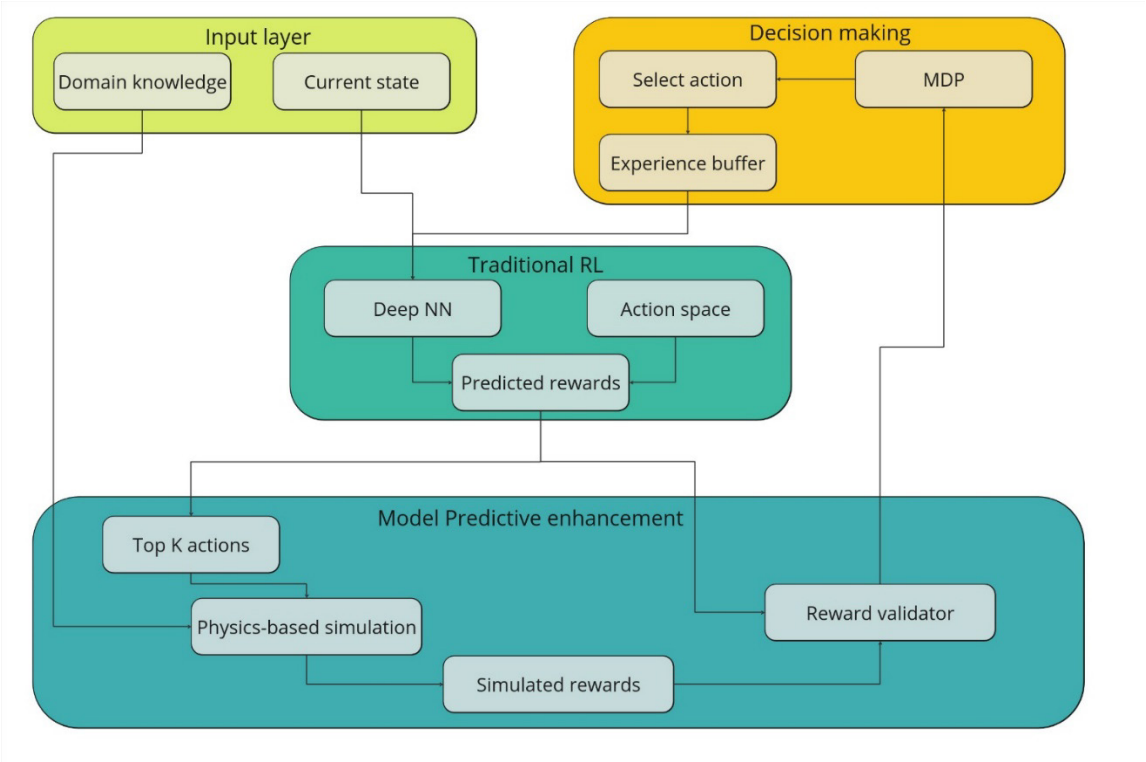

Figure 6 **Model predictive reinforcement learning flow chart with a decision making based on traditional predicted and physics-based simulated rewards.**

2.3 MODEL-FREE TRACK CONTROLLERS

For model-free track controllers errors comparing the actual and desired state are used for control decisions so that none of behavioral constraints are directly included in the decision process. In this research PID and Fuzzy controllers are used to compare the control with model-based controllers.

2.3 (a) PID controller

The proportional-integral-derivative (PID) controller is generally used in ship control. The error on the actual ψ and desired ψ_d heading angles, is evaluated and controlled by setting the rudder angle, depending on the proportional, integral and derivative gains K_P, K_I and K_D:

$$\delta = K_P(\psi_d - \psi) + K_I \int_0^t (\psi_d - \psi) d\tau - K_D \dot{\psi} \quad (2)$$

2.3 (b) Fuzzy controller

The Fuzzy controller which was elaborated and tested in the PhD work of Changyuan Chen (2021), Figure 7, consists of four blocks: fuzzification, fuzzy rules, fuzzy inference and defuzzification, to control an actual situation, described by a heading angle deviation e and the change in time of this deviation de/dt, through the setting of a rudder angle δ.

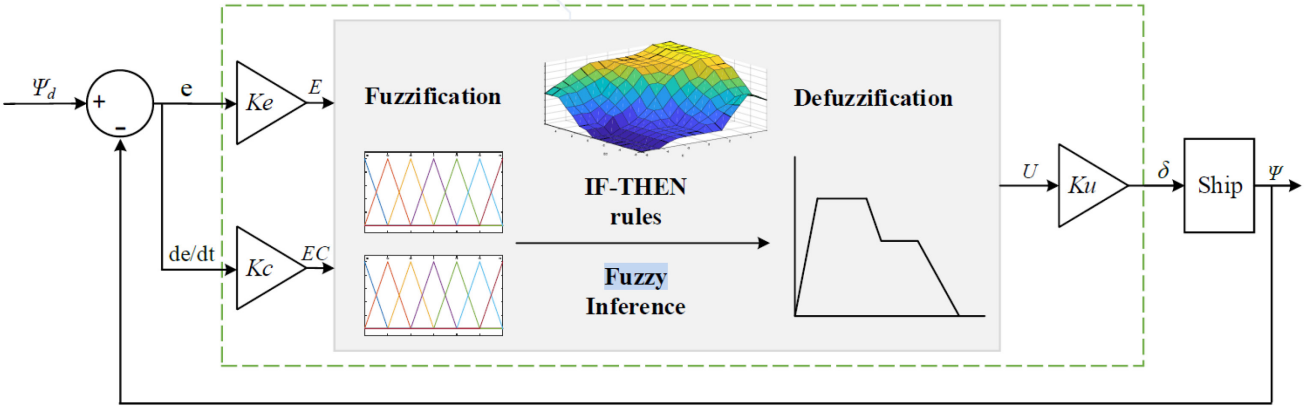

Figure 7 **Overview of the Fuzzy controller from Changyuan Chen (2021).**

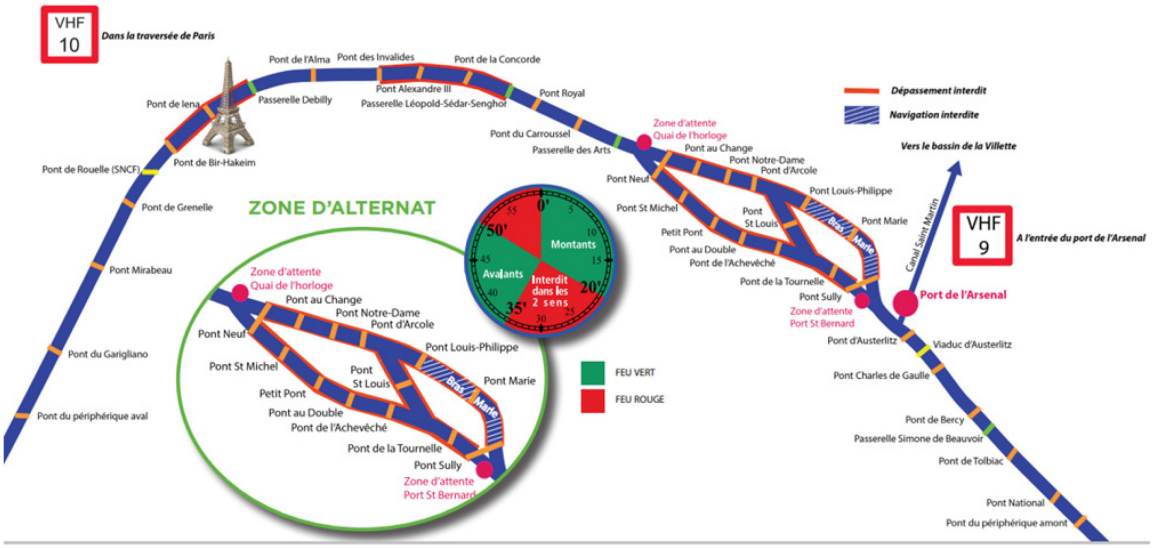

Figure 8 **Navigational procedures on the river Seine and the bridges in Paris (Voies Navigables de France).**

3 SIMULATIONS IN SHALLOW AND CONFINED WATER

To visualize the performance of model-based and model-free track controllers for manoeuvres in shallow and confined water an investigation is made for inland ships passing the city of Paris on the Seine and preliminary results for control through reinforcement learning for inland ships on the Western Scheldt in Belgium. The waterborne transport on the Seine is characterized by merchant ships bringing goods from inland Europe to the harbour of Le Havre and vice versa but in the meantime letting tourist enjoy the historic and modern scenery. The challenges are closely related to follow a path designed depending on the highly varying current, water level and wind conditions with restrictions due to the air draft and narrow width under arch bridges and alternate or dense traffic in different sections. The Western Scheldt is for inland ships much wider and thus the challenges are less so that this environment is taken for a proof of principle on reinforcement learning in autonomous navigation.

3.1 PASSING THE CITY OF PARIS ON THE SEINE

The use of the PMTC and model-free track controllers is demonstrated through the passage of the Seine for the alternate zone in Paris between Pont d'Austerlitz and Passerelle des Arts (Figure 8). The simulation environment was developed in the framework of an accessibility study for larger commercial and passenger ships (Marc Mansuy et al., 2023) under different discharges (water level and current) and wind conditions. Before executing real time simulations on a ship manoeuvring simulator with French professional skippers with ample experience on the river Seine, the trial matrix was reduced by executing fast time simulations with the PMTC as autopilot. A qualitative comparison between simulations with a human (skipper) and the PMTC was summarized in Eloot & Mansuy, (2024) and revealed good correspondence between the tracks realized by the high-fidelity PMTC and French skippers.

For the demonstration of the performance of model-based and model-free controllers a 110 m inland containership with a reduced beam of 10.55 m and two loading conditions of 1.7 m and 2.8 m are track-controlled on a predefined track at a water level of 120 cm at Pont d'Austerlitz, an increased current corresponding with 140 cm water level and a variable wind field of 2 to 4 Bft from a southwestern direction. Consecutively, as human controlled simulations from Marc Mansuy et al. (2023) were available, at an increased water level of 280 cm and corresponding current field, additional PMTC simulations were executed at this higher current. All conditions that are simulated with the ship and environmental parameters are summarized in Table 1.

Table 1 Ship and environmental parameters for the human, model-based and model-free controlled simulations (SIM, PMTC, FUZZY and PID).

Control/Simulation	Draft	Beam	Water level/current	Wind
Name	[m]	[m]	[cm]	[Bft]
SIM35, human	1.7	10.55	280/280	2-4
SIM36, human	1.7	9.65	280/280	2-4
PMTC0	1.7/2.8	10.55	120/140	2-4
FUZZY0	1.7/2.8	10.55	120/140	2-4
PID0	1.7/2.8	10.55	120/140	2-4
PMTC1	1.7	10.55	280/280	2-4
PMTC2	2.8	10.55	280/280	2-4
PMTC3	1.7	10.55	280/280	2-4
PMTC4	1.7	10.55	280/280	2-4

The predefined track was composed based on tracks sailed on the simulator during validation runs by French skippers and restrictions due to bridge passages. During real life sailing the skippers create margin in counteracting hydro- and a erodynamic influences by taking for example the inner bends of the zigzag manoeuvre to be executed between the islands on the Seine (Ile Saint-Louis and Ile de la Cité). Also the behaviour of the vessel itself, for example depending on the draft, has to be considered to safely pass and avoid under and above water collisions.

3.1 (a) Qualitative comparison

In the qualitative comparison the human and PMTC controlled simulations are first compared as both are considered as containing most knowledge based manoeuvring capacities. For the comparison two real time simulations (SIM35 and SIM36) were available executed by a French skipper but only at a larger water level of 280 cm and related current (Mansuy et al., 2023). An overall view is presented in Figure 9. The reference track for the controller is presented in light blue (with 0.1 km indication) and the PMTC simulation with blue filled black contours. A detail between 168.9 km and 170.3 km is shown in Figure 10 with an extraction of the passage of the bridges between 169.8 km and 170.3 km. All human and PTMC controlled ship tracks are free from depth lines (red at 1.7 m depth) and thus grounding but in SIM35 the skipper collided with the portside bridge pillar at Pont Neuf (170.3 km, red ship contour and green arch air draft). It can be seen on Figure 10 that the largest deviations are seen compared to the predefined track for SIM35 with continuous adjustments to keep back on track.

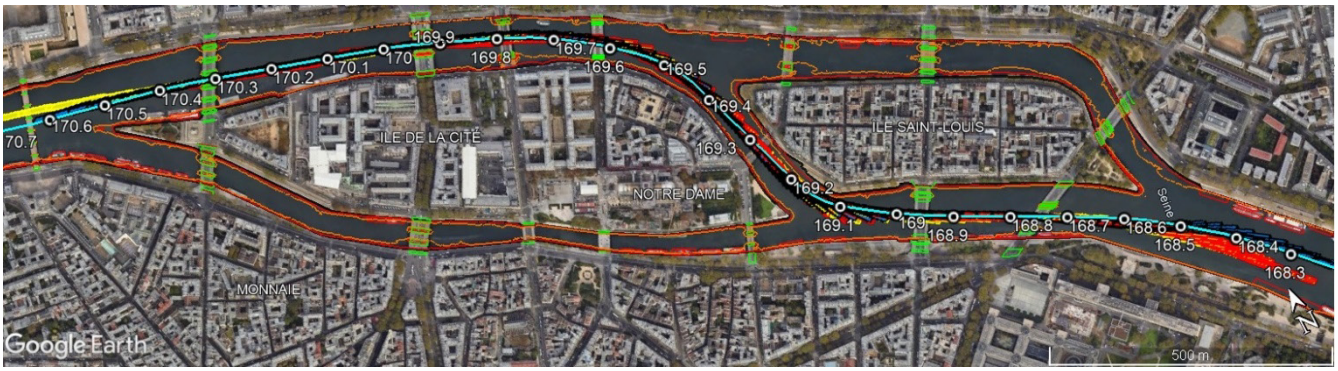

Figure 9 Overall view of the tracks of human (SIM35, SIM36) and PMTC0 simulations for a 110 m vessel at 1.7 m draft (120 cm water level, 140 cm current and SW 2 to 4 Bft wind) – km indication along the (light blue) preference track.

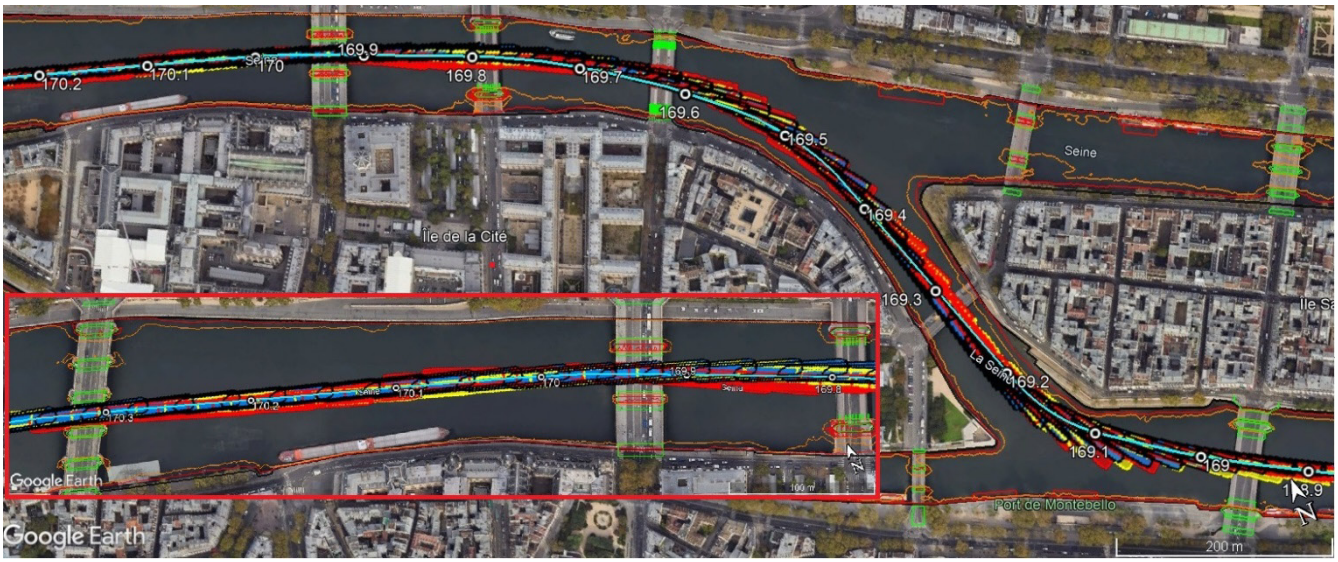

Figure 10 **Detail of the zigzag manoeuvre between Ile Saint-Louis and Ile de la Cité with a closer view to the passages of the bridges between km 169.8 and 170.3 (blue with black contour = PMTC0, red = SIM35 and yellow = SIM36 by skipper).**

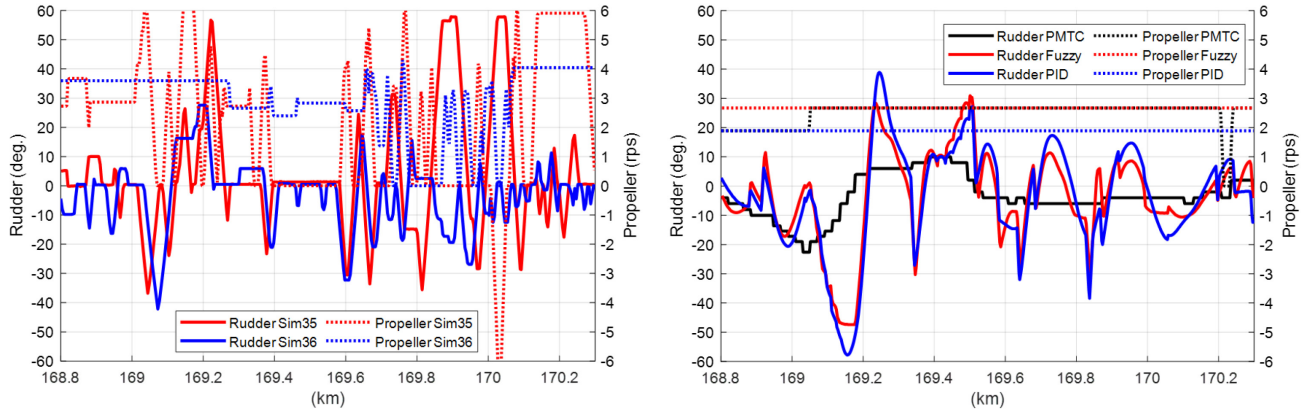

Figure 11 **Use of rudder angle (deg) and propeller rate (rps) for human controlled (SIM35 and SIM36, left) and PMTC0, Fuzzy0 and PID0 simulations within the track between 168.8 and 170.2 km on the Seine in Paris, 110 m vessel at 1.7 m draft.**

The control by setting propeller rate and rudder angle is shown in Figure 11 with the human controlled settings left and the track controller settings right. Now the model-free controllers are also compared. In SIM35 the propeller rate is often put to zero rps to control the speed with a higher variation of the rudder angle compared to SIM36 (smaller beam). The PMTC was restricted in changing the rudder angle in steps of 2 degrees with a maximum of 20 deg in one setting while the skipper and model-free controllers take large steps in rudder angle setting. The comparable rudder settings of the two model-free controllers are remarkable. This could be attributed to the same line of sight (LOS) method as input for both controllers and the linear interpolation scheme for the Fuzzy controller. For the propeller rate, the skippers often stopped the engine (especially in SIM35) while speed control was considered for the PMTC (with two different values during the shown track) and constant propeller rate for the Fuzzy or PID controller. Different gain settings for the PID controller have been checked and only a PD control with finally a negligible D gave the best control. Also increasing the propeller rate for the PID controller did not decrease the heading error.

The PMTC0, FUZZY0 and PID0 simulated paths are shown for the loading condition of 1.7 m in Figure 12 and for the maximum draft of 2.8 m in Figure 13. Thanks to the higher mass at the larger draft, the effect of wind and current on the ship behaviour and track reduces, so that the paths of model-free controlled simulations (Fuzzy and PID) are closer to the predefined track. But for both drafts and the model-free controlled simulations, the passage of a narrow bridge's arch followed by a small heading change, leads to a quick change of the rudder angle and overshoots in swept paths with touching of the bridge arch with the ship contour (downstream 169.9 km and 170.3 km).

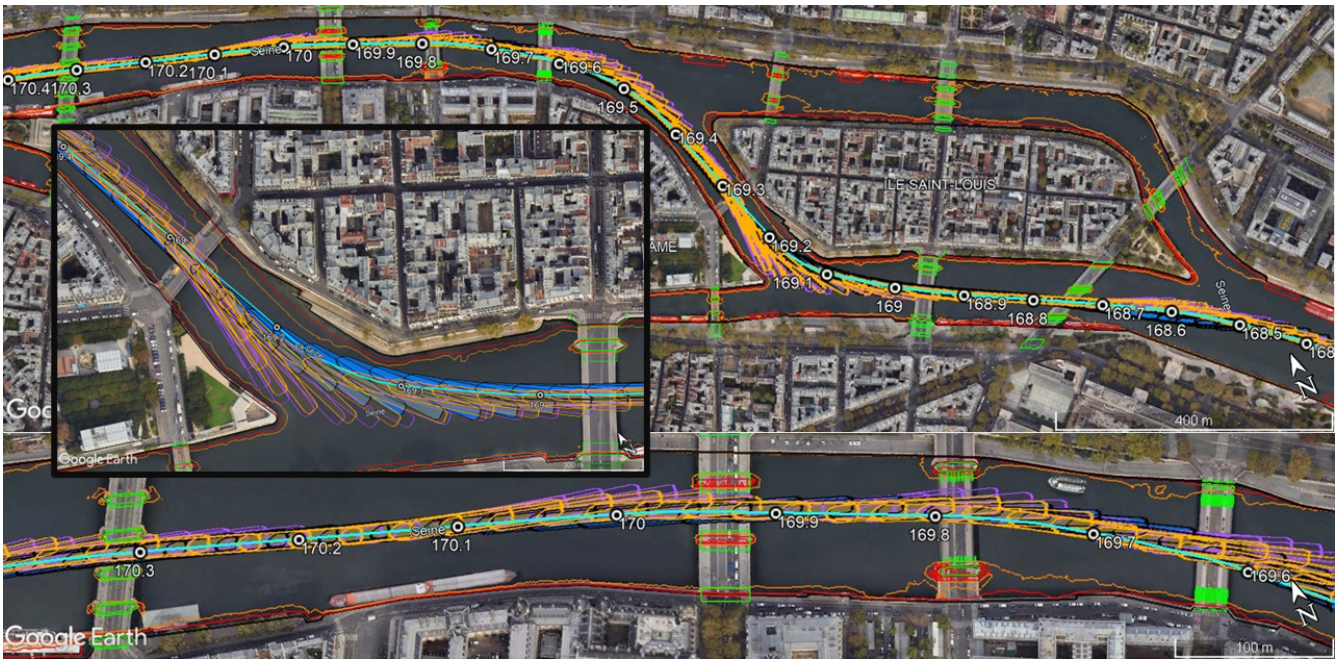

Figure 12 **Overview and detailed extractions of the PMTC0 (blue with black contour), FUZZY0 (orange) and PID0 (purple) simulated tracks of the 110 m vessel at 1.7 m draft.**

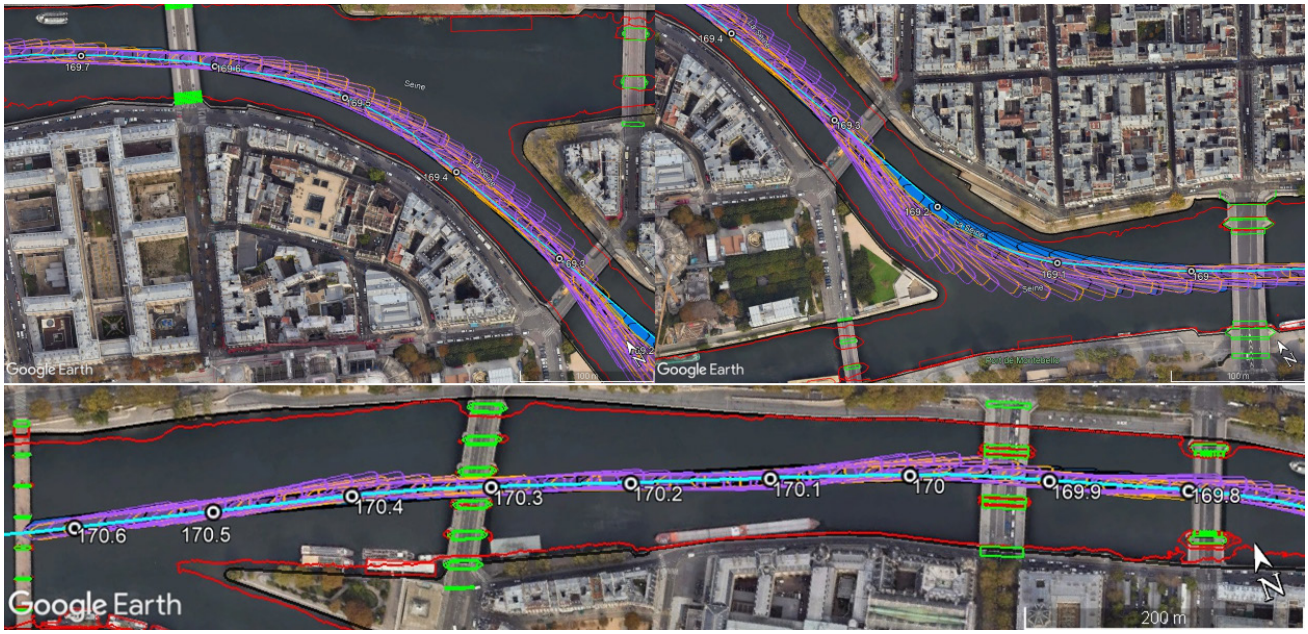

Figure 13 **Detailed extractions of the PMTC0 (blue with black contour), FUZZY0 (orange) and PID0 (purple) controlled tracks of the 110 m vessel at 2.8 m draft.**

The settings of the PMTC required weights for the cost function in equation (1) of 5, 5 and 1 (fore, mid and aft) so that the fore body of the ship should be close to the reference path and a lookahead time of 50 seconds or approximately 125 to 150 m or thus more than one ship length, taken the ship speed into account. The settings of the controllers were not changed for the considered loading conditions (first tuning for smallest draft and reuse for highest draft).

To further investigate the human or PMTC control for the specific environmental conditions at 280 cm water level, four simulations were conducted (Figure 14: SIM36, PMTC2 and PMTC4 are shown):

1. PMTC1: 1.7 m draft, same settings as previous PMTC simulations, except increased desired speed of 4 m/s and rps
2. PMTC2: 2.8 m draft, same settings as Sim1
3. PMTC3: 1.7 m draft, settings as Sim1, changed path between 170.3 and 170.6 km to correspond to human selected path

4. PMTC4: 1.7 m draft, settings as Sim3, decreased look-ahead distance (± 50% of Sim1) for better path following

Drifting is larger for the PMTC controlled vessel at 1.7 m draft compared to the human at the same draft or PMTC controlled vessel at 2.8 m draft. Loading condition has a clear influence and the use of more frequently changing rudder angles with higher values for the French skipper steered simulation gives closer tracks to the reference path.

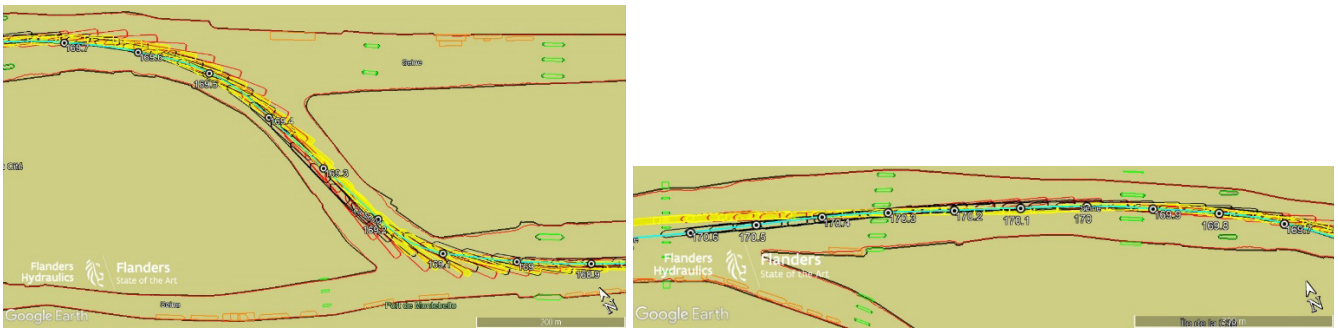

Figure 14 Zigzag manoeuvre and passage of bridges for human controlled simulation SIM36 (yellow) and PMTC controlled simulations PMTC2 (black) and PMTC4 (red) for 280 cm water level.

3.1 (b) Quantitative comparison

A quantitative comparison is made based on different control performance indexes defined by Changyuan Chen et al., (2020) and repeated in He et al. (2023). The cross track error e is the distance from point C to the reference line (W_{k-1},W_k) in Figure 15 and the heading error e_ψ is the difference between the heading of the ship (line CB) to the heading of the reference line (AB). The look-ahead distance ξ for the LOS for PID or Fuzzy controller is given as a percentage of the length between perpendiculars (0.5 to 2 L_{PP}).

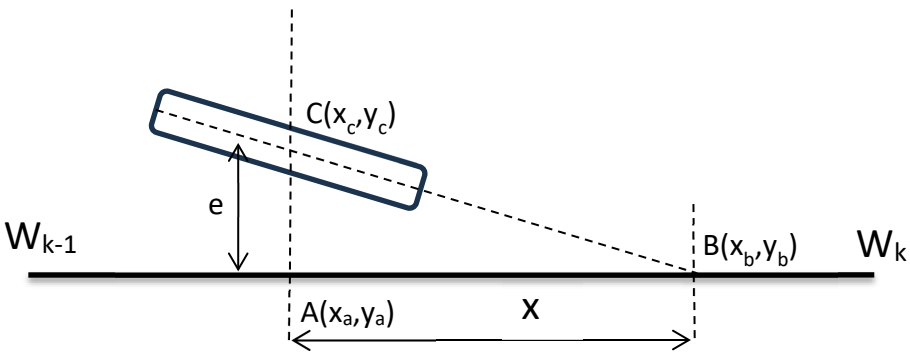

Figure 15 Cross track error e and look-ahead distance ξ for the ship with origin C in relation to the line with waypoints W_{k-1} and W_k

The performance indexes are, with N_0 and N_1 the starting and end time steps for evaluation:

1) Mean track error integral, mTEI (path following accuracy)

$$mTEI = \frac{1}{N_1 - N_0 + 1} \sum_{k=N_0}^{N_1} |e(k)| \tag{3}$$

2) Maximum track error, MTE

$$MTE = \max\{|e(N_0)|, |e(N_0+1)|, \dots, |e(N_1)|\} \tag{4}$$

3) Mean rudder integral, mRI (aggressiveness of rudder control)

$$mRI = \frac{1}{N_1 - N_0 + 1} \sum_{k=N_0}^{N_1} |\delta(k)| \tag{5}$$

4) Mean rudder total variation, mRTV (energy consumption on rudder)

$$mRTV = \frac{1}{N_1 - N_0} \sum_{k=N_0+1}^{N_1} |\delta(k) - \delta(k-1)| \tag{6}$$

5) Mean heading error integral, mHEI (heading control accuracy)

$$mHEI = \frac{1}{N_1 - N_0 + 1} \sum_{k=N_0}^{N_1} |e_\psi(k)| \tag{7}$$

The performance indexes for the different controller types and the human controlled simulations for the 110 m vessel at both drafts are shown in Table 2. The lowest value for each index is shown in bold. The parameters, draft and water level/current, are retaken from Table 1 to clearly show the influence of the loading condition and the discharge on the indexes. The Fuzzy and PID controllers give the largest values for the track and heading errors and for the mean rudder integral comparable values as the human controlled simulations. They do not succeed in coming close to the predefined track and the conclusion could be that model-free controllers should accept more variability in combined engine and rudder settings as is clearly seen for human controlled SIM35 and SIM36 in Figure 11.
Comparing the values for 1.7 m draft the skipper can maintain a closer track to the predefined but with much more rudder use and variability. With the PMTC controlled PMTC2 at 2.8 m draft and PMTC4 at 1.7 m, track errors are 19 to 70% higher, with the maximum track error up to 58 and 92% higher than SIM36. The heading error is lower for PMTC2 (-8%) and 40% higher for PMTC4 compared to SIM36. The mean rudder integral is approximately half of the human controlled value for all PMTC controlled simulations and by decreasing the look-ahead distance in PMTC4 the mean rudder total variation increases a bit, but far from the value skippers induce. This is clearly due to the obligation of only 2 degrees steps of rudder angle difference in consecutive decisions which will have an effect also on the track and heading errors.

Table 2 The performance indexes for the different controller types (PMTC, FUZZY and PID) compared to human controlled simulations for the 110 m.

Control/Simulation	Draft	Water level/current	mTEI	MTE	mRI	mRTV	mHEI
Name	[m]	[cm]	[m]	[m]	[deg]	[deg]	[deg]
SIM35, human	1.7	280/280	2.83	9.04	16.19	3.72	4.79
SIM36, human	1.7	280/280	2.68	**7.02**	19.78	5.82	4.15
PMTC0	1.7	120/140	**2.45**	9.20	**9.51**	0.30	3.98
FUZZY0	1.7	120/140	4.60	18.43	15.81	2.11	5.03
PID0	1.7	120/140	5.65	20.64	18.39	1.59	6.36
PMTC1	1.7	280/280	5.19	14.50	11.44	0.34	6.51
PMTC2	2.8	280/280	3.19	11.11	10.52	**0.28**	**3.82**
PMTC3	1.7	280/280	5.05	14.50	11.89	0.36	6.53
PMTC4	1.7	280/280	4.58	13.53	11.57	0.44	5.85

3.2 SHIPS ON THE WESTERN SCHELDT

The Western Scheldt, a complex estuarine environment, presents significant challenges for autonomous ship navigation due to its varying depth, strong currents, dense traffic and complex waterway geometry. This section describes the approach to develop and validate an autonomous navigation system using reinforcement learning for this river environment. While this work serves as an initial proof of principle, subsequent research will explore these concepts in greater depth.

3.2 (a) Multi-paradigm simulation methodology

The research develops an innovative methodology for training reinforcement learning (RL) agents for autonomous navigation in shallow and confined waterways using multi-paradigm simulation. Traditional approaches often rely on computationally intensive, high-fidelity simulators, which can make the training process prohibitively expensive and time-consuming. The proposed methodology addresses this challenge by leveraging a hierarchical approach to simulation fidelity. The core of the approach is a modular framework that enables the seamless integration of different simulators and AI solutions. This framework allows training to begin with computationally efficient, low-fidelity simulations and progressively incorporate higher-fidelity models for specific aspects of the system dynamics. By incrementally introducing new paradigms and more detailed physics models, the trade-off between training efficiency and model accuracy can be optimized.

In this initial study, the feasibility of the approach is demonstrated through a two-stage process, starting with a computationally efficient 2D environment before moving to the Flanders Hydraulics simulator. Future work will focus on extending the training methodology to incorporate additional paradigms and simulators, further validating the effectiveness of the modular framework for developing robust autonomous navigation systems.

3.2 (b) Simulation definition

A custom 2D continuous environment was developed that roughly represents the Western Scheldt's navigational challenges. The simulation environment implements a simplified linear ship dynamics model based on three degrees of freedom (surge, sway and yaw). At the core of the simulation is a comprehensive state space that captures relevant aspects of the ship's motion and its relationship to the environment.
The state vector s_t at time t defined in Eq. (8), comprises thirteen variables that describe the ship's condition and its navigational context.

$$s_t = [x,\ y,\ \psi,\ u,\ v,\ r,\ d_c,\ d_{c+1},\ d_{c+2},\ e_c,\ e_h, \delta,\ T] \tag{8}$$

In the state vector defined in Eq. (8), the ship's position is defined by coordinates (x, y) and ψ represents the heading. The vessel's motion is characterized by three velocity components: surge velocity u (longitudinal), sway velocity v (lateral), and yaw rate r (rotational velocity). To enable effective navigation, the state space incorporates several navigational parameters: the distances to three sequential checkpoints (d_c for current, d_{c+1} and d_{c+2} for the next two), along with two error measurements—cross-track error e_c (lateral deviation from the planned path) and heading error e_h (difference between actual and desired heading). The state representation is completed by the actual control inputs: rudder angle δ and propeller thrust T.

This model is described by a set of differential equations that couple these motions while accounting for hydrodynamic effects and control inputs. The ship's equations of motion in the 3-DOF model are expressed as a set of coupled differential equations defined in Eq. (9), (10) and (11). Inertial and centripetal forces and moment are neglected which gives a significantly simplified but first model for training.

$$\frac{du}{dt} = k_t \cdot T + X_u \cdot u \tag{9}$$

$$\frac{dv}{dt} = k_v \cdot \sin(\delta)\ +\ Y_v \cdot v \tag{10}$$

$$\frac{dr}{dt} = k_r \cdot \delta +\ N_r \cdot \frac{v}{L} \tag{11}$$

Eq. (9) models the surge dynamics, where thrust T is scaled by the thrust coefficient k_t and dampened by the hydrodynamic coefficient X_u. Eq. (10) describes sway motion, where the rudder angle δ influences lateral movement through the sway coefficient k_v, with Y_v providing hydrodynamic damping. Eq. (11) governs the yaw motion, coupling the rudder angle effect k_r with the sway-induced moment and damping N_r, scaled by the ship's length L.

The action space for the autonomous navigation system consists of two continuous control variables: rudder angle and thrust. Both actions are mapped in a range [-1, 1] and then transformed to physical parameters. This mapping ensures that the reinforcement learning agent calls realistic bounds while maintaining a normalized action space for training stability.

The reward function synthesizes multiple aspects of navigation performance into a single scalar signal. Distance-based progress is rewarded through a hyperbolic tangent function of position changes, while heading alignment is encouraged through a cosine relationship with the desired course. Cross-track error is penalized using a scaled hyperbolic tangent function, providing strong feedback for path-following behaviour while maintaining smooth gradients for learning. Additional rewards are provided for checkpoint progression, with the magnitude scaled by the relative progress through the course. Terminal rewards and penalties provide clear feedback for successful navigation or various failure conditions.

3.2 (c) Proximal policy optimization (PPO) implementation

The autonomous navigation system employs Proximal Policy Optimization with an actor-critic architecture designed specifically for the complexities of ship navigation. The neural network architecture begins with a shared processing backbone that feeds the 13-dimensional state input through two fully connected layers of 256 and 128 units respectively, each followed by ReLU activation functions. This shared representation captures the fundamental features of the navigation state before branching into specialized actor and critic networks.
The actor network outputs both the mean and standard deviation of a Gaussian policy distribution, with the mean processed through a tanh activation to bound the control outputs appropriately. This stochastic policy enables exploration during training while maintaining smooth control outputs suitable for ship navigation. The critic network provides state value estimates that enable advantage estimation for policy updates.

3.2 (d) Training and validation

As proof of principle, the agent was trained in the low-fidelity computationally efficient 2D environment and then tested in the Flanders Hydraulics simulator. The training process spanned 1300 iterations, with five complete navigation episodes each. Each episode initializes the ship with slight position perturbations around the starting coordinates, introducing variability that promotes robust policy learning.

During each iteration, the collected experiences are used for ten epochs of policy updates. The advantage values are normalized within each batch to improve training stability, and an entropy bonus with coefficient 0.01 encourages exploration of the action space. The PPO algorithm optimizes the policy using a clipped surrogate objective function that balances learning stability with policy improvement. The clipping parameter is set to 0.2, preventing excessive policy updates that could destabilize learning. The advantage estimates utilize Generalized Advantage Estimation (GAE) with a discount factor of 0.99 and a GAE parameter of 0.95, providing a good balance between bias and variance in the policy gradient estimates. The learning process is monitored using metrics including the average episode reward and policy loss. This last is computed using a composite loss function that combines policy improvement with value function learning and entropy regularization. The mTEI, MTE and mHEI metrics defined in equations (3), (4) and (5) respectively, were used to measure the accuracy of the model.

Following initial training in the computationally efficient 2D simulation environment, the agent's performance was validated in the Flanders Hydraulics simulator. This sophisticated simulator provides substantially enhanced physical modeling, including full 6DOF ship dynamics, detailed hydrodynamic current models, high-resolution bathymetry, and realistic environmental conditions.

Table 3 The performance indexes for the trained agent tested in both simulators (mTEI, MTE and mHEI).

	mTEI	**MTE**	**mHEI**
Environment	[m]	[m]	[deg]
2D simulator	0.57	3.95	3.44
FH simulator – no wind and no current	21.38	54.24	6.88
FH simulator – wind and no current	24.91	60.66	8.59
FH simulator – wind and current	46.60	164.28	10.31

The initial testing results presented in Table 3 and visualized in Figure 16 demonstrate varying levels of performance across different simulation environments. While the agent achieved promising accuracy in the 2D environment with relatively low error metrics (mTEI of 0.57 m, MTE of 3.95 m, and mHEI of 3.44 degrees) due to the low fidelity of this environment, performance degraded when tested in the more complex Flanders Hydraulics simulator. The introduction of additional environmental factors led to progressively larger deviations, with the most challenging scenario (including both wind and current) resulting in a mTEI of 46.60 m, MTE of 164.28 m, and mHEI of 10.31 degrees. It is important to note that these results represent preliminary findings from an initial proof-of-principle implementation. Future research will focus on optimizing the training process through enhanced simulation paradigms and more sophisticated training methodologies, which is expected to significantly reduce these error margins and improve overall navigation performance.

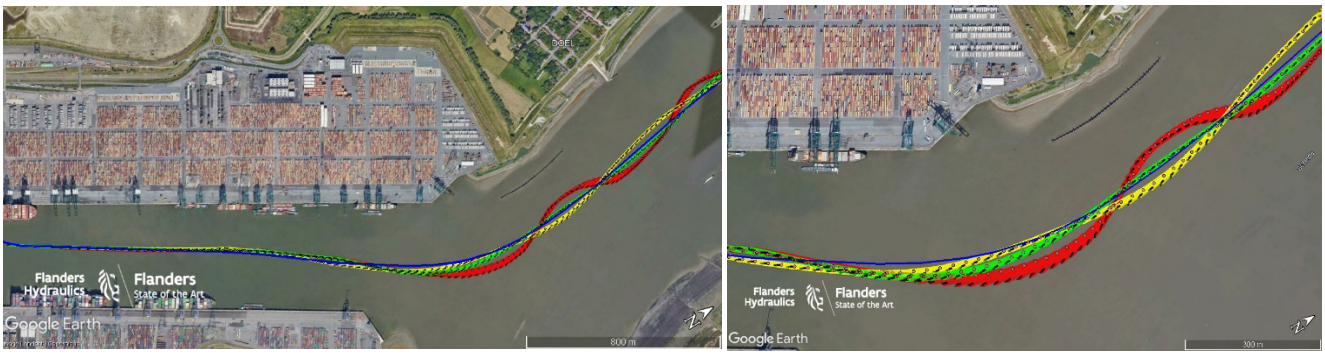

Figure 16 **Test of a trained agent (using low fidelity simulator) in the Flanders Hydraulics research simulator using three different configurations (reference track in blue): no wind and no current (green path), wind and no current (yellow path), wind and current (red path).**

4 CONCLUSIONS

If autonomous navigation in dense harbours and waterways will be made possible, knowledge on different domains will have to be incorporated. In this paper researchers with different backgrounds are joining together through the DDSHIP project for Data-driven Smart Shipping. In the project situational awareness of the surrounding waterborne world for the autonomous ship is combined with model predictive control with models describing the environmental conditions and ship behaviour in very diverse situations and AI trained agents through reinforcement learning.

The paper gives a description of model-based and model-free track controllers that have been used for systematic research on the accessibility of ships in shallow and confined waterways and port areas for sea-going and inland ships. The pre-science model-based track controller (PMTC) applies advanced mathematical models for the prediction of shallow water manoeuvring, ship-bank and ship-ship interaction and environmental models (current, wind) in the prediction phase of the controller. In this phase engine/propeller and rudder settings are providing track predictions which are compared with the predefined track so that the best control setting can be chosen. Many parameters define these decisions and even more are to be included to mimic or replace the human controlled handling. Model-free track controllers, as Fuzzy and PID, do not know the physical constraints for a ship in a dense traffic lane but reduce the deviation and heading errors for the predefined path.

Because in manoeuvring the number of determining parameters are large, the aim is to introduce model predictive reinforcement learning controllers which are enriched by mathematical models on the physics. The question arises in which specific part, path planning or path following, the most domain knowledge should be included or if both, setting the path and following with a controller, are intertwined as the path should be realistic in the given situation for the ship and loading condition and the ship controls should suffice to avoid collisions.

In the examples the PMTC, Fuzzy and PID controllers are compared to each other for the passage of the river Seine in Paris with a zigzag manoeuvre and passages of bridges in a confined river under wind and current. The predefined track which is followed by the controllers, is based on human controlled tracks which were derived from simulations but in real life could be derived from AIS tracks. Nevertheless, the variety in tracks is large so that situational awareness and path planning algorithms should define regularly updated paths for collision avoidance in economical and ecological ways. The performance of the PMTC, due to its large domain knowledge, is coming closest to the human controlled simulations on the same simulator platform of Flanders Hydraulics. The disadvantage of the PMTC is that such high-fidelity models require an enormous amount of physics based data and modelling. Therefore with the proof of principle for an inland ship on the Western Scheldt the University of Antwerp illustrates the multi-paradigm simulation methodology for training of model predictive reinforcement learning controllers. The focus is on path-following but could also be used for path planning. The simplified ship behaviour model on which the control agent is trained, does not suffice if the performance is tested on the Flanders Hydraulics simulator but at least the start is given for a further exploration of adding more precise surrogate models to improve the setup. The DDSHIP project will run until end 2026.

5 ACKNOWLEDGEMENTS

The authors want to acknowledge the subsidy organization VLAIO from the Flemish Government for the DDSHIP project. De Blauwe Cluster is the agency that led the proposals request and that supports the cluster strategic research for the partners: Flanders Hydraulics (coordinator), University of Antwerp and Ghent University. Acknowledgements are also for the valuable insights the project “Etude des conditions de navigation dans la traversée de Paris” for the French waterway authority Voies Navigables de France gave on traffic handling on the river Seine in Paris.

6 REFERENCES

CCNR (2022). https://www.ccr-zkr.org/files/documents/AutomatisationNav/Note_explicative_en.pdf

Chen, C; Verwilligen, J.; Mansuy, M.; Eloot, K.; Lataire, E.; Delefortrie, G. (2021). Tracking controller for ship manoeuvring in a shallow or confined fairway: design, comparison and application. *Appl. Ocean Res. 115*. Available at: https://dx.doi.org/10.1016/j.apor.2021.102823

Chen, C.. (2021). Numerical and Experimental Study on Ship Motion Control Systems in Shallow Water. ISBN 9781119130536

Chen, C.; Delefortrie, G.; Lataire, E. (2020). Experimental investigation of practical autopilots for maritime autonomous surface ships in shallow water. *Ocean Eng. 218*(*October*): 108246. doi:10.1016/j.oceaneng.2020.108246

Chen, C.; Verwilligen, J.; Mansuy, M.; Eloot, K.; Lataire, E.; Delefortrie, G. (2021). Tracking controller for ship manoeuvring in a shallow or confined fairway: Design, comparison and application. *Appl. Ocean Res. 115*: 102823

DNV (2025). https://www.dnv.com/maritime/webinars-and-videos/on-demand-webinars/

Eloot, K.; Mansuy, M. (2024). Manoeuvring in shallow and confined water with model predictive track controllers. *J. Phys. Conf. Ser. 2867*(*1*): 012021. doi:10.1088/1742-6596/2867/1/012021

He, H.; Van Zwijnsvoorde, T.; Lataire, E.; Delefortrie, G. (2023). Model predictive controller for path following ships validated by experimental model tests. *Ocean Eng. 288*(*P2*): 115971. doi:10.1016/j.oceaneng.2023.115971

Mansuy, M; Candries, M.; Eloot, K.; Page, S. (2023). Simulation study to assess the effect of ship beam on the navigable flow conditions in Paris. *TransNav. Int. J. Mar. Navig. Saf. Sea Transp. 17*(*1*): 25–31. Available at: https://dx.doi.org/10.12716/1001.17.01.01

Mansuy, M.; Candries, M.; Eloot, K.; Page, S. (2023). Simulation Study to Assess the Maximum Dimensions of Inland Ships on the River Seine in Paris. *Lect. notes Civ. Eng.* (*264*): 186–200

NIPPON Foundation, https://en.nippon-foundation.or.jp/what/projects/ocean/meguri2040

Potgraven, P. (2024). Track pilots in inland shipping: Steering clear of too much trust [PRESENTATION]. *MTEC/ICMASS 2024, Trondheim, Norway, 29–30 Oct. 2024*. Ministerie van Infrastructuur en Waterstaat. 16 slides pp.

Vantorre, M.; Laforce, E.; Claeyssens, P. (1997). Development of an autopilot for fast-time simulation in confined waterways, *in*: (1997). *11th Ship control systems symposium, Vil 1*, Southampton. pp.203–2017. Available at: https://biblio.ugent.be/publication/398813 [date of retrieval: 13/07/2015]

Verwilligen, J.; Eloot, K.; Meire, D.; Delefortrie, G. (2024a). Historical evaluation of the navigability of the Western Scheldt for ultra large container ships, *in*: (2024a). *Proceedings of the 35TH PIANC WORLD CONGRESS 2024, Cape Town, South Africa, 29 April – 03 May 2024*. PIANC. ISBN 978-2-87223-041-9. pp.770–776. Available at: https://documentatiecentrum.watlab.be/owa/imis.php?module=ref&refid=395777

Verwilligen, J.; Panahi, S.; Eloot, K. (2024b). Study of Navigation and Trajectory Analysis on the Walloon Waterway Network: Software Manual for AIS Processing Toolbox SPW. *FH reports*, 22_012_9. Flanders Hydraulics: Antwerp

7 AUTHORS BIOGRAPHY

Katrien Eloot, PhD, naval architect, is senior expert nautical research at Flanders Hydraulics and chair of the Knowledge Centre (www.shallowwater.be). She is responsible for research on ship manoeuvring in shallow and confined water for private and public agencies worldwide. Her PhD focused on mathematical modelling and validation of ship behaviour based on experimental fluid dynamics in towing tanks. Through real time simulation with pilots and skippers on in house developed full mission simulators, accessibility studies are executed for harbours and waterways.

Luca Donatini, naval architect, is a researcher and PhD candidate at the Ships and Marine Technology Division (SMTD) of Ghent University. He is currently working on several projects in which SMTD provides scientific support to Flanders Hydraulics in improving and expanding the functionality of FH's simulators, with a non-exclusive focus on the effects of hydro/meteo data. His previous experience include a full implementation of spectral waves and seakeeping in the simulators of FH.

Cisneros Matteo holds the current position of PhD student in the modelling for sustainability (M4S) research team at the UAntwerp. He is part of the DDSHIP research project, his research focusses on data driven control for autonomous shipping.

Mansuy Marc, naval architect, is a researcher at the Ships and Marine Technology Division (SMTD) of Ghent University. He is currently working on several projects concerning the evaluation of the accessibility of (inland) ships through fast-time and real-time simulation on the FH simulators and also system identification and control for zero-emission autonomous vessels.

Verwilligen Jeroen holds the current position of senior expert in nautical research at Flanders Hydraulics. He is experienced with simulation studies, nautical accessibility studies, full scale measurements and AIS analysis.

Daems Walter J.F. holds the current position of senior software developer at the Department of Applied Engineering (UAntwerpen). He holds a master's degree in physics. He is currently participating in the creation of a framework for multi-paradigm reinforcement learning.

Hellinckx Peter is a full professor at the UAntwerpen and the head of the department of Electronics-ICT and the M4S (Modelling for Sustainability research team). His research focusses on data driven control of sustainable systems in domains like but not limited to renewable energy, HVAC and autonomous shipping. He is co-founder of 4 (spin-offs) companies: Hysopt, Hi10, Digitrans and Rollo.ai.

ENHANCED FREE-RUNNING MANOEUVRING TESTS OF INLAND VESSELS IN MODEL SCALE

Matthias Tenzer, DST - Development Centre for Ship Technology and Transport Systems, Germany
Felix Roettig, DST - Development Centre for Ship Technology and Transport Systems, Germany
Rainer Kaiser, DST - Development Centre for Ship Technology and Transport Systems, Germany
Justin Jasa, DST - Development Centre for Ship Technology and Transport Systems, Germany
Benjamin Friedhoff, DST - Development Centre for Ship Technology and Transport Systems, Germany

ENHANCED FREE-RUNNING MANOEUVRING TESTS OF INLAND VESSELS IN MODEL SCALE

MATTHIAS TENZER, DST - DEVELOPMENT CENTRE FOR SHIP TECHNOLOGY AND TRANSPORT SYSTEMS, GERMANY
FELIX ROETTIG, DST - DEVELOPMENT CENTRE FOR SHIP TECHNOLOGY AND TRANSPORT SYSTEMS, GERMANY
RAINER KAISER, DST - DEVELOPMENT CENTRE FOR SHIP TECHNOLOGY AND TRANSPORT SYSTEMS, GERMANY
JUSTIN JASA, DST - DEVELOPMENT CENTRE FOR SHIP TECHNOLOGY AND TRANSPORT SYSTEMS, GERMANY
BENJAMIN FRIEDHOFF, DST - DEVELOPMENT CENTRE FOR SHIP TECHNOLOGY AND TRANSPORT SYSTEMS, GERMANY

SUMMARY

The transformation of inland shipping towards an automated mode of transport with clean propulsion concepts is initiated. While the path of automation with its intermediate steps is largely defined and first solutions for partial automation and remote control are available on the market, the race for technologies to decarbonise the drivetrain is completely open. However, it is evident that the operating costs of the drives and the investment costs for the drive power will increase significantly. As a result, the expected decline in the availability of power reserves for critical situations links the topics of automation and decarbonisation. Both fields of research require an improved knowledge of the manoeuvring behaviour of existing and future inland vessels. Free-running manoeuvring tests in model scale are of great importance in this development process, offering direct insight into manoeuvring characteristics. For example, evasive manoeuvres according to the European Standard laying down Technical Requirements for Inland Navigation vessels (ES-TRIN) are mandatory for ship's approval. In order to meet this increasing demand, a novel concept for this type of test has been developed at DST. Manoeuvres with a wooden model, equipped with remote-controlled propulsion and steering systems, are performed in front of the towing carriage. An optical motion tracking system tracks the model's movement, which is converted in real-time to full-scale GPS coordinates, enabling the use of real-world navigation technology. The technology integrates a rate-of-turn controller, a track-control system, and other automated functions for precise rudder control during predefined manoeuvres. Special attention is given to improving the reliability and repeatability of these tests, achieved through partial automation of the manoeuvres. A special focus of this paper is the investigation of the manoeuvring performance of ship models in shallow water condition and different water depths. Based on ongoing and completed research projects, examples of the system application and the results obtained are presented and discussed. In addition to evaluating the results in relation to ES-TRIN requirements, the findings also serve as a valuable basis for refining mathematical manoeuvring models. By ensuring repeatable and reliable model-scale manoeuvres, the accuracy of full-scale manoeuvre predictions can be enhanced, along with a deeper understanding of potential measurement uncertainties.

NOMENCLATURE

AHRS	Attitude and Heading Reference System	
BAW	Federal Waterways Engineering and Research Institute (Germany)	
BMWK	Federal Ministry for Economic Affairs and Climate Action (Germany)	
CFD	Computational Fluid Dynamics	
DST	Development Centre for Ship Technology and Transport Systems	
EOT	Engine Order Telegraph	
ES-TRIN	European Standard laying down Technical Requirements for Inland Navigation vessels	
GPS	Global Positioning System	
NMEA	National Marine Electronics Association	
RC	Remote Control	
WLAN	Wireless Local Area Network	
λ	Scale	-
C_B	Block Coefficient	-
h	Water depth	m
L	Length	m
L_{PP}	Length between Perpendiculars	m
L_{WL}	Length of Waterline	m
r	Rate of Turn	°/min

S_{wett}	Wetted Surface	m^2
T	Draft	m
t	Time	s
V	Displacement	m^3
v_M	Model Velocity	ms/s
v_S	Ship Velocity	km/h
δ	Rudder angle	°
σ	Standard Deviation	-

1 INTRODUCTION

With decarbonisation and automation, inland waterway shipping is facing a profound transformation that has already begun in recent years. The work is currently focussing strongly on various propulsion systems using alternative forms of energy (batteries, hydrogen, methanol, ammonia, etc.). At the same time, the spread of market-ready partial automation systems (such as track guidance assistants) is increasing rapidly and extensive research is being conducted into fully automated systems.

Both aspects also relate to a large extent to the knowledge of the manoeuvring characteristics of the ship. In the field of alternative propulsion technologies, it can be assumed that overpowering – as it is often found on current ships – will no longer be present to the same extent in the future. The determination of a realistic and sufficient propulsion power for defined purposes of an inland vessel is also enabled by the use of modern computer-aided methods and the inclusion of detailed data sets of the boundary conditions (e.g. water depths and current velocities) as part of the ship development process. The reduction in available propulsion power can lead to a significant change of the manoeuvring capability. This can either result in the vessel's non-compliance with the applicable regulations or a restriction of the usual ease of manoeuvring due to a limited power reserve. In any case, early knowledge of the manoeuvring behaviour is crucial in order to initiate technical revisions and/or develop and implement suitable training concepts.

In the context of automation, determining the manoeuvring behaviour as precisely as possible is a central component for implementing the required algorithms. In addition to the simplified approaches commonly used to date (e.g. model by Nomoto et al. (1957)), increasingly complex modelling is required. Even if the use of artificial intelligence is promising for this field of research, defined reference and validation tests are an important element. Furthermore, as long as humans remain part of an automated system, training measures will play a decisive role.

Free-running manoeuvring tests at model scale are one option to determine the manoeuvring behaviour of a ship. All relevant hydrodynamic effects of the ship in interaction with the environmental conditions (shallow water, banking, etc.) become directly effective. The normally moderate scale factors of the models of inland vessels (approx. 10 to 16) usually mean that scale effects are of minor importance. However, the accuracy of the manoeuvres depends crucially on the starting phase (acceleration of the ship model) and the initial state of the vessel before the manoeuvre begins. To achieve repeatable test results, the model must be kept parallel to the tank centreline at always the same distance to the tank walls with as few control commands as possible to achieve a steady approach speed with minimal rate of turn. If one of the two requirements is not fulfilled, the manoeuvre is not repeatable. Signal flows and filter algorithms have already been discussed in a first publication (see Roettig et al. (2023)).

These type of tests have been carried out for many years to determine the ship's manoeuvring behaviour and to develop mathematical manoeuvring models. However, the complexity of the ship model (especially for inland waterway vessels with multiple propellers and rudders) and the test setup (appropriate data transmission and motion capturing) has meant that this type of experiment has tended to be carried out in an academic context. A categorisation of the various options can be found, for example, in Quadvlieg (2016) and Stern et al. (2011). Examples of full-scale sea trials and free-running manoeuvring tests as well as strategies for their evaluation can be found, for example, in Oltmann (1973), Oltmann (1978), Abkowitz (1980), Rhee and K.-H. Kim (1999), Artyszuk (2003), Quadvlieg and Brouwer (2011), Im, Han, and Nguyen (2011), Araki et al. (2012), Sutulo and Guedes Soares (2014), Eloot et al. (2015), H. Xu, Hinostroza, and Guedes Soares (2018), Suzuki, Tsukada, and Ueno (2019), Hinostroza, H. T. Xu, and Guedes Soares (2019), Mei, Sun, and Shi (2020), Jin et al. (2021), I.-T. Kim et al. (2021), Yasukawa, Hasnan, and Matsuda (2021) and Kulbiej (2021). All of these publications deal with seagoing vessels. The only known work to date that uses the method of free-running manoeuvres for inland waterway vessels are the publications by Mucha et al. (2019) and Chillcce and el Moctar (2023).

This paper shows the development and implementation of a concept for free-running model tests in the large shallow water towing tank at DST. With a modern optical motion tracking system and a fibre-optic gyroscope as well as a commercial track guidance assistant (track pilot) for the control and automation of the models, the accuracy and effectiveness of these tests are significantly increased. First results show the possible applications for different research questions.

2 OBJECTIVES AND MANOEUVRING REQUIREMENTS

The presented concept for free-running model tests allows different objectives for the evaluation of obtained ship motions. A central aspect here is the assessment of compliance with the applicable minimum standard for the evasion and turning characteristics of inland waterway vessels, as published in the *European Standard Laying Down Technical Requirements For Inland Navigation Vessels (ES-TRIN)* (2025). Figure 1 shows the evasive manoeuvre with an example time series for the rate of turn (yaw rate) r and the rudder angle δ as well as the important times t_0 to t_4. The times required, depending on the water depth/draught ratio, are given in Table 1.

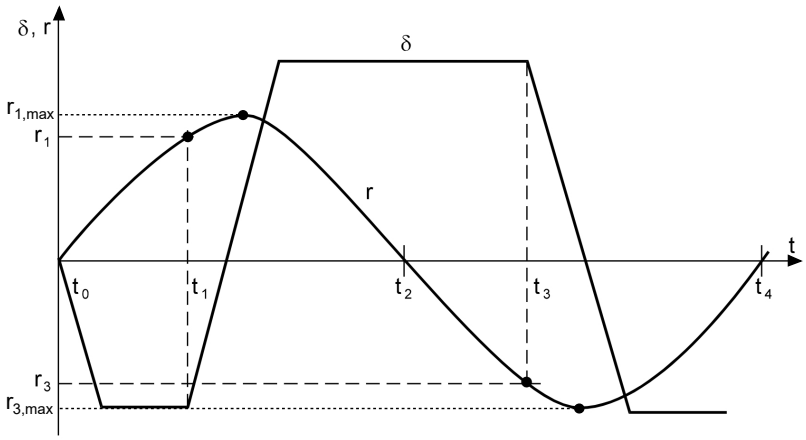

Figure 1: Diagram of the evasive action manoeuvre with extension of maximum yaw rates

Table 1: Rudder angle, rate of turn and limit values for evasive manoeuvres according to ES-TRIN

Rudder angle $\delta\,[°]$	Required rate of turn $r_1 = r_3\,[°/min]$	Limit values for the time $t_4\,[s]$ in shallow and deep water $1.2 \leq h/T \leq 1.4$	$1.4 \leq h/T \leq 2$	$h/T > 2$
20	20	150	110	110
45	28			

This manoeuvre is very similar to a zigzag-manoeuvre used in maritime navigation and considers the yaw rate instead of the course angle and can therefore be carried out on rivers and in the towing tank with limited width. The requirements for these manoeuvres are usually a deadweight of at least $70\,\%$ and a constant initial ship velocity of 13 km/h. DST has extended the official parameters to include the maximum values for rate of turn $r_{1,max}$ and $r_{3,max}$ (see Figure 1). It is expected that these – analogous to the overshoot angles in the zig-zag-manoeuvre – will allow statements to be made about the ship's ability to stop turning. In addition to the motion parameters, other parameters of the manoeuvre are also determined. This includes, for example, the sway velocity and lateral offset of the ship.

In addition to determining compliance with the regulations, parametric analyses can also be carried out with regard to the ship design or different rudder profiles. The limit of manoeuvrability can also be determined by gradually reducing the ship velocity. This is reached when the times for t_4 are exceeded or can no longer be determined because the yaw rate is no longer reached. In addition to the official 20-20 and 45-28 manoeuvres, any combination – for example for low ship velocity – can, of course, be carried out.

Furthermore, evasive manoeuvres can also be used for configuration and parametrisation of the track pilot itself. The existing implementation and performance can be compared and improved using different ship models. For example, tests can also be carried out close to the wall, which result in additional banking effects and challenging for the track guidance system to keep on the desired trajectory.

3 EXPERIMENTAL SETUP

3.1 SHIP MODEL

The wooden ship model used corresponds to a typical inland container vessel (model 1) and a tanker vessel (model 2). Both models have a scale of 1:17 and are described in detail in Tables 2 and 3.

The model propellers are driven by electric 24 V-motors that are powered by two lead-acid batteries. All propulsion parameters are determined using appropriate propeller dynamometers and duct thrust sensors. Each of the rudders is actuated

Table 2: Dimensions of ship models

Parameter	Symbol	Unit	Model 1 Model	Model 1 Ship	Model 2 Model	Model 2 Ship
Scale	λ	[−]	17	1	17	1
Length	L	[m]	7.94	134.98	6.471	110
Length between Perpendiculars	L_{PP}	[m]	7.919	134.63	6.368	108.25
Breadth	B	[m]	0.832	14.15	0.674	11.45
Propulsion			Twin screw		Single screw	
Rudders			Four blades		Two blades	

Table 3: Draught-dependent parameters of ship models

Parameter	Symbol	Unit	Model	Ship
			Model 1	
Draught	T	[m]	0.153	2.6
Length of Waterline	L_{WL}	[m]	7.885	134.05
Displacement	V	[m^3]	0.905	4444.6
Wetted Surface	S_{wett}	[m^2]	8.291	2396.0
Block Coefficient	C_B	[−]	0.897	0.897
Draught	T	[m]	0.100	1.7
Length of Waterline	L_{WL}	[m]	7.746	131.68
Displacement	V	[m^3]	0.581	2854.1
Wetted Surface	S_{wett}	[m^2]	7.318	2115.0
Block Coefficient	C_B	[−]	0.881	0.881
			Model 2	
Draught	T	[m]	0.165	2.8
Length of Waterline	L_{WL}	[m]	6.434	109.38
Displacement	V	[m^3]	0.627	3080.5
Wetted Surface	S_{wett}	[m^2]	5.917	1710.0
Block Coefficient	C_B	[−]	0.874	0.874

by a servo from RC model making. When controlling the rudders via software, the actual rudder kinematics were also taken into account, which ensures that the rudder on the inside of the curve has a larger rudder angle. On board of an inland waterway vessel this kinematic is ensured by mechanical connections between both rudder shafts.

Each model is fully remote-controlled via a real track-keeping system, as it is installed on many ships in practice. This system was slightly adapted for use in the model tests. In addition to manual control via engine order telegraph and rudder lever (track pilot off), rate-of-turn control (river pilot) and track guidance (track pilot on), there is an additional mode for automated execution of evasive manoeuvres.

3.2 MOTION CAPTURING AND MEASUREMENT

The motion of the ship model is recorded in two separate ways, which are partly redundant and can be compared to each other. On the one hand, the position and motion data is recorded by an optical motion tracking system provided by Qualisys AB, using four infrared motion capturing cameras and one video camera. All cameras are installed at the front of the towing carriage (see green circles in Figure 2). The motion capturing is performed via passive spherical markers, which are placed on the side wall of the model (see red circles in Figure 2). Placing two cameras on each front bumper of the carriages provides an effective side view for detecting ship movements close to the basin walls. With this setup, a distance of approximately 25 metres in front of the towing carriage can be covered. During the test, the carriage is manually controlled to follow the sailing ship model keeping it inside the optical range of the motion tracking system. The recorded data in the longitudinal direction of the tank is therefore initially relative to the carriage and converted to global coordinates in real time using the known position and velocity of the carriage, which are measured by a laser distance meter and an encoder wheel.

On the other hand an iXblue Octans Surface gyrocompass and motion sensor is installed in the model. This is an attitude and

Figure 2: Ship model 1 in front of the carriage

heading reference system (AHRS) which is used to measure the models orientation and the linear accelerations in all three dimensions of space. Especially the heading and the rate of turn are used during the automated manoeuvring of the model.

3.3 DATA HANDLING

All data between the carriage and the model is transmitted via a local WLAN. For this purpose, both the carriage and the model are equipped with appropriate antennas. The data processing and handling between the used systems, including the data acquisition system, is realised via an in-house software. The model's position relative to the carriage is gathered from the motion capture system, while heading, rate of turn and accelerations are measured by the AHRS on board of the model. Data combination, calculation, filtering and scaling to full scale is done in real time by the developed software. To use the track pilot in the same way as on a real ship, the model position is transformed into artificial GPS coordinates.

The final data is sent as NMEA 0183 data packets via Ethernet to the track pilot. The track pilot internally calculates the corresponding motions and the necessary rudder angle to keep the model on the guiding line. Using the wireless connection to the model, the desired rudder angles are transmitted using again NMEA 0183 sentence. In addition, the control commands for the drives are transmitted in the same way. It should be noted that the rotational motions of the model are by the square root of the scale factor faster, compared to full scale, what has to be considered in terms of processor performance and signal transmission.

3.4 TEST PROCEDURE

All tests are performed in DST's large shallow water basin with a total length of 200 m and a breadth of 10 m. The test procedure usually consists of four steps, after releasing the model in front of the towing carriage (see Figure 2).

1. Manual steering of the model to the guiding line used
2. Switching on the track controller (track pilot)
3. Triggering the manoeuvre start
4. Manual stopping of the ship model

The released ship model can be steered like a real ship using the engine order telegraph (EOT) and the rudder lever. Experience has shown that an activation of the track controller near the intended guiding line shows the best results for the repeatability of the tests. In this case, the controller only has to process minor position and motion deviations and the starting conditions for the subsequent manoeuvre are optimal, as the model moves straight ahead in the towing tank with only minor deviations. During the period in which the track controller is active, it is possible to fine-tune the intended ship velocity, which is displayed

with good accuracy by the Kalman filter used (see Roettig et al. (2023)). The guiding line is usually defined parallel to the centreline of the tank depending on the expected space needed during the manoeuvre to reduce the distance and possible influence to the outer tank walls. Figure 3 shows the principle experimental setup and test procedure.

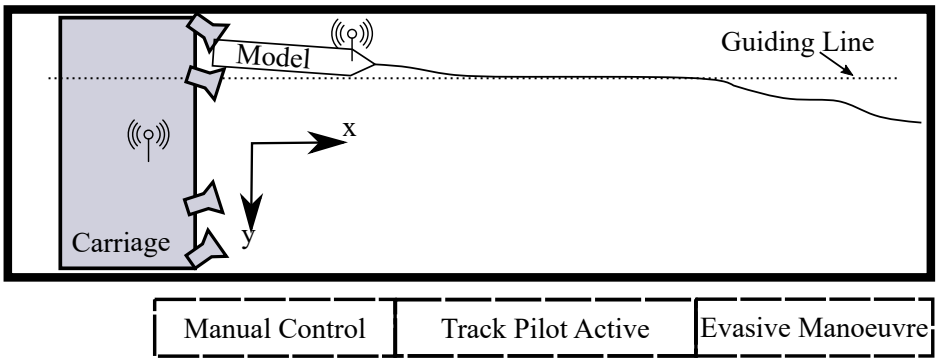

Figure 3: Experimental setup and test procedure

3.5 MANOEUVRE EXECUTION

As soon as the starting conditions are met, the manoeuvre is triggered. The rudders are then automatically set to the target value and automatically set to the opposite value when the target rate of turn is reached (see Figure 1). For example, a 45-28 evasive manoeuvre means that the rudder is set to +45 degrees. As soon as the rate of turn reaches -28 degrees per minute (turn over portside), the rudder is moved to the opposite side (-45 degrees). As soon as the rate of turn has reached +28 degrees per minute (turn over starboard), the rudder is again moved to the opposite side (+45 degrees). This sequence is executed and repeated automatically until it is stopped manually.

In this case a positive rudder angle leads to a negative yaw rate and vice versa. The coordinate system is thus defined analogue to the definitions in *European Standard Laying Down Technical Requirements For Inland Navigation Vessels (ES-TRIN)* (2025) (see Figure 1). It is expected that the overshoot of the yaw rate when the rudder is turned to the opposite side will not be very large. This means that the further acceleration of the yaw rate can be quickly stopped by moving the rudder, but the rotation of the ship itself only stops when the yaw rate has reached zero.

Finally, the automatic manoeuvre execution is stopped and the ship is manually decelerated.

4 RESULTS

The available data is analysed with regard to the following aspects. The presentation of good repeatability is a central component of the test technique described. Determining compliance with the regulations is highly relevant when evaluating ship designs prior to construction. However, the data shown was not recorded for this purpose, but is intended to serve as a validation basis for CFD calculations and simulations with a ship handling simulator. Particularly for the scenarios in shallow water, the test execution has been modified to lower ship velocities and lower target rates of turn (20-10 instead of 20-20 and 45-18 instead of 45-28). This means that no direct statement can be made about the conformity of the manoeuvring behaviour.

However, this problem raises important questions in connection with the permissible manoeuvring behaviour of inland vessels in very shallow water and laterally restricted fairway. For ongoing efforts to make inland navigation suitable for these restricted conditions, extended procedures are needed to adequately assess manoeuvring behaviour in these situations. Indirectly, the shown results can already make a small contribution to these questions.

4.1 REPEATABILITY

Figures 4 and 5 show examples of the repeatability of the model tests (model 1) for 20-20 and 45-28 manoeuvres with a ratio of $h/T = 1.5$ and a draught of $T = 1.7$ m. The legend labels, Port1, Port2, and Stbd2, refer to the respective rudder positions on the ship model 1, from portside to starboard. The signal for the rudder Stbd1 is missing due to a fault. The 80 seconds of negative time represent the test conditions before the start of the manoeuvre and correspond to approximately 20 seconds in model scale. It can be seen that both the rate of turn and the rudder angle differ only slightly. The still visible deviations are due to the slightly different starting conditions and residual currents in the tank. Figure 6 shows the repeatability of two 20-20 manoeuvres with model 2 and equally good agreement. The legend labels, Rudder Port and Rudder Stbd, refer to the respective rudder positions on the ship model 2, from portside to starboard.

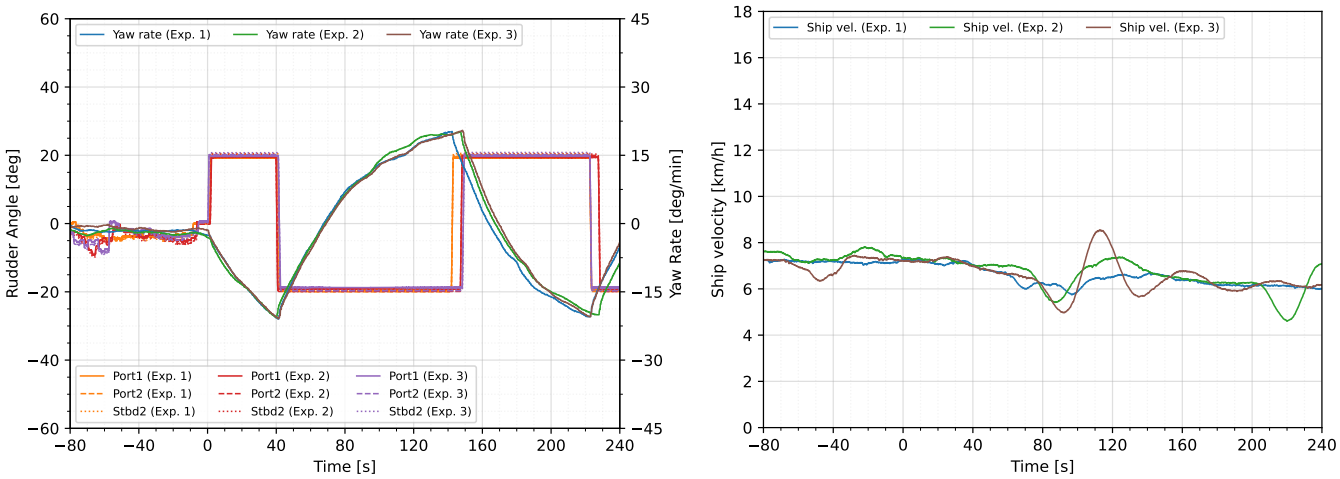

(a) Rate of turn in full scale and rudder angle

(b) Ship velocity in full scale

Figure 4: Repeatability of a 20-20-manoeuvre (Model 1 – h/T = 1.5 and T = 1.7 m)

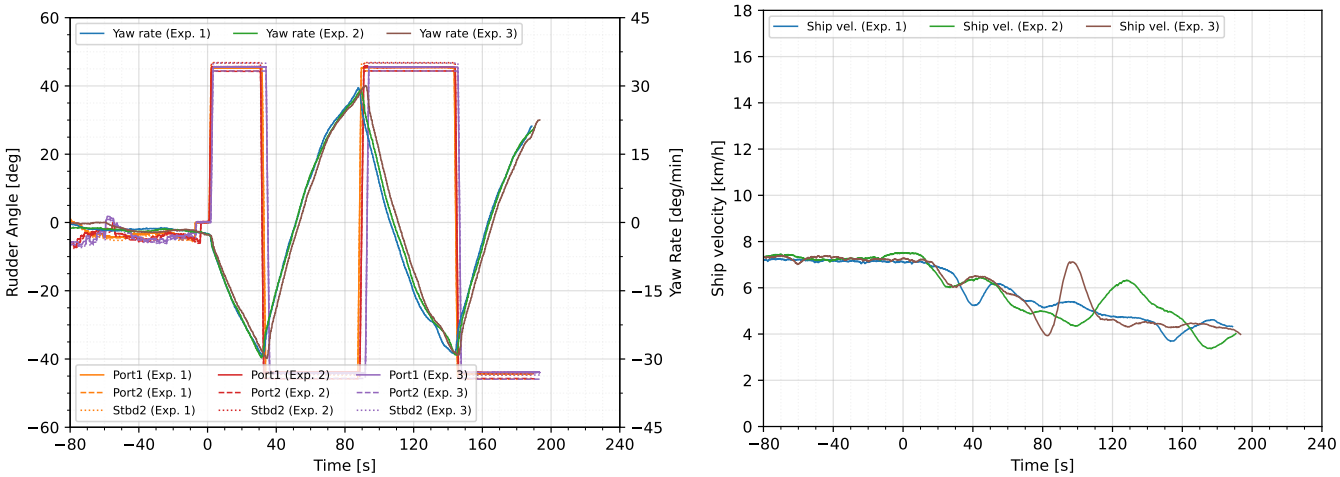

(a) Rate of turn in full scale and rudder angle

(b) Ship velocity in full scale

Figure 5: Repeatability of a 45-28-manoeuvre (Model 1 – h/T = 1.5 and T = 1.7 m)

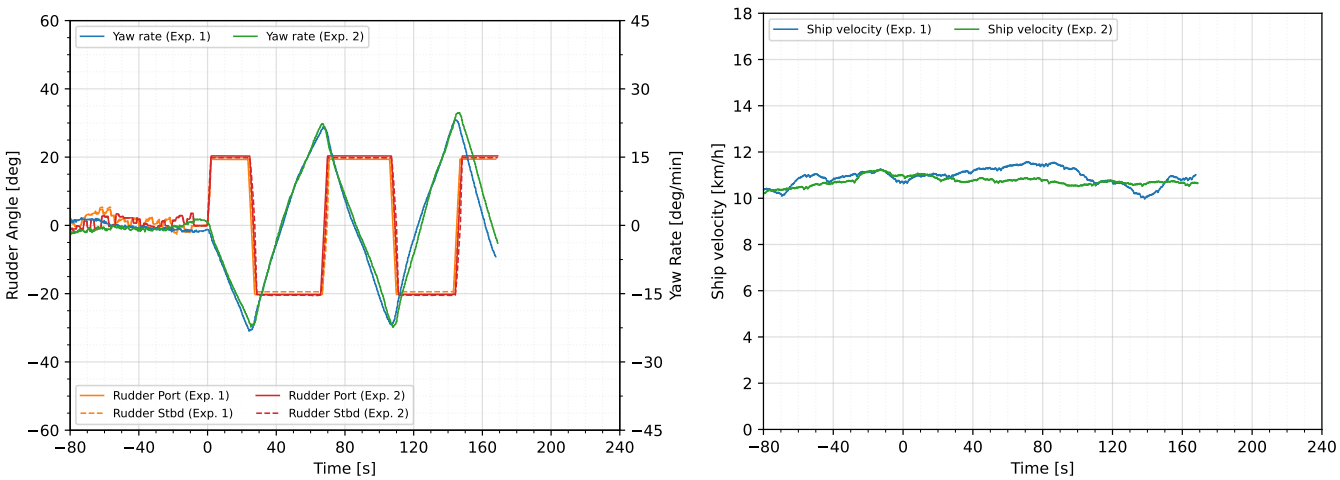

(a) Rate of turn in full scale and rudder angle

(b) Ship velocity in full scale

Figure 6: Repeatability of a 20-20-manoeuvre (Model 2 – h/T = 1.3 and T = 2.8 m)

The evaluation of the ship's velocity with the Kalman filter also shows good agreement before the test. The figures show the absolute value of the velocity vector of longitudinal and lateral velocity, which can also increase during the course of the manoeuvre, as the lateral velocity has a significant influence. Overall, however, the velocity slowly decreases due to manoeuvring. Based on the experience gained during the campaign, some tests were not repeated. As far as possible, Tables 4 and 5 show the mean values for the ship velocity at the start of the manoeuvre and the evaluated time points t_4.

Table 4: Results of evasive manoeuvres 20-20 (20-10) for model 1 in full scale

h/T	T [m]	$\overline{v_S}$ [km/h]	$\sigma(v_S)$ [%]	Manoeuvre	$\overline{t_4}$ [s]	$\sigma(t_4)$ [%]	Test runs	$\overline{\Delta r}$ [°/min]
7.34	1.7	11.0	0.26	20-20	63.1	-	1	0.3
		6.9	2.71	20-20	173.7	-	1	0.1
2.0	2.6	10.8	0.32	20-20	76.1	-	1	0.4
		7.2	0.56	20-20	192.2	1.66	2	0.1
	1.7	10.7	0.50	20-20	67.6	-	1	0.4
		7.0	0.77	20-20	149.0	3.56	2	0.2
1.5	2.6	10.6	0.72	20-20	87.4	-	1	0.5
		7.1	2.91	20-20	208.7	4.02	4	0.1
	1.7	11.4	2.81	20-20	72.5	-	1	0.7
		7.3	3.10	20-20	166.9	1.39	3	0.1
		4.3	4.83	20-20	230.5	-	1	0.0
1.2	2.6	6.9	1.75	20-10	115.8	3.91	2	0.1
		5.5	1.11	20-10	231.9	-	1	0.0
	1.7	6.1	1.52	20-10	103.5	3.41	2	0.1

Table 5: Results of evasive manoeuvres 45-28 (45-18) for model 1 in full scale

h/T	T [m]	$\overline{v_S}$ [km/h]	$\sigma(v_S)$ [%]	Manoeuvre	$\overline{t_4}$ [s]	$\sigma(t_4)$ [%]	Test runs	$\overline{\Delta r}$ [°/min]
7.34	1.7	11.0	0.26	45-28	48.8	-	1	1.3
		6.9	2.71	45-28	114.3	-	1	0.2
2.0	2.6	10.8	0.32	45-28	60.4	-	1	0.8
		7.2	0.56	45-28	129.8	1.47	3	0.3
	1.7	10.7	0.50	45-28	51.8	-	1	1.4
		7.0	0.77	45-28	106.0	0.59	2	0.2
1.5	2.6	10.6	0.72	45-28	63.5	-	1	0.8
		7.1	2.91	45-28	129.7	1.41	2	0.3
	1.7	11.4	2.81	45-28	55.5	-	1	0.9
		7.3	3.10	45-28	108.5	1.74	3	0.3
		4.3	4.83	45-28	244.0	-	1	0.0
1.2	2.6	6.9	1.75	45-18	90.6	1.09	3	0.4
		5.5	1.11	45-18	161.0	-	1	0.1
	1.7	6.1	1.52	45-18	92.2	1.56	3	0.2

4.2 COMPLIANCE WITH REGULATIONS IN SHALLOW WATER

As the data was not explicitly recorded for the purpose of analysing compliance with the regulations, only some values can be evaluated in this respect. Initially, only the data for draught $T = 2.6$ m (load greater than 70%) and ship speed $V_S \approx 11$ km$/h$ for the two ratios $h/T = 2.0$ and $h/T = 1.5$ are suitable for this purpose. Although the ship velocity is less than 13 km$/h$, these requirements are fully met. Unfortunately, the evaluation of the influence of shallow water is only possible to a very limited extent with the available data.

Unsurprisingly, the data show that the draught and thus the displacement volume have a strong influence on manoeuvrability and the important time t_4 is reached much faster. By analogy with zig-zag manoeuvres for seagoing vessels with corresponding overshooting angles, the further increase in the rate of turn (from r_1 to $r_{1,max}$ and from r_3 to $r_{3,max}$) in an evasive manoeuvre is comparable. The following average of the "overshooting rate of turn" Δr was used to analyse the results. Normally, the values are well below one degree per minute, which means that the increase in the ship's rotation can be stopped almost instantly by applying counter rudder.

$$\Delta r = \frac{|r_{1,max}| + |r_{3,max}|}{2} - \frac{|r_1| + |r_3|}{2} \tag{1}$$

Table 6 shows some results for the single screw model 2. Although the ship velocity is again a little too low, all manoeuvring requirements are already met. In this case, all tests were carried out at 80% engine order telegraph (set in shallow water $h/T = 1.3$), which explains the higher ship velocities in deeper water. It is also clearly recognisable that the overshooting rate of turn Δr is higher for the single screw vessel.

Table 6: Results of evasive manouvres 45-28 for model 2 in full scale

h/T	Rudder	$\overline{v_S}$ [km/h]	Evasive side first	t_4 [s]	Test runs	$\overline{\Delta r}$ [°/min]
1.3	1	11.2	Port	63.8	1	3.7
			Stbd	69.5	1	3.0
	2	11.1	Port	84.5	1	1.5
			Stbd	84.2	1	1.7
	3	11.1	Port	90.0	1	1.3
			Stbd	89.2	1	1.1
1.79	3	11.6	Port	85.9	1	2.8
			Stbd	96.3	1	2.9
4.46	3	12.3	Port	83.9	1	3.3
			Stbd	92.4	1	2.9

4.3 INFLUENCE OF DIFFERENT RUDDER PROFILES

Figure 7 shows the result of an approach to determine the effect of different rudder profiles on the manoeuvring characteristics. Three different rudder profiles were tested for model 2, which differed significantly in size and shape (see Table 7). The exact profile definitions cannot be published for reasons of confidentiality. Rudder 1 describes a realistic rudder of an inland vessel with a wedge on the trailing edge. Rudder 2 has a similar profile but is more slender and has a shorter chord length. Rudder 3 was created on the basis of modified NACA profile definitions with curved centrelines, having the same main dimensions as rudder 2. The results show a clear influence of the rudder size and profile. The good characteristics of rudder 1 are certainly due to the low ratio of height to chord length. The difference between rudder 2 and rudder 3 lies in the modified profile shape. This difference can also be clearly determined from the tests.

Table 7: Rudder parameters

Rudder	Profile	Rudder height $[mm]$	Chord length $[mm]$	Profile thickness $[mm]$	Height-length-ratio $[-]$
1	Schilling type (modified)	105.9	112.4	16.4	0.94
2	Schilling type	105.9	84.1	11.1	1.26
3	Curved Centreline	105.9	84.1	11.1	1.26

5 SUMMARY AND CONCLUSION

Free-running manoeuvring tests in model scale offer the possibility of a wide range of detailed investigations of the manoeuvring behaviour of ships. With the presented test setup and the model equipment, this type of investigation can now

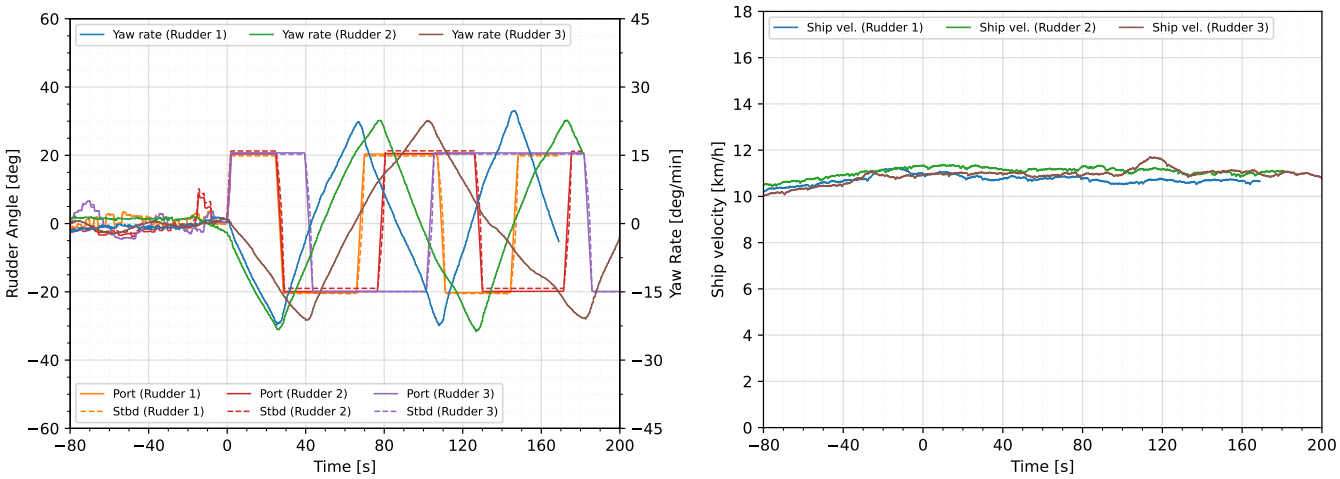

(a) Rate of turn in full scale and rudder angle

(b) Ship velocity in full scale

Figure 7: Influence of rudder profile in a 20-20-manoeuvre ($h/T = 1.3$ and $T = 2.8$ m)

be carried out for inland waterway vessels in DST's shallow water towing tank. The inclusion of a real track guidance system simplifies the control of the ship model and provides the prerequisites for repeatable model tests. The illustrations of repeatability shown are very promising, but with the experience gained so far, some optimisation is still possible and necessary. In particular, the implementation of a speed controller, would increase the repeatability of the approach speed, which is now given by a known propeller revolution.

In addition, only limited systematic analyses are possible for the results presented in this publication, due to the test restrictions in shallow water with regard to the achievable ship velocity and the feasibility of the defined standard manoeuvres 20-20 and 45-28. The lower ship velocity means that the target values for the rate of turn can no longer be achieved in the given tank space. For future applications of this technology, parameters and manoeuvres will be defined in advance that can be implemented in the same way at all water depths. These can be, for example, the shown manoeuvres 20-10 and 45-18 at a ship velocity of 6 km/h.

The investigation of manoeuvring behaviour in general and at low velocities in particular will continue to gain in importance in the future. Areas of application include the development of automated shipping and manoeuvring in designated low water periods with restricted fairways. The parameters of the evaluation will then also include the specific space requirements of the manoeuvring ship.

6 ACKNOWLEDGEMENTS

This project was partly supported by the Federal Ministry for Economic Affairs and Climate Action (BMWK) on the basis of a decision by the German Bundestag. The authors would also like to thank the Federal Waterways Engineering and Research Institute (BAW) for funding, support and permission to publish.

7 REFERENCES

Abkowitz, M. A., 1980. Measurement of hydrodynamic characteristics from ship maneuvering trials by system identification. In: Transactions of SNAME 88, pp. 283–318.

Araki, M., H. Sadat-Hosseini, Y. Sanada, K. Tanimoto, N. Umeda, and F. Stern, Sept. 2012. Estimating maneuvering coefficients using system identification methods with experimental, system-based, and CFD free-running trial data. In: Ocean Engineering 51, pp. 63–84. DOI: 10.1016/j.oceaneng.2012.05.001.

Artyszuk, J., 2003. A Novel Method of Ship Manoeuvring Model Identification from Sea Trials. In: Annual of Navigation 6.

Chillcce, G. and O. el Moctar, May 2023. Data-driven system identification of hydrodynamic maneuvering coefficients from free-running tests. In: Physics of Fluids 35.5. DOI: 10.1063/5.0148219.

Eloot, K., G. Delefortrie, M. Vantorre, and F. Quadvlieg, 2015. Validation of Ship Manoeuvring in Shallow Water Through Free-Running Tests. In: Proceedings of the ASME 2015 34th International Conference on Ocean, Offshore and Arctic Engineering (OMAE2015).

European Standard Laying Down Technical Requirements For Inland Navigation Vessels (ES-TRIN) 2025. 2025/1. European Committee for drawing up Standards in the field of Inland Navigation (CESNI).

Hinostroza, M. A., H. T. Xu, and C. Guedes Soares, Aug. 2019. Manoeuvring test for a self-running ship model in various water depth conditions. In: Sustainable Development and Innovations in Marine Technologies. Ed. by P. Georgiev and C. Guedes Soares. CRC Press, pp. 187–196. DOI: 10.1201/9780367810085-24.

Im, N.-K., S.-H. Han, and T. Nguyen, 2011. A Study on Ship's Maneuverability Evaluation by Real Ship Test. In: Journal of the Korean Society of Marine Environment & Safety.

Jin, Y., L. J. Yiew, Y. Zheng, A. R. Magee, J. Duffy, and S. Chai, Dec. 2021. Dynamic manoeuvres of KCS with CFD free-running computation and system-based modelling. In: Ocean Engineering 241, p. 110043. DOI: 10.1016/j.oceaneng.2021.110043.

Kim, I.-T., C. Kim, S.-H. Kim, D. Ko, S.-H. Moon, H. Park, J. Kwon, and B. Jin, 2021. Estimation of the manoeuvrability of the KVLCC2 in calm water using free running simulation based on CFD. In: International Journal of Naval Architecture and Ocean Engineering 13, pp. 466–477. DOI: 10.1016/j.ijnaoe.2021.05.004.

Kulbiej, E., Nov. 2021. Full Sea Trial Based Estimation of Hydrodynamic Derivatives of a Research Vessel. In: EUROPEAN RESEARCH STUDIES JOURNAL XXIV.Special Issue 4, pp. 469–489. DOI: 10.35808/ersj/2731.

Mei, B., L. Sun, and G. Shi, July 2020. Full-Scale Maneuvering Trials Correction and Motion Modelling Based on Actual Sea and Weather Conditions. In: Sensors 20.14, p. 3963. DOI: 10.3390/s20143963.

Mucha, P., T. Dettmann, V. Ferrari, and O. el Moctar, Feb. 2019. Experimental investigation of free-running ship manoeuvers under extreme shallow water conditions. In: Applied Ocean Research 83, pp. 155–162. DOI: 10.1016/j.apor.2018.09.008.

Nomoto, K., T. Taguchi, K. Honda, and S. Hirano, 1957. On the steering qualities of ships. In: International Shipbuilding Progress 4.35, pp. 354–370.

Oltmann, P., 1973. Auswertung von Bahnkurven freifahrender Schiffsmodelle. Tech. rep. Technische Universität Hamburg-Harburg.

– 1978. Bestimmung der Manövriereigenschaften aus den Bahnkurven freimanövrierender Schiffsmodelle. Tech. rep. Technische Universität Hamburg-Harburg.

Quadvlieg, F., 2016. Current status of manoeuvring prediction methods, their mutual pros and cons and ways to quantify the capabilities. In: Yucel Odabasi Colloquium Series - 2nd International Meeting Recent Advances in Prediction Techniques for Safe Manoeuvring of Ships and Submarines, Istanbul, Turkey.

Quadvlieg, F. and J. Brouwer, 2011. KVLCC2 Benchmark Data Including Uncertainty Analysis To Support Manoeuvring Predictions. In: IV International Conference on Computational Methods in Marine Engineering (ECCOMAS MARINE), Lisbon, Portugal.

Rhee, K.-P. and K.-H. Kim, 1999. A New Sea Trial Method for Estimating Hydrodynamic Derivatives. In: Journal of ship and ocean technology 3, pp. 25–44.

Roettig, F., B. Friedhoff, M. Tenzer, J. Jasa, and A. Lachmeyer, 2023. Automation of Manoeuvring Tests in a Towing Tank Using Real-World Navigation Technology. In: Proceedings of the 7th International Conference on Advanced Model Measurement Technology for The Maritime Industry (AMT'23), Istanbul, Turkey.

Stern, F., K. Agdrup, S. Y. Kim, A. C. Hochbaum, K. P. Rhee, F. Quadvlieg, P. Perdon, T. Hino, R. Broglia, and J. Gorski, 2011. Experience from SIMMAN 2008 - The First Workshop on Verificationand Validation of Ship Maneuvering Simulation Methods. In: Journal of Ship Research 55.2, pp. 135–147.

Sutulo, S. and C. Guedes Soares, Mar. 2014. An algorithm for offline identification of ship manoeuvring mathematical models from free-running tests. In: Ocean Engineering 79, pp. 10–25. DOI: 10.1016/j.oceaneng.2014.01.007.

Suzuki, R., Y. Tsukada, and M. Ueno, Jan. 2019. Estimation of full-scale ship manoeuvring motions from free-running model test with consideration of the operational limit of an engine. In: Ocean Engineering 172, pp. 697–711. DOI: 10.1016/j.oceaneng.2018.12.044.

Xu, H., M. A. Hinostroza, and C. Guedes Soares, Sept. 2018. Estimation of Hydrodynamic Coefficients of a Nonlinear Manoeuvring Mathematical Model With Free-Running Ship Model Tests. In: International Journal of Maritime Engineering Vol 160.A3. DOI: 10.3940/rina.ijme.a3.2018.448.

Yasukawa, H., M. A. A. Hasnan, and A. Matsuda, Feb. 2021. Validation of 6-DOF motion simulations for ship turning in regular waves. In: Journal of Marine Science and Technology 26.4, pp. 1096–1111. DOI: 10.1007/s00773-020-00793-8.

8 AUTHORS BIOGRAPHY

Matthias Tenzer holds a diploma degree in naval architecture and marine engineering obtained in 2011 at the University of Duisburg-Essen. Afterwards he worked for five years as a researcher at the Institute of Ship Technology and Transport Systems (DST). Since 2016 he is working at the Development Centre for Ship Technology and Transport Systems where he is responsible for ship manoeuvring related topics and the ship handling simulator SANDRA II. His previous experience includes experimental as well as numerical investigations in the field of ship hydrodynamics.

Felix Roettig holds a Master of Science in Naval Architecture and Marine Engineering, obtained in 2016 from the University of Duisburg-Essen. From 2014 to 2016, he worked as a research associate at the Institute of Ship Technology and Transport

Systems. Since 2016, he has been part of the Development Centre for Ship Technology and Transport Systems (DST), where he is responsible for measurement technology in model testing. His tasks also include conducting measurements on inland waterway vessels and at port facilities. His background as a Electrical Engineering Assistant in the field of Communications Technology has proven valuable in areas such as measurement systems, software development, database systems, data analysis, and the evaluation of navigation electronics on board inland waterway vessels.

Rainer Kaiser holds a diploma degree in mathematics obtaind in 2000 at the Gerhard Mercator University Gesamthochschule Duisburg. Afterwards he worked for five years as a researcher at the Institute of Combustion and Gasdynamic in the field of numerical methods in CFD. In 2006 numerical developments were done for the numrax GmbH and the institute of Ship Technology and Transport Systems in the field of ship hydrodynamics. Since autumn 2006 he is employed at the Development Centre for Ship Technology and Transport Systems (DST) and worked in a wide range of research fields. Expertise includes numerical developments and investigations in CFD, simulating operational profiles of vessels, developing manoeuvring models for inland vessels.

Justin Jasa is a researcher at the Development Centre for Ship Technology and Transport Systems (DST) in Germany, specialising in experimental investigations in ship hydrodynamics, fleet greening, and emission reduction. He holds a master's degree in Naval Architecture and Marine Engineering from the University of Trieste, Italy. Passionate about programming, he develops custom codes and tools to simulate processes, such as ship manoeuvrability, and to optimise engineering workflows.

Benjamin Friedhoff studied naval architecture at the University of Duisburg-Essen, where he subsequently worked for three years as a researcher. In 2008 he changed to the Development Centre for Ship Technology and Transport Systems (DST), where he worked on a wide range of research topics in the fields of hydrodynamics and renewable energies. Since 2014 he is head of the Hydrodynamics Department and has worked on various greening projects, including alternative energy carriers and zero-emission ships. As part of the restructuring of the DST, his department was renamed "Experiments, Fleet Modernisation and Emissions" in January 2020 taking account of current societal challenges.

COURSE-KEEPING SIMULATIONS OF A SHIP IN CONFINED WATERWAYS BASED ON INTEGRATED CFD METHOD AND CONTROL ALGORITHM

Zi-Qiang Zheng, School of Ocean and Civil Engineering, Shanghai Jiao Tong University, China

Yu He, School of Ocean and Civil Engineering, Shanghai Jiao Tong University, China

Lu Zou, School of Ocean and Civil Engineering, Shanghai Jiao Tong University, China

Zao-Jian Zou, School of Ocean and Civil Engineering, Shanghai Jiao Tong University, China

COURSE-KEEPING SIMULATIONS OF A SHIP IN CONFINED WATERWAYS BASED ON INTEGRATED CFD METHOD AND CONTROL ALGORITHM

ZI-QIANG ZHENG, SCHOOL OF OCEAN AND CIVIL ENGINEERING, SHANGHAI JIAO TONG UNIVERSITY, CHINA
YU HE, SCHOOL OF OCEAN AND CIVIL ENGINEERING, SHANGHAI JIAO TONG UNIVERSITY, CHINA
LU ZOU*, SCHOOL OF OCEAN AND CIVIL ENGINEERING, SHANGHAI JIAO TONG UNIVERSITY, CHINA
ZAO-JIAN ZOU, SCHOOL OF OCEAN AND CIVIL ENGINEERING, SHANGHAI JIAO TONG UNIVERSITY, CHINA

SUMMARY

The course-keeping problem of a ship model in confined waterways is investigated by numerical simulations coupled with a control algorithm in the present study. The URANS method is applied to simulate viscous flows around the ship, and the overset mesh technique combined with the PD algorithm is adopted to realize the rudder action during course keeping. To improve simulation efficiency, the body-force propeller is applied and a virtual bank method is developed to simplify the modeling of bank effects. The results of free-running simulations indicate that the bank-induced yaw moment is the dominant factor causing ship-bank collisions in confined waterways. Applying the controller in simulations, the ship successfully achieves course keeping with either initial off-centerline deviation or heading angle. Furthermore, the simulated flow field indicates that the ship deviates a small distance from the waterway centerline during course keeping to overcome the additional sway force and yaw moment induced by propeller-rudder interaction.

NOMENCLATURE

B	Breadth (m)
d	Draft (m)
D	Propeller diameter (m)
Fr	Froude number based on ship length (-)
Fr_h	Froude number based on water depth (-)
g	Acceleration of gravity (m/s^2)
h	Water depth (m)
K_d	Derivative gain (-)
K_p	Proportional gain (-)
L_{pp}	Length between perpendiculars (m)
N	Yaw moment (Nm)
N_{bank}	Bank yaw moment (Nm)
N_{hydro}	Hydrodynamic yaw moment (Nm)
r	Yaw rate (rad/s)
u	Surge velocity (m/s)
U_0	Nominal speed (m/s)
v	Sway velocity (m/s)
W	Channel width (m)
X	Surge force (N)
Y	Sway force (N)
Y_{bank}	Bank sway force (N)
Y_{hydro}	Hydrodynamic sway force (N)
β	Drift angle (°)
δ	Rudder angle (°)
η	Off-centerline deviation (m)
η_0	Initial off-centerline deviation (m)
λ	Scale ratio (-)
ρ	Fluid density (kg/m^3)
ψ	Heading angle (°)
ψ_0	Initial heading angle (°)

1 INTRODUCTION

Ship maneuverability in confined waterways has garnered continuous attention. The increase in ship size causes reductions in the under keel clearance (UKC) and the navigable waterway width, leading to more significant shallow-water and bank effects. Under the influences of shallow-water and bank effects, a ship navigating in confined waterways experiences additional sway force and yaw moment (Delefortrie, 2024a). These additional force and moment tend to push the ship off its intended course, increasing the collision risks with the banks (Yuan, 2019). This issue becomes particularly pronounced with the rapid development of large-scale ships. Consequently, ship steering and control become significantly more difficult. A reliable autopilot control strategy for keeping ship course in confined waterways could effectively improve navigation efficiency and safety. Therefore, investigations on ship maneuverability and control strategies are of critical importance.

So far, significant progress has been made in studying ship hydrodynamic performances in confined waterways with the perspective of the quasi-steady assumption (the ship is fixed and water flows to the ship) or captive state (the ship moves along a specified trajectory), by applying model tests (Norrbin, 1975; Vantorre et al., 2002; Vantorre et al., 2003; Lataire et al., 2009; Van Zwijnsvoorde et al., 2022; Delefortrie, 2024a; Delefortrie, 2024b), potential flow theory (Yao and Zou, 2010; Zhou et al., 2012; Yuan, 2016; Ren et al., 2020; Degrieck et al., 2021; Xu et al., 2024; Terziev et al., 2024), and viscous flow methods (Zou, 2012; Zou and Larsson, 2013; Van Hoydonck et al., 2019; Liu et al., 2021; Lee, 2023; Terziev et al., 2024). These studies focused on evaluating the hydrodynamic performance of ships in captive motions, without considering motions in multiple freedoms or dynamic rudder action, which were inadequate for practical navigation applications. Consequently, there is a pressing need for studies focusing on ship maneuvering and control under such conditions. The most common approach is computational simulations based on mathematical models (i.e., ship motion equations). By solving the ship motion equations, the motion parameters and ship trajectory at specified rudder angle and propeller speed can be directly calculated. The key and premise of this approach are to establish an appropriate mathematical model.

Captive model tests are the most reliable approach to identify the hydrodynamic parameters in mathematical model. For instance, Fujino (1968, 1970), Sano et al. (2012, 2014), and Yasukawa (2019) carried out captive model tests for different ships and waterway configurations. The mathematical models were established based on the measured forces and moments in the model tests, and then the corresponding maneuverability was investigated. However, such model tests require specialized facilities, such as shallow-water towing tanks or facilities with “false” bottoms and banks, significantly increasing their complexity and cost. Furthermore, these tests fail to provide detailed flow information, limiting their ability to analyze the underlying mechanisms of shallow-water and bank effects on ship maneuverability and control performance. Although the numerical methods can provide detailed flow mechanisms, the mathematical modeling based on numerically determined hydrodynamic parameters from prescribed captive motions is still confronted with challenges in practical applications.

In contrast, direct simulations of maneuvering motions based on the Computational Fluid Dynamics (CFD) method tend to be a viable alternative for this problem. CFD-based approaches address many limitations of model tests, eliminating the need for extensive physical experiments (so-called free-running tests) and enabling the interpretation of detailed flow field results. The CFD simulations provide deeper insights into hydrodynamic interactions and offer practical guidance for ship navigation in confined waterways. Up to now, direct simulations have been successfully applied to ship maneuvering and control in open water, shallow waters, and waves (Carrica et al., 2016; Wang et al., 2017; Kim et al., 2022; Kim et al., 2023), demonstrating their satisfactory abilities. However, their applications to confined-water problems remain challenging due to the complexities of simulating both the fully coupled hull-propeller-rudder system and the surrounding viscous flows within these restricted environments.

Based on the above background, this paper employs CFD-based simulations coupled with control actions to address the course-keeping problem of a ship in confined waterways. The objective is to improve the capability of CFD simulations for providing in-depth analyses of hydrodynamic mechanism for a moving ship under bank effects in confined waterways, and to offer control guidance coupled with the simulations for keeping ship course in such environments. To this end, the unsteady Reynolds Averaged Navier-Stokes (URANS) method is utilized to simulate the viscous flows around the ship, and the overset mesh technique is adopted to realize the dynamic rudder deflection during the control action. In addition, a virtual bank treatment is developed to significantly simplify the inherent numerical complexity and to improve computing efficiency while considering the bank effects on the ship motion. Two typical types of scenarios in confined waterways are investigated: one is the ship navigating with an initial off-centerline deviation and the other is the ship navigating with an initial heading angle, representing common scenarios in practical applications where external disturbances or improper operations may influence the ship course.

2 STUDY OBJECT AND SIMULATION CONDITIONS

2.1 SHIP MODEL

The benchmark ship model: KRISO Container Ship (KCS) is selected as the target ship for this study. The main particulars of the hull, propeller, and rudder are presented in Table 1, and their geometries are illustrated in Figure 1. It should be noted that the rudder stock is also ignored for simplification.

Table 1. Main particulars of hull, propeller and rudder

	Parameter	Symbol	Unit	Value
Hull	Scale ratio	λ	-	1:52.667
	Length between perpendiculars	L_{pp}	m	4.367
	Breadth	B	m	0.611
	Draft	d	m	0.205
Propeller	Diameter	D	m	0.15
	Blade number	-	-	5
	Hub ratio	-	-	0.227
	Rotation direction	-	-	right
Rudder	Rudder area	-	m^2	0.0415
	Lateral area	-	m^2	0.0196

Figure 1. KCS model geometry

2.2 COORDINATE SYSTEMS

Two right-handed coordinate systems are adopted to describe the ship location and motion parameters, as shown in Figure 2. The first one is the earth-fixed coordinate system o_0-$x_0y_0z_0$, where the o_0-x_0y_0 plane is placed on the undisturbed water surface, the x_0-axis is along the waterway centerline, and the z_0-axis points vertically downward. The other one is the ship-fixed coordinate system *o-xyz*. Its origin is set at the midship, the *x*-axis and the *y*-axis point toward the bow and the starboard, respectively. The position and direction of the target ship are described by the midship coordinates (x_0, y_0) in o_0-$x_0y_0z_0$ and the heading angle ψ (angle between x_0 and *x* axes). The positive heading angle ψ and rudder angle δ are illustrated in Figure 2. In addition, force components: *X* (surge force), *Y* (sway force), *N* (yaw moment) and velocity components: *u* (surge velocity), *v* (sway velocity), *r* (yaw rate) are defined in *o-xyz*. The off-centerline deviation η is the distance between the midship and the centerline (η=y_0). The ship location is also presented in nondimensional form:

$$x_0' = x_0 / L_{pp},\ \eta' = y_0 / L_{pp} \tag{1}$$

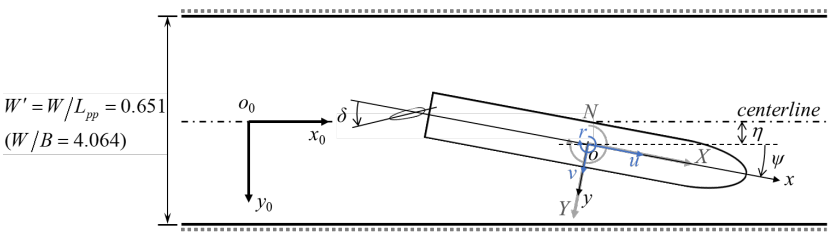

Figure 2. Definition of coordinate systems

2.3 SIMULATION CONDITIONS

The course-keeping performance of the target ship in the waterway is numerically investigated in this paper. The waterway cross-section is rectangular with a water depth h = 0.41m (h/d = 2.0) and a width W = 2.483m ($W' = W/L_{pp}$ = 0.651, W/B = 4.064). The blockage factor is defined as the ratio of the midship-sectional area below the water surface to the cross-sectional area of the waterway. The value is 0.122 in the present study, corresponding to a moderate confined-water condition. Two types of scenarios in confined waterways are investigated: one is the ship navigating with an initial off-centerline deviation $\eta_0' = \pm 0.127$ (Case1), and the other is the ship navigating with an initial heading angle $\psi_0 = \pm 2°$ (Case2), as shown in Table 2 and Figure 3. In the simulations, the target ship starts to move in the straight-ahead motion and is free to surge, sway and yaw (three degrees of freedom). The propeller revolution rate is fixed at 330 RPM according to the self-propulsion point in model tests (Delefortrie et al., 2012), corresponding to the nominal ship speed U_0 = 0.62 m/s. The Froude

number based on ship length $Fr = U_0 \big/ \sqrt{gL_{pp}}$ is 0.095, while the Froude number based on water depth $Fr_h = U_0 \big/ \sqrt{gh}$ is 0.309.

Table 2. Simulation conditions

	Case No.	η_0'	ψ_0 (°)	h/d	W'
Initial off-centerline deviation	Case1-1	0.127	0	2.0	0.651
	Case1-2	−0.127	0		
Initial heading angle	Case2-1	0	2		
	Case2-2	0	−2		

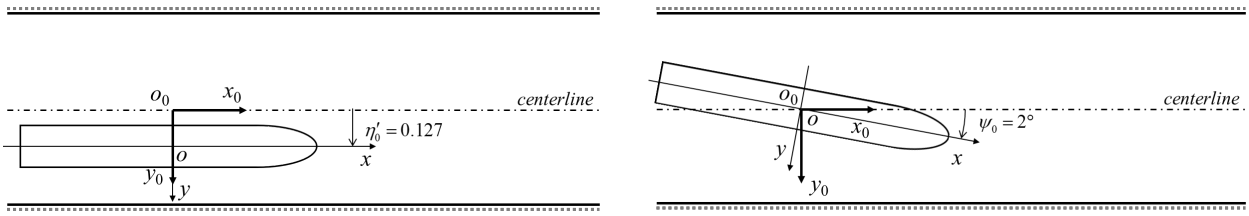

(a) Case1-1 ($\eta_0' = 0.127$) **(b) Case2-1 ($\psi_0 = 2°$)**

Figure 3. Diagram of simulation conditions

3 NUMERICAL METHODS AND SETTINGS

3.1 GOVERNING EQUATIONS

The viscous flow around the ship is assumed to be incompressible. The time-averaged continuity equation and unsteady RANS equations are adopted as the governing equations:

$$\begin{cases} \dfrac{\partial \overline{u}_i}{\partial x_i} = 0 \\ \dfrac{\partial \overline{u}_i}{\partial t} + \dfrac{\partial}{\partial x_j}\left(\overline{u}_i \overline{u}_j\right) = -\dfrac{1}{\rho}\dfrac{\partial \overline{p}}{\partial x_i} + \dfrac{1}{\rho}\dfrac{\partial}{\partial x_j}\left(\overline{\sigma}_{ji} - \rho \overline{u_i' u_j'}\right) + f_i \end{cases} \tag{2}$$

where $\overline{u}_{i(j)}$, $\overline{p}$ and $\overline{\sigma}_{ji}$ denote the time-averaged velocity, pressure and stress tensor components (i, j=1, 2, 3); f_i is the body force, which is regarded as a constant term; $-\rho \overline{u_i' u_j'}$ represents the Reynolds stresses. In this study, the SST k-ω turbulence model (Menter, 1993) is applied to close the governing equations. Simulations are conducted by the STAR-CCM+ software.

3.2 VIRTUAL BANK METHOD

The strategy for free-running simulations of ship maneuvering motion under rudder actions in confined waterways differs significantly from those in open waters, as illustrated in Figure 4. Due to relative motions between the ship and the bank, the narrow waterway with physical bank walls (no-slip walls) in close proximity to the ship must be accurately modeled to mimic the real-world scenario of a ship navigating a confined waterway. It is flexible to apply the dynamic overset mesh technique to handle the complex relative motions between ship and bank. Furthermore, appropriate mesh refinements along the ship trajectory are essential to ensure interpolation accuracy between the background and overset domains (Zheng et al., 2023). These constraints significantly increase computational complexity and cost. To address these challenges, the present study adopts a simplification that effectively reflects the confined-waterway effects while reducing computational costs.

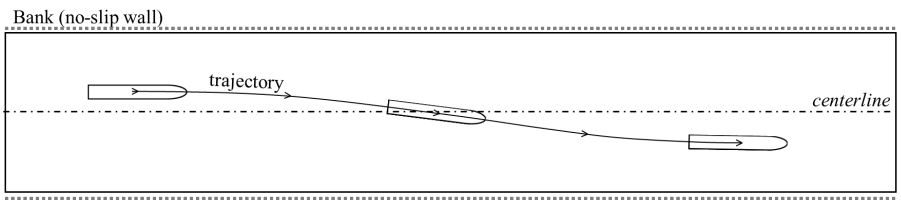

Figure 4. Numerical simulation strategy for confined waterways

A virtual bank method is developed in the present study to simplify the physical wall modeling while still accounting for the bank effects, as shown in Figure 5. In this method, the ship motion in open water with limited water depth is directly simulated, while the additional forces and moments caused by the side bank are directly imposed on the ship in the simulation by formulating the bank effects based on hydrodynamic parameters, without modeling the real bank walls in the simulations. The formulas describe the functional correlation between the bank-induced sway force, yaw moment, and relevant hydrodynamic parameters, which may affect the ship course-keeping motions. This treatment effectively addresses the inherent limitations in traditional numerical simulation strategies for confined-water problems. According to the mathematical model of a ship navigating in confined waterways (Sano et al., 2014), the sway force Y_{bank} and yaw moment N_{bank} induced by the bank can be expressed by the following formulas:

$$\begin{cases} Y_{bank} = 0.5\rho L_{pp} d U_0^2 \left(Y'_\eta \eta' + Y'_{\beta\beta\eta} \beta^2 \eta' + Y'_{\beta\eta\eta} \beta \eta'^2 + Y'_{\eta\eta\eta} \eta'^3 + Y'_{\eta\eta\delta} \eta'^2 \delta \right) \\ N_{bank} = 0.5\rho L_{pp}^2 d U_0^2 \left(N'_\eta \eta' + N'_{\beta\beta\eta} \beta^2 \eta' + N'_{\beta\eta\eta} \beta \eta'^2 + N'_{\eta\eta\eta} \eta'^3 + N'_{\eta\eta\delta} \eta'^2 \delta \right) \end{cases} \tag{3}$$

where ρ denotes fluid density, and β is the drift angle. In this paper, the hydrodynamic derivatives in Eq. (3) are obtained by regressing the Froude number Fr using the experimental results (Sano et al., 2014). As a result, the resultant sway force Y and yaw moment N acting on the ship can be expressed as follows:

$$\begin{cases} Y = Y_{hydro} + Y_{bank} \\ N = N_{hydro} + N_{bank} \end{cases} \tag{4}$$

where Y_{hydro} and N_{hydro} denote the hydrodynamic sway force and yaw moment respectively in shallow- and open-water simulations without the impacts by the side bank.

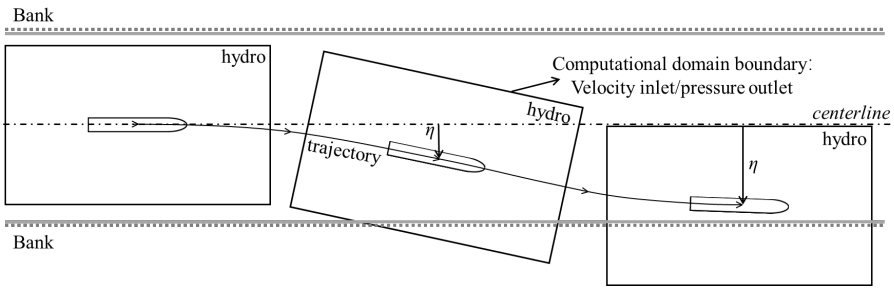

Figure 5. Schematic diagram of virtual bank method

3.3 CONTROL ALGORITHM

The course keeping in simulations is achieved by maintaining the heading angle ψ close to zero under rudder actions. The rudder is controlled by a Proportional-Derivative (PD) algorithm with the following control mechanism:

$$\delta = -K_p \psi - K_d r \tag{5}$$

where K_p and K_d represent proportional and derivative gains, respectively. Both gains are determined through a systematic tuning process, guided by the objective of achieving stable and satisfactory control performance for the course-keeping purpose in the confined waterway. During the tuning process, the proportional gain K_p is first adjusted to achieve a reasonable response speed of the ship, then the derivative gain K_d is applied to improve stability and reduce oscillations in the ship motion. The final set of gains is selected based on a balance between response speed and robustness under the studied conditions. Based on the tuning process, both are set to 10.

3.4 BODY-FORCE PROPELLER MODEL

Since modeling the actual propeller rotation in numerical simulations requires extremely small time steps and highly refined mesh discretization (Deng et al., 2022), it becomes computationally expensive, especially for course-keeping simulations involving rudder actions. Therefore, in the present study, the propeller is modeled using the body-force method (Sørensen, 2022), as its performance and accuracy for simulating ship maneuvering motions have been validated by Aram and Mucha (2023) and Mucha et al. (2023). This approach does not model the geometry and rotation of the propeller blades. Instead, the propeller effects are represented by introducing body forces into the momentum conservation equations. The propeller thrust and torque are derived from open-water propeller performance curves, which provide the thrust coefficient (K_T) and torque coefficient (K_Q) as functions of the advance ratio (J). By distributing these forces over the region where the propeller operates, the body-force method efficiently captures the propeller impact on the flow field while significantly reducing computational costs.

3.5 COMPUTATIONAL DOMAIN

The computational domain is illustrated in Figure 6. The overset mesh technique is utilized to simulate the relative motion between the hull and rudder. Consequently, there are two domains in the simulations: a background domain and an overset domain for the rudder. The distances between the boundaries of the background domain and the ship are sufficient to ensure that these boundaries do not disturb the flow around the ship. In the simulations, the ship is moving forward at a self-propulsion state by the body-force propeller model. The boundary conditions are set as: bottom plane, hull and rudder surfaces are specified as the no-slip walls, while the other boundaries of the background domain are set as the pressure outlet. The overset domain closely envelops the rudder and rotates with it during the simulation, as shown in Figure 6(b).

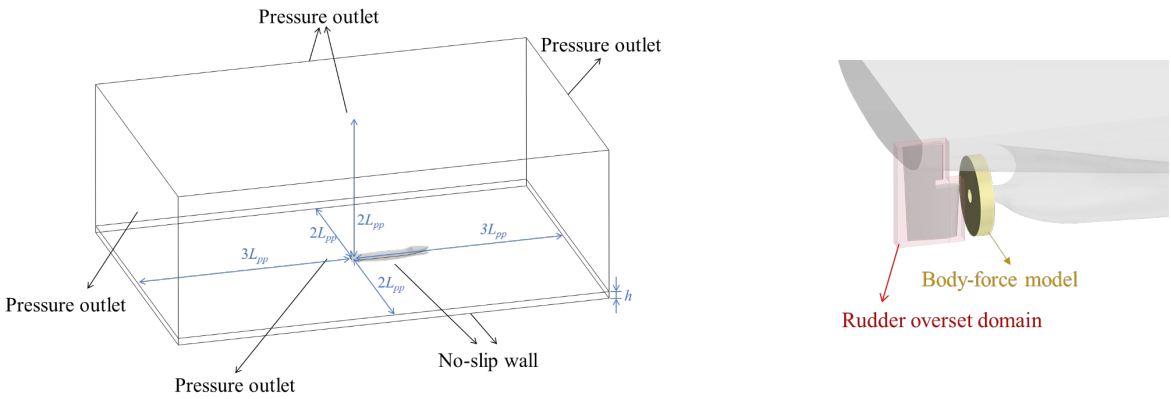

(a) Background domain **(b) Rudder overset domain**

Figure 6. Computational domain

3.6 MESH DISCRETIZATION

The trimmed mesh and prism layer mesh are applied to discretize the computational domain, and an illustration of the mesh distribution is shown in Figure 7. The prism layer mesh is used to generate orthogonal prismatic cells next to the hull and rudder surfaces. For these complex simulations involving rudder rotation and propeller propulsion, mesh refinements for these critical regions are employed to more precisely capture the details in the flow field, as shown in Figures 7(b)–(d). As a result, a total of 2.75 million mesh cells (2.63 million for the background domain and 0.13 million for the overset domain) are generated for the simulation. Given the more frequent rudder deflections during the initial navigation phase in confined waterways, the time step is set to 0.01 s for the first 100 s simulation and adjusted to 0.02 s thereafter.

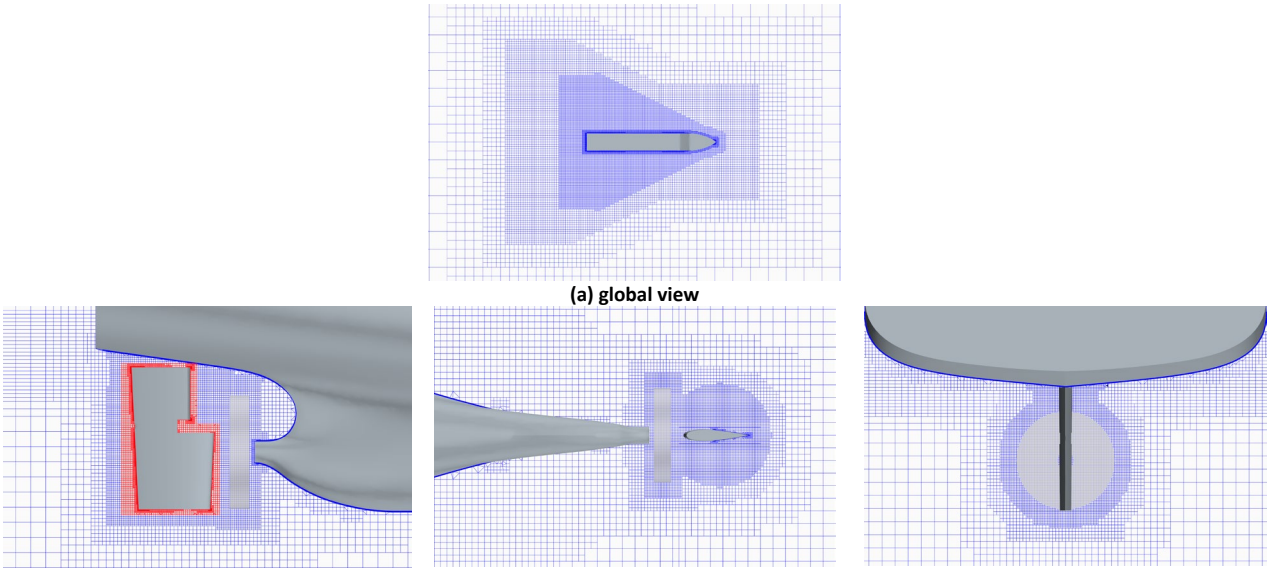

(a) global view

(b) local side view **(c) local bottom view** **(d) local stern view**

Figure 7. Mesh distributions

4 SIMULATION RESULTS

4.1 UNCONTROLLED CONDITIONS

Two scenarios with a total of four cases under both uncontrolled and controlled conditions are simulated for comparison. First, in order to demonstrate the feasibility of the applied virtual bank method and highlight the significance of the controller for ship navigation in confined waterways, Figure 8 shows the ship trajectory under the uncontrolled condition until it collides with the bank. The figure includes a set of simplified ship profiles indicating its position and orientation at several snapshots in time (red lines). The results indicate that even minimal initial disturbances (an initial off-centerline deviation or an initial heading angle) will lead to ship collisions with the waterway bank. Furthermore, the simulations reveal that all collisions occur in less than 40 s, implying that a ship navigating in confined waterways under the uncontrolled condition will be apt to collide with the bank walls. The results confirm that the virtual bank method effectively models the bank effects that cause the ship to deviate from its intended course. It is also observed that the time to collision with the starboard bank is significantly shorter than that with the port bank with the same amount of initial disturbance or deviation. It may be attributed to the right-handed propeller, which generates the wake flow interacting with the rudder. Overall, these findings emphasize the necessity of applying a ship controller for maintaining course-keeping in confined waterways.

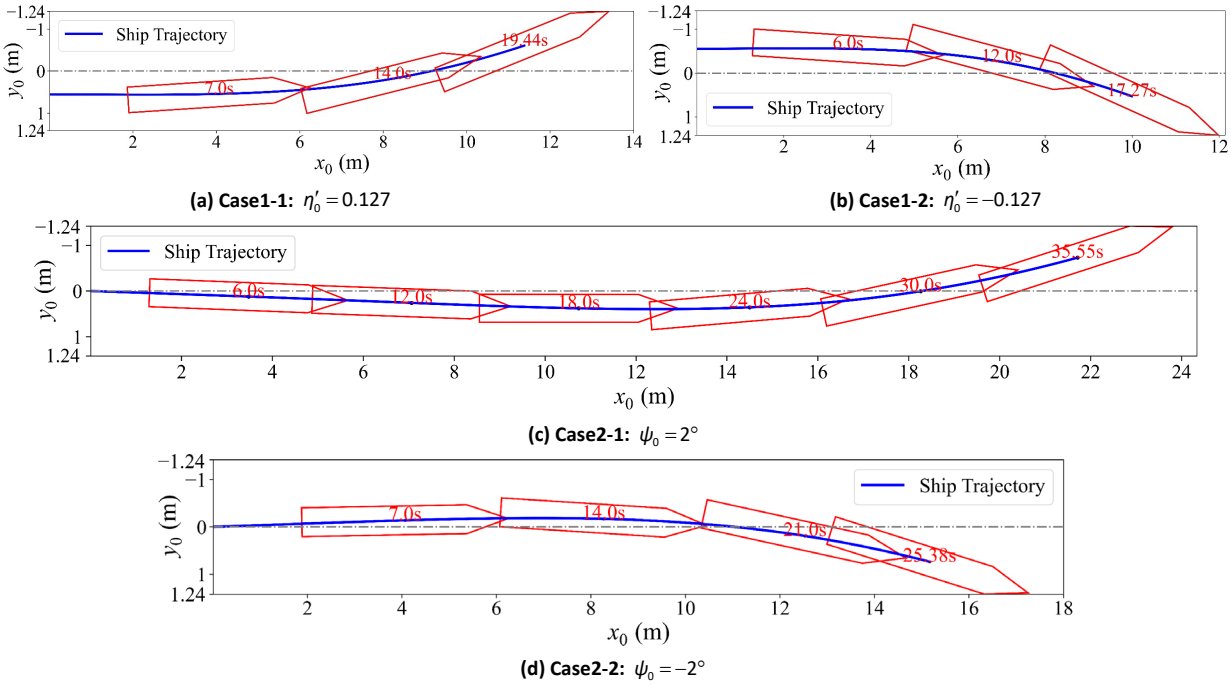

(a) Case1-1: $\eta_0' = 0.127$

(b) Case1-2: $\eta_0' = -0.127$

(c) Case2-1: $\psi_0 = 2°$

(d) Case2-2: $\psi_0 = -2°$

Figure 8. Ship trajectory under the uncontrolled condition

To further analyze the mechanism of bank effects, taking Case1-2 and Case2-2 as examples, the nondimensional off-centerline deviation η, heading angle ψ, sway force Y, yaw moment N, and velocity components u, v, r are shown in Figure 9. For Case1-2, although the ship is initially closer to the portside bank, the consistent impact of the bank effects causes the bow to be attracted to the bank on the other side. From the perspective of forces and moments acting on the ship, the resultant sway force Y repels the ship toward the starboard bank throughout most of the motion in the waterway. Meanwhile, the variation of the resultant yaw moment N is more complex, exhibiting a pattern of bow attraction, repulsion, and then attraction to the starboard bank. Regarding the sway force, positive values indicate a motion tendency of the ship toward the bank wall on the starboard side, while negative values signify a tendency toward the wall on the port side. The initial off-centerline deviation generates a bank-induced sway force Y_{bank}. During the navigation process, Y_{bank} consistently attracts the ship toward the closer bank wall. However, since the magnitude of Y_{hydro} is larger than that of Y_{bank}, it is demonstrated that Y_{hydro} attracting the ship to the starboard side is more dominant.

For the yaw moment, positive values indicate that the ship turns the bow toward the wall on the starboard side, while negative values mean that the ship turns the bow toward the wall on the port side. The direction of N_{bank} is opposite to that of N_{hydro} nearly all the time, but N_{bank} with a greater magnitude has a more pronounced effect than N_{hydro} during the motion. The variation of N_{bank} is more complex: firstly, it is imposed on the ship from the beginning of the motion and consistently exists until the ship passes through the centerline ($0 < x_0' < 1.887$). At this phase, N_{bank} tends to repel the bow away from the closer bank on the port side, hence the yaw rate r and the heading angle ψ continuously increase. After the ship crosses

the centerline ($x_0' > 1.887$), N_{bank} turns positive and then negative, inducing a bow repulsion-attraction trend. Consequently, the yaw rate r first increases and then decreases, while the heading angle ψ continues to increase due to the consistently positive r. Along with the large heading angle, the ship forward motion ultimately leads to a collision with the bank.

For Case2-2 with an initial heading angle $\psi_0 = -2°$, as shown in Figure 9(b), it can be similarly observed that the Y_{hydro} and N_{bank} with greater magnitudes are more dominant during the navigation process. The former attracts the ship toward the starboard bank consistently, while the latter firstly tends to turn the bow toward the starboard bank before the ship crosses the centerline ($0 < x_0' < 2.528$), and then changes its direction after crossing the centerline ($x_0' > 2.528$). Consequently, the yaw rate r firstly increases and then decreases correspondingly. Due to the constantly positive value of r, the heading angle ψ is consistently increasing throughout this process. With the continuous propulsion, the ship ultimately collides with the starboard bank.

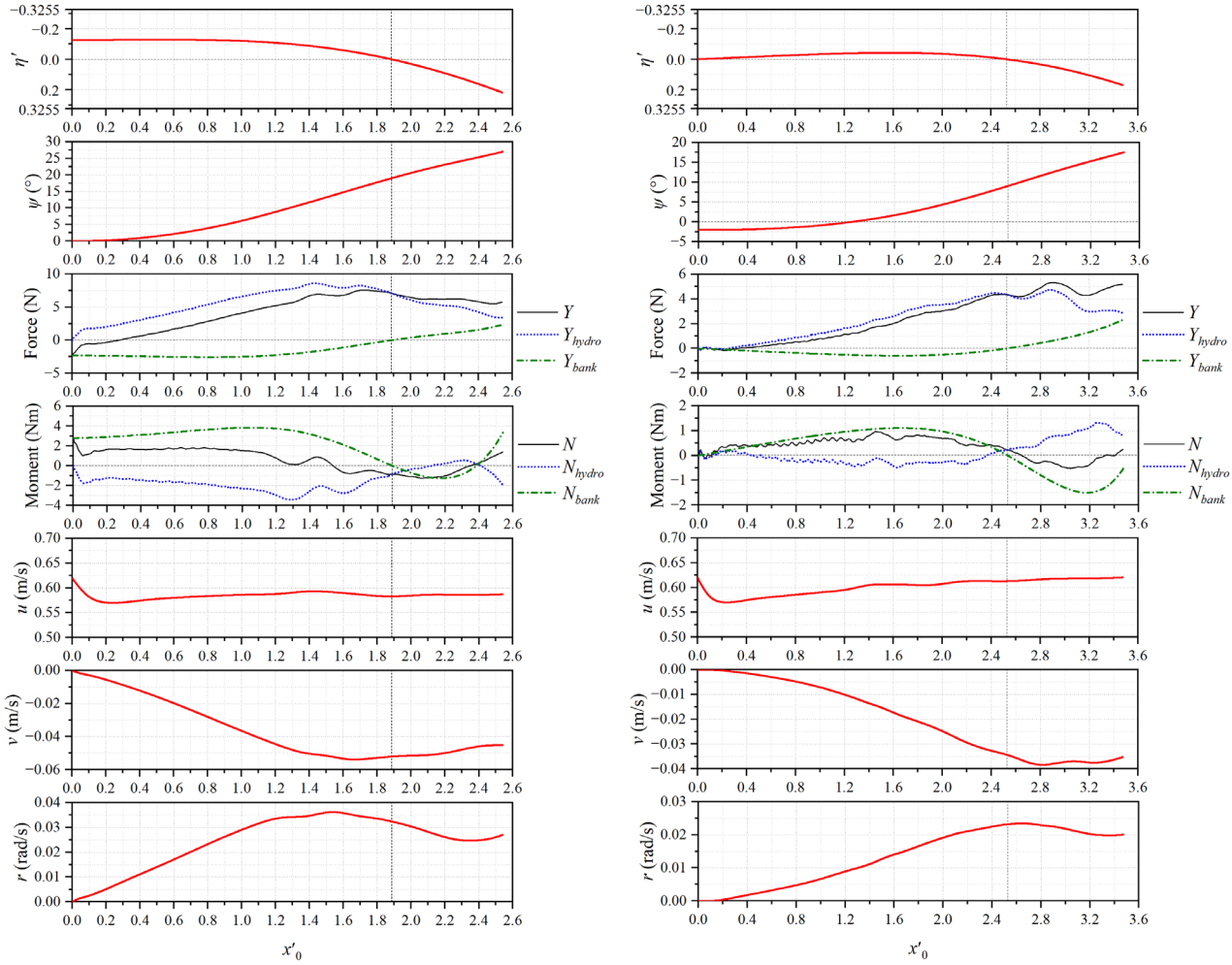

(a) Case1-2: $\eta_0' = -0.127$ **(b) Case2-2:** $\psi_0 = -2°$

Figure 9. Simulation results under the uncontrolled condition

4.2 CONTROLLED CONDITIONS

The results in Section 4.1 highlight the significance of the rudder controller for course keeping when the ship moves in confined waterways. In this section, the simulations for the same scenarios but under the controlled condition are conducted to illustrate the effectiveness of the controller formulated by Eq. (5). The actual trajectories for the four cases are presented in Figure 10, with y_0 magnified 10 times for clarity. It can be observed that after approximately 160 s the trajectories stabilize into quasi-linear paths, indicating successful course-keeping performances. This confirms the effectiveness of the applied control algorithm for course-keeping. In particular, it is interesting to note that in all cases the controlled ship course deviates by approximately 0.2 m from the centerline, since the zero heading angle is selected as the control goal, not the zero deviation from the waterway centerline.

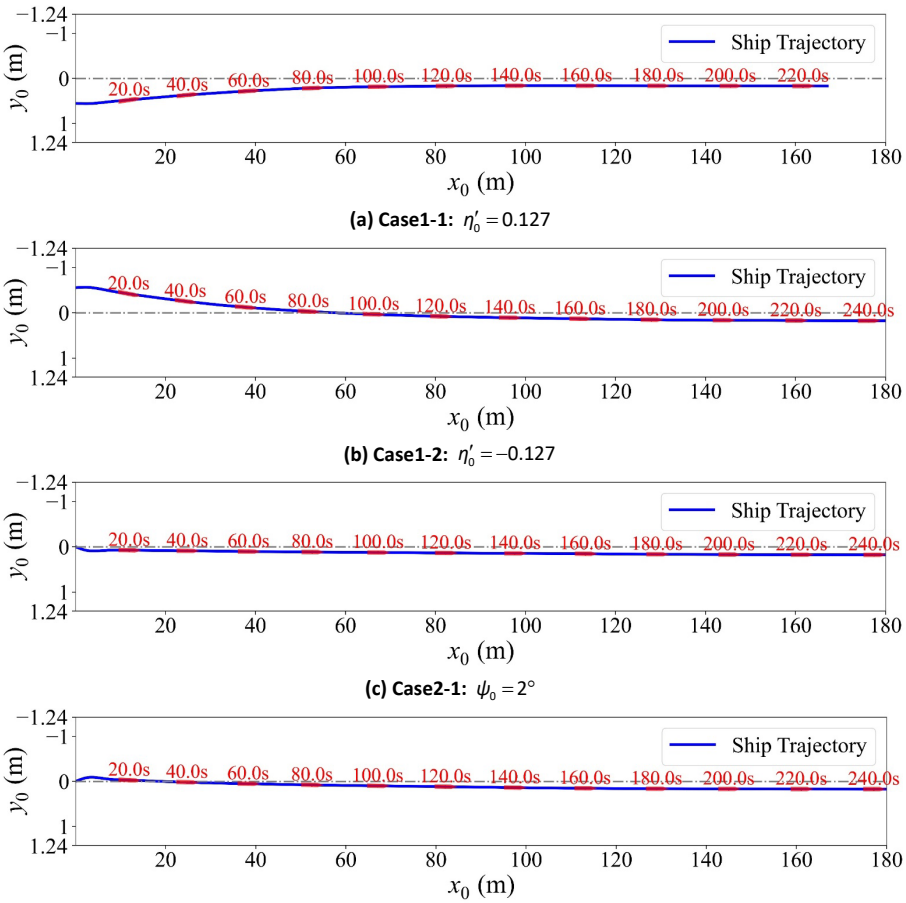

(a) Case1-1: $\eta_0' = 0.127$

(b) Case1-2: $\eta_0' = -0.127$

(c) Case2-1: $\psi_0 = 2°$

(d) Case2-2: $\psi_0 = -2°$

Figure 10. Ship trajectory under the controlled condition

Similar to Section 4.1, the nondimensional location, heading angle ψ, rudder angle δ, sway force Y, yaw moment N, and velocity components u, v, r for Case1-2 and Case2-2 are shown in Figure 11. The time histories of the heading angle ψ demonstrate that the applied controller effectively guides the heading angle to approach zero and maintain this target course in both cases. From the time histories of the rudder angle δ, significant rudder deflection is observed during the initial phases of both cases to control the heading angle. It is noteworthy that after the ship motion tends to be stable with zero heading angle, the ship experiences two pairs of stable sway forces (Y_{hydro} and Y_{bank}) and yaw moments (N_{hydro} and N_{bank}), which have nearly equal magnitudes but opposite directions. As a result, the resultant sway force Y and yaw moment N are close to zero. The stable bank sway force Y_{bank} and yaw moment N_{bank} are attributed to the constant off-centerline deviation $\eta' \approx 0.046$, while the inherent hydrodynamic sway force Y_{hydro} and moment N_{hydro} on the ship in straight-ahead motions are likely induced by the asymmetrical flow field generated by the propeller rotation, and propeller-induced flows are interacted with the rudder.

To confirm it, Figure 12 exhibits the streamlines around the rudder and the pressure distributions on the surface during the course-keeping process. It illustrates that the rotating propeller generates a circumferential flow downstream passing the rudder. This asymmetric flow between the port and starboard sides of the rudder leads to an imbalance in the pressure distributions, producing a lateral force on the rudder. Consequently, the ship experiences additional sway force Y_{hydro} and yaw moment N_{hydro} in straight-ahead motions even without a rudder angle. Finally, the ship is forced to slightly deviate from the centerline to allow the bank force Y_{bank} and moment N_{bank} to counterbalance the additional hydrodynamic sway force Y_{hydro} and yaw moment N_{hydro}.

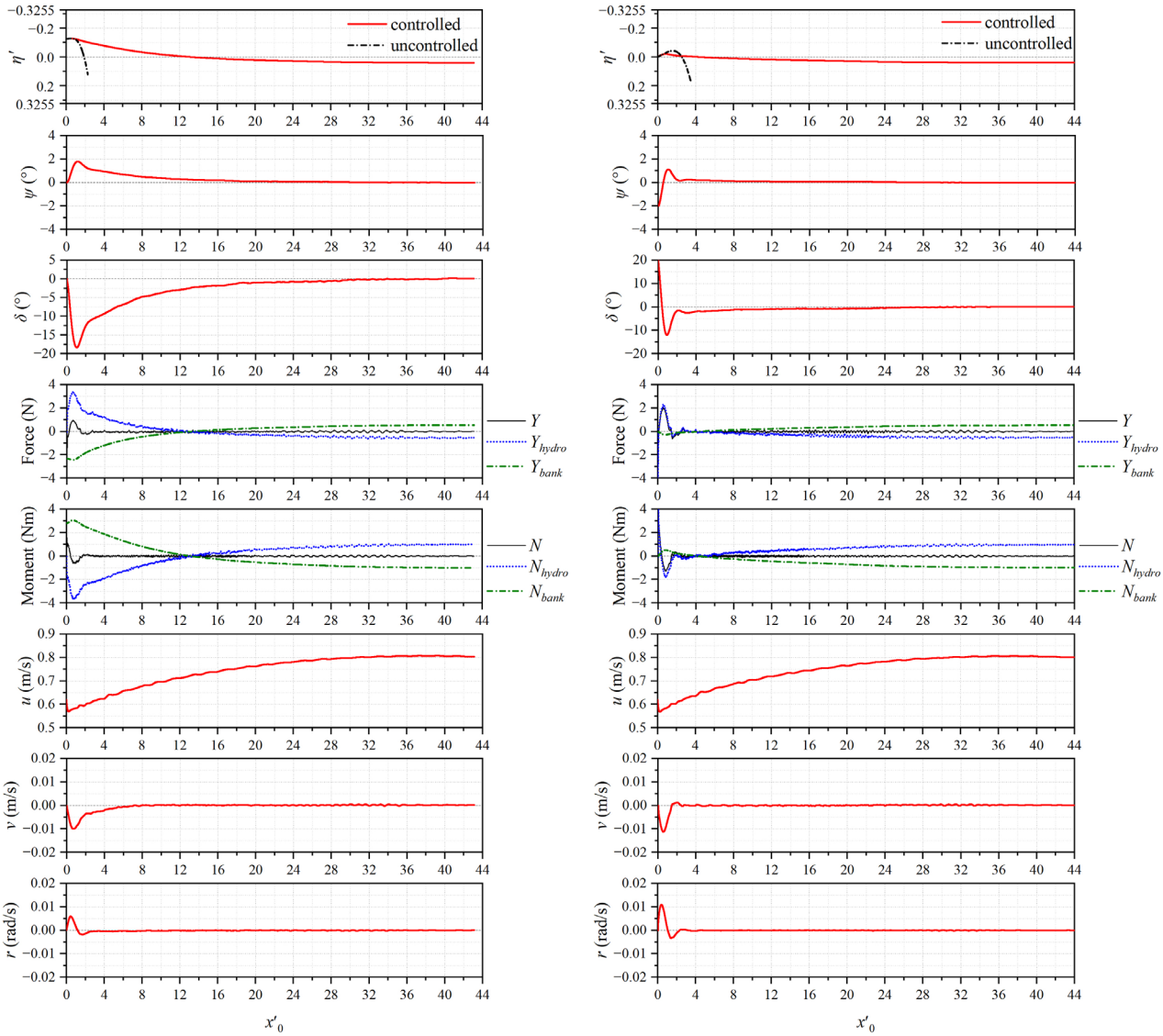

(a) Case1-2: $\eta_0' = -0.127$ **(b) Case2-2:** $\psi_0 = -2°$

Figure 11. Simulation results under the controlled condition

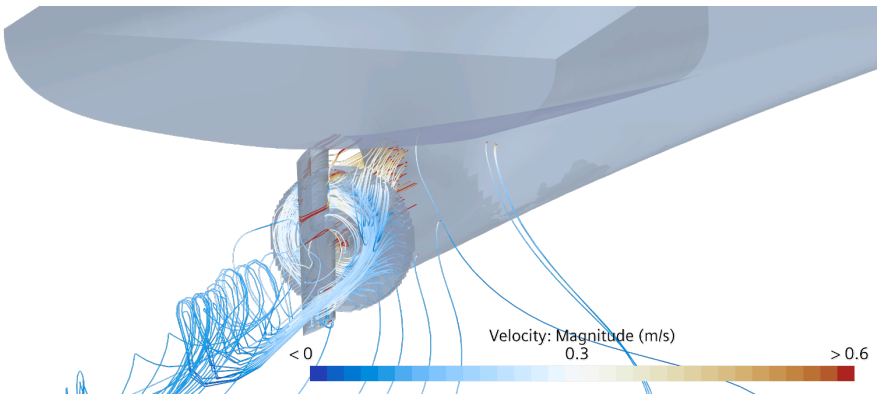

(a) streamlines around rudder

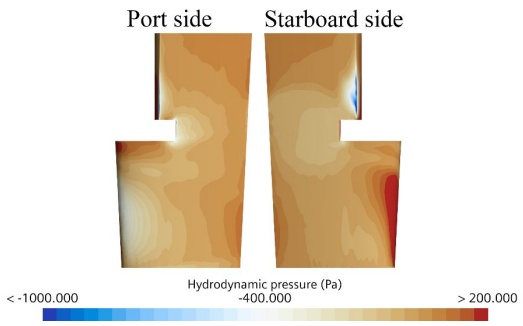

(b) pressure on rudder surface

Figure 12. Flow field results in the course-keeping process

5 CONCLUSIONS

In order to provide an in-depth analysis of the bank-effect mechanism and its influences on a moving ship in confined waterways, particularly to offer practical control guidance for ship operations in such environments, this study employs the coupled CFD method and control algorithm to investigate the course-keeping problem by direct simulations. The unsteady Reynolds Averaged Navier-Stokes (URANS) method is applied to simulate the viscous flows around the ship, and the overset mesh technique combined with the PD algorithm is adopted to realize the dynamic rudder deflection during course keeping. To address the challenges in traditional free-running simulations, this study develops a virtual bank method to simplify the modeling of bank wall effects with appropriate effectiveness. In this approach, the bank-induced forces and moments are directly imposed on the ship through formulas in terms of hydrodynamic parameters, and are added to the open-water simulations as external forces and moments.

Based on the developed method, two types of scenarios of a KCS model moving in confined waterways are investigated: one is the ship navigating with an initial off-centerline displacement, and the other is the ship navigating with an initial heading angle. Free-running simulations of the ship in a confined waterway are performed, where the rudder is controlled to maintain the zero heading angle. The predicted ship trajectories demonstrate that, the ship without the controller gradually deviates from the desired course and ultimately collides with the waterway bank in both scenarios. In contrast, the simulation results under the controlled condition show that the ship successfully achieves course-keeping in the same scenarios. However, the ship trajectory under control actions deviates approximately 0.2 m from the centerline, attributed to the selected course-keeping goal with zero heading angle only. The flow field analyses further reveal that this deviation is also caused by the asymmetrical flow field around the rudder, generated by the propeller rotation. The asymmetrical flow induces additional hydrodynamic sway forces and yaw moments, forcing the ship to deviate from the centerline slightly. This deviation allows the bank-induced forces and moments to counterbalance the additional hydrodynamic impacts, enabling the ship to maintain the target course.

In this paper, a moderate confined-water condition (h/d = 2.0 and Fr_h = 0.309) is selected to assess the feasibility of the developed method. In the future, more challenging conditions, such as smaller under-keel clearance, narrower waterways, or higher ship speeds, will be investigated to provide a more comprehensive evaluation of the robustness and applicability of the method. In addition to the course keeping without variation of heading angle by the developed method, the path following along a predetermined course to keep a distance from the bank for safe navigation in the practical application will be considered in the future study as well.

6 ACKNOWLEDGEMENTS

This work is supported by the State Key Laboratory of Maritime Technology and Safety, the National Natural Science Foundation of China (Grant No. 51979164) and the Fundamental Research Funds for the Central Universities.

7 REFERENCES

Aram, S., Mucha, P., 2023. Computational fluid dynamics analysis of different propeller models for a ship maneuvering in calm water. Ocean Eng. 276, 114226. https://doi.org/10.1016/j.oceaneng.2023.114226.

Carrica, P.M., Mofidi, A., Eloot, K., Delefortrie, G., 2016. Direct simulation and experimental study of zigzag maneuver of KCS in shallow water. Ocean Eng. 112, 117–133. https://doi.org/10.1016/j.oceaneng.2015.12.008.

Degrieck, A., Uyttersprot, B., Sutulo, S., Guedes Soares, C., Van Hoydonck, W., Vantorre, M., Lataire, E., 2021. Hydrodynamic ship-ship and ship-bank interaction: A comparative numerical study. Ocean Eng. 230, 108970. https://doi.org/10.1016/j.oceaneng.2021.108970.

Delefortrie, G., Eloot, K., Mostaert, F., 2012. SIMMAN 2014 report: Execution of Model Tests with KCS and KVLCC2. Flanders Hydraulics Research.

Delefortrie, G., Verwilligen, J., Eloot, K., Lataire, E., 2024a. Bank interaction effects on ships in 6 DOF. Ocean Eng. 310, 118614. https://doi.org/10.1016/j.oceaneng.2024.118614.

Delefortrie, G., Verwilligen, J., Kochanowski, C., Pinkster, J.A., Yuan, Z.M., Liu, Y.H., Kastens, M., Van Hoydonck, W., Pinkster, H.J.M., Lataire, E., 2024b. Unsteady ship–bank interaction: a comparison between experimental and computational predictions. Ship Technol. Res. 71 (1), 33–57. https://doi.org/10.1080/09377255.2023.2275372.

Deng, G., Queutey, P., Wackers, J., Visonneau, M., Guilmineau, E., Leroyer, A., 2022. Assessment of ship maneuvering simulation with different propeller models. J. Hydrodyn. 34 (3), 422–433. https://doi.org/10.1007/s42241-022-0039-y.

Fujino, M., 1968. Experimental studies on ship manoeuvrability in restricted waters - Part I. Int. Shipbuild. Prog. 15 (168), 279–301. https://doi.org/10.3233/ISP-1968-1516801.

Fujino, M., 1970. Experimental studies on ship manoeuvrability in restricted waters - Part II. Int. Shipbuild. Prog. 17 (186), 45–65. https://doi.org/10.3233/ISP-1968-1516801.

Kim, D., Tezdogan, T., Incecik, A., 2022. Hydrodynamic analysis of ship manoeuvrability in shallow water using high-fidelity URANS computations. Appl. Ocean Res. 123, 103176. https://doi.org/10.1016/j.apor.2022.103176.

Kim, D., Yim, J., Song, S., Park, J.B., Kim, J., Yu, Y., Elsherbiny, K., Tezdogan, T., 2023. Path-following control problem for maritime autonomous surface ships (MASS) in adverse weather conditions at low speeds. Ocean Eng. 287, 115860. https://doi.org/10.1016/j.oceaneng.2023.115860.

Lataire, E., Vantorre, M., Eloot, K., 2009. Systematic model tests on ship-bank interaction effects, in: Proceedings of the International Conference on Ship Manoeuvring in Shallow and Confined Water: Bank Effects, Antwerp, Belgium, 9–22. http://hdl.handle.net/1854/LU-663477.

Lee, S., 2023. Hydrodynamic interaction forces on different ship types under various operating conditions in restricted waters. Ocean Eng. 267, 113325. https://doi.org/10.1016/j.oceaneng.2022.113325.

Liu, H., Ma, N., Gu, X., 2021. CFD prediction of ship-bank interaction for KCS under extreme conditions. J. Mar. Sci. Technol. 26 (4), 1062–1077. https://doi.org/10.1007/s00773-021-00798-x.

Menter, F., 1993. Zonal two equation k-ω turbulence models for aerodynamic flows, in: Proceedings of the 24th Fluid Dynamics Conference. Orlando, Florida, USA. https://doi.org/10.2514/6.1993-2906.

Mucha, P., Aram, S., Radosavljevic, D., Singh, J., Wheeler, M., 2023. Propeller modeling for ship maneuvering simulations in Simcenter STAR-CCM+, in: Proceedings of the 25th Numerical Towing Tank Symposium (NuTTS). Ericeira, Portugal.

Norrbin, N.H., 1975. Manoeuvring in confined waters: interaction phenomena due to side banks or other ships, in: Proceedings of the 14th International Towing Tank Conference. Ottawa, Canada, pp. 450–486.

Ren, H., Xu, C., Zhou, X., Sutulo, S., Guedes Soares, C., 2020. A numerical method for calculation of ship–ship hydrodynamics interaction in shallow water accounting for sinkage and trim. J. Offshore Mech. Arct. Eng. 142 (5). https://doi.org/10.1115/1.4046484.

Sano, M., Yasukawa, H., Hata, H., 2012. Experimental study on ship operation in close proximity to bank channel, in: Proceedings of the International Conference on Marine Simulation and Ship Maneuverability (MARSIM 2012). Singapore.

Sano, M., Yasukawa, H., Hata, H., 2014. Directional stability of a ship in close proximity to channel wall. J. Mar. Sci. Technol. 19 (4), 376–393. https://doi.org/10.1007/s00773-014-0271-4.

Sørensen, J.N., 2022. Aerodynamic Analysis of Wind Turbines, in: Comprehensive Renewable Energy (Second Edition). pp. 172–193. https://doi.org/10.1016/B978-0-12-819727-1.00127-8.

Terziev, M., Liu, Y., Yuan, Z., Incecik, A., 2024. The resistance of a trans-critically accelerating ship in shallow water. Ship Technol. Res. 71 (1), 14–32. https://doi.org/10.1080/09377255.2023.2252232.

Van Hoydonck, W., Toxopeus, S., Eloot, K., Bhawsinka, K., Queutey, P., Visonneau, M., 2019. Bank effects for KVLCC2. J. Mar. Sci. Technol. 24 (1), 174–199. https://doi.org/10.1007/s00773-018-0545-3.

Van Zwijnsvoorde, T., Delefortrie, G., Lataire, E., 2022. Passing ship effects in shallow and confined water: open model test data for validation purposes, in: Proceedings of the 6th MASHCON International Conference on Ship Manoeuvring in Shallow and Confined Water. Glasgow, UK, pp. 255–283. http://hdl.handle.net/1854/LU-01H0HW8J5FDQDVEMB3PGZ2ZSX2.

Vantorre, M., Delefortrie, G., Eloot, K., Laforce, E., 2003. Experimental investigation of ship-bank interaction forces, in: Proceedings of the International Conference on Marine Simulation and Ship Maneuverability. Kanazawa, Japan, pp. RC-31-31–RC-31-39. http://hdl.handle.net/1854/LU-298476.

Vantorre, M., Verzhbitskaya, E., Laforce, E., 2002. Model test based formulations of ship-ship interaction forces. Ship Technol. Res. 49, 124–141. http://hdl.handle.net/1854/LU-160369.

Wang, J., Zou, L., Wan, D., 2017. CFD simulations of free running ship under course keeping control. Ocean Eng. 141, 450–464. https://doi.org/10.1016/j.oceaneng.2017.06.052.

Xu, C., Zhou, X., Ren, H., Sutulo, S., Guedes Soares, C., 2024. Real-time calculation of ship to ship hydrodynamic interaction in shallow waters with adaptive mesh refinement. Ocean Eng. 295, 116943. https://doi.org/10.1016/j.oceaneng.2024.116943.

Yao, J.X., Zou, Z.J., 2010. Calculation of ship squat in restricted waterways by using a 3D panel method. J. Hydrodyn. 22 (5, Supplement 1), 489–494. https://doi.org/10.1016/S1001-6058(09)60241-9.

Yasukawa, H., 2019. Maneuvering hydrodynamic derivatives and course stability of a ship close to a bank. Ocean Eng. 188, 106149. https://doi.org/10.1016/j.oceaneng.2019.106149.

Yuan, Z.M., Incecik, A., 2016. Investigation of ship-bank, ship-bottom and ship-ship interactions by using potential flow method, in: Proceedings of the 4th International Conference on Ship Manoeuvring in Shallow and Confined Water. Hamburg, Germany, pp. 83–92.

Yuan, Z.M., 2019. Ship hydrodynamics in confined waterways. J. Ship Res. 63 (01), 16–29. https://doi.org/10.5957/JOSR.04170020.

Zheng, Z.Q., Zou, L., Zou, Z.J., 2023. A numerical study of passing ship effects on a moored ship in confined waterways with new benchmark cases. Ocean Eng. 280, 114643. https://doi.org/10.1016/j.oceaneng.2023.114643.

Zhou, X., Sutulo, S., Guedes Soares, C., 2012. Computation of ship hydrodynamic interaction forces in restricted waters using potential theory. J. Mar. Sci. Appl. 11 (3), 265–275. https://doi.org/10.1007/s11804-012-1132-3.

Zou, L., 2012. CFD Predictions Including Verification and Validation of Hydrodynamic Forces and Moments on a Ship in Restricted Waters. Chalmers University of Technology, Gothenburg, Sweden.

Zou, L., Larsson, L., 2013. Computational fluid dynamics (CFD) prediction of bank effects including verification and validation. J. Mar. Sci. Technol. 18 (3), 310–323. https://doi.org/10.1007/s00773-012-0209-7.

8 AUTHORS BIOGRAPHY

Zi-Qiang Zheng is a PhD student at School of Ocean and Civil Engineering, Shanghai Jiao Tong University. He majors in ship hydrodynamic performances in restricted waters based on numerical methods, etc.

Yu He is a PhD student at School of Ocean and Civil Engineering, Shanghai Jiao Tong University. He majors in ship motion control, etc.

Lu Zou holds the current position of Associate Professor at School of Ocean and Civil Engineering, Shanghai Jiao Tong University. Her major research interest is ship hydrodynamic problems in confined waters, modeling of ship maneuvering motion, ship motion control, etc.

Zao-Jian Zou is a retired professor at School of Ocean and Civil Engineering, Shanghai Jiao Tong University. His previous experience includes PI of projects on maneuvering and control of ships and other marine vehicles. He was a member of the 22nd, 23rd, 25th and 26th ITTC Maneuvering Committee.

VALIDATION OF SLENDERFLOW IN SHIP - SHIP INTERACTION SCENARIOS

Andreas VERBEKE, Ships and Marine Technology, Ghent University, Belgium
Tim GOURLAY, Perth Hydro, Australia
Guillaume DELEFORTRIE, Ships and Marine Technology, Ghent University, Belgium
Maxim CANDRIES, Ships and Marine Technology, Ghent University, Belgium
Wim VAN HOYDONCK, Flanders Hydraulics, Belgium
Evert LATAIRE, Ships and Marine Technology, Ghent University, Belgium

VALIDATION OF SLENDERFLOW IN SHIP - SHIP INTERACTION SCENARIOS

ANDREAS VERBEKE, GHENT UNIVERSITY, BELGIUM
TIM GOURLAY, PERTH HYDRO, AUSTRALIA
GUILLAUME DELEFORTRIE, GHENT UNIVERSITY, BELGIUM
MAXIM CANDRIES, GHENT UNIVERSITY, BELGIUM
WIM VAN HOYDONCK, FLANDERS HYDRAULICS, BELGIUM
EVERT LATAIRE, GHENT UNIVERSITY, BELGIUM

SUMMARY

Ship-to-ship interactions can induce significant vertical motions, increasing grounding risks. Experimental data on this phenomenon remain scarce, so numerical methods could provide an alternative to assess these risks. A numerical method based on slender-body theory was implemented by Gourlay (2009), who used a linear superposition of ship-bound pressure fields in open water to calculate ship sinkage and trim during ship-to-ship interactions. A Fourier solution of these pressure fields was implemented in the computer code *SlenderFlow* (SF). In this paper, Gourlay's superposition method was implemented using SF and validated with experimental data obtained at Flanders Hydraulics (FH). The results showed that SF captures qualitative trends, but its predictions underestimate the peak magnitudes of the unsteady sinkages. This discrepancy is attributed to model simplifications, such as the linearization of the hull and free-surface boundary conditions, but also the superposition of separate pressure fields is questioned.

NOMENCLATURE

A_{M}	Surface area of midship section (m^2)
A_{W}	Waterplane area (m^2)
B	Maximum moulded breadth (m)
$\bar{B}(k)$	Fourier transform of $B(x)$ (m^2)
B_{i}	Maximum moulded breadth of ship I (m)
$B(x)$	Ship breadth on the waterline at longitudinal position x(m)
Fr_h	Depth-based Froude number (-)
$Fr_{h,\mathrm{crit1}}$	First critical Froude depth number (-)
$Fr_{h,\mathrm{i}}$	Depth-based Froude number of ship i (-)
g	Gravitational acceleration constant (9.81 m/s^2)
h	Water depth (m)
I_{LCF}	Second moment of waterplane area (m^4)
k	Dimensional wave number (1/m)
$K(k)$	Kernel function determined by canal bathymetries (-)
L	Submerged length of the own ship (m)
$L_{\mathrm{PP,i}}$	Length between perpendiculars of ship i (m)
m	Canal blockage (-)
$p_i(x_j, y_j)$	Pressure field due to ship i in ship-bound reference system of ship j (N/m^2)
U	Free stream velocity (m/s)
U_{i}	Ship speed magnitude of ship i (knots or m/s)
U_{rel}	Relative speed of target vessel w.r.t. own ship (knots or m/s)
s_0	Sinkage at midships (m)
s	Sinkage (m)
s_{AP}	Sinkage at the aft perpendicular (m)
s_{FP}	Sinkage at the fore perpendicular (m)
s_{LCF}	Sinkage at LCF (m)
s_{peak}	Peak magnitude of the unsteady sinkage (m)
s_{steady}	Steady sinkage (m)
$\bar{S}'(k)$	Fourier transform of derivative of $S(x)$ (m^3/m)
$S(x)$	Hull cross-sectional area at station x (m^2)
$S'(x)$	Derivative of hull cross-sectional area at station x (m^2/m)

t	Time (s)
T	Ship draft (m)
T_i	Draft of ship i (m)
w	Canal width (m)
x	Longitudinal coordinate in ship-bound reference system (m)
X	Variable of integration (m)
$\overline{xB}(k)$	Fourier transform of $(x - x_{\mathrm{LCF}})B(x)$ (m^3)
x_{cc}	Longitudinal distance between midship sections (m)
x_{i}	Longitudinal coordinate (in reference system i) (m)
$x_{\mathrm{i,LCF}}$	Longitudinal coordinate of centre of floatation in reference system of ship i (m)
y	Transverse coordinate in ship-bound reference system (m)
y_{cc}	Transverse distance between symmetry planes (m)
y_{i}	Transverse coordinate (in reference system i) (m)
z	Vertical coordinate in ship-bound reference system(m)
z_i	Vertical coordinate (in reference system of ship i) (m)
Z_{steady}	Steady vertical heave force (positive upwards) (N)
$Z(t)$	Unsteady vertical heave force (positive upwards) as function of time (N)
Z_{total}	Vertical heave force, sum of steady and unsteady component (N)
θ_{LCF}	Trim about LCF (radians)
λ	Scale factor (-)
∇	Moulded volume (m^3)
ξ	Stagger distance (-)
ρ	Density of water (kg/m^3)
ϕ	Disturbance velocity potential (m^2/s)
Ω	Cross-section area of the canal (m^2)
Exp	Experiment
FH	Flanders Hydraulics
LCF	Longitudinal centre of floatation
SF	SlenderFlow
UKC	Under Keel Clearance (-)
$_0$	Subscript, indicating the inertial frame of reference2
$_{\mathrm{own}}$	Subscript, indicating the own ship
$_{\mathrm{tar}}$	Subscript, indicating the target ship

1 INTRODUCTION

Ships manoeuvring in close proximity generate interaction forces due to overlapping ship-bound pressure fields. With increasing ship sizes, the frequency of interaction-related accidents rises, highlighting the relevance of this issue. This problem is not new and has been the topic of many publications (see Zhou et al. (2023) and references therein). However, the main focus of these investigations lies on the forces acting in the horizontal plane due to the passage of another vessel. The specific problem of vertical motions caused by ship interactions has received comparatively little attention (Gourlay, 2009).

Eloot et al. (2011) pointed out that squat and trim during ship-to-ship interaction play an important role in the design of two-way navigation channels, in which vertical dimensions should be sufficient to account for the additional squat caused by ship-to-ship interactions. However, experimental data on this topic remains scarce. Experimental data was reported by Dand (1981). It was shown that large changes in trim and sinkage can occur, increasing the grounding risk. Vantorre et al. (2002) conducted extensive ship-to-ship interaction tests but did not analyse vertical displacements.

Numerical models offer an alternative to experimental data. Gourlay (2009) applied slender-body theory to calculate ship sinkage and trim during ship interaction using an integral expression from Tuck (1966) to calculate the pressure field of a ship in open water. This approach assumes linear superposition of pressure fields but lacked experimental validation.

The pressure field calculated by Tuck (1966) involves the direct integration of a singular integral. To overcome this singularity, Gourlay (2008) proposed an alternative solution involving a Fourier transform. This Fourier transform solution was implemented in the computer code *SlenderFlow* (SF) (Gourlay, 2008; Ha, 2018). The computer code also incorporates the solution to other bathymetries (Gourlay, 2008). With the ship geometry, velocity and bathymetry as input, SF calculates the hydrodynamic pressure fields, steady sinkage and trim of a single ship.

The goal of this paper is to validate the linear superposition method proposed by Gourlay (2009) with data obtained by Vantorre et al. (2002). Instead of Tuck's integral expression of the pressure field in open water, the Fourier-based solutions presented by Gourlay (2008) are modified to calculate the pressure field of a passing target ship.

The paper first presents the slender-body theory of Tuck and his integral solution. The shortcomings of this solution are explained, after which the alternative solution using Fourier transforms is presented. Then, the solution of the flow field around a ship in a canal of constant width is presented, since validation is performed with model test results obtained in a towing tank of constant width. This bathymetry was also included in SF. Subsequently, the superposition method is explained. Finally, the numerical results are compared to experimental results.

2 THEORETICAL METHOD

2.1 THEORETICAL BACKGROUND OF SLENDERFLOW

The computer code *SlenderFlow* calculates the hydrodynamic pressure fields, steady sinkage and trim of a single ship sailing in different bathymetries. The code assumes the ship-bound coordinate systems as shown in Figure *1*. To explain the theoretical background of SF, consider the own ship with ship-bound coordinate system $(x_{\text{own}}, y_{\text{own}}, z_{\text{own}})$. This coordinate system will be denoted with (x, y, z) in this section for ease of notation.

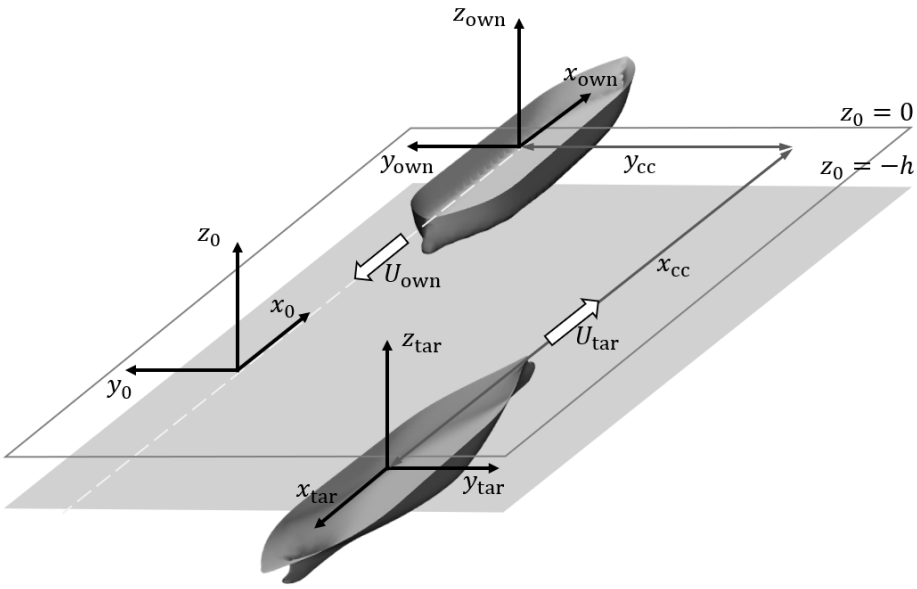

Figure 1 Coordinate systems and notation

The longitudinal coordinate x is centred at midships (positive towards the stern). The transverse coordinate y is centred on the ship's centreline (positive to starboard) and the vertical coordinate z lies at the undisturbed free surface (positive upwards). In this ship-fixed coordinate system, the ship is stationary and is subjected to a steady incoming freestream of magnitude U, which equals the own ship speed U_{own}.

All solutions implemented in *SF* were derived from a partial differential equation derived by Tuck (1966). He derived that the leading order disturbance velocity potential ϕ should satisfy the linearized shallow-water equation in the outer region

$$(1 - Fr_h^2)\frac{\partial^2 \phi}{\partial x^2} + \frac{\partial^2 \phi}{\partial y^2} = 0. \tag{1}$$

Fr_h is the depth-based Froude number ($U/\sqrt{gh}$), with h the water depth. It is subject to a modified linearised hull boundary condition (the inner boundary condition)

$$\frac{\partial \phi}{\partial y} = \pm \frac{U}{2h} S'(x) \text{ on } y = 0_{\pm}, \tag{2}$$

where $S(x)$ is the hull cross-sectional area at station x and $S'(x)$ is the derivative of this section area with respect to x. According to linear theory the ship is fixed in its rest position when calculating the flow, so the increase of the immersed volume due to sinkage is neglected when calculating $S(x)$ in Eq. (*2*) (Gourlay, 2008).

Depending on the specific bathymetry, additional boundary conditions are introduced. For open water of constant depth, Eq. (*1*) is subject to the far-field boundary condition

$$\frac{\partial \phi}{\partial x}, \frac{\partial \phi}{\partial y} \to 0 \text{ as } y \to \pm\infty. \tag{3}$$

In a canal of constant depth h and canal width w, with the ship sailing at the canal centreline, a wall boundary condition at the sides of the canal is introduced (Tuck, 1967):

$$\frac{\partial \phi}{\partial y} = 0 \text{ on } y = \pm \frac{w}{2}. \tag{4}$$

Other bathymetries require additional details (Gourlay, 2008).

The velocity potential can be calculated from the elliptic partial differential equation ($Fr_h < 1$) Eq. (*1*) by considering the boundary conditions. This potential can then be employed to derive the hydrodynamic pressure. This pressure is given from the linearized Bernoulli equation as (Gourlay, 2014)

$$p(x, y) = -\rho U \frac{\partial \phi}{\partial x}. \tag{5}$$

Higher-order (quadratic) terms are neglected in the Bernoulli equation, since these are of the same order as other terms already neglected in the derivation of the linearized shallow-water equation Eq. (*1*) and hull boundary condition Eq. (*2*) (Gourlay, 2014).

Tuck (1966) solved this boundary value problem for the case of a ship sailing in open water by considering the velocity potential for a line of moving sources (Gourlay, 2008). The pressure field around this ship moving at a steady velocity U is equal to

$$p(x, y) = -\frac{\rho U^2}{2\pi h\sqrt{1 - Fr_h^2}} \int_{-\frac{L}{2}}^{\frac{L}{2}} \frac{x - X}{(x - X)^2 + (1 - Fr_h^2)y^2} \frac{dS}{dX} dX, \tag{6}$$

In Eq. (*6*) X represents the variable of integration along the length of the ship. L is the submerged length of the ship and equals the distance between the foremost and aftmost point.

For locations away from the ship's centreline ($y \neq 0$), the integrand in Eq. (*6*) is non-singular and the integral may be evaluated using Simpson's rule (Gourlay, 2014). Additionally, the singularity at $y = 0$ is integrable except right at the bow or stern where $S'(x)$ is discontinuous.

To address this issue, (Gourlay, 2008) proposed an alternative solution which uses Fourier transforms rather than source summations, which was implemented in SF (Ha, 2018). The pressure field surrounding a ship in open water of constant depth may be written as

$$p(x, y) = -\frac{\rho U^2}{4\pi h\sqrt{1 - Fr_h^2}} \int_{-\infty}^{\infty} i \operatorname{sgn}(k) \overline{S'}(k)\, e^{-\sqrt{1 - Fr_h^2}|k||y|} e^{-ikx} dk. \tag{7}$$

The real part of Eq. (7) is considered for physical quantities. The Fourier transform of the derivative of the section area $\overline{S'}(k)$ is calculated directly as (Gourlay, 2014)

$$\overline{S'}(k) = \int_{-\infty}^{\infty} \frac{dS}{dx} e^{ikx} dx. \tag{8}$$

Since this integral is highly oscillatory for large values of $|k|$, Filon's method is employed to evaluate this integral. This Fourier transform does not quite tend to zero as $|k| \to \infty$, due to the discontinuities in $S'(x)$ at the bow and stern. Consequently, the singularity at the bow and stern remains in Eq. (7), but the singularity at other locations on the hull ($y = 0$) is lifted, allowing the use of Simpson's rule.

The expression for the pressure Eq. (7) can be generalized to other bathymetries as

$$p(x,y) = -\frac{\rho U^2}{4\pi h\sqrt{1-Fr_h^2}}\int_{-\infty}^{\infty} i\,K(k)\bar{S}'(k)\,e^{-\sqrt{1-Fr_h^2}|k||y|}e^{-ikx}dk. \tag{9}$$

The function $K(k)$ depends on the transverse geometry (Gourlay, 2008). For instance, in open water

$$K(k) = \mathrm{sgn}(k), \tag{10}$$

which can be derived from Eq. (7). In a rectangular canal

$$K(k) = \coth\left(\left(\frac{w}{2}\right)\sqrt{1-Fr_h^2}k\right). \tag{11}$$

The pressure on the hull $p(x,0)$ can be used to calculate the vertical heave force Z and bow-down trim moment about the longitudinal centre of floatation (LCF) M_{LCF} to first order (Tuck, 1966). Using the slender-body approximation, these are calculated as

$$Z = \int_{-L/2}^{L/2} p(x,0)B(x)\,dx = -\frac{\rho U^2}{4\pi h\sqrt{1-Fr_h^2}}\int_{-\infty}^{+\infty} i\bar{S}'(k)\overline{B^*}(k)K(k)dk, \tag{12}$$

$$M_{LCF} = \int_{-\frac{L}{2}}^{\frac{L}{2}} p(x,0)B(x)\,(x-x_{LCF})dx = -\frac{\rho U^2}{4\pi h\sqrt{1-Fr_h^2}}\int_{-\infty}^{+\infty} i\bar{S}'(k)\overline{xB^*}(k)K(k)dk. \tag{13}$$

$\bar{B}(k)$ denotes the Fourier transform of $B(x)$. The asterisk denotes the complex conjugate. $\overline{xB}(k)$ is the Fourier transform of $(x - x_{\mathrm{LCF}})B(x)$. SlenderFlow includes additional bathymetries, such as a dredged and stepped canal. More details can be found in (Gourlay, 2008).

The upwards vertical force Z is related to the sinkage of the LCF s_{LCF}. and waterplane area A_{W} through hydrostatic balancing via (Gourlay, 2009)

$$Z = -\rho g A_{\mathrm{w}} s_{\mathrm{LCF}}. \tag{14}$$

Similarly, the steady bow-down trim θ_{LCF}(in radians) is related to the bow-down moment through

$$M_{\mathrm{LCF}} = \rho g I_{\mathrm{LCF}}\theta_{\mathrm{LCF}}, \tag{15}$$

$$I_{\mathrm{LCF}} = \int_{-L/2}^{L/2}(X - x_{\mathrm{LCF}})B(X)dX. \tag{16}$$

x_{LCF} is the coordinate of the longitudinal centre of floatation in the ship-bound reference system.

It is clear that a number of assumptions are made when developing the code. Firstly, the slender-body is based on the potential flow assumptions, so boundary layer thickening along the hull is absent. This is especially important at model scale, where the boundary layer is thicker and more likely to separate, increasing the difference in results between experiments and SF results. Additionally, the absence of self-propulsion in SF, might aggravate these effects.

The water depth is small compared to the ship's length, so vertical velocities are assumed to be much smaller than horizontal flow components. Consequently, the flow is essentially horizontal.

Finally, both the free-surface and hull boundary conditions are linearized. The linear solution uses only the leading-order dynamic free surface boundary conditions, assuming free surface displacements to be small (Gourlay, 2008). Hull-boundary

conditions are linearized by assuming that the ship's beam is much smaller than its length. Neglecting these non-linearities are especially important for fuller ship shapes, such as bulk carriers and tankers.

2.2 SHIP INTERACTION WITH SLENDERFLOW

The calculation of sinkages due to ship interaction is based on Gourlay (2009). The unsteady sinkage of a ship (called the own ship) due to a passing ship (called the target ship) was calculated via linear superposition of the pressure fields attached to the own and target ship. Each of these pressure fields is calculated as if the ship were sailing alone in the canal (section 2.1), so unsteady effects, related to the passing ship, are neglected according to this method.This linear superposition was based on Yeung (1978), who found analytically that the dominant heave force and pitch moment were due to linear superposition of the pressure fields produced by each ship (Gourlay, 2009).

The examples studies in this paper consider two ships sailing along parallel trajectories (Figure *1*). It was assumed that the distance between both ships $y_{\mathrm{cc}}$is large compared to each ship's beam and of similar order to each ship's length. In this way, each ship lies entirely in the far field of the other vessel. A ship-fixed coordinate system is attached to the own ship $(x_{\mathrm{own}}, y_{\mathrm{own}}, z_{own})$ and the target ship $(x_{\mathrm{tar}}, y_{\mathrm{tar}}, z_{\mathrm{tar}})$. The own ship and target ship have a constant forward velocity of U_{own} and U_{tar} respectively. An earth-fixed reference frame is introduced as well (x_0, y_0, z_0). The y_0-coordinate is chosen such that the centreline of the own ship lies on y_0 = 0. The centreline of the target vessel lies on y_0 = y_{cc}. The (x_0, t) coordinates are chosen such that the submerged midships of both ships pass through $x_0 = 0$ at time $t = 0$.

With the coordinate systems in Figure 1, Gourlay's (2009) approach is applied. The superposed pressure on the own vessel consists of two terms. The first term is the pressure due to the own ship, which is calculated by taking y = 0in Eq.(9). The second term is the pressure due to the target ship on the own ship. It is found by expressing the target ship-bound pressure field $p_{\mathrm{tar}}(x_{\mathrm{tar}}, y_{\mathrm{tar}})$ in the coordinate system $(x_{\mathrm{own}}, y_{\mathrm{own}})$. For an encounter manoeuvre $x_{\mathrm{tar}} = -x_{\mathrm{own}} + (U_{\mathrm{own}} + U_{\mathrm{tar}})t = -x_{\mathrm{own}} + x_{\mathrm{cc}}$. It follows that, if t is negative before the encounter manoeuvre, x_{cc} is negative when both ships are approaching and positive once both ships have passed each other. Similarly, $y_{\mathrm{tar}} = -y_{\mathrm{own}} + y_{\mathrm{cc}}$, where y_{cc} is negative in Figure 1. This results in the pressure acting on the own ship, due to an encountering target ship, by taking $y_{\mathrm{own}} = 0$in the following expression,

$$p_{\mathrm{tar}}(x_{\mathrm{own}}, y_{\mathrm{own}}, t) = -\frac{\rho U_{\mathrm{tar}}^2}{4\pi h\sqrt{1 - Fr_{h,\mathrm{tar}}^2}} \int_{-\infty}^{\infty} i\, K(k)\overline{S'_{\mathrm{tar}}}(k)\, e^{-\sqrt{1-Fr_{h,\mathrm{tar}}^2}|k||y_{\mathrm{cc}}-y_{\mathrm{own}}|} e^{-ik(-x_{\mathrm{own}}+x_{\mathrm{cc}}(t))} dk, \tag{17}$$

where $Fr_{h,\mathrm{tar}} = U_{\mathrm{tar}}/\sqrt{gh}$. This pressure can be integrated over the own ship to obtain the unsteady sinkage force:

$$Z(t) = \int_{-\frac{L}{2}}^{\frac{L}{2}} p_{\mathrm{tar}}(x, 0, t)B(x)\, dx. \tag{18}$$

This integration is performed numerically to evaluate the unsteady sinkage term. The unsteady trim moment is found by replacing $B(x)$ with $(x - x_{\mathrm{LCF}})B(x)$ in Eq. (*18*). The total vertical force on the own vessel during the encounter manoeuvre is calculated as

$$Z_{\mathrm{total}} = Z_{\mathrm{steady}} + Z(t), \tag{19}$$

where Z_{steady} is calculated with Eq. (*12*).

Similarly, the pressure field of a target ship when overtaking a slower own ship becomes

$$p_{\mathrm{tar}}(x_{\mathrm{own}}, y_{\mathrm{own}}, t) = -\frac{\rho U_{\mathrm{tar}}^2}{4\pi h\sqrt{1 - Fr_{h,\mathrm{tar}}^2}} \int_{-\infty}^{\infty} i\, sgn(k)\overline{S'}(k)\, e^{-\sqrt{1-Fr_{h,\mathrm{tar}}^2}|k||y_{\mathrm{own}}-y_{\mathrm{cc}}|} e^{-ik(x_{\mathrm{own}}+x_{\mathrm{cc}}(t))} dk, \tag{20}$$

where $x_{\mathrm{cc}} = (U_{\mathrm{tar}} - U_{\mathrm{own}})t$. Since t is negative before the target ship overtakes the own ship, x_{cc} is negative before the overtaking manoeuvre and positive once the target ship has passed the own ship.

With the total vertical force and moment, the total sinkage and trim angle can be calculated again via Eq. (*14*) and Eq. (*15*), since it was shown through a dynamic motion analysis that changes in sinkage and trim are sufficiently slow for a quasi-steady method to be employed (Gourlay, 2009).

The unsteady interaction phenomenon is simplified considerably with this approach, as proposed by (Gourlay, 2009). In essence, the unsteadiness only arises through the fact that the ship-bound coordinate systems are moving in space with respect to each other. After all, the interaction is approximated as a superposition of two pressure fields. Each of these ship-bound pressure fields is calculated as if the ship is sailing alone through a canal. The pressure fields were calculated using a linearized Bernoulli equations which neglected the time derivative of the potential. Therefore, the effect of unsteadiness is greatly simplified in the current approach.

3 EXPERIMENTAL DATA

3.1 EXPERIMENTAL PROGRAM

The SF results will be compared to a selection of experimental results obtained by Vantorre et al. (2002). They provided a summary of the ship-ship test program performed in the Towing Tank for Manoeuvres in Confined Water at FH, as well as a description of the test setup and tested parameters. The lines plans of all 4 tested ship models are given in Fig. 3 (from Vantorre et al., 2002).

A selection of experiments was made, which included only three of the 4 tested ship models. The dimensions and drafts of these ships are presented in Table *1* at model scale and full scale. The scale factor λ equals 75. Ship E (T0E)[1] and ship H (T0H) are both used as own vessel in the validation. In each test, the own vessel was fitted with a propeller and rudder and each test was executed at the model self-propulsion point. T0E is a large tanker, while T0H is a smaller tanker. T0E and ship D (C0D) are used as target vessel. No propeller or rudder was fitted to the target ship. C0D is a container ship of similar length as T0 E, but with a smaller width.

Table 1. Dimensions of ship models

	Model scale			Full scale (λ=75)		
Ship code	T0E	T0H	C0D	T0E	T0H	C0D
L_{PP} (m)	3.824	2.211	3.864	286.8	165.8	289.8
B (m)	0.624	0.296	0.536	46.80	22.20	40.25
T (m)	0.207	0.178	0.180	15.53	13.35	13.50
∇ (m^3)	0.4029	0.0989	0.2914	169 981	41 706	92 578

SF requires knowledge on the precise hull geometry. Two offset files are created for each ship (at a specific draft) containing the breadth on the waterline at every station $B(x)$ and the submerged cross section at each station $S(x)$ respectively. The geometry of the ship models is used to generate the offset files. The section area $S(x)$ and half ship width is given in Figure 2.

Both encounters and overtaking scenarios are included in the validation. Only overtaking scenarios where the own ship is being overtaken are considered, since these scenarios result in stronger interaction forces compared to the cases where the own ship overtakes a target vessel. An overview of tested parameters was provided in Table *2*.

[1] D,E,H are the ship codes used by Vantorre et al. (2002). Nowadays, FH uses the codes C0D, T0E and T0H for these ship models respectively. These codes are also used in the remainder of the paper.

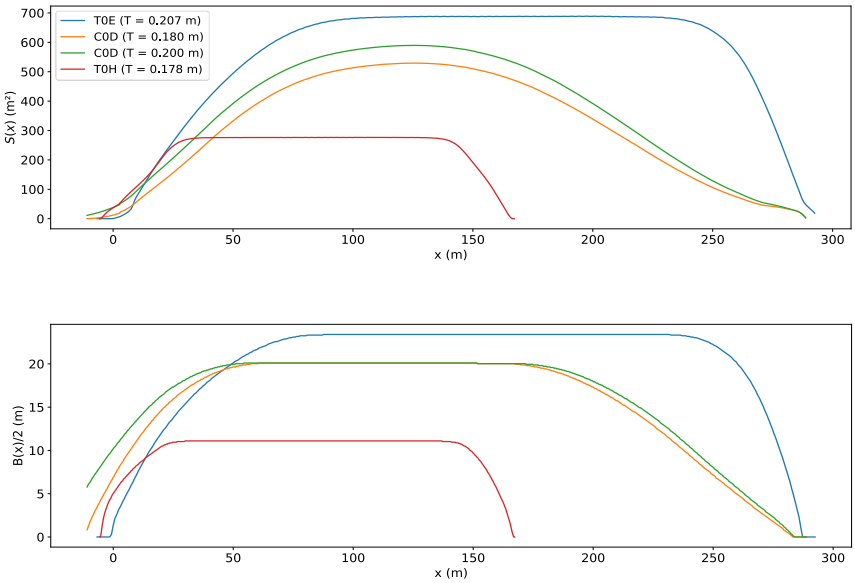

Figure 2 Submerged cross-section area at each station $S(x)$ (top figure) and half width at the waterline at each station $B(x)/2$ (bottom figure). $S(x)$ and $B(x)$ are inputted in SF. The aft perpendicular lies at x=0.

Table 2. Parameters included in the validation study (at model scale). The ship code of the own vessel is given in y_{cc}/B_{own} column.

Manoeuvre	U_{own}(m/s)	U_{tar} (m/s)	y_{cc}/B_i (-)		h (m)
			T0E	T0H	
Encounter	0.238	0.475	1.2	*2.1*	0.228
Overtaking ($U_{tar} > U_{own}$)	0.475	0.713	1.4	*3.7*	0.248
		0.950	1.9	*4.6*	0.307
			2.8	*5.6*	
				6.6	

3.2 SINKAGE MEASUREMENTS

The vertical displacements at four positions (fore/aft; port/starboard) are measured during the model tests. Measurements were only taken on the own vessel attached to the main carriage. These measurements are converted to the vertical displacements at three locations: at the fore perpendicular s_{FP}, at midships s_0 and at the aft perpendicular s_{AP}.

The measurements corresponding to an encounter and overtaking manoeuvre are shown in Figure 3 and Figure 4 respectively. Only the forces on the own vessel (T0E) are given. These are plotted against the non-dimensional stagger distance calculated as

$$\xi = \frac{x_{cc}}{\frac{1}{2}\left(L_{PP,own} + L_{PP,tar}\right)}. \tag{21}$$

In this expression, $x_{cc}$is the longitudinal distance between midship sections (Figure 1) and L_{PP} refers to the length between perpendiculars. Given the definition of x_{cc} in section 2.2, ξ is negative before the passing and positive after. During an encounter, the bows of both ships pass at ξ =-1. The sterns of both ships are aligned when $\xi = 1$. When the own ship is overtaken, ξ =-1 when the bow of the target ship passes the stern of the own ship. Conversely, ξ =1 when the stern of the target ship passes the bow of the own ship. $\xi = 0$ when the midship sections cross. All model test results are scaled to full scale. Scaling is achieved by multiplying the measured sinkage with the scale factor ($\lambda = 75$).

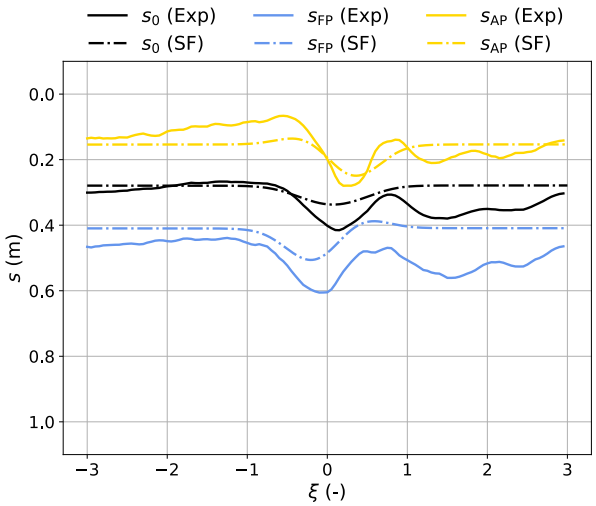

Figure 4 Comparison between sinkages calculated with SF and experimental results amidhips (s_0), at the fore perpendicular (s_{FP}) and at the aft perpendicular (s_{AP}). Encounter of T0E (own ship) and C0D (target ship), both sailing at 8 knots, Fr_h =0.305, h = 18.6 m and y_{cc} = 131 m.

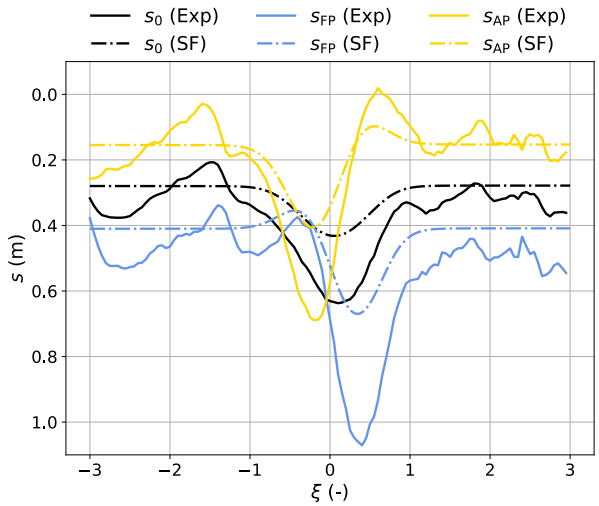

Figure 3 Comparison between sinkages calculated with)SF and experimental results amidhips (s_0), at the fore perpendicular (s_{FP}) and at the aft perpendicular (s_{AP}). T0E (own ship sailing at 8 knots, Fr_h = 0.305) is overtaken by C0D (target ship, sailing at 12 knots, Fr_h=0.457), h = 18.6 m, y_{cc} = 131 m.

In contrast with the experiments, SF calculates the sinkage of the LCF s_{LCF} and the bow-down trim angle θ_{LCF} (Eq. (*15*) and Eq. (*16*) respectively). These values were combined to calculate the sinkages at the three experimental locations:

$$s_{\mathrm{FP}} = s_{\mathrm{LCF}} + \left(\frac{1}{2}L_{\mathrm{PP,own}} + x_{\mathrm{LCF}}\right) \cdot \tan\left(\theta_{\mathrm{LCF}}\right) \tag{22}$$

$$s_{\mathrm{AP}} = s_{\mathrm{LCF}} - \left(\frac{1}{2}L_{\mathrm{PP,own}} - x_{\mathrm{LCF}}\right) \cdot \tan\left(\theta_{\mathrm{LCF}}\right) \tag{23}$$

$$s_0 = s_{\mathrm{LCF}} + x_{\mathrm{LCF}} \cdot \tan\left(\theta_{\mathrm{LCF}}\right) \tag{24}$$

Both s_{LCF} and θ_{LCF} consist of a steady sinkage value caused by the own ship's movement through the water, and an unsteady contribution due to the passing ship.

4 COMPARISON OF SLENDERFLOW WITH MODEL TESTS

4.1 METHODOLOGY

Experimentally obtained trendlines are compared to SF trendlines in Figure 3 and Figure 4. Three sinkages are investigated: s_0, s_{FP} and s_{AP}. These sinkages consists of two contributions: a steady sinkage, corresponding to a single ship sailing through a canal and an unsteady sinkage, corresponding to the passing target ship.

The performance of SF when calculating steady sinkages was discussed before (Gourlay, 2014). SF tended to underestimate the average sinkage and overestimate the bow-down trim when compared to model tests, primarily due to the linearization of the free surface (Gourlay, 2008). The overestimation of the bow-down trim corresponds to under-estimating $s_{\mathrm{AP}}$and over-estimating s_{FP}. However, this observation was not confirmed by Figure 3, since the propulsion and flow separation near the stern in the experiments decreases the bow-down trim.

In general, SF succeeds to predict some qualitative trends present in the experimental results. Firstly, Figure 3 and Figure 4 show that the sinkage near the aft s_{AP} is smaller than the sinkage at the bow s_{FP}, both in the experiments and SF. This bow-

down trim is typical for tankers, which have a large part of their volume in the fore part of the ship (Figure 2). Container ships usually show a bow-up moment (Eloot et al., 2011). Secondly, the number and location of peaks in the sinkage trend is predicted reasonably well by SF. The midship sinkage s_0 predicts a single peak near ξ=0. The sinkages at the bow and stern s_{FP} and s_{AP} predict a smaller peak and a larger peak. Lastly, both the experiments and SF show larger interaction peak magnitudes during an overtaking manoeuvre than during the encounter.

On the other hand, differences are observed as well. The main differences are the peak magnitudes and the fact that the experimental measurements show additional oscillations, which are related to the interaction of the Kelvin wave patterns.

Given these differences between the theoretical and experimental results, the validation will be limited to a comparison of peak magnitudes of the unsteady sinkage. After all, this maximum peak magnitude is the most important part of the sinkage analysis. The unsteady part is obtained by deducting the steady sinkage from the total sinkage trend line. This is straightforward for the SF result. For the experimental results, a steady state value was calculated by computing the average sinkage over the range $\xi = -3$ and $\xi = -2.5$. The maximum value of the unsteady trend line is determined and compared in the next sections.

4.2 INFLUENCE OF SEPARATION

The experimental program tested a range of lateral separations. However, the focus of the experimental test program was on close ship passings, so the maximal full-scale y_{cc} equalled 131 m. Theoretically, SF cannot be used to replicate these tests, since the target vessel is not entirely in the far field of the own vessel. Since the separations were larger than the own ship's breadth, it was assumed that the theory is approximately valid.

Figure 5 compares the experimental peak magnitudes with the unsteady SF peaks. Overall, it is clear that both for encountering and overtaking, the peak magnitudes decrease as y_{cc} increases. This decrease is more pronounced for the experimental peaks, so the comparison between experiment and software improves as the separation increases. In general however, the SF peak is an underestimation of the actual peak. This suggest that the target ship's water level depression amidships is underestimated in SF, which could be due to the linearisation of the hull and free surface boundary condition.

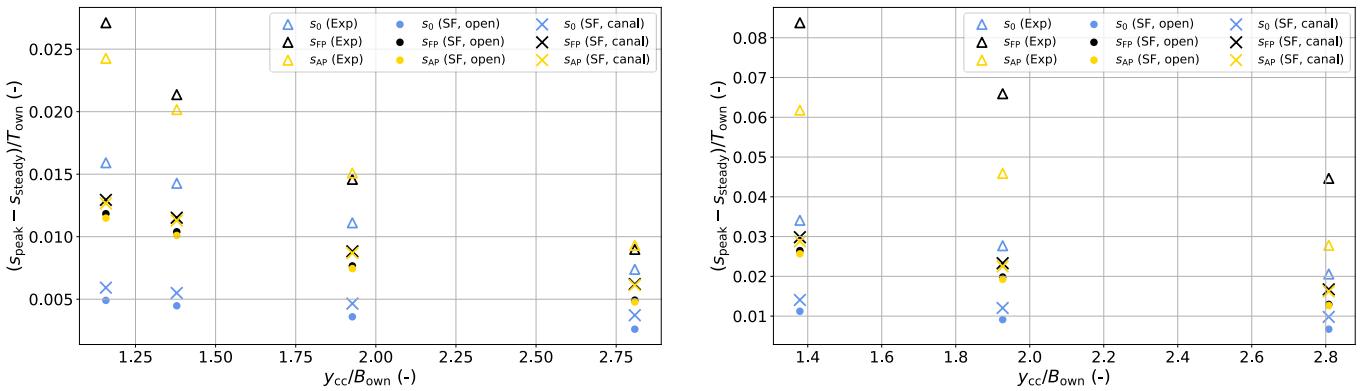

Figure 5 Influence of separation on the interaction peak size. Left: Large tanker T0E (own ship) and large container ship C0D (target ship) encounter at equal speed (8 knots) in a water depth of 18.6 m. Right: Large container ship C0D (target ship), sailing 12 knots, overtakes large tanker T0E (own ship), sailing 8 knots, in a water depth of 18.6 m. The legend indicates whether the pressure field of the target ship was calculated with an 'open' or 'canal' bathymetry.

Additionally, it was investigated whether the target ship's pressure field should be computed using an open water or canal bathymetry. Gourlay (2009) stated that for ships in a canal with reasonable width, the single ship flows as calculated by SF can be linearly superimposed to describe the total flow around two ships travelling on parallel courses. However, a single ship flow, corresponding to a ship in a canal, assumes that the ship sails along the centre line. In Figure 6 both ships were resolved in a canal bathymetry. Clearly, the pressure field due to the container ship is not physically possible near the wall. However, since the canal geometry results in a larger pressure close to this container ship, the interaction peak magnitudes increase slightly over the entire range of y_{cc}, improving the comparison between experiment and SF.

It is concluded that, even though using a canal bathymetry for the target ship results in a non-physical pressure field, the proposed superposition of single canal flows is useful as long as the own ship is not sailing through this zone with incorrect pressure prediction. This is the case when the canal is wide enough.

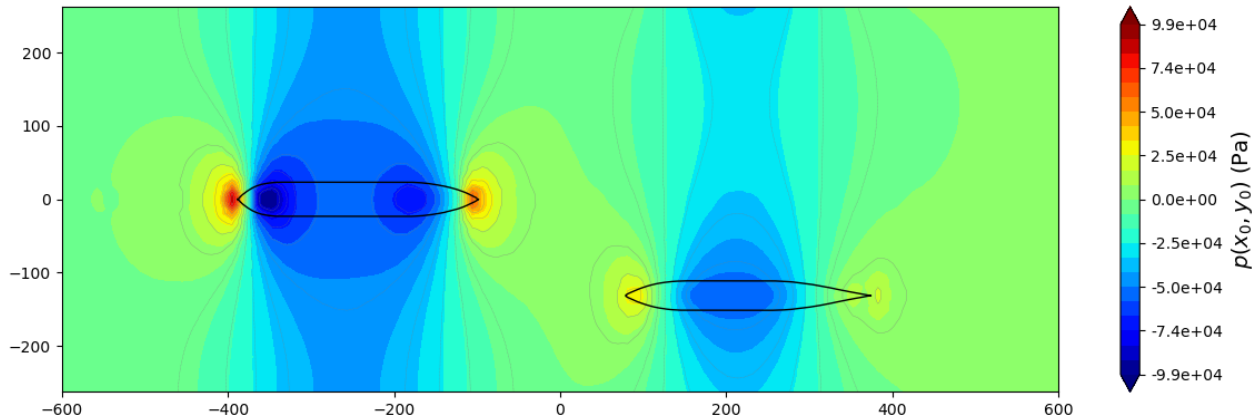

Figure 6 Pressure field after an encounter manoeuvre. Large tanker T0E (sailing to the left) encountered the large container ship C0D (sailing to the right) at equal velocities of 8 knots in a canal of 525 m (= $\lambda \cdot w$). The pressure fields are calculated assuming a canal bathymetry, assuming each ship lies on the centreline of the respective canal.

4.3 INFLUENCE OF UKC

For 20% UKC (calculated as $(h - T_{\text{own}})/T_{\text{own}}$) and 50% UKC of the own ship, similar observations are made as before: the SF interaction peaks underpredict the actual peak sizes, but as the UKC increases the peak magnitudes decrease, improving the prediction. The sinkage at the bow s_{FP} is also larger than the peak sinkage at the stern s_{AP}.

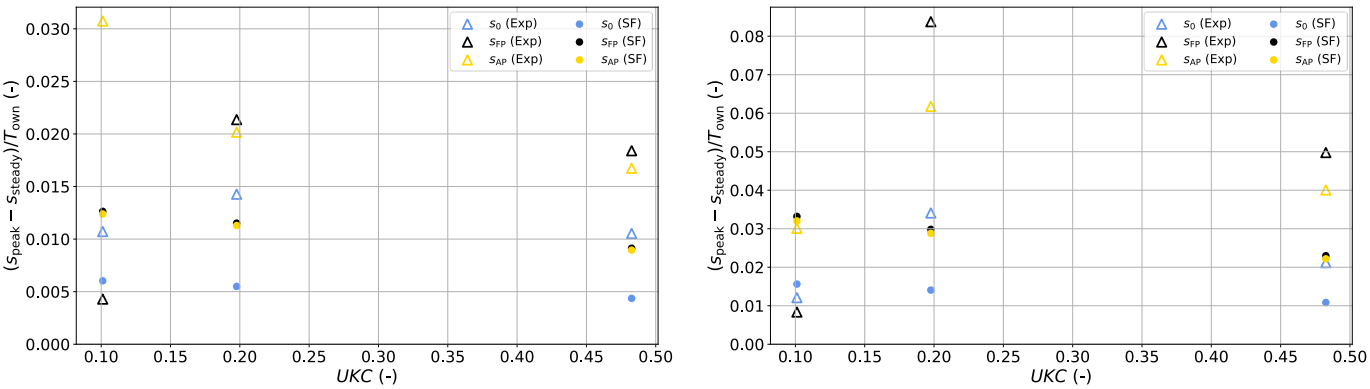

Figure 7 Influence of the UKC (of the own ship) on the interaction peak size. Left: Large tanker T0E (own ship) and large container ship C0D (target ship) encounter at equal speed (8 knots) with a lateral separation y_{cc} = 64.5 m. Right: Large container ship C0D (target ship), sailing 12 knots, overtakes large tanker T0E (own ship), sailing 8 knots, with a lateral separation y_{cc} = 64.5 m.

At a small UKC of 10%, the experimental sinkages deviate from the general pattern. At this UKC, the water flow beneath the keel is blocked, reducing the sinkage at the bow, while the sinkage aft is influenced by low pressure zone created by the propeller action (Eloot et al., 2011). Additionally, the trim of the own ship, and thus the sinkages s_{FP} and s_{AP}, depends simultaneously on the pressure near the forward and aft shoulders. These pressures depend in turn on the longitudinal volume and waterplane area of both ships sailing in shallow water (Gourlay, 2014). Further research is required to understand the combined effect of these observations on the experimentally determined interaction peaks.

In contrast to the experiments, the sinkages calculated with SF increase steadily with decreasing UKC. The UKC does not appear explicitly in the calculation of the unsteady vertical force, rather through the water depth h and the ship section distribution $S(x)$. Consequently, differences are expected between theoretical results and model test results at very small UKC.

4.4 INFLUENCE OF VELOCITY

Both the velocity of the own and target ship determine to great extent the interaction forces. In Figure 8 the interaction peaks obtained with SF and experiments during encounter manoeuvres at different speeds are compared. The relative speed is calculated as U_{rel} = U_{tar}-U_{own}, where $U_{\mathrm{own}}$is a negative value for the encounter manoeuvre. Three speed combinations are considered (U_{own} -U_{tar}): 4 knots – 8 knots; 8 knots – 8 knots; 8 knots – 12 knots.
The experimental peaks increase with increasing U_{rel}, even when the target ship speed remains constant. The theoretical peaks increase at well, but the SF peaks at 12 knots and 16 knots are identical. Clearly, in Eq. (*17*) and Eq. (20), the unsteady vertical force only depends on the speed of the passing vessel. This implies that the superposition of pressure fields as investigated in this paper was an oversimplification.

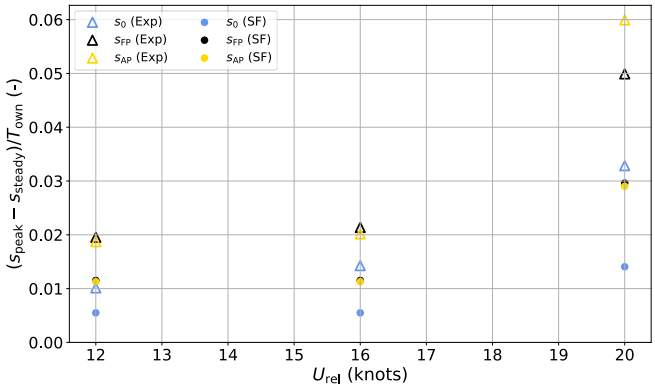

Figure 8 Influence of relative velocity on the interaction peak size. Large tanker T0E (own ship) and large container ship C0D (target ship) encounter in water of depth h = 18.6 m with a lateral separation y_{cc} = 64.5 m.

4.5 INFLUENCE OF SHIP SHAPE

The results presented so far were limited to the interaction between a large tanker (T0E, own ship) and container ship (C0D, target ship) of similar length. However, the ship shapes have an important effect on the pressure fields. When calculating the unsteady interaction, the hull shape of the target ship appears in Eq. (*17*) and Eq. (20). The length and waterplane of the own vessel influence the sinkage values via Eq. (*22*) through (*24*).

To verify the effect of the hull shape, both the interaction between a smaller tanker (T0H) and a large tanker (T0E) and between a smaller tanker (T0H) and large container ship (C0D) was investigated (Figure 9). The smaller tanker is the own ship. The influence of y_{cc} is very comparable to the result of Figure 5. By comparing the results of Figure 9 with those of Figure 5, the effect of the own shape ship is assessed. The interaction between the small tanker and the container ship shows smaller s_{FP} and s_{AP} peaks (experimentally) than the interaction between the large tanker and the container ship. The shorter length of T0H seems an important reason. SF on the other hand predicts larger s_{FP} and s_{AP} peaks for the interaction between the small tanker and container ship as compared to the interaction between the large tanker and container ship. Further examination into this issue is required.

Figure 9 also includes the interaction peaks corresponding to the interaction between a smaller tanker and a large tanker. The large container ship is wider and has a longer parallel midship than the large container ship (Figure 2). When changing the target ship, all peaks (experimental and theoretical) increase. The longer parallel midship causes a greater sinkage of the water level compared to the container ship (Eloot et al., 2011), which increases the interaction sinkage. The increase of interactions peak when changing the container ship with a large tanker is relatively larger for the experiments, which again indicates that the pressure field predicted by SF is underestimated because the free-surface and hull boundary conditions are linearized.

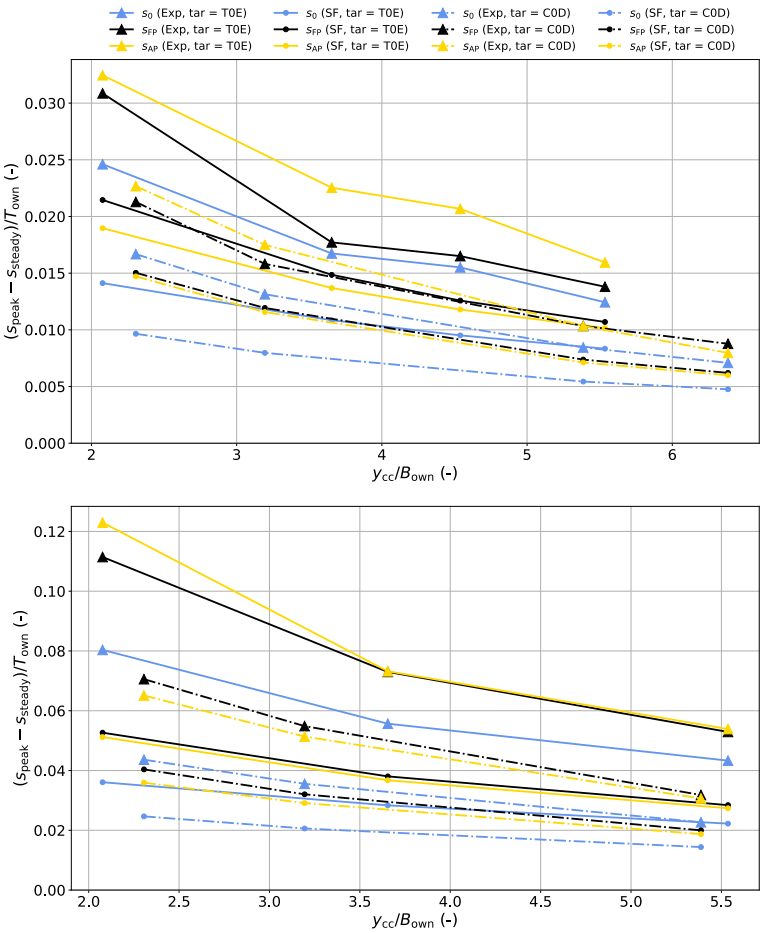

Figure 9 Influence of the hull shape and lateral separation on the interaction peak size. Top figure: Encounter of small tanker T0H (own ship) with large tanker T0E (target ship) (solid line) or large container ship C0D (target ship) (dashed line). Both ships are sailing at 8 knots in a water depth of 18.6 m. Bottom figure: Small tanker T0H (own ship) is overtaken by a large tanker T0E (target ship) (solid line) or large container ship C0D (target ship) (dashed line). T0H is sailing at 8 knots, while the target ships is sailing at 12 knots at h = 18.6 m.

4.6 INFLUENCE OF PROBLEM FORMULATION

All solutions implemented in SF were derived starting from the partial differential equation proposed by Tuck (1966). These solutions have a singularity as Fr_h approaches 1, which corresponds to a transition from subcritical to trans-critical flow. Gourlay (2000) attributed the failing of the basic shallow-water theory close to Fr_h = 1 to the neglect of dispersive effects. By modifying the shallow-water theory to include dispersive effects in open water, the sinkage at transcritical Froude numbers could be calculated.

However, ships such as bulk carriers displace water in confined waters, which has to return along the hull. At some combinations of ship speed and canal confinement, the water can no longer be evacuated along the ship's hull, resulting in a pile-up in front of the vessel. This speed is also known as the first critical speed and it is shown by Delefortrie et al. (2024) that this critical speed depends on the blockage m of the canal:

$$Fr_{h,\mathrm{crit1}} = \left(2\sin\left[\frac{\arcsin(1-m)}{3}\right]\right)^{3/2}. \tag{25}$$

Here is m the blockage factor, calculated as A_M/Ω. A_M is the surface area of the midship section and Ω is the total cross-section area of the canal. This expression is commonly attributed to Schijf (1949), although he only presented a formula for the critical blockage without showing expressions for the critical speed (Delefortrie et al., 2024).

In case of a target container ship (C0D) moving in the towing tank, A_{M} = 589.59 m^2, Ω=9765 m^2, m =0.0604 and the critical water depth dependent Froude number equals 0.705. Comparing this to a critical Fr_h=1 in open water, it could be concluded that the shallow-water continuity equation Eq. (*1*) overestimates the critical velocity in case of confined channels.

To test the influence of the critical speed, the shallow-water equation Eq. (*1*) was, without mathematical derivation, re-written to

$$\left(Fr_{h,\mathrm{crit1}}^2 - Fr_h^2\right)\frac{\partial^2\phi}{\partial x^2} + \frac{\partial^2\phi}{\partial y^2} = 0. \tag{26}$$

Since $Fr_{h,\mathrm{crit1}}$ is not dependent on x or y, re-deriving Eq. (*17*) in a canal of constant width results in

$$p_{\mathrm{tar}}(x_{\mathrm{own}}, y_{\mathrm{own}}, t) = -\frac{\rho U_{\mathrm{tar}}^2}{4\pi h\sqrt{Fr_{h,\mathrm{crit1}}^2 - Fr_{h,\mathrm{tar}}^2}}\int_{-\infty}^{\infty} i\,K(k)\overline{S'_{\mathrm{tar}}}(k)\,e^{-\sqrt{Fr_{h,\mathrm{crit1}}^2 - Fr_{h,\mathrm{tar}}^2}|k||y_{\mathrm{cc}}-y_{\mathrm{own}}|}e^{-ik(-x_{\mathrm{own}}+x_{\mathrm{cc}}(t))}dk, \tag{27}$$

$$K(k) = \coth\left(\left(\frac{w}{2}\right)\sqrt{Fr_{h,\mathrm{crit1}}^2 - Fr_{h,\mathrm{tar}}^2}\,k\right). \tag{28}$$

The interaction peaks during an encounter manoeuvre of the large tanker T0E and large container ship C0D, as function of the lateral separation, are shown in Figure 10. The reformulated SF solution improves the peak magnitudes at smaller separations. However, the reformulated SF solution decreases less with y_{cc}, resulting in an overestimation of the interaction peaks at larger separation distances. It should be kept in mind that Eq. (1) was developed for a single ship in open water. The current correction only addressed the confinement of the canal. However, the unsteady effect, due to the presence of another ship, is still simplified according to this correction. A new slender-body shallow water equation should be derived, which considers the (moving) target ship.

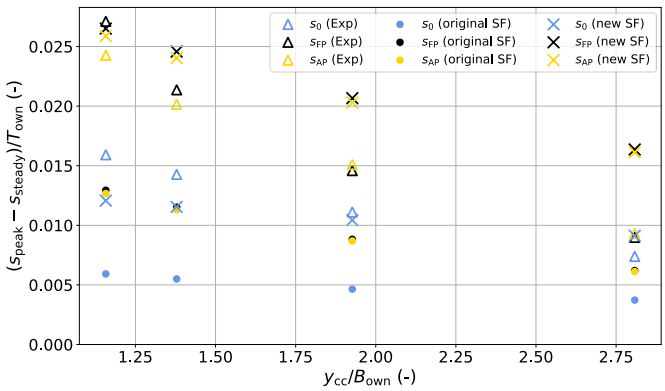

Figure 10 Influence of the lateral separation on the interaction peak size. Tanker E and container ship D encounter at equal speed (8 knots) in a water depth of 18.6 m. Three results are compared: interaction peak sizes of the experiments, interaction peak sizes solved with the original boundary value problem (original SF) and interaction peak sizes solved with the reformulated boundary value problem (new SF).

5 CONCLUSIONS

Significant changes in trim and sinkage can occur when two ships pass in a narrow canal, increasing the risk of grounding. Despite this risk and the high frequency of ship interactions in port areas, limited experimental data exists on vertical ship motions during such interactions. A method was presented by Gourlay (2009) involving the superposition of ship-bound pressure fields to estimate these effects. However, due to lack of experimental data, the accuracy of this approach remained uncertain.

This paper implements Gourlay's method via the *SlenderFlow* (SF) computer code, which uses Fourier transforms to calculate the ship-bound pressure field. An unsteady sinkage could be calculated via the pressure field attached to the target ship and was validated against experimental data.

SF accurately predicts qualitative characteristics of the trend lines, such as the location and number of peaks. Additionally, overtaking manoeuvres induce larger interaction effects than encounter manoeuvres both in the experiments and SF calculations. Also, the distribution of volume in the ship is included correctly.

The qualitative effect of separation y_{cc}, UKC and relative speed is predicted correctly in some cases. For instance, reducing the lateral separation increases sinkages both in the experiments and calculations. On the other hand, SF predicts monotonically increasing sinkages with decreasing UKC or increasing relative velocity, while this is contradicted by the experimental results.

SF systematically underestimates unsteady peak sinkages. Its predictions improve when interaction forces are low, such as at lower speeds, larger separation distances, or greater under-keel clearance (UKC).The underprediction of the interaction sinkages by SF is both related to the simplifications of the theoretical model and the superposition assumption. The main simplifications used in the theory include: ignoring self-propulsion effects, neglecting boundary layer thickening (especially during model tests), linearization of the hull boundary condition and linearization of the free surface condition (Gourlay, 2014). Since these limitations influence the pressure field of the target vessel, the sinkage due to interaction will also be affected by these limitations. For instance, linearization of the hull boundary condition and free-surface result in an underprediction of the low pressure zone amidship of the target vessel, especially for bulky ships such as tankers. This implies that the drawdown force on the own ship due to the passage of a target ship is larger in the experiments, resulting in larger experimental sinkages. Propulsion effects and boundary layer thickening decrease the pressure near the stern during the experiment, further influencing the pressure field.

It was also shown that the superposition method is an oversimplification. After all, the sinkage of the own vessel, due to the passing of a target ship, increases the submerged volume of the own ship. This in turn will influence the own ship's pressure field, resulting in larger experimental sinkages. This effect depends on different parameters such as the separation and ship velocities. Additionally, a target ship is an obstruction for the water flow around the own ship, which will in turn influence the pressure field of the own ship. Lastly, the proposed superposition method ignores unsteady effects, which also contributes to the difference between experimental and numerical results.

Additional investigations into the use of SF for assessing ship interactions are required. Firstly, the comparison in this paper was between the theoretical method and scaled model test results. However, at model scale (low Reynolds number), the boundary layer is thick compared to the ship's dimensions and more likely to separate near the stern, which may markedly change the hull pressure near the stern (Gourlay, 2008). At full scale the boundary layer is thinner and exerts less influence on the hull. Therefore, it is expected that the flow characteristics at full scale better resemble the potential flow assumption used in the theoretical method. Comparison with full-scale results could therefore prove useful.

Secondly, SF results under-predicted the experimental results. It could be investigated whether a correction factor can be found, depending on relevant parameters, to enhance the prediction by SF. However, reformulating the boundary value problem showed an improvement for smaller separations, so it should also be investigated under what conditions the mathematical basis remains valid. Also the lack of unsteadiness in the current method deserves further attention.

Lastly, a superposition of two single flows in a specific bathymetry was used in this paper. It was illustrated that this approach leads to unphysical pressure fields, since it is assumed that a ship sails along the canal's centre line when calculating the pressure field. A cross-flow should be included in the theoretical model to extend the approach to ships sailing off-centre.

6 REFERENCES

Dand, I.W., 1981. Some measurements of interaction between ship models passing on parallel courses, in: National Maritime Institute. National Maritime Inst., Feltham, pp. 1–92.

Delefortrie, G., Verwilligen, J., Vantorre, M., Lataire, E., 2024. Exact and Approximated Solutions to the Critical Ship Speeds in Canals, in: Schoonhees, J.S. (Ed.), Proceedings of the 35th PIANC World Congress 2024. PIANC, Capetown, South Africa, pp. 649–654.

Eloot, K., Vantorre, M., Verwilligen, J., Prins, H., Hasselaar, T.W.F., Mesuere, M., 2011. Squat during ship-to-ship interactions in shallow water, in: Pettersen, B., Berg, T.E., Eloot, K, Vantorre, M (Eds.), Proceedings of the 2nd International Conference on Ship Manoeuvring in Shallow and Confined Water (MASHCON), 18 - 20 May 2011, Trondheim, Norway. R.I.N.A, pp. 117–126.

Gourlay, T., 2014. ShallowFlow: A Program to Model Ship Hydrodynamics in Shallow Water, in: OMAE 2014. San Francisco, USA, p. V01AT01A018.
Gourlay, T., 2009. Sinkage and trim of two ships passing each other on parallel courses. Ocean Eng. 36, 1119–1127. https://doi.org/10.1016/j.oceaneng.2009.06.003
Gourlay, T., 2008. Slender-body methods for predicting ship squat. Ocean Eng. 35, 191–200. https://doi.org/10.1016/j.oceaneng.2007.09.001
Gourlay, T., 2000. Mathematical and Computational Techniques for Predicting the Squat of Ships. The University of Adelaide, Adelaide, Australia.
Ha, J.H., 2018. Measurement and Simulation of Ship Under-Keel Clearance in Port Approach Channels. PhD Thesis. Centre for Marine Science and Technology, Curtin University.
Schijf, J.B., 1949. Protection of Embankments and Bed in Inland and Maritime Waters, and in Overflow or Weirs, in: XVII International Navigation Congress, Lisbon, Section I. pp. 61–78.
Tuck, E.O., 1967. Sinkage and trim in shallow water of finite width. Schiffstechnik 73, 92–94.
Tuck, E.O., 1966. Shallow-Water Flows Past Slender Bodies. J. Fluid Mech. 26, 81–95.
Vantorre, M., Verzhbitskaya, E., Laforce, E., 2002. Model test based formulations of ship-ship interaction forces. Sh. Technol. Res. 49, 124–141.
Yeung, R.W., 1978. On the interactions of slender ships in shallow water. J. Fluid Mech. 85, 143–159.
Zhou, J., Ren, J., Bai, W., 2023. Survey on hydrodynamic analysis of ship–ship interaction during the past decade. Ocean Eng. 278, 114361. https://doi.org/10.1016/J.OCEANENG.2023.114361

7 AUTHORS BIOGRAPHY

Andreas Verbeke, mechanical engineer, is a PhD researcher at the Ships and Marine Technology Division at Ghent University, Belgium. His research focuses on the development of an improved real-time model to calculate hydrodynamic ship-to-ship interaction in 6 degrees of freedom. The model is to be implemented in the ship simulators at Flanders Hydraulics.

Tim Gourlay is a mathematician specializing in ship hydrodynamics. Through his company, Perth Hydro, Tim undertakes consulting work in ship manoeuvring, seakeeping, under-keel clearance and dynamic mooring.

Guillaume Delefortrie: naval architect (MSc, Ghent University 2001, PhD, Ghent University, 2007), associate professor at the Ships and Marine Technology Division of Ghent University, lecturer in charge of courses in marine hydrodynamics. Experienced in EFD based research, with focus point on ship manoeuvring in shallow and confined water. He has been a member of the 27*th*-29*th* ITTC Manoeuvring Committee. Member of the organization and scientific committees of MASHCON conferences since their creation (2009).

Maxim Candries is a postdoctoral researcher at the Ships and Marine Technology Division of Ghent University.

Wim Van Hoydonck obtained his PhD at Delft University of Technology and is nautical researcher at Flanders Hydraulics. His research interests include the application of numerical methods to ship hydrodynamics and aerodynamics.

Evert Lataire is head of the Ships and Marine Technology Division at Ghent University. His research focuses on the behaviour of ships in shallow and confined waters and is often based on model tests. In recent years his division diversified to other floating devices subject to waves and current such as aquaculture in open sea and floating PV-panels in an offshore environment. Member of the organization and scientific committees of all MASHCON conferences .

A SYSTEMATIC STUDY ON ROPES MODELLING OF THE INTERAC- TION FORCES BETWEEN A SAILING SHIP AND A SHIP MOORED AT A QUAY WALL WITH A COMPLEX GEOMETRY

Sara Sanz Sáenz, IMDC, Belgium

Wojciech Misiag, IMDC, Belgium

A SYSTEMATIC STUDY ON ROPES MODELLING OF THE INTERACTION FORCES BETWEEN A SAILING SHIP AND A SHIP MOORED AT A QUAY WALL WITH A COMPLEX GEOMETRY

SARA SANZ SÁENZ, IMDC, BELGIUM
WOJCIECH MISIAG, IMDC, BELGIUM

SUMMARY

This study aims to present the feasibility to model complex quay wall structures in ROPES, to obtain passing ship forces on a moored ship to be subsequently used in mooring analysis. As a case study, a composite quay wall is modelled. The quay consist of a submerged sheet pile, slightly deviating from vertical position, and whirl chambers constructed atop of the sheet pile. The whirl chambers are sloped spaces, subdivided by vertical walls placed along the berth line. The whirl chambers block the longitudinal flow, while they allow for emptying and filling the chambers by flows perpendicular to the berth line.

The quay model is built following a step-wise approach to control the results of modelling, to correct modelling inaccuracies and to gain confidence in the final results. Different test results and conclusions are presented, as well as unexpected behavior of ROPES as found for some parameters.

NOMENCLATURE

LOA	Length overall (m)
B	Beam (m)
d	Draught (m)
TAW	Reference level for vertical coordinates (like a bottom level, a water level)

1 INTRODUCTION

During the assessment of the safety of a moored ship it was necessary to determine the forces caused by a ship sailing in the port basin alongside of the moored ship. The purpose of the assessment was to define the limiting sailing ship speeds. The limiting sailing ship speeds were obtained by analyzing the responses of the moored ships that were to be obtained after feeding the passing ship forces into a dynamic mooring analysis software. The mooring analysis were to be performed with dynamic module of OPTIMOOR package, which is a rather simple version of DMA package, but it allows for rapid analysis of multiple cases. OPTIMOOR model has simple method of calculating passing ship forces, but only for very simple open water case and vertical wall case. More complex berth configurations put a question whether OPTIMOOR built-in models correctly approximate the passing ship forces.

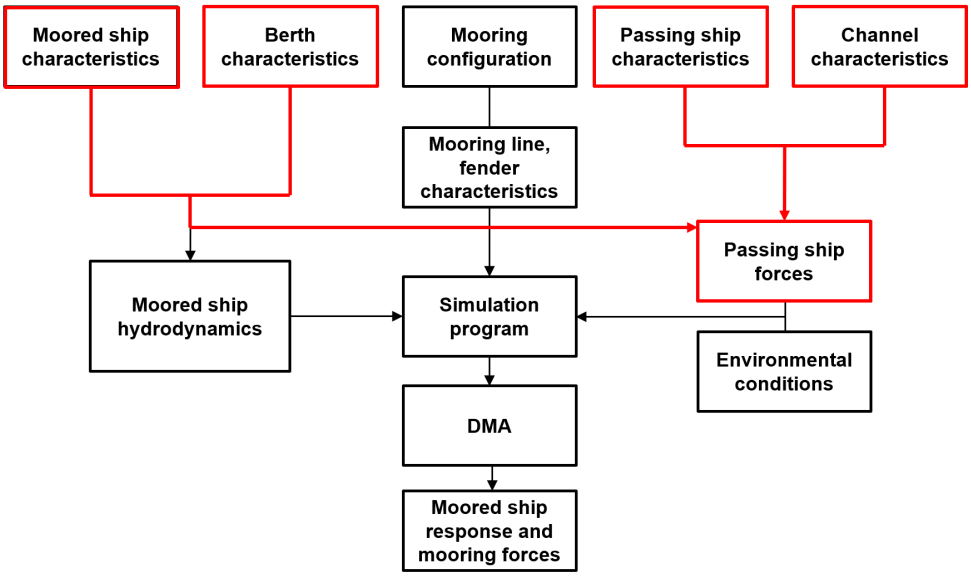

Figure 1. Project (responses of moored ship to passing ship forces) structure

The geometry of the berth is unusual, because it consist of a composite quay wall: a submerged sheet pile, slightly deviating from vertical position, and whirl chambers constructed atop of the sheet pile. The whirl chambers are sloped spaces, subdivided by vertical walls placed along the berth line. The whirl chambers block the longitudinal flow, while they allow for emptying and filling the chambers by flows perpendicular to the berth line. The cross section is presented in Figure 2.

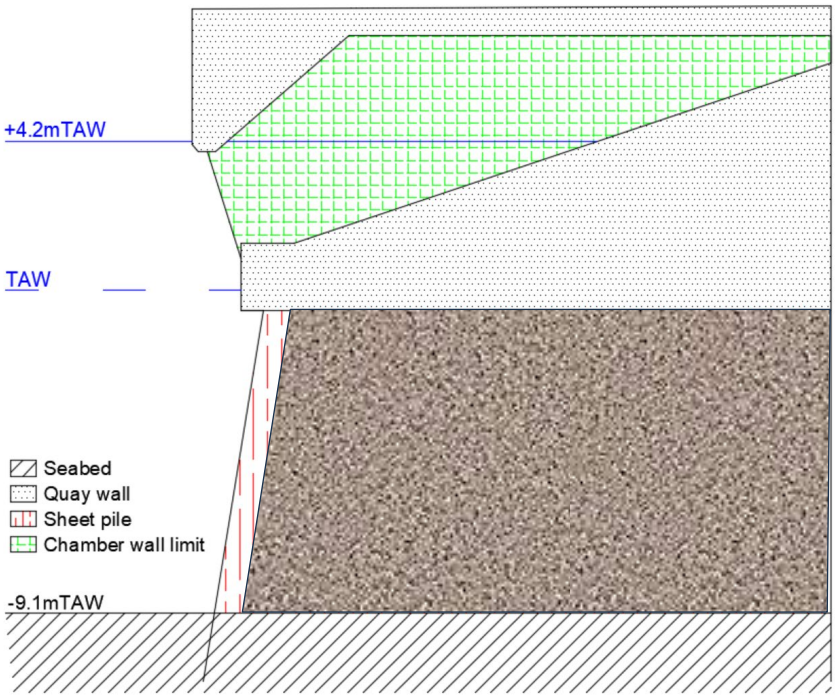

Figure 2. Cross section of the quay wall

ROPES package was developed to calculate interaction forces between sailing ships and between a sailing and moored ships. ROPES package is typically used for relatively simple geometries of the berths. However, it was also used for more complex situations, like modelling of groynes, submerged quays, passages between bridge pillars, berth pockets with conical connections to the basin slopes. This is why ROPES is also selected for modelling of this composite quay wall.

Different approaches can be followed to derive the passing ship forces on the moored vessel for this specific quay wall:

- CFD approach
- Increasing the distance between the moored ship and the wall, in the simple (vertical) quay wall model in ROPES
- More complex panel method in ROPES

The CFD approach is resource-consuming and is not suitable for providing data for mooring analysis involving larger number of sailing/passing ship combinations, with varying passing distance and passing speed, and when the mooring analysis is to be performed with OPTIMOOR package.
The increase of distance between the ship side and the quay wall is a heuristic approach, the increased volume between the ship side and the wall is to model the effect of the whirl chamber volume. The amount of the necessary distance increase is unknown and it is unknown whether the obtained forces would be a good approximation of the situation.
The last approach was chosen for the task. The panel models of the berth are developed sequentially, increasing the complexity of these models: a simple wall, a wall with slopes but without lateral baffles, and finally a wall with slopes and added lateral baffles. The development of the described final model is done stepwise to control the results of modelling, to correct modelling inaccuracies and to gain confidence in the final results. As a result, the final model captures all important components of the quay wall with whirl chambers as described.

2 OBJECTIVES

The objectives of the study include first the explanation of the modelling approach of the passing ship forces for a case of complex berth geometry consisting of a composite quay wall with a submerged sheet pile and whirl chambers. Then, the presentation of the sensitivity analysis of passing ship forces calculated for the different studied berth geometry models and panel sizes. Finally, the description of the quality check issues that appeared during the study for this complex berth modelling.

3 METHODOLOGY

3.1 PASSING SHIP FORCES MODEL ROPES

Passing ship forces exerted on the moored ship are obtained with the Software ROPES, developed by PMH (Pinkster Marine Hydraulics) for the prediction of ship-ship 6-degrees of freedom interaction forces in (shallow) water. The resulting time series of forces and moments can later be used in a dynamic mooring model.

Ships have significantly increased in size and number over the last decades. Ports and waterways are accommodating these ships and at the same time new terminals are designed in the existing infrastructure. In restricted water, the moored vessels can be strongly affected by hydrodynamic forces induced by passing ships. The Joint Industry Project (JIP) ROPES project was initiated to investigate these effects, to develop a numerical model for predicting these loads and to validate this model.

To this end, systematic scale model tests as well as extensive full-scale measurements were conducted. The research was conducted as a joint industry project (JIP) with the support of port authorities, terminal operators, vessel operators, engineering companies, suppliers of mooring equipment and research institutes, mainly led by MARIN, DELTARES, SVASEK and PMH (van den Boom et al., 2014). The detailed description of the ROPES software (equations, applications, constrains on the use) is given in PIANC publication (J.A. Pinkster, H.J.M. Pinkster, 2014), in IOP (J.A. Pinkster, 2004) and in SNAME paper (J.A. Pinkster, 2009).

The effect of passing ships is complicated to analyze as it involves complicated physics, as defined by Talstra and Bliek (2014), which include the following parameters:

- 3-D geometry of the port

- Bathymetry of the waterway
- Displacements and draughts of involved vessels
- Passing distance, and sailing ship trajectory wrt moored ship
- Passing speed

Note that in the ROPES model, the effect of passing vessel speed variations on the passing ship forces is accounted for during post-processing, by quadratic scaling of the forces and re-scaling of time points labelling these forces.

The ROPES computational tool assumes that the pressures originating from the passing vessel can be described by double body 3-D potential theory, so neglecting free surface effects, vorticity of fluid flow and viscous effects. The obtained results proved that ROPES compute the passing forces exerted on the moored ship accurately. Pinkster (J.A. Pinkster, M.N. Ruijter, 2004, J.A. Pinkster, 2009, J.A. Pinkster, 2004) developed two different methods to calculate passing ship forces – without and with accounting for free surface effects (the first is so called double body flow, while the second combines the first one and the diffraction analysis program). For relatively slowly ships sailing in a channel, when the moored ship is placed along the channel side, the results obtained separately by these two methods are practically the same, so the ROPES system implementing the double body flow model is judged as suitable one for the presented analysis. The second model (coupled double body and diffraction analysis) is used when the energy transfer via surface waves is important (channel-attached port basins or other channels where the soliton propagation is to be accounted for).

Vessels navigating in restricted waters create a pressure wave which is observed as a water draw down. When sailing in a shallow and narrows waterways, this effect can be relevant. The water level raises ahead of the vessel and the flow accelerates alongside the hull to fill up behind the vessel. When there is a ship moored in the waterway, this water dray down can create resonant horizontal motions and large loads in the mooring lines. Besides, this increase in motions may also imply a stop in cargo handing operations, such as using container cranes, loading arms for oil and LNG and automated dry bulk excavators that normally allow only limited horizontal vessel motions.

3.2 MODELING OF PASSING SHIP FORCES IN COMPLEX BERTH SITUATION

ROPES is considered adequate for this study for the following reasons:

- The critical aspect of the studied berth is a potential problem, accelerated flows, which makes it feasible to be modelled with the panel method.
- The berth is located along a channel side and it is therefore not required to use the coupling with a diffraction model like XBEACH, DIFFRAC or similar (cf. discussion above).

The channel (port basin) is modelled along a sufficient length in order to exclude the effect of the channel ends on the passing ship forces. The channel panel model includes both channel sides modelled with panels, while the channel bottom is considered to be a horizontal plane without panels to model it. The berth area model differs from the channel side model, and the berth area is modelled separately to capture the complex berth geometry. The more complex berth model is developed near the moored ship, a simpler model is used further from the berth. It is assessed that the details of the complex whirl chambers located far from the moored ship will have negligible effect on the flow near the moored ship and on the sailing ship.

The quay wall consist of an inclined sheet pile which continues up to the whirl chambers section. The final model of the quay geometry has been built in several steps, from an almost vertical wall, through a two slopes model, till the model with two slopes and the chamber walls blocking the longitudinal flow. This was done to control the modelling results by monitoring the trends in the results.
The whirl chambers are modelled on the quay segment only slightly longer than the length of the moored vessel (see Figure 10), considering that the flow acceleration outside of the berth is not affecting the results. The sizes of the panels was also decreased for the quay part with whirl chambers, comparing to the panels on the channel side outside of the berthing area.

For the quay and channel side models we used squared panels, as much as possible, to avoid the numerical problems related to high aspect ratios of rectangular panel sides; where it was needed we used triangular panels. The panel models of the vessel hulls were adopted from ROPES library of ships, and they were originally developed by ROPES authors (prof. Pinkster).

The results between the simple wall model and the whirl chambers model are expected to be similar in patterns of forces, while the differences are expected in peak forces. The lateral baffles of the whirl chambers are expected to block the longitudinal flow, so the longitudinal forces would be similar in cases of the wall-only model and whirl chambers model, while some flows may occur in the lateral direction, thus changing slightly the lateral and the yaw forces. It is so, because the volume of the whirl chambers is relatively small comparing to the volume of the whole water column along the ship between the ship side and the berth wall.

4 DATA

Figure 3 shows the geometry of the channel, fairway and berth as implemented in this case study. One side of the channel (marked black) is sloped, and the banks have two different slopes, and part of it is at angle to the channel axis. The other side of the channel (marked red) is straight, and it has the quay wall with whirl chambers.

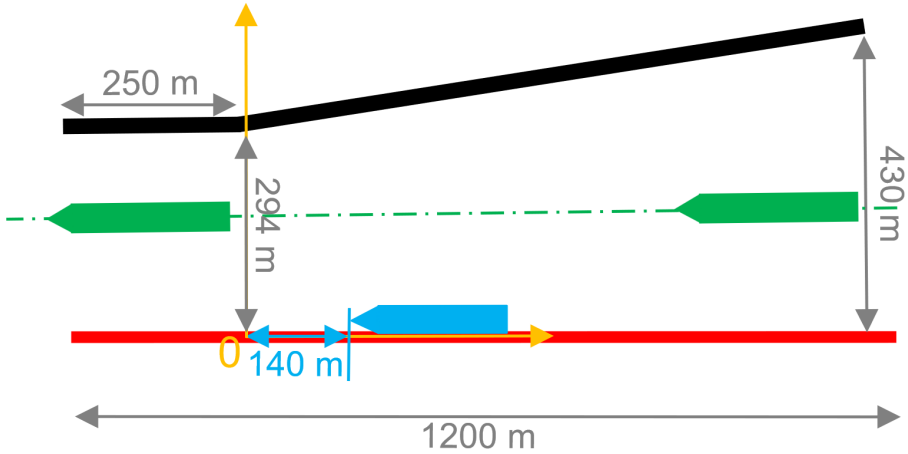

Figure 3. Sketch of the channel, fairway and moored vessel at berth

The bottom in the channel is modelled in ROPES as a horizontal plane, resulting in constant water depth of 13.3 m. The channel bottom level is at -9.1 mTAW and the still water level is at +4.2 mTAW. The cross section of the moored vessel at berth is presented in Figure 4.

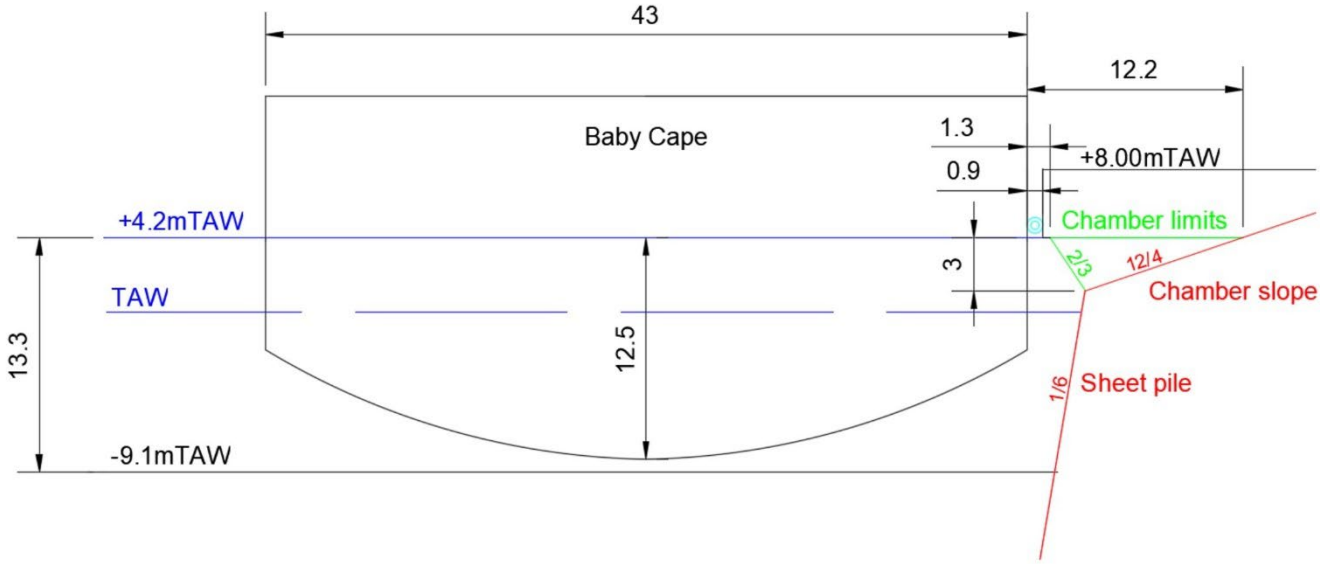

Figure 4. Cross section of the berth with the whole chambers model and a moored vessel at berth as defined in ROPES

The distance between the sheet pile and the center of the fairway is 125 m. The passing distance hull-hull between the passing and moored vessel is defined as presented in Figure 5.

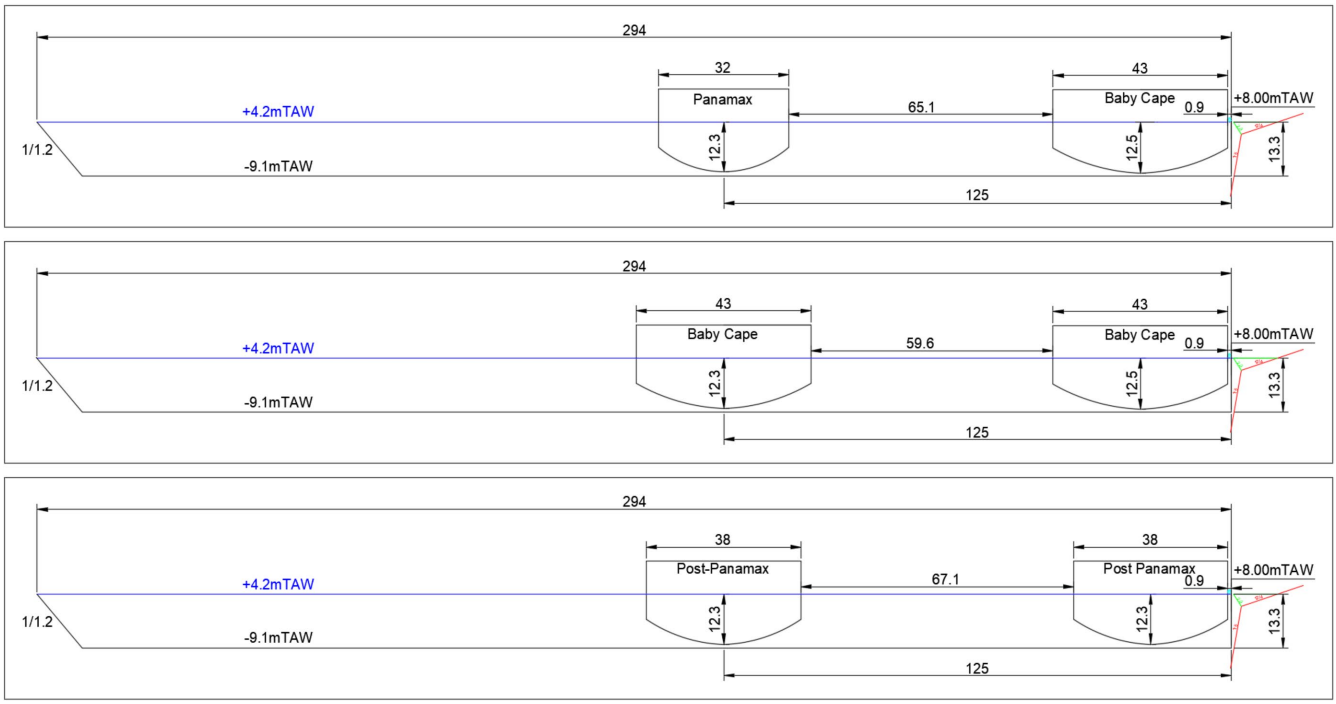

Figure 5. Schematization of the cross section of the channel and vessels for scenario 1 Panamax-Baby Cape

Table 1 shows the characteristics of the different vessels used for the simulations in ROPES. The initial simulations are performed with the first scenario, Baby cape moored and Panamax passing. However, additional checks are performed for the Baby cape moored and Baby cape passing and also the Post Panamax moored and passing. The moored and sailing ship are placed in the ROPES channel and berth models in accordance with the selected scenario. The sailing ship follows a straight line trajectory, parallel to the berth line, with a prescribed constant speed, and on the sailing distance as shown in Figure 3. The passing speed is 1m/s, and the results were later scaled to the actual passing speed (about 5 knots).

Table 1. List of vessels simulated in ROPES and vessel characteristics

	moored ship					passing ship						
nr.	**Class**	**LOA**	**B**	**d**	**UKC**	**Class**	**LOA**	**B**	**d**	**UKC**	**passing dist.**	**sailing speed**
[-]	[-]	[m]	[m]	[m]	[m]	[-]	[m]	[m]	[m]	[m]	[m]	[m/s]
1	Baby Cape	255	43	12.5	0.8	Panamax	229	32	12.3	1.0	65.1	1.0
2	Baby Cape	255	43	12.5	0.8	Baby Cape	255	43	12.3	1.0	59.6	1.0
3	Post-Pana-max	229.2	38	12.5	0.8	Post-Pana-max	229.2	38	12.3	1.0	67.1	1.0

5 MODELING AND RESULTS

5.1 MODELING

The quay wall is modelled as a set of more complex panels. As mentioned, the panes were squares in most cases (sometimes triangles were used). Note that screenshots from ROPES contain diagonals for better visualization. The different panel models defined in ROPES are presented in Figure 6. A systematic development is performed and a check of ROPES model of increased complexity:

- Step 0: a complete vertical wall
- Step 1: a wall with 2 inclined sheets, one almost vertical, and the other virtually closing the space of whirl chambers, to investigate the forces at different distances from the berthing line,

- Step 2: a wall with the inclined submerged sheet pile and the bottom slope of the whirl chambers, to investigate the effect of the additional volume of the whirl chambers, but without the blockage of the longitudinal flow,
- Step 3: a wall with the inclined sheet pile and the whirl chambers with transversal vertical walls blocking the longitudinal flow, the final model.

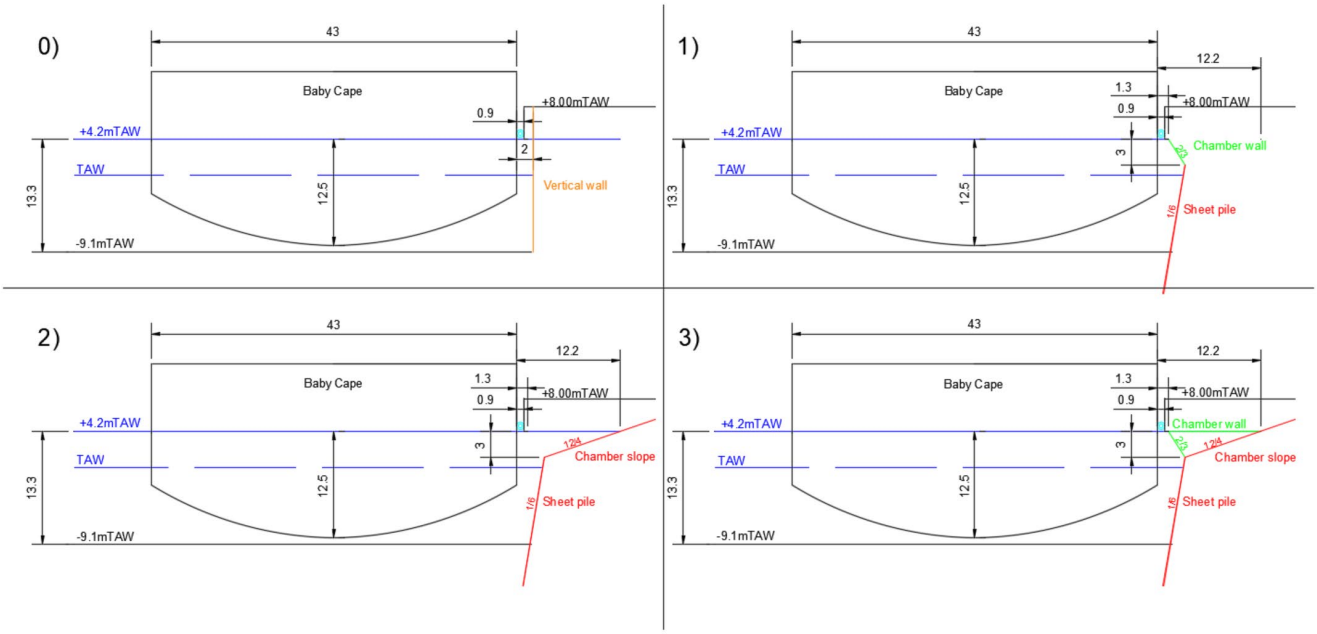

Figure 6. Cross section of the moored vessel at berth as defined in ROPES for the different step-wise models (marked 0) 1) 2) 3))

Figure 7 shows the 3D view of the panel model in Step1, the almost vertical wall, and Step 2, the two slopes model; the translucent blue surface is the water level, the grey surface is the channel bottom and the red/green surfaces are the parts of the quay wall. The development of the described models was done stepwise to control the results of modelling, to correct modelling inaccuracies and to gain confidence in the final results. As a result, the final model (Step 3) captured all important components of the quay wall with whirl chambers as described.

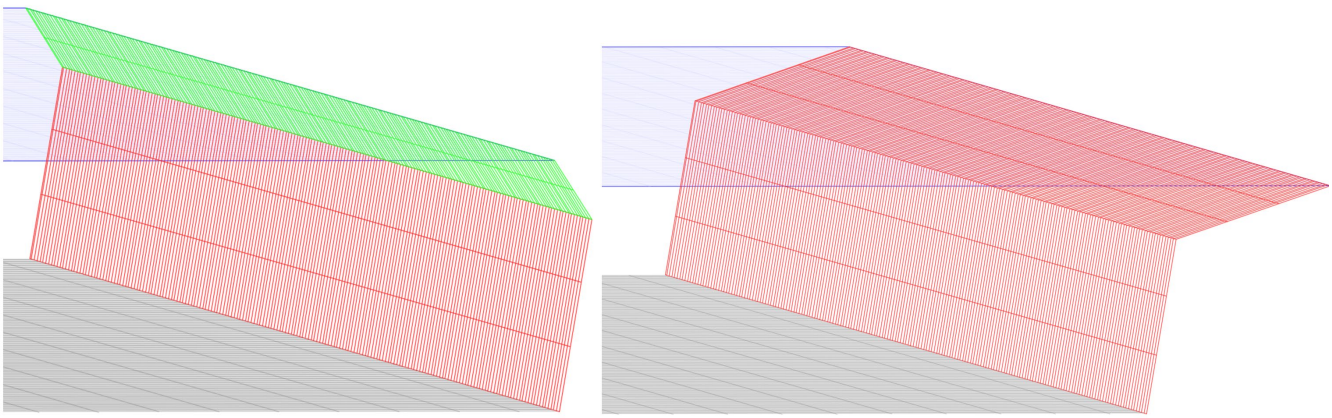

Figure 7. 3D view of the panel models in Step 1 (left figure) and Step 2 (right figure)

Figure 8 shows the schematization of the channel sides and of the berth, i.e., the details of the ROPES panel models. The bank slope opposite to the berth is defined in ROPES with a panel size of 5 m. The channel on the berth side uses model from Step 2 (no transversal walls of whirl chambers) and it is defined with a panel size of 3 m, except for the berth area. The panel model of the berth covers the location of the moored ship and extends slightly over the bow and stern of the moored ship; it is more detailed, with a panel size of 1.5 m. The whirl chambers are modeled in the berth area; they are spaced every 12.5 m and the perpendicular walls of chambers have a wall thickness of 1 m. The model with whirl chambers has the length of 374m, so it is abut 50% longer than the maximum length of the moored vessels.

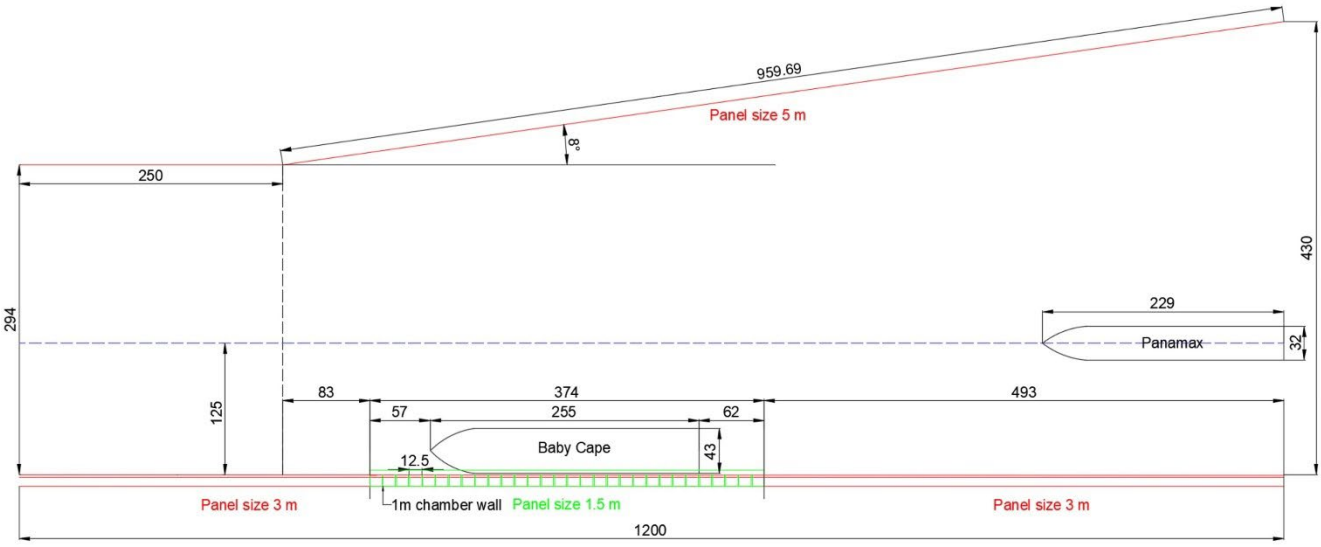

Figure 8. Schematization of the channel and berth panel model

Figure 9 and Figure 10 show the 3D views of the panel model in ROPES for the Step 3 final model. In these figures it is possible to identify the different panel sizes and how the whirl chamber walls have been fitted into the berth panel model.

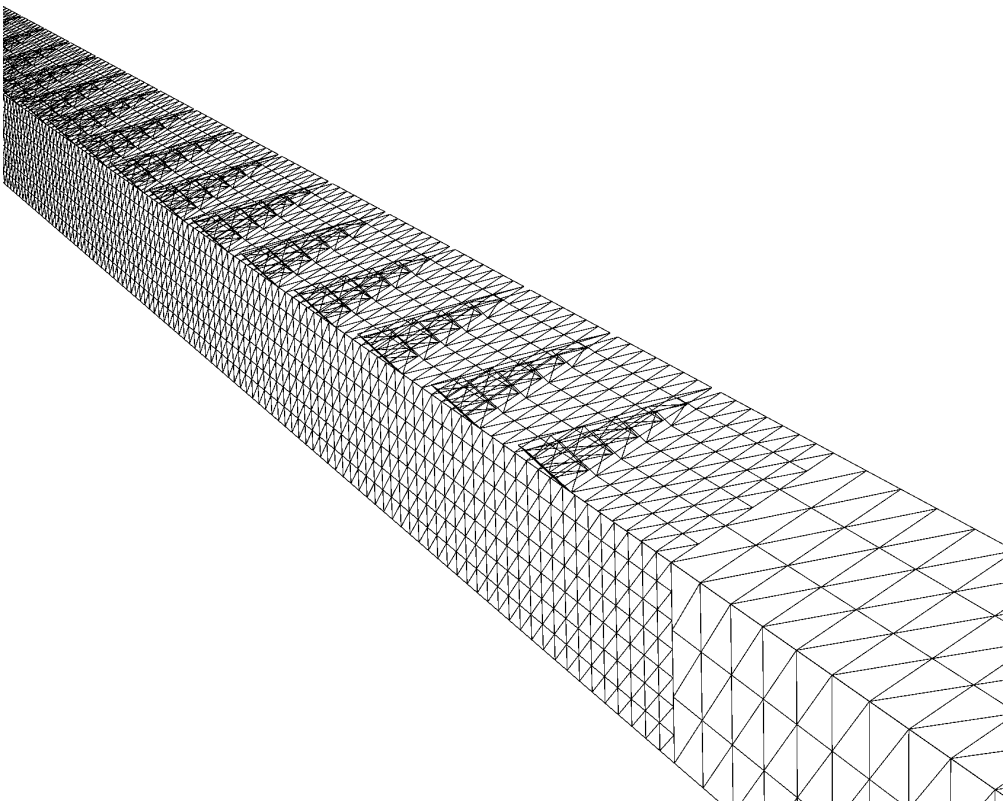

Figure 9 3D view of the different panel sizes used in the Step 3 ROPES model

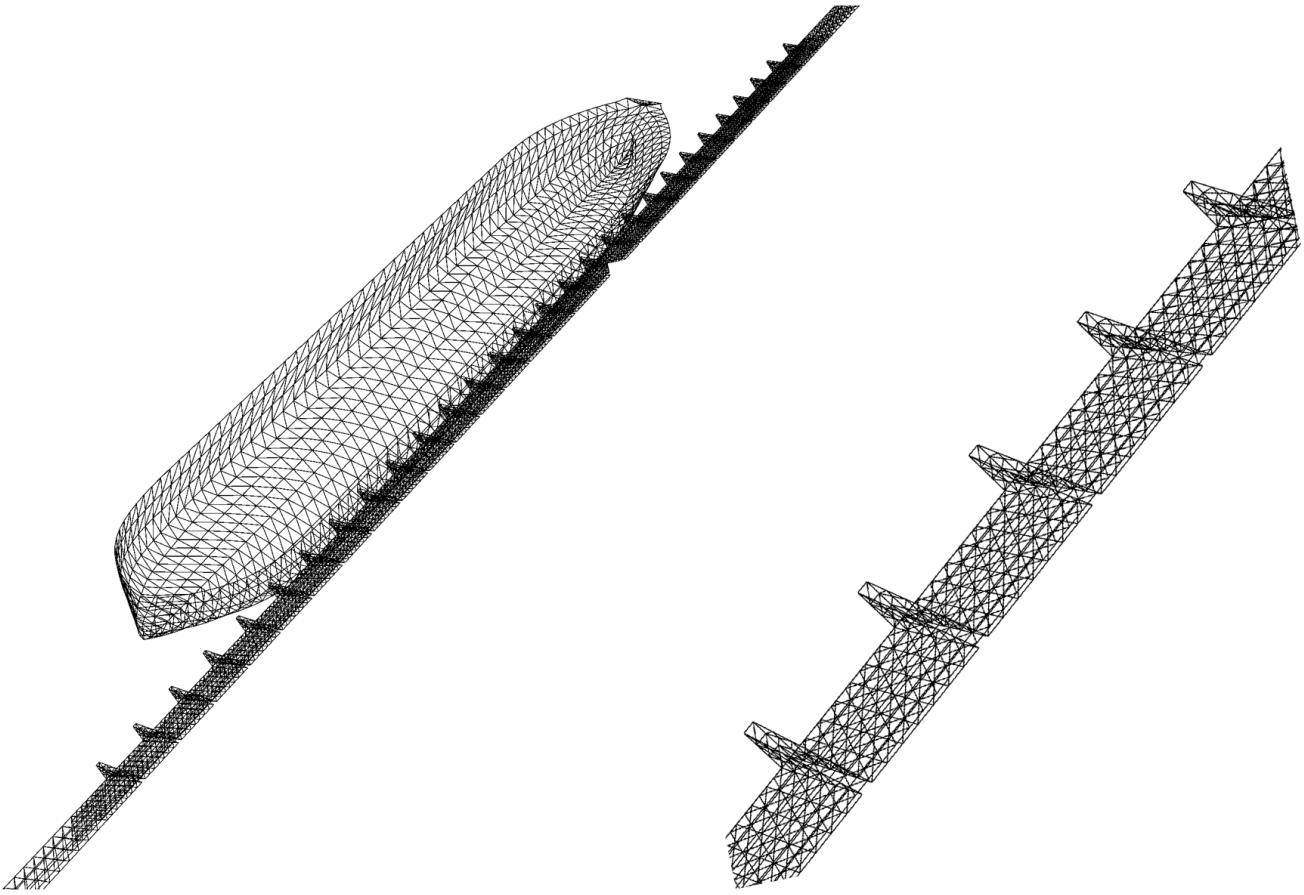

Figure 10. 3D view of the Step 3 panel model in ROPES with the moored vessel (left figure) and detailed 3D view of the whirl chamber walls (right figure)

In ROPES all simulations are done for a speed of 1 m/s in order to obtain results of better quality (the subsequent positions of the sailing ship on its trajectory are obtained by multiplication of velocity by the time step). The time varying forces to be applied to the moored ship at another sailing speed are then obtained by scaling the ROPES results by the squared passing speed and also the time steps are scaled by inverse of the passing speed.

The passing ship forces presented in the results refer to the forces on the moored vessel, unless otherwise mentioned. As it was described in the Methodology, when a ship navigates in restricted waters, there is a pressure wave which is observed as a water draw down. Water level raises ahead of the vessel and there is a return flow that accelerates alongside the hull to fill up behind the vessel. This is observed in the surge graphs as a negative surge motion when the passing ship approaches the moored ship, making the moored ship move towards the passing ship, and as the positive surge motion when the ship has passed the moored ship. In the sway graphs, it is represented as the positive peak when the passing ship sails right in front of the moored ship.

5.2 RESULTS

5.2 (a) Effect of panel size

The sensitivity of the forces to the panel sizes were checked in tests for each of the panel models in Step 0, Step 1 and Step 2. The resulting surge and sway forces are presented in Figure 11 to Figure 13. The peak force magnitude decreases when reducing the panel size from 3m to 1.5 m (more effect seen in sway force peak). This is specially visible for the Step 1 model – an almost vertical quay wall. For other models the variations in panel model sizes have not large results. However, the final model of the whirl chambers part of the berth was made with small panels.

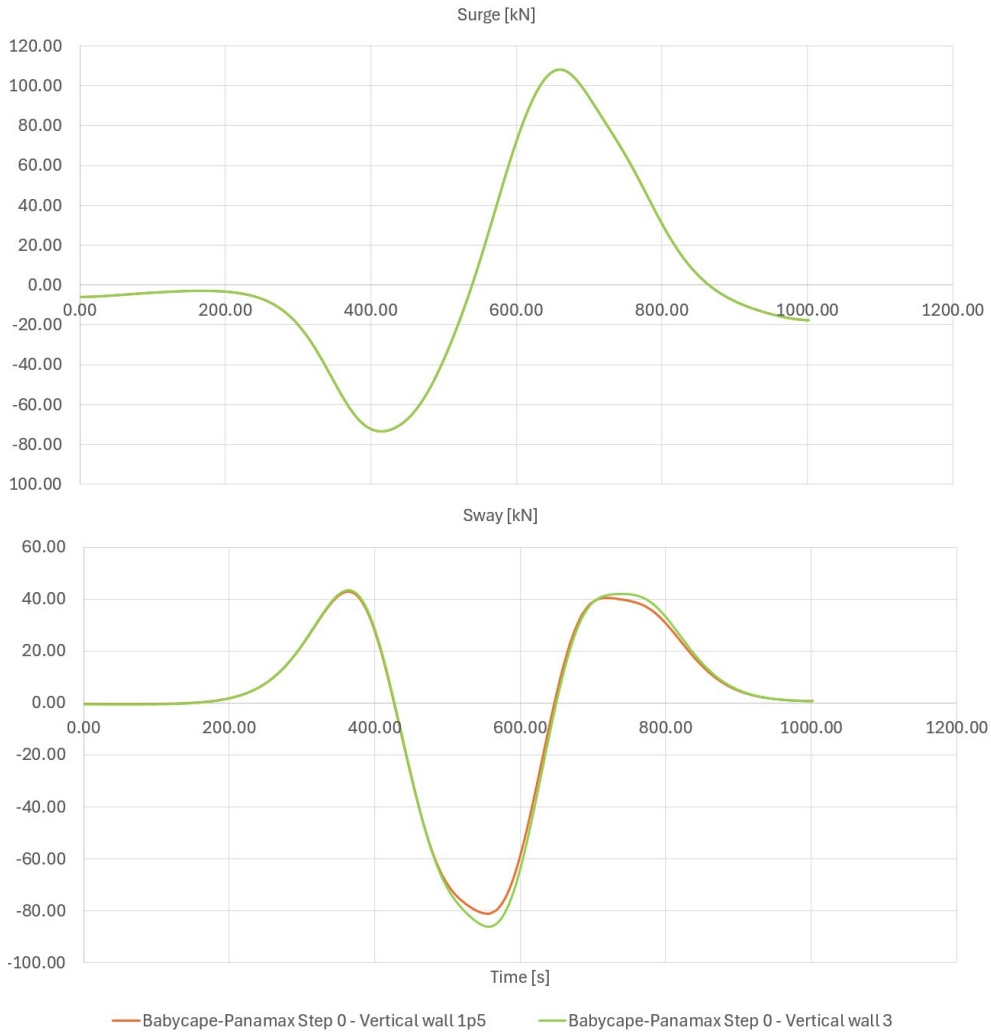

Figure 11. Passing surge and sway forces for the model Step 0 – Vertical wall with a panel size of 1.5 m and 3 m

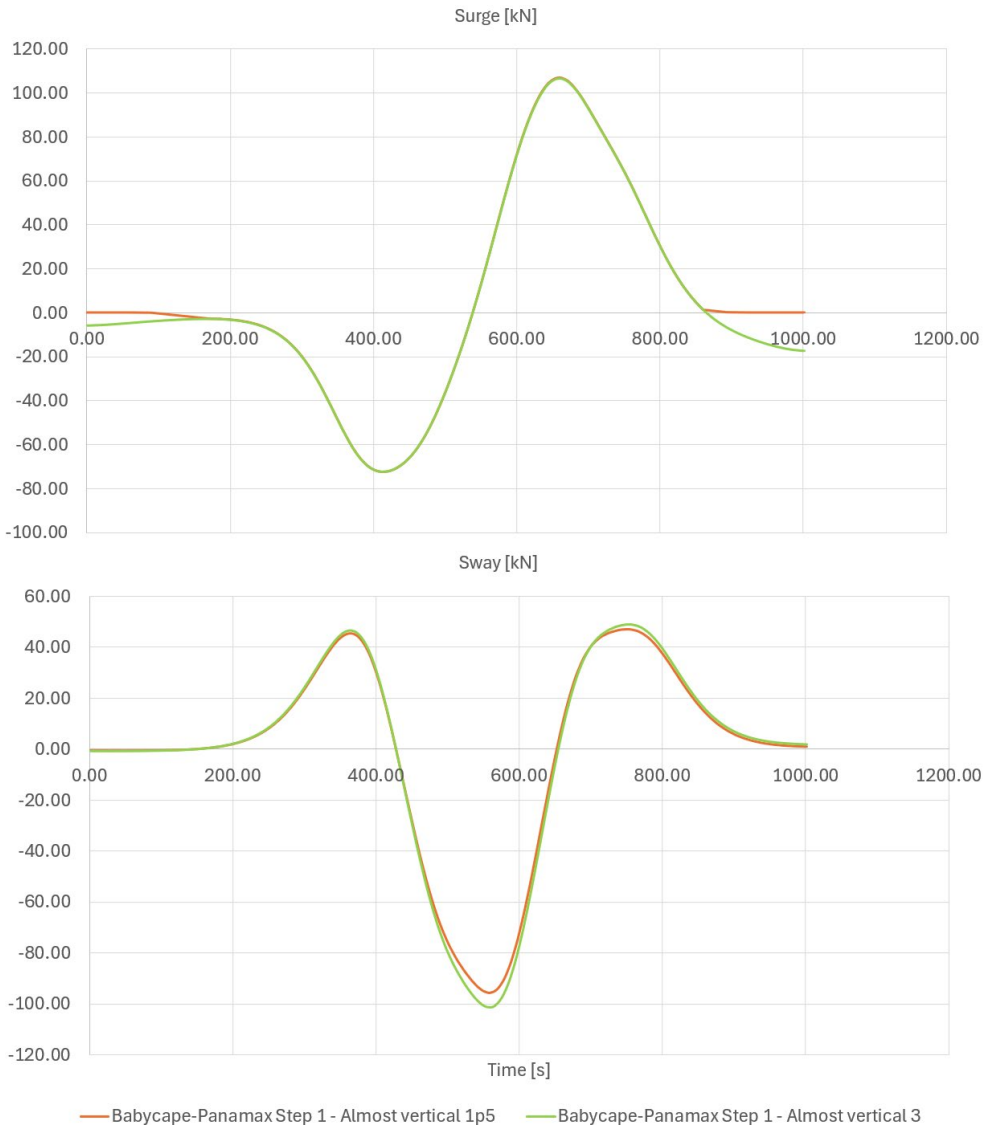

Figure 12. Passing surge and sway forces for the model Step 1 – Almost vertical with a panel size of 1.5 m and 3

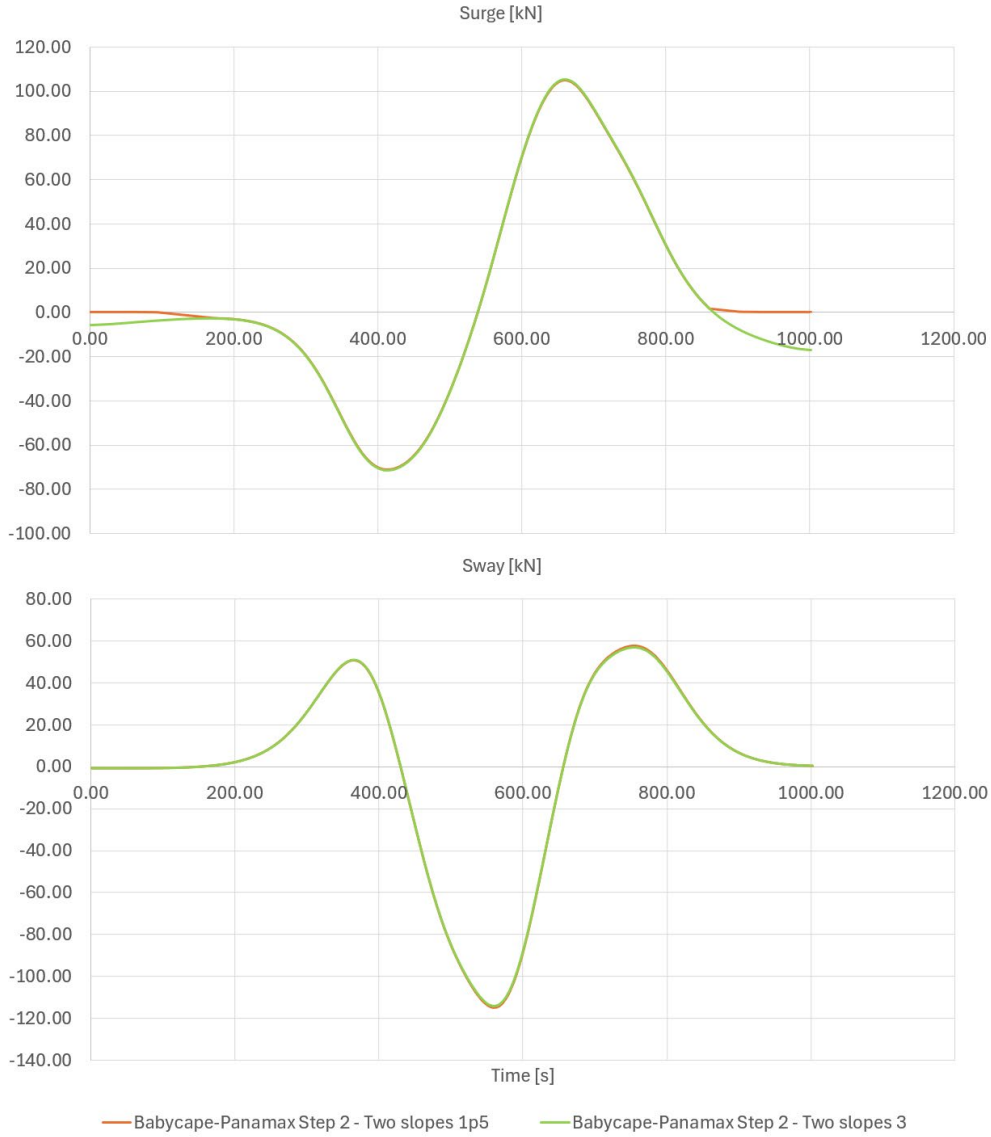

Figure 13. Passing surge and sway forces for the model Step 2 – Two slopes with a panel size of 1.5 m and 3

5.2 (b) Closed quay Vs Open water

The qualitative check of results included also a comparison of forces for a ship moored at a jetty (open water model) and at a vertical quay 2 m distance from the moored vessel. The Step 0 model results were compared with open water in order to better understand the effect of the defined quay wall. The resulting passing surge and sway forces are presented in Figure 14. Open water results presents higher sway forces, while surge increases due to the effect of the Step 0 quay. This is the expected qualitative behavior of models.

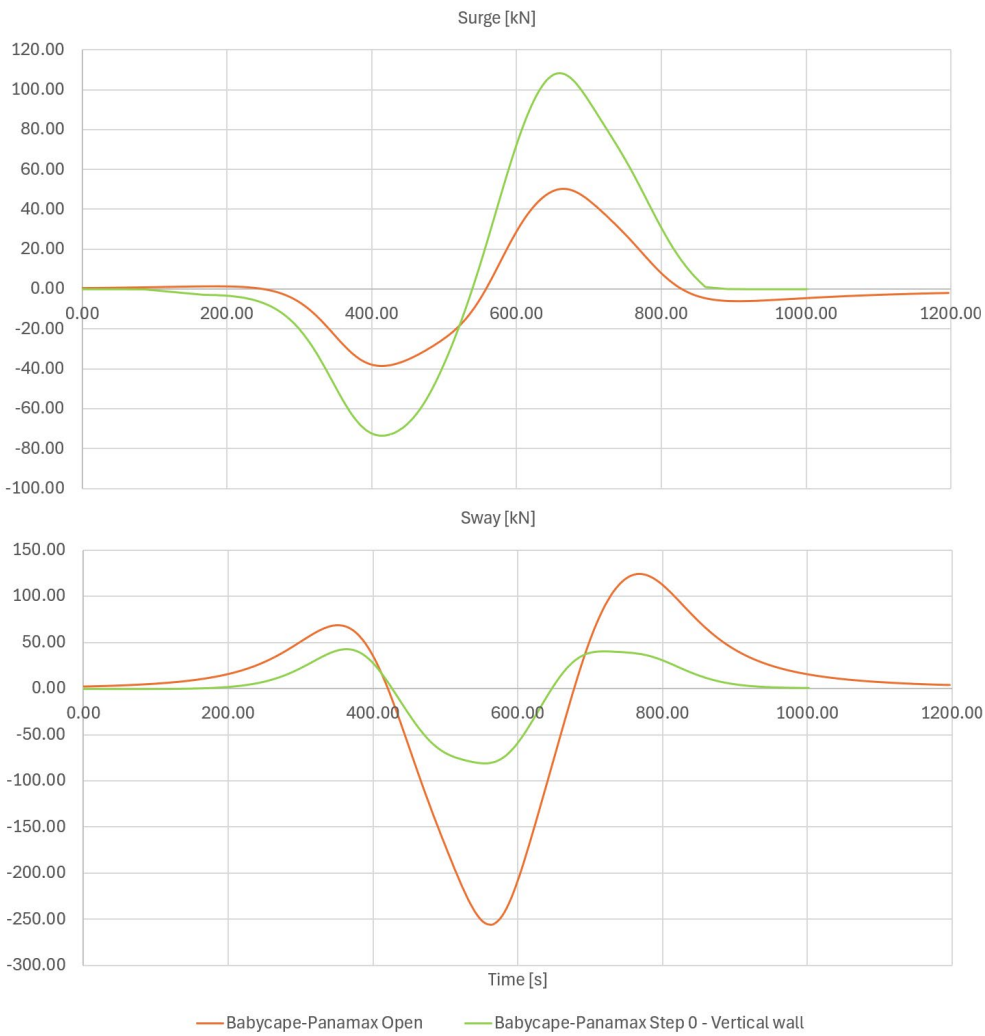

Figure 14. Passing surge and sway force for the Baby cape moored and Panamax passing with an open quay and Step 0 model

5.2 (c) Shift in the longitudinal position

In order to confirm that the position of the vessel with respect to the location of the whirl chambers did not have any effect on the results, one simulation was performed with the moored vessel shifted 3.5 m in the longitudinal position. The possible inaccuracies in results might originate from the relative shifts of panels of the moored vessel model and the quay wall model.

The passing surge and sway forces are presented in Figure 15, showing no noteworthy differences in the results. Therefore, it is safe to place the moored vessel at any location along the whirl chambers.

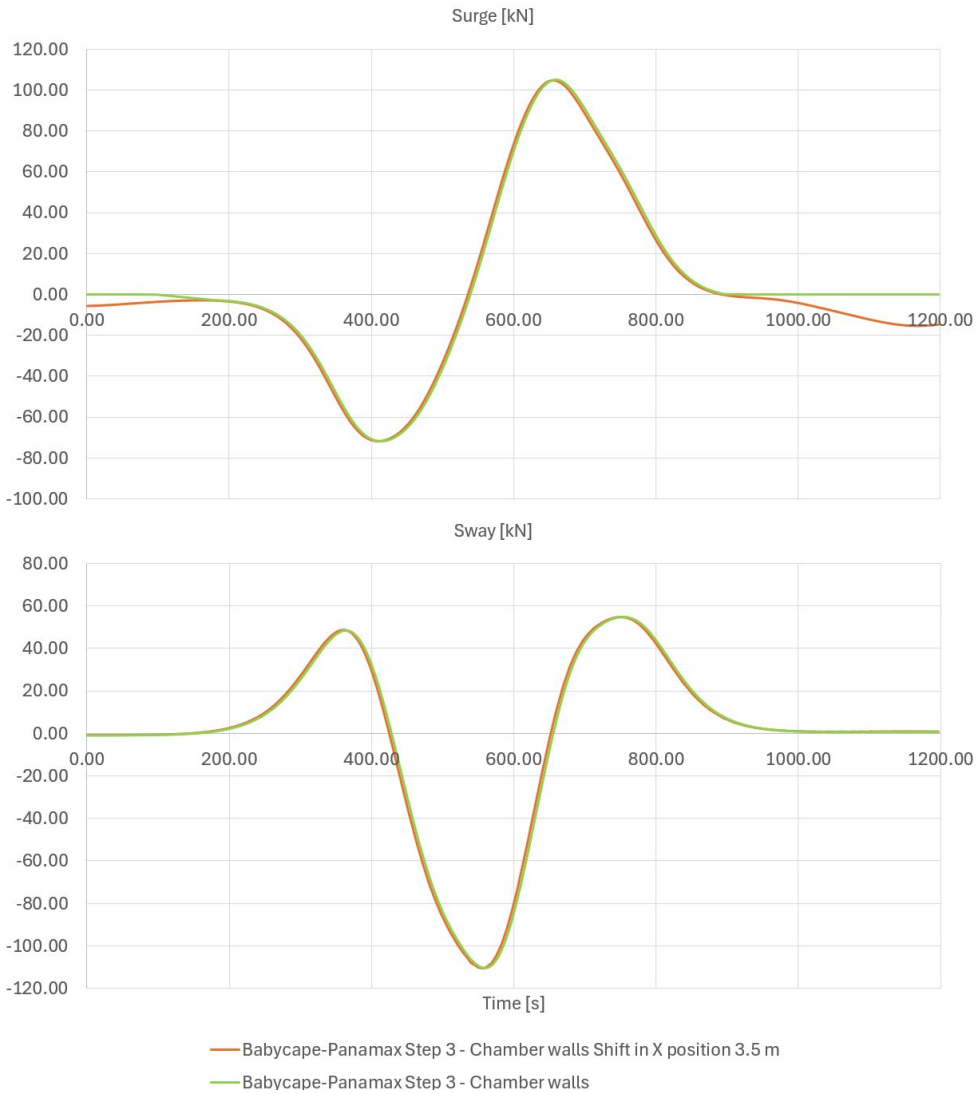

Figure 15. Passing surge and sway force for the Baby cape moored and Panamax passing with Step 3 model and the moored vessel shifted 3.5m in the longitudinal position

5.2 (d) Moored vessel

The strengths of sources modelling the sailing ship depend on the vessel speed and its geometry, as well as on the strengths of sources on panels modelling the geometry of the channel and berth (and the moored vessel). Therefore the resulting forces acting on it can be seen whether the channel model length and the extent of the berth panel model are correctly chosen to minimize their influence on the forces on the moored ship (because the latter depend on the strength of the sources on the sailing ship). The observation of the forces on the sailing ship serves to determine the effect of whirl chambers geometry on the strength of sources on the sailing ship (so, indirectly, on the forces on the moored ship), and on the extent the whirl chambers need to be modelled, considering the position of the sailing ship when the forces on moored ships become non-zero.

Following this concept, the forces acting on the passing vessel have been checked with and without moored vessel to verify whether the complex panel model at berth in Step 3 can be limited to the (extended) length of the moored vessel.

By observing the earlier presented time histories of the forces acting on the moored vessel we see that they are non-zero in time segments between 200s and 1000s, so the model edge effects do not visibly influence them.

The variations of surge forces on the sailing ship, presented in Figure 16, show that in case of no moored ship the forces on the sailing ship depend only on the channel blockage factor (the channel becomes narrower), not on details of the whirl chambers. When there is a moored ship, then the forces on the sailing vessel indicate when the sailing ship begins to “feel” the moored ship presence, thus indicating the necessary extent of modelling of quay wall sloped and whirl chambers (here it is about 400m).

The sway force on the sailing ship (lower plate of Figure 16) confirms that the details of the whirl chambers do not influence the forces on the sailing ship (case with no moored ship). The addition of the moored ship shows that its presence changes the forces on the sailing ship in time segment between 200s and 1000s. This confirms that the length of the whole channel model is sufficient.

These observations show that the whirl chambers have little effect on the sailing ship, confirming the hypothesis that their effect is specific to the near-field model of the moored ship and the berth. Therefore, the length of the whirl chamber model needs to be larger than the moored ship length but does not need to extend over the whole berth length, so it is why the berth model can be simplified when far from the moored ship.

Figure 16. Passing surge and sway forces in the passing ship with Step 3 model for the Panamax passing with and without moored vessel

5.2 (e) Bank slope (opposite side of the channel)

The effect of the opposite bank slope on the results was also checked in order to simplify the model, as presented in Figure 17. The effect of removing the bank slope in sway forces is not relevant and in surge it slightly reduces the forces. Therefore, it is concluded that the bank slope should be included in the model, but it can be modelled with bigger panel size due to the reduced effect in the final results (the bank slopes panels are placed in large distance from the panels on the sailing ship).

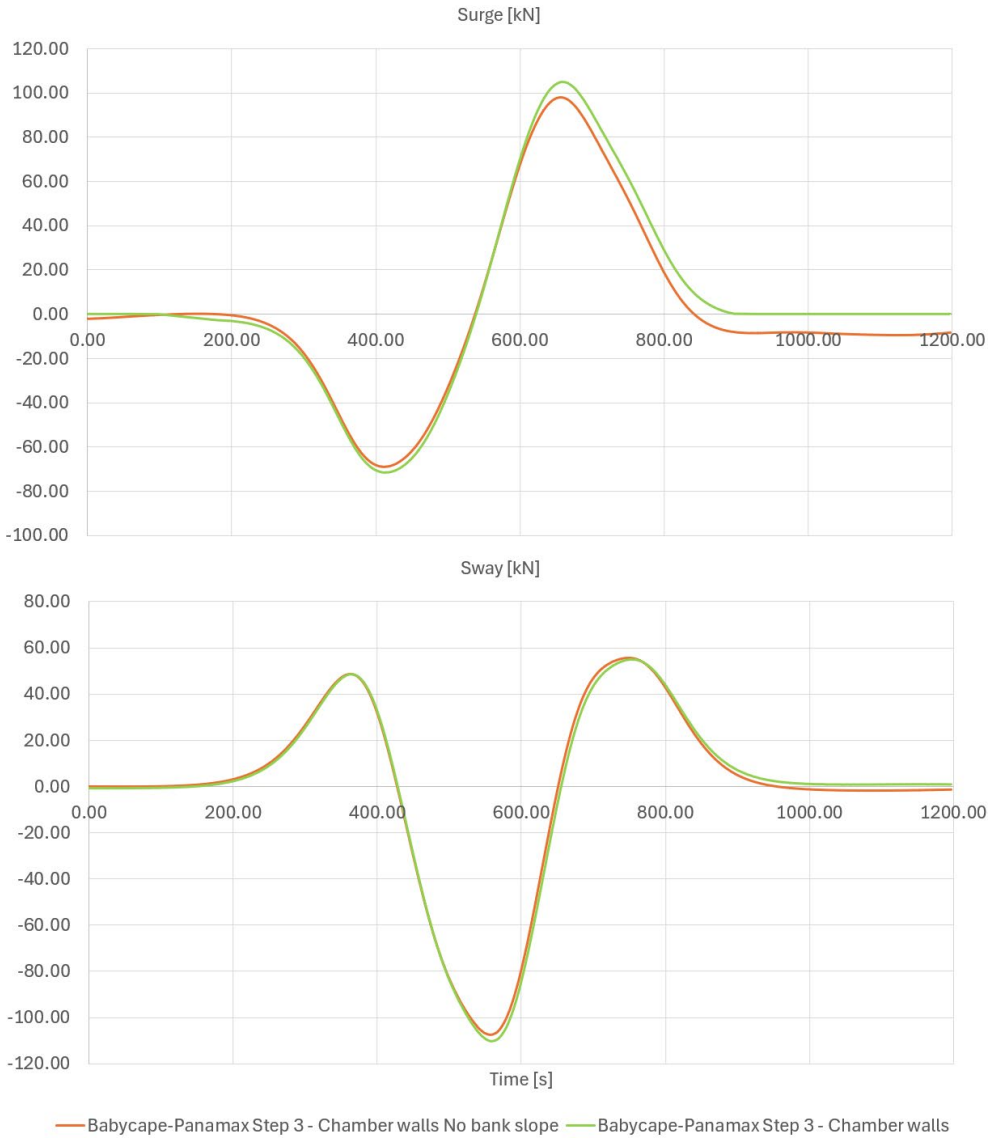

Figure 17. Passing surge and sway forces with Step 3 model with and without bank slope

5.2 (f) Step-wise models

The final model test with the different models was tested for Scenario 1. Figure 18 and Figure 19 show the surge and sway force signal variability for the different ROPES panel models built, from Step 0 to Step 3.

The vertical wall and almost vertical wall result in the highest surge forces compared to the cases with the chamber slopes and the whirl chambers. This is because surge forces increase when there is less water volume between the vessel side and the quay wall.

On the contrary, when the water volume between the moored vessel side and the quay walls increases, the sway forces also tend to increase. The highest sway force is obtained for the chamber slope scenario (Step 2) followed by the case with the chamber walls (Step 3), which creates higher blockage in the longitudinal flow and slightly reduces the volume between vessel side and quay/chamber walls.

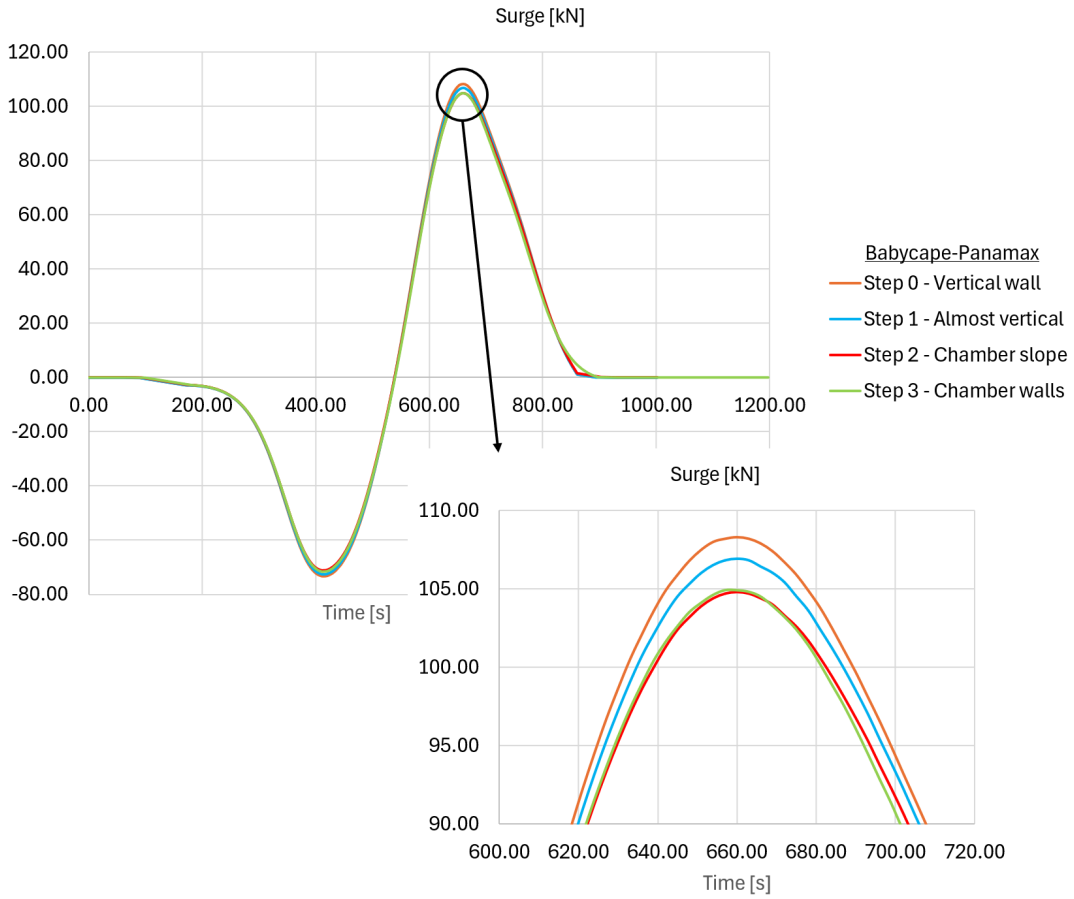

Figure 18. Passing surge motions for the different ROPES panel models Step 0 to Step 3 (top figure). Zoom to the peak in surge force (bottom figure)

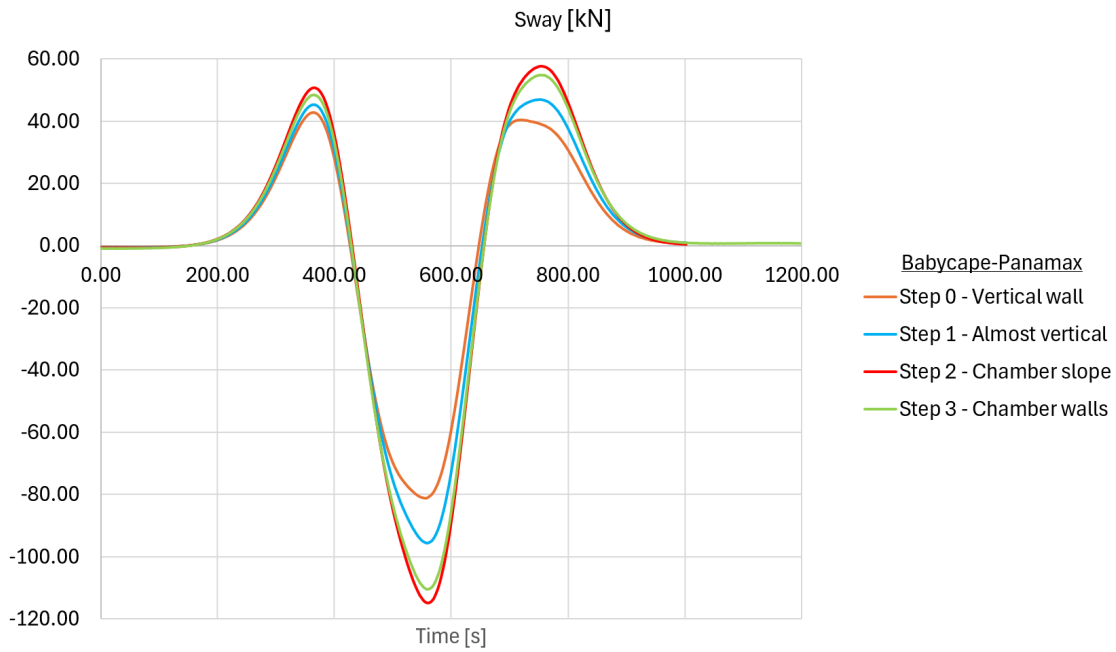

Figure 19. Passing sway forces for the different ROPES panel models Step 0 to Step 3

5.2 (g) Passing ship

The model was also validated with different passing ship size, Baby cape size moored and Baby cape size passing. The results are presented in Figure 20, showing a 70% and 40% increase in the surge and sway forces respectively.

This behavior is expected: a larger passing ship size (volume and the blockage factor due to increased midship area) increases the peak forces, and the larger passing ship length increases the length of passing force signal. Also, the qualitative behavior of passing ship forces is similar, which is expected considering that the data for the numerical models are just scaled.

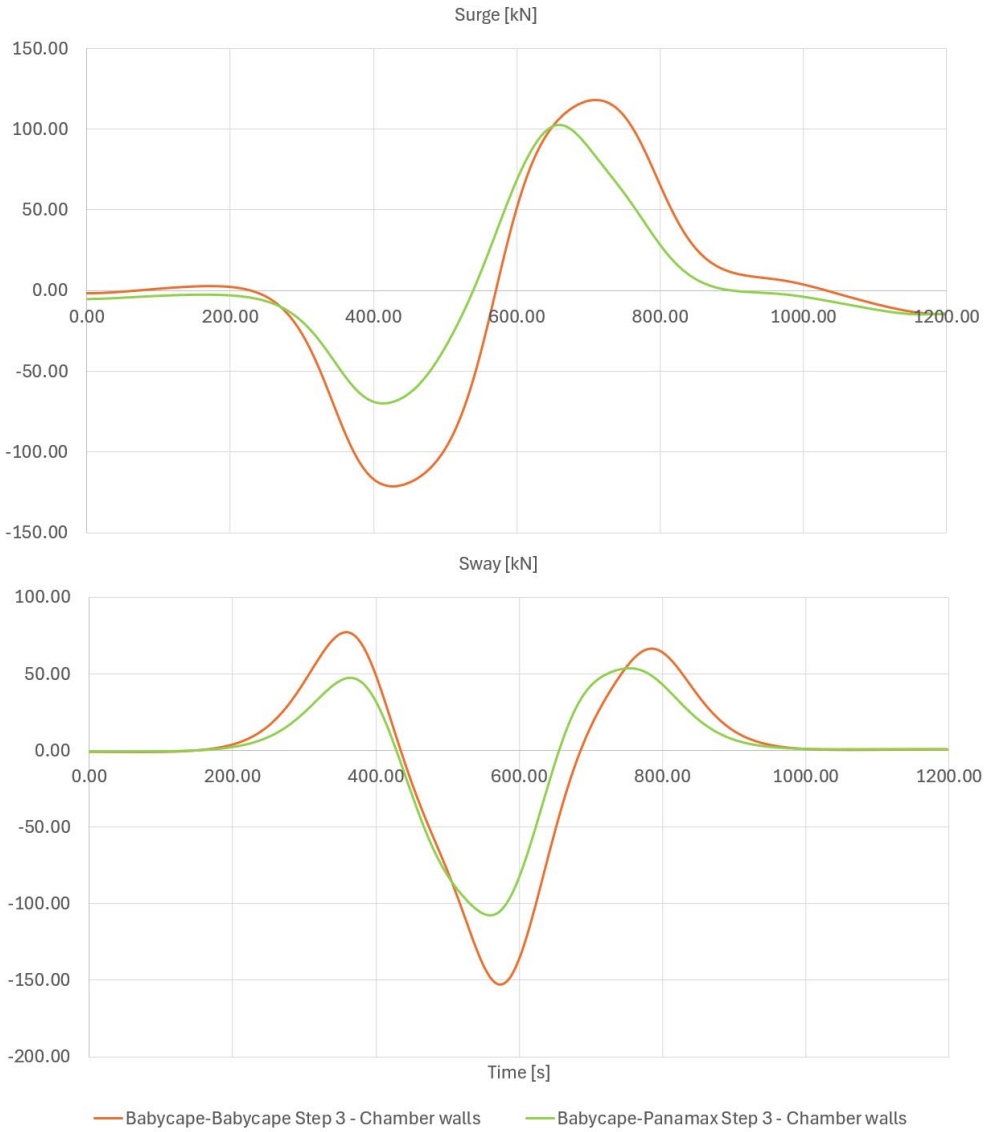

Figure 20. Passing surge and sway forces with Step 3 model for a Panamax and Baby cape size vessel passing

5.3 UNEXPECTED BEHAVIOR OF THE NUMERICAL MODEL

5.3 (a) Effect of the water depth

During the analysis it was observed how sensitive the ROPES model is to changes in the water depth, leading to incorrect results. Unexpected passing ship forces (large peaks and qualitatively different behavior) were noted in a quay model with panels. The initial water depth simulated was 13.25 m, which lead to the results presented in Figure 21. The peak forces are unexplainably high and the qualitative behavior of forces is not as expected for passing ship forces.

Sensitivity checks with the selected vessels and analytical quay were performed to investigate what causes these unexpected forces. The quay wall was modelled in the simplest way, using either large panels on vertical quay wall or the analytical quay. Then the water depth was also varied. When the water depth was modified to 13.3 m and 13.35 m, the model resulted in reasonable passing ship forces, as presented in Figure 22. Therefore, it is very critical to perform initial sensitivity runs with the different parameters before running the final simulation program.

These observed results can be thus attributed to internal implementations in ROPES, not to the specifics of the vessel and/or quay models. Any numerical model may have some implementation deficiencies and it is important to check the results and to detect such cases, if they occur.

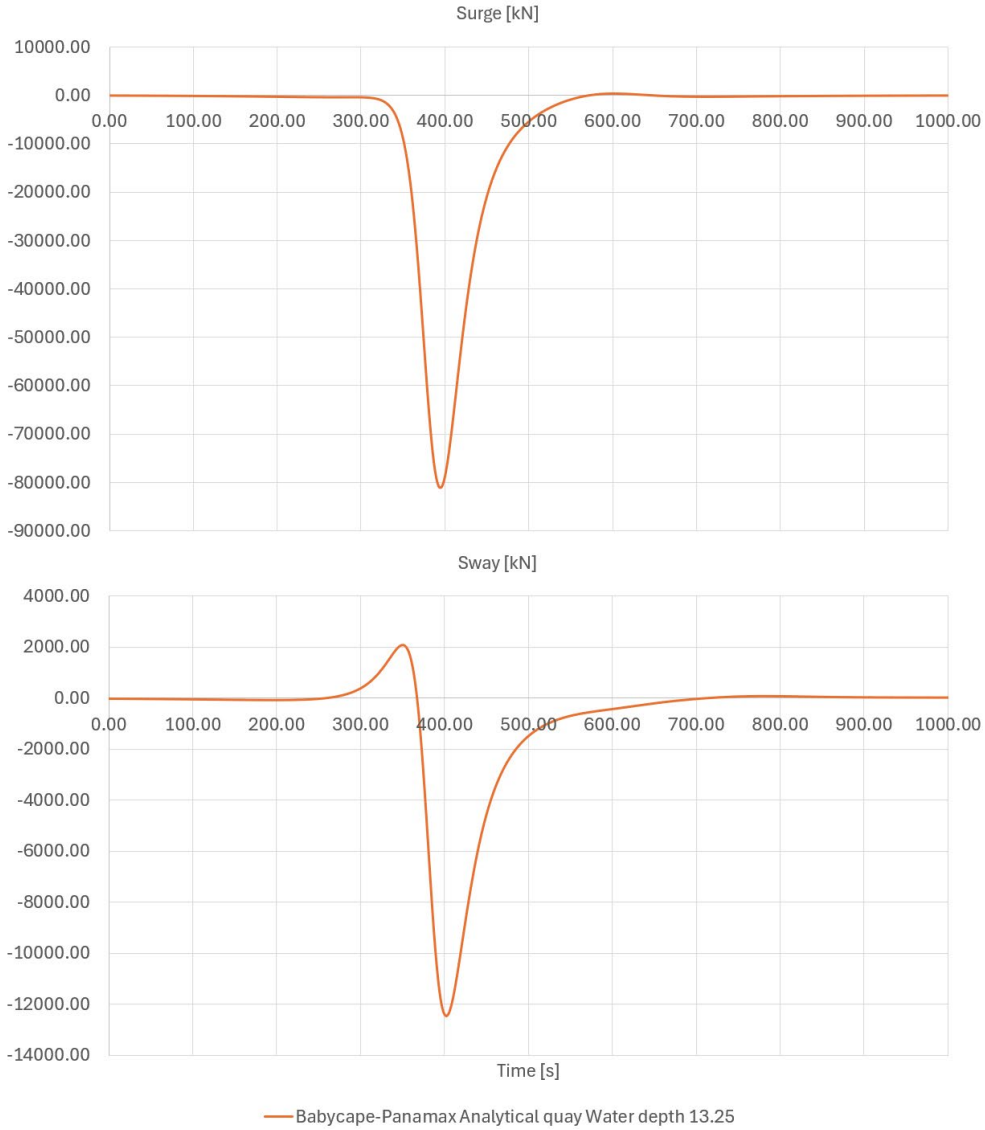

Figure 21. Passing surge and sway force for the Baby cape moored and Panamax passing with an analytical quay and water depth 13.25

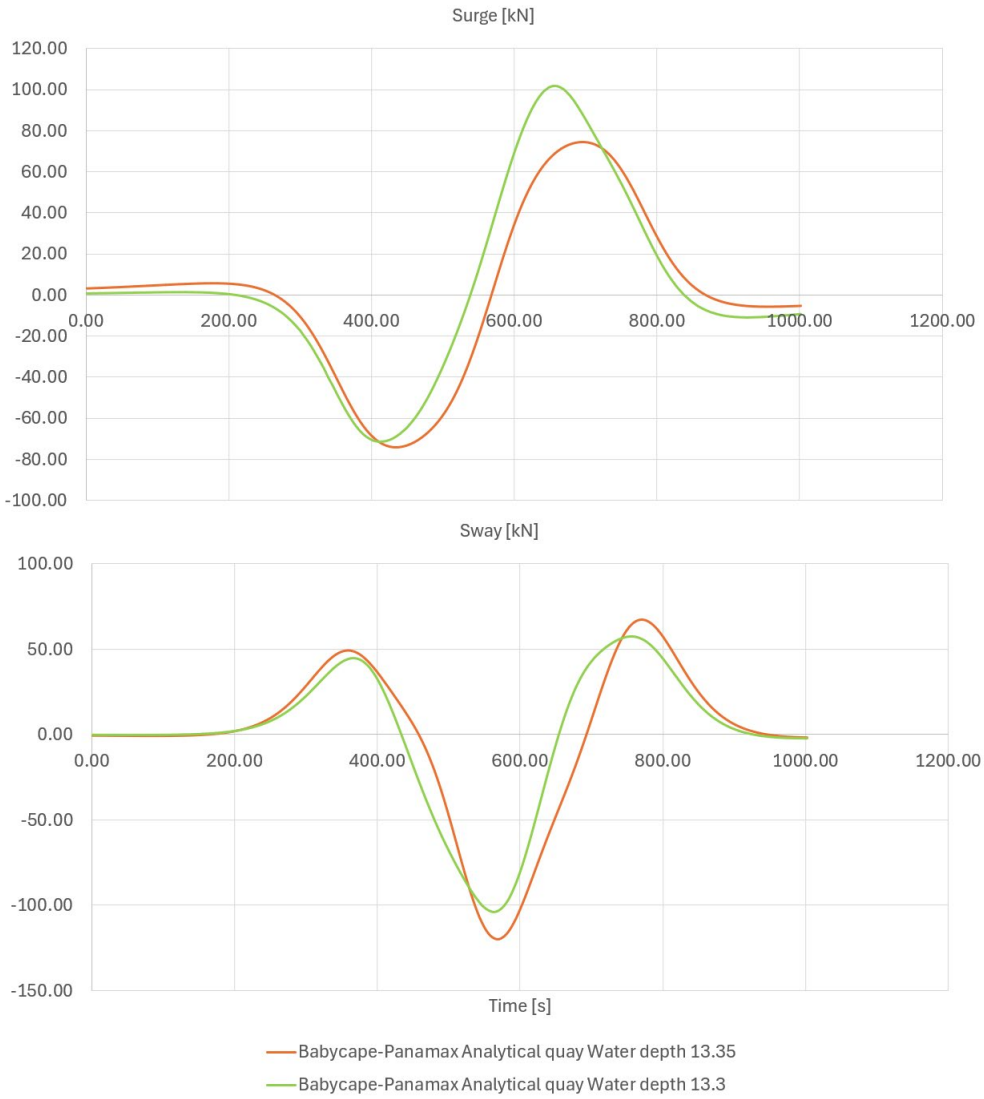

Figure 22. Passing surge and sway force for the Baby cape moored and Panamax passing with an analytical quay and water depth 13.3 m and 13.35 m

5.3 (b) Different hull shapes

Pasing ship scenarios were simulated for different passing and moored ship sizes. For one of the cases, the Post Panamax moored and passing vessels, an unexpected behavior was found in the sway forces, see Figure 25. This was unexplainable, since other combinations of vessels also used the tanker hull model from ROPES library, with its panels, and produced qualitatively similar behavior. ROPES tanker hull shape scaled for the Post Panamax is presented in Figure 23.

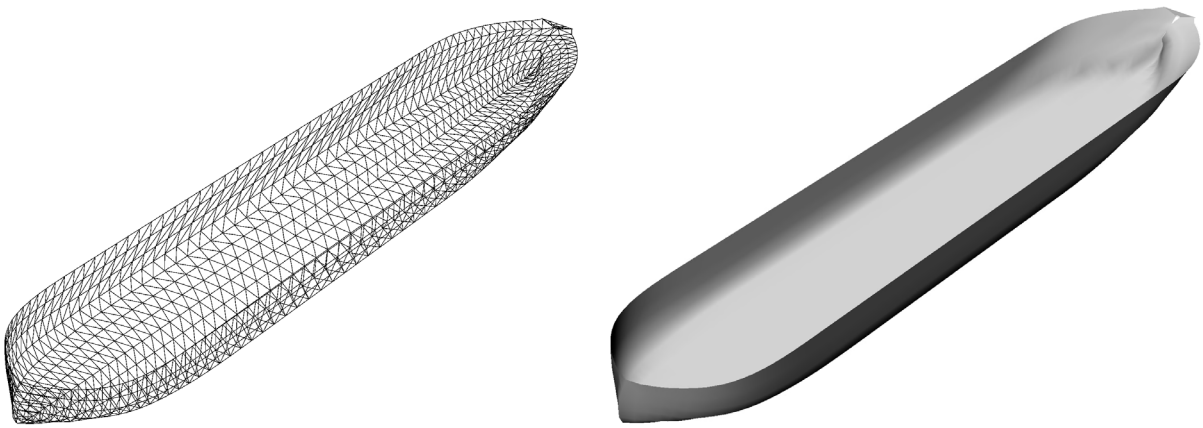

Figure 23. ROPES library tanker hull shape scaled for the Post Panamax

In order to correct this, it was necessary to select a different hull shape for the moored vessel, so a different panel model; while modeling principal dimensions and the block coefficient (hull volume) of Post Panamax vessels. After the change of the Post Panamax moored vessel hull panel model to LNG one, also from ROPES library, the results were qualitatively similar to results for other bulker vessels sizes, obtained with the tanker model. ROPES LNGC hull shape scaled for the Post Panamax is presented in Figure 24.

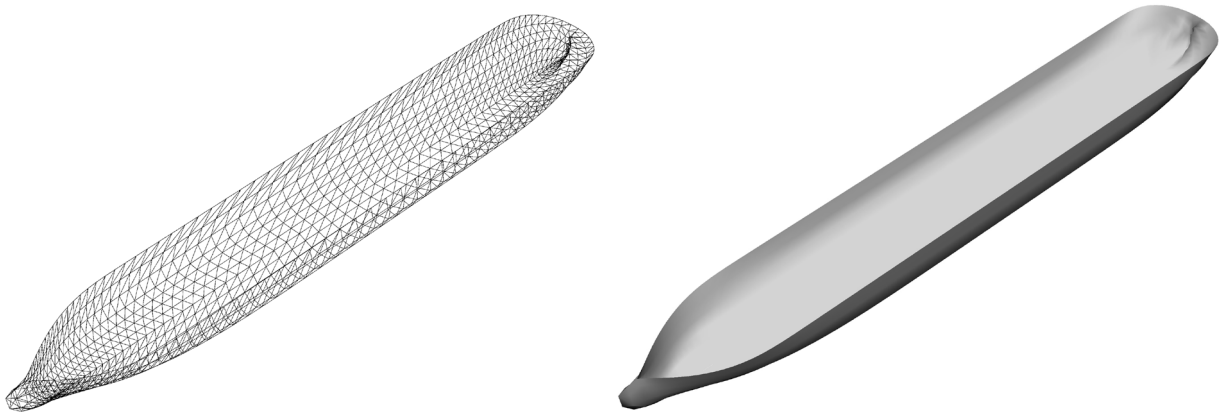

Figure 24. ROPES library LNGC hull shape scaled for the Post Panamax

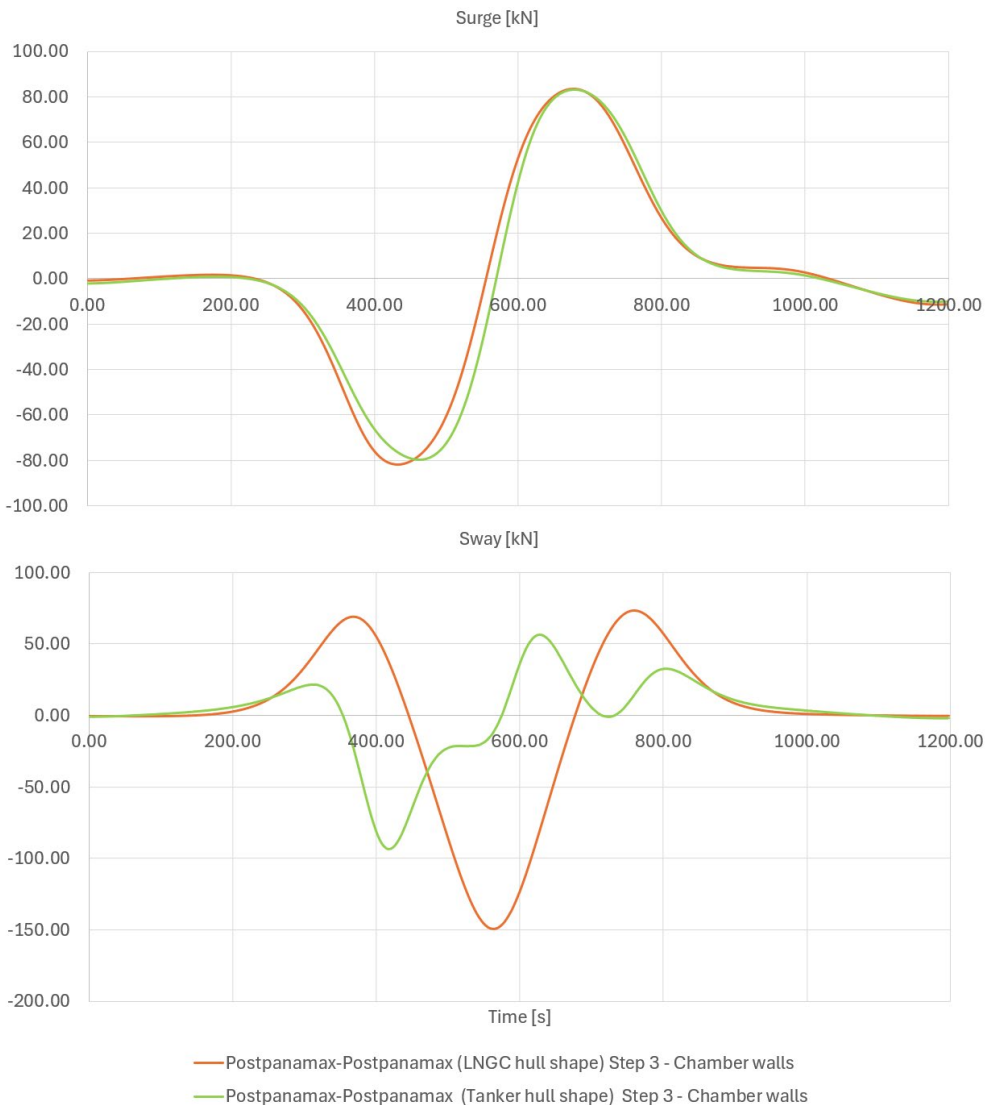

Figure 25. Passing surge and sway force for the Post Panamax moored and Post Panamax passing for Step 3 model considering different hull shapes for the moored vessel

The scaling inside the ROPES to obtain a desired hull volume consists of stretching/squeezing of the cylindrical part of the hull and doing the reverse for the bow and stern part; the number of panels do not change. The scaling of vessel dimensions results in expanding / contracting of panels sides. These two actions are improbable to result in the observed unusual behavior of forces in case of PostPanamaxes. Based on authors' experience with panel models (SHIP-PASSING) it is rather combination of integration method and relative positions of panels of various models (ship and quay wall).

6 CONCLUSIONS

The following conclusions can be formulated.

- The peak forces due to passing ships vary relatively little when comparing quay with whirl chambers and continuous vertical quay. However, these differences in peak forces may have effect on the final vessel responses, thus for the limiting speed of sailing vessel
- The forces due to passing ships at the complex quay behave as expected (less surge due to blocking of longitudinal flow, more sway because of increased volume between the quay and ship side)
- Full complex quay model (particularly, implementing of lateral baffles between chambers) may be implemented over a limited length of the quay, slightly larger than the length of moored ship. The remaining parts of the quay may be modelled with a simpler model that captures remaining features of the flow (sloped quay sides responsible for the increased volume of the space between ship hull side and the quay wall)
- The peak forces are sensitive to panel sizes on the quay next to the ship side; the decrease of panel size decreases the peak of forces
- ROPES, being example of panel method potential flow solver, can be used for calculation of passing ship forces acting on a ship moored along a complex quay.
- ROPES is suitable for fast development of geometrical models and produces the results (forces) fast, thus allowing for step-wise development of complex models, controlling the quality of models and allowing for testing of sensitivities to variations of these models.

The following recommendations can be formulated:

- Develop the final complex model through a sequence of simpler models, capturing important features and allowing to observe the resulting changes in forces. This approach gives a confidence in obtained results and allows to detect and assess irregularities that may occur
- Perform sensitivity checks of model parameters, like panel size, water depth and passing ship draught, distance of the moored ship to the quay side and along the quay side
- Check for the behavior of obtained forces whether this behavior qualitatively conforms to the expected one,
- Check for unexplainable results (both the qualitative behavior of forces and the values of peak forces) and whether the numerical implementation of the models produces stable results.

7 ACKNOWLEDGEMENTS

The authors wish to acknowledge IMDC for the support in writing this paper.

8 REFERENCES

Talstra, H. and Bliek, A.J., 2014. Loads on moored ships due to passing ship events in a straight harbour channel, in: PIANC World Congress San Francisco

van den Boom, H., Pluijm, M. and Pauwand, W., 2014. ROPES; Joint industry project on effect of passing ships on moored vessels, in: PIANC World Congress San Francisco

J.A. Pinkster, 2004. The Influence of a free surface on passing ship effects, in: Int. Shipbuilding Progress, 51, no 4, pp.313-338

J.A. Pinkster, H.J.M. Pinkster, 2014. A fast, user-friendly, 3-D potential flow program for the prediction of passing ship forces, in: PIANC World Congress San Francisco, USA 2014

J.A. Pinkster, 2009. Suction, Seiche and Wash Effects of Passing Ships in Ports, in SNAME 2009

J.A. Pinkster, M.N. Ruijter, 2004. The Influence of passing ships on ships moored in restricted waters, in: Offshore Technology Conference, OTC 16719, Houston, 2004.

9 AUTHORS BIOGRAPHY

Sara Sanz Sáenz is a Civil Engineer with experience in Ports and Coastal Engineering working for IMDC in Dynamic Mooring Analysis (DMA) an passing ship studies. She counts with experience in DMA Software and ROPES since her master thesis called “Impact of increasing container ship sizes on moored ships at container terminals next to busy fairways”

Wojciech Misiag is a Naval Architect (mechanical engineer) with experience in port and waterway design, risk assessment, dynamics of floating structures, mooring and maneuvering of vessels. He developed DMA methods and software, passing ship forces methods and software, performed mooring simulations. He works at IMDC as Principal Engineer.

EXPLORING THE HYDRODYNAMIC EFFECTS AT HIGH RUDDER ANGLES ON INLAND VESSELS

Justin Jasa, DST - Development Centre for Ship Technology and Transport Systems, Germany

Matthias Tenzer, DST - Development Centre for Ship technology and Transport Systems, Germany

Benjamin Friedhoff, DST - Development Centre for Ship technology and Transport Systems, Germany

EXPLORING THE HYDRODYNAMIC EFFECTS AT HIGH RUDDER ANGLES ON INLAND VESSELS

JUSTIN JASA, DST - DEVELOPMENT CENTRE FOR SHIP TECHNOLOGY AND TRANSPORT SYSTEMS, GERMANY
MATTHIAS TENZER, DST - DEVELOPMENT CENTRE FOR SHIP TECHNOLOGY AND TRANSPORT SYSTEMS, GERMANY
BENJAMIN FRIEDHOFF, DST - DEVELOPMENT CENTRE FOR SHIP TECHNOLOGY AND TRANSPORT SYSTEMS, GERMANY

SUMMARY

Studies on inland vessel manoeuvrability remain limited, making it difficult to establish trends and regression models similar to those for seagoing ships. The influence of shallow water, restricted channels, and variable water currents further complicates manoeuvring analysis. Due to lack of dedicated data, many existing studies from maritime are adapted to inland vessels despite their limitations. In particular, wake modelling, originally developed for single-propeller, single-rudder ships, is often applied to multi-propeller, multi-rudder inland vessels. However, it assumes wake variations occur solely due to vessel kinematics, overlooking confined water effects, multi-rudder asymmetries, and direct propeller-rudder interactions. This study experimentally examines rudder deflection effects on thrust and mathematically evaluates wake characteristics using a twin-propeller, quadruple-rudder (TPQR) inland ship model under varying loading conditions, speeds, rudder deflections, and water depths, including shallow water. Results show that high rudder deflections increase propulsion system thrust, reduce aft flow, and generate asymmetries in thrust and wake at lower h/T ratios between port and starboard, offering insights for refining inland vessel manoeuvring predictions.

NOMENCLATURE

DST	Development Centre for Ship Technology and Transport Systems	
TPQR	Twin-Propeller Quadruple-Rudder	
A_{R}	Lateral projected area of single rudder	m^2
B	Breadth	m
C_{B}	Block coefficient	–
D	Propeller diameter	m
h	Water depth	m
L_{PP}	Lenght between perpendiculars	m
L_{WL}	Lenght of the waterline	m
m	Blockage parameter: maximum transverse area of model ship divided by tank cross section area	–
n	Propeller revolution rate	Hz
T	Draft	m
T_{P0}	Thrust measured under neutral rudder angle ($0°$)	N
$T_{\mathrm{P}\delta}$	Thrust measured with rudders deflected at angle δ	N
u	Surge velocity during tests	m/s
w_{P0}	Wake fraction at propeller position under neutral rudder angle ($0°$)	–
$w_{\mathrm{P}\delta}$	Wake fraction at the propeller position with rudders deflected at angle δ	–
Λ_{R}	Geometric aspect ratio of the rudder	–
δ	Rudder angle (also referred to as rudder deflection)	°
λ	Scale ratio bewteen ship in model and full scale	–

1 INTRODUCTION

Understanding the interaction between the hull, rudder, and propeller, or more generally, between the hull, steering, and propulsion systems, is important for predicting and optimizing a vessel's manoeuvrability. This interplay is highly complex: the hull alters the incoming flow to both the rudder and propeller, while the propeller accelerates the wake behind the hull. In turn, the rudder not only deflects the slipstream flow but also modifies the upstream conditions experienced by the propeller. These interdependencies create a continuous feedback loop, making it challenging to isolate individual effects with simplistic assumption and theoretical models.

Most research on vessel manoeuvrability has primarily focused on seagoing ships due to the availability of extensive data and the relative form-uniformity among them, as many seagoing vessels are mass-produced. A comprehensive collection of manoeuvrability studies is documented in Sukas, Kinaci, and Bal (2019), where the majority of references pertain to seagoing or coastal vessels. As noted by Liu et al. (2017), studies on inland vessel manoeuvrability remain limited, making it difficult to establish generalised trends and regression models similar to those developed for maritime ships. However, inland vessels operate in highly constrained environments, where additional hydrodynamic effects, such as shallow water, restricted channels, and variable water currents (not to mention navigating through dense traffic, manoeuvring in confined port areas, and passing through locks) play a significant role in shaping their manoeuvring characteristics. These factors introduce complexities not typically encountered in maritime navigation, where vessels are primarily designed with other priorities in mind, such as seakeeping and stability in waves and wind in open waters, making manoeuvrability a less critical aspect.

Due to this data gap, many of the existing theories, formulations, and assumptions used to predict inland vessel manoeuvrability are derived from maritime studies and extrapolated to inland navigation to compensate for the lack of dedicated data. An example of this approach is the work of Liu et al. (2017), in which several existing methods developed for seagoing ships were combined and compared to identify the most suitable one for application to inland vessels. While this approach provides a basis for manoeuvring predictions, its accuracy and applicability to inland vessels remain an open question, particularly when considering the hydrodynamic complexities of confined waterways.

In particular, wake modelling in manoeuvring simulations, initially formulated for single-propeller single-rudder ships, as reported in Hirano (1980), has been adopted for twin-propeller, twin-rudder inland vessels (Liu et al. 2017). These models assume that wake variations occur solely due to the vessel's kinematics (e.g., drift and yaw), without accounting for asymmetries in multiple-rudder, multiple-propeller configurations, which are common in inland navigation. Moreover, direct propeller-rudder interactions are not explicitly modeled but are instead incorporated indirectly through rudder interaction coefficients, commonly referred to as steering resistance deduction factors (Yasukawa and Yoshimura 2015; *Report of Research committee on standardization of mathematical model for ship maneuvering predictions [P-29]* 2012), rather than being represented as an explicit change in wake characteristics. Additionally, these models were developed under deep-water assumptions, further limiting their applicability to inland vessels, where shallow water effects significantly alter hydrodynamic interactions.

With this in mind, this study provides a foundation for refining wake modelling in the manoeuvring of inland vessels by incorporating the influence of rudder deflection angles, with the aim of encouraging a reassessment, re-evaluation, and rethinking of the traditional approach used in maritime, fostering the exploration of new methodologies better suited to inland navigation. Specifically, it investigates how rudder deflections influence the thrust, and therefore the wake, generated by the propulsion system of an inland vessel in straight-moving conditions across various scenarios, including shallow water. To analyse these effects, an experimental campaign was conducted on a ship model equipped with two ducted propellers and four rudders (TPQR), representing a typical large inland vessel operating on the Rhine. The tests covered a wide range of conditions, including different loading conditions, water depths, speeds, and rudder deflections from $0°$ to $58°$.

2 EXPERIMENTAL CAMPAIGN

The experimental campaign aimed to gather data on propulsion system thrust under varying loading conditions, water depths, speeds, and rudder angles during steady-straight motion. Tests were conducted in the large shallow water tank at DST (Development Centre for Ship Technology and Transport Systems) in Duisburg, Germany. This facility is approximately 200 m long and 10 m wide, with a continuously adjustable water depth ranging from 0 to 1200 mm. This adjustability ensures that the water depths in the model tests are scaled appropriately, fully accounting for the effects of limited water depth.

2.1 SAMPLE INLAND MODEL

The experimental evaluation used a twin-propeller quadruple-rudder (TPQR) ship model, representing a CEMT Class Va vessel operating on the Rhine. The stern design, as depicted in Figure 1, includes a flow-separation plate at the stern, two ducted propellers positioned at the end of the propeller tunnels, and four Schilling-type (fish-tail) rudders arranged in pairs behind each propeller at the edge of the propeller disk. Each rudder is equipped with an end plate at the root and is positioned close to the flow-separation plate at the tip to minimize tip vortices. Two loading cases were considered, including full and reduced draught scenarios in an even keel configuration. In both cases, the flow-separation plate, the propulsion system and rudders remained fully submerged. Table 1 summarises the primary dimensions of the ship model, where L_{WL} is the length of the waterline, T is the draft, C_{B} is the block coefficient, L_{PP} is the length between perpendiculars, B is the breadth, A_{R} is the lateral projected area of single rudder, Λ_{R} is the geometric aspect ratio of the rudder, and D is the propeller diameter. The scale ratio λ between the model and the full-scale ship is 11.

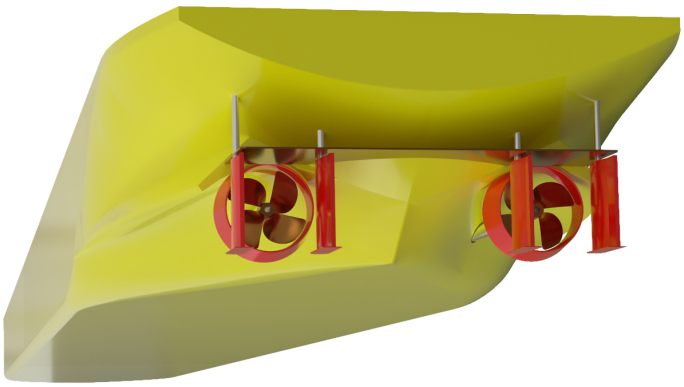

Figure 1: Rendered stern view of the studied inland vessel, featuring a flow-separation plate, two ducted propellers, and four Schilling-type rudders.

Table 1: Main data in model (MS) and full scale (FS). The scale ratio λ between the model and the full-scale ship is 11.

		L_{WL} [m]	T [m]	C_B [-]	L_{PP} [m]	B [m]	A_R [m^2]	Λ_R [-]	D [m]
Full draught	MS	9.935	0.255	0.901	10.000	1.036	0.0196	1.256	0.145
	FS	109.29	2.800	0.901	110.00	11.40	2.372	1.256	1.600
Reduced draught	MS	9.813	0.182	0.887	10.000	1.036	0.0196	1.256	0.145
	FS	107.94	2.000	0.887	110.00	11.40	2.372	1.256	1.600

2.2 TEST CAMPAIGN

2.2.1 Test conditions

The tests were conducted under four different combinations of two loading conditions (full and reduced draught) in even keel configurations and three water depths. This approach enabled a detailed analysis of the results, examining both the influence of changing water depth under the same loading condition and the impact of different loading conditions at the same water depth. Table 2 summarises in model scale the loading configurations, the water depths, the speeds and the rudder angles tested, where h represents the water depth, m is the blockage parameter defined as the ratio between the maximum transverse area of the ship model and the tank cross section area, u is the surge velocity and δ is the rudder deflections (to portside). The loading condition is represented here by the draught of the ship.

Table 2: Matrix of the test campaign in model scale (scale $1{:}11$).

$\downarrow T$ [m] | h [m] $\rightarrow$	0.682	0.318	0.227
0.255 (even keel)	✓($h/T = 2.67;\ m = 0.039$) $\delta = 0, 20, 40, 58$ ° * $u = 0.670, 0.838, 1.005,$ $1.173, 1.339$ m/s	✓($h/T = 1.25;\ m = 0.083$) $\delta = 0, 20, 40, 58$ ° * $u = 0.670, 0.838$ m/s	
0.182 (even keel)		✓($h/T = 1.75;\ m = 0.059$) $\delta = 0, 20, 40, 58$ ° * $u = 0.670, 0.838, 1.005$ m/s	✓($h/T = 1.25;\ m = 0.083$) $\delta = 0, 20, 40, 58$ ° * $u = 0.670, 0.752, 0.838$ m/s

* The rudder angles provided are purely indicative of the test conditions and follow the applied control logic reported in Figure 2.

The study employed a specific rudder kinematic approach used in inland waterway vessels, where the innermost rudder, referring to the rudder that would be closest to the centre of rotation during a steady circular motion, deflect more. In a manoeuvre where the rudders turn to port, the innermost port rudder rotates the most. Conversely, in a manoeuvre where the rudders turn to starboard, the innermost starboard rudder experiences the greatest deflection, while the others follow the standard control logic. Figure 2 illustrates the rudder angles used in the tests. In this case, the extreme port rudder rotated to $22°$, $46°$, and $78°$, while the other rudders followed with deflections of $20°$, $40°$, and $58°$, respectively. These values were derived from the rudder kinematics of a European inland container vessel. Therefore, the rudder angles shown in Table 2 are representative of the test conditions rather than fixed values.

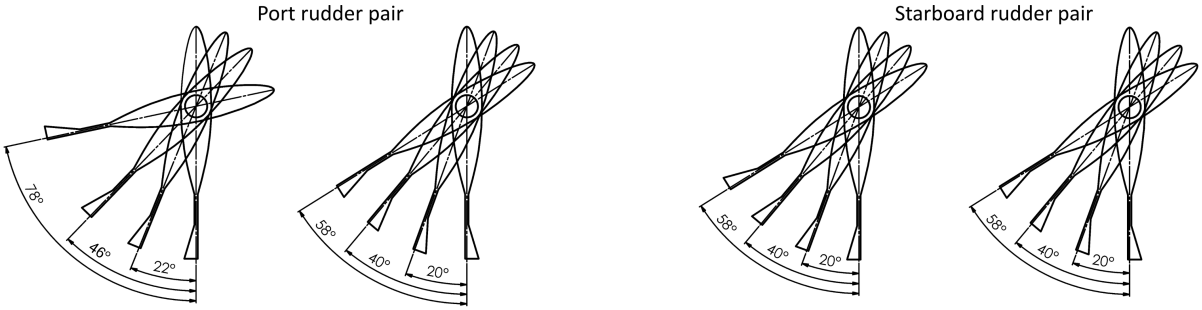

Figure 2: Schematic representation of the rudder kinematic logic used in the tests for port deflections.

2.2.2 Type of tests

The campaign included self-propulsion tests conducted with rudders and propulsion tests with deflected rudders in straight moving. All tests were conducted in accordance with ITTC procedures at varying conditions. Table 2 summarises the loading configurations, the water depth, the speeds and rudder deflections tested for each type of test. In advance of the captive model tests, propeller open water tests were carried out.

The self-propulsion tests were performed with the model in a configuration with rudders in a neutral position, defined as $0°$, where the rudders are parallel to the ship's centreline. Here the self-propulsion point of the ship at model scale was determined by applying the thrust deduction force. The propulsion tests with deflected rudders in straight moving were conducted to measure the thrust of the propulsion system at different rudder angles. During these tests, the model was positioned in the basin and towed by the carriage to have no sway. In each combination of water depth, loading conditon and speed, the same propeller rates of the ship self-propulsion points determined with neutral rudders were maintained. Rudder deflection angles of $20°$ and $40°$ and $58°$ to the port side were tested[1]. The propeller open-water characteristics were used to determine the wake fractions for each condition using the thrust identity method, which is based on the measured propeller thrust.

All measurements were taken under steady-state conditions. After an initial transient phase, the model moved in a steady motion with the carriage before measurements were recorded.

2.3 SHIP MODEL SETUP

The experimental campaign employed a series of high-precision instruments to measure hydrodynamic forces and propellers' performance under different conditions. A load cell recorded the longitudinal force acting on the hull to get the ship self-propulsion point via the British method. Propeller performances were assessed using high-precision dynamometers mounted on each propeller shaft, measuring both thrust and torque (though torque was not used in this analysis). Additional thrust from the ducts was measured with dedicated thrust sensors. Two engines ensured that the propellers maintained the desired rotational speeds throughout the tests. Rudder deflections were controlled using high-precision rotary encoders, ensuring accurate and repeatable angles. Lastly, the towing carriage provided precise speed control, ensuring consistent velocities across all tests.

3 RESULTS AND DISCUSSION

In the experimental campaign, ship self-propulsion tests were conducted with rudders in a neutral position, as well as propulsion tests in straight moving with deflected rudders under different operating conditions. The objective of the campaign was to measure the thrust of the propulsion system across all aforementioned scenarios. For the tests with rudders in a neutral position, the ship self-propulsion point was determined, defined as the propeller rotational speed that, in full scale, would generate the required thrust for the vessel to maintain the desired speed in straight ahead motion. In tests with deflected rudders, the previously determined self-propulsion point was maintained for the same operating condition.

The thrust results are presented as the ratio of the thrust with deflected rudders to the thrust in the neutral rudder condition for the same operating scenario, illustrated in Figure 3. Each subfigure represents a different combination of water depth and loading condition. Additionally, the thrust values for the port and starboard sides are considered separately to account for potential asymmetries in the flow and rudder-propeller interactions. It should be noted that all rudder deflections occur to port side.

[1]These angles are representative of the applied control logic rather than fixed values. For further details, refer to Section 2.2.1 and Figure 2.

Subsequently, using the thrust identity method and open-water propeller characteristics, the wake fractions for each condition listed in Table 2 were determined for port and starboard sides. These are presented in Figure 4 as the ratio of the complement of the wake fraction $(1 - w)$ with deflected rudders to the complement of the wake fraction in neutral rudders for the same operating scenario. Each subfigure represents a different combination of water depth and loading condition. It is important to note that the thrust identity method allows for the determination of an effective wake factor, assuming that the characteristics of the propulsion system remain unchanged between the open-water condition with homogeneous inflow and the behind-hull condition, where the propeller is influenced by the stern, rudders, and confined waters. At this stage, this principle has been used as the basis for obtaining the parameter. More precisely, the wakes calculated in this manner implicitly account for variations in the behavior of the propulsion system under non-open-water conditions.

In this analysis, a parametric approach is considered, where surge velocity u and propeller rotation rate n vary together. However, thrust and wake exhibit different degrees of dependency on these parameters. Given this, the focus is placed on evaluating the effects of rudder angles at the self-propulsion points.

For a smoother interpretation, reference is made to the representative values of the rudder deflection logic, i.e., $20°$, $40°$, and $58°$. See Section 2.2.1 and Figure 2 for further details.

3.1 THRUST ANALYSIS

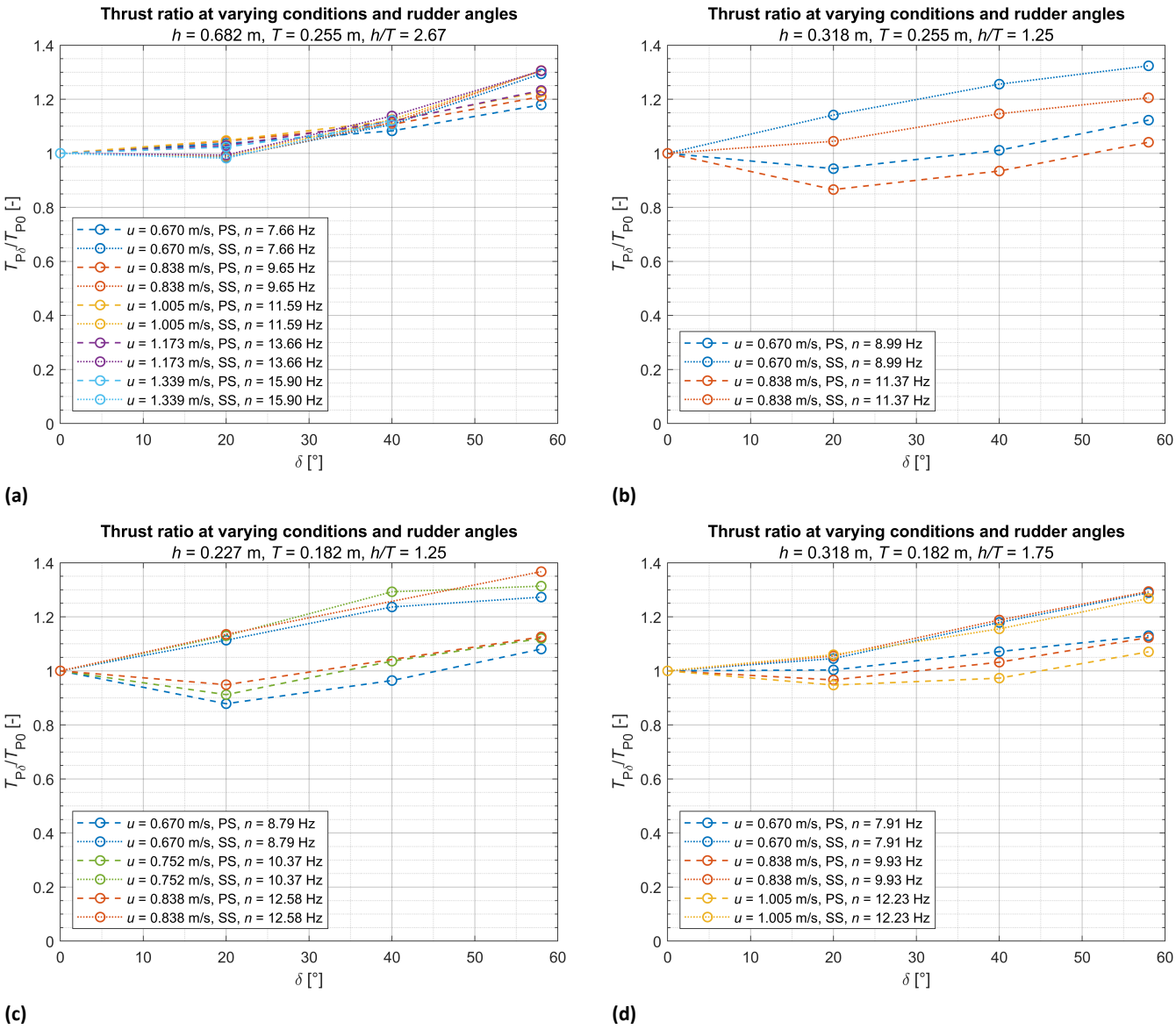

Figure 3: **Ratio of thrust with deflected rudders to thrust in the neutral rudders angle across various loading conditions, water depths, and speeds. Port (PS) and starboard (SS) ratios are shown separately. Rudder deflections are toward the port side.**

In Figure 3, the thrust ratio $T_{\mathsf{P}\delta}/T_{\mathsf{P}0}$, i.e., the thrust at deflected rudders with respect to the thrust with neutral rudders, is primarily influenced by the overall h/T ratio rather than by the individual values of h and T. This is evidenced by the fact that subfigures (b) and (c) exhibit very similar behavior, while subfigure (d) shows an intermediate trend between subfigure (a) and subfigures (b) and (c). The thrust ratio between the port and starboard sides becomes increasingly asymmetric as h/T decreases, whereas for higher ratios of h/T these asymmetries are reduced. The velocity, together with the corresponding self-propulsion point, plays a more significant role in terms of thrust variation at low h/T ratios. A more detailed analysis of these aspects is provided below.

3.1.1 Condition $h/T = 2.67$

In this condition, the asymmetries between the port and starboard sides are not very pronounced. The thrust ratio increases with higher rudder deflections on both the port and starboard sides, except for an initial plateau in the starboard propulsion system up to $\delta = 20^\circ$. Similar CFD results were found by Guo and Zou (2021), where a twin-propeller, twin-rudder vessel, with rudders positioned off-centre relative to the propeller disk, was tested in straight motion at various rudder angles up to $30°$ in deep water. At a rudder angle of $58°$, the thrust ratio reaches a maximum of approximately 1.30 on the starboard side and around 1.25 on the port side. This difference may be also attributed to the asymmetry of the rudders deflection kinematic. The speed parameter has a minor influence on the thrust ratio, leading only to small variations up to $5\,\%$ on portside, within the tested range, at the highest rudder angles without significantly altering the overall trend.

3.1.2 Condition $h/T = 1.75$

In this condition, the asymmetries between the port and starboard sides are more pronounced, than in the previous condition. The thrust ratio on the starboard side constantly increases with higher rudder deflections, whereas the thrust ratio on the port side initially decreases before increasing again at higher deflection angles. The starboard thrust ratio is consistently higher than the port thrust ratio, reaching a maximum of approximately 1.30 at $\delta = 58^\circ$, while the port thrust ratio reaches a maximum of approximately 1.15, among the considered scenarios. Velocity plays a more significant role in varying the thrust ratio on the port side, causing variations from $5\,\%$ to approximately $10\,\%$ within the tested range, while its influence remains negligible for the starboard propulsion system.

Notably, higher velocities lead to lower thrust ratio on the port side.

3.1.3 Condition $h/T = 1.25$

Considering both scenarios with $h/T = 1.25$, the thrust ratio on the starboard side constantly increases with higher rudder deflections, whereas the thrust ratio on the port side initially decreases before increasing again at higher deflection angles, more pronounced than in the previous condition. The starboard thrust ratio is consistently higher than the port thrust ratio, reaching a maximum of approximately 1.35 at $\delta = 58^\circ$, while the port thrust ratio reaches a maximum of approximately 1.10, among the considered scenarios. In this case, velocity plays a significant role for both the port and starboard thrust ratio, causing variations that can reach approximately $10\,\%$ for both within the tested range.

Notably, at higher velocities, the thrust ratio decreases on both the port and starboard sides for the condition of T = 0.255 m (subfigure b), whereas the opposite occurs in the condition T = 0.182 m (subfigure c).

3.2 WAKE ANALYSIS

From Figure 4, it can be observed that the behavior of the wake ratio $(1 - w_{\mathsf{P}\delta})/(1 - w_{\mathsf{P}0})$ inversely reflects the thrust ratio trends shown in Figure 3. This is also one direct consequence of the method used to derive the wake fractions. Nevertheless, the resulting ratios provide valuable insights for evaluating the propeller inflow under different operating conditions at different rudder angles.

It is noted that, in all the scenarios tested, the wake ratio reaches a minimum at the highest rudder deflections. The starboard side exhibits a more pronounced decrease in wake ratio at lower h/T ratios compared to the port side. The velocity, together with the corresponding self-propulsion point, plays a more significant role in terms of wake variation at low h/T ratios. Additionally, the rudder angle has different effects depending on the h/T ratio. A more detailed analysis of these aspects is provided below.

3.2.1 Condition $h/T = 2.67$

The wake ratio varies smoothly and almost symmetrically between the port and starboard sides. However, it decreases with higher rudder deflections on both the port and starboard sides, except for an initial plateau in the starboard propulsion system up to $\delta = 20^\circ$. This may suggest that the flow is being slowed down. In this case, the rudders might act as a barrier that

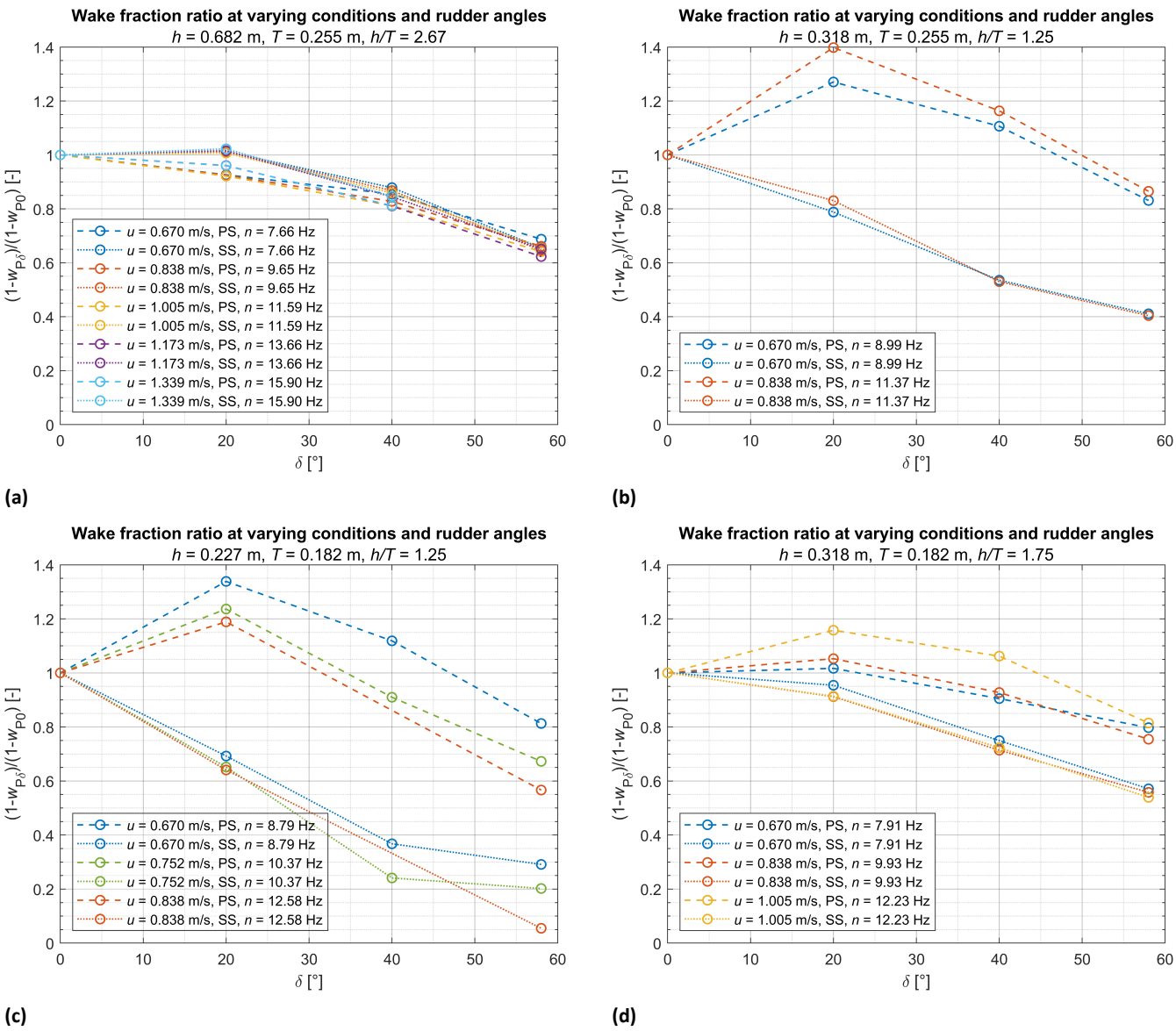

Figure 4: **Ratio of the complement of the wake fraction with deflected rudders to the complement of the wake fraction in the neutral rudders angle across various loading conditions, water depths, and speeds. Port (PS) and starboard (SS) ratios are shown separately. Rudder deflections are toward the port side.**

obstructs the passage of the flow, creating a sort of blockage effect. Nevertheless, the flow remains free to pass beneath, through and along the sides of the rudders. At a rudder angle of $58°$, the wake ratio reaches a minimum of approximately 0.65 on both port and starboard side. The speed parameter has a minor influence on the thrust ratio, leading only to small variations.

3.2.2 Condition $h/T = 1.75$

In this condition, asymmetries emerge between the port and starboard ratios, falling between the cases with $h/T = 2.67$ and $h/T = 1.25$. The wake ratio on the starboard side constantly decreases with higher rudder deflections, whereas the wake ratio on the port side initially increases before decreasing again at higher deflection angles. The starboard ratio is consistently lower than the port ratio, reaching a minimum of approximately 0.55, while the port ratio reaches a minimum of approximately 0.80 at $\delta = 58°$, among the considered scenarios. Velocity plays a more significant role in the propulsion system on the port side, causing variations of up to approximately $15\,\%$ within the tested range, while its influence remains negligible for the starboard propulsion system. Notably, higher velocities lead to higher wake ratio on the port side, suggesting a reduced blockage effect, with reference to the same scenario, but lower velocities.

The difference between the port and starboard sides indicates that shallow water effects cannot be neglected. Considering

that the rudder deflections occur to the port side, it appears that the port side propulsion system benefits from the rudder deflection in that direction, experiencing less flow reduction. However, a more detailed analysis of the flow dynamics is needed to fully understand the differences in behavior between the port and starboard sides. The smaller clearence between bottom of the basin and rudders may prevent the flow from passing directly beneath the rudders, potentially forcing it to seek escape routes through and along the sides instead.

3.2.3 Condition $h/T = 1.25$

The wake ratio on the starboard side consistently decreases with higher rudder deflections, whereas on the port side, it initially increases before decreasing again at higher deflection angles, a trend more pronounced than in the previous condition. The starboard wake ratio remains consistently lower than the port ratio, reaching minimum values that vary with speed, ranging approximately between 0.30 and 0.05 for the condition with T = 0.182 m and around 0.40 for the condition with T = 0.255 m, at $\delta = 58^\circ$ among the considered scenarios. Conversely, the port wake ratio reaches minimum values ranging between approximately 0.85 and 0.55 for T = 0.182 m and around 0.85 for T = 0.255 m at $\delta = 58^\circ$ among the considered scenarios.

For the case of T = 0.182 m (subfigure c), velocity plays a significant role for both the port and starboard propulsion systems, causing variations of up to approximately $25\,\%$ within the tested range. For the case of T = 0.255 m (subfigure b), velocity influences the port side, causing variations of up to about $15\,\%$, while its effect remains negligible on the starboard side. Despite the impact on thrust, the wake exhibits a nonlinear relationship with thrust, as described by the thrust identity method.

As explained in the previous condition, the difference between the port and starboard sides indicates that shallow water effects and speeds dependence cannot be neglected.

4 CONCLUSION

Studies of inland vessel manoeuvrability have remained limited, with many mathematical models and approaches derived from the maritime field, despite the significant differences between seagoing and inland vessels, not only in terms of design but also in terms of the environment in which they sail. In particular, wake modelling in manoeuvring simulations has been developed for single-propeller, single-rudder ships in deep water. The formulations assumes that wake variations occur solely due to the vessel's kinematics (drift and yaw). Direct propeller-rudder interactions are not explicitly modeled but are instead partly incorporated indirectly through rudder interaction coefficients rather than being represented as an explicit change in wake characteristics. Multi-rudder and multi-propeller configurations, typical of inland vessels, require a more tailored approach to account for asymmetries between port and starboard sides, especially in confined waters and at different speeds.

Starting from the evidence of this missing link, this study has investigated the effects of rudder deflection angle on thrust and wake field under different scenarios, including varying speeds, loading conditions, and water depths, particularly considering shallow water effects. By means of an experimental campaign on an inland model ship equipped with two ducted propellers and four rudders, thrust measurements were collected, and the wake fractions were identified through the thrust identity method. Results have been provided in the form of the thrust ratio between the thrust with deflected rudders and the thrust in the neutral rudder condition, and the wake ratio, defined as the ratio of the complement of the wake fraction $(1-w)$ with deflected rudders to the complement of the wake fraction with neutral rudders, depending on the scenario.

Key findings indicate that high rudder deflections lead to increased thrust and reduced flow, with notable asymmetries between the port and starboard sides becoming more pronounced as the h/T ratio decreases and speed varies. Specifically, at a rudder deflection of 58°, the thrust ratio reaches approximately 1.30 on the starboard side and around 1.25 on the port side in deeper water conditions ($h/T = 2.67$). However, in shallower conditions ($h/T = 1.25$), the starboard thrust ratio reaches 1.35, whereas the port side remains lower at approximately 1.10. Additionally, wake ratios exhibit a significant reduction at high rudder angles of 58°, decreasing to approximately 0.65 at $h/T = 2.67$ for both port and starboard sides, and dropping as low as 0.05 at $h/T = 1.25$, while the port side follows a less pronounced decline. Speed plays a significant role in these interactions, particularly at lower h/T ratios. It can change thrust ratio up to about $10\,\%$ and the wake ratio up to about $25\,\%$, depending on the scenario.

By introducing the wake ratio parameter, it becomes possible to account for asymmetry between the port and starboard propulsion systems due to rudder deflections during manoeuvring, even in shallow water. However, to effectively integrate this parameter into current manoeuvring prediction models, a new modelling approach is required. In existing manoeuvring models, the mutual influence between the rudder and propellers is partially incorporated through rudder interaction coefficients, commonly referred to as steering resistance deduction factors. These models, however, were developed under deep-water assumptions for single-propeller, single-rudder seagoing ships, thereby neglecting the potential asymmetry

between port and starboard steering and propulsion systems (Yasukawa and Yoshimura 2015; *Report of Research committee on standardization of mathematical model for ship maneuvering predictions [P-29]* 2012). Recent developments have attempted to account for asymmetry in multiple-propeller and multiple-rudder configurations. Nevertheless, the lack of sufficient data and reliable methods for estimating the behavior of port and starboard interactions often leads to the assumption of symmetry between the two sides, as done, for example, by Liu et al. (2017).

The present study highlights the need to reassess traditional maritime-derived approaches and promote the development of methodologies that better account for the differences between inland and seagoing vessels and environments. As Richard Feynman described in *The Feynman Lectures on Physics (Vol. 1, Chapter 2)*, science progresses by approximating reality, continuously refining its models to enhance understanding.

As a future development, it would be beneficial to experiment with various inland vessel configurations, ranging from single-propeller, single-rudder designs to multi-propeller, multi-rudder setups, while considering shallow water effects. This would provide a more comprehensive understanding of the variations in thrust and wake under these conditions. Additionally, the development of a new mathematical modeling framework is essential to properly integrate the updated wake modeling. Future studies should also focus on further refining the interactions between the hull, propeller, and rudder, specifically tailored to inland vessels and the unique environmental constraints in which they operate.

5 ACKNOWLEDGEMENTS

Special thanks to Nathalie Reinach for rendering the model and designing the schematic representation of the rudder deflection logic.

6 REFERENCES

Guo, H. and Z. Zou, 2021. A RANS-based study of the impact of rudder on the propeller characteristics for a twin-screw ship during maneuvers. In: Ocean Engineering 239.

Hirano, M., 1980. A practical calculation method of ship maneuvering motion at initial design stage. In: Journal of The Society of Naval Architects of Japan 147, pp. 68–80.

Liu, J., R. Hekkenberg, F. Quadvlieg, H. Hopman, and B. Zhao, 2017. An integrated empirical manoeuvring model for inland vessels. In: Ocean Engineering 137, pp. 287–308.

Report of Research committee on standardization of mathematical model for ship maneuvering predictions [P-29] 2012. Tech. rep. Japan Society of Naval Architects and Ocean Engineers (in Japanese).

Sukas, O. F., O. K. Kinaci, and S. Bal, 2019. Theoretical background and application of MANSIM for ship maneuvering simulations. In: Ocean Engineering 192.

Yasukawa, H. and Y. Yoshimura, 2015. Introduction of MMG standard method for ship maneuvering predictions. In: Journal of Marine Science and Technology 20, pp. 37–52.

7 AUTHORS BIOGRAPHY

Justin Jasa* is a researcher at the Development Centre for Ship Technology and Transport Systems (DST) in Germany, specialising in experimental investigations in ship hydrodynamics, fleet greening, and emission reduction. He holds a master's degree in Naval Architecture and Marine Engineering from the University of Trieste, Italy. Passionate about programming, he develops custom codes and tools to simulate processes, such as ship manoeuvrability, and to optimise engineering workflows.

Matthias Tenzer holds a diploma degree in naval architecture and marine engineering obtained in 2011 at the University of Duisburg-Essen. Afterwards he worked for five years as a researcher at the Institute of Ship Technology and Transport Systems. Since 2016 he is working at the Development Centre for Ship Technology and Transport Systems where he is responsible for ship manoeuvring related topics and the ship handling simulator SANDRA II. His previous experience includes experimental as well as numerical investigations in the field of ship hydrodynamics.

Benjamin Friedhoff studied naval architecture at the University of Duisburg-Essen, where he subsequently worked for three years as a researcher. In 2008 he changed to the Development Centre for Ship Technology and Transport Systems - DST, where he worked on a wide range of research topics in the fields of hydrodynamics and renewable energies. Since 2014 he is head of the Hydrodynamics Department and has worked on various greening projects, including alternative energy carriers and zero-emission ships. As part of the restructuring of the DST, his department was renamed "Experiments, Fleet Modernisation and Emissions" in January 2020 taking account of current societal challenges.

* Corresponding author. E-mail address: jasa@dst-org.de

NUMERICAL STUDY ON THE RUDDER INFLOW BEHIND THE HULL AND THE PROPELLER IN FOUR QUADRANTS

Suli Lu, Ships and Marine Technology, Ghent University, Belgium, Suli.Lu@UGent.be
Wim Van Hoydonck, Flanders Hydraulics, Belgium
Santiago Lopez Castaño, Flanders Hydraulics, Belgium
Evert Lataire, Ships and Marine Technology, Ghent University, Belgium
Guillaume Delefortrie, Ships and Marine Technology, Ghent University, Belgium

NUMERICAL STUDY ON THE RUDDER INFLOW BEHIND THE HULL AND THE PROPELLER IN FOUR QUADRANTS

SULI LU*, SHIPS AND MARINE TECHNOLOGY, GHENT UNIVERSITY, BELGIUM, SULI.LU@UGENT.BE
WIM VAN HOYDONCK, FLANDERS HYDRAULICS, BELGIUM
SANTIAGO LOPEZ CASTAÑO, FLANDERS HYDRAULICS, BELGIUM
EVERT LATAIRE, SHIPS AND MARINE TECHNOLOGY, GHENT UNIVERSITY, BELGIUM
GUILLAUME DELEFORTRIE, SHIPS AND MARINE TECHNOLOGY, GHENT UNIVERSITY, BELGIUM

SUMMARY

The inflow to the rudder behind the hull and the propeller in four quadrants is studied numerically by CFD (Computational Fluid Dynamics) with the KCS benchmark ship. The HPR (Hull-Propeller-Rudder) interactions without the free surface effect in all four quadrants are investigated and the inflow to the rudder is analysed. Rudder inflow velocities are extracted to compare the impact of propeller loadings in different quadrants, and vortex structures around the rudder are visualised to show the flow field coherence. Overall, this study provides a view into rudder hydrodynamics in four quadrants, and CFD simulations of the rudder behind the hull and the propeller under different direction combinations of the ship velocity and the propeller rate present a quantitative description of rudder inflow variations.

NOMENCLATURE

CFD	Computational Fluid Dynamics
DDES	Delayed Detached Eddy Simulation
EFD	Experimental Fluid Dynamics
HPR	Hull-Propeller-Rudder
LES	Large Eddy Simulation
RANS	Reynolds-Averaged Navier-Stokes

$(P/D)_{0.7\mathrm{R}}$	Propeller pitch ratio at 70% propeller radius	-
$A_{\mathrm{E}}/A_{\mathrm{O}}$	Propeller area ratio	-
A_{R}	Rudder lateral area	m^2
B	Ship beam	m
c_{m}	Rudder mean chord length	m
C_P	Pressure resistance coefficient	-
$C_{T,\mathrm{DB}}$	Total resistance coefficient of double-body hull	-
C_V	Viscous resistance coefficient	-
D	Drag force	N
D_{P}	Propeller diameter	m
Fr	Froude number	-
K_Q	Torque coefficient	-
K_T	Thrust coefficient	-
L	Lift force	N
L_{PP}	Ship length between perpendiculars	m
n	Propeller rate	rps
Q'	Dimensionless Q-criterion	-
T	Ship draft	m
u	Longitudinal ship velocity	$\mathrm{m\,s^{-1}}$
u_x	Velocity component along x axis	$\mathrm{m\,s^{-1}}$
u_y	Velocity component along y axis	$\mathrm{m\,s^{-1}}$
u_z	Velocity component along z axis	$\mathrm{m\,s^{-1}}$
$\vec{U}$	Velocity vector	$\mathrm{m\,s^{-1}}$
Λ_{G}	Rudder geometric aspect ratio	-
δ	Rudder angle	°
λ	Scale ratio	-

1 INTRODUCTION

For conventional ships equipped with propellers and rudders, harbour manoeuvres require adequate propulsion and steering capabilities. Different scenarios such as sailing forward and backward, together with the propeller rotating ahead and astern, lead to the four quadrants motions of a ship. The combination of the hull wake and the propeller jet constitutes the rudder inflow that affects rudder performance during manoeuvres, and the resulting stern flow has a significant impact on the rudder hydrodynamic performance. Using the directions of the ship's longitudinal speed u and the propeller rate n, the four quadrants motions of the ship can be defined as:

- Quadrant 1 (Q1): $u > 0 \wedge n > 0$,
- Quadrant 2 (Q2): $u > 0 \wedge n < 0$,
- Quadrant 3 (Q3): $u < 0 \wedge n < 0$,
- Quadrant 4 (Q4): $u < 0 \wedge n > 0$.

For the open water rudder, Van Hoydonck et al. (2018) simulate the full-scale KCS rudder numerically and obtain the rudder force in the $[-180^\circ, 180^\circ]$ range. Considering the propeller impact on rudder hydrodynamics, Molland and Turnock (1993) test propeller-rudder interactions in the wind tunnel. The rudder force variations and pressure distributions on the rudder surface are measured in four quadrants. Hu et al. (2019) investigate the effect of the propeller tip vortex on the rudder by LES (Large Eddy Simulation), and a strong periodicity of the pressure fluctuation is presented on the rudder surface. In addition, numerical simulations on the propeller-rudder configuration are also executed to obtain lift and drag forces of the rudder with different deflections in Q1 (Lu et al. 2022) and in bollard pull conditions (Villa et al. 2018).

The rudder inflow becomes complex under hull-propeller-rudder interactions, and four quadrants variations make the stern flow even more complicated especially when the propeller characteristics are highly unstable in Q2/Q4. LES simulations in Q2 from Jang and Mahesh (2013) show the vortex ring around the propeller changing violently over time, which brings challenges for rudder inflow predictions. From the perspective of manoeuvring modelling, Delefortrie, Wim Van Hoydonck, and Eloot (2022) formulate rudder inflow expressions in four quadrants based on momentum theory. The proposed mathematical manoeuvring model has introduced coeffcients that need to be determined by a significant amount of model tests and dedicated regression analysis. The utilization of numerical techniques can possibly enhance the model, while the related rudder inflow study in literature is limited. Jin et al. (2023) compare two propeller modelling methods for the KCS self-propulsion without the rudder in Q1, and show that the real propeller modelling gives more accurate downstream axial velocity distributions than the body force method. Verma, Jang, and Mahesh (2012) simulate a propeller in reverse rotation behind the hull and find that the hull-propeller interactions under high negative advance ratios make the vortex ring closer to the blades.

Following this introduction, computation details of numerical simulations are described in Section 2. After the convergence study in Section 3, the four quadrants simulation results are analysed in Section 4, and conclusions are presented in Section 5.

2 COMPUTATION DETAILS

The model scale KCS benchmark ship with the scale ratio of $1/31.6$ is studied in this paper. The KP505 propeller and the NACA 0018 based semi-balanced rudder are equipped on the ship for HPR interaction simulations. Geometrical details of the KCS ship are shown in Table 1. The KP505 propeller has five blades and rotates right-handed when the propeller rate is positive. The semi-balanced rudder is composed of two parts, i.e. the horn that is fixed to the hull body and the blade that can rotate with respect to the rudder stock. Only the zero angle condition is investigated in this study.

Table 1: Main particulars of the KCS hull, propeller, and rudder.

Hull		Propeller		Rudder	
Particular	Value	Particular	Value	Particular	Value
$L_{\mathsf{PP}}(m)$	7.278	$D_{\mathsf{P}}(m)$	0.250	$c_{\mathsf{m}}(m)$	0.174
$B(m)$	1.109	$A_{\mathsf{E}}/A_{\mathsf{O}}(-)$	0.448	$\Lambda_{\mathsf{G}}(-)$	1.799
$T(m)$	0.342	$(P/D)_{0.7\mathsf{R}}(-)$	1.000	$A_{\mathsf{R}}(m^2)$	0.054
$\lambda(-)$	1/31.6	$\lambda(-)$	1/31.6	$\lambda(-)$	1/31.6

The computation domain of the HPR interaction simulation with the positive inflow velocity is shown in Figure 1. A double-body hull is used. The computation domain extends $3L_{\mathsf{PP}}$ upstream and $4.16L_{\mathsf{PP}}$ downstream, and the lateral distance is $2.25L_{\mathsf{PP}}$. The domain top is at the same level as the design waterline of the model scale KCS, and the bottom is set as $2.20L_{\mathsf{PP}}$ from the

ship bottom. For cases with $u < 0$, the upstream and the downstream directions are reversed compared with $u > 0$, while the extension distances are kept the same.

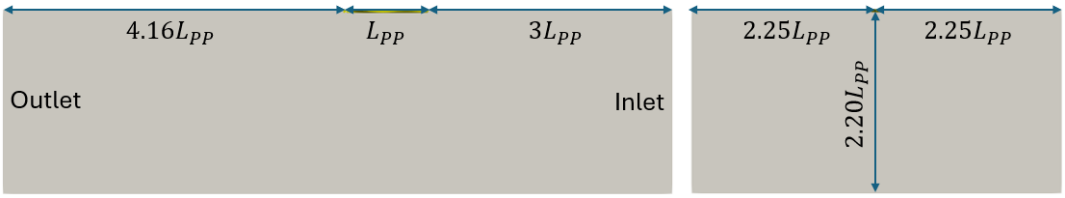

Figure 1: Computation domain of the HPR interaction simulation in Q1/Q2.

The propeller rotation is simulated by the sliding mesh method, and a cylindrical Arbitrary Mesh Interface (AMI) is built around the propeller for the flow field information exchange between the static and the rotating domain. Due to the constrained space between the hull and the rudder, the AMI cylinder has a $1.12D_P$ diameter and a $0.34D_P$ height.

Considering the relative direction of the inflow and the propeller jet, HPR interaction simulations in four quadrants can be classified into two types. In Q1/Q3, the inflow and the jet evolve in the same direction, while in Q2/Q4 the two are opposite. For the current research, DDES (Delayed Detached Eddy Simulation) is applied to capture massive flow separations in Q2/Q4, and RANS (Reynolds-Averaged Navier-Stokes) is applied in Q1/Q3 to lighten the computational burden. The open-source software package OpenFOAM v2206 is used for numerical simulations, and the pimpleFoam solver is applied. The pressure-velocity coupling is implemented with the PIMPLE algorithm, and the numerical schemes applied are shown in Table 2.

Table 2: Numerical schemes applied in RANS and DDES simulations.

Scheme		Setting
Time	$\frac{\partial \phi}{\partial t}$	CrankNicolson 0.9
Gradient	∇p	cellLimited Gauss linear 0.5
	$\nabla \vec{U}$	cellLimited Gauss linear 1
	∇k	cellLimited Gauss linear 1
	$\nabla \omega$	cellLimited Gauss linear 1
Convection	$\nabla \cdot (\vec{U}\vec{U})$	Gauss linearUpwind grad(U)
	$\nabla \cdot (\vec{U}k)$	Gauss limitedLinear 1
	$\nabla \cdot (\vec{U}\omega)$	Gauss limitedLinear 1
	$\nabla \cdot \nu(\nabla \vec{U})^T$	Gauss linear
Laplacian		Gauss linear limited 0.5
Interpolation		linear
Surface-normal gradient		limited 0.5

3 CONVERGENCE STUDY

A convergence study with the bare KCS hull is conducted to obtain an appropriate mesh size around the double-body hull. Wall functions are used, and the target y^+ is set to 50. Three meshes with a relative refinement ratio of $\sqrt{2}$ are generated with snappyHexMesh. The boundary layer mesh settings for three meshes are kept the same. The viscous resistance coefficient C_V obtained from the simulations is compared with the ITTC 1957 formula in Table 3, and deviations from three cases are all smaller than 3%. The numerical uncertainty is estimated with Grid Convergence Index (GCI) method from Celik et al. (2008), as shown in Table 4. Monotonic convergence is achieved for both C_V and C_P, and the medium mesh sizes are used in the remainder of this study.

Table 3: Comparison of the resistance coefficients from meshes with different refinement ratios.

Mesh	Number of cells $(-)$	$C_V(-)$	$C_P(-)$	C_V Error $(-)$
Coarse	$814\,036$	2.942×10^{-3}	2.741×10^{-4}	0.67%
Medium	$1\,882\,360$	2.928×10^{-3}	2.868×10^{-4}	1.52%
Fine	$4\,607\,171$	2.903×10^{-3}	2.069×10^{-4}	2.02%

Table 4: Uncertainty estimation of the resistance coefficients from meshes with different refinement ratios.

	$C_V(-)$	$C_P(-)$
ϵ_{21}	-1.452×10^{-5}	1.273×10^{-5}
ϵ_{32}	-2.441×10^{-5}	2.009×10^{-5}
$\epsilon_{21}/\epsilon_{32}$	0.595	0.634
Convergence	Monotonic	Monotonic
p	2.030	1.811
$U_{G_{21}}$	1.482×10^{-3}	1.620×10^{-2}
$U_{G_{32}}$	2.730×10^{-3}	2.657×10^{-2}

With the medium size mesh around the hull, the mesh for the self-propulsion validation in Q1 is generated, as shown in Figure 2. The rudder is omitted to be consistent with the hull-propeller configuration in the experiment (Hino et al. 2021), and regions close to the propeller are refined to capture the stern flow. The time step independence study is conducted with three time steps, i.e. $\Delta t = 1.462 \times 10^{-4}s$, $2.060 \times 10^{-4}s$, and $2.924 \times 10^{-4}s$, which correspond to the time propeller rotates 0.5°, 0.707°, and 1° respectively. The first order numerical schemes are applied for the time independence study. As shown in Table 5, no significant changes are observed for obtained force coefficients of the hull and the propeller. Therefore, $\Delta t = 2.924 \times 10^{-4}s$ is applied for following hull-propeller-rudder simulations.

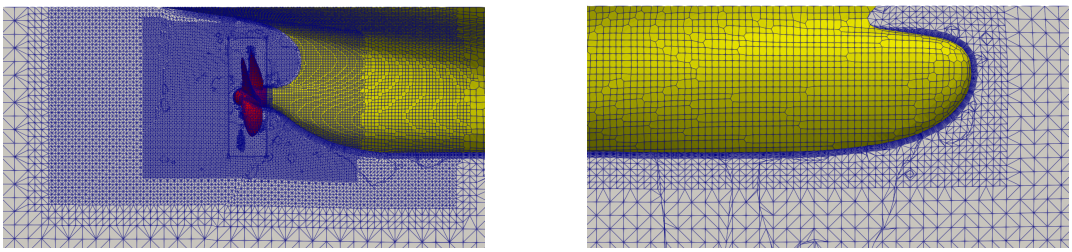

Figure 2: Mesh in the self-propulsion case.

Table 5: Comparison of the self-propulsion results from different time steps.

$\Delta t(s)$	$\Delta\theta(^\circ)$	$C_{T,\mathsf{DB}}(-)$	$K_T(-)$	$10K_Q(-)$
1.462×10^{-4}	0.5	3.651×10^{-3}	0.174	0.368
2.060×10^{-4}	0.707	3.620×10^{-3}	0.173	0.362
2.924×10^{-4}	1.0	3.594×10^{-3}	0.172	0.362

4 RESULTS AND DISCUSSIONS

4.1 VALIDATION IN Q1

To validate the numerical method, the self-propulsion point in Q1 under the design speed $Fr = 0.26$ is simulated. The propeller rate is set as $n = 9.5rps$, which is the same as the value from the model test (Hino et al. 2021). The self-propulsion simulation is conducted with the first order numerical schemes for $t = 0 \sim 6s$ to speed up the computation, get converged results, and then switched to the numerical schemes in Table 2.

The double-body self-propulsion result is compared with the experimental data in Table 6. Both the thrust and torque coefficients are overestimated, with 3.91% in K_T and 28.09% in $10K_Q$ deviating from the experiment. The large deviation in $10K_Q$ is possibly caused by the treatment of the viscous components, and will be carefully investigated in future research. Regarding the momentum prediction that correlates with the velocity field, the distribution of the axial velocity u_x downstream of the propeller at $x/L_{\mathsf{PP}} = 0.0089$ is compared with the EFD (Experimental Fluid Dynamics) data, as shown in Figure 3. The u_x distribution from CFD shows accelerated velocities inside the propeller plane like EFD, and the gradual u_x changes with hook-shaped isolines are observed in both contours.

Table 6: Comparison of the double-body self-propulsion simulation result with the experimental data.

	CFD		EFD		Error	
$C_{T,\mathrm{DB}}(-)$	$KT(-)$	$10K_Q(-)$	$KT(-)$	$10K_Q(-)$	$KT(-)$	$10K_Q(-)$
3.566×10^{-3}	0.177	0.369	0.170	0.288	3.91%	28.09%

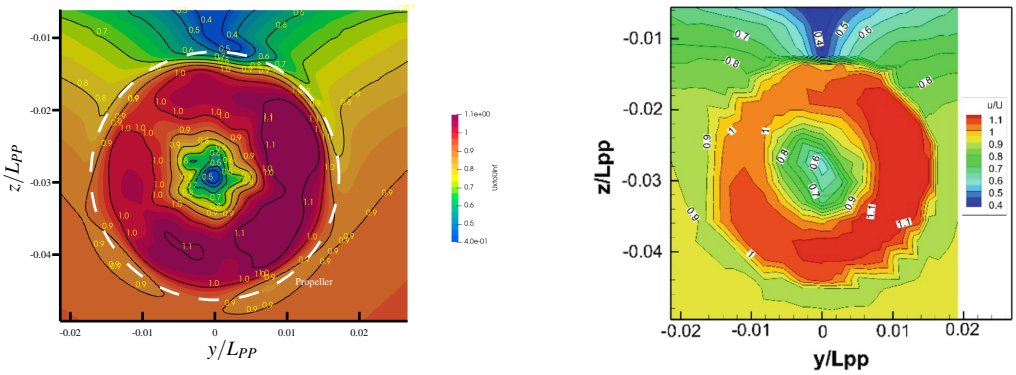

(a) CFD

(b) EFD, NMRI (Hino et al. 2021)

Figure 3: Comparison of the axial velocity distribution in the self-propulsion case at $x/L_{\mathrm{PP}} = 0.0089$ from CFD and EFD.

4.2 VORTEX STRUCTURES IN FOUR QUADRANTS

Vortex structures around the ship are visualized by the isosurface of the dimensionless Q-criterion Q':

$$Q' = \frac{Q_{cri}}{||\nabla \vec{U}||}, \tag{1}$$

where Q_{cri} is the Q-criterion for vortex visualizations, and $\vec{U}$ is the velocity vector, which can be expressed as:

$$\vec{U} = (u_x, u_y, u_z), \tag{2}$$

where u_x, u_y, u_z are velocity components along x, y, and z direction. Vortex structures in four quadrants are shown in Figure 4 with $|Fr| = 0.028$ and Figure 5 with $|Fr| = 0.26$. The simulation time for Q1/Q3 cases is 16.84 s (160 propeller revolutions) and for Q2/Q4 cases is extended to 26.32 s (250 propeller revolutions) to evaluate the highly unstable flow field from a longer time scale. u_x is made dimensionless by the positive inflow velocity value in Q1/Q2 for four quadrants cases. In Figure 4.(a), the hull wake is accelerated by the propeller in Q1. Under higher inflow velocity in Figure 5.(a), the acceleration ratio of u_x decreases, and the break-up of the tip vortices downstream the rudder becomes less significant. For the Q3 case in Figure 4.(c), the inflow towards the bow is accelerated by the reverse rotating propeller, leaving the rudder out of the propeller jet impact and facing the astern inflow. The propeller jet evolves along the hull length and gradually dissipates after interacting with the hull. The rudder under the lighter loading in Figure 5.(c) is also positioned in the astern flow, and the propeller jet dissipates faster than Figure 4.(c). Due to the opposite relative direction of the inflow and the propeller jet, vortex structures in Q2 and Q4 show more chaotic states than Q1 and Q3. In Figure 4.(b), the reverse rotation pushes the flow upstream as the inflow goes downstream, indicating that the propeller jet dominates the stern flow when $|Fr| = 0.028$. In contrast, the intensified uniform inflow in Figure 5.(b) moves the propeller jet downstream and then impacts the rudder along the whole span length. A similar shift of the dominant flow from the propeller jet to the inflow in Q4 occurs from Figure 4.(d) to Figure 5.(d).

4.3 AXIAL VELOCITY DISTRIBUTIONS IN FOUR QUADRANTS

The axial velocity distributions near the rudder under $|Fr| = 0.028$ and $|Fr| = 0.26$ in Q1/Q3 are shown in Figure 6 and Figure 7, and the projections of the propeller disk plane and the rudder outline are denoted as dashed lines. One xoz and two yoz planes are extracted to show the flow around the rudder. The Q1 case in Figure 6.(a) shows the high velocity regions affected by the tip vortex and the blocked region between the hub and the rudder leading edge. The rudder experiences the accelerated flow along a portion of the span that is approximately on the same height level of the propeller plane. The accelerated flow upstream is wrapped by the projected propeller plane in Figure 6.(b), and the flow deforms after interacting with rudder as shown in Figure 6.(c). The Q1 case with a larger $|Fr|$ in Figure 7 shows similar u_x distributions but smaller u_x/u. The Q3 cases accelerate the flow towards the hull, so most part of the rudder is not in the downstream propeller

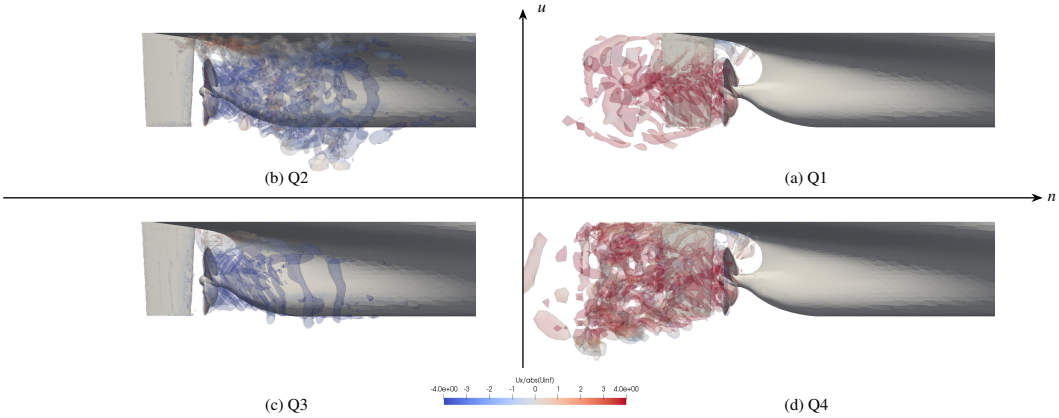

Figure 4: **Isosurface of $Q' = 4$ around the ship in four quadrants with $|Fr| = 0.028$.**

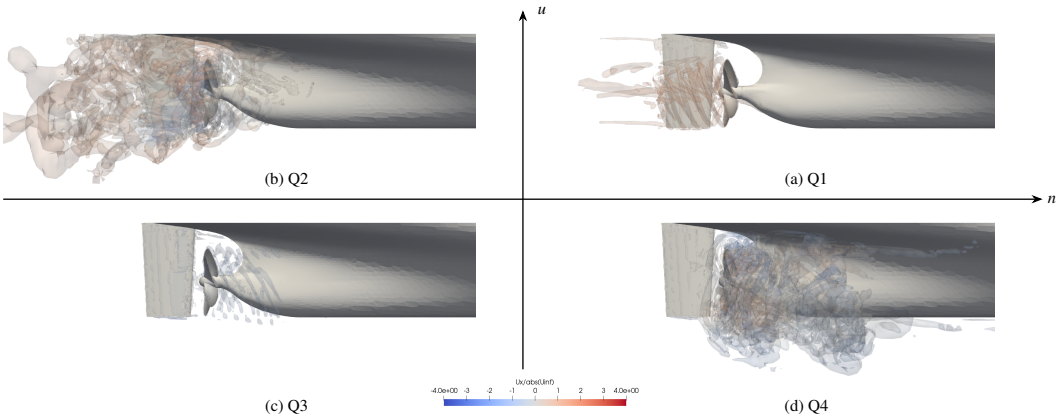

Figure 5: **Isosurface of $Q' = 4$ around the ship in four quadrants with $|Fr| = 0.26$.**

slipstream. However, the pumping effect of the propeller still increases upstream u_x in the vicinity of the rudder leading edge.

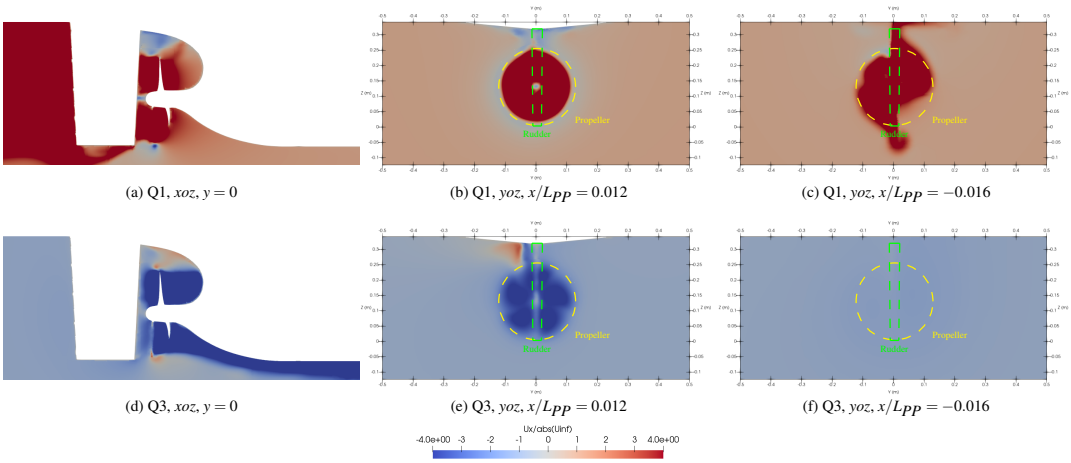

Figure 6: **The axial velocity distributions near the rudder with $|Fr| = 0.028$ in Q1/Q3.**

Figure 8 and Figure 9 show u_x distributions in Q2/Q4 under two $|Fr|$. Unlike in the Q1/Q3 cases when inflow velocity variations mainly alter the magnitude of the acceleration ratio of u_x, in Q2/Q4 the overall rudder inflow direction can also be changed due to the switch in the dominant flow. With the inflow velocity increasing, the inflow impact on the rudder in Q2 is more significant than the propeller. In Q4, especially, the propeller jet in Figure 8.(d) evolves upstream despite the reverse inflow. u_x distributions in Figure 8.(d) and (f) resemble Figure 6.(b) and (c) in Q1, while in Figure 9.(d), the acceleration is very limited.

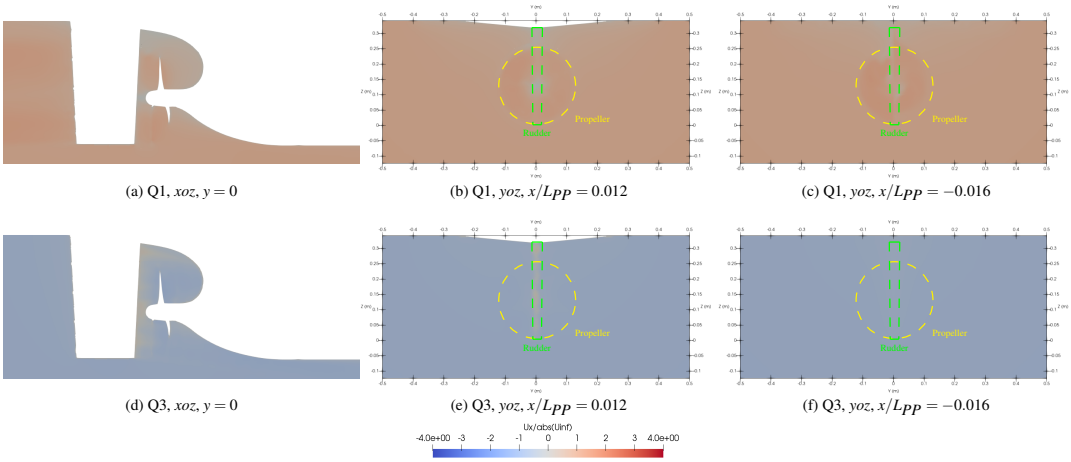

(a) Q1, xoz, $y = 0$ (b) Q1, yoz, $x/L_{PP} = 0.012$ (c) Q1, yoz, $x/L_{PP} = -0.016$

(d) Q3, xoz, $y = 0$ (e) Q3, yoz, $x/L_{PP} = 0.012$ (f) Q3, yoz, $x/L_{PP} = -0.016$

Figure 7: The axial velocity distributions near the rudder with $|Fr| = 0.26$ in Q1/Q3.

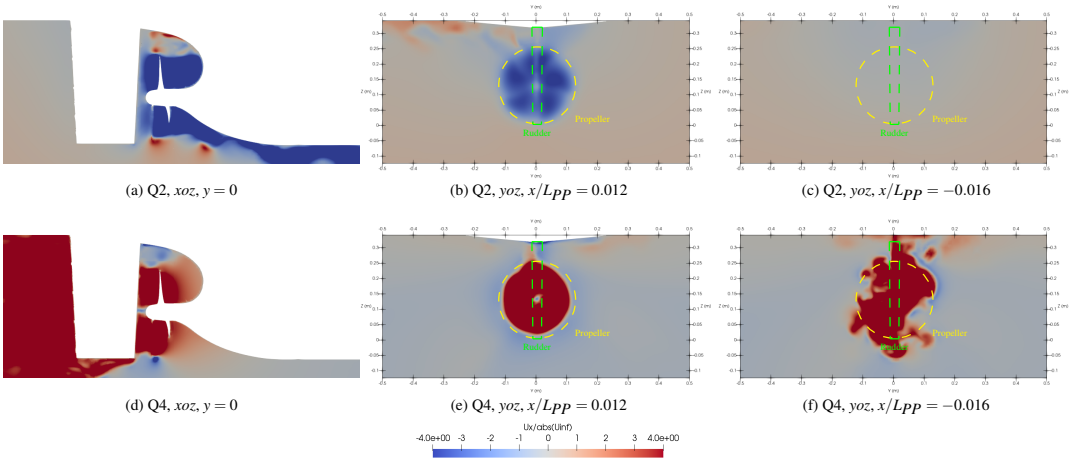

(a) Q2, xoz, $y = 0$ (b) Q2, yoz, $x/L_{PP} = 0.012$ (c) Q2, yoz, $x/L_{PP} = -0.016$

(d) Q4, xoz, $y = 0$ (e) Q4, yoz, $x/L_{PP} = 0.012$ (f) Q4, yoz, $x/L_{PP} = -0.016$

Figure 8: The axial velocity distributions near the rudder with $|Fr| = 0.028$ in Q2/Q4.

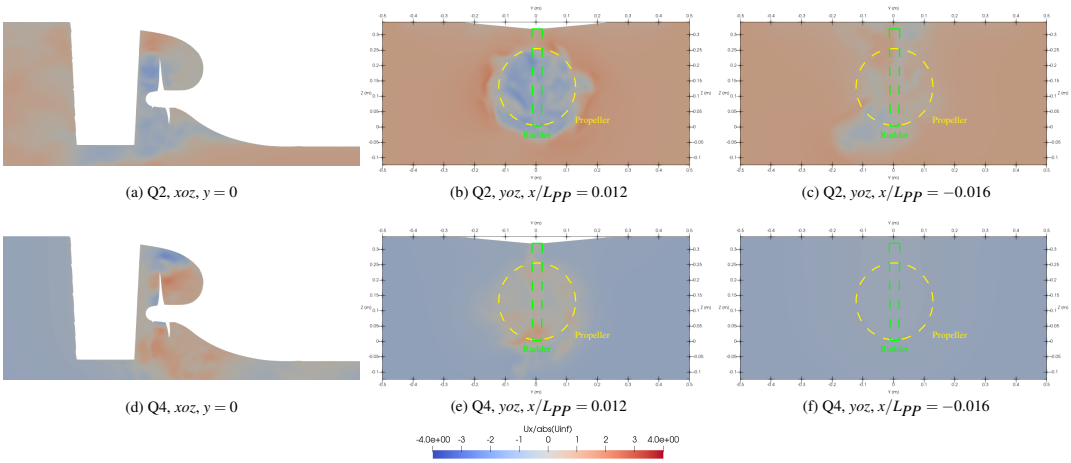

(a) Q2, xoz, $y = 0$ (b) Q2, yoz, $x/L_{PP} = 0.012$ (c) Q2, yoz, $x/L_{PP} = -0.016$

(d) Q4, xoz, $y = 0$ (e) Q4, yoz, $x/L_{PP} = 0.012$ (f) Q4, yoz, $x/L_{PP} = -0.016$

Figure 9: The axial velocity distributions near the rudder with $|Fr| = 0.26$ in Q2/Q4.

4.4 TIME HISTORIES OF THE RUDDER FORCES IN FOUR QUADRANTS

Time histories of the lift force L and drag force D of the rudder with $\delta = 0°$ under $|Fr| = 0.028$ are shown in Figure 10. L and D are calculated by summing up force components from the rudder horn and the rudder blade. L is positive to the portside of the hull, and D is positive forward. In Q1, L oscillates around a non-zero value, indicating the impact of the propeller slipstream on the lateral force of the rudder. A positive D (thrust) with a small magnitude is observed, which is caused by

the heavy propeller loading. Induced strong swirl components increase the rudder inflow angle significantly, so the direction of D changes. The rudder in Q3 with $|Fr| = 0.028$ experiences the inflow in upstream of the reverse rotating propeller, hence L is close to 0 and the direction of D is the same as the inflow. The propeller slipstream in Q2 evolves towards the upstream hull and L of the rudder downstream fluctuates around 0. A larger positive D than Q1 shows the effect of the flow acceleration downstream the propeller, as shown in Figure 8.(b). L in Q4 shows large fluctuations, which coincides with the experiment in Delefortrie, Wim Van Hoydonck, and Eloot (2022). Such drastic changes originate from the opposite motion of the inflow and the propeller jet, and the combined stern flow makes the high and the low pressure region on the rudder surface alternate rapidly. D in Q4 is more stable than L and points ahead, and the magnitude is larger than the Q1 case with the same propeller rate due to the astern inflow.

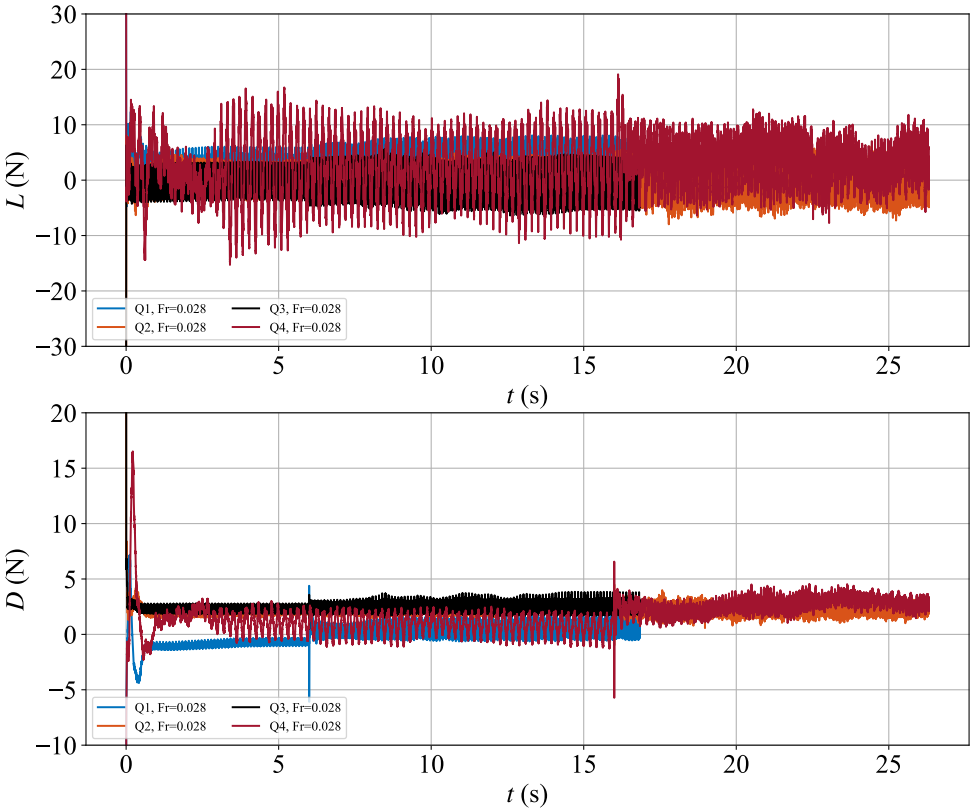

Figure 10: Time histories of the lift and drag forces of the rudder with $\delta = 0°$ under $|Fr| = 0.028$.

With the higher velocity, L and D under $|Fr| = 0.26$ are shown in Figure 11. The averaged L in Q1 is closer to 0 due to weaker swirl flows compared with Figure 10. The rudder in Q3 also has a similar L since it is mainly in the uniform astern inflow. The rudder lateral force in Q2 has more severe fluctuations than Q4 in Figure 10. Judging from the vortex structures in Figure 5.(b), the dominant inflow pushes the propeller jet downstream to the rudder, which resembles the wake pattern when the fluid flows around the bluff body. Highly unstable vortices detached from propeller blades lead to L with varied directions and magnitudes, and D is also increased. Although the interaction between the inflow and the propeller jet is also violent in Q4, the dominant inflow moves most vortex structures downstream to the hull rather than the rudder, as shown in Figure 5.(d). Hence L and D are relatively stable like Q1 and Q3.

5 CONCLUSIONS

Considering hull-propeller-rudder interactions, the rudder flow in four quadrants motions is studied in this paper. In Q1 when the inflow and the propeller jet are in the same direction, the rudder inflow upstream is accelerated and the acceleration becomes more significant under heavier loadings. As both the inflow and the propeller rate reversed, i.e. in Q3, the propeller jet evolves towards the hull and the rudder experiences astern inflow. The lift and drag forces of the rudder with $\delta = 0°$ in Q1 and Q3 inflow show small-scale oscillations, indicating relatively stable inflow conditions. In Q2 and Q4, the opposite relative directions of the inflow and the propeller jet lead to unstable flow fields around the rudder, and the rudder force oscillations are more severe. Such instability characteristics embody more on the lateral rudder force than the longitudinal. When the propeller jet concentrates near the rudder, either under the jet-dominant condition in Q4 or the inflow-dominant

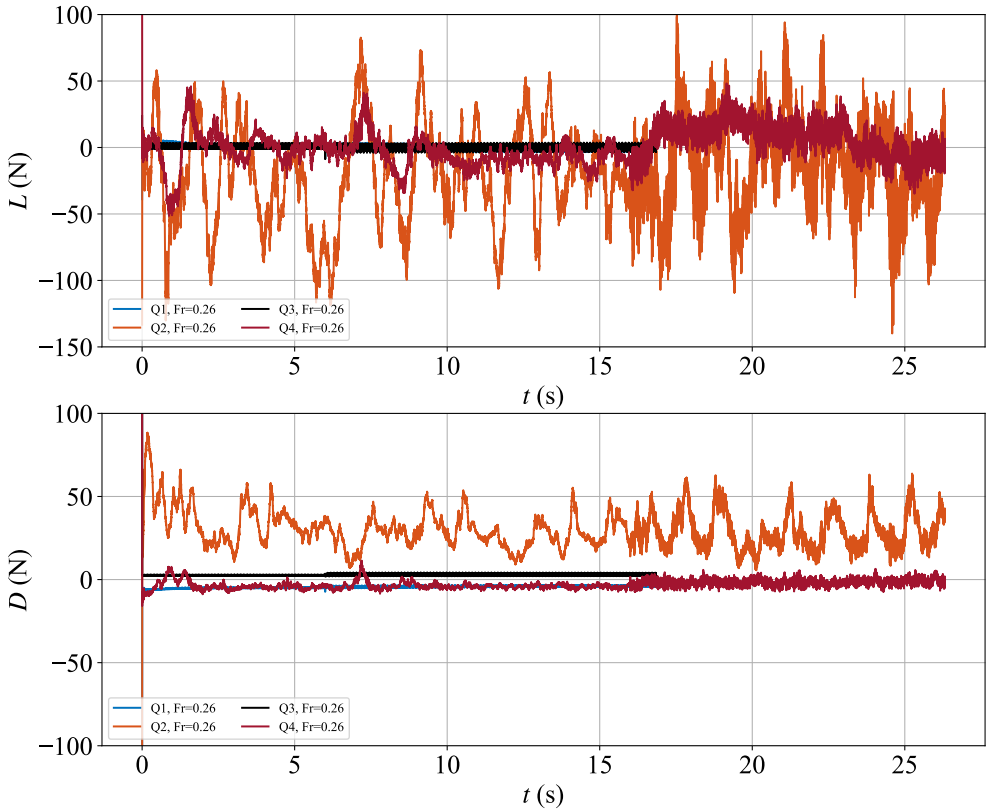

Figure 11: Time histories of the lift and drag forces of the rudder with $\delta = 0^\circ$ under $|Fr| = 0.26$.

condition in Q2, the lateral force oscillations are significant. However, as most inflow-jet interactions occur along the hull, i.e. the jet-dominant condition in Q2 or the inflow-dominant condition in Q4, the disturbances on rudder inflow can be less.

The current numerical model replaces the free surface with a symmetry plane, hence the free surface effect on the rudder inflow is not captured. The effect can be significant in the stern especially when the flow field is highly unstable in Q2 and Q4, as the free surface variation can change the rudder inflow velocity profile. Therefore, the free surface will be implemented in four quadrants conditions in the future. Besides, rudder angles covering a wider range will be investigated to show rudder force changes in four quadrants inflow conditions. The study of the hull-propeller-rudder interactions in four quadrants can quantify rudder inflow velocities, which can provide essential coefficients for ship manoeuvring modelling in four quadrants and enhance the realism of harbour manoeuvring in ship simulators.

6 ACKNOWLEDGEMENTS

The first author Suli Lu is financed by the China Scholarship Council under Grant 202206950018. The computational resources (Stevin Supercomputer Infrastructure) and services used in this work were provided by the VSC (Flemish Supercomputer Center), funded by Ghent University, FWO and the Flemish Government - department EWI.

7 REFERENCES

Celik, Ismail, Urmila Ghia, Patrick Roache, Christopher Freitas, Hugh Coleman, and Peter Raad, 2008. Procedure for estimation and reporting of uncertainty due to discretization in CFD applications. In: Journal of Fluids Engineering 130.7.

Delefortrie, Guillaume, Wim Van Hoydonck, and Katrien Eloot, 2022. Forces and Torque acting on a Rudder while Manoeuvring. In: Journal of Marine Science and Technology 27.1, pp. 383–407.

Hino, Takanori, Frederick Stern, Lars Larsson, Michel Visonneau, Nobuyuki Hirata, and Jin Kim, eds., 2021. Numerical Ship Hydrodynamics: An Assessment of the Tokyo 2015 Workshop. Vol. 94. Lecture Notes in Applied and Computational Mechanics. Springer International Publishing.

Hu, Jian, Weipeng Zhang, Shili Sun, and Chunyu Guo, 2019. Numerical simulation of Vortex–Rudder interactions behind the propeller. In: Ocean Engineering 190, p. 106446.

Jang, Hyunchul and Krishnan Mahesh, 2013. Large eddy simulation of flow around a reverse rotating propeller. In: Journal of Fluid Mechanics 729, pp. 151–179.

Jin, Shanqin, Heather Peng, Wei Qiu, Chad Oldfield, and Barton Stockdill, 2023. Best modeling practice for self-propulsion simulation of ship model in calm water. In: Physics of Fluids 35.10, p. 105129.

Lu, Suli, Xide Cheng, Jialun Liu, Shijie Li, and Hironori Yasukawa, 2022. Maneuvering modeling of a twin-propeller twin-rudder inland container vessel based on integrated CFD and empirical methods. In: Applied Ocean Research 126. Publisher: Elsevier, p. 103261.

Molland, A. F. and S. R. Turnock, 1993. Wind tunnel tests on the influence of propeller loading on ship rudder performance: four quadrant operation, low and zero speed operation. Monograph. University of Southampton.

Van Hoydonck, W, G Delefortrie, B De Maerschalck, and M Vantorre, 2018. Open-water rudder tests using CFD. In: 32nd Symposium on Naval Hydrodynamics. Hamburg, Germany.

Verma, Aman, Hyunchul Jang, and Krishnan Mahesh, 2012. The effect of an upstream hull on a propeller in reverse rotation. In: Journal of Fluid Mechanics 704, pp. 61–88.

Villa, Diego, Michele Viviani, Giorgio Tani, Stefano Gaggero, Dario Bruzzone, and Carlo Bonvino Podenzana, 2018. Numerical Evaluation of Rudder Performance Behind a Propeller in Bollard Pull Condition. In: Journal of Marine Science and Application 17.2, pp. 153–164.

8 AUTHORS BIOGRAPHY

Suli Lu is a PhD student at Ships and Marine Technology, Ghent University. His research interest includes CFD and ship hydrodynamics.

Wim Van Hoydonck obtained his PhD at Delft University of Technology and is nautical researcher at Flanders Hydraulics. His research interests include the application of numerical methods to ship aerodynamics and hydrodynamics.

Santiago Lopez Castaño is a Researcher at Flanders Hydraulics, he holds a PhD in Earth sciences from University of Trieste. His focus is on turbulence, earth science, and Engineering sciences.

Evert Lataire is head of the Ships and Marine Technology Division at Ghent University. His research focuses on the behaviour of ships in shallow and confined waters and is often based on model tests. In recent years, his division diversified to other floating devices subject to waves and current such as aquaculture in open sea and floating PV-panels in an offshore environment. Member of the organization and scientific committees of all MASHCON conferences.

Guillaume Delefortrie is naval architect (MSc, Ghent University 2001, PhD, Ghent University, 2007), associate professor at the Ships and Marine Technology Division of Ghent University, lecturer in charge of courses in marine hydrodynamics. Experienced in EFD based research, with focus point on ship manoeuvring in shallow and confined water. He has been a member of the 27th-29th ITTC Manoeuvring Committee. Member of the organization and scientific committees of MASHCON conferences since their creation (2009).

HYDRODYNAMIC PERFORMANCE OF A NEWLY DESIGNED RHINE VESSEL INTEGRATED WITH VARIOUS PROPULSION IMPROVEMENT DEVICES FOR SHALLOW WATER OPERATIONS

Nathalie Reinach, Development Centre for Ship Technology and Transport Systems (DST), Germany
Ravindu Us Gamaralalage, Development Centre for Ship Technology and Transport Systems (DST), Germany
Jens Ley, Development Centre for Ship Technology and Transport Systems (DST), Germany

HYDRODYNAMIC PERFORMANCE OF A NEWLY DESIGNED RHINE VESSEL INTEGRATED WITH VARIOUS PROPULSION IMPROVEMENT DEVICES FOR SHALLOW WATER OPERATIONS

NATHALIE REINACH, DEVELOPMENT CENTRE FOR SHIP TECHNOLOGY AND TRANSPORT SYSTEMS (DST), GERMANY
RAVINDU US GAMARALALAGE, DEVELOPMENT CENTRE FOR SHIP TECHNOLOGY AND TRANSPORT SYSTEMS (DST), GERMANY
JENS LEY, DEVELOPMENT CENTRE FOR SHIP TECHNOLOGY AND TRANSPORT SYSTEMS (DST), GERMANY

SUMMARY

Reduced water levels in inland waterways caused by the frequent and prolonged dry periods due to climate change could significantly hinder the inland waterway transport (IWT). Inland ships operating in shallow waterways face reduced efficiency due to hydrodynamic challenges such as increased resistance and propeller ventilation. This paper details the development of a twin-propeller Rhine vessel (GMS class), specially optimized for shallow water operation. Several hull designs focused on the aft section were iteratively optimized using computational fluid dynamics (CFD) simulations. The final hull design, appended with different configurations of three propulsion optimization devices—a flow separation plate, an outer tunnel, and a fixed inner tunnel—was tested in a towing tank. Their impact on propulsion efficiency and trade-off between performance in shallow and deep water were analyzed. With the capability to transport substantial amounts of cargo at drafts as low as 1.1 m, the proposed design appended with recommended propulsion improvement devices, could have carried over 10% additional cargo in 2018 compared to a conventional Rhine vessel.

NOMENCLATURE

Δ	Total mass displacement of the ship [t]
λ	Scaling factor [–]
B	Breadth (beam) of the ship [m]
C_{B}	Block coefficient [–]
DWT	Deadweight [t]
h	Water depth [m]
LOA	Length overall [m]
LCB	Longitudinal center of buoyancy [m]
P_{D}	Power demand [kW]
$P_{\mathrm{D,S}}$	Specific power demand [kW/t]
T	Draft [m]
T_{D}	Design draft [m]
T_{min}	Minimum draft [m]
U	Velocity of the ship [km/h]
U_{D}	Ship velocity at the design draft [km/h]

1 INTRODUCTION

Inland waterway transport (IWT) is a safer and more sustainable alternative to increasingly overloaded and congested rail and road transportation. Generally, it is considered that approximate demands of energy to carry a unit cargo weight [J/t-km] for inland water means are 17% lesser than that of road transportation and 50% less than that of rail transport, while being cost effective[1]. Owing to these favorable conditions, the European Union, in conjunction with European Green Deal and Sustainable and Smart Mobility Strategy projects, has already set goals to increase inland waterways and short sea

[1] Source: Official website of European Union, *Inland Waterways*, accessed January 3, 2025, https://transport.ec.europa.eu/transport-modes/inland-waterways_en.

transportation by 25% by 2030, and by 50% by 2050[2]. This underscores the importance of future-proofing the whole inland transportation system to keep up with the demand. This paper focuses on future-proofing of inland waterway cargo transport of the Rhine River, with particular emphasis on countering challenges faced by low water levels through improved ship design.

As one of the major rivers in Europe, the Rhine River runs through Switzerland, Liechtenstein, Austria, Germany, France and the Netherlands. With a fleet of close to 7000 ships, around 300 million tons of goods are transported on the Rhine every year (Woehrling, 2013). The portion of the river that spans through Germany traverses numerous cities that hold economic and industrial importance (Köln, Düsseldorf, Duisburg, etc.), signifying its importance to the country. Consequently, continuous improvement of IWT sector around Rhine River is of utmost importance when safeguarding the country's economic integrity for the future.

Even though inland water transportation must be adopted as a better alternative to land transportation in terms of sustainability and climate change, it is also the one worse affected by climate volatility in turn. These adverse effects are mostly linked to the vulnerability of ship operations to changing hydrological features of the river. For instance, the severe drought that prevailed during 2018 caused the river discharge volumes to plummet drastically, along with the water levels (Vinke et al., 2022). This consequently hindered a considerable portion of ship transportation through the river since most vessels in the current IWT fleet were not optimized for low draught operations, thus were susceptible to damages due to bottom contact and grounding. Also, as water levels decline, the navigable width of the river narrows.

Although dry periods have been natural occurrences in historical weather cycles, the concerns have arisen that these will become more prolonged, intense, and frequent due to climate change (Christidis and Stott, 2021). The general frequency of critical dry periods that lead to discharge volumes down to 2018 lows is 17.6 years, but this is projected to be uncertain and range between 6.5 – 22.6 years in the future (Brenk, 2021). Discharges are projected to continually increase in winter periods due to accelerated melting of mountainous ice caps. In summer periods, they are projected to gradually decline synonymous with frequent and prolonged dry periods (International Commission for the Protection of the Rhine, 2024). Contrary to the claims of climate change-based increased dry periods, a study conducted by Christodoulou et al. (2020) suggests that effects of climate change on inland waterways could be beneficial for IWT in some (Kaub on the Middle Rhine and Hofkirchen on the Upper Danube) since the utilized weather models have predicted overall increase in water levels. Yet, it is noteworthy that regions like Duisburg-Ruhrort were still projected to have lowered water levels, yielding net negative profits from IWT.

As described in coming sections, the current inland fleet operating on Rhine river consists to a major extent of the largest possible vessels to maximize profits. These vessels are far from being optimized to navigate at very low water levels. This is already factually proven from the experience gained through the 2018 dry period where economic momentum has been slowed down due to hindered IWT operations (Ademmer et al., 2019). Therefore, it is always prudent to maintain a universally capable vessel fleet that can perform well in either scenario. The burden of "future-proofing" the ships thus will be eased.

Various solutions can be proposed to address the problem of "future-proofing" the IWT sector against reducing water levels, encompassing aspects such as policy development, infrastructure improvements, logistical strategies and innovative design approaches (Hendrickx and Breemersch, 2012). Among the innovative design solutions proposed in the literature—such as reducing structural weight, designing smaller vessels, and adopting pusher-barge configurations—this paper specifically focuses on the promising aspect of improving the hydrodynamic performance of vessels in shallow water (Bačkalov et al., 2022, 2016; Radojčić et al., 2021). A new and optimized hull design is proposed, which will be evaluated with the integration of three shallow-water propulsion improvement devices that perform as hull appendages, namely, (a) flow-separation plate, (b) outer tunnel in retractable and fixed forms, and (c) fixed inner tunnels (see Figure 1). The ship configurations assessed were derived by alternatively appending these devices to the base hull. Systematic model tests were performed in the shallow water towing tank of Development Centre for Ship Technology and Transport Systems (DST).

[2] Source: Official website of European Union, *NAIADES III action plan*, accessed January 3, 2025, https://transport.ec.europa.eu/transport-modes/inland-waterways/promotion-inland-waterway-transport/naiades-iii-action-plan_en.

2 HULL DEVELOPMENT AND MODEL TESTS

2.1 DESIGN OBJECTIVES AND SPECIFICATION

In a collaborative meeting with inland shipping industry partners, key factors affecting ship operations in low water were identified. Analysis of hydrological and geographical data from the Rhine and its tributaries focused on water levels and flow characteristics. This analysis highlighted critical shallow areas and challenging river cross-sections, crucial for defining the ship's dimensions.

To accommodate the demand of increasing cargo volumes, IWT stakeholders throughout the past decade had resorted to developing increasingly larger ships. Larger ships were ultimately reducing the operational cost for unit cargo transported, thus remained favorable in economic terms too. During the period of 1996–2008, the average deadweight of new inland ships had nearly doubled (Hekkenberg, 2013). However, it remains doubtful whether advancements in ship design have kept pace with this rapid growth in size. The significant impairment of the inland traffic in Rhine during the 2018 dry season is a prominent example for this. It is also stated that the innovative vessels within the Rhine inland fleet make less than 0.2% (CCNR, 2024). Therefore, a mere maximization of dimensions would not make a compelling shallow-water efficient Rhine ship (Hekkenberg, 2016). Nevertheless, referring to these dimensions of current ships when deciding the dimensions of the intended ship design is prudent, as they have already been complying with the waterway constraints such as river locks.

The largest length and breadth dimensions of the vessels currently traversing the Rhine are 135 m and 22.90 m respectively. For pusher-barge configurations, these values could go up to 269.60 m in length and 34.35 m in breadth. However, the operability of these vessels is limited to specific sections of the river as steeply curved or narrow spans could hinder their maneuverability. The GMS (Großmotorgüterschiff) class on the other hand represents the most universally navigable ships with dimensions $110\ \mathrm{m} \times 11.45\ \mathrm{m}$ (length × breadth). This is classified under the CEMT class Va internationally. Some extra-long vessels that retain the breadth of the GMS class but extend its signature length up to 135 m have also become popular in the past decade (Bundesanstalt für Wasserbau, 2016). Typically, the carrying capacities for single Rhine vessels falls between $1{,}500 - 4{,}000$ t.

A comparison between numerous Rhine vessels led to the decision that the intended ship should be of GMS class with $110\ \mathrm{m} \times 11.45\ \mathrm{m} \times 2.8\ \mathrm{m}$ (length × breadth × design draft) dimensions with the carrying capacity (deadweight) of about 2,300 t at the design draft. Further studies and discussions led to the discovery that a ship with the draft of 1.1 m could have managed to operate for 336 days in 2018, even during the dry period. Subsequently, 1.1 m was picked as the minimum operational draft. The static under-keel clearance was set at 0.3 m for improved safety measures with mitigated risk against ground contact and grounding avoidance (Renner and Bialonski, 2004). Furthermore, requirements for ship strength, stability, maneuvering, and other criteria were defined according to European standards and technical regulations for inland navigation (ES-TRIN).

Table 1. Summary of design objectives and specifications

Attribute	Value
Class	GMS (CEMT class Va internationally)
Length overall (LOA)	110 m
Beam (B)	11.45 m
Design draft (T_{D})	2.8 m
Deadweight at design draft (DWT)	2370 t
Block coefficient at C_{B}	0.89
Cruising speed at T_{D} (U_{D})	16 km/h
Minimum draft (T_{min})	1.1 m

2.2 PROPULSION IMPROVEMENT DEVICES

The propeller diameter for CEMT class Va vessels is between 1.6 – 1.8 m (Bundesanstalt für Wasserbau, 2016, p. 15). Once a portion of the propeller has emerged in the air (partially immersed in water) due to low water, or when operating close to the water surface, air from the surface is sucked into its rotational volume, causing propeller ventilation. Subsequently, a number of adverse events are set off, such as main engine over speeding, excessive eccentric thrust, vibration and erosion due to cavitation. Altogether, the propulsion efficiency of the ship plummets drastically (Ghaemi and Zeraatgar, 2022; Taskar

et al., 2016). Therefore, among other things, propeller ventilation is one of the reasons that makes shallow water navigation challenging for this vessel class. Scaling the propeller down in size while increasing its rotational speed to eliminate this issue is a suboptimal solution since this combination would generally result in propulsion efficiencies inferior to those of larger, slower propellers (Majumder and Maity, 2023; Tadros et al., 2021). Instead, the discussed propulsion enhancement devices (appendages) herein discussed are intended to counter ventilation by: (a) reconditioning the water flow into and around the partially-emerged propeller to cover it better through the flooding of tunnels, and (b) blocking the intruding air stream into the propeller volume even when it is operating near the surface. A visual arrangement of all three devices appended to the hull is presented in Figure 1.

2.2.1 Flow-separation plate

The flow separation plate is a horizontal plate that stems from the hull, located above the propeller and extends behind it. The rudder shafts are penetrated through it while allowed to rotate freely. Historically, the flow-separation plate was invented to support long rudder shafts against high bending moments. According to Zöllner (2015, 2006), the plate also possesses a drag-reducing effect since it modifies the flow both into and behind the propeller, as well as further downstream. Furthermore, by blocking the area above the propeller, the plate could help with propeller ventilation in shallow water.

2.2.2 Outer tunnel (fixed form and flex form)

Typical tunnels on inland vessels are pairs of side skirts fixed in front of the propellers. Their objective is to prevent air from being sucked into the propeller with the inlet waterflow, at low water levels and partially loaded conditions. The so called Flex-tunnel is an improved version of conventional fixed outer tunnels: firstly, it can be retracted into the hull at design draft; secondly, it can be folded-out in shallow water to benefit the water flow to the propeller (Förster, 2016; Zöllner, 2006). The flooding of the tunnel volume could reduce ventilation. In contrast to a fixed tunnel, a flexible tunnel offers the possibility of optimizing the entire aft section of a ship. This is possible because the ship's lines can initially be designed without a tunnel and the Flex Tunnel can be fitted later. Although this approach does not allow complete freedom in the design of the lines—due to the need to create a movable connection between the flex tunnel and the hull, usually using hinges that must be aligned on a single plane and line to function properly— it does offer considerable freedom in deciding on the design of the stern lines. In this way, the ship's design significantly reduces hull resistance, resulting in considerable fuel savings[3,4]. Mainly, the main functions of a Flex-tunnel are (Förster, 2016):

- Significantly improving the propeller inflow, particularly in shallow water, by ensuring more water is channeled into the propeller area. This results in an increase in propeller efficiency due to reduced ventilation.
- Reducing the flow resistance of the ship by optimizing the water flow around the propeller.
- Providing flexibility over fixed conventional tunnels by being able to hydraulically deploy/retract as the crew desired, allowing adaptation to various travelling conditions and water depths.
- Improving propeller inflow efficiency through the vacuum effect created at the connection between the tunnel and nozzle. This ensures optimal propeller operation even under minimal load and shallow water conditions.

2.2.3 Fixed inner tunnel

As with the outer tunnel, the inner tunnel is designed to work against ventilation. It is particularly needed for slender aft ship lines. Combined with the outer tunnel skirt, the inner tunnel skirt forms a complete tunnel section leading flow up to the inlet of the propeller duct. This completed tunnel section is supposed to be flooded more easily than a semi-tunnel section which is formed with just the outer tunnel skirt. This component would be permanently installed in the aft ship.

[3] Source: Official website of Damen, *Flex Tunnel*, accessed January 3, 2025, https://www.damenmc.com/flex-tunnel/#tab-1731943398133-10.

[4] Source: Official website of Damen, *FLEX Tunnelsystem*, accessed January 3, 2025, https://damenmc.com/wp-content/uploads/2023/04/FLEX_tunnel_system_DE-2.pdf

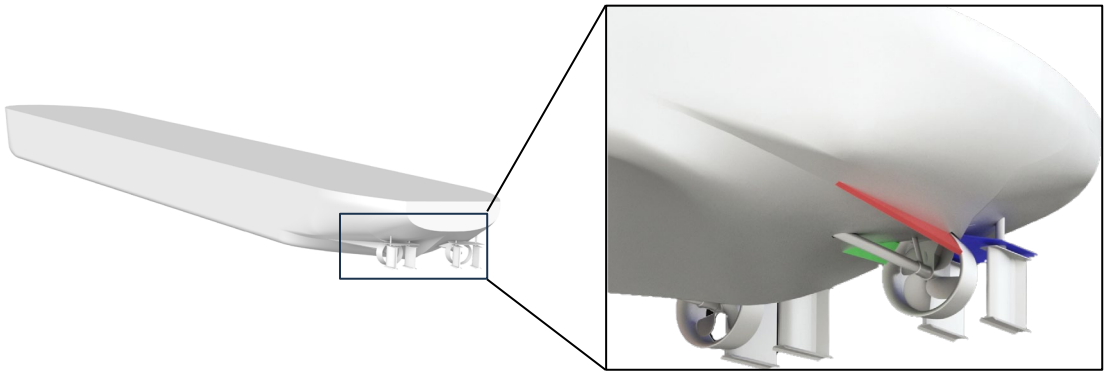

Figure 1. Visualization of the arrangement of considered propulsion improvement devices appended to a bare hull. Here, each device is depicted in different colors: (a) flow-separation plate in blue, (b) outer tunnel is red, and (c) fixed inner tunnel in green

2.3 DEVELOPMENT OF THE HULL DESIGN

An iterative optimization process (see Figure 2), directed by the observations of CFD simulations at each step, was employed to develop the final hull design[5]. This process consisted of four distinct steps, each progressively refining the stern to enhance performance for efficient shallow water operation. Throughout the process, the signature dimensions and characteristics of the hull were kept unchanged: a Rhine ship measuring $110\ \mathrm{m} \times 11.45\ \mathrm{m}$ with a design draft of 2.8 m and two propellers.

- The first iterative version (HV1) closely resembled a typical GMS class vessel, directly inheriting many of its features. The water flow was found to be struggling to follow along the bulky stern portion in the forward motion. The flow separation caused by this led to additional resistance on the hull.
- Adopting the findings made by Friedhoff et al. (2018), the stern was refined with reduced volume and smoothly transitioning contour lines in the second iterative version (HV2). The shape of the propeller tunnel integrated into the hull was extended behind the propeller to minimize any discontinuities, leaving a semi-circular opening at the transom. The retractable tunnel skirt was reshaped to have a smooth transition with the hull lines. The aft ship lines were smoothed out.
- With HV3, a transom with a raised lowest edge was introduced to reduce the transom wetting that leads to increased resistance (Carlton, 2007).
- In HV4, the point where the bottom-most (base) hull edges converge together was moved forward compared to its location in HV3.

Consequently, further trimmed down stern volume and better directed flow into the propeller resulted in a further reduction in drag and improved the propulsion conditions. Ultimately, HV4 was declared as the final design with a drag reduction of about 12.7% and a power requirement reduction of about 21.5% compared to the initial design HV1, when sailing at the design draft and 16 km/h, in deep water. Figure 3 shows the lines plan of the selected design.

[5] The detailed CFD study is included in the final report of the research project “FlaBi”, which is being prepared for publication.

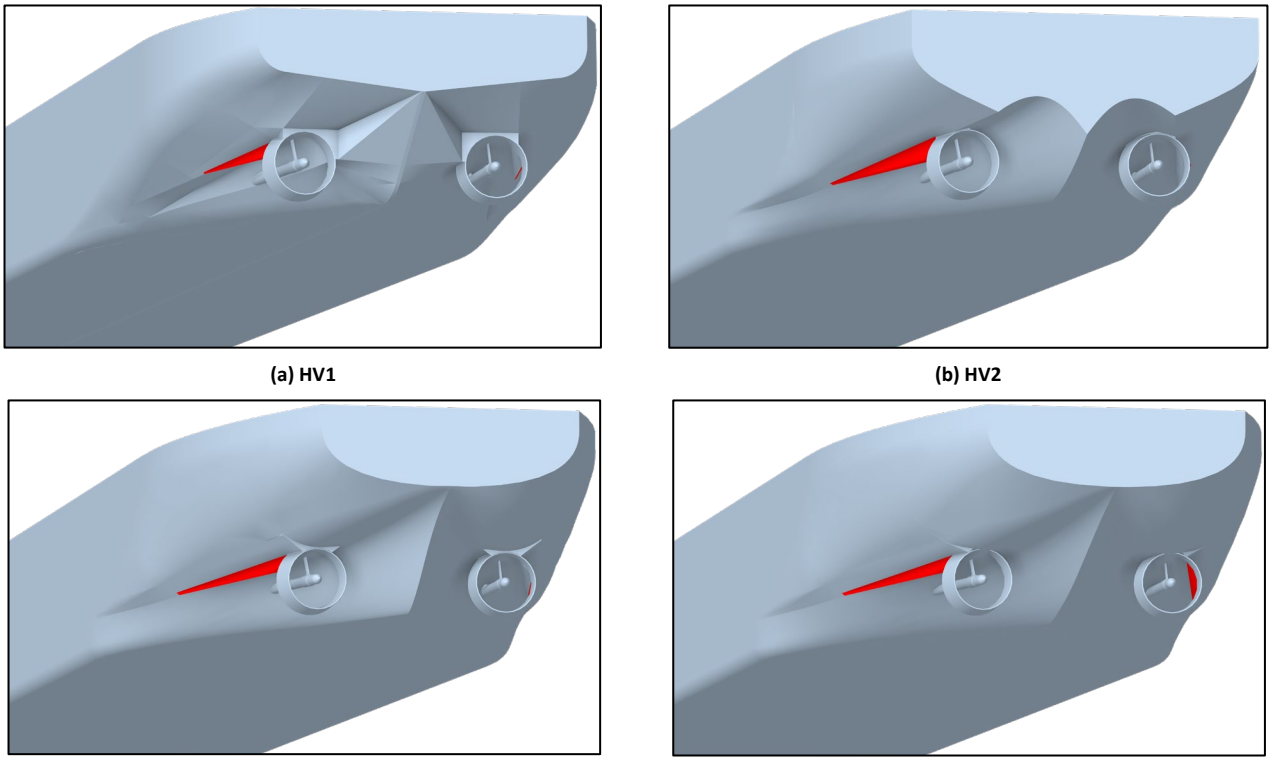

(a) HV1 (b) HV2

(c) HV3 (d) HV4

Figure 2. The optimization of stern shapes through the iterative process, shown with the corresponding outer tunnel flaps and without rudders

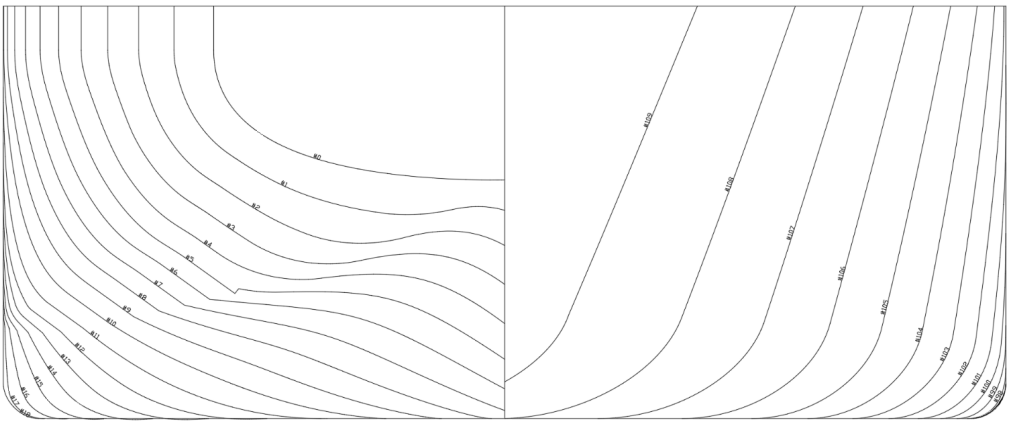

Figure 3. Hull lines of the finalized design HV4

The potential cargo capacity can be determined from the hydrostatics (see Table 2) of the ship and its calculated lightweight (660 t) (Hekkenberg, 2013).

Table 2. Hydrostatic table of the finalized HV4 hull design for drafts between T_{min} and T_D

T [m]	Δ [t]	LCB [m]	C_B [–]	Load carrying capacity (DWT) [t]
1.1	**1218.3**	**57.779**	**0.871**	**558.0**
1.5	1670.7	57.615	0.877	1010.4
2.0	2253.3	57.181	0.889	1593.0
2.5	2845.0	56.796	0.899	2184.7
2.8	**3204.2**	**56.579**	**0.904**	**2543.9**

2.4 MODEL TESTING OF HULL-APPENDAGE CONFIGURATIONS

The self-propulsion model tests with a 1:10 scale ratio were carried out in the shallow water towing tank at DST, which has a width of 10 m and a length of 200 m. The propeller is characterized by the following parameters: a scale factor λ = 10, a pitch-to-diameter ratio $\mathrm{P/D}$ = 0.955, a number of blades Z = 4, an expanded area ratio A_{E}/A_0 = 0.800, a diameter D = 0.110 m, and a chord length at 70% of the radius $\mathrm{C}_{0.7R}$ = 0.04965125 m.
Five distinct test configurations were established by attaching different combinations of aforementioned three propulsion improvement devices to the finalized hull HV4 (Figure 4). These configurations were then subjected to an extensive model testing phase to assess their hydrodynamic performance. The derived configurations are as follows. Note that the term 'base hull' is used for the hull assembly, including the twin propellers, propeller nozzles, and rudders.

K1: HV4 base hull appended with all three devices: flow-separation plate, outer tunnel, and inner tunnel

K2: HV4 base hull appended with flow-separation plate and outer tunnel

K3: HV4 base hull appended with flow-separation plate

K4: HV4 base hull appended with outer tunnel

K5: HV4 base hull without any propulsion improvement devices appended

Since the Flex-tunnel can be retracted in deep water, it essentially transforms the hull into the base configuration. Therefore, while configuration K4 represents the outer tunnel in both its fixed and folded-out (Flex) forms in shallow water, it exclusively represents the fixed form in deep water. Conversely, in deep water, the retracted Flex-tunnel is represented by configuration K5.

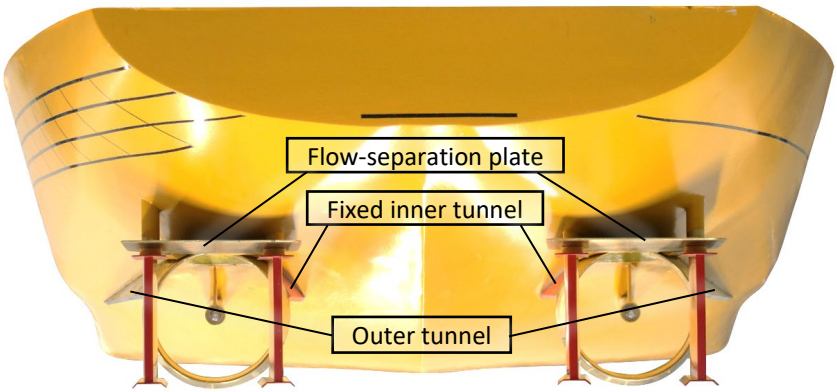

Figure 4. Test model of the K1 configuration, the base hull HV4 is appended with all three propulsion improvement devices (scaling factor $\lambda = 10$)

The model testing procedure was carried for each test configuration under varying combinations of draft (T), velocity (U), and depth (h) combinations (Table 3). Velocity in the range $U \in [4, 16]$ km/h, depth in the range $h \in [1.4, 7.5]$ m were considered with minimum and design draft values $T \in \{1.1, 2.8\}$ m. The minimum depth was determined based on the minimum draft and the required under-keel clearance, calculated as, ($h_{\min} = T_{\min} + 0.3$ m). However, the achievable velocity range was limited to low values at the minimum depth $U|_{h=1.4} \in [0, 5]$ km/h. This was a safety measure taken to prevent the model from getting damaged by bottom contact due to strong sinkage at higher speeds.

Table 3. Test matrix developed for model testing, with the considered draft (T), depth (h), and velocity (U) values in full-scale, for each configuration

Configuration	*T* [m]	*h* [m]	*U* [km/h]
K1	1.1, 2.8	[1.4, 5.0]	[5, 16]
K2	1.1, 2.8	[1.6, 5.0]	[5, 16]
K3	2.8	[3.5, 5.0]	[8, 16]
K4	1.1, 2.8	[1.6, 5.0]	[5, 16]
K5	2.8	[3.5, 7.5]	[7, 18]

2.5 MODEL TEST RESULTS

2.5.1 Results for $h = 5$ m & $T = 2.8$ m

Table 4 summarizes the total power demand (P_D) corresponding to all velocities tested under the test condition, water depth h = 5 m and draft T = 2.8 m. The P_D values in model scale were measured without accounting for wind effects on the superstructure, roughness effects on the hull, or the impact of hull openings (e.g. bow thrusters). The model test results were then extrapolated to ship scale using Froude scaling based on the ITTC 1957 correlation line and DST's empirical correlation allowance (CA) including blockage correction. The power requirement clearly diminishes as the number of appendages decreases. Fully equipped K1 configuration demands the highest power, and a continuous decline can be seen as the appendages are stripped off. Ultimately, the completely stripped base hull configuration, which also resembles the base hull with retracted Flex-tunnel (K5), demonstrates the lowest power requirement, particularly at greater speeds.

In the tables dedicated to the test results, the relative change in power demand for each configuration is indicated with colored dots and arrows.

- Colored dots represent the change in power demand with respect to the base hull configuration (K5), for each velocity value
  - red: increased power demand w.r.t. K5
  - yellow: reference configuration K5
  - green: reduced power demand w.r.t. K5
- The direction of gray colored arrows below each case indicates the relative change in power demand with respect to the immediate preceding configuration (in Table 4, power demand of K2 has decreased by 3.1%, with respect to K1).

At this depth and draft level, flow-separation plate, fixed outer tunnel, and the inner tunnel merely burden the ship by increasing the power demand, most probably by introducing additional drag. At design draft, in absence of propeller ventilation to work against, they appear redundant. Subsequently, use of a Flex-tunnel proves beneficial in design draft as it can be retracted, effectively forming the base hull configuration (K5). According to the results, the opportunity cost of using a fixed tunnel instead of a retractable Flex-tunnel at design draft at the maximum speed of $U_{\max} = 16\ \mathrm{km/h}$ would be about 4% of increased power demand (K4→K5). However, the installation and maintenance costs of Flex-tunnel system are significantly higher than a fixed tunnel structure. To comprehensively evaluate the real economic benefits of a Flex Tunnel, these additional costs must be weighed against the cost benefit gained by lowered fuel consumption in deep water conditions. A comparison of the configurations K5→K1 shows that all three appendices together add 5.2% (at 16.1 km/h) to the power demand at design draft.

Table 4. Power demands recorded for the test cases with $h = 5$ m and $T = 2.8$ m

U [km/h]	P_D [kW]					Trend visualization sparkline
	K1	K2	K3	K4	K5	
9.00	78	75.6 ↓ -3.1%	67.8 ↓ -10.3%	66.4 ↓ -2.1%	67.7 ↑ 2.0%	
11.60	162.5	163.9 ↑ 0.9%	156.2 ↓ -4.7%	151.4 ↓ -3.1%	148.4 ↓ -2.0%	
14.10	373	366.5 ↓ -1.7%	338.1 ↓ -7.7%	350 ↑ 3.5%	338.8 ↓ -3.2%	
15.10	513.4	479.1 ↓ -6.7%	491.1 ↑ 2.5%	492.3 ↑ 0.2%	478.9 ↓ -2.7%	
16.10	811.9	801 ↓ -1.3%	779.9 ↓ -2.6%	801.5 ↑ 2.8%	771.8 ↓ -3.7%	

2.5.2 Results for $h = 3.5$ m & $T = 2.8$ m

A simple comparison of data given in Table 5 with data given in Table 4 reveals that the propulsion power for the same speed is consistently higher in shallower water, across all configurations. The comparison between configurations K1→K2 implies that the inner tunnel skirt has a negligible influence on performance at low speeds. However, this situation overturns

at an increased speed of $U = 12.11\ \mathrm{km/h}$, where the presence of inner tunnel has significantly increased the power demand.

The comparison of configurations K4→K5 led to the observation that the outer tunnel results in an increased power requirement at all examined velocities. This assessment underscores that, removing the fixed outer tunnel or replacing it with a retractable Flex-tunnel at the design draft leads to a decreased resistance, improved propulsion conditions, and consequently a lower power requirement. The benefit at forward speeds between 11 and $12.11\ \mathrm{km/h}$ is reaching from about 4% to 7.7%. In comparison with the power demand reductions in the previous case at $h = 5\ \mathrm{m}$, the positive effect of retracting the tunnel seems to be even increased at $h = 3.5\ \mathrm{m}$; most likely because of improved propulsion conditions.

The effect of flow-separation plate cannot be clearly understood from the results. Even though the comparison between K3→K5, which is the removal of flow-separation plate is positive at some speeds, the general trend seems to an increase in power demand. However, the potential utility of this component under conditions of reduced water depths should be examined before hypothesizing its universal effectiveness or ineffectiveness.

Table 5. Power demands recorded for the test cases with $h = 3.5\ \mathrm{m}$ and $T = 2.8\ \mathrm{m}$

U [km/h]	P_D [kW] K1	K2	K3	K4	K5	Trend visualization sparkline
8.07	87.9	87.3 ↓ -0.7%	79.4 ↓ -9.0%	80.9 ↑ 1.9%	69.3 ↓ -14.3%	
10.07	196.7	192.5 ↓ -2.1%	165 ↓ -14.3%	189.7 ↑ 15.0%	185.1 ↓ -2.4%	
11.10	326.3	349.6 ↑ 7.1%	315.2 ↓ -9.8%	322 ↑ 2.2%	307.6 ↓ -4.5%	
11.60		425	407.5 ↓ -4.1%	424.5 ↑ 4.2%	391.8 ↓ -7.7%	
12.11	603.7	559.8 ↓ -7.3%	525.4 ↓ -6.1%	579.6 ↑ 10.3%	555.6 ↓ -4.1%	

2.5.3 Results for $h = 1.6\ \mathrm{m}$ and $T = 1.1\ \mathrm{m}$

Following the test runs at the design draft, the performance at the minimum draft T_{min} = 1.1m was investigated. The results made it clear that the shallow water effects significantly restrict operation. Particularly, the achievable maximum speeds were limited up to $8.6\ \mathrm{km/h}$ since any higher speeds caused the ship model to rapidly sink and collide with the tank bottom. Despite these limitations, it was possible to demonstrate that the ship was able to accelerate without additional assistance such as a bow thruster.

Table 6 lists the results of the tests. Note that the reference configuration here has been changed to K4 from K5. The propeller is 30% emerged from the water surface at the minimum draft. The ship was unable to move forward without the outer tunnel as verry low thrust was generated by the propeller due to severe ventilation and the ventilated tunnel volume. Consequently, configurations that do not accommodate the outer tunnel were proven completely ineffective at the minimum draft and thus were omitted from the test runs. The inclusion of the fixed inner tunnel had a positive influence on the performance (K2→K1) at minimum draft, yet it is not significant.

The reduction in power demand after removing the flow-separation plate (K2→K4) is significant, even though the plate is positioned entirely above the water surface at the minimum draft. The plate does not contribute to any flow modification or assist against ventilation. One possible explanation is that the propeller jet above the water surface impacts on the underside of the flow-separation plate, altering the pressure difference in the propeller plane. Also, this may have generated additional resistance on the ship.

Table 6. Power demands recorded for the test cases with $h = 1.6$ m and $T = 1.1$ m

U [km/h]	P_D [kW]			Trend visualization sparkline
	K1	K2	K4	
5.1	14.2	16.5 ↑ 16.2%	13.3 ↓ -19.4%	
6.1	28.9	30.3 ↑ 4.8%	25.3 ↓ -16.5%	
7.1	51.5	54.1 ↑ 5.0%	48.3 ↓ -10.7%	
8.1	106	105.2 ↓ -0.8%	95.3 ↓ -9.4%	
8.6	186.6	206.1 ↑ 10.5%	176.3 ↓ -14.5%	

3 DISCUSSION

To decide whether the proposed ship design and shallow water propulsion improvement devices provide a sophisticated solution for 'future-proofing' the Rhine River IWT sector against extended period of shallow water, the decreased power demand and the extended operational days must be investigated.

3.1 PERFORMANCE IN SHALLOW WATER

It was technically not possible to operate the model at the minimum draft without the outer tunnel. This appendage is therefore essential for a ship that is optimized for shallow water.

Observations at the minimum draft further suggest that the inner tunnel can potentially reduce power consumption by around 10% (K2→K1). The photos shown with Figure 5 are taken from below the hull, through an observation window, during the minimum draft model tests. The dashed-blue line marks the boundary between the water and air. In K1, this boundary is pulled closer to the propeller inlet compared to the other two configurations. This means that more water is directed to the propeller when the inner tunnel is present. Boundary lines of K2 and K4 configurations without the inner tunnel are located at the same position relative to the propeller, indicating that the inner tunnel assisted against ventilation, ultimately improving the thrust generated.

Yet, the power demanded by the K4 configuration is the lowest for each speed, suggesting that positive effect of the inner tunnel may have been nullified. At the same time, the removal of the flow-separation plate (K2→K4) revealed a 14% reduction in power requirements (Table 6), showcasing its negative effect on the proposed ship design. Combination of this, and the additional resistance generated by the inner tunnel itself might have led the configuration K1 to have a higher power demand. This could have indeed been the reason that, even with an increased thrust provided by the inner tunnel, the configuration K1 shows a higher power demand compared to K4.

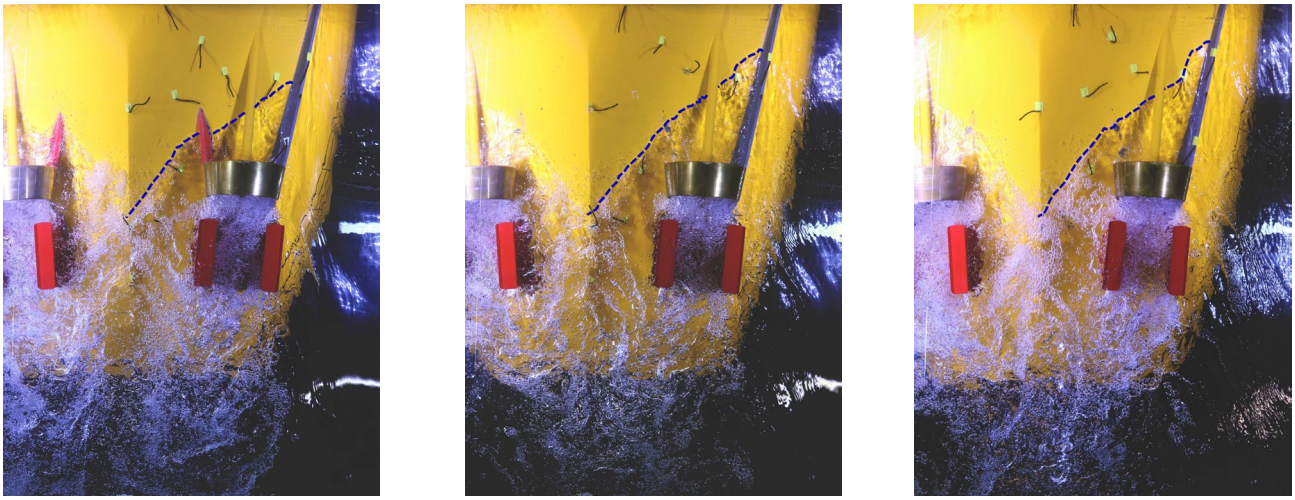

(a) K1 – all devices appended (b) K2 – outer tunnel + flow-separation plate (c) K4 - outer tunnel only

Figure 5. The photos captured during the model test at $h = 1.6$ m and $U = 8.1$ km/h, showcasing the state of ventilation of the partially emerged propeller for different configurations

In both water depth scenarios tested at the design draft ($h = 3.5$ m and $h = 5.0$ m), the flow separation plate, fixed inner tunnel, and outer tunnel proved to be detrimental to the performance of the proposed hull. When appended to the base hull, their protruding silhouettes appeared to disturb the flow around the hull, generating additional drag and adversely increasing the power demand. Therefore, the necessity of incorporating the flow-separation plate and the fixed inner tunnel to the proposed hull design is especially conflicted since they are not integral for shallow water operation. It is noted that the stern section of the proposed hull is explicitly optimized for shallow water through an iterative process. Hence, the effectiveness of these devices is not universally dismissed here, but it is simply implied that they are not necessary for the already optimized proposed hull. However, they might still serve as effective retrofitting options for existing, non-optimized hulls (Zöllner, 2006).

The outer tunnel on the other hand, was proven to be essential for shallow water operation based on the test runs conducted at the minimum draft. No thrust has been generated by any configuration without the outer tunnel. Any detrimental effect a fixed outer tunnel has on the ship performance at design draft can be easily circumvented by the usage of a Flex-tunnel. A Flex-tunnel can be simply retracted at the design draft, effectively transforming ship back to the base hull configuration (K4→K5), eliminating any added resistance. The retracted flex tunnel has a reduced power requirement of 4-7% at high speeds for both $h = 3.5$ m and $h = 5.0$ m cases (Table 4 and Table 5). For a new build, however, the question arises as to whether this performance enhancement justifies the significant capital investments for a Flex-tunnel over a relatively cheaper fixed tunnel.

To appraise the developed vessel design its competitiveness against the current Rhine fleet, a comparative analysis was conducted including a cohort of contemporary vessels. The evaluation, depicted in Figure 6, focuses on the propulsion power requirement for a unit displacement relative to the total displacement. The specific power requirement per displacement matrix serves as an indicator of efficiency, as both are directly proportional. To ensure the validity, uniform conditions were maintained across all assessments, including the water level ($h = 5$ m), vessel speed ($U = 16$ km/h), and the channel width. Yet, this approach may not be perfectly standardized in the absence of information on other potentially influential factors, such as the exact vessel's lightweight or specific ship type. The new design for a Rhine vessel, represented by the red dot, demonstrated a commendable specific performance per unit volumetric displacement. This achievement not only highlights the design’s efficiency but also its potential to stand competitively in the market, affirming the design's viability under the standardized test conditions employed in this analysis.

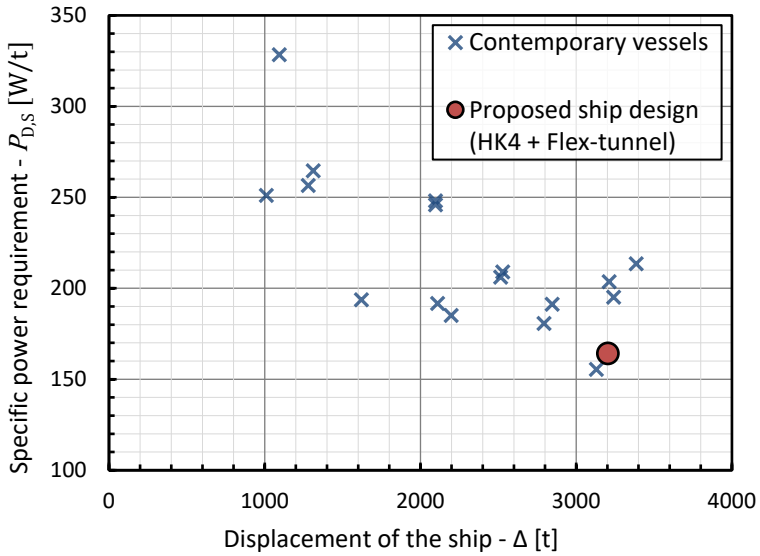

Figure 6. **The comparison of specific power requirement against the cargo carrying capacity of the proposed ship design with respect to several Rhine vessels in operation (Source: the inland vessel database of Development Centre for Ship Technology and Transport Systems - DST, Germany)**

3.2 INCREASED CARGO CARRYING DAYS

The German Federal Institute of Hydrology (BfG) collected water level data along the Rhine in 2018 (German Federal Institute of Hydrology, 2018). The data set includes recordings of the water levels at intervals of 100 m. The specific data corresponding to the German section of the Rhine (362.3 km to 865.4 km) can be utilized to calculate the number of days the vessel would experience downtime. For the vessel proposed in this study, a minimum allowable under keel clearance of 0.3 m results in an operable minimum depth of $h_{\min}|_{T_D} = 3.1\ \mathrm{m}$ at the design draft $T_{\mathrm{D}} = 2.8\ \mathrm{m}$. In 2018, water levels below this depth persisted for 237 days. However, if the minimum draft $T_{\min} = 1.1\ \mathrm{m}$ is taken into consideration, the minimum operable water depth reduces to $h_{\min}|_{T_{\min}} = 1.4\ \mathrm{m}$, leading to only 10 days of downtime for the vessel.

Table 7 provides information on cargo that can be transported at various drafts of the proposed ship. Here, it is assumed that the proposed ship would operate as same as a typical GMS vessel, accounting for about 60 journeys annually. Some existing Rhine vessels in the GMS class can attain drafts as low as 1.4 m, requiring a minimum water level of 1.7 m. This water level was not reached for 90 days in 2018. This indicates that a significant portion of the German Rhine fleet remained idle for at least 25% of the year, unable to transport goods due to insufficient water levels. Smaller ships could be operated, but the loading capacity of these ships was not sufficient to adequately supply all the industrial sites along the Rhine. This situation has compelled the IWT stakeholders to adopt alternative modes of transport, namely rail and road, which consequently imposed significant operational pressures and financial challenges. With the reduced downtime (additional 80 operational days) with nearly 10% extra cargo with respect to the existing Rhine GMS fleet, the proposed ship design poses as a promising solution to mitigate the challenges faced by the industry. However, it is important to recognize that a reduced draft, while offering increased operational days, comes with the trade-off of reduced cargo capacity. Also, the speed attainable at lower h/T ratios is limited. This analysis does not account for this reduction in speed because it is based on the assumption of possible number of journeys annually through the Middle Rhine. Note that the cargo capacity of an existing GMS ship is assumed to be the same as the cargo capacity of the proposed vessel at the same draft since they have similar overall dimensions.

Table 7. Cargo carrying capacity of the proposed vessel for water depths seen in Rhine during 2018

Water depth [m]	Draft [m]	Load carrying capacity at draft [t]	Annual days operable [-]	Tonnage for 60 journeys per year [t]	Remarks
> 3.1	2.8	2543.9	140 (38.4%)	58544.5	- Load carrying capacities for each draft were extracted from the hydrostatic table (Table 2) - Total possible cargo for an existing GMS ship= 94891.2 t
3	2.7	2424.0	16 (4.4%)	6375.5	
2.9	2.6	2304.2	14 (3.8%)	5302.8	
2.8	2.5	2184.7	6 (1.6%)	2154.8	
2.7	2.4	2065.5	11 (3%)	3734.9	
2.6	2.3	1946.8	6 (1.6%)	1920.1	
2.5	2.2	1828.5	7 (1.9%)	2104.0	
2.4	2.1	1710.5	7 (1.9%)	1968.2	
2.3	2	1593.0	5 (1.4%)	1309.3	
2.2	1.9	1475.6	9 (2.5%)	2183.1	
2.1	1.8	1358.7	3 (0.8%)	670.0	
2	1.7	1242.1	8 (2.2%)	1633.4	
1.9	1.6	1126.2	13 (3.6%)	2406.7	
1.8	1.5	1010.4	9 (2.5%)	1494.8	
1.7	1.4	894.8	21 (5.8%)	3088.9	
1.6	1.3	780.5	28 (7.7%)	3592.4	- Additional cargo gained by the proposed ship optimized for low draft and shallow water= 8973.6
1.5	1.2	670.7	33 (9%)	3638.3	
1.4	1.1	558.0	19 (5.2%)	1742.8	
1.3	1	–	–	–	- Inoperable water depth
		∑ 365	97.3%	∑ 103864	

4 CONCLUSIONS

Inland waterway transportation (IWT) is a sustainable and efficient alternative to road and rail transport. Europe boasts a comprehensive inland shipping network, with the Rhine River serving as one of its most vital corridors. However, the inland shipping sector is projected to face significant challenges due to climate change, particularly from disruptions caused by declining water levels. For example, the prolonged dry period in 2018 resulted in substantial economic losses for the unprepared inland shipping industry as most of the vessels were unable to operate in shallow water. As a solution for this, in order to “future proof” the industry against climate change, a new ship design optimized for low-draft, shallow water operations was proposed. The proposed design was further evaluated with the attachment of three different propulsion improvement devices, especially intended to counter propeller ventilation. The three devices were, (a) flow separation plate, (b) outer tunnel attachment in retractable and fixed forms, and (c) fixed inner tunnel.

- The hull was designed through a four-step iterative optimization process, with a particular focus on improving the stern shape for shallow water operations. The finalized design retained the characteristic dimensions of a typical GMS-class vessel. Compared to the initial design, which closely resembled a contemporary GMS vessel, it demonstrated a 12.7% reduction in drag and a 21.5% decrease in power demand to achieve a 16 km/h speed at the design draft.
- The self-propulsion model tests were conducted at a scale of 1:10 for five configurations of base hull appended with different combinations of shallow water improvement devices. The last configuration was the base hull without the shallow water appendages.
- In deepest water depth investigated, at design draft, no propeller ventilation was seen. All three appendages were found to exert extra drag on the hull and lower the ship’s performance.
- In the shallow water scenario, the configurations with inner tunnel and flow-separation plate did not improve in overall performance. In contrast, the outer tunnel was absolutely necessary to operate the ship at minimum draft. And addition to that, the Flex Tunnel can decrease the power demand by extra 4-7% at design draft.

- The developed vessel design was compared against a number of vessels within the current Rhine fleet, focusing on the propulsion power requirement per unit displacement as an indicator of efficiency, where a sufficient improvement was found to have achieved.
- In addition, the ship design is capable of operating in extremely shallow water due to its low minimum draft. Utilizing it during the dry period of 2018 could have resulted in uninterrupted operation of an additional 80 days compared to an existing GMS class vessel. This would have accounted for close to a 10% increment in total cargo transported.
- All in all, the proposed ship appended with the outer tunnel provides a robust solution for 'future-proofing' the Rhine IWT sector against reducing water levels.

5 ACKNOWLEDGEMENTS

The analysis presented in this paper is part of the research project 'FlaBi – Development of Inland Waterway Vessels for Extreme Low Water Conditions' (Project No. 03SX532A) which was funded by Federal Ministry for Economic Affairs and Climate Action (BMWK). The broader scope of FlaBi encompassed activities like, evaluation of various propulsion trains through experimental and numerical means and a full CFD study leading up to the finalization of the final hull, and etc. The authors would like to express their gratitude to all parties involved in the FlaBi project. Readers are encouraged to refer to the main FlaBi report, which will be published in the near future, for a full understanding of the project's scope.

6 REFERENCES

Ademmer, M., Jannsen, N., Kooths, S., Mösle, S., 2019. Niedrigwasser bremst Produktion. Wirtschaftsdienst 99, 79–80. https://doi.org/10.1007/s10273-019-2399-7

Bačkalov, I., Kalajdzic, M., Momčilović, N., Rudaković, S., 2016. A study of an unconventional container vessel concept for the Danube.

Bačkalov, I., Kalajdzic, M., Momčilović, N., Rudaković, S., Vidić, M., 2022. Shallow-draught vessels for the Vessel Train.

Brenk, S.H. van, 2021. Return period of low water periods in the river Rhine.

Bundesanstalt für Wasserbau, 2016. Driving dynamics of inland vessels: vessel behaviour on European inland waterways and waterway infrastructure with special respect to German waterways. Karlsruhe.

Carlton, J.S., 2007. Ship resistance and propulsion, in: Carlton, J.S. (Ed.), Marine Propellers and Propulsion (Second Edition). Butterworth-Heinemann, Oxford, pp. 286–318. https://doi.org/https://doi.org/10.1016/B978-075068150-6/50014-0

CCNR, 2024. Inland navigation in Europe: annual market observation 2024. Central Commission for the Navigation of the Rhine, Strasbourg.

Christidis, N., Stott, P.A., 2021. The influence of anthropogenic climate change on wet and dry summers in Europe. Sci Bull (Beijing) 66, 813–823. https://doi.org/https://doi.org/10.1016/j.scib.2021.01.020

Christodoulou, A., Christidis, P., Bisselink, B., 2020. Forecasting the impacts of climate change on inland waterways. Transp Res D Transp Environ 82, 102159. https://doi.org/https://doi.org/10.1016/j.trd.2019.10.012

Förster, K., 2016. Mehr Flexibilität mit einem Flextunnel. Zeitschrift für die Binnenschifffahrt Band 9.

Friedhoff, B., List, S., Hoyer, K., Tenzer, M., 2018. Bestimmung des effektiven Propellerzustroms für die Binnenschifffahrt. Duisburg.

German Federal Institute of Hydrology, 2018. Climate level - Metstat.

Ghaemi, M.H., Zeraatgar, H., 2022. Impact of propeller emergence on hull, propeller, engine, and fuel consumption performance in regular head waves. Polish Maritime Research 29, 56–76. https://doi.org/10.2478/pomr-2022-0044

Hekkenberg, R., 2016. Optimization of the dimensions of dry bulk ships: the case of the river Rhine. Maritime Economics & Logistics 18, 211–229. https://doi.org/10.1057/mel.2014.36

Hekkenberg, R.G., 2013. Inland ships for efficient transport chains (PhD thesis). Delft university of Technology, Delft.

Hendrickx, C., Breemersch, T., 2012. The Effect of Climate Change on Inland Waterway Transport. Procedia Soc Behav Sci 48, 1837–1847. https://doi.org/https://doi.org/10.1016/j.sbspro.2012.06.1158

International Commission for the Protection of the Rhine, 2024. Climate change induced discharge scenarios for the Rhine basin: update of the discharge scenarios for the Rhine basin using latest climate change findings. Koblenz.

Majumder, P., Maity, S., 2023. A critical review of different works on marine propellers over the last three decades. Ships and Offshore Structures. https://doi.org/10.1080/17445302.2022.2058767

Radojčić, D., Simić, A., Momčilović, N., Motok, M., Friedhoff, B., 2021. Concepts of Contemporary and Innovative Vessels, in: Radojčić, D., Simić, A., Momčilović, N., Motok, M., Friedhoff, B. (Eds.), Design of Contemporary Inland Waterway Vessels: The Case of the Danube River. Springer International Publishing, Cham, pp. 269–325. https://doi.org/10.1007/978-3-030-77325-0_10

Renner, V., Bialonski, W., 2004. Technische und wirtschaftliche Konzepte für flussangepasste Binnenschiffe. Duisburg.

Tadros, M., Ventura, M., Guedes Soares, C., 2021. Design of propeller series optimizing fuel consumption and propeller efficiency. J Mar Sci Eng 9. https://doi.org/10.3390/jmse9111226

Taskar, B., Yum, K.K., Steen, S., Pedersen, E., 2016. The effect of waves on engine-propeller dynamics and propulsion performance of ships. Ocean Engineering 122, 262–277. https://doi.org/https://doi.org/10.1016/j.oceaneng.2016.06.034

Vinke, F., van Koningsveld, M., van Dorsser, C., Baart, F., van Gelder, P., Vellinga, T., 2022. Cascading effects of sustained low water on inland shipping. Clim Risk Manag 35, 100400. https://doi.org/https://doi.org/10.1016/j.crm.2022.100400

Woehrling, J.M., 2013. The Central Commission for the Navigation of the Rhine: In the service of the Rhine economy, in: 4th Transnational Rhine Conference. Erasmus School of History, Culture and Communication, Rotterdam .

Zöllner, J., 2015. Moderner Binnenschiffbau zur Verbesserung der Propulsion und damit zur Reduzierung schiffsinduzierter Einflüsse. Bundesanstalt für Wasserbau (Hg.): Wechselwirkung Schiff/Wasserstraße mit Auswirkungen auf Nautik und schiffsinduzierte Belastungen. 27–33.

Zöllner, J., 2006. New inland container vessels for transport to the hinterland. PIANC Magazine 30.

7 AUTHORS BIOGRAPHY

Nathalie Reinach holds the current position of research associate at Development Centre for Ship Technology and Transport Systems (DST), Germany. She is responsible for design, construction, and testing ship models. She was directly involved with the project 'FlaBi – Development of Inland Waterway Vessels for Extreme Low Water Conditions', which this research is based on.

Ravindu U.S., Gamaralalage holds the current position of research associate at DST. He has been involved with the FlaBi project and is currently preparing for his PhD studies.

Jens Ley graduated in 2009 in Naval Architecture at the University of Duisburg-Essen (UDE). His research activities covered ship motions and loads in waves, hydroelasticity effects and wave induced added resistance. Since 2018 he has been heading the department for ship design and simulations at DST. His current research is related to hydrodynamics of inland waterway ships and shallow water effects. He is an assistant lecturer at UDE.

COMPUTATIONAL MODELLING OF SQUAT AND RESISTANCE OPTIMISATION IN FULLY CONFINED WATER

Momchil Terziev - Department of Naval Architecture, Ocean and Marine Engineering, University of Strathclyde, Glasgow, UK
Muhammad Iqbal - Department of Naval Architecture, Faculty of Engineering, Universitas Diponegoro, Indonesia
Yujia Wei - School of Aerospace, Transport and Manufacturing, University of Cranfield, UKAtilla Incecik - Department of Naval Architecture, Ocean and Marine Engineering, University of Strathclyde, Glasgow, UK

COMPUTATIONAL MODELLING OF SQUAT AND RESISTANCE OPTIMISATION IN FULLY CONFINED WATER

MOMCHIL TERZIEV - DEPARTMENT OF NAVAL ARCHITECTURE, OCEAN AND MARINE ENGINEERING, UNIVERSITY OF STRATHCLYDE, GLASGOW, UK.
MUHAMMAD IQBAL - DEPARTMENT OF NAVAL ARCHITECTURE, FACULTY OF ENGINEERING, UNIVERSITAS DIPONEGORO, INDONESIA.
YUJIA WEI - SCHOOL OF AEROSPACE, TRANSPORT AND MANUFACTURING, UNIVERSITY OF CRANFIELD, UK.
ATILLA INCECIK - DEPARTMENT OF NAVAL ARCHITECTURE, OCEAN AND MARINE ENGINEERING, UNIVERSITY OF STRATHCLYDE, GLASGOW, UK.

SUMMARY

Ship squat in confined waters is of critical importance for safe and efficient operations. However, little is known about the relationship between the magnitude of the maximum squat and the resistance, and if it is possible to reduce squat by imposing changes in trim through variations in the position of the centre of gravity of a ship. The present paper investigates these questions through the use of Reynolds Averaged Navier-Stokes modelling, applied to the KRISO container ship at a scale of 1:75. It is found that at the low speed investigated of F_h =0.303, the dynamic trim is dominated by the initial assignment and changes in sinkage are responsible for a complex behaviour exhibited by the total resistance. The set of optimum values expressing the trade-off between squat and resistance is found to be such that higher squat values are predicted to be able to improve resistance at the investigated speed.

NOMENCLATURE

B	Ship beam (m)
C_F	Frictional resistance coefficient (-)
CFD	Computational Fluid Dynamics
C_M	Midship section coefficient (-)
C_P	Pressure resistance coefficient (-)
C_T	Total resistance coefficient (-)
dy	Wall-normal distance to first cell centre (m)
F_h	Depth Froude number = $V/\sqrt{gh}$ (-)
h	Canal depth (m)
h/T	Depth-to-draft ratio (-)
L	Ship length (m)
LC	Loading condition (-)
p	Observed order of accuracy = $\log(\varepsilon_{21}/\varepsilon_{32})$ /log (r) (-)
R	Convergence ratio= $\varepsilon_{32}/\varepsilon_{21}$ (-)
r	Refinement factor = $\sqrt{2}$ (-)
S	Common ratio in geometric series expressing the distribution of near-wall layers (-)
s	Ship sinkage (m)
S_w	Wetted surface area
T	Ship draft (m)
U	Discretisation uncertainty (%)
U_E	Experimental uncertainty (%)
U_N	Numerical uncertainty (%)
U_V	Validation uncertainty (%)
w/L	Width to length ratio (-)
y^+	Dimensionless wall-normal distance (-)
B_R	Blockage ratio

δ	Boundary layer thickness $= 0.382L/Re^{1/5}$ (m)
ε	Difference between the coarse and medium solutions (ε_{32}) and medium and fine solutions (ε_{21}).
θ	Ship trim (°)
λ	Scale factor (-)
μ	Dynamic viscosity (Pa-s)
ν	Kinematic viscosity (m^2/s)
ρ	Density of water (kg/m^3)
τ_w	Shear wall stress (Pa)

1 INTRODUCTION

Much attention has been paid to trim optimisation as a rational and low-cost approach to reduce the power requirements of a vessel sailing in calm water. However, the dynamic attitude of a hull is influenced by the fore-aft imbalance in forces and moments while underway, modifying the running trim and sinkage from the condition assigned at rest. Such effects are small in unrestricted waters, but may pose a threat of grounding in shallow and laterally restricted waterways. Therefore, one may ask if it is possible to cancel squat-induced trim by modifications to the loading condition, for example by moving ballast water within the hull. It is widely believed that such modifications can only magnify squat, but Härting et al. (2009) questioned the validity such assertions and demonstrated that it may be possible to reduce overall squat. Alternatively, it may be asked what the relationship between an optimum squat and resistance is.

Unlike deep water performance, to the best of the authors' knowledge, confined water performance through the lens of trim optimisation has received little attention since the work of Härting et al. (2009). In the field of trim optimisaiton, many researchers have recently opted to use statistical and AI type models which typically employ full-scale data (Cisek, 2025; Panagiotakopoulos et al., 2022; Tu et al., 2023). Regrettably, the necessary datasets are usually proprietary and to the best of the authors' knowledge, there exist no openly available full-scale datasets, including the ship geometry where confined and shallow water performance is concerned. Since each ship's performance, and therefore, dynamic attitude while underway, are unique, models built on proprietary data featuring a single hull or a limited number of hulls cannot yet replace the need for deterministic models, an overview of which was recently given by Korkmaz et al. (2023). A widely used alternative in practice due to the speed of the prediction are empirical methods, summarized by Barrass & Derrett (2012). However, empirical models are simplistic and tend to significantly overestimate squat. While that ought to mean fewer groundings, data from the European Maritime Safety Agency data consistently shows that groundings are in the top accident categories and that the majority of accidents occur in shallow water (EMSA (European Maritime Safety Agency), 2023).

The present paper uses Computational Fluid Dynamics (CFD) to assess the possibility of simultaneously negating changes dynamic in trim and reducing resistance through modifications of the static trim by modifying the loading condition of a ship. CFD has the advantage of solving the viscous effect which is likely of considerable importance in very shallow and narrow conditions. Viscous effects have been recently shown to be of critical importance in the calculation of the trim, first by Chillcce & Moctar (2022) who modelled various approaches of accounting for the viscous term in computational squat modelling and more recently by Le Strat & Terziev (2025) who investigated the scale effect acting on the force causing sinkage and trim finding that the trim moment exhibits sensitivity to the Reynolds number, and therefore, viscosity.

The approach taken herein is to employ the response surface methodology requiring a set of 9 results to produce the optimum. Each of the 9 data points for squat and resistance, respectively, are obtained using the commercially available Navier-Stokes solver Star-CCM+, and which are used to construct a Pareto front showing the trade-offs between squat and resistance. This study proceeds with a laying out of the employed case studies and validation condition, followed by the numerical model and details of the computational mesh. Results and discussion are preceded by a brief overview of the optimisation procedure. Finally, conclusions and recommendations for future work are given.

2 CASE STUDIES

To maximise the reproducibility of the subsequently presented results, the KRISO Container Ship (KCS) in model scale of 1:75 is used throughout. The scale factor is chosen to match that experimented upon by Elsherbiny et al. (2019), whose study included a rectangular canal of dimensions shown in Table 1.

Table 1. Ship principal dimensions and basis bathymetry geometry

Parameter	Symbol	Full-scale	Model-scale	Units
Scale factor	λ	1	75	-
Ship length	L	230	3.067	m
Beam	B	23.2	0.429	m
Draft	T	10.8	0.144	m

Midship area coefficient	C_M	0.985	0.985	-
Depth-to-draft ratio	h/T	2.22	2.22	-
Width-to-length ratio	w/L	1.5	1.5	-
Depth Froude number	F_h	0.303	0.303	-

The conditions given in Table 1 are used for validation to ensure the numerical model has sufficient accuracy against a basis condition, which is subsequently modified to explore the effects of depth and width on the resulting optima. Once the above condition is validated following the ITTC (2008) procedure, a set of alterations are imposed on the canal geometry to gauge the sensitivity of the optimum loading condition on the length and width of the waterway. The full description of the loading conditions and canal geometry variations are given in Table 2.
The loading conditions given in Table 2 are replicated for each of the canal geometry condition. The values moment of inertia result from the difference in the position of the centre of gravity, measured from the aft perpendicular of the ship and varied within ±2.5% of the initial condition in the horizontal and ±5% in the vertical direction.

Table 2. Investigated loading conditions and canal geometries. LC stands for loading condition; the initial condition is labelled 0. The vase studies were obtained using a systematic variation determined by the optimisation procedure

LC	Parameter										
	LCG (m)	KG (m)	Rx (m)	Ry (m)	Rz (m)	I_{xx} (kgm^2)	I_{yy} (kgm^2)	I_{zz} (kgm^2)	h/T	w/L	F_h
0*	1.487	0.149	0.134	0.791	0.796	1.099	38.408	38.851	2.22, 2, 1.8	1.5, 1	0.303
1	1.524	0.156	0.135	0.791	0.795	1.111	38.369	38.801			
2	1.524	0.142	0.135	0.791	0.795	1.093	38.351	38.801			
3	1.450	0.156	0.135	0.794	0.798	1.111	38.638	39.070			
4	1.450	0.142	0.135	0.793	0.798	1.093	38.621	39.070			
5	1.434	0.149	0.135	0.795	0.800	1.099	38.773	39.217			
6	1.540	0.149	0.135	0.791	0.796	1.099	38.387	38.831			
7	1.487	0.138	0.133	0.791	0.796	1.092	38.401	38.851			
8	1.487	0.160	0.135	0.791	0.796	1.120	38.429	38.851			

*Condition used for validation

3 NUMERICAL MODEL

All results are obtained using the commercially available Navier-Stokes solver, Star-CCM+, version 18.02.010. The set up explained herein is replicated across case studies and intended to maximise reproducibility of the results.
The solver makes use of the Finite Volume method to discretise the computational domain into a finite number of adjoining cells. For the purposes of the present paper, the Reynolds Averaged Navier-Stokes approach was used throughout with the standard *k*-ω turbulence model following the recommendations of Terziev et al. (2019). Second order discretisation was used for all parameters except time marching where a first order scheme was used to improve stability and relax the conditions of the Courant number on the free surface. The value of the time step was selected by $\Delta t = 0.0035 V/L$ following Terziev et al. (2018). Multiphase flow was modelled in all cases where the air-water interface is resolved using the Volume of Fluid method (Hirt & Nichols, 1981).

3.1 COMPUTATIONAL DOMAIN AND BOUNDARY CONDITIONS

The computational domain consisted of a rectangular box with a global coordinate system coincident with the ship aft perpendicular. Half of the problem was modelled to reduce the number of required cells. The boundary bisecting the ship was assigned a symmetry plane boundary condition, the domain bottom and side were no-slip walls placed according to the conditions given in Table 1, and assigned a tangential velocity equal and opposite that of the ship's. The ship geometry was set as a no-slip wall, while the upstream boundary was assigned a velocity inlet condition and the downstream boundary - a pressure outlet condition which maintained the hydrostatic pressure. The upstream and downstream boundaries were placed at 3.5 and 2.5 ship lengths in the respective direction from the global coordinate system, resulting in 2.5 ship lengths clearance from each perpendicular. The computational domain and assigned boundary conditions are depicted in Figure 1.

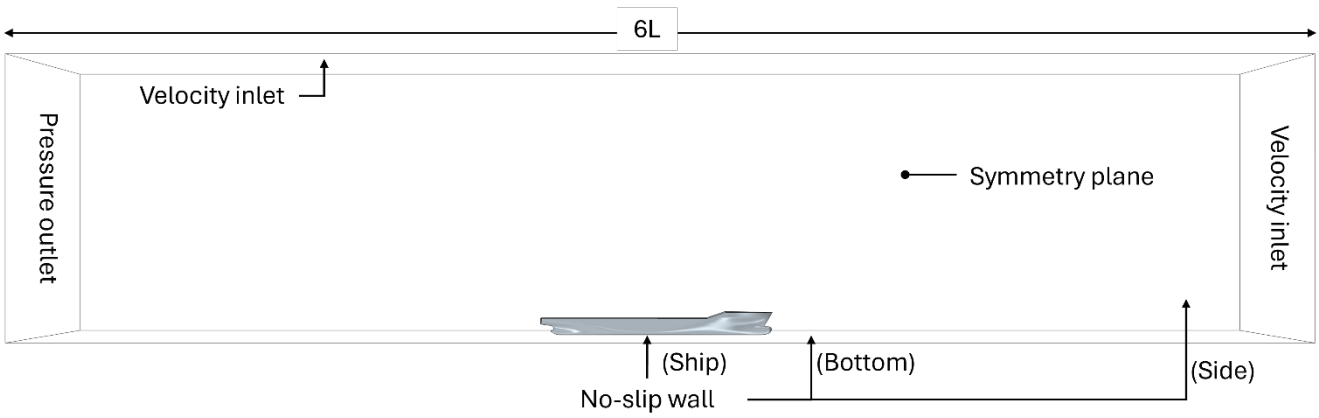

Figure 1. Computational domain and boundary conditions.

3.2 COMPUTATATIONAL MESH

The computational mesh was generated within the automatic facilities of Star-CCM+, consisting of flow-aligned hexahedral cells. A series of concentric refinements were created in the Kelvin wedge region in addition to a rectangular box encompassing the water surface in the entire computational domain where high-aspect ratio cells were created to capture deformations.

3.2 (a) Near-wall modelling approach

Near-wall modelling of turbulent flows is of critical importance to ensure the forces and moments acting on the vessel are accurately solved for. The approach laid out in (Terziev et al., 2022) was used to set the y^+ value to approximately 50 for the basis condition. The resulting near-wall mesh was copied to all conditions, which resulted in a y^+ of approximately 33 in the lowest speed case. The procedure for setting the y^+ *a priori* begins by approximating the ship's boundary layer as that of a flat plate with the same Reynolds number ($\delta = 0.382L/Re^{1/5}$, where δ is the boundary layer thickness and Re is the Reynolds number) and discretising the first 20% of the boundary layer where the majority of the flow velocity gradient is concentrated. The target y^+ = 50 is used in conjunction with the fluid density, ρ = 997.561 kg/m^3 and dynamic viscosity μ = 8.8875×10^{-4} Pa-s to estimate the thickness of the first cell layer ($2dy$) as shown in Eq. (1):

$$dy = y^+\nu/\sqrt{\tau_w/\rho} \quad (1)$$

Where τ_w is the shear wall stress, predicted using the ITTC correlation line and $\nu = \mu/\rho$. The number of layers (n) to be distributed over the discretised distance can be expressed through a geometric progression with a common ratio S=1.2 as shown in Eq. (2):

$$n = \log[1 - \delta(1 - S)/2dy]\,/\log\,(S) \quad (2)$$

A top view of the computational mesh is depicted in Figure 2, while the total number of cells was approximately 1.5 million cells with a small change in the number of cells depending on the water depth.

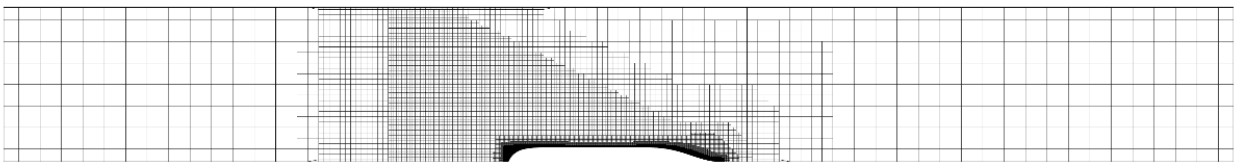

Figure 2. Computational mesh: top view of a slice through the mean water surface

3.3 MODELLING OF SHIP SQUAT

The account for the motion of the ship as a result of the hydrodynamic interaction between it and the bathymetry, a morphing mesh was utilised. This approach deforms the computational mesh to allow for 2-degrees of motion in the present case, namely, rotation around the y-axis (trim) and motion in the z-direction (sinkage). To prevent excessive mesh deformation and potential problems with stability of the solution, motion was initiated at least 5 seconds after the impulsive start of the simulation with hydrodynamic forces applied gradually following a further 10 seconds of simulation time. All simulations were allowed to run for a minimum of 150 seconds which also allowed the residuals to stabilise with a reduction of at least 3 orders of magnitude. In all cases, a combination of these criteria was used to judge convergence of the solution.

4 OPTIMISATION PROCEDURE

The optimisation procedure is based on the work of (Iqbal et al., 2025). The centre of gravity (CoG) optimisation technique to minimise squat and total resistance in fully confined water was conducted using a systematic approach that combines the response surface method (RSM) and a multi-objective genetic algorithm. The two key design variables in altering the CoG were the longitudinal centre of gravity (LCG) and the vertical centre of gravity (KG) of the ship. These variables significantly influence the ship's hydrodynamic performance, particularly squat and resistance, and were bounded within the range of −2.5 to 2.5 as codes. The conversion from codes to actual value is shown in Table 3, where -1, 0, and 1 indicate the minimum, initial, and maximum variation of design variables. The range between initial to maximum and minimum for LCG is ±2.5% and the KG is ±5%.

Table 3. Codification of design variables

Code	-1.414	-1	0	1	1.414
LCG	1.434	1.450	1.487	1.524	1.540
KG (0.75KM)	0.138	0.142	0.149	0.156	0.160

The two objective functions targeted for minimisation were squat and total resistance. To model the relationship between the design variables and the objective functions, a Central Composite Design (CCD) for two variables was employed, resulting nine combinations of load cases of two variables, including the initial condition. The nine combinations are shown in Table 4. The responses generated by this experimental design efficiently captures the nonlinear interactions between the variables while minimising the number of required simulations or experiments.

Table 4. Sample data generated from central composite design for two variables

No	Load Cases	x_1 code	x_2 code	LCG (m)	KG (m)
1	Initial	0	0	1.487	0.149
2	LC 1	1	1	1.524	0.156
3	LC 2	1	-1	1.524	0.142
4	LC 3	-1	1	1.450	0.156
5	LC 4	-1	-1	1.450	0.142
6	LC 5	-1.414	0	1.434	0.149
7	LC 6	1.414	0	1.540	0.149
8	LC 7	0	-1.414	1.487	0.138
9	LC 8	0	1.414	1.487	0.160

The results of the CCD procedure is a polynomial regression model which was developed for each objective function, squat and resistance. The general form of the regression model is shown in Eq. (3), where x_1 represents the LCG, $x_2$represents KG, and the coefficients a, b, c, d, e, f were determined from the CCD results after conducting the regression analysis. Then, these regression models formed the mathematical basis for optimisation

$$F(x_1, x_2) = a + bx_1 + cx_2 + d{x_1}^2 + e{x_2}^2 + f{x_1}^2{x_2}^2 \quad (3)$$

Where x_1 has a boundary condition of ±2.5% and x_2 a boundary condition of ±5%. To address the trade-off between minimising squat and resistance, a multi-objective genetic algorithm was applied. The algorithm began by generating an initial population of 500 solutions. Through iterative processes involving intermediate crossover and mutation, the algorithm explored the design space to produce new solutions. The fitness of each solution was evaluated using the polynomial regression models for squat and resistance, and non-dominated solutions were identified to construct a Pareto front. The optimisation process continued for 500 generations or until a maximum stall generation of 500 was reached, with tolerances set for function and constraint violations to ensure robust convergence.

The result of this process was a Pareto front representing the optimal trade-offs between squat and total resistance. Each point on the Pareto front corresponded to a solution where neither squat nor resistance could be improved without adversely affecting the other. These solutions were visualised in a Pareto plot, with squat and resistance represented on the x-axis and y-axis, respectively. The Pareto front provides insights into the relationship between the design variables and the objective functions, enabling decision-makers to select an optimal configuration of LCG and KG based on specific performance priorities. This approach effectively integrates RSM for efficient modelling and multi-objective genetic algorithm for robust multi-objective optimisation, offering a comprehensive framework for optimising ship performance in fully confined waters.

5 RESULTS AND DISCUSSION

5.1 VALIDATION AND VERIFICATION

The validation and verification process follows the norms set out by the ITTC (2008). Namely, the Grid Convergence Index procedure (Roache, 1997) was used to estimate the discretisation uncertainty. The numerical uncertainty is assumed to equal the discretisation uncertainty since iterative errors are negligible as explained in section 3.3. To obtain the discretisation uncertainty, a so-called grid triplet is required, which is obtained through a systematic change in the discretisation interval. The approach taken herein to satisfy the conditions of Richardson Extrapolation regarding cell aspect ratio and Courant number across the grid triplet is to magnify the spatial and temporal interval simultaneously (Salas, 2006). Then, the result from the Grid Convergence Index exercise is to obtain the spatio-temporal discretisation uncertainty, which begins with the definition of the convergence ratio (R) and observed order of accuracy (p):

$$R = \varepsilon_{32}/\varepsilon_{21} \quad (4)$$

$$p = \log(\varepsilon_{21}/\varepsilon_{32})\,/\log\,(r) \quad (5)$$

Where ε_{32} and ε_{21} are the difference between the coarse and medium, and medium and fine solution, respectively, while r is the refinement factor, chosen as $\sqrt{2}$, following ITTC (2008) and American Society of Mechanical Engineers (2009) guidelines. Once the observed order of accuracy is known, the uncertainty (U_N) follows:

$$U = 1.25\varepsilon_{21}/(r^p - 1) \quad (6)$$

Where the factor 1.25 is known as the factor of safety, used to increase the error's confidence interval from 50% to 95% and may be used when p is calculated using three solutions. A solution can be said to be validated if the error relative to the experiment is less than the validation uncertainty, defined as shown in Eq. (7). The results of the uncertainty estimation exercise and validation are shown in Table 4.

$$U_V = \sqrt{U_N^2 + U_E^2} \quad (7)$$

Where U_E is the experimental uncertainty. The experimental uncertainty in the present case was reported as 2.2% for resistance, and while the trim and sinkage show large uncertainties of approximately 90% at the low speed examined herein (Elsherbiny et al., 2019). To enable some measure of quality in sinkage and trim, the high-speed values of 3.47% and 4.64% are used, respectively.

Table 5. Discretisation uncertainty and validation exercise.

Parameter	Sinkage	Trim	Total resistance
Experimental value	2.09mm	0.022°	1.301N
Fine solution	2.03mm	0.009°	1.278N
Medium solution	2.05mm	0.001°	1.294N
Coarse solution	2.09mm	0.012°	1.317N
Convergence ratio	0.705	0.590	0.443
Observed order of accuracy	2.350	1.52	1.010
Discretisation uncertainty	0.794%	13.752%	3.825%
Experimental uncertainty	3.47% | 90%	4.64% | 90%	2.2%
Validation uncertainty	3.560% | 90.004%	14.514% | 91.045%	4.412%
Error (Fine – Experiment)	2.65%	60.02%	1.79%
Validated?	Yes | Yes	No | Yes	Yes

Table 5 shows that the solution is validated in sinkage regardless of whether the experimental uncertainty is taken as the low of high value reported by Elsherbiny et al. (2020) because the error relative to the experimental value is 2.65%. In the case of resistance, the experimental error is also sufficiently small to allow a successful validation. Although the disagreement in trim value is small, the relative percentage difference is significant, meaning that only the high level of experimental uncertainty permits the validation to be successful. An important aspect of the discretisation uncertainty estimate is to ensure the observed orders of accuracy are close to or not significantly higher than the theoretical value of $p = 2$. The results reported in Table 5 show that the order of accuracy predicted for sinkage is close to the theoretical value, while trim and total resistance exhibit smaller values, which are known to magnify the uncertainty. These properties of the approach to the asymptotic range give confidence in the robustness of the solution.

5.2 SINKAGE, TRIM AND RESISTANCE COEFFICIENTS

Presentation of the results from the systematic variation in position of the LCG proceeds with a description of the obtained values. To facilitate interpretation of the data, the results are presented by showing the property of interest, such as sinkage in the case of Figure 3, against relative changes in the position of the LCG while changes in the position of the KG are included via variations in the colour.

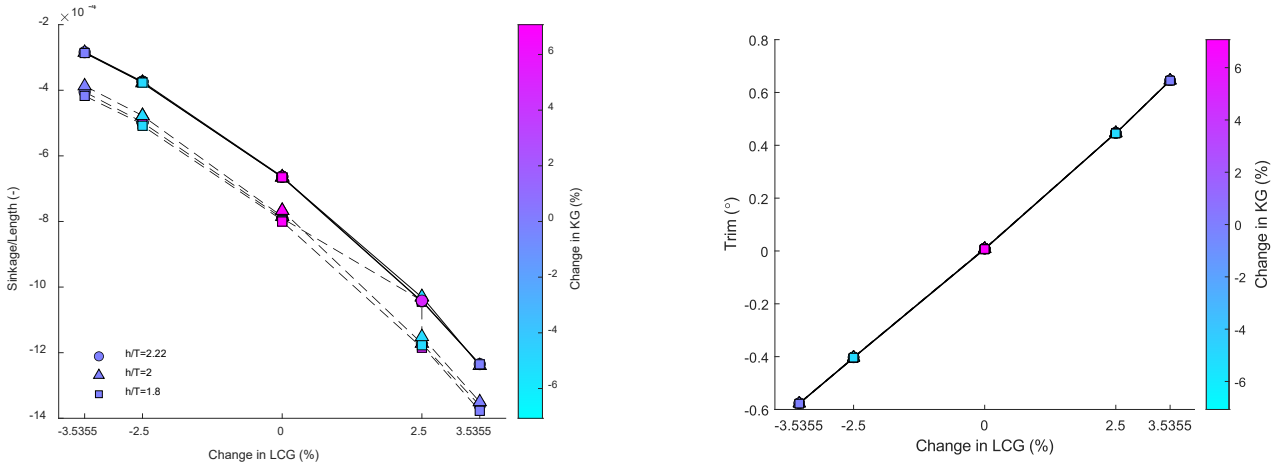

Figure 3. Sinkage and trim values obtained for all case studies. Solid lines show w/L = 1.5, while dashed lines show w/L = 1.

Figure 3 shows that sinkage is affected weakly by the position of the KG. All points except when the LCG is moved forward by 2.5% show that the sinkage change between case studies, for example the difference between h/T=2.2, h/T=2, and h/T=1.8 are within 1.5%. The aforementioned variation is within the uncertainty band reported in section 5.1. Thus, the variation with KG could be explained by the limitations of the computational model. Nevertheless, the results demonstrate that LCG has a significant effect on sinkage, which may increase by a factor of 7 across the examined case studies. Similarly, the trim is dominated by changes in the position of the LCG and shows negligible dependence on the KG. These results can be explained by the low value of the depth Froude number. At such speeds, the hydrodynamic moment generating trim is small, hence, the results are dominated by the initial trim.

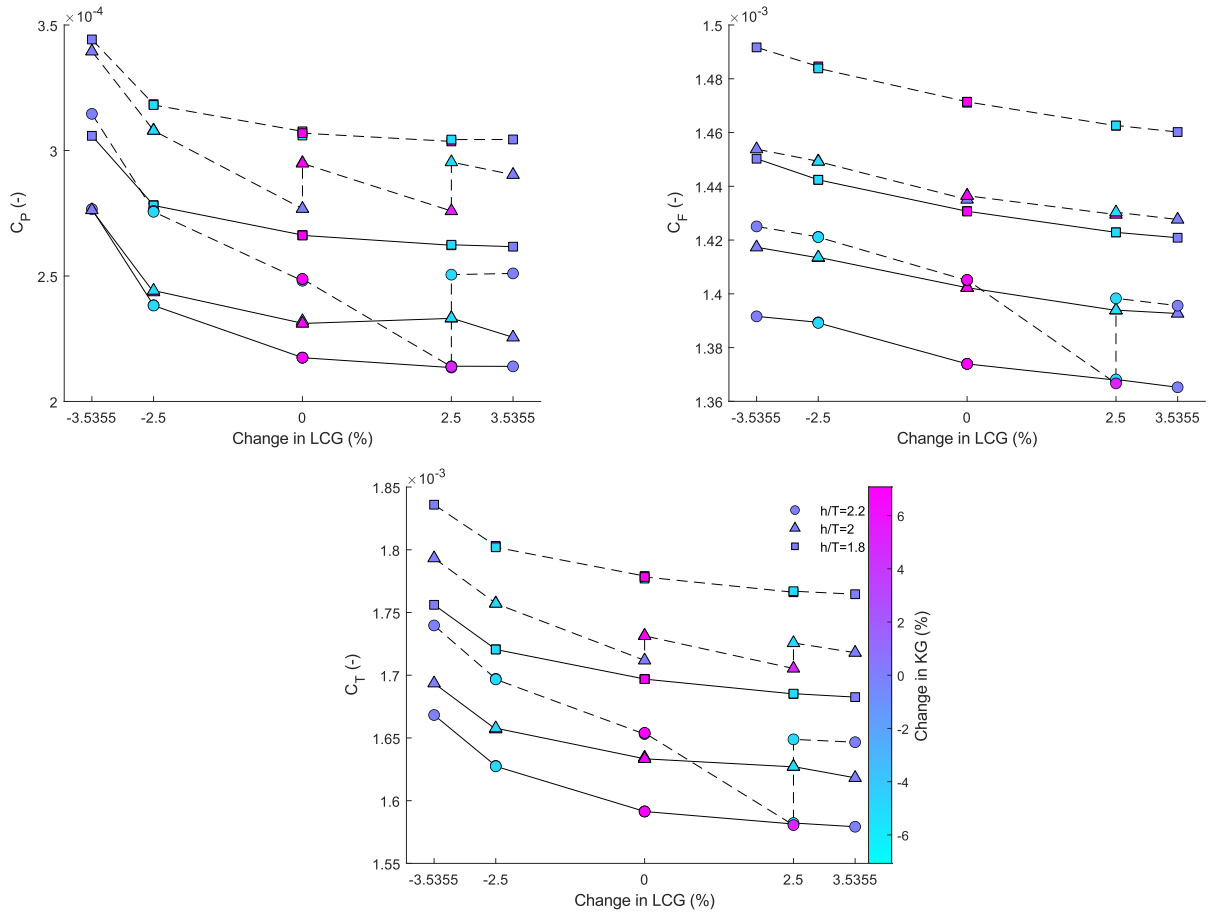

Figure 4. Pressure, Frictional, and total resistance coefficient values obtained for all case studies. Solid lines show w/L=1.5 and dashed lines show w/L=1.

Unlike sinkage and trim, the total resistance exhibits a more complex pattern owing to the change in width and depth of the waterway. When the dimensionless width of the waterway corresponds to w/L=1.5, the influence of KG is limited, as evidenced by the smooth curved described by the total resistance coefficient values in those cases across the range of LCG values. However, when the dimensionless width is reduced, the KG shows an influence on the results driven by apparent

changes in sinkage rather than trim. Figure 3 and Figure 4 jointly show that the variations in KG are responsible for the changes in the resistance. Unlike potential flow models which are not able to model the frictional component change, the computational model captures these and shows that the spike in resistance at ΔLCG=2.5% with variations in KG occurs not solely due to pressure resistance or its component, the wave resistance, which is typically isolated and optimised for. Instead, the frictional resistance and the pressure resistance show a similar pattern, particularly for the deepest case (h/T=2.2). With decreases in water depth, hydrodynamic forces and moments increase, and hence, the influence of variations in KG appears to decrease so that when h/T=1.8, the resistance curve versus LCG becomes smooth and shows no influence on the KG.

5.3 PARETO FRONTS

As described previously, the systematic variations in the LCG and KG were used to construct a mathematical model which is fed into a multi-objective genetic optimisation model with the purpose of defining the set of optimum solutions. This set of optima, known as the Pareto front, can be used to establish the trade-off in optimum arrangement directly through parameters of interest. For the purposes of this paper, the total resistance coefficient and squat, defined as the maximum vertical deviation of the ship, taking into account the sinkage and trim, was used. It should be noted that unlike sinkage, squat is defined positive downwards to facilitate the minimisation process of the multi-objective optimiser. The results, separated for w/L=1.5 and w/L=1 are shown in Figure 5.

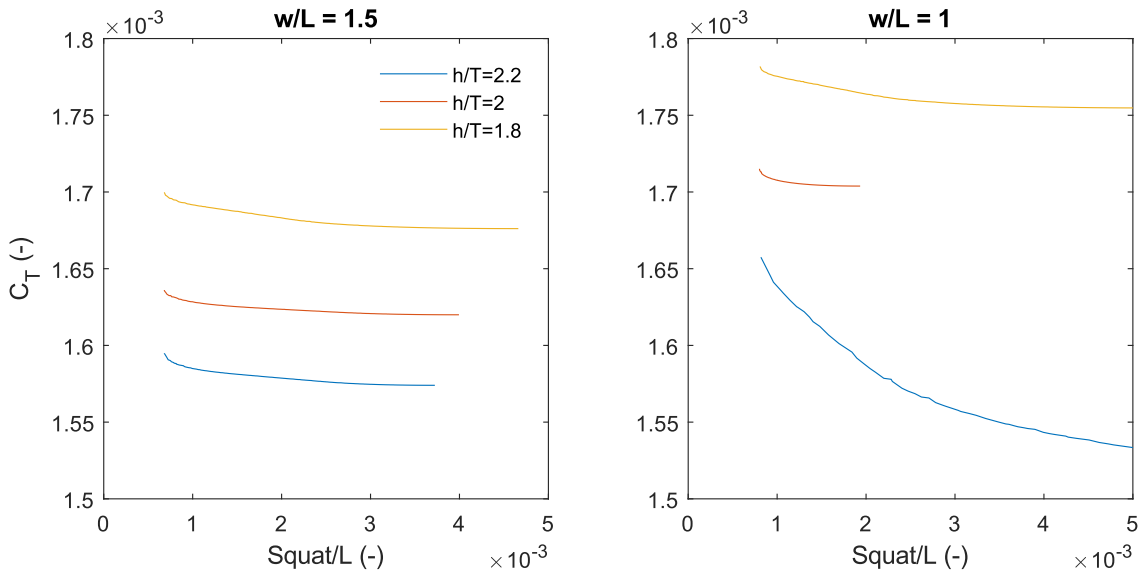

Figure 5. Pareto fronts of the total resistance coefficient and dimensionless squat for w/L=1.5 and w/L=1.

Figure 5 shows that despite the identical value in the depth Froude number across the case studies, there are significant variations in the set of possible optima. Specifically, the h/T=1.8 case is always characterised by a higher total resistance coefficient by no less than approximately 6.5% and 3.4% relative to h/T=2.2 and h/T=2, respectively, for the same dimensionless squat values at w/L=1.5. Similarly, the maximum differences in this case are 6.75% and 3.93%. Reducing the channel width causes a shift of the maximum disagreement magnifying the difference to up to 16.65% and 3.9%. More importantly, a consequence of the pareto fronts shown in Figure 5 is that an increase in squat can be linked to a reduction in resistance – a trend preserved across all case studies in varying degrees. Generally, a lower squat was associated with a trim by stern, hence, the results can be interpreted by the fact that the vessel ought to have a small trim by bow to reduce resistance; a result previously observed for the KCS by Campbell et al. (2022).

6 CONCLUSIONS AND FUTURE WORK

The effect of variation in the position of centre of gravity on ship hydrodynamics in fully confined water were examined using Computational Fluid Dynamics based on the Reynolds Averaged-Navier Stokes approach. Results were validated for a depth Froude number of 0.303 and a sample channel geometry against experimental results. Then, six channel geometries and nine systematically varied centre of gravity positions within the range ±2.5% horizontally and ±5% vertically were modelled for a depth Froude number of 0.303.

The obtained results show that trim is influenced weakly by the hydrodynamic moment generated due to forward motion, allowing the initial trim due to the change in centre of gravity to dominate the response. While the main response in sinkage was also dominated by the initial trim, it was found that the highest position of the centre of gravity resulted in a change in

sinkage which caused a spike in resistance coefficients. Interestingly, the pressure and shear force coefficients acting on the hull were affected causing in the same trend, hence, the effect on the total resistance coefficient was significant.
A complex interaction is revealed that depends on the vertical and horizontal position of the centre of gravity. Specifically, it is shown that sinkage is affected weakly by variations of the centre of gravity in the vertical direction, which were predicted to be around 1.5%, a value that lies within the discretisation uncertainty band. Conversely, variations in the LCG may alter the sinkage by a factor of 7. Resistance coefficients curves show spikes, only explainable through changes in the vertical position of the centre of gravity. For example, C_T may change by approximately 4% solely due to variations in VCG in a given case study. It is also revealed that such changes due to the position of vertical position of the entre of gravity become apparent only when the waterway width is small or equivalently, when the blockage is high.
The results obtained from systematically varying the centre of gravity were fed to a multi-objective genetic algorithm after a response surface model of the data was constructed. The multi-objective optimisation algorithm was used to construct Pareto fronts describing the trade-off between squat, the maximum reduction in underkeel clearance, and the total resistance coefficient which showed that a small squat is linked to elevated resistance. This was interpreted through the lens of the direction of trim since it is known that a small trim by bow contributes to energy efficiency of the target ship.
There are several ways in which the present study may be extended, ranging from the incorporation of other velocities to changes in blockage and self-propulsion. The former two are of particular interest since the depth Froude number was preserved for all case studies in the present paper rather than maintaining the velocity. It is interesting to observe how changes such as the speed and further reductions in the channel width may impact the results, particularly in cases where the hydrodynamic moment may cause trim of similar magnitude to the initial trim.

7 ACKNOWLEDGEMENTS

Results were obtained using the ARCHIE-WeSt High Performance Computer (www.archie-west.ac.uk) based at the University of Strathclyde.

8 REFERENCES

ASME (American Society of Mechanical Engineers). (2009). Standard for Verification and Validation in Computational Fluid Dynamics and Heat Transfer - ASME V&V 20-2009. In *ASME International*.

Barrass, C. B., & Derrett, D. R. (2012). Chapter 42 – Ship Squat in Open Water and in Confined Channels. *Ship Stability for Masters and Mates*, 367–388. https://doi.org/10.1016/B978-0-08-097093-6.00042-6

Campbell, R., Terziev, M., Tezdogan, T., & Incecik, A. (2022). Computational fluid dynamics predictions of draught and trim variations on ship resistance in confined waters. *Applied Ocean Research*, *126*(August), 103301. https://doi.org/10.1016/j.apor.2022.103301

Chillcce, G., & Moctar, O. (2022). Viscous effects on squat. *Applied Ocean Research*, *125*(July), 103252. https://doi.org/10.1016/j.apor.2022.103252

Cisek, J. M. (2025). Weather-driven variations in optimum trim of a refrigerated cargo carrier: insights from ocean crossing voyage. *Journal of Ocean Engineering and Marine Energy*. https://doi.org/10.1007/s40722-024-00378-2

Elsherbiny, K., Terziev, M., Tezdogan, T., Incecik, A., & Kotb, M. (2020). Numerical and experimental study on hydrodynamic performance of ships advancing through different canals. *Ocean Engineering*, *195*(106696). https://doi.org/10.1016/j.oceaneng.2019.106696

Elsherbiny, K., Tezdogan, T., Kotb, M., Incecik, A., & Day, S. (2019). Experimental analysis of the squat of ships advancing through the New Suez Canal. *Ocean Engineering*, *178*(November 2018), 331–344. https://doi.org/10.1016/j.oceaneng.2019.02.078

EMSA (European Maritime Safety Agency). (2023). *Annual Overview of Marine Casualties and Incidents*.

Härting, A., Laupichler, A., & Reinking, J. (2009). Considerations on the squat of unevenly trimmed ships. *Ocean Engineering*, *36*(2), 193–201. https://doi.org/10.1016/j.oceaneng.2008.10.003

Hirt, C. W. W., & Nichols, B. D. D. (1981). Volume of fluid (VOF) method for the dynamics of free boundaries. *Journal of Computational Physics*, *39*(1), 201–225. https://doi.org/10.1016/0021-9991(81)90145-5

Iqbal, M., Terziev, M., Tezdogan, T., & Incecik, A. (2025). Hull form optimisation to minimise the total resistance and dynamic responses of small fishing vessels. *Ocean Engineering*, *321*, 120357. https://doi.org/10.1016/j.oceaneng.2025.120357

ITTC. (2008). Uncertainty Analysis in CFD Verification and Validation Methodology and Procedures. *25th ITTC 2008, Resistance Committee*, 12. http://ittc.info/media/4184/75-03-01-01.pdf

Korkmaz, K. B., Werner, S., & Bensow, R. (2023). Investigations on experimental and computational trim optimisation methods. *Ocean Engineering*, *288*. https://doi.org/10.1016/j.oceaneng.2023.116098

Le Strat, M., & Terziev, M. (2025). Scale effects on ship vertical force and trim moment in calm water. *Physics of Fluids*, *37*(1). https://doi.org/10.1063/5.0243505

Panagiotakopoulos, T., Filippopoulos, I., Filippopoulos, C., Filippopoulos, E., Lajic, Z., Violaris, A., Panagiotis Chytas, S., & Kiouvrekis, Y. (2022, July 18). Vessel's trim optimization using IoT data and machine learning models. *13th International Conference on Information, Intelligence, Systems & Applications (IISA)*. https://marantankers.gr/

Roache, P. J. (1997). Quantification of Uncertainty in Computational Fluid Dynamics. *Annual Review of Fluid Mechanics*, *29*(1), 123–160. https://doi.org/10.1146/annurev.fluid.29.1.123

Salas, M. D. (2006). Some observations on grid convergence. *Computers and Fluids*, *35*(7), 688–692. https://doi.org/10.1016/j.compfluid.2006.01.003

Terziev, M., Tezdogan, T., & Incecik, A. (2019). Application of eddy-viscosity turbulence models to problems in ship hydrodynamics. *Ships and Offshore Structures*, 1–24. https://doi.org/10.1080/17445302.2019.1661625

Terziev, M., Tezdogan, T., & Incecik, A. (2022). Scale effects and full-scale ship hydrodynamics: A review. *Ocean Engineering*, *245*(November 2021), 110496. https://doi.org/10.1016/j.oceaneng.2021.110496

Terziev, M., Tezdogan, T., Oguz, E., Gourlay, T., Demirel, Y. K., & Incecik, A. (2018). Numerical investigation of the behaviour and performance of ships advancing through restricted shallow waters. *Journal of Fluids and Structures*, *76*, 185–215. https://doi.org/10.1016/j.jfluidstructs.2017.10.003

Tu, H., Xia, K., Zhao, E., Mu, L., & Sun, J. (2023). Optimum trim prediction for container ships based on machine learning. *Ocean Engineering*, *277*. https://doi.org/10.1016/j.oceaneng.2022.111322

9 AUTHORS BIOGRAPHY

Brief biographies are required for all authors e.g.:

Momchil Terziev is assistant professor in naval architecture at the Department of Naval Architecture, Ocean and Marine Engineering at the University of Strathclyde. His research interests lie in scale effects and shallow water ship hydrodynamics.
Muhammad Iqbal is assistant professor at Diponegoro University within the Faculty of Engineering. His research interests include modelling and performance of small fishing boats.
Yujia Wei is research fellow in fellow in multiphysics modelling at the University of Cranfield. His research interests include computational modelling of hydroelasticity of marine structures and AI applications in the maritime field.
Atilla Incecik is professor of offshore engineering at the Department of Naval Architecture, Ocean and Marine Engineering at the University of Strathclyde. His research interests span ocean and marine engineering with applications to ships and offshore structures.

A ONE DIMENSIONAL HYDRAULIC MODEL FOR CONFINED NAVIGATION WITH A LONGITUDINAL VARIATION OF THE HULL

Julien Dambrine, Laboratoire de Mathématiques et Applications (UMR 7348), CNRS, University of Poitiers, France.

Valentin Jules, Institut Pprime (CNRS UPR 3346), CNRS, University of Poitiers, ISAE-ENSMA, France.

Pierre-Jean Pompée, Voies Navigables de France, France.

Morgan Pierre, Laboratoire de Mathématiques et Applications, (UMR 7348) University of Poitiers, France.

Germain Rousseaux, Institut Pprime (CNRS UPR 3346), CNRS, University of Poitiers, ISAE-ENSMA, France.

A ONE DIMENSIONAL HYDRAULIC MODEL FOR CONFINED NAVIGATION WITH A LONGITUDINAL VARIATION OF THE HULL

JULIEN DAMBRINE, LABORATOIRE DE MATHÉMATIQUES ET APPLICATIONS (UMR 7348), CNRS, UNIVERSITY OF POITIERS, FRANCE.
VALENTIN JULES, INSTITUT PPRIME (CNRS UPR 3346), CNRS, UNIVERSITY OF POITIERS, ISAE-ENSMA, FRANCE.
PIERRE-JEAN POMPÉE, VOIES NAVIGABLES DE FRANCE, FRANCE.
MORGAN PIERRE, LABORATOIRE DE MATHÉMATIQUES ET APPLICATIONS, (UMR 7348) UNIVERSITY OF POITIERS, FRANCE.
GERMAIN ROUSSEAUX, INSTITUT PPRIME (CNRS UPR 3346), CNRS, UNIVERSITY OF POITIERS, ISAE-ENSMA, FRANCE.

SUMMARY

This paper addresses some aspects of shallow water theories used for the description of the flow around boats in the context of confined navigation. We start by giving a brief account of the derivation of the most general version of the shallow water system of equations for a boat with non-constant beam and draught profiles. We will also consider the boat to be able to trim and sinkage by hydrostatic effects. Then, we present a quick review of the two classical families of theories of the literature on the matter: the energy and momentum approaches. We will comment their consistencies or inconsistencies with regards to the aforementioned general model. Finally, some numerical results are presented on the general model and comparisons with classical approaches such as the one proposed by Kreitner (1934), Schijf (1949) and Constantine (1960) will be shown.

NOMENCLATURE

CFD	Computational Fluid Dynamics
CNR	Compagnie Nationale du Rhône
KSC	Kreitner-Schijf-Constantine
t-KSC	trapezoidal Kreitner-Schijf-Constantine

An	Anthony number (Fourdrinoy et al. 2019)	
B	Boat's beam (function)	m
B_{max}	Boat's maximal beam	m
Fn_h	Froude number based on h and V	
Fn_{Hm}	Froude number based on the average depth $Hm = A_c/W$ (trapezoidal channel)	
g	Earth's gravitational acceleration (9.81m/s^2)	m/s^2
h	Canal's section maximal depth	m
I_b	Tensor of inertia of the boat	kg m^2
L_{wl}	Length of the boat (at the waterline, at rest)	m
m	Blockage ratio or Bossut number (Bossut 1775)	
m_b	Mass of the boat	kg
p	Canal's walls slope with respect to the vertical direction	
R_i	Moment of inertia ratio	
R_m	Mass ratio	
Sr	Sretensky number (Sretensky 1936)	
T	Boat's draught (function)	m
Td	Trapezoidal deviation	
T_{max}	Boat's maximal draught	m
u	Return current velocity	m/s
V	Horizontal speed of the boat	m/s
W	Canal's section maximal width	m
w	Canal's section minimal width	m
x^*	Centre of mass relative position (0 : stern ; 1 bow))	
x_b	Horizontal coordinate of the bow (w.r.t the centre of mass)	m
x_s	Horizontal coordinate of the stern (w.r.t the centre of mass)	m
z	Water level drawdown	m

$\overline{z}$	Boat's squat (from rest)	m
θ	Boat's trim (from rest)	rad
μ	Water depth to boat length ratio	
ρ	Water's mass density (1000kg/m^3)	kg/m^3

1 INTRODUCTION

The launch of major waterway expansion projects for inland water transport is currently driving the development of inland navigation, which is recognised as a mode of transport with significant economic and environmental potential (Bouman et al. 2017; Pompée 2015). However, this type of navigation has a direct impact on the balance of river ecosystems, as the waves generated by boats disturb the banks of rivers and canals.

In contrast to maritime navigation, inland navigation takes place in a confined environment in which the waterways are limited in both width and depth. These special conditions significantly influence the behaviour of boats, leading to pronounced effects such as increased squat, greater resistance to forward motion, lower propulsion efficiency, and reduced manoeuvrability.

These phenomena are inherently complex and depend on a variety of factors: the geometry of the waterway, the shape and speed of the boat, the velocity and direction of the current, and the presence of sediments and obstacles. A thorough understanding of these interactions is crucial, not only to minimise the environmental impact of inland navigation, but also to ensure safety and optimise the efficiency of navigation operations.

Several attempts have been made in the literature to describe the mechanisms governing these phenomena: vertical, lateral, and/or sectional confinement. Ranging from early studies based on fundamental physical theories proposed by Thiele (1901) or Rassmussen (Biles 1908) to more recent investigations employing advanced CFD (Computational Fluid Dynamics) techniques as in (Gourlay 2000; Bechthold and Kastens 2020; Nieutin-Redon 2024).

This paper addresses key aspects of shallow water theories applied to confined navigation. We begin by deriving the most general formulation of the shallow-water equations, which has been adapted to account for boats with non-uniform beam and draught profiles. The model also incorporates hydrostatic effects that allow for trim and sinkage (lowering of the centre of gravity) of the boat, thus extending its relevance to practical applications. In the context of the current article, we will call this model the "general model".

This is followed by a brief overview of the two classical families of theories in the literature: the energy-based and the momentum-based approaches. In most of these works, the flow is considered one-dimensional, with no head losses, and assumes a constant canal cross section that is rectangular or, more generally, trapezoidal. Similarly, the boat is modelled as a rectangular block with a constant cross section. This simplification underpins the works of Thiele (1901), Kreitner (1934), Schijf (1949), and Constantine (1960), which we will refer to as the KSC (Kreitner-Schijf-Constantine) theory throughout this article.

More recently, an analytical calculation has been provided (Pompée 2015; Delefortrie et al. 2024), ultimately offering a comprehensive summary and detailed mathematical formulations of these theories, offering valuable insights into their underlying principles and calculations. These studies used the energy-based approach, as did Marchal (1975), who extended the framework by incorporating head losses due to wall friction, as well as those occurring in wave crests, troughs, and hydraulic jumps. In addition, Marchal accounted for dynamic squat effects, providing a more comprehensive representation of real-world conditions.

In contrast, other research work, such as those of Sharp and Fenton (1968), Bouwmeester, Drost, and Van der Meer (1986) and Tenaud & CNR (Compagnie Nationale du Rhône) (1977) adopted the so-called "momentum conservation" approach. Although this method offers an alternative perspective, it is ultimately limited by the discontinuity of the flow at the bow of the vessel, which renders the momentum-based approach inconsistent with the classical shallow-water theory (and thus our model). We mention that Chen (2013) proposed a model that is very similar to the one shown here, but with additional terms (transverse flow, thickening of the boat by boundary layer effects, first-order dispersive effects), which takes into account phenomena that are far beyond the scope of the present work.

Their consistencies and limitations are critically assessed in light of the aforementioned "general model". This comparative analysis highlights the conditions under which these traditional theories align or deviate from the behaviour predicted by the general model in the limit of a block boat.

Finally, numerical simulations of the general model are performed, and the results are compared with the classical KSC theories adapted to trapezoidal section canals (Jules et al. 2024), called t-KSC (trapezoidal Kreitner-Schijf-Constantine) in the context of this article. The results provide valuable insight into the dynamics of confined navigation and suggest possible improvements to existing theoretical frameworks. Further, the results compared with classical theories illustrate the impact of this asymmetry on the boat's trim and overall hydrodynamic behaviour.

2 DERIVATION OF THE GENERAL SHALLOW-WATER MODEL

Let us consider a waterway with a constant trapezoidal section, we denote $\vec{e}_x$ the unit vector indicating the longitudinal direction (pointing forward), $\vec{e}_y$ the transverse unit vector, and $\vec{e}_z$ the upward unit vector. We denote Ω the fluid domain, Γ_f the free surface (time dependent), Γ_c the walls and bottom of the waterway, and Γ_b the boundary (time dependent) of the boat immersed in fluid. We assume that the boat is moving at a constant speed V along the $\vec{e}_x$ axis and is free to move vertically and to trim. The frame of reference is following the boat that is moving forward with constant speed V. The origin of the frame of reference is set at the intersection between the vertical axis passing through the centre of mass of the boat and the horizontal plane that coincides with the water level at rest. Let $S(x) = (]x-\varepsilon/2, x+\varepsilon/2[\times \mathbb{R}^2) \cap \Omega$ be a transverse

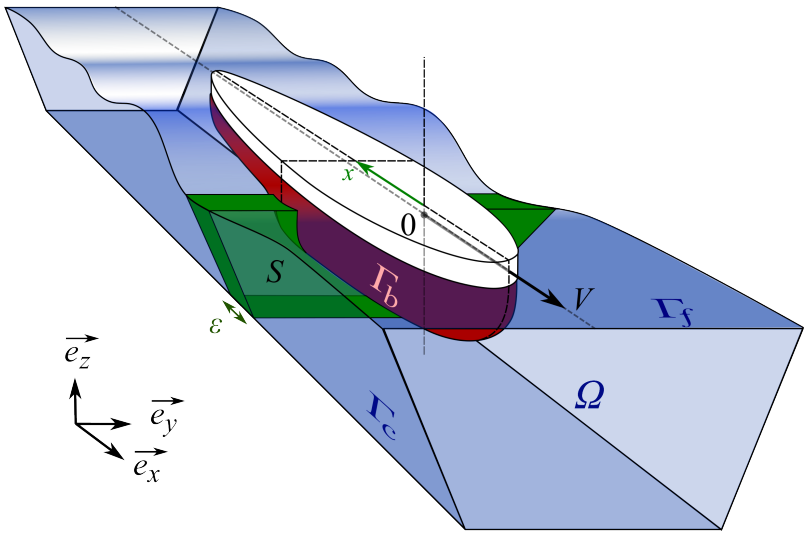

Figure 1: Geometric setting of the problem and main notations for the fluid and boat's domains.

slab of the fluid domain, centred on the longitudinal coordinate $x \in \mathbb{R}$, with thickness ε (see figure 1). Let us denote Σ_+ and Σ_- the front and back boundaries of the slab, and let us denote, respectively, Σ_c, Σ_b, Σ_s, the boundaries of S in contact, respectively, with the waterway, the boat and the free surface. The conservation of mass and momentum in S for an inviscid incompressible fluid write (Batchelor 1967):

$$\frac{d}{dt}|S| = \int_{\Sigma_\pm} \vec{U}\cdot\vec{n}\, ds, \tag{1}$$

$$\frac{d}{dt}\int_S \vec{U} d\vec{r} = -\int_{\Sigma_\pm} \left(\vec{U}\otimes\vec{U}\right)\vec{n} ds - \frac{1}{\rho}\int_S \nabla P dx - g\,|S|\,\vec{e}_z, \tag{2}$$

where $|S|$ denotes the volume of S, $\vec{U}$ is the fluid's velocity, P is the fluid's pressure, ρ is the water's mass density and g is the Earth's gravitational acceleration. In addition to these conservation equations for the fluid, we shall consider the following equations for the conservation of the linear and angular momentum of the boat (Landau and Lifshitz 1976):

$$\frac{d}{dt}\left(m_b\vec{U}_b\right) = -\int_{\Gamma_b} P\vec{n}\,\mathrm{d}s - m_b g\vec{e}_z\,, \tag{3}$$

$$\frac{d}{dt}\left(I_b\,\vec{\omega}_b\right) = -\int_{\Gamma_b} P\,\vec{r}\wedge\vec{n}\,\mathrm{d}s - m_b g\,\vec{r}_g\wedge\vec{e}_z, \tag{4}$$

where $\vec{U}_b$ is the velocity of the boat's centre of mass, m_b is the mass of the boat, $\vec{\omega}_b$ is the boat's angular speed, and I_b is its inertia tensor. Since the origin of the reference frame is placed on a vertical line that passes through the centre of gravity of the boat, we have $\vec{r}_g \wedge \vec{e}_z = 0$. The next section introduces some hypotheses about the dynamics of the boat along with some notation of its geometric parameters and kinematic variables.

2.1 BOAT'S GEOMETRY AND KINEMATICS

Recall that it is assumed that the boat moves horizontally at constant speed V. The displacement and rotation of the boat are governed by equations (3), (4). In the context of this article, we will call "sinkage" the vertical displacement of the boat and "trim" the angle of rotation of the boat along the $\vec{e}_y$ axis starting from the rest configuration. It is important to note that in the literature a distinction is made between sinkage and trim induced by hydrostatic effects (solely due to the buoyancy forces)

and sinkage and trim induced by hydrodynamic effects. In the scope of this paper, as we will see later, the only components of the sinkage and trim are the hydrostatic ones. Let $\overline{z}$ be the sinkage and let θ be the trim angle (positive for an upward displacement of the bow). We have, in the frame of reference following the horizontal motion of the boat (as described in the previous section):

$$\vec{U}_b(t) = -\dot{\overline{z}}(t)\vec{e}_z\,, \quad \vec{\omega}_b(t) = \dot{\theta}(t)\vec{e}_y\,. \tag{5}$$

The left-right symmetry of the boat implies that:

$$I_b\vec{e_y} = I_y^0 m_b\,\vec{e_y}\,, \tag{6}$$

where I_y^0 is the boat's principal moment along $\vec{e}_y$. For simplicity, we also assume that all sections of the boat are rectangular (with a beam B and a draught T).

The domain of the boat at rest is hence (see figure 2, top row):

$$\Omega_b^0 = \{\vec{r} \in \mathbb{R}^3 \ \mid |r_y| < B(r_x)/2, \text{ and } r_z > T(r_x)\}. \tag{7}$$

With a vertical displacement $\overline{z}(t)$ and trim angle $\theta(t)$ (see figure X, bottom row), it can be shown that, at first order with respect to θ the domain of the boat becomes:

$$\Omega_b^{\overline{z},\theta} = \{\vec{r} \in \mathbb{R}^3 \ \mid |r_y| < B(r_x)/2, \text{ and } r_z > T(r_x) \ + r_x\theta - \overline{z}\}. \tag{8}$$

The hypothesis that the trim angle is small is consistent with the "long boat hypothesis" that will be introduced in the next section. This implies that, in first order, the effect of a sinkage and trim can be seen as a modification of the draught profile of the boat. Let us also introduce the following notation:

- The surface area of the section of the waterway at rest:

  $$A_c = \frac{W+w}{2}\,h\,, \tag{9}$$

  where W (respectively w) is the canal's section maximal (respectively minimal) width, and h is the canal's section maximal depth. Since $w = W - 2ph$ (by definition of p, see figure 2), we have:

  $$A_c = \frac{W + (W-2ph)}{2}\,h = (W - ph)\,h\,. \tag{10}$$

- The surface area of the section the immersed part of the hull at longitudinal coordinate x and time t:

  $$A_b(x,z,\overline{z},\theta) = B(x)\left(\overline{z} - x\theta + T(x) - z\right)^+\,, \tag{11}$$

  where $(\cdot)^+$ denotes the positive part, and we recall, from figure 2 that z is the free surface drop profile. Since it introduces both theoretical and numerical challenges, this threshold effect will be ignored later on as we will assume that the free surface shall never drop below the boat in reasonable situations.

- The surface area of the section of the waterway at longitudinal coordinate x and time t:

  $$A_w(x,z,\overline{z},\theta) = A_c - A_b(x,z,\overline{z},\theta) - z(W - pz)\,. \tag{12}$$

Let us note that in the above definitions, A_b and A_c appear to be independent of time, which is wrong in general: both A_b and A_c depend on the functions θ, $\overline{z}$, and z, which, depending on the context, can be functions of time. For example, the surface area of the boat at time t and longitudinal coordinate x is given by $A_b(x, z(t,x), \overline{z}(t), \theta(t))$.

2.2 FLOW HYPOTHESES

We now assume that the variations of the boat's geometrical parameters $T(x)$ and $B(x)$ are slow along the longitudinal coordinate, *i.e.*:

$$hT'(x)/T_{max} << 1\,, \quad hB'(x)/B_{max} << 1\,, \tag{13}$$

where T_{max} and B_{max} are respectively the maximum draught and beam of the boat. Note that, for a boat with length L_{wl}, if we suppose that the dimensionless beam and draught profiles ($T(x/L_{wl})/T_{max}$ and $T(x/L_{wl})/T_{max}$) are fixed, then assuming (13) is equivalent to suppose that:

$$h/L_{wl} << 1\,. \tag{14}$$

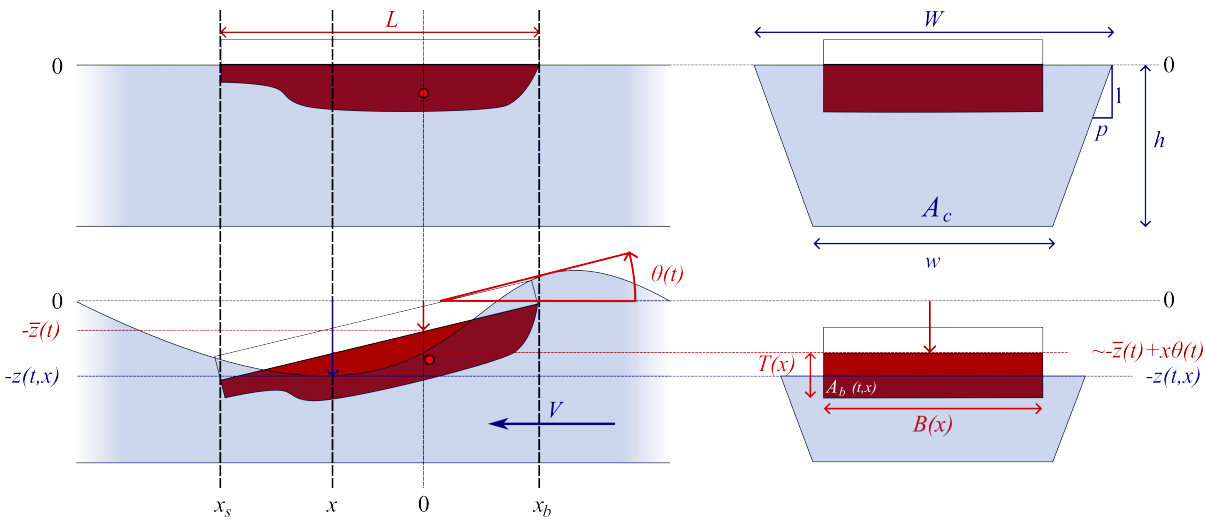

Figure 2: **Notation for the main geometrical variables involved in the model. Top row: boat at rest : bottom row: boat in motion. left column: side view, right column: front view for a slice at longitudinal coordinate x**

These assumptions, which we will refer to as the "long boat hypothesis", will lead us to assume that the flow is slowly varying along the longitudinal axis of the waterway and that the pressure can be assumed to be at hydrostatic equilibrium on every section of the canal (Saint-Venant hypotheses on the flow). We hence first assume that the flow is unidirectional and uniform across each section:

$$\vec{U}(\vec{r}) = -\left(u(r_x) + V\right)\vec{e_x}\,, \tag{15}$$

where u is the return current velocity (negative in the $\vec{e}_x$ direction). Second, the pressure is at hydrostatic equilibrium for each section:

$$P(\vec{r}) = -\rho g\left(r_z + z(r_x)\right)\,. \tag{16}$$

The first consequence of this is that no transverse variations are taken into account, and hence the free surface elevation is constant on each section:

$$\Gamma_f = \left\{(r_x, r_y,\ -z(r_x))\,;\ r_x \in \mathbb{R}\,, r_y \in]-W/2, W/2[\right\}\,, \tag{17}$$

where z is a function that represents the water drawdown longitudinal profile. Note that this hypothesis was already implicitly introduced in the previous section (through the definitions of A_c and A_w). Since the hypotheses (13) are consistent with a flow forced by a smooth and long obstacle (albeit not necessarily thin), it is, in principle, excluded to consider boat geometries that have discontinuous variations, such as "block"-type boats. We will therefore assume that, at least, the beam profile B is continuous and that there exist two longitudinal coordinates x_s (for stern) and x_b (for bow) such that $B(x_s) = B(x_b) = 0$.

By injecting (15), (16) and (17) into the mass and momentum balance equations (1)-(2) and taking the limit $\varepsilon \to 0$ we obtain after some calculations (which will be detailed in an upcoming review paper on this topic) :

$$\underbrace{\partial_t A_w}_{\frac{1}{\varepsilon}\frac{d}{dt}|S|} + \underbrace{\partial_x\left(A_w\left(V+u\right)\right)}_{-\frac{1}{\varepsilon}\int_{\Sigma_\pm}\vec{U}\cdot\vec{n}\,ds} = 0\,, \tag{18}$$

$$\underbrace{\partial_t\left(A_w(V+u)\right)}_{-\frac{1}{\varepsilon}\frac{d}{dt}\int_S\vec{U}d\vec{r}} - \underbrace{\partial_x\left(A_w(V+u)^2\right)}_{\frac{1}{\varepsilon}\int_{\Sigma_\pm}\left(\vec{U}\otimes\vec{U}\right)\vec{n}ds} + \underbrace{gA_w\partial_x z}_{-\frac{1}{\varepsilon}\frac{1}{\rho}\int_S\nabla P dx - g|S|\vec{e}_z} = 0\,. \tag{19}$$

where the terms indicated below the following equations show the origin of the terms above in the limit $\varepsilon \to 0$. Note that in the above equation, we identified, by a small abuse of language, the function $(t,x) \mapsto A_w(x, z(t,x), \overline{z}, \theta)$ with a function of space and time A_w taken as an unknown of the system. The system (18)-(19) is a generalised version of the classical Saint-Venant system, that has been adapted to take into account the geometry of the boat implicitly through the relation between z and A_w (that we recall from 12):

$$A_w(x, z, \overline{z}, \theta) = A_c - B(x)\left(\overline{z} - x\theta + T(x) - z\right) - z(W - pz) \tag{20}$$

Let us now describe the simplified dynamics of the boat by introducing the Saint-Venant hypotheses (15), (16) and (17) in the expression of the hydrostatic forces applied to the boat's hull.

2.3 DESCRIPTION OF THE BOAT'S DYNAMICS

For $\vec{r} \in \Gamma_b$, let $\vec{F}_w(\vec{r})$ be the force exerted by the fluid on the boat at $\vec{r}$, we have:

$$\vec{F}_w = -P\,\vec{n} \tag{21}$$

Consistently with (13), since the variations of the boat's beam and draught profile are assumed to be slow with respect to the longitudinal coordinate x, we neglect the component of $\vec{F}_w$ along $\vec{e}_x$. At a given section of longitudinal coordinate x (see figure 3), we have:

$$\vec{F}_w(x, r_y, r_z) = \begin{cases} \pm\,\rho g(r_z + z(x)) & \text{on the sides } (y = \pm B(x)) \\ \rho g(-\overline{z} + x\theta - T(x) + z(x)) & \text{at the bottom } (z = \overline{z} + x\theta(t) - T(x)) \end{cases} \tag{22}$$

by symmetry, we then obtain the resultant force $\overline{\vec{F}_w}(x)$ applied at $(x, 0, -\overline{z} + x\theta - T(x))$ on the boat:

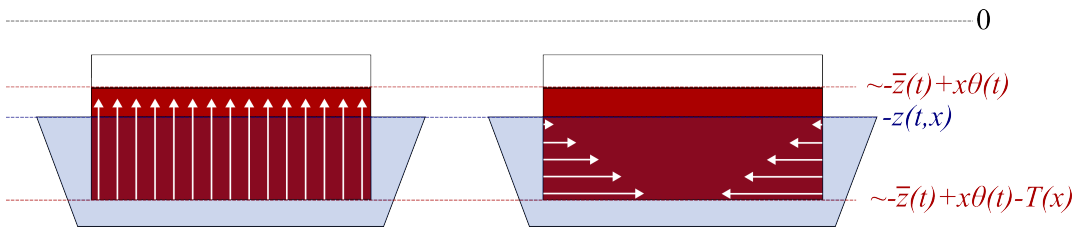

Figure 3: Schematic description of the forces exerted by the fluid on the boat (white arrows) at a given section of longitudinal coordinate x. Left: vertical forces; right: horizontal forces.

$$\overline{\vec{F}_w}(x) = \rho g B(x)(-\overline{z} + x\theta - T(x) + z(x))\,\vec{e}_z \tag{23}$$

Thus the total resultant force applied by the fluid on the boat writes:

$$\int_{\Gamma_b} \vec{F}_w\,\mathrm{d}s = \rho g \int_{x_s}^{x_b} \overline{\vec{F}_w}(x)\mathrm{d}x = \rho g \int_{x_s}^{x_b} B(x)(-\overline{z} + x\theta - T(x) + z(x))\mathrm{d}x\,\vec{e}_z \tag{24}$$

And the corresponding total resultant force moment writes:

$$\begin{aligned} \int_{\Gamma_b} \vec{r} \wedge \vec{F}_w\,\mathrm{d}s(\vec{r}) &= \rho g \int_{x_s}^{x_b} (x\vec{e}_x + B(x)(-\overline{z} + x\theta - T(x))\,\vec{e}_z) \wedge (-\overline{z} + x\theta - T(x) + z(x))\vec{e}_z\,\mathrm{d}x \\ &= -\rho g \int_{x_s}^{x_b} xB(x)(-\overline{z} + x\theta - T(x) + z(x))\,\mathrm{d}x\,\vec{e}_y \end{aligned} \tag{25}$$

Recalling (3)-(4) we hence have, for $(\overline{z}, \theta)$:

$$\ddot{\overline{z}}(t) = \frac{\rho g}{m_b} \int_{x_s}^{x_b} B(x)\,(\overline{z}(t) - x\theta(t) - z(t,x) - T(x))\;\mathrm{d}x + g \tag{26}$$

$$\ddot{\theta}(t) = -\frac{\rho g}{I_y^0} \int_{x_s}^{x_b} xB(x)\,(\overline{z}(t) - x\theta(t) - z(t,x) - T(x))\;\mathrm{d}x \tag{27}$$

Finally we point out the fact that at rest ($\overline{z} = 0$, $\theta = 0$, $z = 0$), the boat must be at equilibrium, hence we must have:

$$\int_{x_s}^{x_b} B(x)T(x)\,\mathrm{d}x = \frac{m_b}{\rho}\,, \quad \int_{x_s}^{x_b} xB(x)T(x)\,\mathrm{d}x = 0\,. \tag{28}$$

The first condition states that the mass of the boat must be equal to the mass of a volume of water equivalent to the immersed part of the boat at rest. It is important to note that T represents the boat's draught at rest (which will be affected, in motion, by the boat's sinkage and trim). The second condition states that, at rest, the centre of buoyancy of the boat must be at the same longitudinal coordinate as its centre of mass. Therefore, taking into account the conditions (28) in (26)-(27), we obtain:

$$\ddot{\overline{z}}(t) = \frac{\rho g}{m_b} \int_{x_s}^{x_b} B(x)\,(\overline{z}(t) - x\theta(t) - z(t,x))\;\mathrm{d}x \tag{29}$$

$$\ddot{\theta}(t) = -\frac{\rho g}{I_y^0} \int_{x_s}^{x_b} xB(x)\,(\overline{z}(t) - x\theta(t) - z(t,x))\;\mathrm{d}x \tag{30}$$

2.4 THE COMPLETE DIMENSIONLESS MODEL

In this section we rewrite our model in a dimensionless form in order to identify the key parameters of our problem. For the sake of simplicity, instead of giving a different name for the dimensionless variables, we rather rename our variables in their dimensionless form:

$$\tilde{t} = \frac{V}{L_{wl}} t\,, \quad \tilde{x} = \frac{x - x_s}{L_{wl}}\,, \quad \tilde{B}(x) = \frac{B((x-x_s)/L_{wl})}{B_{max}} \quad \tilde{T} = \frac{T((x-x_s)/L_{wl})}{T_{max}} \tag{31}$$

$$\tilde{A}_w(\tilde{t},\tilde{x}) = \frac{A_w(\tilde{t}\,L_{wl}/V, x_s + \tilde{x}\,L_{wl})}{A_c}\,, \quad \tilde{z}(\tilde{t},\tilde{x}) = \frac{z(\tilde{t}\,L_{wl}/V, x_s + \tilde{x}\,L_{wl})}{h}\,, \quad \tilde{u}(\tilde{t},\tilde{x}) = \frac{u(\tilde{t}\,L_{wl}/V, x_s + \tilde{x}\,L_{wl})}{V} \tag{32}$$

$$\tilde{\overline{z}} = \frac{\overline{z}}{h}\,, \quad \tilde{\theta} = \frac{L_{wl}\theta}{h} \tag{33}$$

where $L_{wl} = x_b - x_s$, B_{max}, T_{max} represent respectively the length, maximum beam and draught of the boat (in meters). We also recall that h is the maximum upstream depth of the canal, and that:

$$A_c = h\frac{W+w}{2} = h(W - ph) \tag{34}$$

where p is the slope of the waterway with respect to the vertical direction at the border of the banks. Then, gathering the equations (18)-(19)-(29)-(30)-(12), we get the following system of dimensionless equations (again, the details will be shown in an upcoming review paper):

$$\partial_{\tilde{t}}\tilde{A}_w + \partial_{\tilde{x}}(\tilde{A}_w(1+\tilde{u})) = 0\,, \tag{35}$$

$$\partial_{\tilde{t}}(\tilde{A}_w(1+\tilde{u})) - \partial_{\tilde{x}}(\tilde{A}_w(1+\tilde{u})^2) + \frac{1}{\mathsf{Fn}_h^2}\tilde{A}_w\partial_{\tilde{x}}\tilde{z} = 0\,, \tag{36}$$

$$\tilde{A}_w(\tilde{t},\tilde{x}) = 1 - \mathsf{Sr}\,\tilde{B}(x)(\tilde{\overline{z}}(\tilde{t}) - \tilde{z}(\tilde{t},\tilde{x}) + \mathsf{An}\,\tilde{T}(\tilde{x}) - (\tilde{x} - x^*)\tilde{\theta}(\tilde{t}) - \frac{1}{1-\mathsf{Td}}\tilde{z}(1 - \mathsf{Td}\,\tilde{z})\,, \tag{37}$$

$$\ddot{\tilde{\overline{z}}}(\tilde{t}) = \frac{\mu^{-2}}{\mathsf{Fn}_h^2}\mathsf{R}_m\int_0^1 \tilde{B}(\tilde{x})\left(\tilde{\overline{z}}(t) - (\tilde{x}-x^*)\tilde{\theta}(\tilde{t}) - \tilde{z}(\tilde{t},\tilde{x})\right)\,\mathrm{d}\tilde{x}\,, \tag{38}$$

$$\ddot{\tilde{\theta}}(t) = \frac{\mu^{-3}}{\mathsf{Fn}_h^2}\mathsf{R}_m\mathsf{R}_i\int_0^1 (\tilde{x}-x^*)\tilde{B}(x)\left(\tilde{\overline{z}}(t) - (\tilde{x}-x^*)\tilde{\theta}(\tilde{t}) - \tilde{z}(\tilde{t},\tilde{x})\right)\,\mathrm{d}\tilde{x}\,, \tag{39}$$

where, in addition to the non-dimensional beam and draught profiles B and T, the parameters of the problem are :

- Fn_h represent the maximum height-based Froude number:

  $$\mathsf{Fn}_h = \frac{V}{\sqrt{gh}}\,. \tag{40}$$

  Note that in Pompée (2015), rather than the Froude number based on h, the (cross-sectional) averaged depth based Froude number was considered:

  $$\mathsf{Fn}_{Hm} = \frac{V}{\sqrt{gH_m}} \tag{41}$$

  where $H_m = A_c/W$. This definition of the Froude number is useful in cases where p is neglected, in order to obtain an equivalent rectangular canal section for a given trapezoidal section. In our case, we retain (40) since p is taken into account in the model.

- Sr (Sretensky number) accounts for the beam to average width ratio :

  $$\mathsf{Sr} = \frac{B_{max}}{W - ph} = \frac{B_{max}}{\frac{W+w}{2}}\,, \tag{42}$$

  and An (Anthony number) accounts for the draught to depth ratio :

  $$\mathsf{An} = \frac{T_{max}}{h}\,. \tag{43}$$

  These two quantities are of crucial importance in confined hydrodynamics since they both appear in fully dispersive linear theories developed, either by Sretensky (1936) and Sretensky (1937) for the wave-making resistance in finite

depth or width, or by Keldysh and Sedov (1937) for rectangular canals. Our previous work on the battle of Actium (Fourdrinoy et al. 2019) have shown the importance of the draught to depth ratio in the outcome of this historical event, which is why we have chosen the terminology An for this ratio.

Although our model (35)-(39) is fully non-linear but non-dispersive, it is worth noticing that Sr and An also play a role here, in contrast with the KSC theory where the only geometrical ratio that matters is the blockage (or Bossut number) factor m (we recall from (10) that $A_c = (W - ph)\,h$ for a trapezoïdal canal):

$$m = \frac{B_{max}T_{max}}{(W - ph)h} = \text{Sr An} \tag{44}$$

- μ is the depth to length ratio :

$$\mu = \frac{h}{L_{wl}} \tag{45}$$

in principle this quantity is assumed to be small from (13). This suggests that the system (35)-(39) should have properties of a slow-fast system, and that a quasi-static version of (38)-(39) should be considered even in the case of a time-dependent solution of the full system. This is of little importance here as we will only seek stationary solutions.

- Td is the trapezoidal deviation :

$$\text{Td} = p\frac{h}{W} = \frac{1}{2}\frac{W - w}{W} \tag{46}$$

that measures how much the section of the canal deviates from a rectangle (in which situation its value is 0).

- R_m and R_i are mass and moment of inertia ratios:

$$\text{R}_m = \frac{\rho h L_{wl} B_{max}}{m_b}\,, \quad \text{R}_i = \frac{h L_{wl} m_b}{I_0^y}\,. \tag{47}$$

which are of few importance here since these constant disappear for the stationary problem.

- x^* is the relative position (between 0 and 1) of the centre of mass of the boat:

$$x^* = -\frac{x_s}{L_{wl}} \tag{48}$$

In the following section, we shall drop the $\sim$ symbol over the variables in equations (35)-(39) for the sake of clarity.

3 SUB/SUPER CRITICAL FLOWS

In this section, we seek stationary solutions of (35)-(39) , which might only exist in a particular range of the above-mentioned parameters. First, the stationary version of (35) give the flow rate conservation equation:

$$A_w(1 + u) = 1\,. \tag{49}$$

Second, the stationary version of the momentum conservation equation (36) give an equation that describes the variation of the flux of fluid momentum caused by the presence of the boat:

$$-\partial_x\left(A_w(1 + u)^2\right) + \frac{1}{\text{Fn}_h^2}A_w\partial_x z = 0\,. \tag{50}$$

Let us develop the first term in the above equation:

$$-A_w(1 + u)\partial_x(1 + u) - (1 + u)\partial_x(A_w(1 + u)) + \frac{1}{\text{Fn}_h^2}A_w\partial_x z = 0\,. \tag{51}$$

On one hand using (49) , we remark that $\partial_x(A_w(1 + u)) = \partial_x(1) = 0$; on the other hand, assuming $A_w \neq 0$ everywhere, we have:

$$-(1 + u)\partial_x(1 + u) + \frac{1}{\text{Fn}_h^2}\partial_x z = 0\,, \tag{52}$$

which leads to :

$$\partial_x \left(\frac{(1+u)^2}{2} - \frac{1}{\mathsf{Fn}_h^2} z \right) = 0 \,. \tag{53}$$

and so, integrating with respect to x, and noting that, in the absence of a current:

$$u(x), z(x) \underset{x \to +\infty}{\longrightarrow} 0 \,, \tag{54}$$

we have:

$$(1+u)^2 - \frac{2}{\mathsf{Fn}_h^2} z = 1 \,. \tag{55}$$

Finally, we recall the equations (38)-(39) in the steady state :

$$\int_0^1 \begin{pmatrix} 1 \\ x - x^* \end{pmatrix} B(x) \left(\overline{z} - (x - x^*)\theta - z(x) \right) \, \mathsf{d}x = 0 \,, \tag{56}$$

which can be recast as a linear system of unknowns $(\overline{z}, \theta)$:

$$\begin{pmatrix} 1 & -\overline{x} \\ -\overline{x} & (\sigma^2 + \overline{x}^2) \end{pmatrix} \begin{pmatrix} \overline{z} \\ \theta \end{pmatrix} = \int_0^1 \begin{pmatrix} 1 \\ x^* - x \end{pmatrix} z(x) b(x) \, \mathsf{d}x \,, \tag{57}$$

where $\overline{x}$ and σ are respectively the mean and variance associated with the normalized beam profile b:

$$b(x) = B(x) / \int_0^1 B(s) \, \mathsf{d}s \,, \tag{58}$$

$$\overline{x} = \int_0^1 (x - x^*) \, b(x) \, \mathsf{d}x \,, \tag{59}$$

$$\sigma^2 = \int_0^1 (x - x^*)^2 \, b(x) \, \mathsf{d}x - \overline{x}^2 \,. \tag{60}$$

Provided that σ is non-zero (which is true provided that the boat is not described by a singular mass), the system (57) has a unique solution that writes:

$$\overline{z} = \int_0^1 \frac{\sigma^2 + \overline{x}^2 - \overline{x} \, (x - x^*)}{\sigma^2} \, b(x) z(x) \mathsf{d}x \,, \tag{61}$$

$$\theta = \int_0^1 \frac{\overline{x} + x^* - x}{\sigma^2} \, b(x) z(x) \mathsf{d}x \,. \tag{62}$$

Our problem is therefore to solve the system of equation (49) and (55), along with the relations (61)-(62). Injecting (49) in (55) and recalling the expression (37) of A_w, our problem can be reformulated as finding z satisfying

$$\left(\frac{2}{\mathsf{Fn}_h^2} z + 1 \right) \left(1 - \mathsf{Sr} \, B(x) (\overline{z} - z + \mathsf{An} \, T - (x - x^*)\theta) - \frac{1}{1 - \mathsf{Td}} z (1 - \mathsf{Td} \, z) \right)^2 = 1 \tag{63}$$

where $\overline{z}$ and θ are given by (61) and (62). We call an "admissible solution" any continuous function $z : [0,1] \to \mathbb{R}$ satisfying equation (63), with the boundary conditions (upstream and downstream): $z(0) = z(1) = 0$. From a numerical point of view, the integrals in (61) and (62) are approached with the rectangle method, and all functions z, B, T, are uniformly discretized in the interval $[0,1]$. The solution of (63)-(61)-(62) is then sought using a quasi-Newton method implemented in python with Numpy/Scipy (Harris et al. 2020; Virtanen et al. 2020). All the results obtained in this article have been produced by a Python code available at: `https://github.com/jdambrin/MASHCON/` .

3.1 RELATIONSHIPS WITH OTHER MODELS

In this section, we stress the differences between the model presented in the previous sections and some of the models of the same family (based on a shallow water approach) that can be found in the literature. The predictions of the hydrostatic sinkage and return current are usually presented in the literature as belonging to one of the two following families of physical approaches.

- Momentum-based approaches such as those found in the works of Sharp and Fenton (1968), Bouwmeester, Drost, and Van der Meer (1986) and Tenaud & CNR (1977) in which the variation of the flux of momentum between the upstream region and the region abreast of the boat is determined by a term that is supposed to model the effect of the boat's bow on the fluid. Here, the term "momentum-based approach" is an abuse of language, since the quantity of interest is the flux of momentum (or the impulsion, when divided by ρ) rather than the momentum itself.
- Energy-based approaches such as those found in the works of Kreitner (1934), Schijf (1949), Constantine (1960) in which the conservation of the total energy (or the hydraulic head, when divided by ρg) is invoked to obtain a relation between the quantities of interest (return current and waterlevel drawdown) upstream and abreast of the boat.

It should be noted that these two approaches have been shown to produce different predictions of θ and $\overline{z}$ (Sharp and Fenton 1968). This might be counter-intuitive since a balance of momentum and a balance of energy of a mechanical system should lead to the same set of equations. The key of this paradox is that both approaches, that are based on the same Saint-Venant assumptions are equivalent (indeed (50) and (55) have been shown to be equivalent in the previous section) only when B is continuous, which is not the case in all the references mentioned above in this section, in which the boat is assumed to be a block, *i.e.*:

$$B(x) = \begin{cases} 1 & \text{if } x \in [0,1] \\ 0 & \text{if } x \notin [0,1] \end{cases} . \tag{64}$$

The approach of the present paper is to suppose beforehand that B is continuous and supported in $[0,1]$, and to eventually investigate the limit where B degenerates towards (64).

We remark that by setting $B \equiv 1, T \equiv 1$, then z is constant (and equal to $\overline{z}$), $\theta = 0$, and then equation (63) becomes:

$$\left(\frac{2}{\mathsf{Fn}_h^2} z + 1\right)\left(1 - m - \frac{1}{1-\mathsf{Td}} z(1-\mathsf{Td} z)\right)^2 = 1\,, \tag{65}$$

where $m = \mathsf{SrAn}$ is the obstruction parameter. We will call this equation the "t-KSC equation" (for trapezoidal Kreitner-Schijf-Constantine), that has been studied revently by Jules et al. (2024). Moreover, for a rectangular channel ($p = 0$) we retrieve the usual equation of the classical KSC theory:

$$\left(\frac{2}{\mathsf{Fn}_h^2} z + 1\right)(1 - m - z)^2 = 1\,. \tag{66}$$

In (63), (65) and (66) it is expected that, for given values Sr, An, Td, there exist two critical values of the Froude number Fn_h^- and Fn_h^+ which are such that, only for $\mathsf{Fn}_h \in [\mathsf{Fn}_h^-, \mathsf{Fn}_h^+]$ the equation does not have a solution. For $\mathsf{Fn}_h < \mathsf{Fn}_h^-$, the flow is called subcritical ; for $\mathsf{Fn}_h > \mathsf{Fn}_h^+$, the flow is called supercritical. For the KSC equation (66) the critical Froude values can be determined analytically as calculated by Pompée (2015) and ultimately proven completely by Delefortrie et al. (2024):

$$\mathsf{Fn}_h^- = \left(2\sin\left(\frac{\arcsin(1-m)}{3}\right)\right)^{3/2} \tag{67}$$

$$\mathsf{Fn}_h^+ = \left(2\sin\left(\frac{\pi - \arcsin(1-m)}{3}\right)\right)^{3/2} \tag{68}$$

For the other models (63) and (65) these critical values will be estimated numerically with a search by dichotomy.

4 NUMERICAL EXPERIMENTS

In this section we present some numerical tests with a range of parameters that are chosen to be close to realistic situations, and we aim to show the effect of the boat's end profiles and the influence of the asymmetry on the main characteristics of the flow around the boat (sinkage, trim, free-surface elevation). All the tests presented here have been produced using a script developed by the authors of the present article, and available at: `https://github.com/jdambrin/MASHCON/`.

4.1 PARAMETERS

Let us consider the following set of parameters for the boat:

$$L_{wl} = 100\text{m}\,, \quad B_{max} = 11.4\text{m}\,, \quad T_{max} = 2.5\text{m} \tag{69}$$

Which corresponds to a large Rhine class boat as defined by the European Conference of Ministers of Transport (ECMT) (1992). We will also consider two different waterways, as in Pompée (2015). However, unlike Pompée (2015), we deliberately use the same single vessel CEMT class Vb in both class IV and Vb cross sections to simplify our comparisons:

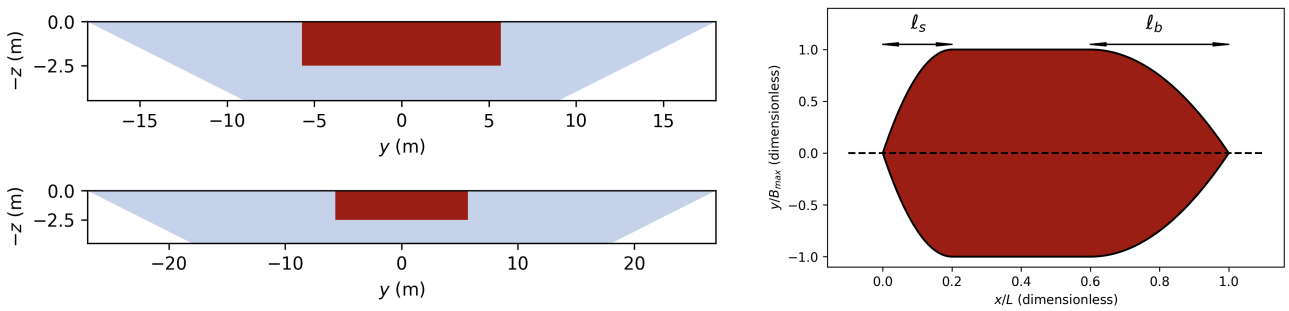

Figure 4: Left: cross section of the canal with the boat at rest for the CEMT class IV (top) and Vb (bottom) canals; right: schematic view of the boat's beam profile, with the geometrical parameters ℓ_s and ℓ_b.

- CEMT class IV

$$W = 36\text{m}\,, \quad p = 2\,, \quad h = 4.5\text{m} \tag{70}$$

- CEMT class Vb

$$W = 54\text{m}\,, \quad p = 2\,, \quad h = 4.5\text{m} \tag{71}$$

The figure 4 shows the cross section of the waterway and the boat at rest at the midpoint of the boat (maximum beam and draught); it shows that the main difference lies in the blockage factor (or Bossut number according to our terminology) $m = (B_{max}T_{max})/((W - ph)h)$ (which is 23% for the class IV canal and 14% for the class Vb canal). For simplicity, we will consider $T \equiv 1$ (constant draught profile), but more general profiles can be considered without any technical difficulty. The longitudinal change of the boat's section will be induced by the beam profile (prismatic boat):

$$B(x/L_{wl}) = \begin{cases} -(x/(L_{wl}\ell_s) - 1)^2 + 1 & \text{if } x/L_{wl} \in [0, \ell_s] \\ 1 & \text{if } x/L_{wl} \in [\ell_s, 1 - \ell_b] \\ -((x/L_{wl} - 1)/\ell_b + 1)^2 + 1 & \text{if } x/L_{wl} \in [1 - \ell_b, 1] \end{cases} \tag{72}$$

where ℓ_s and ℓ_b are two dimensionless parameters representing the ratio between the length of the smooth transition between the stern (respectively the bow) of the boat and the position beyond which the beam can be considered constant (see figure 4). These parameters can be related with the boat's block coefficient:

$$C_B = \int_0^1 B(s)\,\mathrm{d}s = 1 - \frac{(\ell_s + \ell_b)}{3} \tag{73}$$

and so it is clear that, as $\ell_s, \ell_b \to 0$, we have $C_b \to 1$. In this "block limit", the shape of the boat converges towards a "shoe's box" shape. The contrast between ℓ_s and ℓ_b can be related to the asymmetry of the boat :

$$a = 1 - 2x^* = -1 + 2\int_0^1 xB(x)\mathrm{d}x / \int_0^1 B(x)\mathrm{d}x\,. \tag{74}$$

A positive (r.p. negative) value of a means that the centre of gravity of the boat is towards the bow (r.p. the stern), and its maximum value is 1 (r.p. -1).

In the next sections, we will study the effect of these two geometrical parameters on the behaviour of the boat for different speeds (or Froude numbers) in the subcritical and supercritical regimes. Note that we are fully aware that such boats are never in the supercritical regime due to their incapacity to overcome the wall of resistance that appears at the end of the subcritical regime. The results in the supercritical regime are shown for theoretical interest only.

4.2 INFLUENCE OF THE END PROFILES OF THE BOAT

In this section we set $\ell_s = \ell_b = \ell$, and we investigate the behaviour of the boat as $\ell \to 0$. By symmetry arguments, it can be shown that in this particular situation we expect the trim θ to vanish. For the aforementioned values of the parameters (both class IV and Vb canals), we will compare the sinkage $\overline{z}$ as a function of the Froude number for values of ℓ ranging from 0.05 to 0.4 (which corresponds to block coefficients ranging from 0.96 to 0.73). These profiles will also be compared with the results

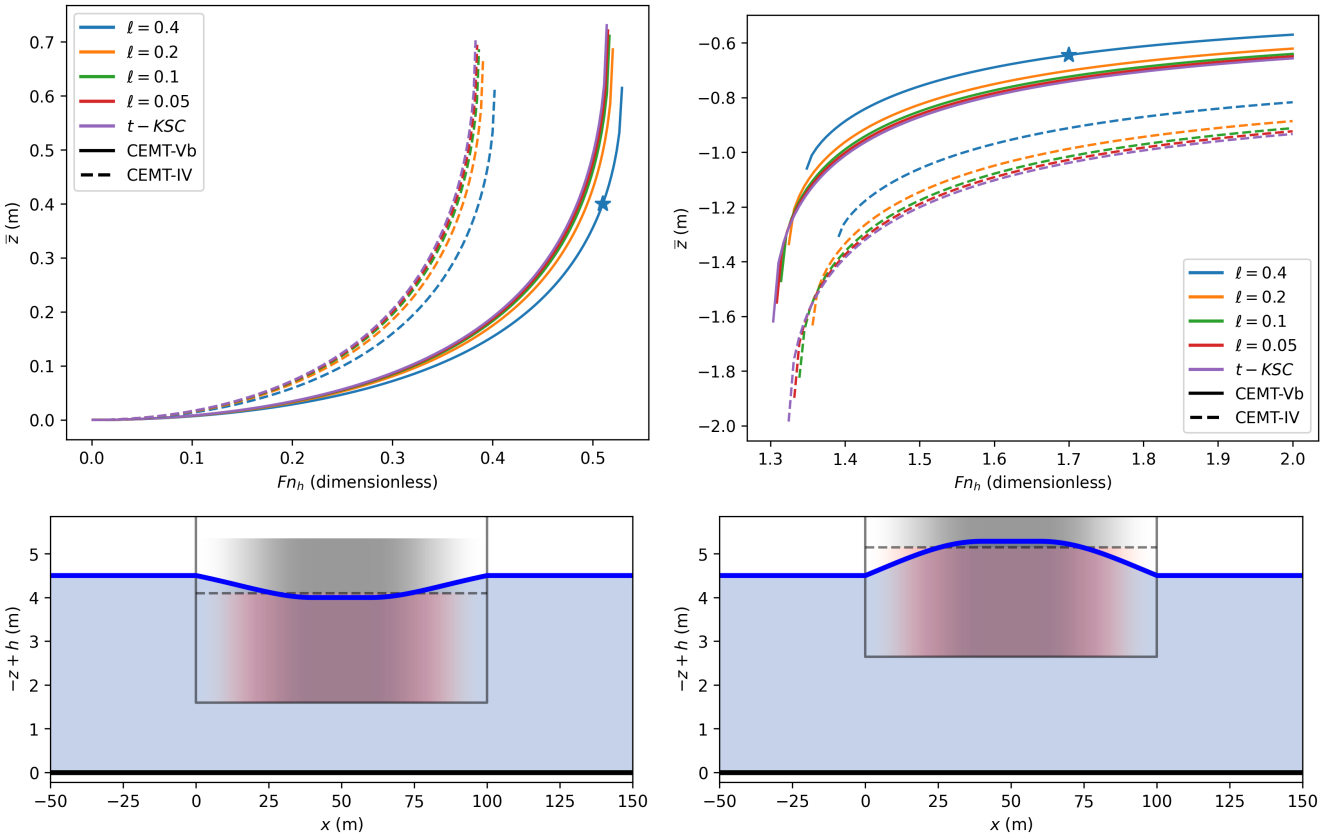

Figure 5: Top : boat sinkage $\overline{z}$ as a function of the Froude number for the class Vb (plain) and IV (dashed) canal, and different values of the geometrical parameter ℓ. Left : sub-critical solutions ; right : supercritical solutions. Bottom : instances of the longitudinal profile of the free-surface elevation, and position of the boat (shades of red indicate the beam values), for parameters indicated by a star on the figure above.

of the t-KSC theory (block limit). In figure 5 (top row) we can remark that, as ℓ becomes smaller, the sinkage of the boat $\overline{z}$ becomes closer and closer to the prediction of z given by the t-KSC model (purple lines), showing that the energy approach for the prediction of the hydrostatic sinkage is consistent with the Saint-Venant theory in the block limit. The tendency shown is that larger values of ℓ will give slightly larger values of the critical Froude numbers Fn_h^- and Fn_h^+ (defined in the previous section), along with a smaller maximum sinkage in the subcritical regime. The effect of larger values of ℓ therefore seems to be similar (in a nontrivial way) to smaller values of the blockage factor. For the supercritical case, the effect is inverse, as larger values of ℓ are associated with higher values of the elevation of the boat. The figure 5 (bottom row) shows instances of the longitudinal profiles of the free surface along with the boat's position for the parameters indicated by a star on the top row. These figures show that the trim is indeed null in this symmetric case.

4.3 INFLUENCE OF THE ASYMMETRY OF THE BOAT

Here, we will choose different values for ℓ_s and ℓ_b, ranging from $\ell_s = 0.4$ and $\ell_b = 0.05$ to $\ell_s = 0.05$ and $\ell_b = 0.4$ (asymmetry coefficient a ranging between -10% and 10%). The figure 6 (top) shows the trim angle as a function of the Froude number for subcritical flows (left) and supercritical flows (right). We can notice that the trim angle grows sharply in magnitude as the Froude number approaches Fn_h^-, and changes sign in the supercritical regime (where the angle seems to be changing more slowly with respect to the Froude number). One important fact to be noted here is that the sign of the angle depends on the direction of the asymmetry of the boat: if the centre of gravity is closer to the stern, the trim is bow up in the subcritical regime, and conversely, if the centre of gravity of the boat is closer to the bow, the trim is bow down in the subcritical regime.

5 CONCLUSIONS

In this article, we derived from general principles a one-dimensional hydraulic model for the flow around a boat in the context of inland navigation, that allows for regular shape profiles of the boat's beam and draught. The first feature of this model, in contrast with the more classical KSC theory, is that it requires a distinction between the water drawdown and the boat's

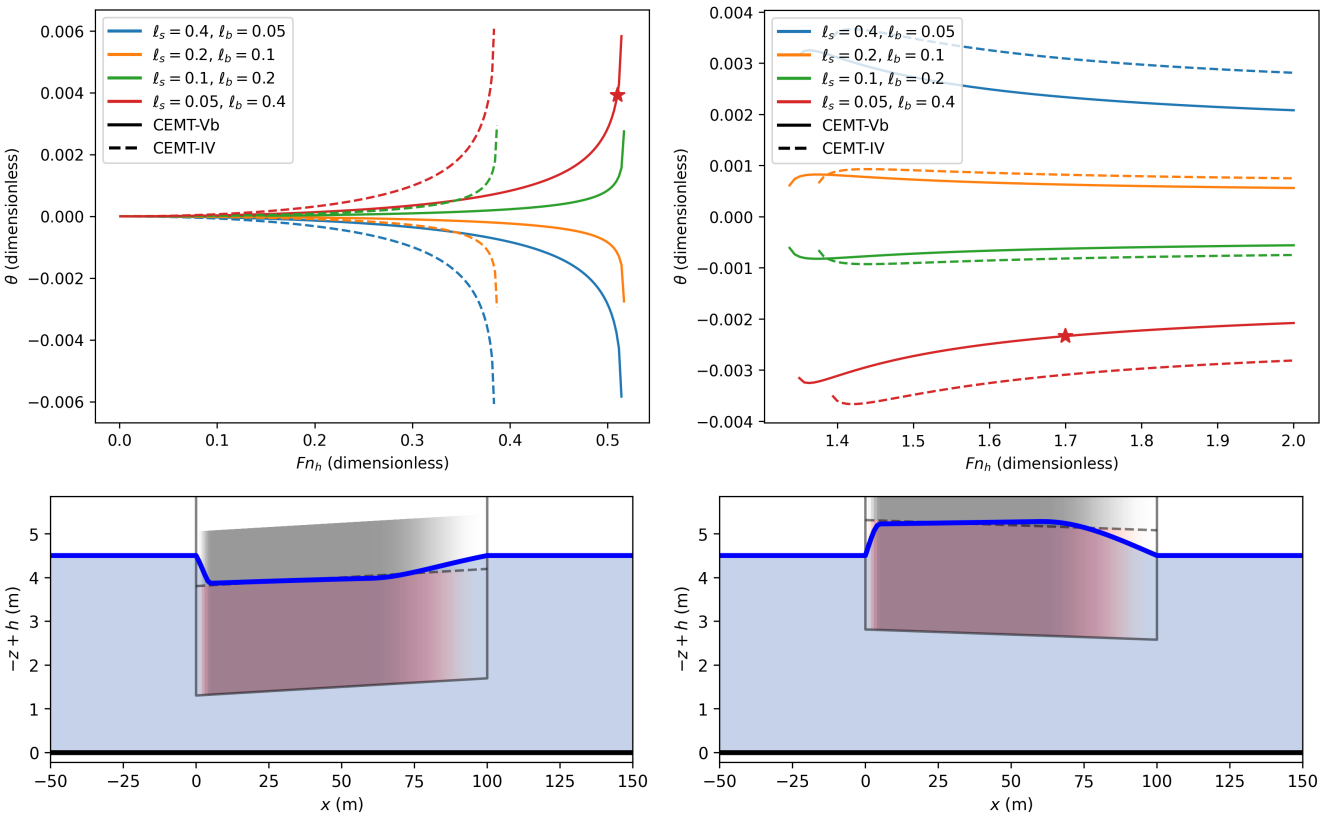

Figure 6: **Boat trim θ as a function of the Froude number for the class Vb (plain) and IV (dashed) canal, and different values of the geometrical parameters ℓ_s and ℓ_b. Left : sub-critical solutions ; right : supercritical solutions. Bottom : instances of the longitudinal profile of the free-surface elevation, and position of the boat (shades of red indicate the beam values), for parameters indicated by a star on the figure above.**

vertical displacement. The second consequence of allowing non-block boats is the emergence of a trim, merely by hydrostatic effects, induced by the longitudinal asymmetry.

Our numerical simulations, restricted to subcritical and supercritical flows, have shown that, first, when the boat's profile degenerates towards a block boat, our results converge towards the classical KSC theory adapted for canals with trapezoidal sections (t-KSC). This fact can be demonstrated formally on the systems of equations being solved, but it ought to be proven rigorously by a convergence theorem (this is a work in progress that will be the occasion of a future, more mathematical paper). Second, is the existence of the hydrostatic trim effect, which sign depends on the position of the boat's center of gravity and which is maximal in amplitude at the subcritical critical value of the Froude number Fn_h^-. We have shown that, when the centre of gravity of the boat is closer to the bow (r.p. the stern), the trim is nose-down (r.p. nose-up) in the subcritical regime and that the effect is reversed in the supercritical regime. In this study, we have always considered the draught to be constant at rest and the asymmetry being induced by variations of the beam, but it is very easy to consider, with the same model, a longitudinal variation of the draught at rest (caused, for example, by an uneven loading of the boat).

The trans-critical regime $\mathrm{Fn}_h^- < \mathrm{Fn}_h < \mathrm{Fn}_h^+$ has not been investigated here. In fact, stationary solutions to this problem do not exist in this particular situation (there is no continuous profile z of a constant specific head along the canal). This problem is usually resolved by the appearance of several hydraulic jumps: one in front of the bow (in a forward relative motion), one behind the stern (in a backward relative motion), and one abreast (stationary). Then, in the absence of friction, there is a lack of uniqueness of the position of the later stationary hydraulic jump. This suggests a position that is history dependent and justifies a future work, focused on numerical simulations of (35)-(39) which will require the design of well-balanced schemes to capture correctly the dynamics of this hyperbolic system.

These purely hydraulic models are only valid in situations of significant blockages ($m \sim 1$) and for very long vessels ($h/L_{wl} << 1$). In particular, frictional head losses, which play a role not only in the dynamics of the fluid around the vessel but also in the dynamics of the vessel itself, have been neglected here. We aim to include these effects in a future study. Finally, shallow-water theory also neglects the dispersive effects of surface waves, which are also significant in the forces exerted by the fluid on the vessel (wave resistance, lift). Accounting for precise hydraulic effects alongside dispersive effects within a framework consistent with the Euler equations poses a major challenge, which we intend to address in future work.

6 ACKNOWLEDGEMENTS

This work is funded by the French Waterways Voies Navigables de France (VNF). This work pertains (namely, is not funded but enters in the scientific perimeter) to the French government programme "Investissement d'Avenir" EUR INTREE (reference ANR-18-EURE-0010) and LABEX INTERACTIFS (reference ANR-11-LABX-0017-01).

7 REFERENCES

Batchelor, G. K., 1967. An Introduction to Fluid Dynamics. Cambridge University Press. DOI: 10.1017/CBO9780511800955.

Bechthold, Jonas and Marko Kastens, 2020. Robustness and quality of squat predictions in extreme shallow water conditions based on RANS-calculations. In: Ocean Engineering 197, p. 106780.

Biles, John Harvard, 1908. The Design and Construction of Ships (1908). Vol. 2. BoD–Books on Demand.

Bossut, Charles, 1775. Traité élémentaire d'hydrodynamique. Vol. 2.

Bouman, Evert A, Elizabeth Lindstad, Agathe I Rialland, and Anders H Strømman, 2017. State-of-the-art technologies, measures, and potential for reducing GHG emissions from shipping–A review. In: Transportation Research Part D: Transport and Environment 52, pp. 408–421.

Bouwmeester, J, JC Drost, and MT Van der Meer, 1986. Scheepssnelheiden op beperkt water met gegeven motorvermogen. Tech. rep. TH Delft.

Chen, Xue-Nong, 2013. Study of one-dimensional ship squat theories. In: Chinese Journal of Hydrodynamics 28.4.

Constantine, T, 1960. On the movement of ships in restricted waterways. In: Journal of Fluid Mechanics 9.2, pp. 247–256.

Delefortrie, Guillaume, Jeroen Verwilligen, Marc Vantorre, Evert Lataire, and Flanders Hydraulics, 2024. Exact and Approximated Solutions to the Critical Ship Speeds in Canals. In: Proceedings of the 35th PIANC World Congress.

European Conference of Ministers of Transport (ECMT), 1992. Resolution No. 92/2 on New Classification of Inland Waterways.

Fourdrinoy, Johan, Clément Caplier, Yann Devaux, Germain Rousseaux, Areti Gianni, Ierotheos Zacharias, Isabelle Jouteur, Paul-Marius Martin, Julien Dambrine, Madalina Petcu, and Morgan Pierre, 2019. The naval battle of Actium and the myth of the ship-holder: the effect of bathymetry. In: 5th MASHCON - International Conference on Ship Manoeuvring in Shallow and Confined Water with non-exclusive focus on manoeuvring in waves, wind and current, Flanders Hydraulics Research; Maritime Technology Division, Ghent University, May 2019, Ostend, Belgium. WWC007 (pp 104 - 133).

Gourlay, Tim Peter, 2000. Mathematical and computational techniques for predicting the squat of ships. PhD thesis.

Harris, Charles R., K. Jarrod Millman, Stéfan J. van der Walt, Ralf Gommers, Pauli Virtanen, David Cournapeau, Eric Wieser, Julian Taylor, Sebastian Berg, Nathaniel J. Smith, Robert Kern, Matti Picus, Stephan Hoyer, Marten H. van Kerkwijk, Matthew Brett, Allan Haldane, Jaime Fernández del Río, Mark Wiebe, Pearu Peterson, Pierre Gérard-Marchant, Kevin Sheppard, Tyler Reddy, Warren Weckesser, Hameer Abbasi, Christoph Gohlke, and Travis E. Oliphant, Sept. 2020. Array programming with NumPy. In: Nature 585.7825, pp. 357–362. DOI: 10.1038/s41586-020-2649-2.

Jules, Valentin, Pierre-Jean Pompée, Julien Dambrine, Morgan Pierre, and Germain Rousseaux, 2024. A revisit of confined medium navigation theories. In: 19e Journées de l'Hydrodynamique, Nantes.

Keldysh, M. and L. Sedov, 1937. The theory of wave drag in a channel of finite depth. In: Journal of Applied Mathematics and Mechanics 75. In "The papers of M.V. Keldysh in the field of mechanics and applied mathematics (On the centenary of his birth)", pp. 123–131.

Kreitner, J, 1934. Über den Schiffswiderstand auf beschränktem Wasser. In: Werft, Reederei, Hafen 15.7, pp. 77–82.

Landau, L. D. and E. M. Lifshitz, Jan. 1976. Mechanics, Third Edition: Volume 1 (Course of Theoretical Physics). 3rd ed. Butterworth-Heinemann.

Marchal, Jean, 1975. Contributions théorique et expérimentale au calcul de la résistance à l'avancement des convois poussés en navigation dans les voies d'eau de sections limitées. In: Collection des Publications de la FSA de l'ULg 55.

Nieutin-Redon, Pablo, 2024. Étude expérimentale et numérique des phénomènes hydrodynamiques liés au passage d'un navire dans une voie navigable confinée : quantification des ondes de batillage et de leur impact sur les berges. PhD thesis. Université de Poitiers.

Pompée, Pierre-Jean, 2015. About modelling inland vessels resistance and propulsion and interaction vessel-waterway key parameters driving restricted/shallow water effects. In: Proceedings of Smart Rivers 2015, Buenos Aires, Argentina, paper 180, September 2015.

Schijf, J.B., 1949. Protection of embankments and bed in inland and maritime waters, and in overflows or weirs. In: Proceedings of the 17th International Navigation Congress, Lisbon. SI - C2. Permanent International Association of Navigation Congresses. PIANC.

Sharp, BB and JD Fenton, 1968. A model investigation of squat. In: DOCK & HARBOUR AUTHORITY 49.577, p. 242.

Sretensky, L.N., 1936. On the wave-making resistance of a ship moving along in a canal. In: Phil. Mag. Pp. 1005–1013.

– 1937. Theoretical investigation of wave resistance. In: Transactions of the TsAGI (Central Aerohydrodynamic Institute) 319.

Tenaud & CNR, Renaud, 1977. Essais sur modèles réduits et modèles mathématiques pour l'étude du passage des convoi poussés dans un canal et des défenses des berges. In: 24th AIPCN.

Thiele, A, 1901. Schiffswiderstand auf canalen. In: Centralblatt der Bauverwaltung.

Virtanen, Pauli, Ralf Gommers, Travis E. Oliphant, Matt Haberland, Tyler Reddy, David Cournapeau, Evgeni Burovski, Pearu Peterson, Warren Weckesser, Jonathan Bright, Stéfan J. van der Walt, Matthew Brett, Joshua Wilson, K. Jarrod Millman, Nikolay Mayorov, Andrew R. J. Nelson, Eric Jones, Robert Kern, Eric Larson, C J Carey, İlhan Polat, Yu Feng, Eric W. Moore, Jake VanderPlas, Denis Laxalde, Josef Perktold, Robert Cimrman, Ian Henriksen, E. A. Quintero, Charles R. Harris, Anne M. Archibald, Antônio H. Ribeiro, Fabian Pedregosa, Paul van Mulbregt, and SciPy 1.0 Contributors, 2020. SciPy 1.0: Fundamental Algorithms for Scientific Computing in Python. In: Nature Methods 17, pp. 261–272. DOI: 10.1038/s41592-019-0686-2.

8 AUTHORS BIOGRAPHY

Julien Dambrine is assistant professor at the University of Poitiers and a member of the Laboratoire de Mathématiques et Application, as an applied mathematician working on theoretical and numerical problems involving partial differential equations for fluid dynamics. Over time he became a specialist in the mathematical modeling of wave/ship interactions in naval and, more recently, fluvial hydrodynamics.

Valentin Jules is a postdoctoral researcher at the CNRS (French National Scientific Research Center). His work focuses on theoretical modeling of navigation in confined environments.

Pierre-Jean Pompée is the responsible for Innovation Engineering at VNF (Voies Navigables de France). He is an expert in the engineering of waterways and hydraulic problems in inland navigation.

Morgan Pierre is an Associate Professor at the University of Poitiers (France). He is the head of the team "Partial Differential Equations and Applications" at the Department of Mathematics.

Germain Rousseaux is a research director at the CNRS (French National Scientific Research Center). With his team, he explained the reason for the defeat of Marc-Anthony and Cleopatra against Octavian at the naval battle of Actium because of the difference in boat draughts between both fleets and the resulting peak of wave resistance with a dedicated free surface wake. He is now interested in navigation in confined media and the effect of the return current and the water level drawdown. He is also an expert in Analogue Gravity where waterfalls mimic black holes in the laboratory.

INTEGRATING POTENTIAL FLOW CODE FOR SHIP BANK INTERACTION AT REAL TIME SIMULATIONS

Ibarrondo, Marta, MARIN, The Netherlands

Gornicz, Tomasz, MARIN, The Netherlands

Kleermaker, Wim, MARIN, The Netherlands

INTEGRATING POTENTIAL FLOW CODE FOR SHIP BANK INTERACTION AT REAL TIME SIMULATIONS

IBARRONDO, MARTA, MARIN, THE NETHERLANDS
GORNICZ, TOMASZ, MARIN, THE NETHERLANDS
KLEERMAKER, WIM, MARIN, THE NETHERLANDS

SUMMARY

The MARIN simulator utilizes an advanced method that runs on graphics processing units (GPUs) to estimate the hydrodynamic loads that occur when a ship navigates near a bank. This method is based on potential flow theory, which is particularly useful for modeling fluid flow around ships in various maritime conditions. Series of model tests, Computational Fluid Dynamics simulations, RAPID calculations and Extensible Modelling Framework (XMF) simulations using the Flow Interaction node were conducted using a 135-meter inland ship, which was equipped with two ducted propellers and four Schilling-type rudders. This study investigated the impact of key parameters—such as sailing speed, water depth, and proximity to the bank—on suction/repulsion forces. The results were analyzed with the initial aim of assessing the feasibility of the Flow Interaction code for practical applications at real time simulator. At this stage, the research focuses on understanding and refining the code's behavior in shallow water.

NOMENCLATURE

δ	Rudder angle (deg)
∇	Displacement volume (m^3)
λ	Linear scale ratio (-)
ρ	Fresh-water density (999,1 kg/m^3)
θ	Pitch angle (deg)
A_C	Cross-sectional area of the waterway (m^2)
A_S	Ship's underwater midship cross-sectional area (m^2)
B	Ship breadth (m)
C_P	Dynamic pressure coefficient (-)
d	Distance between the ship side and the bank (m)
d/B	Non-dimensional distance to bank (-)
F_r	Froude number (-)
F_{rh}	Depth Froude number (-)
F'_X or C_x	Ship surge force coefficient (-)
F'_Y or C_y	Ship sway force coefficient (-)
h	Water depth (m)
h/T	Water depth-to-draught ratio (-)
L_{PP}	Ship length between perpendiculars (m)
M'_Z or C_z	Ship yaw moment coefficient (-)
P/D	Pitch ratio at 70% radius (-)
RPM	Propeller revolution rate (1/min)
S	Blockage factor A_S/A_C (-)
T	Ship draught at rest (m)
V_{cr}	Critical canal speed (km/h or m/s)
V_s	Ship speed (km/h or m/s)
Z	Number of blades (-)
XMF	Extensible Modelling Framework
CPU	Central Processing Unit
GPU	Graphics Processing Unit
CFD	Computational Fluid Dynamics
RAPID	Raised Panel Iterative Dawson
RAPID NO TRIM	Raised Panel Iterative Dawson taking out trim and sinkage
BASIN	Experimental model test results
MARIN	Maritime Research Institute Netherlands
DST	Development Centre for Ship Technology and Transport Systems
SHINING	Shallow Water Inland Ships Manoeuvring working group
BAW	German Federal Waterways Engineering and Research Institute

1 INTRODUCTION

As ships grow in size and navigate more confined waterways, understanding ship-bank interactions has become crucial. Research focuses on predicting resistance, squat, and hydrodynamic forces near banks, with reduced-order models for suction and repulsion forces (Norrbin, 1985; Delefortrie et al., 2024) integrated into ship-handling simulators for training, waterway design, and accident analysis. Recent studies emphasize real-time predictions for safe navigation, including irregular banks (Bedos et al., 2019), shallow water maneuvering (Mai et al., 2021), and canal accessibility (Verwilligen et al., 2022). Model tests are resource-intensive, but advances in CFD provide a cost-effective alternative, although benchmarking remains critical. Van Hoydonck et al. (2019) highlight the importance of validating CFD methods, particularly for inland waterways with fluctuating water levels and narrow corridors. To overcome the limitations of traditional methods, the MARIN simulator uses advanced time domain computations and GPU power to improve hydrodynamic load estimations' in real time simulations.

The MARIN simulator's methodology is grounded in potential flow theory, a well-established approach for modeling fluid flow around ships. This theory offers a computationally efficient means of estimating the forces acting on a vessel without the heavy resource demands of full-scale CFD simulations. By leveraging GPU acceleration, the simulator enables faster and more efficient real-time predictions, making it an invaluable tool for ship designers, operators, and researchers aiming to enhance vessel performance in complex maritime environments. In this paper, the potential code will be referred to as the Flow Interaction Code within the XMF simulation package.

An extensive study was undertaken using a 135-meter inland vessel equipped with two ducted propellers and four Schilling-type rudders. This study integrated physical model tests (Bedos et al. 2025), high-fidelity CFD simulations, RAPID potential flow code based on a raised-panel method (Raven, 1995, 1996 and 1998) and Flow Interaction code in XMF (GPU-based) computations to rigorously assess the accuracy of the MARIN simulator's ship-bank interaction models. By comparing Flow Interaction generated results with CFD simulations and RAPID output, it is possible to evaluate the distribution of hydrodynamic loads along the ship's hull and identify key areas where the XMF based approach could be further refined.

This work explores how key parameters—such as sailing speed, water depth, and distance to the bank—affect suction forces. The results are compared with the ultimate goal of trying to make a first attempt to confirm the usability of the Flow interaction code for practical applications at real time simulator. At this stage the research is centred entirely on understanding behaviour of the code and improve its behaviour in shallow water rather than correction methods for including the viscous effects.

2 FLOW INTERACTION CODE

The flow interaction code was developed as the successor to PASSCAL and based on the work of Korsmeyer et al. 1993, was initially introduced as a CPU-based tool in 2017. However, it lacked the necessary computational speed and validation. In 2021, a GPU version was released, significantly improving speed but still facing robustness challenges. By 2023, the initiative was launched to validate the enhanced GPU code, which had become more stable but still required further refinements.

The Flow Interaction code assumes an idealized potential flow by neglecting viscosity, free-surface effects, and simplifying cross-flow vorticity using thin-wing theory. Various geometric simplifications are made based on the specific problem. For conventional ships at low Froude numbers, the assumptions about viscosity and free-surface effects are considered reasonable, as viscosity has minimal impact except in cases of cross-flow vorticity, and waves generated by ship motion are generally insignificant. However, the treatment of cross-flow vorticity is more uncertain and depends on the particular case.

Cross-flow drag along a ship's hull plays a crucial role in large-amplitude maneuvers, and similar effects may apply to ship interactions if transverse flow velocities are significant. In such cases, these effects can be idealized using a trailing vortex sheet downstream of the stern, with a Kutta condition applied by analogy to low-aspect-ratio wing theory. While this approach, as outlined by Newman. 1977, provides qualitative insights into maneuvering behavior, experimental comparisons show that it lacks quantitative accuracy due to the complexity of stern flow and interactions with propellers. Traditional slender-body theories approximate ship interactions based on their relative distances, but these methods only provide qualitative accuracy. To improve precision, the Flow Interaction code employs a numerical approach using three-dimensional panel methods, avoiding previous geometric assumptions.

The method computes interaction forces based on the panel method pioneered by Hess & Smith (1964), this is the first known application to ship interactions. By neglecting free-surface effects and shed vorticity, memory effects are removed, allowing time-stepped hydrodynamic calculations. The process involves deriving an integral equation for velocity potential, discretizing it using quadrilateral panels, solving the resulting algebraic system, and computing force and moment histories for each ship.

3 TEST CASES

The study focuses on a 135m CEMT-class Vb inland ship, commonly operating on the Rhine. Designed in 2014 by BAW and DST, this benchmark vessel has been used in experimental studies on resistance, propulsion, and maneuvering in shallow water (Mucha et al., 2017, 2018, 2019). More recently, it was selected in the SHINING workshop to evaluate CFD techniques for predicting maneuvering forces and moments in shallow water (Chilcee et al., 2025).

Table 1 details the inland waterway ship's main particulars and appendages at full scale and a linear scale ratio of 1:16. Experimental and CFD were conducted at model scale, while RAPID and Flow Interaction simulations were run full scale. The ship features a twin-shaft arrangement with two ducted propellers (1.6 m diameter, inward rotation) and four fishtail-type rudders with endplates. The duct geometry resembles the 19A type but is horizontally trimmed at the baseline. The rudders' projected lateral area is approximately 4 x 2.36 m^2 times, equating to 4 x 0.50%·L_{PP}·T. Further aft-ship details are provided by Mucha et al. 2017.

Table 1. Main particulars of the inland waterway ship and its appendages.

Designation	Symbol	Full scale	Model scale
Linear scale ratio (-)	λ	1	16
Length between perpendiculars (m)	L_{PP}	135.0	8.438
Breadth moulded on waterline (m)	B	11.44	0.715
Draught at rest, even keel (m)	T	3.50	0.219
Displacement volume (m^3)	∇	4,991.5	1.219
Propeller diameter (m)	B	1.6	0.100
Pitch ratio at 70% radius (-)	P/D	1.000	1.000
Expanded blade area ratio (-)	A_E/A_0	0.679	0.679
Number of blades (-)	Z	4	4
Rudder height (m)	b	1.726	0.108
Rudder chord (m)	c	1.370	0.086

This work compares experimental and numerical methods to analyse ship-bank interactions for a reference ship in shallow water, ensuring a fair comparison with a consistent setup. The ship sails along a vertical wall on its port side, with a parallel wall farther on the starboard side. The distance between them is 22.1 times the ship's width. The distance towards the closest bank varies between 2.0 to 1.0 B, therefore the system can be considered confined. The ship is towed in a semi-captive condition, with imposed surge, sway, roll, and yaw motions, while heave and pitch remain free, ensuring realistic force equilibrium. The study examines various portside bank distances (d/B) and water depths (h/T). The ship moves straight at a constant speed with fixed propeller RPM and neutral rudders. Dynamic squat, highly sensitive to hydrodynamic loads in shallow waters, is considered. Tests were conducted at 0.972 m/s (14 km/h full scale, Fr = 0.107) with a 4.5% blockage factor.

The tests used the ship model under two propeller regimes: self-propulsion and water milling, the latter aiding CFD comparisons. Experiments were conducted at three water depths (3.0, 1.5, and 1.2 h/T) to study deep and shallow water effects. Four bank distances (2.5, 2.0, 1.5, and 1.0 d/B) and four speeds (8, 10, 12, and 14 km/h) were tested to simulate real-life conditions and improve result reliability. Details on the setup of both the model tests and CFD calculations are provided in Bedos et al. (2025).

An overview of the runs carried out is presented in Table 2.

Table 2. Matrix of stationary conditions (quantities are indicated at model scale)

Run	h/T (-)	Vs (m/s)	d/B (-)	RPM (1/min)	δ (deg)	FI (-)	CFD (-)	RAPID (-)	RAPID NO TRIM (-)
02010401	3.0	0.972	1.5	303	0	✓	✓	✓	✓
03010201	1.5	0.972	2.0	322	0	✓	✓	✓	✓
03010301	1.5	0.972	1.5	322	0	✓	✓	✓	✓
03010401	1.5	0.972	1.0	322	0	✓	✓	✓	✓
04010301	1.2	0.972	1.5	341	0	✓	✓	✓	

4 RAPID/ FLOW INTERACTION CODE SETUPS

In order to perform the assessment, potential flow simulations were conducted using the XMF simulation package with the GPU[1] implementation.

As expected both in RAPID and Flow interaction code in XMF, elements such as ducts, rudders, and other intricate details can be omitted, as they are not incorporated into the simulation framework. The banks are represented as simplified flat vertical walls positioned on both sides of the vessel. Both numerical setups were done using full scale values. For sailing with the heading parallel to the bank only the u-velocity is set, for sailing with a 0 drift angle the u- and v-velocity are set such that the speed vector is pointing parallel to the bank. Table 3 summarises the main particulars of the numerical domains. Figure 1 and Figure 2 show a 3D view of the domain in both numerical tools.

Table 3. Numerical domain in Flow Interaction code and RAPID

Parameter name	FI	RAPID
Computational domain size (m)	2840	413.5 x 157.8
Vessel Grid Number of panels (-)	2246	7198
Port Bank Grid. Number of panels (-)	800	2370
Starboard Bank Grid. Number of panels (-)	800	2370

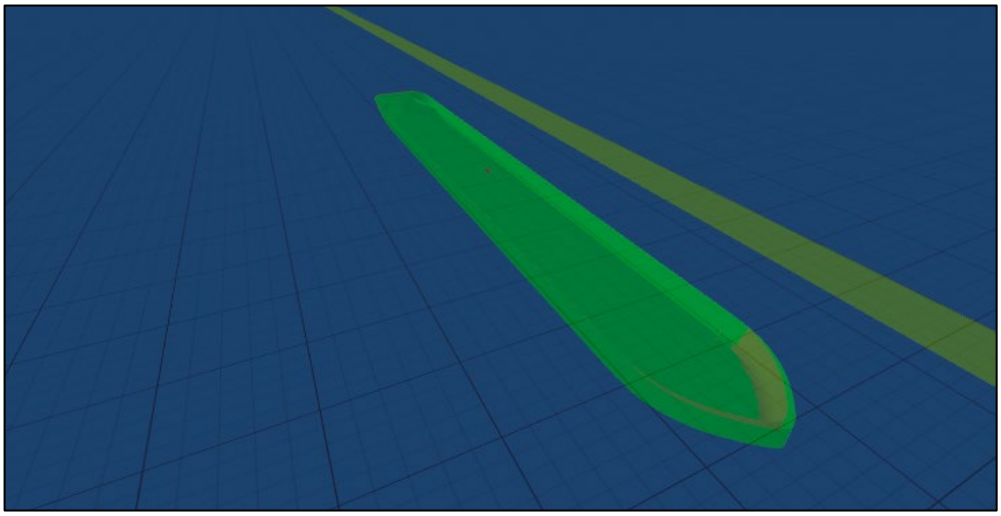

Figure 1. Computational domain in Flow Interaction

[1] The Parallel Flow Interaction between ships was verified against Flow Interaction via the test scripts used in the 2017 XMF-PASSCAL-Ropes comparison. These 35 scripts specified container-container and tanker-tanker interaction. Forces and moments showed a good resemblance but in some cases there were small differences due to calculation inaccuracies. GPU's floating point calculation is performed in single precision instead of double precision on a CPU.

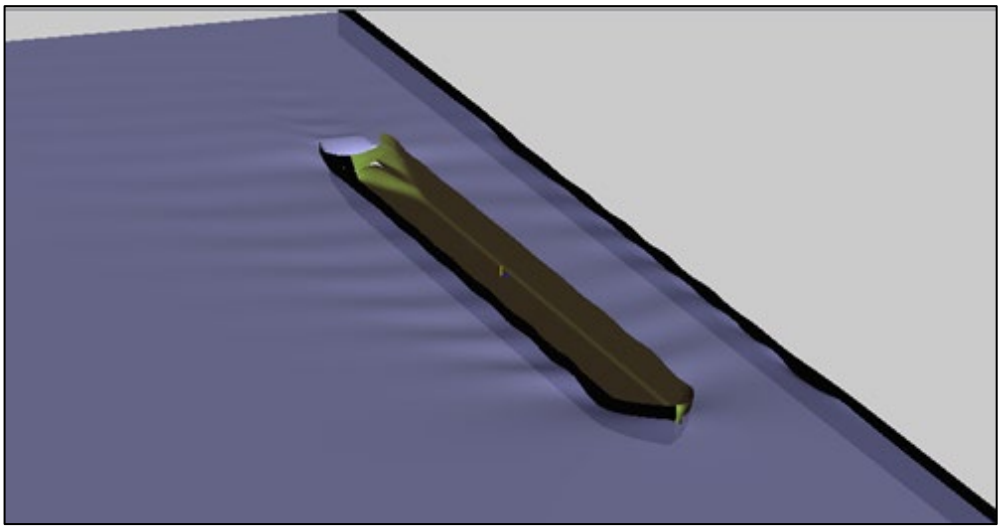

Figure 2. Computational domain in RAPID

To assess the influence of grid resolution on computational accuracy, five vessel grids were employed, ensuring that the aspect ratio and relative panel sizes remained consistent across refinements. The grid specifications are detailed in Table 4. Figure 3 presents a comparative analysis of the first, third, and fifth grid resolutions, highlighting the impact of grid refinement on the computational results.

Table 4. Flow Interaction set up. Hull grid number associated with number of panels.

Grid number	Panels
1	386
2	958
3	2246
4	3832
5	6138

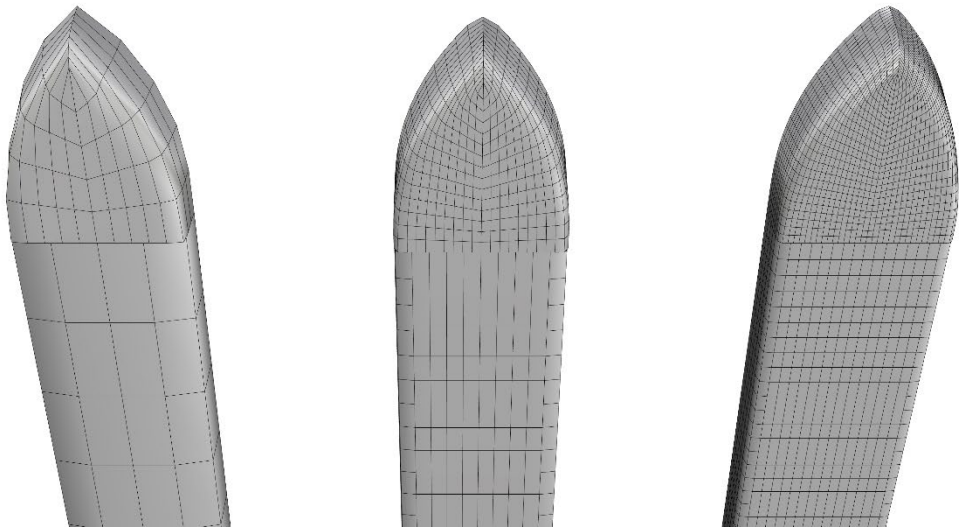

Figure 3. Hull grid 1 (left), 3 (centre) and 5 (right)

Figure 4 shows a longitudinal distribution of the side force Fy and yawing moment Mz. The plot is obtained by splitting the hull into a series of slices (sections) with a constant width. For every slice, the forces and moments are calculated. Then, the values are summed in the flow direction from the bow (x/Lpp=1) towards the transom (x/Lpp=0). The plot illustrates a build-up of Fy and Mz along the ship, starting with value zero at the bow and total force and moment acting on the ship given at x/Lpp=0.

For a single time step, the results across different grid resolutions are analyzed based on the integrated load distribution along the hull. Notably, the first two grids exhibit significant deviations, particularly in the moment calculations, compared to the finer grids. From grid 3 onward, the variation in results decreases, indicating improved numerical stability. Consequently, grid 3 is selected for all subsequent simulations in this study.

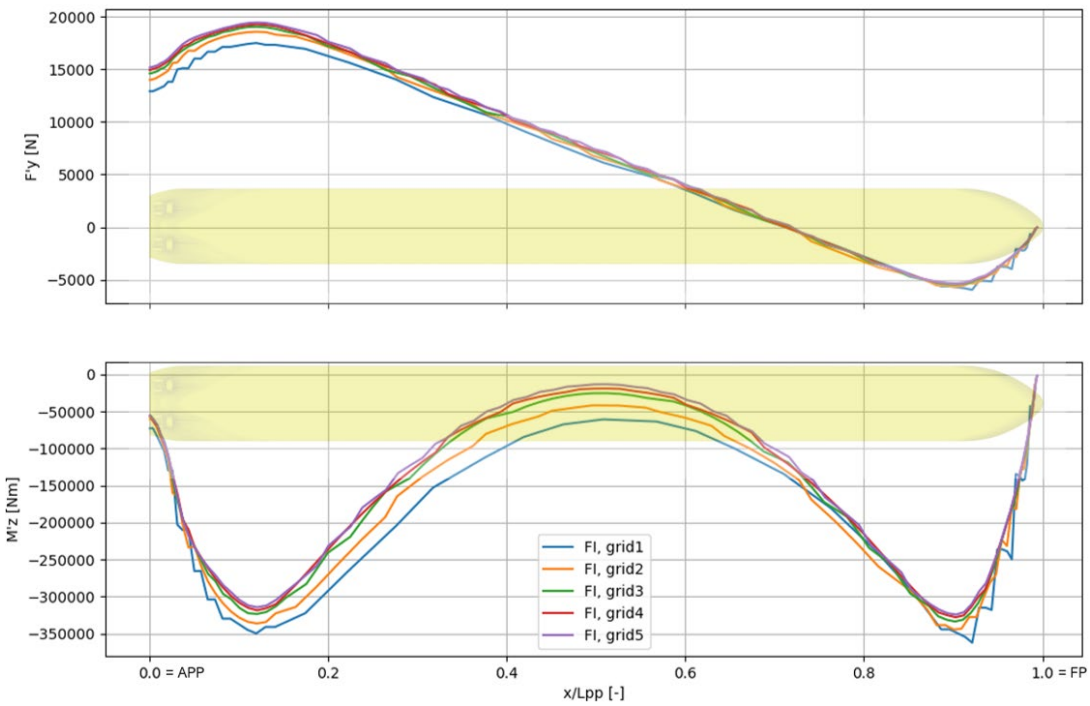

Figure 4. Comparison of longitudinal side force (Fy) and yawing moment distribution, integrated from the bow to the stern, for different grids

5 COMPARISON BETWEEN TOOLS AND DISCUSSION OF RESULTS

This section provides a comparative analysis of the numerical tools and examines the key findings of the study, with a specific focus on their dependency on water depth and closeness to the bank.

Ship forces and moments are expressed in the yawed-only coordinate system, which is nearly ship-fixed but remains level, excluding roll and pitch. This ensures the longitudinal and transverse axes stay in the earth-fixed horizontal plane. The origin is at the midsection centerline of the waterline intersection, with x-, y-, and z-axes directed forward, portside, and upward, respectively. The ship sway force and yaw moment are given in a non-dimensional form, using the ship speed V_s, water density ρ and draught at rest T. CFD calculations were performed at model scale, whereas RAPID and Flow Interaction code in XMF simulations were conducted at full scale. These non-dimensional loads are defined as follows:

$$F_Y' = \frac{F_Y}{0.5\,\rho\,L_{PP}\,T\,V_S^2} \qquad M_Z' = \frac{M_Z}{0.5\,\rho\,L_{PP}^2\,T\,V_S^2} \tag{1}$$

With F_Y and M_Z being the sway force and yaw moment respectively. The influence of confinement on surge force, having minimal impact, will be explored further in future studies.

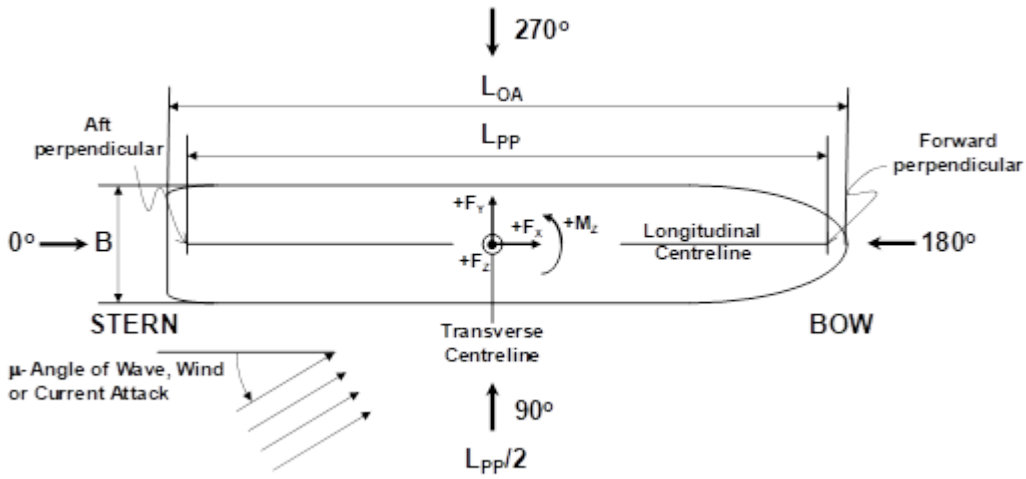

In all conditions, the ship experiences a transversal suction force (positive F_Y) directed towards the vertical bank, with the point of application located aft of midship, as indicated by the bow-out yaw moment (negative M_Z). The intensity of the bank effect increases as the under-keel clearance decreases. General observations from the tests show that forces tend to increase with higher speeds and closer proximity to the bank. The variation in the h/T plot indicates that at h/T = 3.0, there is strong agreement between the model test results, CFD simulations, and Flow Interaction calculations. Furthermore, the CFD results demonstrate improved alignment with model test data in shallow water conditions (h/T = 1.5 & 1.2), marking a significant step forward in using CFD as a reliable comparative tool for ship hydrodynamic analysis. However, the Flow Interaction results showed that the lateral force (F_Y) was approximately half the value measured in the basin, and the calculated moment was nearly negligible compared to the basin measurements. This suggests that the moment is significantly underestimated in both h/T = 1.5 and 1.2.

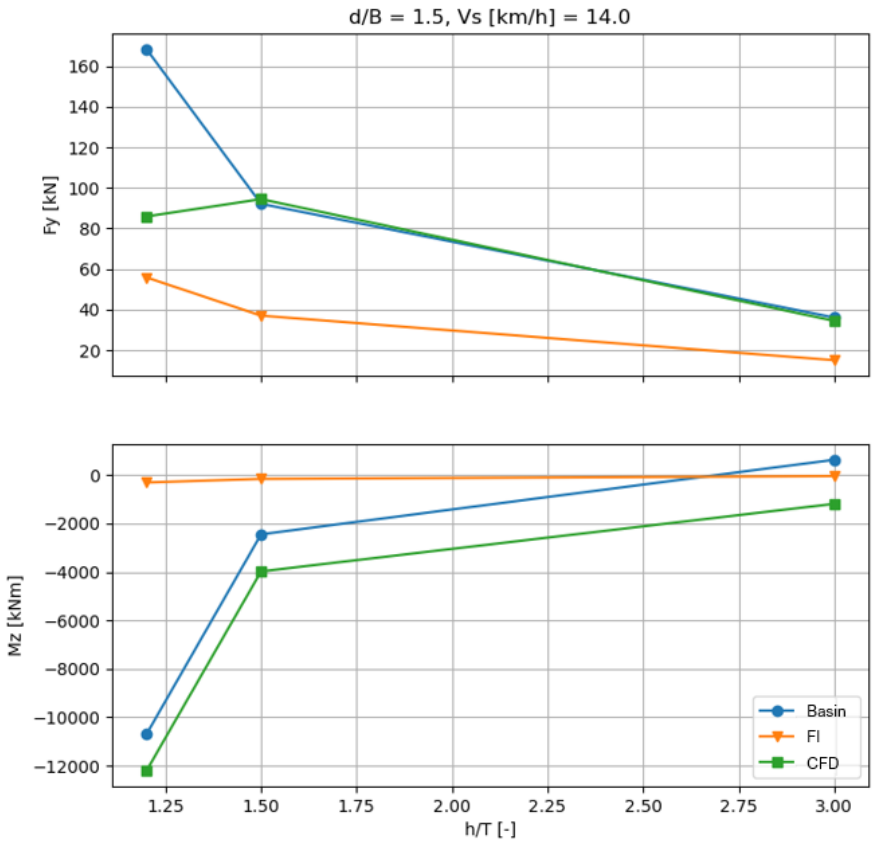

Figure 5. Suction force/moment trends in h/T in d/B=1.5 and speed 14 km/h.

Based on the findings, the focus is directed toward enhancing the Flow Interaction code by including alternative potential flow solvers like RAPID and systematically cross-referencing discrepancies between them. This approach aims to identify critical areas requiring refinement, ultimately improving the accuracy and reliability of the computational framework.

RAPID is one of the flow interaction codes that could provide valuable solutions for our analysis. It solves the exact fully non-linear potential flow problem by an iterative procedure, based on raised panel method (Raven, 1995, 1996 and 1998). The inviscid flow method neglects boundary layers and flow separation, overestimating stern waves, especially for fuller hulls. While wave resistance predictions are not fully accurate, the method is useful for hull design ranking. Wave breaking and spray are not modeled. RAPID has been extensively validated against MARIN's model test results, accurately predicting flow and wave patterns. It outperforms linearized methods in bow wave height and diverging wave predictions. While absolute wave resistance may vary, it is effective for comparing hull designs in optimization.

5.1 VARYING WATER DEPTH

For the case of h/T = 3.0, as illustrated in Figure 6, the plots present a comparison between CFD, RAPID (with and without trim and sinkage considerations) and Flow Interaction calculations. In this case, the trim has a negligible impact on the RAPID results. Specifically, RAPID demonstrates closer alignment with CFD results at both the bow and stern of the vessel, while Flow Interaction provides a marginally better match at midship. At the stern, both RAPID and Flow Interaction, as potential flow solvers, fail to accurately predict the increase in lateral force F_Y', which is primarily driven by viscous effects that are not captured by potential flow theory. These discrepancies highlight the limitations of potential flow methods in regions where viscous effects become significant.

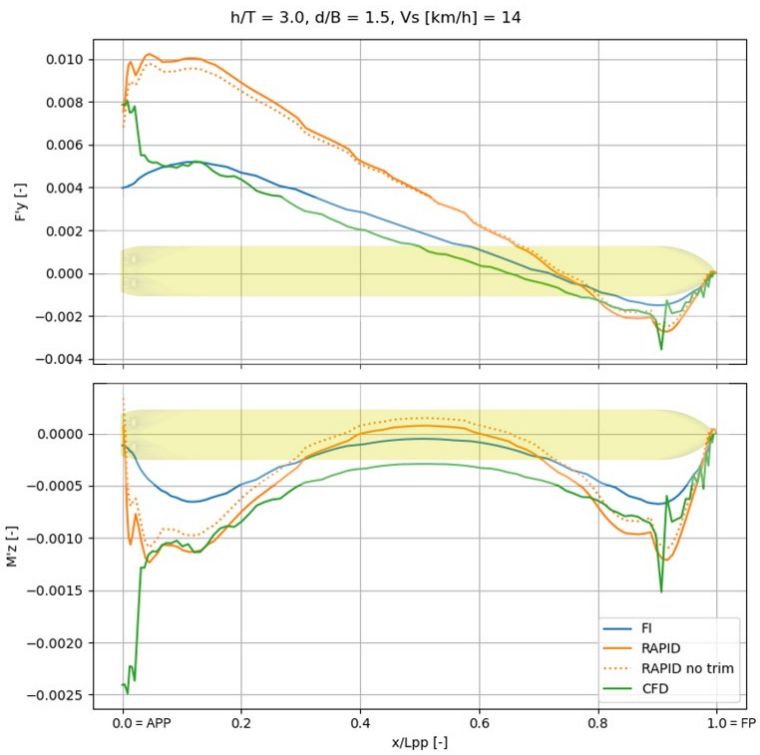

Figure 6: Case 02010401. Comparison of the integrated F'y and M'z.

This limitation becomes more evident when examining the pressure distribution comparison shown in Figure 7. In this comparison, the Flow Interaction results indicate an unrealistic pressure recovery near the stern, a characteristic that is typical of potential flow methods due to their inability to model viscous effects. This unrealistic recovery further underscores the challenge of accurately capturing flow behavior in the stern region using inviscid flow models.

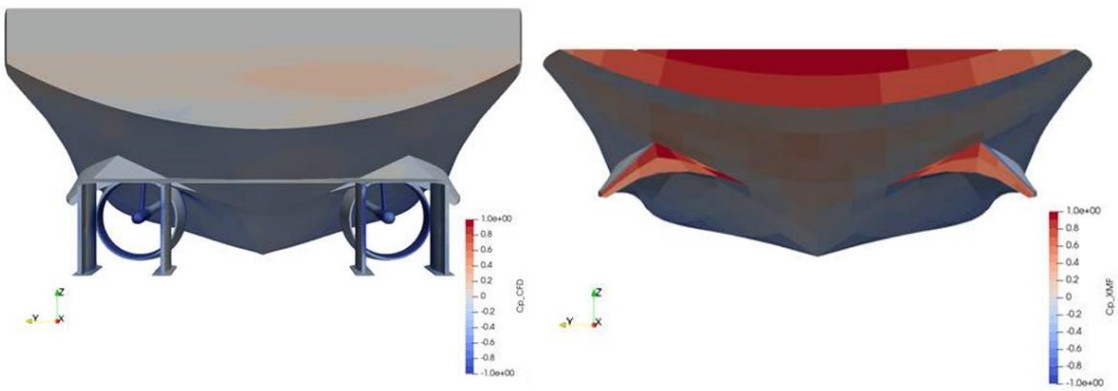

Figure 7. Case 02020401. Stern body. CFD results (left) and Flow Interaction calculations (right)

At the reduced water depth (h/T=1.5, see Figure 8), the Flow Interaction results exhibit a significant discrepancy with the CFD data, particularly at the bow. In contrast, RAPID more closely follows the CFD trend, effectively capturing the peak near the bow. Omitting trim and squat effects in RAPID improves the prediction of the lateral force (F_Y') compared to CFD; however, the deviations in the yaw moment (M_Z') are amplified. The primary distinction between RAPID and Flow Interaction lies in RAPID's incorporation of the free surface effects in its calculations, which could account for the observed differences between the two codes.

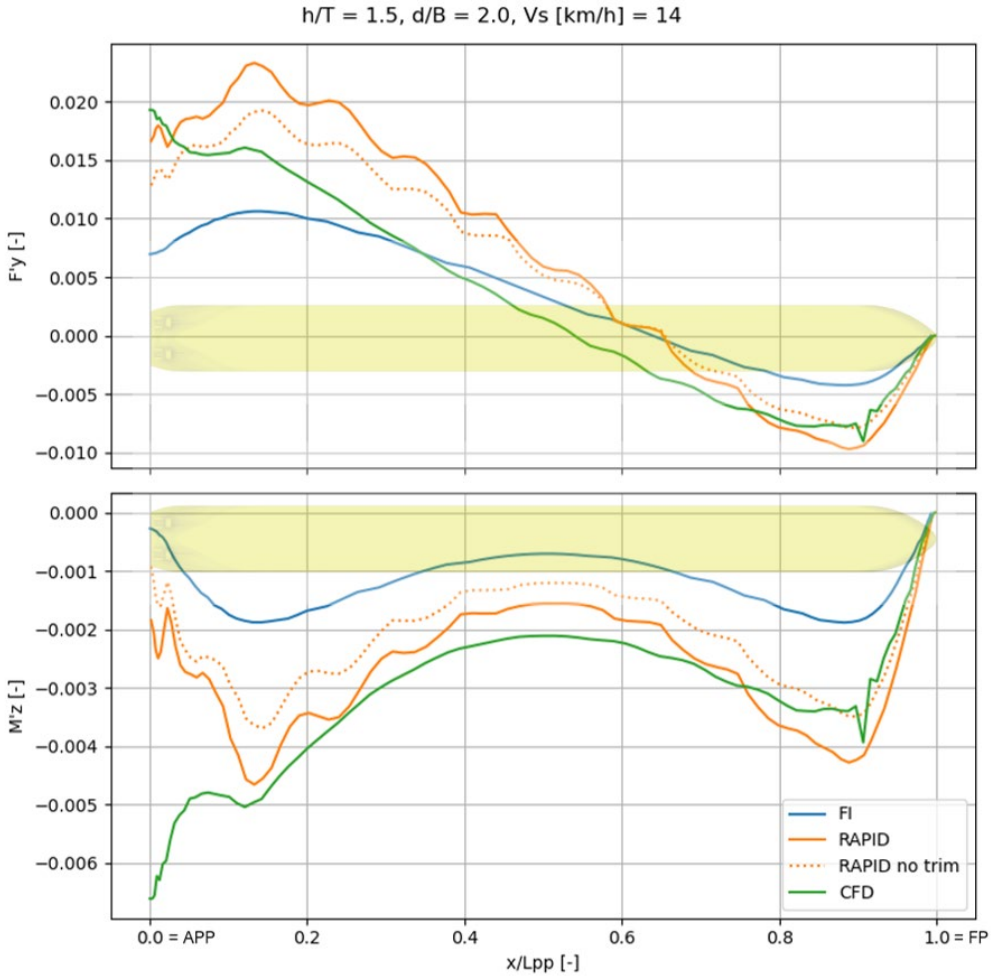

Figure 8. Case 03010201. Comparison of the integrated F'y and M'z.

At a water depth ratio of 1.2, the cumulative distributions for the lateral force F_Y' and yaw moment M_Z' coefficients, shown in Figure 9, reveal that RAPID aligns better with the CFD results. However, neither potential flow code accurately predicts the distribution at this shallow depth. This discrepancy is likely due to the increased significance of viscous effects, which are not captured by the potential flow models.

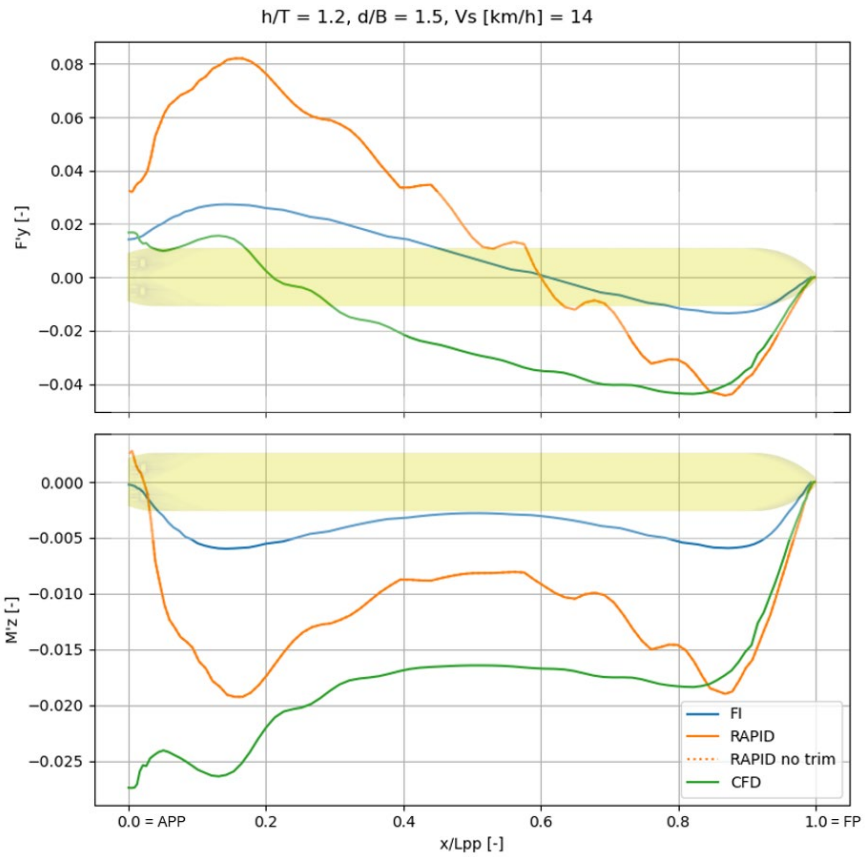

Figure 9. Case 04010401. Comparison of the integrated F'y and M'z.

A comparison between h/T = 1.2 (Figure 9) and h/T = 1.5 (middle plot in Figure 11) revealed that the M_Z' values at the bow are approximately three times greater in h/T = 1.2 in both CFD and RAPID results, see Figure 10.

For h/T = 1.5, the CFD maintains a smooth decline, while the RAPID shows pronounced fluctuations. Similarly, for h/T = 1.2, the CFD has a consistent trend, whereas the RAPID displays noticeable peaks and troughs. Overall, the CFD method is more stable and reliable for smooth trends, while the RAPID captures detailed changes, making it useful for applications requiring high sensitivity.

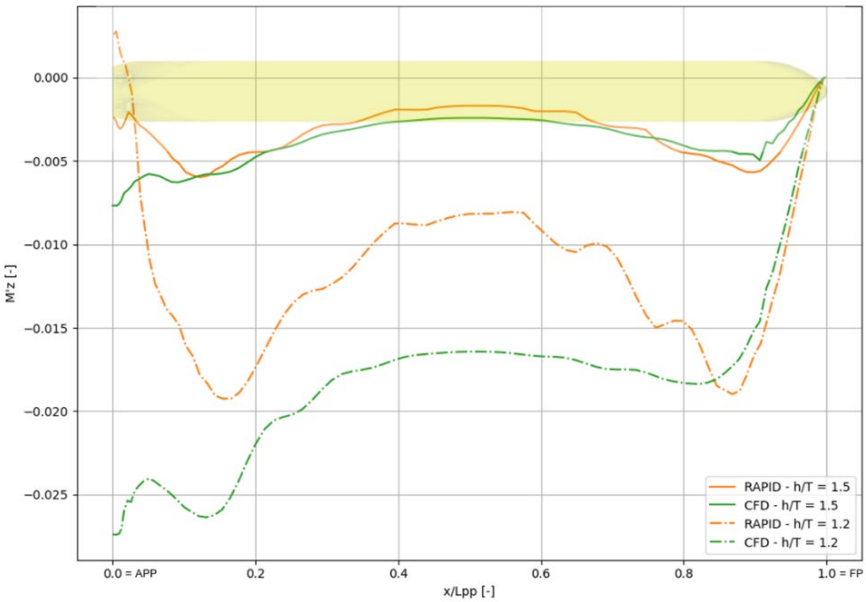

Figure 10. Comparison of the integrated M'z for h/T = 1.5 and h/T = 1.2

Figure 11 displays the dynamic pressure coefficient along the bow and stern at h/T=1.2. The high and low-pressure regions are consistent across all water depths, with increasing intensity as under-keel clearance decreases. At h/T = 1.2, the pronounced low-pressure zone beneath the hull indicates accelerated flow under the keel. Moreover, the pressure distribution exhibits greater asymmetry between the port and starboard sides, especially at the bow.

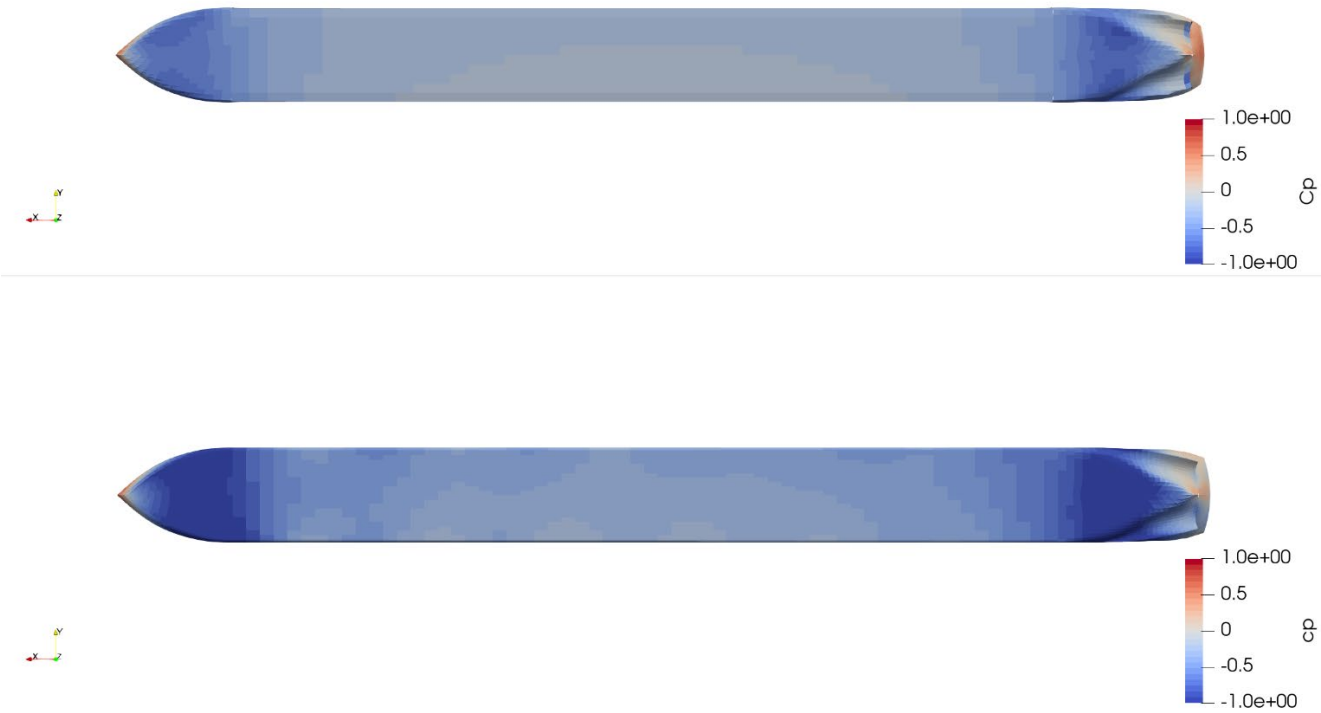

Figure 11. Dynamic pressure coefficient on the appended ship at Flow Interaction (top) and RAPID (bottom)

The differences between the Flow interaction code and RAPID can have different origins. The two more probable are free surface effects and dynamic trim and sinkage. Both of these phenomena are not taken into account in the Flow Interaction code. A small CFD study was conducted to estimate the importance of those effects on the side force. Figure 12 and Figure 13 show a comparison of between three cases: FreeSurf (with both free surface effect and dynamic trim and sinkage), Double body trim&sink (no waves but with dynamic trim and sinkage) and DoubleBody (no waves, no dynamic trim and sinkage). If we consider the free surface computations as the most accurate, then it seems that taking into account only dynamic trim and sinkage improves results, but it does not solve all of the issues. Hence, considering both seem to be required to predict ship bank interactions accurately.

Figure 12. Longitudinal distribution of side force along the ship.

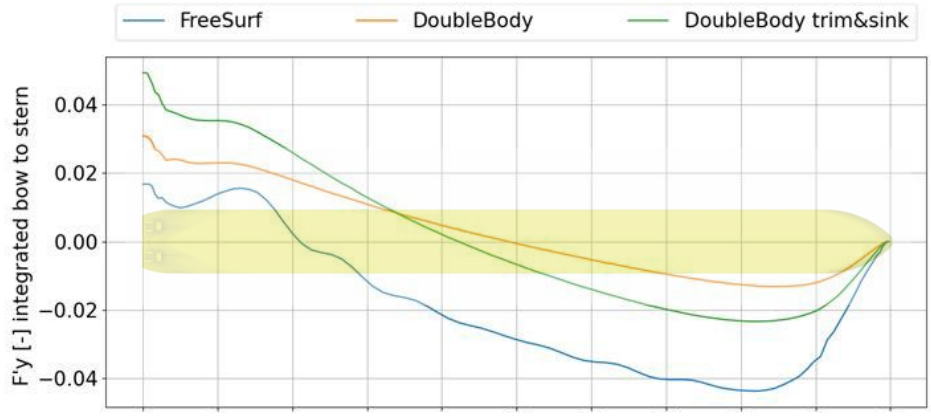

Figure 13. Longitudinal distribution of side force along the ship integrated from the bow to stern.

5.2 VARYING DISTANCE TO THE BANK

Figure 14 presents the integrated loads for various distances to the bank (2.0, 1.5, and 1.0 d/B). As the vessel approaches the bank, both F'_Y and M'_Z exhibit an increase. The differences between the results for 2.0 and 1.5 d/B are minimal. However, when reducing the distance to 1.0 d/B, a significant increase in forces is observed at the bow. This is attributed to the restricted flow of water between the vessel and the bank, resulting in enhanced interaction effects.

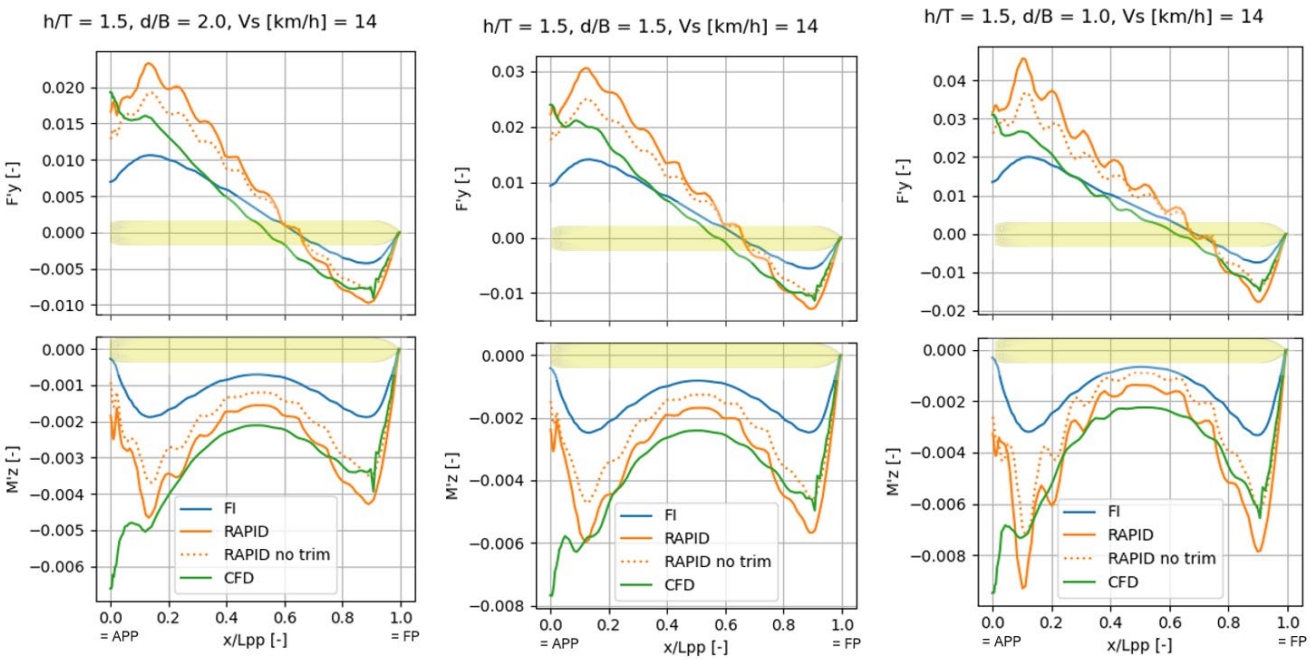

Figure 14. Comparison of the integrated F'y and M'z for h/T=1.5 at d/B=2.0 (left), 1.5 (middle) and 1.0 (right)

Based on the comparisons, it can be concluded that the influence of the h/T ratio (ranging from 1.5 to 1.2) has a more significant impact on the results than the effect of bank proximity at 1.5B. Furthermore, the distance to the nearest bank is sufficiently large to minimize any substantial viscous effects resulting from bank-induced interactions.

6 CONCLUSIONS

This research examines ship-bank interactions for a 135 m inland vessel in shallow water, using experimental and numerical methods under consistent conditions. The ship sails near a vertical bank in a shallow channel with a rectangular cross-section. The total width of the channel is 22.1B. The distance towards the closest bank varies between 2.0 to 1.0 B, therefore the system can be considered confined. Tests were conducted in a semi-captive setup with imposed surge, sway, roll, and yaw, while heave and pitch remained free. The analysis covers various bank distances (d/B) and water depths (h/T) at a speed of 14 km/h full scale. Experiments were performed under self-propulsion and water milling conditions for CFD validation, at three water depths (h/T = 3.0, 1.5, 1.2), four bank distances (d/B = 2.5, 2.0, 1.5, 1.0), and four speeds (8, 10, 12, 14 km/h).

Results show a transversal suction force (F_Y) toward the bank, with its point of application aft of midship, as indicated by the bow-out yaw moment (M_Z). The bank effect intensifies with reduced under-keel clearance, increased speed, and shorter bank distance. At h/T = 3.0 CFD, RAPID and Flow Interaction results align well. In shallower waters (h/T = 1.5 and 1.2), CFD more accurately predicts forces, while Flow Interaction code underestimates F_Y by approximately 50% and fails to capture M_Z. This suggests limitations in Flow Interaction XMF's modeling of bank-induced forces at low h/T. These findings support refining XMF simulations for improved hydrodynamic modeling in restricted waters.

The key findings from the study are as follows:

- **Deep Water Conditions (h/T > 3):** The Flow interaction code model performs reliably in deeper waters, showing reasonable agreement with CFD and RAPID simulations. The lower impact of viscosity in these conditions allows for accurate predictions. However, discrepancies arise near the stern, where Flow Interaction (as well as RAPID) fails to capture flow separation and other viscous effects, leading to deviations in the computed forces.
- **Moderate to Transitional Water Depths (1.2 < h/T < 1.5):** In moderately shallow waters, FI does not accurately predict the peak loads at the bow, resulting in significant differences from CFD results. RAPID, which accounts for free surface effects, provides a more accurate representation of these forces. This indicates that incorporating free surface modeling into FI could improve its predictive capability in transitional water depths.
- **Shallow Water Conditions (h/T= 1.2):** At very shallow depths, discrepancies between Flow Interaction, RAPID and CFD become more pronounced due to the increased influence of viscous effects such as turbulence and flow separation. The inability of the potential flow codes to account for these factors makes them unsuitable for precise force predictions in shallow water, highlighting the necessity for more advanced modeling techniques in these conditions.
- A CFD study demonstrated that while considering dynamic trim and sinkage improves results, it does not fully resolve all issues. Therefore, to accurately predict ship-bank interactions, both free surface effects and dynamic trim and sinkage must be taken into account.

The next phase of research will focus on evaluating the influence of trim, sinkage, and free surface effects—factors that are incorporated in RAPID but currently absent in Flow Interaction code in XMF. The primary objective is to enhance the Flow Interaction code in XMF's capability to accurately model ship-bank interactions in shallow water conditions (h/T = 1.5) by integrating these effects into the computational framework. It was confirmed by the CFD study that these effects have an important impact on hydrodynamic loads on the ship sailing along the regular bank.

To achieve this, a new computational module is planned for implementation. Once integrated, all test cases will be re-run to assess its impact on simulation accuracy and overall model performance. Additionally, an alternative approach under consideration involves developing an empirical correction node to account for the missing hydrodynamic effects, providing an adaptive solution to improve accuracy in shallow water conditions.

These enhancements will improve Flow Interaction code predictive accuracy, enabling more reliable simulations of ship-bank interactions across different water depths, particularly for typical cases encountered in real-time simulators.

7 REFERENCES

Bedos, A., Oud, G., De Boer, W., 2019. Impact of an Irregular Bank on the Sailed Trajectory of an Inland Ship. In: Proceedings of the Smart Rivers 2019 Conference. Lyon, France.

Bedos, A. Tonelli, R. Gornicz, T., 2025. Combining Numerical and Experimental Methods to Explain Ship Bank Interactions. MASHCON7.

Chillcce, G., Zentari, L., Van Hoydonck, W., Bedos, A., Ley, J., Gornicz, T., Yang, Y., Oud, G., Tenzer, M., Rzeszutko, J., el Moctar, O., 2025. Numerical Calculation of Hydrodynamic Forces on Inland Waterway Vessels During Circular Motion in Shallow and Extreme Shallow Waters. Ocean Engineering. Vol. 318. https://doi.org/10.1016/j.oceaneng.2024.120095.

Delefortrie, G., Verwilligen, J., Eloot, K., Lataire, E., 2024. Bank Interaction Effects on Ships in 6 DOF. Ocean Engineering. Vol. 310, Part 1. https://doi.org/10.1016/j.oceaneng.2024.118614.

Hess, J.L., Smith A. M. O. 1964. Calculation of Non-lifting Potential Flow about Arbitrary Three Dimensional Bodies. Journal of Ship Research, 6.

Korsmeyer, F. T, Lee C. H., Newman, J. N, 1993. Computation of Ship interaction forces in Restricted Waters. Journal of Ship Research. Vol. 37. No 4, pp 298-306.

Mai, T.L., Jeon, M., Vo, A.K., Yoon, H.K., 2023. A Numerical Study on the Ship–Bank Interaction at Various Water Depths of a Surface Ship. Science Progress. Vol. 106(1). https://doi.org/10.1177/00368504221149624.

Mucha, P., el Moctar, O., Dettmann, T., Tenzer, M., 2017. Inland Waterway Ship Testcase for Resistance and Propulsion Prediction in Shallow Water. Ship Technology Research. Vol. 64 (2), pp.106-113. https://doi.org/10.1080/09377255.2017.1349723.

Mucha, P., el Moctar, O., Dettmann, T., Tenzer, M., 2018. An Experimental Study on the Effect of Confined Water on Resistance and Propulsion of an Inland Waterway Ship. Ocean Engineering. Vol. 167, pp.11-22. https://doi.org/10.1016/j.oceaneng.2018.08.009.

Mucha, P., Dettmann, T., Ferrari, V., el Moctar, O., 2019. Experimental Investigation of Free-Running Ship Manoeuvres Under Extreme Shallow Water Conditions. Applied Ocean Research. Vol. 83, pp.155-162. https://doi.org/10.1016/j.apor.2018.09.008.

Newman, J. N. 1977. Marine Hydrodynamics. MIT. Press Cambridge.

Norrbin, N., 1985. Bank Clearance and Optimal Section Shape for Ship Canals. In: Proceedings of the 26th PIANC International Navigation Congress. Brussels, Belgium, pp. 167-178.

Raven, H. C., Valkhof, H. H. 1995 Application of Non-linear Ship Wave Calculations in Design. 6th PRADS Symposium, Seoul.

Raven, H. C.. 1996. A Solution Method for the Non-Linear Ship Wave Resistance Problem. PhD. Thesis, Delft University Technology.

Raven, H. C.. 1998. Inviscid Calculations of Ship Wavemaking Capabilities Limitations and Propect. 22nd Symposium on Naval Hydrodynamics. Washington DC.

Van Hoydonck, W., Toxopeus, S., Eloot, K., Bhawsinka, K., Queutey, P., Visonneau, M., 2019. Bank effects for KVLCC2. Journal of Marine Science and Technology. Vol. 24, pp. 174-199. https://doi.org/10.1007/s00773-018-0545-3.

Verwilligen, J., Lataire, E., Tello Ruiz, M., Eloot, K., 2022. Evaluation of Bank Effects on a Bulk Carrier in a Confined Channel Cased on Towing Tank Tests and Full-Scale Measurement. In: Proceedings of the 6th International Conference on Ship Manoeuvring in Shallow and Confined Water: Port Manoeuvres (MASHCON). Glasgow, UK, pp.285-298.

8 AUTHORS BIOGRAPHY

Marta Ibarrondo holds the position of Senior Project Manager at the Maritime Research Institute Netherlands (MARIN). She specializes in real-time simulators, modeling complex maritime and offshore operations for feasibility studies and crew training. She has conducted numerical research on shallow-water and maneuvering applications and advises Young NL PIANC's Maritime Navigation Commission on port and navigation guidelines.

Tomasz Gornicz holds the position of CFD Specialist at the Maritime Research Institute Netherlands (MARIN). He graduated from a technical university in Poland, where his professor, Jan Kulczyk, introduced him to the fascinating world of inland shipping hydrodynamics. For more than 10 years, he has been conducting numerical studies in ship manoeuvring and non-conventional propulsion systems.

Wim Kleermaker holds the position of Project Engineer within the Offshore department at the Maritime Research Institute Netherlands (MARIN). In this role, his main focus is on modelling all kinds of complex offshore systems in MARINs time domain software XMF.

LOCAL HYDRODYNAMICS EFFECTS IN NARROW AND SHALLOW CHANNELS. ITS IMPORTANCE IN DESIGN AND TRAINING

Rafael Ros, Siport21, Spain

Raul Redondo, Siport21, Spain

Lourdes Pecharroman, Siport21, Spain

LOCAL HYDRODYNAMICS EFFECTS IN NARROW AND SHALLOW CHANNELS. ITS IMPORTANCE IN DESIGN AND TRAINING

RAFAEL ROS, SIPORT21, SPAIN
RAUL REDONDO, SIPORT21, SPAIN
LOURDES PECHARROMAN, SIPORT21, SPAIN

SUMMARY

This paper analyses the manoeuvring performance of large vessels in narrow (width < 2.0·*B*) and shallow waters (*H/T* < 1.1), where hydrodynamic effects such as squat, blockage, bank, and piston effects significantly impact navigation. A comprehensive methodology was developed to model and calibrate these effects through numerical simulations, pilot expertise, and real-time manoeuvring simulations.

Key hydrodynamic influences, including canal geometry, squat, bank, and piston effects, were incorporated into simulation models using specialised geographic and hydrodynamic modelling tools to enhance predictive accuracy. A case study involving a New Panamax container ship (366 m length, 51.2 m beam, 10.5 m draught) demonstrated the model's accuracy in predicting manoeuvrability in restricted channels.

Validation was conducted with local pilots and port authorities, ensuring operational feasibility and safety. The findings highlight the importance of precise modelling and simulation-based training for improving manoeuvring strategies and ensuring safe port operations in challenging environments.

NOMENCLATURE

B	Beam (m)
c	Chamber congestion
c_1	Coefficient of strength of the effect due to fore and aft width difference
c_2	Coefficient of strength of the effect due to canal narrowness
c_A	Coefficient related to the mean chamber width
c_a	Aft chamber congestion coefficient
c_B	Blockage coefficient
C_{BN}	Coefficient for yaw moment
C_{BY}	Coefficient for lateral force
c_f	Fore chamber congestion coefficient
c_S	Coefficient related to the mean submergence
d_B	Distance to the bank (m)
F	Volume rate of water pressed into the chamber (m^3/s)
$f_A(l_{int}/l_{max})$	Function dependent on the ratio l_{int}/l_{max}
F_E	Canal entrance force (N)
F_H	Hydrostatic force (N)
F_p	Volume flow induced by the ship's propulsors (m^3/s)
Fr	Froude number
Fr_∇	Froude displacement number
Fr_h	Depth Froude number
G	Gravity (m/s^2)
H	Depth (m)
H_B	Bank depth (m)
L	Ship's Length (m)
l	Distance to the integration point from the chamber's start, measured along the canal's centre (m)
L_i, R_i	Interval consisting of points on the left and right banks of the canal
l_{int}	Distance at which integration stops (m)

l_{max}	Predefined maximum integration distance (m)
m	Ship's mass (kg)
N	Yaw moment (N*m)
O_a	Aft Chamber
O_f	Fore Chamber
S	Mean submergence (m)
$s_l(l)$	Local left submergence (m)
$s_r(l)$	Local right submergence (m)
T	Draught (m)
u	Speed of the ship (m/s)
u_1	Ship speed relative to water (m/s)
UKC	Under Keel Clearance (m)
v	Counter-current velocity of water (m/s)
W	Canal width (m)
$w(l)$	Local canal width (m)
w_a	Width of the aft chamber (m)
w_f	Width of the fore chamber (m)
W_{min}	Minimal width of the canal (m)
X	Longitudinal Force Component (N)
Y	Lateral Force Component (N)
ΔH	Difference in water levels between fore and aft chambers (m)
ΔT	Change in draught (m)
$\Delta \tau$	Change in trim (°)
$\overline{\Delta T}$	Coefficient for draught change
$\overline{\Delta \tau}$	Coefficient for trim change
∇	Ship's displacement volume (m^3)
ϕ_B	Angle to the bank (rad)
α	Water surface inclination angle (rad)
τ	Relative position within a canal section

1 INTRODUCTION

The manoeuvring performance of vessels in confined areas has become a critical area of study due to the increasing scale of modern fleets. While inland waterway vessels have historically been the primary focus of shallow water navigation studies, the growing size of seagoing vessels has amplified the importance of assessing their behaviour in restricted channels and shallow waters. These conditions introduce complex hydrodynamic effects, including squat, piston effects, and significant resistance increases, causing speed reductions and significant blockage effects

The ratio between water depth and vessel draught (*H/T*) is typically greater than 4 in open water for seagoing vessels but often below 2.5 for inland waterway ships, particularly during dry seasons. The influence of water depth becomes noticeable in medium-depth waters (1.5 <*H/T*< 3.0), significant in shallow waters (1.2 <*H/T*< 1.5), and dominant in very shallow waters (*H/T*<1.2). Shallow waters introduce complex effects on the primary manoeuvring forces (*X*, *Y*) and moments (*N*), which directly impact a vessel's manoeuvring performance.

In shallow water, limited depth significantly impacts a vessel's resistance, which is the main component of hull forces in the longitudinal direction. Additionally, in confined waterways, horizontal restrictions also affect resistance, leading to the so-called blockage effect.

This paper focuses on the methodology, calibration and impact of these hydrodynamic effects in order assess their influence on the vessel and define strategies to perform manoeuvres ensuring port operations with reasonable safety level. Accurate numerical models and scenarios of local conditions, based on pilot information and experience, and real-time simulations are employed to evaluate vessel performance under these constrained conditions. A case study is included, where real-time manoeuvres were performed with local pilots in a full mission simulator, demonstrating the effectiveness of the methodology in reproducing realistic conditions and ensuring operational safety.

Accurate numerical models and scenarios of local conditions, based on pilot information and experience, are essential for assessing manoeuvrability under such constraints

2 METHODOLOGY

This section explains the methodology used for assessing complex hydrodynamic effects in manoeuvring large vessels in confined areas (narrow canals and shallow water).

2.1 CANAL GEOMETRY AND HYDRODYNAMIC EFFECTS

As a vessel progresses through a narrow channel, it displaces a significant volume of water astern. Due to the limited lateral clearance and insufficient depth, the water encounters resistance in flowing around the hull, resulting in an increased current in the direction opposite to the vessel's movement. This phenomenon resembles the action of a piston within a tube, forcing water backwards. Consequently, it induces a blockage effect, increasing hydrodynamic resistance and leading to a reduction in the vessel's speed.

To understand the methodology used for the sizing of narrow canals, the importance of the canal geometry, the effects produced by narrow canals and how they have been calculated are explained below.

For clarity, the following image shows a narrow canal with its sections and nomenclature.

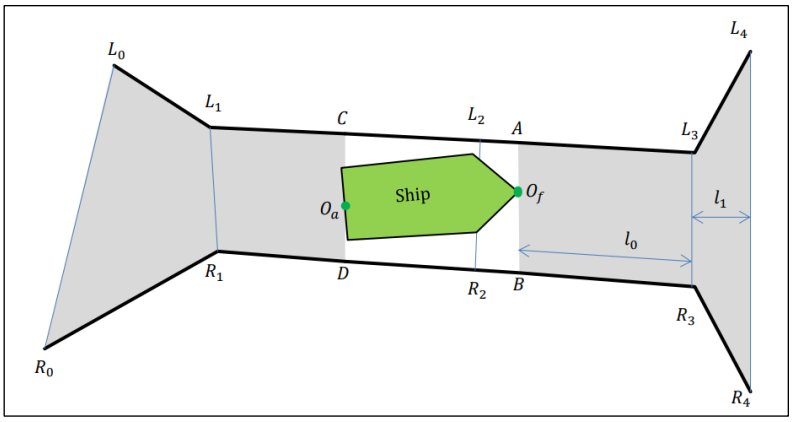

Figure 1. Sections and nomenclature of a narrow canal.

2.1 (a) Geometry of the Canal

The geometry of the canal is represented by two chambers: the fore chamber which is the part of the canal located to the front of the ship's bow O_f and the aft chamber which is the part of the canal behind the ship's stern O_a. Each of the chambers is characterized by the congestion c, which is a fraction of total outflow of combusted water which passes back ship along its hull. Congestion takes values from 0 to 1, where 0 corresponds to the case of infinitely wide chamber, while 1 corresponds to the chamber which encompasses ship tightly. Chamber congestion is calculated as follows:

$$c = c_S \frac{c_A + c_B}{2} \quad (1)$$

Here c_S is related to the mean submergence S of the left and right-side banks of the chamber:

$$c_S = \begin{cases} 1 - \frac{2S}{H}, & S < \frac{H}{2} \\ 0, & otherwise \end{cases} \quad (2)$$

Where H is the depth of the canal. According to formula (2) c_S takes values from the interval [0, 1]. Blockage coefficient $c_B \in [0, 1]$ is defined via minimal width W_{min} of the canal along the ship's hull:

$$c_B = \frac{B \cdot T}{H \cdot W_{min}} \quad (3)$$

where T is the draught and B is the beam of the ship.

Coefficient $c_A \in [0, 1]$ is related to the mean chamber width W

$$c_{\mathrm{A}} = \frac{B}{W} \cdot f_A\left(\frac{l_{int}}{l_{max}}\right) \quad (4)$$

Where $f_A(l_{int}/l_{max})$ will be explained later.

Mean values S and W are calculated as simple averages of local left and right submergences, $s_l(l)$ and $s_r(l)$, and local canal width $w(l)$ along the banks of the chamber as follows

$$\mathrm{S} = \frac{1}{l_{int}} \int_0^{l_{int}} \frac{s_l(l)+s_r(l)}{2} dl, \quad W = \frac{1}{l_{int}} \int_0^{l_{int}} w(l)\, dl \quad (5)$$

Where l is a distance to the integration point from the beginning of the chamber, measured along the middle of the canal; l_{int} is the distance at which integration stops, it is not less than some predefined integration distance l_{max}, $l_{int} \leq l_{max}$. The value of l_{max} is taken to be equal to the ship's length, L. So, integration should be stopped if integrated distance l_{int} has exceeded l_{max}, or if the canal has ended with the locked gate or an open water. Each of these events yield an upper integration boundary, l_{int}, and a value of the function $f_A(l_{int}/l_{max})$,

$$\mathrm{f_A}(x) = \begin{cases} 0.5, & x \geq 1 \\ 1 - 0.5x, & x < 1, locked\ water \\ 0.5x, & x < 1, open\ water \end{cases} \quad (6)$$

2.1 (b) Canal Effect

The canal effect on ship's hull compromises three components:

- **Counter-current v [m/s]** of water which is combusted in a chamber by moving ship. Volume rate of water F which is pressed in the chamber by moving ship is

  $$\mathrm{F} = \mathrm{u} \cdot \mathrm{B} \cdot \mathrm{T} - \mathrm{F_p} \quad (7)$$

  where u is speed of the ship; F_p is the volume flow induced by working propulsors pumping water out of the chamber. It is assumed here that ship is sailing forward, and that part of this flow, proportional to the congestion of the chambers, yields the return flow in the canal along the ship's hull which is directed from fore to the aft chamber. Hence the corresponding current v is:

  $$v = \frac{F}{W_{min} \cdot h - B \cdot T} \cdot \frac{c_f + c_a}{2} \quad (8)$$

  Where c_f and c_a are the fore and aft chamber congestions, correspondingly.

- **Hydrostatic force F_H:** This force is induced by the difference ΔH in water levels of fore and aft chamber, which is assumed to depend on the counter-current as follows

  $$\Delta H = \frac{v^2}{2g} \quad (9)$$

  Where g is the gravity acceleration. Hence, F_H can be expressed via the angle α of water surface inclination as follows

  $$F_H = mg \tan\alpha \approx mg \frac{\Delta H}{L} \quad (10)$$

  where m is a mass of the ship.

- **Canal entrance force F_E:** This force appears due to the change of water flow-over pattern around the ship when it enters the canal from open water. Generally, it is assumed that whenever width w_f of fore chamber is smaller than width w_a of aft chamber, the flow-over pattern change takes place. Force is defined as

$$F_E = c_f c_1 c_2 \frac{mu^2}{2\,L} \quad (11)$$

Here c_f is the maximal fraction of the total ship energy $mu^2/2$ which can be dissipated due to pattern change, and it is taken as $c_f = 0.02$. The c_1 is strength of the effect due to the difference in fore and aft canal widths,

$$c_1 = 1 - \frac{w_f}{w_a} \quad (12)$$

Where $c_1 \in [0, 1]$ due to $w_f < w_a$. The c_2 is strength of the effect due to narrowness of the canal itself. It is assumed that the narrower is the canal, the stronger will be the effect. Hence

$$c_2 = \frac{1}{2}\left(\frac{B}{W_{min}} + \frac{T}{h}\right) \quad (13)$$

Where $c_2 \in [0, 1]$ and value 1 is reached for completely tight canal.

2.1 (c) Canal Calculation

A canal is represented by its cross-sections, the intervals $[L_0,R_0]$, …, $[L_N,R_N]$, consisting of points on the left and right banks of the canal, which are characterized by their coordinates and submergence s in the water.

The values of formula (5) are calculated as follows:

$$S = \frac{1}{l}\sum_{i=0}^{K}\frac{s_{l,i}+s_{r,i}}{2}l_i, \quad W = \frac{1}{l}\sum_{i=0}^{K} w_i l_i, \quad l = \sum_{i=0}^{K} l_i \quad (14)$$

Where $s_{\ldots,i}$ and w_i are the average submergence and width in the *i-th* section of the canal which is delimited by cross-sections, counted from the fore point O_f (or aft point O_a). For example, for the fore chamber in the case as on the Figure 1, we get

$$S = \frac{1}{l}\left(\frac{s_{l,0}+s_{r,0}}{2}l_0 + \frac{s_{l,1}+s_{r,1}}{2}l_1\right), \quad W = \frac{1}{l}(w_0 l_0 + w_1 l_1), \quad l = l_0 + l_1 \quad (15)$$

And

$$s_{l,0} = \frac{s(A)+s(L_3)}{2}, \quad s_{l,1} = \frac{s(L_3)+s(L_4)}{2}, \quad s_{r,0} = \frac{s(B)+s(R_3)}{2}, \quad s_{r,1} = \frac{s(R_3)+s(R_4)}{2}, \quad w_0 = \frac{AB+L_3R_3}{2}, \quad w_1 = \frac{L_3R_3+L_4R_4}{2}, \quad (16)$$

where, e.g. submergence in point *A*, *s(A)*, is calculated as

$$s(A) = s(L_2)(1-\tau) + s(L_3)\tau \quad (17)$$

where $\tau \in [0 \ldots 1]$ is relative position of point O_f in the section delimited by the cross-sections $[L_2R_2]$ and $[L_3R_3]$, where $\tau = 0$ if $O_f \in [L_2R_2]$ and $\tau = 1$ if $O_f \in [L_3R_3]$.

Numerical integration stops when integrated length, *l*, reaches $l_{max} = L_{ship}$. In this case the last section, in which limit was reached, is considered partially, similarly as it was done for the first cross-section, i.e. from the beginning up to the cross-section, at which $l = l_{max}$. Alternatively, integration stops if canal finishes before l_{max} is reached, in this case $l < l_{max}$.

2.2 SQUAT EFFECT

The ship's draught and trim are known to change as the ship moves through the water. There are two parameters that influence the squat: ship speed u_1 relative to water and water depth *H*.

In this case the change in draught ΔT and change in trim $\Delta\tau$ are calculated according to the formulas:

$$\Delta T = L\overline{\Delta T}\left(Fr, \frac{H}{T}\right) \; where \; Fr = \frac{u_1}{\sqrt{g\,L}} (Froude\ Number) \; and \; \overline{\Delta T} \; is \; individual \; for \; each \; ship \quad (18)$$

$$\Delta\tau = T\overline{\Delta\tau}\left(Fr_\nabla, \frac{H}{T}\right) \; where \; Fr_\nabla = \frac{u_1}{\sqrt{g\,\nabla^{\frac{1}{3}}}} (Froude\ displacement\ Number) \; and \; \overline{\Delta\tau} \; is \; individual \; for \; each \; ship \quad (19)$$

The selection of the Froude number *Fr* and the Froude displacement number Fr_∇ in the squat and trim equations is based on their well-established use in hydrodynamic studies related to ship behaviour in shallow waters. The conventional Froude number *Fr*, defined in terms of ship length, is commonly used in wave resistance and wake formation analyses, while the displacement-based Froude number Fr_∇ is relevant for capturing dynamic effects related to the ship's buoyancy and hydrodynamic forces acting on the hull.

A key consideration in shallow water dynamics is the depth-based Froude number Fr_h, which directly accounts for the influence of limited water depth on flow acceleration and pressure distribution around the hull. Although this parameter is not explicitly included in the current formulation, its effects are indirectly incorporated through the depth-to-draught ratio *H/T*. The term *H/T* plays a crucial role in adjusting the squat and trim predictions by reflecting the confinement of flow under the ship and the increase in hydrodynamic pressure gradients as the under-keel clearance decreases.

Furthermore, the use of *Fr* and Fr_∇ is consistent with empirical models and databases that have been extensively validated in experimental and numerical studies. Many of these models rely on ship-specific coefficients $\overline{\Delta T}$ and $\overline{\Delta\tau}$, which have been derived from datasets where squat and trim behavior is correlated with these Froude number formulations. Changing the formulation to directly include Fr_h would require recalibrating the empirical coefficients and potentially modifying the underlying assumptions of the model.

Therefore, the approach adopted in this study ensures consistency with previous research while still accounting for the effects of shallow water through the inclusion of *H/T*. Future investigations may explore the explicit incorporation of Fr_h to assess whether it provides additional accuracy in specific cases of extreme shallow-water conditions.

2.3 BANK EFFECT

The bank effect is a critical hydrodynamic phenomenon in narrow canals, where the proximity of the channel banks significantly influences a ship's manoeuvrability. It arises due to asymmetric flow patterns around the hull caused by the ship's proximity to one or both banks, resulting in lateral forces (*Y*) and yawing moments (*N*) that can destabilize the vessel. In narrow canals, these effects are amplified due to the reduced distance between the hull and the banks.

2.3 (a) Forces and Moments in Narrow Canals

In narrow canals, where the channel width is less than twice the ship's beam ($W < 2B$), the forces are calculated as:

$$Y = mgFr^2 C_{BY}, \;\; N = mgLFr^2 C_{BN} \quad \left(Fr = \frac{u}{\sqrt{g\,L}} (Froude\ Number)\right) \quad (20)$$

Where C_{BY} and C_{BN} are coefficients that depend on:

- Non-dimensional distance to the bank (d_B/B): Proximity to the bank, critical in narrow canals.
- Water depth ratio (*H/T*): Shallow water amplifies bank effects.
- Angle to the bank (ϕ_B): Orientation of the vessel relative to the bank.
- Bank depth difference ($H-H_B$): Variations in water depth across the canal.

2.3 (b) Amplified Effects on Narrow Canals

- Lateral Forces: In a narrow canal, the reduced distance to banks (d_B) intensifies the lateral force (*Y*), pulling the vessel toward the nearest bank.
- Yawing Moments: Asymmetric flow around the hull generates significant yawing moments (*N*), requiring active rudder corrections to maintain course.

- Constrained Water Flow: Limited space amplifies flow velocities, increasing hydrodynamic pressures and force asymmetries.

2.3 (c) Dependence on Canal Geometry

- Non-Uniform Banks: Irregular slopes or varying depths along canal banks exacerbate force asymmetry, making precise navigation more challenging.
- Equivalent Blockage: The narrow geometry increases blockage effects, where the channel constrains the flow, further amplifying hydrodynamic resistance.

2.3 (d) Practical Implications

In narrow canals, the combination of lateral forces, yawing moments, and increased flow resistance poses significant challenges:

- Course Keeping: Continuous rudder adjustments are required to counteract the yawing moment.
- Safety Risks: Proximity to banks increases the risk of grounding or collision.
- Design and Training Needs: Ship designs must account for amplified bank effects, and simulator training should include scenarios replicating these confined water conditions.

3 MODELLING AND CALIBRATION

It is important to note that the accurate calibration of these phenomena in a real-time ship manoeuvring simulator to evaluate its performance depends on the software used. The following is a brief explanation of how these hydrodynamic phenomena have been modelled and calibrated.

3.1 CANAL GEOMETRY AND HYDRODYNAMIC EFFECTS

For the accurate modelling and calibration of these hydrodynamic effects, it is essential to have precise knowledge of both the canal geometry and the main characteristics of the study vessel.

The study vessel is a New Panamax container ship, with a length of 366 metres, a beam of 51.2 metres, a draught of 10.5 metres and a displacement of 119,240 tonnes.

The access channel to the port extends approximately 13.5 km with a depth of 10.4 metres. The first 5.5 km of the channel has a width of 150 metres (2.93*B), which narrows to 130 metres (2.54*B) between kilometres 7.7 and 5.5. The final section of the channel, from approximately kilometre 5.5 to the turning basin, has a width of 100 metres (1.95*B). The turning basin has a diameter of 450 metres and connects with the last section of the access channel.

The following figures present a plan view of the access channel and a cross-section illustrating both the channel and the study vessel.

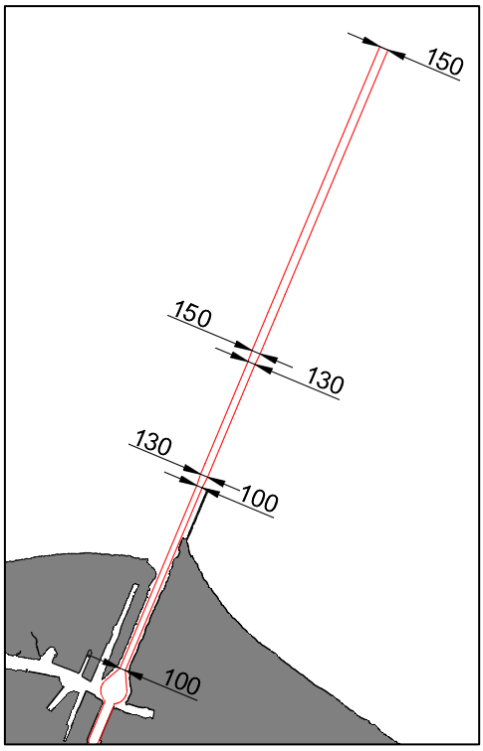

Figure 2. Plan view of the access channel

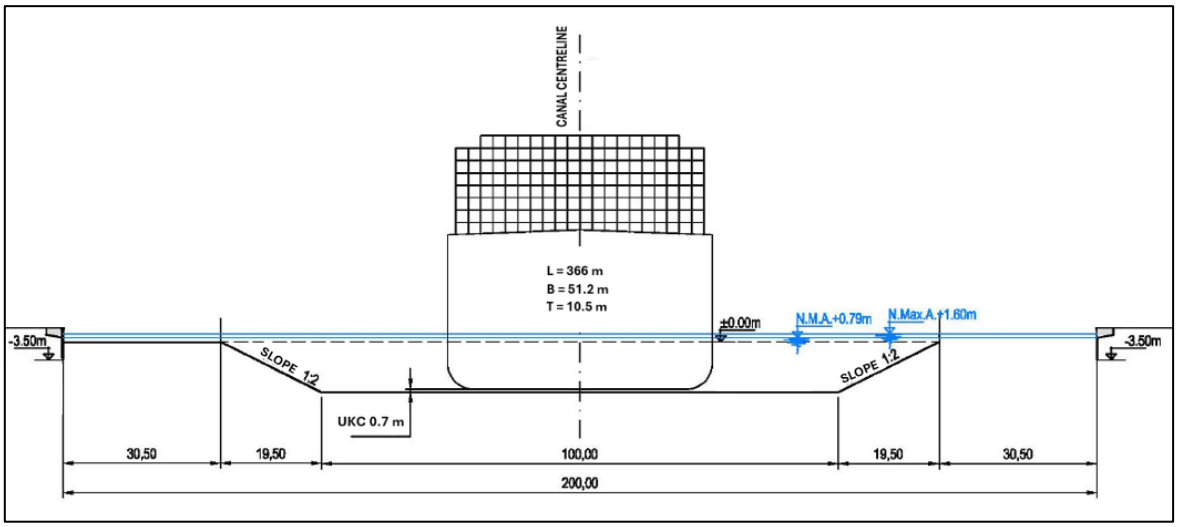

Figure 3. Cross section of the channel and the study vessel

The piston effect occurs when there is a reduction in channel width, meaning that in the study area, there are two distinct braking effects caused by the piston effect:

- When the channel width decreases from 150 m to 130 m
- When the channel width further reduces from 130 m to 100 m

To achieve the accurate modelling and calibration, an iterative process was carried out to adjust and calibrate the results based on the information and assessments provided by local pilots, who are experts in the study area and the hydrodynamic effects experienced by vessels. This iterative process involved modelling four different hydrodynamic effects induced by the canal geometry, each with distinct velocity reduction and blockage coefficients. The following image illustrates the modelling of one of these effects.

Figure 4. Modelling of one of the hydrodynamic effects induced by the canal geometry using the Geographic Information System *(GIS)* software plug-in

According to local pilots with extensive experience in the study area and vessels of this size, the expected piston effect in the region corresponds to an approximate speed reduction of two knots without any engine intervention.

To accurately model and calibrate this effect, four simulations were conducted using four different representations of the piston effect. These simulations were performed considering:

- Mean high tide water level (+0.80 m), resulting in a H/T ratio of 1.07
- No external environmental factors, such as wind, currents, or waves
- A target speed of 10 knots, meaning the vessel automatically adjusted its engine power to maintain this velocity

Under these conditions, and in the absence of a piston effect, the vessel requires 23% main propulsor level order to sustain a speed of 10 knots.

The results of the four simulations are presented in the following figures, where the vessel's speed and the percentage of main propulsor usage are plotted against time. The shaded regions (red, blue, and green) highlight the channel width reduction zones, which correspond to the sections where the vessel experiences the piston effect.

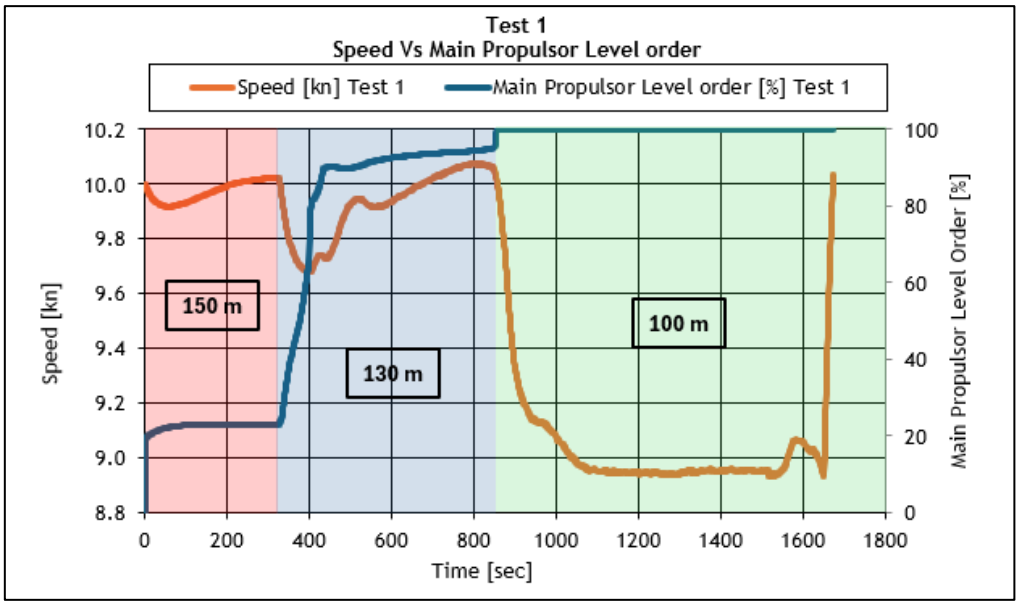

Figure 5. Piston effect Test 1 – Speed (knots) and Main Propulsor Level Order (%)

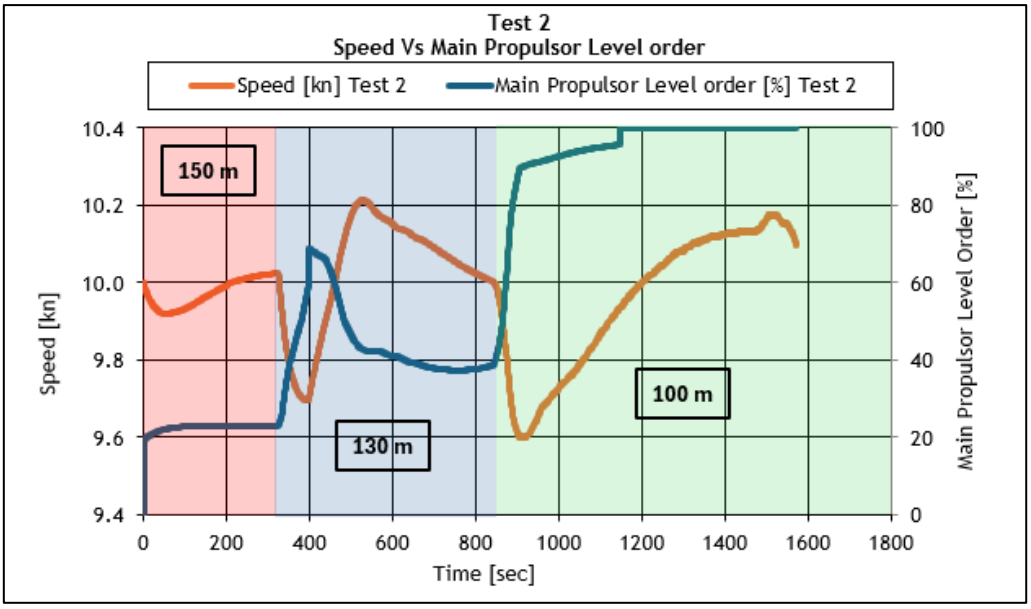

Figure 6. Piston effect Test 2 – Speed (knots) and Main Propulsor Level Order (%)

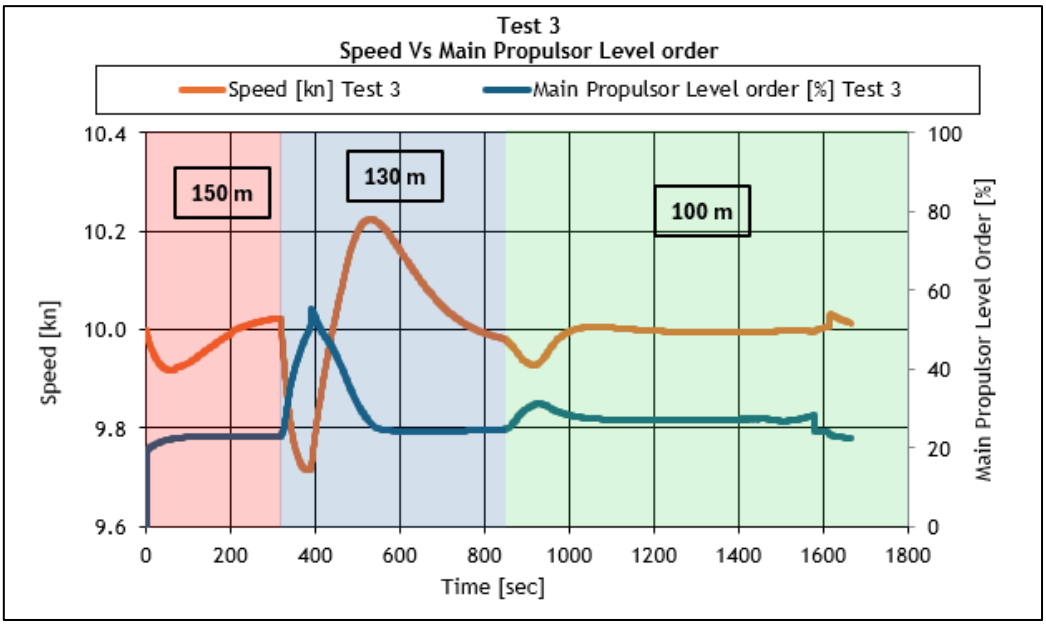

Figure 7. Piston effect Test 3 – Speed (knots) and Main Propulsor Level Order (%)

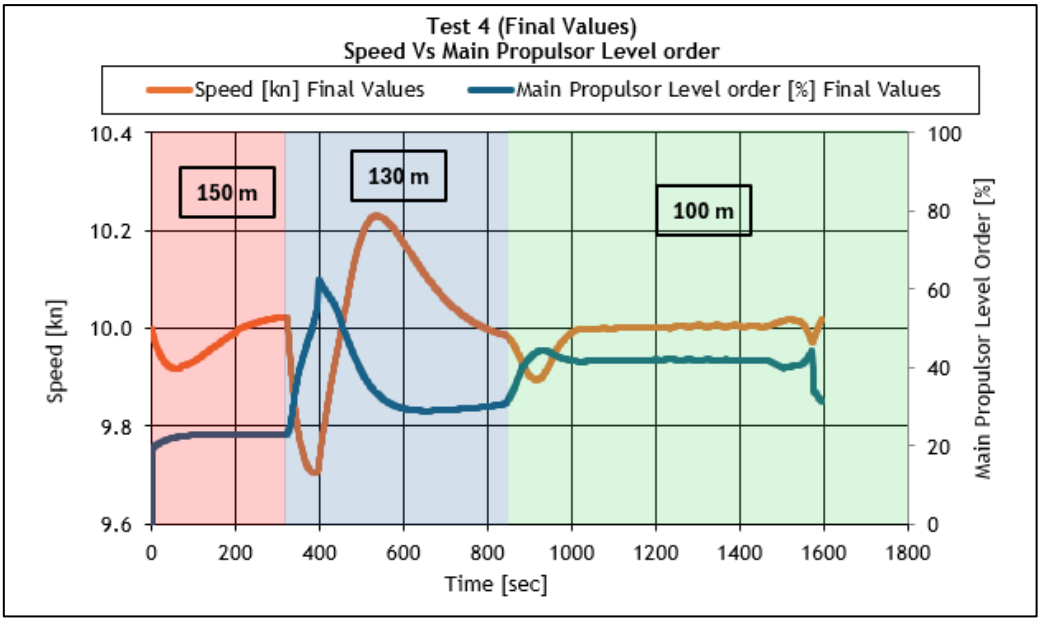

Figure 8. Piston effect Test 4 (Final Values) – Speed (knots) and Main Propulsor Level Order (%)

Analysing the results of the simulations shown in the figures and, considering that the vessel needs a 23% of propulsor usage in the absence of the piston effect to maintain a speed of 10 knots, as well as the expected results from local pilots, it can be concluded that:

- Test 1: This represents an overestimated piston effect, where the vessel needs to use 100% propulsor usage and still fails to maintain 10 knots.
- Test 2: Although the piston effect is slightly reduced compared to Test 1, it remains overestimated, requiring full propulsor usage and still being unable to overcome the speed loss.
- Test 3: Here, the piston effect is practically negligible, as the vessel consistently operates at approximately 23% propulsor usage, indicating that the braking effect is too weak.
- Test 4 (Final Values): The piston effect in this test aligns well with the expected values reported by local pilots. The vessel requires a reasonable increase in engine power to overcome the effect, reflecting a realistic representation of the hydrodynamic phenomenon.

The iterative modelling and simulation process allowed for a refined calibration of the piston effect, ensuring that the final model accurately represents the hydrodynamic resistance induced by channel width reductions. The first two tests demonstrated an overestimated effect, leading to unrealistic propulsion demands, while the third test underestimated the effect, failing to capture the braking force observed in real-world conditions. The final model provides a balanced representation, in agreement with expert pilot assessments, effectively replicating the vessel's speed loss and recovery dynamics as it navigates through the channel.

This calibrated model ensures a more precise assessment of navigational performance in constrained waterways, which is crucial for operational planning, safety assessments, and future optimisation of transit strategies in the study area.

3.2 SQUAT AND BANK EFFECTS

For the precise modelling of the squat and bank effects, a specialised Hydrodynamic Modelling Tool (*HDMT*) was used. This tool includes various applications for the accurate development of ship hydrodynamic models, which are employed in a real-time manoeuvring simulator. Specifically, the following applications were used:

- Ship Database Manager: Its purpose is to create and modify ship database files, including a wide range of wizards and other tools designed to streamline the model development process, modify or add specific functionalities, and facilitate adjustments.

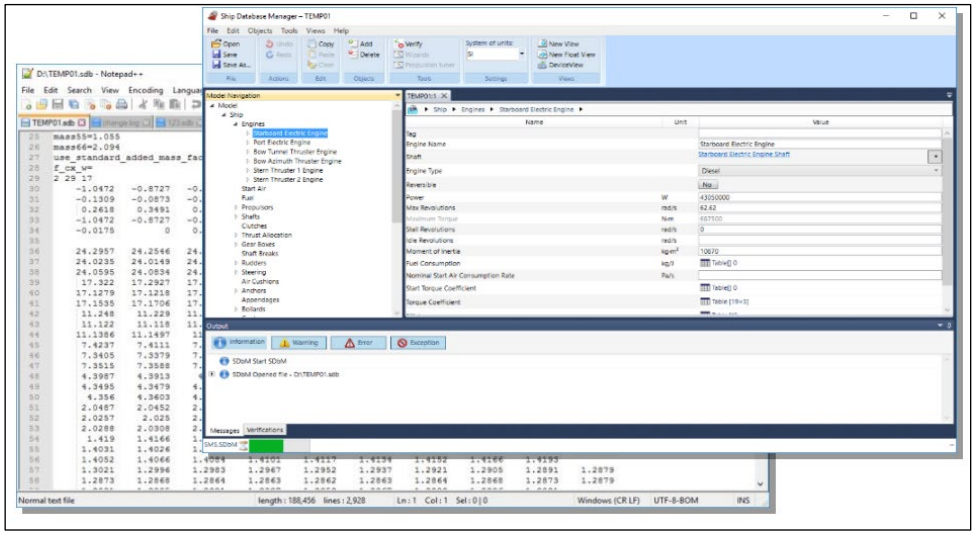

Figure 9. **Ship Database Manger Application.**

- Ship Simulator: A real-time deck-top simulation platform that provides real-time controls for testing, handling and manoeuvring, propulsion, bank/canal/squat effects, environmental conditions (including ice formation), and energy management. The features include 2D and 3D visualization of models both above and below the water, as well as live graphs of simulation parameters.

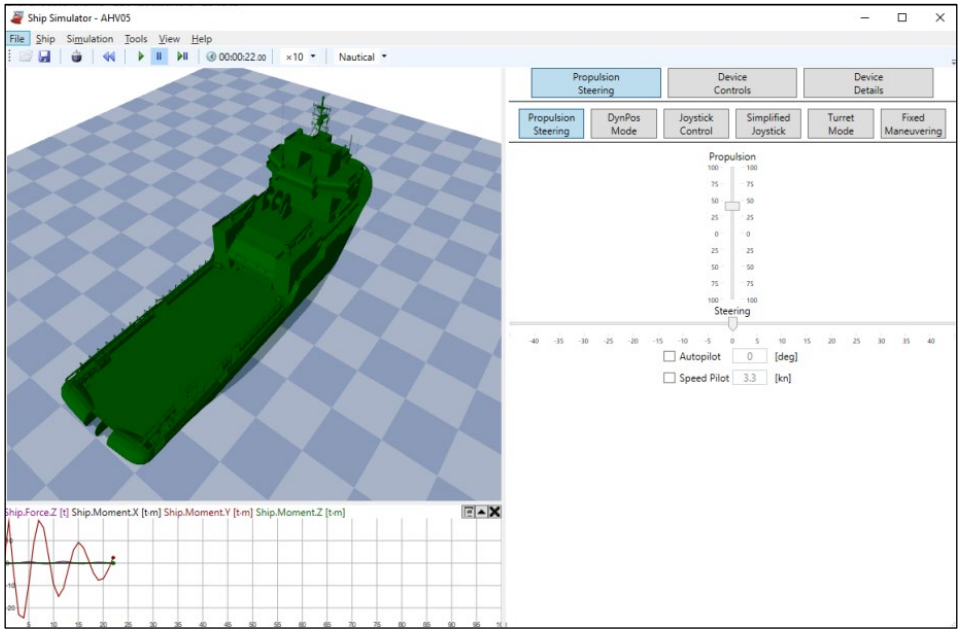

Figure 10. Ship Simulator Application.

3.2 (a) Squat Effect

For the modelling of the squat effect, the Hydrodynamic Modelling Tool allows the use of various formulations (Ankudinov et al., 1996; Barrass, 1995; Eryuzlu et al., 1994; Huuska, 1976; Millward, 1992; Norrbin, 1986; Romisch, 1989; Yoshimura, 1986; and Standard), enabling the selection of the most appropriate formulation for each specific case study. It is important to note that great differences on squat results can be observed depending on the formulation selected. Hence the importance of making a prior assessment of the most appropriate option.

After a detailed analysis of the various formulations available for calculating the squat effect, the Standard formulation was selected. This approach for determining dynamic ship squat is based on the approximation data provided in:

- Millward. Comparison of Theoretical and Empirical Prediction of Squat in Shallow Water. Int. Shipbuild. Progr., 39, No. 417, 1992, pp. 69-78.
- A.M. Basin et al. Hydrodynamics of Ships in Shallow Water. Shipbuilding, St. Petersburg, 1976, p. 319.

It is important to highlight that this formulation enables the calculation of the coefficients, $\overline{\Delta T}\left(Fr, \frac{H}{T}\right)$ and $\overline{\Delta\tau}\left(Fr_{\nabla}, \frac{H}{T}\right)$, as defined in Equations 18 and 19 of this paper. These coefficients allow for the determination of both the change in draught in meters and trim in degrees due to the squat effect by multiplying the ship's length by the coefficient $\overline{\Delta T}\left(Fr, \frac{H}{T}\right)$ and the ship's draught by the coefficient $\overline{\Delta\tau}\left(Fr_{\nabla}, \frac{H}{T}\right)$.

For the precise calibration of the squat effect in the study area, local pilots noted that, although it is a highly challenging phenomenon to quantify in this specific region, for the vessel under study at a speed of 6 knots, with the channel depth conditions (10.4 m) and water level (+0.8 m), corresponding to a H/T ratio of 1.07, the squat effect experienced would be expected to fall within the range of approximately 0.5 to 0.55 metres of settlement.

In this context, the aim is to calibrate the squat effect in the most conservative manner, and therefore, the calibration is performed to achieve a draught settlement value of 0.55 metres for the vessel's speed of 6 knots and an H/T ratio of 1.07.

For the precise calibration of this effect, three tests were conducted, as outlined below. For each test, two figures are presented: one showing, for various H/T ratios, the coefficient of draught increase ($\overline{\Delta T}\left(Fr, \frac{H}{T}\right)$) plotted against the Froude number, and another displaying, for various H/T ratios, the coefficient of trim increase ($\overline{\Delta\tau}\left(Fr_{\nabla}, \frac{H}{T}\right)$) plotted against the volume Froude number.

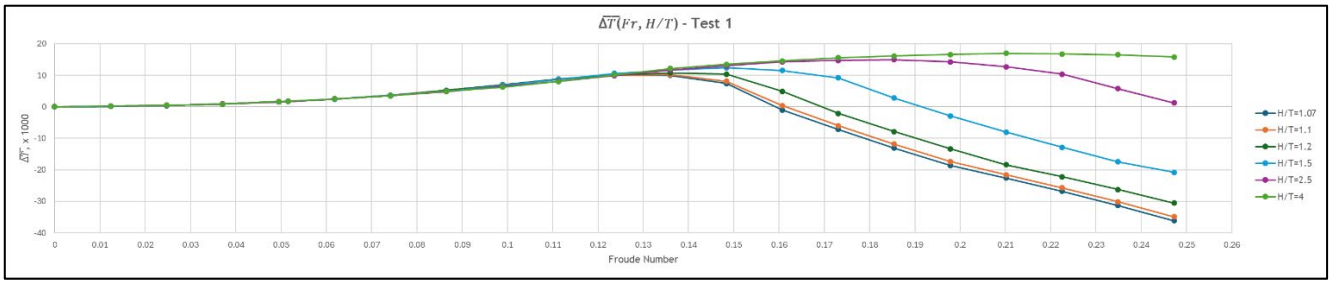

Figure 11. Draught Increase Coefficient for Test 1.

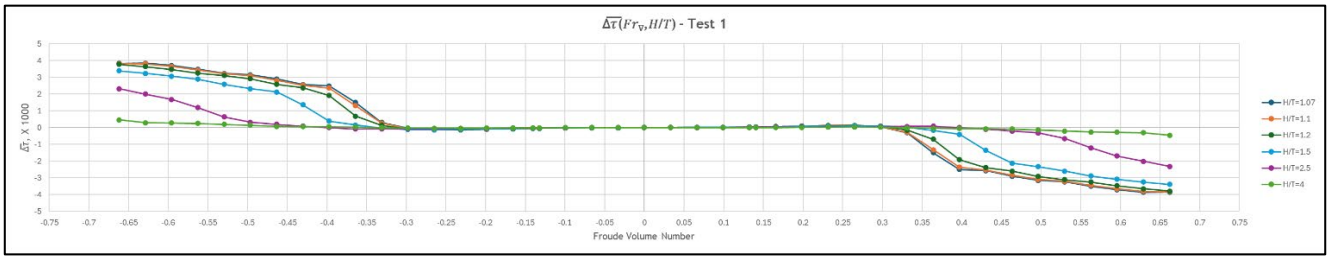

Figure 12. Trim Increase Coefficient for Test 1.

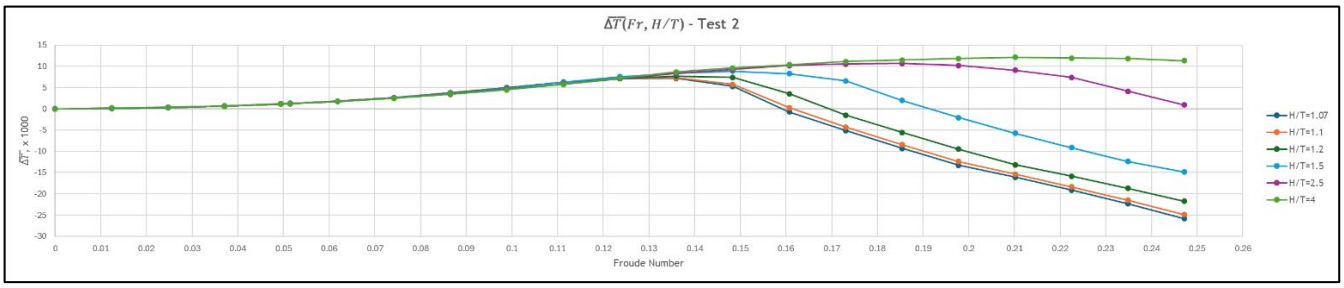

Figure 13. Draught Increase Coefficient for Test 2.

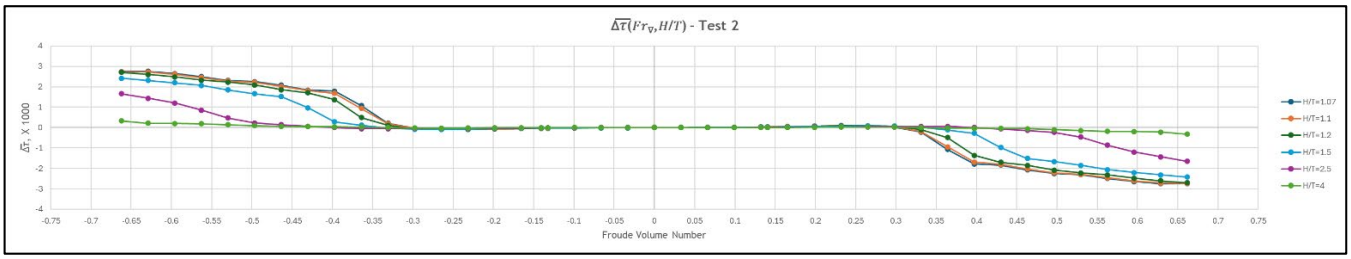

Figure 14. Trim Increase Coefficient for Test 2.

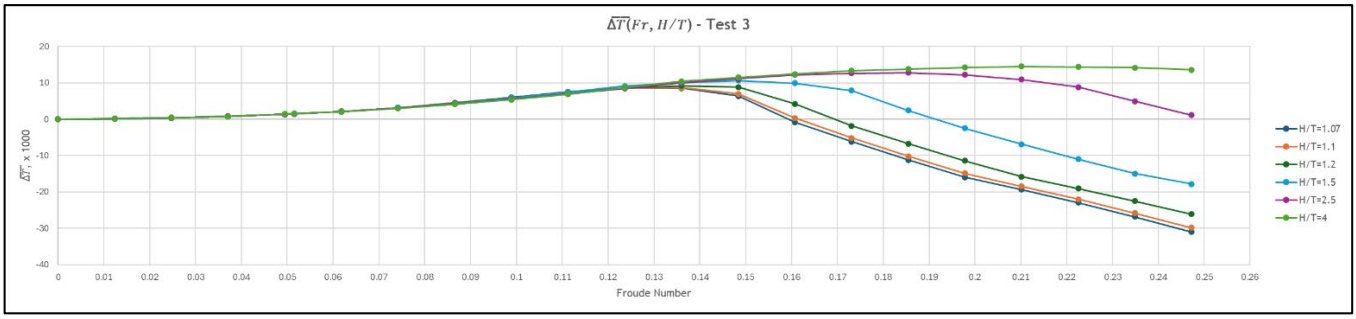

Figure 15. Draught Increase Coefficient for Test 3.

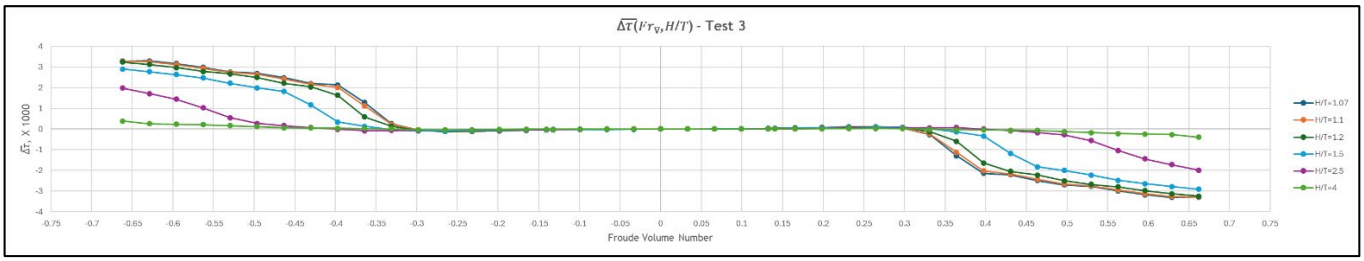

Figure 16. Trim Increase Coefficient for Test 3.

Finally, by inputting the Froude number and volume Froude number at 6 knots of speed and the H/T ratio of 1.07 for each of the tests, and multiplying these values by the vessel's length and draught (as shown in Equations 18 and 19 of the paper), the values for the increase in draught (m) and trim (°) due to the squat effect were obtained for each test. These values are summarised in the table below:

Table 1. Draught and Trim Increase Obtained in the Different Tests Conducted

	Test 1	Test 2	Test 3
Draught Increase (ΔT)	0.642 m	0.458 m	0.550 m
Trim Increase (Δτ)	-0.000160 ° 0.000160 °	-0.000114 ° 0.000114 °	-0.000137 ° 0.000137 °

As observed in the table, the values obtained in Test 1 exceed the target values, the results from Test 2 fall below the target values, and the values from Test 3 match the expected results. Thus, the final values derived from the modelling and calibration of the squat effect correspond to those of Test 3.

The results of the squat effect calibration demonstrate that Test 3 provides the most accurate and reliable values for the study area, aligning closely with the target draught increase of 0.55 metres at a vessel speed of 6 knots and an H/T ratio of 1.07. Furthermore, the minimal impact on trim observed across all tests highlights that the draught change is the primary factor influencing squat, reinforcing the importance of accurately quantifying this effect for safe and efficient navigation in shallow waters.

Additionally, simulations were carried out using both the Ship Simulator application and the real-time manoeuvring simulator, where it was confirmed that the values obtained from the modelling and calibration of the squat effect aligned with the expectations of the local pilots.

3.2 (b) Bank Effect

In the present study, the bank effect has not been considered in the simulations. According to information provided by local pilots, this effect is negligible compared to the piston effect and squat in the study area. Given the dominant influence of these two phenomena on ship manoeuvrability, the modelling and calibration efforts have focused on capturing their impact with higher accuracy, while the bank effect has been disregarded as a secondary influence.

4 CASE STUDY AND VALIDATION BY LOCAL PILOTS

After detailing the methodology, modelling, and calibration of local hydrodynamic effects in narrow and shallow channels, their importance in ship design and training is demonstrated through a case study conducted using a real-time ship manoeuvring simulator.

Manoeuvres of a New Panamax container ship, 366 meters in length, 51.2 meters in beam, and with a draught of 10.5 meters, were conducted using a real-time ship manoeuvring simulator. The objective was to verify the feasibility of these manoeuvres by evaluating the available navigational spaces and determining the hydro-meteorological limits under which the operations are feasible with the resources available at the port. To achieve this, initial working sessions were conducted on the Real-Time Manoeuvring Simulator with the participation of local pilots to validate and calibrate the numerical model.

Once the model was calibrated and validated by the local pilots, representatives from the Port Authorities attended as observers to evaluate and ultimately approve or reject the feasibility of the manoeuvres in the area.

For the manoeuvres, the mean high tide water level (+0.80 *m*) was considered, which means navigating with an *H/T* of 1.07. Additionally, the manoeuvres were conducted with the assistance of tugboats, consisting of a formation of three Azimuth Stern Drive (*ASD*) units, each with a bollard pull of 70 tons, using one of them at the stern to help control the speed and steering of the ship.

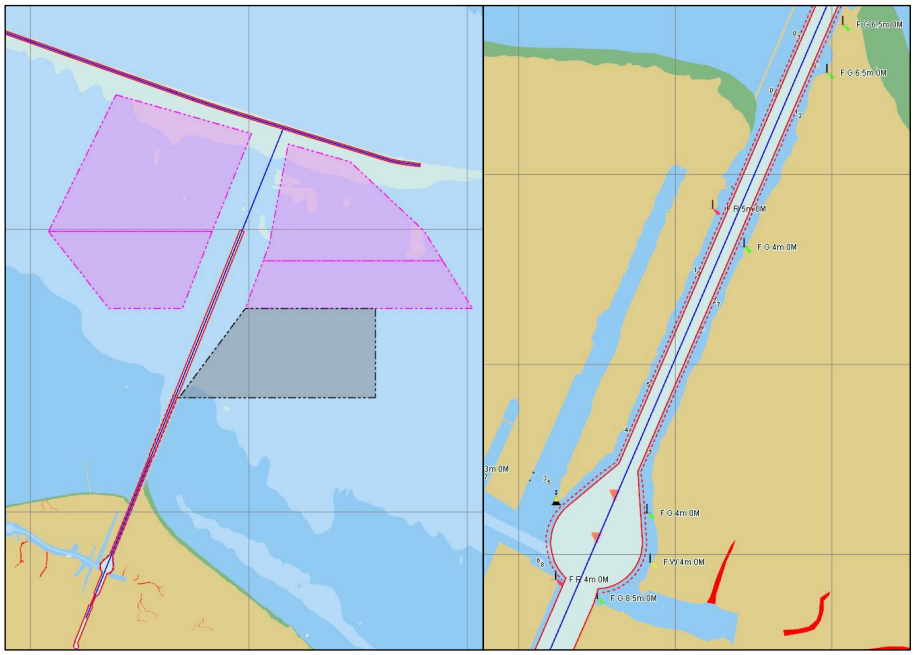

Figure 17. Modelling of Port in the simulator

Figure 18. Visual model of Port

The project faced several technical challenges, summarized as follows:

- Wind Conditions: Manoeuvring in winds of up to 15 knots and cross direction, including a gust factor that increases wind intensity by up to 33% above the average considered.
- Cross Currents: in addition to the restricted area and the effect associated, manoeuvres had to contend with cross currents in the access channel exceeding 0.5 knots.

- Very Low Under Keel Clearance (*UKC*): The selected study draught (10.5 m) ensured a minimum static under keel clearance (UKC) of 0.7 *m* in the channel, accounting for a 0.8 *m* water level (*H/T* = 1.07)
- Numerical Model Accuracy: The numerical model incorporated local hydrodynamic effects, as conveyed by pilots during the initial phases of the study. This included precise modelling of the channel's hydrodynamic forces.
    - Piston Effect: The model accounted for the "piston effect," which reduces vessel speed due to increased drag forces caused by the restricted channel dimensions (width and depth) relative to the vessel's size.
    - Squat Effect: The increase in the vessel's draught with speed (squat effect) was incorporated, reflecting its impact on under keel clearance in the channel.

Finally, it is worth highlighting that the local pilots expressed their satisfaction with the modelled local hydrodynamic effects during the manoeuvres. They noted that these effects closely mirrored their real-world experiences, thereby validating the accuracy of the modelling. Similarly, representatives of the port authorities, who attended as observers, also validated the hydrodynamic effects and ultimately approved the manoeuvres. This approval marked a significant milestone for the port, making it the first terminal in the country to be certified by the port authorities for the access of Neo-Panamax container ships.

5 CONCLUSIONS

The study presented in this paper demonstrates the critical importance of accurately modelling and calibrating local hydrodynamic effects for the safe and efficient operation of large vessels in narrow and shallow channels, when these aspects are of great impact on the safety and feasibility of manoeuvres. Key findings and remarks are summarized below:

- Precise Hydrodynamic Modelling:
    - The integration of advanced tools, including Geographic Information System (*GIS)* software for canal geometry modelling and the Hydrodynamic Modelling Tool (*HDMT*) for effects such as squat, proved essential for replicating real-world conditions with high fidelity.
    - Iterative calibration, informed by local pilot expertise, ensured that the numerical models captured nuanced local conditions, including the piston effect and squat effect in narrow and shallow canals.
    - The final calibrated squat model determined that, for a vessel speed of 6 knots and an H/T ratio of 1.07, the draught increase reached **0.55 metres**, with negligible trim variation, aligning with pilot expectations.
    - For the piston effect, the iterative modelling process revealed that under the conditions of a 10-knot target speed and a channel with reduced widths (from 150m to 130m, and then from 130m to 100m), the vessel experienced a speed reduction of approximately 2 knots, which matched local pilot assessments. The calibrated model showed that the vessel required a reasonable increase in engine power to overcome the piston effect, aligning with the real-world hydrodynamic forces observed.
- Validation through Real-Time Simulation:
    - The use of a real-time ship manoeuvring simulator enabled the effective validation of the numerical models. The simulator accurately reproduced local conditions, such as winds, cross currents, very low under keel clearance (*UKC*), squat and piston effects, allowing for realistic testing of manoeuvring scenarios.
    - Participation from local pilots and representatives of port authorities further reinforced the reliability and accuracy of the modelling.
- Operational Feasibility and Certification:
    - The validated models confirmed the feasibility of manoeuvres for a New Panamax container ship in the access channel to the port under predefined hydro-meteorological conditions and resource constraints.
    - The approval of the manoeuvres by port authorities established the port as the first terminal in the country certified to accommodate Neo-Panamax container ships, marking a milestone for the region's maritime infrastructure.
- Challenges and Innovations:
    - The study highlighted significant technical challenges, including low *UKC*, and the combined effects of squat and piston forces in narrow channels.

    - The application of real-time modelling and pilot calibrations provided innovative solutions to these challenges, ensuring operational safety and efficiency.
- Implications for Design and Training:
    - The findings underscore the importance of incorporating complex hydrodynamic effects into both the design phase of vessels and training programs for pilots and crews.
    - Real-time simulators proved to be very helpful for training, allowing seafarers to experience and prepare for the challenges posed by confined navigation conditions.

This paper highlights the necessity of site-specific calibration when applying hydrodynamic models to ensure accurate predictions. The robust methodology, including modelling and calibration, presented here can be applied to similar confined waterway environments, improving safety and operational efficiency in complex maritime settings.

6 REFERENCES

Zaikov, S., & Nikushchenko, D. 2021. Hydrodynamic Modelling Tool (HDMT)-Mathematical Model of Ship Dynamics (Internal document). Kongsberg Digital AS.

Nikitina, E. 2021. Hydrodynamic Modelling Tool Ship Database Manager User Guide (Internal document). Kongsberg Digital AS.

Nikitina, E. 2021. Hydrodynamic Modelling Tool: Overview (Internal document). Kongsberg Digital AS.

Ankudinov, V. K., and B. K. Jakobsen. 1996. Squat predictions at an early stage of design. Workshop on Ship Squat in Restricted Waters (4 October, Washington). Jersey City, NJ: SNAME, 48-69.

Ankudinov, V., L. L. Daggett, J. C. Hewlett, and B. K. Jakobsen. 2000. Prototype measurement of ship sinkage in confined water. Proceedings International Conference on Marine Simulation and Ship Maneuverability (MARSIM 2000). Orlando, FL, 8-12 May.

Dr. C.B.Barrass. 1995. Ship Squat – Method 1.

Eryuzlu, N. E., Y. L. Cao, and F. D'Agnolo. 1994. Underkeel requirements for large vessels in shallow waterways. 28th International Navigation Congress, PIANC, Paper S11-2, Sevilla, 17-25.

Huuska, O. 1976. On the evaluation of underkeel clearances in Finnish waterways, Report No.9. Otaniemi: University of Technology, Ship Hydrodynamics Laboratory.

Millward, A. 1992. A comparison of the theoretical and empirical prediction of squat in shallow water. International Shipbuilding Progress 39(417); 69-78.

Norrbin, N.H. 1986. Fairway design with respect to ship dynamics and operational requirements. SSPA Research Report No.0102.Gothenburg, Sweden: SSPA Maritime Consulting.

Romisch, K. 1989. Empfehlungen zur Bemessung von Hafeneinfahrten. Wasserbauliche Mitteilungen der Technischen Universitat Dresden, Heft 1, 39-63.

A.M. Basin et al. 1976. Hydrodynamics of Ships in Shallow Water. Shipbuilding., St. Petersburg, p.319.

Yoshimura, Y. 1986. Mathematical model for the maneuvering ship motion in shallow water, J. Kansai Society of Naval Architects, Japan, No 200.

7 AUTHORS BIOGRAPHY

Rafael Ros currently holds the position of Project Engineer of the Manoeuvring and Nautical Studies Area at Siport21. He is responsible for carrying out manoeuvring studies using numerical tools (fast and real-time simulation). He is specialized in numerical models of ports.

Raul Redondo holds the current position of Director of Manoeuvring and Nautical Studies Area at Siport21. He coordinates and checks the technical projects. He specializes in ship manoeuvrability in port areas, both using numerical models and real-time simulation.

Lourdes Pecharroman holds the current position of Project Manager of the Manoeuvring and Nautical Studies Area at Siport21. She is responsible for managing manoeuvring studies carried out with numerical tools (fast-time and real-time simulation). She is specialized on numerical models of vessels.

HYDRODYNAMIC INFLUENCE OF WAVY SEABED ON SHIP-SEABED INTERACTION

Yunxin Xu, School of Engineering, Newcastle University, UK
Weichao Shi, School of Engineering, Newcastle University, UK

HYDRODYNAMIC INFLUENCE OF WAVY SEABED ON SHIP-SEABED INTERACTION

YUNXIN XU, SCHOOL OF ENGINEERING, NEWCASTLE UNIVERSITY, UK
WEICHAO SHI, SCHOOL OF ENGINEERING, NEWCASTLE UNIVERSITY, UK

SUMMARY

The interaction between a vessel and an uneven seabed is a critical factor in ship performance and safety, particularly in depth-restricted conditions where shallow water effects are significant. While most existing research focuses on ship-seabed interaction analysis using a flat seabed, an uneven seabed introduces far more intricate hydrodynamic effects. This study employs a high-fidelity transient numerical simulation method with a sliding mesh to investigate the hydrodynamic response of a self-propulsion ship navigating over a wavy seabed. Key findings demonstrate the substantial impact of the wavy seabed on vessel motion. Several regions of pronounced vessel sinkage were identified, revealing differences compared to flat sea-bed conditions as the ship moves over the wavy surface. These results emphasize the importance of accounting for seabed topography in accurately predicting vessel behaviour and ensuring navigational safety in such environments.

1 INTRODUCTION

Compared to deep-water conditions, vessels operating in depth-restricted conditions are more sensitive to environmental factors, which play a crucial role in determining hydrodynamic performance. Understanding the interaction between a vessel and its surrounding environment, particularly the seabed, is critical for ensuring the safety, efficiency, and environmental sustainability of marine operations. While a significant body of research has focused on ship-seabed interactions over flat and constant-depth seabed (Gourlay, 2008; Sun et al., 2013), real-world conditions often present uneven seabed with varying topographies, introducing complex hydrodynamic challenges (Carrica et al., 2012; Shi et al., 2021). Among these, tidal sand waves are commonly found in shallow continental shelf regions with water depths of 20 m to 50 m, such as those near the Rotterdam harbour in the North Sea and the Mouth of San Francisco Bay in California (Figure 1). The features are typically described by their wave height and wavelength, with typical heights ranging from 4 to 10 meters, with extreme cases reaching up to 30 meters, and wavelengths from several tens to hundreds of meters (Besio et al., 2008; Hulscher et al., 1993; Krabbendam et al., 2021).

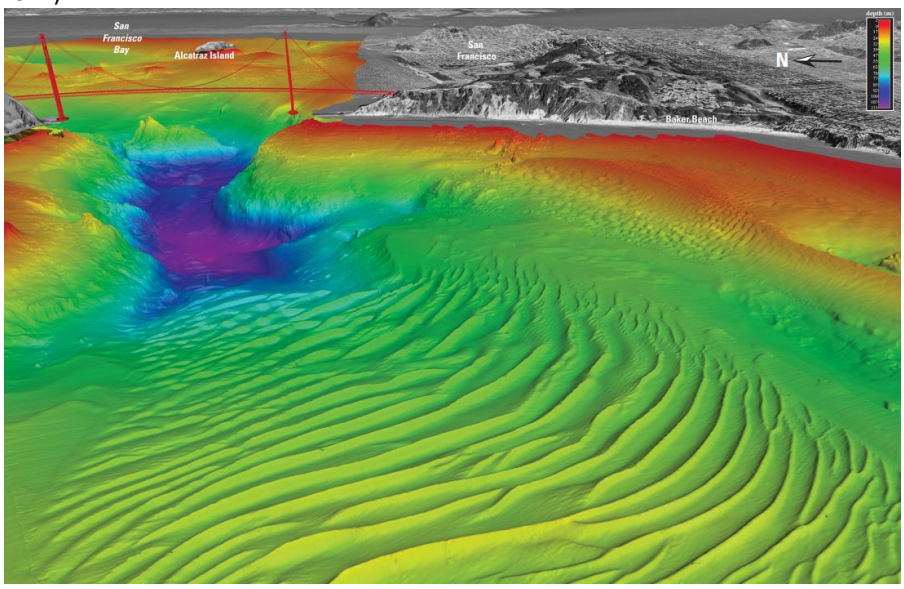

Figure 1. Seabed topography at the Mouth of San Francisco Bay, California (Adapted from U.S. Geological Survey, Public domain, photo by Patrick L. Barnard, Daniel M. Hanes, Rikk G. Kvitek, and Pat J. Iampietro, https://pubs.usgs.gov/sim/2006/2944/).

Unevenness of the seabed, such as wavy profiles, significantly affect hydrodynamic forces and flow patterns. These effects are especially pronounced in depth-restricted conditions, where proximity to the seabed amplifies interactions, altering resistance, sinkage, and trim. Gourlay's application of slender-body methods extended theoretical predictions to container ships in restricted waters, offering valuable insights into squat and resistance under varying depth conditions (Gourlay,

2008). Similarly, recent research by Terziev et al. demonstrated the utility of CFD in capturing critical phenomena like wave generation and flow separation over abrupt seabed transitions, in cases with depth-to-draft ratios of 1.1–2.2 and depth Froude numbers ranging from 0.8 to 1.2 (Terziev et al., 2021, 2024). Song et al. (2023) showed that increased seabed roughness modifies resistance and turbulence characteristics, influencing vessel performance, particularly under shallow-water conditions with depth-to-draft ratios of 1.1–1.3 and depth Froude numbers of 0.29–0.45.

The advent of computational fluid dynamics (CFD) has advanced the study of ship-seabed interactions. High-fidelity methods, such as Reynolds-Averaged Navier-Stokes (RANS) solvers and dynamic overset grids, now enable detailed simulations of unsteady hydrodynamic phenomena (Carrica et al., 2016; Kim et al., 2022; Song et al., 2023). CFD studies have highlighted the intricate interactions between hull form, seabed, and hydrodynamic forces, emphasizing the role of viscous effects in enhancing prediction accuracy. However, gaps remain in understanding the full scope of uneven seabed effects, particularly under varying Froude number regimes and complex geometrical configurations.

Building upon these foundational studies, a high-fidelity transient numerical simulation method was developed employing a sliding mesh to analyse the hydrodynamic effects of ship-seabed interactions over a step change in seabed depth (Shi et al., 2021). This work revealed the substantial influence of seabed geometry on wave elevations, wake development, and vessel sinkage, highlighting the delayed effects of depth transitions, where extreme sinkage occurs after a significant travel distance rather than immediately upon entering shallow regions. This detailed analysis provides a robust computational framework for understanding ship behaviour in complex seabed environments.

This study builds upon prior research by employing a high-fidelity transient numerical simulation with a sliding mesh to investigate the hydrodynamic response of a vessel navigating over a wavy seabed. Unlike traditional flat-seabed models, this research emphasizes the role of uneven topographies in influencing vessel motion. By capturing these effects, the findings aim to contribute to improved design and operational strategies for navigating vessels in shallow and restricted waters.

2 CFD SIMULATION METHODOLOGY

2.1 MODEL INFORMATION AND COMPUTATIONAL DOMAIN

The simulations were conducted to analyse the motion response of a ship navigating over a wavy seabed using the Computational Fluid Dynamics (CFD) software STAR-CCM+. A Reynolds-averaged Navier–Stokes (RANS) model, coupled with a K-ω Shear Stress Transport (K-ω SST) turbulence model, was employed to ensure accurate representation of the flow dynamics (Singh et al., 2011).

For this study, the benchmark ship model, KRISO Container Ship (KCS), was selected due to its extensive use in experimental and numerical validations. Experimental data for the KCS model are available from Hino et al. (2020). In the simulations, the model-scale KCS without a rudder was investigated under self-propulsion conditions to avoid the high computational cost for full-scale simulation. Meanwhile, the simulation result can have a direct comparison with the model test results.

In the self-propulsion simulation, the virtual disk module was utilized to replicate the KP505 propeller, as Figure 2 shows below. This propeller is identical to the one employed in the experiments, and the open-water propeller curves were sourced from MOERI (*SIMMAN 2008*, 2008). The main parameters of the ship model are detailed in Table 1. In addition, since the experimental test was conducted at the ship point, an additional towing force for skin friction correction (SFC) of 30.25 N was added on the model during the simulation.

Figure 2. Model-scale KCS model with the virtual disk model.

Table 1. Main parameters of the KCS models

	Symbol	Unit	Full Scale	Model Scale (MOERI)
Scale Factor				31.60
Length between the perpendiculars	L_{pp}	m	230.00	7.28
length of the waterline	L_{wl}	m	232.50	7.36
Beam at waterline	B_{wl}	m	32.50	1.02
Depth	D	m	19.00	0.60
Design draft	T	m	10.80	0.34
Displacement		m^3	52030.00	1.65
Longitudinal Centre of Gravity (From Aft Perpendicular Point)	LCG	m	111.60	3.53

In this study, four types of seabed were analysed. The first was a flat seabed, which served as a reference case for comparison. The other three were wavy seabed, generated using a first-order wave equation (Equation 1). The wave height (H) was set to 0.5, 1, and 1.5 times the ship's draft (T), while the wavelength (λ) was equal to the ship's length between perpendiculars (L_{pp}). In all cases, the under-keel clearance for the flat seabed and the mean clearance for wavy seabeds were set to 3T. The depth Froude number (Fr_h) was calculated by Equation 2, where V is the ship velocity and h is the local water depth. For the flat seabed, Fr_h was 0.70, while for the wavy seabed cases it ranged between 0.62 and 0.80. All values fall within the range associated with pronounced shallow-water effects, as defined by ITTC (Proceedings, 2017). An overview of the seabed geometry in relation to the ship is illustrated in Figure 3. In all simulations, the ship travelled a distance (d) equal to 80 times its length to ensure result stabilization. The analysis focused on the range from 70L_{pp} – 80L_{pp}, representing a steady-state region where the hydrodynamic responses of the vessel had stabilized.

$$z_w(x_w) = \frac{H}{2}\sin\left(\frac{2\pi}{\lambda}x_w\right) \tag{1}$$

$$Fr_h = \frac{V}{\sqrt{gh}} \tag{2}$$

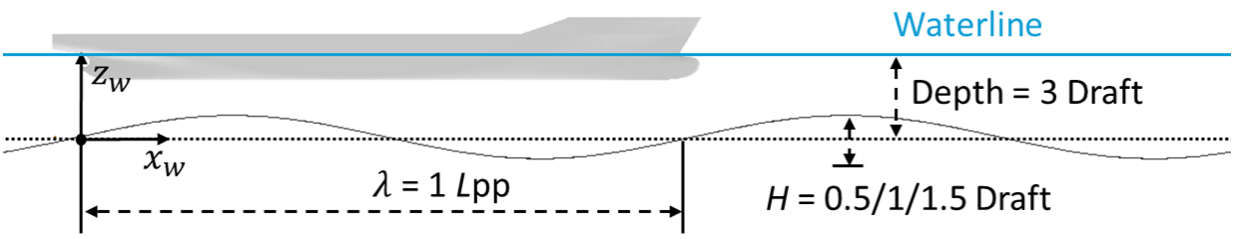

Figure 3. Overview of seabed and ship geometries.

In the pre-processing stage, to enhance computational cost efficiency and improve mesh performance compared to traditional CFD simulation methods, a novelty simulation setting method was introduced which includes three computational regions: the ship motion region (Region A), the free surface region (Region B), and the seabed region (Region C). The configuration details are illustrated in Figure 4.

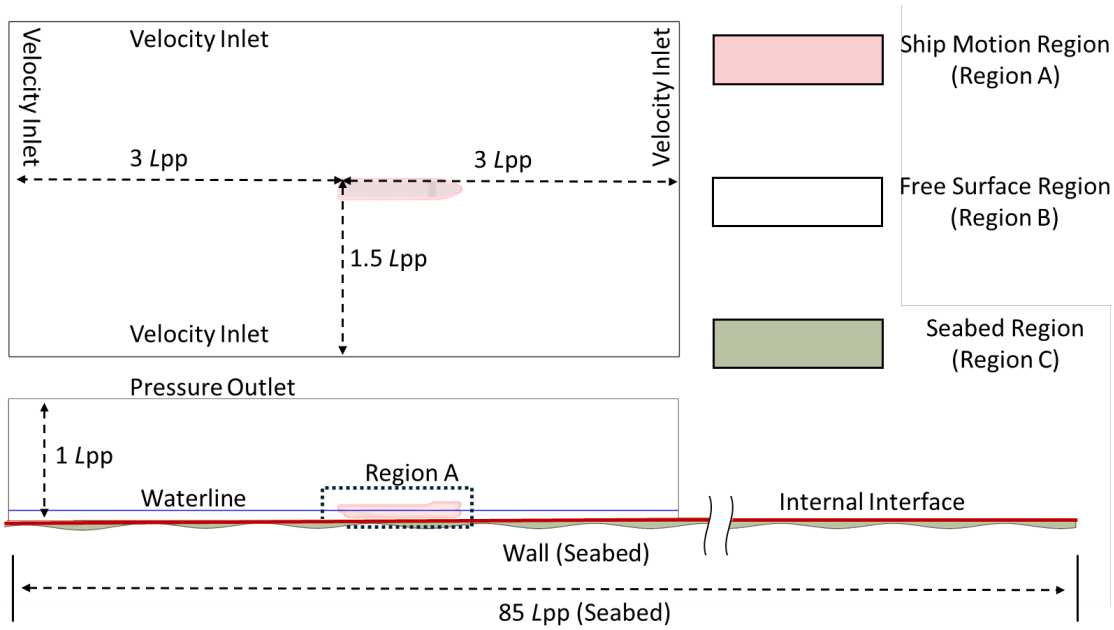

Figure 4. Overview of the computational domain.

Region A was designed to enable the ship model to move within the computational domain. It consisted of an offset surface positioned 0.2 m from the KCS model and functioned as an overset mesh region. The DFBI (Dynamic Fluid Body Interaction) module was applied to allow three degrees of freedom (pitch, heave, and surge), and the rotation speed for the virtual disk was fixed at 9.5 rps; Region B was constructed to simulate the free surface conditions around the ship, excluding seabed. It moved in sync with the surge motion of Region A. At the bottom of Region B, a sliding mesh interface facilitated the exchange of flow information with Region C. This configuration enabled the seabed conditions around the ship to be extracted from Region C without requiring Region B to cover the entire seabed, resulting in a significant reduction in domain size. The dimensions of Region B were determined in accordance with the Practical Guidelines for Ship CFD Applications ITTC (Proceedings, 2014); Region C was fixed to an global coordinate system as a stationary region, providing seabed conditions. The top of this region was configured as an interface for exchanging flow information with region B.

2.2 MESH GENERATION AND VALIDATION

An automatic meshing tool with volumetric control was utilized to generate computational mesh. As depicted in Figure 5 (a), key areas such as the overset mesh region, the free surface, virtual disk region, and the interface connecting Region B and Region C were refined to better resolve the flow field details. The simulations implemented the all y+ treatment method, which integrates high-y+ treatment for coarser meshes and low-y+ treatment for finer meshes, as recommended by Siemens PLM Software (2023). To ensure sufficient near-wall resolution, the average y+ was maintained above 30. The time step of 0.02s was employed according to the recommendations from the International Towing Tank Conference (ITTC) (Proceedings, 2014)(Proceedings, 2014)(Proceedings, 2014).

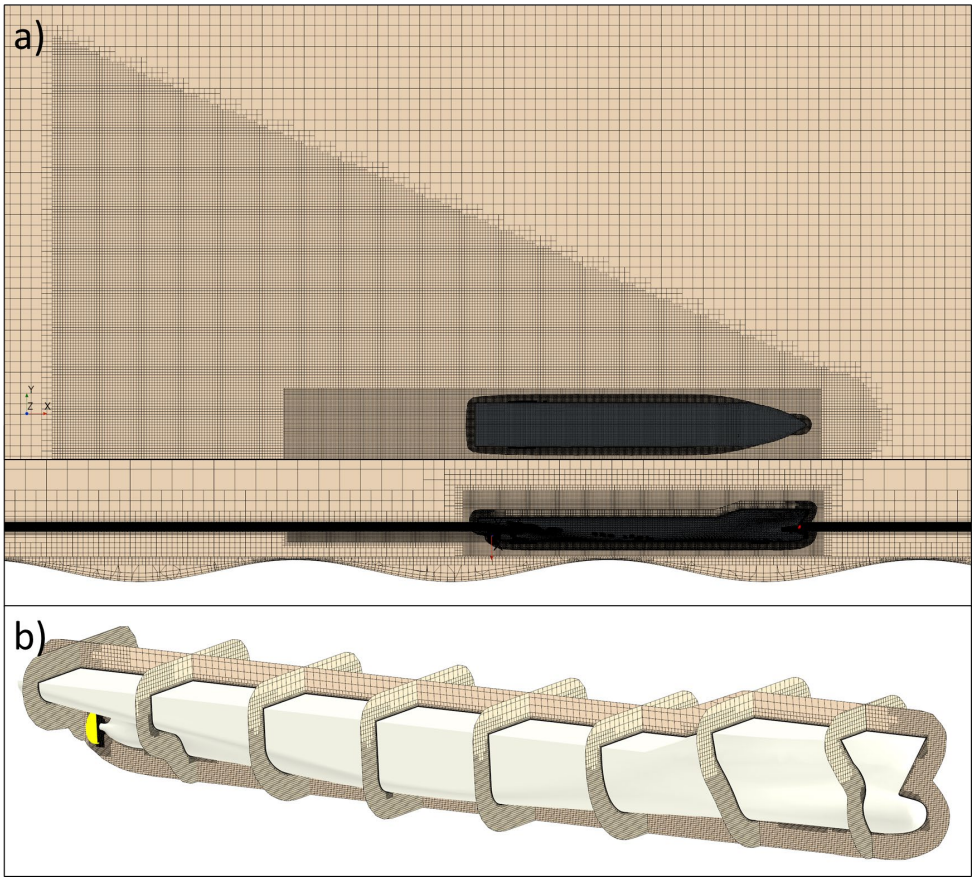

Figure 5. (a) Overview of the mesh and (b) offset surface for overset mesh region.

To evaluate the numerical accuracy and verify the independence of the computational grid, a grid convergence index (GCI) study was carried out. This investigation employed three different grid resolutions (Fine, Medium, and Coarse grid) during the model-scale self-propulsion analysis. The comparative results of these grid resolutions are presented in Table 2, and considering the computational cost, the Medium Grid was chosen in the simulations. In addition, the CFD setup also has been validated against the model test results (Hino et al., 2020), the results show good agreement with the test. The detailed results are shown below Table 3.

Table 2. Grid independent studies of self-propulsion analyses in deep-water condition.

Parameter	Grid Count	Drag Coefficient, $*10^3$	Velocity, m/s
Coarse Grid	3069007	3.296	2.057
Medium Grid	7648501	3.933	2.147
Fine Grid	17082767	3.942	2.151
GCI_{fine}		-0.27%	-0.22%

Table 3. Validation of self-propulsion analyses in deep-water condition.

Parameter	CFD	Experimental Test	Difference
Resistance Coefficient, $*10^3$	3.933	3.966	0.83%
Velocity	2.147	2.196	2.23%

3 RESULTS ANALYSIS AND DISCUSSION

The results presented in Figures 5–9 and Tables 4–6 highlight the significant influence of seabed geometry on ship hydrodynamics in depth-restricted conditions. The comparison between flat and wavy seabed cases reveals distinct variations in vessel resistance, velocity, sinkage and pitch behaviours.

3.1 RESISTANCE AND VELOCITY

Figure 6a and 6b present the normalized resistance ($\text{Resistance}_0/\text{Resistance}_{\text{deep water}}$) and normalized velocity ($V_0/V_{\text{deep water}}$) as a function of the travelled distance (d/L_{pp}) across various seabed conditions. All shallow-water cases exhibit increased resistance and reduced velocity compared to deep-water conditions, primarily due to intensified ship-seabed interactions and the influence of shallow-water hydrodynamics. The wavy seabed cases, in particular, introduce periodic fluctuations in resistance directly linked to the undulating geometry of the seabed. As the seabed wave height increases from 0.5*T* to 1.5*T*, the amplitude of resistance and velocity fluctuations grows proportionally, leading to more pronounced variations in hydrodynamic forces. In contrast, the flat seabed condition produces relatively stable resistance and velocity with only minor fluctuations. These oscillations suggest that vessels navigating over wavy seabed experience periodic variations in hydrodynamic forces due to flow disturbances induced by the seabed's topography, which could impact vessel control and stability. A similar trend is observed for velocity. The amplitude of velocity fluctuations increases with wave height. As resistance increases, the vessel's speed decreases correspondingly. In the 1.5*T* wavy seabed case, the velocity drops by approximately 4% compared to the deep-water condition. These fluctuations indicate that the wavy seabed not only affects resistance but also leads to periodic speed variations, which may result in unsteady propulsion performance. The continuous adjustments required to maintain speed in response to these fluctuations could increase fuel consumption and reduce propulsion efficiency due to the additional energy needed to counteract the increased hydrodynamic drag.

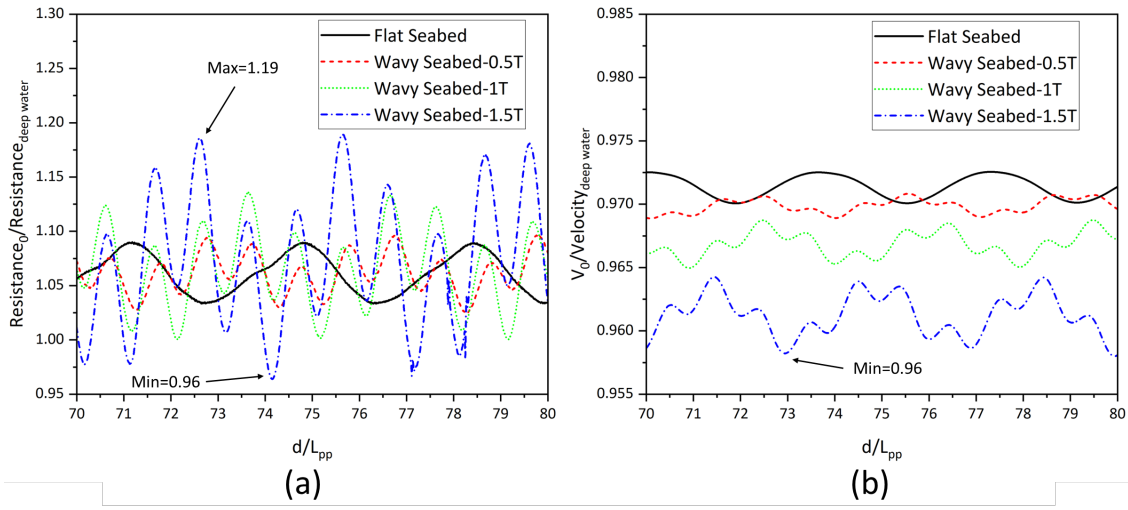

Figure 6. (a) Normalized resistance variations and (b) Normalized velocity variations of the vessel under shallow-water condition.

Tables 4 and 5 provide a detailed comparison of mean values and standard deviations for velocity, resistance, and delivered power across different seabed conditions. As the seabed wave height increases, the differences in both mean values and fluctuation amplitudes between the flat and wavy seabed cases become more pronounced. The mean resistance gradually increases with higher seabed wave height. However, it is important to note that while the mean resistance rise is relatively moderate, the peak resistance values increase significantly, showing a much stronger impact from the seabed undulations. At a wave height of 1.5*T*, the peak resistance reaches an increase of 18.94% compared to the deep-water condition, highlighting the substantial impact of larger seabed undulations on hydrodynamic performance. The standard deviation increases significantly as the wave height increases, expanding from ± 1.675 at 0.5T to ± 5.134 at 1.5T, indicating stronger variations in resistance due to increased wave-seabed interactions. Interestingly, despite the general increase in resistance, localized reductions are observed in specific regions for the 1.5T case, where resistance is reduced by approximately 3.62% compared to the deep-water condition. This suggests that in certain geometric alignments, favourable flow interactions may temporarily reduce resistance. The delivered power follows a similar trend to resistance. Compared to deep-water conditions, the required power increases significantly with seabed undulations. The flat seabed results in a 7.31% increase in power demand. As the seabed wave height increases, power consumption rises further, reaching 8.03% for 1.0T and 8.98% for 1.5T, and the fluctuation range of power also increases. However, the overall increasing fluctuation range implies that

ships navigating over wavy seabed will experience greater resistance variations, leading to higher energy demands to maintain a steady operational speed.

Table 4. Comparison of mean velocity, resistance, and required power for various seabed conditions.

Conditions	Mean Velocity, m/s	Mean Resistance, N	Required Power, W
Flat Seabed	2.085(-2.87%)	93.098 (+6.06%)	159.564 (+7.31%)
Wavy Seabed-0.5T	2.082(-3.01%)	93.170 (+6.14%)	159.853 (+7.50%)
Wavy Seabed-1T	2.076(-3.32%)	93.466 (+6.48%)	160.631 (+8.03%)
Wavy Seabed-1.5T	2.064(-3.87%)	94.224 (+7.34%)	162.053 (+8.98%)
*Comparison with the deep-water condition: '+' indicates an increase, while '-' indicates a decrease.			

Table 5. Standard deviation of velocity, resistance, and required power for various seabed conditions.

Conditions	Velocity	Resistance	Required Power
Flat Seabed	1.906E-03	1.675	0.370
Wavy Seabed-0.5T	1.256E-03	1.638	0.841
Wavy Seabed-1T	2.167E-03	3.146	1.846
Wavy Seabed-1.5T	3.495E-03	5.134	3.145

3.2 HEAVE MOTION

Figure 7 and Table 6 present the heave response of the vessel under different shallow-water conditions compared to deep-water conditions. In Figure 7, the normalized heave ($Heave_0/Heave_{deep\ water}$) clearly shows a significant increase in heave when the vessel operates in depth-restricted conditions compared to deep-water conditions. The wavy seabed cases, in particular, introduce periodic oscillations in heave, with the amplitude of these oscillations increasing gradually as the seabed wave height increases. The flat seabed case exhibits minimal fluctuations, indicating relatively stable vertical motion due to the uniform flow distribution below the hull. In contrast, the wavy seabed cases display intensified vertical oscillations, primarily driven by ship-seabed interactions. These periodic fluctuations closely correspond to the undulating seabed geometry, reinforcing the strong correlation between seabed topography and vessel response. As the wave height of the seabed increases from 0.5*T* to 1.5*T*, the amplitude of these oscillations becomes more pronounced, with the 1.5*T* case exhibiting the highest peak values, showing a 125.47% increase compared to the deep-water condition. This indicates that larger seabed undulations induce stronger flow disturbances below the hull, leading to greater vertical forces acting on the vessel.

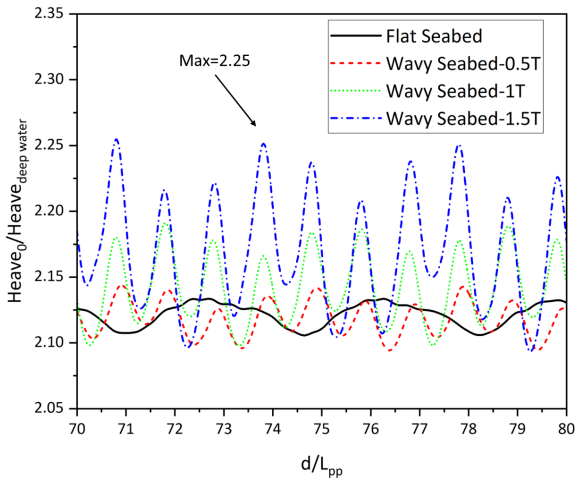

Figure 7. Normalized heave variations of the vessel under shallow-water condition.

The mean, maximum and standard deviation of heave values presented in Table 6 further support this observation. Compared to the deep-water condition, all shallow-water cases result in larger negative heave values, indicating a greater downward displacement of the vessel's midship due to increased flow disturbances. Although the mean heave values show only slight variations among different seabed cases, the extent of heave fluctuations increases significantly. The maximum heave values exhibit a sharp increase with larger seabed wave heights, reaching a 125.47% increase at 1.5T, which implies that the vessel experiences more extreme vertical motion peaks as seabed undulations grow. Similarly, the standard deviation of heave follows this trend, increasing substantially with wave height. The 1.5T wavy seabed case shows the highest standard

deviation, nearly 5 times that of the flat seabed condition. These findings suggest that while the overall downward displacement is influenced by shallow-water effects, the dominant impact of increasing seabed undulations is the amplification of heave fluctuations rather than a significant shift in mean displacement. This intensified vertical motion could lead to greater instability, increased structural loads, and potential operational challenges for vessels navigating over highly undulating seabed, particularly in shallow-water environments with limited under-keel clearance.

Table 6. Mean, maximum and standard deviation of heave for various seabed conditions.

Conditions	Mean Heave, m	Max Heave, m	Standard deviation
Flat Seabed	-2.925E-02 (+112.23%)	-2.944E-02 (+113.59%)	1.294E-04
Wavy Seabed-0.5T	-2.920E-02 (+111.81%)	-2.960E-02 (+114.76%)	1.803E-04
Wavy Seabed-1T	-2.953E-02 (+114.20%)	-3.020E-02 (+119.11%)	3.508E-04
Wavy Seabed-1.5T	-2.991E-02 (+116.99%)	-3.108E-02 (+125.47%)	5.901E-04
*Comparison with the deep-water condition: '+' indicates an increase, while '-' indicates a decrease.			

3.3 PITCH AND SINGKAGE AT FORWARD AND AFT PERPENDICULAR

Figure 8 illustrate the effects of varying seabed geometries on the vessel's longitudinal dynamics, including pitch, forward sinkage, and aft sinkage, under shallow-water conditions. In Figure 8a, the normalized pitch ($Pitch_0/Pitch_{deep\ water}$) exhibits distinct trends across different seabed configurations. Contrary to the initial expectation that the amplitude of oscillations in wavy seabed would increase compared to the flat seabed, the 0.5*T* wavy seabed case actually demonstrates a reduction in pitch fluctuations relative to the flat seabed case. This suggests that minor seabed undulations have a dampening effect on pitch oscillations. As the wave height increases to 1.0*T*, the pitch oscillations become similar to those observed for the flat seabed, suggesting a transitional state where the seabed undulations begin to offset the damping effect. When the wave height reaches 1.5*T* that the oscillation amplitude increases significantly compared to the flat seabed condition, reflecting a more pronounced destabilizing effect from the larger seabed undulations. Despite these variations, the maximum pitch values for all wavy seabed cases remain lower than those observed for the flat seabed condition, suggesting that while pitch oscillations grow with increasing wave height, extreme pitch angles are reduced slightly.

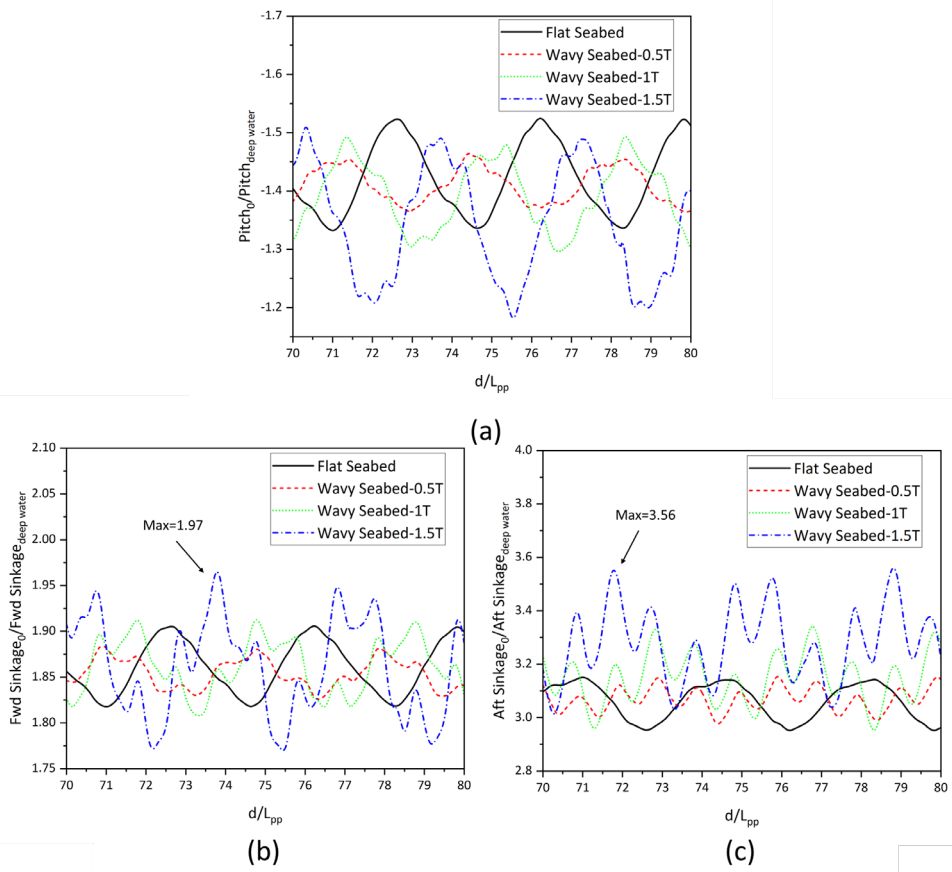

Figure 8. (a) Normalized pitch variations (b) Normalized forward sinkage variations and (c) Normalized aft sinkage variations of the vessel under shallow-water condition.

In Figures 8b and 8c, which display the normalized forward sinkage (Fwd $Sinkage_0$/Fwd $Sinkage_{deep\ water}$) and aft sinkage (Aft $Sinkage_0$/Aft $Sinkage_{deep\ water}$), a similar trend is observed. For the 0.5*T* wavy seabed case, both the forward and aft sinkage fluctuations show a reduction in amplitude compared to the flat seabed case, indicating that minor seabed undulations have a stabilizing effect on the vessel's longitudinal sinkage response. As the wave height increases to 1.0*T* and 1.5*T*, the amplitude of fluctuations increases. The aft sinkage response exhibits a strong correlation with the seabed undulations, similar to the heave response observed in Figure 7. This highlights the vessel's sensitivity to changes in seabed depth, particularly below the stern. In contrast, the forward sinkage displays more irregular fluctuations, likely influenced by the complex flow interactions and wave impacts occurring around the bow, which become more pronounced as the wave height increases.

Tables 7 and 8 provide a comparative analysis of pitch, forward sinkage , and aft sinkage under different seabed conditions, offering insights into how seabed topography influences vessel motion in depth-restricted conditions . The results indicate that, compared to deep-water conditions, shallow-water conditions lead to a more pronounced bow-down tendency. However, compared to the flat seabed case, the increasing wave height of the wavy seabed appears to suppress this bow-down effect. While the maximum pitch values in wavy seabed cases remain lower than those observed for the flat seabed, the oscillation amplitude increases with rising seabed wave height. In addition to pitch, sinkage variations become significantly more pronounced in depth-restricted conditions , with both forward and aft sinkage increasing substantially compared to deep-water conditions. The maximum forward and aft sinkage values rise sharply, particularly in the wavy seabed cases, where increasing seabed wave amplitude leads to even higher sinkage fluctuations. The aft sinkage , in particular, exhibits a strong correlation with the seabed undulations, reinforcing the role of seabed topography in shaping vessel dynamics. These variations are of critical concern for vessels operating in restricted waters, as excessive sinkage may reduce under-keel clearance, increasing the risk of grounding or affecting maneuverability. The combination of higher oscillation amplitudes and growing sinkage values underscore the need for careful assessment of seabed-induced hydrodynamic effects when planning navigation strategies in depth-restricted conditions .

Table 7. Comparison of mean pitch under various seabed conditions.

Conditions	Mean Pitch, degree	Standard deviation
Flat Seabed	-1.793E-01 (+42.70%)	8.365E-03
Wavy Seabed-0.5T	-1.773E-01 (+41.07%)	4.299E-03
Wavy Seabed-1T	-1.752E-01 (+39.44%)	7.602E-03
Wavy Seabed-1.5T	-1.694E-01 (+34.79%)	1.281E-02

*Comparison with the deep-water condition: '+' indicates an increase, while '-' indicates a decrease.

Table 8. Comparison of mean and maximum forward sinkage, and aft sinkage under various seabed conditions.

Conditions	Mean Fwd Sinkage, m	Max Fwd Sinkage, m	Mean Aft Sinkage, m	Max Aft Sinkage, m
Flat Seabed	4.099E-02 (+86.25%)	4.203E-02 (+91.00%)	1.797E-02 (+205.80%)	1.855E-02 (+215.64%)
Wavy Seabed-0.5T	4.080E-02 (+85.38%)	4.160E-02 (+89.04%)	1.804E-02 (+207.02%)	1.856E-02 (+215.91%)
Wavy Seabed-1T	4.099E-02 (+86.27%)	4.218E-02 (+91.69%)	1.850E-02 (+214.81%)	1.966E-02 (+234.62%)
Wavy Seabed-1.5T	4.099E-02 (+86.27%)	4.328E-02 (+96.67%)	1.925E-02 (+227.61%)	2.093E-02 (+256.19%)

*Comparison with the deep-water condition: '+' indicates an increase, while '-' indicates a decrease.

3.4 WAVY SEABED EFFECTES ON THE WAVE PATTERNS

Figure 9 illustrates the wave patterns around the KCS ship under different seabed conditions, highlighting the impact of depth-restricted conditions and wavy seabed on the generation and propagation of ship-induced waves. The comparison between deep water, flat seabed, and wavy seabed cases reveals significant variations in wave behaviour, particularly in how wave interactions evolve at the bow, midship, and stern as the seabed undulation increases. In the deep-water case (Figure 9a), the Kelvin wave system is well-developed, characterized by distinct transverse and divergent waves propagating symmetrically away from the ship. When transitioning to depth-restricted conditions with a flat seabed (Figure 9b), the wave patterns become more confined, and wave amplitudes increase slightly due to enhanced ship-seabed interactions and reduced under-keel clearance. The bow wave system becomes more pronounced, with higher wave elevations forming near the ship's forebody, which suggests stronger hydrodynamic pressure buildup. However, the stern wake structure remains largely similar to that of deep water, indicating that shallow-water effects primarily modify wave amplitude rather than the overall wake shape. For wavy seabed conditions (Figures 9c–9e), localized variations in bow, midship, and stern wave dynamics become more pronounced. At the bow, the presence of a wavy seabed leads to wave accumulation near the forebody, forming a more elevated bow wave. As the seabed undulation increases, the wave height at the bow fluctuates more,

particularly in the 1.5T case, where stronger interactions between the incoming flow and seabed disturbances lead to significant wave buildup ahead of the ship. The midship region experiences continuous variations in wave amplitude along the hull, resulting in alternating wave reinforcement and reduction. These variations increase with seabed wave height, making the wave pattern less uniform, particularly in the 1.5T case, where stronger undulations lead to pronounced wave height differences along the ship's length. Flow disturbances appear more irregular along the sides of the hull, suggesting that the unsteady flow field is further amplified by the wavy seabed conditions. Despite these changes, the stern wake remains relatively stable across different cases, showing only minor disturbances compared to midship and bow regions. This suggests that while seabed undulations have a strong influence on wave formation at the bow and along the hull, the stern wake remains primarily governed by the ship's hull shape and shallow-water constraints rather than direct seabed interactions. however, the increased wave accumulation at the bow, combined with unsteady wave variations along the hull, highlights the need to consider seabed irregularities when assessing wave-induced resistance and vessel stability in depth-restricted conditions.

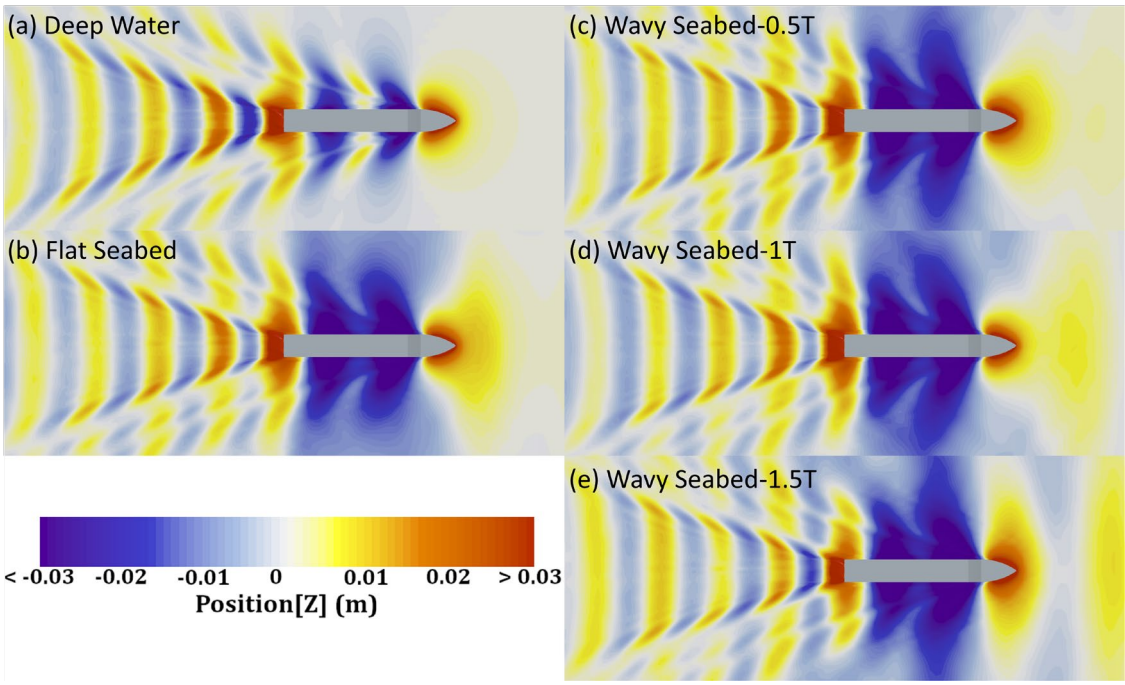

Figure 9. Wave patterns around KCS ship in difference conditions.

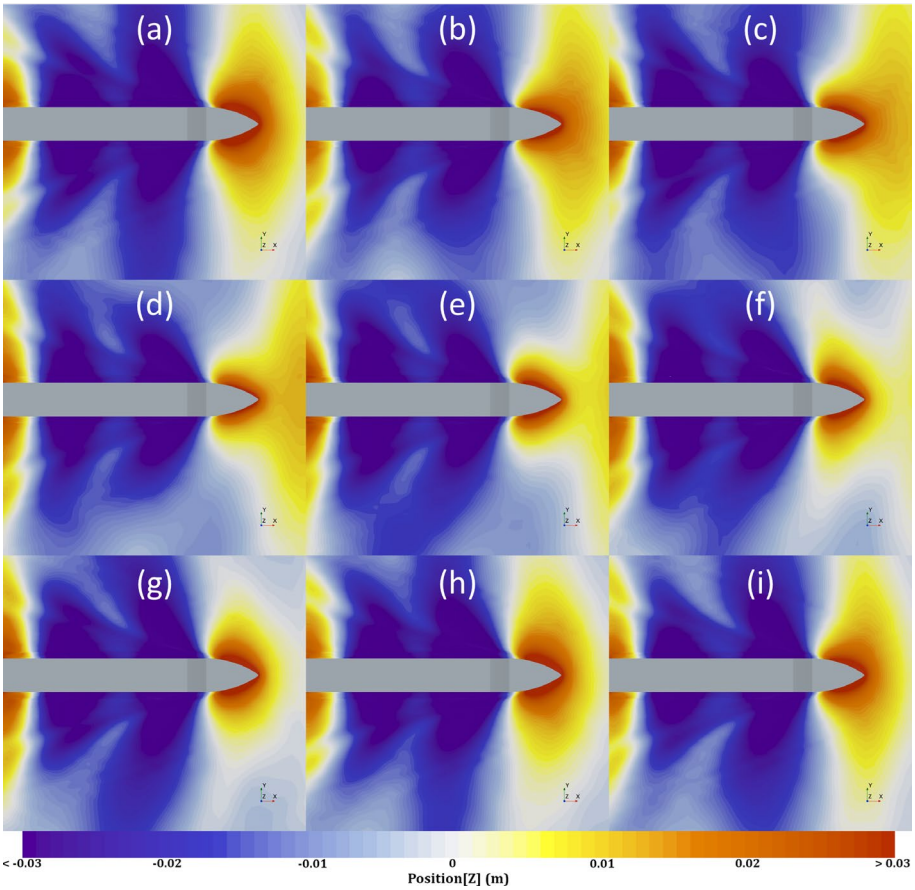

Figure 10. Temporal evolution of wave patterns around the vessel for the 1.5T wavy seabed condition. The time interval between each subfigure (a-i) is 1.6 seconds.

In addition, under deep-water conditions, the wave patterns remain stable over time. In the flat seabed case, slight fluctuations can be observed, whereas in wavy seabed conditions, the wave field exhibits more pronounced and periodic variations. This is particularly evident for the 1.5T case. Figure 10 presents the time-dependent evolution of the wave field surrounding the vessel under the 1.5T wavy seabed condition, with each subfigure (a–i) representing a 1.6 second interval. The yellow-orange region near the bow indicates elevated wave heights that fluctuate in both shape and intensity, suggesting cyclic variations in wave resistance resulting from the seabed undulations. Meanwhile, the midship wave field displays alternating regions of wave reinforcement and cancellation, driven by the interactions among Kelvin waves, ship-induced pressure waves, and seabed-induced disturbances. Over time, certain frames (e.g., Figure 10a) show localized wave amplification, while others (e.g., Figure 10d) reveal reduced amplitude due to wave cancellation effects, thereby illustrating the unsteady evolution of the wave field along the midship region. Although the stern wake maintains a relatively consistent shape throughout, minor variations in its strength and divergence angles are observed as time progresses.

4 CONCLUSIONS

This study investigated the hydrodynamic effects of wavy seabed on ship motion in depth-restricted conditions with shallow water effects, using high-fidelity CFD simulations. The results demonstrate that seabed undulations significantly influence vessel dynamics. As the seabed wave height increases, and under a constant propeller rotation speed, both resistance and power consumption rise, while ship velocity decreases due to ship-seabed interactions. Periodic fluctuations in resistance, heave, and aft sinkage closely follow the amplitude of wavy seabed, with larger amplitude leading to more pronounced oscillations. Additionally, for the pitch and sinkage , minor seabed undulations exhibit a stabilizing effect. Notably, the increase in maximum forward and aft sinkage values reduce under-keel clearance, increasing the potential risk of grounding for vessels operating in depth-restricted conditions where shallow water effects are significant. The analysis of wave patterns further reveals that wavy seabed induce unsteady wave behaviours, particularly near the bow and midship, where wave accumulation and oscillatory variations are more prominent. These findings highlight the importance of considering seabed geometry in ship performance assessments and operational planning. Future work will extend this analysis to account for varying amplitude and wavelengths of the wavy seabed, offering further insights into vessel behaviour in complex depth-restricted environments.

5 ACKNOWLEDGEMENTS

Results were obtained using the Rocket High-Performance Computer at Newcastle University. The authors would also like to acknowledge the funding received in the RESHIP project. RESHIP project has received funding from both the European Union's Horizon Europe research and innovation programme (Grant agreement: 101056815) and the Innovate UK's Horizon Europe Guarantee scheme (Ref: 10052906, 10051800, 10059974).

6 REFERENCES

Besio, G., Blondeaux, P., Brocchini, M., Hulscher, S. J. M. H., Idier, D., Knaapen, M. A. F., Németh, A. A., Roos, P. C., & Vittori, G. (2008). The morphodynamics of tidal sand waves: A model overview. *Coastal Engineering*, *55*(7–8), 657–670.

Carrica, P. M., Mofidi, A., Eloot, K., & Delefortrie, G. (2016). Direct simulation and experimental study of zigzag maneuver of KCS in shallow water. *Ocean Engineering*, *112*, 117–133.

Carrica, P. M., Sadat-Hosseini, H., & Stern, F. (2012). CFD analysis of broaching for a model surface combatant with explicit simulation of moving rudders and rotating propellers. *Computers & Fluids*, *53*, 117–132.

Gourlay, T. (2008). Slender-body methods for predicting ship squat. *Ocean Engineering*, *35*(2), 191–200.

Hino, T., Stern, F., Larsson, L., Visonneau, M., Hirata, N., & Kim, J. (2020). *Numerical ship hydrodynamics: An assessment of the Tokyo 2015 workshop* (Vol. 94). Springer Nature.

Hulscher, S. J. M. H., de Swart, H. E., & de Vriend, H. J. (1993). The generation of offshore tidal sand banks and sand waves. *Continental Shelf Research*, *13*(11), 1183–1204.

Kim, D., Tezdogan, T., & Incecik, A. (2022). Hydrodynamic analysis of ship manoeuvrability in shallow water using high-fidelity URANS computations. *Applied Ocean Research*, *123*, 103176.

Krabbendam, J., Nnafie, A., de Swart, H., Borsje, B., & Perk, L. (2021). Modelling the past and future evolution of tidal sand waves. *Journal of Marine Science and Engineering*, *9*(10), 1071.

Proceedings, I. (2014). Practical Guidelines for Ship CFD Applications ITTC–Recommended Procedures and Guidelines. *International Towing Tank Conference Section*, *7*, 2–3.

Proceedings, I. (2017). Propulsion Test ITTC- Recommended Procedures and Guidelines. *International Towing Tank Conference*.

Shi, W., Li, M., & Yuan, Z. (2021). Investigation of the ship–seabed interaction with a high-fidelity CFD approach. *Journal of Marine Science and Technology*, *26*(3), 931–946.

Siemens PLM Software. (2023). *STAR-CCM+ Documentation*.

SIMMAN 2008. (2008). Maritime and Ocean Engineering Research Institute (MOERI). http://www.simman2008.dk/KCS/kcs_link.htm

Singh, H., Fletcher, D. F., & Nijdam, J. J. (2011). An assessment of different turbulence models for predicting flow in a baffled tank stirred with a Rushton turbine. *Chemical Engineering Science*, *66*(23), 5976–5988.

Song, S., Terziev, M., Tezdogan, T., Demirel, Y. K., Muscat-Fenech, C. D. M., & Incecik, A. (2023). Investigating roughness effects on ship resistance in shallow waters. *Ocean Engineering*, *270*, 113643.

Sun, X., Yan, X., Wu, B., & Song, X. (2013). Analysis of the operational energy efficiency for inland river ships. *Transportation Research Part D: Transport and Environment*, *22*, 34–39.

Terziev, M., Liu, Y., Yuan, Z., & Incecik, A. (2024). The resistance of a trans-critically accelerating ship in shallow water. *Ship Technology Research*, *71*(1), 14–32.

Terziev, M., Tezdogan, T., & Incecik, A. (2021). Modelling the hydrodynamic effect of abrupt water depth changes on a ship travelling in restricted waters using CFD. *Ships and Offshore Structures*, *16*(10), 1087–1103.

7 AUTHORS BIOGRAPHY

Yunxin Xu is a Research Associate at Newcastle University, specializing in computational fluid dynamics (CFD) and marine hydrodynamics. His research focuses on ship hydrodynamics, energy efficiency, and advanced numerical modelling. He has contributed to projects on hydrogen-powered ships and innovative propulsion systems funded by Innovate UK. His expertise includes ship towing tank test, marine multiple-body motion simulation, and advanced CFD applications.

Weichao Shi is a Reader at Newcastle University, researching in the field of marine renewable energy and marine propulsion system with specialities in experimental and numerical marine hydrodynamics. Weichao is currently leading a research team developing applied biomimetics marine hydrodynamics technology with the ambition of providing the maritime industry with effective and feasible solutions inspired by mother nature.

MANEUVERING OF A MODEL SCALE SHIP IN NATURAL FLUID MUD

Jan Mense, Federal Waterways Engineering and Research Institute, German
Carl-Uwe Böttner, Federal Waterways Engineering and Research Institute, Germany

MANEUVERING OF A MODEL SCALE SHIP IN NATURAL FLUID MUD

JAN MENSE, FEDERAL WATERWAYS ENGINEERING AND RESEARCH INSTITUTE, GERMANY
CARL-UWE BÖTTNER, FEDERAL WATERWAYS ENGINEERING AND RESEARCH INSTITUTE, GERMANY

SUMMARY

An experimental study was conducted on a free-running model of the Japan Bulk Carrier maneuvering in and over natural fluid mud sourced from Hamburg Port. The study included zig-zag maneuvers, turning circles and straight runs across a range of under keel clearances, from -10% draft to 20% draft relative to the fluid mud inte rface. Rheological properties and the fluid mud interface were consistently monitored to ensure reproducibility and support the validation of numerical models. Although the study aims primarily at providing validation data for numerical models, several maneuvering parameters will be evaluated and discussed. Where available, the results will be compared with experiments over hard bottom.

NOMENCLATURE

aFM	artificial Fluid Mud
BAW	German Federal Waterways Engineering and Research Institute
FM	Fluid Mud
HB	Hard Bottom
JBC	Japan Bulk Carrier
UKC	Under Keel Clearance

δ	Rudder angle	°
λ	Scale factor	-
ρ	Density	kg/m^3
τ_y	Yield stress of the fluid mud	N/m^2
ψ	Heading	°
ψ_{010}	Course change of 10°	°
ψ_{030}	Course change of 30°	°
B	Ship beam	m
C_{B}	Block coefficient	-
$CI_{95\%}$	95% confidence interval	-
D'_C	Non-dimensional steady turning diameter	-
Fr_h	Froude depth number $= u/\sqrt{h \cdot L_{\mathsf{PP}}}$	-
h_{HB}	Water depth w.r.t hard bottom	m
h_{fm}	Height of FM layer	m
h_w	Height of water column (above FM layer)	m
$\overline{h_w}/T$	Spacial average of h_w by T	-
$\langle \overline{h_w}/T \rangle_t$	$= \frac{1}{t_1 - t_0} \int_{t_0}^{t_1} \overline{h_w}/T \, dt$ Spacial and temporal average of $\overline{h_w}/T$	-
L_{PP}	Length between perpendiculars	m
n	Propeller frequency of revolution	1/min
P_T	Thrust	N
Q	Propeller shaft moment	Nm
r	Yaw rate	°/s
$\dot{r}$	$\partial r/\partial t$	°/s^2
R_T	Total longitudinal resistance	N
T	Draft	m
t_{10}	Time to reach 10° change of heading	s
t_{30}	Time to reach 30° change of heading	s
u	Ship velocity	m/s
x'_{090}	Advance at 90° change of heading	L_{PP}

1 INTRODUCTION

With ship dimensions and traffic increasing drastically over the past centuries (e.g. Hoffmann et al. 2021), port operators are constantly challenged to keep up with the ever increasing demand for deeper harbor approaches and basins. As the associated annual dredging volumes increase likewise, harbors like Hamburg Port spend millions per year just on maintaining water depths in the fairways. As most of the excavated material consists of FM (Fluid Mud), the question arises, whether this FM layer actually decreases the safety and ease of shipping. Thereby, PIANC (PIANC 2014) defined the nautical depth as the depth at which both safety and navigational ease are not compromised. As yield point and density both slowly increase until a sudden rise (lutocline) within the FM layer, referencing the nautical depth down to this step has been actively discussed in the past. Several ports have already implemented alternative definitions of the nautical depth based either on the yield stress, for instance river Ems at Emden, or density of the fluid, for instance harbor of Rotterdam, Zeebrugge, Delfzijl, Cayenne and others. Typically densities of $1150\,\mathrm{kg/m^3}$ to $1270\,\mathrm{kg/m^3}$ are used as reference (e.g. Delefortrie 2007). Other ports, like Hamburg Port, define nautical depth as the layer where a 200 kHz echo reflects, i.e. the uppermost layer is detected by a multi frequency echo (Kirichek et al. 2020). The specific situation at Port of Hamburg is described in (Shakeel et al. 2022). In order to define alternative depth references, a profound knowledge of the implications on the maneuverability of ships is essential.

A small number of experimental studies on model ships maneuvering in and above artificial mud have been published in the past (Sellmeijer et al. 1983; Brossard et al. 1990; Delefortrie 2007). Delefortrie (2007) also gives an overview of a number of experiments performed at Flanders Hydraulic Research from 1984-1989. Aside of a preliminary analysis given by Vantorre et al. (Vantorre et al. 1988), this study has been primarily published in the form of reports in Dutch. The studies were mainly performed using aFM (artificial Fluid Mud) of chlorinated paraffin and kerosene or petroleum in various densities, viscosities and layer heights. With most studies being performed over a homogenous layer of aFM, Brossard et al. (Brossard et al. 1990) also tested aFM with an density gradient over depth. In these studies, captive model tests have been generally preferred. The principal findings are complementary and will be shortly summarized in the following.

Generally an increase in shallow water resistance is found in the presence of aFM. While Sellmeijer et al. (1983) found an increase over the whole range of UKC (Under Keel Clearance), others primarily found a steep increase in resistance as soon as the hull comes into contact with the aFM (Brossard et al. 1990; Delefortrie 2007), while in some cases, Brossard et al. (Brossard et al. 1990) even observed a maximum in resistance when the ship was sailing just above the aFM interface. Moreover, the effect of the aFM is found to be most prominent at low velocities (Sellmeijer et al. 1983; Brossard et al. 1990). The largest effect on static maneuvers was observed at very small UKC, where turning circle diameters reached a maximum. At the same time, reactivity is found to be increased in the presence of aFM, thereby dynamic maneuvers like zig-zag tests were observed to be faster with lower overshoot angles in the presence of aFM (Sellmeijer et al. 1983; Delefortrie et al. 2016).

Internal undulations at the interface between aFM and water were observed in all studies. The wave pattern appears to be highly dependent on velocity, water depth and the viscosity of the aFM layer, featuring a velocity-dependent transition both in wave pattern and position (Delefortrie et al. 2016; Kaidi et al. 2020). Additionally, Sellmeijer et al. (1983) describe a dependence of the wave pattern on the aFM layer thickness. Generally, a decrease in amplitude with diminishing UKC and disappearing at negative UKC was observed. As Kaidi et al. (Kaidi et al. 2020) later showed in a numerical study, those internal waves are significantly dampened when the non-Newtonian properties of the FM are considered, particularly for FM with higher viscosity.

The experimental studies are accompanied by a very limited number of full scale measurements that have been performed for validation purposes. There is a high reluctance to perform tests in full scale, due to the immense effort and the inherent risk. Naturally within those studies, the control of boundary conditions is quite limited as well as the number of performed maneuvers. The first known full scale experiment was performed in the harbor of Rotterdam in 1975 (Wens et al. 1984). In 2013, there was a full scale measurement and sea trials campaign in the Zeehavenkanaal Delfzijl performed by Flanders Hydraulics (Verwilligen et al. 2014), in addition to a successful ship handling simulation campaign before.

A detailed overview of the current knowledge on ships maneuvering in FM areas can be found in (Delefortrie et al. 2016).

Since numerical models allow studies in arbitrary scales, they are particularly valuable for systematic studies hard to conduct under real-world scenarios. The challenge is generated by a stratification of three entirely different fluids, i.e. air, water, fluid mud, and the non-Newtonian rheological behavior of the latter. There were different models invented to include fluidic non-Newtonian behavior in Reynolds-Averaged Navier Stokes Equations solvers, with the rheological behavior described by an addition to the apparent viscosity (Yan et al. 1994; Le Hir et al. 2000; Watanabe et al. 2000; Guan et al. 2005; Knoch et al. 2011; Wehr et al. 2014; Chmiel et al. 2020; Kaidi et al. 2020; Sotelo et al. 2024; Lovato et al. 2024). While most models simplify or neglect the thixotropic (shear thinning) behaviour of the FM, first efforts have been taken to include these effects into the models (Knoch et al. 2011; Kaidi et al. 2020; Lovato et al. 2022). So far, only a small number of experiments utilizing natural FM, focusing on the validation of such numerical models, have been performed, focusing on simple geometries like a

flat plate (Lovato et al. 2022), a cylinder (Toorman et al. 2015; Sotelo et al. 2022) and a hydrofoil (Sotelo et al. 2024).

Specifically aiming at the validation of ship maneuvering simulations, this study provides multi-dimensional test cases for ship models sailing in and closely above natural FM.

2 EXPERIMENTS

The aim of this study was to accurately incorporate all interactive effects between FM and the model ship in order to provide reliable validation data for numerical models. Therefore, the FM substance had to be selected carefully. Since substitutes such as paraffin, petroleum or kerosene used in previous studies were out of the question for ecological and environmental concerns, it was decided to also take the non-Newtonian properties of the material into account. Multiple substitute materials offering similar properties to natural FM such as apple fiber where tried out, promising a good temporal stability and control over the rheological properties. However, no suitable material was found, with the required amount of material and the rot resistance being significant limiting factors. Thereby the use of natural FM was seen as the only viable alternative, where the properties are mainly controlled by the source of origin.

It was decided to use the widely known JBC (Japan Bulk Carrier) test case (Hino et al. 2016) for this study, at it is geometrically similar to the biggest carriers regularly embarking at Hamburg Port. The JBC test case has been analyzed intensively both numerically and experimentally during the 2015 Tokyo Workshop (Hino 2021) for deep water condition and is presumably sensitive to shallow water effects due to its fullness ($C_B = 0.858$). The model used for the experiments was build at SVA Potsdam to the requirements of ITTC 7.5-01-01-01:2017 in the scale of 1:60 (Hull No. 1827).

2.1 EXPERIMENTAL SETUP

The experimental series was carried out in the ship wave basin at BAW (German Federal Waterways Engineering and Research Institute) Hamburg, with dimensions of ~ 33 m $\times 100$ m and a maximum water depth of 0.6 m. The water and air temperature within the facility where constantly monitored during the series and where constant at 14.76 ± 0.38 °C and 14.40 ± 0.89 °C respectively.

The semi automated model was free running and remotely controlled by a human. Its position including heading, heave, pitch and roll along with the state of and forces acting on rudder and drive-train were constantly monitored and centrally collected in a 10 Hz frequency. The ship's position was recorded using a *Trimble SPS930* total station in tracking mode. With this setup, a positional accuracy of ± 4 mm can be achieved in all directions within the measured region. At the given sample rate, this would result in the velocity being accurate to < 0.085 m/s. As these accuracies refer to the absolute position, the relative inaccuracy is expected to be much lower and with u being a derived value its accuracy was estimated to be below ± 0.025 m/s in a $95\,\%$ confidence interval using the experimental data from this study. The position of the center of gravity, being the model reference position in this study, was calculated by correcting for prism offset, pitch and roll. The ship's orientation, rudder angle and the forces and moments acting on rudder and drive where also recorded. The technical data of the respective instruments can be found in Table 1. The revolution frequency of the propeller shaft n was read out from

Instrument (Manufacturer)	Measured values	Range	Accuracy
Octans Subsea optical gyro compass (IXBlue)	Heading ψ	$360°$	$0.01°$
	Pitch & Roll	$360°$	$0.001°$
K6D40 50N/5Nm (ME Messsysteme)	Rudder forces (6 DOF)	50 N/5 N m	$0.5\,\%$RD (DC)
K3D60a 100N (ME Messsysteme)	Thrust P_T	100 N	$0.5\,\%$RD (DC)
DR 2477 (Lorenz)	Torque Q	5 N m	0.0075 N m
Posirot PRAS3-H-120-l1-CW-M12R5 (ASM)	Rudder angle δ	$120°$	$0.036°$
UltraLab UWS 1M (General Acoustics)	Echo sounding 1 MHz	0.02 to 15 m	$1\,\%$RD

Table 1: Utilized instruments and sensors. DC: dynamically calibrated in setup.

the motor controller, thereby some noise is to be expected. Wherever analog sensors were used, data acquisition modules were selected whose accuracy was several orders of magnitude higher than that of the sensors. The data was bundled and recorded on a computer placed inside the model ship, where the temporal synchronization was realized using GPS time. As the respective modules were not synchronized, the data from the different sensors might be shifted by up to -100 ms relative to the reference time. The module acquiring data for δ, n and Q did only supply those values with about 5 Hz resulting in missing data in the time series that had to be re-interpolated.

2.2 EXECUTION

A large number of zig-zag maneuvers and turning circles were performed at various n and δ. The selection of the performed maneuvers is leaning on specified maneuvers from IMO (IMO Resolution MSC.137(76)) with variations regarding course change angles $\Delta\psi$ and δ. Straight sections in the approach to the circle maneuvers were evaluated as additional runs. An overview of the performed runs can be found in Table 2. The selection of maneuvers allows for the evaluation of characteristic maneuvering parameters, typically evaluated during ship acceptance trials as well.

Maneuver		circle		zig-zag			straight
Naming		**C 35**	**C 45**	**z-20-10**	**z-35-10**	**z-35-20**	**Straight section**
δ		35°	45°	20°	35°	35°	0°
$\Delta\psi$		>90°	>90°	10°	10°	20°	0°
n [1/min]	400	3/-	3/-	4/-	-	3/-	-
	620	3/4	4/4	3/3	-	3/3	-
	710	-	4/-	4/3	-	4/-	-
	880	3/-	3/-	4/-	-	4/-	-
	900	-	7/-	6/4	10/4	-	-
	1050	9/10	19/5	17/4	-	3/-	-
	1100	-	-	-	38/38	-	-
	1300	-	5/-	-	11/-	-	2

Table 2: Number of performed maneuvers at given n. no1/no2: number of runs (starting) with starbord/port rudder.

A reference measurement was done every time after the model was moored, giving a baseline for the following measurements. All maneuvers were performed in line with the ITTC Guidelines (ITTC 7.5-02-06-01:2008) at constant n starting from a steady initial state, targeting constant values of speed u, heading ψ and δ. Motor and rudder were controlled manually using a programmable digital remote control enabling a reliable wireless connection. During the maneuvers, preset values of n and δ could be selected to ensure reliability, while during run up δ was controlled manually for better control. When executing zig-zag maneuvers, the change of rudder direction was initiated manually.

2.3 FLUID MUD

The FM used in this study was sourced shortly prior to the experimental series in Köhlfleet, Hamburg Port and was constantly mixed before being poured into the basin, where it was manually distributed and carefully covered with a layer of water. The thickness of the FM layer ($14\,\text{cm}\rightarrow 10\,\text{cm}$ due to consolidation) was chosen in order to minimize effects from the hard bottom on the maneuverability. Since achieving a uniform FM surface was found to be more challenging than expected, several attempts of reconditioning and leveling the FM layer were performed over the duration of the experimental series. Additionally, frequent monitoring of the FM interface via echo sounding using a lab echo sounder (see Table 1) was established. The soundings were conducted along straight paths across the basin, with the number of paths increasing over the course of the experiments. On the final day, a control sounding was performed using a random pattern. The mud layer monitoring allows to calculate an in-situ depth of the ship during the maneuvers as will be later described in Section 3. The water level from the solid bottom h_{HB} was regularly monitored using a surface-piercing micrometer gauge, which provided an accuracy of ± 0.1 mm. Since some degree of consolidation was witnessed over the duration of the test series, the water level above the FM had to be varied accordingly, a range of different h_w/T was observed (see Figure 1).

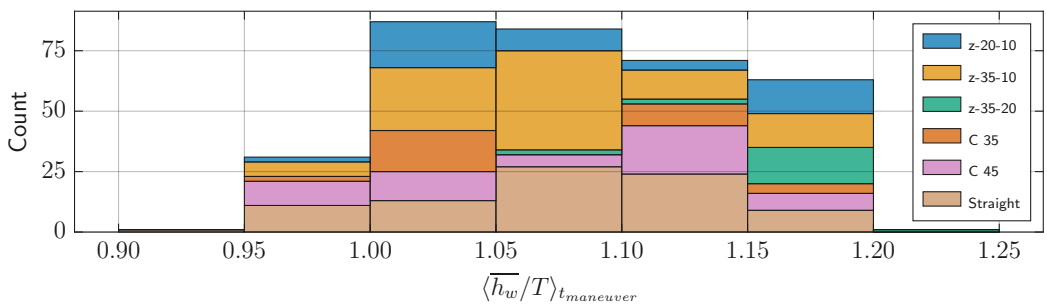

Figure 1: Characteristic $\langle \overline{h_w}/T \rangle_t$ during maneuver section. Naming as described in Table 2.

An overview of the FM properties relevant to this study has been provided by McAnally et al. (McAnally et al. 2007). During

the series, the rheological properties were monitored regularly at 3 fixed locations along the rim of the basin, complemented by irregular measurements inside the basin. The sample frequency varied from 5 measurements per day in the beginning to a single sample a day in the end, accounting for the decreasing consolidation rate. Samples were taken mostly at recorded heights using a syringe and additional vertical profiles were taken using the same technique. Due to significant scatter in the

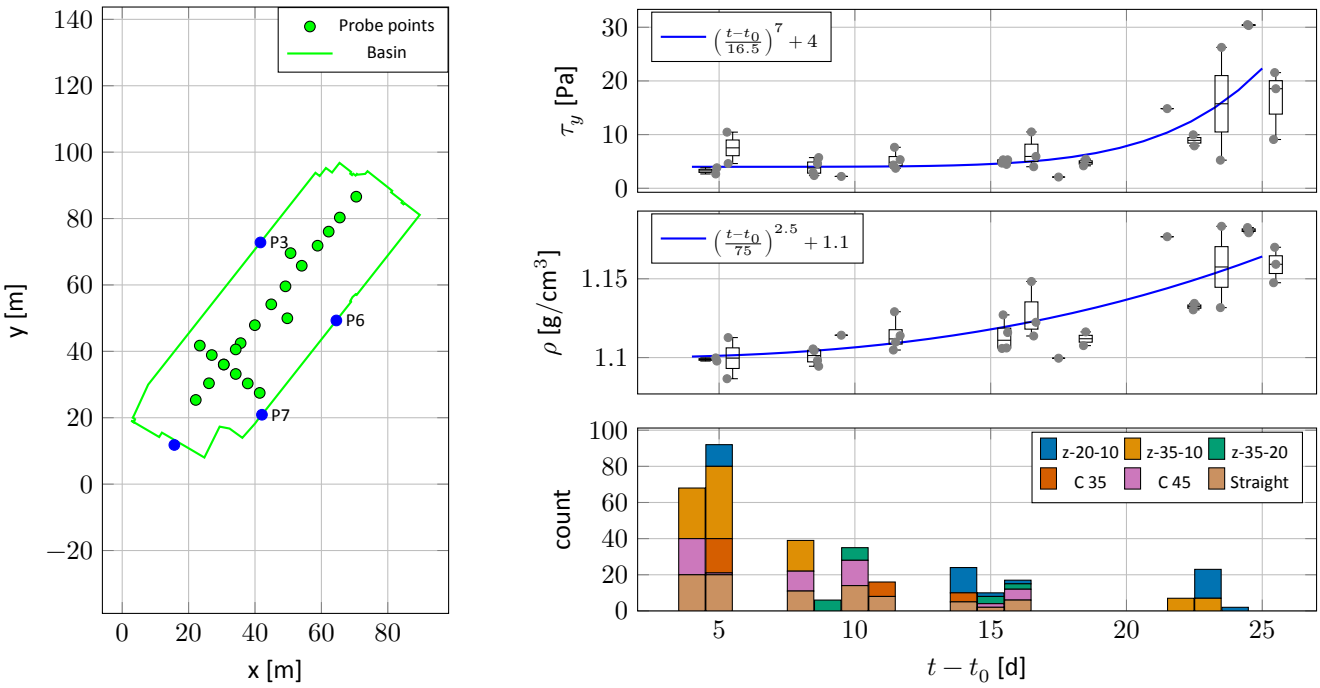

(a) (b)

Figure 2: 2a: Probe positions. Frequent reference measurements at the blue positions. 2b: Measured yield stress (upper plot) and density (middle plot) over the experimental series (combined measurements of P3, P6, P7), number of runs performed on the respective days (lower plot). X axis as days since start of the series. A significant scatter in τ_y and ρ can be observed especially in the end of the series. Values interpolated from the blue fit lines are used for qualitative comparison within the series.

rheological properties throughout the experimental series, yield stress (τ_y) and density (ρ) above the lutocline (zone of sharp vertical gradient in ρ) were approximated using a smooth fitting function, as they can be assumed to change continuously. This allows for a qualitative comparison within the experimental series. An overview of the measured values as well as the used fit functions can be found in Figure 2. While preliminary consolidation trials using FM from the same origin suggested a steep increase in τ_y after about 4-5 days due to consolidation, this increase was only observed after around 18 days in the presented test series. In a recent study of Brouwers et al. (Brouwers et al. 2023) the authors showed, that while the duration of the settling phase is dependent on the reconditioning intensity, the transitions into the consolidation phase occurs within a couple of hours. Accounting for the limited intensity of reconditioning during the experimental series and the long waiting periods after reconditioning, it is safe to say that the experiments were performed exclusively during the consolidation phase, where the settling rate can be approximated by a power law (Brouwers et al. 2023).

3 DATA PROCESSING

3.1 WATER-MUD INTERFACE

As stated in Section 2, it was observed early on, that the desired flatness of the water-mud interface was difficult to achieve over the basin dimensions (size relation $1\times10^{-4} - 1\times10^{-5}$) and that the interface exhibited larger irregularities. Although the interface height only differs by a few mm over several m, it imposes unsteady conditions on the model tests. In order to counteract the resulting uncertainty, the systematic soundings allowed reconstructing the actual in-situ mud level during the experiments. The soundings were performed in a line type manner parallel to the longer basin dimension, at first the raw data was filtered for obvious outliers and averaged using the 75% quantile over a Gaussian type rolling window of 4 m (0.85 Lpp) for further usage. To counteract the different measurement densities longitudinally and laterally along the basin, the lines were re-sampled to data points 0.5 m apart in preparation for surface interpolation. As it will be discussed in Section 3.2, the region of ship-mud interaction is about one magnitude larger than the re-sampling distance. Thereby, no considerable influence on

the results is expected by this re-sampling. Reconstructing a surface on a regular grid from the line measurements was done using scipy's Radial Basis Function interpolation. Missing values where filled from linear interpolation and nearest neighbor extrapolation to avoid gaps within the data set.

In order to quantify the accuracy of the derived surface, additional measurements were performed following the experimental series with the echo attached to a floating body that was randomly maneuvered through the basin (referred to as random soundings later). This allows to compare the in-situ water depth with its corresponding value derived from surface interpolation (Figure 3). With the number of sounding lines gradually increasing over the duration of the series, the comparison was done both for a full set of sounding lines as well as for a reduced set. The goodness of fit was determined based on the confidence interval width $CI_{95\%}$ of the difference between the chaotic measurements and the corresponding mud bed elevation received from surface interpolation. It has to be noted that the results obtained from the random soundings where solely filtered for outliers, while the interpolated surface inherently exhibits spacial averaging. The differences were calculated as an average over a fixed-length window along the path of the random soundings, using various window lengths (see Figure 3).

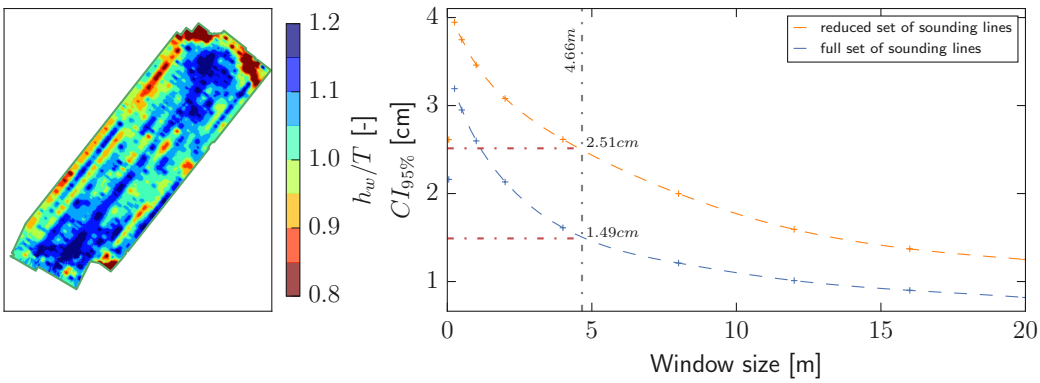

Figure 3: **Left: Example of h_w above the interpolated FM interface, the sounding paths are still recognizable. Right: $CI_{95\%}$ depending on the length of the averaging window, from statistical comparison with the random soundings.**

3.2 IN-SITU WATER DEPTH

Several studies suggest that the hydrodynamic effective depth experienced by the vessel appears to be spatially averaged longitudinally (Flügge et al. 2001) and laterally (Lataire et al. 2007) over at least the footprint of the vessel (Schoeneich 2011), in line with the guidelines given by PIANC (PIANC 2014) speaking of a minimum time-averaged UKC impacting maneuverability. Thereby evaluating $CI_{95\%}$ at a window length of L_{PP} is most likely to be a conservative assumption of the accuracy reached by the surface interpolation (see Figure 3). Based on these conclusion, the in-situ water depth h_w below the model ship in this study is determined as the weighted mean $\overline{h_w}$ within a box with the dimensions L_{PP} by $2B$, applying a trapezoidal weighting function. Full weighting is assigned between $-0.5B$ and $0.5B$. $\overline{h_w}$ was calculated for each data point, using the positional data and heading.

3.3 SHIP DATA PROCESSING

Potentially missing values within the absolute positioning data were interpolated for consistency. The northerly and easterly velocity components were calculated by differencing the position over time to then be converted into a longitudinal and transverse velocity relative to the ships coordinate system using the heading. The velocities were then filtered using a Hampel filter followed by a butter low pass filter, cutting off frequencies above 0.5 Hz. As stated in Section 2.1, the slightly varying data rate of the measurement unit responsible for the measurements of n, Q and δ required a coupled filtering of the respective measurements. As n was kept constant for the maneuvers, it was used to indicate and filter outliers induced by the measurement unit to all three quantities, to which a Hampel filter was applied afterwards. The measured P_T was corrected by a correlation determined from dynamic calibration of the sensor inside the arrangement and smoothed using a rolling mean over a window of 1 s. Quantities that have been measured and postprocessed separately like ambient temperatures, mud rheology (see Section 2.3) and in-situ water depth (see Section 3.2) where evaluated and added for each data point.

4 RESULTS

The results were clustered according to the local $\overline{h_w}/T$ within intervals of 0.05 $\overline{h_w}/T$. If not stated otherwise, all available data points were used for the evaluation. Aside from the longitudinal resistance, parameters characterizing the maneuverability of the ship in static and dynamic conditions like the initial course-changing ability, steady turning circle diameter and advance will be discussed. At close inspection, certain systematic asymmetries in regard to the distribution of runs within the parameter space of τ_y, u and $\overline{h_w}/T$ are evident (see also Figure 2 and Figure 4). With $\tau_y(t)$ showing a highly exponential trend over time, essentially two clusters are visible in the data. While most runs were performed at 4 Pa $\lessapprox \tau_y \lessapprox 6$ Pa, with τ_y being almost constant over time, a second cluster evolves at an average τ_y of about 14 Pa (see Figure 2). Due to the rapid temporal change within the second cluster, only a very limited amount of runs were performed within that period, mainly at higher u. With the variance of the τ_y measurements being quite significant, the temporal development of τ_y will only be described qualitatively during this study.

Several observations were made, regarding the possible combination of parameters during the runs. The thrust P_T was observed to be constant with n and almost independent of u. With P_T usually being dependent on the propeller advance ratio (and thereby u), this occurs to be quite remarkable. It was also found, that a a minimum P_T was needed to overcome resistance in cases of constant contact with the FM layer, as the model repeatedly got stuck otherwise. Considering the thixotropic properties of the FM, it is not surprising that sailing at low velocities could not be steadily reached while contacting FM, leading to a lack of data in this area (see Figure 4). In cases sailing clearly above the FM layer, high n could only be used in selected cases, as some maneuvers significantly exceeded the basin dimensions. Determination of trends thereby has to be done with utmost care and due to the assumingly nonlinear relation $R_T = f(u, \tau_y, \overline{h_w}/T)$ extrapolation shall be avoided.

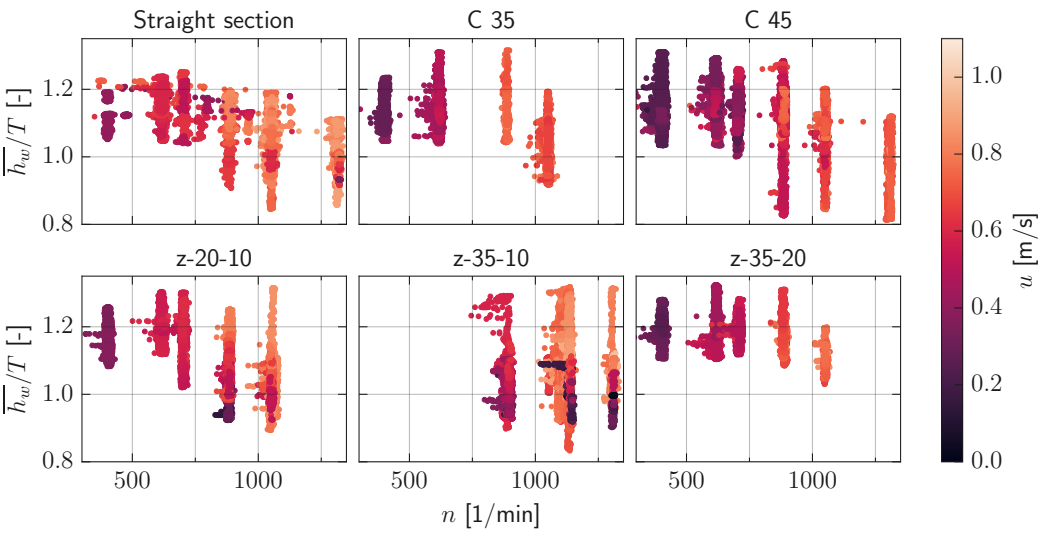

Figure 4: Distribution of $\overline{h_w}/T$ at different propeller revolutions n for the respective types of maneuver. Due to the thixotropic properties of the FM, runs at $\overline{h_w}/T \lessapprox 1.05$ can only be performed at higher n. Each datapoint represents a sample from the time series of the different runs. The in-situ velocity u is represented by color.

4.1 SHIPS RESISTANCE

With the experimental setup being based around a free running model ship, the measured thrust P_T has to be used as proxy for the ship's longitudinal resistance R_T, as no direct measurement of R_T is possible. It is generally assumed that R_T is lowest for a ship running straight, with factors line residual rate of turn r and rudder angle δ causing an increase of R_T. As this ideal state ($R_{T_{theor}}$) is rarely reached in a free running model, it is assumed to closely correspond to the lower envelope curve of the measurements done for a respective state (see Figure 5). The measurements can than be compared to baseline measurements of over HB (Hard Bottom) in the absence of FM for $h_{HB}/T \in \{1.1, 1.15, 1.2, 1.5, 2.0\}$, complemented by the deep water resistance results presented at the Tokyo workshop (Hino 2021) (referred to as $R_{T_{HB}}$ in the following).

When looking at the $R_{T_{theor}}$ curves for different $\overline{h_w}/T$ in comparison with the $R_{T_{HB}}$ curves (Figure 6), a few observations can be made:

- The resistances can essentially be separated into two groups: $h_w/T \gtrapprox 1.1$ and $h_w/T \lessapprox 1.0$ with the curve for $h_w/T \approx 1.05$ being in between. For the cases of $h_w/T \gtrapprox 1.1$, $R_{T_{theor}}$ appears to follow the $R_{T_{HB}}$ curves at low u, with $R_{T_{theor}}$ being lower compared to HB cases of similar UKC. At higher velocities ($u \gtrapprox 0.65$ m/s), $R_{T_{theor}}$ in this group seems to

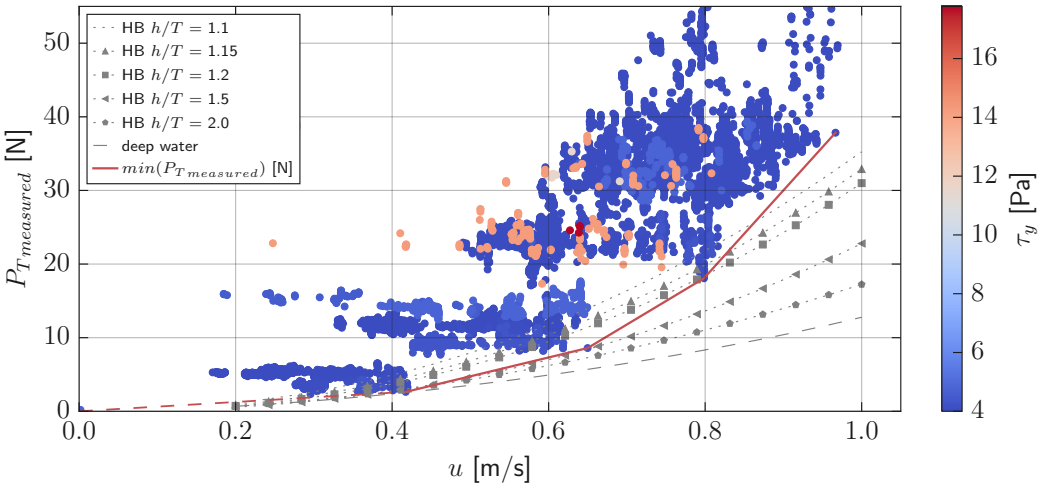

Figure 5: **Exemplary plot of measured P_T over u at $\overline{h_w}/T = 1.10$ along with reference measurements for different h_{HB}/T over hard bottom. Note the red line marking the undisturbed resistance $R_{T_{theor}}(h_w/T)$ as defined in Section 4.1. τ_y as described in Section 2.3.**

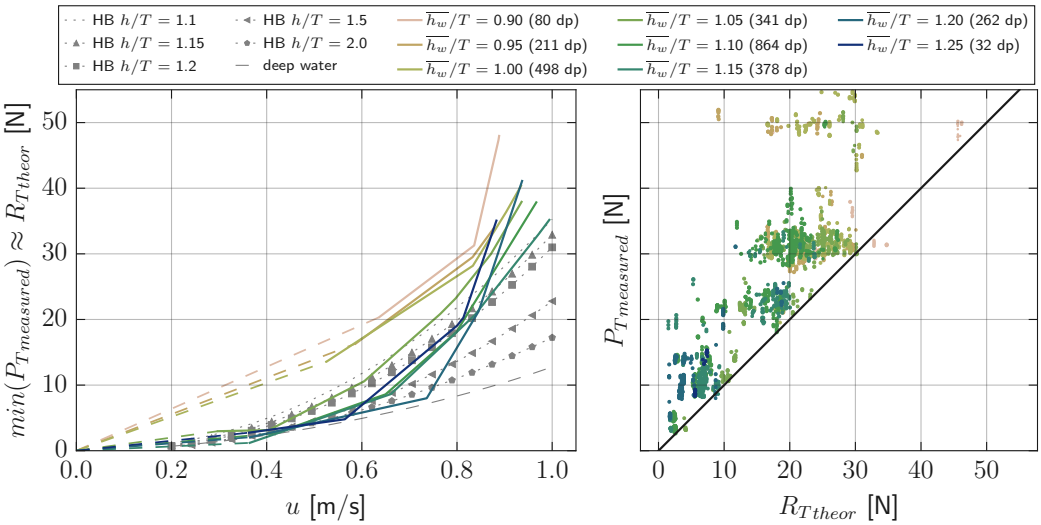

Figure 6: **Left: Velocity dependent resistance over hard bottom (HB) and in FM for different $\overline{h_w}/T$. Right: measured P_T over $R_{T_{theor}}$.**

increase much more drastically compared to the HB cases, especially for the runs at $h_w/T \gtrapprox 1.05$. This is presumably due to the formation of an internal wave system at the water—FM interface.

- In the second group of $\overline{h_w}/T \lessapprox 1.05$ $R_{T_{theor}}$ shows significantly higher values. Due to constant contact with the FM layer in these cases, viscous effects are assumed to be dominant for resistance here. As stated earlier, no runs were performed at low u for negative UKC, thereby no information is available for this area, although R_T is assumed to increase for lower u, due to the thixotropy.

- Generally, a significant increase of resistance was observed with higher τ_y (see Figure 5). However this can only be seen as indication, as only a few runs were performed at higher τ_y.

- The strong non-linearity in resistance is especially prominent when looking at iso-curves of u in the R_T over $\overline{h_w}/T$ parameter space as displayed in Figure 7. Similar to runs over hard bottom, where R_T typically increases exponentially with decreasing h_{HB}/T , an increase of resistance with diminishing UKC can be observed for $\overline{h_w}/T \gtrapprox 1.0$, with the steepest slope just before touching the FM layer. After making contact to the FM layer, R_T appears to increase only slightly when $\overline{h_w}/T$ is further decreased. Assuming dominance of viscous resistance for this case, this may be accounted to the contact area between hull and FM barely increasing after first contact.

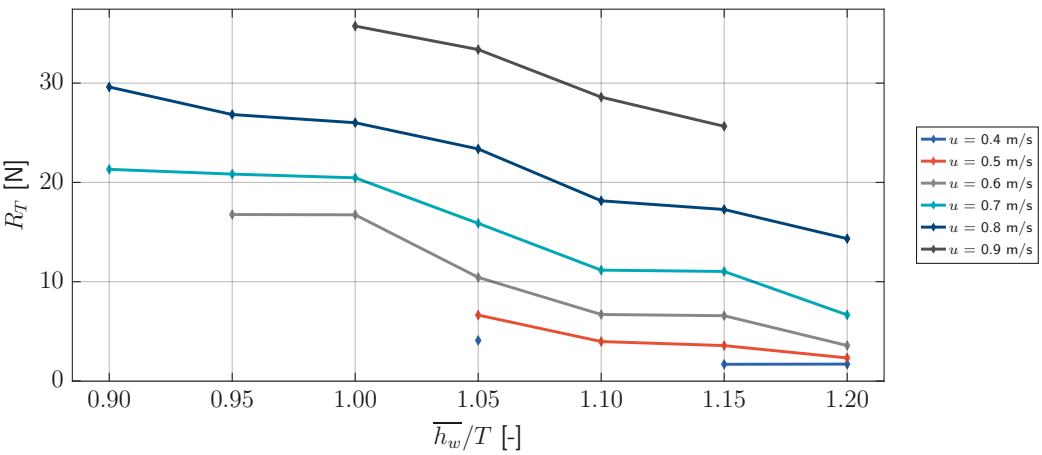

Figure 7: R_T **depending on** $\overline{h_w}/T$ **for different iso curves of** u**. A distinct non linearity can be observed at** $\overline{h_w}/T \approx 1.0$**.**

4.2 INITIAL COURSE-CHANGING ABILITY

With the initial course-changing ability being one of the most important parameters of ship acceptance trials according to IMO (IMO Resolution MSC.137(76)), it may be considered a good proxy for the reactivity of a ship under certain conditions. While typically being expressed as distance traveled until a certain change of course is realized, it will here be evaluated in terms of the time needed to alter the course, for different rudder angles δ and n. The data was batched according to n and the type of maneuver. As dependencies on the direction of turn, often found in shallow water maneuvering (e.g. Eloot et al. 2006) have not been observed here, turns to port and starboard will be evaluated together. On a general note, it is expected that the initial state of the circle maneuvers is better converged in comparison to the initial state of the zig-zag maneuvers, due to the longer approach distance. To evaluate the initial reactivity, a change of course of $10°$ (ψ_{010}) was chosen, as it can be evaluated both for the circle maneuvers and for the zig-zag maneuvers. As a high dependency on the initial state is assumed at those small course alterations, the time to alter the course by $30°$ (ψ_{030}) was evaluated as well in order to get a second measure for the evolving rate of turn, while still being highly influenced by dynamic effects. Quite remarkably, the response time was observed to be almost independent of the temporal averaged water depth $\langle \overline{h_w}/T \rangle_t$, n and initial direction of turn for the whole observed range of $\langle \overline{h_w}/T \rangle_t$ (see Figure 8). At ψ_{010} and low δ ($20°$) the response time appears to be slightly increased and shows a higher scatter compared with the higher rudder angles, while no significant difference is evident between $\delta = 35°$ and $\delta = 45°$. When looking at ψ_{030}, a slight decrease in response time can be observed with increasing δ. The absence of a further reduction of response time at high rudder angles during the initial phase (ψ_{010}) of the turn does not seem too surprising, considering that el Moctar et al. (el Moctar et al. 2022) found the acceleration dependent hydrodynamic masses to increase exponentially with decreasing UKC.

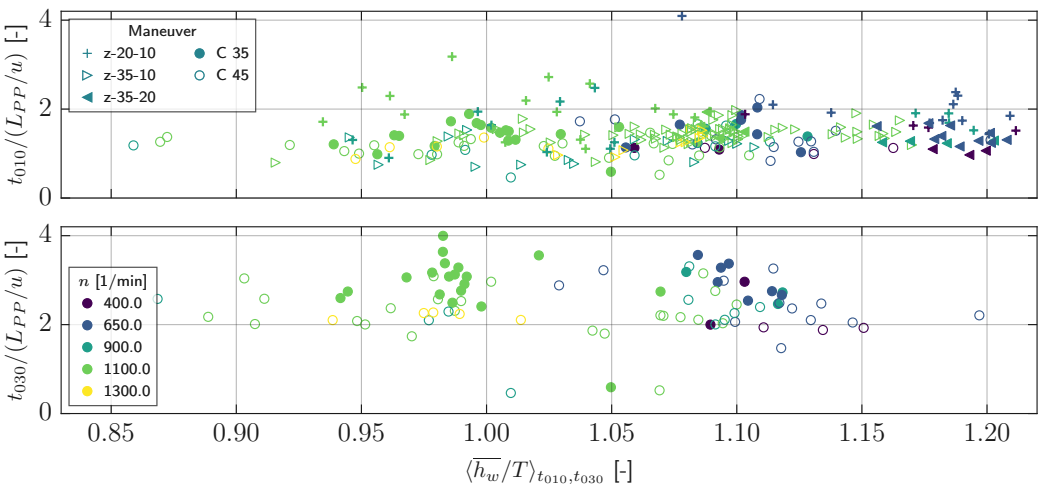

Figure 8: **Rudder responsiveness as time to reach** ψ_{010} **(upper) and** ψ_{030} **(lower) respectively. The color reflects the** n **used within the maneuver. Different markers are used for different maneuvers.** $\overline{h_w}/T$ **time-averaged over the duration of the maneuver**

4.3 STEADY DIAMETER

Another typical parameter for describing the maneuvering behavior is the steady diameter (D'_C), determined during the shipyard acceptance trials as well (IMO Resolution MSC.137(76)). It is usually determined for a constant water depth and converges when a ship reaches equilibrium during the maneuver. Typically, a nonlinear increase of D'_C is expected for $h_w/T \lesssim 2.0$ in shallow water (Vantorre et al. 2017; Gokarn 2024). As an equilibrium was only reached temporarily during the experiment due to height variations of the FM interface, D'_C could not be calculated directly from the path, but from its derivatives r and u instead. Therefore, sections of at least 3 s have been selected from the circular runs, where $\overline{h_w}/T$, r, u and n were approximately constant. By temporal averaging over the section duration, D'_C can be approximated as:$D'_C(\langle \overline{h_w}/T \rangle_t) \approx \langle \frac{u \cdot 360°}{r \cdot \pi} \rangle_t$. It should be noted, that this method is not very robust and should therefore only be used for qualitative analysis. Interpretation of the results has to be done carefully, as the datapoints are not equally spaced over the investigated domain. A strong dependence of D'_C on n can be observed, being especially prominent at a smaller δ of $35°$. This is remarkable, as only a slight dependence on n is expected from comparable experiments in shallow water over a hard bottom.

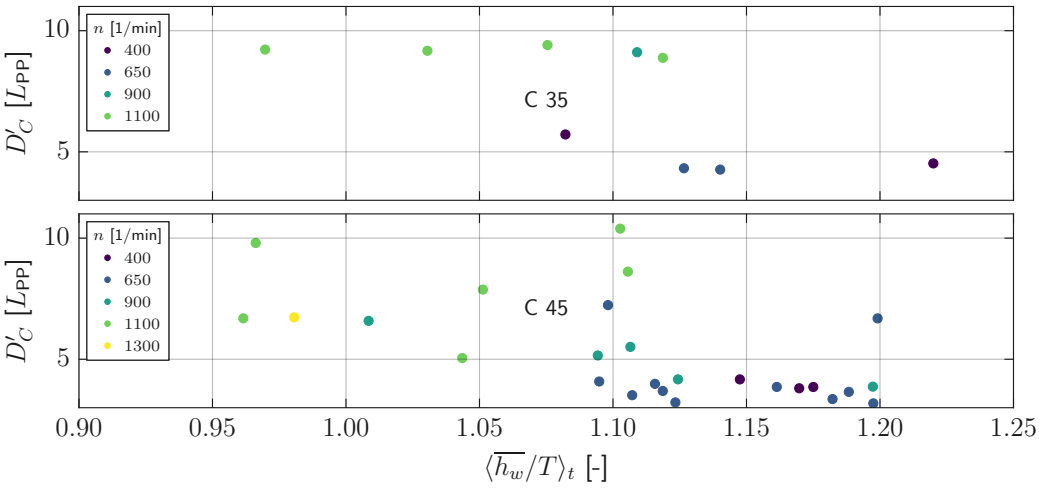

Figure 9: Final diameter D'_C for δ $35°$ (upper) and δ $45°$ (lower) depending on n and $\langle \overline{h_w}/T \rangle_t$.

4.4 ADVANCE

The advance distance x'_{090} is likewise evaluated as part of the shipyard acceptance trials and of the classification procedures (IMO Resolution MSC.137(76)). It marks the distance in the initial direction of travel until a heading change of $90°$ is reached. With it often being the minimal distance to avoid large obstacles, it is a critical measure to look at, with deep water limits below $4.5\,L_{PP}$ (IMO Resolution MSC.137(76)).

As with D'_C, the data points were batched by δ and n. However, as x'_{090} describes a dynamic maneuver, the $\overline{h_w}/T$ distribution over the maneuver section has been taken into account. As apparent from the upper graph of Figure 10, a negative correlation between δ and x'_{090} is found. While higher n correlates with likewise higher x'_{090}, the spread in x'_{090} is significant, in parts more than $100\,\%$, even for a constant $\overline{h_w}/T$. This indicates a high temporal dependency of the actual sequence of the maneuver, leading to the conclusion that $\overline{h_w}/T$ cannot be used as an estimator for x'_{090}. While overall a slight negative correlation between $\overline{h_w}/T$ and x'_{090} is indicated by the results, the data suffers from slight systematic shortcomings, as the runs are not equally distributed within the n over $\overline{h_w}/T$ parameter space, final conclusions cannot be drawn from that observation.

5 DISCUSSION

While the experiments conducted for this study were performed with utmost care, due to the systematic shortcomings discussed earlier and the large number of parameters accounting for the unsteady conditions, the results presented here are not sufficient for a comprehensive analytical description of the maneuvering behavior of a model ship in fluid mud. However, the results are highly valuable for the comparison with numerical, time resolved methods, allowing the verification of the latter with cases of different levels of complexity. Due to the limited time frame in which the natural FM retains the desired properties, captive model test should be preferred over free running setups, offering results of reduced complexity and increased repeatability.

The largest factor for uncertainty in this study is found in the natural FM layer distribution. Although several attempts were made trying to even out the FM surface, the unevenness over the basin reaching the same order of magnitude as $0.1T$. This

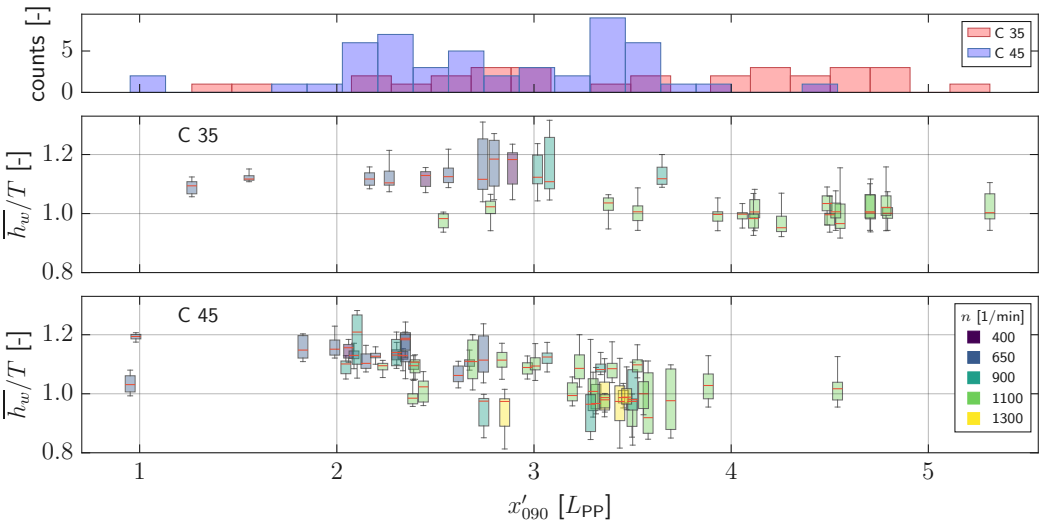

Figure 10: Advance (on x axis), number of occurrences for $\delta\,35°$ and $\delta\,45°$ (upper graph). Advance depending on n and $\overline{h_w}/T$ distribution for $\delta\,35°$ (middle graph) and $\delta\,45°$ (lower graph) .

lead to unavoidable changes in h_w/T during the maneuvers. Combined with the uncertainty due to the surface interpolation this makes an isolated evaluation of different impact factors very challenging. Thereby methods to reliably distribute and level the FM layer should be established before repeating such experiments. Despite of extensive mixing of the FM before introducing it to the experimental facility, slight inconsistencies have been detected in the temporal development of the FM properties at different locations. With h_{fm} of only a few centimeters, determining the actual probe height of the rheological measurements and ensuring that no material from other layers is mixed under the sample turned out to be quite challenging, making it a potential source of error.

To avoid these error sources and to enable a precise control of the FM properties, artificial FM layers have been used in the past Delefortrie (2007). Although this allows for a better parameterization, the non-Newtonian properties of the FM are neglected with this approach, potentially not detecting non-linear effects that might occur. While Kaidi et al. (Kaidi et al. 2020) concluded from the results of numerical studies, that the effect on R_T is negligible, it seems reasonable to assume that the effect is much more prominent during maneuvers with the ship being at drift. Nevertheless, with the viscous forces being highly scale dependent, the effects at full scale are expected to be much less pronounced than at model scale.

Quite remarkably, shallow water effects expected from experiments over hard bottom, like a significant dependence of D'_C and x'_{090} on h_w/T , have not been observed in this study. While h_w/T with respect to the mud interface was varied between 0.9 and 1.2, the distance to the hard bottom was much less variable within the range of $1.38 \gtrapprox h_{HB}/T \gtrapprox 1.52$, with only two runs performed at a smaller h_{HB}/T of ≈ 1.23. Following Delefortrie et al. (Delefortrie et al. 2009) it can be assumed, that the hydrodynamic equivalent water depth is enlarged in the present of a FM layer, reducing the sensitivity on variations of h_w/T . This is further supported by the observations made for the longitudinal resistance (see Section 4.1), where R_T for low u and positive UKC in the presence of FM was observed to correlate with R_T for significantly higher UKC over hard bottom.

While an almost constant FM layer thickness of $0.52T \rightarrow 0.36T$ (due to consolidation) was used in this study in order to minimize effects from the hard bottom, previous studies (Vantorre et al. 2006; Kaidi et al. 2020) utilized a significantly smaller layer thickness, that was varied during the studies. They found the internal wave system to be significantly influenced by the layer thickness, with the largest amplitude at higher thicknesses. Although the utilization of a thick layer is assumed to represent a conservative approach in order to produce a validation case, the influence of mud layer thickness should be added as additional parameter in future studies.

As shown in Section 4.1, a distinct non-linearity in resistance is found when the ship sails very closely to the FM interface ($h_w/T \approx 1.05$). As the first contact between hull and FM is quite likely to be established at that point due to internal waves deforming the interface, this might be due to a significant increase of viscous resistance based on the FM rheology. This is further supported by the observation that no remarkable change in resistance is evident between $h_w/T \approx 1.0$ and $h_w/T \approx 0.9$, as the contact area between hull and FM is assumed to increase only slightly after the ships bottom made contact. Moreover a distinct amplification of resistance compared to runs over hard bottom can be observed when a certain velocity is exceeded. This may be accounted to an internal wave system evolving at the FM interface, gaining significance at higher u.

6 CONCLUSIONS

An experimental series of a free running model ship over a layer of natural fluid mud was performed, in order to generate validation cases for numerical models. However, a distinct non-linear dependency between total resistance and distance between the ship's keel and the fluid mud interface (h_w/T) was observed. Moreover the results showed a significantly increased resistance for higher velocities compared to baseline measurements performed in shallow water over hard bottom. Quite remarkably, no unambiguous influence of h_w/T on the initial course-change ability, advance or steady turning circle diameter was found. With this study being the first of its kind using natural fluid mud, suggestions for improvements of the experimental setup and execution are given as aid for future studies. The experimental results obtained in this study are available on request.

7 ACKNOWLEDGMENTS

The research leading to this study was funded by BAW and Hamburg Port Authority (HPA) in equal parts in the scope of the project 'Nautical Depth'. While employees of HPA significantly supported the preparation and execution of the experimental series, no influence was applied on the outcomes of this study. The authors thereby declare no conflict of interest.

8 REFERENCES

Brossard, C., Delouis, A., Galichon, P., Granboulan, J., and Monadier, P., 1990. Navigability in Channels Subject to Siltation. Physical Scale Model Experiments. In: Coastal Engineering Proceedings 1(22). DOI: 10.9753/icce.v22.%25p.

Brouwers, B., Meire, D., Toorman, E. A., van Beeck, J., and Lataire, E., 2023. Conditioning procedures to enhance the reproducibility of mud settling and consolidation experiments. In: Estuarine, Coastal and Shelf Science 290. DOI: 10.1016/j.ecss.2023.108407.

Chmiel, O., Naulin, M., and Malcherek, A., 2020. Combining Turbulence and Mud Rheology in a Conceptual 1DV Model – An advanced continuous modeling concept for fluid mud dynamics. 27. In: Die Küste 89. DOI: 10.18171/1.089101.

Delefortrie, G., 2007. Manoeuvring Behaviour of Container Carriers in Muddy Navigation Areas. Faculty of Engineering. PhD Thesis. Gent: Universiteit Gent. 295 pp.

Delefortrie, G. and Vantorre, M., 2009. Prediction of the forces acting on container carriers in muddy navigation areas using a fluidization parameter. In: Journal of Marine Science and Technology 14.1, pp. 51–68. DOI: 10.1007/s00773-009-0041-x.

Delefortrie, G. and Vantorre, M., 2016. Ship Manoeuvring Behaviour in Muddy Navigation Areas: State of the Art. en. In: 4th MASHCON Proceedings. International Conference on Ship Manoeuvring in Shallow and Confined Water with Special Focus on Ship Bottom Interaction (Hamburg, Germany), pp. 26–36. DOI: 10.18451/978-3-939230-38-0_4.

el Moctar, O., Lantermann, U., and Chillcce, G., 2022. An efficient and accurate approach for zero-frequency added mass for maneuvering simulations in deep and shallow water. In: Applied Ocean Research 126. DOI: 10.1016/j.apor.2022.103259.

Eloot, K., Vantorre, M., and Delefortrie, G., 2006. Prediction of Ship Manoeuvrability of an 8000 TEU Containership in Deep and Shallow Water: mathematical modelling and captive model testing. In: Proceedings MARSIM 2006. Maritime Institute Willem Barentsz.

Flügge, G. and Uliczka, K., 2001. Dynamisches Fahrverhalten und Wechselwirkungen mit der Fahrrinnensohle von sehr großen Containerschiffen unter extremen Flachwasserbedingungen. German. In: Hansa 12.138.

Gokarn, R. P., 2024. A Study of Ship Manoeuvrability. 1st ed. 2024. Singapore: Springer Nature. DOI: 10.1007/978-981-97-0625-9.

Guan, W. B., Kot, S. C., and Wolanski, E., 2005. 3-D fluid-mud dynamics in the Jiaojiang Estuary, China. In: Estuarine, Coastal and Shelf Science 65.4, pp. 747–762. DOI: 10.1016/j.ecss.2005.05.017.

Hino, T., 2021. Numerical Ship Hydrodynamics. An Assessment of the Tokyo 2015 Workshop. In collab. with F. Stern, L. Larsson, M. Visonneau, N. Hirata, and J. Kim. Vol. v.94. Lecture Notes in Applied and Computational Mechanics Ser. Springer International. 1442 pp. DOI: 10.1007/978-3-030-47572-7.

Hino, T., Hirata, N., Ohashi, K., Toda, Y., Zhu, T., Makino, K., Takai, M., Nishigaki, M., Kimura, K., and Anda, M.: Shingo, S., 2016. Hull Form Design and Flow Measurements of a Bulk Carrier with an Energy-Saving Device for CFD Validations. In: 2016 PRADS 13th triennial. Proceedings of the 13th International Symposium on Practical Design of Ships and Other Floating Structures : 4th-8th September, 2016, Copenhagen, Denmark, pp. 159–166.

Hoffmann, J. and Hoffmann, J., Jan. 11, 2021. Bigger ships and fewer companies - two sides of the same coin. Article No. 70. UNCTAD Transport and Trade Facilitation Newsletter N°89 - First Quarter 2021. UN Trade and Development.

International Maritime Organization, Dec. 4, 2002. Standards for Ship Maneuvrability. MSC 76/23/Add.1.

ITTC 7.5-01-01-01:2017: Ship Models Sept. 1, 2017. ITTC Procedure. Version 04.

ITTC 7.5-02-06-01:2008: Free Running Model Tests 2008. ITTC Procedure. Version 03.

Kaidi, S., Lefrançois, E., and Smaoui, H., 2020. Numerical modelling of the muddy layer effect on Ship's resistance and squat. In: Ocean Engineering 199. DOI: 10.1016/j.oceaneng.2020.106939.

Kirichek, A., Shakeel, A., and Chassagne, C., 2020. Using in situ density and strength measurements for sediment maintenance in ports and waterways. In: Journal of Soils and Sediments 20.6, pp. 2546–2552. DOI: 10.1007/s11368-020-02581-8.

Knoch, D. and Malcherek, A., 2011. A numerical model for simulation of fluid mud with different rheological behaviors. In: Ocean Dynamics 61.2-3, pp. 245–256. DOI: 10.1007/s10236-010-0327-x.

Lataire, E., Vantorre, M., Laforce, E., Eloot, K., and Delefortrie, G., 2007. Navigation in Confined Waters: Influence of Bank Characteristics on Ship-Bank Interaction. In: Proceedings of the 2nd International Conference On Marine Research And Transportation. ICMRT 07 (Ischia, Naples, Italy), pp. 1–9.

Le Hir, P., Bassoullet, P., and Jestin, H., 2000. Application of the continuous modeling concept to simulate high-concentration suspended sediment in a macrotidal estuary. In: Coastal and Estuarine Fine Sediment Processes. Vol. 3. Proceedings in Marine Science, pp. 229–247. DOI: 10.1016/S1568-2692(00)80124-2.

Lovato, S., Kirichek, A., Toxopeus, S. L., Settels, J. W., and Keetels, G. H., 2022. Validation of the resistance of a plate moving through mud: CFD modelling and towing tank experiments. In: Ocean Engineering 258. DOI: 10.1016/j.oceaneng.2022.111632.

Lovato, S., Toxopeus, S. L., Settels, J. W., Keetels, G. H., and Kirichek, A., 2024. CFD analysis of the full-scale resistance of an oil tanker in presence of a mud–water interface. In: Ocean Engineering 294. DOI: 10.1016/j.oceaneng.2024.116700.

McAnally, W. H., Friedrichs, C., Hamilton, D., Hayter, E., Shrestha, P., Rodriguez, H., Sheremet, A., and Teeter, A., 2007. Management of Fluid Mud in Estuaries, Bays, and Lakes. I: Present State of Understanding on Character and Behavior. In: Journal of Hydraulic Engineering 133.1, pp. 9–22. DOI: 10.1061/(ASCE)0733-9429(2007)133:1(9).

PIANC, 2014. Harbour Approach Channels. Design Guidelines. Brussels, Belgium. 320 pp.

Schoeneich, M., 2011. Probabilistic Model of Under-Keel Clearance Assessment As a Practical Tool for Ships' Safety Determination in Existing and Designed Ports. In: ICTIS 2011. First International Conference on Transportation Information and Safety (ICTIS) (Wuhan, China). Reston, VA: American Society of Civil Engineers, pp. 2690–2696. DOI: 10.1061/41177(415)339.

Sellmeijer, R. and van Oortmerssen, G., 1983. The Effect of Mud on Tanker Manoeuvres. In: Spring Meetings, RINA, Paper No. 7.

Shakeel, A., Chassagne, C., Bornholdt, J., Ohle, N., and Kirichek, A., 2022. From fundamentals to implementation of yield stress for nautical bottom: Case study of the Port of Hamburg. In: Ocean Engineering 266, p. 112772. DOI: 10.1016/j.oceaneng.2022.112772.

Sotelo, M. S., Boucetta, D., Doddugollu, P., Toorman, E., Brouwers, B., Delefortrie, G., and van Hoydonck, W., 2022. Experimental Study of a Cylinder Towed Through Natural Mud. In: 6th MASHCON Proceedings. International Conference on Ship Manoeuvring in Shallow and Confined Water, with special focus on port maneuvres. Glasgow, pp. 222–231.

Sotelo, M. S., Boucetta, D., van Hoydonck, W., Praveen, D., Vantorre, M., Toorman, E. A., and Delefortrie, G., 2024. Experimental and numerical study of the hydrodynamic forces acting on a surface-piercing hydrofoil in muddy environments. In: Ocean Engineering 294. DOI: 10.1016/j.oceaneng.2024.116816.

Toorman, E. A., Vandebeek, I., Liste-Munoz, M., Heredia, M., Rocabado, I., Vanlede, J., Delefortrie, G., Vantorre, M., and Meerschaut, Y., 2015. Drag on an Object Towed Through a Fluid Mud Layer. CFD versus experiment. In: 13th International Conference on Cohesive Sediment Transport Processes. Leuven, Belgium.

Vantorre, M. and Coen, I., 1988. On sinkage and trim of vessels navigating above a mud layer. In: 9th International Harbour Congress. Koninklijke Vlaamse Ingenieursvereniging. Antwerpen.

Vantorre, M., Eloot, K., Delefortrie, G., Lataire, E., Candries, M., and Verwilligen, J., 2017. Maneuvering in Shallow and Confined Water. In: Encyclopedia of Maritime and Offshore Engineering, pp. 1–17. DOI: 10.1002/9781118476406.emoe006.

Vantorre, M., Laforce, E., and Delefortrie, G., 2006. A novel methodology for revision of the nautical bottom. In: Seminar: Flanders, a maritime region of knowledge (MAREDFlow). Vlaams Instituut voor de Zee (VLIZ), pp. 15–34.

Verwilligen, J., Vantorre, M., Delefortrie, G., Kamphuis, J., Meinsma, R., and van der Made, K.-J., 2014. Manoeuvrability in proximity of nautical bottom in the Harbour of Delfzijl. In: Proceedings. 33rd PIANC world congress (San Francisco, USA), pp. 581–598.

Watanabe, R., Kusuda, T., Yamanishi, H., and Yamasaki, K., 2000. Modeling of fluid mud flow on an inclined bed. In: Coastal and Estuarine Fine Sediment Processes. Vol. 3. Proceedings in Marine Science, pp. 249–261. DOI: 10.1016/S1568-2692(00)80125-4.

Wehr, D. and Kuratorium für Forschung im Küsteningenieurwesen, 2014. A Numerical Model for Fluid Mud Dynamics in Estuarine Systems – Overview and Outlook. In: Die Küste 81, pp. 463–472.

Wens, F., Coen, I., and Roovers, P., 1984. Nautische Bodem in Slibrijke Gebieden. Report MOD. 428. Dutch. Flanders Hydraulics Research.

Yan, Y. and Hayter, E. J., 1994. Numerical Modeling of Fluid Mud Transport in Estuaries. In: Hydraulic engineering '94. Proceedings of the 1994 conference, Buffalo, New York August 1 - 5, 1994. New York, NY: American Society of Civil Engineers.

9 AUTHORS BIOGRAPHY

Jan Mense is researcher at the Federal Waterways Research and Engineering Institute Germany. He studied Naval Architecture and Maritime Engineering and specialized on experimental and numerical fluid dynamics. He previously worked on scientific projects developing, executing and processing experimental studies as well as developing numerical models in the field of ocean engineering.

Carl-Uwe Böttner currently works as senior researcher with the Federal Waterways Engineering and Research Institute (BAW) in Hamburg on the fields of hydrodynamics, ship dynamics and ship handling simulation. He is responsible for consulting the German waterways authorities in every aspect of ship handling simulation.

FULL SCALE MANOEUVRING TESTS WITH A SMALL, FLEXIBLE AUTOMATED, ZERO-EMISSION (SFAZ) VESSEL

Mansuy, M., Delefortrie, G., Candries, M., Ships and Marine Technology, Ghent University, Belgium

Alliot, A., Mesnil, L., Alliot, I., NEAC-INDUSTRY, France

FULL SCALE MANOEUVRING TESTS WITH A SMALL, FLEXIBLE AUTOMATED, ZERO-EMISSION (SFAZ) VESSEL

MANSUY, M., DELEFORTRIE, G., CANDRIES, M., SHIPS AND MARINE TECHNOLOGY – GHENT UNIVERSITY, BELGIUM
ALLIOT, A., MESNIL, L., ALLIOT, I., NEAC-INDUSTRY, FRANCE

SUMMARY

The roadmap for transitioning to zero-emission transport and logistics in Europe promotes the use of waterborne transport, specifically inland waterway transport (IWT) and coastal shipping, to shift goods from road to water. In congested, urban areas that are characterized by shallow waterways and low bridges, the use of smaller vessels for IWT may offer a more environmentally attractive option.

FOREMAST aims at facilitating the movement of goods using Small, Flexible Automated, Zero-emission (SFAZ) vessels. Solutions are developed and validated in three Living Labs (LLs) in Europe with three different types of SFAZ vessels, exploring different levels of automation and autonomy combined with innovative green propulsion.

In order to understand how the different SFAZ vessels will react to a control command, the manoeuvring characteristics of the vessels need to be known. A Living Lab in Romania considers new concepts, of which the resistance and manoeuvring characteristics can be derived based on CFD computations. For the LL in France, full scale manoeuvres have been carried out. This paper will focuses on the French LL and explains how the measured data from zig-zag, turning circle and other manoeuvres were pre-processed in order to be able to apply system identification techniques to establish a mathematical manoeuvring model of the SFAZ vessel. The same methodology will be used applied for the LL in Belgium.

1 INTRODUCTION

The “SFAZ” concept is relatively new. It stands for Small Flexible Automated Zero-Emissions vessels, which addresses several of the challenges that inland shipping faces.

Inland waterway navigation is one of the most environmentally friendly modes of transport (Barros et al., 2022). The European Commission introduced the European Green Deal as a new sustainable growth strategy, with a commitment to shift a substantial part of current inland freight transport by road to railways and inland shipping (European Commission, 2021). However, inland shipping has been struggling with a shortage of skippers (CCNR, 2024; Kriedel and Roux, 2024). From an economical point of view, it is more interesting for skippers to work on larger inland vessels. Kloch and Kristiansen (2024) studied the viability of existing inland navigation vessels and found that smaller vessels are disappearing faster than larger vessels (Kloch and Kristiansen, 2024). In terms of CEMT classes, virtually no CEMT class I inland navigation vessels have been built in Europe since 1970 (Bačkalov et al., 2024). As a consequence, some smaller waterways are underutilised to the point that some of them risk falling into disuse, only to be used by the occasional pleasure craft. This raises the question whether these underutilized waterways can be used by a new type of small vessel.

At first instance, urban waterways seem the most interesting for re-development, as changes in logistical planning are required in order to develop an optimal distribution network that integrates transport via urban waterways and last-mile delivery. The economy and liveability of cities depends to a large degree on efficient urban logistics. In many cities, this efficiency is under pressure due to factors such as increasing population and faces challenges such as congestion, emissions, noise, and safety issues. Historically, many cities were founded near a waterway because transport by water was easier than over land. Over the last couple of centuries, road transport has replaced transport by water as the main mode of transport. Over time, this gradual shift in transport habits has often overlooked the spatial correlation between waterway and urban development (Pourmohammad-Zia and van Koningsveld, 2024). Several sources have pointed out that inland waterways present untapped potential that can improve urban logistics in many cities and examples have been given of successful solutions worldwide (Wojewódzka-Król and Rolbiecki, 2019).

The World Economic Forum has projected a 32% increase in urban delivery-related traffic emissions and a 21% increase in congestion from 2020 to 2030 (World Economic Forum, 2020). The majority of these emissions originate from the 'last mile' delivery stage, an inherently inefficient process characterised by low product volume and a high number of destinations. Several companies have looked at waterways for last mile deliveries (CCNR, 2022). Alternative routes between ports and consignors/consignees using different models of transport can be explored using methods, such as graph theory (Paulauskas et al., 2022). Pourmohammad-Zia and van Koningsveld (2024) evaluated the benefits of transitioning from a roadway-centric to a waterway-based system for the city of Amsterdam as a case study. By formulating the problem as a location routing problem with time windows, they obtained significant cost savings (approximately 28 %), reductions in vehicle weight (approximately 43 %), and minimized travel distances (approximately 80 %) within the city centre. Traditional inland vessels are used to move cargo from a central hub to several transshipment locations and the last-mile delivery is carried out with Light Electric Vehicles or moving jacks (Pourmohammad-Zia and van Koningsveld, 2024). Jaegler et al. (2024) analysed the economic feasibility of urban distribution where inland waterway transport is used for transshipment and cargo bikes/vans are deployed for last-mile delivery (Jaegler et al., 2024). Small and flexible vessels could in that sense be an interesting proposition for many cities.

Consensus has grown that automated/autonomous inland navigation can help in reviving transport on small waterways in particular (Pauwelyn and Turf, 2023). The distinction between the terms "automation" and "autonomy" has been discussed in detail by Rødseth et al. (2022). Both terms are used to express the same concept, but the Central Commission for the Navigation of the Rhine (CCNR), refers to "levels of automation", so it has become (slightly more) common to use "automated" for inland navigation and "autonomous" for seagoing vessels. Essentially, it means that one or more of a ship system's processes or equipment, under certain conditions, is designed and verified to be controlled by automation, without human assistance (Rødseth et al., 2022).

Several projects have investigated the technical feasibility of automated inland navigation purposes. The feasibility was first demonstrated with ferries, which offer the advantage that they usually operate continuously between two fixed destination points. Rolls-Royce and Finnferries demonstrated automated navigation on a 1.8 km long trajectory with a 53.8 m double-ended car ferry, which was remotely controlled from a centre some 50 kilometres away. The vessel detects objects by fusing sensor data and using artificial intelligence and is able to conduct collision avoidance and automatic berthing (Rolls-Royce, 2018). In another project, NTNU put a self-propelled electric passenger ferry into trial operation along the urban waterways of Trondheim (Haugan, 2022). As part of the AUTOSHIP Horizon 2020 research project, remote-controlled automated vessel operations were demonstrated in Belgium with an inland waterway barge. The Zulu 4 completed a 16.5 km long circuit that included traversing locks and passing several bridges (Taylor, 2023).

The AEGIS research project aims to develop a transport system that can better compete with road transport by using more and smaller vessels to increase frequency, differentiate speeds, reduce terminal costs and reducing port times. They point out that the main advantage of remote-controlled vessels is the possibility to operate a fleet of vessels from a single remote control centre and therefore be more flexible and efficient. Several shallow draughted (≤ 3.3 m) concept vessels are included in the project, such as a 61m long container shuttle, and a push convoy with three different types of 33 m long barges and fully electric inland waterway RORO vessels, ranging from CEMT class II to IV+ that are able to carry trailers (Krause et al., 2022). Roboat aims to make use of the existing infrastructure with novel automated surface vessels that could eventually be used for urban transportation of passengers or freight (Wang et al., 2020).

From an environmental point of view and with an increasing amount of low-emission zones in urban areas, these small, flexible and automated vessels would only make sense if they are zero-emission. Inland navigation has long had an advantage over road transport in terms of the sustainability of transport (i.e. lower emissions per transported unit). This advantage has decreased considerably in recent years, as the road transport sector is able to adopt and install new techniques more quickly than is possible in the inland navigation sector. It Is therefore important for the inland navigation sector to realise gains in terms of emissions, in order to reinforce its image as a sustainable mode of transport (Sys et al., 2020).

Based on a systematic literature review of emissions, decarbonization, and alternative fuels in inland navigation, Raftis et al. (2023) point out that majority of the studies come from outside Europe, especially China, where considerable effort has been put into utilizing inland corridors and switching to alternative power sources for inland vessels and their propulsion systems. As the European region has extensive networks of inland waterways and the European Commission has set a goal for net zero, it seems that there is plenty of space for additional actions to stimulate environmentally friendly inland navigation. Within Europe, the focus so far is on the optimization of the inland corridors as a first step, and the focus on

switching to alternative power sources for inland vessels is only a second step which merits higher research efforts (Raftis et al., 2023).

The concept of using Small, Flexible Automated, Zero-emission (SFAZ) vessels is therefore promising. FOREMAST (Freight vOlumes transfer from Road to waterborne transport, using zero-EMission, Automated, Small, and flexible vessel (SFAZ) protoTypes) builds on the findings from projects such as ReNEW (Resilience-centric Smart, Green, Networked EU Inland Waterways), which creates and tests new solutions for both climate-neutral and climate-resilient transport systems via inland waterways, and IW-NET (Innovation-Driven Collaborative European Inland Waterways Transport Network), which focuses on developing a multimodal optimisation process across the EU transport system. FOREMAST aims to explore areas which other research projects do not address. AUTOFLEX (AUTOnomous small and FLEXible vessels), for example, looks into the modernization of the design of traditional inland navigation vessels. One of the findings is that the modification of a traditional CEMT Class I reference design to a container carrier is not viable, as the vessel could not comply with the intact stability criteria for container carriers, which rendered the analysis of the further modernization steps superfluous (Bačkalov et al., 2024).

Within FOREMAST, several different SFAZ designs are studied, which are fundamentally different from traditional inland navigation vessels, in the hope that these SFAZ concepts can revive underutilized class I waterways. FOREMAST principally aims at facilitating the movement of goods using SFAZ. Solutions are developed and validated in three Living Labs (LLs) in Europe with three different types of SFAZ vessels, exploring different levels of automation and autonomy combined with innovative green propulsion.

One of the aims within FOREMAST is to develop suitable mathematical models for the different SFAZ, considering both independent operation and platooning. The mathematical model is the cornerstone of ship manoeuvring theory. Over the years, various models of different complexity and adequacy have been proposed, ranging from relatively full and complex manoeuvring models based on fundamental physical principles and much simpler models usually associated with the name Nomoto (Sutulo and Guedes Soares, 2024). In order to understand how the different SFAZ vessels will react to a control command, the manoeuvring characteristics of the vessels need to be known. A Living Lab in Romania considers new concepts, of which the resistance and manoeuvring characteristics can be derived based on CFD computations. For the LL in France, full scale manoeuvres have been carried out.

This paper will focus on the LL In France, which aims to develop and test a new vessel design and prototype of a SFAZ concept that can be used for urban and intra-urban transport of goods in Caen, France. Section 2 of the paper briefly describes why manoeuvring models are important within the development of automated inland navigation. Section 3 describes the environment in which the full scale trials were carried out, the ship characteristics and the test protocol. Section 4 describes the pre-processing of the collected data. Section 5 concludes the paper and describes the prospects for further developments.

2 DIGITAL TWIN AND AUTONOMOUS NAVIGATION

Digital twins provide a comprehensive virtual representation of the vessel and its environment. In the design phase, these virtual replicas enable early-stage optimization of hull forms, propulsion systems, and other critical components, facilitating performance analysis and risk mitigation before physical construction. This reduces development time and costs while improving overall design quality. During operation, digital twins integrate real-time sensor data from the physical ship, enabling continuous performance monitoring, predictive maintenance, and optimized route planning. By simulating various scenarios, including weather changes and potential equipment solutions, digital twins can help in making decisions, enhance crew training, and contribute to improved safety, efficiency, and sustainability throughout the ship's lifecycle. These improvements translate into significant economic benefits for ship owners and operators. Optimized energy consumption through route planning and performance monitoring directly reduces operational expenses. Furthermore, improved operational efficiency and reduced risks can enhance profitability and competitiveness of inland waterway transportation. Moreover, digital twins play a crucial role in the development and validation of autonomous navigation systems. By providing a virtual testing ground, they allow for the safe and cost-effective evaluation of autonomous algorithms and sensor integration in various simulated conditions, accelerating the development and deployment of autonomous vessels.

Both digital twins and autonomous navigation require precise prediction of ship dynamics for safe and efficient operation. Accurate ship manoeuvring models are fundamental for robust path planning and collision avoidance in dynamic

environments. Moreover, model-based simulations provide a cost-effective and safe platform for testing and validating autonomous navigation algorithms.

This is even more true when vessels train need to be simulated to analyse and optimize complex interactions between autonomous vessels ensuring safe distances, synchronized movements and for effective reaction to unexpected events and emergency situations.

These models enable prediction of ship response to control inputs (e.g. rim-driven thrusters, conventional propellers) and environmental disturbances (wind, currents). Reliable motions prediction facilitates the generation of optimal trajectories, minimizing fuel consumption and transit time.

Developing accurate manoeuvring models, especially complex six degrees of freedom (6DOF) models (Delefortrie et al., 2016), is challenging and time consuming. Determining the required hydrodynamic parameters usually involves computationally expensive captive model tests or Computational Fluid Dynamics (CFD) simulations, frequently combined with system identification. This process is time consuming and not particularly suitable for the design of different types of vessels considered within the FOREMAST project, where evaluating the impact of minor hull variations, propulsion system changes, and other modifications requires rapid assessment.

Therefore, a simplified model including dominant hydrodynamics is sufficient for the present study. Such model still requires identifying several manoeuvring characteristics of the vessel. Standard manoeuvres recommended for sea trials are representative of the main manoeuvring characteristics of a ship, those tests are therefore used as a base for system identification.

The idea behind the methodology presented is to be able to have a fast and easy method to build a model which can be used for several ship versions and different purposes. Therefore, very simple pre-processing techniques are applied to investigate the quality of the data.

3 FULL SCALE TRIALS

3.1 SHIP PARTICULARS

The vessel is a trimaran of 6.5 m by 3.0 m from NEAC-INDUSTRY (shown in Figure 1) with main particulars listed in Table 1 and electronic connected architecture shown in Figure 4. The vessel is equipped with an RIM 6kW electric driven thruster of Hy.G Motors (shown in Figure 2). The energy pack has a 7,2 kWh (150 Ah) capacity, providing 1 – 3 hours of autonomy.

Figure 1. Development vessel for experimenting and testing, Living Lab France. Outside view (left) and ship bridge (right).

Table 1. Ship main particulars

Symbol	Unit	Description	portside hull	central hull	starboard side hull
L_{PP}	m	Length	5.40	6.40	5.40
B	m	Breadth	0.50	0.80	0.50
B_{total}	m	Total breadth		3.00	
T	m	Draught	0.20	0.20	0.20
∇	m^3	Displacement volume	0.27	0.78	0.27
C_B	-	Block coefficient	0.50	0.76	0.50
A_L	m^2	Longitudinal windage area		6.15	
A_T	m^2	Lateral windage area		11.00	
x_G	m	Longitudinal position of the centre of gravity (measured from midship)		-0.07	
y_G	m	Transversal position of the centre of gravity (measured from centreline)		0.00	
z_G	m	Vertical position of the centre of gravity (measured from keel, z+ pointing upwards)		0.52	

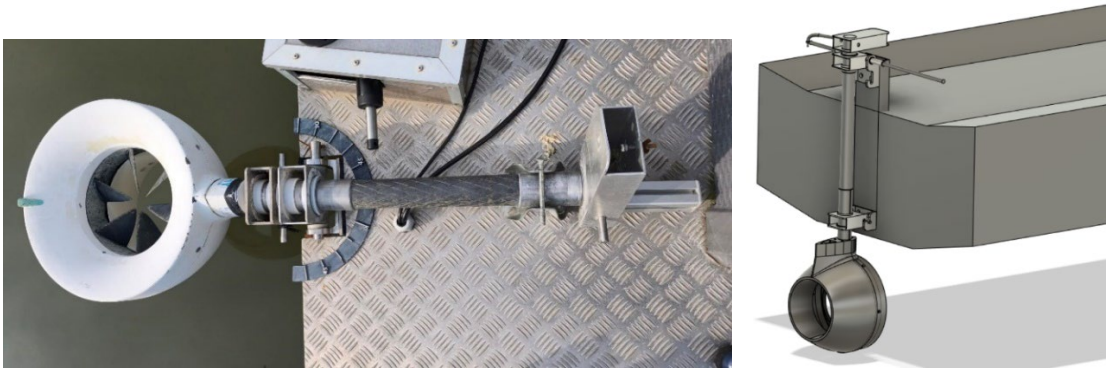

Figure 2. Hy.G Motors, RIM6kW - electric driven thruster lifted on the deck (left) and in operating position (right).

3.2 ENVIRONMENT

The Caen Canal is a 15km waterway connecting the port of Caen with the port of Ouistreham on the English Channel (La Manche). Traversing the municipalities of Hérouville-Saint-Clair, Bénouville, Blainville-sur-Orne and Ouistreham, this canal is considered a maritime zone, subject to a speed limit (RPP, 2024). Key features include three bridges (Fonderie, Colombelles, and Bénouville) and two locks in Ouistreham, each measuring 225m by 29m. The canal experiences a relatively small tidal range of 70-80 cm and low current velocities (< 0.1 m/s). With a consistent depth of 10 m and a width of 100 m. This controlled setting offers an ideal testbed for ship manoeuvring trials and autonomous vessel research.

The manoeuvres were executed in or near the Hérouville basin, as shown in Figure 3. The basin offers a free sailing area of approximately 200m by 300m, which is large enough for turning circle manoeuvres. This basin is almost unaffected by the current in the canal. However, the presence of traffic and moored vessels can introduce ship-generated waves and wind shielding effects respectively and influence the measurements. Acceleration tests and zigzag tests, requiring longer straight runs, were performed within the canal itself. This section is relatively sheltered from wind due to the presence of mature trees lining the canal banks.

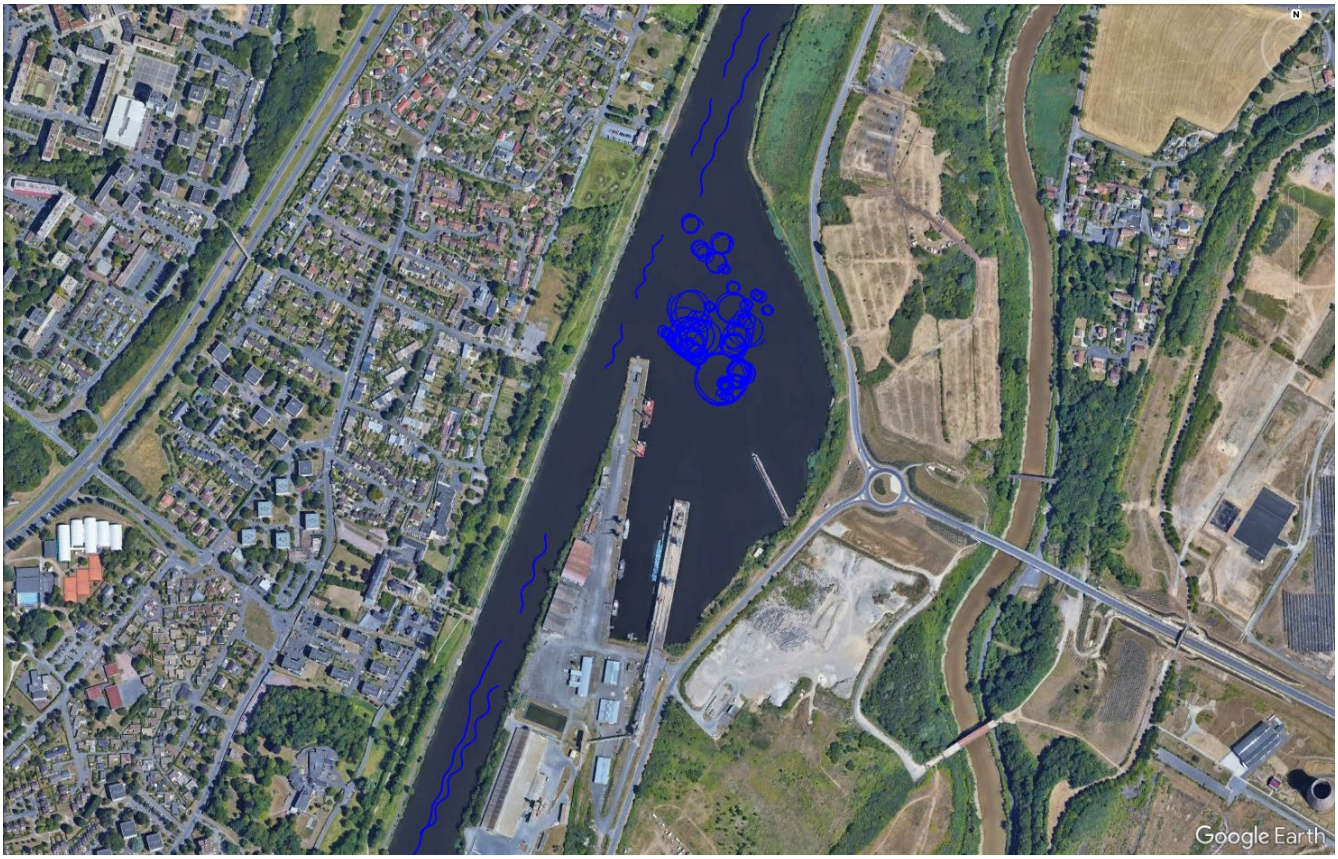

Figure 3. The Caen canal and the Hérouville Bassin in which the tests were performed. Examples of manoeuvres that were executed are shown in blue.

3.3 SHIP INSTRUMENTATION

The vessel was equipped with different sensors measuring position, heading, heave, roll, pitch and speed over ground with a compact satellite compass (Furuno SCX-20) installed on the roof of the vessel (as shown in Figure 4. This compass provides longitude, latitude at 5 Hz, heading, heave, pitch, roll, yaw at 10Hz, speed over ground at 1 Hz with 3 to 5 m accuracy for the positions, 0.1 m/s for the speed and 0.5° accuracy for heading/roll/pitch.

The relative wind direction and speed were recorded by an anemometer. The data are collected on the NMEA2000 network (Figure 7). A first pre-processing was executed by NEAC in France to select useful data and provide a user-friendly format to for further processing. The positions and speed were recalculated at the position of the centre of gravity. The data transfer was rather smooth and can be easily replicated on another vessel.

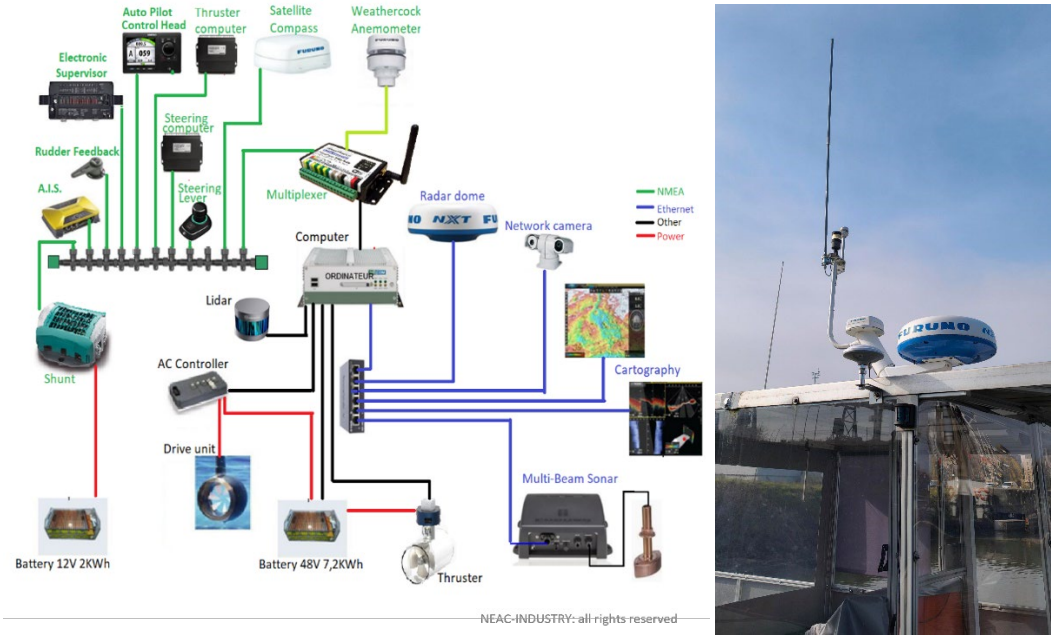

Figure 4. Connected electronic architecture of sensors on vessel (left) and sensors installed on the roof of the vessel (right).

3.4 TRIALS PROTOCOL

To identify manoeuvring characteristics, the full scale measurements have been conducted following the guidelines of relevant ITTC procedures, notably the procedure for full scale manoeuvring trials (ITTC, 2024a) and also the procedure for free running model tests (ITTC, 2024b), considering the size of the vessel. One can observe that the required accuracies were not met, which added challenges to the post-processing of the result.

A tailor-made test protocol was prepared for the manoeuvring trials in France. This test campaign was completed in three days. Prior to this campaign, several preliminary tests were conducted and analysed to check the quality of the data measured by the different sensors. This iterative process of testing, analysis, and refinement provided valuable feedback on measurement techniques and data processing, leading to significant optimization of the overall methodology and the upgrading of certain sensors.

It is worth noting that the rim-driven thruster (i.e. thrust magnitude and direction) was not controlled by an autopilot. At times, differences and delays were observed between the setting indicated by the protocol and the command given by the pilot.

Another complicating factor is that the loading condition was not always the same. Three persons were onboard during the measurements (cf. Figure 1), who did not always stay in exactly the same position. In addition, the amount and mass of the batteries onboard varied during the measurement campaign. Given the relatively small displacement of the vessel of 1.32 tons, the loading condition and particularly the trim of the vessel changed quite significantly.

One of the main challenges was to find a time window with good weather, i.e. no wind and no traffic. Moreover, the vessels relied on batteries which limited the testing time and maximum power.

3.4 (a) Acceleration tests

Acceleration tests are meant to give information on the self-propulsion points, i.e. what speed is reached with a given propeller setting and how fast this equilibrium is reached. The ship accelerates from rest (or a smaller speed) to the final speed on a straight line. The speed extends from the lowest (20% throttle) to the highest speed (100% throttle).

Speed ranges correspond to telegraph positions, 20%, 40%, 60%, 80% and 100% rpm setting. The runs were performed along and against current so that the speed through water could be determined. The acceleration tests were not corrected for wind as they were executed in the canal, which is quite sheltered from wind.

3.4 (b) Turing circle tests

Turning circle tests were performed to both port and starboard at approach speed with a maximum rim-driven thruster angle. During the turning circle tests, the ship completed a total heading angle change of 720 degrees, which corresponds to two full circles. This allows to investigate a possible drift motion due to wind or current. The tactical diameter, advance, and transfer derived from turning circle manoeuvres provide essential quantitative measures of a vessel's course changing ability (cf. Figure 5).

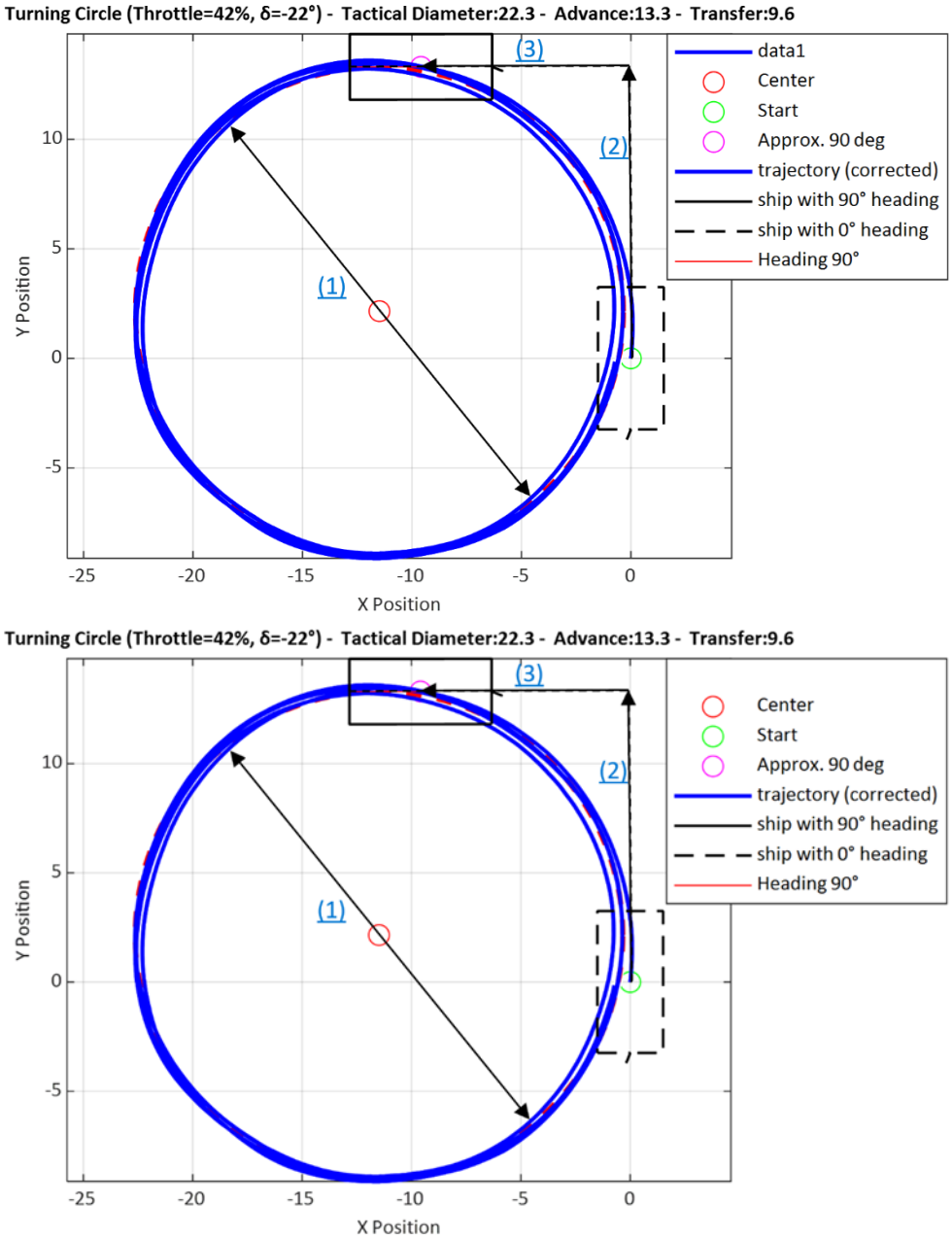

Figure 5. Example of turning circle manoeuvres with tactical diameter (1), advance (2) and transfer (3) characteristics.

3.4 (c) Zigzag tests

Zigzag manoeuvres involve alternating the azimuth angle by δ degrees when the ship deviates ψ degrees from its initial course. The rim-driven thruster angle is reversed multiple times (typically four) during each trial, causing the ship to yaw in alternating directions. The manoeuvre is defined by the azimuth angle(δ) and heading deviation (ψ), and denoted as δ/ψ (e.g., 10/10 or 20/20).

Zigzag tests were performed to both starboard and port direction to account for environmental factors, but starboard turns are of particular interest for emergency situations. A vessel may need to alter its course quickly. Therefore, the capacity to perform a zigzag manoeuvre is a crucial aspect of a ship's handling capabilities.

The zigzag manoeuvre begins with the azimuth angle at zero (i.e. straight ahead) and the vessel maintains a constant rpm setting. Subsequently, the rim-driven thruster is turned to the desired angle δ and held until the ship's heading changes by the desired angle ψ. The rim-driven thruster is then turned to opposite angle -δ and held until the vessel's heading reaches the heading -ψ. This process is then repeated.

The analysis of the results uses characteristic steering values plotted against δ to assess the ship's response.

3.4 (d) Random manoeuvres

With the increasing use of machine learning for system identification and model validation, random manoeuvring tests have gained prominence. Consequently, random navigation data were also collected. Drifting manoeuvres were performed to estimate both the speed of the current in the canal and to estimate the drift caused by the wind. However, accurate quantification of the drift was hampered by the difficulty in obtaining precise speed through water measurements.

4 DATA PROCESSING AND ANALYSIS

4.1 Data filtering and Pre-Processing

The different sensor data were resampled to 10hz and synchronized to a common timestamp. Any blank data entries were filled in by values recorded in the previous timestamp. Filtering techniques were applied to remove outliers and to smoothen the recorded data and filter out sensor noise. Only low frequency motions are of interest for manoeuvring in inland waterways (and not high frequency wave induced motions caused by passing ships), therefore a moving average with a window of 3s was applied to filter sensor noise.

The true wind speed and direction were recomputed based on the relative wind speed and direction measured onboard and the vessel’s speed and heading.

Due to the relatively large superstructure and the small draught, the vessel is very sensitive to wind and a large drift can be observed during a steady turn, as shown in Figure 6. The velocity components are then influenced by the drift (Figure 7). Although very small current velocities are present in a canal, current also had an influence on the ship when sailing close to the entrance of the basin in the channel. If a turn takes about 1 min to be completed, a current velocity of 0.1 m/s can already produce a drift of 6 m.

Mei et al. (2020) proposed a more advanced trials correction method suitable for varying environmental disturbances (Mei et al., 2020); however, this paper employs the simpler ITTC recommended approach of comparing vessel positions at identical headings during consecutive turning circles after a steady rate of turn is reached to accurately estimate and correct for drift due to wind or current, which is deemed sufficient for estimating basic turning circle parameters. This method assumes uniform current or wind creating steady and linear drift. Future work will incorporate wind forces into the system identification to model and reproduce drift from quasi-steady winds. For example, the drift during the turning manoeuvre shown in Figure 6 was estimated at 0.06 m/s in the direction of -90° from the initial heading.

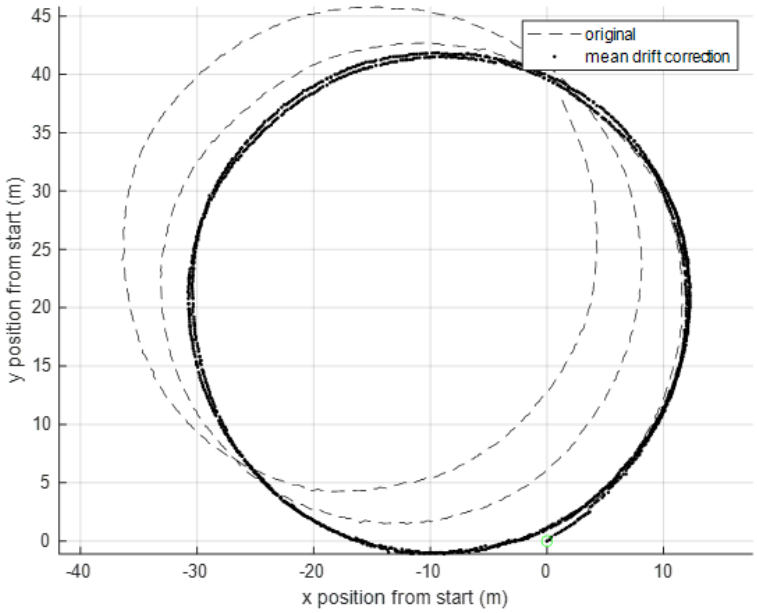

Figure 6. Correction of ship motions assuming mean drift due to wind and current.

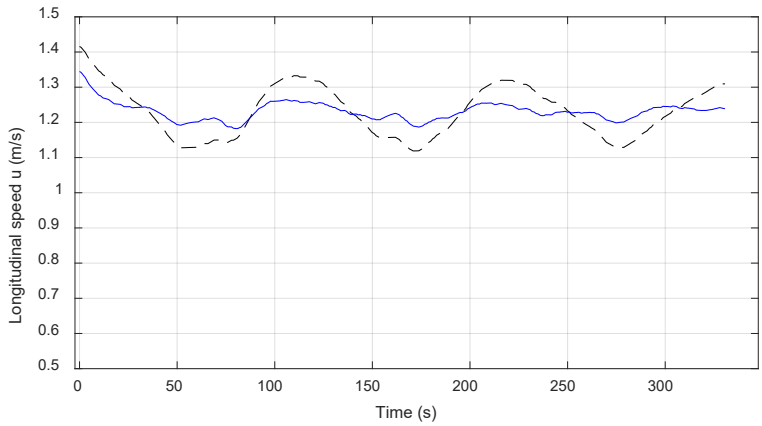

Figure 7. Comparison of measured longitudinal velocity before (dashed line) and after (blue full line) drift correction for a 10° turning circle to starboard side with 40% throttle

4.2 EXTRACTION OF THE MANOEUVRING CHARACTERISTICS

4.2 (a) Acceleration tests

Based on the different acceleration tests executed in upstream and downstream direction the maximum speed reached for different telegraph positions from 20% to 80% can be estimated, as throttle position (n) and speed (u) are proportional (as shown in Table 2 and Figure 8). The acceleration tests can also be used to estimate the reaction time to reach a steady speed related to inertial properties of the vessel.

Table 2. Results from acceleration tests.

	Speed (m/s)		
Throttle (%)	upstream	downstream	no wind
0	0.00	0.00	0.00
20	0.63	0.60	0.61
40	1.26	1.19	1.23
60	1.89	1.79	1.84
80	2.52	2.38	2.45

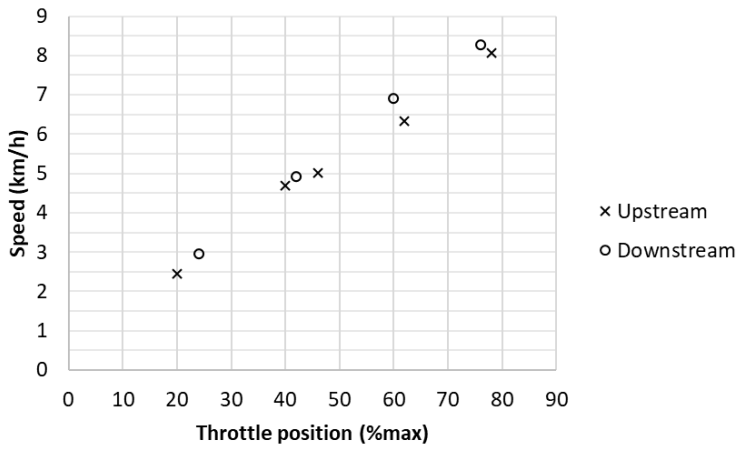

Figure 8. Speed in function of throttle position

4.2 (b) Turning circles

Figure 9 shows an example of output trajectories at 80% throttle for various rim-driven thruster orders. The manoeuvres begin immediately before rim-driven thruster application, following a period of straight, constant-speed running. Applying a thruster angle initiates sway and yaw motions until reaching a steady turn.

The final rate of turn gives an indication of the turning ability of the ship. The final speed gives an indication of the speed loss during a steady turn. The tactical diameter, representing the maximum width of the turning path (cf. Figure 5), is crucial for assessing the space required to execute a turn, particularly in confined waters or during collision avoidance manoeuvres. The advance, which is the distance the vessel travels in its original direction before reaching a 90° heading change, and the transfer, the perpendicular distance travelled during that same 90° turn, further refine the understanding of the ship's turning response. Consequently, accurate determination and analysis of these turning circle characteristics are paramount for ensuring safe and effective shipping in diverse operational scenarios.

Turning circle characteristics, corrected for drift, are presented in Figure 10. While large differences in transfer and advance characteristics are observed, the tactical diameter, final rate of turn and final longitudinal speeds shows clear trends as functions of throttle position and rim-driven thruster angle.

The influence of throttle position on tactical diameter appears limited. However, significant variations in tactical diameter were observed in repeated tests with 10° rim-driven thruster angles, suggesting sensitivity to environmental conditions. The difference between starboard turning circles at 80% throttle is attributed to substantial speed variations between the tests of November 6th and 7th, 2024. This speed difference may be due to the different test location, which spanned both the canal and the basin. Hence, current velocities are expected to differ. Furthermore, the tactical diameters obtained for 10° starboard at 80% and 60% throttle (tested on October 15th and November 7th, 2024, respectively) are relatively large compared to the 40% throttle case. This is also attributed to the test location near the basin entrance, where large moored ships create irregular wind speeds due to shielding effects. The 10° portside turning circle at 60% throttle also exhibited a larger tactical diameter than the 40% throttle case, likely due to significant wind speed variations during the turn.

These variations underscore the importance of accurate speed through water measurements given the uncertainty over environmental conditions. Unlike readily available speed over ground measured by GPS, speed through water is affected by dynamic factors (Dalheim and Steen, 2021). Traditional speed logs (e.g., impeller and doppler logs) are susceptible to these influences, leading to potential inaccuracies, especially in dynamic conditions or near other vessels and structures where wave reflections and flow interference occur. Therefore, careful consideration of environmental factors and appropriate sensor selection and placement are essential for reliable speed through water measurements.

The trials reported here were carried out in fairly good weather conditions with maximum current speeds of 0.1 m/s and mean wind speed of maximum 11 km/h with gusts of 18 km/h, but it can be seen from the analysis in Figure 10 that even then current and wind have an influence. Other factors, such as limited time windows imposed by canal and port traffic, and restricted space, may also render trials complicated. Consequently, these variations must be carefully considered when interpreting the derived manoeuvring characteristics from full scale trials. Non uniform current velocities can be corrected

by simply recalculated the speed through water if the current field is known. Wind forces need to be modelled to correct drift induced by non-uniform wind.

In practice, small angles are typically used for course corrections, rarely resulting in full turning circles. The differences observed between the repeated tests is also relatively small compared to the space occupied by a full turning circle, as shown in Figure 9.

Figure 10 gives an overview of the turning circle characteristics. Small asymmetry between portside and starboard side can be observed Figure 10. The lateral speed is around 0.1 m/s (positive toward starboard side) during the turns to portside and -0.05 m/s (negative toward portside) during the turn to starboard side and is not significantly influenced by the thrusters settings.

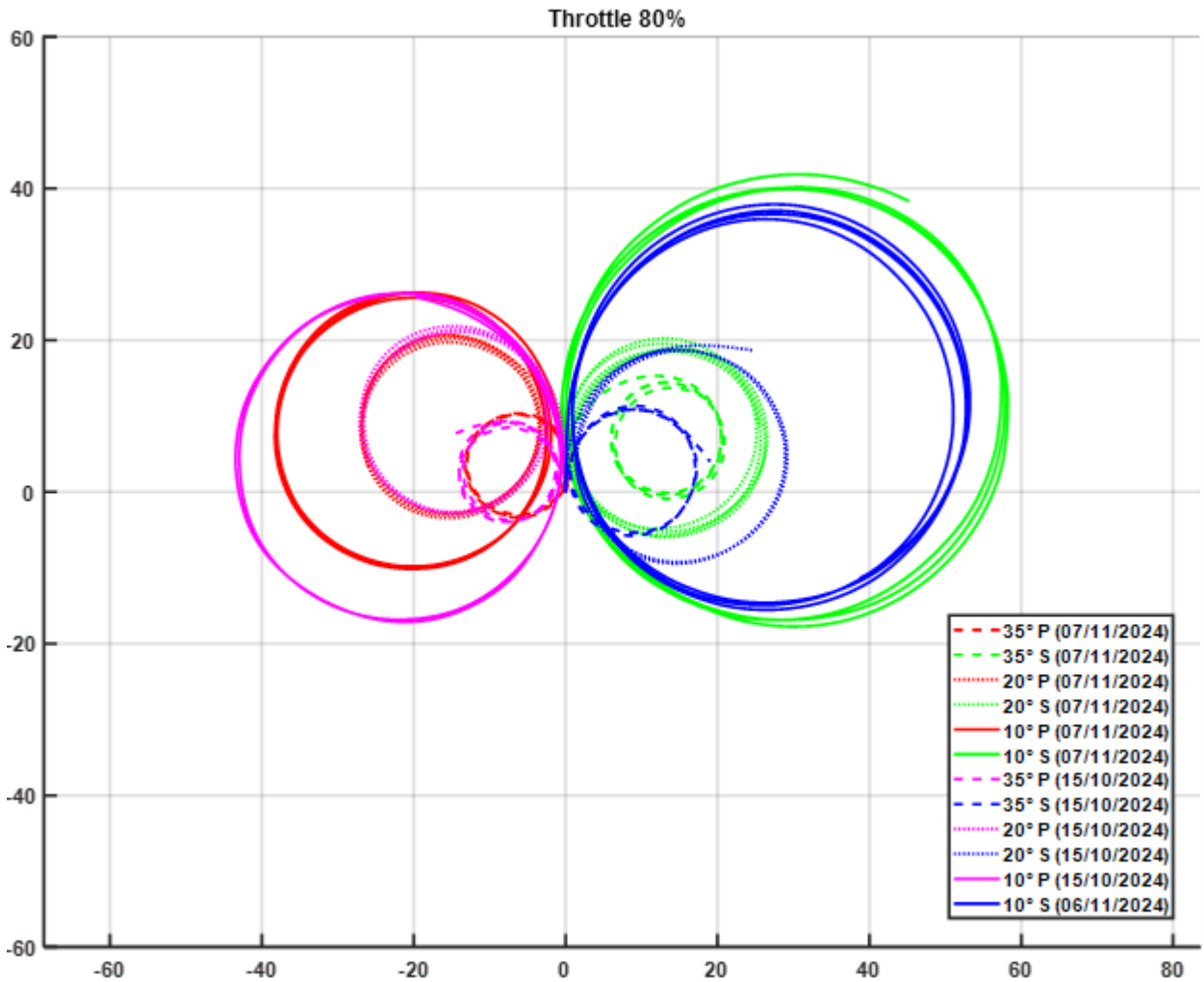

Figure 9. Trajectory of turning circles manoeuvres obtained with 80% throttle.

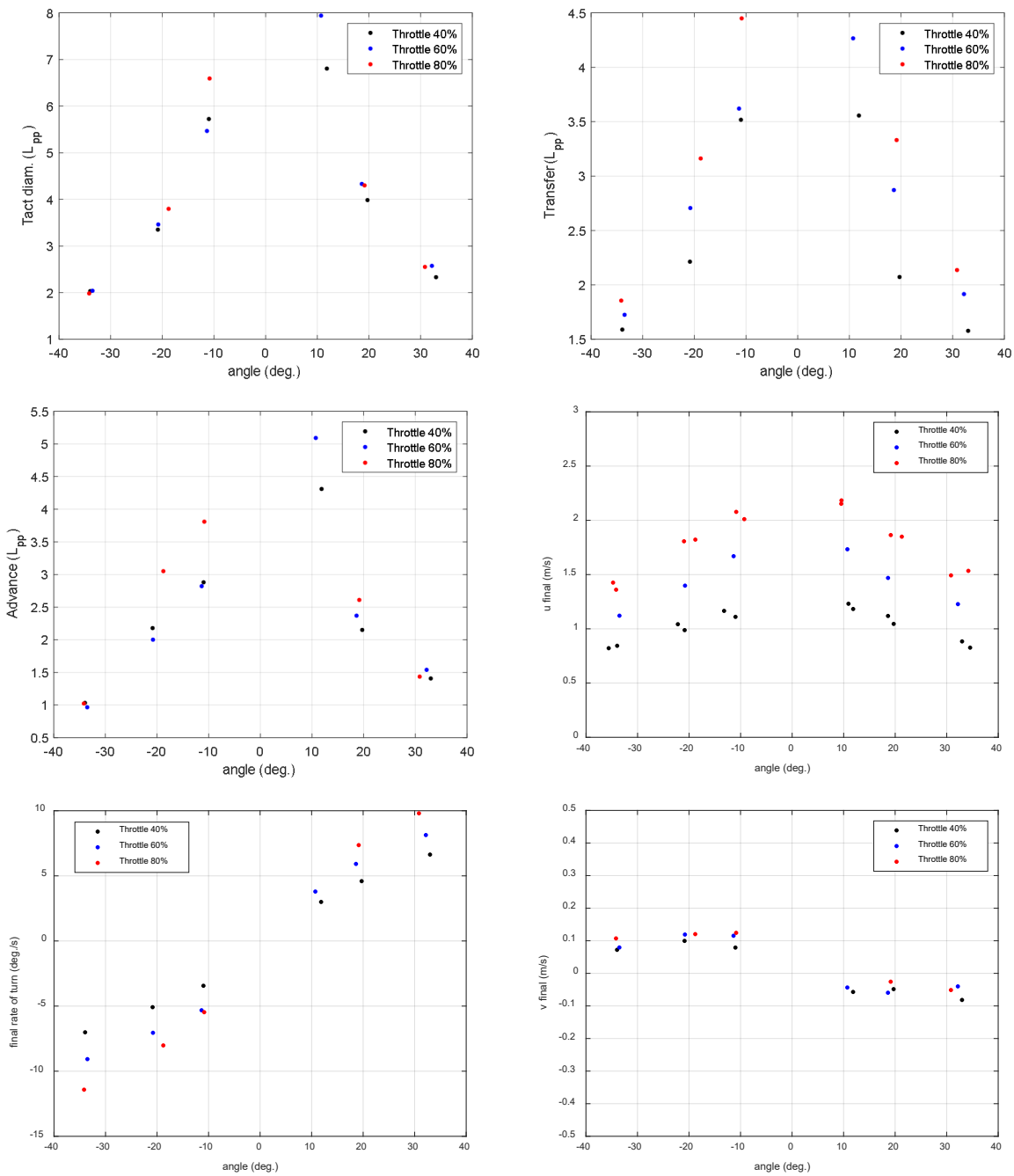

Figure 10. Turning circles characteristics.

4.2 (c) Zigzag tests

A key method for evaluating a ship's ability to maintain a desired course and control unwanted yawing motions is the zigzag test. This standard test involves applying alternating rim-driven thruster commands and provides essential information for ensuring safe navigation and preventing collisions. The test parameters, rim-driven thrust angles (δ) and heading angles (ψ), offer insight into the vessel's response to rapid steering inputs and its effectiveness in mitigating yaw oscillations. Important metrics obtained from this test include the initial and subsequent overshoot angles, the time taken to achieve a specific heading change, and the heading change rate. Lower overshoot values generally indicate better directional stability and improved yaw control, while higher values may point to an excessive response to steering inputs. These factors are particularly relevant when navigating in difficult environments, such as those with substantial wind or current effects, and are essential for performing quick avoidance actions. Zigzag tests outputs (rim-driven thruster angle, heading, rate of turn and trajectory) are also extensively used for system identification of manoeuvring models because of their ability to excite coupled motions, revealing nonlinear dynamic behaviour.

Figure 11 shows an example of 20/20 test from which the rate of turn time response and magnitude can be clearly identified in function of the rim-driven thruster angle order. The longitudinal speed loss is also clearly influenced by the lateral speed and the rate of turn.

During the first part of the manoeuvre, the longitudinal speed decreases due to non-zero thruster angle. In a second part, The speed oscillates around a mean value of about 1 m/s. The maximum speed loss is then reached when v and r reach both their maximum absolute value.

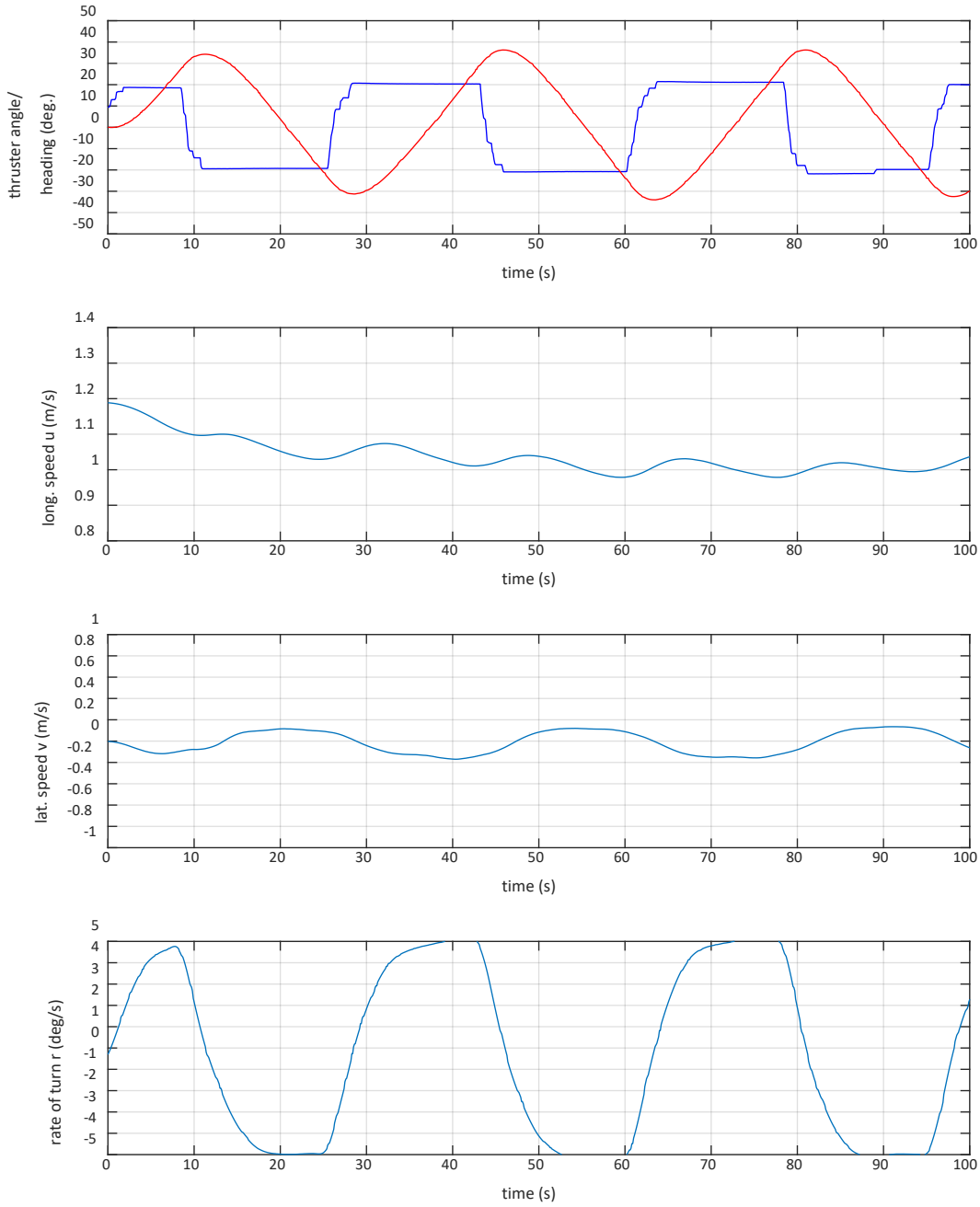

Figure 11. Example 20/20 zigzag test to starboard side - throttle 40%

10/10 and 20/20 zigzag tests starting to portside and to starboard side have been executed at 40%, 60% and 80% throttle. Figure 12 reveals substantial overshoots, with no discernible correlation between these overshoots and either rim-driven

thruster angles or throttle positions. This lack of a clear trend likely stems from human operation of the rim-driven thruster, which may introduce inaccuracies in timing and execution of the intended course alterations, as illustrated in Figure 11. Hence standard parameters such as overshoot angles and overshoot times may not be accurate. Additional tests with 10/05, 15/15, 20/10 and 30/30 have also been executed in order to refine the ship's initial steering response and its behaviour during more aggressive manoeuvres which can be used as input for system identification.

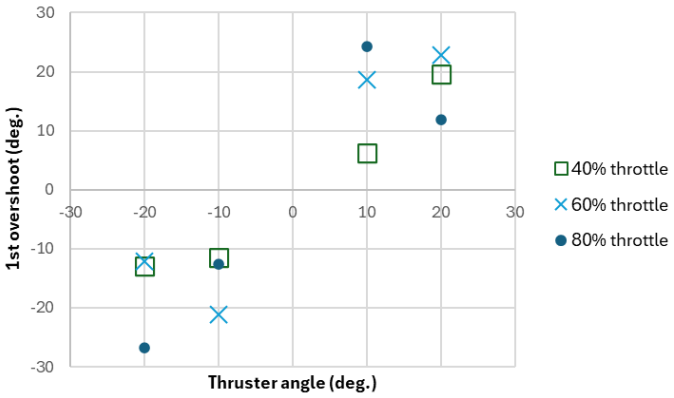

Figure 12. Zigzag test characteristics

5 FURTHER OUTLOOK

Future research will build upon these findings by focusing on several key areas. This includes refining the system identification process through simplified parameter estimation techniques to develop a simplified 3DOF manoeuvring model and exploring the influence of environmental factors such as wind, on the SFAZ's manoeuvring characteristics. The same methodology will be applied to a second LL in Belgium replicating the measurement setup on a different vessel. Furthermore, the derived manoeuvring models will be integrated into the vessel's autonomous control system to enhance its performance and robustness in challenging operational scenarios such as vessels train configuration. Investigations into an adaptive model that can be adjusted to varying design solutions are also planned. The use of such a model at a scale which is suitable for logistical and economic planning will also be investigated. This would allow making data-driven decisions to optimize vessel operations, reduce costs, improve safety, and minimize environmental impact.

6 CONCLUSIONS

The EU Horizon project FOREMAST aims at facilitating the movement of goods using Small, Flexible Automated, Zero-emission vessels (SFAZ). SFAZ is a concept that answers to the challenges facing inland shipping, aiming to revitalize small (urban) waterways offering environmentally friendly solutions.

This paper details the results of a comprehensive series of full-scale manoeuvring trials conducted using a SFAZ prototype. The trials were designed to assess the vessel's dynamic behaviour. The test program included turning circle manoeuvres, zig-zag tests, and acceleration/deceleration tests. These standard tests provide a framework for characterizing a vessel's manoeuvring characteristics. The data collected during these trials provided useful information for quantifying the SFAZ's manoeuvring performance.

The subsequent analysis of the collected data and simple sampling and filtering techniques as well as correction for drift due to environmental disturbances enabled the precise derivation of several key manoeuvring characteristics. These included essential parameters such as advance (i.e. the distance gained in the original direction when turning 90 degrees), the tactical diameter (i.e. the diameter of the turning circle), the overshoot angle (I.e. the angle the vessel deviates from the intended course after a rim-driven thruster input), the speed loss and the turning rate (i.e. the rate at which the vessel changes heading). These metrics are crucial for understanding and predicting the vessel's response to control inputs and external disturbances. Moreover, ship motions in the horizontal were accurately measured and show clear correlation with

rim-driven thruster and propeller. The obtained results establish a robust baseline for the future development and validation of a comprehensive manoeuvring model of the SFAZ.

Beyond the specific results for the SFAZ, this work also demonstrates the practical feasibility and significant cost-effectiveness of utilizing small inland vessels for conducting full-scale manoeuvring studies. Compared to traditional methods involving extensive model tests programs and/or CFD or even large crewed vessels, the use of small platforms offers substantial advantages in terms of reduced operational costs, increased flexibility in testing locations and conditions. This approach opens up new possibilities for efficient and frequent testing, accelerating the development and validation of advanced autonomous navigation and control strategies.

Building upon the findings presented in this paper, future research efforts will focus on several key areas. Firstly, the influence of various environmental factors, such as wind on the vessel's manoeuvring behaviour will be systematically investigated. Finally, a simplified, yet comprehensive, 3 degrees-of-freedom (3DOF) manoeuvring model will be developed. This model will balance computational efficiency with sufficient accuracy for practical applications, enabling prediction of the SFAZ's motion in diverse operational environment and configurations.

7 ACKNOWLEDGEMENTS

The authors gratefully acknowledge the invaluable support and expertise provided by the staff of NEAC Industry. In particular, we would like to express our sincere appreciation to their flexibility and their diligent efforts in operating the facilities and equipment during the experimental campaign. Their technical assistance, meticulous data collection, and logistical support were essential to the successful completion of the full-scale trials and the acquisition of high-quality data. In addition, former colleague Hongwei He is thanked for supervising the tests in Caen.

The research reported here has been carried out in the framework of HORIZON Project 101138261 — FOREMAST — HORIZON-CL5-2023-D5-01. The partners within FOREMAST are thanked for their feedback during the meetings.

8 REFERENCES

Bačkalov, I., Burmeister, H.-C., Isidorović, L., Jasa, J., Josipović, M., Kloch, K., Koimtzoglou, A., Krasilnikov, V., Krause, S., Mateienko, D., Nordahl, H., Reinach, N., 2024. Impact of automation and zero-emission propulsion on design of small inland cargo vessels. J. Phys. Conf. Ser. 2867, 012018. https://doi.org/10.1088/1742-6596/2867/1/012018

Barros, B.R.C. de, Carvalho, E.B. de, Brasil Junior, A.C.P., 2022. Inland waterway transport and the 2030 agenda: Taxonomy of sustainability issues. Clean. Eng. Technol. 8, 100462. https://doi.org/10.1016/J.CLET.2022.100462

CCNR, 2024. The labour market of the European inland navigation sector. Thematic report. Central Commission for the Navigation of the Rhine.

CCNR, 2022. An assessment of new market opportunities for inland waterway transport. Thematic report. Central Commission for the Navigation of the Rhine.

Dalheim, Ø.Ø., Steen, S., 2021. Uncertainty in the real-time estimation of ship speed through water. Ocean Eng. 235, 109423. https://doi.org/10.1016/J.OCEANENG.2021.109423

Delefortrie, G., Eloot, K., Lataire, E., Van Hoydonck, W., Vantorre, M., 2016. Captive Model Tests Based 6 DOF Shallow Water Manoeuvring Model, in: Proceedings of the 4th International Conference on Ship Manoeuvring in Shallow and Confined Water (MASHCON), 23 - 25 May 2016, Hamburg, Germany. Bundesanstalt für Wasserbau (BAW), Karlsruhe, Germany, pp. 273–286. https://doi.org/10.18451/978-3-939230-38-0

European Commission, 2021. Sustainable & smart mobility strategy. Putting European transport on track for the future.

Haugan, I., 2022. NTNU trials world's first urban autonomous passenger ferry [WWW Document]. URL https://norwegianscitechnews.com/2022/09/ntnu-trials-worlds-first-urban-autonomous-passenger-ferry/ (accessed 1.10.25).

ITTC, 2024a. ITTC - Recommended Procedures and Guidelines. Full Scale Manoeuvring Trials, 7.5-04-02-01. Revision 04.

ITTC, 2024b. ITTC - Recommended Procedures and Guidelines. Free Running Model Tests, 7.5-02-06-01. Revision 05.

Jaegler, A., Randrianarisoa, L.M., Yahyaoui, H., 2024. Policy decision-support for inland waterway transport in sustainable urban areas: an analysis of economic viability. Ann. Oper. Res. 1–19. https://doi.org/10.1007/S10479-024-06034-0/TABLES/5

Kloch, K., Kristiansen, J.N., 2024. The economic and environmental viability of green and autonomous ships in inland shipping ecosystems. J. Phys. Conf. Ser. 2867. https://doi.org/10.1088/1742-6596/2867/1/012030

Krause, S., Wurzler, L., Mørkrid, O.E., Fjørtoft, K., Psaraftis, H.N., Vilanova, M.R., Zis, T., Coelho, N.F., Van Tatenhove, J., Raakjær, J., Kloch, K., Billesø, M.B., Kristiansen, J.N., 2022. Development of an advanced, efficient and green intermodal system with autonomous inland and short sea shipping - AEGIS. J. Phys. Conf. Ser. 2311, 012031. https://doi.org/10.1088/1742-6596/2311/1/012031

Kriedel, N., Roux, L., 2024. The labour market in the European inland waterway transport sector, in: Workshop on the Inland Navigation Labour Market and Its Attractiveness. Strasbourg, France, pp. 1–25.

Mei, B., Sun, L., Shi, G., 2020. Full-Scale Maneuvering Trials Correction and Motion Modelling Based on Actual Sea and Weather Conditions. Sensors 2020, Vol. 20, Page 3963 20, 3963. https://doi.org/10.3390/S20143963

Paulauskas, V., Henesey, L., Plačiene, B., Jonkus, M., Paulauskas, D., Barzdžiukas, R., Kaulitzky, A., Simutis, M., 2022. Optimizing Transportation between Sea Ports and Regions by Road Transport and Rail and Inland Waterway Transport Means Including "Last Mile" Solutions. Appl. Sci. 2022, Vol. 12, Page 10652 12, 10652. https://doi.org/10.3390/APP122010652

Pauwelyn, A.S., Turf, S., 2023. Smart Shipping on Inland Waterways. In: Proceedings of PIANC Smart Rivers 2022. PIANC 2022. Lecture Notes in Civil Engineering.

Pourmohammad-Zia, N., van Koningsveld, M., 2024. Sustainable urban logistics: A case study of waterway integration in Amsterdam. Sustain. Cities Soc. 105, 105334. https://doi.org/10.1016/J.SCS.2024.105334

Raftis, C.C., Vanelslander, T., Van Hassel, E., 2023. A Global Analysis of Emissions, Decarbonization, and Alternative Fuels in Inland Navigation—A Systematic Literature Review. Sustain. 2023, Vol. 15, Page 14173 15, 14173. https://doi.org/10.3390/SU151914173

Rødseth, Ø.J., Wennersberg, L.A.L., Nordahl, H., 2022. Levels of autonomy for ships. J. Phys. Conf. Ser. 2311, 012018. https://doi.org/10.1088/1742-6596/2311/1/012018

Rolls-Royce, 2018. Rolls-Royce and Finferries demonstrate world's first Fully Autonomous Ferry [WWW Document]. URL https://www.rolls-royce.com/media/press-releases/2018/03-12-2018-rr-and-finferries-demonstrate-worlds-first-fully-autonomous-ferry.aspx (accessed 1.10.25).

RPP, 2024. Arrêté conjoint portant application du règlement particulier de police du port de Caen-Ouistreham.

Sutulo, S., Guedes Soares, C., 2024. Nomoto-type manoeuvring mathematical models and their applicability to simulation tasks. Ocean Eng. 304, 117639. https://doi.org/10.1016/J.OCEANENG.2024.117639

Sys, C., Van de Voorde, E., Vanelslander, T., van Hassel, E., 2020. Pathways for a sustainable future inland water transport: A case study for the European inland navigation sector. Case Stud. Transp. Policy 8, 686–699. https://doi.org/10.1016/J.CSTP.2020.07.013

Taylor, C., 2023. KONGSBERG successfully demonstrates autonomous vessel operations on Belgium's inland waterway network [WWW Document]. URL https://www.kongsberg.com/maritime/news-and-events/news-archive/2023/trial-of-autonomous-shipping/ (accessed 1.10.25).

Wang, W., Shan, T., Leoni, P., Fernandez-Gutierrez, D., Meyers, D., Ratti, C., Rus, D., 2020. Roboat II: A novel autonomous surface vessel for urban environments. IEEE Int. Conf. Intell. Robot. Syst. 1740–1747. https://doi.org/10.1109/IROS45743.2020.9340712

Wojewódzka-Król, K., Rolbiecki, R., 2019. The role of inland waterway transport in city logistics. Transp. Econ. Logist. 84, 103–114. https://doi.org/10.26881/ETIL.2019.84.09

World Economic Forum, 2020. The Future of the Last-Mile Ecosystem. Transition Roadmaps for Public- and Private-Sector Players.

9 AUTHORS BIOGRAPHY

Marc Mansuy holds the current position of research staff at the Ships and Marine Technology Division of Ghent University. Ship manoeuvring expert with 10 years of experience in nautical research. Proven ability to identify and solve bottlenecks in inland waterways and harbours using ship simulators. Expertise in navigation under bridges, turning manoeuvres, and ship meetings in narrow channels. Associated with the Knowledge Centre Manoeuvring in Shallow and Confined Water and member of PIANC WG 237.

Guillaume Delefortrie: naval architect (MSc, Ghent University 2001, PhD, Ghent University, 2007), associate professor at the Ships and Marine Technology Division of Ghent University, lecturer in charge of courses in marine hydrodynamics. Experienced in EFD based research, with focus point on ship manoeuvring in shallow and confined water. He has been a member of the 27*th*-29*th* ITTC Manoeuvring Committee. Member of the organization and scientific committees of MASHCON conferences since their creation (2009).

Maxim Candries is a postdoctoral researcher at the Ships and Marine Technology Division of Ghent University. A substantial part of his research involves inland navigation.

Alain Alliot is a co-founder and president of NEAC-INDUSTRY, an engineering French company developing Connected Autonomous Electric Navigation (NEAC) for inland and coastal waters. Has been managing small and medium-sized businesses and the activities of major industrial groups over 45 years. Held corporate offices in several different countries for 17 years. Contributed to developing new markets in technical composites and biomaterials, as well as managing the engineering and implementation of industrial production lines. Founded Normandie Mobilité Électrique, an organization dedicated to promoting electric mobility and federating eco-responsible initiatives in this field in Normandy, France. Held project management positions at Alstom Power, AXA/EMC and SAFRAN. Graduated from the École Nationale Supérieure d'Ingénieurs de Caen (ENSICAEN) and the Université de Caen Basse-Normandie.

Lionnel MESNIL is a co-founder and technical director of NEAC-INDUSTRY. Managed the company MARELEC ELECTRONICS NAVIGATION (involved in electricity, electronics and marine computing, professional training on real equipment & on navigation simulators, etc.). As a design engineer at THALES Airborne System and SEXTANT AVIONNIQUE, participated in exploratory research and development work on new waveforms for radar mapping (emission, reception and signal processing) and data acquisition systems for air/ground fire control on helicopters.
As head of department at THALES AVIONICS, led the development and implementation of simulators (airbus, rafale, mirage) and the integration of on-board radar systems. Was responsible for flight tests and radar on the Rafale aircraft (Istres air base) with Dassault Aviation and the DGA. Graduated from l'Institut Polytechniques des Sciences Appliquées (IPSA) in aerospace science and technology.

Inna Alliot is a co-founder, European Project and Communication Manager at NEAC-INDUSTRY. Participated in the setting up of international projects and consortiums to respond to several calls for tenders, particularly for the protection against lightning of the Chernobyl Arch, Ukraine and its associated equipment's. Graduated from Kyiv Slavonic University, Ukraine, master's degree in international relations with focus point on international policy analysis, translation and interpretation.

EVALUATING THE IMPACT OF WIND-ASSISTED SHIP PROPULSION ON THE MANEUVERABILITY OF A SUEZMAX TANKER

Gustavo L. de O. Santana, Ferdinando R. Freire, Maria E. F. Chame, Claudio M. Sampaio, Eduardo A. Tannuri, TPN-USP (Numerical Offshore Tank - University of São Paulo), Brazil

Lucia B. F. Logsdon, Nathalie Sanghikian, Petrobras Petróleo Brasileiro S.A., Brazil

EVALUATING THE IMPACT OF WIND-ASSISTED SHIP PROPULSION ON THE MANEUVERABILITY OF A SUEZMAX TANKER

GUSTAVO L. DE O. SANTANA[1], FERDINANDO R. FREIRE[1], JUNGEUI CHOI[1], MARIA E. F. CHAME[1], CLAUDIO M. SAMPAIO[1], EDUARDO A. TANNURI[1], LUCIA B. F. LOGSDON[2], NATHALIE SANGHIKIAN[2]
[1]TPN-USP, BRAZIL
[2]PETROBRAS PETRÓLEO BRASILEIRO S.A., BRAZIL

SUMMARY

Recent regulations introduced by the International Maritime Organization (IMO) have significantly impacted the naval indus-try, compelling designers to create more efficient ships to comply with minimum energy efficiency standards. Wind-assisted ship propulsion (WASP) has emerged as a promising solution, gaining widespread attention and adoption in many ships over recent years, with reported energy savings of up to 24% for tankers. However, the WASP technologies may affect a ship's maneuverability, leading to safety concerns during operations. Wind loads acting on a ship's hull are typically estimated using standard drag force formulations, with coefficients obtained from OCIMF (Oil Companies International Marine Forum) database curves (for tankers), wind tunnel tests, or computational fluid dynamics (CFD). Herein, the latter method was em-ployed to evaluate the aerodynamic forces on a tanker with and without WASP. A convergence study on spatial discretization was conducted to assess numerical uncertainty. These coefficients were incorporated into a mathematical model to estimate changes in hydrodynamic derivatives for different shallow water h/T ratios. This study investigated how implementing four rotors on a Suezmax tanker affects its maneuverability by evaluating standard maneuvers, including Zig-zag, Turning Circle, and Crash Stop tests in both deep and shallow waters. In this initial study, only a typical maneuver was assessed. For the loaded condition and moderate velocity, the maneuvering parameters showed slight variations between cases with and with-out WASP technology for zig-zag tests. In contrast, some notable aspects of the drift-away characteristics evaluated through the turning circle and a loss in stopping ability observed during the crash tests were identified when comparing both cases.

NOMENCLATURE

ALS	Air Lubrication System
CFD	Computational Fluid Dynamics
GCI	Grid Convergence Index
GHG	Greenhouse Gas
IMO	International Maritime Organization
ITTC	International Towing Tank Conference
OCIMF	Oil Companies International Marine Forum
SINTEF	Foundation for Industrial and Technical Research
SST	Shear Stress Transport
TPN-MM	Numerical Offshore Tank - Mathematical Model
TPN-USP	Numerical Offshore Tank - University of São Paulo
URANS	Unsteady Reynolds Averaged Navier-Stokes
VIV	Vortex-Induced Vibration
V&V	Verification and Validation
WAMIT	Wave Analysis Massachusetts Institute of Technology
WASP	Wind-Assisted Ship Propulsion

AD	Advance	$[m]$
A_L	Longitudinal area of the ship	$[m]$
A_T	Cross-sectional area of the ship	$[m]$
B	Breadth	$[m]$
C_X	Force Coefficient on the X-axis	[-]
C_Y	Force Coefficient on the Y-axis	[-]
C_Z	Moment Coefficient around the Z-axis	[-]
D	Depth	$[m]$

DWT	Deadweight	$[t]$
F_D	Drag Force	$[N]$
F_L	Lift Force	$[N]$
$F_{Richardson}$	Richardson extrapolation	$[N]$
F_{tot}	Total force acting on the ship	$[N]$
F_X	Forces Acting on the X-axis	$[N]$
F_Y	Forces Acting on the Y-axis	$[N]$
h	Water depth	$[m]$
H_D	Drift distance	$[m]$
k	Turbulent kinetic energy	$[m^2/s^2]$
L_{BP}	Length between perpendiculars	$[m]$
L_{OA}	Length Overall	$[m]$
M	Ship's Mass	$[kg]$
M_Z	Moment Acting on the Z-axis	$[Nm]$
N_Z	Yaw Moment	$[Nm]$
$r'c$	Non-dimensional rate of turn	[-]
T	Draft	$[m]$
TD	Tactical Diameter	$[m]$
V_C/V_0	Speed loss in the steady part of the turn	[-]
V_W	Relative Wind Velocity	$[m/s]$
∇	Displacement	$[t]$
β_C	Drift angle	$[^\circ]$
θ_W	Relative Wind Incidence Angle	$[^\circ]$
μ_D	Drift direction	$[^\circ]$
ρ	Fluid Density	$[kg/m^3]$
ω	Specific dissipation ratio	$[s^{-1}]$
ϵ	Rate of dissipation of turbulence kinetic energy	$[m^2/s^3]$

1 INTRODUCTION

Fossil fuels have raised awareness about the environmental impacts caused by their use. Numerous studies on clean energy and decarbonization have been published in this context, aiming to implement these solutions in various vehicles and devices. Commercial ships are responsible for a considerable amount of CO2 emissions among these vehicles. They are also central to decarbonization plans, particularly by International Maritime Organization (IMO), which envisions a zero CO2 emissions goal for these ships until 2050, as highlighted by IMO (2023). In this context, IMO (International Maritime Organization) suggests strategies for shipowners among the viable technologies for GHG (Greenhouse Gas) emission reduction; key measures include vessel speed and power reduction, devices to reduce required propulsion thrust (such as ALS (Air Lubrication System) and WASP (Wind-Assisted Ship Propulsion)), propulsion system optimization (such as gate rudders), and potential fuels, including ammonia, biofuels, electric power, fuel cells, hydrogen, and methanol.

A recent review conducted by the ITTC (International Towing Tank Conference) on the development of energy-saving technologies for the propulsion of commercial ships evaluated different devices, highlighting the high potential of the WASP. According to ITTC (2021), WASP can offer energy savings of up to 24%, with rotor sails (originally conceptualized by Anton Flettner) being frequently chosen for tankers. The rotor sails, also known as Flettner rotors, enhance a ship's propulsion by utilizing the Magnus effect, where the velocity of the incident wind interacting with the rotating sail creates a pressure gradient, generating a force directed toward the area of lower pressure when combined with higher wind speed (Nuttall et al. 2016).

Despite the potential of this technology to decrease fuel consumption, the integration of WASP could impact a ship's maneuverability, leading to safety concerns during operations. Maneuver simulations are essential for assessing a vessel's dynamic stability and response under operational conditions, addressing yaw checking ability, course-keeping ability, and initial turning/course-changing ability (ABS 2017). These assessments were conducted using TPN-MM (Numerical Offshore Tank - Mathematical Model), designed to analyze hydrodynamic, propulsive, wind, wave, rudder, ship-to-ship, bank, tug, and mooring forces, integrating them as needed. A key consideration that arises with the application of rotor sails is how to incorporate the aerodynamic forces of these devices on simulators. Typically, OCIMF coefficients are used to model aerodynamic forces, but this applies only to conventional vessels without wind-assisted devices. In the past years, coefficients obtained by virtual captive tests have been extensively employed since this approach allows for modeling the geometry and operational conditions of interest. Kume et al. (2022) state that for a Reynolds number of 10^6 or more, the aerodynamic coefficients of the ship should not be sensitive to velocity changes, followed by results from wind tunnel tests that show almost constant aerodynamic coefficients for the range mentioned.

Fuel consumption savings on vessels equipped with WASP technology depend on various factors, including their rotation, number of rotors, size, and arrangement on the deck. Wind forces, which vary with velocity and incidence angle, also affect the consumption, requiring a route evaluation. Given the many factors that can affect the efficiency of WASP ships, a method that is feasible in time and cost is favorable. In this context, virtual simulations are favorable instead of towing tanks or wind tunnel tests. CFD also benefits from conducting tests on full-scale Reynolds numbers, disregarding any errors when applying extrapolation methods from model scale to full scale. In this way, the coefficients can be ascertained without scaling effects. Further, the confined water effect, influenced by water depth-to-draft ratio, proximity to banks, vessel speed, and loading, significantly affects ship behavior. These factors, especially in shallow water, alter hydrodynamic coefficients and force distributions, making their accurate representation essential for understanding and simulating ship performance in restricted waterways.

Forsberg (2020) assessed the impact of cylindrical rotors on vessel maneuverability. This study was carried out in the simulator Transas virtual shipyard at Aboa Mare, with rotor force data provided by Norsepower. The study compared the standard maneuvers, turning circle, zig-zag, Williamson turn, and crash stop with and without rotors under constant wind conditions of $25m/s$ at a range of wind incidence. Results showed minor differences, such as higher speed reduction during maneuvers with WASP devices, and the author emphasized the importance of further studies involving varied rotor configurations. Sampaio et al. (2024) analyzed the wind pattern along the route of a 325,000 DWT ore carrier and simulated different apparent/relative wind conditions based on CFD (Computational Fluid Dynamics) to obtain the optimum rotational speed for the rotor sails for each condition. A numerical investigation was conducted by Azcueta et al. (2023) to investigate different numerical parameters in a virtual resistance test and 6-DoF simulations for a bulk carrier with WASP devices, including the turbulence model, the y+ value, domain size, spatial and temporal discretization, and scale effects. The numerical results were validated against the SINTEF (Foundation for Industrial and Technical Research) Ocean bulk carrier benchmark. The authors highlighted the importance of conducting verification and validation procedures, especially when investigating these new technologies. Additionally, they established some numerical guidelines to follow when conducting these tests. The mentioned studies confirmed CFD's applicability and effectiveness by achieving strong agreement between computational and experimental methods in reproducing maneuvers.

This paper describes the potential of using CFD to predict aerodynamic forces, mainly to analyze the WASP devices to improve vessel performance and acquire aerodynamic coefficients required to predict standard maneuvers. A convergence study on spatial discretization was conducted to assess the numerical uncertainty following the ITTC guidelines. Once the aerodynamic coefficients were ascertained, virtual simulations were conducted using an in-house mathematical model to assess the maneuverability of a Suezmax tanker ship in standard maneuvers in deep and shallow waters. This study gives an insight into how to approach a maneuver problem with these new devices in a ship maneuvering simulator.

2 ROTOR SAILS

The rotor sails technology was first implemented in 1925 on the Buckau ship, as shown in Figure 1. Since then, the technology has been the focus of many studies, both experimental and computational, regarding the decarbonization criteria set by IMO.

Figure 1: Photography of the first ship to implement rotor sails, the Buckau ship. Source: De Marco et al. (2016)

.

The basic concept behind the rotor sails is the Magnus effect; that is, once the rotating cylinder is exposed to wind, the air in contact with the cylinder will have its speed changed in such a way that from one side, the wind will experience a slowdown, while on the opposite side, the wind will be accelerated, generating a pressure gradient that will result in a force acting from the highest to the lowest pressure around the cylinder. This force is called lift, which in the context is expected to generate the majority of the auxiliary propulsion for the ship, while the other force generated by the wind is the drag, acting in the direction of the flow. These forces act perpendicular to each other and are called aerodynamic forces; in this sense, it is

expected that the composition of such forces acts in favor of the movement of the ship. Figure 2 illustrates the aerodynamic forces acting on a rotor sail.

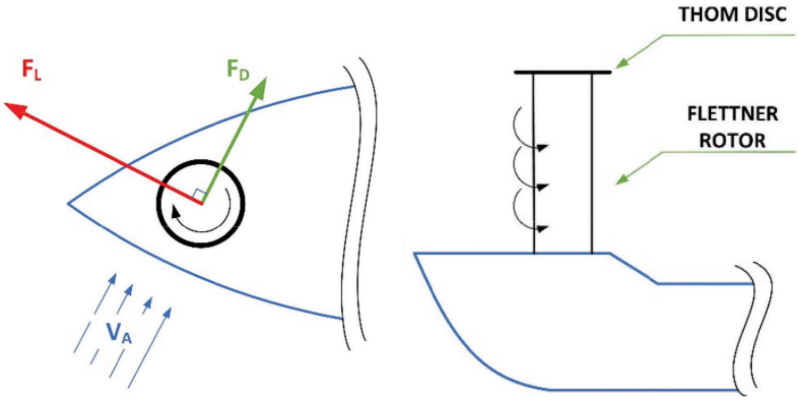

(a) (b)

Figure 2: (a) Illustration of the Magnus effect; Lift force (F_L), Drag force (F_D); (b) Illustration of a rotor sail on a ship from a side view. Source: Petković et al. (2021)

For a proper simulation of the aerodynamic forces acting on the rotor, the main parameters used for non-dimensionalization are shown in Figure 3. The angle of the incident wind is also vital for computing the aerodynamic forces; in this sense, an angle of 90° in relation to the ship's forward speed is the scenario with the maximum lift, although the drag can also contribute positively to the propulsion.

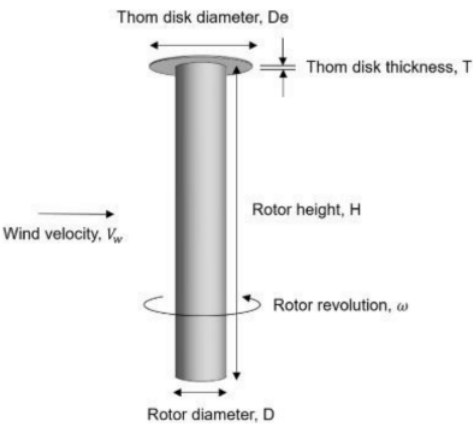

Figure 3: Main parameters used for non-dimensionalization of a flow around a rotor sail. Source: Kwon et al. (2022)

In order to account for the aerodynamic forces, non-dimensional parameters are also used, in this case, the force coefficient on the X-axis (C_X), force coefficient on the Y-axis (C_Y), as well as moment coefficient around the Z-axis (C_Z), which are nondimensionalized, respectively, by the Equation 1:

$$C_X = \frac{F_X}{\frac{1}{2}\rho V_W^2 A_T}, \quad C_Y = \frac{F_Y}{\frac{1}{2}\rho V_W^2 A_L}, \quad C_Z = \frac{M_Z}{\frac{1}{2}\rho V_W^2 A_L L_{BP}}. \tag{1}$$

F_X and F_Y are the forces acting on the X-axis and Y-axis, respectively, and M_Z is the moment acting on the Z-axis. ρ is the fluid density, V_W is the relative wind velocity, θ_W is the relative wind incidence angle, A_T is the cross-sectional area of the ship, A_L is the longitudinal area of the ship, and L_{BP} is the length between perpendiculars.

Considering that the ship in question is subject to a test maneuver, it is expected that the angle between the wind and the ship heading is changed constantly; in this sense, the impact of the rotors on the aerodynamic forces acting on the ship is evaluated, assessing the main parameters regarding the maneuverability of the ship. Rotor sails can generate thrust ranging from 175 to 385 kN, depending on their size (EMSA 2023). Numerous trials and simulations have been conducted to evaluate their potential in reducing fuel consumption and emissions. According to EMSA (2023), some key findings using rotor sails include the ships presented in Table 1:

Table 1: Average fuel savings measured on ships using rotor sails.

Ship Name	Ship Type	Nº of Rotors	Rotor Height [m]	Rotor Diameter [m]	Average Fuel Savings
M/V Annika Braren	General Cargo	1	18.0	3.0	2.0% - 4.5%
M/V Estraden	Ro-Ro	2	18.0	3.0	6.1%
M/V Copenhagen	Hybrid Ferry	1	30.0	5.0	4.0%
M/T Maersk Pelican	Tanker	2	30.0	5.0	8.2%
M/V SC Connector	Ro-Ro	2	35.0	5.0	20.0% - 25.0%
M/V Afros	Bulk Carrier	4	16.0	2.0	12.5%
M/T Sea Zhoushan	VLOC	5	24.0	4.0	8.0%

Based on: EMSA (2023)

According to Chou et al. (2021), fuel savings from rotor sails vary significantly, from 1% to 30%, depending on the type of vessel, its displacement, the number of sails, and the route conditions, based on information available up to 2019. European Commission et al. (2016) estimate a 5-17% power saving for higher speed vessels and a 7-23% power saving for lower speeds. However, the savings do not necessarily increase proportionally with the number of sails due to aerodynamic interactions between them, as highlighted by Bordogna et al. (2020). Route optimization and wind conditions can further increase savings, with potential gains ranging from 9% to 25% when voyage optimization is applied, as indicated by Paakkari et al. (2022). A parametric study made by Lu et al. (2020) showed that fuel savings depend on factors like ship type, speed, and route, emphasizing the need to adjust rotor usage based on these variables for maximum fuel efficiency.

Although this research aims to investigate the maneuvering of ships equipped with WASP, it is relevant to establish the potential of this technology and how fast it is growing and spreading in the naval industry. This fact underscores the significance of the proposed investigation and initiates a discussion on how these new technologies will be incorporated into the established mathematical models used for predicting standard maneuvers.

3 MATHEMATICAL MODEL AND TPN SHIP MANEUVERING SIMULATION CENTER

Marine simulators are used for many applications, such as predicting the vessel's trajectory in arbitrary maneuvers, training naval officers, and navigability analysis in restricted areas. These simulators replicate the bridge of a ship and allow up to 360° vision of the outside environment as viewed from the bridge. The landscape usually seen by the vessel's crew is represented by a graphical interface, ranging from low to high degree of sophistication. Motion prediction is given by the mathematical model and may include several phenomena. The hydrodynamic model will cover the physics involved in the interaction between ship and water, and the aerodynamic coefficients will model the air-structure interaction experienced by the hull top sides, superstructure, and WASP devices at a certain wind speed and direction.

The TPN-USP Ship Maneuvering Simulation Center is the largest of its kind in Brazil. The center comprises six simulators, three classified into full-mission, which means an immersive system with more than 270° of projection, and three tug stations. Figure 4 shows the main full-mission simulator. Furthermore, the simulators can be adapted to represent different kinds of vessels and operate individually or combined. The simulator center is a powerful facility that allows evaluating new routes, tugboat requirements, environmental scenarios, dynamic positioning systems, or even defining the optimum dimensions of ships during conceptual design, among other engineering questions. TPN-USP Maneuvering Simulation Center has its own mathematical model, TPN-MM, based on long-term experience in ship hydrodynamics; this has been described in detail in Tannuri, Rateiro, et al. (2014). It follows ITTC procedures for calibration and validation of maneuvering models.

When analyzing the ship maneuvering dynamics, a three-degree-of-freedom plane motion is typically adequate to describe this low-speed operation. The surge, sway, and yaw motions can be expressed as a function of the forward speed, acceleration, mass, and moment of inertia. The forces and motion can be described by Equation 2.

$$\begin{gathered}(M+M_{11})\dot{u}-(M+M_{22})vr-(Mx_G+M_{26})r^2=F_{X,tot},\\(M+M_{22})\dot{v}+(Mx_G+M_{26})\dot{r}+(M+M_{11})ur=F_{Y,tot},\\(I_Z+M_{66})\dot{r}+(Mx_G+M_{26})(\dot{v}+ur)+(M_{22}-M_{11})uv=N_{Z,tot}.\end{gathered} \tag{2}$$

In this case, M is the ship mass, M_{11} represents the ship-added mass in the surge direction and M_{22} the ship-added mass in the sway direction. M_{66} is the ship-added moment of inertia, and M_{26} is the coupled sway-yaw added moment of inertia. I_Z stands by the correspondent yaw moment of inertia, r is the yaw angular velocity, and u and v are the surge and sway velocities, respectively. F_X, F_Y, and N_Z are, respectively, the longitudinal force, lateral force, and yaw moment components.

Figure 4: TPN-USP maneuvering full-mission simulator.

The physical problem involves many components, and dealing with all these coupled phenomena is challenging. So, in this model, these are treated separately. Based on this, external loads can be decomposed into several forces, enlarging the variables shown before and expressed by Equation 3.

$$F_{tot} = F_{hydro} + F_{wind} + F_{wave} + F_{rudder} + F_{prop} + F_{ship-ship} + F_{bank} + F_{tug} + F_{mooring}. \quad (3)$$

The subscript *tot* represents the total force, which may be defined as the sum of potential and external loads. Due to the purpose of simulations, these forces should be pre-calculated as much as possible to enable the model to be used in real-time or even for fast-time simulations. Considering low-speed maneuvers, the hydrodynamic component is the most significant among these forces. An empirical method for modern commercial ships will be used to estimate the hydrodynamic coefficients, as proposed in Chame (2024). Regarding wave loads, potential theory using WAMIT (Wave Analysis Massachusetts Institute of Technology) is employed, see Lee et al. (2013). Ship-to-bank interactions are predicted following Silva et al. (2015), and the passing ship problem is based on Watai et al. (2018). Shallow water effects are computed as a correction applied to the hydrodynamic potential and non-potential loads. Two alternatives are available in the TPN-MM to model such a phenomenon, as shown in Tannuri and Martins (2018): pre-calculated coefficients or real-time corrections. Herein, the first method is employed; thus, these coefficients were incorporated into the mathematical model to estimate modifications in hydrodynamic derivatives considering different shallow water h/T ratios. Standard maneuvers were then evaluated by considering different h/T ratios and comparing the maneuvers of the Suezmax tanker with and without WASP.

Wind loads acting on the ship hull are defined considering the typical drag force formulation. The coefficients may be obtained from OCIMF database curves (for tankers), wind tunnel tests, or numerically. However, WASP devices will affect the ship's response, which was previously obtained for conventional ships (w/o WASP devices). In this sense, the aerodynamic inputs must be updated to incorporate these forces in the mathematical model. The method herein employed will be modified to accommodate the coefficients obtained numerically for ships with and w/o WASP devices. In this context, a CFD-based method for calculating the aerodynamic coefficients will be employed for both cases: ships without rotors and those equipped with them. This approach will be explained in the next section.

4 METHOD

4.1 CASE

A typical Suezmax tanker vessel is evaluated herein on the presence of a WASP system. The main characteristics of the vessel are given in Table 2.

Table 2: Main Characteristics of the Suezmax Tanker used in this study.

	Unit	Value
Lenght Between Perpendiculars (L_{BP})	[m]	264.0
Lenght Overall (L_{OA})	[m]	275.0
Breadth (B)	[m]	48.0
Draft (T)	[m]	16.0
Depth (D)	[m]	21.0
Displacement (∇)	[t]	166229
Deadweight (DWT)	[t]	157700

Four Flettner rotors were included to investigate the aerodynamic forces acting on the ship at different wind incidence angles. The rotors were arranged symmetrically, with two on the port side and two on the starboard side. The installation feasibility was assessed using the ship's general arrangement plan and the rotor sails' base dimensions, considering the presence of pipelines, walkways, winches, and other systems that could obstruct installation. This thorough analysis was crucial to determining the final symmetrical arrangement of the rotors on the main deck.

More complex geometry parts that could complicate the numerical simulation, like winches, anchors, and bollards, are not considered in the CFD simulation. Sampaio et al. (2024) performed simulations to account for the individual contribution of these parts, concluding that their contribution to the total drag was less than 0.37%. Additionally, for the present study, the contribution of the rotors to the aerodynamic forces on the ship can be up to 96% for 90° and 270° of relative wind incidence. As a result, the geometries used are simplified to avoid the complexity and computational time that some minor geometry components would add to the case. Figure 5 shows the geometries used for both cases, with and without rotor sails.

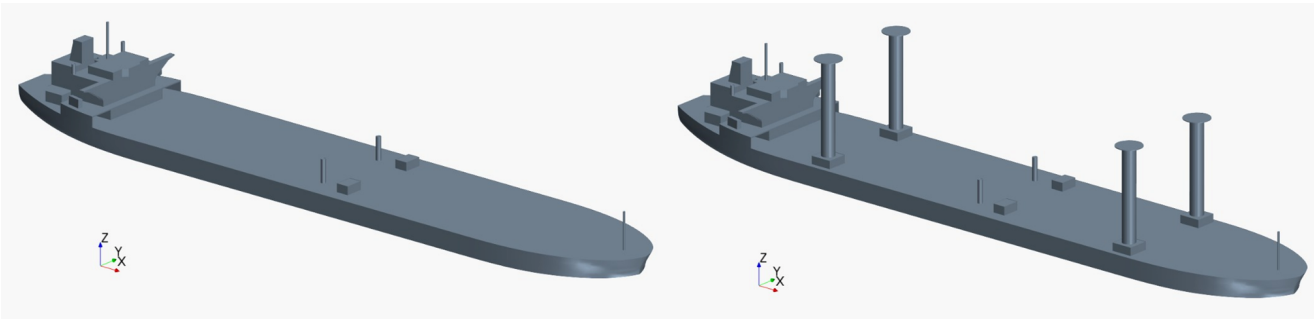

Figure 5: Simplified geometries used for the numerical simulation. On the left, the ship without rotor sails. On the right, the ship with the rotor sails in a symmetrical arrangement.

The rotor sails modeled for the numerical simulation are based on commercial sails, with an aspect ratio of 7, that is, the ratio between its height and diameter. The end disc thickness is 5% of the rotor diameter, and its diameter is twice the rotor diameter. The rotational speed applied to each rotor is identical, set as positive 100 rpm. Considering an incident wind and the ship in movement, there is a relative wind velocity to be considered, which results from the vector sum of the ship and the wind velocities. To simplify the analysis, the relative wind velocity is considered in the numerical simulation, in this case, 10 m/s. Table 3 presents the main characteristics considered in the analysis, including the air draft increase with WASP.

Table 3: Main Characteristics of the Analysis and Air Draft Change With and Without WASP.

	θ_W	V_W (m/s)	Air Draft (m)	Rotational Speed (rpm)
W/O WASP	0° to 180° (22.5° step)	10.0	35.6	-
W WASP	0° to 360° (22.5° step)	10.0	45.2	100

For proper orientation of the forces acting on the case, the coordinate system and the geometry parameters used are shown in Figure 6. As adopted by OCIMF, the wind incidence angle grows counterclockwise, with 0° on the stern, and the X-axis points to the heading of the ship. Additionally, the positive rotation direction points to the positive Z-axis.

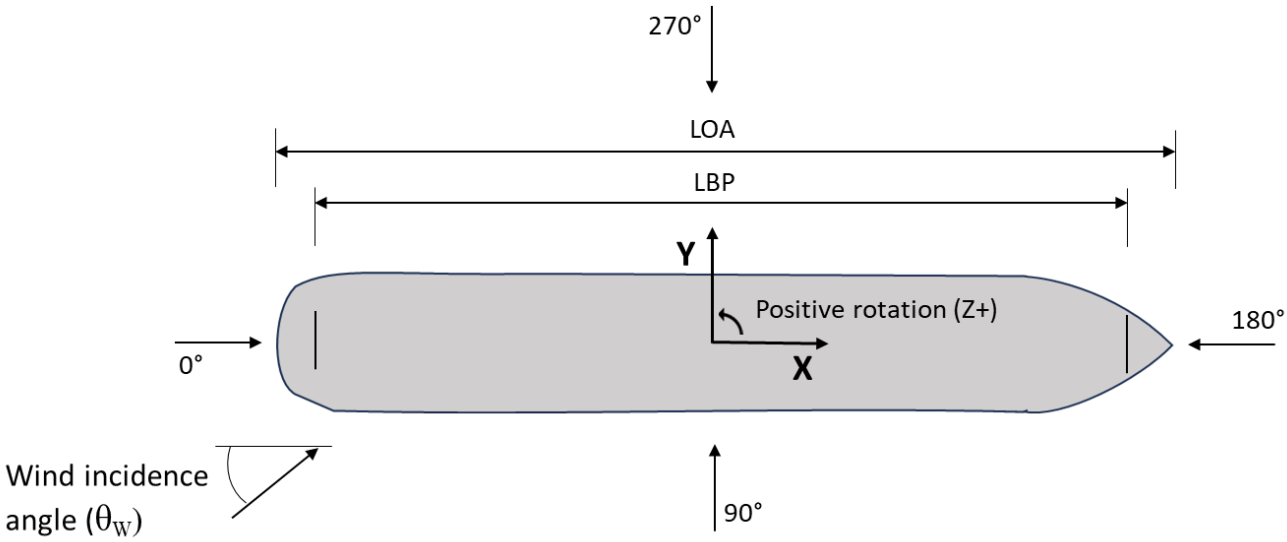

Figure 6: Coordinate system and geometric references used for the study.

4.2 NUMERICAL METHOD

The analysis is carried out through numerical simulation using CFD, employing the finite volume method, where the fluid domain is filled by a mesh with a large number of elements, allowing the Navier-Stokes equations to be integrated within the generated volumes. All the numerical setups and solutions of the CFD cases were obtained using the software Star-CCM+. At the lateral sides and top, a symmetrical boundary condition was employed. For the bottom boundary condition, i.e., water surface, assuming calm water, a no-slip wall condition is also applicable for a non-uniform velocity profile or a free slip wall for a uniform profile. However, a near-wall treatment is used for such cases, demanding more computational resources. Typically, the flow around a ship can be split into underwater and above-water domains for a low Froude regime. Since the problem herein investigated is interested only in the wind loads acting in the structures above a certain distance from the waterline, the physical phenomenon can be modeled considering that the velocity profile will be uniform in the interest region (rotors) and a symmetrical boundary condition can be applied to reduce the computation domain size. In this context, a uniform velocity profile was prescribed at the inlet plane, which was placed at $2L_{BP}$ from the midship, and the domain outlet was placed at $2L_{BP}$ from the midship. The computational domain spans $2L_{BP}$ between the port and starboard boundaries and has a vertical extent of 132 m. The boundary condition used for the geometry of the ship and the rotors is a no-slip wall, while the boundary conditions for the limits of the domain are shown in Figure 7a. To impose rotation on each rotor, the overset mesh method is applied, using a linear interpolation. Besides, the region near the vessel is shown in Figure 7b.

A turbulence model is required to properly represent the flow during the simulation. In order to achieve accurate results in an appropriate computational time, the k-ω SST (Shear Stress Transport) model is implemented. As mentioned by Azcueta et al. (2023), this model is highly efficient in predicting the forces at full-scale Reynolds number. The k-ω model aims to solve two transport equations: k, which is the turbulent kinetic energy, and ω, the specific dissipation rate. The chosen model, in particular, is a hybrid model, combining the k-ω model near walls and the k-ϵ model far from walls, assuring a more accurate solution and avoiding complex wall functions. Additionally, the simulations were conducted using the URANS (Unsteady Reynolds Averaged Navier-Stokes) model for a full-scale geometry with a time step of 0.01 s.

The V&V (Verification and Validation) processes in CFD simulations are fundamental for modeling the aerodynamic effects of Flettner rotors. Verification ensures numerical precision through grid convergence studies and error quantification, such as using GCI (Grid Convergence Index) and evaluating solution monotonicity. Validation confirms the physical accuracy by comparing simulation results against experimental data. However, for the study case selected, there is no benchmark case available to validate the solution. In this case, only the numerical uncertainty will be carried out; that is, a specific case is solved for three different meshes, which have their element base size refined by a systematic refinement ratio from coarse to medium and finer case, accounting for the numerical uncertainty and assuring the simulation is a proper representation of the physics embedded in the real case.

To evaluate the forces at different angles, simulations were conducted with relative wind angles ranging from 0° to 180° from the stern for the case without rotors (assuming a symmetrical ship). Due to the break of symmetry caused by the unchanged rotation of the sails, the angles from 180° to 360° are also considered for the case with rotors. The geometry remained stationary in all simulations, while the fluid domain was rotated in 22.5° increments to capture force variations across the full range of angles.

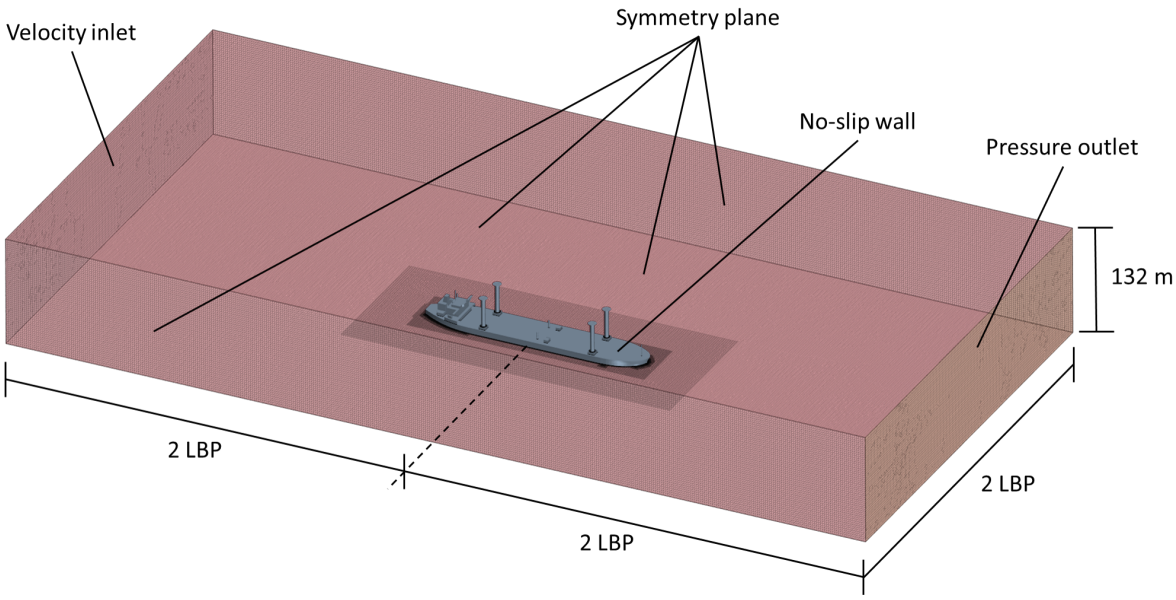

(a) Boundary conditions of the domain.

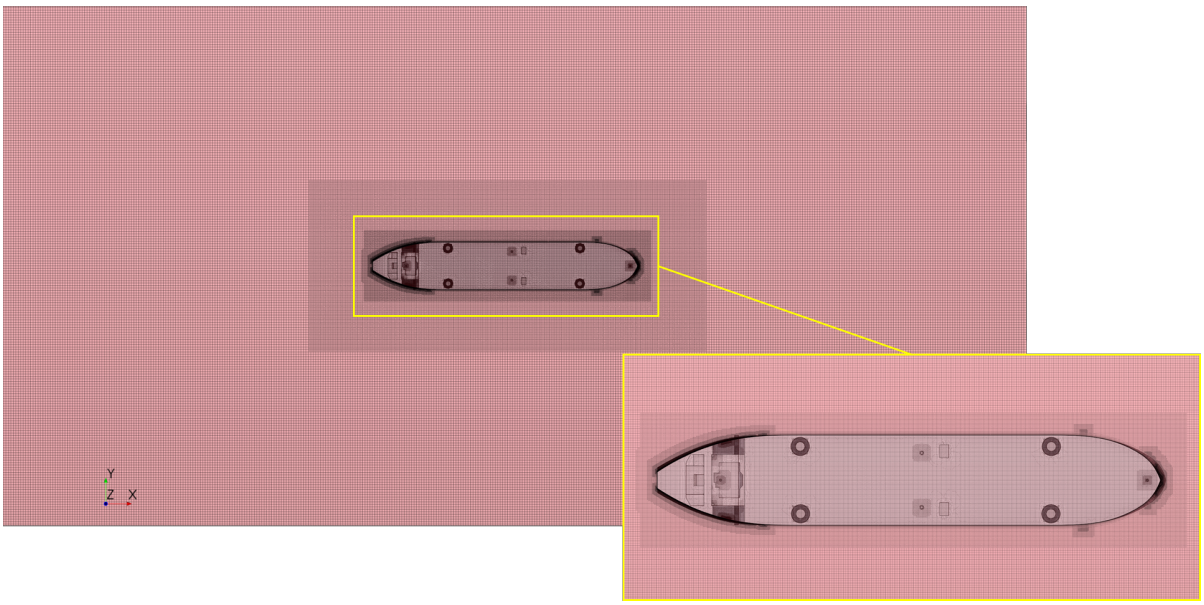

(b) Detailed mesh.

Figure 7: Computational domain.

5 RESULTS AND DISCUSSION

5.1 AERODYNAMIC FORCES

Using the described computational domain, the CFD results are generated for each desired angle. Once the forces are assessed and their coefficients calculated, the results are used in the mathematical model for the virtual simulation of the desired maneuvers. To strengthen the confidence in the CFD results, a verification is executed. The verification procedure was performed using three systematically refined meshes: G_3 (coarse), G_2 (medium), and G_1 (fine), with 13.91M, 17.07M, and 20.12M elements, respectively. The evaluated quantities included forces on the X and Y axes.

As a result of the verification procedure, the forces on the X and Y axes achieved oscillatory convergence. The numerical uncertainty achieved for F_X and F_Y is, respectively, 5.68% and 2.51%, considering the grid convergence index method described by Chame (2024).

Figure 8 illustrates the coefficients with and without WASP devices. Additionally, Figure 9 represents the same coefficients as a radar plot. Since the X-axis aligns with the ship's heading, Figure 9a illustrates the coefficients derived from total aerodynamic

thrust, highlighting the significant influence of rotor forces. The maximum ahead thrust occurs at relative wind angle of 67.5°. It is important to note that the peak lateral force coefficient (C_Y) is reached at a slightly greater angle when rotors are present compared to the reference case without rotors. Conversely, the absolute maximum moment (C_Z) is observed at 45 and 315 degrees the reference case and at 45 and 157.5 degrees for the case with rotors.

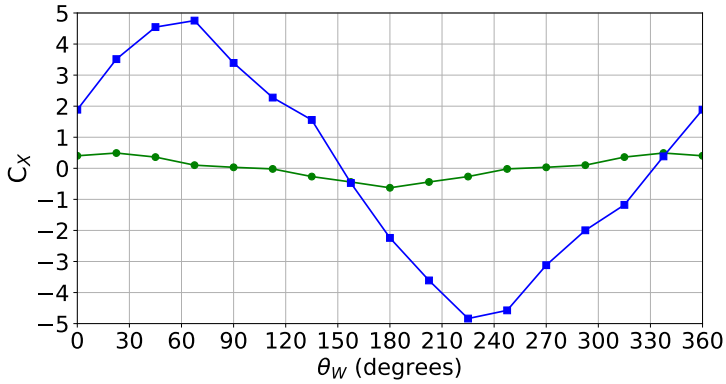

(a) C_X

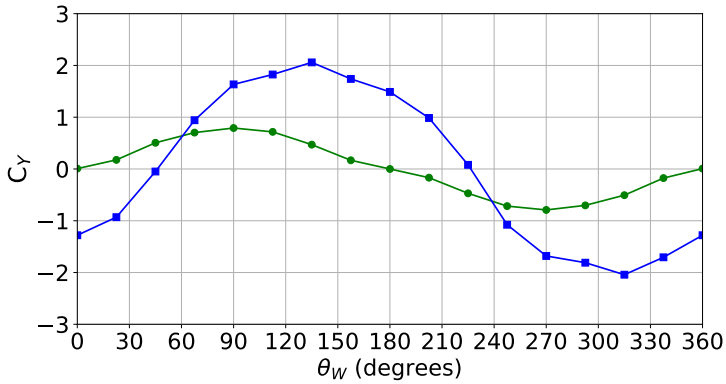

(b) C_Y

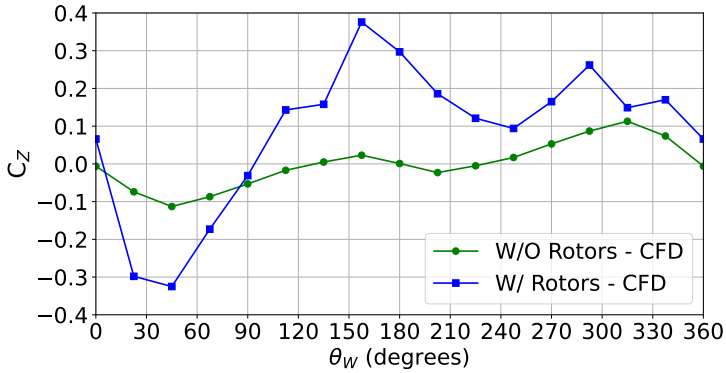

(c) C_Z

Figure 8: Total aerodynamic coefficients for the reference case (no rotors) and with rotors.

To further analyze the flow, the pressure field is evaluated on a section plane positioned 26m above the deck. As the wind flows around the rotor sails, a region of lower and a region of higher velocity are expected on opposite sides of the rotors due to their rotation, which causes velocity changes due to the friction with the incident wind, resulting in a pressure gradient that indicates the direction of the force. The pressure field generated for angles from 0° to 180° for the case with the rotor sails is shown in Figure 10. Starting from the upper left, at 0°, the incident relative wind angle simulated for each image is increased by 22.5°. By analyzing the dark blue areas of the pressure field, the direction of the total aerodynamic force on the rotors can be assessed. These areas represent regions of lower pressure, which contribute to the aerodynamic thrust the more they are aligned with the ship's heading; consequently, the higher lift contribution occurs for the case with 67.5° of relative wind incidence.

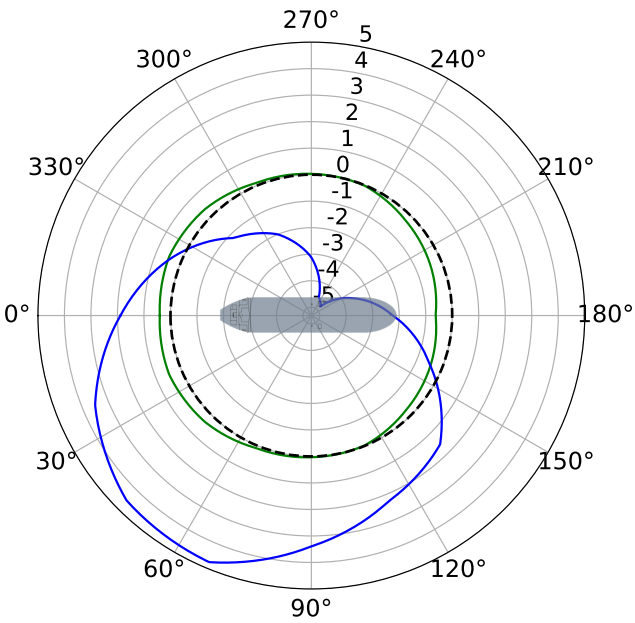

(a) C_X

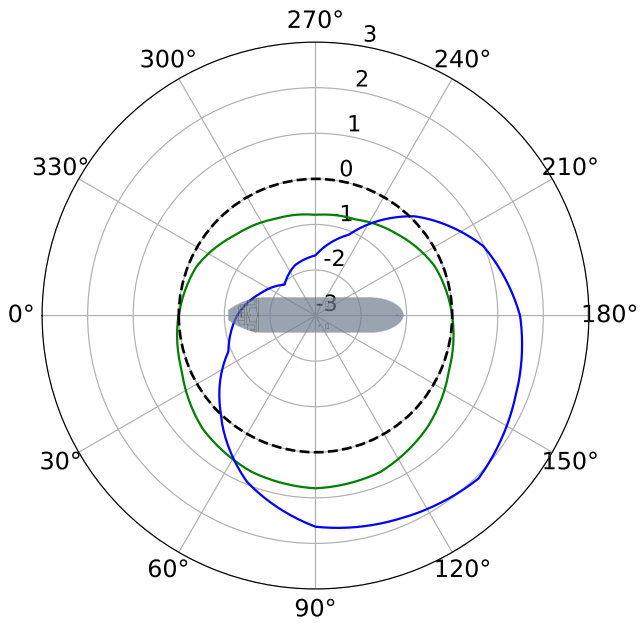

(b) C_Y

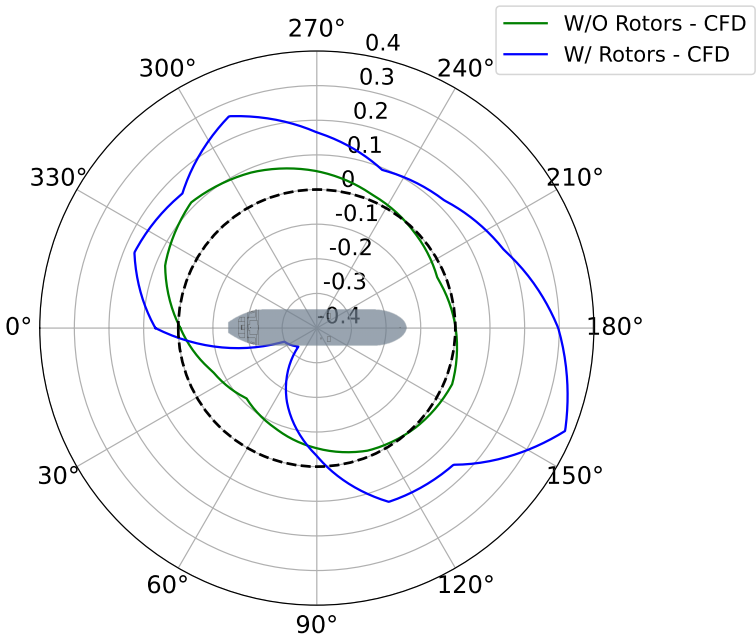

(c) C_Z

Figure 9: Radar Plot of the total aerodynamic coefficients.

It is possible to note that the highest thrust force magnitude, that is, the force aligned with the heading of the ship (positive X axis), occur at the angle of 67.5° of relative wind incidence for the cases with rotors. The total thrust for this angle results from the lift force with a minor contribution of the total drag force acting on the structures of the ship and on the rotors. If a comparison is made between the angles of 67.5° and 90°, the CFD results show that the contribution of the deckhouse and hull for the aerodynamic thrust is 5.35% and 3.75%, respectively. For these angles, Figure 11 details how the total force is composed on a rotor. Figure 9 shows that the forces on the Y-axis peak at 135°, which is caused by the large lateral area of the ship, mostly due to the hull and the direction of the lift force due to the rotors. In this case, the contribution of the deckhouse and hull sums for a total of 33.54% of the total aerodynamic force on the Y-axis, with the hull being responsible for 29.25% of this force.

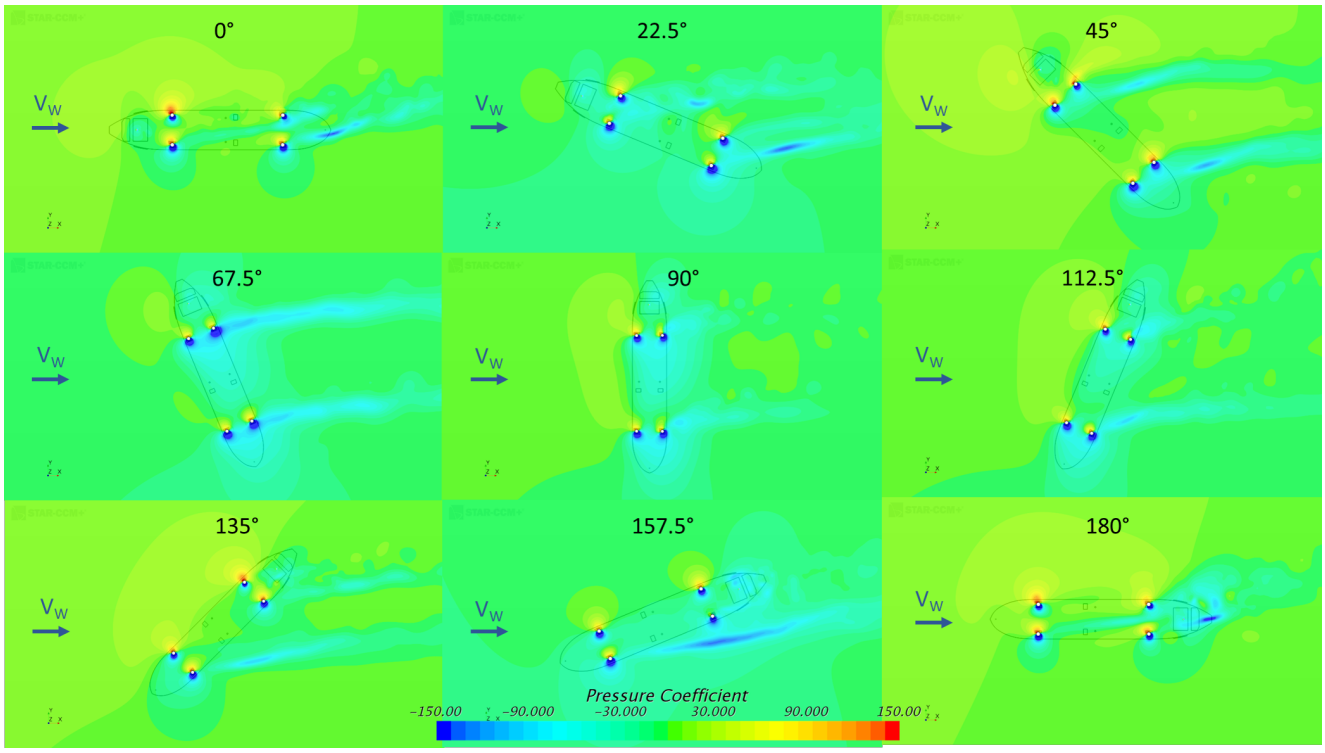

Figure 10: **Pressure field on a section plane of the cases simulated with rotors, from 0° to 180° of incident relative wind angle.**

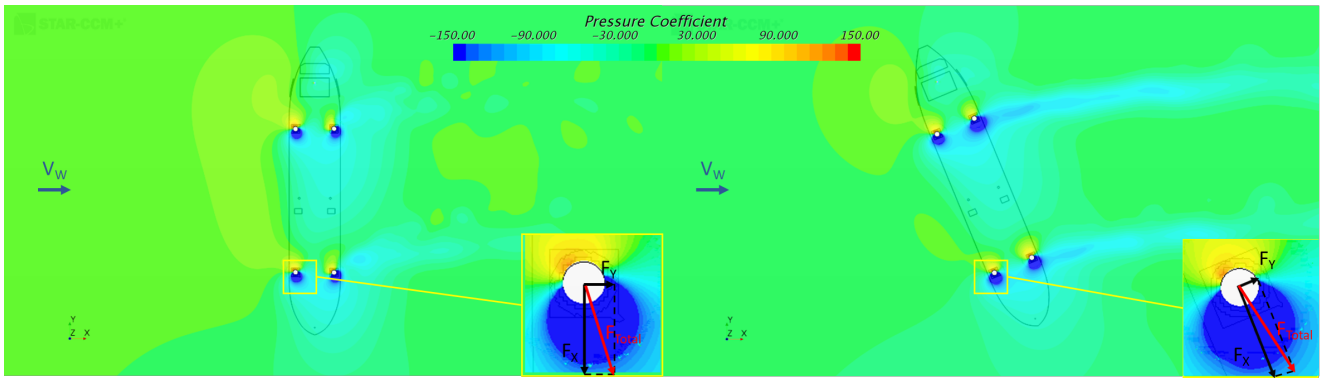

Figure 11: **Pressure field on a section plane 26m above the deck for cases with rotors with 90° (left) and 67.5° (right) of relative wind incidence.**

5.2 STANDARD MANEUVERS

This section aims to evaluate the maneuverability of the Suezmax tanker by comparing its performance with and without rotor sails at different wind speeds (V_W) and incidence angles (θ_W). The test maneuvers for which commercial ships are subject are defined by IMO and also well described in the ABS (2017). It is crucial to evaluate key maneuvering characteristics, including turning, course changing, yaw checking, initial turning and stopping ability, with and without rotor sails. The turning circle, zig-zag, and crash stop tests were conducted using TPN-MM to evaluate the ship's maneuvering performance.

A previous comparison can be drawn by analyzing the straight-ahead velocity at service speed. Figure 12 presents the speeds under varying V_W, θ_W, and h/T conditions. Notably, vessels equipped with rotors in deep water exhibit higher velocities. This effect results from the additional thrust the rotor generates with beam wind incidence, as illustrated in Figure 9. Given the higher C_X in the rotor-assisted case, the vessel maintains a higher speed. Specifically, at V_W = 20 m/s and θ_W = 90°, the vessel's velocity was approximately 1.4 m/s higher with rotors compared to the non-WASP configuration (21% increase).

After this first discussion about the advance speed, the manoeuvering characteristics can be assessed. Initially, the typical maneuvering characteristics of turning circle trajectories were compared for cases with and without rotors performed on starboard and port sides.

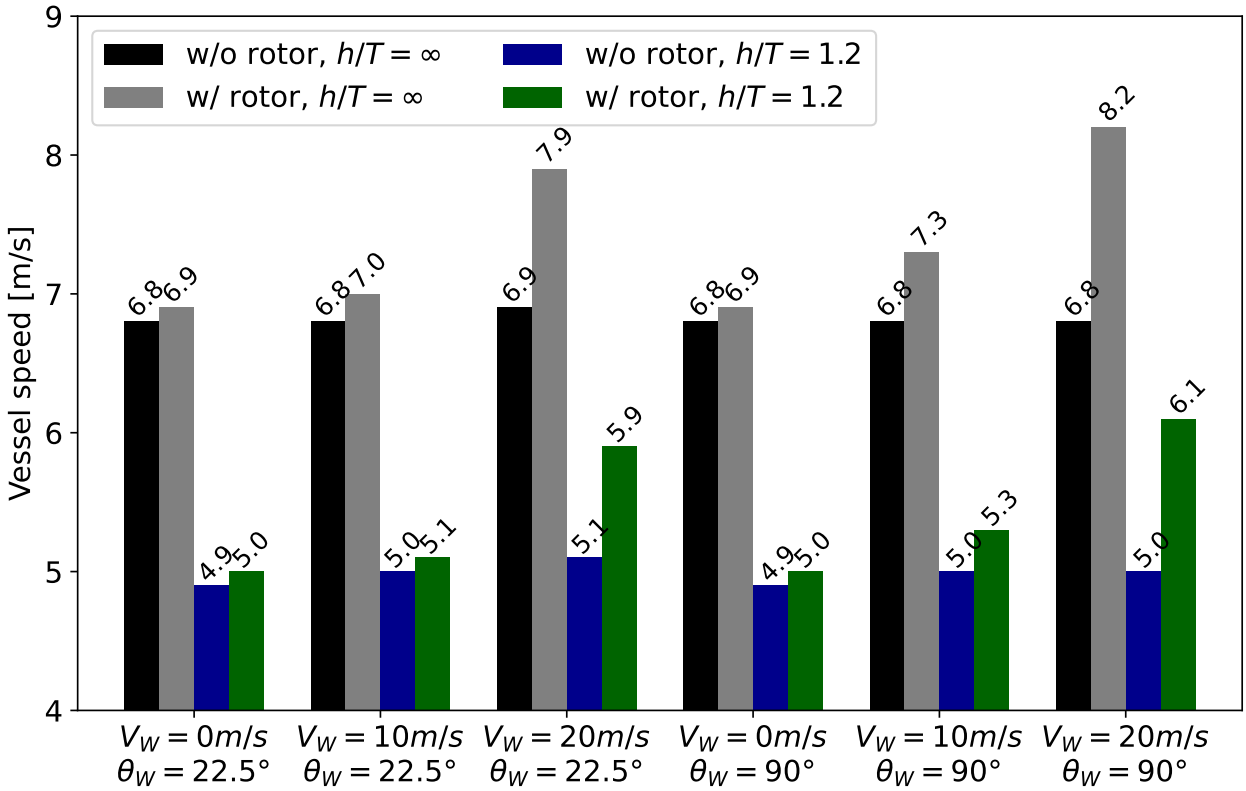

Figure 12: Straight-ahead velocity at different V_W and θ_W.

Table 4 presents, in the upper section, the turning circle main parameters (relative to the first turn): Advance (AD), Tactical Diameter (TD), non-dimensional rate of turn ($r'c$), speed loss in the steady part of the turn (V_C/V_0), and drift angle (β_C) for all tests conducted. An average difference of roughly 5% is observed for all parameters when comparing the cases with and without the rotor at a wind speed of 10 m/s. This average difference rises to about 17% at a wind speed of 20 m/s.

Table 4: Maneuvering characteristics from the turning circle in windy conditions.

	Cases															
	1	2	3	4	5	6	7	8	9	10	11	12	13	14	15	16
Side	SB	SB	SB	SB	SB	SB	SB	SB	PS	PS	PS	PS	PS	PS	PS	PS
Rotor		x		x		x		x		x		x		x		x
V_W [m/s]	10	10	20	20	10	10	20	20	10	10	20	20	10	10	20	20
h/T	∞	∞	∞	∞	1.2	1.2	1.2	1.2	∞	∞	∞	∞	1.2	1.2	1.2	1.2
Turning Circle Characteristics																
AD/L	3.45	3.60	3.46	3.84	3.63	3.51	3.58	4.15	3.45	3.53	3.49	3.72	3.66	3.80	3.77	4.28
TD/L	3.57	3.71	3.50	3.93	4.78	4.83	4.66	5.63	3.64	3.75	3.69	4.04	4.86	5.06	4.96	5.69
r'_c	-0.79	-0.72	-0.79	-0.60	-0.51	-0.47	-0.51	-0.39	0.79	0.77	0.80	0.69	0.50	0.48	0.50	0.43
$\frac{V_C}{V_0}$	0.28	0.30	0.28	0.35	0.50	0.52	0.50	0.54	0.28	0.29	0.28	0.33	0.50	0.51	0.50	0.54
β_C	26.25	24.61	26.00	21.28	8.91	8.44	8.85	7.24	-26.31	-25.09	-26.17	-22.33	-8.92	-8.47	-8.84	-7.50
Drift-Away Characteristics																
H_D/L	0.17	0.15	0.50	0.48	0.12	0.05	0.44	0.25	0.14	0.49	0.48	1.33	0.10	0.36	0.41	1.28
μ_D	103.5	52.9	107.7	70.1	-68.3	-116.4	-162.1	-87.8	-99.7	-160.6	-153.4	-168.3	133.1	166.6	161.0	155.8

Notes: SB stands for starboard and PS means portside.

The presence of wind induced a noticeable drift in the vessel's trajectory for the next turns. In the absence of wind and rotors (the reference case), turns were nearly concentric. However, this pattern was disrupted when wind was introduced. Figure 13 illustrates this difference, highlighting the trajectory of the case with rotors and a 20 m/s, 90-degree wind. The vessel's path deviates significantly from the reference trajectory (black line), exhibiting both an angular displacement and a lateral shift. These deviations are quantified by two "drift-away characteristics" as defined by Quadvlieg et al. (2023).

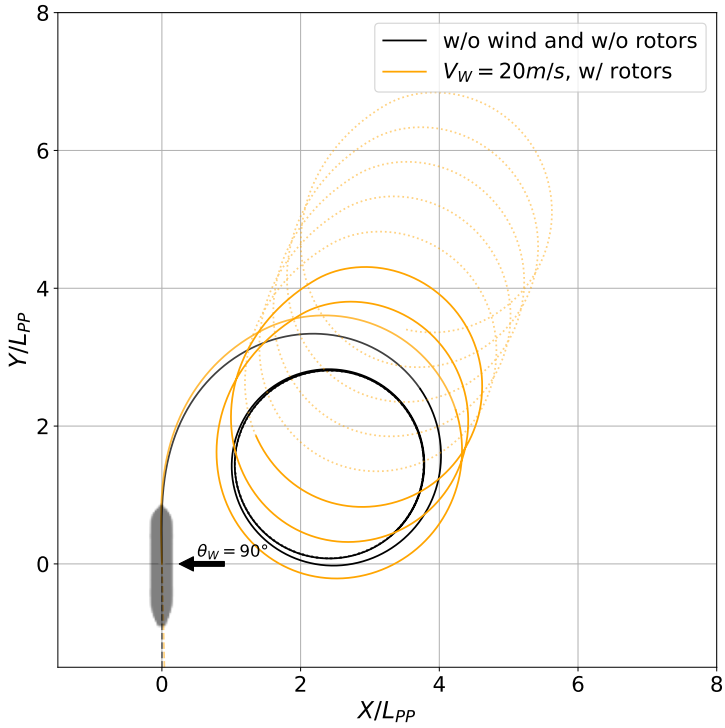

Figure 13: Turning circle test for a reference case (no wind, no rotors) and WASP vessel (beam 20m/s wind).

Due to the lack of procedures for addressing maneuvering tests under wind conditions, the same approach introduced in the last SIMMAN Conference Quadvlieg et al. (2023) for turning circle in waves will be employed herein. Figure 14 shows the eleven points used to evaluate the drift-away behavior for an example case.

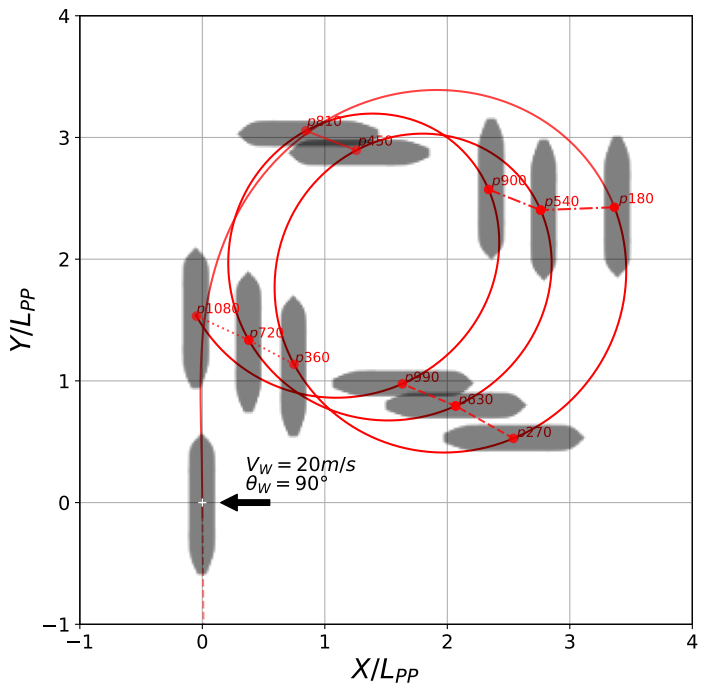

Figure 14: Drift-away analysis.

Both distance and angle between these points are computed to obtain the final parameters: drift distance (H_D) and drift angle (μ_D). Equation 4 describes the Euclidean distance calculation $(H_{D(\theta+360^\circ)-\theta})$ using the angle θ starting from 180° to 1080° and the drift direction $(\mu_{D(\theta+360^\circ)-\theta})$ determined by the angle between those two points.

$$H_{D(\theta+360^\circ)-\theta} = \sqrt{(x_{\theta+360^\circ} - x_\theta)^2 + (y_{\theta+360^\circ} - y_\theta)^2}, \qquad \mu_{D(\theta+360^\circ)-\theta} = \text{arctan}\,(x_{\theta+360^\circ} - x_\theta, y_{\theta+360^\circ} - y_\theta) \tag{4}$$

The procedure outlined above was applied to assess three distinct weather conditions: no wind, V_W = 10 m/s, and V_W = 20 m/s. Simulations were conducted for vessels both with and without rotors under each condition, and the resulting trajectories are presented in Figure 15. Maneuvers to both starboard and portside were performed using the TPN-MM. Table 4 summarizes the maneuvering characteristics derived from the turning circle in windy conditions. These values enable the evaluation of drift-away characteristics.

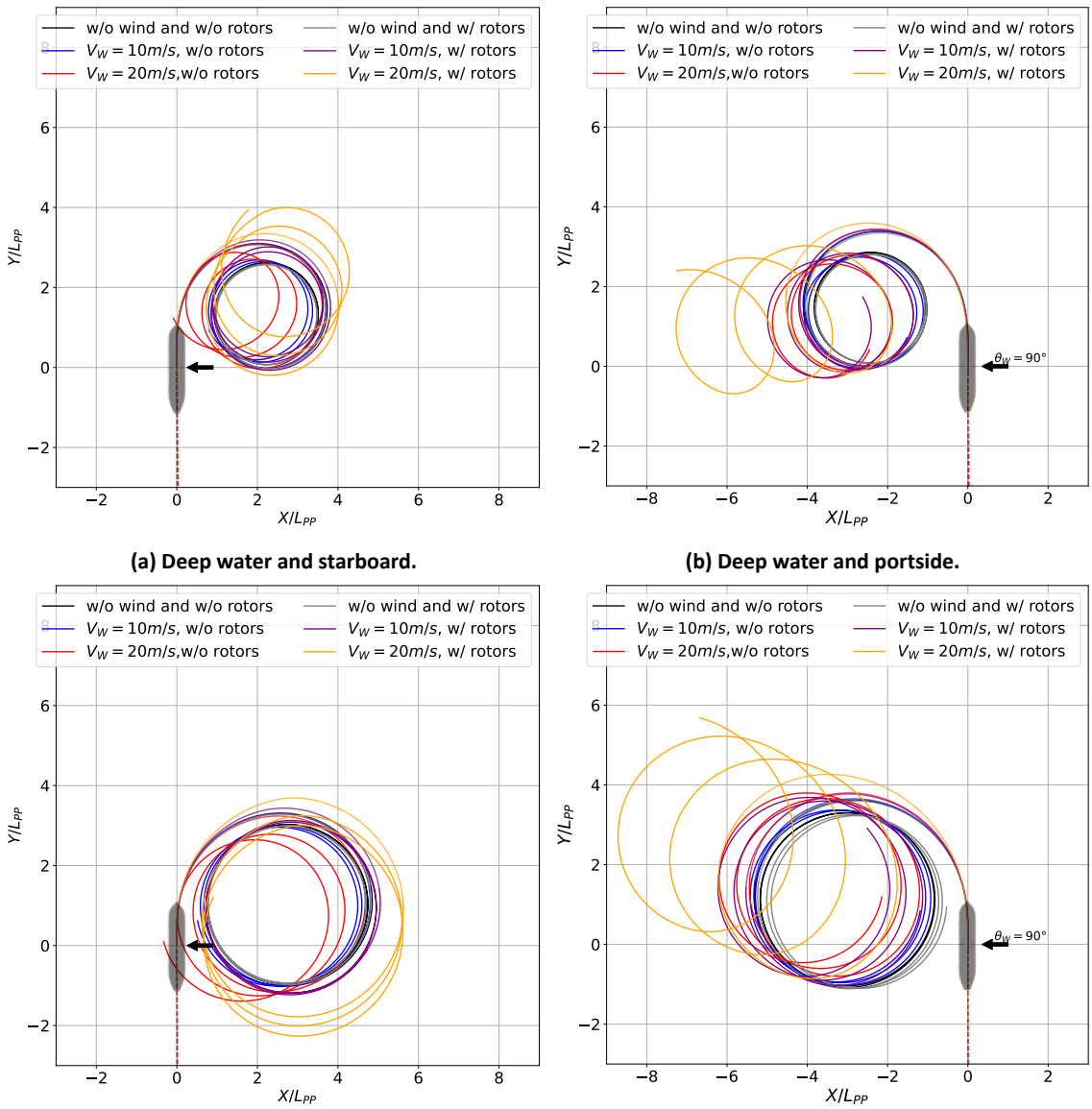

(a) Deep water and starboard. **(b) Deep water and portside.**

(c) Shallow water (h/T =1.2) and starboard. **(d) Shallow water (h/T =1.2) and portside.**

Figure 15: Drift-away characteristics.

The drift-away parameters exhibited considerably larger differences between the cases with and without rotor sails. The maximum variation in H_D exceeded 0.87 L_{pp}, while the drift angle (μ_D) varied by up to 74°, as shown in Figure 16. For $V_W = 20$ m/s, substantial drift distances were observed, reaching 1.32 L_{pp}. Furthermore, the shallow-water condition was evaluated following the methodology described in Section 3. As expected, maneuvers in shallow water resulted in larger turning diameters compared to deep-water conditions, as illustrated in Figures 15c and 15d.

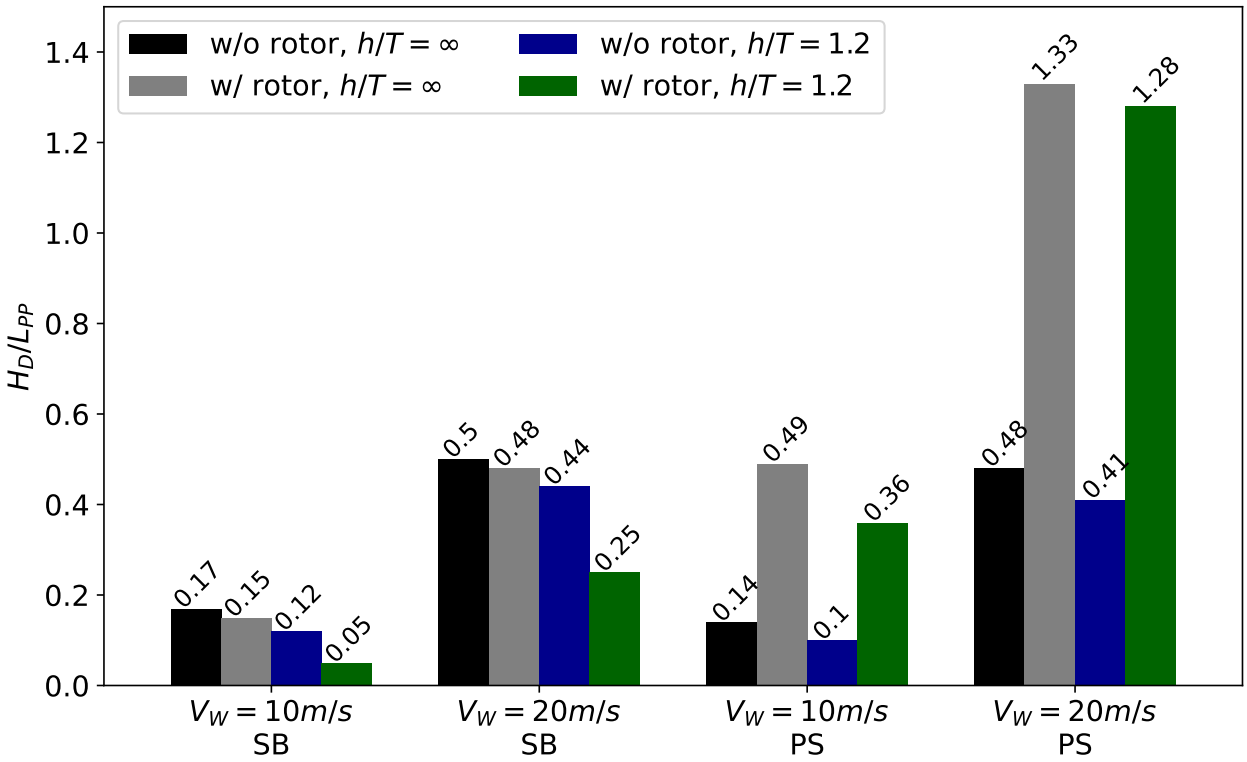

Figure 16: Drift distance for θ_W = 90°wind cases.

When the wind acts on the ship, the speed increases when moving with the wind and decreases when sailing against the wind, and no steady turn can be observed. Therefore, an extended drift-away analysis was proposed in Quadvlieg et al. (2023). A sectorial analysis method obtains the parameters of the first three turns and evaluates the not-so-steady behavior of the turn. Figure 17 shows the impact of the winds on the turning characteristics, and the sectors employed to describe the turning circle in windy conditions are shown in Figure 17. The speed, drift angle, and rate of turn are interpreted as a function of the position in the turning circle, which were derived by sectors of the circle. In this way, the speed, drift, and rate of turn are evaluated for different wind headings, and the wind incidence and vessel's heading are included in the analyses. These are non-dimensionalized by the calm water, no wind, and no rotor values and are a function of the ship's heading with respect to wind incidence, called wind heading (x-axis). A variation can be noted by comparing the case with and w/o rotors for the non-dimensional drift (Fig 17c), average rate of turn (Fig 17d), and average speed loss (Fig 17b).

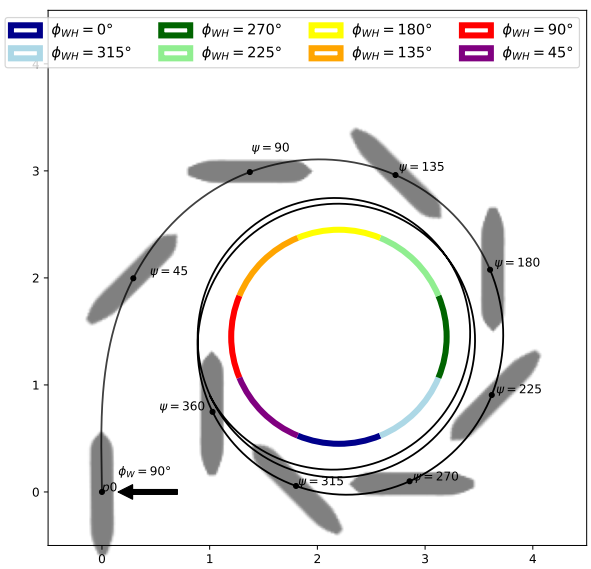

(a) Sectors used to describe the turning circle in windy conditions

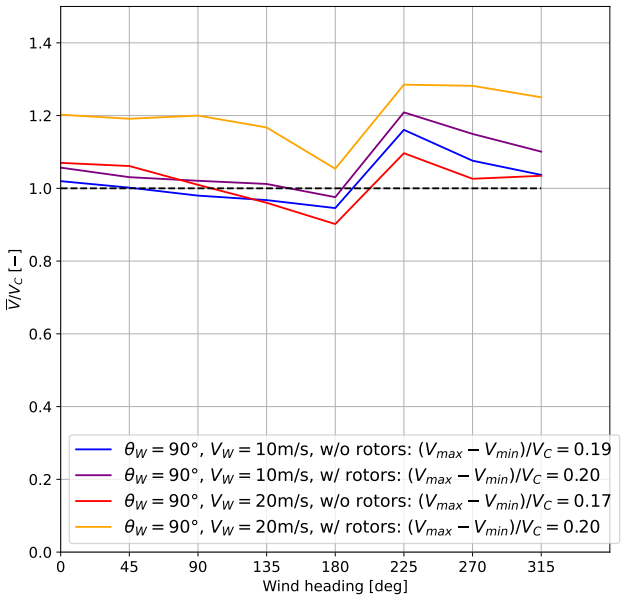

(b) $\bar{V}/V_C$

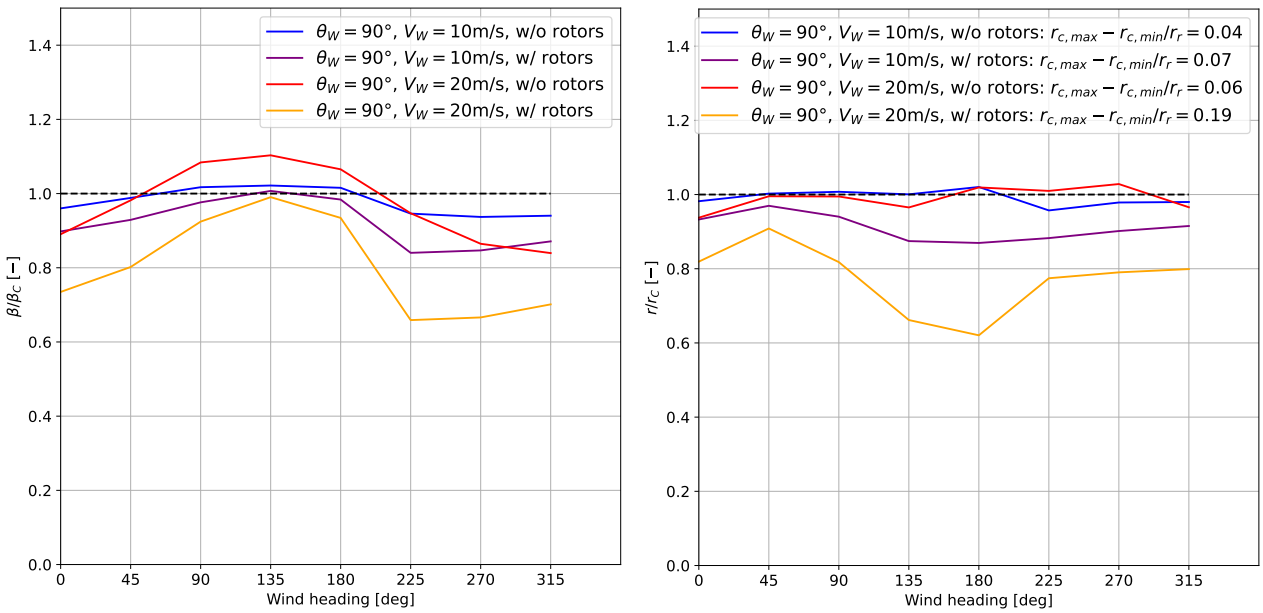

(c) $\bar{\beta}/\beta_C$ **(d)** $\bar{r}/r_C$

Figure 17: The impact of the wind on the maneuvering characteristics.

Figure 18 presents the results of two stopping ability tests: one for the reference case without rotors and another for a vessel equipped with rotors, both conducted under identical wind conditions. The case with rotors exhibits a track reach approximately $1L_{PP}$ longer than the reference case, indicating a reduced stopping performance. Additionally, lateral deviation and head reach are more pronounced, further highlighting a deterioration in stopping ability for vessels equipped with WASP technology.

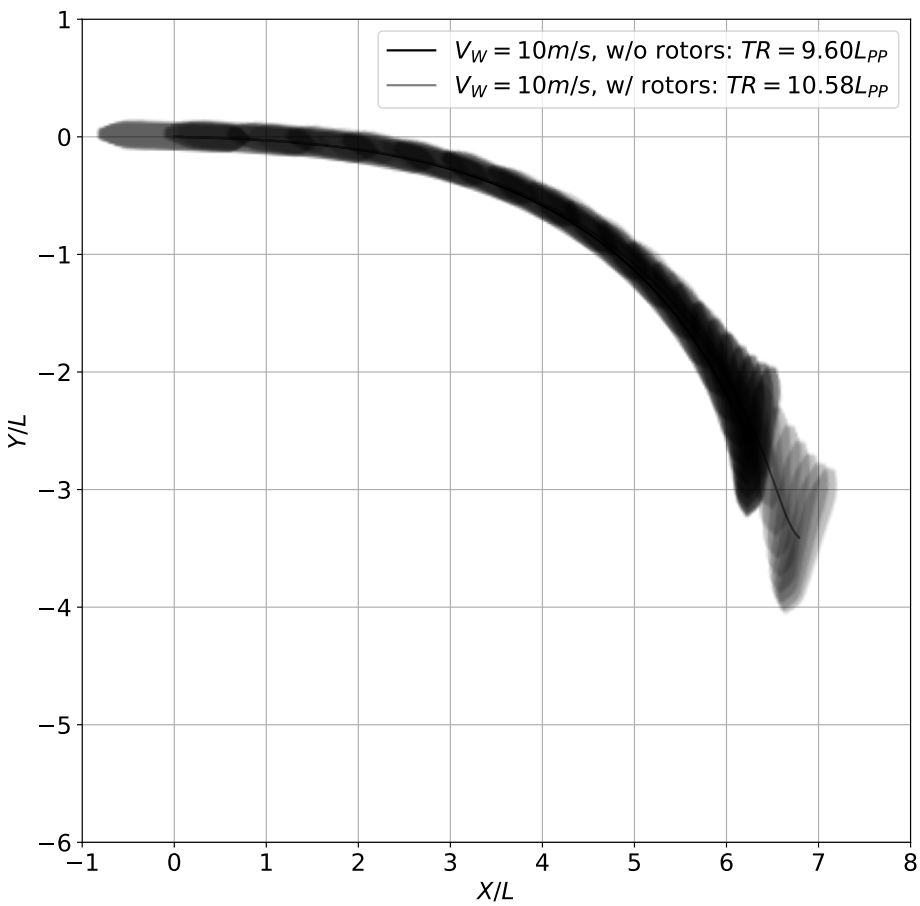

Figure 18: Stopping ability test at $\theta_W = 22.5°$.

Initial course change and yaw-checking ability can be assessed by conducting a zig-zag test. In this maneuver, the vessel's overshoot angle—defined as the deviation angle following the reversal of the rudder—along with the execution times for the first and second maneuvers, are measured as the primary characteristics. The variations observed for these parameters were around 10% for the case illustrated in Figure 19. By comparing both cases, the second overshoot was larger (12%) for the rotor case, meaning a less efficient yaw-checking ability.

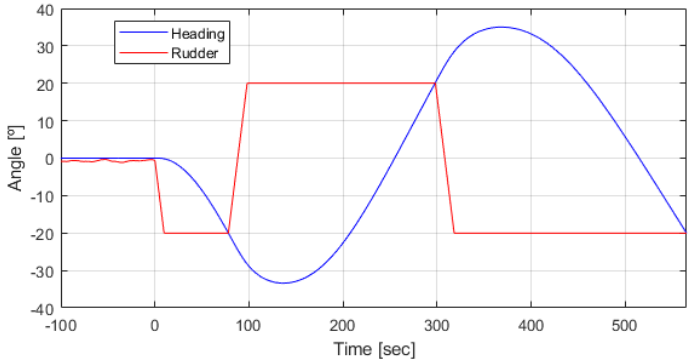

(a) Without rotors.

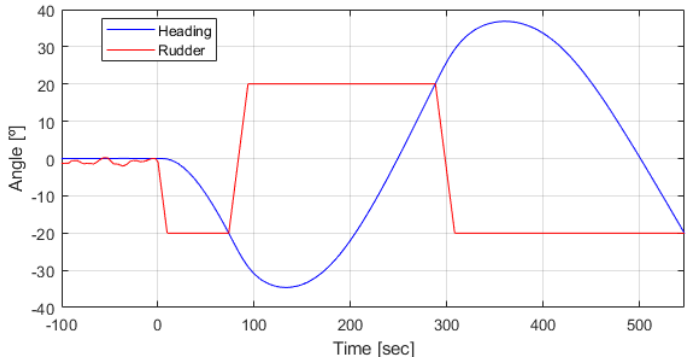

(b) With rotors.

Figure 19: Zig-zag test with 20° of rudder angle at $V_W = 20m/s$ and $\theta_W = 22.5^\circ$.

6 CONCLUSIONS

This study used computational fluid dynamics (CFD) to model the aerodynamic wind coefficients for a Suezmax class tanker, with and without rotor sails. These coefficients were then used in a maneuvering simulator to conduct simulations of standard maneuvers, including turning circles, zig-zag tests, and crash stops.

The turning circle tests showed an average variation in the main maneuvering characteristics of 5% at a wind speed of 10 m/s and 17% at a wind speed of 20 m/s. An interesting discussion emerged once the drift-away aspect was addressed, employing a novel methodology to deal with the wind effects on vessels equipped with rotors. It is important to note that the methodology employed in this research was based on the maneuvering in waves SIMMAN approach. This was a preliminary investigation of how the WASP devices would affect the vessel's maneuverability and an attempt to propose a methodology for processing the turning trajectories. Significant variations were found in the drift distance (H_D) and drift angle (μ_D) for the cases evaluated (up to 0.87 L_{pp} and 74°, respectively). Although few cases have been investigated, the results so far demonstrate the need to thoroughly investigate the maneuverability of the ship equipped with rotors for different operational and weather conditions. The stopping ability was also affected by the rotors, suggesting that the rotor sails may reduce the turning ability of a vessel. The assessment of the zig-zag manoeuvres indicated that the presence of the rotors can degrade the vessel's yaw-checking ability by approximately 10%.

This study provides a preliminary investigation into the influence of WASP ships on maneuverability. Although this initial work examined a limited set of conditions for obtaining the nondimensional wind coefficients (one wind speed, one rotor speed, vessel fully loaded), future research will address several key areas. These include the impact of varying the rotor operational parameters (e.g. rotation speed, arrangement, and size), environmental conditions (currents and waves), and different vessel loading scenarios. Although some studies suggest that aerodynamic coefficients are insensitive to velocity changes, the novel nature of these cases necessitates further investigation, particularly regarding the coefficients used in the maneuvering model.

7 ACKNOWLEDGEMENTS

The authors gratefully acknowledge the support from ANP/PETROBRAS, Brazil (project 2023/00126-6). Eduardo A. Tannuri acknowledges the CNPq – Brazilian National Council for Scientific and Technological Development for the research grant (process 310127/2020–3).

8 REFERENCES

ABS; 2017. Guide for Vessel Maneuverability. In: Act of Legislature of the State of New York.

Azcueta, R. and Ward, H.; 2023. Performance Prediction of Wind Propulsion Technologies Via CFD. In: Wind Propulsion 2023.

Bordogna, G. et al.; 2020. The effects of the aerodynamic interaction on the performance of two Flettner rotors. In: Journal of Wind Engineering and Industrial Aerodynamics 196, p. 104024. DOI: https://doi.org/10.1016/j.jweia.2019.104024.

Chame, Maria Eduarda Felippe; 2024. CFD-based method for calculating ship maneuvering coefficients. PhD thesis. Universidade de São Paulo. DOI: https://doi.org/10.11606/T.3.2024.tde-09122024-093018.

Chou, Todd et al.; 2021. A Comeback of Wind Power in Shipping: An Economic and Operational Review on the Wind-Assisted Ship Propulsion Technology. In: Sustainability 13.4. DOI: 10.3390/su13041880.

De Marco, A. et al.; 2016. Flettner Rotor Concept for Marine Applications: A Systematic Study. In: International Journal of Rotating Machinery 2016.1, p. 3458750. DOI: https://doi.org/10.1155/2016/3458750.

EMSA; 2023. Potential of Wind-Assisted Propulsion for Shipping. Accessed: 2025-01-14.

European Commission et al.; 2016. Study on the analysis of market potentials and market barriers for wind propulsion technologies for ships – Final report. Publications Office. DOI: doi/10.2834/68747.

Forsberg, J.; 2020. Impact of Cylindrical Rotors on Vessel Maneuverability. In: Journal of Marine Engineering and Technology.

IMO; 2023. 2023 IMO Strategy on Reduction of GHG Emissions from Ships. In: THE MARINE ENVIRONMENT PROTECTION COMMITTEE RESOLUTION MEPC.377(80) - ANNEX 15.

ITTC; 2021. The Specialist Committee on Energy Saving Methods. In: Final Report and Recommendations to the 29th ITTC.

Kume, Kenichi et al.; 2022. Evaluation of aerodynamic characteristics of a ship with flettner rotors by wind tunnel tests and RANS-based CFD. In: Ocean Engineering 254, p. 111345. DOI: https://doi.org/10.1016/j.oceaneng.2022.111345.

Kwon, Chang Seop et al.; 2022. A parametric study for a flettner rotor in standalone condition using CFD. In: International Journal of Naval Architecture and Ocean Engineering 14, p. 100493. DOI: https://doi.org/10.1016/j.ijnaoe.2022.100493.

Lee, Chang-Ho and Newman, John Nicholas; 2013. WAMIT user manual, version 7.0. In: WAMIT Inc, Chestnut Hill, Massachusetts.

Lu, Ruihua and Ringsberg, Jonas W.; 2020. Ship energy performance study of three wind-assisted ship propulsion technologies including a parametric study of the Flettner rotor technology. In: Ships and Offshore Structures 15.3, pp. 249–258. DOI: 10.1080/17445302.2019.1612544.

Nuttall, Peter and Kaitu, John; Jan. 2016. The Magnus Effect and the Flettner Rotor: Potential Application for Future Oceanic Shipping. In: Journal of Pacific Studies 36. DOI: 10.33318/jpacs.2016.36(2)-9.

Paakkari, Ville; Wang, H, and Stigler, C; Sept. 2022. VOYAGE OPTIMIZATION WITH WIND PROPULSION. In: ICCAS 2022. DOI: 10.3940/rina.iccas.2022.28.

Petković, Miro et al.; Nov. 2021. Wind Assisted Ship Propulsion Technologies – Can they Help in Emissions Reduction? In: Nase More 68, pp. 102–109. DOI: 10.17818/NM/2021/2.6.

Quadvlieg, Frans and Stern, Fred; 2023. SIMMAN 2020 Workshop on Verification and Validation of Ship Maneuvering Simulation Methods. In: Simman 2020. Korea Research Institute of Ships, Ocean Engineering (KRISO), and The Society of Naval Architects of Korea (SNAK). Korea.

Sampaio, Joao et al.; 2024. Prediction of Rotor Sails Performance on Large Ore Carriers. In: Proceedings of the 9th International Symposium on Marine Propulsors (SMP 2024). Rome, Italy: Marine Propulsors. DOI: 10.15480/882.9316.

Silva, Gustavo O; Tannuri, Eduardo Aoun, and Ruggeri, Felipe; 2015. Real-time prediction of ship interaction forces using simplified models. In: International Conference on Offshore Mechanics and Arctic Engineering. Vol. 56475. American Society of Mechanical Engineers, V001T01A017.

Tannuri, Eduardo Aoun and Martins, Gabriel Henrique Antunes; 2018. Application of a maneuvering simulation center and pilots expertise to the design of new ports and terminals and infrastructure optimization in Brazil. In: PIANC-World Congress Panama City. PIANC.

Tannuri, Eduardo Aoun; Rateiro, Felipe, et al.; 2014. Modular mathematical model for a low-speed maneuvering simulator. In: International Conference on Offshore Mechanics and Arctic Engineering. American Society of Mechanical Engineers.

Watai, Rafael de Andrade et al.; 2018. An analysis methodology for the passing ship problem considering real-time simulations and moored ship dynamics: Application to the Port of Santos, in Brazil. In: Applied Ocean Research 80, pp. 148–165.

9 AUTHORS BIOGRAPHY

Gustavo Santana holds the current position of Junior Researcher at Numerical Offshore Tank, TPN-USP. He is responsible for the numerical study of the impact of rotor sails on Aframax and Suezmax tanker vessels. He is mastering in Marine Engineering at the University of São Paulo with emphasis on CFD.

Ferdinando Freire Naval Engineer currently holding the position of Junior Researcher at the Numerical Offshore Tank, TPN-USP, responsible for conducting numerical studies on the analysis of Air Lubrication Systems for Aframax and Suezmax tanker vessels. He is mastering in Marine Engineering at the University of São Paulo with emphasis on CFD to assess energy efficiency technologies, particularly air lubrication systems.

Jungeui Choi holds a bachelor's degree in Naval Architecture and Ocean Engineering at the Polytechnic School of USP. Currently is pursuing a Ph.D degree in Mechanical Engineering with a focus on Deep Generative Networks applied in Inverse Problems. Researcher in Computer Fluid Dynamics at the Numerical Offshore Tank (TPN-USP), responsible for numerical study of flettner rotors and trim optimization.

Maria Chame earned her Master's degree in Naval Engineering in 2019, subsequently completing her Doctoral degree in 2024, both from the University of São Paulo. During her Master's, she studied VIV (Vortex-Induced Vibration) and CFD Verification and Validation (V&V) of hydrodynamic problems in collaboration with the Maritime Institute of Netherlands (MARIN) and the University of Tokyo. During the PhD, she participated in an exchange program with the Norwegian University of Science and Technology (NTNU). Her research relies on computational fluid dynamics using the open-source code OpenFOAM, new energy devices, and ship maneuverability. Recently, she was nominated as a member of the ITTC Wind Propulsion Committee (2024-2027).

Claudio Mueller holds both a Bachelor's and a Master's degree in Naval Architecture from the University of São Paulo, as well as a PhD in Naval and Ocean Engineering from Yokohama National University, Japan. He is currently a Senior Lecturer/Assistant Professor in the Department of Naval and Ocean Engineering at Escola Politécnica, University of São Paulo, where he teaches Ship Design courses. His research focuses on ship design and hydrodynamics, with a particular emphasis on computational fluid dynamics (CFD) to assess energy efficiency technologies, including wind-assisted propulsion and air lubrication systems.

Eduardo Tannuri holds the current position of Full Professor at the Department of Mechatronics Engineering, University of São Paulo (USP), and director of the Maneuvering Simulation Center of the Numerical Offshore Tank (TPN). Member of ITTC Maneuvering Committee (2012-2021). Works on Dynamic Positioning (DP) Systems applied to offshore vessels and platforms, Maneuvering and Sea-keeping time-domain simulators development with applications to ports, vessels and floating structures design. He was graduated in Mechatronics Engineering, in 1998, and completed his doctorate degree in 2002, both at USP. He already coordinated more than 300 maneuvering simulation studies in different Brazilian Ports and offshore operations.

Lucia Logsdon currently holds the position of Logistics researcher at the Petrobras research center, where she works on the development of technologies to reduce vessel fuel consumption. She is currently studying for a PhD in Production Engineering at the Federal University of Rio de Janeiro.

Nathalie Sanghikian currently holds the position of Logistics researcher at the Petrobras research center, where she works on the development of technologies to reduce vessel fuel consumption. She is currently studying for a PhD in Production Engineering at the Pontifícia Universidade Católica - RJ.

APPLICATION OF THE MMG-METHOD TO PREDICT THE PROPULSIVE PERFORMANCE OF A BULK CARRIER WITH FLETTNER ROTORS

Hironori Yasukawa, Hiroshima University, Japan

APPLICATION OF THE MMG-METHOD TO PREDICT THE PROPULSIVE PERFORMANCE OF A BULK CARRIER WITH FLETTNER ROTORS

HIRONORI YASUKAWA, HIROSHIMA UNIVERSITY, JAPAN

SUMMARY

The number of ships equipped with Flettner rotors (known as rotor ships) has increased recently to reduce fuel consumption and greenhouse gas emissions. To capture the energy-saving effect of a rotor ship, it is necessary to evaluate its steady sailing conditions, including the check helm, hull drift angle, and heel angle, as it moves straight in wind and waves, and predict the engine power and ship speed under these conditions. In this study, a calculation method based on the MMG-method was used to predict the steady sailing conditions and propulsive performance of a bulk carrier with four Flettner rotors. Compared with the same ship without rotors, the energy-saving gains were 4 – 6% under the full-load condition and 5 – 7% under the ballast-load condition in an absolute wind speed range of 10 – 12 m/s. The proposed method is useful for predicting the propulsive performance of rotor ships.

NOMENCLATURE

A_F	Rotor profile area (m^2)
A_R	Movable rudder area (m^2)
A_X, A_Y	Front- and side-profile areas of the ship in air, respectively (m^2)
a_H	Rudder force increase factor (–)
B	Ship breadth (m)
C_b	Block coefficient (–)
C_{LF}, C_{DF}, C_{PF}	Lift, drag, and power coefficients of the rotor, respectively (–)
D	Ship depth (m)
D_{Fi}	Drag of the *i*-th rotor (N)
D_P	Propeller diameter (m)
d, d_f, d_a	Mean, fore, and aft drafts, respectively (m)
e_P	Power reduction ratio due to rotor operation (–)
e_U	Ship speed increase ratio due to rotor operation (–)
$\overline{GM}$	Metacentric height (m)
g	Gravitational acceleration (m/s^2)
$H_{1/3}$	Significant wave height (m)
H_R	Rudder span length (m)
L	Ship length between perpendiculars (m)
L_{Fi}	Lift of the *i*-th rotor (N)
L_{oa}	Length overall (m)
N_{FR}	Rotor revolution (rps)
$N_v{}'$, $N_\phi{}'$, $N_{vvv}{}'$	Hydrodynamic derivatives with respect to the yaw moment
n_F	Number of the Flettner rotors (–)
$o_0 - x_0y_0z_0$	Space fixed-coordinate system
$o - xyz$	Horizontal body-fixed coordinate system
P_D	Delivered power (kW)
P_{DRA}	Average total power of delivered power and rotor power in all wind directions (kW)
P_{Fi}	Rotational power of the *i*-th rotor (kW)
P_R	Total rotor power (kW)
p	Propeller pitch ratio (–)
R	Ship resistance in straight motion (N)
R_R	Rotor radius (m)
S_r	Rotor spin ratio (–)
T	Propeller thrust (N)
T_{01}	Mean wave period (s)
t_R	Steering resistance reduction factor (–)
U	Ship speed ($= \sqrt{u^2 + v^2}$) (m/s)

U_{Ave}	Average ship speed in all wind (wave) directions (m/s)
U_W	Absolute wind speed (m/s)
u,v	Surge and lateral velocities of the ship, respectively (m/s)
V_A	Relative wind speed (m/s)
X, Y, N, K	Surge force, lateral force, yaw moment, and roll moment acting on the ship, respectively (N or Nm)
X_A, Y_A, N_A, K_A	Surge force, lateral force, yaw moment, and roll moment due to wind, respectively (N or Nm)
X_F, Y_F, N_F, K_F	Surge force, lateral force, yaw moment, and roll moment due to rotor operation, respectively (N or Nm)
X_{Fi}, Y_{Fi}, N_{Fi}, K_{Fi}	Surge force, lateral force, yaw moment, and roll moment due to the *i*-th rotor operation, respectively (N or Nm)
X_H, Y_H, N_H	Surge force, lateral force, and yaw moment acting on the ship hull, respectively (N or Nm)
X_P	Surge force due to the propeller (N)
X_R, Y_R, N_R	Surge force, lateral force, and yaw moment due to steering, respectively (N or Nm)
X_W, Y_W, N_W, K_W	Wave-induced steady surge force, lateral force, yaw moment, and roll moment, respectively (N or Nm)
X_{vv}', $X_{\phi\phi}'$, X_{vvvv}'	Hydrodynamic derivatives with respect to the surge force (–)
x_{Fi}, y_{Fi}, z_{Fi}	Representative coordinates of the force acting on the *i*-th rotor (m)
x_G	Longitudinal coordinate of the ship's center of gravity (m)
x_H	Longitudinal coordinate of the acting point of the hull lateral force component induced by steering (m)
Y_v', Y_ϕ', Y_{vvv}'	Hydrodynamic derivatives with respect to the lateral force (–)
Z	Number of propeller blades (–)
z_H	Vertical coordinate of the acting point of the hull lateral force (m)
z_R	Vertical coordinate of the acting point of the rudder force (m)
β	Hull drift angle at midship (rad)
γ_R	Flow straightening coefficient (–)
δ	Rudder angle (check helm) (rad)
ε	Ratio of wake fractions at the propeller and rudder positions (–)
θ_A	Relative wind direction (rad)
θ_W	Absolute wind direction (rad)
κ	Experimental constant for expressing the rudder inflow velocity (–)
ρ_a	Air density (kg/m^3)
ϕ	Roll angle (rad)
ω	Rotor angular velocity (rad/s)
χ	Absolute wave direction (rad)
ψ	Ship heading (rad)
∇	Ship displacement volume (m^3)

1 INTRODUCTION

To reduce fuel consumption and greenhouse gas (GHG) emissions from ships, the use of natural wind is considered following the example of sailing ships. One such idea is to use rotating cylinders called Flettner rotors to assist the ship's thrust. Flettner rotors are smooth-surfaced cylinders with a disk end plate that rotates along the vertical axis. Flettner rotors use the principle that when horizontal air passes through the rotor, the Magnus effect generates horizontal lift perpendicular to the airflow.

Ships equipped with Flettner rotors (known as rotor ships) were developed in the early 1920s; however, they were abandoned afterwards due to maintenance costs. Nevertheless, since the 1980s, rotor ships have gradually been revived, and their number has increased in recent years, taking the advantage that they are less expensive than other sailing rigs owing to their simple structure.

According to Tillig and Ringsberg (2020), the potential energy-saving gain is 30% for a tanker with six rotors and 14% for a RoRo ship with four rotors. Rotor ships use the lift force acting on the rotors; therefore, an offset rudder angle (check helm) is required to navigate the ship straight ahead; simultaneously, a hull drift angle appears in the ship. To capture the energy-saving effect of a rotor ship, it is necessary to evaluate its steady sailing conditions, including the check helm, hull drift angle, and heel angle, as it moves in wind and waves, and predict the engine power and ship speed under these

conditions. However, Tillig and Ringsberg (2020) employed a simple method to predict steady sailing conditions, and their handling appeared to be inadequate. Additionally, the effect of wave-induced steady forces acting on the ship was not considered.

Meanwhile, in the field of ship maneuvering simulations, a method has been established (Yasukawa and Sakuno, 2019c) to predict the steady sailing condition of an obliquely moving ship with a check helm in wind and waves and to investigate the course stability under such condition, based on the MMG-method (Yasukawa and Yoshimura, 2015). In this study, we extend the MMG-method to rotor ships. Such an endeavor was previously attempted by Sogihara and Kume (2022). However, because rolling motion was not considered in their calculations and the simple estimation formulas by Kijima et al. (1990) and Kijima and Nakiri (1999) were used to calculate the hull hydrodynamic and rudder forces, their steady sailing condition prediction results need to be verified.

In this study, a calculation method based on the MMG-method (Yasukawa and Yoshimura, 2015, and Yasukawa and Sakuno, 2019c) was developed to predict the steady sailing condition and propulsive performance of a rotor ship. The developed calculation method was applied to a bulk carrier with four Flettner rotors to predict its propulsive performance and energy-saving gain. Many of the hydrodynamic forces required for the calculations are estimated using captive model test results based on the MMG-method. The method proposed by Tillig and Ringsberg (2020) was used to calculate the drag, lift, and rotational torque on the Flettner rotors. Based on the obtained calculation results, the energy-saving gain of the bulk carrier equipped with the Flettner rotors is discussed.

2 CALCULATION METHOD

2.1 COORDINATE SYSTEMS

Figure 1 shows the coordinate systems used in this study. Consider the space-fixed coordinate system o_0-$x_0y_0z_0$, where the x_0-y_0 plane coincides with the still water surface, and the z_0-axis is vertically downwards. Additionally, consider a horizontal body-fixed coordinate system (Hamamoto and Kim, 1993) *o-xyz*. The *x*-axis is considered as the ship's bow direction, the *y*-axis is the lateral direction, and the *z*-axis is considered vertically downwards. The *x-y* plane also coincides with the still water surface. The origin *o* is located at the midship position on the still-water surface. The heading angle ψ is defined as the direction between the x_0 and *x* axes and the roll angle is denoted by ϕ. Clockwise rotation is positive for roll when observed from the ship's stern in the fore direction. *u* and *v* denote the velocity components in the *x*- and *y*-axis directions, respectively, and *r* denotes the yaw rate around the *z*-axis. δ denotes the rudder angle. The hull drift angle at the midship position β is evaluated as follows.

$$\beta = \tan^{-1}\left(-\frac{v}{u}\right) \tag{1}$$

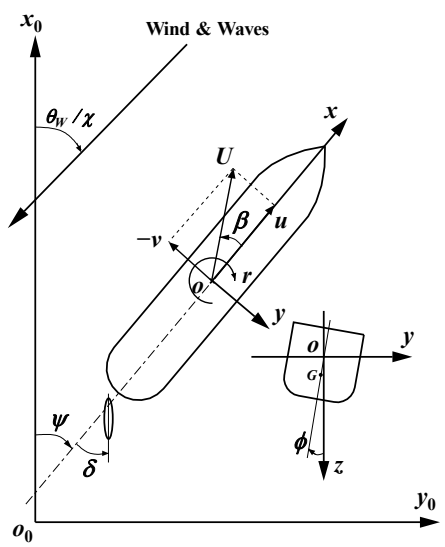

Figure 1. Coordinate systems used in this study

and the ship speed U is defined as

$$U = \sqrt{u^2 + v^2} \tag{2}$$

The wind is assumed to be constant and uniform, with the absolute wind speed (U_W) blowing from the θ_W direction relative to the x_0-axis. The waves are assumed to be long-crested irregular waves with a significant wave height ($H_{1/3}$) and mean wave period (T_{01}) entering from the χ direction relative to the x_0-axis. To simplify the problem, we assumed that the wind (θ_W) and wave (χ) directions were the same.

2.2 CALCULATION OUTLINE

Consider a ship sailing obliquely in wind and waves with the Flettner rotors operating under constant propeller revolution conditions. The ship is in a steady-state condition with a certain check helm (δ), hull drift angle (β), and zero-heading angle ($\psi = 0$) in the wind and waves. Therefore, the time derivative terms of the ship motion and yaw rate (r) are all zero. Wave-induced motion is not considered. When considering four ship motions, namely, surge, sway, yaw, and roll, the basic equations assume that the four forces acting on the ship, namely, surge force (X), lateral force (Y), yaw moment (N), and roll moment, (K) are zero. The unknowns are the surge velocity (u), lateral velocity (v), heel angle (ϕ), and check helm (δ). The number of unknowns corresponds to the number of basic equations. The basic equations need to be solved numerically because they are nonlinear with respect to the unknowns. For the detailed calculations, please refer to Yasukawa and Sakuno (2019c).

2.3 EXPRESSION OF THE FORCES AND MOMENTS ACTING ON THE SHIP

X, Y, N, and K are assumed to consist of the hull forces/moments, propeller force, rudder forces, and the forces due to the Flettner rotors, as well as the wind and wave-induced steady forces. The X, Y, and N acting on a ship are expressed as

$$\left.\begin{aligned} X &= X_H + X_R + X_P + X_A + X_W + X_F \\ Y &= Y_H + Y_R + Y_A + Y_W + Y_F \\ N &= N_H + N_R + N_A + N_W + N_F \end{aligned}\right\} \tag{3}$$

The subscripts H, R, and P on the right-hand side of Eq.(3) denote the hull, rudder, and propeller, respectively. Subscripts A, W, and F are the aerodynamic (wind) forces, wave-induced steady forces, and forces due to the Flettner rotors, respectively. Additionally, the roll moment K is expressed as

$$K = -Y_H z_H - Y_R z_R - mg\overline{GM}\phi + K_A + K_W + K_F \tag{4}$$

In the right-hand side of Eq.(4), the first term is the roll moment acting on the hull, except for the roll restoring moment, and the second term is the roll moment owing to steering and is expressed by multiplying the lateral force components (Y_H, Y_R) by their vertical acting points (z_H, z_R). The expressions for the forces and moments acting on a ship except the forces due to the Flettner rotors have been presented by Yasukawa and Yoshimura (2015), and Yasukawa and Sakuno (2019c). Here we present the expression of the forces due to the Flettner rotors.

2.4 FORCES AND MOMENTS DUE TO THE DUE TO THE FLETTNER ROTORS

Consider the forces and moments due to the Flettner rotors. Assume that there are n_F identical Flettner rotors installed on the ship. The lift (L_{Fi}), drag (D_{Fi}), and power (P_{Fi}) generated by the i-th rotor are respectively expressed as

$$L_{Fi} = (1/2)\rho_a A_F V_A^2 C_{LF}(S_r) \tag{5}$$

$$D_{Fi} = (1/2)\rho_a A_F V_A^2 C_{DF}(S_r) \tag{6}$$

$$P_{Fi} = (1/2)\rho_a A_F V_A^3 C_{PF}(S_r) \tag{7}$$

where ρ_a is the air density; V_A is the relative wind speed; A_F is the rotor lateral area; and C_{LF}, C_{DF}, and C_{PF} are the lift, drag, and power coefficients, respectively. These are functions of spin ratio (S_r) defined as $\omega R_R/V_A$, where R_R is the rotor radius, ω is the rotor rotational angular velocity, and clockwise rotation is positive. Following Tillig and Ringsberg (2020), C_{LF}, C_{DF}, and C_{PF} are expressed as quantic equations with respect to S_r as follows:

$$\left.\begin{aligned} C_{LF}(S_r) &= \sum_{j=0}^{5} C_{Lj} S_r^j \\ C_{DF}(S_r) &= \sum_{j=0}^{5} C_{Dj} S_r^j \\ C_{PF}(S_r) &= \sum_{j=0}^{5} C_{Pj} S_r^j \end{aligned}\right\} \tag{8}$$

The surge force (X_{Fi}), lateral force (Y_{Fi}), yaw moment (N_{Fi}), and roll moment (K_{Fi}) generated by the i-th rotor are respectively expressed as

$$X_{Fi} = -\mathrm{sgn}(\omega) L_{Fi} \sin\theta_A - D_{Fi} \cos\theta_A \tag{9}$$

$$Y_{Fi} = \mathrm{sgn}(\omega) L_{Fi} \cos\theta_A - D_{Fi} \sin\theta_A \tag{10}$$

$$N_{Fi} = Y_{Fi} x_{Fi} - X_{Fi} y_{Fi} \tag{11}$$

$$K_{Fi} = -Y_{Fi} z_{Fi} \tag{12}$$

where θ_A is the relative wind direction. (x_{Fi}, y_{Fi}, z_{Fi}) is the acting point on the force generated by the rotor. Specifically, (x_{Fi}, y_{Fi}) are the coordinates of the rotor rotation axis when the rotor stands vertically, and z_{Fi} is half the height of the rotor installed on the deck. Assuming that the n_F rotors do not interfere with each other aerodynamically, the surge force (X_F), lateral force (Y_F), yaw moment (N_F), and roll moment (K_F) due to all rotors can be calculated by taking the sum of X_{Fi}, Y_{Fi}, N_{Fi}, and K_{Fi} for n_F as follows:

$$X_F = \sum_{j=1}^{n_F} X_{Fj}\,, \qquad Y_F = \sum_{j=1}^{n_F} Y_{Fj}\,, \qquad N_F = \sum_{j=1}^{n_F} N_{Fj}\,, \qquad K_F = \sum_{j=1}^{n_F} K_{Fj}$$

The total power required to rotate the rotors can be calculated as

$$P_R = \sum_{j=1}^{n_F} P_{Fj}$$

3 STUDIED SHIP

3.1 BULK CARRIER

We studied a Handymax bulk carrier (Yasukawa et al., 2019a). Figure 2 shows the ship's body plan, and Table 1 lists the its principal particulars. The loading conditions were full load (even keel) and ballast load (trimmed by stern). In the table, L_{oa} is the overall length, L is the length between perpendiculars, B is the breadth, D is the depth, d_f is the draft at the fore perpendicular, d_a is the draft at the aft perpendicular, d is the mean draft, ∇ is the displacement volume, x_G is the longitudinal position of the center of gravity from the midship, C_b is the block coefficient, and $\overline{GM}$ is metacentric height.

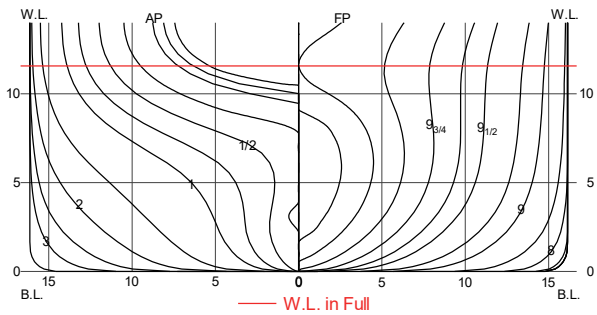

Figure 2. Body plan of the studied bulk carrier

Table 2 lists the propeller and rudder dimensions. In the table, Z is the number of propeller blades, D_P is the propeller diameter, p is the pitch ratio, H_R is the rudder height (span length), and A_R is the movable rudder area (excluding the horn area). Under ballast load conditions, the upper part of the rudder is exposed above the water surface, and the immersed portion is regarded as the actual rudder. For this reason, rudder dimensions, such as H_R and A_R, are different under full- and ballast-load conditions, despite the ship being equipped with the same rudder.

Table 1. Principal particulars of the studied bulk carrier

	Full	Ballast
L_{oa} [m]	185.9	
L [m]	178.0	
B [m]	32.26	
D [m]	17.27	
d_f [m]	11.57	5.30
d_a [m]	11.57	7.84
d [m]	11.57	6.57
∇[m^3]	55,810	29,680
x_G [m]	5.33	2.82
C_b	0.840	0.786
$\overline{GM}$ [m]	3.2	5.7
A_X [m^2]	535.0	696.0
A_Y [m^2]	1,923.2	2,824.8

Table 2. Principal dimensions of the propeller and rudder

	Full	Ballast
Z [–]	4	
D_P [m]	5.483	
p [–]	0.690	
H_R [m]	8.787	7.734
A_R [m^2]	35.3	31.7

In this study, it was necessary to consider the superstructure of the ship. Figure. 3 shows the frontal and lateral projections of the superstructure and part of the hull above the waterline (Yasukawa, et al., 2021) under full-load conditions without the rotors. In Table 1, A_X and A_Y denote the frontal and lateral projected areas of the ship above the waterline, respectively.

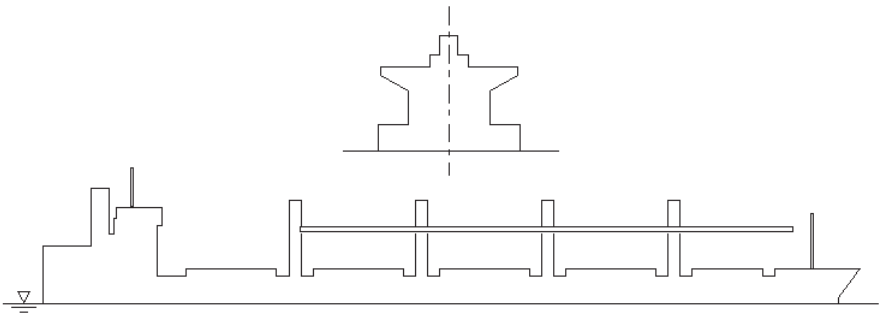

Figure 3. Frontal and lateral projections of the superstructure and part of the hull above the waterline of the studied bulk carrier under full-load conditions (without the Flettner rotors)

3.2 FLETTNER ROTORS

Four rotors were arranged lengthwise on the starboard deck, as shown in Figure. 4. All four rotors were assumed to have the same shape. The rotors are 3 m in diameter and 18 m in height, with a 5.25-m-diameter endplate at the top of the rotors. A cylindrical platform 1 m in height and 5 m in diameter was installed on the deck, and the rotors were placed on top of it.

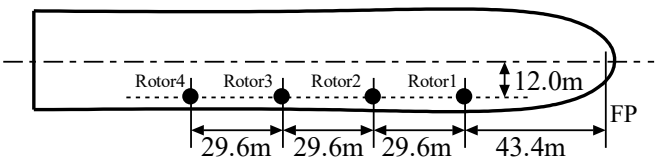

Figure 4. Arrangement of the Flettner rotors

3.3 CALCULATION CONDITIONS

3.3 (a) Ship speed

The ship speed (U) in the case with no environmental disturbances was assumed to be 13.5 kn under full-load conditions. The propeller revolution (n_P) was 120 rpm, and the delivered power (P_D) was 6570 ps (4832 kW). The ship speed was 14.1 kn under ballast-load conditions. Assuming a sea margin of 15%, the normal output was 7730 ps (5685 kW).

3.3 (b) Hydrodynamic force coefficients used in the calculations

Table 3 lists the hydrodynamic force coefficients used to predict the rotor ship propulsive performance. Most of these coefficients were determined based on measured data from captive model tests (Yasukawa and Hirata, 2023). Note that the flow-straightening coefficient (γ_R) has a different value depending on whether β is positive or negative.

Table 3. Comparison of the hydrodynamic derivatives and parameters while maneuvering

	Full	Ballast
X_{vv}'	-0.0767	0.0413
X_{vvvv}'	0.6579	0.6146
$X_{\phi\phi}'$	-0.0267	-0.1351
Y_v'	-0.3308	-0.3181
Y_{vvv}'	-1.3985	-0.6915
Y_ϕ'	-0.0044	0.0195
N_v'	-0.1476	-0.0707
N_{vvv}'	-0.0449	-0.0257
N_ϕ'	-0.0041	-0.0095
z_H/d	0.614	0.392
t_R	0.297	0.306
a_H	0.492	0.343
x_H/L	-0.410	-0.429
ε	1.2	1.4
κ	0.47	0.38
γ_R (β<0)	0.346	0.379
γ_R (β>0)	0.435	0.565

3.3 (c) Aerodynamic characteristics of the Flettner rotors

The aerodynamic characteristics of the Flettner rotor were estimated using Eq.(8). Following Tillig and Ringsberg (2020), the C_{LF}, C_{DF}, and C_{PF} coefficients in the equation are listed in Table 4.

Table 4. C_{LF}, C_{DF}, and C_{PF} coefficients of the Flettner rotors

i	C_{Li}	C_{Di}	C_{Pi}
0	0.0	0.6375	0.0
1	-0.1039	-1.6410	0.0234
2	3.1309	1.7243	-0.0168
3	-0.9817	-0.4424	0.0143
4	0.1145	0.0464	-0.0004
5	-0.0046	-0.0017	0.0001

Figure 5 shows the lift (C_{LF}), drag (C_{DF}), and power (C_{PF}) coefficient curves estimated using Eq.(8). In the figure, the horizontal axis represents the rotor spin ratio (S_r). C_{LF} increases with S_r; however, once S_r exceeds a value 3, the increase in C_{LF} gradually decreases. C_{DF} already acts as a resistance at S_r=0 (zero rotor revolutions), but the resistance temporarily decreases as the rotor rotates. As S_r increases, the resistance begins to increase and the increase in resistance gradually decreases. C_{PF} increases significantly with S_r.

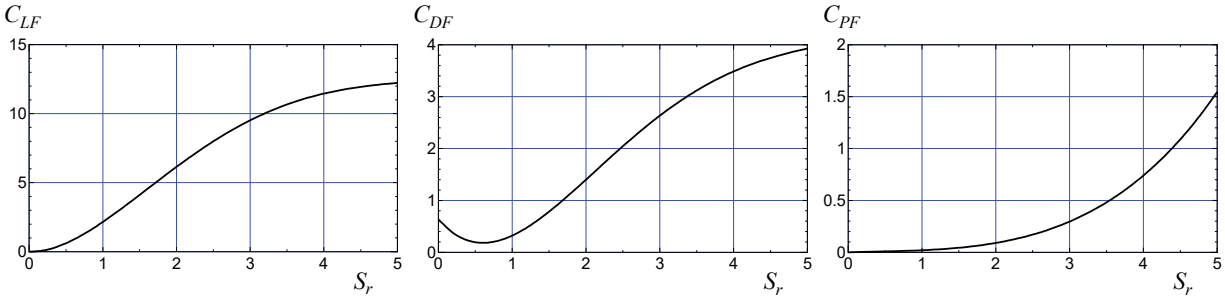

Figure 5. C_{LF}, C_{DF}, and C_{PF} curves according to spin ratio S_r

3.3 (d) Environmental disturbance conditions

The environmental disturbance conditions used in the calculations (absolute wind speed (U_W), significant wave height ($H_{1/3}$), and mean wave period (T_{01})) are listed in Table 5. This was determined based on the Beaufort wind scale and tables in WMO codes 3155 and 3700. Wave conditions, such as $H_{1/3}$ and T_{01}, were assumed to change according to U_W. The ITTC spectrum was used as the wave spectrum. The wave direction was assumed to be the same as the absolute wind direction (θ_W). The absolute wind direction (wave direction) was set as 0° for the head wind (waves), 90° for the starboard side, and -90° for the port side. Finally, the wind (waves) from behind the ship was $\pm 180°$. In the calculations, wind (waves) from all directions (-180° – 180°) were considered. The aerodynamic force coefficients were predicted using the method described in Fujiwara et al. (2005a). The wave-induced steady forces in regular waves were estimated using the strip method and 3D panel method (Yasukawa et al., 2019a). Based on the calculated results of the wave-induced steady forces in regular waves, short-term predictions in long-crested irregular waves were performed, and the average values were assumed to act on the ship.

Table 5. Absolute wind speed (U_W), significant wave height ($H_{1/3}$), and mean wave period (T_{01}) used in the calculations

U_W [m/s]	$H_{1/3}$ [m]	T_{01} [s]
5	0.8	3.44
7.5	1.4	4.51
10	2.1	5.53
12.5	2.9	6.52
15	3.8	7.49

3.4 ROTOR REVOLUTION CONTROL

The relative wind direction (θ_A) and speed (V_A) were assumed measurable onboard the ship, and the rotor revolutions (N_{FR}) were controlled. The relationship between N_{FR} and S_r is as follows:

$$N_{FR} = \omega/(2\pi) = S_r V_A/(2\pi R_R) \tag{13}$$

The control is outlined as follows:

- N_{FR} is set such that S_r is 4.0. In this case, N_{FR} is proportional to V_A. If N_{FR} exceeds the maximum rotor revolutions, a limiter is automatically set at 180 rpm (18.85 rad/s in ω). In this paper, the value of 4.0 was selected, which is larger than the S_r at which the optimum lift-to-drag ratio of the rotor appears, to achieve a greater energy saving effect.
- When θ_A is negative (wind from the port side), the rotor rotates to the right (N_{FR}>0). Conversely, when θ_A is positive (wind from the starboard side), the rotor rotates to the left (N_{FR}<0). However, when the absolute value of θ_A is smaller than 10°, the absolute value of N_{FR} is proportionally reduced to θ_A. Additionally, for θ_A = 0°, we set N_{FR}=0. When the wind comes from ship's fore, the rotor cannot generate sufficient thrust force and would become a resistance. Therefore, the rotor revolutions are stopped/reduced in the relative wind direction range (-10° < θ_A < 10°) to conserve the rotors' rotational energy.

4 CALCULATION RESULTS

4.1 STEADY SAILING CONDITION AND DELIVERED POWER OF THE ROTOR SHIP

As an example, Figure 8 shows the steady sailing conditions, including the ship speed (U), check helm (δ), hull drift angle (β), and heel angle (ϕ), of the bulk carrier with and without rotors under full- and ballast-load conditions in the environmental disturbance of U_W=10 m/s; $H_{1/3}$=2.1 m. In the figure, the horizontal axis represents the absolute wind-wave direction (θ_W). Although the rotors are arranged asymmetrically on the port and starboard sides, the calculated results are almost symmetrical. U increases under both full- and ballast-load conditions because of the rotor operation, except when the absolute wind direction θ_W is in the range of -20° – 20°. When θ_W is in this range, the absolute value of the lift force generated by the rotors is small, and the rotors act as a resistance; therefore, U does not increase. The lift generated by the rotors can cause the ship to change its course. To prevent this and sail straight, it is necessary to apply a check helm (δ). This also results in a hull drift angle (β). For U_W=10 m/s and $H_{1/3}$=2.1 m, under full-load conditions, δ and β are at most 3° and 1°, respectively. Under ballast-load conditions, δ and β are at most 1° and 2°, respectively; therefore, δ and β are small under both full- and ballast-load conditions. The maximum ϕ value is also small, less than 1°. δ, β, and ϕ exhibit opposite signs at θ_W = 0°. This is because the rotor rotation direction is reversed depending on the sign of θ_W.

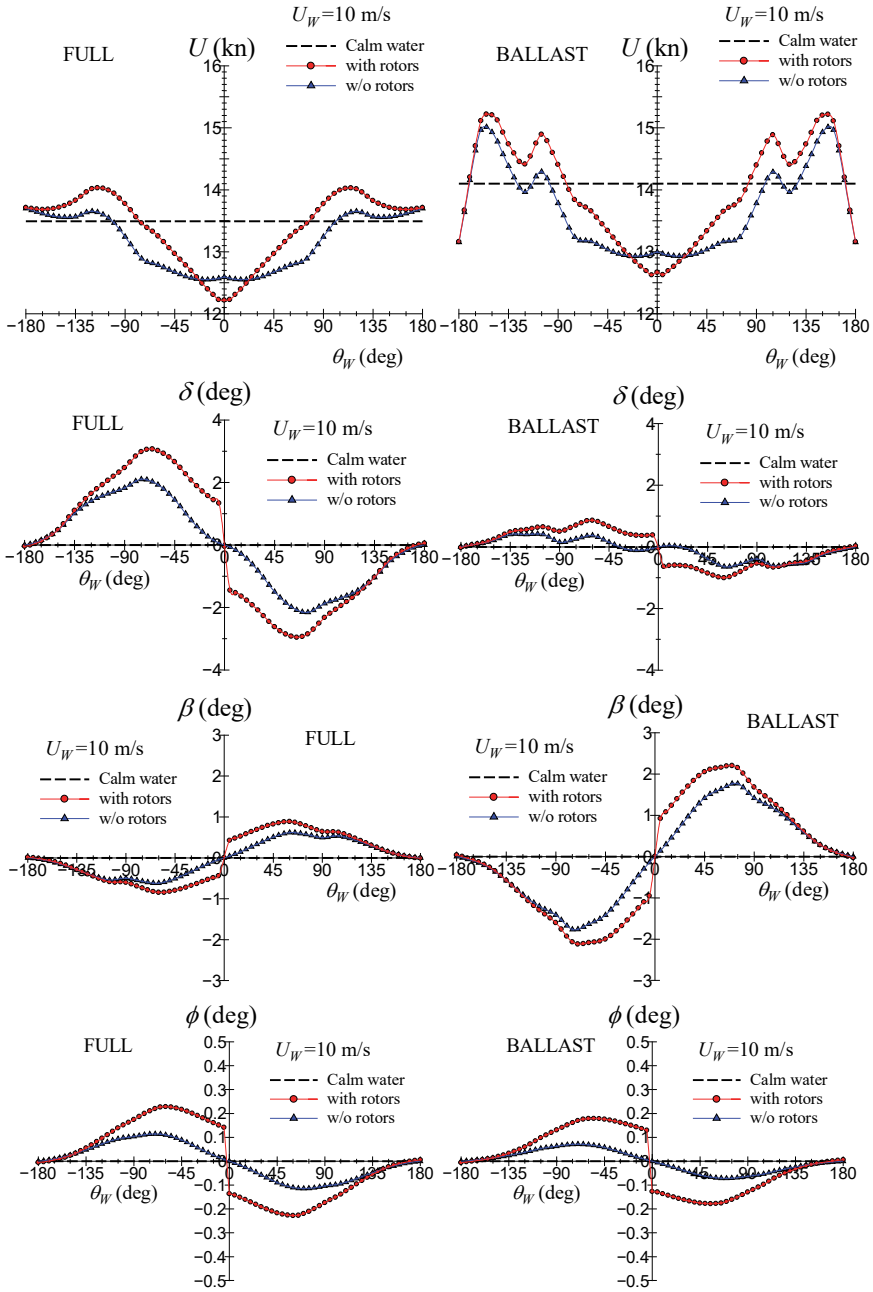

Figure 8. Calculation results for ship speed (U), check helm (δ), drift angle (β), and heel angle (ϕ) in full- and ballast-load conditions (U_W=10 m/s; $H_{1/3}$=2.1 m)

Figure 9 shows the delivered power (P_D) and rotor rotational power (P_R) of the bulk carrier. P_D decreases owing to the rotor operation, except when θ_W is in the -20° – 20° range, because the propeller load decreases owing to the thrust force generated by the rotors. P_R was a maximum of 50 ps, which is very small, less than 1% of P_D.

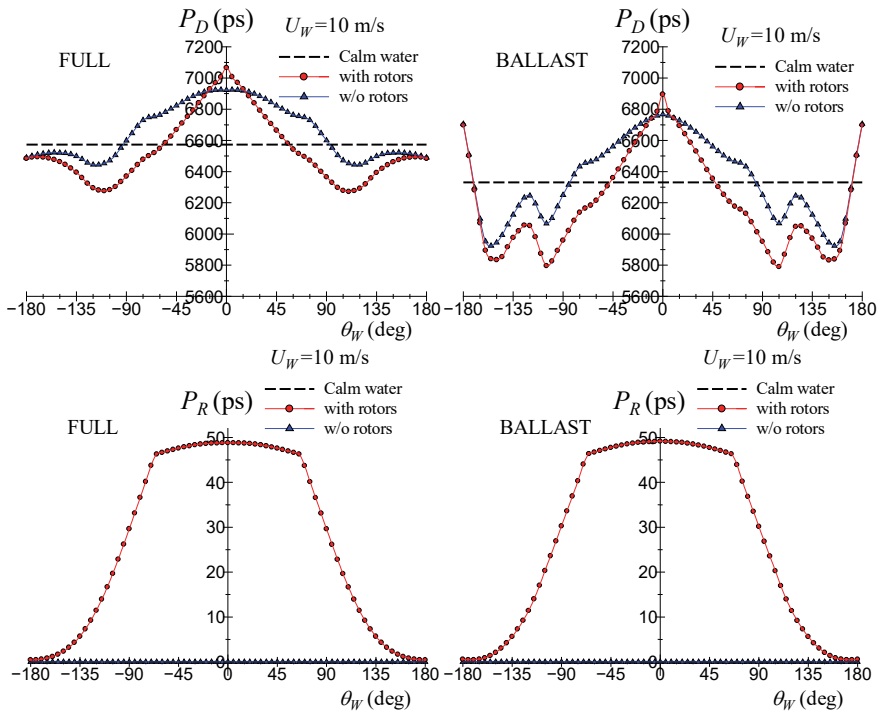

Figure 9. Calculation results for delivered power (P_D) and rotor rotational power (P_R) in full- and ballast-load conditions (U_W=10 m/s; $H_{1/3}$=2.1 m)

4.2 RESISTANCE COMPONENT COMPARISON

We investigated which resistance components act on the ship when U_W = 10 m/s and $H_{1/3}$ = 2.1 m. Figure 10 shows the

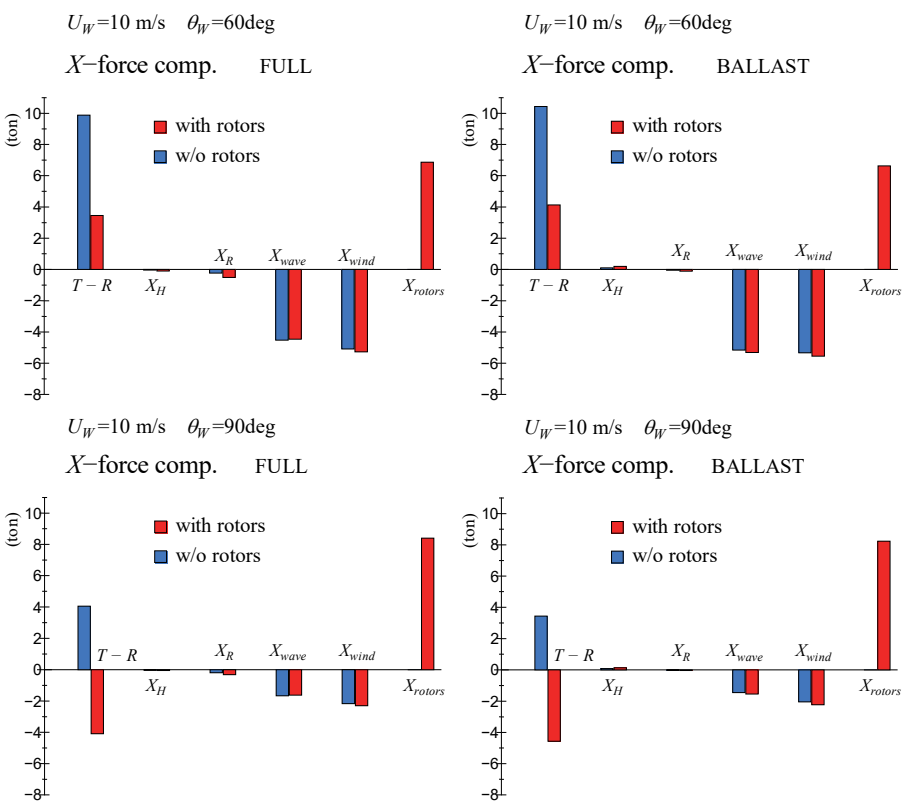

Figure 10. *X*-force components for two different wind (wave) directions with and without rotors (U_W=10 m/s; $H_{1/3}$=2. 1 m)

components of the surge force (X) acting on the ship under θ_W = 60° and 90°. In the figure, (T-R) is the difference between the propeller thrust (T) and the ship resistance (R) when moving straight, X_H is the resistance increase due to oblique movement, X_R is the steering resistance, X_{wave} is the added resistance in waves, X_{wind} is the wind resistance, and X_{rotors} is the thrust force due to the rotors. The values for each of these are shown with and without the rotors. The signs are positive and negative for thrust and resistance, respectively. For θ_W = 60°, X_{rotors} generates a relatively large thrust, and (T-R) decreases accordingly. It can be observed that the propeller load decreases owing to rotor operation. Meanwhile, under this condition, the wind and waves come from the quartering head wind/wave direction, and thus X_{wind} and X_{wave} become large in the negative direction. Consequently, the energy-saving effect of the rotors is reduced. For θ_W = 90° (beam wind, beam waves), X_{rotors} is larger and the absolute X_{wind} and X_{wave} values are smaller than those for θ_W = 60°; therefore, the effect of the rotor becomes significant. The thrust generated by the rotors was approximately 20% of the propeller thrust. Moreover, the absolute values of both the check helm (δ) and drift angle (β) were small, as shown in Figure 8; therefore, the absolute values of the resistance components (X_R, X_H) are small. No significant differences were observed in the qualitative trends of the resistance components between the full- and ballast-load conditions.

4.3 ENERGY-SAVING PERFORMANCE EVALUATION

The calculation results for the ship without the Flettner rotors and with them installed and operated under wind and waves were compared to determine the energy-saving gain. In practice, the energy-saving gain differs for different wind (wave) directions. Therefore, the average values of the obtained U and the sum of P_D and P_R for all wind (wave) directions were calculated. These are the average ship speed (U_{Ave}) and average power (P_{DRA}). Figure 11 shows the U_{Ave} and P_{DRA} results with and without the rotors under full- and ballast-load conditions. In the figure, the horizontal axis represents the absolute wind speed U_W. U_{Ave} with rotors is larger than that without rotors, and P_{DRA} with rotors is smaller than that without rotors. The effect of the rotors manifests as an increase in the ship speed and a decrease in the delivered power. The increment in U_{Ave} and the decrease in P_{DRA} owing to the rotor operation increase as U_W increases.

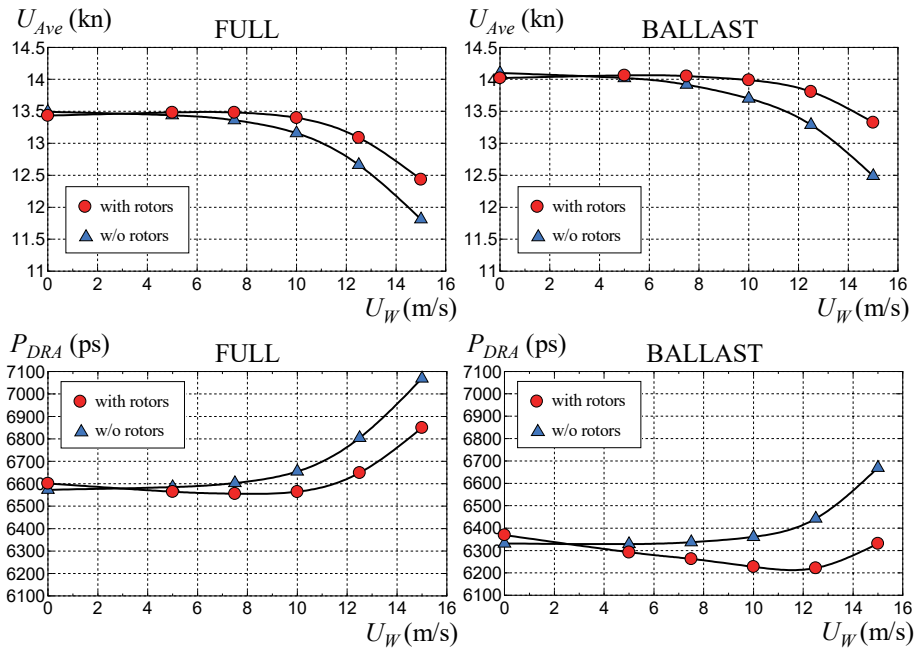

Figure 11. Average ship speed (U_{Ave}) and average delivered power (P_{DRA}) according to absolute wind speed (U_W)

Here, the ship speed increase ratio (e_U) and delivered power decrease ratio (e_P) owing to the rotor operation are respectively defined as follows:

$$e_U = U_{Ave}^{(with)} / U_{Ave}^{(wo)} - 1 \tag{14}$$

$$e_P = 1 - P_{DRA}^{(with)} / P_{DRA}^{(wo)} \tag{15}$$

The superscripts (*with*) and (*wo*) indicate operation with and without the rotors. In this study, the sum of e_U and e_P is considered as the energy-saving ratio of the ship. Figure 12 shows the calculation results for e_U, e_P, and their sum (Gain total) against the absolute wind speed (U_W) under full- and ballast-load conditions. At a wind speed of U_W =10 – 12 m/s,

the energy-saving ratio was 4 – 6% and 5 – 7% under full- and ballast-load conditions, respectively. At a wind speed of U_W = 15 m/s, the energy-saving ratio was 9% under full-load conditions and over 12% under ballast-load conditions. However, it should be noted that P_{DA} exceeded the normal power in the head wind under full-load conditions.

At the same wind speed, the thrust generated by the rotors is almost the same in full- and ballast-load conditions. However, the average ship speed loss and power increase at the larger wind speed are smaller in ballast-load condition than in full-load condition, as shown in Figure 11. This is because the hull resistance in ballast-load condition is originally smaller than that of full-load condition, so the energy saving gain is calculated to be larger in ballast-load condition than in full-load condition.

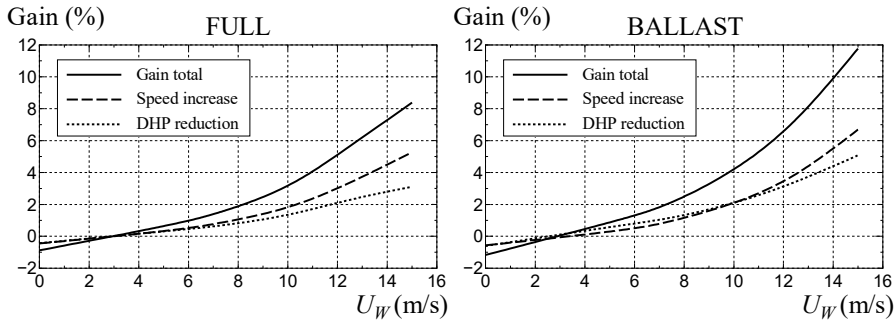

Figure 12. Speed increase ratio (e_U) and delivered power decrease ratio (e_P) by the rotors and total gain

5 CONCLUSION

In this study, a calculation method was developed for predicting the steady sailing condition and propulsive performance of a ship equipped with Flettner rotors based on the MMG-method. The developed method was applied to a bulk carrier with four Flettner rotors to predict its propulsive performance and energy-saving gain. It was found that the ship speed increased and the delivered power decreased owing to the thrust force generated by the rotors. Compared to the same ship without rotors, the energy-saving gains were 4 – 6% and 5 – 7% under full- and ballast-load conditions, respectively, for an absolute wind speed range of U_W = 10 – 12 m/s. The calculation results demonstrate that the proposed method is useful for predicting the propulsive performance of ships with Flettner rotors.

In future work, we plan to investigate basic design issues, such as the influence of the number and arrangement of rotors on the energy-saving effect of the Flettner rotors.

6 ACKNOWLEDGEMENT

We would like to thank Mr. Y. Wada for his support during the analysis.

7 REFERENCES

Fujiwara, T., Ueno, M., Ikeda, Y., 2005a, A new estimation method of wind forces and moments acting on ships on the basis of physical component models, J. Japan Society of Naval Architects and Ocean Engineers 2, 243-255. (in Japanese)

Fujiwara, T., Ueno, M., Ikeda, Y., 2005b, Cruising performance of ships with large superstructures in heavy sea –1st report: added resistance induced by wind–, J. Japan Society of Naval Architects and Ocean Engineers 2, 257-269 (in Japanese).

Hamamoto, M., Kim, Y., 1993, A new coordinate system and the equations describing manoeuvring motion of a ship in waves, J. Society of Naval Architects of Japan 173, 209-220 (in Japanese).

Hasnan, M. A. A., Yasukawa, H., Hirata, N., Terada, D., Matsuda, A., 2020, Study of ship turning in irregular waves, J. Marine Science and Technology 25(4), 1024-1043.

Kijima, K., Katsuno, T., Nakiri, Y., Furukawa, Y., 1990, On the manoeuvring performance of a ship with the parameter of loading condition, J. Society of Naval Architects of Japan 168, 141-148.

Kijima, K., Nakiri, Y., 1999, Approximate expression for hydrodynamic derivatives of ship manoeuvring motion taking into account of the effect of stern shape, Trans. West Japan Society of Naval Architects 98, 67-77, (in Japanese)

Sogihara, N., Kume, K., 2022, Fuel saving Evaluation of a rotor ship in actual sea, J. Japan Society of Naval Architects and Ocean Engineers 35, 29-41. (in Japanese)

Tillig, F., Ringsberg, J. W., 2020, Design, operation and analysis of wind-assisted cargo ships, Ocean Engineering 211, 107603,

Yasukawa, H., Yoshimura, Y., 2015, Introduction of MMG standard method for ship maneuvering predictions, J. Marine Science and Technology 20(1), 37-52.

Yasukawa, H., Hirata, N., Matsumoto, A., Kuroiwa, R., Mizokami, S., 2019a, Evaluations of wave-induced steady forces and turning motion of a full hull ship in waves, J. Marine Science and Technology 24(1), 1-15.

Yasukawa, H., Sakuno, R., Yoshimura, Y., 2019b, Practical maneuvering simulation method of ships considering the roll-coupling effect, J. Marine Science and Technology 24(4), 1280-1296.

Yasukawa, H., Sakuno, R., 2019c, Application of the MMG-method for prediction of steady sailing condition and course stability of a ship under external disturbances, J. Marine Science and Technology 25(1), 196-220.

Yasukawa, H., Hirata, N., Nakayama, Y., Matsuda, A., 2021, Drifting of a dead ship in wind, Ship Technology Research 70(1), 26-45.

Yasukawa, H., Hirata, N., 2023, Effects of wave direction on the ship turning in regular waves, Ocean Engineering 286, 115581.

8 AUTHORS BIOGRAPHY

Hironori Yasukawa is a professor at the Graduate School of Advanced Science and Engineering, Hiroshima University, Japan. His specialty is ship maneuverability. He was ITTC member of maneuverability committee (2005 to 2011), the member of specialist committee on performance of ship in service (2014 to 2017), and the chairman of specialist committee on maneuvering in waves (2017 to 2021).

DEVELOPMENT OF A PUSH BOAT BARGE UNIT WITH AN AUXILLARY SHALLOW WATER PROPULSION SYSTEM

Benjamin Kossmann, Ould el Moctar, Thomas E. Schellin, University of Duisburg-Essen, Germany

DEVELOPMENT OF A PUSH BOAT BARGE UNIT WITH AN AUXILLARY SHALLOW WATER PROPULSION SYSTEM

BENJAMIN KOSSMANN, OULD EL MOCTAR, THOMAS E. SCHELLIN, UNIVERSITY OF DUISBURG-ESSEN, GERMANY

SUMMARY

For several years, European inland shipping has been affected by prolonged periods of extremely shallow water levels. To navigate under these unfavorable conditions, we developed a push boat for the Elbe River with a draft of only 0.7 m, capable of operating in water levels down to 1.0 m. This push boat is equipped with a primary propulsion system consisting of two Voith Linear Jets (VLJs) and, for shallow waters, a secondary propulsion system consisting of two smaller outer VLJs. Employing experimental and numerical methods, we analyzed the flow surrounding a scaled down push boat barge unit operating at two representative drafts. We carried out systematic URANS resistance and propulsion studies up to a full-scale speed of 10 km/h and, under shallow water conditions, up to a full-scale speed of 6 km/h. We employed a virtual disc model of the VLJs to carry out the propulsion simulations.

NOMENCLATURE [Summary]

AP	Aft perpendicular (m)
B	Ship breadth (m)
B_{Tank}	Tank width (m)
c_B	Block coefficient (-)
F_n	Froude number (-)
F_{nh}	Deep Froude number (-)
FP	Forward perpendicular (m)
h	Water depth (m)
J	Advance coefficient (-)
KQ	Moment coefficient (-)
KT_T	Total thrust coefficient (-)
L_B	Length of barge (m)
L_{OA}	Convoy`s length over all (m)
L_{PB}	Length of push boat (m)
MS	Midship (m)
O	Origin (m)
R_e	Reynolds number (-)
R_{TM}	Total longitudinal model resistance (N)
S_{wett}	Wetted surface of ship`s hull (m²)
T_{B_max}	Maximum draft of the barge (m)
T_{B_min}	Minimum draft of the barge (m)
T_{PB_max}	Maximum draft of the push boat (m)
T_{PB_min}	Minimum drat of the push boat (m)
T_1	Thrust of outer Linear Jet (N)
UKC	Under keel clearance (m)
u/u_0	Normalized longitudinal velocity (-)
v/u_o	Normalized transversal velocity (-)
v	Velocity component in Y-direction (m/s)
Y	Grid refinement ratio (-)
z_{MS}	Ship`s vertical displacement (mm)
Δ	Displacement freshwater (m³)
ρ	Density of fresh water (kg/m³)
λ	Scale factor (-)
η_T	Total open water efficiency (-)

1 INTRODUCTION

The Elbe River is of central importance as it connects the harbor of Hamburg with Germany's eastern canal network. Only one lock near Geesthacht interrupts inland shipping on the Elbe River along its German course. At this lock, the river's tidal currents are slowed down shortly before Hamburg, which improves shipping conditions from here on (Federal Waterways and Shipping Administration, 2021). The long-standing trend of declining freight transport has continued, declining to 12,774 transports in 2019. One problem for inland shipping has always been the prolonged shallow water periods (Schifffahrtsverlag Hansa GmbH & Co. KG, 2020). According to shipping police regulations, single vessels with a maximum length of 110 m and a maximum width of 11.45 m are permitted on the Elbe River. Regarding convoys, their maximum dimensions are specified for different areas. This means that all areas of the Elbe are passable for convoys not exceeding the dimensions of the largest single vessels.

The average flow velocity of the Elbe River between the Czech border and the Geesthacht lock is 3 km/h. (Kurs Elbe. Hamburg bis Wittenberge., 2021) In the area of the Lower Elbe River, which stretches from Geesthacht to Cuxhaven, the flow velocity is significantly higher: on average it is 5 km/h, and this flow velocity is highly dependent on the water level. At the Dresden gauge station, the flow velocity varies from 3.6 km/h at a water level of 1.0 m to 6.1 km/h at a water level of 5.5 m (Adam, 2001). The navigable channel depth is particularly critical in the Dömitz, Magdeburg, and Dresden areas in shallow waters. The water level in these areas can frequently drop to a depth of one meter, which makes it difficult to maintain a sufficient draft with conventional single vessels. The Elbe River is characterized by a sandy, partly very shallow waterway. In contrast to the Rhine River, the Elbe River is only seldomly used for classic freight transports. In this context, a push boat with a small draft has proved to be the optimum solution. The push boats of the type "Oberelbe" developed in the German Democratic Republic (GDR) have a minimum draft of 0.8 m. This means that large parts of the Elbe can be navigated even at low water levels. To reduce the cargo on other modes of transport, the operation of inland waterway vessels with smaller drafts needs to be made even more reliable. Heuser et al. (1979) established general guidelines for the design of aft ship geometries of pusher boats, encompassing the geometry, arrangement of the propulsors, as well as use and placement of rudders and flank rudders. At the beginning of the 1980s, the VEB Deutsche Binnenwerft Genthin (Bin2022) developed a series of push boats of type KSS-300, which were designed to address the specific requirements for navigating in the shallow waters of the upper Elbe. These vessels have a length of 28.68 m, a width of 10.27 m, and a draft of 0.8 m. Their propulsion system comprises two ducted propellers. Zöllner et al. (1994) designed an Upper Elbe River push boat as part of the VEBIS project OSTWESTSCHUB, with the objective of adapting to the challenging conditions of the upper Elbe. The push boat considered has a length of 27.0 m, a width of 10.5 m, and its draft is 0.8 m. This design is similar to the last GDR river push boats of the "flachgehend" type. The vessel is powered by two pump jets. Guesnet et al. (2004) undertook the design of multiple barge trains, with a particular focus on their utilisation under shallow water conditions. In conjunction with these designs, their study encompassed the formulation of performance predictions and estimates of propulsion and steering forces. This comprehensive approach was further complemented by an analysis of local conditions of waterways and waterway structures, a pivotal aspect of the INBAT project. Kulczyk et al. (2003) studied the comparative analysis of aft ship geometries and propulsion configurations for pusher craft, drawing upon existing designs and paying particular attention to the navigability in shallow waters. Towards this end, a range of experimental and numerical analyses were conducted and validated through the implementation of the HPSDK calculation system developed at the Wroclaw University of Technology. Zentari et al. (2022) explored the impact of shallow water conditions on the hydrodynamic performance, including the resistance and propulsion of coupled pusher-barge convoys. They developed numerical models to simulate the hydrodynamic behavior of the convoy in shallow waters. They employed CFD tools to analyze the flow around the vessels in shallows and to predict the resistance experienced by the convoy. They found that shallow water significantly increases resistance due to additional frictional losses and hydrodynamic effects, such as water constriction and flow disturbance. Besides, it is well known that water depth affects the clearance between a vessel's hull and the seabed, leading to increased hull friction and altered flow patterns. Yuba et al. (2013) analyzed the effect of different maneuvering and propulsion devices for different configurations.

For this purpose, a particularly shallow-water-capable push boat barge convoy was designed for navigating on the Elbe River. The advantages of a pushed convoy lie in its particularly high cargo capacity of barges with small drafts (Renner et al., 2004). The propulsion of the pushed barge can also be optimized for very small drafts as the loaded cargo hardly causes the ship's draft to vary. Based on the general conditions of the Elbe River, a push boat was developed that can be operated with a minimum draft of 0.7 m. If sufficient water is available, the draft can be increased to 1.0 m. The push boat is equipped with four Voith Linear Jets (VLJs). The outer VLJs have a rotor diameter of 630 mm and provide propulsion for shallow drafts and low power requirements. For the barge with a higher load, the inner VLJs with a rotor diameter

of 730 mm are switched on and serve as boosters. To prevent ventilation at shallow drafts, the outer VLJs are each mounted in a skeg, and they are supplied with water from specially shaped intake tunnels at the sides of the chine radius.

2 TEST CASE DESPRIPTION

The developed convoy has a total length of 110 m and a width of 11.45 m, while the push boat is 30 m long, and the barge is 70 m long. The push boat is capable of operating at two drafts. The standard draft is 1.0 m, with the capability of being reduced to 0.7 m when navigating in shallow waters is necessary. This draft reduction is achieved by proper ballasting of the vessel and a corresponding reduction in bunker fuel. Table 1 lists the principal dimensions of the push boat and the barge at model-scale and at full-scale.

Table 1: Principal dimensions of the Elbe River convoy.

Principal dimension	*Acronym*	Value		Unit
		Model Scale	Full Scale	
Length push boat	L_{PB}	3.75	30.00	m
Length barge	L_B	5.00	80.00	m
Length overall	L_{OA}	8.75	110.00	m
Width	B	1.43	11.45	m
Minimum draft push boat	T_{PB_min}	0.0875	0.70	m
Maximum draft push boat	T_{PB_max}	0.125	1.00	m
Minimum draft barge	T_{B_min}	0.0875	0.70	m
Maximum draft barge	T_{B_max}	0.2625	2.10	m
Block coefficient push boat	c_{B_PB}	0.89		-
Block coefficient barge	c_{B_B}	0.94		-

The developed convoy has a high block coefficient, which makes it possible to generate sufficient buoyancy even at lowest drafts. For this purpose, the push boat is equipped with two lateral skegs which, in addition to increasing buoyancy, serve to accommodate the outer Linear Jets, while the integration of the VLJs into the skegs ensures protection in the event of grounding. Water is drawn in through two lateral intake tunnels, which suck in the water as far away from the free surface as possible and therefore without ventilation, making the outer VLJs function more like water jets. The design of the intake tunnels favors the lateral intake of water in extremely shallow waters and enables a sufficient water supply for the VLJs. Maneuverability is ensured by two twin rudders with an asymmetrical profile mounted behind each of the outer VLJs, whereby a transverse force can be generated by differential thrust with the inner VLJs. The stern of the push boat is extended to below the waterline at 0.7 m to improve the stopping and astern characteristics. This prevents ventilation when navigating at shallow drafts. The barge lines are based on the lines of a Europa-IIa barge with a wedge frame bow, but with a more rounded design to increase the load capacity at shallow drafts. Figure 1 shows stern and bow body plans of the push boat and the barge.

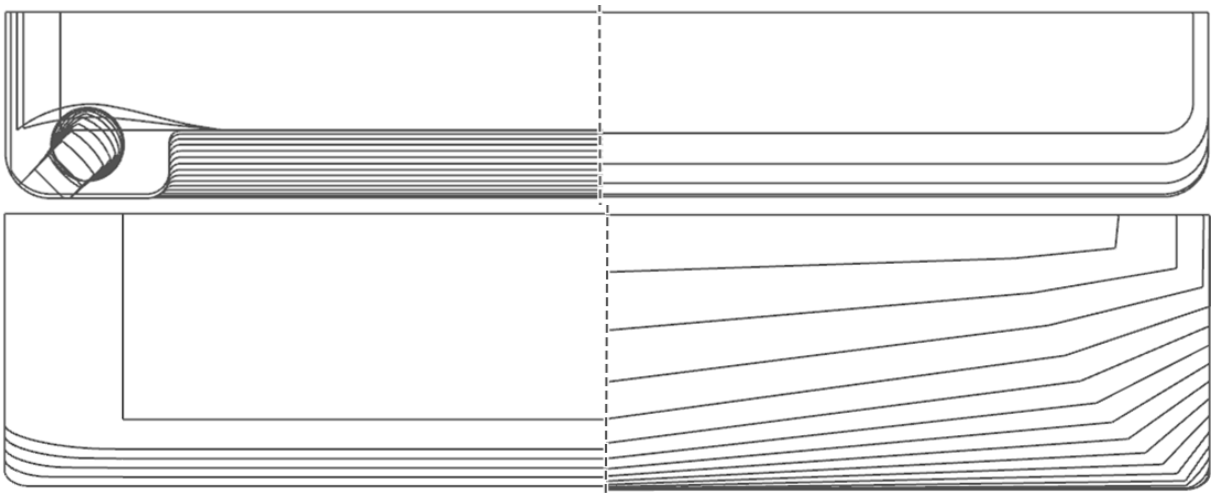

Figure 1: Body plans of the stern (left) and the bow (right) for the push boat (top) and the barge (bottom).

3 NUMERICAL METHOD

The simulations were conducted using version 2302 of the Siemens StarCCM+ numerical flow solver. The unsteady Reynolds-Averaged Navier-Stokes (URANS) equations were solved using the k-ω SST model to account for turbulence. Second-order methods were employed to discretize the conservation equations in space and time. The Volume of Fluid (VoF) method was used to model the free surface. The propulsion of the VLJs were modeled using a virtual disk approach. The free surface in the vicinity of the ship, the coupling mechanism, and stern was subject to local refinement. The computational domain was designed as a mesh of trimmed cells. The ship´s motion was achieved by a mesh deformation algorithm. By employing suitable initial and boundary conditions and a series of discrete approximations, an algebraic system of equations was derived, which was subsequently solved numerically. The spatial solution domain was initially divided into a finite number of contiguous control volumes (CVs). The equations of interest were found to contain surface and volume integrals as well as temporal and spatial derivatives. The derivatives were suitably approximated for each control volume at each time step. It was assumed that the Reynolds-Averaged Navier-Stokes (RANS) equations adequately described the flow, with turbulence effects accounted for via an eddy viscosity model. The equations to be solved are comprised of the continuity equation, the three momentum component equations, and the two equations for turbulence properties (Ferziger et al., 2019). In the equations for conservation of momentum (1) and mass (2), *V* describes the CV, *S* its surface, *T* the stress tensor, *v* the velocity, *ρ* the density, and *b* the body forces per unit mass. Free surface effects (3) were captured with the volume of fluid method, where *c* describes the alpha value (Ferziger et al., 2019):

$$\frac{\delta}{\delta t}\int_V \rho v \, dV + \int_S \rho v v \cdot n dS = \int_S T \cdot n \, dS + \int_V \rho b \, dV \tag{1}$$

$$\frac{\partial}{\partial t}\int_V \rho \, dV + \int_S \rho v \cdot n dS = 0 \tag{2}$$

$$\frac{\delta}{\delta t}\int_V c \, dV + \int_S c v \cdot n \, dS = 0 \tag{3}$$

4 NUMERICAL SETUP

As in the model tests, the side boundaries were placed 5.0 m from the convoy's symmetry plane; the inlet boundary, three ship lengths from the convoy's AP; and the outlet boundary, four ship lengths from the ship's AP. At the outlet boundary, the hydrostatic pressure determined the pressures. At the inlet boundary, velocity and free surface height were prescribed. The bottom of the computational domain was considered as a non-slip wall moving with the flow. Therefore, the relative velocity at the bottom of the computational domain was zero. The hull surface was also considered as a no-slip wall. At the outlet boundary, hydrostatic pressures defined the pressure distribution. Small control volumes discretized the flow in the numerical domain. We used the trimmed cell mesher Simcenter in STAR-CCM+ (Siemens 2302) to create hexahedral cells in a grid across the entire region being meshed. The grid was locally refined near the bow, near the stern, near the coupling area, and between the underside and the bottom boundary of the domain. Our grid included six prismatic layers near the hull to model the boundary layer. To model the inner region of the boundary layer, we used a y+ of about 50. Figure 2 shows the grid structure utilized in the simulations.

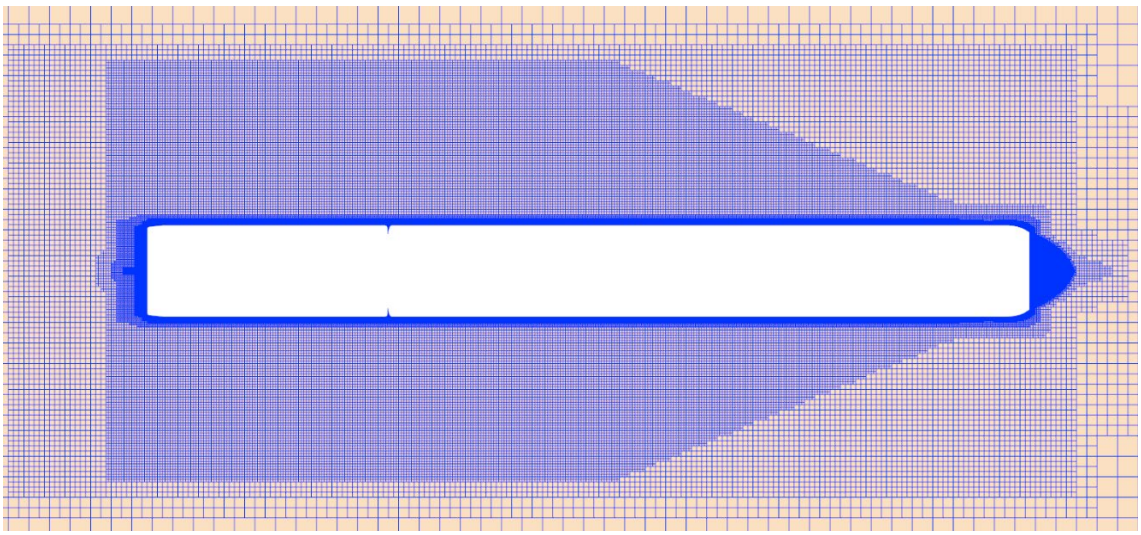

Figure 2: Numerical domain for the Elbe River convoy.

To describe the motions of the ship, two right-handed coordinate systems were used, with the origin located at the point of intersection between the initial vertical symmetry plane of the ship, its initial aft perpendicular (AP), and the plane of the stationary water line. The origin (O) of the initial coordinate system was defined as the point of intersection of the initial vertical symmetry plane of the ship, its initial aft perpendicular (AP), and the plane of the water's surface. A second, fixed-body coordinate system was defined with the origin (O) situated at the intersection of the displaced vertical symmetry plane of the ship, its displaced midship plane, and the plane of the water's surface. The X-coordinate points towards the bow of the ship, the Y-coordinate points towards starboard, and the Z-coordinate points upwards. Table 2 lists these coordinates. The longitudinal coordinates indicate the distance in meters between the AP and the FP relative to the centerline of the ship.

Table 2: Coordinates of the initial and body-fixed coordinate system (0) and the points of the forward (FP) and aft (AP) perpendicular and midship (MS) of the convoy at model scale.

Symbol	Initial CS [m]	Body-fixed CS [m]
O	[6.87; 0.00; 0.00]	[0.00; 0.00; 0.00]
AP	[0.00; 0.00; 0.00]	[-6.87; 0.00; 0.00]
FP	[13.75; 0.00; 0.00]	[6.87; 0.00; 0.00]
MS	[6.87; 0.00; 0.00]	[0.00; 0.00; 0.00]

Table 3 summarizes the parameters of the numerical simulations in model-scale of the convoy at the two operating states considered. The list includes the *h/T* ratio, the under-keel clearance (UKC), the water depth *h*, the ship speed *v*, as well as the depth Froude number Fn_h, the Froude number *Fn*, and the tank width. Note that all cases considered parameters were in the subcritical speed range.

Table 3: Test matrix of the convoy for a model-scale of 8.

Operating point	h/T [-]	UKC_{PB} [m]	UKC_B [m]	T_{PB} [m]	T_B [m]	h [m]	v [m/s]	Fn_h [-]	B_{Tank} [m]
'Minimum'	1.43	0.0375	0.0375	0.0875	0.0875	0.125	0.393	0.35	10.00
							0.442	0.40	
							0.491	0.44	
							0.541	0.49	
							0.589	0.53	
'Maximum'	1.43	0.25	0.1125	0.125	0.2625	0.375	0.491	0.26	10.00
							0.589	0.31	
							0.786	0.41	
							0.982	0.51	
							1.277	0.67	

The simulation of the Voith Linear Jet was carried out with the aid of the virtual disk model in StarCCM+ as the detailed geometry of the rotor and stator was not available. Table 4 lists the open water characteristics of the VLJs. The open water tests were performed at Schiffbau-Versuchsanstalt Potsdam GmbH (SVA-Potsdam) with a propeller diameter D_P = 0.23 m and a revolution of n = 7.5 s^{-1}(SVA3428).

Table 4: Open water characteristics of the VLJs with advance coefficient *J*, total thrust coefficient KT_T, torque coefficient *KQ*, and total open water efficiency η_T.

J	0	0.2599	0.5204	0.7809	1.0388	1.2971	1.5679	1.8307	2.0802	2.338	2.6012
KT_T	1.5041	1.3803	1.215	1.0424	0.8877	0.7443	0.5953	0.4501	0.2995	0.1314	-0.064
KQ	0.2852	0.2777	0.267	0.2589	0.2512	0.2429	0.2302	0.2148	0.1956	0.1714	0.1432
η_T	0	0.2002	0.367	0.4873	0.5688	0.6158	0.6284	0.5944	0.4935	0.2779	-0.179

5 DISCRETIZATION STUDY

To guarantee adequate grid quality for our simulations, we conducted studies on the discretization of space and time. The approach proposed by Oberhagemann et al. (2016) was employed to calculate discretization errors. In accordance with their procedure, the simulations were conducted on three progressively finer grids, commencing with a coarse grid. The absolute thickness of the boundary layer and the cells in closest proximity to the wall were maintained at a consistent

value across all three grids. Table 5 lists the number of control volumes of each grid and the associated grid spacing (Δ_{x1}, Δ_{x2}, Δ_{x3}) and time step size (Δ_{t1}, Δ_{t2}, Δ_{t3}) for ship resistance at a velocity of 0.589 m/s at the operating point 'Minimum'. Additionally, the table presents the spatial grid refinement ratio γ, along with the longitudinal ship resistance R_{TM} and the ship's sinkage z_{MS} obtained on the three grids. Furthermore, it includes the comparative extrapolated (grid-independent) and the measured resistance and sinkage, along with their absolute and percentage errors.

Table 5: Grid Spacing, time step, number of cells, refinement ratio, vertical midship displacement and longitudinal force obtained on the coarse, the medium, and the fine grids and the extrapolated (grid-independent) and measured vertical amidship displacement, the longitudinal force and errors of the convoy at 0.589 m/s.

	Δx [m]	**Δt** [s]	**Number of cells** [-] Mio	**γ** [-]	**z_{MS}** [mm]	**R_{TM}** [N]
Coarse	0.113	0.0141	7.53	1.0	-8.1	20.76
Medium	0.080	0.0100	14,14	0.66	-8.5	-22.78
Fine	0.057	0.0071	45.78	0.44	-8.6	-23.55
Extrapolated	- -	-	-	0.0	-8.8	-24.02
Measured	- -	-	-	-	-9.0	-24.39
Absolute computed error	- -	-	-	-	0.2	0.37
Percentual computed error	- -	-	-	-	2.27%	1.53%

In this study, we conducted a discretization analysis under turbulent flow conditions, with the primary focus being on the ship's vertical displacements z_{MS} and the total longitudinal force R_{TM}. As the grid fineness, i.e., the refinement ratio γ, decreased, the computed variables z_{MS} and R_{TM} obtained on the three grids, as well as the extrapolated (grid-independent) and measured values, converged monotonically towards the grid-independent solution at $\gamma = 0$. It was observed that absolute values of vertical displacement increased and absolute values of the longitudinal force increased with increasing grid fineness. The maximum error for midship sinkage was observed at z_{MS} = -8.8 mm for the extrapolated mesh, and the measurement uncertainty was determined to be about 1.0 mm. Consequently, the computed midship sinkage was found to be underestimated with a discrepancy of around 0.2 mm from the measured values. The values for longitudinal resistance were underestimated with a discrepancy of around 0.37 N for the extrapolated mesh. The numerical simulations presented herein were performed using the medium-sized grid, which represented a compromise between accuracy and computing effort.

6 NUMERICAL RESULTS

6.1 COMPARISON OF EXPERIMENTAL (EFD) AND COMPUTED (CFD) RESULTS

The numerical results (CFD) were validated against model experiments (EFD) conducted at the Institute of Sustainable and Autonomous Maritime Systems (INAM). Due to the considerable length of the scale model, a shortened barge was employed. The numerical approach was validated against comparative model test measurements. The remaining investigations of the thrust coupling were conducted purely numerically. Figure 3 (left) plots the longitudinal resistance R_{TM} for the midship sinkage z_{MS} of the convoy with the shortened barge at the 'Minimal' operating point versus the model speed v_M. As seen, there is a high degree of correlation between the ship resistances obtained from the EFD and CFD models, with a maximum deviation of less than 2 % in resistance. The magnitude of the sinkage is frequently underestimated, with the maximum discrepancy of about 6 %. As demonstrated in Figure 4 (right), a comparison of the propulsion is provided. It plots the thrust T_1 and the rotation rate n_1 of the port side VLJ versus the model velocity v_M. A substantial agreement between the experimental model and the simulation is evident. The generated thrust of the Virtual Disk model and the determined rotational speed are found to be lower than the measured values due to the slightly underestimated resistance.

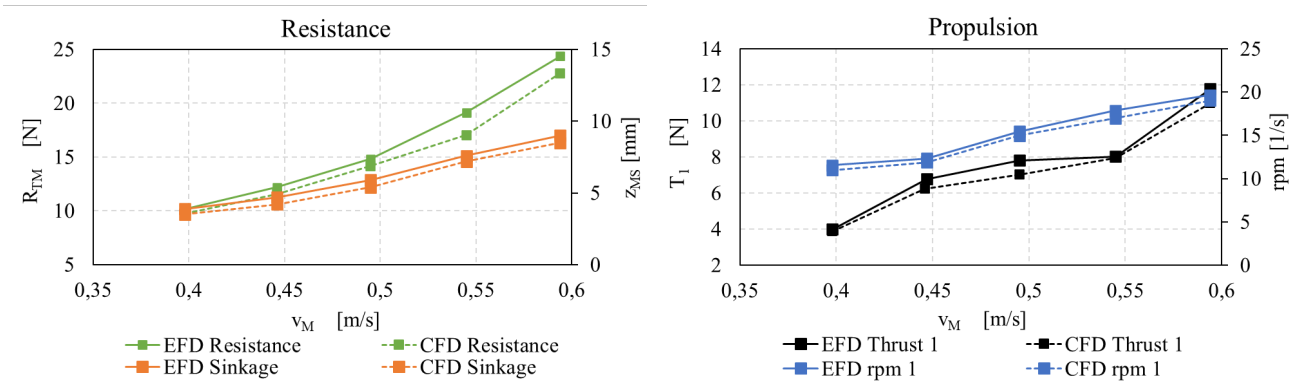

Figure 3: Comparison of longitudinal resistance R_{TM} and midship sinkage z_{MS} over the model velocity v_M of the convoy with shortened barge between EFD and CFD at operating point 'Minimum' (left) and comparison of VLJ port thrust and revolution over the velocity v_M of the convoy with shortened barge between EFD and CFD at operating point 'Minimum' (right).

6.2 RESISTANCE SIMULATIONS

Based on this setup, the resistance and propulsion simulations were carried out with an unabridged barge. The results of the resistance tests at the 'Minimum' and 'Maximum' operating points are shown in Figure 4 (left). As can be deduced from the evidence presented, the longitudinal resistance is primarily contingent on the breadth of the vessel rather than its length. At the 'Minimum' operation point, the resistance with standard barge is found to be 25% higher than that achieved with the use of the shortened barge. The 'Maximum' operating point demonstrates a maximum longitudinal resistance of 158 N at a velocity of 0.982 m/s. This velocity is equivalent to a full-scale vessel speed of 10 km/h and is identified as the critical velocity for navigating the Elbe River according to the ES-TRIN criteria (CESNI2019).

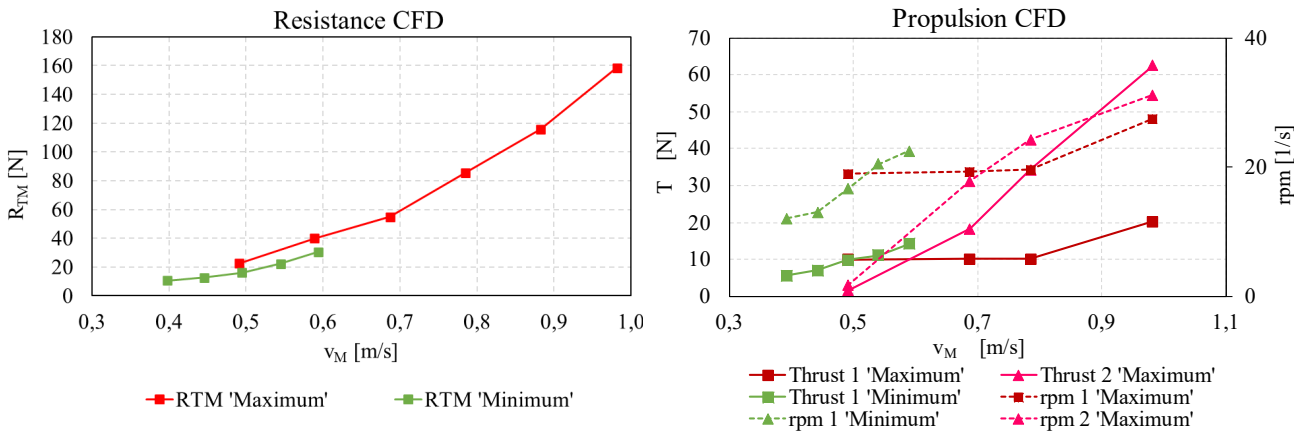

Figure 4: Computed longitudinal resistance R_{TM} vs. model velocity v_M of the convoy with standard barge at operating point 'Minimum' and 'Maximum' (left) and the VLJ's primary (T_2) and secondary thrust (T_1) and revolution vs. model velocity v_M.

Figure 5 shows the Q-criterion of the vorticity magnitude in the coupling area of the barge at the operating point 'Maximum' for the barge advancing at its highest model speed of 0.982 m/s. In this figure, looking from aft and bottom up, a massive flow detaches around the barge's stern. Two dominant vortices can be seen at the outer corners of the barge, which continue below the push boat. Such detaching vortices contribute significantly to the overall resistance of the convoy. Furthermore, the dynamic pressure on the barge hull (white grey color bar) is shown. Strong pressure jumps can be identified on the outer skin of the push boat (black areas), which are caused by the two dominant vortices generated by the barge. A negative pressure area is seen below the entire barge up to the coupling area. A jump to positive pressure is observed in the dominant vortices. In areas without dominant vortices, a negative pressure is still observed, as also in the rest of the barge's hull.

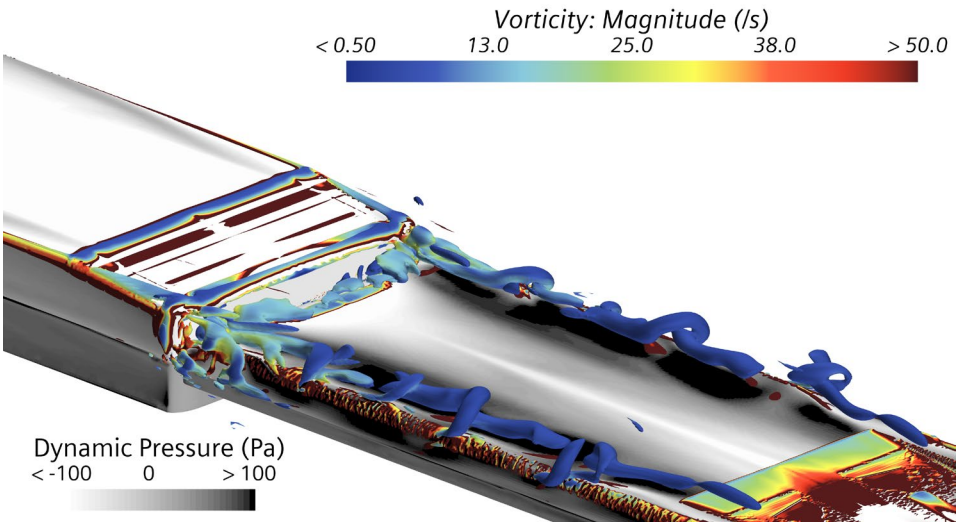

Figure 5: Q-criterion of volume fraction of water in the coupling area, showing the vorticity in the i-direction for the convoy at its 'Maximum' operating point advancing at 0.982 m/s.

6.3 PROPULSION SIMULATIONS

As only a virtual disc model was available for the VLJs and the operation of these VLJs, the present installation situation is more like that of a water jet. Thus, the investigations for this case differ significantly from the classical propulsion tests. In this case, the investigation of the VLJs is carried out via a bollard pull test, corresponding to the actual operating conditions. Consequently, no propeller open water test was carried out. The thrust generated by the VLJs was set in the simulation to compensate for the total resistance of the convoy. At the 'Minimum' operating point, only the two outer VLJs were used, as the inner VLJs could not be operated due to insufficient water supply. At the 'Maximum' operating point, all four VLJs were used. The inner VLJs acted as boosters. Maneuverability is provided by a twin rudder system on the outer VLJs and the differential thrust on the inner VLJs.

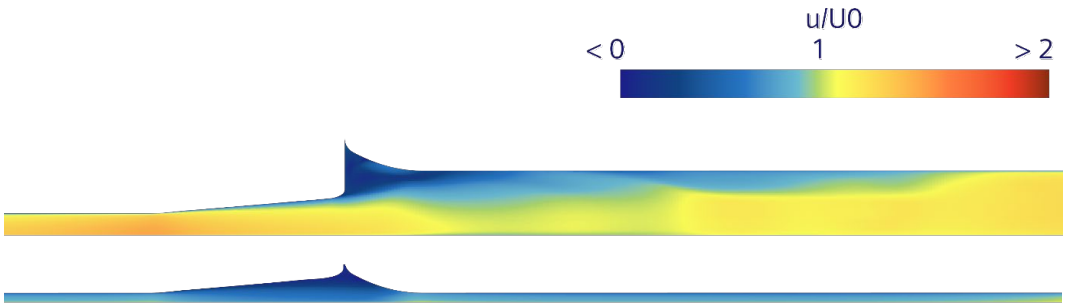

Figure 6: For the self-propulsion point on the midship plane in the coupling area, normalized velocity u/u_0 at the operating point 'Maximum' (top) for the convoy advancing at 0.982 m/s (top) and at the operating point 'Minimum' for the convoy advancing at 0.589 m/s (bottom).

Figure 6 illustrates the normalized velocity u/u_0 in the coupling area at the 'Maximum' and at the 'Minimum' operating points in the midship plane. At the 'Maximum' operating point, a recirculating zone with a relative velocity of zero is clearly visible behind the barge below the push boat. Below the barge, the surrounding water is accelerated more strongly due to the small UKC. At the 'Minimum' operating point, almost no relative velocity of the water can be seen below the barge and the push boat. This can be explained by an almost completely pronounced boundary layer that extends to the domain bottom. For this reason, the inner VLJs cannot be operated sensibly, as only an insufficient water supply can be guaranteed under such inflow conditions.

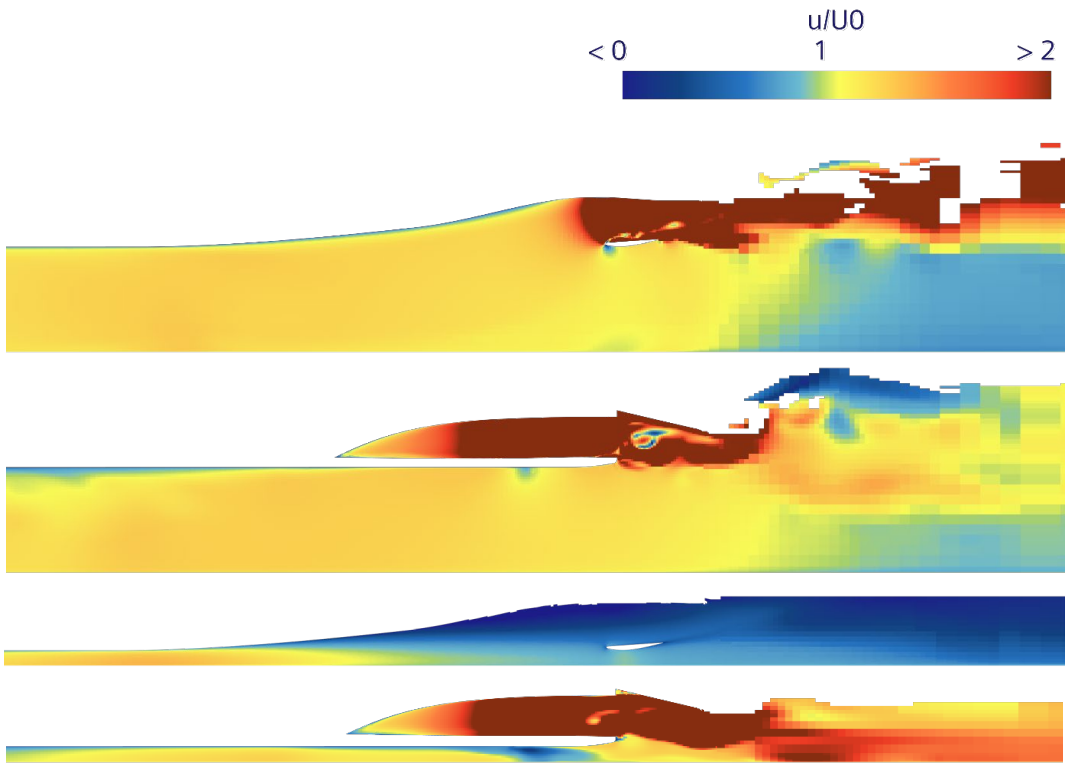

Figure 7: Normalized velocity u/u_0 at the 'Maximum' operating point for the convoy advancing at 0.982 m/s on the inner VLJ plane (top), on the outer VLJ plane (upper center) and at the 'Minimum' operating point for the convoy advancing at 0.589 m/s on inner the VLJ plane (lower center) and on the outer VLJ plane (bottom) in the longitudinal direction at the self-propulsion point in the stern area.

Figure 7 illustrates the normalized velocity u/u_0 in the volume fraction water at the operating points 'Maximum' and 'Minimum' in the inner and outer propeller plane at the self-propulsion point for the convoy advancing at 0.982 and 0.589 m/s, respectively. All VLJs are in operation at the 'Maximum' operating point. The inflow conditions for the inner and outer linear jets can be rated as good, with a very pronounced stern sea and a larger dead water area above the mirror of the outer VLJs. At the 'Minimum' operating point, corresponding to a model speed of 0.589 m/s, the situation is reversed. Due to the limited UKC clearance, a significant dead water area is formed in the middle section below the push boat, which prevents the effective use of the inner VLJs. The specially shaped intake tunnel of the outer VLJ with suction in the chine radius, on the other hand, allows water to be aspirated from the side and thus ensures a sufficient water supply. A strong interaction can also be seen around the intake tunnel at the chine radius. The water is not only drawn in from the front of the area of the tank bottom and from the rear (Figure 7, fourth), but also from the side (Figure 8).

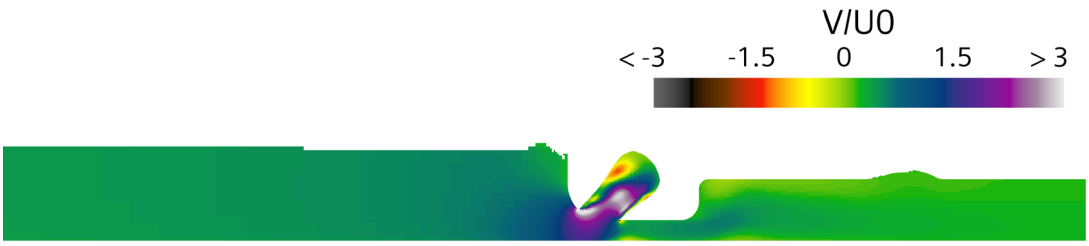

Figure 8: Normalized velocity v/u0 of the volume fraction of water at the 'Minimum' operating point for the convoy advancing at 0.589 m/s in lateral direction in the area of the intake of the outer VLJ.

The intake in the area of the chine radius enables ventilation to be effectively avoided when starting up on small drafts. This ensures a safe start-up. The small air volumes in the tunnels can be vented quickly and also guarantee clean inflow conditions during operation.

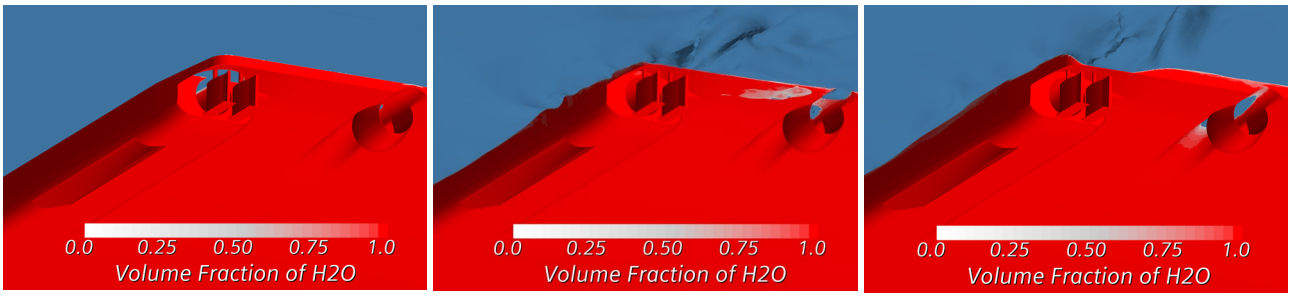

Figure 9: Elevation of free surface (light blue) and volume fraction of water with α = 0 (white) and α = 1 (red) on the ship's hull at stand still (left), after 2s (center), and after 20s (right) for the convoy accelerating at 0.589 m/s in the stern area of the push boat at the operating point 'Minimum'.

Figure 9 shows the acceleration process of the convoy in the 'Minimum' operating point from standstill to a speed of 0.589 m/s. The images show the times 0, 2, and 20 s. The free surface is shown in light blue, while the alpha value of the water volume fraction is shown in white (0 %) to red (100 %). It can be seen that the air in the outer tunnels is expelled within a very short time, and during further operation the water intake of the outer VLJ is free of ventilation.

7 CONCLUSION

A push boat equipped with primary and secondary propulsion devices, capable of operating in extremely shallow waters, was developed and experimentally and numerically investigated. The flow around a barge train in extremely shallow waters was presented, and the push boat's propulsion in extremely shallow water was demonstrated using a virtual disc model. The draft of this developed push boat is 0.1 m below the minimum draft of today's push boats. This opens up a wider range of applicability for navigating the Elbe River.

8 ACKNOWLEDGEMENTS

The authors acknowledge the financial support from the Federal Ministry for Economic Affairs and Energy (Bundesministerium für Wirtschaft und Energie) of Germany in project FlaBi (Project number 03SX532B). The authors also acknowledge the computing time granted by the Center for Computational Sciences and Simulation (CCSS) of the University of Duisburg–Essen on its supercomputer magnitude (DFG grants INST 20876/209-1 FUGG, INST 20876/243-1 FUGG) at the Zentrum für Informations- und Mediendienste (ZIM).

9 REFERENCES

1 Adam, P., 2004. Hochwasserforschung an der Elbe und ihren Nebenflüssen, in: Ufordat – Datenbank zur Umweltforschung, Umweltbundesamt, Germany.
2 Broß, H., 2002. Innovative Barge Trains for Effective Transport on Shallow Waters, in: 5th Framework Program, Bericht 1652, Duisburg, Germany.
3 Ferziger, J. H., Perić, M., & Street, R. L. 2019. Computational methods for fluid dynamics. Fourth edition, Springer.
4 Guesnet, T., Delius, A., Jastrzebski, T., 2004. Efficient Freight Transport on Shallow Inland Waterways – Results of the INBAT R&D Project, in: PRADS conference, Travemünde, Germany.
5 Heuser, H., 1979. Optimierung der Hinterschiffsform von Schubbooten, in: Bericht 853 a+b, Duisburg, Germany.
6 Kulczyk, J., Tabaczek, T., Werszko. R., 2003. An idea of the propulsion system and the pusher aft shape of a shallow water barge train, in: Transactions of the Built Environment vol 68.
7 Oberhagemann, J., 2016. On prediction of wave-induced loads and vibration of ship structures with finite volume fluid dynamic methods. PhD thesis, University of Duisburg-Essen, Germany.
8 Renner, V., Bialomski, W., 2004. Technische und wirtschaftliche Konzepte für flußangepaßte Binnenschiffe. In: Bericht 1701, Duisburg, Germany.
9 Wasserstraßen- und Schifffahrtsverwaltung des Bundes, 2020, in: Verkehrsbericht 2018.
10 Yuba, D. T., & Tannuri, E. A., 2013. Analysis of Pusher-Barge System With Different Maneuvering and Propulsion Devices. In International Conference on Offshore Mechanics and Arctic Engineering (Vol. 55393, p. V005T06A036). American Society of Mechanical Engineers.

11 Zentari, L., el Moctar, O., Lassen, J., Hallmann, R., & Schellin, T. E. 2022. Experimental and numerical investigation of shallow water effects on resistance and propulsion of coupled pusher-barge convoys, in: Applied Ocean Research, 121, 103048. https://doi.org/10.1016/j.apor.2022.103048
12 Zöllner, J., Heuser, H., 1994. Modellversuche mit Schubverbänden für den Einsatz in den Kanälen im Ost- und West-Verkehr und auf der Elbe und Oder, in: VEBIS, Ost-West-Schub, Bericht 1374, Duisburg, Germany.
13 (Bin2022), https://www.ddr-binnenschifffahrt.de/schiffstyp-sch-sss-elbe.htm.
14 (Siemens 2302), Siemens Simcenter STAR-CCM+ 2302, User Guide.
15 (Schiffahrts-Verlag Hansa GmbH & Co. KG, 2020), https://binnenschifffahrt-online.de/2020/01/haefen-wasserstrassen/12570/guetertransporte-in-der-elbe-region-brechen-ein/.
16 (SVA3428), Bericht 3428, Schiffbau-Versuchsanstalt Potsdam GmbH, 2008, Blatt Nr. 2.1.
17 (CESNI2019), Europäischer Ausschuss zur Ausarbeitung von Standards im Bereich der Binnenschifffahrt (CESNI), Europäischer Standard der technischen Vorschriften für Binnenschiffe (ES-TRIN), 2019, Artikel 5.06.

10 AUTHORS BIOGRAPHY

Benjamin Kossmann studied mechanical engineering at the University of Duisburg-Essen, Germany, and graduated in 2020. He continued working at the university as a research associate and started working on his doctorate at Institute of Sustainable and Autonomous Maritime Systems (INAM). In his range of research, he investigates numerically and experimentally shallow water effects on inland waterway vessels with a focus on resistance, propulsion, power requirement and emissions.

Bettar O. el Moctar studied Naval Architecture and Ocean Engineering at the University of Hamburg/Germany. He graduated in 1997 and has since then worked as a research assistant in different departments of the University of Technology Hamburg, where he has specialized in computational fluid dynamics. He completed his doctorate at the University of Technology Hamburg with a dissertation entitled "Numerical Computation of Forces Acting on Maneuvering Ships." In 2000 he joined the Hamburg Ship Model Basin (HSVA) and worked as a research engineer. He was head of department of fluid dynamics at Germanischer Lloyd/Germany from 2002 to 2008 and global head of research at DNV GL advisory services from 2013 to 2016. Since 2008 he has been working at the University Duisburg-Essen as a full professor for ship technology and Ocean Engineering and member of the Board of Directors of the shallow water model basin DST/Germany. He is editor and co-editor for several international journals and has been member of different international committees. His publications cover various aspects of hydrodynamics and Fluid-Structure-Interaction. The focus of his research is the development of numerical and experimental methods for seakeeping, hydroelasticity, cavitation, slamming and sloshing, maneuvering and propulsion in waves.

Thomas E. Schellin has been lecturing at the Institute of Sustainable and Autonomous Maritime Systems (INAM) of the University of Duisburg-Essen since the beginning of 2016. Currently, he also works on a freelance relationship for DNV acting as a Marine Warranty Surveyor. In 2004, after his formal retirement from Germanischer Lloyd (now DNV), he spent a semester teaching Ship Dynamics at Virginia Tech University, Blacksburg, and from 2007 to 2014 he taught also at the Technical University of Berlin. His work at Germanischer Lloyd (GL) comprised the development of hydrodynamic analysis methods for ships and offshore structures, coordination of nationally and internationally sponsored research projects, and formulation of class rules for fast ships, offshore structures, and offshore service vessels. He was GL's representative in the IACS AHG on Mooring and Anchoring, served on the 2001 and 2003 ISSC Committee I.2 Loads, and was the official discusser of the 2009 ISSC I.2 Loads Committee Report. He has published widely and is a Life Fellow of ASME and SNAME. Born in Germany, in 1964 he obtained his M.S. in Naval Architecture from the Massachusetts Institute of Technology and, in 1971, his Ph.D. in Mechanical Engineering from Rice University, Houston.

A METHOD TO ESTIMATE EMISSIONS OF AN INLAND WATERWAY SHIP MANEUVERING IN RESTRICTED WATERS

Jakob Rzeszutko, University of Duisburg-Essen (UDE), Germany
Daniel Weber, Federal Waterways Engineering and Research Institute (BAW), Germany
Lahbib Zentari, Federal Waterways Engineering and Research Institute (BAW), Germany
Christian Noss, Federal Waterways Engineering and Research Institute (BAW), Germany
Ould el Moctar, University of Duisburg-Essen (UDE), Germany

A METHOD TO ESTIMATE EMISSIONS OF AN INLAND WATERWAY SHIP MANEUVERING IN RESTRICTED WATERS

JAKOB RZESZUTKO, UNIVERSITY OF DUISBURG-ESSEN (UDE), GERMANY
DANIEL WEBER, FEDERAL WATERWAYS ENGINEERING AND RESEARCH INSTITUTE (BAW), GERMANY
LAHBIB ZENTARI, FEDERAL WATERWAYS ENGINEERING AND RESEARCH INSTITUTE (BAW), GERMANY
CHRISTIAN NOSS, FEDERAL WATERWAYS ENGINEERING AND RESEARCH INSTITUTE (BAW), GERMANY
OULD EL MOCTAR, UNIVERSITY OF DUISBURG-ESSEN (UDE), GERMANY

SUMMARY

Inland waterway transportation is highly energy-efficient compared to on-road transportation and hence provides an appropriate means to reduce overall transportation greenhouse gas emissions. The effects of intermodal transportation instead of purely on-road transportation, can be evaluated by emission models. However, existing emission models for inland waterway ships overlook the impact of maneuvering situations, particularly in varying water depths and directions of travel. For this reason, we present in this study four power prediction models to investigate the influence of different maneuvering situations on CO_2 emissions for inland waterway ships on the Rhine river. The goal is to improve the accuracy of CO_2 emission predictions and highlight the importance of model selection for reliable assessments.

NOMENCLATURE

BAW	Federal Waterways Engineering and Research Institute	
CFD	Computional Fluid Dynamics	
CO	Carbon Monoxide	
CO_2	Carbon Dioxide	
DST	Development Center for Ship Technology and Transport Systems e. V.	
EEDI	Energy Efficiency Design Index	
FaRAO	Dynamic Route Analysis and Optimization	
GNSS	Global Navigation Satellite Systems	
IMO	International Maritime Organization	
1978 ITTC	1978 ITTC Performance Prediction Method	
IWS	Inland Waterway Ship	
MPEC	Marine Environment Protection Committee	
MMM	Modular Maneuvering Model	
MRF	Moving Reference Frame	
NDIR	Non-Dispersive Infrared	
NO_x	Nitrogen Oxides	
O_2	Oxygen	
PMM	Planar Motion Mechanism	
RANS	Reynolds-Averaged Navier–Stokes	
RSM	Reynolds Stress Model	
UMTS	Universal Mobile Telecommunications System	
A_e/A_0	Propeller disc area ratio	—
A_R	Rudder area	m^2
B	Breadth	m
B_i	Bank inclination	m
$BSFC$	Brake specific fuel consumption	$gkW^{-1}h^{-1}$
C_A	Correlation allowance	—
C_{AAS}	Air resistance coefficient	—
C_B	Block coefficient	—
C_{FS}	Frictional resistance coefficient	—
$C_{P_{0.7}}$	Propeller chord length	m

C_R	Rudder chord length	m
C_{TS}	Total resistance coefficient	—
C_W	Wave resistance coefficient	—
D_{Di}	Duct inner diameter	m
D_P	Propeller diameter	m
EF_i	Emission factor	$g_{Emission} g_{fuel}^{-1}$
ER_i	Emission rate	$gkW^{-1} h^{-1}$
F	Resistance force	N
F_H	Total hull force	N
F_P	Total propulsion force	N
F_R	Total rudder force	N
F_X	Longitudinal force	N
F_Y	Lateral force	N
h	Water depth	m
h'	Draft to water depth ratio	—
h/T	Water depth to draft ratio	—
k	Form factor	—
L_D	Duct length	m
L_D/D_{Di}	Duct length to diameter ratio	—
L_{PP}	Length between perpendiculars	m
n_P	Propeller revolution rate	rpm
$P_{0.7}/D_P$	Propeller pitch ratio	—
P_B	Brake power	kW
P_E	Effective power	kW
r	Yaw rate	s^{-1}
r_C	Curve radius	m
$\dot{r}$	Yaw acceleration	s^{-2}
S_W	Wetted surface	m^2
T	Draft	m
T/h	Draft to water depth ratio	—
t_R	Rudder thickness	m
u	Longitudinal speed	$m\,s^{-1}$
U	Ship speed	$m\,s^{-1}$
U_0	Reference ship speed	$m\,s^{-1}$
U_{stw}	Ship speed through water	$m\,s^{-1}$
$\dot{u}$	Longitudinal acceleration	$m\,s^{-2}$
v	Lateral speed	$m\,s^{-1}$
$\dot{v}$	Lateral acceleration	$m\,s^{-2}$
w	Channel or river width	m
x_g	Center of gravity	m
ΔC_F	Roughness allowance	—
Λ_R	Rudder aspect ratio	—
β	Drift angle	°
δ	Rudder angle	°
ζ_P	Number of propellers	—
η_D	Propulsive efficiency	—
η_T	Transmission efficiency	—
λ	Scale factor	—
ρ	Density	$kg\,m^{-3}$

1 CHANGES

2 INTRODUCTION

Reducing anthropogenic greenhouse gas emissions is crucial to effectively mitigate climate change and its impacts. The transportation sector, which continues to rely predominantly on fossil fuels, remains a significant contributor to these emissions (Crippa et al. (2022)). Among the available alternatives, inland waterway transportation emerges as a particularly energy-efficient option for the movement of goods, due to a more favorable emissions-per-tonne-kilometer ratio, as highlighted by

the Central Commission for the Navigation of the Rhine, see CCNR (2022). As a viable substitute for road transportation, it has considerable potential to reduce overall transportation emissions.

The MPEC (Marine Environment Protection Committee) under the IMO (International Maritime Organization)'s remit focused on reducing ship-source emissions, including air pollutants and greenhouse gases, as mandated under the MARPOL treaty (IMO (2022b)). A resolution of the IMO (2022a) provided guidelines on the method of calculation of the EEDI (Energy Efficiency Design Index), served as a metric of the ship specific CO_2 (Carbon Dioxide) emissions of sea-going ships. Various studies were conducted on this subject to propose additional modeling approaches. For instance, a study by Bouman et al. (2017) examined the potential especially for sea-going ships to save CO_2 emissions. The study indicated that the most promising avenues for reducing carbon dioxide emissions in the shipping sector are ship size, bio fuels, and speed optimization. Brown et al. (2019) presented in their study a set of power models for sea-going ships that estimate CO_2 emissions. The models under consideration can be classified into two categories: resistance-based and load-factor-based models.

Several numerical models were available for modeling exhaust emissions from inland waterway ships (e.g. Zhou et al. (2022), Chen et al. (2017), and Dippold (2016)). In mechanistic models that considered individual ships, the calculation of the applied engine brake power was a crucial component. Maneuvering situations had an important influence on that. Emission models utilized numerous ship parameters as inputs, yet they neglect to consider the impact of maneuvering behavior in detail. Jiang et al. (2021) divided a journey into port departure, cruise and port arrival and added low load adjustments for the most accurate brake power prediction, Dippold (2016) calculated the resistance of the hull already very detailed. However, current exhaust emission models do not sufficiently account for the incident flow on the hull, propeller, and rudder.

This paper investigates the influence of different maneuvering situations on CO_2 emissions for inland waterway ship during a voyage on the Rhine, presenting four power prediction models. By investigating the influence of different maneuvering situations on emissions for ships on the Rhine, we present four power prediction models incorporating ship, kinematic, and bathymetry parameters. In the first method, we couple the resistance performance prediction method by the Resistance and Propulsion Committee of the 29th ITTC (2021) to estimate the necessary engine brake power using the ship's speed as an input variable. The second method, presented by Linke et al. (2015) and Weber et al. (2025), is an BAW (Federal Waterways Engineering and Research Institute) in-house development called FaRAO (Dynamic Route Analysis and Optimization), which is based on the longitudinal resistance force, thereby accounting for the draft-to-water-depth ratio and bathymetry of the river. It also incorporates a lateral component depending on the longitudinal force and curve radius. Furthermore, we apply the modular maneuvering model by Rzeszutko et al. (2025) to predict total hydrodynamic forces acting on a inland waterway ship as the sum of the hull, rudders, and propulsion units based on numerical simulations. This method provides a more detailed or comprehensive understanding of the individual modules, taking into account speeds, accelerations, propeller revolution rates, rudder angles, and draft-to-water-depth ratios. The modular maneuvering model is enabled to facilitate a differentiated consideration in the determination of performance between the hull forces and propulsion forces. These approaches are used to estimate CO_2 emissions proposed by Weber et al. (2025) of an inland waterway ship along a recorded voyage and compared with on-board exhaust emission measurements. Finally, the advantages and disadvantages of the examined approaches are discussed.

In this paper, we present a detailed analysis of measured CO_2 emissions compared to four models predicting the engine brake power of a typical full-scale twin-screwed inland waterway ship during a voyage. This study aims to understand the discrepancies between the performance prediction methodologies employed in the early design stage and maneuvering models.

3 TEST CASE

In this study, we considered the full-scale representation of the MS *Monika Deymann*, a representative IWS (Inland Waterway Ship) operating on German and Dutch waterways under the flag of the inland shipping company Reederei Deymann. This 135-meter container ship was extensively described and investigated during the PROMINENT project, as detailed by Orlovius (2020). The project aimed to conduct full-scale trials to measure emissions on the ship, with the overarching goal of proposing innovative solutions to reduce the energy consumption and carbon footprint of inland waterway transportation. Table 1 summarizes the main particulars of the IWS, including its propellers, ducts, and rudders, at the loading condition under investigation. A distinctive feature of this design was the availability of a model scale representation at a scale of λ=17. Additionally, a comprehensive experimental campaign was conducted at DST (Development Center for Ship Technology and Transport Systems e. V.), see DST (2023), in Duisburg as part of a joint research project with the BAW. Results from these experiments were expected to be published in a dedicated journal paper.

Figure 1 presents the lines plan of the IWS without propellers, ducts, and rudders, along with photographs of the ship, in both model scale and full-scale. The designs of the propellers, ducts, and rudders were proprietary and therefore not publicly available. Consequently, we scaled the designs from the model tests to full scale, which were then used in our numerical simulations.

Table 1: Main particulars of the inland waterway ship, propellers, ducts, and rudders in full scale.

Ship type	L_{PP} (m)	B (m)	T (m)	C_B $(-)$	x_g (m)	S_W (m^2)
Container ship	135.0	14.15	2.1	0.889	2.574	2249.0
Propeller type	No.	ζ_P $(-)$	D_P (m)	$C_{P_{0.7}}$ (m)	A_e/A_0 $(-)$	$P_{0.7}/D_P$ $(-)$
P40167, P40168	2	4	1.6	0.693	0.71	1.052
Duct type	No.	L_D (m)	D_{Di} (m)	$L_D/D_{Di}(-)$		
D358/e, D358/f	2	0.859	1.734	0.493		
Rudder type	No. $(-)$	A_R (m^2)	C_R (m)	Λ_R $(-)$	t_R (m)	
Fish tail	4	3.352	1.817	0.983	0.245	

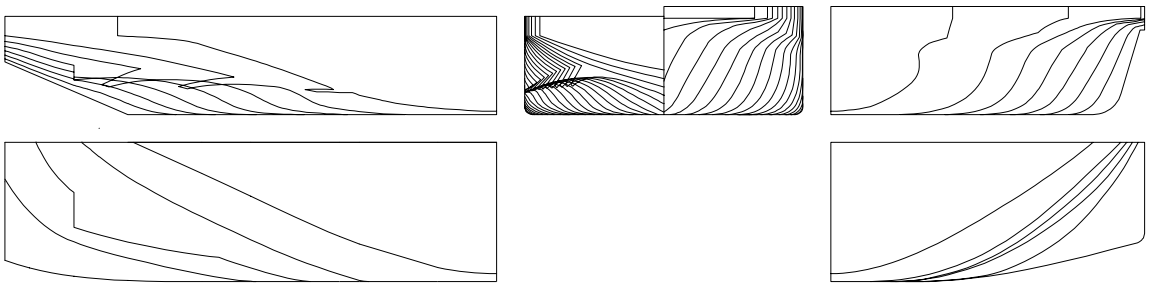

(a) Lines plan of the Monika Deymann in bare hull configuration.

(b) model scale photograph of the Monika Deymann. Courtesy of DST.

(c) Full-scale photograph of the Monika Deymann. Courtesy of Reederei Deymann.

Figure 1: Visual representations of the considered inland waterway ship, the Monika Deymann. Full-scale and model scale representations of the ship exist.

4 COORDINATE SYSTEM

The inertial coordinate system, denoted as $O_0x_0y_0z_0$, had its origin O_0 located at the calm water plane. In contrast, the body-fixed coordinate system, denoted as $Sxyz$, had its origin at the midship section, centerline, and calm water plane. In both systems, the axes were oriented such that the x-axis pointed towards the bow, the y-axis towards port, and the z-axis upwards. All hydrodynamic forces and kinematic parameters were referenced to the body-fixed coordinate system S.

5 EXPERIMENTAL SETUP

In this study, we utilized on-board emission data measured and captured by our experimental apparatus, which was already in operation during the PROMINENT project. The following sensors were installed on the IWS (Orlovius (2020)): a 1D acoustic

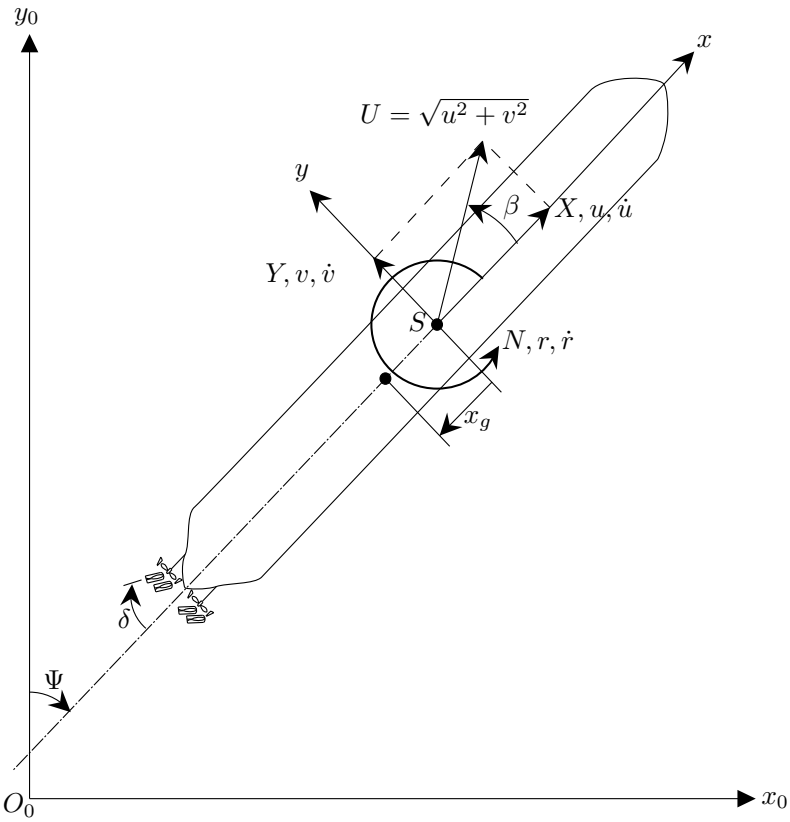

Figure 2: Inertial and body-fixed coordinate system, reproduced from Rzeszutko et al. (2025).

doppler current profiler, four echo sounders, a GNSS (Global Navigation Satellite Systems) heading receiver, load sensors, an engine data logger, and an inclinometer. Additionally, AIS data, rudder angle, and shaft generator power were continuously recorded. The echo sounders and the GNSS receiver operated at a sampling rate of 5 Hz, while all other sensors had a sampling rate of 1 Hz. All measured values were processed and georeferenced every second, and data were transmitted to a BAW server in 10-minute blocks via UMTS (Universal Mobile Telecommunications System). A temporary exhaust emission measurement was carried out on board the test ship during a journey down the Rhine from Mainz (Rhine km 500) to Rotterdam (Rhine km 1034). The measurement was performed on the exhaust duct of the port side engine. The air sample was taken through a 1.905 cm sampling port two meters behind the engine with a measuring probe that was bent by $90°$ and thus aligned parallel to the flow. The extracted air sample was dried and introduced into a Horiba PG 350 E multi-component analyzer to quantify gas concentrations in the exhaust gas. CO (Carbon Monoxide) and CO_2 concentrations were measured via NDIR (Non-Dispersive Infrared)-spectroscopy, NO_x (Nitrogen Oxides) via chemiluminescence, and remaining O_2 (Oxygen) via magnetic susceptibility. The exhaust gas volume flow was reported by the engine system.

The recorded data arev isualized in Figure 3, with results plotted against longitude and kilometer. The analyzed section of the IWS spanned the Rhine river between Bonn at Rhine kilometer 654.80 km and Duisburg at 780.80 km. The dataset was processed using a Discrete FFT (Fast Fourier Transform), adhering to the Nyquist-Shannon Sampling Theorem. Subsequently, Kalman filtering was employed to recursively estimate the system state, mitigate Gaussian noise, and enhance the signal-to-noise ratio (SNR). This approach yielded a more robust signal representation. Figure 3 is divided into several subplots, which presents the following data: Figure 3a displays the Rhine river, with longitude on the x-axis and latitude on the y-axis from Bonn to Duisburg. Major cities along the analyzed river section are highlighted with markers. Figure 3b illustrates the measured longitudinal speed u (dotted green) between 3.65 m s^{-1} to 6.06 m s^{-1} and lateral speed v (dashed orange) between -1.39 m s^{-1} to 1.95 m s^{-1} of the ship's speed through water U_{stw} (blue) between 3.64 m s^{-1} to 6.07 m s^{-1} along the Rhine kilometers. Figure 3c shows the measured water depth h (blue) between 4.35 m to 5.82 m, the water depth-to-draft ratio h/T (orange) 2.56 to 3.42, and the draft T (green) of 1.70 m along the Rhine kilometers. Figure 3d depicts the rotation rate r (blue) between $-52.63\,°$ min^{-1} to $38.93\,°$ min^{-1} and β (green) between $-20.31°$ to $27.58°$ over the Rhine kilometers. Figure 3e presents the measured starboard (blue) and port side (green) rudder angle δ between $-41.01°$ to $31.80°$. Figure 3f shows the starboard (blue) and port side (green) propeller revolution rates n_P between 216.13 rpm to 230.81 rpm, over the Rhine kilometers. The outliers below 109.87 rpm and above 926.72 rpm were not filtered even after processing and were not included in the performance prediction modeling. The Rhine river, with longitude on the x-axis and latitude on the y-axis from Bonn to Duisburg is shown.

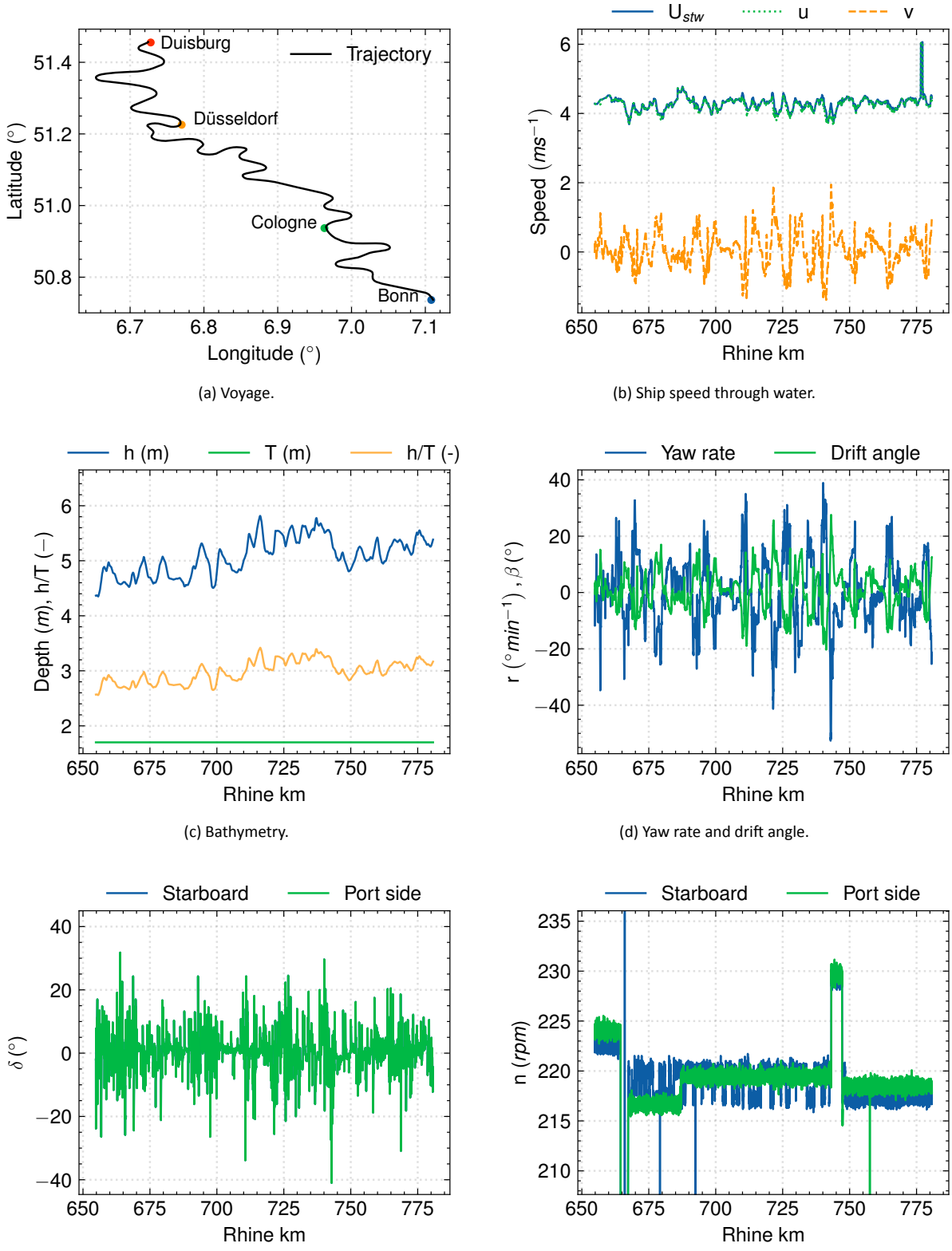

(a) Voyage.

(b) Ship speed through water.

(c) Bathymetry.

(d) Yaw rate and drift angle.

(e) Rudder angle.

(f) Propeller revolution rate.

Figure 3: **Measured data from a voyage of an inland waterway vessel on the Rhine. Plotted via longitude and the Rhine kilometer. The longitudinal u and lateral v speed components of the ship's speed through water U_{stw} are shown; the water depth h, draught T and water depth to draught ratio h/T, as well as the rate of turn r, rudder angle δ and propeller rotation speed n.**

6 METHODS

6.1 POWER PREDICTION MODELING

One crucial aspect of our emission model is the accurate prediction of the required engine brake power (P_B) of the inland waterway ship engine, as described by Equation (1). This prediction depended on the effective power (P_E), propeller efficiency (η_D), and transmission efficiency (η_T), which accounted for losses in the gear, bearings, and engine. The effective power (P_E) was determined by the resistance force (F) and ship speed through water (U_{stw}). To determine the propeller efficiency (η_D), open-water, resistance, and propulsion model tests were performed for the IWS by the DST at a model scale of λ=17. These tests yielded a range of values between η_D=0.45 to 0.55 . For our power prediction, we applied a propeller efficiency (η_D) of 0.5, see DST (2023). For the transmission efficiency (η_T), we assumed a value of 0.95, based on the work of Molland et al. (2017).

$$P_B = \frac{P_E}{\eta_D \eta_T} = \frac{F}{\eta_D \eta_T} U_{stw} \tag{1}$$

The first modeling approach employed was the 1978 ITTC (1978 ITTC Performance Prediction Method) method, as described in Resistance and Propulsion Committee of the 29th ITTC (2021), to estimate the resistance characteristics of the ship. Equation (2) was utilized to model the total resistance coefficient (C_{TS}) of the inland waterway ship, which accounted for the form factor (k), frictional resistance coefficient (C_{FS}), roughness allowance (ΔC_F), correlation allowance (C_A), wave resistance coefficient (C_W), and air resistance coefficient (C_{AAS}). Based on the methodology proposed by Zeng et al. (2019), the calculation of the frictional resistance coefficient (C_{FS}) was facilitated, enabling a more accurate determination of this parameter as a function of the water depth to draft ratio (h/T). The model tests conducted by the DST provided the necessary coefficients for this calculation. Specifically, the following coefficients were held constant at the following values: k=0.14, C_A=0.002, and C_{AAS}=6.6×10^{-5}. By using these constant values, we ensured a consistent and reliable estimation of the resistance characteristics.

$$C_{TS} = (1 + k)\, C_{FS} + \Delta C_F + C_A + C_W + C_{AAS} \tag{2}$$

Equation (3) presents the calculation of the total resistance force (F) as a function of the density (ρ), wetted surface area (S_W), and ship speed through water (U_{stw}).

$$F = \frac{1}{2} C_{TS} \rho S_{Wett} U_{stw}^2 \tag{3}$$

The second modeling approach utilized is a proprietary development of the BAW, denoted as BAW - FaRAO, which was previously presented by Weber et al. (2025). This approach calculates the total resistance force (F) as a function of the longitudinal force (F_X) and lateral force (F_Y), as expressed in Equation (4).

$$F = \sqrt{F_X^2 + F_Y^2} \tag{4}$$

Additional details on the modeling approach can be found in Linke et al. (2015) and Spitzer (2021), which provided a comprehensive overview of the underlying methodology. The forces predicted by this model, as given in Equation (5), are dependent on a range of ship and bathymetry parameters, including the ship speed through water (U_{stw}), length between perpendiculars (L_{PP}), breadth (B), draft (T), and block coefficient (C_B), as well as the water depth (h), river or channel width (w), bank inclination (B_i), and curve radius (r_C). Equation (5) provides a mathematical representation of the relationship between these parameters and the resulting forces.

$$F = f\left(U_{stw}, L_{PP}, B, T, C_B, h, W, B_i, r_C\right) \tag{5}$$

The modular maneuvering model developed by Rzeszutko et al. (2025) was employed to calculate the total hydrodynamic force (F) acting on the ship as presented in Equation (6). This model was also developed by the BAW. As this MMM (Modular

Maneuvering Model) only evaluated the ship in straight-ahead conditions, we extended it to take into account the effects of the rudder and lateral flow on the propulsion forces. The calculation of the total hydrodynamic force (F) represented the sum of the hydrodynamic hull force (F_H), hydrodynamic propulsion forces (F_P), and hydrodynamic rudder forces (F_R), where the indices i and j denote the number of ducted propellers and rudders, respectively. This modular maneuvering model replacedenablesenabled a differentiated consideration in the determination of performance between the hull forces and propulsion forces. Consequently, a decision based on the guidelines by IMO (2022a) was made to examine them individually, namely, the BAW - MMM Hull and the BAW - MMM Propulsion.

$$F = F_H + \sum_i F_{P_i} + \sum_j F_{R_j} \tag{6}$$

Equation (7) shows that the total force (F) was a function of the kinematic parameters, including the longitudinal velocity (u), lateral velocity (v), yaw rate (r), longitudinal acceleration ($\dot{u}$), lateral acceleration ($\dot{v}$), and yaw acceleration ($\dot{r}$), as well as the propeller revolution rate (n_P), rudder angle (δ), and draft to water depth ratio (h'=T/h).

$$F = f\left(u, v, r, \dot{u}, \dot{v}, \dot{r}, n_P, \delta, h'\right) \tag{7}$$

The third model, BAW - MMM Hull, calculates the effective power (P_E) using the scalar product of the longitudinal (F_X) and lateral (F_Y) hull forces and rudder forces, and the longitudinal (u) and lateral (v) components of the ship speed (U), as shown in Equation (8).

$$P_E = \left(F_{X_H} + \sum_j F_{X_{R_j}}\right) u + \left(F_{Y_H} + \sum_j F_{Y_{R_j}}\right) v \tag{8}$$

The fourth model, designated as BAW - MMM Propulsion, considers the propulsion forces (F_P) as defined in Equation (9). These forces represented the cumulative sum of the forces generated by all propulsion units, multiplied with their respective speed components. These propulsion units constituted a module within the modular mathematical model.

$$P_E = \sum_i \left(F_{X_{P_i}} u + F_{Y_{P_i}} v\right) \tag{9}$$

A wind resistance term was not incorporated in any of the methods since wind affects inland vessels much less than seagoing vessels. In general, the resistance force modeling was limited to typical cruise mode because, firstly, steady state conditions were assumed which were not fulfilled when maneuvering at locks or harbors and, secondly, engine speed related emission factors would be necessary for maneuvering. However, moderate speed adjustments as a result of waterway traffic were covered by the model.

6.2 EMISSION MODELING

The BAW exhaust emission model, as given in Equation (10), is based on the determination of the current required engine brake power (P_B) and brake-specific emission factors (EF_i). This allows for the calculation of time-related emission rates (ER_i), where the subscript i indicated the specific exhaust gas component.

$$ER_i = P_B EF_i \tag{10}$$

The emission factors of $6.0\,\mathrm{g_{NO_x}kW^{-1}h^{-1}}$ for NO_x and $1.5\,\mathrm{g_{CO}kW^{-1}h^{-1}}$ for CO were applied here, which were the legal limits for engines of this model year, as specified by European Union (2004). The time-related CO_2 emission rate $\left(ER_{CO_2}\right)$, as given in Equation (11), is proportional to the fuel consumption rate, which in turn depends on the current engine brake power (P_B). The fuel consumption rate was calculated using the brake-specific fuel consumption ($BSFC$) of $0.2\,\mathrm{kg_{fuel}kW^{-1}h^{-1}}$ and the CO_2 emission factor $\left(EF_{CO_2}\right)$ of $3.2\,\mathrm{kg_{CO_2}kg_{fuel}^{-1}}$, as reported by Fridell et al. (2008).

$$ER_{CO_2} = P_B EF_{CO_2} BSFC \tag{11}$$

6.3 NUMERICAL METHOD

We utilized the numerical solver of STAR-CCM+ from Siemens (2023) for our numerical simulations. Our numerical setup reflected the need to populate the maneuvering model with hydrodynamic derivatives using a robust and computationally efficient approach. To this end, we employed a double-body, single-phase, steady-state method based on the numerical solution of the RANS (Reynolds-Averaged Navier–Stokes) equations. Turbulence closure was provided by the RSM (Reynolds Stress Model) to account for anisotropic turbulence near the walls. As shown by Rzeszutko et al. (2025), this model yields improved accuracy for shallow water maneuvering applications involving inland waterway vessels. The double-body approach, which neglects free-surface effects, was valid when wave-making resistance was negligible. According to 1978 ITTC, this held for Froude numbers below 0.12. In our case, the target ship velocity at model scale was $0.539\,\mathrm{m\,s^{-1}}$, corresponding to a Froude number of approximately 0.061. Even at the highest measured velocities, the Froude number remained below 0.1.

The ship geometry was fully appended and included rotating propellers. We modeled propeller rotation using the MRF (Moving Reference Frame) method, where the propeller was resolved within a dedicated subdomain. The flow field rotates within this subdomain, and field quantities were exchanged with the main domain.

In this study, we followed a twofold approach. First, we adapted the numerical setup for validation at model scale. Second, we scaled the setup to compute hydrodynamic forces and moments at full scale.

At model scale, the computational domain was modeled after DST's shallow water tank, which is 200 m long and 9.5 m wide. The domain extended $2L_{PP}$ upstream and $3.5L_{PP}$ downstream of the ship. Aiming for a y^+ value below unity, we fully resolved the boundary layer. Squat effects were accounted for using the hydrostatic balancing approach by Chillcce et al. (2025) Trim was neglected, as measured values during the experiments did not exceed $0.5°$. Refinement zones were placed around the hull, appendages, and between the keel and tank bottom to capture the complex interactions between hull, propeller, rudder, and waterway in very shallow water. Figure 4 provides an overview of the surface mesh and refinement zones.

At full scale, the numerical setup was retained, except for a widened domain to avoid wall-induced confinement effects. A wall-function approach was applied, targeting a y^+ value of approximately 300, as fully resolving the boundary layer at full scale would require prohibitively high grid resolution and computational cost.

The numerical approach was validated using model-scale experimental data from an extensive campaign conducted at DST. The ship was towed using the computerized PMM (Planar Motion Mechanism) carriage in DST large towing tank. The campaign was designed to provide a comprehensive validation basis for numerical captive maneuvering tests. For three water depth-to-draft ratios (2.0 to 1.2), resistance, propulsion, drift, and combined drift–rudder tests were conducted. During the experiments, time series of hydrodynamic forces (X, Y, Z) and moments (N, K, M) acting on the hull were recorded, along with propeller and duct forces for each individual unit. Selected tests were repeated to quantify experimental uncertainty and ensure data quality. A detailed description of the experimental procedures will be provided in a dedicated publication.

Figure 5 presents a validation of the longitudinal force (F_X), lateral force (F_Y), and propulsion force (F_P) as a function of the drift angle (β), comparing experimental and numerical CFD (Computional Fluid Dynamics) data. The longitudinal force (F_X) in Figure 5a decreases with increasing drift angle (β) for both datasets, with the experimental data consistently exhibiting higher values compared to the numerical data of the CFD. The deviations of the experimental and numerical data are between a range of $16\,\%$ to $21\,\%$. In contrast, the lateral force (F_Y) in Figure 5b shows a strong positive correlation with the drift angle (β) in both datasets, converging at higher values. However, the propulsion force (F_P) in Figure 5c exhibits distinct behaviors. The numerical data (CFD) demonstrate a non-monotonic trend, characterized by a sharp increase followed by a decrease, whereas the experimental data remain relatively stable with minor fluctuations. A comparison of the experimental and numerical data sets reveals favorable results.

7 RESULTS AND DISCUSSION

Figure 6 presents the brake power along a section of the Rhine river, plotted against Rhine kilometer, based on four distinct modeling approaches. The blue line represents the predictions obtained using the 1978 ITTC model, while the green line depicts the results from the BAW - FaRAO model. The orange line corresponds to the BAW - MMM Hull model, and the red line represents the BAW - MMM Propulsion model. The 1978 ITTC model predicts a relatively constant brake power of approximately 0.142 kW, with minor fluctuations. In contrast, the BAW - FaRAO model exhibits a higher brake power of approximately 0.193 kW, but with greater variability. Notably, the peaks observed at Rhine kilometers 721 km and 743 km illustrate the influence of lateral speed, rudder angle and yaw rate r on the predicted brake power, whereas at 777 km the longitudinal speed influences the predicted brake power. Among the four models, the hydrodynamic forces acting on the hull, as predicted by the BAW - MMM Hull model, produce the highest mean brake power of 0.226 kW. The fluctuations in this model are attributed to the influence of velocity components, acceleration phases, draft-to-water-depth ratio, rudder angle, and propeller revolution rates. Conversely, the BAW - MMM Propulsion model demonstrates the lowest magnitude of

(a) Plane at z=0.

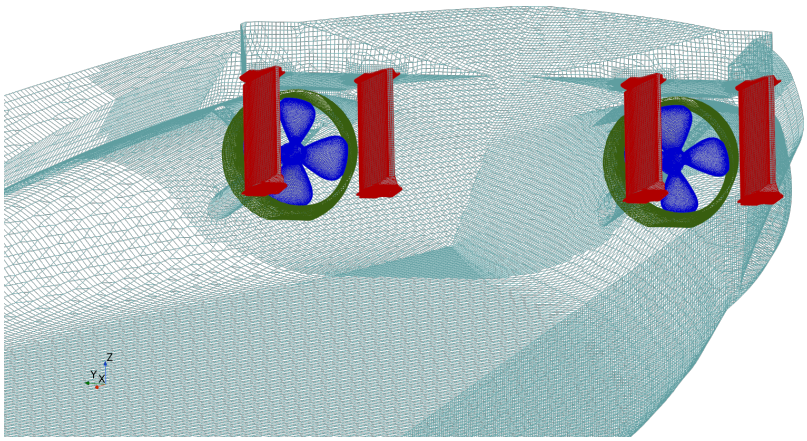

(b) Aft view.

Figure 4: Mesh settings for numerical calculations.

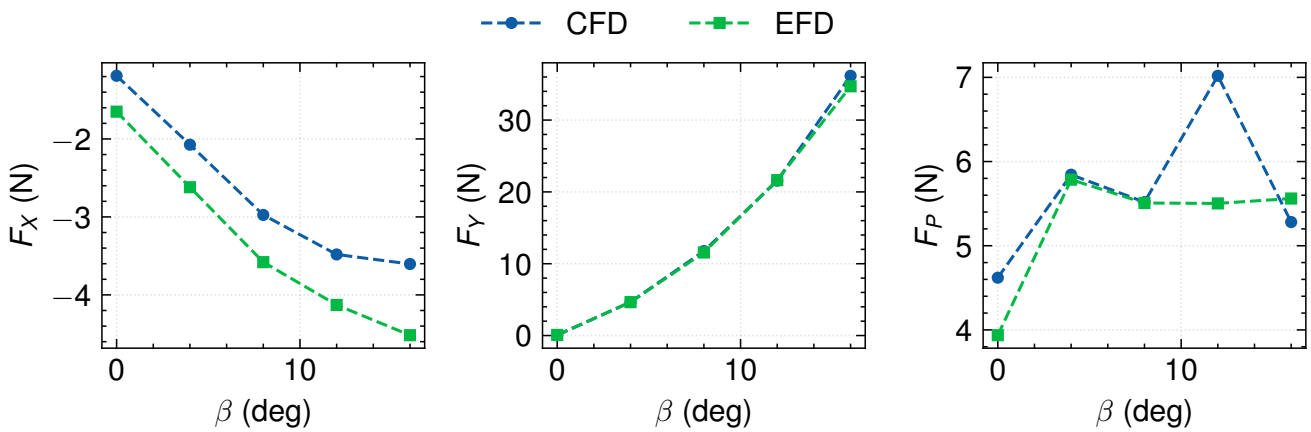

(a) Longitduinal force. (b) Lateral force. (c) Propulsion force.

Figure 5: Validation of the numerical longitudinal force F_X, lateral force F_Y, and propulsion force F_P over the drift angle β, comparing experimental measurement and numerical CFD data at a reference ship speed U_0=$0.539\,\mathrm{m\,s^{-1}}$, propeller revolution rate n_P=$140\,\mathrm{rpm}$, and water depth to draft ratio h/T=2.0.

brake power, fluctuating around $0.124\,\mathrm{kW}$ across the entire range, with minimal variability.

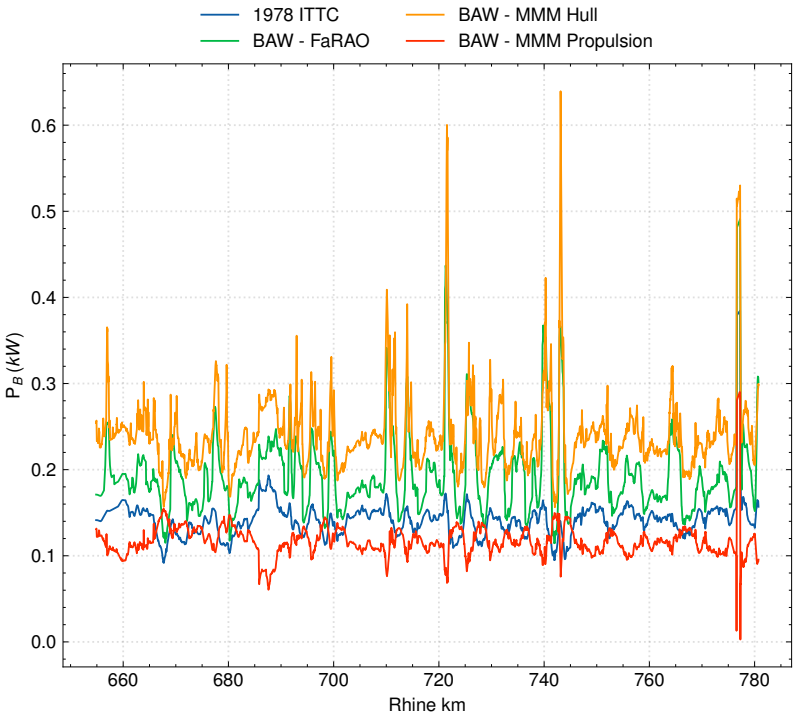

Figure 6: Comparison of the brake power P_B over the Rhine kilometers for four different modeling approaches.

Figure 7 presents ship-specific CO_2 emissions along the Rhine River, spanning from Bonn to Duisburg, derived by the emission model based on the brake power from the four methods discussed above and supplemented by the results of the on-board exhaust emission measurement. The blue line represents the predictions generated by the 1978 ITTC model, while the green line depicts the results from the BAW - FaRAO model. The orange line corresponds to the BAW - MMM Hull model, and the red line represents the BAW - MMM Propulsion model. The black line denotes the actual measurements, with the dashed black lines indicate a $\pm 20\,\%$ confidence interval around the measured values due to measurement uncertainties. The measurement data exhibits relatively constant and low emission values with minimal variability. The 1978 ITTC model predicts moderately higher CO_2 emissions compared to the measurements. In contrast, the BAW - FaRAO model predicts higher emissions that exceed the measurement by more than $\pm 20\,\%$. The BAW - MMM Hull model predicts significantly higher CO_2 emissions, characterized by substantial variability and multiple peaks that consistently deviate above the expected values. Notably, the brake power prediction has a pronounced effect on emission prediction, resulting in the highest CO_2 emissions being predicted at Rhine kilometers 721 km, 743 km and 777 km for the BAW - FaRAO and BAW - MMM Hull models. Conversely, the BAW - MMM Propulsion model predicts the lowest CO_2 emissions, occasionally approaching the expected values but generally underestimating emissions in specific regions. This analysis indicates that the BAW - FaRAO and BAW - MMM Hull models are insufficient for accurately predicting CO_2 emissions. In contrast, the 1978 ITTC model, which is based on model tests, and the BAW - MMM Propulsion model, which utilizes propulsion forces directly obtained from numerical simulations, demonstrate the best overall performance.

Figure 8 presents violin plots comparing the distributions of ship-specific CO_2 emissions from the four modeling methods and the on-board exhaust emission measurement, presented on a logarithmic scale. Each method's data is represented by a vertical distribution of individual data points, where the blue violin represents the 1978 ITTC model, the green violin depicts the BAW model, the orange violin represents the BAW - MMM Hull model, the red violin corresponds to the BAW - MMM Propulsion model, and the black violin represents the measured data. The black line in each violin represents the mean value of the dataset. The measured dataset exhibits a compact and homogeneous distribution, characterized by low variability. The median emission value is 3.91×10^{-2} kg s^{-1}, indicating a relatively narrow range of emission rates within the dataset. In contrast, the 1978 ITTC model provides a reliable estimation of the measured emissions, with a median of 4.68×10^{-2} kg s^{-1} and a range of 6.58×10^{-4} kg s^{-1} to 3.41×10^{-1} kg s^{-1}. However, the probability distribution shows a high density around the median, with a tendency to overestimate emissions. The BAW - FaRAO model, with a median of 7.76×10^{-2} kg s^{-1}, significantly overestimates the measurement. The distribution reveals that most of the data tends to overestimate the measurement, spanning a range of 1.06×10^{-3} kg s^{-1} to 5.57×10^{-1} kg s^{-1}. Similarly, the BAW - MMM Hull model exhibits an overestimation of emissions, with a median of 1.11×10^{-1} kg s^{-1} and a range of 1.45×10^{-3} kg s^{-1} to 8.52×10^{-1} kg s^{-1}. On the other hand, the BAW - MMM Propulsion model provides closer predictions to the measurement, with a median of 3.49×10^{-2} kg s^{-1}. Although the emissions are underestimated between 4.90×10^{-4} kg s^{-1} to 1.58×10^{-1} kg s^{-1}, this model demonstrates the most accurate predictions despite its high variability. Overall, the computational

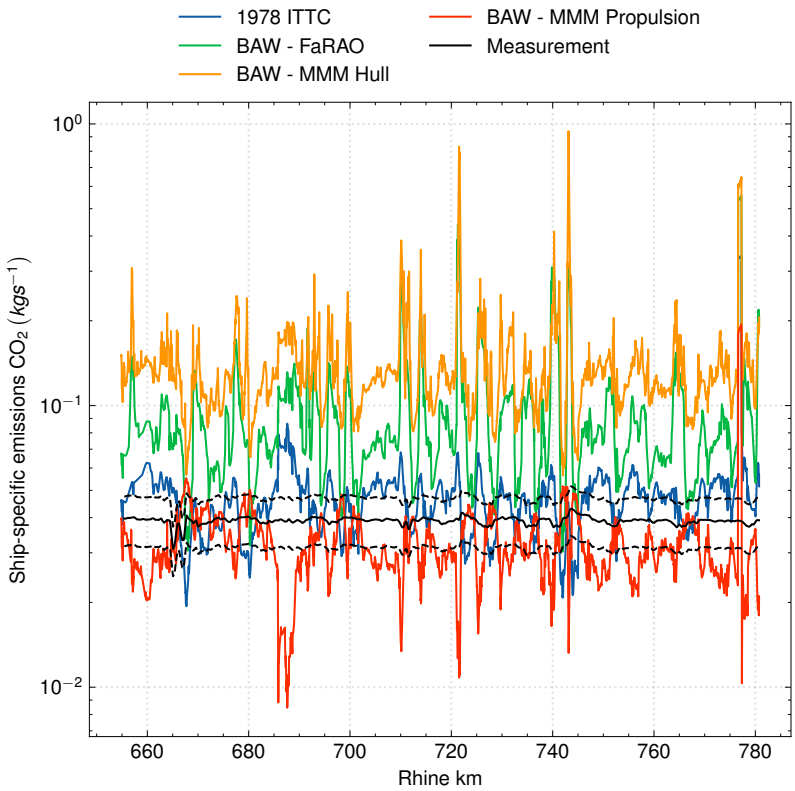

Figure 7: Comparison of the modeled and measured ship-specific CO_2 emissions over the Rhine kilometers for four different modeling approaches. The black dashed lines show a $\pm 20\,\%$ deviation of the processed measured emissions due to uncertainties and simplifications.

models exhibit greater variability compared to the measurement. The BAW - MMM Propulsion model provides the most accurate prediction of emissions, while the BAW - MMM Hull, BAW - FaRAO, and 1978 ITTC models demonstrate significant overestimation in their upper tails.

Table 2 presents statistical measures comparing the deviation of the four models (1978 ITTC, BAW - FaRAO, BAW - MMM Hull, and BAW - MMM Propulsion) from the experimental data (measurement) in percentage terms. These deviations provide insight into the accuracy and consistency of each model relative to the experimental baseline. The BAW - MMM Hull model exhibits a significant tendency to underestimate the measurement values, with a mean deviation of $214\,\%$. In contrast, the 1978 ITTC model demonstrates an accurate prediction of the emissions compared to the measurement, with a mean deviation of $22\,\%$ and a median deviation of $19\,\%$. Although the variability is still significant, with a standard deviation of $1691\,\%$, the interquartile range spans from $1\,\%$ to $34\,\%$, further highlighting its tendency to overestimate. The BAW - FaRAO model shows a strong tendency toward overestimation, with a mean deviation of $135\,\%$ and a median deviation of $98\,\%$. This model exhibits extreme variability, as shown by a standard deviation of $4199\,\%$. The interquartile range is between $65\,\%$ and $160\,\%$, indicating consistent overestimation within this range. The BAW - MMM Hull model also demonstrates a tendency toward overestimation, with a mean deviation of $214\,\%$ and a median deviation of $183\,\%$, and the highest standard deviation of $4642\,\%$. The interquartile range suggests consistent overestimation, with values of $146\,\%$ and $224\,\%$. In contrast, the BAW - MMM Propulsion model shows the most accurate prediction, with a mean deviation of $-7\,\%$ and a median deviation of $-11\,\%$, indicating a slight underestimation compared to the measurement. It also exhibits the lowest standard deviation, with $777\,\%$. The interquartile range of $-20\,\%$ and $3\,\%$ indicates that most predictions are close to the measurement, with occasional underestimations. In summary, the BAW - MMM Propulsion model performs closest to the measurement, followed by the 1978 ITTC model, which tends to slightly overestimate. The BAW - MMM Hull and BAW - FaRAO models show consistent overestimation with much higher variability, making them less reliable for predicting values consistent with the measurement.

8 CONCLUSIONS

In this paper, we present a comprehensive evaluation of ship-specific CO_2 emissions using four power prediction models (1978 ITTC, BAW - FaRAO, BAW - MMM Hull, and BAW - MMM Propulsion) and compare their predictive power performance to measured emission data. The analysis reveals the complexities of predicting ship-specific CO_2 emissions, highlighting the

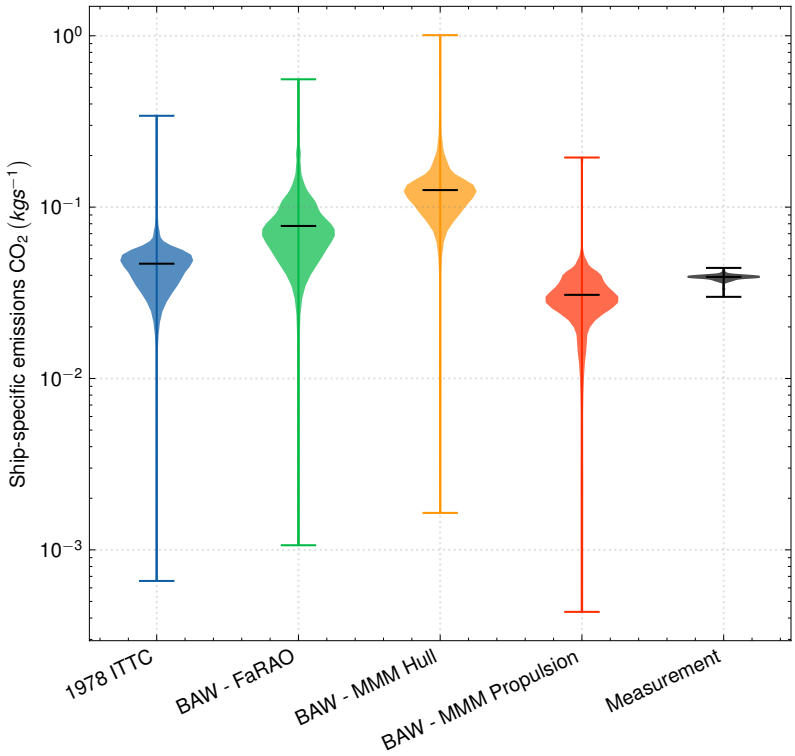

Figure 8: **Comparison of the modeled and measured ship-specific CO_2 emissions in a violin plot for four different modeling approaches.**

	1978 ITTC	BAW - FaRAO	BAW - MMM Hull	BAW - MMM Propulsion
Mean	22 %	135 %	214 %	−7 %
Median	19 %	98 %	183 %	−11 %
Std.	1691 %	4199 %	4642 %	777 %
25 %	1 %	65 %	146 %	−20 %
50 %	19 %	98 %	183 %	−11 %
75 %	34 %	160 %	224 %	3 %

Table 2: **Statistical measures comparing the deviation of the four distinct models from the measured data in percentage terms. Positive percentages indicate an overestimation of the deviation, while negative percentages indicate an underestimation.**

varying approaches from preliminary design to advanced numerical simulations. This study underscores the knowledge gap in predicting CO_2 emissions during the voyage of an inland waterway ship. It is structured as follows: First, a test case is introduced, featuring a typical full-scale twin-screw inland waterway ship. Next, the experimental setup, including all sensors, is described along with details of the analyzed voyage. Then, the four power prediction models, the emission model, and the numerical method are explained. Finally, a discussion of the obtained results is provided. The findings indicate that the 1978 ITTC, BAW - FaRAO and BAW - MMM Hull models consistently overestimate CO_2 emissions, whereas the BAW - MMM Propulsion model tends to underestimate them. Despite limitations in processing the measured field data, the 1978 ITTC and BAW - MMM Propulsion models demonstrate intermediate performance, falling within an acceptable uncertainty range and aligning with the IMO's EEDI calculation guidelines. The analysis suggests that hydrodynamic hull forces estimations, used for mathematical maneuvering models, may contribute to overestimation, based on the current results. Furthermore, this study highlights the critical role of model selection in ensuring accurate CO_2 emission assessments for ships and underscores the need for further research to enhance the predictive capabilities of these models. In light of these findings, the study underlined the necessity of a multifaceted approach to effectively reduce emissions in inland waterways. First, politically, establishing environmental zones near ecologically sensitive areas or urban centers, in conjunction with rewarding the adoption of climate-neutral propulsion systems, would be a viable option. Second, from an operational point of view, ship owners should develop specific operational strategies. Such strategies include real-time emission monitoring and dynamic route optimization, which incorporates weather, hydrodynamic conditions, and traffic patterns. Thirdly, at the design level, the use of advanced numerical methods to accurately predict emissions and optimize hull and propulsion performance would

help attain the goal of emission reduction. Overall, the combined efforts of policymakers, shipowners and designers have the potential to accelerate progress towards the goal of environmentally sustainable shipping.

Future work should focus on improving the accuracy and reliability of ship-specific CO_2 emission models, particularly for those exhibiting high variability. Refining these models through enhanced calibration with experimental data and incorporating more detailed physical processes could reduce deviations. Additionally, integrating real-time operational data and exploring machine learning approaches may further enhance predictive capabilities.

9 ACKNOWLEDGEMENTS

The results presented in this paper originated from a joint research project between the Federal Waterways Engineering and Research Institute (BAW) and the Institute for Sustainable and Autonomous Maritime Systems (INAM) at the University of Duisburg-Essen (UDE). We extend our gratitude to Reederei Deymann for kindly granting permission to share the figures and data of the MS Monika Deymann, which were recorded by the Federal Waterways Engineering and Research Institute (BAW). The work presented was funded by the Federal Waterways Engineering and Research Institute (BAW).

10 REFERENCES

Bouman, Evert A. et al., 2017. State-of-the-art technologies, measures, and potential for reducing GHG emissions from shipping – A review. In: Transportation Research Part D: Transport and Environment 52, pp. 408–421. DOI: 10.1016/j.trd.2017.03.022.

Brown, Isabela N. et al., 2019. Power models and average ship parameter effects on marine emissions inventories. In: Journal of the Air & Waste Management Association 69.6. PMID: 30794070, pp. 752–763. DOI: 10.1080/10962247.2019.1580229.

CCNR, Mar. 2022. CCNR ROADMAP for reducing inland navigation emissions. Central Commission for the Navigation of the Rhine.

Chen, Dongsheng et al., 2017. High-spatiotemporal-resolution ship emission inventory of China based on AIS data in 2014. In: The Science of the total environment 609, pp. 776–787. DOI: 10.1016/j.scitotenv.2017.07.051.

Chillcce, Guillermo et al., 2025. Numerical calculation of hydrodynamic forces on inland waterway vessels during circular motion in shallow and extreme shallow waters. In: Ocean Engineering 318, p. 120095. DOI: 10.1016/j.oceaneng.2024.120095.

Crippa, M. et al., 2022. CO2 emissions of all world countries: JRC/IEA/PBL 2022 report. Vol. 31182. EUR. Luxembourg: Publications Office of the European Union.

Dippold, Martin, 2016. Entwicklung eines Simulationsmodells zur Ermittlung von Energieverbrauch und Emissionen auf Verkehrsnetzwerken. Dissertation. Graz: TU Graz.

DST, May 2023. Modellversuche mit dem Modell des GMS Monika Deymann. DST Report 2343. Development Centre for Ship Technology and Transport Systems.

European Union, 2004. Directive 2004/ 26/EC of the European Parliament and of the Council of 21 April 2004 amending Directive 97/68/EC on the approximation of the laws of the Member States relating to measures against the emission of gaseous and particulate pollutants from internal combustion engines to be installed in non-road mobile machinery. In: Office Journal of the European Union L 146, pp. 1–107.

Fridell, Erik et al., 2008. Primary particles in ship emissions. In: Atmospheric Environment 42.6, pp. 1160–1168. DOI: 10.1016/j.atmosenv.2007.10.042.

IMO, 2022a. 2022 Guidelines on the method of calculation of the attained energy efficiency design index (EEDI) for new ships. MEPC 364 (79). Available at: https://www.imo.org/en/OurWork/Environment/Pages/Index-of-MEPC-Resolutions-and-Guidelines-related-to-MARPOL-Annex-VI.aspx. International Maritime Organization.

– 2022b. List of MEPC resolutions. In: MARPOL. International Maritime Organization, pp. 357–372.

Jiang, Han et al., 2021. Comparison of Inland Ship Emission Results from a Real-World Test and an AIS-Based Model. In: Atmosphere 12.12. DOI: 10.3390/atmos12121611.

Linke, T. et al., Sept. 2015. Recent developments in the application of shallow water ship hydrodynamics in inland waterway design. In: Smart Rivers 2015. PIANC, p. 7. DOI: 10.13140/RG.2.1.2810.7928.

Molland, Anthony F. et al., 2017. Ship Resistance and Propulsion: Practical Estimation of Ship Propulsive Power. Cambridge University Press. DOI: 10.1017/9781316494196.

Orlovius, Andreas, Dec. 2020. Automatisierte Erfassung von Sohlenhöhen und Strömungsgeschwindigkeiten im laufenden Schiffsbetrieb. BAW-Nr. B3953.04.04.70007. Bundesanstalt für Wasserbau.

Resistance and Propulsion Committee of the 29th ITTC, June 2021. Recommended Procedures and Guidelines - 1978 ITTC Performance Prediction Method. Tech. rep. 7.5-02-03-01-01.4. The International Towing Tank Conference.

Rzeszutko, Jakob et al., 2025. Mathematical modeling of propulsion forces in shallow waters. In: Applied Ocean Research 154, p. 104417. DOI: 10.1016/j.apor.2025.104417.
Siemens, 2023. Simcenter STAR-CCM+ 2310 User guide. 2310.0001. Siemens PLM Softwares.
Spitzer, Detlef, 2021. Resistance and Economic Speed of Ships and Tows in Inland Waterways. In: Journal of Waterway, Port, Coastal, and Ocean Engineering 147.6. DOI: 10.1061/(ASCE)WW.1943-5460.0000672.
Weber, Daniel et al., 2025. Exhaust Emission Rates along German Inland Waterways. In Review.
Zeng, Qingsong et al., 2019. On the viscous resistance of ships sailing in shallow water. In: Ocean Engineering 190, p. 106434. DOI: 10.1016/j.oceaneng.2019.106434.
Zhou, Chunhui et al., 2022. Meso-level carbon dioxide emission model based on voyage for inland ships in the Yangtze River. In: The Science of the total environment 838.3, p. 156271. DOI: 10.1016/j.scitotenv.2022.156271.

11 AUTHORS BIOGRAPHY

Jakob Rzeszutko is a PhD student at the Institute for Autonomous and Sustainable Maritime Systems (INAM) at the University of Duisburg-Essen (UDE). His research focuses on ship maneuverability, with a particular emphasis on the influence of shallow water on inland waterway ships.

Lahbib Zentari holds the position of research engineer at the Federal Waterways Engineering and Research Institute (BAW) in Karlsruhe. His research interests include computational fluid dynamics (CFD) methods applied to shallow water maneuvering problems, ship-waterway interaction, and ship-handling simulators.

Daniel Weber is a researcher at the Federal Waterways Engineering and Research Institute (BAW) in Karlsruhe. His research focuses on the measurement and numerical modeling of gaseous and particulate exhaust emissions from inland waterway ships.

Christian Noss is the head of the Department of Waterways and Environment at the Federal Waterways Engineering and Research Institute (BAW) in Karlsruhe. His research focuses on the physical processes and ecological development of waterways.

Ould el Moctar, Prof. Dr.-Ing., is a full professor at the Institute for Autonomous and Sustainable Maritime Systems (INAM) at the University of Duisburg-Essen (UDE). His publications cover various aspects of hydrodynamics and fluid-structure interaction. The focus of his research is on seakeeping, hydroelasticity, slamming and sloshing, cavitation, maneuvering, and propulsion in waves. He is an editor and co-editor of numerous international journals.

APPROACH TO ELIMINATE TANK WALL EFFECTS FROM OPEN WATER MANOEUVRING MODELS

Guillaume Delefortrie, Ships and Marine Technology, Ghent University, Belgium
Arghya Kamol Roy, Ships and Marine Technology, Ghent University, Belgium
Katrien Eloot, Flanders Hydraulics, Belgium
Evert Lataire, Ships and Marine Technology, Ghent University, Belgium

APPROACH TO ELIMINATE TANK WALL EFFECTS FROM OPEN WATER MANOEUVRING MODELS

GUILLAUME DELEFORTRIE, GHENT UNIVERSITY, BELGIUM
ARGHYA KAMOL ROY, GHENT UNIVERSITY, BELGIUM
KATRIEN ELOOT, FLANDERS HYDRAULICS, BELGIUM
EVERT LATAIRE, GHENT UNIVERSITY, BELGIUM

SUMMARY

A ship manoeuvring simulator which is designed for training in (and/or redesign of) harbour areas needs to be fed with highly realistic mathematical manoeuvring models that allow the accurate prediction of the ship motions while simulating complex manoeuvres. These manoeuvring models can be designed based on captive model tests carried out in a towing tank. However, when performing such tests, the ship is subjected to possible towing tank wall interaction and thus blockage, a risk that increases with decreasing water depth, increasing ship velocity and increasing obliqueness of the ship with respect to the towing tank's longitudinal axis. The present paper gives an overview of the research that the authors have carried out in the field and the work to be performed to be able to correctly isolate the open water behaviour of the ship from the captive model test results or mathematical models. The isolation of these effects will enable the correct superposition of the hydrodynamic forces when carrying out manoeuvring simulations in complex harbour environments.

NOMENCLATURE

A	towing tank cross section area (m^2)
A_{M}	midship area of the vessel (m^2)
A_{R}	rudder area (m^2)
A_{E}/A_0	expanded area ratio of the propeller (-)
B	breadth (m)
C_{B}	block coefficient (-)
D'	non-dimensional drag force (-)
D_{P}	propeller diameter (m)
Fr_h	Froude depth number (-)
K'	non-dimensional roll moment (-)
$\overline{KM_{\mathrm{L}}}$	position longitudinal metacenter above the keel (m)
$\overline{KM_{\mathrm{T}}}$	position transverse metacenter above the keel (m)
L'	non-dimensional lift force (-)
L_{OA}	length overall (m)
L_{PP}	length between perpendiculars (m)
m	blockage (-)
m	mass (kg)
M'	non-dimensional pitch moment (-)
m_{eq}	equivalent blockage (-)
N'	non-dimensional yaw moment (-)
$\frac{P}{D_{\mathrm{P}}}$	pitch-to-diameter ratio of the propeller (-)
T	draft (m)
X'	non-dimensional surge force (-)
X_{BANK}	increase in longitudinal force due to tank confinement (N)
x_v	non-dimensionalized point of application of lateral force on the hull (-)
Y'	non-dimensional sway force (-)
y_{infl}	influence width (m)
Z'	non-dimensional heave force (-)
β	drift angle (°)
ξ	regression coefficient (-)
ξ_y	regression coefficient (-)
ξ_z	regression coefficient (-)

χ_{ocean}	the 'weight' of an infinite large cross section (-)
χ_p	the 'weight' of the port side cross section (-)
χ_s	the 'weight' of the starboard side cross section (-)
χ_{ship}	the 'weight' of the ship section (-)

1 INTRODUCTION

A ship manoeuvring simulator designed for training in and/or redesign of harbour areas requires highly realistic mathematical ship manoeuvring models to accurately predict the ship motions while simulating complex manoeuvres. These manoeuvring models are typically designed based on captive tests carried out in a towing tank. The ship manoeuvring simulators, present at Flanders Hydraulics (FH) in Antwerp, Belgium, are fed with such a sophisticated 6 Degrees of Freedom (DOF) mathematical model.

In harbour areas, the limited water depth leads to shallow water effects affecting the hydrodynamic behaviour of the vessel. This effect, when combined with the horizontal restrictions imposed by physical boundaries like banks, generates what is referred to as *confinement effects*. Due to this confinement, the vessel's resistance increases and the speed is therefore reduced. Voluntary speed reductions may also be required to mitigate squat and to accommodate the need for external manoeuvring assistance, such as tug support. Squat refers to the phenomenon where a vessel experiences both sinkage and a change in trim. For a given speed the squat increases in confined areas, because the latter induces an increase of return flow speed around the hull. This increased flow velocity results in a pressure drop (Bernoulli's principle). The pressure drop lowers the local free surface level near the hull which in turn decreases the free surface of the water leading to decrease of the ship's buoyancy (which is directly proportional to the displaced water volume). Depending on the hull form, the propulsion and the loading condition, the local pressure drop might vary at the stern and bow. This leads to a difference in sinkage at the stern and bow and hence a trimming of the ship.

Another significant issue is that at low forward speeds, the proportional influence of lateral forces caused by wind and currents, becomes more pronounced. Consequently, from the kinematic relationship between drift angle, forward velocity, and lateral velocity, it can be inferred that drifting behaviour increases at lower speeds. Usually at higher speeds the drifting is less prominent compared to that at lower speeds. So in order to create a realistic mathematical model for ships manoeuvring in shallow water, ship manoeuvring tests at low speeds need to be carried out at a full 360° range of drift angles in a towing tank.

The tank width plays an important role in shallow water towing tank tests. The tank width should be large enough compared to the model size to avoid confinement effects. The latter can be directly linked with the so-called blockage ratio, which is the ratio of the cross sectional area of the ship and the cross section of the canal: $m = A_M/A$. A higher magnitude of the blockage parameter, m, indicates a stronger confinement effect within a given towing tank environment for a specific ship model size. For a ship sailing in a deep and an unrestricted environment (e.g. ocean) the blockage will be zero ($A \sim \infty$). In case of a towing tank environment, the confinement effects experienced by the ship model due to the horizontal restrictions or the towing tank walls is denominated as tank wall effects. Similar to the shallow water effect, the tank wall effect increases with decreasing water depth, increasing ship velocity and increasing obliqueness of the ship with respect to the towing tank's longitudinal axis. Equations 1 and 2 offer a comprehensive way to represent the hydrodynamic forces experienced by a ship hull in a tank area. The main challenge to isolate the tank wall effects from the total forces experienced by the ship is that the tank wall effect is highly coupled with shallow water effects and other factors.

$$F_{\text{open water}} = F_{\text{deep}} + F_{\text{shallow}} \tag{1}$$

$$F_{\text{Total}} = \underbrace{F_{\text{open water}} + F_{\text{tank wall}}}_{\text{Coupled}} \tag{2}$$

A researcher may opt to neglect this tank wall interaction but must be aware of the fact that the obtained manoeuvring model is not necessarily an open water manoeuvring model. A clear example of this problem can be found in the shallow water contributions to the SIMMAN 2020 workshop (Delefortrie et al. 2024a). Within the framework of this workshop, FH submitted results of drift forces for the KVLCC2 with 20% Under Keel Clearance (ukc) based on tests executed in the Towing

Tank for Manoeuvres in Confined Water (co-operation with Ghent University) (Delefortrie and Eloot 2022). Figure 1 shows a comparison of different submissions [1].

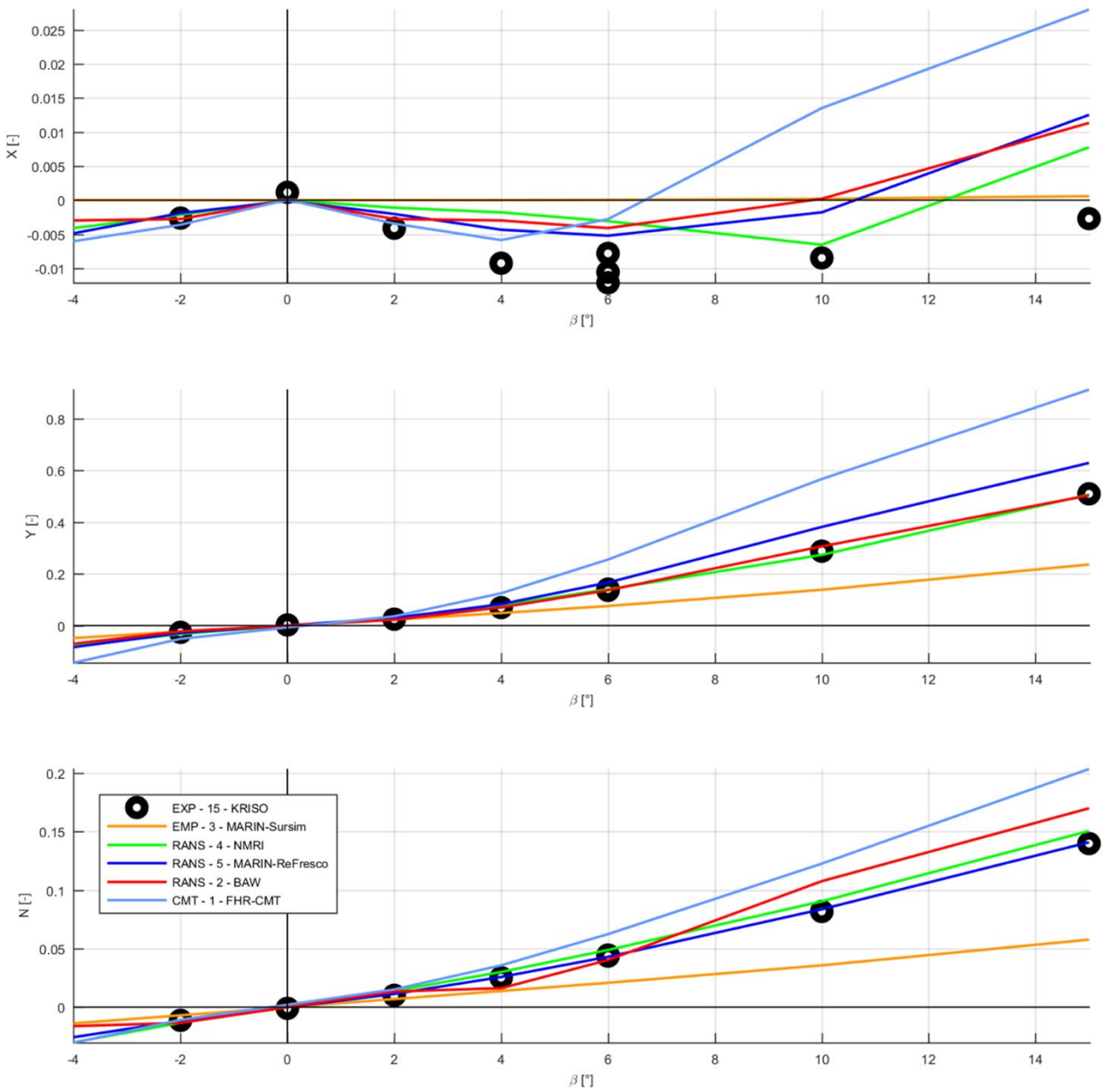

Figure 1 Comparisons between the (offsets of the) drift forces using different methods: preliminary assessment of KVLCC2 submissions to SIMMAN 2020

One can observe from Figure 1 that the largest non-dimensional offsets are predicted by FH. Although the trends are well captured, the overestimation tends to increase with increasing drift angle. Again with the benchmark vessel KVLCC2, a second example of such overestimation was observed in the technical report of Van Hoydonck et al. (2017). The tests were carried out at FH with KVLCC2 (model scale 1 : 75) at a drift angle of 30°. Experimental results were compared with different Computational Fluid Dynamics (CFD) methods. Some CFD methods used the towing tank as a computational domain, whereas others (MARIN's in particular (Van Hoydonck et al. 2017)) performed computations without walls. The CFD computations performed with walls better captured the towing tank effects, whereas the computations without walls significantly 'underestimated' (as mentioned in the report) the measurements.

[1] Thanks to Frans Quadvlieg (MARIN, The Netherlands) for sharing the data. The data were shared by e-mail, June 3, 2020.

The above suggests that there is an influence of the towing tank walls on the shallow water results for the KVLCC2. Historically, this problem is treated from the viewpoint of the ship's resistance only. An example of this was discussed by Raven at the 2019 MASHCON conference (Raven 2019), which lead to a new shallow water correction procedure for the resistance. This correction factor was developed based on potential flow theory and is further adopted in the 2021 ITTC conference (*ITTC Recommended Procedures and Guidelines: Resistance Tests - 7.5-02-02-01, rev-05 2021*). Such tank wall effect is observed previously applicable to any DOF. An analogous phenomenon was discussed at the 2022 MASHCON conference with the use of a false bottom to test the drift induced forces acting on a ship. These measured forces became smaller as the false bottom was moved towards the true bottom of the tank (Hachiya et al. 2022).

Table 1. Full scale data of the KVLCC2.

KVLCC2 – single propeller – single rudder			
L_{OA} (m)	325	#propeller blades	4
L_{PP} (m)	320	D_{P} (m)	9.86
B (m)	58	P/D_{P} (-)	0.721
T (m)	20.8	A_{E}/A_0 (-)	0.431
C_{B} (-)	0.81	A_{R} (m²)	111.7
m (kg)	3.130×10^8	Model scale	1:75 & 1:150
$\overline{KM_{\mathrm{T}}}$ (m)	24.29	$\overline{KM_{\mathrm{L}}}$ (m)	398.5

As understood earlier tank wall effects have a strong dependency on various factors. Progress made by the authors in this field with the benchmark ship KVLCC2's data at two different scales are already published in Delefortrie et al. (2023) & Delefortrie et al. (2024b). This paper intends to supplement these observations with a discussion of Geosim test results and tries to put light on the fact that there is a need of introduction of a drift dependent correction factor for the towing tank manoeuvring tests in order to isolate the tank effects from open water data obtained from the towing tank tests.

To aid the development of the correction factor, the ship-bank interaction model by Lataire (2014) is utilized as an approach. This model quantifies the bank effect experienced by a vessel shipping close to the wall. A crucial term used in this model is the influence width (Lataire and Vantorre 2008) which is defined as the (horizontal) distance between a ship and bank where the bank effects can be neglected. This term was initially derived for ships with zero drifting conditions. The ship-bank interaction model uses the influence width and another term called "equivalent blockage" m_{eq}, to quantify the longitudinal contribution of the banks. The requirement for the introduction of this new term is because of the fact that for a ship moving parallel to the tank walls, with zero drift angle and at the center of the tank, the contribution of the horizontal confinement from the tank walls is equal. However if the vessel travels in close vicinity of one of the walls then the effect from the closest wall will be more pronounced. By definition the value of the (classic) blockage m does not change if the same vessel is located at a different position in the same cross section. To address this issue, a weighted parameter called the equivalent blockage, m_{eq} is introduced by Lataire (2014). It takes into account the horizontal distance between the vessel and the tank wall on both sides.

In 2023 the definition of the influence width was extended to drifting ships. In drifting cases the nearest point along the longitudinal axis of the ship is to be considered and the distance from this point to the bank is counted as the influence width (Delefortrie et al. 2023). Observing the offset from Figure 1 at higher drift angles, it is imperative that the tank wall effect is more pronounced at higher drift angle and hence to correct these experimental values a drift angle dependent correction factor is required. A proof of concept of a drift angle dependent equivalent blockage, $m_{\mathrm{eq}}(\beta)$, is proposed in this paper as a correction factor. However, further investigation using RANS (Reynolds-Averaged Navier-Stokes equations) based CFD calculation seems to be an ideal solution to explore this further.

2 IDENTIFICATION OF FACTORS THAT INFLUENCE THE OPEN WATER MODEL AT HIGHER DRIFT ANGLES

2.1 OVERVIEW

In shallow water conditions, a restricted tank width primarily affects the flow by causing an increased velocity near the ship model, which is greater than in an unbounded tank domain, as the water is forced to pass through the confined space. For a particular towing tank, the extent of this confinement effect is defined as blockage. Historically the establishment of blockage formulation is done based on experiments conducted with zero drift angles. As a ship drifts, the horizontal distance

between the bow or stern part of the ship to the tank decreases and intuitively the confinement effect increases. This means for a particular towing tank and for a particular ship model size, the equivalent blockage changes as the ship's drifting angle increases. To reduce the effect of equivalent blockage, it is required to increase the horizontal distance between the ship's bow or stern to the tank wall. As the dimension of a towing tank cannot be increased, it is more practical to reduce the model size. However, decreasing the model size can lead to change in flow dynamics. Hence an investigation is required to understand how the model size effects the towing tank's test measurements at various drifting angles.

The latter tests are used as input to establish an open-water mathematical model of the ship's manoeuvring behaviour. A valid mathematical model needs to fulfill a number of requirements, for instance regression coefficients should be independent of test parameters like speed distributions. Hence a core investigation of such factors is executed first and presented in the following sections.

2.2 DESCRIPTION OF THE EXPERIMENTAL CASES OF THE GEOSIM CONDITIONS

To study the influence of different factors, captive model tests have been carried out in the Towing Tank for Manoeuvres in Confined Water at FH. All the tests were conducted in Froude scaled Geometrically similar (Geosim) conditions, which means that everything is scaled, except for the towing tank dimensions. For these tests, the benchmark model KVLCC2 has been used at two model scales, namely 1/75 (T0Z, L_{PP} = 4.267 m) and 1/150 (T20, L_{PP} = 2.13 m). Table 1 lists all the full scale data of the KVLCC2. At both scales the ship was loaded to an even maximum full scale draft of 20.8 m. An important difference is that T0Z was equipped with rudder and propeller while the smaller T20 only had a rudder which was neither used nor measured upon during the tests.

The experimental program consisted of three datasets:

- **Dataset 1:** T0Z (model scale 1/75) has been tested at three under keel clearances: 80%, 30% and 20%. A full open water manoeuvring program was carried out and the mathematical model was already presented at the 2016 MASHCON conference (Delefortrie et al. 2016).
- **Dataset 2:** In 2021 T20 (model scale 1/150) has been tested at five under keel clearances: 260%, 80%, 30%, 20% and 10%. The ship was tested with straight line tests only at different drift angles and along different lateral positions in the tank. The results were used to update the influence width definition with inclusion of the drift angle effect (Delefortrie et al. 2023). The speeds of that test program are not Froude scaled speeds of T0Z. This dataset is identified as T2001 in the following sections.
- **Dataset 3:** A full open water manoeuvring program (hull only) was executed with T20 (model scale 1/150) at under keel clearances 30% and 20%. The speeds were Froude scaled from the open water program of T0Z. This dataset is identified as T2002 in the following sections.

Table 2. Speed Ranges for T0Z and T20 Programs

Model	Program	Speed (m/s)	Equivalent Full Scale Speed (knots)
T0Z	Open Water Manoeuvring	0.0000	0.0
		± 0.1250	2.1
		± 0.2080	3.5
		0.3330	5.6
		0.4160	7.0
		0.6530	11.0
		0.9209	15.5 (only at the largest water depth)
T20	Influence Width Program	0.1250	Not necessarily corresponding to full-scale
		0.1875	
		0.2500	
		0.3750	
		0.5000	
		0.7500	
		1.0000	
	Open Water Manoeuvring	± 0.0884	2.1
		± 0.1471	3.5
		0.2942	7.0

2.3 EFFECT OF A DIFFERENT SPEED SET FOR A PARTICULAR MODEL SIZE OF KVLCC2

The difference between the datasets 2 (T2001) and 3 (T2002) is that they are based on different speed sets. In Figure 2, the different components of the non-dimensionalized hydrodynamic forces and moments acting on the KVLCC2 (model scale 1:150) in 6 DOF as a function of drift angles obtained from the regression analysis using the T2001 and T2002 datasets are plotted for 30% and 20% ukc. Using the non-dimensionalized surge and sway magnitudes (see Delefortrie et al., 2016, for the way the forces are non-dimensionalized), the drag coefficient ($D'(\beta)$) and lift coefficient ($L'(\beta)$) are derived and plotted as a function of drift angle. The legend denotes the ukc from the two datasets. The 30%T2002A03 means the data obtained from the dataset T2002 for 30% ukc. Similarly the legend, 20%T2002A04 means the dataset T2002 for 20%. The other two legend 30% and 20% denotes the dataset T2001 for 30% and 20% ukc. Roll moment plots are not included because these were not measured during the tests.

As in harbour areas the ships travel below the critical speed, the speed sets for certain ukc were modified such that speeds above the sub-critical velocity are eliminated before performing the regression analysis. For example, although at 90° drift, the speed 0.25 m/s was included for 30% ukc, it was removed for 20% ukc as it was above the sub-critical velocity. Similarly it was necessary to remove the speed 0.25 m/s for 20% ukc at 70° drift angle. More information on the assessment of critical velocities in drifting conditions is available in Delefortrie et al. (2023).

Figure 2 shows that the change in the difference between the magnitude of the forces with respect to the drift angles between the two datasets for the same ukc, gradually increases. This implies that for a particular model size and ukc, the discrepancy increases as the drift angle increases. This discrepancy is less pronounced for the lift coefficient. Strong variations for the pitch moment at larger drift angles appear.

2.4 EFFECT OF THE MODEL SCALE

2.4 (a) Effect of the model scale as a function of drift angle

The results obtained from the dataset 1 (T0Z) and dataset 3 (T2002) are used to understand the impact of model size on the hydrodynamic forces. Here the dataset T2002 is used for comparison as the speed sets in prototype scale are similar to those of the dataset T0Z. The mathematical drift functions have been plotted in Figure 3, which compares the results for the tests carried out with the above mentioned two model scales under three under keel clearances: 80%, 30% and 20%. From the plots of the figure, the following observations can be made:

- The ship model size has a significant influence on the drag, lift and heave force. Similar to the speed set effect, the differences between the non-dimensionalized forces obtained from the tests of the two model size for the same ukc increase with increasing drift angle. Also for a particular model size, the forces increase as the ukc decreases. In terms of drag and lift a deviation is seen for:
  - 80% ukc: drift angles of 55° and above;
  - 30% ukc: drift angles of 40° and above;
  - 20% ukc: drift angles of 25° and above.

  For the heave force this deviation is already noted at smaller drift angles than the ones mentioned above.
- The non-dimensionalized pitch moment, $M'(\beta)$ is more or less similar for 80% ukc, whereas for the smaller water depths similar variations as the ones caused by the speed dependency are observed;
- The non-dimensionalized yaw moment, $N'(\beta)$ is primarily affected by the changed lift and drag. However, there is a tendency that the point of application (x_v) of the sway force is located slightly more towards the aft for the smaller ship model.

2.4 (b) Effect of the model scale as a function of yaw angle

Figure 4 plots the non-dimensionalized hydrodynamic forces and moments as a function of yaw angle. The speed sets considered while performing these tests were scaled with respect to the 1/75 model sized KVLCC2 (T0Z).

Excluding the non-dimensionalized yaw moment plot, the yaw effect is significantly smaller by an order of magnitude when compared to the drift effect of the ship as explained in the previous section. Even for the yaw moment, the largest variations occur at yaw angles of ±90°. The repeatability of pure yaw tests is relatively poor; particularly for the 1/150 scale model. It is due to the fact that for such a small model, applied yaw rates and the resulting forces and moments are smaller. Consequently, it can be concluded that for most degrees of freedom, the ship model size does not have a substantial impact on the yaw functions. The only noteworthy effect of ship model size is observed in the sway force plot.

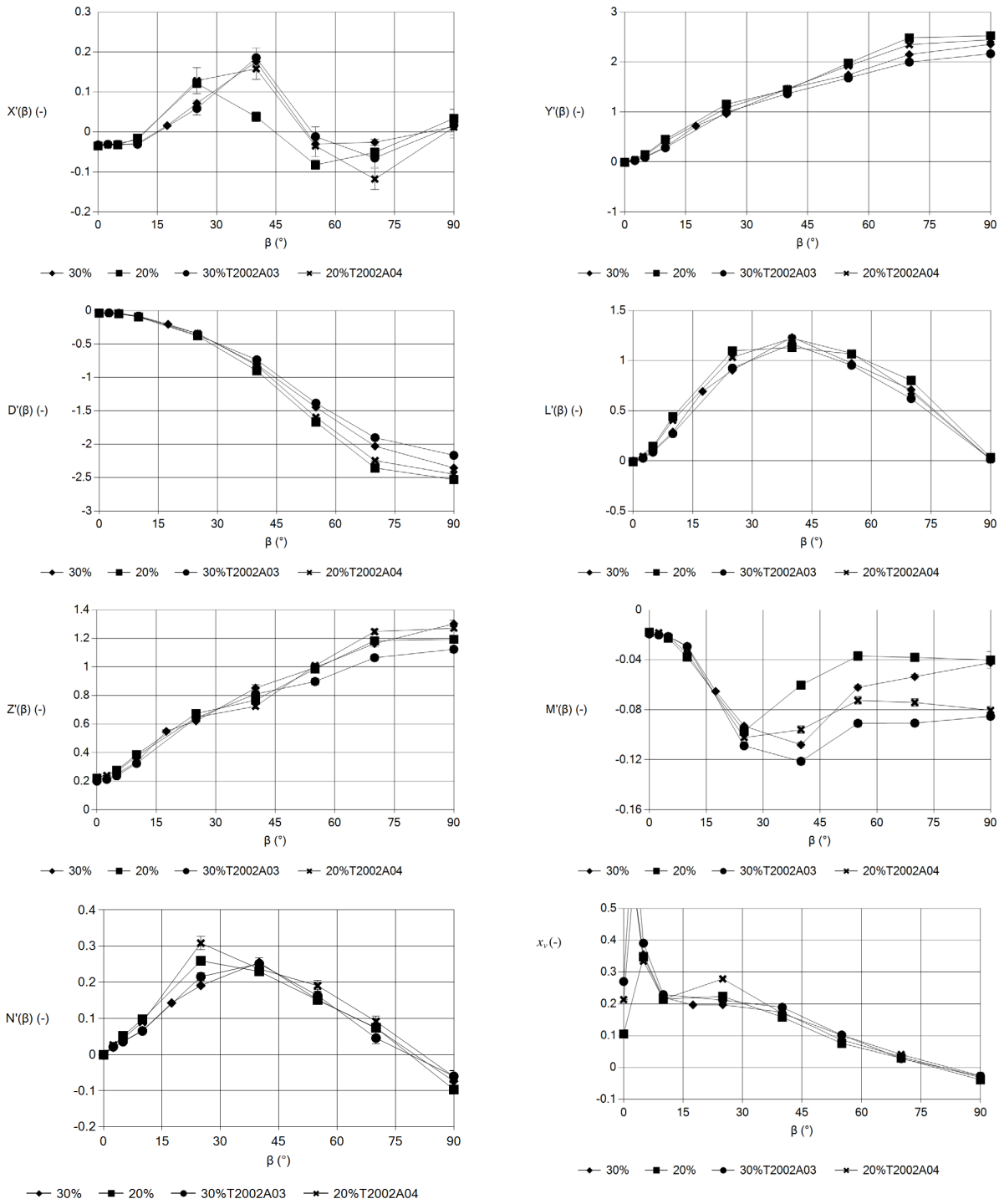

Figure 2. Evaluation of speed set effect on the different components of non-dimensionalized hydrodynamic forces as a function of drift angle using two different datasets of 1/150 scale model at various under keel clearances (Delefortrie and Eloot, 2022).

2.5 DISCUSSION OF GEOSIM RESULTS

From the speed set effect and model scale effect analysis, it is evident that the existing open-water mathematical model which is based on the regression analysis, shows discrepancy at higher drift angles. This discrepancy arises primarily from the confinement of the towing tank, which becomes more pronounced at higher drift angles. Such an effect calls for the introduction of a correction factor to accurately adjust the test results. To address this, a correction factor in the form of an equivalent blockage parameter must be established. For a particular ukc, towing tank and model size, this equivalent blockage parameter is a function of drift angle.

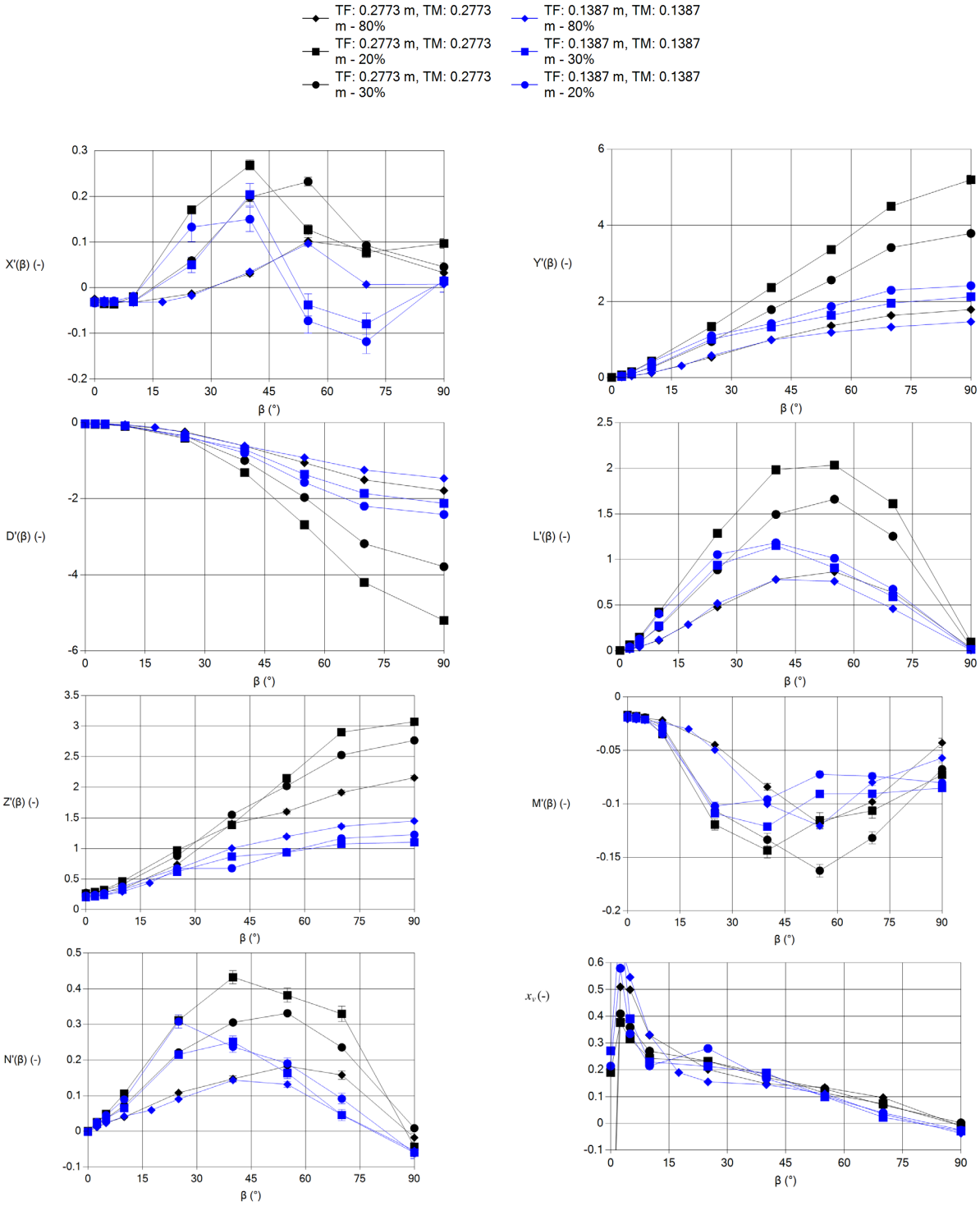

Figure 3. **Evaluation of model size effect on the different components of non-dimensionalized hydrodynamic forces as a function of drift angle using both 1/150 and 1/75 scale models at various under keel clearances (Delefortrie and Eloot 2022).**

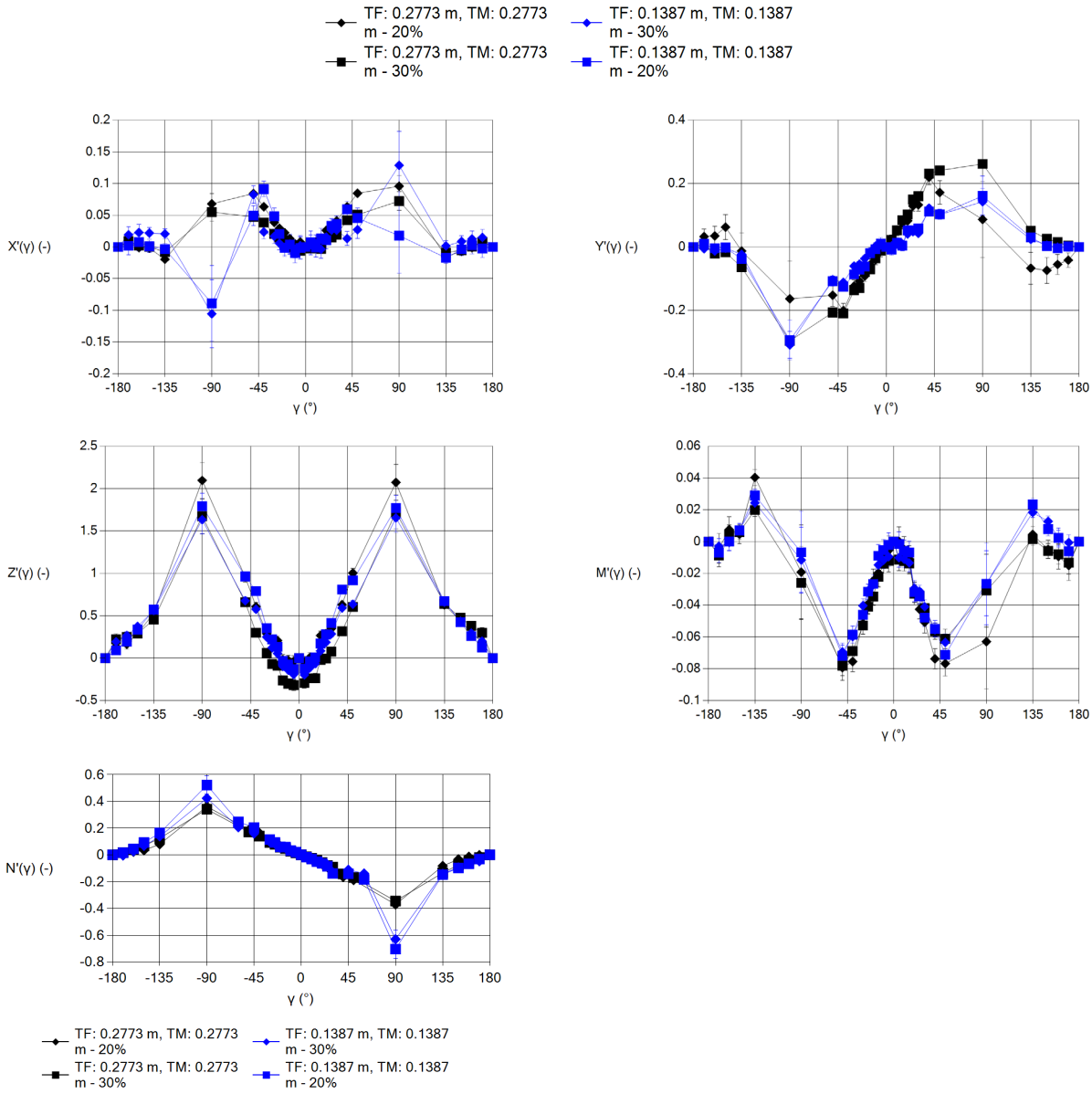

Figure 4. **Evaluation of model size effect on the different components of non-dimensionalized hydrodynamic forces as a function of yaw angle using both 1/150 and 1/75 scale models at various under keel clearances (Delefortrie and Eloot 2022).**

3 ESTABLISHMENT OF EQUIVALENT BLOCKAGE FORMULATION AS A FUNCTION OF DRIFT ANGLE

3.1 PROBLEM STATEMENT

So far the dependencies of the hydrodynamic forces and moments on various factors have been addressed. However as discussed earlier tank wall effect can influence the hydrodynamic forces and flow patterns experienced by the model, leading to deviations from the conditions expected in open water. Hence the tank wall effect can lead to faulty results and need to be quantified.

This section aims to develop a drift-dependent equivalent blockage correction factor, allowing towing tank results, accounting for confinement effects, to be adjusted to represent open-water conditions accurately.

3.2 PRINCIPAL CHARACTERISTICS OF THE SHIP BANK INTERACTION MODEL

A comprehensive mathematical model for the prediction of ship-bank interaction forces and moments in the horizontal plane was developed by Lataire (2014). Recently an updated model to 6 DOF was developed by Delefortrie et al. (2024b). The **first pillar** of the previous research is the establishment of influence width and this is also the foundation pillar to establish the correction factor.

$$y_{\text{infl}} = 5B(Fr_h + 1) \tag{3}$$

Equation 3 indicates at which horizontal distance an obstacle should be in order to be considered as having no effects on the ship. As such this equation gives a limit for restricted water effects. In Delefortrie et al. (2023) this definition was extended towards drifting ships as well, where the distance should be expressed between the closest point along the centerline of the ship and the obstacle.

This influence width is then used in the **second pillar** in equation 4, which considers a weighted integration of the available cross section. Each water particle at coordinates (y, z) with respect to the ship has a weight:

$$w = e^{-\left(\xi_y \frac{|y|}{y_{\text{infl}}} + \xi_z \frac{|z|}{T}\right)} \tag{4}$$

ξ_y and ξ_z are regression coefficients which are determined based on the outcome of the tests. ξ_z is a constant for the present towing tank, while ξ_y is a constant for each ship-draft combination.

The integration of the cross section at both sides of the vessel can be calculated with equations 5 and 6. Here the ship dependent weight factor (w) can be seen as an overlay sheet which is placed on the cross section under consideration. All 'water particles' are taken into account including the particles at a distance far away from the vessel. However, the weight value for these particles will be insignificant as the influence of these particles on the ship will be negligible.

$$\chi_{\text{s}} = \int_0^h \int_0^{y_{\text{s}}} e^{-\left(\xi_y \frac{|y|}{y_{\text{infl}}} + \xi_z \frac{|z|}{T}\right)} dy\, dz \tag{5}$$

$$\chi_{\text{p}} = \int_0^h \int_0^{y_{\text{p}}} e^{-\left(\xi_y \frac{|y|}{y_{\text{infl}}} + \xi_z \frac{|z|}{T}\right)} dy\, dz \tag{6}$$

$$\chi_{\text{ship}} = 2\int_0^T \int_0^{\text{B}/2} e^{-\left(\xi_y \frac{|y|}{y_{\text{infl}}} + \xi_z \frac{|z|}{T}\right)} dy\, dz = 2\frac{y_{\text{infl}}\, T}{\xi_y \xi_z}\left(1 - e^{-\frac{\xi_y B}{2 y_{\text{infl}}}}\right)\left(1 - e^{-\xi_z}\right) \tag{7}$$

$$\chi_{\text{ocean}} = 2\frac{y_{\text{infl}}\, T}{\xi_y \xi_z} \tag{8}$$

The **third pillar** is then the definition of an equivalent blockage as mentioned in the equation 9

$$m_{\text{eq}} = \frac{1}{2}\left(\frac{\chi_{\text{ship}}}{2\chi_{\text{s}}} + \frac{\chi_{\text{ship}}}{2\chi_{\text{p}}}\right) - \frac{\chi_{\text{ship}}}{\chi_{\text{ocean}}} \tag{9}$$

This equivalent blockage becomes zero in an open and deep water section. Equation 10 portrays a nice proportionality relationship which was established between the square of this blockage and the increased longitudinal force due to the confinement.

$$X_{\text{BANK}} \propto m_{\text{eq}}^2 \tag{10}$$

3.3 DEVELOPMENT OF DRIFT ANGLE DEPENDENT CORRECTED EQUIVALENT BLOCKAGE

3.3 (a) Methodology

The ship bank interaction model is established and validated for tests with zero drift angle. However to incorporate a corrected equivalent blockage as a function of drift angle, the ship-bank interaction model needs to be improved. As a proof of concept a methodology with a correction factor is introduced in this section and was also applied on test runs in the towing tank for a variety of drift angles of the KVLCC2. By this approach one can estimate the additional open-water forces acting on the ship model due to the confinement in the presence of a non-zero drift angle too. By definition the hull drag can be formulated as:

$$D'(\beta) = X'(\beta)\cos\beta - Y'(\beta)\sin\beta \tag{11}$$

as the drag is calculated in the flow direction. The relation represented in equation 10 can be adopted to $D'(\beta)$ as mentioned in equation 12.

$$D'(\beta) \propto m_{\mathrm{eq}}^2 \tag{12}$$

However the equivalent blockage parameter, m_{eq} incorporates the influence width which needs to be redefined as the ships are drifting. As a proof of concept a modified influence width formulation is represented by equation 13.

$$y_{\mathrm{infl}} = 5B^*(\beta)(Fr_h + 1) \tag{13}$$

$B^*(\beta)$ in equation 13 represents the "corrected" ship's breadth. Assuming the corrected breadth as a function of B, L and β as mentioned in equation 14, an empirical example is shown in this paper.

$$B^*(\beta) = B|\cos\beta| + L\sin^2\beta \tag{14}$$

Using this influence width the drag $D'(\beta)$ has been modelled as mentioned in equation 15 where ξ is a regression coefficient which needs to be identified.

$$D'(\beta) = D'_{\mathrm{deep}}(\beta) + \xi(\beta)m_{\mathrm{eq}}^2 \tag{15}$$

This is how the correction factor, i.e the corrected m_{eq} can be developed as a function of drift angle. It can be utilized to obtain the open water data (D'_{deep}) provided the experimental data are available. Considering $F' = [X', Y', Z', K', M', N']$ to be a set of non-dimensionalized hydrodynamic forces, the correction equation can be generalized as mentioned in equation 16.

$$F'(\beta) = F'_{\mathrm{deep}}(\beta) + \xi(\beta)m_{\mathrm{eq}}^2 \tag{16}$$

3.3 (b) Application example

To show the applicability of the correction factor another benchmark hull, the KRISO Container Ship (KCS) is taken. Here a comparison is made between the drag on a 1/52.667 scale model of the KCS and the drag on a 1/75 scale model of the rudder of the Esso Osaka. The latter is chosen, because the model scale rudder is much smaller than the ship model, and as such it will sense less the tank walls and this is why the forces measured by the rudder are assumed to be close to the order of magnitude of open water result as seen from the Figure 5. These results are marked with the red points in the figure.

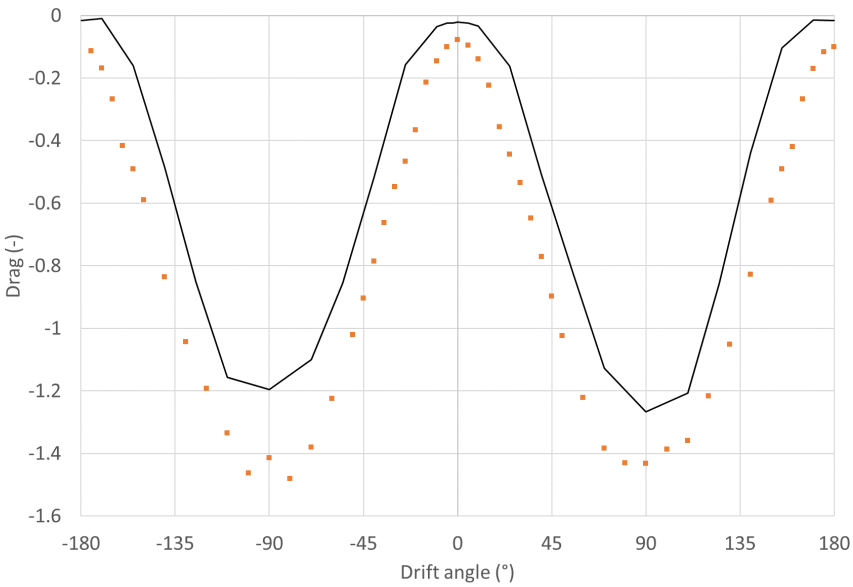

Figure 5. Comparison of Predicted non-dimensionalized deep water component of the drag $D'_{\mathrm{deep}}(\beta)$ of the KCS with that of rudder Esso Osaka

The predicted open water component of drag force of KCS is demarcated by the black line which is obtained using the equation 15. The corrected blockage m_{eq} is already known with the ship bank interaction model and the assumption of the corrected ship's breadth as mentioned in equation 14. Hence from the confined results of KCS model a predicted $D'_{\mathrm{deep}}(\beta)$ can be determined of similar magnitude as the Esso Osaka rudder drag. This finding underscores the substantial impact of lateral confinement (tank wall effects) on the hydrodynamic forces experienced by the ship model under these conditions.

If all the coefficients of equation 15 are known, this equation can be used to compute the drag of a ship tested in different environments. An example of such exercise is represented in Figure 6. On that figure:

- The drag functions for 100% ukc and 10% ukc are known functions and stem from the measurements of captive model tests carried out in the 7 m wide Towing Tank for Manoeuvres in Confined Water.
- The deep water ocean drag corresponds to a $D'_{\mathrm{deep}}(\beta)$ that was now determined in such way that in a 2D case the drag coefficient C_D increases to around 2 at 90° inflow. The 2D case can be computed by computing m_{eq} for a zero under keel clearance. Mind that this $D'_{\mathrm{deep}}(\beta)$ at 90° is different from Fig. 5 and the flat plate computation where the drag C_D should be approximately 1.3 in 3D scenario, which also implies further work is needed to establish this difference.

Based on the model the suggested drag of the ship can be computed for an environment as the 20 m wide Towing Tank for Manoeuvres in Shallow Water and an open shallow water ocean environment (without horizontal boundaries). This model indicates that in the confined towing tank of Antwerp starting from 25° drift a severe confinement occurs. In the shallow water towing tank in Ostend, for a 4 m long ship model this bifurcation starts at 55° drift. However it seems less severe compared to the severity experience in Antwerp's tank.

3.4 PRELIMINARY CFD COMPUTATIONS

Some preliminary exercises where performed using CFD.

- The results at 30° drift of the KVLCC2 without walls seem to approach the CFD results of MARIN without the walls. Detailed information is published in the technical report of Van Hoydonck et al. (2017).
- CFD tests were executed with large drift angles for different widths of the towing tank walls. A first hand computation reveals that for a barge drifting at an angle of 90°, the drift force decreases from 56 kN to 33 kN when carried out in a wider domain. It implies again the severity of lateral confinement (also termed as the tank wall effects).

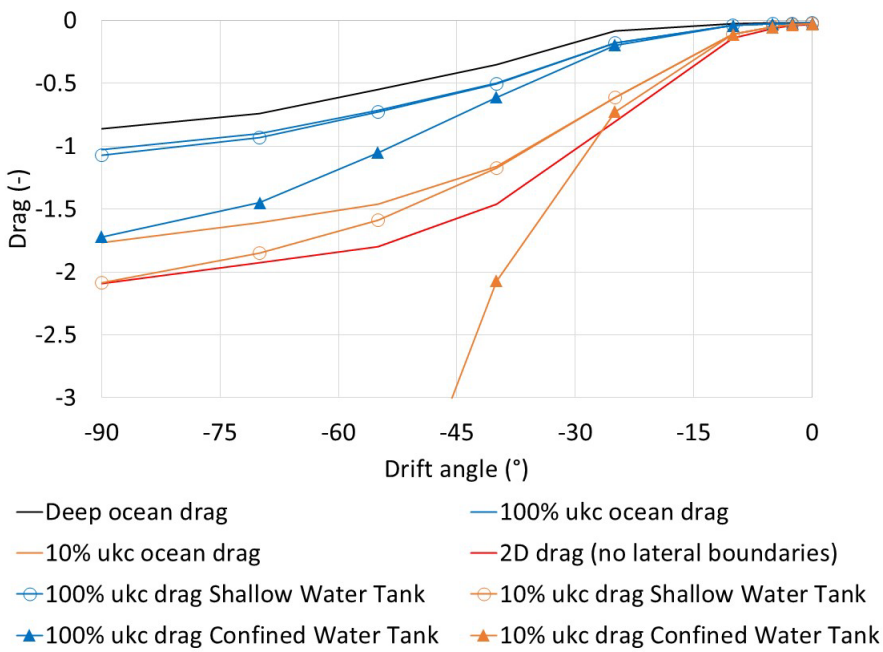

Figure 6. Predicted drag of the 1/52.667 scaled model KCS in a given environment.

4 CONCLUSION

Significant variations in force components (surge, sway, and heave) have been observed due to the drift angle of the ship model. These variations become more pronounced with increasing drift angles and decreasing under-keel clearance. Larger dimensionless values are recorded for the larger ship model, which can be attributed to the increased flow velocity around the ship caused by the influence of towing tank walls. In contrast, yaw forces appear to be less influenced by the size of the ship model, with the only notable difference occurring in the sway force.

While the influence of scale effects on drag has been omitted from the current discussion, it is worth noting that these effects appear less dominant. However, they are increasingly challenging to study as the ship model size decreases. The reduction in scale introduces complexities in accurately capturing flow characteristics and their implications on drag behaviour.

The current framework for describing ship-bank interactions is limited to qualitative trends. A drift-dependent model is required to account for the dynamic interaction between the ship and its environment during drift manoeuvres. However, the absence of comprehensive experimental data, such as tests in shallow open-water environments or virtual Towing Tank for Manoeuvres in Shallow Water, limits validation efforts. Future work is therefore oriented towards CFD based research.

5 REFERENCES

Delefortrie, G. and K. Eloot, 2022. Confinement Effects in Open Water Manoeuvring: Sub Report 1 – KVLCC2 Geosim Test Results. Tech. rep. 20_105_1. Version 3.0. Antwerp: Flanders Hydraulics Research.

Delefortrie, G., K. Eloot, and E. Lataire, 2023. The influence width of drifting ships. eng. In: APPLIED OCEAN RESEARCH 141, p. 13. ISSN: 0141-1187.

Delefortrie, G., K. Eloot, E. Lataire, W. Van Hoydonck, and M. Vantorre, 2016. Captive model tests based 6 DOF shallow water manoeuvring model. eng. In: Hamburg, Germany: Bundesanstalt für Wasserbau, pp. 273–286. ISBN: 978-3-939230-38-0.

Delefortrie, G., K. Eloot, and W. Van Hoydonck, 2024a. EFD based submissions for the shallow water cases of SIMMAN 2020. eng. In: SIMMAN 2020 Workshop on Verification and Validation of Ship Manoeuvring Simulation Methods Incheon, Republic of Korea 17–19 July 2023 Volume IV : Workshop Proceedings. Incheon, Republic of Korea, 19–24.

Delefortrie, G., J. Verwilligen, K. Eloot, and E. Lataire, 2024b. Bank interaction effects on ships in 6 DOF. In: Ocean Engineering 310.Part 1, p. 118614. ISSN: 0029-8018. DOI: 10.1016/j.oceaneng.2024.118614.

Hachiya, Y., M. Sano, R. Okuda, Y. Furukawa, and H. Yasukawa, 2022. False bottom effect on the hydrodynamic forces acting on a ship hull during an oblique test and countermeasures. In: Proceedings of MASHCON 2022, Glasgow, UK, pp. 59–71.

ITTC-Recommended Procedures and Guidelines: Resistance Tests - 7.5-02-02-01, rev-05 2021. International Towing Tank Conference (ITTC).

Lataire, E., 2014. Experiment based mathematical modelling of ship-bank interaction. PhD thesis. Ghent University, XXIX, 269. ISBN: 9789085787488.

Lataire, E. and M. Vantorre, 2008. Ship-bank interaction induced by irregular bank geometries. eng. In: Symposium on Naval Hydrodynamics, 27th, Proceedings. Vol. 2. Seoul, Korea, 511–524.

Raven, Hoyte C., 2019. Shallow-water effects in ship model testing and at full scale. In: Ocean Engineering 189, p. 106343. ISSN: 0029-8018. DOI: https://doi.org/10.1016/j.oceaneng.2019.106343.

Van Hoydonck, W., K. Eloot, S. Toxopeus, M. Visonneau, P. Schiller, and M. Abdel-Maksoud, 2017. Chapter 8 – Experimental and numerical investigations of KVLCC2 at 30° static-drift angle in shallow water. In: STO Technical Report TR-AVT-183. 1354 pp., pp. 8-1–8-34.

6 AUTHORS BIOGRAPHY

Guillaume Delefortrie, naval architect (MSc, Ghent University 2001, PhD, Ghent University, 2007), associate professor at the Ships and Marine Technology division (SMTD) of Ghent University, lecturer in charge of courses in marine hydrodynamics. Experienced in EFD (Experimental Fluid Dynamics) based research, with focus point on ship manoeuvring in shallow and confined water. He has been a member of the 27th-29th ITTC Manoeuvring Committee. Member of the organization and scientific committees of MASHCON conferences since their creation (2009).

Arghya Kamol Roy is a mechanical engineer currently working as a scientific researcher in the Ships and Marine Technology division (SMTD) at Ghent University (https://ships.ugent.be/staff.php), Belgium. With a specialization in computational fluid dynamics (CFD), he is advancing the team's manoeuvring models by integrating state-of-the-art CFD techniques. He is an

Erasmus mundus scholarship awardee and has completed his master's degree in Advanced Ship Design through a joint program at the University of Liège, Belgium, and École Centrale Nantes, France.

Katrien Eloot, PhD, naval architect, is senior expert nautical research at Flanders Hydraulics (FH) and chair of the Knowledge Centre (www.shallowwater.be). She is responsible for research on ship manoeuvring in shallow and confined water for private and public agencies worldwide. Her PhD focused on mathematical modelling and validation of ship behaviour based on experimental fluid dynamics in towing tanks.

Evert Lataire, PhD, naval architect, is professor and head of the Ships and Marine Technology division (SMTD) at Ghent University. He has written a PhD on the topic of bank effects mainly based upon model tests carried out in the shallow water towing tank of FHR. His fifteen year experience includes research on ship manoeuvring in shallow and confined water such as ship-ship interaction, ship-bottom interaction and ship-bank interaction.

INFLUENCE OF THE RETURN CURRENT AND THE PRIMARY WAVE OF A PASSING SHIP ON HARBOUR HYDRODYNAMICS

Ina Teutsch, Federal Waterways Engineering and Research Institute (BAW), Germany
Marko Kastens, Federal Waterways Engineering and Research Institute (BAW), Germany

INFLUENCE OF THE RETURN CURRENT AND THE PRIMARY WAVE OF A PASSING SHIP ON HARBOUR HYDRODYNAMICS

INA TEUTSCH, FEDERAL WATERWAYS ENGINEERING AND RESEARCH INSTITUTE (BAW), GERMANY
MARKO KASTENS, FEDERAL WATERWAYS ENGINEERING AND RESEARCH INSTITUTE (BAW), GERMANY

SUMMARY

Large sea-going vessels with a displacement hull create a return current and a primary wave. This pressure-generated system induces loads beyond the immediate surroundings of the ship. By applying a Reynolds-averaged Navier–Stokes (RANS) method, it is demonstrated how the return current of a ship passing a harbour entrance in a channel induces a water outflow of the harbour basin. The primary wave diffracts around the edges of the harbour entrance and propagates into the harbour basin before it is damped. Depending on the channel geometry and the ship velocity, the primary wave affects different areas of the basin. Especially in narrow waters, it is advisable to pass harbour entrances with an appropriate distance and at low speeds, as to reduce the primary wave height.

NOMENCLATURE

CFD	Computational Fluid Dynamics	
HRIC	High Resolution Interface Capturing	
VoF	Volume of Fluid	
A_c	Canal cross section	[m^2]
A_s	Wetted ship cross section	[m^2]
B	Channel width	[m]
b	Ship beam	[m]
c_B	Block coefficient	[-]
CFL	Courant–Friedrichs–Lewy number	[-]
h	Water depth	[m]
H_p	Primary wave height	[m]
K_d	Damping coefficient	[-]
L	Distance to the wall	[m]
L_{PP}	Length between perpendiculars	[m]
n	Ratio between canal cross section and wetted ship cross section	[-]
S	Gap width	[m]
t	Draught	[m]
t_d	Design draught	[m]
v_s	Ship velocity	[m/s]

1 INTRODUCTION

Large sea-going vessels with a displacement hull displace water that is transported along their hull to the back, inducing a pressure drop as described by Bernoulli (1738)'s law. The movement of water to the aft of the ship is termed return current. The pressure reduction leads to a depression of the water surface along the ship's hull, referred to as drawdown (Bhowmik et al., 1981). The pressure system enforces the formation of a primary wave, which consists of a bow wave, the drawdown, and a stern wave (Fig. 1).

The effect of primary ship waves is not limited to the direct surroundings of the ship. Previous studies treated the propagating primary wave as a solitary wave (Parnell et al., 2015). The primary wave propagates from the fairway into adjoining areas and affects built and natural environments (Scarpa et al., 2019). It has been observed to initiate erosion processes (Duró et al., 2020), put pressure on marine habitats (Gabel et al., 2017) and damage coastal protection structures (Melling et al., 2021). Moreover, in the past decades, ship traffic has increased and merchant vessels have become larger (UNCTAD, 2024). In addition to the interaction of ship waves with the shore, ship-to-ship interactions have become difficult to avoid. Cases have been documented in which the primary wave of a passing ship pulled off the lines of moored ships, which led to collisions between ships in a harbour area (Heijboer, 2024).

The effect of the primary ship wave increases in narrow conditions, such as laterally restricted channels or shallow water, in which the water is forced to flow faster and primary waves become higher (Constantine, 1960, e.g.).
An example of an adjoining area is a harbour basin that is connected to a channel. Kunz (1977) described the effect of primary ship waves originating in a channel on the wave climate in a connected harbour basin and found wave heights to be dependent on the ship velocity and on the ratio between the fairway cross section and the wetted ship cross section. Building on the findings in Kunz (1977)'s laboratory experiments, the present numerical study considers a ship moving in a narrow channel at constant speed. The channel opens to a sideward gap, which represents the entrance to a harbour basin. The primary wave propagates through the gap into the adjacent harbour. It transports wave energy and influences the movement of the water body inside the harbour. The present study investigates damping and diffraction of the primary wave in the harbour basin. Furthermore, light is shed on the influence of the return current on the hydrodynamics in the harbour basin.
The findings may be used as a basis in the planning stage of harbour dimensioning, to reduce the effect of primary waves on the surface elevation in the harbour. Moreover, the study sheds light on the role of ship velocity, draught, and channel geometry on the generation, propagation and damping of return current and primary wave. Based on these insights, strategies on how to reduce the amount of wave energy that enters the harbour, can be derived.

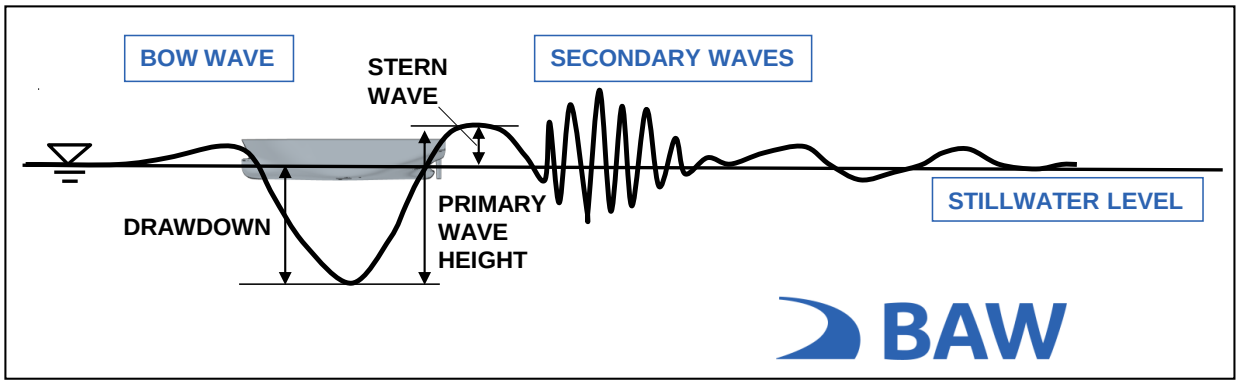

Figure 1: Stationary wave profile as generated by a large sea-going vessel with a displacement hull, travelling to the left of the figure at constant speed in a constant geometry. The wave system is represented schematically at a location close to the ship. The figure introduces the terminology used in the present study. Secondary waves are not subject of this analysis.

2 METHODS

Reynolds-averaged Navier-Stokes (RANS) equations were applied to investigate the situation of a ship passing a harbour entrance while moving at constant speed in a narrow channel. The commercial CFD (Computational Fluid Dynamics) code Simcenter Star-CCM+ Version 19.04.007-R8 (Siemens Digital Industries Software, 2024) was used. The CFD model consisted of a channel, amid which the ship moved along a wall from the left to the right of the domain (Fig. 2). After a runup length of 10 ship lengths, the wall opened on the ship's port side to a harbour entrance. The gap width S was defined to equal the ship length L_{pp}. In the CFD model, domain and ship were scaled down by a factor of 60 , which facilitated comparison with earlier CFD experiments (Bundesanstalt für Wasserbau, 2023, e.g.). The model domain included damping zones at the inlet and outlet of the domain to avoid reflections at the ends. Furthermore, the use of damping zones minimises the effect of a ship-generated pre-cursor soliton, which develops as a disturbance during the acceleration phase (Kochanowski & Kastens, 2022). To reduce the initial soliton height, an additional damping zone was established just ahead of the ship's starting position. The choice of dimensions and parameters of the damping zones were based on Peric (2019). The (full-scale) dimensions of the harbour basin were 4500 x 2220 m, large enough to avoid disturbances of the water surface by wave reflection at the walls, in agreement with common ocean wave diffraction diagrams (O'Sullivan, 1992). A post-panamax container ship with a beam of 52 m (PPM52) and a length between perpendiculars of L_{pp} = 347.2 m, as well as a design draught of t_d = 16 m and a block coefficient of c_B = 0.67 was chosen for the investigations. PPM52 is a ship that frequently uses German navigation channels. An overset technique was used in the simulation (Volkov, 1970). Motion of the ship in all degrees of freedom was suppressed, as the impact of the fluid body on the ship was not of interest. The mesh consisted primarily of hexahedral grid cells. The base sizes of both the overset and the background mesh were 0.4 m, which corresponds to approximately $1/15$ of the investigated ship's length in model scale. A grid study showed that the propagating primary wave was well resolved by 15 cells. The mesh was refined near the free surface to 12.5% of the base size in z direction and 50% of the base size in x and y directions. The boundaries near the walls and the ship hull were represented by prism layers containing four cells, for which an all-y+ wall treatment was adopted (Ferziger & Perić, 2002). The mesh consisted of approximately 2 million cells. The

VoF (Volume of Fluid) method was applied to track the free surface in the simulation of the multiphase flow (Hirt & Nichols, 1981). The HRIC (High Resolution Interface Capturing) of Muzaferija et al. (1998) was used to capture the surface between water and air. Menter (1994)'s Shear Stress Transport turbulence model with all-y+ treatment was used. An implicit unsteady solver was applied in the simulation. Its time step was adjusted to the respective ship speed of the experiment, estimated to satisfy the Courant–Friedrichs–Lewy condition (Courant et al., 1928), with a chosen value for the Courant number of CFL = 0.04 with reference to the grid base size. An experimental matrix of 64 cases was designed by varying the draught t and the velocity v_s of the ship PPM52, as well as the ratio n = A_c/A_s between the channel cross section A_c = $B \cdot h$, with channel width B and water depth h, and the ship's wetted cross section $A_s \approx b \cdot t$ (Table 1). These parameters were identified by Flügge and Uliczka (1996) as essential for the ship-induced loads in maritime waterways. Throughout the experiments, the water depth was kept constant at h = 30 m. The study was designed to yield results as general as possible to be of use for considerations in harbour design. Shallow-water effects, introduced by a more realistic water depth, will make the results very specific to each considered geometry, preventing the general use of the study. Therefore, the water depth was increased above the realistic water depth in a typical harbour. Since the experiments were designed in a way that the ship was always located in the middle of the channel (Fig. 2), the variation of n had a direct influence on the channel width B and the distance to the wall L = $B/2$.

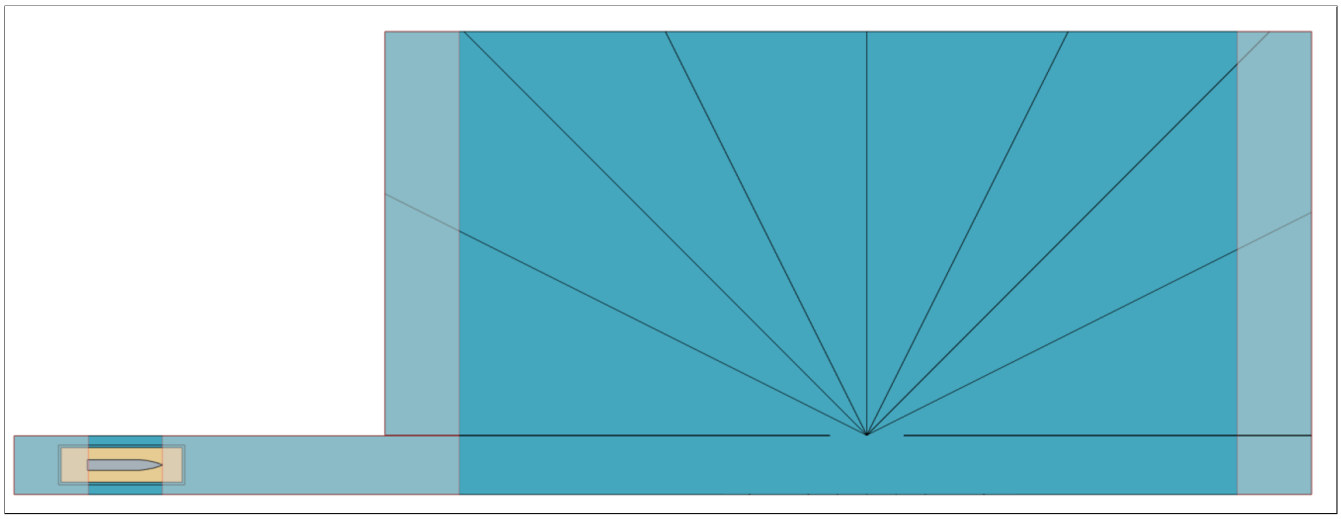

Figure 2: Top view of the CFD model with the ship and overset block (orange) in their starting position. The harbour basin at the top is separated from the channel at the bottom by a wall with a gap in the middle of the figure. The wavecuts used for the analysis share a common origin in the middle of the gap. Damping zones are represented by hatched areas.

3 RESULTS

3.1 RETURN CURRENT

As the moving vessel reaches the harbour entrance, the return current emerges from the spatial restrictions of the wall and propagates into the harbour basin (Fig. 3). Starting from the gap, it then distributes radially and almost symmetrically into the harbour basin (Fig. 4). The diagrams display relative values with respect to the maximum return current at the harbour entrance. The absolute values have been added to the captions. The influence of the return current in the propagation direction of the ship is restricted to the width of the gap, which is equivalent to $x/S = \pm 0.5$. Depending on the focus on absolute or relative values, two observations can be made from Fig. 4: (i) The highest return current values were reached by fast ships and for low n ratios, implying that passing at slow speed and with an adequate distance will reduce the load on the area of the harbour entrance. (ii) From a relative perspective, damping of the initial return current was also dependent on ship speed and n ratio. As the ship passed faster, the influence of the return current reached slightly further into the harbour (from top to bottom plots in Fig. 4). Cases of ship speeds below 9 kn are not displayed. Slow ships induced only a small return current, whose damped values were not distinguishable from signal noise in the harbour basin. For the same reason, 50% curves are not shown when their absolute values fall below 6 cm/s. Furthermore, the wider the channel, the further the influence of the return current seems to reach into the harbour basin (from left to right in Fig. 4). However, this observation is not equally evident in all cases. The draught was observed to have negligible influence on all presented results. From the displayed diagrams, it can be concluded that the spatial distribution of the return current around the ship was comparable for all experiments with ship type PPM52.

Table 1: Experimental matrix, containing the parameters of the CFD experimental runs. Horizontal lines separate classes of common draught. In each draught class, four groups of experiments were conducted, with one n ratio per group. In order to obtain nearly constant n ratios, the channel width B was varied. Each group consisted of four experiments with ship velocities of 12 kn, 10 kn, 8 kn and 5 kn, respectively. All parameters are given in full scale.

	Draught t	n ratio	Channel width B
Group 16-01	16 m	≈ 10	288 m
Group 16-02		≈ 12.5	336 m
Group 16-03		≈ 17.5	480 m
Group 16-04		≈ 20	552 m
Group 14-01	14.5 m	≈ 10	240 m
Group 14-02		≈ 12.5	312 m
Group 14-03		≈ 17.5	432 m
Group 14-04		≈ 20	504 m
Group 13-01	13 m	≈ 10	216 m
Group 13-02		≈ 12.5	288 m
Group 13-03		≈ 17.5	384 m
Group 13-04		≈ 20	456 m
Group 11-01	11.5 m	≈ 10	192 m
Group 11-02		≈ 12.5	240 m
Group 11-03		≈ 17.5	336 m
Group 11-04		≈ 20	408 m

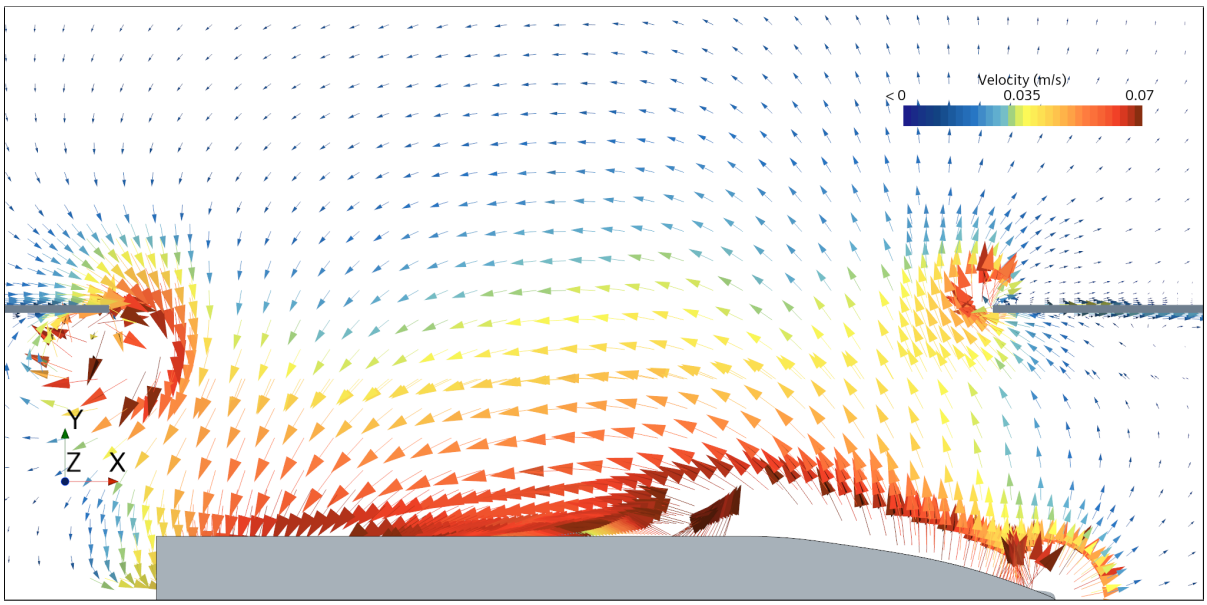

Figure 3: Vector plot showing the return current of the vessel PPM52 in the numerical model with t= 14.5 m and v_s = 10 kn, passing the harbour entrance in a channel with an n ratio of 9.5 Only the port side of the ship is displayed. The velocity is presented in model scale.

3.2 PRIMARY WAVE

As the ship moves through the channel and passes the gap in the wall, first the drawdown and subsequently the stern wave propagate from their origin at the ship hull into the harbour basin (Fig. 5). In contrast to the previously analysed return current, the primary wave shows propagation properties comparable to an ocean wave. Here, the term diffraction as opposed to decay is used in connection with the primary wave. Damping of the primary wave in the harbour basin is compared to the damping of the drawdown. The comparison of drawdown and primary wave diffraction is strongly dependent on the role of the stern wave, as summed up in Table 2. At slow ship speeds and especially for wide channel geometries, the stern wave is fully damped before reaching the harbour entrance. At medium ship speeds, the stern wave accounts only for a small fraction of

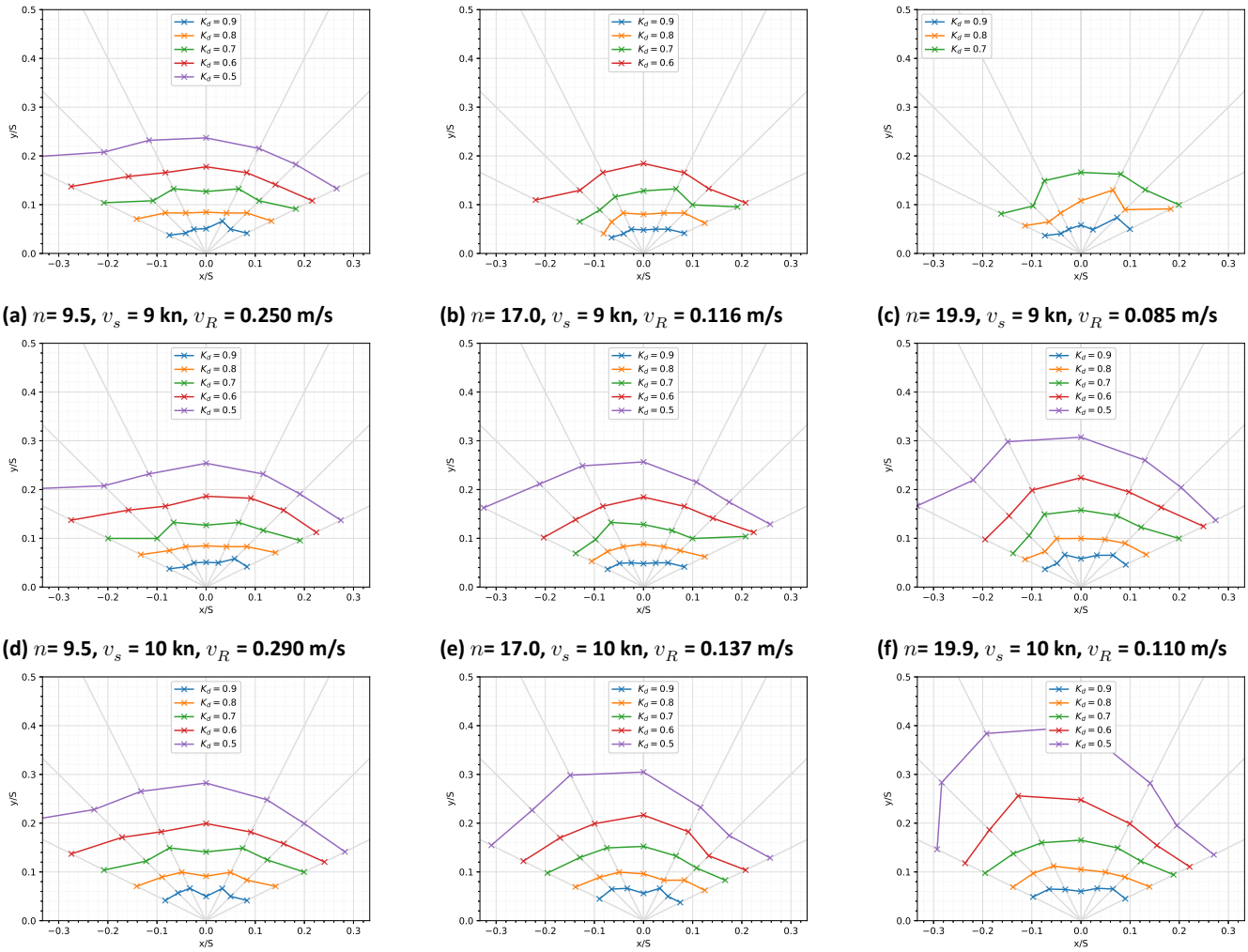

(a) n**= 9.5,** v_s **= 9 kn,** v_R **= 0.250 m/s** **(b)** n**= 17.0,** v_s **= 9 kn,** v_R **= 0.116 m/s** **(c)** n**= 19.9,** v_s **= 9 kn,** v_R **= 0.085 m/s**

(d) n**= 9.5,** v_s **= 10 kn,** v_R **= 0.290 m/s** **(e)** n**= 17.0,** v_s **= 10 kn,** v_R **= 0.137 m/s** **(f)** n**= 19.9,** v_s **= 10 kn,** v_R **= 0.110 m/s**

(g) n**= 9.5,** v_s **= 12 kn,** v_R **= 0.406 m/s** **(h)** n**= 17.0,** v_s **= 12 kn,** v_R **= 0.205 m/s** **(i)** n**= 19.9,** v_s **= 12 kn,** v_R **= 0.160 m/s**

Figure 4: Decay of the return current as it enters the harbour basin at y = 0. The gap in the harbour wall extends from $x = -0.5$ **to** $x = +0.5$**. The damping coefficient** K_d **represents the ratio between the decayed and the initial return current.**

the primary wave height at the harbour entrance. At higher ship speeds, the significance of the stern wave for the height of the primary wave at the harbour entrance increases.

It was found that damping of the primary wave occurred less strongly than damping of the drawdown alone (Fig. 6). This may be explained by the increased water depth in the primary wave case, which includes the stern wave crest. As a result, the influence of the primary wave reaches further into the harbour basin than the influence of the drawdown. In cases of medium ship speeds, the shape of the diffraction diagram of the primary wave resembles that of the diagram of the drawdown, while damping of the primary wave occurs less strongly than damping of the drawdown alone (upper and middle row in Fig. 6). For high ship speeds, both the drawdown and the primary wave propagate asymmetrically into the harbour basin.

In addition to the ship speed, the width of the channel plays a role for the damping behaviour of the primary wave. As the channel width increases (from left to right in Fig. 6), the absolute values reduce, but the primary wave propagates further into the basin, in agreement with the observations for the drawdown. In the cases of v_s = 12 kn that correspond to asymmetric diagrams, the primary wave propagates further in the rear direction of the ship than the drawdown. As a result, a larger region of the basin becomes affected by the induced wave motion. To conclude, the influence of the primary wave on the water body in the harbour is not necessarily restricted to the same region as the influence of the drawdown alone.

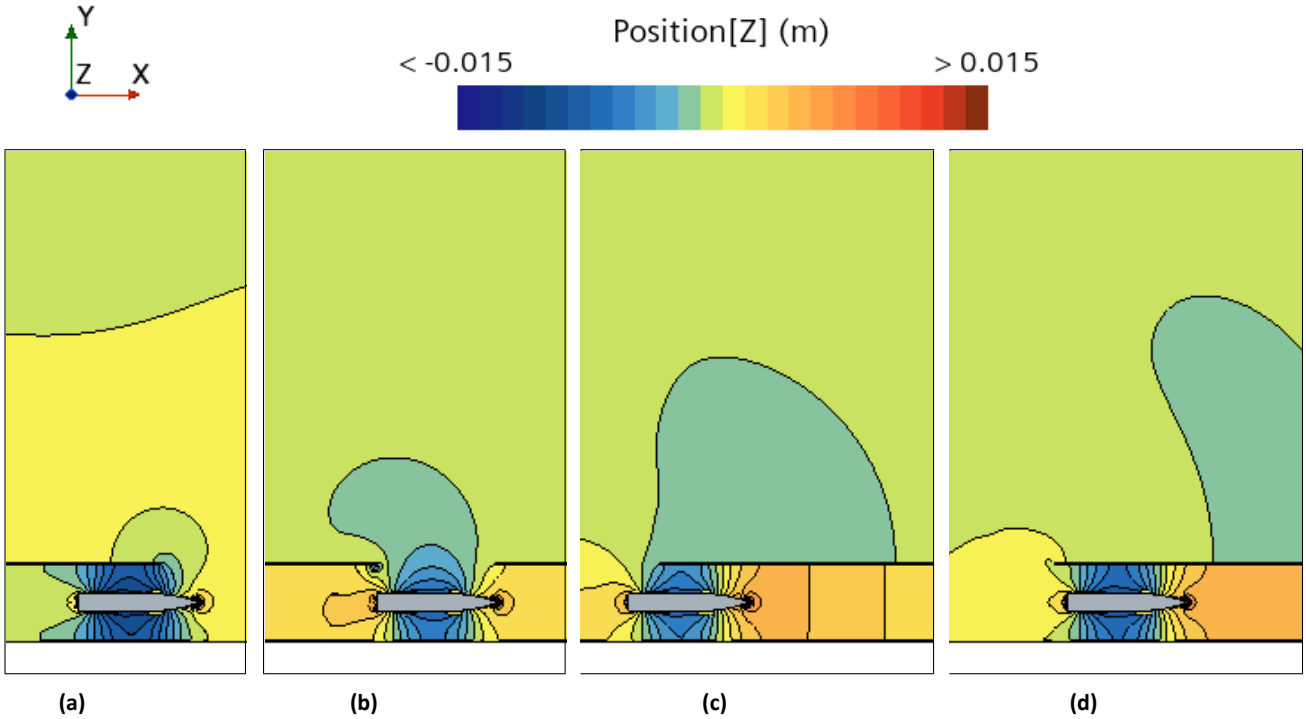

Figure 5: **Top view of the numerical model, showing the elevation of the water surface in model scale as (a) the ship approaches the gap; (b) the drawdown enters the harbour basin; (c) the ship has passed the gap and (d) the stern wave enters the harbour basin.**

Table 2: **Significance of the stern wave in the primary wave system, and resulting influence on the characteristics of the diffraction diagram.**

Ship speed	Role of stern wave	Influence on diagram
5 kn	None	Use damping diagram for drawdown only
9 kn - 10 kn	Minor	Slower damping than drawdown
12 kn	Major	Shape of diagram changes

4 DISCUSSION

The numerical setup, in which the vessel PPM52 with different draughts passed a harbour entrance connected to a channel at different velocities, has shown that ship-induced loads do not only influence the water in the direct vicinity of the ship. While the return current was strictly bound to the ship and its influence did not reach far beyond the area of the harbour entrance, the primary wave propagated into the basin and distributed wave energy also into the geometrical shadows. The present analysis showed that the influence of the primary wave reached beyond the influence of the drawdown. In agreement with findings of Heijboer (2024), it is advisable to pass harbour entrances at low speed and with an adequate distance. This will reduce the return current, possibly even lead to a full decay of the return current before it has reached the harbour entrance. Moreover, both a reduction in speed and an increased distance to the wall will reduce the initial height of the primary wave that propagates into the basin. Although in a relative consideration, damping of a smaller primary wave occurs slower than damping of a larger primary wave, this refers to the initial value of the wave. For the wave climate in the harbour basin, a small initial primary wave is preferable. The developed diffraction diagrams are informative on the region that should be expected to be influenced by a primary ship wave before it is damped in the harbour basin. The information can be considered when designing harbour dimensions, with the aim of minimising wave action. It is also valuable when planning activities in a harbour basin in which primary ship waves play a significant role.
The damping behaviour of a primary ship wave differed from the damping of an ocean wave, although the primary ship wave includes a wave crest. According to Goda (2000), a random ocean wave entering a harbour at a perpendicular angle has decayed to 70% (60%, *50%*) of its initial value at approximately 0.95 (1.35, *2.1*) times the width of the harbour entrance. In principle, these values compare well with the primary wave damping at 90° for a setup with a ship speed of 10 kn and an n

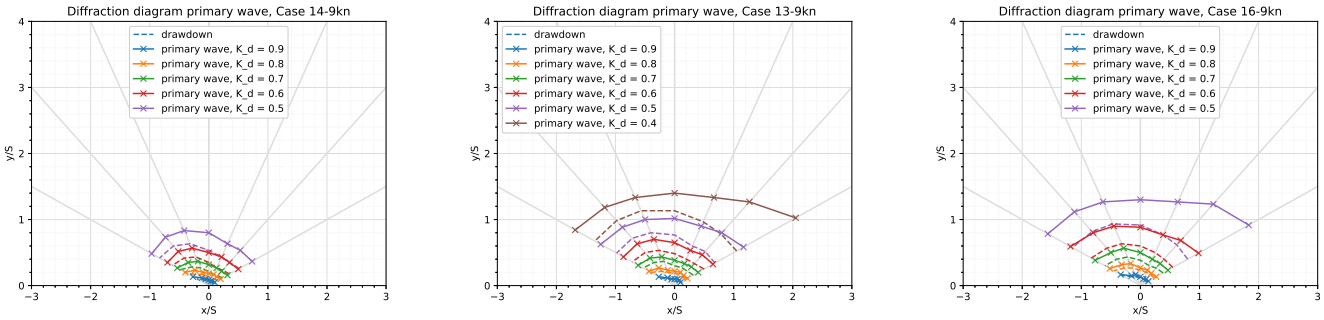

(a) n= 9.5 , v_s = 9 kn, H_p = 12.9 cm **(b)** n= 17.0 , v_s = 9 kn, H_p = 7.1 cm **(c)** n= 19.9 , v_s = 9 kn, H_p = 5.3 cm

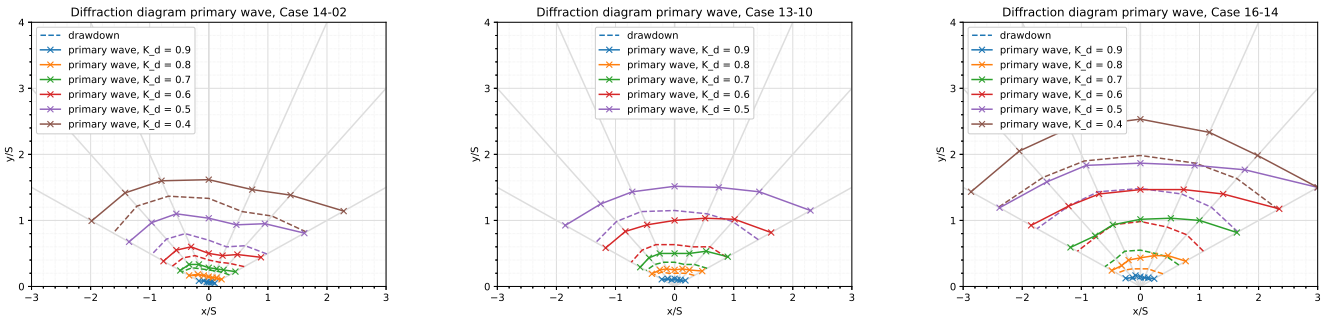

(d) n= 9.5 , v_s = 10 kn, H_p = 17.4 cm **(e)** n= 17.0 , v_s = 10 kn, H_p = 9.1 cm **(f)** n= 19.9 , v_s = 10 kn, H_p = 7.2 cm

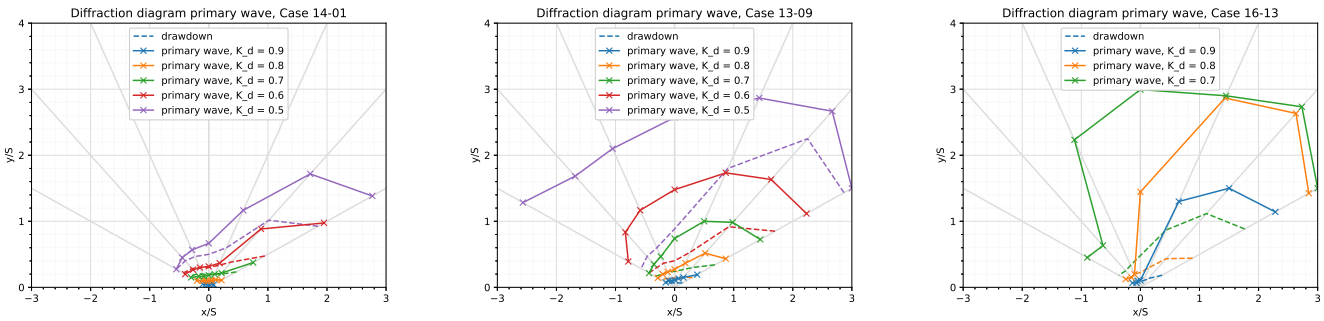

(g) n= 9.5 , v_s = 12 kn, H_p = 22.4 cm **(h)** n= 17.0 , v_s = 12 kn, H_p = 16.2 cm **(i)** n= 19.9 , v_s = 12 kn, H_p = 8.4 cm

Figure 6: Diffraction diagrams of ship-generated wave that entered the harbour basin at y = 0. Solid lines represent the full primary wave, while dashed lines show diffraction of the isolated drawdown. The absolute values of the primary wave height refer to full scale.

ratio of approximately 20 (Fig. 6f). However, in Goda (2000)'s diagrams the lines of equal K_d are more attached to the wall ends at the harbour entrance, while the K_d lines of primary ship waves in the present case reach further into the region of the geometrical shadow. For lower n ratios than 20 , the primary wave was damped earlier than ocean waves. At the highest considered ship speed of 12 kn, the diffraction diagrams of the primary ship wave became asymmetric and were no longer comparable to the diffraction diagrams of ocean waves.

The presented results are restricted to the investigated cases and parameter ranges. They serve as indicators of the damping behaviour of primary waves in a harbour basin than can be used as a basis for the investigation of basins with different dimensions, other ship types and circumstances. In the present study, only one basin geometry was considered. The results should however be expected to differ for harbour basins of different shapes, as observed in the physical model tests of Kunz (1977). Some of the results of that study are summarised in the following. For example, the author found wave loads to be less severe in larger basins. In addition, the study identified larger wave heights in square-shaped than in rectangular basins. These differences increased with increasing ship speeds. The author pointed out that in a coextensive elongated basin, reflections at the harbour walls can play a significant role for the resulting wave height in the basin. Finally, the study identified the width of the harbour entrance to be an essential parameter for the wave heights in the basin. This confirms results by Johnson (1951), who pointed out that the wider the gap, the longer it takes for the waves to be damped. A change in gap width, in order to observe this effect for the damping of primary ship waves, exceeds the scope of the present study.

In the present study, a simplified geometry was assumed, which included e.g. the assumption of a flat bottom. A possible influence of a natural bathymetry, as described by Johnson (1951), was not considered. Neither were shallow-water effects,

which are expected to play a major role in the damping of primary ship waves, as the propagation speed of shallow-water waves is different from that of deep-water or intermediate-water waves.
The presented results revealed an influence of the ship speed and channel width on damping and diffraction of the primary wave. An effect of the draught could not be observed, although an increased draught yields a larger displacement, which is expected to result in higher ship-induced loads. A reason for the negligible influence of the draught is its small range of variation among the experimental cases, as opposed to the ranges of ship speed and n ratio. However, a stronger variation of the draught, which could shed light on its influence, would result in unrealistic values and is therefore out of scope.

5 CONCLUSIONS

The passage of a vessel by a harbour entrance influences harbour hydrodynamics. The return current of the passing vessel affects the flow behaviour of the water in the region of the entrance. The spatial extent of this influence was comparable in each numerical experiment with ship type PPM52, even with varying ship speed, draught and channel width. The primary wave, consisting of a drawdown of the water surface and a subsequent stern wave, propagates into the harbour basin. In contrast to the return current, the influence of the primary wave reaches far beyond the harbour entrance and into the geometrical shadows, distributing wave energy in the harbour basin. Due to the relevance of the stern wave, the influence of the primary wave reaches further into the harbour basin than the influence of the drawdown alone. The channel width and especially the speed of the passing ship influence the propagation direction of the primary ship wave and its damping strength in the harbour basin. To avoid a strong increase of wave energy and disturbances of the water surface in the harbour, it is recommended to pass harbour entrances slowly and with an appropriate distance, in agreement with common standards.

6 ACKNOWLEDGEMENTS

The results of this study were derived in the scope of the research project “Investigation of the effective range of ship waves in shallow water” (Wish-F), funded by the German Federal Waterways Engineering and Research Institute (BAW) with grant number B3955.01.04.70385.

7 REFERENCES

Bernoulli, D., (1738). Hydrodynamica, sive de viribus et motibus fluidorum commentarii [in Latin, source ETH-Bibliothek Zürich, Rar 5503]. Sumptibus Johannis Reinholdi Dulseckeri. https://doi.org/10.3931/e-rara-3911

Bhowmik, N., Demissie, M., & Osakada, S., (1981). Waves and drawdown generated by river traffic on the Illinois and Mississippi rivers (tech. rep. No. SWS Contract Report 271). University of Illinois, State Water Survey Division.

Bundesanstalt für Wasserbau, (2023). Integration der dreidimensionalen Wasserstraße in die Berechnung der Schiffshydrodynamik im Flachwasser (Integra3D-SHD-F) (BAW-FuE-Abschlussbericht, B3955.01.04.70379) (tech. rep.). Bundesanstalt für Wasserbau.

Constantine, T., (1960). On the movement of ships in restricted waterways. Journal of Fluid Mechanics, *9*(2), 247–256. https://doi.org/10.1017/S0022112060001080

Courant, R., Friedrichs, K., & Lewy, H., (1928). Mathematische Annalen. Verlag von Julius Springer.

Duró, G., Crosato, A., Kleinhans, M. G., Roelvink, D., & Uijttewaal, W. S. J., (2020). Bank erosion processes in regulated navigable rivers. Journal of Geophysical Research: Earth Surface, *125*(e2019JF005441). https://doi.org/https://doi.org/10.1029/2019JF005441

Ferziger, J. H., & Perić, M., (2002). Computational methods for fluid dynamics (3rd ed.). Springer.

Flügge, G., & Uliczka, K., (1996). Schiffsbedingte Wellen unter den spezifischen Randbedingungen von Seewasserstraßen (tech. rep. No. 9) (Wellen. Dresdner Wasserbauliche Mitteilungen). Technische Universität Dresden, Institut für Wasserbau und technische Hydromechanik. Dresden.

Gabel, F., Lorenz, S., & Stoll, S., (2017). Effects of ship-induced waves on aquatic ecosystems. Science of The Total Environment, *601-602*, 926–939. https://doi.org/https://doi.org/10.1016/j.scitotenv.2017.05.206

Goda, Y., (2000). Random seas and design of maritime structures (Vol. 15). WORLD SCIENTIFIC.

Heijboer, D., (2024, February). The effects of passing seagoing vessels on the inland ships in the outer harbour and locks of Hansweert [Master’s thesis, Delft University of Technology].

Hirt, C., & Nichols, B., (1981). Volume of fluid (VOF) method for the dynamics of free boundaries. Journal of Computational Physics, *39*(1), 201–225. https://doi.org/https://doi.org/10.1016/0021-9991(81)90145-5

Johnson, J., (1951). Generalized wave diffraction diagrams. Coastal Engineering Proceedings, *1*, 6–23. https://doi.org/10.9753/icce.v2.2

Kochanowski, C. A., & Kastens, M., (2022, May). Simulation and validation of ship induced waves in shallow and confined water. In C. Maxim, E. Lataire, Z. Yuan, K. Eloot, & G. Delefortrie (Eds.), Proceedings of the 6th mashcon international conference on ship manoeuvring in shallow and confined water, with special focus on port manoeuvres (pp. 89–101, Vol. 6).

Kunz, H., (1977). Schiffsschwall und Sunk in seitlich einer Wasserstraße angeordneten Becken (tech. rep.). Wasserwirtschaft-samt Brake.

Melling, G., Jansch, H., Kondziella, B., Uliczka, K., & Gätje, B., (2021). Evaluation of optimised groyne designs in response to long-period ship wave loads at juelssand in the lower elbe estuary (and Kuratorium für Forschung im Küsteningenieurwesen (KFKI), Ed.). Die Küste, *89*, 29–56.

Menter, F. R., (1994). Two-equation eddy-viscosity turbulence models for engineering applications. AIAA Journal, *32*, 1598–1605.

Muzaferija, S., Perić, M., Sames, P., & Schellin, T., (1998). A two-fluid Navier- Stokes solver to simulate water entry. Proc. Twenty-Second Symposium on Naval Hydrodynamics.

O'Sullivan, E. J., (1992). Wave Reflection Effects Within a Harbour [Master thesis]. The University of British Columbia.

Parnell, K. E., Soomere, T., Zaggia, L., Rodin, A., Lorenzetti, G., Rapaglia, J., & Scarpa, G. M., (2015). Ship-induced solitary Riemann waves of depression in Venice Lagoon. Physics Letters A, *379*(6), 555–559. https://doi.org/https://doi.org/10.1016/j.physleta.2014.12.004

Peric, R., (2019, June). Minimizing undesired wave reflection at the domain boundaries in flow simulations with forcing zones [PhD thesis]. Technischen Universität Hamburg.

Scarpa, G., Zaggia, L., & Manfè, G. e. a., (2019). The effects of ship wakes in the Venice Lagoon and implications for the sustainability of shipping in coastal waters. Sci Rep, *9*, 19014.

Siemens Digital Industries Software, (2024). Simcenter STAR-CCM+, version 2402.

UNCTAD, (2024). Review of maritime transport (tech. rep. No. 978-92-1-003206-3). United Nations Conference on Trade and Development. Geneva.

Volkov, E., (1970). The method of composite meshes for finite and infinite regions with piecewise smooth boundary. Proc. Steklov Inst. Math. *96*, 145–185.

8 AUTHORS BIOGRAPHY

Ina Teutsch is working at Federal Waterways Engineering and Research Institute in Hamburg since 2023. She is responsible for CFD simulations in the field of interaction between ship and waterway focusing on ship-induced loads. Her previous experience includes the analysis of ocean waves.

Marko Kastens is a Senior Research Fellow at Federal Waterways Engineering and Research Institute in Hamburg since 2003. He is responsible for consulting the authorities as well as for scientific research in the area of interaction between ship and waterway.

SHIP-GENERATED WAVES IN CONFINED WATERWAYS: LABORATORY AND NUMERICAL STUDY OF FLOW FEATURES NEAR SLOPING BANKS WITH DIFFERENT ANGLES

Pablo Nieutin, Institut Pprime, CNRS - Université de Poitiers - ISAE-ENSMA, HYDÉE team, France
Clément Maubant, Institut Pprime, CNRS - Université de Poitiers - ISAE-ENSMA, HYDÉE team, France
Gérard Pineau, Institut Pprime, CNRS - Université de Poitiers - ISAE-ENSMA, HYDÉE team, France
Damien Calluaud, Institut Pprime, CNRS - Université de Poitiers - ISAE-ENSMA, HYDÉE team, France

SHIP-GENERATED WAVES IN CONFINED WATERWAYS: LABORATORY AND NUMERICAL STUDY OF FLOW FEATURES NEAR SLOPING BANKS WITH DIFFERENT ANGLES

PABLO NIEUTIN, INSTITUT PPRIME, CNRS - UNIVERSITÉ DE POITIERS - ISAE-ENSMA, HYDÉE TEAM, FRANCE
CLÉMENT MAUBANT, INSTITUT PPRIME, CNRS - UNIVERSITÉ DE POITIERS - ISAE-ENSMA, HYDÉE TEAM, FRANCE
GÉRARD PINEAU, INSTITUT PPRIME, CNRS - UNIVERSITÉ DE POITIERS - ISAE-ENSMA, HYDÉE TEAM, FRANCE
DAMIEN CALLUAUD, INSTITUT PPRIME, CNRS - UNIVERSITÉ DE POITIERS - ISAE-ENSMA, HYDÉE TEAM, FRANCE

SUMMARY

This study investigates ship-generated waves in confined waterways, focusing on flow features near sloping banks with vary-ing angles. Laboratory experiments were conducted using a towing tank, complemented by numerical simulations utilizing the Star-CCM+ software. A Wigley hull model served as the reference vessel, tested under different channel widths and bank inclinations. Stereo-PIV (Stereoscopic Particle Image Velocimetry) and stereo-refraction techniques were employed to mea-sure velocity fields and free-surface elevations. The k–ω SST URANS model is used for turbulence modeling. Results highlight the influence of bank geometry on fluid velocities, emphasizing the impact of inclined banks on flow patterns, return currents, and wave systems. These findings provide valuable insights into the hydrodynamic effects of inland waterway navigation on riverbanks.

NOMENCLATURE

CFD	Computational Fluid Dynamics
CFL	Convective Courant-Friedrichs-Lewy Number
DTC	Duisburg Test Case
GCI	Grid Convergence Index
pHE	plateforme Hydrodynamique Environnementale
Stereo-PIV	Stereoscopic Particle Image Velocimetry
VOF	Volume of fluid
WL	Waterline

B	Beam	m
C_B	Block coefficient	-
h	Water depth	m
L_{WL}	Ship length on waterline	m
R_k	Convergence ratio	-
S	Blockage coefficient	-
S_W	Wetted area	m^2
T	Draft	m
V	Ship speed	m/s
w	Width	m
∇	Displacement	m^3
α	Riverbank angle	°

1 INTRODUCTION

The increase in river traffic, whether in terms of frequency, speed or size of vessel, inevitably increases the deterioration of riverbanks. The primary waves generated by ships, depending on their speed and water level, cause a drawdown, that leads to the resuspension of sediments from the riverbed and organic riverbank. As the size of ships increase, their ship confinement now induces more intense return currents.

Trials can be conducted with ships at full scale, or more commonly at Froude scale, while maintaining the same Froude number. This second solution is generally required due to the limited size of test tanks and available computational capacities.

However, other phenomena are then underestimated, such as the importance of advection, as it is not possible to simultaneously maintain a constant Froude number and a constant Reynolds number. Correction methods exist, such as the application of turbulence generators on ship models and adjustments to the measured forces (Terziev, Tezdogan, and Incecik 2022).

Physical methods are historically the main method to evaluate ships characteristics, especially hull resistance and maneuverability. The principles come from Froude's research who build the first towing tank in Torquay. It is common to measure the forces and the wake generated, but it is generally difficult to obtain velocity measurements without disturbing the flow. However, some towing tanks as the one used for these tests are specifically optimized for non-invasive optical measurements, allowing for a very detailed understanding of the velocity fields throughout the entire channel.

Numerical simulations in fluid mechanics help to complement towing tank tests. Indeed, the limited availability of test facilities limit their use and test facilities are now used in conjunction with numerical simulations. Furthermore, simulations provide access to normally inaccessible measurements and allow for real-scale simulations.

As the flow around a ship is predominantly turbulent, a turbulence model is need for simulations. The movement of the vessel across the free surface generates waves, and the kinetic energy of these waves is dissipated into the small-scale structures of turbulence. However, it is not physically possible to fully resolve turbulence at these small scales due to computational cost. Therefore, RANS models are used to replicate the results as accurately as possible.

For this study, a Wigley hull is used with a rectangular section and the factor n taken equal to 8, hereinafter referred to as CWn8. This is an analytical hull used as a model to inland navigation vessels. However, it remains far from the shape of a real ship and is employed for researches. The main interest of Wigley hulls is the analytical description of their shape which has been studied extensively historically. It is used in particular for ship hull forms optimization (Percival, Hendrix, and Noblesse 2001), but has also been used to study bank effects and ship interactions like during MASHCON conferences, see (Delefortrie et al. 2016; Eloot et al. 2022).

The DTC (Duisburg Test Case) container ship is one of the hulls commonly used for shallow water simulations, after the 2013 workshop on squat simulations (PreSquat) produced numerical and experimental data. Tezdogan, Incecik, and Turan (2016) used the DTC with Star-CCM+ to perform a RANS simulation, with the $k-\epsilon$ model. An asymmetric canal was studied with several drafts, and showed that the ship resistance was very sensitive to the ship draft.

Terziev, Tezdogan, Oguz, et al. (2018) used Star-CCM+ RANS solver to study ship performances and wave system in dredged canals with submerged vertical banks. A good correlation was found with a Slender-Body theory a low speed. The topography of riverbanks had a huge impact on the ship resistance, especially the height between navigation channel and the undredged river.

In this paper, the viewpoint of the riverbanks is taken. The primary and secondary wave systems are therefore preferentially studied. Influences of the angle of riverbank on the wave pattern and the velocity of the flow are emphasised.

2 SHIP HULL AND CHANNEL GEOMETRY

2.1 VESSEL GEOMETRY

The ship was a Wigley CWn8, a rectangular and symmetrical hull with a 0.9 C_B block coefficient (Figure 1). It is close to the typical Freycinet hull shape and other inland ships, and is widely used for simulations. Indeed, inland ships are designed to maximize the dimensions allowed by the gauge limits. The symmetry of the hull makes trials easier by eliminating the need to flip the hull. This Wigley shape is described by the Equation 1, the name CWn8 stands for carene Wigley $n = 8$ in the equation. The shape is cylindrical with a lenticular base.

Moreover, the hull is already available and has been intensively studied in the laboratory (Nieutin et al. 2024; Caplier et al. 2019). Studies with similar shapes have been conducted, including other Wigley hulls such as the CWn2 and taylor series 60. The main dimensions are given in Table 1. Here the section is rectangular ($S_e(z,T) = 1$).

$$\begin{cases} y(x,z) &= S(z,T)\frac{B}{2}\left[1-\left(\frac{2x}{L_{WL}}\right)^n\right] \\ S_e(z,T) &= 1 \end{cases} \tag{1}$$

Other ship models, such as the Duisburg Test Case or the KRISO Container Ship, are often used, but they have an intermediate block coefficient (around 0.65) that is more akin to a river-sea vessel. In this study, the choice was made to get as close as possible to the reals block coefficient in the highly confined configurations studied. This block coefficient apply to all types of existing cargo vessels, whether large ships or barges (CEMT classification).

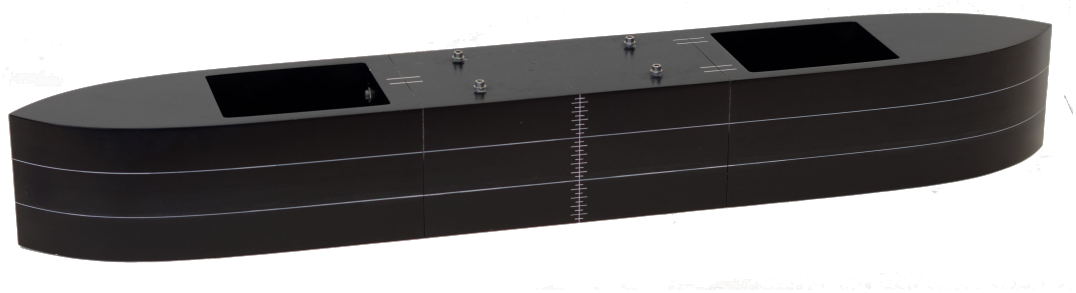

Figure 1: Wigley hull used for towing tank trials

Table 1: Wigley CWn8 main particulars

Property	Unit	Symbol	Value
Length at waterline	m	L_{WL}	1.2
Beam at waterline	m	B	0.18
Draught	m	T	0.075
Displacement	m^3	∇	
Block coefficient	-	C_B	0.889
Wetted surface	m^2	S_W	0.372

2.2 CHANNEL GEOMETRY

To validate the simulation configuration, experimental tests were carried out by varying the velocity, the channel width, and the draft of the hull. A campaign was specifically conducted by Caplier (2015), which allowed for the initial calibration of the simulation. Further testing campaigns were carried out thereafter with more laterally confined configurations conducted by Nieutin (2024). At that time, the riverbank angles were fixed at 90° in the channel, so the simulation was validated with vertical riverbanks and extended to this configuration.

The two configurations are thus represented in Figure 2, with the height h fixed at 10 cm and the angle fixed at $15\,°$. A real river is closer to the inclined, so-called trapezoidal configuration, with the angle varying depending on the nature of the substrate and is typically around 25° for non-cohesive material (see Thorne and Tovey (1981)).

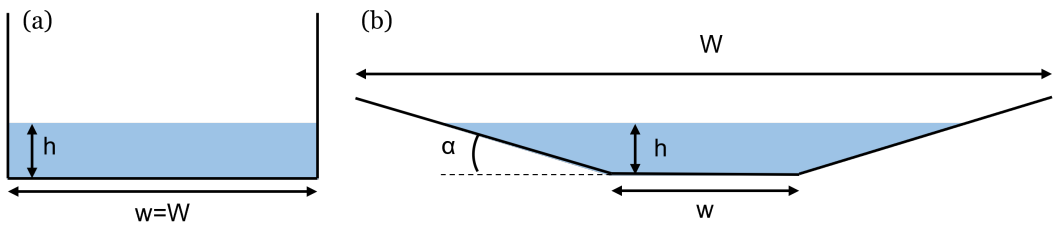

Figure 2: Channel geometry used, vertical riverbanks (a) and inclined riverbanks (b)

The configurations used for this paper were shown in Table 2, where only the configurations compared in this study were considered. Although for the vertical shores, the complete datasets velocities were between 0.2 m/s and 1.6 m/s, draft was between 5.5 cm and 8.5 cm.

Table 2: Trials used to validate the simulation

w (m)	V (m/s)	T (cm)	α (°)	S	h (m)	Origin of the data
1	0.6	7.5	90	0.135	0.10	Numerical / Experimental
0.5	0.6	7.5	90	0.270	0.10	Numerical / Experimental
0.5	0.6	7.5	15	0.155	0.10	Numerical

The blockage coefficient S was defined in Equation (2), were A_c is the transverse section of the channel. The blockage coefficient was used to quantify the flow confinement and thus the intensity of the return current. The configuration with an inclined bank corresponds to a blockage coefficient intermediate between the configurations with w =1 m and w =0.5 m, both with α = 90°.

$$S = \frac{A_b}{A_c} = \frac{BT}{A_c} \tag{2}$$

2.3 APPROACHES

The experimental study was carried out in the pHE (plateforme Hydrodynamique Environnementale) towing tank, at the Institute Pprime, Poitiers, France (Figure 3). The channel is 34 m long, 1.5 m wide and the water level can be adjusted up to 80 cm. The width can also be adjusted to 1m and 0.5m. The towing carriage can travel at a maximum speed of 2.5 m/s. This channel is specifically designed with many optical accesses and to study inland waterway navigation.

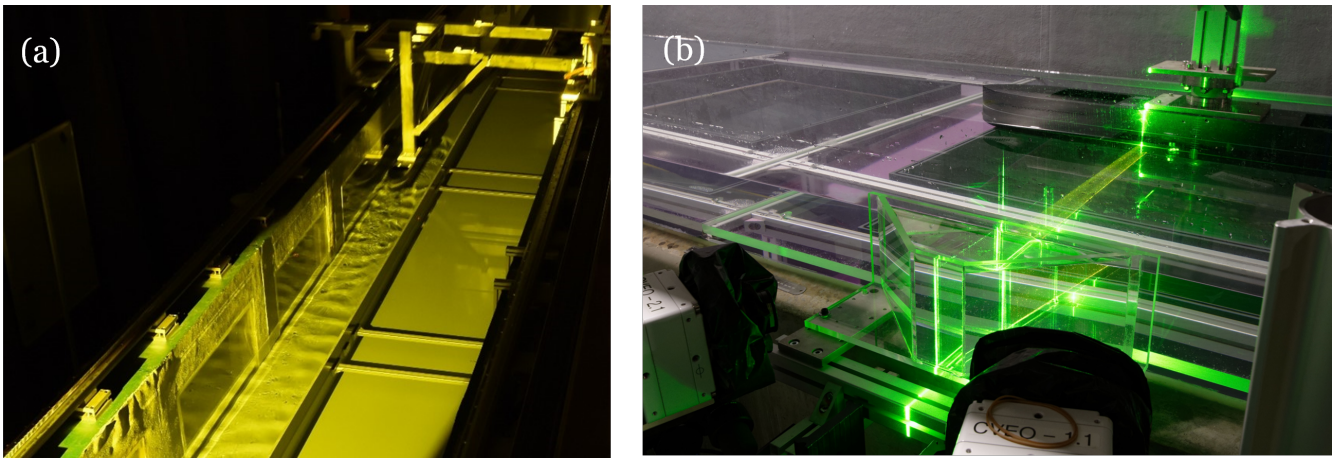

Figure 3: (a) Top view of the channel in the configuration w = 0.5 m **(a), (b) Setup used to perform Stereo-PIV with two high-resolution phantom cameras and a Pulsed Solid-State laser at** 532 nm **(b)**

Stereo-PIV and stereo-refraction technics have been used, to obtain speed vectors and free surface elevation. It provides simultaneous access to the velocity fields and the free surface elevation. The principle of Stereo-PIV is to use a laser sheet to illuminate a set of particles in the same plane and to film them at high speed with two cameras. The calculation of the cross-correlation matrix between the two images provides access to the displacement of each particle (Calluaud and David 2004). The stereo-refraction technic is one of the methods used to reconstruct the free surface by studying the deformation of its patterns. The implementation used for this study was based on patterns created by particles suspended in the fluid and illuminated by a laser sheet (Gomit et al. 2013).

2.4 NUMERICAL MODELLING

The CFD (Computational Fluid Dynamics) simulation was created using classics parameters (Mucha and Moctar 2014; Tezdogan, Incecik, and Turan 2016; Terziev, Tezdogan, Oguz, et al. 2018). The CFD simulations were carried out on the double precision version of Star-CCM+ 17.02.007, which employs a finite volume method. To model the turbulence, a standard $k-\omega$ SST method was used as the results were closer to the reference experimental data, combined with a segregated flow model and a semi-implicit method for pressure linked equations (SIMPLE). The VOF (Volume of fluid) method was used to model the free surface. The boundaries conditions are described in Figure 4, Figure 5 and Figure 6, where a pressure outlet is used in front of the ship to absorb certain waves generated by the stern in highly confined cases (Terziev, Tezdogan, Oguz, et al. 2018).

The adaptive mesher was used, with Star-CCM+ enhanced quality triangles and a prism layer. The base size was 0.16 m, slightly smaller than B. A mesh refinement is applied in the free surface vicinity (Figure 5), with the mesh size fixed vertically at 0.01 m and 0.005 m. An automatic mesh refinement is used of the free surface with a vertical size of 0.0025 m (Figure 6). The resulting consists of 3 million cells.

A convergence study was carried out, on ship resistance force, pressure on the bottom and on the sides. The grid spacing was multiplied by r=2 between coarse, medium and fine mesh configurations. Using the Richardson extrapolation method described in “Procedure for Estimation and Reporting of Uncertainty Due to Discretization in CFD Applications” (2008), the convergence ratio R_k is -0.5 for ship resistance, which indicate an oscillatory convergence. The relative error is e_a^{21} =0.67 % and the fine GCI (Grid Convergence Index) is equal to 0.84< 1 %. This small value ensure negligible numerical discretization error.

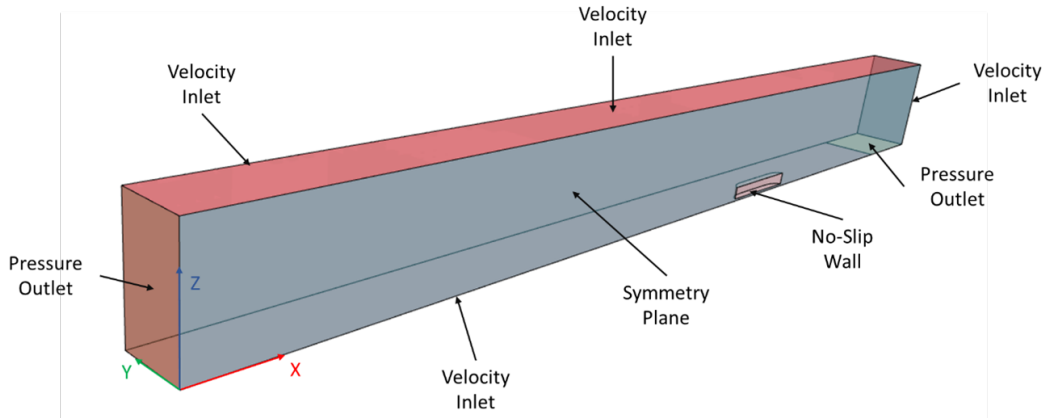

Figure 4: Boundaries conditions, from Nieutin (2024)

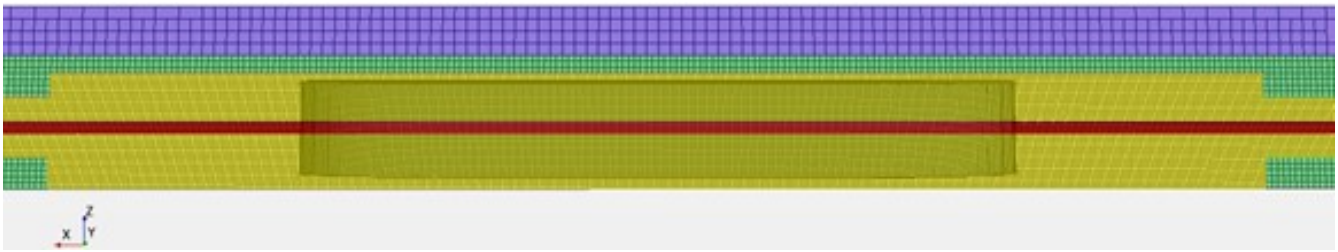

Figure 5: Lateral view of volume mesh refinement. Blue : no refinement, green : refined, yellow : highly refined zone, red : automatic refinement, from Nieutin (2024)

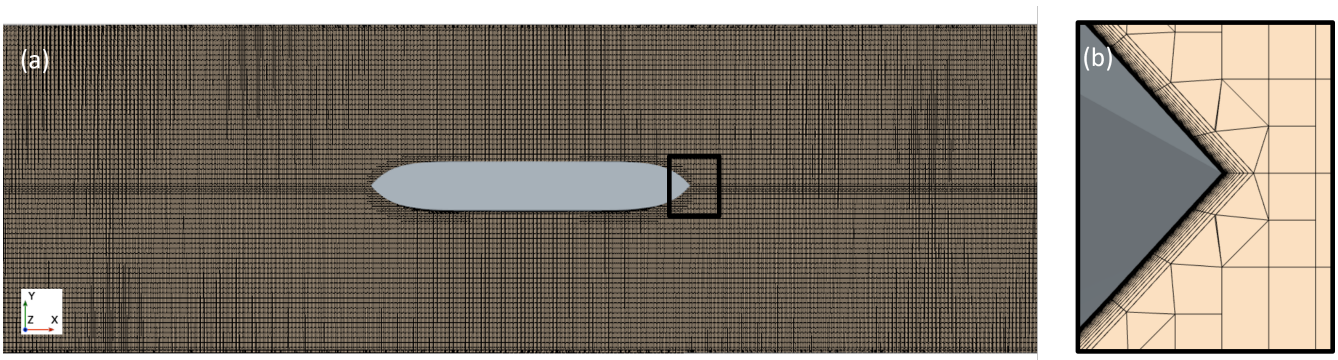

Figure 6: (a) Top view of volume mesh on the free surface, (b) Zoom on the bow

The simulation was run for a total time of 30 s for each configuration. A total of 8 Tflops of computational power is allocated for running the simulation, utilizing 120 cores, with a base time step of 5×10^{-4} s and with the adaptive time-step module to keep the average CFL (Convective Courant-Friedrichs-Lewy Number) at 0.5 (Equation 3). Indeed, depending on the generation, processor type, or clock frequency, the number of cores does not directly correlate with the available computational power[1].

$$CFL = \frac{V_x \Delta t}{\Delta x} \tag{3}$$

2.5 EFD / CFD COMPARISON

In the context of this study, CFD was used to supplement experimental results by reproducing other cases on the same scale. To validate the results, the first configuration in Table 2 was compared ($w = 1$ and $\alpha = 90$).

Figure 7 compared the free surface elevation between a numerical simulation and an experimental test under identical conditions. We could see that the spatial period and the amplitude of the secondary wake are similar, as the wake angle. At the

[1]If we consider the example of two processors from the same generation, an i7 processor provides approximately 50 Gflops per core, whereas a Xeon Gold 6252 processor delivers around 70 Gflops per core and is therefore 30% faster.

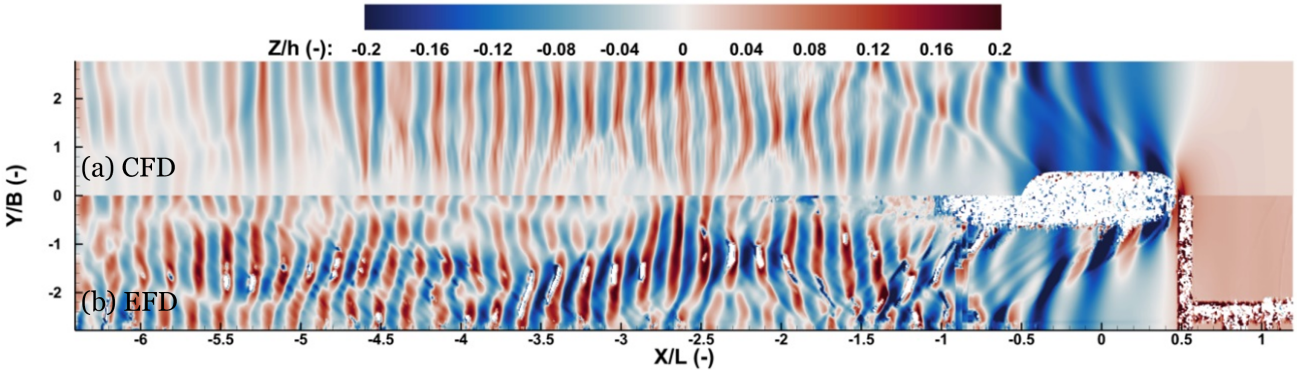

Figure 7: (a) Free surface heights obtained by numerical simulation - (b) Experimental measurements

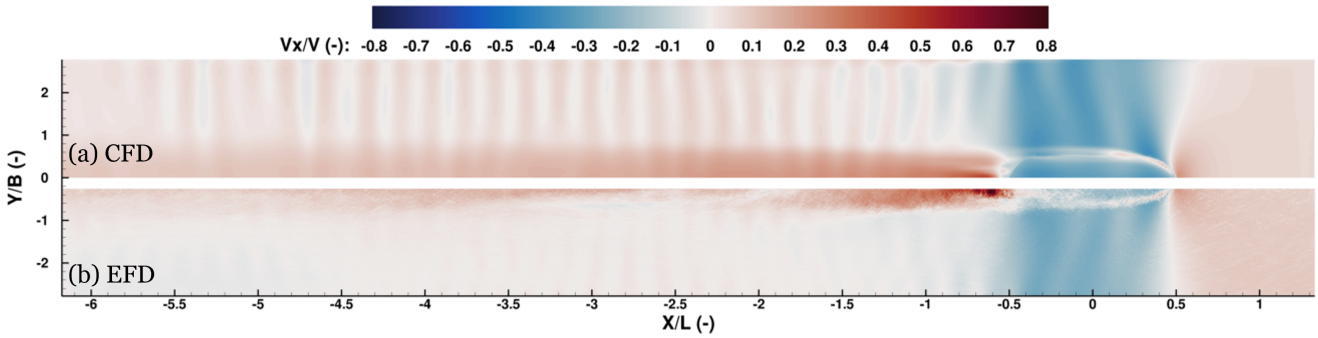

Figure 8: (a) Longitudinal component of speed obtained by numerical simulation - (b) Experimental measurements

contrary, there was some differences : the primary wake was purely below the level at rest in the numerical case, in contrast to the numerical simulations. In addition, the wavefronts remained collinear in the numerical case but became more deformed in the experimental case. One explanation for these differences was the (natural) imperfect geometry of the channel in the real case. Moreover, with CFD, some numerical diffusion is well-known which it tends to attenuate waves amplitude.

The flow velocity is compared in Figure 8, in a plane located 8cm above the waterline. We could see that the waves gradually shifted, because the spatial period was slightly different. The amplitude was also slightly lower in the experimental case, so we could assume that the damping was more intense. The return current is also very close in intensity.

3 RESULTS AND DISCUSSION

The analysis of the influence of the bank shape was achieved thanks to numerical simulations. The angle studied is 15°. The simulated section is shown to scale in Figure 2, with reference to rectangular sections of width w = 0.5 m, 1 m, and 1.5 m. The flat bottom h measures 0.5 m, and the bank has an angle α of 15° to the horizontal. The depth of the water is $h = 10$ cm. The bank rises to a height of 15 cm to prevent overflow in high-speed cases. These cases will be compared to two cases with vertical banks, with widths w = 1 m and w = 0.5 m. Their blockage coefficient (Table 2) is close to that of the inclined case. It should be noted that the free surface is wider in the sloped wall case than in the case with a width of 1 m.

The impact of river navigation on the banks is reflected, among other factors, by the fluid velocities near the walls. Given the predominance of the longitudinal component, this component was addresses in the following analysis. The lengths were made dimensionless using the length L_{WL} and width B of the vessel. Figure 10 and Figure 11 are projections of the longitudinal speed from two planes parallel to the riverbank and the riverbed. The black dashed lines mark the position of the junction between the bottom and the walls, as well as the connection between these two planes.

The results presented are manly numerical data, as the objective is to compare the angle and width of the channel according to Tab. 2 without comparing experimental and numerical data.

3.1 FREE SURFACE EVOLUTION

The free surface is defined by the volume fraction of water variable equal to 0.5. The inclination of the bank primarily results in the creation of a dry zone on the bank, at Y/B = -3 and X/L = -0.5 on field (b) in Figure 9. This is due to the lowering of the

water surface at the stern of the model. The recovery to the initial water height occurs in the form of a wave. Furthermore, it is noteworthy that the water level ahead of the ship (X/L greater than 0.5) increases in cases (b) and (c).

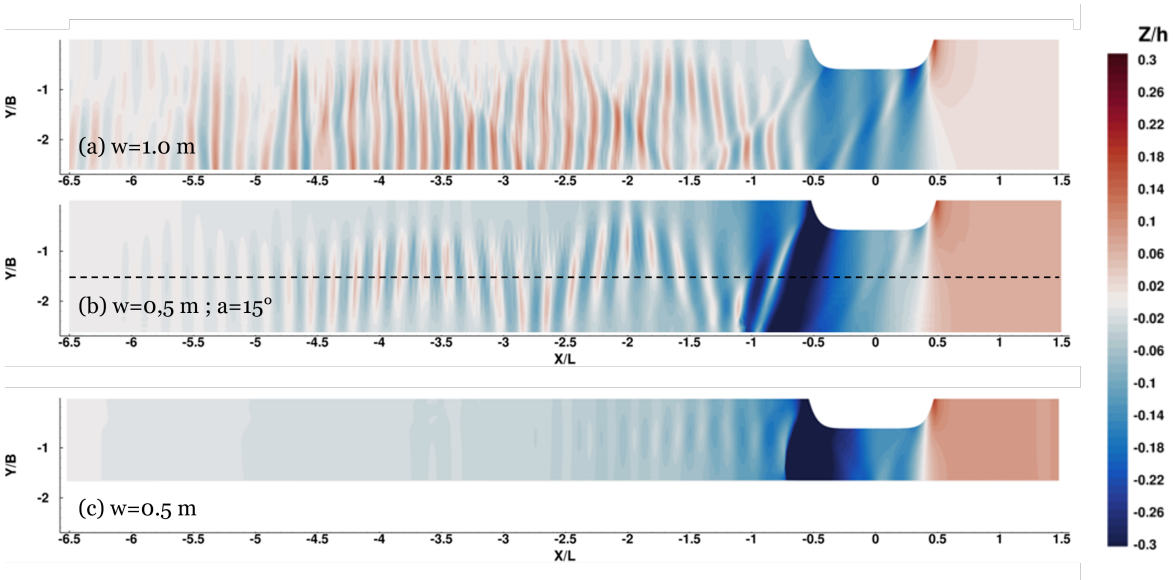

Figure 9: **Free surface elevation with** h = 10 cm, V = 0.6 m/s**.**

3.2 RETURN CURRENT

Figure 10 shows a strong return current visible behind the vessel, with a change in the sign of the velocity. This is the area where the water returns to its original level after the lowering of the level (primary wake). Moreover, a strong velocity gradient is observed at the primary wake along the banks where the zoom is applied, where the speed varies from very positive to very negative value on a short distance, indicating the presence of significant acceleration. The parietal constraint is composed of two components: a viscous component, dependent on the mean velocity gradient at the wall, and a turbulent contribution dependent on velocity fluctuations. In relation with Shields critical velocity (so as function of sediment), the erosion process could be estimated (Shields 1936).

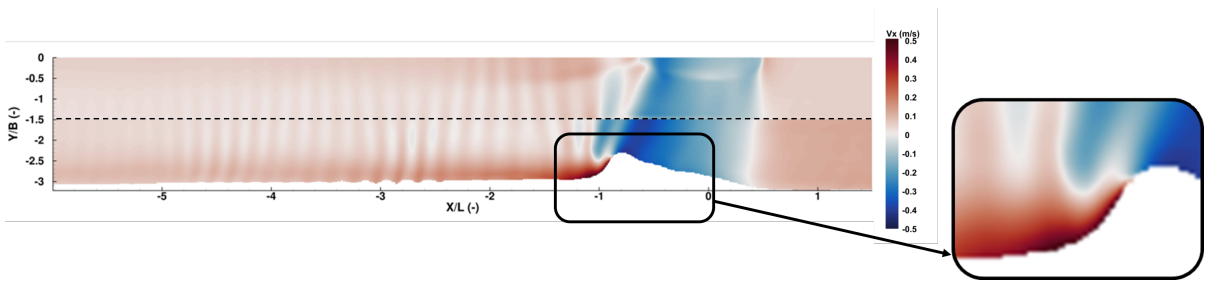

Figure 10: **Longitudinal velocity at the banks with** h = 10 cm**,** w = 0.5 m**,** V = 0.6 m/s **on the horizontal plane located** 2 mm **above the riverbed and the riverbanks.**

Given the constraint, bank erosion is also strongly related to the near-wall velocity in addition to the lowering of the water level. (Hooke 1979) shows that the rate of bank erosion is influenced by low near-bank velocity, among with other parameters such as soil properties. The region along the banks where the zoom was applied follows the ship's longitudinal movement, and thus likely causes a reduction in sediment cohesion at this location. The visible fluctuations in speed will therefore have a major impact on the riverbanks.

Figure 11 shows fluids velocities 4 cm above the riverbed. It compares the flow between the configurations with vertical banks and those with sloped banks of intermediate blockage coefficient.

It can be observed that the return current extends over a greater length in the case of sloped banks. Furthermore, in the vertical bank cases, two zones appear: a main current following the hull and a lateral return current. In the sloped bank case, a second positive current appears along the ship's passage.

There is therefore a significant impact of the bank shape on the current generated by the passage of the hull.

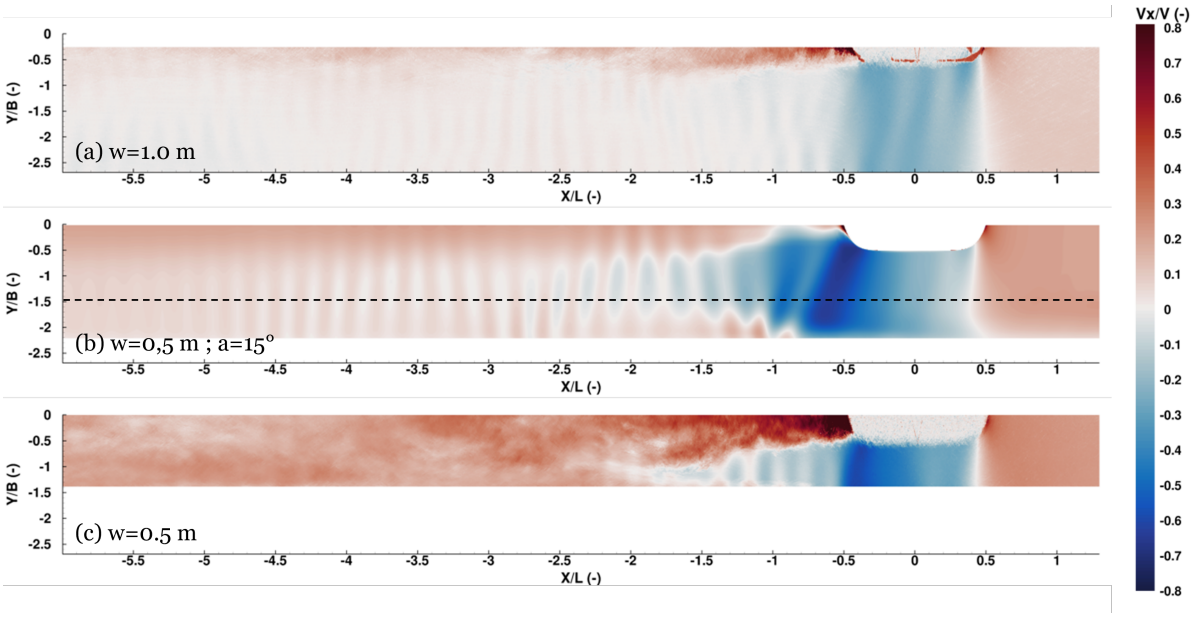

Figure 11: Longitudinal velocities for different configurations on the horizontal plane located 4 cm above the riverbed, V = 0.6 m/s.

4 CONCLUSION

This study highlights the critical influence of bank geometry on the hydrodynamic behavior of ship-generated waves in confined waterways. Inclined banks alter fluid velocity patterns and increase free surface area, leading to significant variations in return flow currents. The integration of experimental and numerical methods has proved to be effective in understanding these interactions.

The slope of the banks has a significant effect on the flow around the towed model. It reduces the wave height near the bank due to the progressive decrease in water depth as the waves approach. The lowering of the water surface at the ship's position creates a dry zone on the sloped bank, followed by a high-velocity wave. These findings underscore the critical role of near-wall velocities in influencing processes such as sediment re-suspension and bank erosion.

Future work should extend this investigation to include additional bank angles and ship speeds, to further improve environmental impact assessments. It is also planned to continue the study of the wake's impact on the banks, particularly on erosion, by evaluating the constraints and forces exerted. This approach, coupled with laboratory experiments and numerical simulations, gives us access to detailed and precise quantities and provides valuable information for managing bank protection against erosion caused by river navigation.

5 ACKNOWLEDGEMENTS

This research was funded in whole or in part by the Agence Nationale de la Recherche (ANR) under project ANR-23-CE51-0032-01 and was supported by the French government program "France 2030" (LABEX INTERACTIFS, reference ANR-11-LABX-0017-01). It was conducted within the INFluE project.

6 REFERENCES

Calluaud, Damien and Laurent David, 2004. Stereoscopic particle image velocimetry measurements of the flow around a surface-mounted block. In: Experiments in Fluids 36.1, pp. 53–61. DOI: 10.1007/s00348-003-0628-7.

Caplier, Clément, 2015. Étude expérimentale des effets de hauteur d'eau finie, de confinement latéral et de courant sur les sillages et la résistance à l'avancement des navires. PhD thesis. Université de Poitiers.

Caplier, Clément, Guillaume Gomit, Germain Rousseaux, Damien Calluaud, Ludovic Chatellier, and Laurent David, 2019. Calibrating and measuring wakes and drag forces of inland vessels in confined water in a towing tank. In: Ocean Engineering 186, p. 106134. DOI: https://doi.org/10.1016/j.oceaneng.2019.106134.

Delefortrie, Guillaume, Katrien Eloot, Evert Lataire, Wim Van Hoydonck, and Marc Vantorre, 2016. Captive model tests based 6 DOF shallow water manoeuvring model. In: 4th MASHCON. Bundesanstalt für Wasserbau, pp. 273–286.

Eloot, Katrien, Guillaume Delefortrie, Wim Van Hoydonck, and José Villagómez, 2022. Wigley hull shallow water manoeuvring and ship to ship interaction. In: 6th Mashcon International conference on ship manoeuvring in shallow and confined water with special focus on port manoeuvres. Knowledge Centre for Manoeuvring in Shallow and Confined Water, pp. 34–48.

Gomit, Guillaume, Ludovic Chatellier, Damien Calluaud, and Laurent David, 2013. Free surface measurement by stereo-refraction. en. In: Experiments in Fluids 54.6, p. 1540. DOI: 10.1007/s00348-013-1540-4.

Hooke, Janet M., 1979. An analysis of the processes of river bank erosion. In: Journal of Hydrology 42.1, pp. 39–62. DOI: 10.1016/0022-1694(79)90005-2.

Mucha, Philipp and Ould el Moctar, 2014. Numerical prediction of resistance and squat for a containership in shallow water. In: Proceedings of the 17th Numerical Towing Tank Symposium. Marstrand Sweden.

Nieutin, Pablo, 2024. Experimental and Numerical Study of Hydrodynamic Phenomena Related to Ship Passage in a Confined Waterway: Quantification of Wake Waves and Their Impact on the Shores. fr. PhD thesis. Université de Poitiers.

Nieutin, Pablo, Damien Calluaud, Malick Ba, and Gérard Pineau, 2024. Towing Tank Stereo-PIV Measurements of the Evolution in Fluid Velocity from Bank to Ship in a Confined Waterway Configuration. en. In: OnePetro.

Percival, Scott, Dane Hendrix, and Francis Noblesse, 2001. Hydrodynamic optimization of ship hull forms. In: Applied Ocean Research 23.6, pp. 337–355. DOI: https://doi.org/10.1016/S0141-1187(02)00002-0.

Procedure for Estimation and Reporting of Uncertainty Due to Discretization in CFD Applications 2008. In: Journal of Fluids Engineering 130.078001. DOI: 10.1115/1.2960953.

Shields, Albert, 1936. Application of similarity principles and turbulence research to bed-load movement. en. PhD thesis.

Terziev, Momchil, Tahsin Tezdogan, and Atilla Incecik, 2022. Scale effects and full-scale ship hydrodynamics: A review. In: Ocean Engineering 245, p. 110496. DOI: 10.1016/j.oceaneng.2021.110496.

Terziev, Momchil, Tahsin Tezdogan, Elif Oguz, Tim Gourlay, Yigit Kemal Demirel, and Atilla Incecik, 2018. Numerical investigation of the behaviour and performance of ships advancing through restricted shallow waters. en. In: Journal of Fluids and Structures 76, pp. 185–215. DOI: 10.1016/j.jfluidstructs.2017.10.003.

Tezdogan, Tahsin, Atilla Incecik, and Osman Turan, 2016. A numerical investigation of the squat and resistance of ships advancing through a canal using CFD. en. In: Journal of Marine Science and Technology 21.1, pp. 86–101. DOI: 10.1007/s00773-015-0334-1.

Thorne, Colin R. and N. Keith Tovey, 1981. Stability of composite river banks. en. In: Earth Surface Processes and Landforms 6.5. _eprint: https://onlinelibrary.wiley.com/doi/pdf/10.1002/esp.3290060507, pp. 469–484. DOI: 10.1002/esp.3290060507.

7 AUTHORS BIOGRAPHY

Pablo Nieutin is an ATER (Temporary Lecturer and Researcher) at the Pprime Laboratory and Poitiers University, after he has defended his PhD thesis on wake waves impact on riverbanks in 2024. He studied Naval Engineering at ENSTA (National Higher School of Advanced Techniques).

Clément Maubant is a PhD student at the Pprime laboratory, his work focuses on the study of wake waves on bench-type banks within a multidisciplinary framework as part of the ANR Influe project. He studied Naval Engineering at ENSTA (National Higher School of Advanced Techniques) and University of Western Brittany. He is member of the RINA (Royal Institution of Naval Architects).

Damien Calluaud is full professor at Poitiers University and ANR Influe project leader. He is the head of the platform of Environmental Hydraulic (pHE) within the Pprime laboratory and head of the scientific section "Hydrodaulique pour l'environnement et le développement durable" HED2 in the Société Hydrotechnique de France (SHF). He is member of International Association of Hydro Environment Engineering and Research (IAHR).

Gerard Pineau is full professor at Poitiers University. He leads the HYDÉE team within the Pprime laboratory.

NUMERICAL PMM TEST IN FINITE DEPTH AND APPLICATION TO MMG MODEL OF SHIP MANOEUVERING

Junhoi Choi, Department of Naval Architecture and Ocean Engineering, Seoul National University, Korea

Shuguang Wang, Department of Naval Architecture and Ocean Engineering, Seoul National University, Korea

Yonghwan Kim, Department of Naval Architecture and Ocean Engineering, Seoul National University, Korea

NUMERICAL PMM TEST IN FINITE DEPTH AND APPLICATION TO MMG MODEL OF SHIP MANOEUVERING

JUNHOI CHOI, DEPARTMENT OF NAVAL ARCHITECTURE AND OCEAN ENGINEERING, SEOUL NATIONAL UNIVERSITY, KOREA
SHUGUANG WANG, DEPARTMENT OF NAVAL ARCHITECTURE AND OCEAN ENGINEERING, SEOUL NATIONAL UNIVERSITY, KOREA
YONGHWAN KIM, DEPARTMENT OF NAVAL ARCHITECTURE AND OCEAN ENGINEERING, SEOUL NATIONAL UNIVERSITY, KOREA

SUMMARY

This study investigates the maneuvering performance of the KRISO container ship (KCS) in finite-depth waters using computational fluid dynamics (CFD) based Planar Motion Mechanism (PMM) tests. Hydrodynamic coefficients were derived through static drift and pure yaw tests performed at different depth-to-draft (H/T) ratios to assess the influence of shallow water conditions. Validation of the CFD model against the data obtained from the SIMMAN 2020 experiments confirmed its accuracy. Uncertainty analyses of grid resolution and timestep were also conducted to guarantee the reliability of CFD. A comparative evaluation of the MMG-based models, including first-, second-, and third-order hydrodynamic coefficients, demonstrated that the MMG model using first- and third-order terms performs effectively in deep water, whereas the model with first- and second-order terms better capture crossflow effects in shallow water. These findings emphasize the necessity of adaptive modeling approaches to enhance the prediction accuracy of ship manoeuvering in restricted waterways.

NOMENCLATURE

C_{cf}	Crossflow drag coefficient (-)
f_{ext}	External force (N)
Fr	Froude number (-)
Fr_H	Depth Froude number (-)
g	Gravitational acceleration (m/s^2)
L	Ship length (m)
o - xyz	Ship-fixed coordinate (-)
o_E - $x_E y_E z_E$	Earth-fixed coordinate (-)
P_{rgh}	Pressure (Pa)
R_i	Convergence ratio (-)
r	Yaw rate (rad/s)
T	Draft (m)
S_i	Solution (-)
U	Ship speed (m/s)
U_i	Uncertainty (-)
u, v	Surge, sway velocity (m/s)
$\vec{u}$	Flow velocity vector (m/s)
X', Y', N'	Nonlinearized surge, sway force, yaw moment (-)
X'_H, Y'_H, N'_H	Nonlinearized surge, sway force, yaw moment acting on ship hull (-)
X'_P	Nonlinearized added mass components by propeller (-)
X'_R, Y'_R, N'_R	Nonlinearized surge, sway force, yaw moment by steering (-)
$y+$	Dimensionless wall distance (-)
β	Drift angle (rad)
ρ	Density of water (kg/m^3)
τ	Shear stress (Pa)
ψ	Yaw angle (rad)

1 INTRODUCTION

Environmental considerations, including contamination caused by ship grounding and collision, have garnered growing attention in recent years. These challenges are particularly in areas with limited water depths, including harbors and riverine channels. The reduced manoeuverability in such conditions, along with limitations on cargo and speed, can result in significant economic losses. Furthermore, restrictions on harbor infrastructure have heightened the significance of assessing ship manoeuverability in confined waters, especially given the trend toward larger modern vessels. Therefore, the influence of shallow water not only constrains ship operations but also further intensifies the issue of navigation and safety in high-traffic ports and narrow waterways.

Traditionally, manoeuverability prediction has relied on methods such as sea trials, experimental model testing, and empirical formulas. These methods are often associated with high cost, long time, or logistical difficulties. Advancements in computational resources have positioned numerical simulations, especially computational fluid dynamics (CFD), as efficient alternatives to traditional approaches. By leveraging high-performance computing, CFD enables the detailed analysis of complex hydrodynamic phenomena across various environmental conditions.

The CFD approach facilitates the calculation of hydrodynamic coefficients, which is critical for assessing ship manoeuvering performance. Planar motion mechanism (PMM) and circular motion tests (CMT) are commonly used to obtain these coefficients. The calculated coefficients are then applied to hydrodynamic models, such as the Abkowitz model by Abkowitz (1969) and the MMG model by Yasukawa and Yoshimura (2015), to estimate the contributions of the hull, propellers, and rudder to overall hydrodynamic forces and moments.

While extensive research has focused on manoeuverability in deep water, investigations into shallow water effects have gained attention only in recent decades. Notable studies include the experimental research by Fujino (1968), mathematical modeling of hull force by Gronarz (1993), and empirical formulation of hydrodynamic coefficients in shallow water by Kijima et al. (1990). More recent experimental work by Eloot and Vantorre (2009) has further advanced the understanding of hull interactions in shallow water. Despite these developments, verifying these coefficients in shallow water remains a critical area for further investigation.

Recent research has increasingly utilized numerical computations to analyze ship manoeuverability in confined waters. For instance, Mucha et al. (2016) and Taimuri et al. (2020) analyzed the hydrodynamic coefficients of various vessels, including KVLCC2 container vessels, using CFD and Rankine panel methods. Additionally, the SIMMAN 2020 workshop provides benchmark results for ship manoeuvering performance in shallow waters, covering hydrodynamic coefficients, hull-propeller interactions, and seakeeping analysis at various water depths.

This study aims to evaluate ship manoeuvering performance in shallow water conditions and to investigate the influence of varying water depths on hydrodynamic coefficients. Prior research has often neglected the second-order terms of hydrodynamic coefficients under shallow water conditions, focusing predominantly on the third-order terms. However, this approach limits the ability to comprehensively capture the nonlinear behaviors that emerge with decreasing depth of water. To overcome these constraints, this research also conducts a comparative analysis of hull force modeling using both first- and second-order terms of hydrodynamic coefficients along with the first- and third-order terms to enhance the accuracy of the MMG model for shallow water computations.

2 METHODOLOGY

2.1 TEST OVERVIEW

2.1 (a) Motion Equations of MMG Model

In ship manoeuverability studies, two primary coordinate systems, as illustrated in Figure 1, are utilized: an earth-fixed ($o_E - x_E y_E z_E$) and ship-fixed coordinate system ($o - xyz$). The ship-fixed coordinate system is originated at the vessel's central point, facilitating the description of the ship's motion relative to its own axes. These coordinate systems are essential for analyzing the dynamic behavior of hull. Figure 1 also highlights the definition of forces, velocities, and angular parameters involved in ship manoeuvering analysis.

The ship's motion is typically described using 3-DOF, namely surge (*X*), sway (*Y*), and yaw (*N*). Force and moment are normalized by $0.5\rho U^2 TL$, and $0.5\rho U^2 TL^2$, respectively, to enhance the consistency. Surge and sway represent translational motions along the x (surge) and y (sway)-axes, respectively, while yaw describes rotational motion about the vertical axis ψ (yaw). Corresponding velocities are represented as *u* (surge velocity), *v* (sway velocity), and *r* (yaw rate). The total velocity

of the hull is given by $U = \sqrt{u^2 + v^2}$, while the drift angle (β) provide additional parameters to define the ship's state during maneuvers.

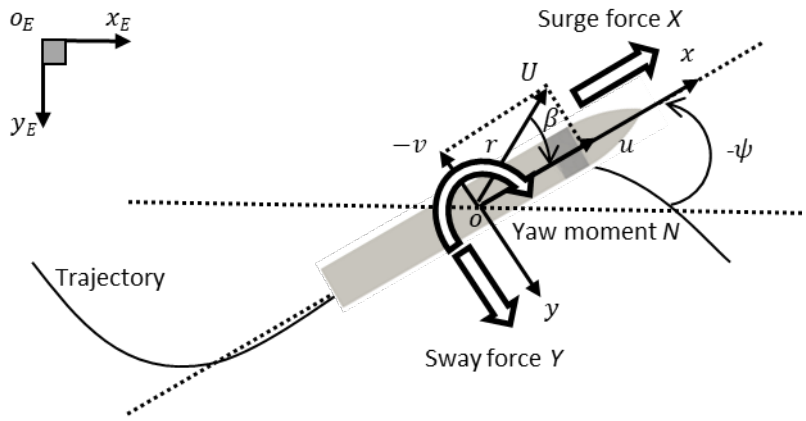

Figure 1. Coordinate system and parameters

The equations of motion for the hull within the 3-DOF of the ship-fixed coordinate system are defined in Equation (1). The forces and moments result from contributions of the hull, propeller, and rudder force, as modeled by the MMG model.

$$\begin{cases} m(\dot{u} - rv) = X_H + X_R + X_P \\ m(\dot{v} + ru) = Y_H + Y_R \\ I_z \dot{r} = N_H + N_R \end{cases} \quad (1)$$

2.1 (b) Hull Force Modeling

The modeling of hull forces, specifically the sway force (*Y*) and yaw moment (*N*), are able to be approached using two main methods. The first method relies on a Taylor series expansion, while the second considers the significance of crossflow effects beneath the hull.

The Taylor series expansion method models the sway force and yaw moment as odd functions, incorporating first- and third-order terms. This approach provides a detailed representation of the odd function behavior of hull forces and moments. Using this formulation, the hull forces can be expressed as:

$$\begin{cases} Y'_H = Y'_v v' + Y'_r r' + Y'_{vvv} v'^3 + Y'_{vvr} v'^2 r' + Y'_{vrr} v' r'^2 + Y'_{rrr} r'^3 \\ N'_H = N'_v v' + N'_r r' + N'_{vvv} v'^3 + N'_{vvr} v'^2 r' + N'_{vrr} v' r'^2 + N'_{rrr} r'^3 \end{cases} \quad (2)$$

An alternative approach emphasizes the hull forces and moments' nonlinear components generated by crossflow beneath the hull. This approach integrates first- and second-order terms to provide a more accurate depiction from a physical perspective. The sway force and yaw moment induced through crossflow are able to be represented through the following equations (Faltinsen, 2006b; Beukelman and Journee, 2001):

$$\begin{cases} Y_{cf} = \frac{1}{2}\rho C_{cf} \int_0^L (v + xr) \,|\, v + xr \,|\, T(x) dx \\ N_{cf} = \frac{1}{2}\rho C_{cf} \int_0^L x(v + xr) \,|\, v + xr \,|\, T(x) dx \end{cases} \quad (3)$$

The crossflow model allows for the sway force and yaw moment to be represented by second-order terms, as opposed to the third-order terms used in the Taylor series method, as expressed in Equation (4). This makes the crossflow approach more suitable for capturing the quadratic damping effects that play a significant role in hull hydrodynamics (Norbin, 1971).

$$\begin{cases} Y'_H = Y'_v v' + Y'_r r' + Y'_{v|v|} v'|v'| + Y'_{r|r|} r'|r'| \\ N'_H = N'_v v' + N'_r r' + N'_{v|v|} v'|v'| + N'_{r|r|} r'|r'| \end{cases} \quad (4)$$

2.1 (c) PMM Tests

The PMM tests are commonly employed to evaluate hydrodynamic coefficients critical for predicting ship manoeuverability. This study utilized two primary PMM tests: static drift tests and pure yaw tests. In static drift tests, hydrodynamic forces and moments are evaluated under steady drift conditions as shown in Figure 2. The drift angle β is defined as $\beta = tan^{-1}(-v/u)$. The hull forces and moments during the test are represented as:

$$\begin{cases} X' = X'^{(0)} = X'_* + X'_{vv} v'^2 \\ Y' = Y'^{(0)} = Y'_v v' + Y'_{vvv} v'^3 \\ N' = N'^{(0)} = N'_v v' + N'_{vvv} v'^3 \end{cases} \quad (5)$$

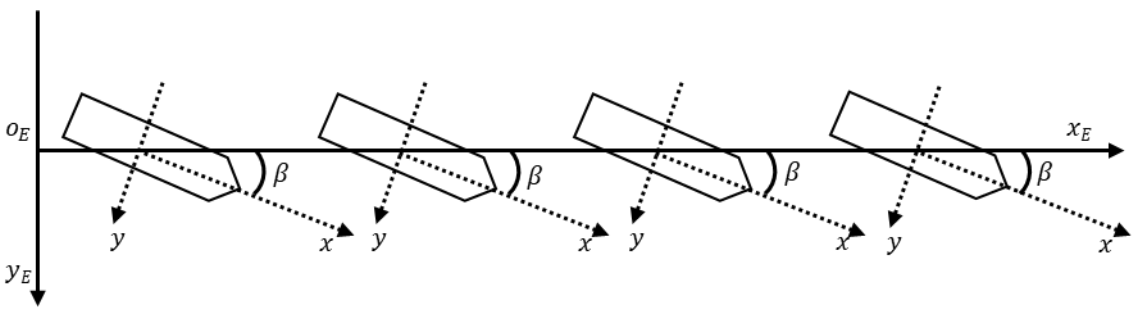

Figure 2. Static drift test

On the other hand, pure yaw tests analyze the ship's response under a sinusoidal yaw motion, as presented in Figure 3. The yaw angle ψ and yaw rate r are represented as $\psi = \psi_{\max} cos\ (\omega t)$ and $r = r_{\max} sin(\omega t)$. Superscripts in the equations indicate specific harmonic elements of the hydrodynamic forces and moments; for example, $Y^{(0)}$ represents the mean sway force, $Y^{(1,\cos)}$ denotes the first-order cosine term of the sway force, and $N^{(1,\sin)}$ refers to the first-order sine term of the yaw moment. The hull forces and moments during the test are expressed as:

$$\begin{cases} X' = X'_* + X'_{rr} r'^2 = X'^{(0)} + X'^{(2,\cos)} \cos(2\omega t) \\ Y' = Y'_r r' + Y'_{rrr} r'^3 = Y'^{(1,\sin)} \sin(\omega t) - Y'^{(3,\sin)} \sin(3\omega t) \\ N' = N'_r r' + N'_{rrr} r'^3 = N'^{(1,\sin)} \sin(\omega t) - N'^{(3,\sin)} \sin(3\omega t) \end{cases} \quad (6)$$

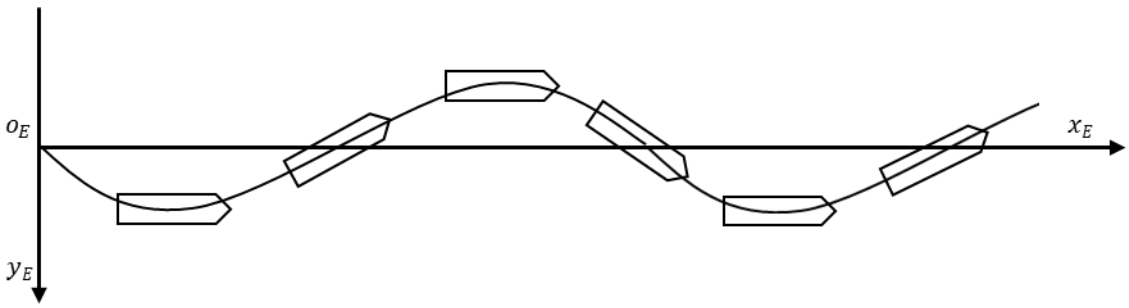

Figure 3. Pure yaw test

For better comparison with benchmark data from SIMMAN 2020, both PMM tests were performed in the same calm-water conditions as model tests. As outlined in Table 1, various drift angles and yaw rates, as well as depth-to-draft ratios (*H/T*), were tested. A scaled KCS model with a rudder, at a scale of 1/31.6, was used in this study to evaluate hydrodynamic behavior under controlled conditions. Figure 4 depicts the hull geometry, and Table 2 summarizes the primary specifications of the test hull model.

Table 1. Summary of test conditions

Model	KCS
Towing velocity (*Fr*)	0.8007m/s (0.09476)
SDT	$\beta = \pm 2°, \pm 4°, 0°, 6°, 10°, 15°$
PYT	$r_{max} = 0.3,\ 0.35,\ 0.4,\ 0.45,\ 0.5$
H/T (Fr_H)	1.2, 1.5, 2.0, deep (< 0.4)
Benchmark data	SIMMAN 2020

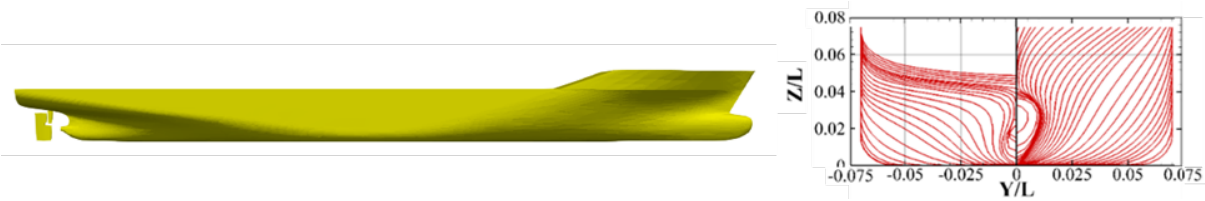

Figure 4. KCS geometry and body plan

Table 2. Details of the KCS model

Scale	λ	31.6
Length	L_{pp} [m]	7.278
Draught	T [m]	0.342
Breadth	B [m]	1.019
Displacement	Δ [m^3]	1.649
GM	[m]	0.019
LCB (%Lpp) fwd+	-	-1.48
KG	[m]	0.283
Moment of Inertia (*x*)	I_{xx} / B	0.4
Moment of Inertia (*z*)	I_{zz} / Lpp	0.25

2.2 NUMERICAL APPROACH

2.2 (a) CFD Slover

The CFD simulations in this study were conducted using a solver developed on the OpenFOAM of open source library, specifically snuMHLFoam, designed by the Marine Hydrodynamics Laboratory (MHL) at Seoul National University. This solver is tailored for various ship seakeeping and maneouvering studies (Zhu et al., 2022; Kim et al., 2023; Wang et al., 2023). The solver implements key governing equations such as the continuity equation and momentum equations, as described in Equations (7) and (8):

$$\nabla \cdot \vec{u} = 0 \qquad (7)$$

$$\frac{\partial(\rho\vec{u})}{\partial t} + (\rho\vec{u} \cdot \nabla\vec{u}) = -\nabla p_{rgh} + \rho g + \nabla \cdot \tau + \rho f_{ext} \qquad (8)$$

To model multiphase flows, the Volume of Fluid (VOF) method was used. For turbulence modeling, the k-ω SST model (Menter et al., 1993) was utilized, enhanced with additional buoyancy term and an artificial viscosity limiter to enhance computational stability. The governing equations were discretized employing the finite volume method, with an implicit Euler scheme for time discretization. Spatial discretization applied central differencing for gradient and Laplacian terms, while divergence terms were handled using variable-specific schemes. Techniques such as the van Leer scheme and linear upwind schemes ensured numerical stability and accuracy for volume fraction, velocity, and turbulence variables. PIMPLE algorithm, which combines PISO and SIMPLE schemes, was used for velocity-pressure coupling.

2.2 (b) Numerical Model

The computational domain for the PMM tests was designed as a cylindrical computational domain, including the ship model, to ensure accurate wave generation and damping. The domain boundaries were labeled as "inlet," "top," "bottom," and "hull." The "inlet" refers to the circular region encompassing the domain, while the "top" and "bottom" correspond to the ceiling and floor of the domain, respectively. The "hull" refers to the ship's surface. Figure 5 illustrates the computational tank and mesh detail designed for the stern and bow parts.

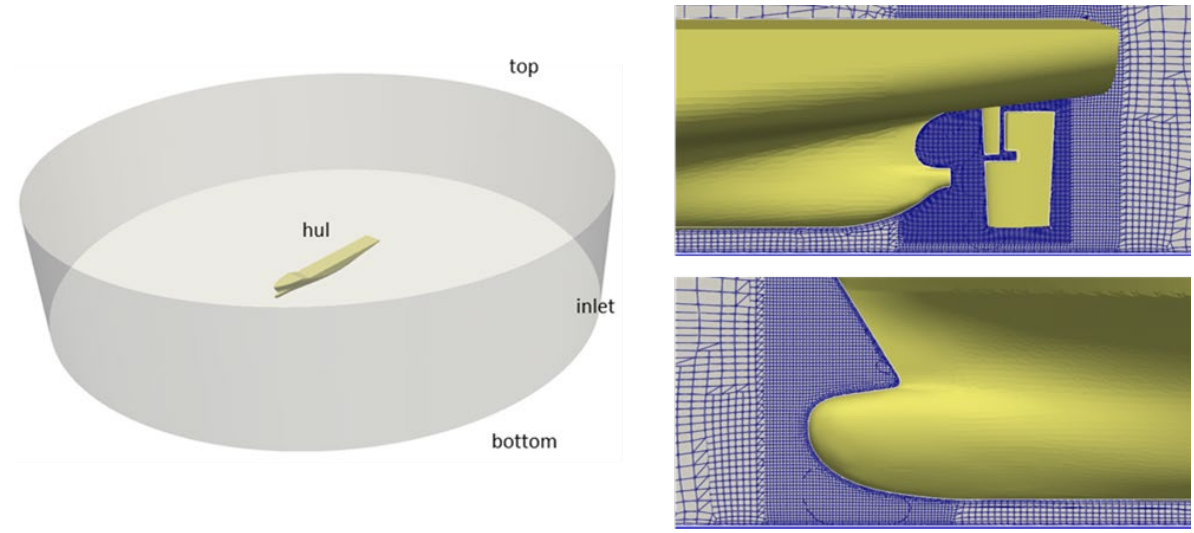

Figure 5. Computational tank and mesh detail

The computational domain was designed to accommodate different depth-to-draft ratios (*H/T*) and ensure accurate simulation results. Additional mesh refinement was applied to critical regions such as the free surface, bow, and stern. The final grid resolution was optimized to minimize uncertainties by testing various grid densities between the keel and the seabed.

Boundary conditions included zero-gradient and fixed-value types. For most variables, the zero-gradient condition was applied to ensure smooth transitions, while fixed-value conditions were used for specific variables like velocity and pressure on the hull and top. Wall functions were implemented to reduce computational costs. The y+ value was set from the recommended ITTC range of 30 to 100. This setup ensured computational stability and accuracy, enabling detailed analysis of hydrodynamic behavior under various test conditions.

3 NUMERICAL SENSITIVITY

In CFD calculations, uncertainties can originate from factors such as grid size and timestep selection in numerical methods. To reduce these uncertainties and enhance the reliability of the computations, numerical sensitivity tests were performed in this research to evaluate the influence of mesh size and temporal step on the accuracy of the computational results.

Uncertainty analyses followed the ITTC 7.5-03-01-01 (2017) guidelines, which require at least three calculated results for convergence evaluation. The convergence ratio (R_i) was used to determine the type of convergence in the results. Depending on the convergence type, different methods were applied to estimate uncertainties. For monotonic convergence ($0<R_i<1$), Richardson extrapolation was utilized to quantify numerical errors and assess uncertainty. For oscillatory convergence ($R_i<0$), uncertainty was estimated using the variation between the maximum and minimum values obtained from the calculations. In cases of divergence ($1<R_i$), uncertainty was not defined. Two approaches were employed in this study to calculate uncertainty: one based on safety factors proposed by Roache (1998) and the other based on correction factors recommended by Wilson et al. (2004) and Stern et al. (2001).

Detailed uncertainty analysis has been performed and presented in our previous work (Choi, 2024). Here are only the summarized results in Table 3. The static drift test with the largest drift angle ($\beta = 15°$) was chosen to test grid size ranging from $L/300$ to $L/600$ and timestep with $U_0\Delta t/\Delta x$ ranging from 0.326 to 0.652. The uncertainty analysis results indicated that

sway force showed monotonic convergence with uncertainties of around 1.0% for both grid size and time step analyses. Surge force and yaw moment demonstrated oscillatory convergence, but their uncertainties also remained low, at around 1.0%. Building on these findings, a mesh size of $L/424$ and a time step of 0.010s were selected for subsequent simulations.

Table 3. Summary of numerical sensitivity test

Uncertainty analysis		Cell size (Δx)			CFL ($U_0\Delta t/\Delta x$)		
Grid # (M)		3	4.49	6.95	4.49		
Solution		X'	Y'	N'	X'	Y'	N'
$S_{i,3}$ (Coarse)		0.01196	0.49521	0.12451	0.01193	0.50815	0.13029
$S_{i,2}$ (Medium)		0.01153	0.50265	0.12715	0.01153	0.50265	0.12715
$S_{i,1}$ (Fine)		0.01188	0.50516	0.12688	0.01167	0.49934	0.12563
Uncertainty	U_i (%S_1)	1.786 %	0.756 %	1.039 %	1.679 %	1.656 %	1.346 %
	$U_{i,C}$(%S_1)	-	0.245 %	-	-	0.335 %	0.269 %

4 RESULTS AND DISCUSSION

4.1 RESULTS OF PMM TESTS

The static drift tests were performed across a range of drift angles between -4° and 15°, while the pure yaw tests were conducted for yaw rates between 0.3 and 0.5 under four different depth conditions (H/T = 1.2,1.5,2.0, and deep water). Taking the static drift test as an example, Figure 6 illustrates representative time signals for the forces and moment, along with their corresponding averaged values. The results demonstrate a good convergence, allowing the averaged values to be easily determined. For the pure yaw tests, time signals are more oscillatory due to the periodic characteristics of the prescribed yaw motion. Therefore, the Fourier transform is utilized to calculate forces and moments to determine the hydrodynamic coefficients.

Figure 6. Time signal of force and moment of SDT (H/T = 1.2, $\beta = 15°$)

Figure 7 illustrates the free surface elevation resulting from the two PMM tests under the previously described conditions. Here, z represents the height of the free surface, non-dimensionalized by the ship's length. For the static drift test, as shown in Figure 7(a), the free surface elevation is higher on the forward-facing side of the bow and lower on the opposite side. For the pure yaw test at a yaw rate of 0.5, as depicted in Figures 7(b) and 7(c), free surface patterns around the hull at time instances $1/4T_0$ and $3/4T_0$ are approximately symmetric but with minor deviations, which results in the generation of sinusoidal forces and moments. This behavior aligns with the periodic motion of the hull observed during the yaw tests.

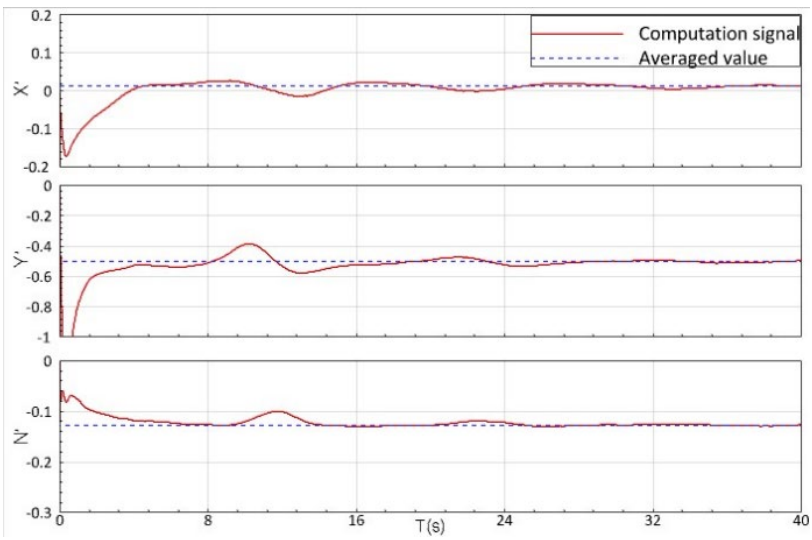

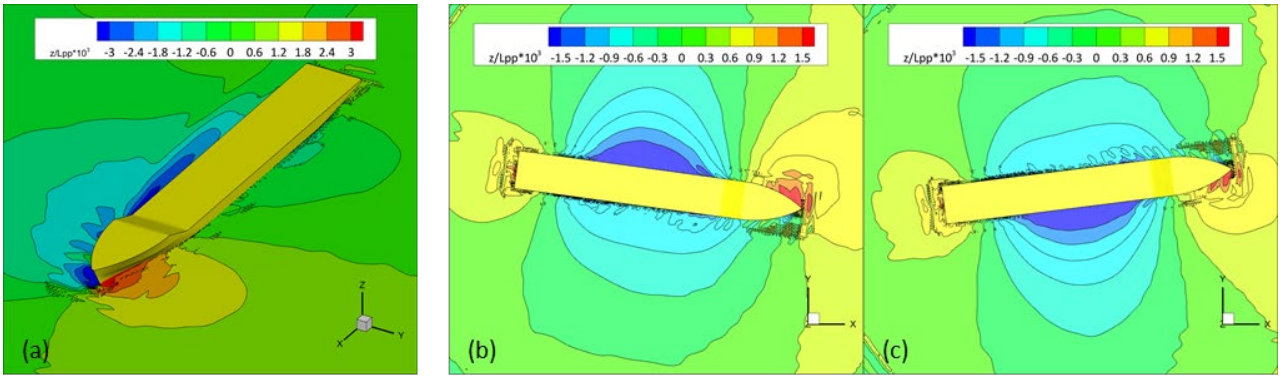

Figure 7. Wave elevation of PMM test ((a) SDT, (b) PYT at t = 1/4T$_0$, (c) pure yaw test at t = 3/4T$_0$)

Table 4 summarizes the comparison of computed sway force and yaw moment against experimental data from KRISO (SIMMAN, 2020). Because the benchmark data for the surge force and sway force of the pure yaw test has a great deal of uncertainty, it was omitted from further comparisons. The results demonstrate strong consistency between the computational and experimental results, indicating the reliability of the numerical method employed in this study. Although some differences appear relatively large, the actual values involved are small, resulting in only minor absolute differences. Additional details and discussions are available in Choi (2024).

Table 4. Validation of forces and moments for the two types of PMM tests. (*H*/*T* = 1.2)

	CFD		EFD		Difference	
Drift angle (β)	Y'	N'	Y'	N'	*Y* (%)	*N* (%)
-4	-0.0708	-0.0265	-0.0627	-0.0264	-12.92	-0.38
4	0.0712	0.0260	0.0696	0.0252	-2.30	-3.17
15	0.5027	0.1271	0.5031	0.1393	0.08	8.76
Yaw rate (*r*)	$Y^{(1,\sin)\prime}$	$N^{(1,\sin)\prime}$	$Y^{(1,\sin)\prime}$	$N^{(1,\sin)\prime}$	*Y* (%)	*N* (%)
0.3	0.0146	-0.0304	-	-0.0275	-	-10.55
0.4	0.0222	-0.0466	-	-0.0461	-	-1.08
0.5	0.0238	-0.0633	-	-0.0666	-	4.95

Four hydrodynamic coefficients (Y_{v} , $Y_{\mathrm{vvv}}, N_{\mathrm{v}}, and\ N_{\mathrm{vvv}}$) from static drift test and four hydrodynamic coefficients (Y_{r} , $Y_{\mathrm{rrr}}, N_{\mathrm{r}}, and\ N_{\mathrm{rrr}}$) from pure yaw test were evaluated across varying water depths. As depicted in Figure 8, the coefficients exhibit an increasing trend as water depth decreases, reflecting the increased forces and moments in shallower water conditions. The comparison of hydrodynamic coefficients obtained from CFD and experimental results revealed that most values exhibit similar trends. For Y_{vvv}, its magnitude is significantly larger than the others, and the underlying cause will be discussed in a subsequent section. In the case of N_{vvv}, there appears to be some discrepancy with the experimental results. However, the computational results show an almost linear behavior, indicating a high sensitivity to this nonlinear term. Consequently, its impact on overall maneuvering performance is negligible. These depth-dependent differences arise from the imbalance in pressure distribution acting on the hull's starboard and port sides.

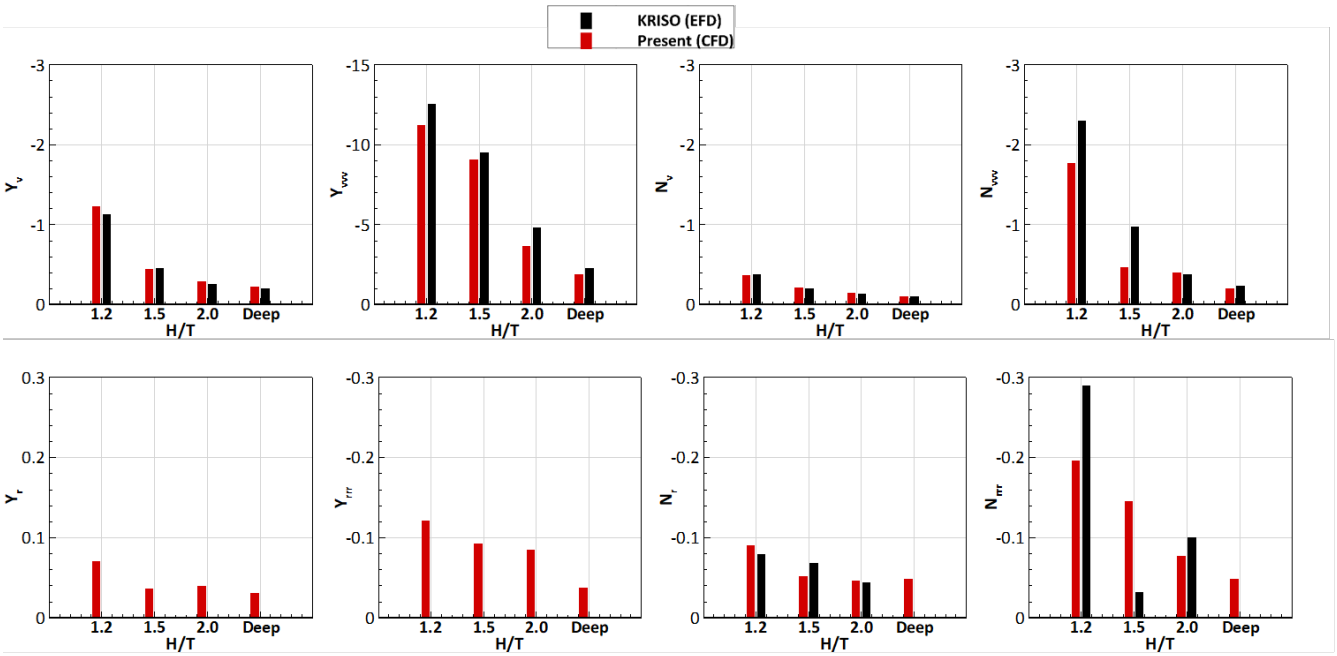

Figure 8. The hydrodynamic coefficients at various water depths comparison with experimental data

4.2 COMPARISON OF HULL FORCES MODELING

As introduced in Section 2.1 (b), there are two approaches to hull force modeling. In this study, an analysis was conducted to determine which order has a more dominant influence. Computations were conducted to examine the differences in hydrodynamic coefficients derived from models combining all of the order terms, as shown in Equation (9).

$$\begin{cases} Y'_H = Y'_v v' + Y'_r r' + Y'_{v|v|} v'|v'| + Y'_{r|r|} r'|r'| + Y'_{vvv} v'^3 + Y'_{rrr} r'^3 \\ N'_H = N'_v v' + N'_r r' + N'_{v|v|} v'|v'| + N'_{r|r|} r'|r'| + N'_{vvv} v'^3 + N'_{rrr} r'^3 \end{cases} \quad (9)$$

Using this combined equation, curve fitting was performed on the PMM test's results to evaluate the influence of the coefficients at different water depths. Table 4 presents a summary of the results obtained by fitting calculation data of PMM tests using an equation that includes all of the order coefficients.

Table 4. Hydrodynamic coefficients derived from combined-order modeling

H/T	1.2	1.5	2.0	Deep
Y_v	-0.8849	-0.2471	-0.1932	-0.1933
$Y_{v\|v\|}$	-4.2537	-2.7279	-1.2826	-0.4634
Y_{vvv}	0.0000	-1.4000	-0.0665	-0.6505
N_v	-0.3321	-0.2099	-0.1524	-0.1101
$N_{v\|v\|}$	-0.5710	-0.0986	0.0000	-0.0007
N_{vvv}	-0.1725	-0.1927	-0.3983	-0.2051
Y_r	0.0889	0.0481	0.0458	0.0312
$Y_{r\|r\|}$	-0.0964	-0.0678	-0.0367	0.0000
Y_{rrr}	0.0000	0.0000	-0.0348	-0.0379
N_r	-0.0664	-0.0389	-0.0383	-0.0466
$N_{r\|r\|}$	-0.1436	-0.0937	-0.0492	-0.0153
N_{rrr}	0.0000	-0.0013	-0.0095	-0.0280

The results indicate that the second-order term coefficients ($Y_{r|r|}$, $N_{v|v|}$) exhibit values near zero in deep water, suggesting minimal second-order contributions under such conditions. For third-order coefficients (Y_{rrr}, N_{vvv}), the values remain consistent between first-, third-order and first-, second-, third-order fits, implying that third-order terms dominate hydrodynamic behavior in deep water. Although second-order terms are evident for (Y_{vvv}, N_{rrr}), their behaviors remain almost linear, indicating that nonlinear terms have a limited impact on maneuvering performance under these conditions. These findings are consistent with earlier studies indicating that third-order terms dominate hydrodynamic behavior in deep water. However, with a reduction in depth of water, the influence of second-order terms becomes increasingly significant. This transition can be attributed to the stronger interaction between the vessel's hydrodynamic forces and the proximity of the seabed, leading to increased contributions from quadratic effects. Specifically, the enhanced second-order effects in shallow waters are closely related to cross-flow effects described earlier, where the lateral flow under the hull significantly alters the hydrodynamic force distribution. Furthermore, it is observed that in shallow waters, the vorticity underneath the ship developed more compared to deep water conditions.

Figures 9(a) and 9(c) compare the results from the third-order equation (Equation 2) and a second-order model (Equation 4) for *N* at H/T=1.2 to evaluate the fitting performance. The latter equation provides a closer fit across most data points than the former. To further verify the suitability of the second-order model in shallow water, additional fitting was performed by excluding the last data point. When the last data point is excluded, the second-order model achieves a significantly closer fit near the removed data point, as shown in Figures 9(b) and 9(d). This demonstrates the importance of second-order terms in accurately representing hydrodynamic behavior in shallow water.

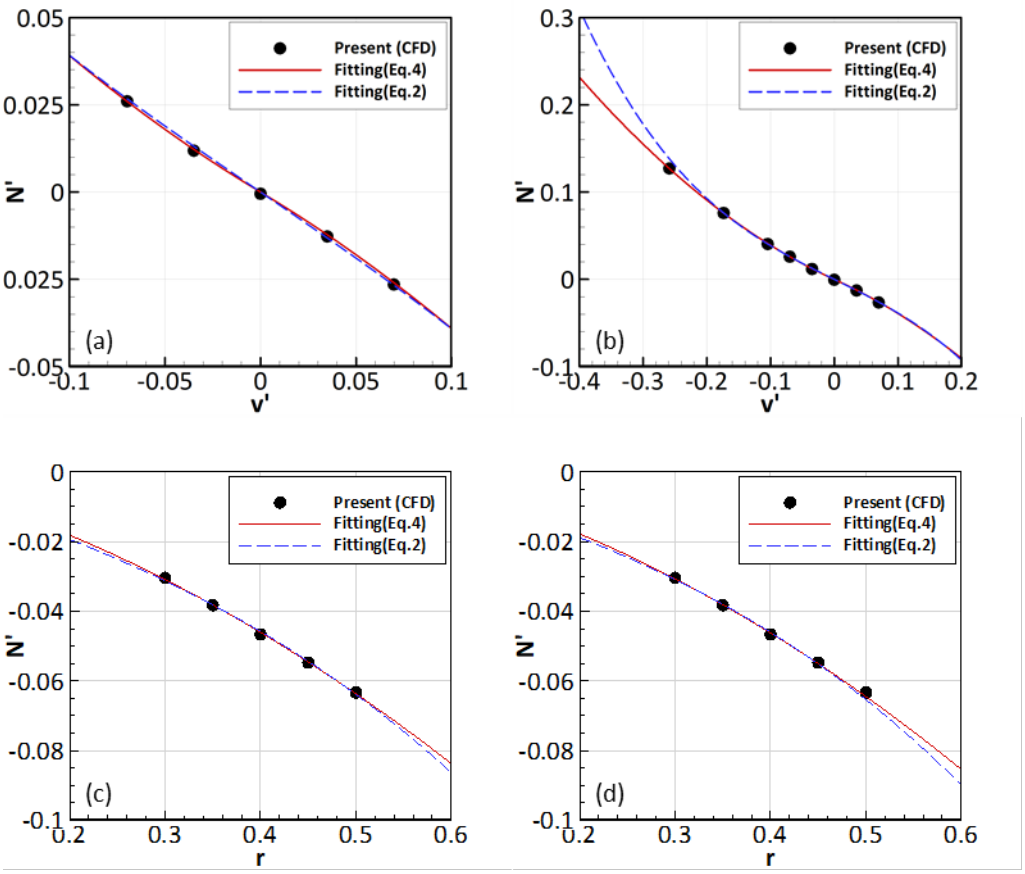

Figure 9. Comparison of fitting performance between third-order and second-order models based on the presence or absence of the last point ((a), (c) w/ last point (zoomed) and (b), (d) w/o last point PMM data curve fitting for *N* at *H/T* = 1.2)

5 CONCLUSIONS

This research utilized a CFD approach based on OpenFOAM to conduct numerical simulations of PMM tests under both deep and shallow water conditions, aiming to evaluate the manoeuvering characteristics of the KCS model. The key findings are summarized as follows:

- Numerical sensitivity tests on mesh size and time step were carried out using the safety and correction factor, yielding uncertainties of approximately 1.0%. The CFD simulations for two kinds of PMM tests demonstrated close agreement with experimental data, confirming the reliability and robustness of the numerical method.

- PMM tests at various water depths revealed an increase in hydrodynamic forces, moments, and consequently coefficients with a reduction in water depth, highlighting the pronounced effects of shallow water on maneouvering performance.

- Regarding hull force modeling, first- and third-order terms of hydrodynamic coefficients were dominant in deep water, whereas second-order terms became increasingly important in shallow water due to cross-flow effects. This underscores the necessity of including second-order terms in models to address shallow water effects.

- Limitations and future work: While individual hydrodynamic coefficients were successfully derived, combined drift-yaw PMM tests were not performed. Consequently, the coupling coefficients could not be entirely integrated into the model. Further studies are required to address this limitation and improve the modeling of coupled hydrodynamic effects.

6 ACKNOWLEDGEMENTS

This study was supported by the Lloyd's Register Foundation Research Center (LRFC) at Seoul National University, South Korea. Their financial support is greatly appreciated. Administrative support from the Institute of Engineering Research (IoER) and the Research Institute of Marine System Engineering (RIMSE), Seoul National University, South Korea, is also acknowledged.

7 REFERENCES

Abkowitz, M.A., 1969. Stability and motion control of ocean vehicles. The MIT Press, USA.

Beukelman, W. and J.M.J. Journee, 2001. Hydrodynamic transverse loads on ships in deep and shallow waters. In: 22nd International Conference on Hydrodynamics and Aerodynamics in Marine Engineering.

Choi, J., Kim, Y., Zhu, Z., Wang, S. 2024. Numerical PMM test in finite depth. Ocean Eng, vol 314 pp 119690.

Eloot, K., Vantorre, M., 2009. Proceedings of the First International Conference on Ship Manoeuvring in Shallow and Confined Water: Bank Effects. RINA. Ghent University.

Faltinsen, O.M., 2006b. Hydrodynamics of High-Speed Vessels. Cambridge University Press. New York City, NY, USA.

Fujino, M., 1968. Experimental Studies on Ship Maneuverability in Restricted Waters. International Shipbuilding Progress, 15:279-301.

Gronarz, A., 1993. A Mathematical Model for Manoeuvring Simulation on Shallow Water. Proc. of MARSIM 1993.

Kijima, K., Nakiri, Y., Tsusui, Y., and Matsunaga, M., 1990. Prediction method of ship manoeuvrability in deep and shallow water. In Proc. of MARSIM, Tokyo, Japan.

Kim, B. -S., Wang, S., Zhu, Z. & Kim, Y. 2023. Numerical Simulation of Free running Turning Test of Ship in Waves. Ocean Eng, vol 228 pp 115951.

Menter, F. R. 1993. Zonal Two Equation k-ω Turbulence Models for Aerodynamic Flows. 23rd Fluid Dynamics, Plasmadynamics, and Lasers Conference, Orlando, Florida, USA.

Mucha P, Deng G, Gourlay T and Moctar O el 2016. Validation studies on numerical prediction of ship squat and resistance in shallow water In Proc. the 4th Int. Conf. on Ship Manoeuvring in Shallow and Confined Water (Hamburg, Germany).

Norrbin, N., 1971. Theory and observations on the use of a mathematical model for ship manoeuvring in deep and confined water. Technical Report 63. Swedish State Shipbuilding Experimental Tank. Gothenburg.

Roache, P.J., 1998. Verification and validation in computational science and engineering. Hermosa Pub, USA.

SIMMAN 2020 Workshop on Verification and Validation of Ship Manoeuvring Simulation Methods (Songdo, Korea).

Stern, F., Wilson, R.V., Coleman, H. & Paterson, E. 2001. Comprehensive Approach to Verification and Validation of CFD-Simulations-Part 1: Methodology and Procedures. Journal of Fluid Engineering, 123(4), 793-802.

Taimuri G, Matusiak J, Mikkola T, Kujala P and Hirdaris S 2020. A 6-DoF maneuvering model for the rapid estimation of hydrodynamic actions in deep and shallow waters. Ocean Eng, vol 218 pp 108103.

Wang, S., Kim, B.-S., Zhu, Z. & Kim, Y. 2022. Enhanced body-force propeller model for non-uniform inflow flow and application to turning circle test of KCS in calm water. Journal of Engineering for the Maritime 169 Environment.

Wilson, R. V., Shao, J. & Stern, F. 2004. Discussion: Criticisms of the "Correction Factor" Verification Method 1. Journal of Fluid Engineering, 126(4), 704-706.

Yasukawa, H., Yoshimura, Y., 2015. Introduction of MMG standard method for ship maneuvering predictions. J. Mar. Sci. and Tech. 20, 37-52.

Zhu, Z., Kim, B.-S., Wang, S. & Kim, Y. 2022. Study on numerical PMM test and its application to KCS hull. Applied Ocean Research, 127.

8 AUTHORS BIOGRAPHY

Junhoi Choi is the Ph.D candidate in the Department of Naval Architecture and Ocean Engineering at Seoul National University. He is responsible for developing the main PMM methodologies, simulating the CFD, and conducting analyses.

Shuguang Wang is the Post-doctoral researcher in the Department of Naval Architecture and Ocean Engineering at Seoul National University. He is responsible for developing the main CFD methodologies.

Yonghwan Kim is the professor in the Department of Naval Architecture and Ocean Engineering at Seoul National University. He is responsible for supervision, providing resources, and overseeing writing tasks, including review and editing.

VISCOUS CFD SIMULATION OF PMM TESTS IN SHALLOW WATER AND IN A CANAL

Takuya Ohmori, National Maritime Research Institute, Japan

Kunihide Ohashi, National Maritime Research Institute, Japan

Yoshitaka Furukawa, Kyushu University, Japan

Hiroshi Ibaragi, Kyushu University, Japan

Yuya Matsunaga, JAPAN MARINE UNITED CORPORATION, Japan

VISCOUS CFD SIMULATION OF PMM TESTS IN SHALLOW WATER AND IN A CANAL

TAKUYA OHMORI, NATIONAL MARITIME RESEARCH INSTITUTE, JAPAN
KUNIHIDE OHASHI, NATIONAL MARITIME RESEARCH INSTITUTE, JAPAN
YOSHITAKA FURUKAWA, KYUSHU UNIVERSITY, JAPAN
HIROSHI IBARAGI, KYUSHU UNIVERSITY, JAPAN
YUYA MATSUNAGA, JAPAN MARINE UNITED CORPORATION, JAPAN

SUMMARY

One of the important situations to consider when discussing maritime traffic safety is restricted water areas such as shallow waters and narrow channels. Despite that being an important issue, evaluation of manoeuvrability in restricted waters, especially in narrow waterways, has not been sufficiently conducted due to technical difficulties.
The viscous flow simulation using CFD (computational fluid dynamics) can be used to evaluate hydrodynamic forces. So, a CFD simulation method for the PMM test in-channel using the NAGISA code developed in-house was applied to this problem and trial calculations using a KCS container ship model were performed to compare and verify the results with the tank test results conducted at Kyushu University. The results of the CFD and tank test showed good agreement. Consequently, viscous CFD can be used to simulate the unsteady hydrodynamic forces acting on a ship undergoing unsteady motion in a narrow waterway.

NOMENCLATURE

P	Pressure (N/m^2)
ν	Kinematic viscosity (m^2/s)
ρ	Density of water (kg/m^3)
L	Ship length (m)
d	Ship mean draft (m)
U	Ship speed (m/s)
lcb	Longitudinal centre of buoyancy (%L, positive in aft direction)
Fr	Froude number
Re	Reynolds number
C_X	Longitudinal force coefficient
C_Y	Lateral force coefficient
C_N	Yawing moment coefficient

1 INTRODUCTION

Narrow waterways are one of the situations that must be considered when discussing ship manoeuvrability. Specifically, these correspond to canal and river traffic. There are only a limited number of situations in which large commercial ships navigate narrow waterways, but there have been accidents in the Suez Canal, and it is becoming increasingly important to know the characteristics of the ships they operate.
There are various conditions to consider when it comes to traffic in narrow waterways, such as two-way traffic, one-way traffic, and the presence or absence of other ships, but here we will consider the case of a large ship navigating a one-way canal.
In order to grasp manoeuvrability in a narrow waterway, it is desirable to construct a manoeuvring simulation based on the manoeuvring equation of motion, and a mathematical model of hydrodynamic force is necessary. However, it cannot be said that a precise formulation has been completed. Fujino's research (Fujino, 1968; Fujino, 1970) is an example of a systematic approach among past studies. Fujino expressed the hydrodynamic force as the sum of the linear terms of the drift angle, the turning angular velocity, and the lateral displacement from the centre of the waterway and determined their linear derivatives by combining PMM tests (pure swaying and pure yawing) in a straight waterway, a steady oblique navigation test, and a straight-line test with changed left and right positions. However, some simplifications have been made,

and it is questionable whether the calculation is sufficiently precise. In fact, there is a discrepancy between the derivative of drift angle obtained from the steady oblique towing test and that obtained from the PMM test shown in the paper.
Conducting a PMM test in a narrow waterway to obtain the hydrodynamic force derivatives is easier than performing a CMT, but a characteristic of the PMM test is that the distance from the side wall also varies periodically and it is supposed that it will be difficult to properly evaluate or remove the side wall effect from PMM test result. Therefore, in this study, we aimed to deepen our understanding of PMM tests in narrow channels by examining how the results change depending on whether or not a side wall is present. CFD was selected as the tool for the study. The authors applied CFD technique to steady circular motion test within canal (Ohmori and Ohashi, 2022) and obtained good results. As the next step, we conduct and evaluate numerical simulations of PMM tests, which is an unsteady test.

2 COMPUTATIONAL AND EXPERIMENTAL METHOD

2.1 CFD SIMULATION

The in-house Reynolds-averaged Navier Stokes (RaNS) CFD code NAGISA(Ohashi et al. 2019) is used in this study, which is based on overset structured grid and finite volume method. Details of NAGISA are described in the reference document. The computational coordinate system is right-handed, x positive from bow to stern, y positive from port to starboard, and z positive from keel to deck. The positive direction of yaw moment is counterclockwise observed from the deck, as summarized in Figure 1. The EASM algebraic turbulence model which is based on the k-ω BSL model is selected from various turbulence models available. Although the computation is conducted in very low Froude number, free surface is modeled by single-phase level-set method. The reason for that is to consider the change of running attitude (pitch and heave motion). The NAGISA has the function of coupling the flow field calculation and the equation of motion up to 6 degrees of freedom.
The multi-block and multi-domain computation is applied using overset grid technique. The computational grid consists of three blocks: hull block, rudder block and external domain block. The hull block with rudder block move according to prescribed PMM motion and free pitch/heave motion against the external domain block by the overset grid technique.
A simplified propeller model is introduced. The number of revolutions is decided from the self-propulsion computation of steady straight course for each external domain condition respectively.

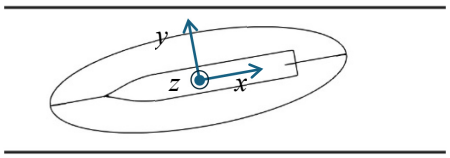

Figure 1. Coordinate system of CFD computation

2.2 TANK EXPERIMENT

The tank experiment to validate the CFD result is conducted in the Seakeeping and Manoeuvring Basin of Kyushu University. The size of the basin is 38.8m in length, 24.4m in width and 2.0m in depth. The bottom of the basin is finished flat in high precision (the error is within 2mm) so as to conduct experiments in shallow water. The X-Y towing carriage with turn table is equipped and various captive model tests can be conducted.

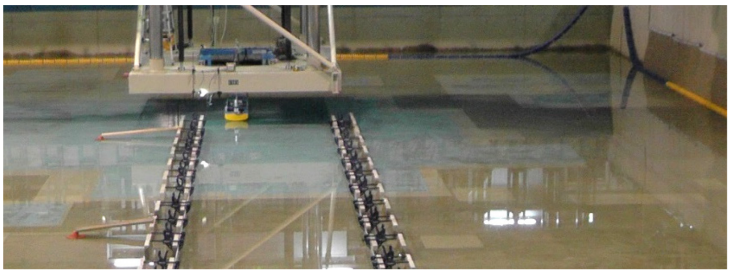

Figure 2. The model of the canal installed in the model basin.

The shallow water condition is produced by changing water depth and the canal condition is produced by placing walls supported by concrete blocks in the model basin as shown in Figure 2. The water depth and canal width are set as same as the computation, shown in Table 2 and details of the condition are described in the next section. The length of the channel is 20m, which is eight times the length of the ship. Both ends of the channel are open to prevent wave reflection.
The model ship is equipped with a rudder and propeller just like the CFD calculations.

3 TEST SHIP AND CONDITIONS

3.1 TEST SHIP

The KCS container ship was selected as the test ship. Principal particulars of the ship are shown in Table 1. CFD computation conditions are based on that of model experiments. The radius of gyration kyy/L is assumed to be 0.25. CFD computations are conducted in nondimensional, in which the water density, the ship length and the flow velocity are 1. The Froude number Fr and the Reynolds number Re are set as the same as in model test.

Table 1. Principal particulars of KCS

Scale	Full	Model Experiment	CFD
L(m)	230	2.5	1(nondim)
d(m)	10.8	0.117	0.047(nondim)
U(m/s)	4.116	0.429	1(nondim)
Lcb(%)	1.48	1.48	1.48
Fr	0.087	0.087	0.087
Re*	7.96e8	9.42e5	9.42e5

*Calculated by water properties at 15deg(C)

3.2 CONDITIONS

The computational grid system consists of three blocks, that is the hull, rudder and external region. Three geometrical conditions are computed by exchanging only the grid of the external region. The geometrical size of the external region is shown in Table 2. The total numbers of computational cells are 6,089,728 (canal), 7,017,984 (shallow water) and 7,931,904 (deep water). The computational region of canal and ship hull are shown in Figure 3. The inflow boundary position is 2.1 times the ship length from the midship, and the outflow boundary position is 3.17 times the ship length from the midship for all case. The outer boundary position in deep water case is 1.37 times the ship length in horizontal direction and 1.22 times the ship length in vertical direction. The side boundary position in shallow water case is the same as that of deep water. The boundary conditions at channel walls and bottom are tunnel conditions (same as the main carriage speed for flow velocity, Neumann condition for level set function and pressure).
The propeller revolution number used in the model tests and CFD calculations are shown in Table 3. Although the CFD calculation is dimensionless, it is shown converted to rps, the same as the model test. Rotational speeds in CFD and tank test are in good agreement. Hull resistance increases in shallow water and canal conditions and so does the propeller speed. Tank experiment for deep water conditions is not conducted and remains as the future task.

Table 2. Computational domain conditions converted to full scale

Type	Deep	Shallow	Canal
Water depth(m)	-	16	16
Canal width(m)	-	-	180

Table 3. Propeller revolution number (converted to model scale, in rps)

	Deep	Shallow	Canal
Experiment	-	6.8	7.1
CFD	6.5	6.7	7.1

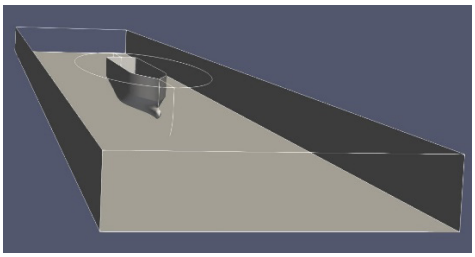

Figure 3. Computational region for canal case.

As for PMM test conditions, one large-amplitude pure swaying motion (sway amplitude=300mm in model scale and 0.123 times ship length) condition and one pure yawing motion condition (nondimensional yaw rate amplitude =0.1) are selected. The PMM motions are given around the centreline of the channel. The period of PMM motion is set to 25sec in model scale, which was determined so that the travel distance for one cycle is just within the length of the channel. The amplitude was decided to prevent the ship from approaching too close to the side wall of the channel.

4 RESULTS AND DISCUSSION

4.1 RESTRICTED WATER EFFECTS ON HYDRODYNAMIC FORCES AND MOMENT

Computed time history of longitudinal force, lateral force and yawing moment are shown in Figure 3. The forces and moment acting on the hull and rudder are integrated and nondimensionalized by ship length L, ship speed U and water density ρ. C_X, C_Y and C_N are nondimensionalized coefficients. The horizontal axis is the nondimensionalized time. The lateral displacement nondimensionalized by ship length is also shown in the figure as “posY”.

The graphs show a strong shallow water effect and a rather weak canal side wall effect. For C_X, the cyclic component appears to increase significantly in the shallow and canal condition. This means that the 2nd-order and higher terms in polynomial hydrodynamic force model have increased. The amplitude of C_Y and C_N in shallow water are almost twice as large as in deep water. The amplitude of hydrodynamic forces and moment in the canal are only slightly larger than in shallow water, but a notable difference is the waveform of the C_Y. When the ship hull approaches the side walls in the canal, the C_Y waveform peak plateaus and becomes different from a sinusoidal waveform. This means that higher-order terms work in the polynomial model of the hydrodynamic force, but at the same time, it also suggests that local fluid phenomena other than the blockage effect occur near the wall. If an analysis of the PMM test is performed by normal procedures in this state, care must be taken because there is a possibility that the effect of the distance between the canal wall and the hull may be mixed with the hydrodynamic derivatives of the sway motion in the analysis.

The results of pure yawing test are also shown in Figure 4. Nondimensional yawing rate is also shown in the figure as “rotZ”. The results are slightly different from pure swaying motion. For C_X, steady resistance component increases in shallow water and canal conditions and change in higher order component is not significant. Small differences are observed in the amplitude of C_Y and C_N, but higher order components are observed in C_Y. However it have to be noted that the amplitude of C_Y is small and might contain errors.

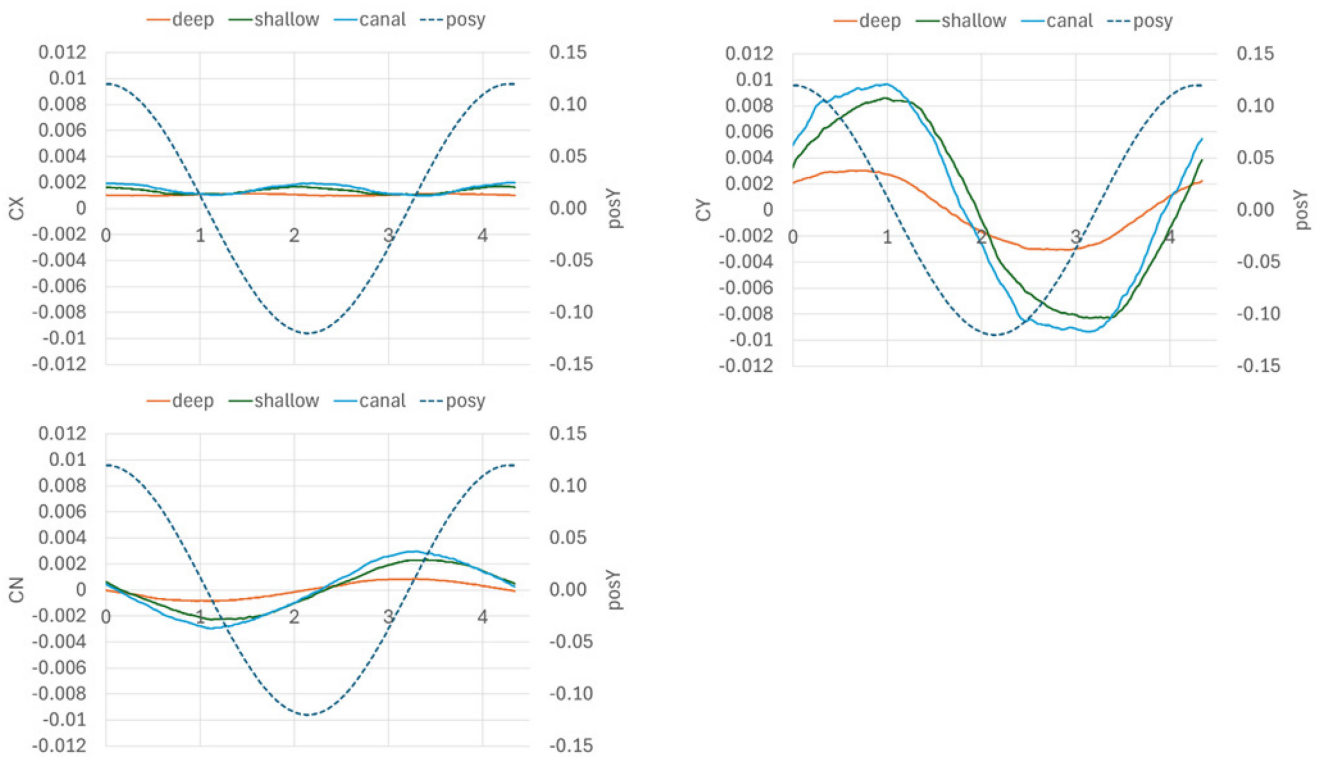

Figure 3. Computed time history of C_X, C_Y, C_N in pure swaying motion.

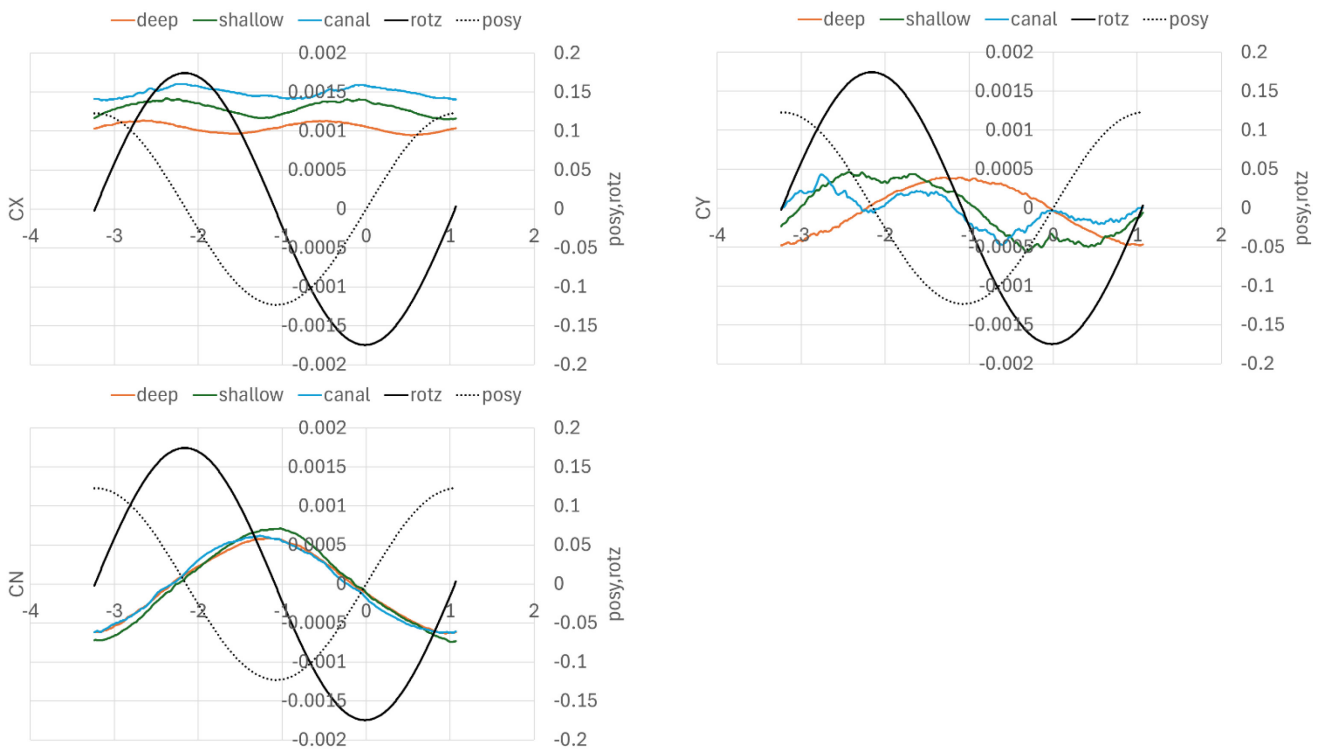

Figure 4. Computed time history of C_X, C_Y, C_N in pure yawing motion.

4.2 COMPARISON OF COMPUTED RESULTS WITH EXPERIMENTAL RESULTS

Computed and experimental results of time variation of hydrodynamic force are shown in Figures 5 and 6. The sampling rate of hydrodynamic force in tank experiment is 100Hz and a low-pass filter was applied with a cutoff frequency of 5 Hz. Ship position and angle are separately recorded by carriage and the sampling rate is 20Hz. Trigger signals are given at the

entrance and exit of the channel, and the measurement data is synchronized later. As for the pure yawing test, small errors are observed between ordered yawing rate (orange solid line) and obtained motion (orange dotted line). There seems to be room for improvement in the precision of the turntable control.

For pure swaying motion, the computed and measured hydrodynamic forces and moment are consistent over time. Their amplitudes match well, but there is a slight error in their phases. On the other hand, for pure yawing motion, the agreement is not so good both in amplitudes and phases. There are several possible reasons for this:

- Lack of precision in calculations and experiments due to small C_Y values in pure yawing motion
- The effect of inertial forces in unsteady motion is large, and measurement errors account for a large proportion of the hydrodynamic forces after inertial forces are subtracted
- Especially in canals, the length of the canal may be insufficient in comparison with the PMM motion period, due to restrictions on the length of the model basin.

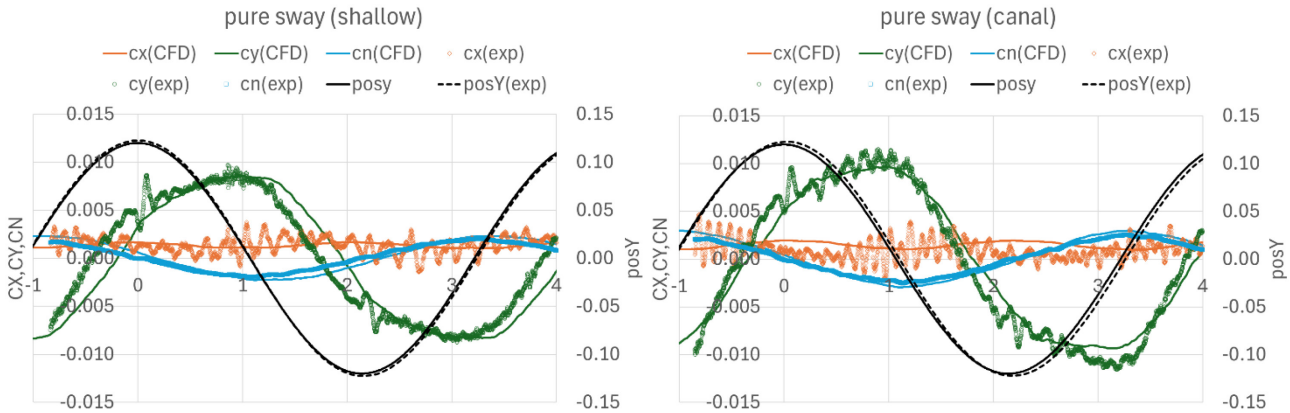

Figure 5. Computed and measured hydrodynamic forces and moment in shallow water (left) and canal (right) conditions during pure swaying motion.

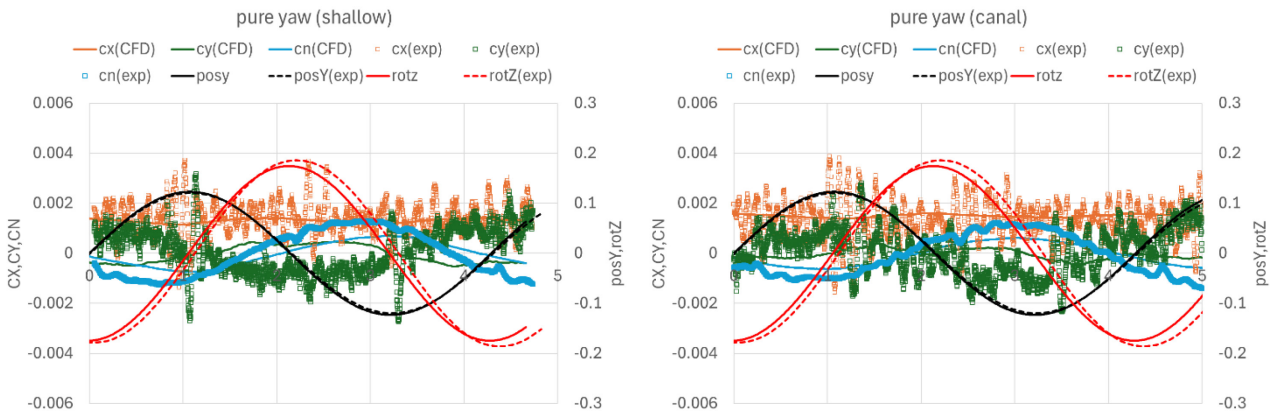

Figure 6. Computed and measured hydrodynamic forces and moment in shallow water (left) and canal (right) conditions during pure yawing motion.

4.3 DISCUSSION ON THE PMM TESTS WITHIN CANALS

The Fourier coefficients obtained by Fourier analysis of the hydrodynamic force are shown in Figure 7. The 0th and 2nd order coefficients of C_X are related to the derivatives of polynomial hydrodynamic force representation. The 1st and 3rd order coefficients of C_Y and C_N are also related to the derivatives of polynomial hydrodynamic force representation. Despite the differences in the time series data, the analyses are in relatively good agreement. Another possible reason is that phase errors do not affect the Fourier analysis results. There is room for improvement in the accuracy of the pure yawing test.

Finally, the pressure distribution at the moment when the hull is closest to the left wall in pure swaying motion is shown in figure 9. In the canal, there is an overall tendency for pressure to decrease around the centre of the ship, which is likely due to blockage effects, but the pressure drop between the portside of the ship and the side wall of the canal is particularly

pronounced. Thus, due to the existence of local interference between the hull and the wall, further research is considered necessary to properly analyse PMM tests in canals and extract the effects of the ship motion parameters.

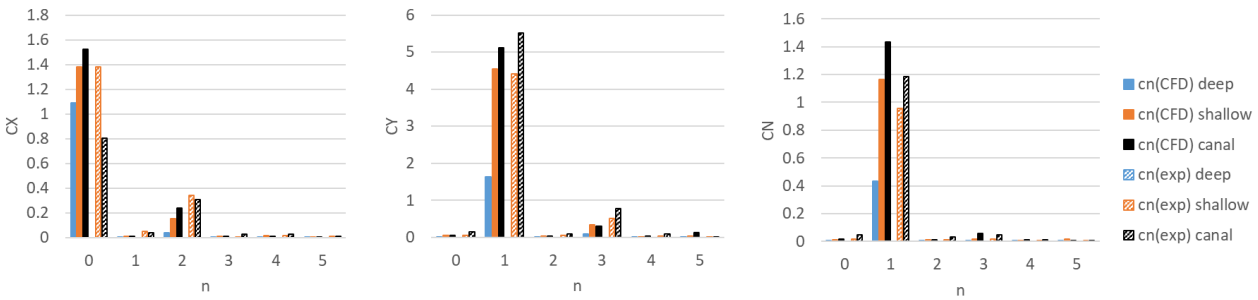

Figure 7. Fourier coefficients in pure swaying motion

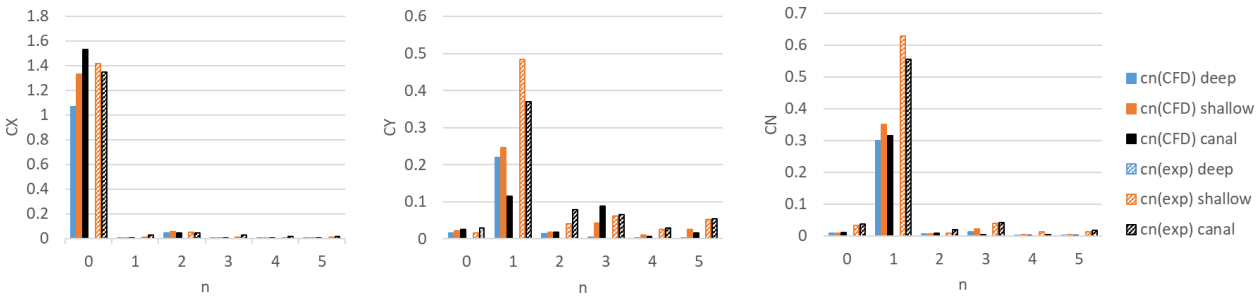

Figure 8. Fourier coefficients in pure yawing motion

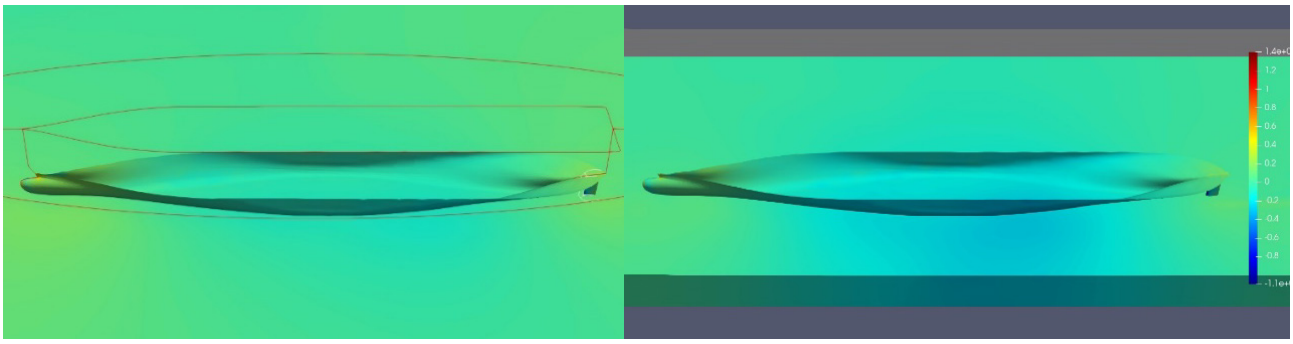

Figure 9. Pressure distribution on hull and bottom during pure swaying motion (left: shallow water, right: canal)

5 CONCLUSIONS

The PMM tests in-channel as a means of obtaining a manoeuvring hydrodynamic force necessary for simulating manoeuvring motions in narrow waterways were investigated using CFD and tank tests. As a result, the following was found.

- For the pure swaying test, the results of the CFD and tank test show good agreement in terms of the Fourier coefficients and time series data.
- For the pure yawing test, the Fourier coefficients of the CFD and tank test are of the same order of magnitude, but the agreement in time series data is lower than for pure swaying case.
- The pure yawing test is difficult to ensure accuracy in terms of experimental measurements.
- In addition to the overall changes in flow velocity and pressure due to blockage effects, there is also local interference between the hull and sidewall, and further research is needed on analysis methods for PMM tests in waterways.

Consequently, viscous CFD can be used to simulate the unsteady hydrodynamic forces acting on a ship undergoing unsteady motion in a narrow waterway.

6 ACKNOWLEDGEMENTS

This work was supported by JSPS KAKENHI Grant Number 24K01104.

7 REFERENCES

Fujino, M., 1968. Experimental Studies on Ship Manoeuvrability in Restricted Waters Part I. International Shipbuilding Progress. Vol. 15, No. 168, pp. 279-301.

Fujino, M., 1970. Experimental Studies on Ship Manoeuvrability in Restricted Waters Part II. International Shipbuilding Progress. Vol. 17, No. 186, pp. 45-65.

Ohmori, T., Ohashi, K., 2022. Numerical Study to Improve the Estimation of Manoeuvring Fluid Force for a Container Ship in Deep and Restricted water, in: Proceedings of the 15th International Symposium on Practical Design of Ships and Other Floating Structures (PRADS 2022), Dubrovnik, Croatia.

Ohashi, K., Hino, T., Kobayashi, H., Onodera, N., Sakamoto, N., 2019. Development of a structured overset Navier-Stokes solver with a moving grid and full multigrid method. J. Mar. Sci. Technol. 24-3, pp. 884-901.

8 AUTHORS BIOGRAPHY

Takuya Ohmori worked at Technical Research Center of Japan Marine United Corporation and is now head of marine dynamics research group at National Maritime Research Institute (NMRI). He is responsible for research on ship manoeuvrability. His previous experience includes application of CFD in various aspects of ship manoeuvrability.

Kunihide Ohashi served as head of CFD research group and is currently deputy director of fluids engineering and ship performance evaluation department at NMRI. He is responsible for the development of CFD software and one of the development members of NAGISA.

Yoshitaka Furukawa currently holds the position of professor at the Department of Marine Systems Engineering, Faculty of Engineering, Kyushu University. He is responsible for research and education regarding ship dynamics.

Hiroshi Ibaragi currently holds the position of professor at the Department of Marine Systems Engineering, Faculty of Engineering, Kyushu University. He is responsible for research and education regarding ship dynamics.

Yuya Matsunaga conducted research on computational fluid dynamics at the master course of Graduate School of Engineering, Kyushu University. He now belongs to the Fabrication Group of the Tsu shipyard of Japan Marine United Corporation.

HYDRODYNAMIC FORCES ACTING ON SHIP RUNNING IN CURVED WATERWAY WITH CONSTANT RADII

Yoshitaka Furukawa, Kyushu University, Japan Hiroshi Ibaragi, Kyushu University, Japan

Takuya Ohmori, National Maritime Research Institute, Japan Kunihide Ohashi,

National Maritime Research Institute, Japan

Yuya Matsunaga, Japan Marine United Corporation, Japan

HYDRODYNAMIC FORCES ACTING ON SHIP RUNNING IN CURVED WATERWAY WITH CONSTANT RADII

YOSHITAKA FURUKAWA, KYUSHU UNIVERSITY, JAPAN
HIROSHI IBARAGI, KYUSHU UNIVERSITY, JAPAN
TAKUYA OHMORI, NATIONAL MARITIME RESEARCH INSTITUTE, JAPAN
KUNIHIDE OHASHI, NATIONAL MARITIME RESEARCH INSTITUTE, JAPAN
YUYA MATSUNAGA, JAPAN MARINE UNITED CORPORATION, JAPAN

SUMMARY

Accurate understanding of a ship's manoeuvrability in confined waterways is extremely important to ensure the safety of ship navigation. In order to establish mathematical models of hydrodynamic forces acting on a ship running in curved confined waterways, it is necessary to investigate the influence of turning motion on the hydrodynamic forces. In this study, hydrodynamic forces acting on a ship model towed in three types of confined waterways, a straight waterway and two curved waterways with constant radii were measured. Furthermore, the hydrodynamic forces were calculated by CFD simulation method using the NAGISA code developed by NMRI. The three types of waterways used in the captive model tests were reproduced in the CFD simulations using overset grid technique. Based on a comparison of the steady values of measured and simulated hydrodynamic forces, the applicability of the CFD simulation method to such problems is discussed.

NOMENCLATURE

L	Ship length (m)
B	Ship breadth (m)
d	Ship draft (m)
C_B	Block coefficient (-)
U	Ship speed (m/s)
n_{PW}	Number of propeller rotations in waterway (rps)
n_{PO}	Number of propeller rotations in open water (rps)
Fr	Froude number (-)
Re	Reynolds number (-)
H	Water depth (m)
W	Width of a waterway (m)
L_W	Length of a waterway (m)
R	Radius of the centerline of a curved waterway (m)
β	Drift angle (deg.)
r	Yaw rate (rad./sec.)
δ	Rudder angle (deg.)
η	Lateral deviation from the centerline of a waterway (m)
η_0	Distance from the centerline of a waterway to the centerline of a ship model touching with sidewall (m)
X	Longitudinal force acting on a ship (N)
Y	Lateral force acting on a ship (N)
N	Yawing moment acting on a ship (N-m)
X_H	Longitudinal force acting on a hull including interaction among a hull, a propeller and a rudder (N)
Y_H	Lateral force acting on a hull including interaction among a hull, a propeller and a rudder (N)
N_H	Yawing moment acting on a hull including interaction among a hull, a propeller and a rudder (N-m)
T	Propeller thrust (N)
F_N	Rudder normal force (N)
F_T	Rudder tangential force (N)
ρ	Density of water (kg/m^3)
$'$	Non-dimensional value (-)

1 INTRODUCTION

Accurate understanding of a ship's manoeuvrability in confined waterways is extremely important to ensure the safety of ship navigation. Although there are many studies dealing with the ship manoeuvrability in confined water, the target of most studies is to tackle with problems related to straight motion of a ship in straight waterways (Vantorre et al., 2003; Lataire et al., 2009; Sano et al., 2012; Furukawa et al., 2015). However, in order to establish mathematical models of hydrodynamic forces acting on a ship running in curved confined waterways, it is necessary to investigate the influence of turning motion on hydrodynamic forces acting on a ship, since the actual waterways are curved. From this point of view, Fujino (1968, 1970) conducted oblique towing tests and PMM tests in a straight waterway and proposed mathematical model to express hydrodynamic forces acting on a ship by the combination of linear terms with respect to drift angle, yaw rate and lateral deviation from the centerline of the waterway. However, it is considered that the effects of variable distance to the sidewalls of the waterway are mixed in the linear terms of drift angle and yaw rate.

In this study, captive model tests both in a straight confined waterway and curved confined waterways with constant radii were conducted to investigate the effect of drift angle, yaw rate and lateral deviation on hydrodynamic forces acting on a ship model. Hydrodynamic forces acting on a hull, propeller thrust and rudder force of a model of KCS of 2.5m in length towed in the confined waterways were measured. Three types of confined waterways, a straight waterway and two curved waterways with radii of 50m and 25m in model scale, were installed in the Seakeeping and Manoeuvring Basin in Kyushu University. Drift angle, rudder angle and lateral deviation from the centerline of the waterways were chosen as parameters for the captive model tests. The measured hydrodynamic forces both in the straight and the curved waterways with constant radii are compared with those measured in open water with the same water depth and the influence of the existence of sidewalls and turning motion in the curved waterways on hydrodynamic forces acting on a ship is discussed.

Furthermore, the hydrodynamic forces were calculated by CFD (Computational Fluid Dynamics) simulation method using the NAGISA code developed by NMRI (National Maritime Research Institute) (Ohashi et al., 2019). The three types of waterways used in the captive model tests were reproduced in the CFD simulations using overset grid technique. Based on a comparison of the steady values of measured and simulated hydrodynamic forces, the applicability of the CFD simulation method to such problems is discussed.

2 MODEL TEST SET-UP

2.1 SHIP MODEL

Captive model tests both in confined waterway condition and in shallow and unrestricted water condition were carried out for a model of KCS. The principal particulars of KCS are shown in Table 1. The ship model is made at a scale of 1:92 and tested as appended hull equipped with a fixed-pitch five-bladed propeller with right rotation and a rudder. Heave and pitch of the ship model are free and roll was fixed during the measurement of hydrodynamic forces.

Table 1. Principal particulars of KCS

	Ship	Model
Ship length, L (m)	230.0	2.50
Ship breadth, B (m)	32.2	0.350
Ship draft, d (m)	10.8	0.117
Block coefficient, C_b (-)	0.661	
Ship speed, U (m/s)	4.116	0.429
Reynolds number, Re (-)	7.96×10^8	9.42×10^5
Froude number, Fr (-)	0.087	

2.2 ENVIRONMENTAL CONDITION

The captive model tests were conducted at the Seakeeping and Manoeuvring Basin in Kyushu University. The principal dimensions of the basin are 38.8 m in length, 24.4 m in width and 0.2-2.0 m of water depth. Shallow water conditions are implemented by draining away water from the basin. The accuracy of the level of flatness of the whole bottom is less than ±2.0 mm. It is sufficiently accurate to investigate shallow water effect on the manoeuvrability of a ship model of 2.5 m long with under keel clearance of 56.2 mm which is discussed later.

Three types of confined waterways with vertical sidewalls, a straight waterway and two curved waterways with radii of 50.0 m and 25.0 m in model scale, were installed in the basin. The cross-sectional shape of those waterways is rectangular. The main dimensions of the waterways are shown in Table 2. The water depth was set based on the ratio of the draft of the

container carrier EVER GIVEN to the average depth of the Suez Canal. The width of the waterways was set so that the ratio of the cross-sectional area of the ship model to the cross-sectional area of the waterway was approximately 12%.

Table 2. Main dimensions of waterways

Water depth, H (m)	0.174
Width of waterway, W (m)	1.957
Length of waterway, L_W (m)	17.71
Radius of the centerline of curved waterway, R (m)	∞, 50.0, 25.0
Width of waterway / ship breadth ratio, W/B (-)	5.59
Water depth / ship draft ratio, $H/\ d$ (-)	1.48

The confined waterways were installed by combining vinyl chloride plates of 1.0 m long and 2.0 m long. The vinyl chloride plates were held in place by vises and U-shaped blocks. Rubber was mounted both in the gaps between the adjacent vinyl chloride plates and the gaps between the vinyl chloride plates and the bottom of the basin to prevent leakage. Overviews of the three types of the installed confined waterways are shown in Figure 1 and the ship model towed in the curved waterway with radius of 25.0 m is shown in Figure 2.

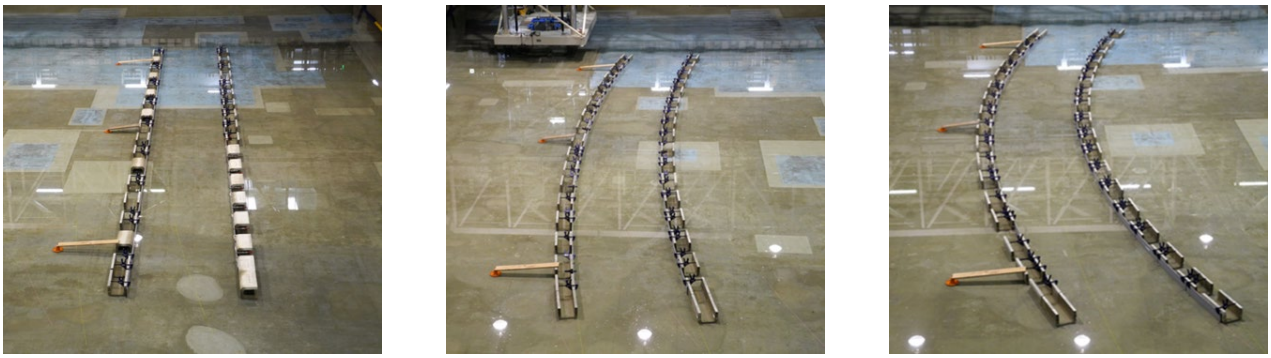

(a) straight waterway ($R = \infty$) **(b) curved waterway ($R = 50.0$m)** **(c) curved waterway ($R = 25.0$m)**

Figure 1. Three types of confined waterways

Figure 2. Ship model towed in curved waterway with radius of 25.0 m

2.3 COORDINATE SYSTEM

Coordinate systems used in the captive model tests are shown in Figure 3. o-xy shown in Figure 3(a) is a ship-fixed coordinate system. The origin o is located at the midship of the ship model. The orientations of the positive coordinate axes are directed from the origin o to bow for the longitudinal axis x and towards starboard side for the lateral axis y. Non-dimensional yaw rate of the ship model is automatically determined from the radii of the curved waterways as follows;

$$r' = \frac{rL}{U} = \frac{rL}{rR} = \frac{L}{R}. \tag{1}$$

Lateral deviation from the centerline of the waterways η shown in Figure 3(b) are presented in non-dimensional form using the following equation;

$$\eta' = \frac{\eta}{\eta_0} = \frac{\eta}{\frac{1}{2}W - \frac{1}{2}B}. \tag{2}$$

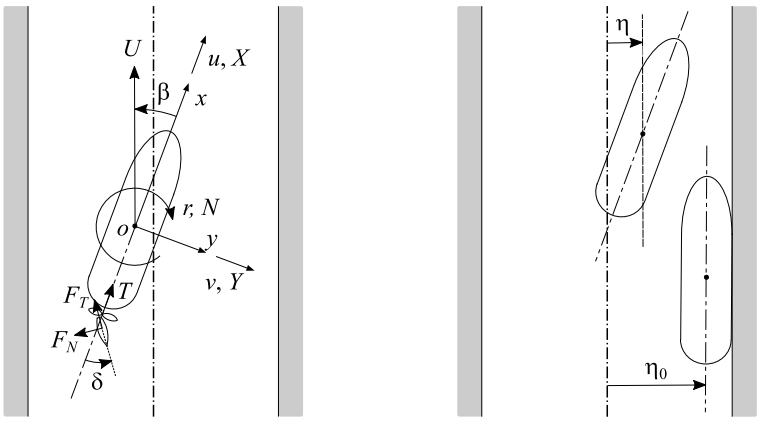

(a) Ship-fixed coordinate system **(b) Definition of η and η_0**

Figure 3. Coordinate systems

η_0 is a distance from the centerline of the waterways to the centerline of a ship model touching with sidewall as shown in Figure 3(b). The signs of η and η' are positive when the ship model deviate to starboard side.

2.4 MODEL TEST PROGRAM

Drift angle β, non-dimensional yaw rate $r'(= rL/U)$, lateral deviation from the centerline of the confined waterways in non-dimensional form η' and rudder angle δ were chosen as parameters for the captive model tests. It was assumed that the ship model was towed keeping constant distance from the centerline of the waterways in the captive model tests. Settings for each parameter are shown in Table 3. Some combinations of the parameters were omitted because of the limitation of variable range of drift angle β near the sidewalls and relation between the signs of drift angle β and yaw rate r. The numbers of propeller rotations n_{PW} and n_{PO} are obtained by conducting self-propulsion test both in the straight waterway and open water, respectively.

When the ship model is towed on an arc line laterally off the centerline in the curved waterways, the radius of the arc line is slightly different from the radius of the centerline. On the other hand, towing speed is constant for all experimental conditions. It implies that the value of non-dimensional yaw rate also differs slightly depending on the radii of the arc lines. Hereafter, the value of non-dimensional yaw rate on the centerline is used for the measurement on the shifted arc lines for convenience.

Table 3. Settings for each parameter

U (m/s)	0.429
n_{PW} (rps)	7.13
n_{PO} (rps)	6.77
β (deg.)	0.0, ±5.0, ±10.0
r'	0.00, ±0.05, ±0.10
η'	0.00, ±0.25, ±0.50, ±0.75
δ (deg.)	0.0, ±15.0, ±30.0

2.5 MEASUREMENTS

Longitudinal force X, lateral force Y and yawing moment N acting on the appended hull with a propeller and a rudder were measured at the midship when the ship model was towed both in the confined waterways and open water at propelled condition. Propeller thrust T, rudder normal force F_N and rudder tangential force F_T were also measured in each condition. Hydrodynamic forces produced by a propeller and a rudder and hydrodynamic interaction among a hull, a propeller and a rudder are included in the measured longitudinal force X, lateral force Y and yawing moment N. Therefore, the hydrodynamic forces produced by the propeller and the rudder were excluded to compare with the results of CFD calculations. Longitudinal and lateral forces acting on a hull X_H, Y_H and yawing moment acting on a hull N_H including interaction among a hull, a propeller and a rudder are obtained as follows;

$$\left.\begin{aligned} X_H &= X - T - F_T\cos\delta + F_N\sin\delta\,, \\ Y_H &= Y + F_T\sin\delta + F_N\cos\delta\,, \\ N_H &= N + \frac{L}{2}(F_T\sin\delta + F_N\cos\delta). \end{aligned}\right\} \tag{3}$$

These hydrodynamic forces are shown in the following non-dimensional form;

$$X'_H, Y'_H, T', F'_N, F'_T = \frac{X_H, Y_H, T, F_N, F_T}{\frac{1}{2}\rho L d U^2}, \quad N'_H = \frac{N_H}{\frac{1}{2}\rho L^2 d U^2}. \tag{4}$$

3 MEASURED HYDRODYNAMIC FORCES

3.1 COMPARISON BETWEEN HYDRODYNAMIC FORCES MEASURED IN WATERWAYS AND OPEN WATER

Comparison between hydrodynamic forces measured in the waterways and open water in non-dimensional form is shown in Figure 4. The ship model was towed on the centerline of the waterways ($\eta' = 0$) at a rudder angle of 0°. Figure 4 shows the variation of hydrodynamic forces with respect to drift angle β and non-dimensional yaw rate r'. The rectangles in the figure indicate hydrodynamic forces measured in the waterways and the triangles show those in open water. Dotted and dashed lines connecting each mark are shown in the figure for reference.

It is observed in Figure 4(a) that the absolute values of the longitudinal force acting on a hull X'_H in the waterways are greater than those in open water. No significant difference is observed in the trend of variation of the values with respect to drift angle β and non-dimensional yaw rate r', though there is some irregular variations in the measurements in the waterways. The variations of lateral force acting on a hull Y'_H with respect β and r' are shown in Figure 4(b). The effect of drift angle and non-dimensional yaw rate is more pronounced in the lateral force measured in the waterways. A similar trend can be observed in Figure 4(c) showing the variations of yawing moment acting on a hull N'_H. Figure 4(d) presents the variations of propeller thrust T'. With the increase in the absolute values of longitudinal force acting on a hull in the waterways, propeller thrust T' which is required to achieve set speed also increases. Figure 4(e) shows the variations of rudder normal force F'_N at a rudder angle of 0°. As in the case of lateral force and yawing moment acting on a hull, the effect of drift angle and non-dimensional yaw rate is more significant in the waterways.

3.2 EFFECT OF LATERAL DEVIATION FROM CENTERLINE IN WATERWAYS ON HYDRODYNAMIC FORCES

Effect of lateral deviation from the centerline in the waterways on hydrodynamic forces is shown in Figure 5. The ship model was towed at a rudder angle of 0°. There are irregular variations in some of the measured longitudinal force acting on a hull X'_H similar to the results shown in Figure 4(a). As explained in the section 2.5, hydrodynamic forces and moment acting on a hull were obtained by excluding hydrodynamic forces and moment produced by the propeller and the rudder from total forces and moment measured at the midship of the ship model. As for X'_H, it is considered that the effect of measurement error included in both X'_H and T' is particularly pronounced. It can be seen that the absolute values of longitudinal force tend to increase as the ship hull approaches the sidewall.

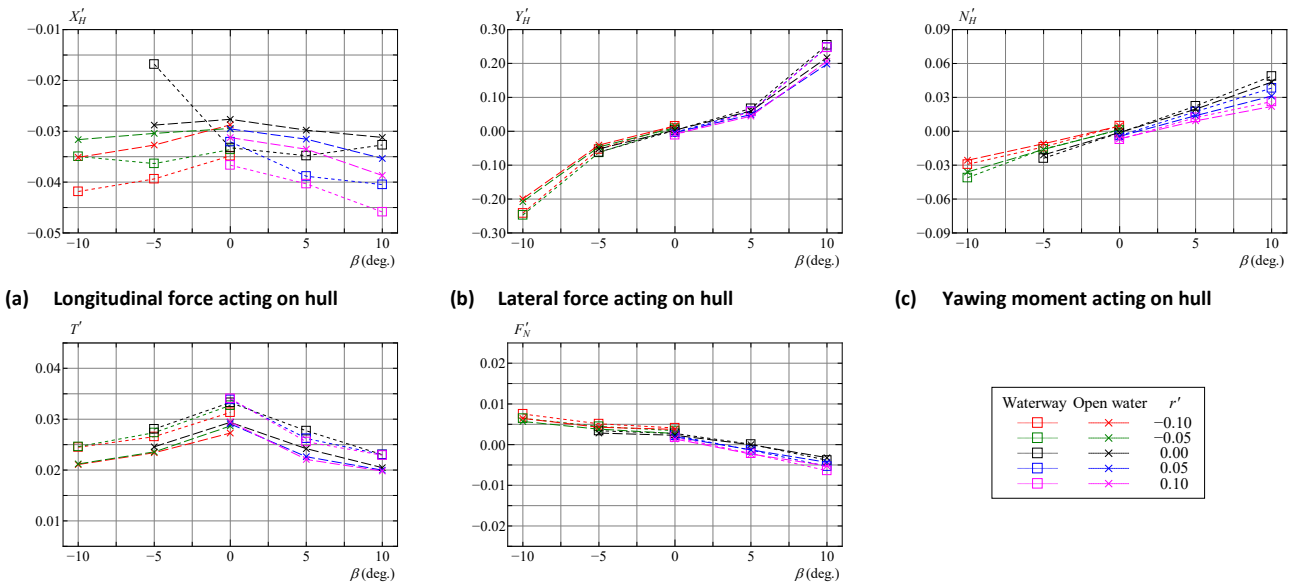

(a) Longitudinal force acting on hull (b) Lateral force acting on hull (c) Yawing moment acting on hull

(d) Propeller thrust (e) Rudder normal force

Figure 4. Comparison between hydrodynamic forces measured in waterways and open water (η'=0, δ=0°)

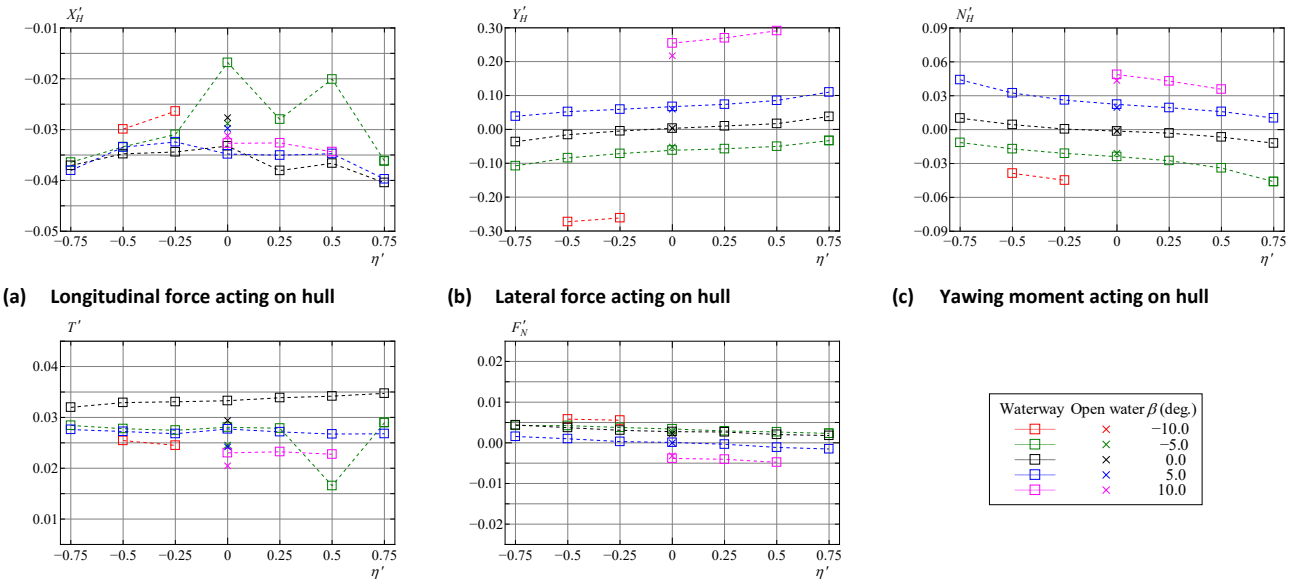

(a) Longitudinal force acting on hull (b) Lateral force acting on hull (c) Yawing moment acting on hull

(d) Propeller thrust (e) Rudder normal force

Figure 5. Effect of lateral deviation from centerline in waterways on hydrodynamic forces (r'=0, δ=0°)

Suction effect due to proximity to the sidewall is observed in lateral force Y'_H and yawing moment N'_H shown in Figure 5(b) and (c). Figure 5(d) presents the variations of propeller thrust T' with respect to non-dimensional lateral deviation from the centerline of the waterways η' and drift angle β. When the drift angle is 0°, the values of propeller thrust T' tend to increase slightly as the ship hull approaches to the sidewall in starboard side. For the other drift angles, there is a minute variation with respect to η', but no clear trend can be identified. On the other hand, as for the rudder normal force F'_N at a rudder angle of 0°, the values tend to change moderately with lateral deviation η'.

4 CFD CALCULATION

4.1 CFD SOLVER AND COMPUATIONAL GRID

CFD Solver NAGISA developed by NMRI (National Maritime Research Institute, Japan) was used to calculate hydrodynamic forces acting on the model of KCS. The NAGISA is a structured overset Navier-Stokes solver with a moving grid and full multigrid method. EASM (Rumsey and Gatski, 2001) is applied to calculate Reynolds stresses. A single-phase localized level-set method is employed for free surface treatments.

The ship model is an appended hull with a propeller and a rudder as same as the ship model used in the captive model tests. Heave and pitch of the ship model are free to take the influence of trim and sinkage in confined waterway into account. Figure 6 shows the global view of a computational grid and Figure 7 indicates the components of the computational grid near the hull. Computational grid consists of three blocks, such as a hull block, a rudder block and an external domain block and number of cells for each block is presented in Table 4. Length of the computation grids of straight and curved waterways is about 5.2 times of ship model length L. The inflow and outflow boundaries are 2.1 L forward and 3.17 L backward from the midship of the ship model, respectively. The boundary conditions on the bottom and sidewalls of the waterways are set as the inflow condition which replicate the experimental condition in the ship fixed coordinate system that the inflow with the ship speed is coming from the inflow boundary and the Neumann condition is applied to the pressure and level-set function. Motions of the ship model are accounted for by a moving grid technique with a grid-deforming methodology.

Propeller thrust is calculated using a simplified propeller model. The number of propeller rotations is determined based on the calculation of self-propulsion test on the centerline of the straight waterway.

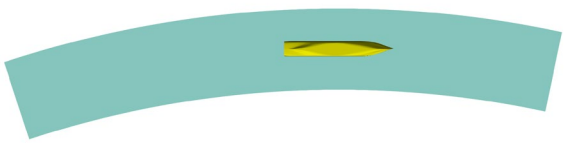

Figure 6. Global view of computational grid

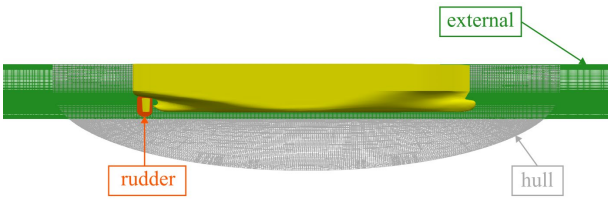

Figure 7. Components of computational grid near hull

Table 4. Number of cells

Hull block		4,822,272
Rudder block	$\delta = 0°, \pm 15°$	395,901
	$\delta = \pm 30°$	378,873
External domain block	Waterway	1,366,875
	Open water	948,750

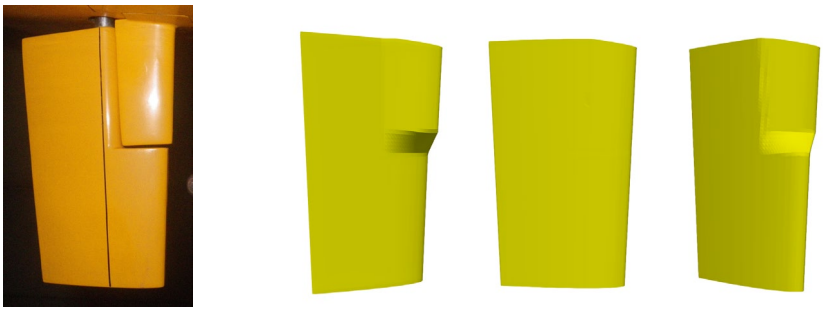

(a) Captive model tests **(b) CFD calculations**

Figure 8. Rudder models used in captive model tests and CFD calculations

Figure 8(a) presents the shape of a rudder which is equipped on the ship model. The rudder is divided into two components, such as a rudder horn and a movable rudder surface. On the other hand, the rudder horn and the movable rudder surface are integrated in a rudder model used in the CFD calculations as shown in Figure 8(b). Considering the comparison with measured rudder force, hydrodynamic forces acting on the rudder horn and the movable rudder surface are calculated separately. Hydrodynamic forces acting on the rudder horn is considered as a part of hydrodynamic forces acting on a hull.

4.2 CALCULATION CONDITIONS

Calculation conditions were set up similarly to the settings for each parameter shown in Table 3. In the CFD calculations, some calculations were carried out for combinations of parameter values that were not measured in the captive model tests.

5 COMPARISON BETWEEN CALCULATION AND MEASURED HYDRODYNAMIC FORCES

5.1 HYDRODYNAMIC FORCES WITH RESPECT TO β AND r'

Comparison between calculated and measured hydrodynamic forces for typical combinations of parameters shown in Table 3 are presented in this section, because the number of the combinations is very large.
Figure 9 shows comparison of the hydrodynamic forces with respect to drift angle β and non-dimensional yaw rate r'. In this comparison, $\eta' = 0$ means that ship was towed on the centerline of the waterways and rudder angle $\delta = 0°$. The circles and rectangles in the figure indicate calculated and measured hydrodynamic forces respectively. Solid and dotted lines connecting each mark are shown in the figure for reference.
It is observed in Figure 9(b) and (c) that calculated lateral force Y'_H and yawing moment N'_H at $\beta = 0°$ and $\pm 5°$ show good agreement with measured results, but they were underestimated at $\beta = \pm 10°$. The difference between the calculated and measured values is remarkable for longitudinal force X'_H and propeller thrust T' as shown in Figure 9(a) and (d). Regardless of the value of non-dimensional yaw rate r', the measured thrusts are symmetric with respect to β, whereas the calculated thrusts show asymmetry. It is observed in Figure 9(e) that the qualitative trends of the variations of F'_N to β can be expressed, but quantitatively there are differences even if $\beta = 0°$. The longitudinal forces which are introduced by the hull, rudder forces and propeller thrust may be unstable due to relatively lower Reynolds number at the captive model tests. Additionally, the simplification of the rudder model shown in Figure 8 resulted in a poor reproduction, however, the things cannot be for certain at this moment.

5.2 HYDRODYNAMIC FORCES WITH RESPECT TO η' AND β

Figure 10 presents comparison between calculated and measured hydrodynamic forces with respect to non-dimensional lateral deviation from the centerline of the waterways η' and drift angle β. It seems that the qualitative trends of the variations of X'_H and T' to β is expressed well, but quantitative agreement is not enough especially for $\beta = \pm 10°$. There is good agreement between calculated Y'_H, N'_H and F'_N and their measurements at $\beta = 0°$ and $\pm 5°$. The tendency of the variations

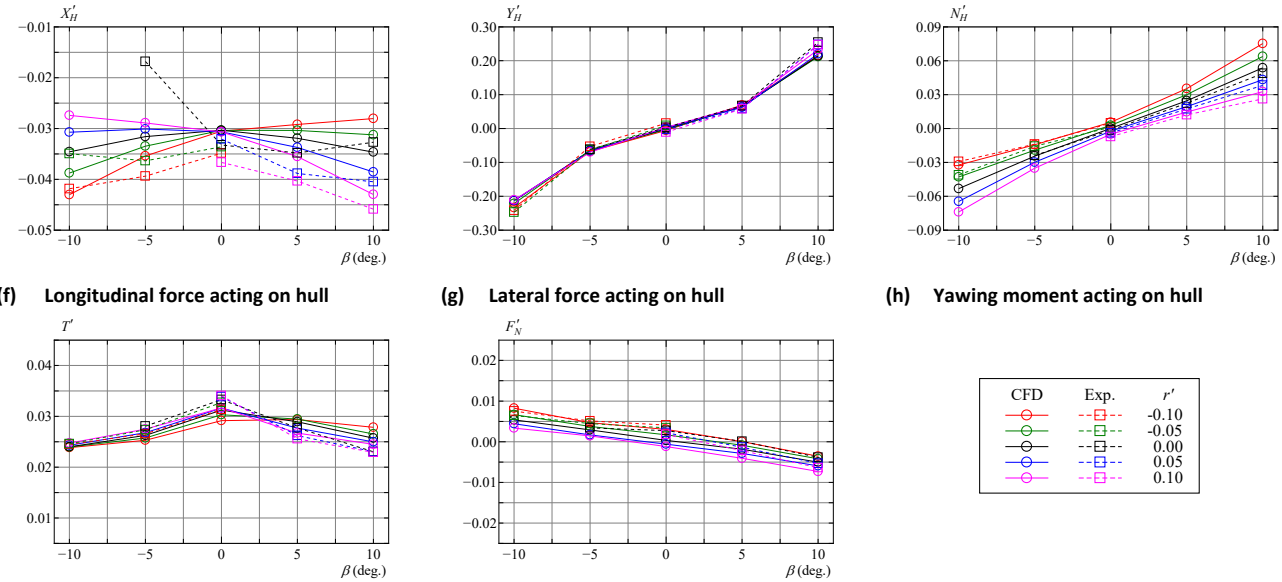

(f) Longitudinal force acting on hull (g) Lateral force acting on hull (h) Yawing moment acting on hull

(i) Propeller thrust (j) Rudder normal force

Figure 9. Comparison between calculated and measured hydrodynamic forces with respect to β and r' (η'=0, δ=0°)

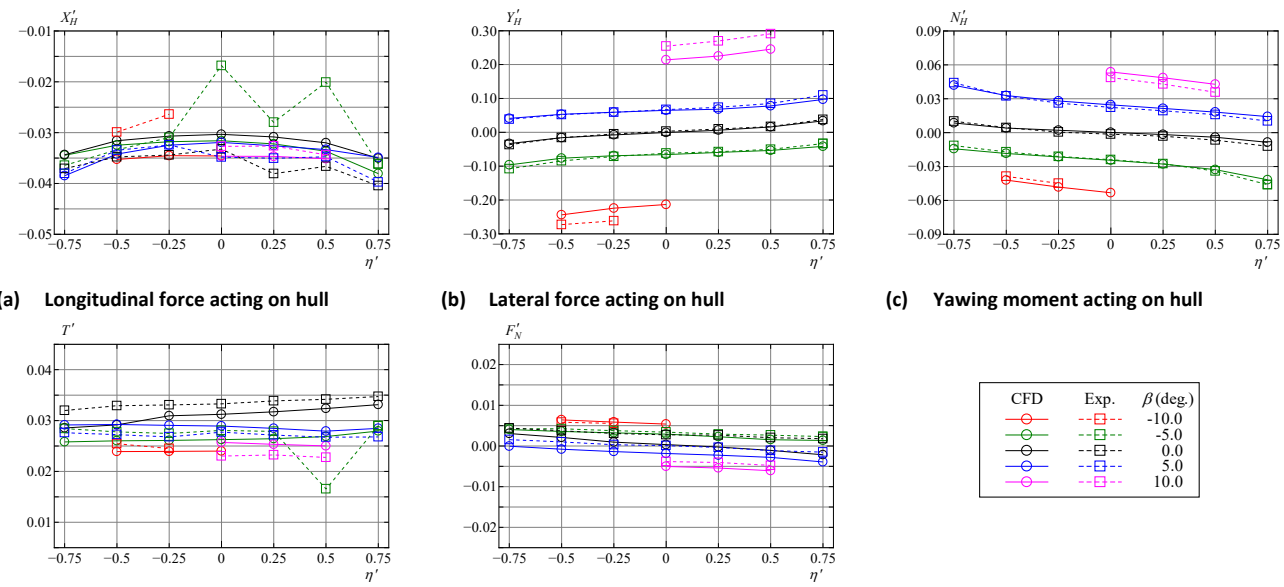

(a) Longitudinal force acting on hull (b) Lateral force acting on hull (c) Yawing moment acting on hull

(d) Propeller thrust (e) Rudder normal force

Figure 10. Comparison between calculated and measured hydrodynamic forces with respect to η' and β (r'=0, δ=0°)

of these hydrodynamic forces with respect to lateral deviation in the waterways is well represented by the CFD calculation. However, the differences between the calculated and measured values widen as drift angle increases.

5.3 HYDRODYNAMIC FORCES WITH RESPECT TO r' AND η'

Figure 11 presents comparison between calculated and measured hydrodynamic forces with respect to non-dimensional yaw rate r' and non-dimensional lateral deviation from the centerline of the waterways η'. The qualitative trends of the variations of all hydrodynamic forces and moment to r' are approximately expressed. Though the quantitative agreement of the hydrodynamic forces and moment is not so good, the variations of them with respect to η' are small.

5.4 RUDDER NORMAL FORCE WITH RESPECT TO β AND δ

The variations of rudder normal force F'_N with respect to drift angle β and rudder angle δ is shown in Figure 12. Figure 12(a) presents comparison between calculated and measured rudder normal forces in the waterways. As the rudder angle increases, the discrepancy between the calculated and measured values clearly increases. Although the degree of difference

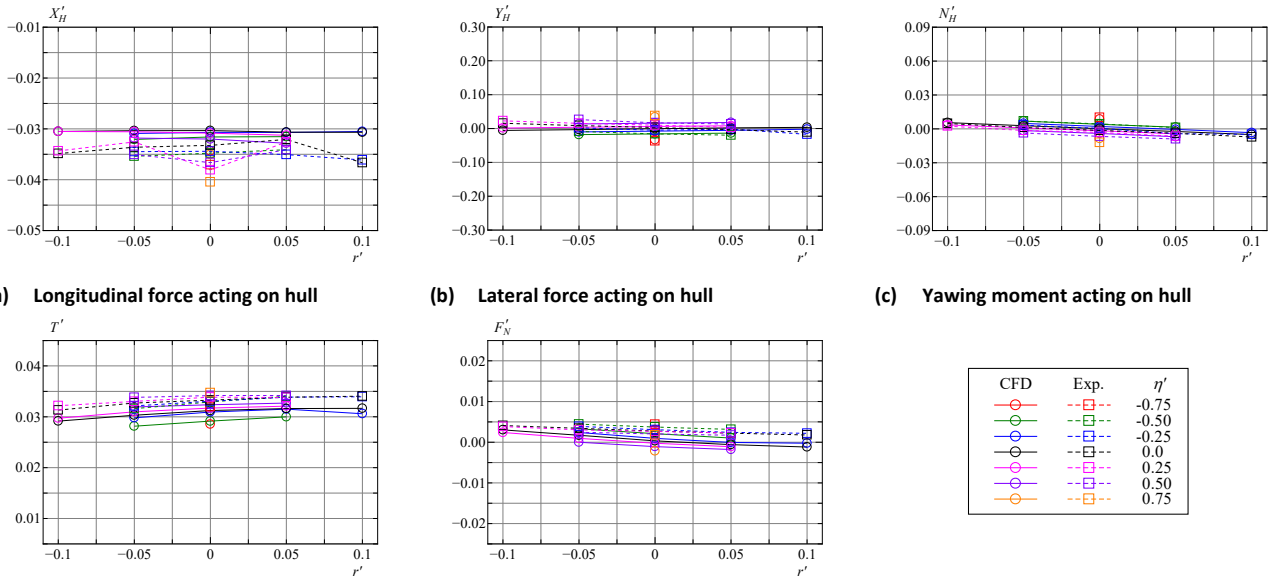

(a) Longitudinal force acting on hull (b) Lateral force acting on hull (c) Yawing moment acting on hull

(d) Propeller thrust (e) Rudder normal force

Figure 11. Comparison between calculated and measured hydrodynamic forces with respect to r' and η' (β=0°, δ=0°)

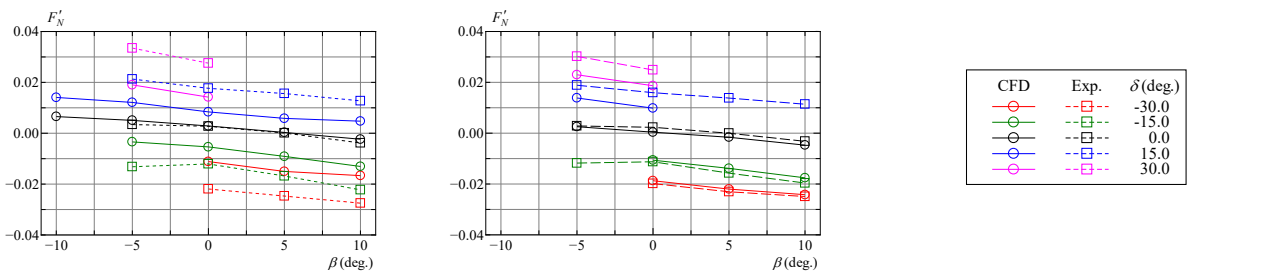

(a) Rudder normal force in waterway (b) Rudder normal force in open water

Figure 12. Comparison between calculated and measured rudder normal force with respect to β and δ (η'=0, r'=0)

is smaller, similar discrepancy between calculated and measured values can be observed in Figure 12(b) showing rudder normal force in open water condition. Therefore, this discrepancy is not a problem unique to the calculations in the waterways.

One possible cause of the discrepancy is the rudder model used in the CFD calculations. As shown in Figure 8(a), there is a small gap between the rudder horn and the movable rudder surface of the rudder equipped on the ship model. On the other hand, the rudder horn and the movable rudder surface are integrated in a rudder model used in the CFD calculations as shown in Figure 8(b). As the rudder angle increases, the difference between the shapes of the rudder models increases, and the flow around the rudder models may differ accordingly. This may have caused the difference in the rudder normal force to increase as the rudder angle increased. Furthermore, this difference in flow around the rudder may have affected the calculation of the propeller thrust and pressure distribution around the stern, so a detailed study of the rudder model is needed.

6 CONCLUSIONS

Hydrodynamic forces acting on a ship model towed in three types of confined waterways, a straight waterway and two curved waterways with constant radii were measured to investigate the influence of turning motion on hydrodynamic forces acting on a ship. Furthermore, the hydrodynamic forces were calculated by CFD simulation method using the NAGISA code developed by NMRI. From the comparison between calculated and measured hydrodynamic forces, the following findings were made.

- The difference between calculated and measured values is remarkable for longitudinal force X'_H and propeller thrust T'.
- Calculated lateral force Y'_H, yawing moment N'_H, rudder normal force F'_N at $\beta = 0°$ and $\pm 5°$ show good agreement with measured results, but they were underestimated at $\beta = \pm 10°$.

- As the rudder angle increases, the discrepancy between the calculated and measured rudder normal force F'_N increases. The discrepancy is observed both in confined waterways and open water.
- One possible cause of the discrepancy is the rudder model used in the CFD calculations. A detailed study of the rudder model is needed.

7 ACKNOWLEDGEMENTS

The computation was carried out using the computer resource offered under the category of General Project by Research Institute for Information Technology, Kyushu University.

8 REFERENCES

Fujino, M., 1968. Experimental Studies on Ship Manoeuvrability in Restricted Waters, Part I, International Shipbuilding Progress. 15-168, pp.279-301.

Fujino, M., 1970. Experimental Studies on Ship Manoeuvrability in Restricted Waters, Part II, International Shipbuilding Progress. 17-186, pp.45-65.

Furukawa, Y., Ibaragi, H., Nakiri, Y., Kijima, K., 2015, Experimental Study of Interaction Forces Acing on Ship Hull by Bank Effect, In: Proceeding of International Conference on Marine Simulation and Ship Maneuverability (MARSIM 2015). Newcastle upon Tyne, United Kingdom, 15 pp.

Lataire, E., Vantorre, M., Eloot, K., 2009, Systematic Model Tests on Ship-Bank Interaction Effects, In: Proceeding of International Conference on Ship Manoeuvring in Shallow and Confined Water: Bank Effects. Antwerp, Belgium, pp.9-22.

Ohashi, K., Hino, T., Kobayashi, H., Onodera, N., Sakamoto, N., 2019. Development of a Structured Overset Navier-Stokes Solver with a Moving Grid and Full Multigrid Method, J. Mar. Sci. Technol. 24-3, pp.884-901.

Rumsey, C. L., Gatski, T. B., 2001, Recent Turbulence Advances Applied to Multielement Airfoil, Computations, J. Aircraft, 38-5, pp.904-910.

Sano, M., Yasukawa, H., Hata, H., 2012, Experimental Study on Ship Operation in Close Proximity to Bank Channel, In: Proceedings of International Conference on Marine Simulation and Ship Manoeuvrability (MARSIM 2012). Singapore, 10 pp.

Vantorre, M., Delefortrie, G., Eloot, K., Laforce, E., 2003, Experimental Investigation of Ship-bank Interaction Forces, In: Proceedings of International Conference on Marine Simulation and Ship Maneuverability (MARSIM '03). Kanazawa, Japan, pp.RC-31-1/9.

9 AUTHORS BIOGRAPHY

Yoshitaka Furukawa currently holds the position of professor at the Department of Marine Systems Engineering, Faculty of Engineering, Kyushu University. He is responsible for research and education regarding ship dynamics.

Hiroshi Ibaragi currently holds the position of assistant professor at the Department of Marine Systems Engineering, Faculty of Engineering, Kyushu University. He is responsible for research and education regarding ship dynamics.

Takuya Ohmori worked at Technical Research Center of Japan Marine United Corporation and is now head of marine dynamics research group at National Maritime Research Institute (NMRI). He is responsible for research on ship manoeuvrability. His previous experience includes application of CFD in various aspects of ship manoeuvrability.

Kunihide Ohashi served as head of CFD research group and is currently deputy director of fluids engineering and ship performance evaluation department at NMRI. He is responsible for the development of CFD software and one of the development members of NAGISA.

Yuya Matsunaga conducted research on computational fluid dynamics at the master course of Graduate School of Engineering, Kyushu University. He now belongs to the Fabrication Group of the Tsu shipyard of Japan Marine United Corporation.

PATH FOLLOWING OF AN UNDERACTUATED SHIP IN RESTRICTED WATERS USING CLOS AND COMPENSATED LQR METHODS

Yu He, School of Ocean and Civil Engineering, Shanghai Jiao Tong University, Shanghai, China

Lu Zou, 1. School of Ocean and Civil Engineering, Shanghai Jiao Tong University, Shanghai, China; 2. State Key Laboratory of Ocean Engineering, Shanghai Jiao Tong University, Shanghai, China

Wei-Min Chen, Shanghai Ship and Shipping Research Institute Co., Ltd., Shanghai, China

Zao-Jian Zou, 1. School of Ocean and Civil Engineering, Shanghai Jiao Tong University, Shanghai, China; 2. State Key Laboratory of Ocean Engineering, Shanghai Jiao Tong University, Shanghai, China

Jin-Lan Li, School of Ocean and Civil Engineering, Shanghai Jiao Tong University, Shanghai, China

PATH FOLLOWING OF AN UNDERACTUATED SHIP IN RESTRICTED WATERS USING CLOS AND COMPENSATED LQR METHODS

YU HE, SCHOOL OF OCEAN AND CIVIL ENGINEERING, SHANGHAI JIAO TONG UNIVERSITY, SHANGHAI, CHINA
LU ZOU*, 1. SCHOOL OF OCEAN AND CIVIL ENGINEERING, SHANGHAI JIAO TONG UNIVERSITY, SHANGHAI, CHINA; 2. STATE KEY LABORATORY OF OCEAN ENGINEERING, SHANGHAI JIAO TONG UNIVERSITY, SHANGHAI, CHINA
WEI-MIN CHEN, SHANGHAI SHIP AND SHIPPING RESEARCH INSTITUTE CO., LTD., SHANGHAI, CHINA
ZAO-JIAN ZOU, 1. SCHOOL OF OCEAN AND CIVIL ENGINEERING, SHANGHAI JIAO TONG UNIVERSITY, SHANGHAI, CHINA; 2. STATE KEY LABORATORY OF OCEAN ENGINEERING, SHANGHAI JIAO TONG UNIVERSITY, SHANGHAI, CHINA
JIN-LAN LI, SCHOOL OF OCEAN AND CIVIL ENGINEERING, SHANGHAI JIAO TONG UNIVERSITY, SHANGHAI, CHINA

SUMMARY

This study presents a control method for ship path following in restricted waters, combining the constrained line-of-sight (CLOS) guidance law with a compensated linear quadratic regulator (LQR) heading controller. In the guidance system, CLOS transforms the path-following task in a narrow channel into a heading control task based on an adaptive look-ahead distance and the tracking error. A sway velocity observer is introduced to eliminate steady-state errors during path following. Furthermore, spatial constraints imposed by channel walls are imposed on the desired heading angle, and the tracking differentiator (TD) is used for smoothing the desired heading angle and yaw rate. In the LQR heading control system, an extended state observer (ESO) is designed for estimating the yaw rate and compensating unmodeled dynamics and external disturbances. Simulation results verify that the proposed controller enables the ship to accurately follow a path in restricted waters while ensuring anti-collision with channel walls.

NOMENCLATURE

$\boldsymbol{A}$	System matrix of the heading control system (-)
A_Y	Lateral projected area of the ship above the waterline (m^2)
B	Breadth (m)
$\boldsymbol{B}$	Input matrix of the heading control system (-)
C_{NA}	Wind pressure-induced yaw moment coefficient (-)
C_{YA}	Wind pressure-induced sway force coefficient (-)
d	Draft (m)
$\boldsymbol{d}$	Disturbance vector of the heading control system (-)
e	Error between the desired and the actual heading angle (°)
$\boldsymbol{e}$	Observer error (-)
$\boldsymbol{G}$	Input matrix of the observer error system (-)
h	Water depth (m)
$\boldsymbol{H}$	System matrix of the observer error system (-)
$\boldsymbol{K}_1$	State feedback gain matrix (-)
$\boldsymbol{K}_2$	Reference gain matrix (-)
K_3	Gain of the total unknown term (-)
K_d	Derivative gain (-)
K_i	Integrate gain (-)
K_p	Proportional gain (-)
L	Ship length (m)
m	Ship mass (kg)
N	Yaw moment (Nm)
$\boldsymbol{P}$	Solution of the algebraic matrix Riccati equation (-)
$\boldsymbol{Q}$	Weight matrix of the state vector (-)
r	Yaw rate (rad/s)
R	Weight of the rudder angle (-)

u	Surge velocity (m/s)
u'_A	Dimensionless relative wind speed in the longitudinal direction (-)
U	Ship speed (m/s)
U'_W	Dimensionless absolute wind speed (-)
v	Sway velocity (m/s)
v'_A	Dimensionless relative wind speed in the lateral direction (-)
V'_A	Dimensionless relative wind speed (-)
W	Channel width (m)
$\boldsymbol{x}$	State of the heading control system (-)
x_G	Longitudinal position of the center of gravity of ship (m)
Y	Sway force (N)
Δ_{LOS}	Look-ahead distance (m)
$\Delta_{\max}$	Maximum value of the look-ahead distance (m)
$\Delta_{\min}$	Minimum value of the look-ahead distance (m)
β	Drift angle (°)
δ	Rudder angle (°)
η	Off-centerline displacement (m)
η_d	Desired off-centerline displacement (m)
η_e	Tracking error (m)
θ_A	Relative wind direction (°)
θ_W	Absolute wind direction (°)
λ_1	Gain of the water depth to draft ratios in the look-ahead distance (-)
λ_2	Gain of the nondimensional off-centerline displacement in look-ahead distance (-)
ξ	Total unknown term of the heading control system (-)
ρ	Water density (kg/m^3)
ρ_A	Air density (kg/m^3)
ψ	Heading angle (°)
ψ_{CLOS}	Desired heading angle generated by the CLOS guidance law (°)
ψ_{LOS}	Desired heading angle generated by the LOS guidance law (°)
ω	Reference vector of the heading control system (-)
κ	Parameter to guarantee the safety of the CLOS guidance law (m)
τ	Parameter to guarantee the safety of the CLOS guidance law (m)

1 INTRODUCTION

Restricted waters, such as narrow channels and ports, are critical regions for ship navigation. In these areas, ship maneuverability changes significantly compared to open waters. These differences in restricted navigation environments bring more challenges to ship motion control, and highlight the significance of the advanced control strategies essential for ensuring safe and efficient ship operations. Among various ship motion control in restricted waters, path following is regarded as a fundamental task that plays an important role in berthing/unberthing, docking, and collision avoidance with static structures (piers, quay walls, etc.) and other ships. As a result, the development of the path-following control method for ships operating in restricted waters has received widespread attention, aiming to enhance control accuracy while minimizing collision risks.

Before the development of the path following control method, it is essential to first establish a ship maneuvering motion model describing the dynamic features in restricted waters. Shallow water and bank effects introduce disturbances on the ship system with additional forces and moments, leading to significant changes in ship maneuverability in restricted waters. Numerous studies investigated ship maneuvering features in restricted waters through experiments (e.g., Lataire et al., 2007; Duffy, 2008; Chen et al., 2020; Van Zwijnsvoorde et al., 2022). Yasukawa (2019) used captive model tests to analyze bank effects on course stability. Xu et al. (2024) applied potential flow theory to simulate hydrodynamic interactions and the impacts on ship maneuverability. With the advancement of numerical methods, the issues related to ship motions and corresponding hydrodynamic mechanisms in restricted waters have been further investigated. Van Hoydonck et al. (2021) employed viscous-flow solvers and CFD methods to predict hydrodynamic forces and moments in ship-bank interaction scenarios. The hydrodynamic interaction between the ship and the bank was analyzed using panel methods (Degrieck et al., 2021). Zheng et al. (2022) studied the effects of passing ships on moored ships in restricted waters based on computational fluid dynamics (CFD) simulations. These investigations provided bases for the study of ship motion control in restricted waters.

In restricted waters, shallow water and bank effects make the ships more difficult to maintain a steady course due to the complicated hydrodynamic disturbances and the consequently reduced rudder effects, thereby putting forward higher requirements on the design of ship controllers. To address these challenges, several control methods have been proposed. Zhang et al. (2000) introduced a sliding mode controller (SMC) to ensure robustness and good performance under the bank effect. Wang et al. (2019) utilized robust H∞ guaranteed cost control (RHGCC) to ensure path-following control for ships in restricted waters. Xu et al. (2023) proposed an adaptive line-of-sight (LOS) guidance combined with a nonlinear terminal sliding mode (NTSM) algorithm to realize precise path following. While these studies focused on mitigating the adverse impacts of shallow water and bank effects on control performance, they often neglected the fact that ship motions in restricted waters are also subject to certain spatial constraints. This oversight may result in safety accidents for ships in practical applications.

The linear quadratic regulator (LQR) is one of the most widely applied techniques in optimal control with numerous applications in ship motion control. For the motion control in restricted waters, Liu et al. (2018) applied multiple-input-multiple-output (MIMO)-based model predictive control (MPC) and LQR for precise course following and course keeping. For ship motion control in open waters, Taghavifar et al. (2021) proposed the disturbance observer-based composite nonlinear feedback (DO-CNF) and robust LQR (RLQR) methods to enhance the path-following performance of ships, ensuring asymptotic stability and robustness against uncertain dynamics and environmental disturbances. Lv and Li (2023) introduced dynamic inverse adaptive LQR (DI-ALQR) control for dynamic positioning of ships, combining strong fixed-time prescribed performance functions (SFPPF) with cascaded fixed-time extended state observers (CFESO) to achieve precise, energy-efficient control. These scholars have proposed improvements to the LQR to enhance the performance of ship motion control in open waters under environmental disturbances, but the studies by LQR on ship control in restricted water are scarce.
To achieve accurate path-following control under the influences of shallow water and bank effects while ensuring the safety of ship navigation in a narrow channel, a control method is proposed integrating the constrained line-of-sight (CLOS) guidance law with a compensated LQR heading controller. The CLOS method transforms the path-following problem while actively avoiding collisions with channel walls into a heading control task. The compensated LQR method addresses unmodeled dynamics and disturbances, improving robustness against the effects of shallow depths and small ship-bank distances, thereby ensuring precise heading control.

2 PROBLEM DESCRIPTIONS

2.1 COORDINATE SYSTEMS

The three-degrees-of-freedom (3-DOF) motion of an underactuated ship in a channel is described by the earth-fixed coordinate system o_n-$x_n y_n z_n$ and the ship-fixed system o_b-$x_b y_b z_b$, as shown in Figure 1. Both o_n-$x_n y_n$ and o_b-$x_b y_b$ are defined in the horizontal plane, with z_n-axis and z_b-axis positively downward. The origin o_n of the earth-fixed coordinate is fixed on the centerline of the channel; x_n-axis is along the centerline and towards the forward motion of the ship; y_n-axis points to the right wall of the channel. The origin o_b of the ship-fixed coordinate system is located at the midship; x_b-axis points towards the ship bow; y_b-axis towards the starboard side. The ship speed is represented by U, with two components u (surge velocity), v (sway velocity) in x_b and y_b directions, respectively, while the heading angle and rudder angle are denoted as ψ and δ, and the yaw rate of the ship is defined as $r = \dot{\psi}$. The drift angle is represented as β, and $\beta = \operatorname{atan}\left(\frac{v}{u}\right)$. η indicates the off-centerline displacement during ship motion in the channel, and W is the channel width.

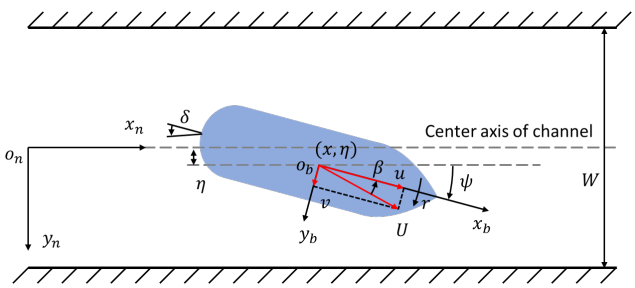

Figure 1. Coordinate systems of a ship in a channel

2.2 EQUATIONS OF SHIP MANEUVERING MOTION

Compared to the case in open waters, ship maneuvering motion in restricted waters is significantly influenced by the shallow-water and bank effects. Consequently, the equations governing a ship maneuvering motion in restricted waters differ from those in open waters. To address this issue, Sano et al. (2014) developed a nondimensional mathematical model specifically for ship motions in channels:

$$\begin{cases}(m' + m'_{22})\dot{v}' + (x'_G m' + m'_{26})\dot{r}' + (m' + m'_{11})r' = Y' \\ \left(I'_z + {x'_G}^2 + m'_{66}\right)\dot{r}' + (x'_G m' + m'_{26})\dot{v}' + x'_G m' r' = N'\end{cases} \tag{1}$$

where m' represents the ship mass; the added mass in i-th direction resulted from a unit acceleration in the j-th direction is denoted by m'_{ij} (1: surge, 2: sway, 6: yaw). v' and r' are the sway velocity and the yaw rate, respectively. Y' denotes the sway force, N' represents the yaw moment, expressed as follows:

$$\begin{cases} Y' = Y'_0 + Y'_\beta \beta + Y'_r r' + Y'_\eta \eta' + Y'_\delta \delta + Y'_{\beta\beta\beta}\beta^3 + Y'_{\beta\eta\eta}\beta\eta'^2 \\ \quad + Y'_{\beta\beta\eta}\beta^2\eta' + Y'_{\eta\eta\eta}\eta'^3 + Y'_{\eta\eta\delta}\eta'^2\delta + Y'_{\beta\delta\delta}\beta\delta^2 + Y'_{\beta\beta\delta}\beta^2\delta \\ N' = N'_0 + N'_\beta \beta + N'_r r' + N'_\eta \eta' + N'_\delta \delta + N'_{\beta\beta\beta}\beta^3 + N'_{\beta\eta\eta}\beta\eta'^2 \\ \quad + N'_{\beta\beta\eta}\beta^2\eta' + N'_{\eta\eta\eta}\eta'^3 + N'_{\eta\eta\delta}\eta'^2\delta + N'_{\beta\delta\delta}\beta\delta^2 + N'_{\beta\beta\delta}\beta^2\delta \end{cases} \tag{2}$$

where η' represents the nondimensional off-centerline displacement. The hydrodynamic derivatives at varying water depths and different ship-bank distances in Eq. (2) are referred to Sano et al. (2014), some of them are presented in Table 1. The quadratic polynomial fitting is applied in the present study to estimate the hydrodynamic derivatives of the ship at different ship-bank distances but the same water depth.

Table 1. Part of hydrodynamic derivatives (F_n=0.084) (Sano et al., 2014)

h/d	2.03	1.37
$\boldsymbol{Y'_0}$	−0.004	0.000
$\boldsymbol{Y'_\beta}$	0.413	1.038
$\boldsymbol{Y'_r}$	0.053	0.002
$\boldsymbol{Y'_\eta}$	0.060	0.228
$\boldsymbol{Y'_\delta}$	−0.041	−0.049
$\boldsymbol{N'_0}$	0.000	0.001
$\boldsymbol{N'_\beta}$	0.191	0.379
$\boldsymbol{N'_r}$	−0.064	−0.098
$\boldsymbol{N'_\eta}$	−0.030	−0.073
$\boldsymbol{N'_\delta}$	0.018	0.017

The kinematic model describing the ship motion in the channel is given as follows:

$$\begin{cases}\dot{x} = u\cos\psi - v\sin\psi \\ \dot{\eta} = u\sin\psi + v\cos\psi \\ \dot{\psi} = r\end{cases} \tag{3}$$

Due to the relatively small magnitudes of the heading angle and surge velocity in the channel, $\sin\psi \approx \psi$,$\cos\psi \approx 1$, $u \approx U$ and $\beta \approx v'$. The kinematic equations can be simplified as follows:

$$\begin{cases}\dot{x}' = 1 \\ \dot{\eta}' = \psi + v' \\ \dot{\psi}' = r'\end{cases} \tag{4}$$

where x' denotes the nondimensional longitudinal position of the ship in the earth-fixed coordinate system, and ψ' represents the nondimensional heading angle.

2.3 COLLISION AVOIDANCE CRITERIA

To facilitate the formulation of collision avoidance for a ship in the channel, the profile of the ship is approximated as a rectangular geometry. The rectangle slightly exceeds the actual ship profile, providing a conservative estimation to enhance safety margins. Based on approximation, the following collision-avoidance criteria is established:

$$f(\eta,\psi) = |\eta| + \sin\left[|\psi| + \operatorname{atan}\left(\frac{B}{L}\right)\right]\frac{\sqrt{L^2+B^2}}{2} < \frac{W}{2} \tag{5}$$

where L is the ship length and B represents the breadth.

The principle of the collision-avoidance criteria is illustrated in Figure 2.

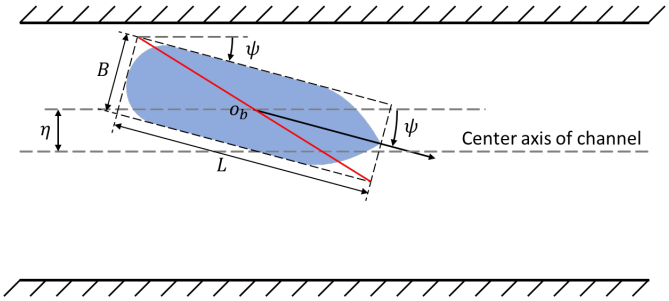

Figure 2. Principle of the collision avoidance criteria

2.4 BASIC ASSUMPTIONS

Assumption 1: The ship position, and heading angle are measurable, whereas its surge velocity, sway velocity, and yaw rate cannot be directly measured.
Assumption 2: There exists a constant M such that the condition $|\dot{v}'| \leq M$ is always valid.
Remark 1: The ship typically relies on global positioning systems (GPS) to provide information about the ship position, heading angle, and velocity. However, GPS generally measures only the ground speed and does not provide surge velocity, sway velocity, or the yaw rate.

3 CONTROL SYSTEM

The control system proposed in this paper is divided into two main components: a CLOS guidance law and a compensated LQR heading controller. The CLOS method addresses the underactuated problem of the ship by transforming the following of the target path into the tracking of the desired heading angle. Furthermore, it enhances the LOS approach by integrating the spatial constraints imposed by channel walls on ship motion, thereby improving navigational safety in the channel. The compensated LQR heading controller is designed to track the desired heading angle generated by the CLOS guidance law. The coupling of CLOS guidance law with a compensated LQR controller ensures precise path-following performance for the ship. The principle of the entire control system is illustrated in Figure 3.

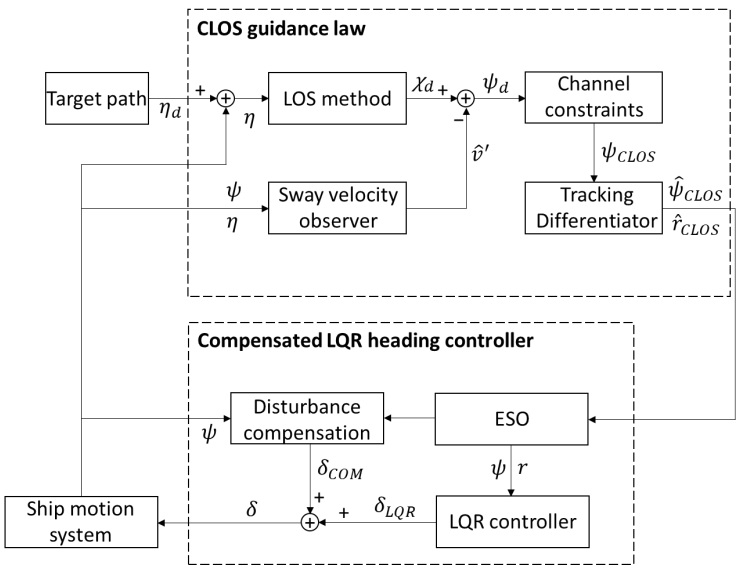

Figure 3. Principle of the proposed control system

3.1 CLOS GUIDANCE LAW

The proposed CLOS guidance law includes four components: LOS method, sway velocity observer, spatial constraints, and tracking differentiator (TD). Firstly, CLOS transforms the path-following task into the desired heading angle tracking task based on the adaptive look-ahead distance and the tracking error. Besides, a sway velocity observer is introduced to eliminate the effect of drift angle. The spatial constraints caused by channel walls are then integrated into the constraints of the desired heading angle. Finally, TD is employed to obtain the smoothed desired heading angle and yaw rate.

3.1 (a) LOS Method

The desired heading angle ψ_{LOS} can be obtained according to the LOS method:

$$\psi_{LOS} = \arctan\left(\frac{\eta_e}{\Delta_{LOS}}\right) - \beta \tag{6}$$

where $\eta_e = \eta_d - \eta$ denotes the tracking error between the ship and the desired off-centerline displacement η_d. Δ_{LOS} is the look-ahead distance. As the water depth decreases, the maneuverability of the ship gets worse. Meanwhile, the desired heading angle must be kept closer to zero to ensure smoother tracking of the target path when the ship is near the channel walls. Thus, the look-ahead distance Δ_{LOS} changes with both water depth to draft ratios h/d and η' in the proposed method:

$$\Delta_{LOS} = \Delta_{\min} + (\Delta_{\max} - \Delta_{\min})\mathrm{e}^{-\lambda_1\frac{h}{d}+\lambda_2\eta'} \tag{7}$$

where $\Delta_{\min}$ and $\Delta_{\max}$ are the minimum and maximum value of Δ_{LOS}, λ_1 and λ_2 denote the gains of h/d and η'.

3.1 (b) Sway Velocity Observer

Since the surge velocity, and sway velocity are unknown during the motion, the drift angle cannot be determined directly from v', and then the sway force and the yaw moment cannot be obtained from Eq. (2). In order to guarantee the accuracy of path following, the sway velocity observer is utilized to estimate v' based on the known motion state with η and ψ:

$$\begin{cases} \dot{\hat{\eta}}' = \hat{v}' + \psi + \gamma_1\tilde{\eta}' \\ \dot{\hat{v}}' = \gamma_1\tilde{\eta}' \end{cases} \tag{8}$$

where $\hat{\eta}'$ and $\hat{v}'$ represent the estimated η' and v', respectively, γ_1 and γ_2 are both positive parameters. $\tilde{\eta}'$ and $\tilde{v}'$ denote the estimation error of $\hat{\eta}'$ and $\hat{v}'$, which can be described as follows:

$$\begin{cases} \tilde{\eta}' = \eta' - \hat{\eta}' \\ \tilde{v}' = v' - \hat{v}' \end{cases} \tag{9}$$

Taking the time derivatives of both sides of Eq. (9) and substituting Eq. (8) into it yields:

$$\begin{cases} \dot{\tilde{\eta}}' = \hat{v}' - \gamma_1\tilde{\eta}' \\ \dot{\tilde{v}}' = \dot{v}' - \gamma_2\tilde{\eta}' \end{cases} \tag{10}$$

Consider $\dot{v}'$ as the input to the observer error system, and rewrite Eq (10) as a state-space expression.

$$\dot{\boldsymbol{e}} = \boldsymbol{H}\boldsymbol{e} + \boldsymbol{G}\dot{v}' \tag{11}$$

$$\boldsymbol{e} = [\tilde{\eta}', \tilde{v}']^T, \boldsymbol{H} = \begin{bmatrix} -\gamma_1 & 1 \\ -\gamma_2 & 0 \end{bmatrix}, \boldsymbol{G} = [0, 1]^T \tag{12}$$

Apply the Laplace transform to Eq. (11) to convert it into the form of a transfer function.

$$\boldsymbol{e}(s) = \frac{1}{s^2+\gamma_1 s+\gamma_2}\begin{bmatrix} 1 \\ s+\gamma_1 \end{bmatrix}\dot{v}'(s) \tag{13}$$

By selecting $\gamma_2 \gg \gamma_1 \gg 1$, $\boldsymbol{e} \to 0$ can be achieved. Therefore, it is assumed that the sway velocity observer can estimate $\dot{v}'$ accurately, such that $\hat{v}' = v'$ in the subsequent stability analysis.

Based on the values obtained from the sway velocity observer, Eq. (6) can be rewritten as follows:

$$\psi_{LOS} = \arctan\left(\frac{\eta_e}{\Delta_{LOS}}\right) - \hat{v}' \tag{14}$$

3.1 (c) Spatial Constraints

The desired heading angle derived from Eq. (14) does not consider the spatial constraints imposed by the sidewalls. Therefore, based on the collision avoidance criteria outlined in Eq. (5), the CLOS guidance law is formulated to guarantee safe navigation as follows:

$$\psi_{CLOS} = \begin{cases} \psi_{LOS} & \text{if } f(\eta, \psi_{LOS}) < \frac{W}{2} - \kappa \\ \mathrm{sgn}(\eta_e)\left[\arcsin\left(\frac{W-2|\eta|-2\tau}{\sqrt{L^2+B^2}}\right) - \arctan\left(\frac{B}{L}\right)\right] & \text{else} \end{cases} \tag{15}$$

where κ and τ are positive parameters to guarantee the safety of the guidance law. There is such a relationship between the parameter κ and τ:

$$\tau = \kappa\left(1 - 2\frac{|\eta|}{W-B}\right) \tag{16}$$

If the proposed controller achieves precise heading control, the CLOS guidance law can ensure that the tracking error gradually converges to zero. Based on the analysis of the Lyapunov function under the aforementioned two conditions, it can be concluded that the ship effectively realizes accurate tracking of the target path without static tracking error.
When $f(\eta, \psi_{LOS}) \geq \frac{W}{2} - \kappa$:

$$\begin{aligned} f(\eta, \psi_{CLOS}) &= |\eta| + sin\left[|\psi_{CLOS}| + \arctan\left(\frac{B}{L}\right)\right]\frac{\sqrt{B^2+L^2}}{2} \\ &\leq |\eta| + \sin\left[\left|\arcsin\left(\frac{W-2|\eta|-2\tau}{\sqrt{L^2+B^2}}\right) - \arctan\left(\frac{B}{L}\right)\right| + \arctan\left(\frac{B}{L}\right)\right]\frac{\sqrt{L^2+B^2}}{2} \end{aligned} \tag{17}$$

Due to the constraints imposed by the channel walls, it is noted that: $W - 2|\eta| > B$. Let $g(|\eta|) = W - 2|\eta| - 2\tau$, then:

$$g(|\eta|) = W - 2|\eta| - 2\kappa\left(1 - 2\frac{|\eta|}{W-B}\right) = W - 2\kappa - 2\left(1 - \kappa\frac{2}{W-B}\right)|\eta| > B \tag{18}$$

It is evident that Eq. (18) is valid when $\kappa < (W - B)/2$ is satisfied. Substituting Eq. (18) into Eq. (17) yields:

$$f(\eta, \psi_{CLOS}) < \frac{W}{2} - \tau < \frac{W}{2} \tag{19}$$

As a result, the CLOS guidance law can ensure that the ship avoids collisions with the sidewalls during navigation in the channel if the ship can track the desired heading angle accurately. The CLOS guidance law is able to prevent ship collisions by adjusting the parameter τ continuously based on the ship position relative to the sidewalls.

3.1 (d) Tracking Differentiator

The TD is employed to obtain the smoothed desired heading angle $\hat{\psi}_{CLOS}$ and nondimensional desired yaw rate $\hat{r}'_{CLOS}$:

$$\begin{cases} \hat{\psi}_{CLOS}(k+1) = \hat{\psi}_{CLOS}(k) + t_s\frac{U}{L}\hat{r}'_{CLOS}(k) \\ \hat{r}'_{CLOS}(k+1) = \hat{r}'_{CLOS}(k) + t_s\frac{U}{L}\left[-q^2\left(\hat{\psi}_{CLOS}(k) - \psi_{CLOS}(k+1)\right) - 2q\hat{r}_{CLOS}(k)\right] \end{cases} \tag{20}$$

where t_s is the sampling time, and $q > 0$ is the tracking speed factor.

3.2 COMPENSATED LQR HEADING CONTROLLER

To achieve precise and safe path following, it is necessary to accurately track the desired heading angle through a heading controller after determining the desired heading angle using the CLOS method. The proposed compensated LQR heading controller includes two components: extended state observer (ESO) and compensated LQR control law. The ESO is capable of estimating the yaw rate, unmodeled dynamics and disturbances. By compensating for these unmodeled dynamics, and disturbances and minimizing the defined cost function, the compensated LQR control law ensures precise and rapid tracking of the desired heading angle.

3.2 (a) Extended State Observer

The yaw dynamics of ships can be described by the following state space equation:

$$\dot{\boldsymbol{x}} = \boldsymbol{A}\boldsymbol{x} + \boldsymbol{B}\delta + \boldsymbol{d} \tag{21}$$

where $\boldsymbol{x} = [\psi, r']^{\mathrm{T}}$ denotes the state of the heading control system. The system matrix $\boldsymbol{A}$, input matrix $\boldsymbol{B}$ and the disturbance vector $\boldsymbol{d}$ are defined as follows:

$$\boldsymbol{A} = \begin{bmatrix} 0 & 1 \\ 0 & -\frac{1}{T} \end{bmatrix}, \boldsymbol{B} = \begin{bmatrix} 0 \\ \frac{K}{T} \end{bmatrix}, \boldsymbol{d} = \begin{bmatrix} 0 \\ \xi \end{bmatrix} \tag{22}$$

where T and K are positive indexes to describe the maneuverability of ships, and ξ is the total unknown term including the unmodeled dynamics and environment disturbances (Li et al., 2021).
The ESO is utilized to address the issue of not being able to directly obtain the yaw rate and to estimate unmodeled dynamics and disturbances:

$$\dot{\hat{\bar{\boldsymbol{x}}}} = \bar{\boldsymbol{A}}\hat{\bar{\boldsymbol{x}}} + \bar{\boldsymbol{B}}\delta + \boldsymbol{\mu}\tilde{\psi} \tag{23}$$

where $\bar{\boldsymbol{x}} = [\psi, r', \xi]^{\mathrm{T}}$ is the extend state vector, $\hat{\bar{\boldsymbol{x}}} = \left[\hat{\psi}, \hat{r}', \hat{\xi}\right]^{\mathrm{T}}$ represents the estimation of $\bar{\boldsymbol{x}}$, and $\tilde{\psi} = \psi - \hat{\psi}$ denotes the estimation error of the heading angle. The matrix $\bar{\boldsymbol{A}}$, vector $\bar{\boldsymbol{B}}$, and $\boldsymbol{\mu}$ are given as follows:

$$\bar{\boldsymbol{A}} = \begin{bmatrix} 0 & 1 & 0 \\ 0 & -\frac{1}{T} & 1 \\ 0 & 0 & 0 \end{bmatrix}, \bar{\boldsymbol{B}} = \begin{bmatrix} 0 \\ \frac{K}{T} \\ 0 \end{bmatrix}, \boldsymbol{\mu} = \begin{bmatrix} \mu_1 \\ \mu_2 \\ \mu_3 \end{bmatrix} \tag{24}$$

3.2 (b) Compensated LQR Control Law

Based on the estimation of $\bar{\boldsymbol{x}}$, the control law can be rewritten as follows:

$$\delta = \bar{\boldsymbol{K}}_1\hat{\bar{\boldsymbol{x}}} + \boldsymbol{K}_2\boldsymbol{\omega} \tag{25}$$

where $\bar{\boldsymbol{K}}_1 = -[\boldsymbol{K}_1, K_3]$ is the extend state feedback gain matrix, $\boldsymbol{K}_1$ denotes the state feedback gain matrix, $\boldsymbol{K}_2$ represents the reference gain matrix and K_3 is the gain of the total unknown term. $\boldsymbol{\omega} = \left[\hat{\psi}'_{CLOS}, \hat{r}'_{CLOS}\right]^{\mathrm{T}}$ represents the reference vector The LQR method is adopted to design $\boldsymbol{K}_1$, which is determined by minimizing the following cost function:

$$J = \int_0^{\infty} (\boldsymbol{x}^T \boldsymbol{Q} \boldsymbol{x} + R\delta^2)\, dt \tag{26}$$

where $\boldsymbol{Q}$ is the weight matrix of the state vector $\boldsymbol{x}$, and $\boldsymbol{Q}$ is a positive diagonal matrix. The positive parameter R is the weight of the rudder angle δ. The gain matrix $\boldsymbol{K}_1$ is given as follows:

$$\boldsymbol{K}_1 = \frac{1}{R} \boldsymbol{B}^T \boldsymbol{P} \tag{27}$$

where $\boldsymbol{P}$ is symmetric positive-definite solution of the algebraic matrix Riccati equation:

$$\boldsymbol{A}^T \boldsymbol{P} + \boldsymbol{P}\boldsymbol{A} + \boldsymbol{Q} - \boldsymbol{P}\boldsymbol{B} R^{-1} \boldsymbol{B}^T \boldsymbol{P} = \boldsymbol{0} \tag{28}$$

In order to compensate the effect of the total unknown term appropriately, the gain K_3 should be designed to make the coefficient of $\boldsymbol{d}$ equal to zero:

$$K_3 = \frac{T}{K} \tag{29}$$

For the purpose of achieving the steady state at $\hat{\psi}'_{CLOS}$, $\boldsymbol{K}_2$ is selected as follows:

$$\boldsymbol{K}_2 = -((\boldsymbol{A} - \boldsymbol{B}\boldsymbol{K}_1)^{-1} \boldsymbol{B})^{\dagger} \tag{30}$$

where the symbol '†' represents the Moore-Penrose pseudoinverse.

4 SIMULATION ANALYSES

To evaluate the effectiveness and robustness of the proposed controller based on CLOS and compensated LQR methods for the path following problem in restricted waters, simulations are performed for two different scenarios. The first scenario assesses the path-following accuracy under the impacts of varying water depths, the second one tests the designed control system for path following performance under combined restricted-water and wind effects, while the third one evaluates the navigation safety of the proposed methods under collision-risk conditions.

4.1 SELECTION OF CONTROL PARAMETERS

The main particulars of the ship are: length *L*=136.7 m, breadth *B*=22.0 m and draft *d*=7.36 m. The channel width is *W*=89 m. The maximum rudder angle and the maximum rudder rate of the ship are set as 35° and 2.7°/s. The surge velocity remains constant at 3.086 m/s. The initial sway velocity and initial yaw rate are defined as: v_0=0 m/s and r_0=0 rad/s.
The parameters of the adaptive look-ahead distance Δ_{LOS} are selected as: $\Delta_{\min}$=2L, $\Delta_{\min}$=L, λ_1=1 and λ_2=1. The look-ahead distance Δ_{LOS} is typically of the same order of magnitude as the ship length to ensure control stability and precision. The parameters of the sway velocity observer are established as: γ_1=20 and γ_2=200. The estimated values of the sway velocity and displacement from the centerline are initialized as follows: $\hat{v}'$=0 and $\hat{\eta}'$=0. The parameter κ to guarantee the safety of the guidance law is set as 4 m. The tracking speed factor q of the TD is 100. According to Sano et al. (2014), the parameters of the yaw dynamic model are determined as: K=0.271 and T=0.393. The parameters of the ESO are selected as: μ_1=24, μ_2=192 and μ_3=512. The estimated values of the heading angle, yaw rate and total unknown term are initialized as: $\hat{\psi}$=0, $\hat{r}'$=0 and ξ=0. The parameters of the LQR are defined as: $\boldsymbol{Q}$=diag ([1, 0.5]) and R=0.01. Based on these parameters, the control gains are obtained as: $\bar{\boldsymbol{K}}_1 = [-10, -5.93, -1.45]$ and $\boldsymbol{K}_2 = diag([10, 0])$. These parameters are tunable in accordance with the practical control objectives and the operational requirements in specific applications.

4.2 PATH FOLLOWING UNDER RESTRICTED-WATER EFFECTS

In this section, the path-following performance of the proposed controller is evaluated under varying restricted-water conditions. To demonstrate the advantages of the compensated LQR heading controller presented in this study, a comparison with a proportional-integral-derivative (PID) controller is performed. The PID control law can be expressed as follows:

$$\delta(k) = K_p e + K_i e_i + K_d \dot{e} \tag{31}$$

where K_p, K_i and K_d are the proportional, integral, and derivative gains of the control law, respectively. In this paper, the values of these three parameters are: K_p=6, K_i=3 and K_d=6. e, e_i and $\dot{e}$ represent the error, its integral item and derivative term related to the heading angle, which are determined as follows:

$$\begin{cases} e(k) = \hat{\psi}_{CLOS}(k) - \hat{\psi}(k) \\ e_i(k) = e_i(k-1) + e(k) t_s \frac{U}{L} \\ \dot{e}(k) = \hat{r}'_{CLOS}(k) - \hat{r}'(k) \end{cases} \tag{32}$$

The simulations with the desired off-centerline displacement η_d=0.1L but varying water depth are conducted. During the simulations, the water depth ratio changes as follows: for x/L≤50, h/d=2.03 and for x/L>50, h/d=1.37. The simulation results are shown in Figure 4.

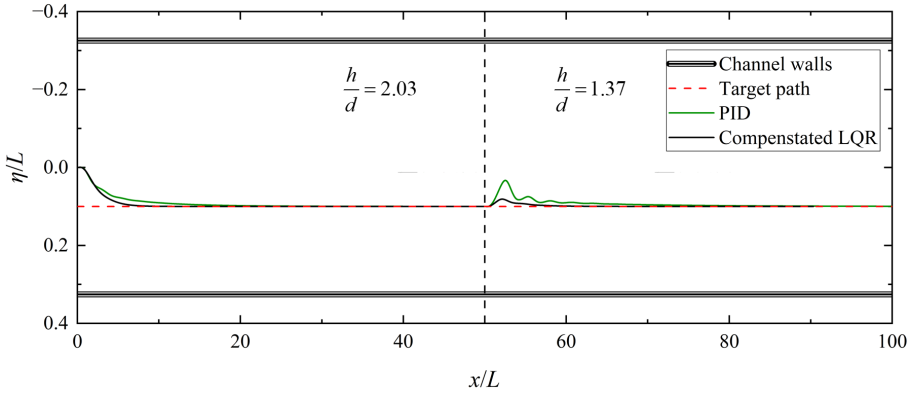

(a) Ship trajectory

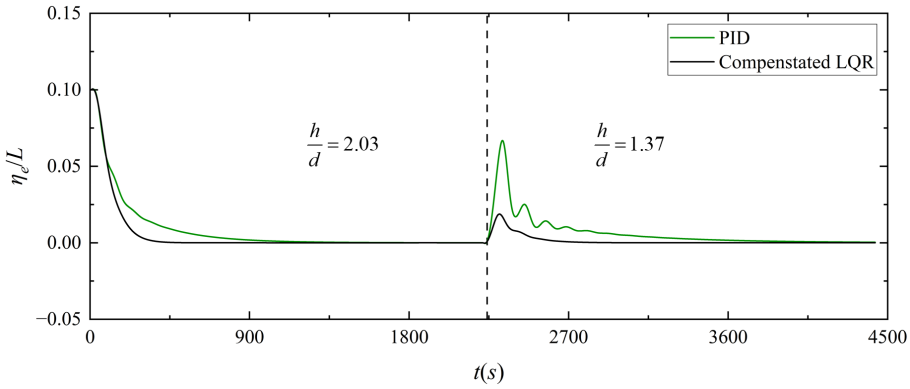

(b) Tracking error

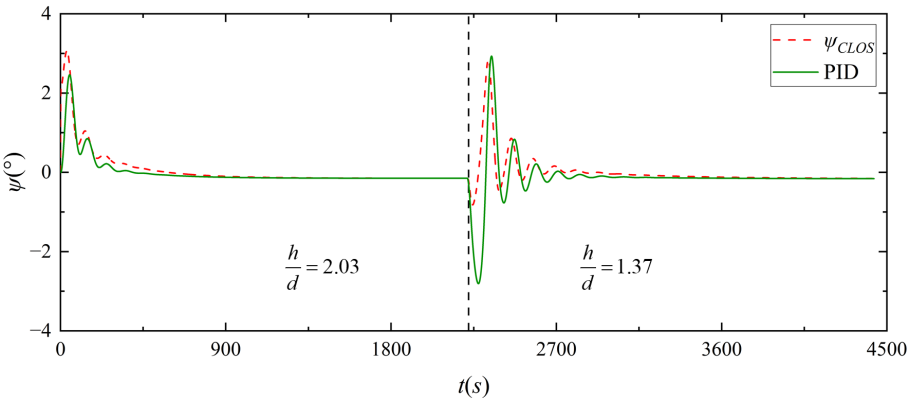

(c) Desired and actual heading angle (PID)

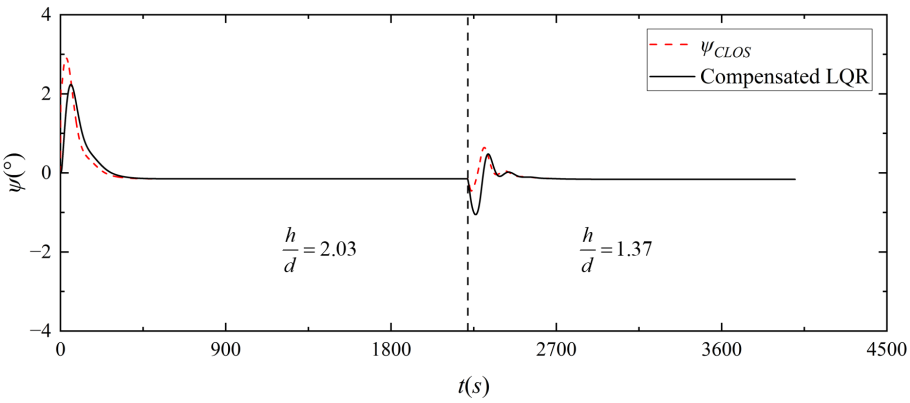

(d) Desired and actual heading angle (Compensated LQR)

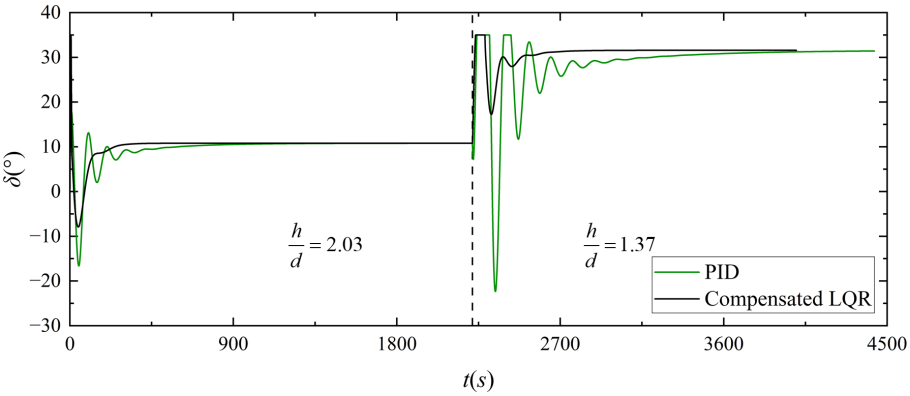

(e) Rudder angle

Figure 4. Path following results under different water depths

Figure 4(a) illustrates the target path and the ship trajectory using different heading controllers. It is observed that the ship eventually follows the target path accurately under PID heading control, while the convergence rate is slow. According to Figure 4(b), the tracking error of PID reduces to 1% of the initial error at x/L≥23.7 when h/d=2.03. However, when h/d changes to 1.37, the tracking error decreases to 1% of the initial value much later at x/L≥86.6. Additionally, the PID controller requires a longer time to make the ship follow the target path when h/d changes from 2.03 to 1.37, and the ship trajectory also displays noticeable oscillations during the control process. In contrast, the compensated LQR enables the ship to achieve prompt path-following performance, and to maintain course stability while returning to the target path when the water depth changes. When h/d=2.03, the tracking error reduces to within 1% of the initial value at x/L≥8.3. When h/d is adjusted to 1.37, the error reduces to within 1% only at x/L≥59.6. Figures 4(c) and 4(d) present the desired and the actual heading angles under different heading controllers. Both PID and compensated LQR methods are combined with the CLOS guidance approach. Therefore, the significant differences in path-following performances result from the different heading controllers. The heading controller must counteract disturbances caused by shallow water and bank effects to achieve precise heading control. The PID controller compensates for disturbances using the integral term, which requires a relatively long integration period. In contrast, the compensated LQR utilizes ESO to estimate disturbances, enabling faster disturbance compensation and achieving superior control performance. In the process of path-following control, the generation of the desired heading angle is coupled with the effectiveness of heading control, which leads to oscillations between the desired and actual heading angles when using PID control. According to Figure 4(e), the changes in the rudder angle are smoother when using the compensated LQR compared to the PID controller.

4.3 PATH FOLLOWING UNDER RESTRICTED-WATER AND WIND EFFECTS

In this section, the path-following performance of the proposed path following controller is evaluated under combined restricted-water and wind effects with η_d=0.1L and h/d=2.03, to demonstrate the robustness of the compensated LQR heading controller under external disturbances. Simulations are conducted with a PID controller as well for comparative analysis. Wind effects are modeled as follows:

$$\begin{cases} Y_A' = (\rho_A/\rho)[A_Y/Ld]V_A'^2 C_{YA}(\theta_A) \\ N_A' = (\rho_A/\rho)[A_Y/Ld]V_A'^2 C_{NA}(\theta_A) \end{cases} \tag{33}$$

where Y_A' and N_A' represent the dimensionless sway force and yaw moment induced by the wind, respectively. C_{YA} and C_{NA} are the wind pressure coefficients, referred to Yasukawa et al. (2013). ρ_A is the air density, ρ is the water density, A_Y=1890 m² is the lateral projected area of the ship above the waterline. V_A' and θ_A represent the dimensionless relative wind speed and relative wind direction, which can be expressed as follows:

$$\begin{cases} V_A'^2 = u_A'^2 + v_A'^2 \\ u_A' = u' + U_W' \cos(\theta_W - \psi) \\ v_A' = v' + U_W' \sin(\theta_W - \psi) \\ \theta_A = arctan\left(\frac{v_A'}{u_A'}\right) \end{cases} \tag{34}$$

where U_W' represents the dimensionless absolute wind speed and θ_W denotes absolute wind direction. u_A' and v_A' denote the dimensionless relative wind speed in the longitudinal and lateral direction, respectively. In this case, U_W'=2.5 and θ_W=45°.

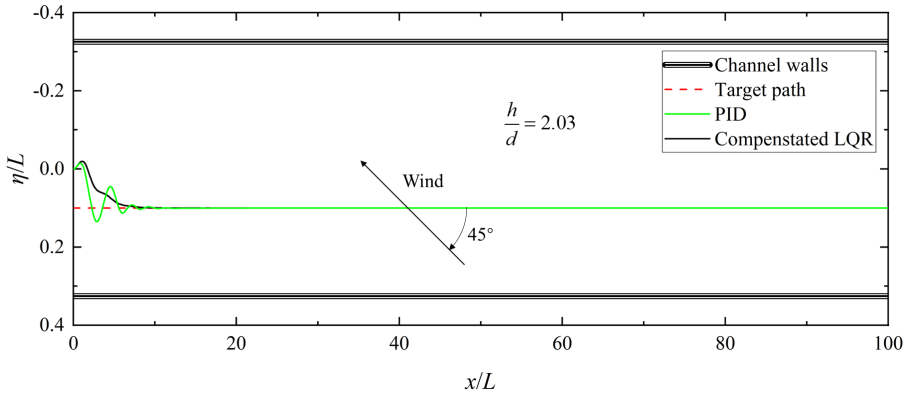

(a) Ship trajectory

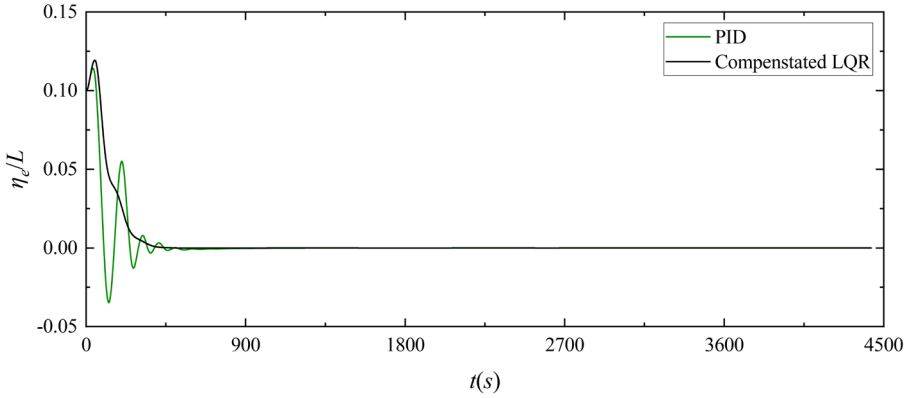

(b) Tracking error

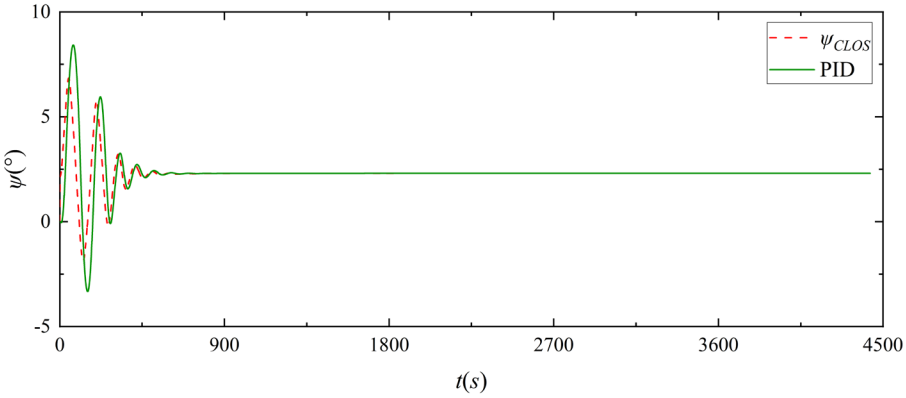

(c) Desired and actual heading angle (PID)

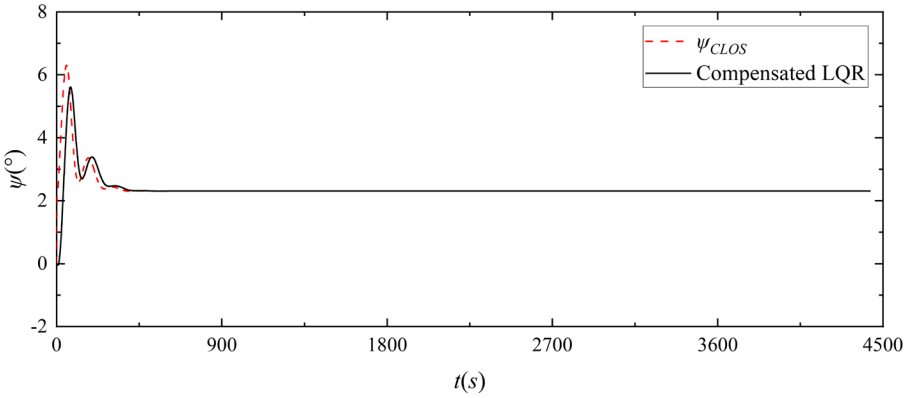

(d) Desired and actual heading angle (Compensated LQR)

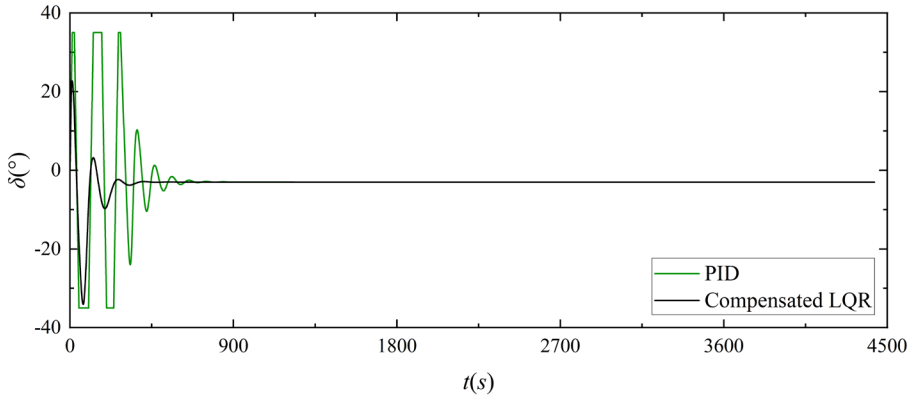

(e) Rudder angle

Figure 5. Path following simulations under combined restricted-water and wind effects

Figure 5(a) illustrates the path-following performances of different controllers under combined restricted-water and wind effects. It is evident that the PID controller induces significant overshoot and oscillations during the path-following process, whereas the compensated LQR controller enables the ship to smoothly and rapidly converge to the desired path. According to Figure 5(b), the tracking error of the PID controller reduces to 1% of the initial error at $x/L \geq 12.9$ when $h/d=2.03$. In contrast, the compensated LQR achieves this reduction in tracking error at $x/L \geq 8.6$, demonstrating its superior performance. Figures 5(c) and (d) depict the desired and actual heading angles with different heading controllers. Both PID and compensated LQR methods are integrated with the CLOS guidance approach, and the notable differences in path-following performance are attributed to the distinct characteristics of the heading controllers. It is observed that the compensated LQR outperforms the PID controller in tracking the desired heading angle. This is because the ESO effectively estimates disturbance terms, and the LQR compensates for these disturbances based on the estimates. Additionally, the LQR inherently provides greater advantages as an optimal control method. Figure 5(e) demonstrates the variations in rudder angle with the two controllers, further highlighting the improved control performance of the proposed approach.

4.4 PATH FOLLOWING UNDER COLLISION-RISK CONDITIONS

In this section, the navigation safety of the CLOS guidance law is evaluated under collision-risk conditions, and a simulation using the LOS algorithm is conducted for comparison. The simulations with a switch between two opposite desired offset distances ($0.2L$ and $-0.2L$) are conducted in a constant water depth of $h/d=2.03$. During the control simulations, the desired offset distance changes as follows: for $x/L \leq 30$, $\eta_d=0.2L$, and for $x/L>30$, $\eta_d=-0.2L$. The simulation results are shown in Figure 6.

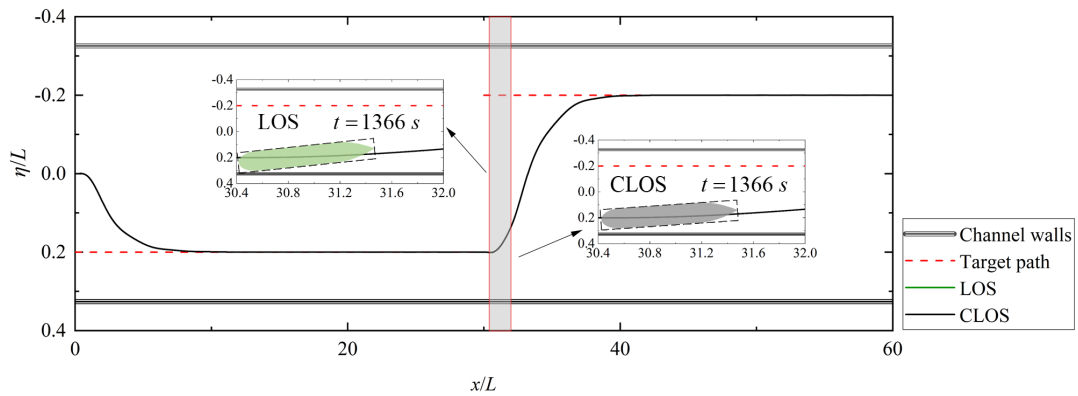

(a) Ship trajectory

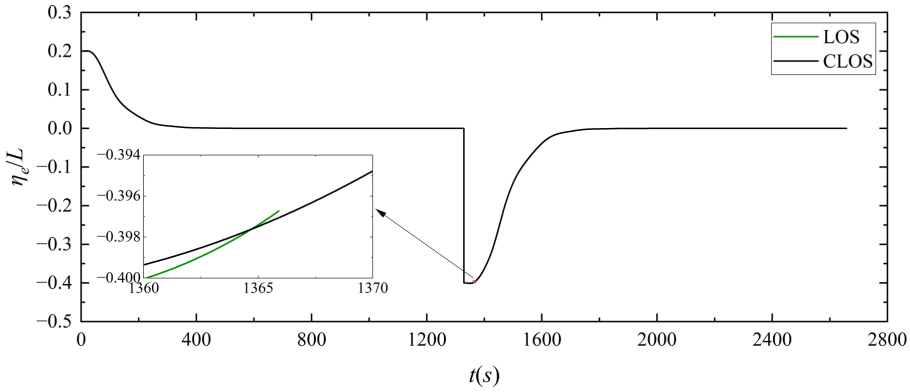

(b) Tracking error

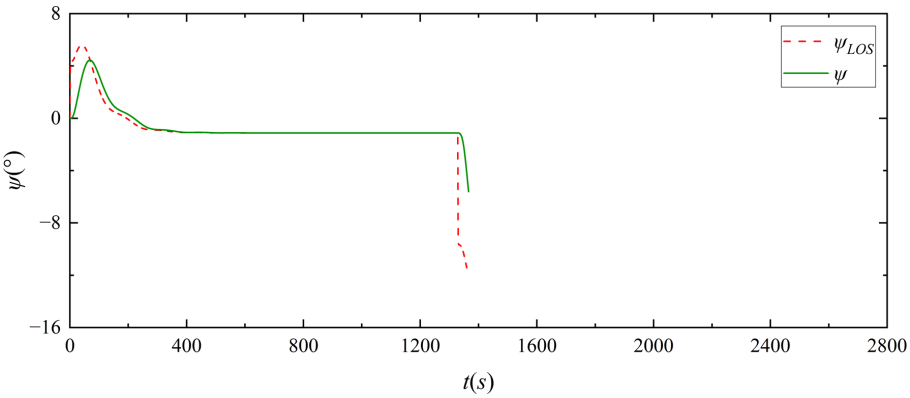

(c) Desired and actual heading angle (LOS)

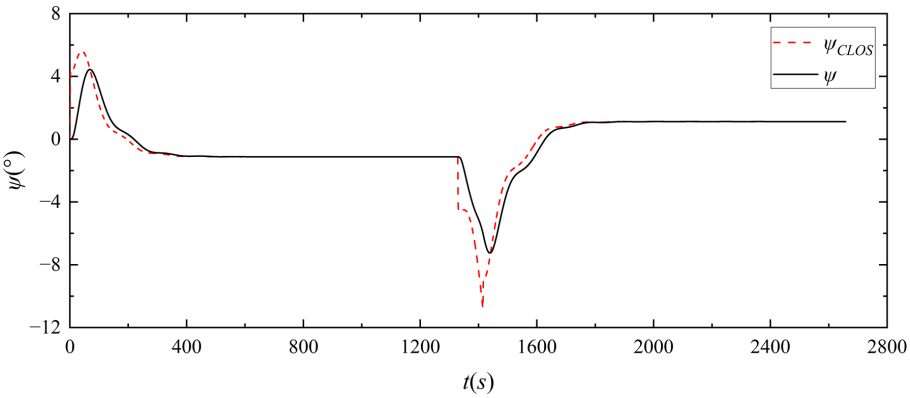

(d) Desired and actual heading angle (CLOS)

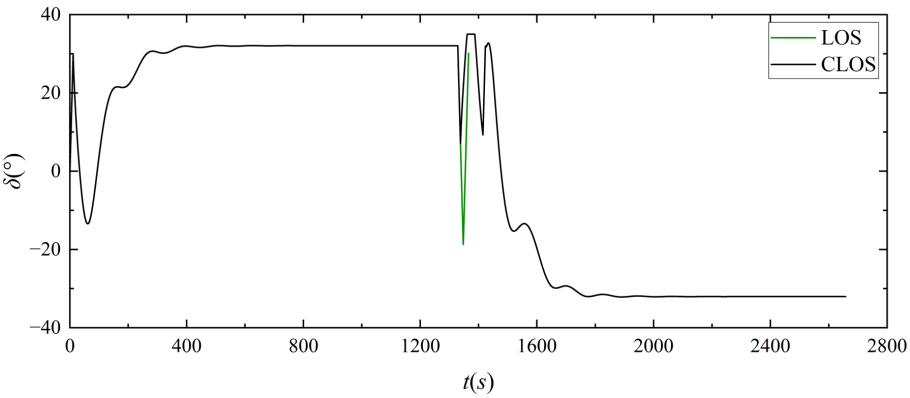

(e) Rudder angle

Figure 6. Path following simulations under different water depths

Figure 6(a) illustrates the target path and the ship trajectory when using different guidance laws. It can be observed that when $x/L \leq 30$, the ship trajectory generated by both LOS and CLOS guidance laws present no difference, indicating that the

heading constraint mechanism has not yet been triggered. However, the ship using the LOS guidance collides with the channel wall when x/L>30. In contrast, the ship using the CLOS strategy continues its navigation. Figure 6(b) shows that the tracking error converges well when using different guidance laws. According to Figures 6(c) and (d), the LOS method aims to track the new target path rapidly for the ship when x/L>30, resulting in a large desired heading angle. However, the ship is already in close proximity to the sidewall at this position, and following the path with a large desired heading angle leads to a collision. The CLOS method provides a smaller desired heading angle by accounting for the spatial constraints imposed by the channel wall, thus avoiding the collision. Figure 6(e) shows that the variation in the rudder angle of the ship using CLOS is relatively smoother when η_d changes. In summary, compared to the LOS algorithm, the CLOS algorithm not only ensures precise tracking of the target path but also guarantees collision avoidance with channel walls throughout the tracking process.

5 CONCLUSIONS

This study proposes a controller integrating the CLOS guidance law with the compensated LQR heading controller for the path following in a narrow channel. In the guidance system, the path-following task is transformed into the task of tracking the desired heading angle by the CLOS method to deal with the underactuation problem. A sway velocity observer is incorporated to mitigate the effect of drift angle. To make the CLOS guidance law more suitable for the restricted-water scenarios, the constraints of channel walls are converted into heading angle constraints based on the current ship position. Furthermore, the TD is employed to obtain the smoothed desired heading angle and desired yaw rate. In the heading control system, the ESO estimates the yaw rate of the ship and the total unknown term in the compensated LQR heading controller. The disturbance compensation is integrated into the LQR controller to enhance the robustness of the control system against the impacts of small ship-bank distances and shallow water depths. The simulation results demonstrate that the proposed compensated LQR controller exhibits significantly enhanced control performance compared to the PID controller. It enables the ship to track the target path more rapidly in the channel, even under varying water depths as well as combined restricted-water and wind effects. The proposed controller effectively ensures the ship to avoid collisions with sidewalls during the path-following task in the channel.

It should be mentioned that shallow water and bank effects are handled in a simplified manner in the present study. In future work, these factors will be further analyzed and incorporated. Moreover, addressing ship encounters and collision avoidance problems in restricted waters is both essential and challenging. Future research will attempt to design appropriate controllers to address common scenarios typically encountered in restricted waters.

6 ACKNOWLEDGEMENTS

This work is supported by the State Key Laboratory of Maritime Technology and Safety, the National Natural Science Foundation of China (Grant Nos. 52211530101 and 51979164), the Fundamental Research Funds for the Central Universities.

7 REFERENCES

Chen, C., Delefortrie, G., Lataire, E., 2020. Experimental investigation of practical autopilots for maritime autonomous surface ships in shallow water. Ocean Eng, 218, 108246. https://doi.org/10.1016/j.oceaneng.2020.108246

Degrieck, A., Uyttersprot, B., Sutulo, S., Guedes Soares, C., Van Hoydonck, W., Vantorre, M., Lataire, E., 2021. Hydrodynamic ship–ship and ship–bank interaction: A comparative numerical study. Ocean Eng, 230, 108970. https://doi.org/10.1016/j.oceaneng.2024.117585

Duffy, J., 2008. Modelling of ship-bank interaction and ship squat for ship-handling simulation, Doctoral dissertation, University of Tasmania.

Lataire, E., Vantorre, M., Laforce, E., Eloot, K., Delefortrie, G., 2007. Navigation in confined waters: influence of bank characteristics on ship-bank interaction. In International Conference on Marine Research and Transportation, ICMRT.

Li, Z.X., Li, R.H., Bu, R.X., 2021. Path following of under-actuated ships based on model predictive control with state observer. J Mar Sci Technol, 26, 408-418.
https://doi.org/10.1007/s00773-020-00746-1

Liu, H., Ma, N., Gu, X.C., 2018. Ship course following and course keeping in restricted waters based on model predictive control. TransNav, 12(2), 305-312.
https://doi.org/10.12716/1001.12.02.1

Lv, Y.Y., Li, H., 2023. Strong fixed-time dynamic inverse adaptive LQR integrated control strategy for dynamic positioning of ship. Ocean Eng, 288, 115969.
https://doi.org/10.1016/j.oceaneng.2023.115969

Sano, M., Yasukawa, H., Hata, H., 2014. Directional stability of a ship in close proximity to channel wall. J Mar Sci Technol, 19, 376-393.
https://doi.org/10.1007/s00773-014-0271-4

Taghavifar, H., Qin, Y.C., Hu, C., 2021. Adaptive immersion and invariance induced optimal robust control of unmanned surface vessels with structured/unstructured uncertainties. Ocean Eng, 239, 109792.
https://doi.org/10.1016/j.oceaneng.2021.109792

Van Hoydonck, W., Toxopeus, S., Eloot, K., Bhawsinka, K., Queutey, P., Visonneau, M., 2015. Bank effects for KVLCC2. In SNAME Maritime Convention, SNAME.
https://doi.org/10.5957/WMTC-2015-132

Van Zwijnsvoorde, T., Delefortrie, G., Lataire, E., 2022. Passing ship effects in shallow and confined water: Open model test data for validation purposes. In Proceedings of the 6th MASHCON International Conference on Ship Manoeuvring in Shallow and Confined Water, Glasgow, UK, 254-283.

Wang, J.H., Zou, L., Wan, D.C., 2017. CFD simulations of free running ship under course keeping control. Ocean Eng, 141, 450-464.
https://doi.org/10.1016/j.oceaneng.2017.06.052

Wang, J.Q., Zou, Z.J., Wang, T., 2019. Path following of a surface ship sailing in restricted waters under wind effect using robust H∞ guaranteed cost control. Int J Nav Arch Ocean, 11(1), 606-623.
https://doi.org/10.1016/j.ijnaoe.2018.10.005

Xu, D.H., Huang, Y.J., Zhou, X.Q., Xu, H.T., 2023. Path following control for large inland ships in a restricted waterway using the nonlinear terminal sliding mode method. Ocean Eng, 284, 115159.
https://doi.org/10.1016/j.oceaneng.2023.115159

Xu, C., Zhou, X.Q., Ren, H.L., Sutulo, S., Guedes Soares, C., 2024. Real-time simulation of ship overtake maneuvering at different water depths with a ship motion controller. Ocean Eng, 311, 119021.
https://doi.org/10.1016/j.oceaneng.2024.119021

Yasukawa, H., 2019. Maneuvering hydrodynamic derivatives and course stability of a ship close to a bank. Ocean Eng, 188, 106149.
https://doi.org/10.1016/j.oceaneng.2019.106149

Yasukawa, H., Sano, M., Amii, H., 2013. Wind effect on directional stability of a ship moving in a channel. J. Japan Soc. Nav. Archit. Ocean Eng., 18.
https://doi.org/10.2534/jjasnaoe.18.45

Zhang, R.J., Chen, Y.B., Sun, Z.Q., Sun, F.C., Xu, H.Z., 2000. Path control of a surface ship in restricted waters using sliding mode. IEEE T Contr Syst T, 8(4), 722-732.
https://doi.org/10.1109/87.852916

Zheng, Z.Q., Zou, L., Zou, Z.J., 2022. A numerical investigation on the ship-ship interaction between a passing ship and a moored ship in restricted waterways. In Proceedings of the 6th MASHCON International Conference on Ship Manoeuvring in Shallow and Confined Water, Glasgow, UK, 22-26.

8 AUTHORS BIOGRAPHY

Yu He is a PhD student at School of Ocean and Civil Engineering, Shanghai Jiao Tong University. He majors in ship path following and collision avoidance, etc.

Lu Zou holds the current position of Associate Professor at School of Ocean and Civil Engineering, Shanghai Jiao Tong University. Her major research interest is ship hydrodynamic problems in confined waters, modeling of ship maneuvering motion, ship motion control, etc.

Wei-Min Chen holds the current position of Senior Researcher at Shanghai Ship and Shipping Research Institute Co., Ltd. His previous experience includes ship performance evaluations, ship maneuvering and control, etc.

Zao-Jian Zou is a retired professor at School of Ocean and Civil Engineering, Shanghai Jiao Tong University. His previous experience includes maneuvering and control of ships and other marine vehicles. He was a member of the 22nd, 23rd, 25th and 26th ITTC Maneuvering Committee.

Jin-Lan Li is a Master student at School of Ocean and Civil Engineering, Shanghai Jiao Tong University. She majors in ship path following and collision avoidance, etc.

BAYESIAN-SVR MODEL FOR PREDICTING SHIP MANEUVERING TRAJECTORIES IN DEEP AND SHALLOW WATER CONDITION

Donghyeong Ko, HD Hyundai Heavy Industries Co., Ltd; Department of Naval Architecture and Ocean Engineering, Seoul National University, Republic of Korea

Seong Ho Moon, HD Hyundai Heavy Industries Co., Ltd, Republic of Korea

Bo Woo Nam, Department of Naval Architecture and Ocean Engineering, Seoul National University, Republic of Korea

BAYESIAN-SVR MODEL FOR PREDICTING SHIP MANEUVERING TRAJECTORIES IN DEEP AND SHALLOW WATER CONDITION

Donghyeong Ko, HD Hyundai Heavy Industries Co., Ltd; Department of Naval Architecture and Ocean Engineering, Seoul National University, Republic of Korea
Seong Ho Moon, HD Hyundai Heavy Industries Co., Ltd, Republic of Korea
Bo Woo Nam, Department of Naval Architecture and Ocean Engineering, Seoul National University, Republic of Korea (Corresponding Author: bwnam@sun.ac.kr)

SUMMARY

Maneuverability is influenced by hydrodynamic interactions between the hull and the fluid, affected by draft, trim, and water depth. Particularly in shallow water (H/D ≤ 1.5), reduced under-keel clearance increases hull loads and decreases maneuverability, raising accident risks. Consequently, accurate trajectory prediction in shallow water conditions is essential for safe navigation. This study proposes a grey-box-based machine learning framework (Bayesian-SVR) to predict VLCC maneuverability in both deep and shallow waters. A physical model based on MMG equations is developed, using Bayesian estimation with empirical formulas as prior information. Machine learning corrects residual errors in the physical model, addressing inaccuracies and overfitting issues. CFD Simulations by STAR-CCM+ were used to generate training and validation data, verifying the influence of water depth on maneuverability and the accuracy of the method. In this study, the results demonstrate that the Bayesian-SVR provides robust performance, offering fast and reliable trajectory prediction, , even with small datasets, making it suitable for on-board maneuvering prediction models.

1 INTRODUCTION

Understanding a ship's maneuverability is important for ensuring safe navigation and improving economic efficiency. The advancement of autonomous navigation technologies has further emphasized the need for rapid and accurate predictions of ship's maneuvering capabilities during voyages. However, evaluating maneuverability in maritime environments presents several challenges. A ship's behavior can vary significantly depending on navigational conditions, such as ship design and loading conditions, all of which notably affect fluid-structure interactions. These variations in hydrodynamic and steering forces complicate the prediction of maneuvering performance. Additionally, in shallow waters with low water depth (h)-to-draft (d) ratios (h/d ≤ 1.5), hydrodynamic forces increase sharply, creating substantial difficulties in accurately estimating maneuvering performance. Thus, developing adaptable and accurate prediction methods for diverse maritime conditions remains imperative.

Traditionally, empirical formula-based MMG (Maneuvering Modeling Group) models have been the standard approach for estimating ship maneuvering performance. These methods derive generalized maneuvering characteristics from captive model tests and full-scale sea trial data. Researchers (Kijima et al, 1990; Lee et al., 2003; Aoki et al, 2006) have proposed empirical formulas based on accumulated datasets. While these methods allow for quick predictions, their reliance on a ship's principal parameters (e.g., length, breadth, draft) makes it difficult to account for subtle variations in loading conditions, hull forms, and water depth, even within similar or identical parameter ranges. Additionally, studies that analyze the impact of water depth changes on maneuvering performance remain limited, highlighting the need for improved accuracy to ensure broader applicability.

Currently, Computational Fluid Dynamics (CFD) techniques have been widely used for maneuverability estimation. Studies (Kim et al., 2022; Yang et al.,2024) have investigated ship maneuverability in shallow waters through virtual captive model tests and free-running tests. Although CFD-based approaches can simulate intricate fluid dynamics around a ship, their reliance on substantial computational resources limits their applicability in real-time onboard navigation.

Recently, machine learning (ML) techniques using navigation data have gained attention for predicting ship maneuverability. These data-driven methods enable recursive estimation of ship dynamics, allowing real time adaptation to variation in environmental and loading conditions. Approaches, such as SVR (Support Vector Regression), GP (Gaussian Process), LSTM (Long Short-Term Memory), and GRU (Gated Recurrent Unit) have demonstrated strong potential in prediction, as evidenced (Wang and Xiao, 2023; Wang et al., 2023). In addition, an ensemble-based online estimation framework for recursive updates (Yu et al.,2024) was proposed. Leveraging navigational data, ML-based methods offer versatility across a wide range of scenarios, presenting the potential to overcome the limitations of traditional and simulation-based methods.

However, these ML models are mostly relied on black-box. As noted (Alexandersson et al.,2023), noise or overfitting issues may lead to overestimated maneuvering trajectories for black-box model. Furthermore, the lack of physical considerations makes it difficult to accurately reflect the hydrodynamic characteristics of a ship. In navigation, rudder commands are often short and infrequent, and since a ship's maneuvering characteristics are independent of temporal relationships (memory effects), methods like LSTM and GRU, which rely on continuous temporal data, may be less efficient in this context.
To address these limitations, this study proposes a new grey-box approach that combines a numerical method using Bayesian estimation with the MMG method and SVR (Bayesian-SVR) to achieve high accuracy and real-time applicability. The validity of the proposed method is verified through CFD-based free-running simulation data in deep and shallow waters. As demonstrated (Xue et al. 2020), Bayesian estimation can be effectively utilized for hydrodynamic coefficient estimation and trajectory prediction in maneuvering. Bayesian estimation incorporates prior information from domain knowledge while accounting for parameter uncertainties and maintain robust even with limited data. In this study, prior information on hydrodynamic coefficients is derived from empirical formulas to minimize discrepancies with measured data. Additionally, SVR is applied to address residual errors between empirical formulas and CFD results, as well as nonlinear maneuvering characteristics observed in low-speed shallow waters. This process enables effective modeling of hydrodynamic coefficients based on physical equations while maximizing performance through machine learning. Both Bayesian estimation and SVR are robust to temporally discontinuous and sparse data, sustaining high accuracy even where rudder commands occur. It means that Bayesian-SVR is well-suited for application as an on-board maneuvering prediction model, providing fast and accurate trajectory predictions in navigation.
The structure of this paper is as follows: Section 2 describes the generation of free-running trajectory data using CFD. Section 3 details the proposed maneuvering estimation methodology based on Bayesian estimation and SVR. Section 4 validates the proposed method using free-running data and analyzes its effectiveness. Finally, Section 5 concludes the study and discusses potential directions for future research.

2 NUMERICAL METHOD

2.1 MATHEMATICAL MODEL

This study evaluates the maneuvering performance of a ship using a grey-box approach that integrates a physics-based model with machine learning techniques. The analysis procedure is described in the flow chart provided in Figure 1. The proposed methodology begins with the construction of a physics-based MMG maneuvering model. Bayesian estimation is then employed to update hydrodynamic coefficients and propeller-rudder interaction coefficients, utilizing empirical formulas as prior information. To address limitations in the maneuvering equations, Support Vector Regression (SVR) is applied to further refine the results for residual errors, particularly under challenging conditions such as large drift angles, low speeds, and shallow water environments. To assess the robustness of the proposed method under low data sampling conditions, 10% and 30% of the entire dataset were utilized for Bayesian estimation and SVR training. In this study, the MMG model proposed by Sung et al. (2009) is adopted, and the corresponding maneuvering equations are expressed as (1)-(3).

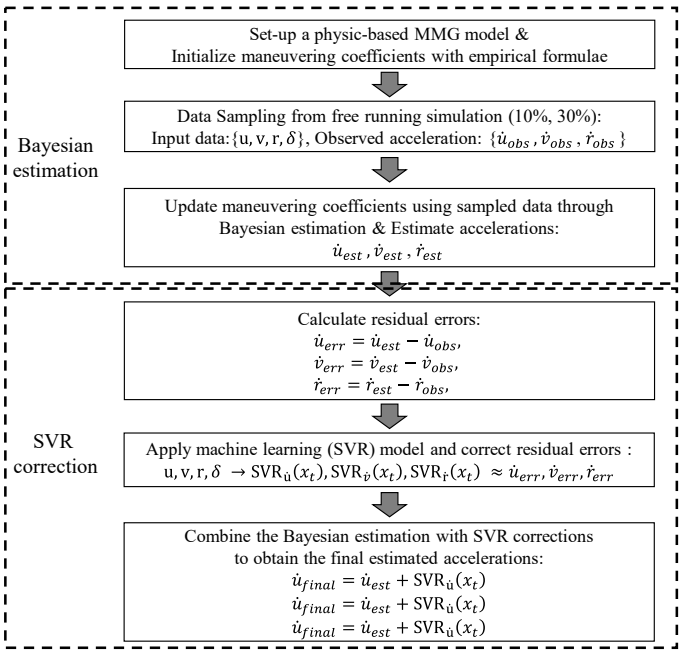

Figure 1 Flowchart of the ship maneuvering model with Bayesian and SVR corrections.

$$(m' + m'_x) \cdot \dot{u}' = \left(X'_{vr} + m' + m'_y\right) \cdot v'r' + X'_{rr}r'^2 + X'_{vv}v'^2 + X'_P + X'_R \tag{1}$$

$$\left(m' + m'_y\right) \cdot \dot{v}' = Y'_v v' + Y'_{vvv}v'^3 + Y'_{vvr}v'^2r' + (Y'_r - (m' + m'_x))r' + Y'_{rrr}r'^3 + Y'_{vrr}v'r'^2 + Y'_R \tag{2}$$

$$(I'_{zz} + J'_{zz}) \cdot \dot{r}' = N'_v v' + N'_{vvv}v'^3 + N'_{vvr}v'^2r' + N'_r r' + N'_{rrr}r'^3 + N'_{vrr}v'r'^2 + N'_R \tag{3}$$

Figure 2 illustrates the coordinate system used in the maneuvering equations. In these equations, primes denote non-dimensional values. Specifically, $u' = \frac{u}{U}$, $v' = \frac{v}{U}$ and $r' = \frac{rL}{U}$ represent the non-dimensional surge velocity, sway velocity, and yaw rate, respectively, where L is the length between perpendiculars and $U = \sqrt{u^2 + v^2}$. The forces X, Y and N correspond to the non-dimensional surge, sway, and yaw forces and moments at the center of gravity scaled by $\frac{1}{2}\rho LTU^2$. The subscripts P and R denote components due to the propeller and rudder, respectively. The expressions for these forces and moments are given in equations (4) and (5), which account for the contributions from the propeller and rudder.

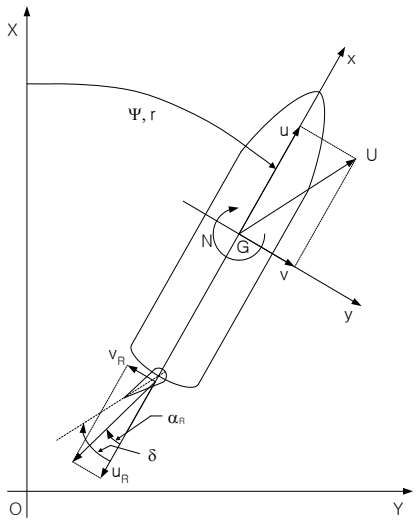

Figure 2 A schematic diagram of coordinate systems

$$X'_P = \frac{(1-t)n^2 D_P^4 K_T}{\left(\frac{1}{2}\right)LTU^2} \tag{4}$$

$$\begin{aligned} X'_R &= -(1 - t_R) \cdot F'_N \cdot \sin\delta \\ Y'_R &= -(1 - a_H) \cdot F'_N \cdot \cos\delta \\ N'_R &= -(x'_R - a_H x'_H) \cdot F'_N \cdot \cos\delta \end{aligned} \tag{5}$$

In the equations, F'_N is defined by (6)

$$F'_N = \frac{A_R}{LT} \cdot \frac{U_R^2}{U^2} \cdot f_\alpha \cdot sin(\alpha_R) \tag{6}$$

Where $U_R^2 = u_R^2 + v_R^2$, and the components u_R and v_R are expressed as equation (7)

$$\begin{aligned} u_R &= \epsilon \cdot (1 - \omega) \cdot u \cdot \left[\eta \cdot \left\{1 + \kappa\left(\sqrt{1 + \frac{8K_T}{\pi J^2}} - 1\right)\right\} + (1 - \eta)\right]^{0.5} \\ v_R &= \gamma_R \cdot (v + rl_R) \end{aligned} \tag{7}$$

Here, γ_R is the flow straightening coefficient, and in this paper, the value of γ_1 is used for port turning and γ_2 for starboard turning conditions. Empirical formulas were utilized as prior information in Bayesian estimation, incorporated into equations (1)-(5). For deep water conditions, the empirical coefficients were referenced from Sung et al. (2009). For shallow water conditions, empirical formulas from the Joint Industrial Project conducted by SSPA, as reported in the SWABE (Shallow Water and Bank Effect) report (Allenström et al., 2009), were utilized to adjust the ship resistance, propeller wake, and linear fluid force coefficients $Y'_v, Y'_r - m' + m'_x, N'_v, N'_r$, as well as the rudder forces.

2.2 BAYESIAN ESTIMATION

The MMG-based maneuvering equations were utilized in this study to predict the maneuverability of the ship, and the relevant coefficients were modified using Bayesian estimation. A random sampling of 10% and 30% of the total dataset, consisting of 3539 sec (deep water) and 3143 sec (shallow water) of free-running CFD simulation results, was selected for random and time-independent maneuvering data, which is visually summarized in Figure 3. The maneuvering equations (1)~(3) were reformulated into a generalized form, as shown in equations (8)-(10):

$$(m' + m'_{\mathrm{x}}) \cdot \dot{\mathrm{u}}' = f_{\mathrm{u}}(\theta, u', v', r', \delta) \tag{8}$$
$$(m' + m'_{\mathrm{y}}) \cdot \dot{\mathrm{v}}' = f_{v}(\theta, u', v', r', \delta) \tag{9}$$
$$(I'_{\mathrm{zz}} + J'_{\mathrm{zz}}) \cdot \dot{\mathrm{r}}' = f_{\mathrm{r}}(\theta, u', v', r', \delta) \tag{10}$$

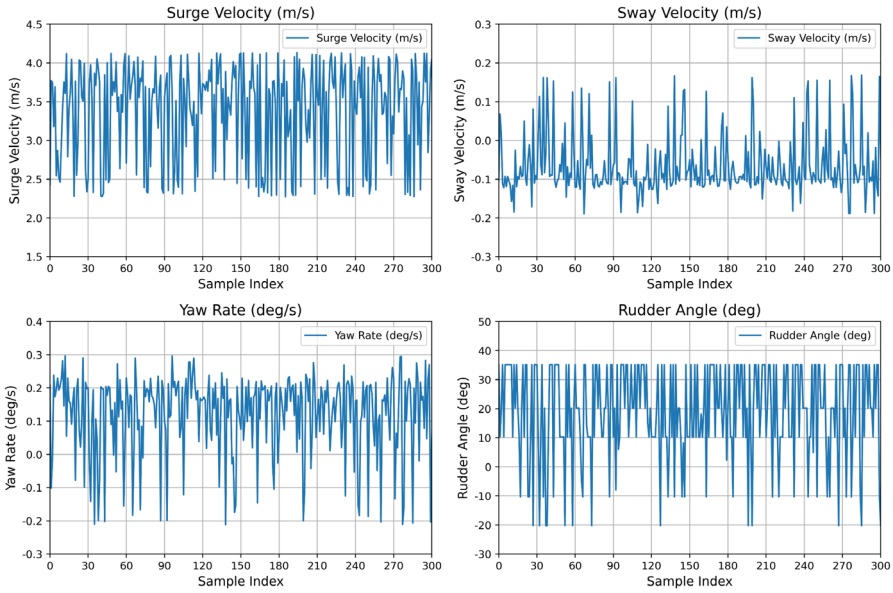

Figure 3 Random Sampling of Maneuvering Dataset for Bayesian Analysis

Here, θ represents the coefficient vector to be estimated, including $\theta_0 = \begin{Bmatrix} \omega, t, \epsilon, \gamma_1, \gamma_2, X'_{\mathrm{vr}}, X'_{\mathrm{vv}}, X'_{\mathrm{rr}}, \\ Y'_{\mathrm{v}}, Y'_{\mathrm{r}} - (m' + m'_{\mathrm{x}}), N'_{\mathrm{v}}, N'_{\mathrm{r}} \end{Bmatrix}$. The functions f_u, f_v and f_r aggregate the terms on the right-hand side of equations (1)-(3), which include hydrodynamic forces, propeller forces, and rudder forces. Given N observed data points $\{\mathrm{x_n}, \mathrm{y_n}\}_{n=1}^{\mathrm{N}}$, the posterior distribution of the model coefficients θ is defined using Bayes' theorem as shown in Equation (11)

$$P(\theta|y_{\mathrm{n}}) = \frac{P(y_{\mathrm{n}}|\theta, x_{\mathrm{n}})P(\theta)}{P(y_{\mathrm{n}})} \propto P(y_{\mathrm{n}}|\theta)P(\theta) \tag{11}$$

In Equation (11), $P(\theta)$ referred to as the prior distribution for θ, $P(y_n|\theta)$ denotes the likelihood, and $P(\theta|y_n)$ corresponds to the posterior distribution. In this study, x_n refers to the n-th data point, which includes the non-dimensional velocity, angular velocity, and rudder angle $(u'_n, v'_n, r'_n, \delta_n)$. The coefficients vector θ in Equation (9) is constructed using prior information derived from empirical formulas for deep and shallow water conditions and is subsequently updated based on the observed acceleration data from free-running simulations $y_n = (\dot{u}'_{\mathrm{obs,n}}, \dot{v}'_{\mathrm{obs,n}}, \dot{r}'_{\mathrm{obs,n}})$.

For the prior distribution in $P(\theta)$, coefficients other than θ_0 defined in Equations (1)-(3) are treated as deterministic values, and θ_0 is assumed to follow a normal distribution with a mean vector, μ_{emp} and a variance vector σ^2_{emp}. The mean vector, μ_{emp} is selected based on empirical formulas, and the variance σ^2_{emp} is set according to the μ_{emp}. Additionally, coefficients such as $Y_{\mathrm{v}}, N_{\mathrm{r}}, Y'_{\mathrm{r}} - (m' + m'_{\mathrm{x}})$, which are physically constrained to be negative, are modeled using truncated normal distributions to reflect the boundary. The likelihood function $P(y|\theta)$ is defined by modeling the residuals between the predicted accelerations $(\dot{u}'_{\mathrm{est,n}}, \dot{v}'_{\mathrm{est,n}}, \dot{r}'_{\mathrm{est,n}})$ from the MMG maneuvering equations and the observed accelerations $(\dot{u}'_{\mathrm{obs,n}}, \dot{v}'_{\mathrm{obs,n}}, \dot{r}'_{\mathrm{obs,n}})$ using a Student-T distribution. This formulation enhances robustness against outliers, prone to large errors, and is expressed as follows in Equation (12).

$$\begin{aligned}\dot{u}'_{\mathrm{obs,n}}|\theta, \mathrm{x_n} &\sim StudentT(\nu_{\dot{u}}, \dot{u}'_{\mathrm{est,n}}, \sigma_{\dot{u}})\\ \dot{v}'_{\mathrm{obs,n}}|\theta, \mathrm{x_n} &\sim StudentT(\nu_{\dot{v}}, \dot{v}'_{\mathrm{est,n}}, \sigma_{\dot{v}})\\ \dot{r}'_{\mathrm{obs,n}}|\theta, \mathrm{x_n} &\sim StudentT(\nu_{\dot{r}}, \dot{r}'_{\mathrm{est,n}}, \sigma_{\dot{r}})\end{aligned} \tag{12}$$

The parameters $\nu_{\dot{u}}, \nu_{\dot{v}}, \nu_{\dot{r}}$ in the Student-T distribution control the tail heaviness, ensuring robustness against outliers. The overall likelihood is expressed as infinite product, $\Pi_{\mathrm{n=1}}^{\mathrm{N}} P(y_{\mathrm{n}}|\theta, x_{\mathrm{n}})$. Since the posterior distribution $P(y_{\mathrm{n}}|\theta)$ is generally intractable in closed form, this study employs automatic differentiation variational inference (ADVI) to approximate Equation (11) for computational efficiency. Once variational inference converges, posterior samples of θ are obtained, providing posterior means, credible intervals, and additional statistics. The posterior means are chosen as the maneuvering coefficient for θ.

2.3 SUPPORT VECTOR REGRESSION

A second-stage correction approach using Support Vector Regression (SVR) is employed to further reduce the residual errors after updating the maneuvering equation coefficients through Bayesian estimation. Although the predicted accelerations $(\dot{u}'_{\mathrm{est,n}}, \dot{v}'_{\mathrm{est,n}}, \dot{r}'_{\mathrm{est,n}})$ can be obtained from the sampled dataset, the maneuvering equations (1)-(3) struggle to fully capture the nonlinear characteristics of free-running maneuvering. Consequently, discrepancies arise relative to the actual observed values $(\dot{u}'_{\mathrm{obs,n}}, \dot{v}'_{\mathrm{obs,n}}, \dot{r}'_{\mathrm{obs,n}})$. Defining these discrepancies as residual errors yields Equation (13)

$$\begin{aligned}\dot{u}'_{\mathrm{err,n}} &= \dot{u}'_{\mathrm{est,n}} - \dot{u}'_{\mathrm{obs,n}}\\ \dot{v}'_{\mathrm{err,n}} &= \dot{v}'_{\mathrm{est,n}} - \dot{v}'_{\mathrm{obs,n}}\\ \dot{r}'_{\mathrm{err,n}} &= \dot{r}'_{\mathrm{est,n}} - \dot{r}'_{\mathrm{obs,n}}\end{aligned} \tag{13}$$

Where, $\mathrm{n} = 1..\mathrm{N}$ indicates the indices of the data points in the sampled dataset used for Bayesian estimation, and these residual errors are subsequently employed as target values for additional machine learning models. To learn the residual errors $(\dot{u}'_{err,n}, \dot{v}'_{err,n}, \dot{r}'_{err,n})$ with respect to the input variable x_n, this study applies Support Vector Regression (SVR). In SVR, slack variables $(\xi_{n,}, \xi_n^*)$ are introduced to build a regression model that is robust to outliers and can capture nonlinearity, represented as follows in Equation (14)

$$\min_{\mathrm{w,b},\xi,\xi^*} \frac{1}{2}||w||^2, \text{ subject to } \begin{cases} y_{\mathrm{n}} - (w \cdot x_{\mathrm{n}} + b) \le \epsilon + \xi_{\mathrm{n}}, \\ (w \cdot x_{\mathrm{n}} + b) - y_n \le \epsilon + \xi_{\mathrm{n}}^*, \\ \xi_{\mathrm{n}}, \xi_{\mathrm{n}}^* \ge 0 \end{cases} \tag{14}$$

The hyper-parameters of SVR include (i) C, which determines the tolerance level for slack variables, (ii) γ, which controls the nonlinearity of the RBF, kernel function, and (iii) ϵ, which defines the acceptable margin of error. During the training process, separate SVR models were utilized for each acceleration error set $\{\dot{u}'_{\mathrm{err}}, \dot{v}'_{\mathrm{err}}, \dot{r}'_{\mathrm{err}}\}_{\mathrm{n=1}}^{\mathrm{N}}$, and GridSearchCV was employed to identify the optimal combination of (C, γ, ϵ). Using the trained SVR model, a second-stage correction was performed on the Bayesian estimation model. Specifically, when a new input variable $x_{\mathrm{t}} = (u'_{\mathrm{t}}, v'_{\mathrm{t}}, r'_{\mathrm{t}}, \delta'_{\mathrm{t}})$ is provided, the errors predicted by SVR $(\mathrm{SVR}_{\dot{u}}(x_{\mathrm{t}}), \mathrm{SVR}_{\dot{v}}(x_{\mathrm{t}}), \mathrm{SVR}_{\dot{r}}(x_{\mathrm{t}}))$ are added to the original predicted values $(\dot{u}'_{\mathrm{est,t}}, \dot{v}'_{\mathrm{est,t}}, \dot{r}'_{\mathrm{est,t}})$ to determine the final results. Equation (13) illustrates this two-step integration process. As a result, the final predicted values $(\dot{u}'_{\mathrm{final,t}}, \dot{v}'_{\mathrm{final,t}}, \dot{r}'_{\mathrm{final,t}})$ represent a combination of the Bayesian-estimated model and the SVR-based error correction model. This integrated approach achieves reduced prediction errors compared to utilizing a single model.

3 CFD SET-UP

In this study, free-running simulations were conducted using commercial CFD software STAR-CCM+ for a model-scale VLCC under both deep-water and very shallow-water conditions of a water depth-to-draft ratio of 1.2. The principal specifications of the model are summarized in Table 1. The flow field was analyzed based on the unsteady incompressible Reynolds-averaged Navier–Stokes (URANS) equations, and the k-ω SST turbulence model was employed to capture complex turbulent behaviors. The Volume of Fluid (VOF) method with High Resolution Interface Capturing (HRIC) scheme was used for free surface modelling.

The computational domain was designed as a cylindrical region with a diameter of 2L, centered at the ship's After Perpendicular (AP). A damping zone was applied at the inlet boundary for a length of 2/3 L to minimize wave reflections and flow disturbances caused by fluid-body interactions. The top boundary of the domain was defined as a pressure outlet, while the bottom boundary was set as a non-slip wall to account for seabed interactions in shallow water as shown in Figure 4. To

accurately resolve the flow around the hull and free surface, a computational grid of approximately 9 million cells was constructed using a combination of trimmer mesh and prism layers.
The time step was set to 0.025 seconds in accordance with the ITTC 2014 guidelines ($\Delta t < 0.01$ L/U), and the Dynamic Fluid Body Interaction (DFBI) technique was applied to simulate the 6-DoF ship motions induced by hydrodynamic forces and moments (ITTC, 2014). The overset mesh technique was used to implement the complex motion of the hull and rudder, allowing the rudder to rotate in response to steering commands. In the case of shallow water condition analysis, a dual overset mesh was applied, as shown in Figure 5, consisting of the rudder, hull, and background region to reflect the flow characteristics between the ship and the seabed. The propeller's rotational effects were simulated using the virtual disk method, incorporating thrust and torque coefficients derived from open water test results. Time-series data for ship speed, angular velocity, and rudder angle were obtained through 10/10 and 20/5 zig-zag maneuvers and turning simulations to analyze the maneuvering characteristics of the vessel.

Table 1 Principal dimensions of the model-scale VLCC

Parameters	Unit	Value
Length Between Perpendicular, L_{pp}	[m]	7.34
Breadth, B	[m]	1.38
Draft, T	[m]	0.50
Block coefficient, C_b	[-]	0.80
Propeller diameter/ Rudder height, η	[-]	0.75
Rudder area ratio, $\frac{\text{Area}}{L_{pp}T}$	[-]	1.70

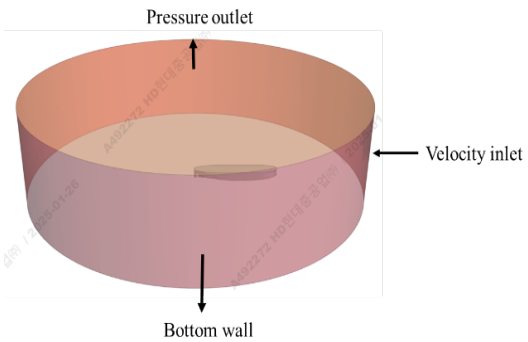

Figure 4 Computational domain for free running simulation

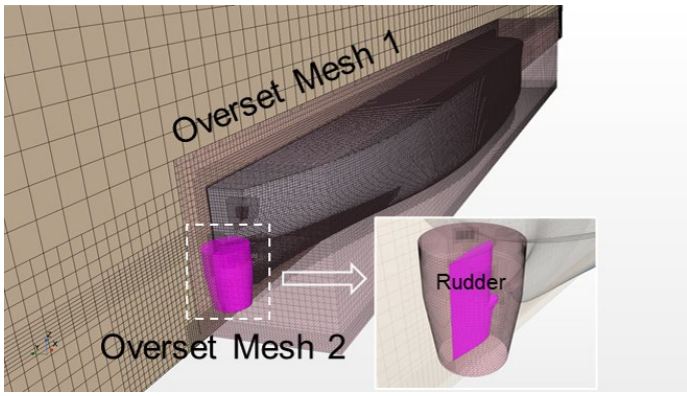

Figure 5 Visualization of the dual overset mesh in shallow water conditions

4 RESULTS

Using sampled data, Bayesian estimation was applied to MMG-based maneuvering equations, followed by an additional correction using SVR, to perform maneuvering test (e.g., turning and 10/10 zigzag test) through recursive time series forecasting. The estimated results were then compared and validated against free-running simulation data in both deep and shallow water conditions with the results converted to full scale. First, Θ was initialized using prior information derived from empirical formulas. Bayesian estimation was then performed by randomly sampling 10% and 30% from the total dataset, updating Θ accordingly. The posterior mean of the estimated maneuvering coefficients and their 94% Highest Density Interval (HDI) are presented in Table 2 and Figure 6.

Analysis of the posterior distribution of the coefficients (Y'_v, Y'_r-$(m'+m'_x)$, N'_v, N'_r, X'_{vr}, X'_{vv},...) revealed that Θ followed mostly a normal distribution while exhibiting a narrow 94% HDI relative to the mean values of each coefficient. This indicates that Θ converged stably during the Bayesian estimation process. Additionally, coefficients that are physically constrained to be negative remained within the negative domain, ensuring consistency with physical expectations. Furthermore, the Monte Carlo Standard Error (MCSE), which quantifies the variability of the posterior mean estimate, was computed. The results showed that MCSE values approached zero, confirming that the posterior mean estimates for the maneuvering coefficients have converged with high stability. These findings suggest that Bayesian estimation effectively integrates prior distributions with observational data, enabling uncertain coefficients to maintain both consistency with physical principles and statistical stability.

Table 2 Bayesian Estimation of Maneuvering Coefficients with 94% HDI in Deep and Shallow Water Conditions

Coefficients		Deep Water Condition		Shallow Water Condition	
		Empirical values [Sung et al., 2009]	Bayesian estimation [10% / 30%, sampling + 94% HDI]	Empirical values [Allenström et al., 2009]	Bayesian estimation [10% / 30%, sampling + 94% HDI]
X'_{vr}		57741	63654/65385 $\pm$350	57741	60172/64536 $\pm$2000
X'_{vv}		6180	5755/5513 $\pm$350	6180	6157/6208 $\pm$500
X'_{rr}		2335	1873/2325 $\pm$200	2334	872/-2020 $\pm$500
Y'_{v}		-33738	-40664/-44308 $\pm$900	-128204	-130087/126898 $\pm$1600
Y'_{vvv}		-82783	-	-	-
$Y'_{\mathrm{r}} - (m' - m'_{\mathrm{x}})$		-23182	-20810/-21716 $\pm$350	-18626	-10557/8678 $\pm$350
Y'_{rrr}		258	-	-	-
Y'_{vvr}	$(\cdot\, 10^5)$	25513	-	-	-
Y'_{vrr}		38623	-	38623	-
N'_{v}		-15146	-8711/-5532 $\pm$100	-39684	-52075/56320 $\pm$350
N'_{vvv}		-45	-	-45	-
N'_{r}		-5050	-2658/-925 $\pm$100	-12677	-8261/8548 $\pm$100
N'_{rrr}		-1177	-	-	-
N'_{vvr}		-23731	-	-	-
N'_{vrr}		1417	-	-	-
ϵ		1.05	1.160/1.084 $\pm$0.005	1.05	0.972/0.943 $\pm$0.005
γ_1		0.300	0.319/0.331 $\pm$0.02	0.300	0.093/0.046 $\pm$0.05
γ_2	(-)	0.300	0.597/0.599 $\pm$0.002	0.300	0.348/0.322 $\pm$0.015
wake		0.333	0.320/0.301 $\pm$0.005	0.456	0.438/0.403 $\pm$0.01
thrust deduction		0.157	0.157/0.157 $\pm$0.005	0.157	0.157/0.157 $\pm$0.01

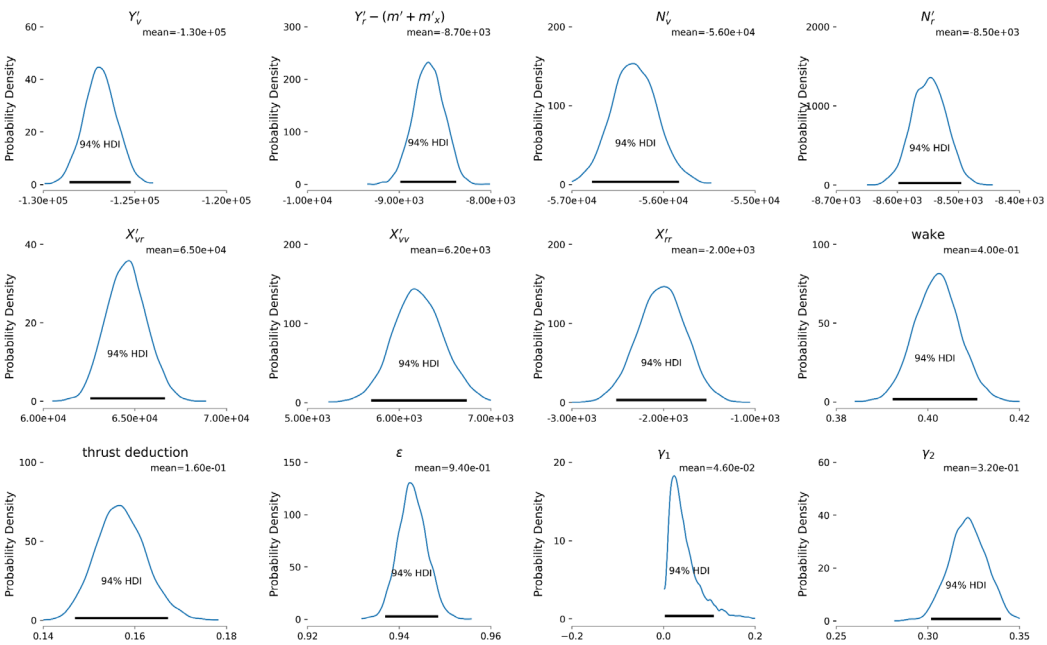

Figure 6 Bayesian Estimation of Maneuvering Coefficients with 94% HDI in Shallow Water Condition(30% sampled data)

Figure 7 and Table 3 illustrate the comparison between the acceleration distribution of the entire dataset calculated through free running simulations and the residuals obtained by applying a Bayesian estimation trained on 30% sampled data, where the residuals represent the differences between the estimated and actual acceleration values. As shown in the figures and tables, the standard deviations of surge, sway, and yaw accelerations markedly decreased under both deep and shallow water conditions after incorporating Bayesian-estimated coefficients into the maneuvering equations. Additionally, the gap between the mean and median values narrowed substantially. For example, in deep water conditions, the surge acceleration ($|\dot{u}|$) exhibited a mean of 1.59· 10^{-3} m/s², a median of 0.95· 10^{-3} m/s², and a standard deviation of 1.96· 10^{-3} m/s² before correction. After Bayesian correction, these values improved to a mean of 1.05×· 10^{-3}m/s², a median of 0.89· 10^{-3}m/s², and a standard deviation of 0.80· 10^{-3} m/s².

While residual bias remains, the overall error distribution became noticeably more concentrated around the mean. This means that the prediction errors are closer to the mean, and the distribution has narrowed, resulting in the predicted values becoming closer to the actual values and improving the stability of the predictions. This characteristic helps reduce the uncertainty of the model and contributes to improving the consistency of the predictions. When the predicted values concentrate, the variability decreases, enabling the development of a simpler and more efficient model. Similar improvements were observed in sway and yaw accelerations, suggesting that Bayesian estimation is effective across all free-running conditions. Ultimately, Bayesian correction not only refines the error distribution but also contributes to achieving a balanced trade-off between accuracy and computational efficiency in subsequent machine learning processes.

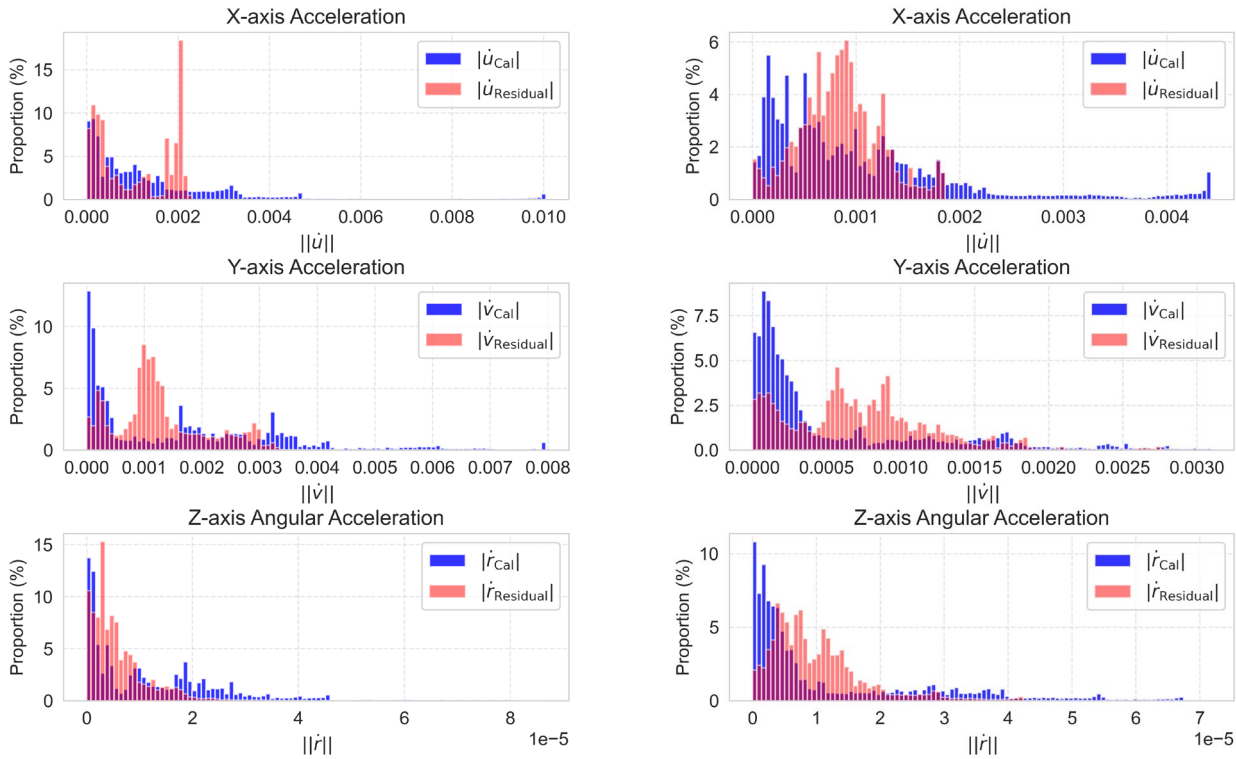

Figure 7 Acceleration Distributions from sampled data and Residuals after Bayesian Estimation.
(Left: Deep water condition, Right: Shallow water condition)

Table 3 Comparison of calculated accelerations from the simulation and residuals after Bayesian correction under deep and shallow water conditions.

Variables	unit	Deep Water Condition ($\cdot 10^5$)			Shallow Water Condition ($\cdot 10^5$)		
		Mean	Median	std	Mean	Median	std
$\lvert\dot{u}_{Cal}\rvert$	m/s²	159.0	95.0	196.0	104.2	77.0	95.7
$\lvert\dot{u}_{Cal} - \dot{u}_{Bayesian}\rvert$		105.0	88.6	80.5	84.9	84.1	38.4
$\lvert\dot{v}_{Cal}\rvert$		175.6	142.1	176.5	57.3	23.5	69.1
$\lvert\dot{v}_{Cal} - \dot{v}_{Bayesian}\rvert$		129.9	113.1	84.5	73.6	68.5	50.4
$\lvert\dot{r}_{Cal}\rvert$	deg/s²	1.33	0.90	1.49	1.24	0.46	1.54
$\lvert\dot{r}_{Cal} - \dot{r}_{Bayesian}\rvert$		0.63	0.44	0.68	1.03	0.82	0.79

Additionally, the performance of the SVR model and the Bayesian-SVR model was compared through turning and zigzag simulations, with quantitative errors evaluated against the free-running simulation results (Reference). Figure 8 provides a visual comparison of trajectories, speeds, and accelerations, while Table 4 presents the Mean Absolute Error (MAE) for each test. In the zigzag test, both models showed similar performance, with error differences in the range of 10^{-2} to 10^{-3}. However, during the turning simulation, the SVR model exhibited a rapid increase in yaw rate and trajectory errors over time, whereas the Bayesian-SVR model maintained high consistency with the reference trajectory (black solid line), regardless of the amount of sample data.

The SVR model encountered increasing prediction errors due to the accumulation of errors in the feedback loop when used with input values close to the boundary of the training data, as seen in the turning simulation. Initial prediction errors were repeatedly fed into the model, gradually accumulating and amplifying, which caused the predicted values to deviate further over time. Specifically, significant increases in error were observed in v (knots) and r (deg/s), with the r (deg/s) error rising from 0.075 in the 10% sampled data to 0.140 in the 30% sampled data. This is assumed to result from the 30% data including more samples, thus learning more complex patterns near the boundary, which accelerated the extrapolation and accumulation of small errors. In contrast, the Bayesian-SVR model effectively addressed the issue of accumulating prediction errors by stabilizing the posterior distribution within physical limits using a physics-based estimation method. This approach alleviated extrapolation problems in the boundary regions, allowing predictions to remain more stable. In particular, the r (deg/s) error was maintained at a low level of 0.007 during the turning simulation, indicating that the Bayesian-SVR model effectively prevented the divergence issues that can occur at the boundaries.

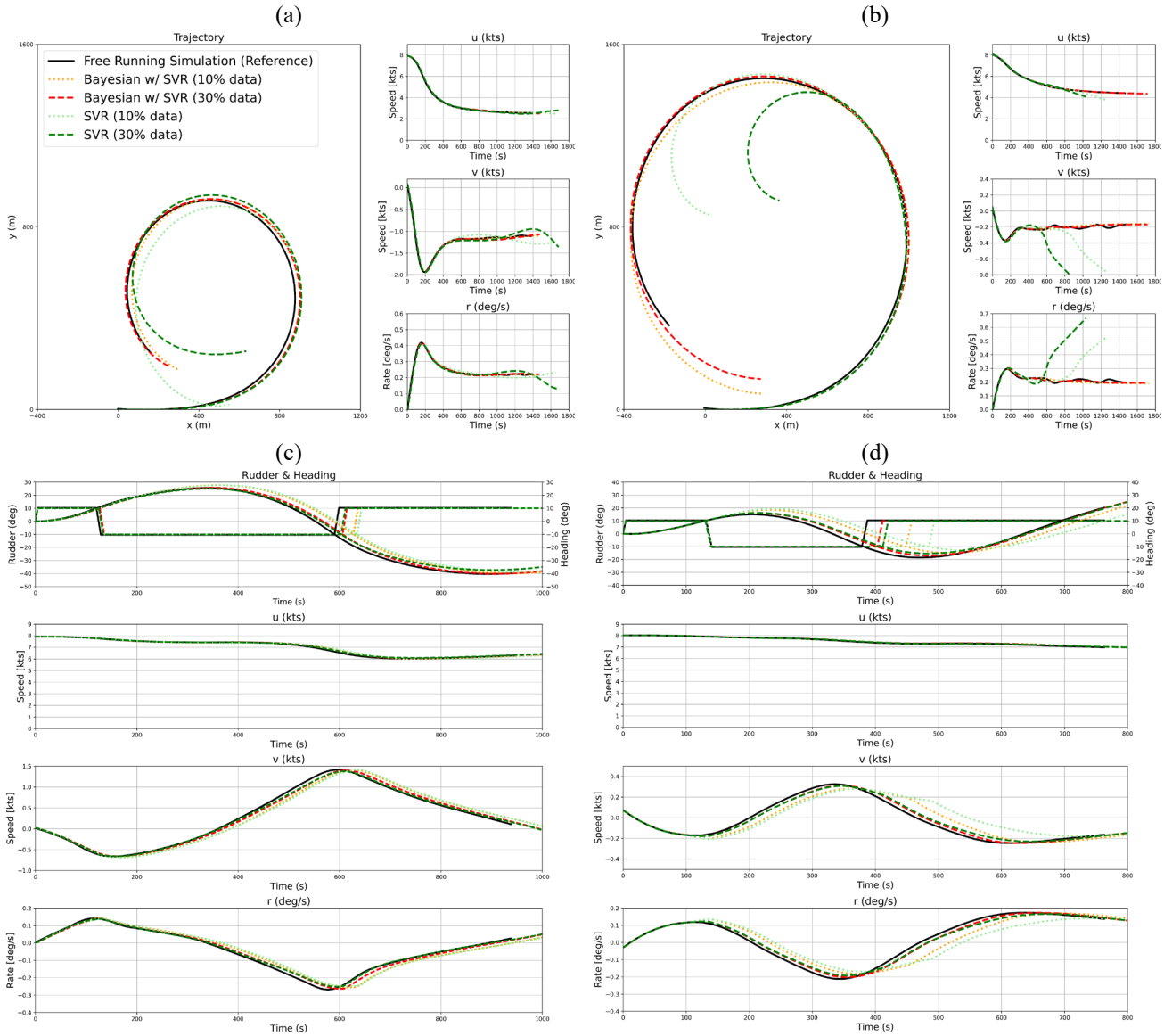

Figure 8 Comparison of SVR and Bayesian-SVR Methods for Turning and Zigzag Simulations under Deep-water and Shallow-water Conditions. (a) Turning in deep water condition, (b) Turning in shallow water condition, (c) 10/10 zigzag in deep water condition, (d) 10/10 zigzag in shallow water condition.

These results suggest that while the SVR model demonstrates stability within the range of the training data (e.g., rudder commands in the zigzag test), the physics-based Bayesian estimation is more effective in situations requiring extrapolation or when operating the training data boundaries (e.g., large turning maneuvers). The proposed Bayesian-SVR method stabilizes the posterior distribution within physical limits, thereby resolving the divergence problem observed with the SVR model that relies solely on sampled data. This ensures reliable trajectory and ship behavior predictions, even under varying environmental conditions.

Table 4 Mean Absolute Errors in Zigzag and Turning Tests for Velocity (u, v in m/s) and Yaw Rate (r in deg/s) Using SVR and Bayesian-SVR Under 10% and 30% Sampled Data in Shallow Water Conditions.

Items	Variable	SVR		Bayesian-SVR	
		10% sampled data	30% sampled data	10% sampled data	30% sampled data
Zigzag test	u (knots)	0.044	0.016	0.036	0.020
	v (knots)	0.086	0.024	0.056	0.019
	r (deg/s)	0.052	0.015	0.037	0.013
Turning test	u (knots)	0.110	0.101	0.016	0.017
	v (knots)	0.135	0.247	0.015	0.011
	r (deg/s)	0.075	0.140	0.010	0.007

5 CONCLUSIONS

A grey-box method (Bayesian-SVR) that integrates a physics-based MMG model with Bayesian estimation and SVR-based residual corrections was developed to evaluate ship maneuvering performance. Bayesian estimation was employed to update the hydrodynamic and propeller–rudder interaction coefficients by integrating prior information based on empirical formulas, ensuring that the coefficients converged stably within physical boundary. Moreover, SVR was applied to the residual errors following the coefficient update, effectively mitigating the divergence issues observed when using a black-box model, particularly in extrapolation scenarios such as low-speed and high-drift conditions. Through random sampling (10% and 30%) of free running simulation data, the robustness with respect to data quantity was evaluated. It was confirmed that, under both deep-water and shallow-water conditions, the posterior distributions of the coefficients converged stably after Bayesian estimation, resulting in a notable reduction in the variances of surge, sway, and yaw accelerations. A comparison of the Bayesian-SVR model and the SVR model based on turning and zigzag simulations indicated that while both the SVR and Bayesian-SVR models produced satisfactory estimates within the training range, the physics-based Bayesian-SVR model demonstrated superior performance—maintaining a high degree of consistency with the reference trajectory—when operating conditions approached the boundaries of the training data. The proposed Bayesian-SVR method ensures stable coefficient estimation and effectively resolves the divergence issues observed when using an SVR model based solely on sampled data. Consequently, this approach enables reliable predictions of trajectories and ship behavior even under various water depth and environmental conditions. Future work will focus on deriving robust maneuvering equations that remain effective under various vessel speeds and draft conditions and on developing corresponding hydrodynamic coefficient estimation techniques to ultimately construct a data-driven, robust model.

6 REFERENCES

Alexandersson, M., Zhang, D., Mao, W., Ringsberg, J.W., 2023. A comparison of ship manoeuvrability models to approximate ship navigation trajectories. *Ships and Offshore Structures* 18(4), 550-557.

Allenström, B., 2009. Joint Industrial Project SWABE: Compilation of SSPA Reports 4006 4341-1 to 4006 4341-14. SWABE Consortium/SSPA Sweden AB, Report no. 4006 4341-15 rev. 5, Stockholm, Sweden.

Aoki, I., Kijima, K., Furukawa, Y., Nakiri, Y., 2006. On the prediction method for maneuverability of a full-scale ship. *Journal of the Japan Society of Naval Architects and Ocean Engineers* 3, 157-165.

ITTC, 2014. ITTC - Recommended Procedures and Guidelines: Practical Guidelines for Ship CFD Applications.

Kim, D., Tezdogan, T., Incecik, A., 2022. Hydrodynamic analysis of ship manoeuvrability in shallow water using high-fidelity URANS computations. *Applied Ocean Research* 123, 103176.

Kijima, K., Katsuno, T., Nakiri, Y., Furukawa, Y., 1990. On the manoeuvring performance of a ship with the parameter of loading condition. *Journal of The Society of Naval Architects of Japan* 168, 141-148.

Lee, T., Ahn, K., Lee, H., Yum, D., 2003. On an empirical prediction of hydrodynamic coefficients for modern ship hulls. In: *International Conference on Marine Simulation and Ship Manoeuvrability*, 555-562.

Wang, X., Xiao, Y., 2023. A deep learning model for ship trajectory prediction using automatic identification system (AIS) data. *Information* 14, 212. https://doi.org/10.3390/info14040212.

Wang, Z., Kim, J., Im, N., 2023. Non-parameterized ship maneuvering model of deep neural networks based on real voyage data-driven. *Ocean Engineering* 284, 115162.
Xue, Y., Liu, Y., Ji C., Xue, G., 2020. Hydrodynamic parameter identification for ship manoeuvring mathematical models using a Bayesian approach. *Ocean Engineering* 195, 106612.
Yang, Y., Chillcce, G., el Moctar, O., 2024. A mathematical model for ships maneuvering in deep and shallow waters. *Ocean Engineering* 295, 116927.
Yu, Y., Hao, H., Wang, Z., Peng, Y., Xie, S., 2024. Online prediction of ship maneuvering motions based on adaptive weighted ensemble learning under dynamic changes. *Engineering Applications of Computational Fluid Mechanics*.
Sung, Y., Ahn, K., Lee, T., 2009. Development of new empirical formulae for manoeuvring coefficients and application on rudder design. In: *Proceedings of 10th International Marine Design Conference*, Vol. I, Trondheim, Norway, 26-29 May 2009, 382-394.

7 AUTHORS BIOGRAPHY

Donghyeong Ko holds the current position of Senior Researcher and Navigation Solution Team Leader at HD Hyundai Heavy Industries Co., Ltd. He is responsible for evaluating hydrodynamics and maneuvering performance of the ships, analyzing ship navigation data, and R&D activities. His previous experience includes evaluating the maneuverability of large merchant vessels and submarines, conducting various model tests and sea trials on maneuvering and seakeeping, and applying machine learning techniques in research for optimal rudder design, maneuverability estimation, and wave prediction using the ship-as-a-buoy method.
Seong Ho Moon holds the current position of Senior Researcher at HD Hyundai Heavy Industries Co., Ltd. He is responsible for ship maneuvering performance evaluation and CFD analysis. His previous experience includes CFD-based seakeeping performance evaluation, research on sloshing analysis, as well as experience in model tests and sea trials.
Bo Woo Nam holds the current position of Associate Professor at the Department of Naval Architecture & Ocean Engineering, Seoul National University. He is responsible for conducting research and teaching in the fields of ship seakeeping, hydrodynamics, and the maneuvering and control of ocean vehicles. His previous experience includes serving as an Assistant Professor at Seoul National University and working as a Principal Researcher at KRISO (Korea Research Institute for Shipbuilding & Offshore Engineering), where he focused on marine energy utilization, ocean space utilization, and various marine operations such as installation, lifting, and towing.

UNBERTHING SIMULATIONS OF A SHIP USING A FIRST-ORDER LAG MODEL TO TAKE THE HYDRODYNAMIC MEMORY EFFECT INTO ACCOUNT

Ryusuke Okuda, National Maritime Research Institute, Japan

Hironori Yasukawa, Hiroshima University, Japan

UNBERTHING SIMULATIONS OF A SHIP USING A FIRST-ORDER LAG MODEL TO TAKE THE HYDRODYNAMIC MEMORY EFFECT INTO ACCOUNT

RYUSUKE OKUDA, NATIONAL MARITIME RESEARCH INSTITUTE, JAPAN
HIRONORI YASUKAWA, HIROSHIMA UNIVERSITY, JAPAN

SUMMARY

When a ship is unberthing, transient hydrodynamic forces act on the ship hull, and these forces vary due to the ship-bank distance. Therefore, hydrodynamic forces may not be treated as quasi-steady when conducting unberthing simulations. This study aims to incorporate the effects of these forces into unberthing simulations to improve the accuracy of the estimation. We focused on the hydrodynamic forces of a single-propeller and single-rudder ship and conducted captive model tests to measure the transient hydrodynamic forces. To capture the tendency of transient hydrodynamic forces during unberthing, a first-order lag and dead-time model were introduced to model the hull force. Furthermore, the model was implemented in unberthing simulations, and the results were compared with the author's free-running model test results for validation, which revealed an improvement in the accuracy of the simulation.

NOMENCLATURE

A_R	Total rudder area (m^2)
B	Ship breadth (m)
B_R	Rudder chord length (m)
C_b	Block coefficient
C_{HX}, C_{HY}, C_{HN}	Hydrodynamic force coefficients with respect to surge, sway, and yaw moment acting on the ship hull
$D_{11}^{(i)}$	Change in hydrodynamic force owing to ship-bank distance during straight moving
D_P	Propeller diameter (m)
d	Ship draft (m)
F_{Bi}	Additional force owing to the bank effect (i = 1, 2, 3) (N)
F_{BTi}	Bow thruster force (i = 1, 2, 3) (N)
F_{Hi}	Hull force (i = 1, 2, 3) (N)
F_N	Total rudder normal force (N)
F_{Pi}	Propeller force (i = 1, 2, 3) (N)
F_{Ri}	Rudder force (i = 1, 2, 3) (N)
$\overline{GM}$	Metacentric height (m)
h	Water depth (m)
H_R	Rudder span length (m)
k_d	Sample time (s)
K_1	System gain for a first-order lag model
L	Ship length between perpendiculars (m)
L_1	Dead time for a first-order lag model
m	Ship mass (kgf s^2/m)
m_{kj}	Added mass components
m_{kjy}	Added mass derivatives
N	Yaw moment (Nm)
n_P	Propeller revolution (rps)
n_B	Bow thruster impeller revolution (rps)
o - xyz	Fixed coordinate system of ship taking the origin at midship
o_0 - $x_0y_0z_0$	Space fixed coordinate system
p	Propeller pitch ratio
r	Yaw rate
T	Propeller thrust (N)
t	Time (s)
t_d	Dead time (s)

T_s	Sampling time (s)
T_1	Time constant for a first-order lag model
U	Resultant speed ($=\sqrt{u^2+v_m^2}$) (m/s)
U_0	Steady speed while unberthing (m/s)
u	Surge velocity (m/s)
v_m	Lateral velocity at the midship (m/s)
x_G	Longitudinal coordinate of the center of gravity of the ship (m)
T_{BT}	Lateral force generated by the bow thruster (N)
X	Surge force (N)
Y	Lateral force (N)
Z	Number of propeller blades
α_r	Yaw rate angle (°)
β	Hull drift angle (°)
δ	Rudder angle (°)
δ	Rudder angle (°)
δ_F	Flap angle (°)
ψ	Heading angle (°)
η_0	Distance from the midship to the bank (m)
ρ	Water density (N/m^3)
∇	Displacement volume of the ship (m^3)
Suffixes 1, 2, 3	Direction of surge, sway, and yaw, respectively.

1 INTRODUCTION

When a ship moves laterally close to the bank, such as during berthing and unberthing, the additional hydrodynamic forces are caused by the bank effect acting on the ship hull, unlike during normal maneuvering motion (e.g., turning, zigzag-maneuver) in the open sea. To advance such automatic berthing technology, it is necessary to predict the ship maneuvering motion during berthing and unberthing with high accuracy.

Previous studies have shown that when a ship moves laterally with large drift angles, e.g., during berthing and unberthing, there is a response delay in the hydrodynamic forces acting on the ship hull. For example, Sadakane and Tsuruta (1993) and Sadakane (1996) measured transient lateral forces on a ship moving pure-laterally from rest and observed the response delay from experiments. Lee et al. (2003) conducted computational fluid dynamics (CFD) calculations to investigate the response delay caused by lateral forces and reported that if the water depth becomes shallower, then the pressure difference between the port and starboard sides due to shed vortices is relevant. Shintani et al. (2020) reported the memory effects that produce the hull lateral force during unberthing on the basis of their CFD results. Yoneda et al. (2018) conducted captive model tests for unberthing with varying water depth, acceleration, and ship-bank distance, and showed differences in the hydrodynamic characteristics acting on the ship hull. However, these studies are only focused on pure-lateral motion and are not useful for modeling the hydrodynamic forces of a single-propeller and single-rudder ship. It cannot move pure-laterally without the assistance of tugs or bow and stern thrusters because the propeller induces forward motion. We believe that oblique sailing conditions should be considered for lateral movement.

This study focused on a single-propeller and single-rudder ship to obtain transient hydrodynamic forces acting on the hull during unberthing with various unberthing angles (drift angles) from the bank. In addition, referring to the formulation of hydrodynamic forces for navigating narrow channels by Yasukawa and Sano (2024), the theoretical hull forces, which consider the change in added mass as the ship approaches the bank, were obtained and compared with the tank test. It was found that the response delay of the hydrodynamic forces, which is remarkable in the captive model tests, cannot be captured by the original theoretical calculation. Therefore, we attempted to approximate the response delay by using a first-order lag and a dead-time model, which is used in the modeling for the control technology. This model, which can reproduce the response delay in hydrodynamic forces, was incorporated into a low-speed ship maneuvering model by Okuda et al. (2023) to perform unberthing simulations of a single-propeller and single-rudder ship with a bow thruster. To confirm the accuracy of the simulations, its results were compared with those of free-running model tests by Okuda et al. (2024).

2 COORDINATE SYSTEMS

Fig. 1 shows the coordinate systems used in this paper. In the ship-fixed coordinate system $o - xyz$, where o is taken at the midship, u and v_m are the velocity components in the x and y directions, respectively. In contrast, we consider the space-fixed coordinate system, where the $x_0 - y_0$ plane coincides with the still water surface and the z_0-axes point vertically downward. The center of gravity G is located at position $(x_G, 0)$. x_G is the longitudinal coordinate of the center of gravity (forward from the midship is positive). An angle generated from x_0 to x is defined by the heading angle ψ. Furthermore, at $y_0 = 0$, a vertical bank in the x_0-direction is assumed to exist, and the distance from the bank wall to the midship position o is defined as η_0. r is the yaw rate around the z-axis, as defined by $d\psi/dt$. The hull drift angle at the midship position β is defined by $\beta = \tan^{-1}(-v_m/u)$, and the total velocity U is defined by $U = \sqrt{u^2 + v_m^2}$. Moreover, δ is the rudder angle, and δ_F is the flap angle. F_N is the rudder normal force, and T is the propeller thrust. T_{BT} is the lateral force generated by the bow thruster.

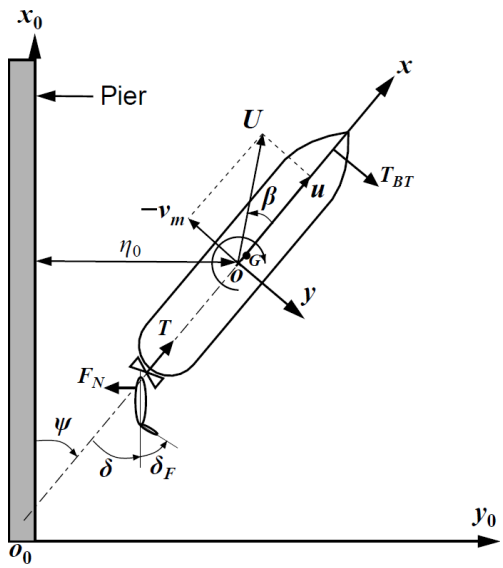

Figure 1. Coordinate systems

3 STUDIED SHIP

3.1 HULL AND PROPELLER

An inland container ship called "Suzaku" was selected as the studied ship (Okuda et al., 2023). Table 1 lists the principal particulars of the full-scale ship and model of the ship. In the table, L denotes the length between the perpendiculars, B is the breadth, d is the draft, ∇ is the displacement volume, C_b is the block coefficient, x_G is the longitudinal coordinate of the center of gravity, $\overline{GM}$ is the metacentric height, D_P is the propeller diameter, p is the propeller pitch ratio, and Z is the propeller blade number. The scale ratio of the model was 1/27.667. Fig. 2 shows a photo of the model ship. The bilge keels attached to the model were fitted between S.S.3.15 and 6.76. The length of the bilge keel model was 1084.3 mm, and the protruding height was 23.5 mm.

Table 1. Principal particulars of the studied ship

	Full-scale	Model
L [m]	83.0	3.000
B [m]	13.5	0.488
d [m]	3.8	0.1376
∇ [m^3]	3146	0.1486
C_b	0.7369	
x_G [m]	0.930	0.034
$\overline{GM}$ [m]	0.91	0.0329
D_P [m]	2.8	0.101
p	0.694	
Z	5	

Figure 2. Photo of the studied ship model (Suzaku)

3.2 BOW THRUSTER

A 4-blade bow thruster model with a diameter of 55.0 mm (1.52 m on the full-scale ship) was attached to the model ship at S.S.9.43. Fig. 3 shows a photo of the bow thruster model. The maximum thrust of the bow thruster was assumed to be 3.04 N at rest (equivalent to 6.5 tons for full scale).

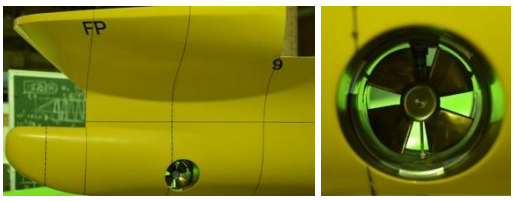

Figure 3. Bow thruster model

3.3 FLAP RUDDER

The studied ship was equipped with a flap rudder, as shown in Fig. 4. The flap rudder provides a higher rudder force than do conventional rudders because the flap part assumes a certain angle with the rudder angle. A large lift force can be expected from the flap part. Table 2 lists the rudder dimensions, where H_R is the rudder span length, B_R is the chord length, and A_R is the total rudder area. The chord length of the main rudder part was 0.050 m, and the chord length of the flap was 0.015 m. The area of the flap part was approximately 23% of the total rudder area.

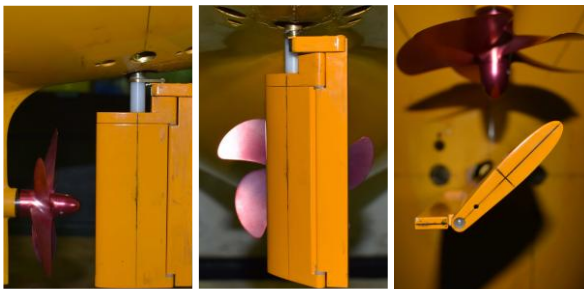

Figure 4. Flap rudder model

Table 2. Principal particulars of the rudder

	Full-scale	Model
H_R [m]	3.49	0.126
B_R [m]	1.60	0.065
A_R [m^2]	6.282	0.00821

4 CAPTIVE MODEL TESTS

Using the model ship described in section 3, captive model tests were conducted to simulate unberthing motions. The tests were conducted at Kyushu University Seakeeping and Manoeuvring Test Basin (tank length; 38.0 m, width; 24.4 m, maximum depth; 2.0 m). The vertical bank model was placed on the bottom of a square tank in shallow water to simulate the ship motion of unberthing, and the transient hydrodynamic forces acting on the ship hull were measured. The length of the vertical wall model is 13.3 m, which is equivalent to 368 m at the full scale. The water depth (h) has two conditions, i.e., $h/d = 1.5$ and 1.2, where d is the ship draft.

The model ship was assumed to leave from the bank parallel to the vertical wall. Here, the ship heading was kept at 0°, and oblique sailing navigation was used. The steady-state speed in the author's free-running model tests (Okuda et al., 2024) was 0.170 m/s (1.7 knots for the full-scale ship), which becomes approximately 60 s after starting unberthing. At $h/d = 1.5$ in the free-running model tests, the subject ship left the vertical bank for approximately 20°. On the basis of these results, we determined the towing speed U_0 and conditions in the captive model tests. Its angle was used as a base, and larger drift angles were also conducted, assuming towing by tugboats. The absolute value of the unberthing angle from the bank (drift angle β) varied between -20°∼-120° as shown in Fig. 5. The ship accelerated from its resting at $\eta_0/L = 0.105$ and began to move laterally. The ship speed U was adjusted to be steady at $\eta_0/L = 0.2$. This is a scenario in which the actual ship starts unberthing at 2.0 m between the vertical wall and the port side of the hull and reaches a steady ship speed at 10.0 m. This was determined by referring to the author's free-running model test results. These changes in ship speed were assumed to be the same regardless of the drift angle. Note that the red marks indicate the final positions of the unberthing motion. The tests were conducted on a bare hull without a propeller and rudder. The measurement items were surge force X, lateral force Y, and yaw moment N acting on the ship hull at the midship.

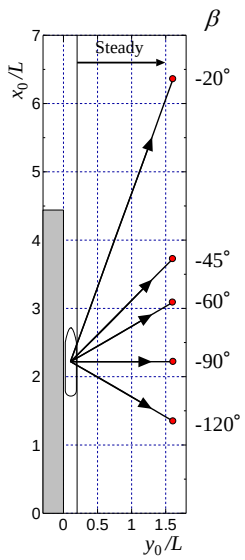

Figure 5. Initial and final positions of the unberthing motion

5 CALCULATION MODEL OF TRANSIENT HYDRODYNAMIC FORCE DURING UNBERTHING

5.1 A CALCULATION MODEL

Since a ship during unberthing has low-speed motion, we consider three equations of motion: surge, sway, and yaw (Yasukawa and Yoshimura, 2015). Close to the bank, all the coupling terms of the added mass (including the added

moment of inertia) appear because the symmetric flow field around the ship is broken, and their values vary with distance from the bank wall (Yasukawa and Sano, 2024). The added mass components denote m_{kj} ($k = 1{\sim}3; j = 1{\sim}3$) to be considered. Note that $k = 1,2,3$ represents the added mass or added moment of inertia for surge, sway, and yaw, respectively. In addition, $j = 1,2,3$ denote the surge, sway, and yaw motions, respectively. The equation of ship motion is expressed as follows:

$$\left.\begin{aligned} (m+m_{11})\dot{u} + m_{12}\dot{v}_m + m_{13}\dot{r} - (m+m_{22})v_m r - mx_G r^2 - m_{23}r^2 &= F_x \\ m_{21}\dot{u} + (m+m_{22})\dot{v}_m + m_{23}\dot{r} + (m+m_{11})ur + mx_G\dot{r} &= F_y \\ m_{31}\dot{u} + m_{32}(\dot{v}_m + ur) + (I_{zz} + m_{33} + mx_G^2)\dot{r} + mx_G(\dot{v}_m + ur) &= M_z \end{aligned}\right\} \tag{1}$$

where m is the ship mass and I_{zz} is the moment of inertia. F_x, F_y, and M_z are the surge force, lateral force, and yaw moment acting on the ship hull, respectively. These are expressed as follows:

$$\left.\begin{aligned} F_x &= F_{H1} + F_{B1} + F_{P1} + F_{R1} + F_{BT1} \\ F_y &= F_{H2} + F_{B2} + F_{P2} + F_{R2} + F_{BT2} \\ M_z &= F_{H3} + F_{B3} + F_{P3} + F_{R3} + F_{BT3} \end{aligned}\right\} \tag{2}$$

Here, F_{Hi} ($i = 1{\sim}3$) is the hull forces, F_{Bi} ($i = 1{\sim}3$) is the additional forces owing to the bank effect, F_{Pi} ($i = 1{\sim}3$) is the propeller forces, F_{Ri} ($i = 1{\sim}3$) is the rudder forces, and F_{BTi} ($i = 1{\sim}3$) is the bow thruster forces. Note that $i = 1$ is the surge force, $i = 2$ is the lateral force, and $i = 3$ is the yaw moment. These do not include the bank effect except for F_{Bi}.

Then, the case is considered where the ship is oblique sailing at a heading angle parallel to the bank, as in captive model tests. By substituting $\dot{r} = r = 0$ into the formula for the hydrodynamic force of a ship navigating near the bank according to Yasukawa and Sano (2024), the changes in hydrodynamic forces acting on the ship hull due to approaching the bank wall, F_{B1}, F_{B2}, and F_{B3}, are expressed as follows:

$$\left.\begin{aligned} F_{B1} &\cong \dot{m}_{11}u + \dot{m}_{21}v_m + D_{11}^{(1)}u|u|/2 \\ F_{B2} &\cong \dot{m}_{21}u + \dot{m}_{22}v_m + D_{11}^{(2)}u^2/2 \\ F_{B3} &\cong \dot{m}_{31}u + \dot{m}_{32}v_m + (D_{11}^{(3)}/2 - m_{21})u|u| \end{aligned}\right\} \tag{3}$$

where $D_{11}^{(i)}$ ($i = 1{\sim}3$) is the hydrodynamic force component proportional to the square of u. The distance variable transformation of the time derivative is formulated as follows:

$$\begin{aligned} \frac{d}{dt} &= \frac{dy_0}{dt}\frac{d}{dy_0} + \frac{d\psi}{dt}\frac{d}{d\psi} \\ &= (u\sin\psi + v_m\cos\psi)\frac{d}{dy_0} + r\frac{d}{d\psi} \\ &\cong v_m\frac{d}{dy_0} \end{aligned} \tag{4}$$

Using this relation and ignoring m_{21} as small, we obtain the following:

$$\left.\begin{aligned} F_{B1} &\cong m_{11y}u|v_m| + m_{12y}v_m^2 + D_{11}^{(1)}u|u|/2 \\ F_{B2} &\cong m_{21y}uv_m + m_{22y}v_m|v_m| + D_{11}^{(2)}u^2/2 \\ F_{B3} &\cong m_{31y}uv_m + m_{32}v_m|v_m| + D_{11}^{(3)}u|u|/2 \end{aligned}\right\} \tag{5}$$

where the subscript y denotes the derivative with respect to y_0, and absolute values are included as appropriate to account for the symmetry of the ship. The first and second terms on the right side of Eq. (5) are the hydrodynamic forces resulting from the change in added mass due to proximity to the bank. Note that m_{11y}, m_{12y}, m_{21y}, m_{22y}, m_{31y}, and m_{32y} are called the added mass derivatives. The third term is the added resistance, added lateral force, and added yaw moment acting on the ship as it moves forward and aftward along the bank wall. Note that $D_{11}^{(i)}$ in Eq. (5) is obtained from the captive model tests. Since $\dot{r} = r = 0$ in the captive model tests that were conducted under the bare hull condition, the propeller, rudder, and bow thruster effects were not considered. The values measured in the captive model tests (X, Y, N) are expressed as follows. They include inertial forces associated with acceleration and deceleration motions.

$$\left.\begin{aligned} X &= F_{H1} + F_{B1} - (m + m_{11})\dot{u} - m_{12}\dot{v}_m \\ Y &= F_{H2} + F_{B2} - m_{21}\dot{u} - (m + m_{22})\dot{v}_m \\ N &= F_{H3} + F_{B3} - m_{31}\dot{u} - (mx_G + m_{32})\dot{v}_m \end{aligned}\right\} \tag{6}$$

In summary, X, Y, N can be calculated by using Eq. (6). To do so, it is necessary to calculate F_{Hi}, F_{Bi} and the added mass terms, which, except for F_{Hi}, vary with the distance to bank η_0. The mathematical model for F_{Hi} was published by Okuda et al. (2023), along with the hydrodynamic force parameters, and is considered in this paper.

5.2 CALCULATION OF ADDED MASS DURING UNBERTHING

The added mass coefficients when the ship keeps heading angle zero and unberthing parallel to the bank are obtained by solving potential theory-based equations using a three-dimensional panel method (Yasukawa et al., 2009) while varying the distance between the ship and the bank (η_0). These calculations are based on potential theory and thus the relation $m_{ij} = m_{ji}$ (Timman and Newman, 1962).

Fig. 6 shows the variation in the nondimensionalized added mass with respect to η_0. m_{11}, m_{21}, and m_{22} are divided by $(\rho/2)L^2d$, m_{33} by $(\rho/2)L^4d$, and m_{31} and m_{23} by $(\rho/2)L^3d$, for nondimensionalization. Prime notation (') indicates the nondimensionalized value of the added masses, and the m'_{11} and m'_{22} values are almost the same for $\eta_0/L > 1$. When the ship is close to the bank, the added mass begins to increase slowly and increases sharply at $\eta_0/L < 0.5$. The m'_{33} value does not change much until the ship approaches the bank. Among the added mass coupling terms, the m'_{21} and m'_{31} values are almost zero at a distance from the bank (approximately $\eta_0/L > 1$) but increase when approaching the bank. The m'_{23} value is almost constant for $\eta_0/L > 0.2$ but begins to change when it approaches the bank to approximately $\eta_0/L = 0.2$. However, m'_{23} will not be zero even if the ship is far enough from the bank. In all the cases, the absolute value of the added mass components is greater for the shallow water depth of $h/d = 1.2$ than for $h/d = 1.5$.

Fig. 7 shows the nondimensionalized added mass derivatives. m_{11y}, m_{21y}, and m_{22y} are divided by $(\rho/2)Ld$, $m_{33y}$by $(\rho/2)L^3d$, and m_{31y} and m_{32y} by $(\rho/2)L^2d$, for nondimensionalization. m_{kjy} is obtained by differentiating the change in η_0/L in m_{kj} by the central difference method. Up to approximately $\eta_0/L = 1$, all added mass derivatives are almost zero, and the bank effect is not observed. Closer to the bank, these values increase in the negative direction except for m_{31y}, which becomes more noticeable if the water depth becomes shallower. However, the m_{21y} value increases in the negative direction as the ship approaches the bank, but its value decreases as $\eta_0/L < 0.2$ increases.

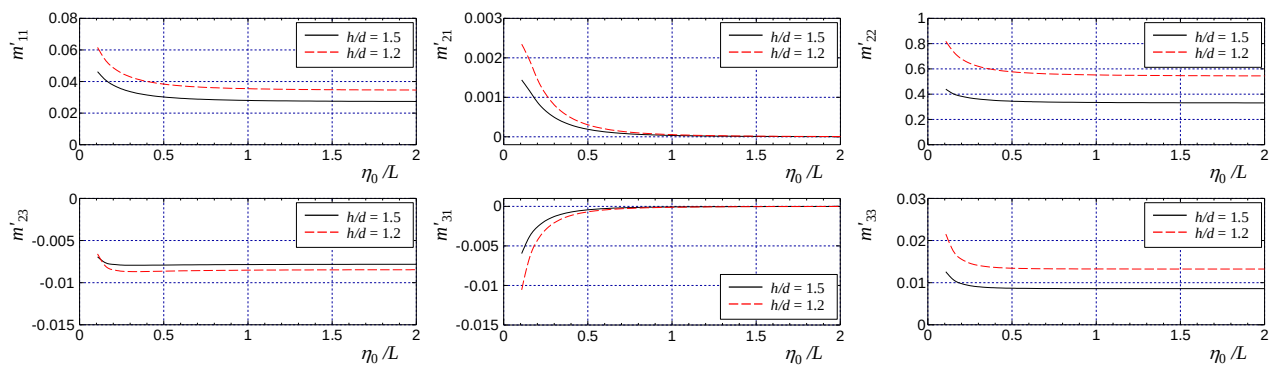

Figure 6. Changes in the added mass coefficients versus the ship-bank distance (η_0/L) at h/d = 1.5 and 1.2

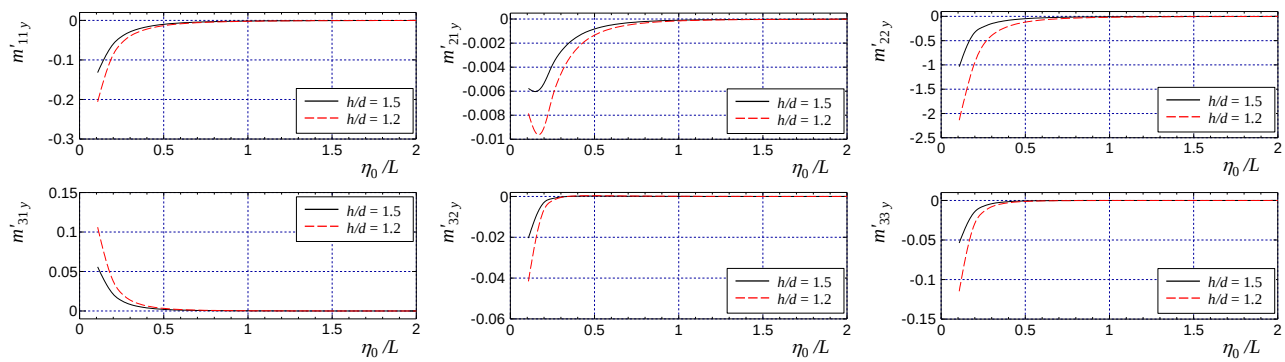

Figure 7. Changes in the added mass derivative coefficients versus the ship-bank distance (η_0/L) at h/d = 1.5 and 1.2

5.3 COMPARISON OF TRANSIENT HYDRODYNAMIC FORCES IN THE CALCULATIONS AND EXPERIMENTS

On the basis of the calculation results of the added mass components described above, the surge force (X), lateral force (Y), and yaw moment (N) acting on the ship hull during unberthing were calculated using Eq. (6) and compared with the captive model test results.

Fig. 8 shows a comparison of the calculated hull hydrodynamic forces during unberthing and the captive model test results in $h/d = 1.5$. The hydrodynamic force and moment are divided by $(\rho/2)LdU_0^2$ and $(\rho/2)L^2dU_0^2$, respectively, for nondimensionalization. These nondimensional values are indicated by a prime notation (′). The horizontal axis is the nondimensional value η_0/L of the distance from the bank wall. Note that a small η_0/L means that the ship is close to the bank. Additionally, after unberthing begins, the ship accelerates until η_0/L reaches 0.2, and at $\eta_0/L > 0.2$, the towing speed becomes constant. In $h/d = 1.5$, X' at $\beta = -120°$ takes a positive value near $\eta_0/L = 0.15$ as the ship starts unberthing. In contrast, X' is a negative value except for $\beta = -120°$. These consist mainly of hydrodynamic force components caused by the acceleration associated with the unberthing motion. The calculated results exhibit the same trend as the tank test results. However, the calculated value peaks at approximately $\eta_0/L = 0.1$ and converges to a steady-state value of almost zero at approximately $\eta_0/L = 0.2$. In comparison, the experimental value peaks first around $\eta_0/L = 0.2$ and then converges to a steady-state value of almost zero around $\eta_0/L = 0.3$. Thus, the experimental value of X' corresponds to the response delay behind the calculated value. This phenomenon of response delay can also be seen in Y' and N'. The delay in Y' becomes more pronounced if the absolute value of β is closer to the pure-lateral movement of $-90°$. The larger the value of Y' is in the negative direction, the greater the lateral force on the ship becomes to prevent unberthing motion. There is no significant difference in N' between the post-acceleration and steady-state conditions. However, the experimental value of the steady-state η_0/L is approximately 0.4. This indicates a response delay relative to the calculated value.

Fig. 9 shows the comparison of the calculated hull hydrodynamic forces during unberthing and the captive model test results in $h/d = 1.2$. From the tank test results, hull hydrodynamic forces become approximately steady at approximately $\eta_0/L = 0.7$, indicating that the bank effect is affected within a wider range. Additionally, Y' and N' at $\beta = -60°$ peak in the negative direction at $\eta_0/L = 0.3{\sim}0.35$, which is approximately twice the calculated value for Y' and approximately eight times the calculated value for N'. As the absolute value of β increases, the values of Y' and N' increase in the negative direction, and their response delays also increase. X' is negative at first and then becomes positive. Thus, at shallower water depths, the memory effect becomes very pronounced. The cause of the response delay is thought to be the memory effect of the fluid due to the shed vortex created at the stern of the ship by the start of the unberthing motion, as already mentioned by Sadakane and Tsuruta (1993), Sadakane (1996), Lee et al. (2003), and Shintani et al. (2020). The theoretical calculations assume quasi-stationary treatment and cannot reproduce such a memory effect.

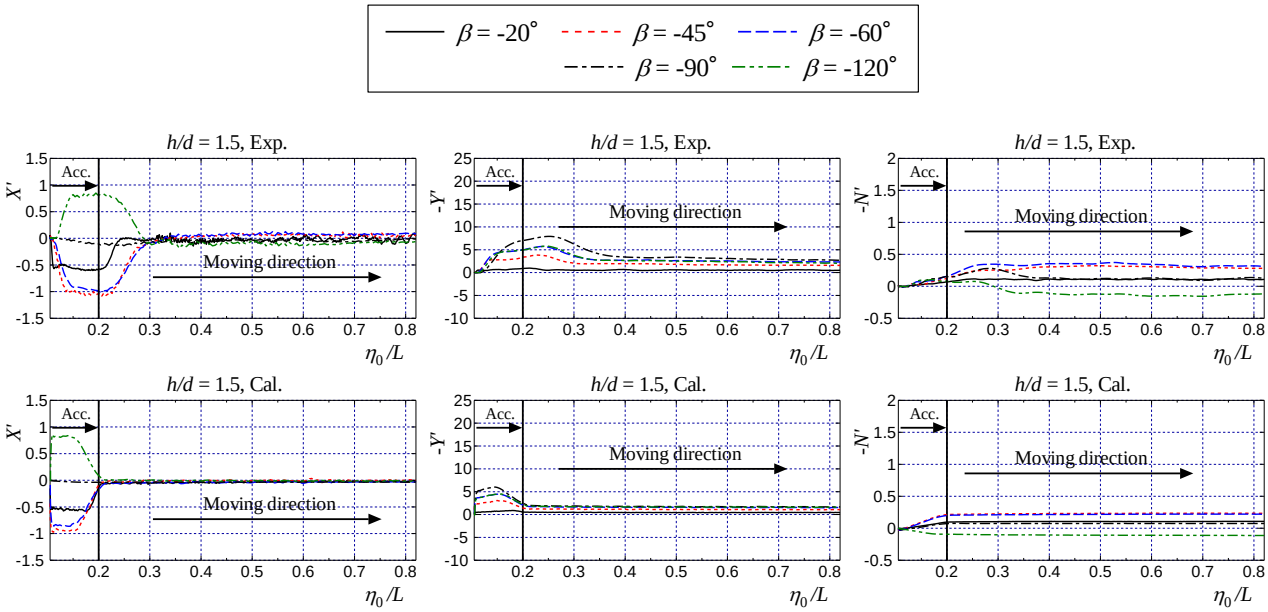

Figure 8. Nondimensionalized transient hydrodynamic forces (X', Y', N') during unberthing for different drift angles at h/d = 1.5

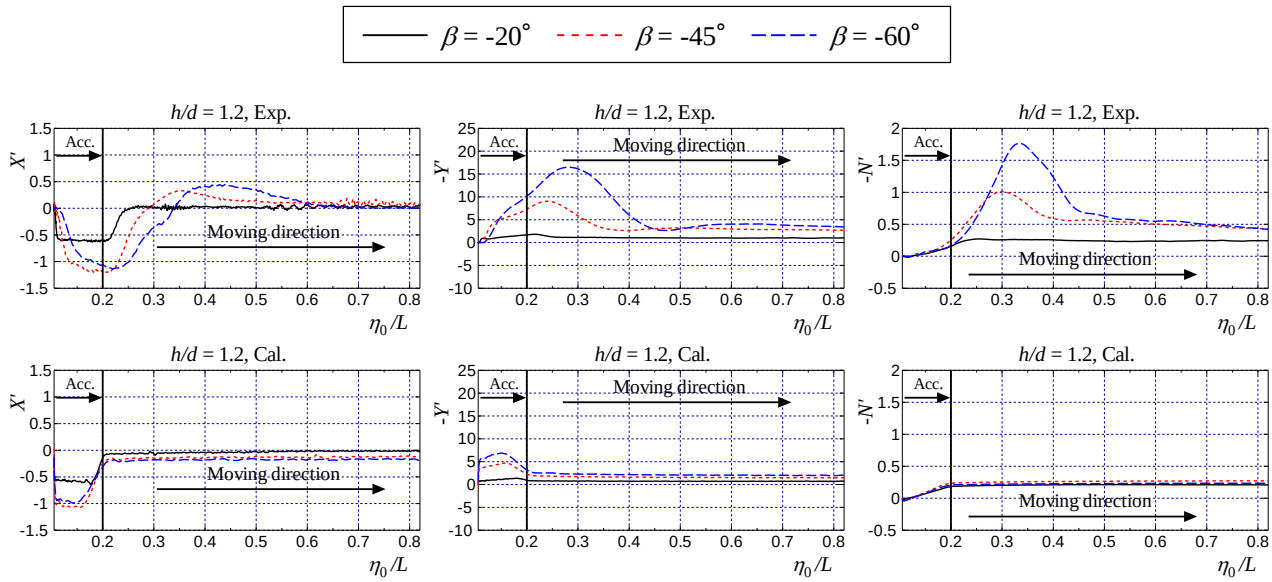

Figure 9. Nondimensionalized transient hydrodynamic forces (X', Y', N') during unberthing for the different drift angles at h/d = 1.2

6 A PRACTICAL METHOD THAT CONSIDERS THE HYDRODYNAMIC MEMORY EFFECT INTO ACCOUNT VIA A FIRST-ORDER LAG MODEL

The calculated hull hydrodynamic force obtained by Eq. (6) cannot capture the response delay due to the memory effect. Thus, we adopted a first-order lag and dead-time model (called a first-order lag model) to approximate the response delay of the hydrodynamic forces during acceleration.

6.1 A FIRST-ORDER LAG MODEL WITH A DEAD TIME

In a first-order lag model, the differential equation is expressed as follows:

$$a(t) + T_1 \frac{da(t)}{dt} = K_1 b(t - L_1) \tag{7}$$

where K_1 is the system gain, T_1 is the time constant, and L_1 is the dead time. K_1 T_1', and L_1' are called "first-order lag parameters". a is the output value considering the response delay, and b is the input value (i.e., X, Y, N). Discretizing Eq. (8) by backward difference approximation, we obtained as follows:

$$a(k_d) = -c_1 a(k_d - 1) + c_2 b(k_d - t_d - 1) \tag{8}$$

where

$$c_1 = -\frac{T_1}{T_s + T_1}, c_2 = \frac{K_1 T_s}{T_s + T_1}, t_d = \frac{L_1}{T_s}$$

Here, T_s is the sampling time, k_d is the sample time, and t_d is the dead time. The three parameters K_1, T_1, and L_1 are determined by referring to the time-history data of the capture test results for each oblique sailing condition and are calculated accordingly so that the theoretical values match the experimental results. Different values are taken for each drift angle for X, Y, and N. By solving Eq. (8) with their parameters, the response delay of the hull hydrodynamic force can be approximated using a first-order lag and dead-time model.

6.2 PARAMETERS FOR A FIRST-ORDER LAG MODEL USED IN SIMULATIONS

To introduce a first-order lag model into the unberthing simulations of the hull hydrodynamic forces (X, Y, N), the system gain K_1, time constant T_1', and dead time L_1' must be determined in advance. These values differ depending on the drift angle β and water depth. The specific procedures for determining the first-order lag parameters are as follows:

- Determine K_1 so that the peak value of the transient hydrodynamic forces during unberthing in the calculation results from Eq. (6) matches that in the captive model tests.
- Next, T_1 and L_1 are determined so that the transient response (response delay) of the hydrodynamic forces during unberthing in the calculation results matches that of the hydrodynamic force in the captive model tests.

Fig. 10 shows the comparison of K_1, T_1', and L_1' for the surge force, lateral force, and yaw moment, respectively. The time-related parameters (T_1' and L_1') are divided by L/U_0 for nondimensionalization, indicating that (') is a nondimensionalized value. In $h/d = 1.5$, K_1 is in the range of 1 to 1.5 for both the surge force, lateral force, and yaw moment. With respect to $h/d = 1.2$, K_1 in the lateral force and yaw moment is larger than $h/d = 1.5$. In particular, K_1 becomes approximately 3.0 in the lateral force. It indicates the larger of K_1, the greater the discrepancy of the peak values between the calculated value and the experiments shown in Figs. 8 and 9. As the water depth becomes shallower and the maximum value of the transient hydrodynamic forces acting on the ship hull increases, the value of K_1 also increases. T_1' is within 0.05 for the surge force, lateral force, and yaw moment, respectively. This value is within 1 s of the model scale. Additionally, the T_1' value changes only slightly when h/d or β changes. L_1' takes a value of approximately 0.1~0.15, except for the surge force and yaw moment at $\beta = -90°$. L_1' indicates that at $\beta = -20°$, there is a response delay of approximately 2 s at the model scale for the surge force and lateral force and approximately 1.5 s at the yaw moment. These parameters are solely based on the studied ship and require the generalization of this method in the future.

The unberthing simulations described in section 7 interpolate these values by β, which changes with time. Note that for $h/d = 1.2$, there are no data for first-order lag parameters more than $|\beta| = 60°$ if the absolute value of β is larger than 60° in the unberthing simulations, then the value of the first-order lag parameters at 60° is used.

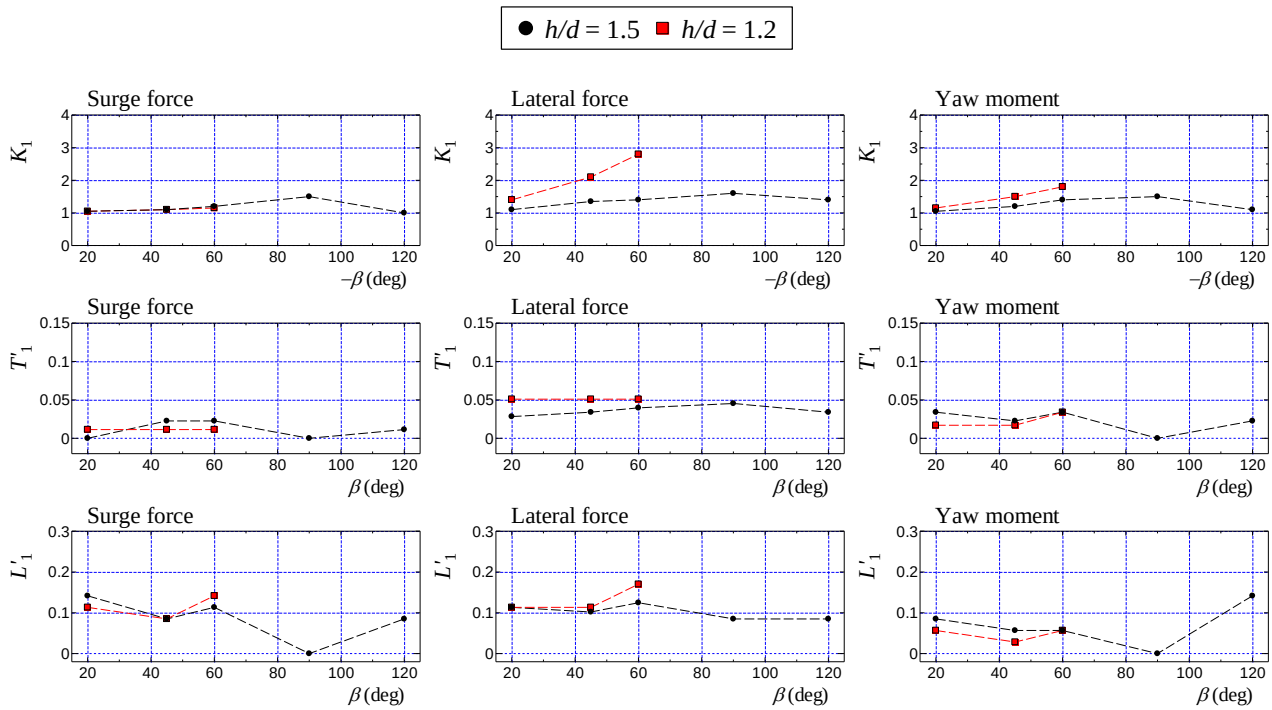

Figure 10. First-order lag parameters (K_1, T'_1, L'_1) used in the calculations

6.3 CALCULATION RESULTS OF THE TRANSIENT HYDRODYNAMIC FORCES

Fig. 11 shows the comparison of the calculated values of the hull hydrodynamic force at $\beta = -20°$ by Eq. (6) (Cal. (original)), the calculated values using a first-order lag model (Cal. (1st lag)), and the experimental results (Exp.). The original calculations cannot capture the response delay caused by the hydrodynamic forces. In $h/d = 1.5$, the values calculated

via a first-order lag model were used to estimate the changes in hydrodynamic forces and the response delay that occurs during unberthing with practical accuracy. Even at $h/d = 1.2$, the trends of X', Y' and N' change can be roughly captured. However, X' immediately after U becomes a steady speed, is slightly greater in the negative direction than the experimental value, and the absolute value of N' is slightly smaller than the experimental value. A first-order lag model cannot approximate the complex changes in hydrodynamic forces during unberthing.

Next, we consider the hull hydrodynamic force at $\beta = -60°$. Fig. 12 compares the originally calculated hull hydrodynamic force at $\beta = -60°$, the value calculated via a first-order lag model, and the experimental value. For $h/d = 1.5$, the hull hydrodynamic force can be calculated accurately by introducing a first-order lag model, as in the case of $\beta = -20°$. Even in $h/d = 1.2$, the trend of Y' can be captured by introducing a first-order lag model. However, the first-order lag model used in this study is insufficient for cases such as X' and N'. A first-order lag model is not suitable for use when the sign of the value is reversed with η_0/L or when a specifically large peak appears.

As a result, by introducing the first-order lag model to the calculation of hydrodynamic forces occurring at the unberthing, the response delay can be captured with practical accuracy for $h/d = 1.5$. Even in extremely shallow water, such as $h/d = 1.2$, the response delay can be approximately captured. However, as the absolute value of the drift angle increases, it becomes difficult to capture the complex behavior of hydrodynamic forces.

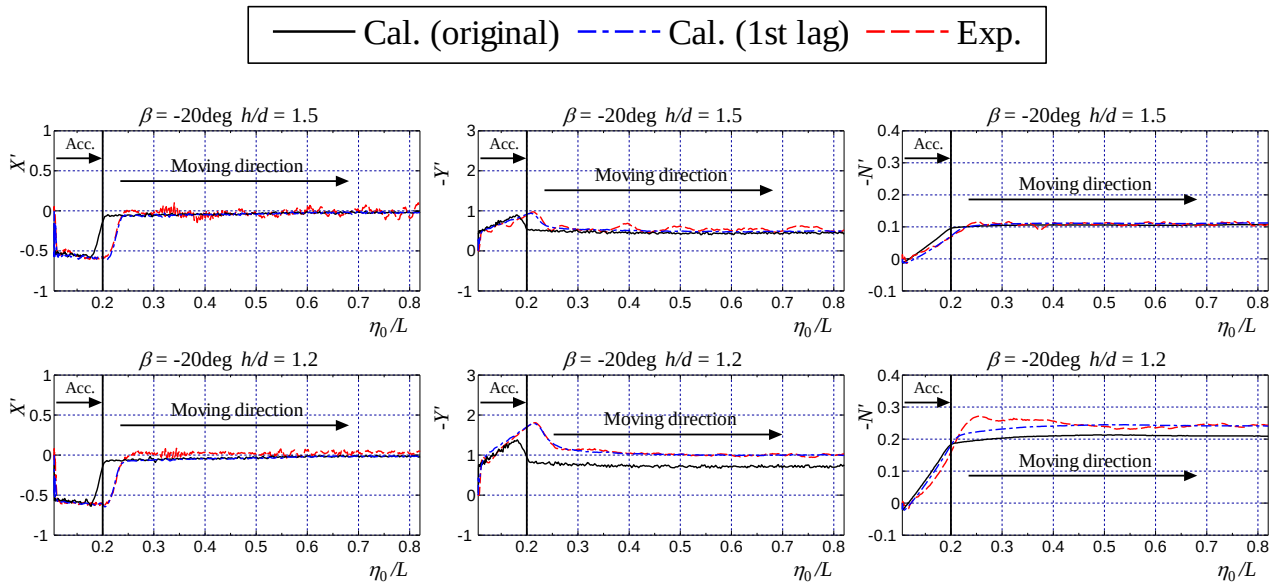

Figure 11. Comparison of the hydrodynamic forces during unberthing ($\beta = -20°$) between the calculations and the experiments of

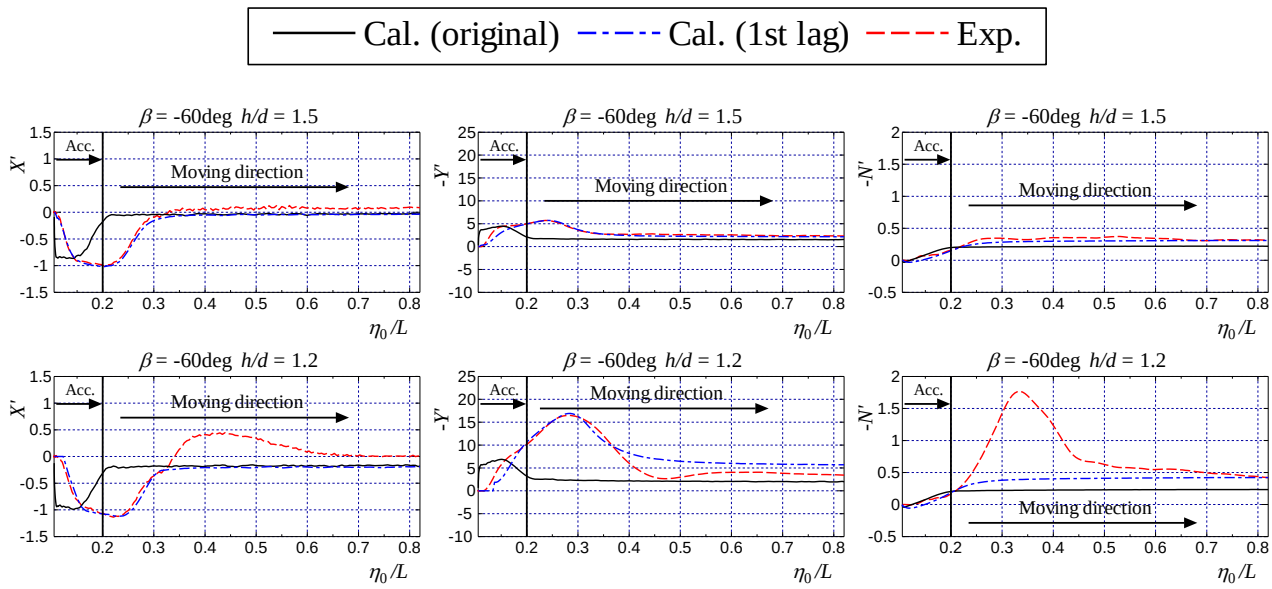

Figure 12. Comparison of the hydrodynamic forces during unberthing ($\beta = -60°$) between the calculations and the experiments

7 UNBERTHING SIMULATIONS USING A FIRST-ORDER LAG MODEL

A first-order lag model and parameters described in section 6 were introduced to calculate the hull hydrodynamic forces, and unberthing simulations of the subject ship were conducted. In the simulations, the bow thruster thrust was controlled so that the rudder angle was taken to $-35°$ and parallel to the bank (i.e., the heading angle was zero), while the propeller was rotated (Okuda et al., 2024). In the experiments, the bow thruster impeller was controlled manually while watching the ship's heading parallel to the vertical bank, and the bow thruster impeller control model used in the simulations mimicked these operations. The propeller revolution was set as 5.8 rps in both the simulations and experiments, corresponding to the propeller speed at which one can navigate at 4 knots for straight movement. When sailing at 20 degrees at 5.8 rps, the ship speed becomes approximately 1.7 knots, which is the same as that in the captive model tests. The propeller revolution and the rudder angle were taken to be constant values during unberthing motions, the same as those used in the author's experiments. Note that the response delay owing to the first-order lag model was considered only in the hull force. The propeller, rudder, and bow thruster forces were used in the original model (Okuda et al., 2023).

Fig. 13 compares the trajectories of the simulation results and the free-running model test results presented by Okuda et al. (2024). In the figure, the ship's shadow indicates the ship position every 10 s from the start of unberthing. The legend ''Cal. (present)/Present'' shows the simulation results considering the change in hydrodynamic forces due to the bank effect and the first-order lag model, and ''Cal. (original)/Original'' shows the simulation results when the bank effect is not considered (the value calculated via Eq. (5) is set to zero). The Present trajectory in $h/d = 1.5$ is closer to the free-running model test results than the Original result, and the simulation accuracy is improved. The "Present" trajectory $h/d = 1.2$ is also close to the free-running model test results, as in the case of $h/d = 1.5$.

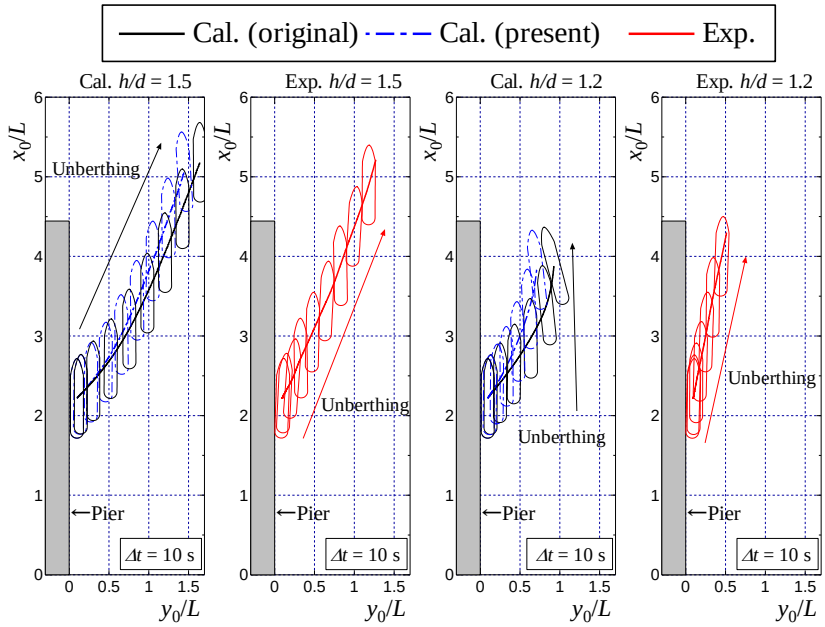

Figure 13. Unberthing trajectories in both the calculations and the experiments

Fig. 14 shows the time histories of the heading angle (ψ), bow thruster impeller revolution (n_B), drift angle (β), propeller thrust (T), and rudder normal force (F_N) during unberthing. The ψ values in Present and Original are approximately zero except after 45 s when $h/d = 1.2$. In contrast, the experimental ψ varies within the range of $\pm 4°$. This is because the heading control in the free-running model tests was performed manually (Okuda et al., 2024). In the Present and Original cases, a large change in heading occurs approximately 45 s after $h/d = 1.2$. This is because the bow thruster thrust, which allows lateral movement while maintaining the heading at zero, was excessive and exceeded the impeller thrust capacity. The n_B of the Present case is smaller than that of the Original case and closer to the experimental n_B. The β of the Present case is generally smaller than that of the Original and is closer to the experimental results. Assuming that the heading is set to 0, β represents the unberthing angle from the bank. In particular, the Present result at the steady state with $h/d = 1.5$ is in good agreement with the experimental results. The tendency to leave the bank at approximately 20 degrees and the steady-state speed are captured. This is also similar to the captive model test conditions described above. The T of the Present case does not differ significantly from that of the Original case and is roughly consistent with that of the experimental results. The F_N of Present is larger than the F_N of Original at $h/d = 1.5$, which is closer to the experimental result. However, the absolute value of F_N immediately after unberthing is smaller than the

simulation result and may be related to the response delay owing to the memory effect. Furthermore, in $h/d = 1.2$, the absolute values of F_N for the Present and Original cases are larger than those in the experimental result, and there is no clear improvement in simulation accuracy. The simulation accuracy improved when the first-order lag model was introduced in the unberthing simulations, and the memory effect was considered. However, there is room for improvement, especially the possibility that the memory effect may also occur in F_N. In addition, refining the modeling of the bow thruster force needs to be considered.

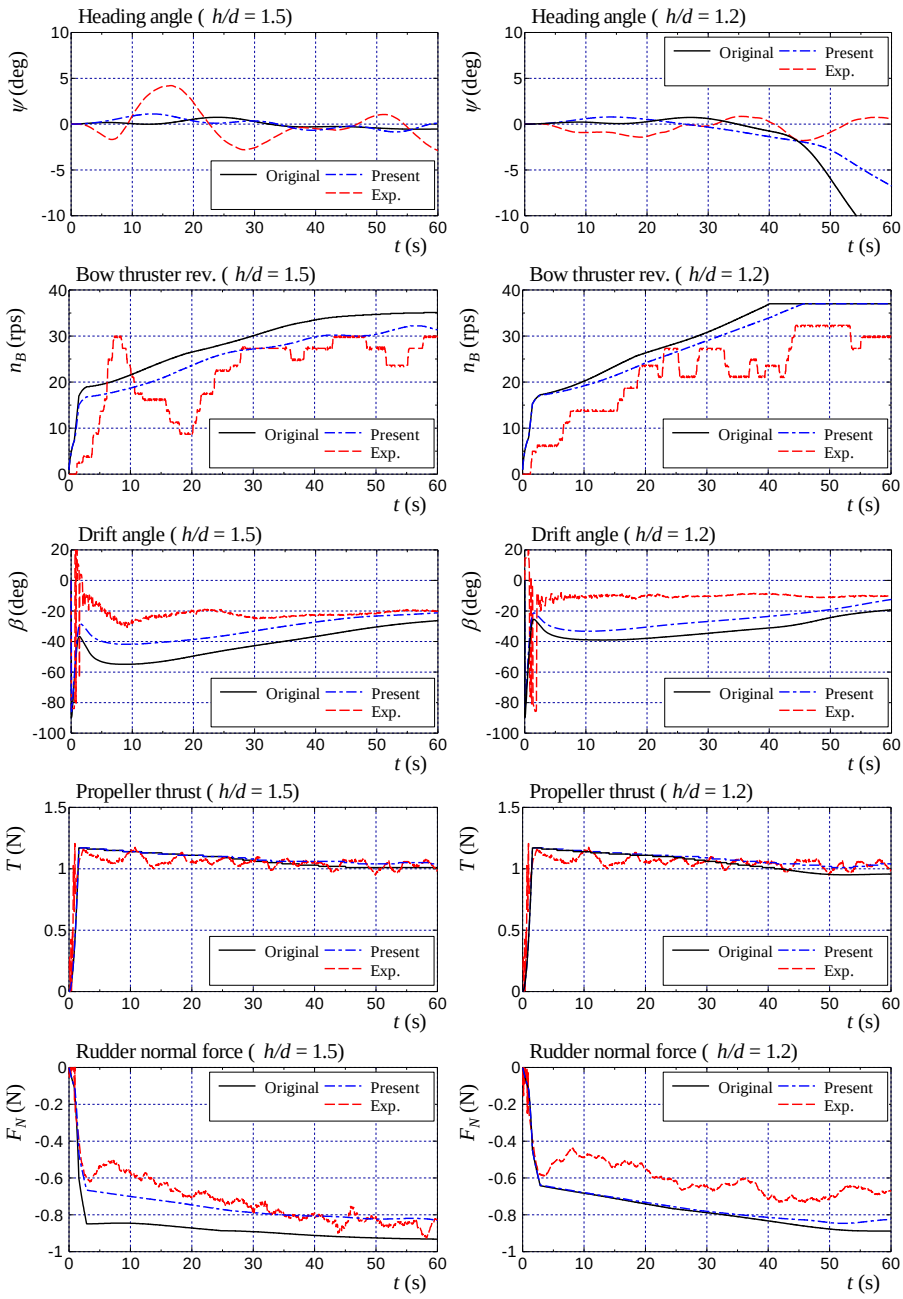

Figure 14. Comparison of the time histories of the heading (ψ), the B/T impeller revolution (n_B), the drift angle (β), the propeller thrust (T), and the rudder normal force (F_N)

8 CONCLUDING REMARKS

In this study, captive model tests were carried out by changing the oblique sailing (drift) angle from the bank to understand the transient hydrodynamic forces acting on the ship hull of a single-propeller and single-rudder ship during unberthing motion. In addition, referring to the formulation of hydrodynamic forces for ships navigating narrow channels

by Yasukawa and Sano (2024), the hull forces were calculated considering the change in added mass with varying distance from the bank and compared with the experimental results. As a result, the response delay of the hydrodynamic force due to the memory effect becomes significant in shallow water, and the present mathematical model cannot produce a response delay in the transient hull forces. Therefore, we attempted to model the response delay caused by the hydrodynamic forces using a first-order lag model and a dead time model (the first-order lag model). The results show that for water depths of approximately $h/d = 1.5$, this model can produce a response delay in which the hydrodynamic forces appear with practical accuracy. Furthermore, the first-order lag model was incorporated and calculated for the hydrodynamic forces, and unberthing simulations were conducted considering the response delay. The simulation results were compared with the free-running model test results of Okuda et al. (2024), and the accuracy of the simulation was confirmed. The first-order lag model is found to be effective in improving the accuracy of unberthing simulations. However, when the water depth is shallow and the drift angle is large, as in the case of $h/d = 1.2$, the transient hydrodynamic forces during unberthing may observe complex changes. The first-order lag model has limitations in modeling such transient hydrodynamic forces.

9 ACKNOWLEDGEMENTS

This study was conducted as a part of a MEGURI 2040 project grant from the Nippon Foundation. A part of this study was supported by the Fundamental Research Developing Association for Shipbuilding and Offshore (REDAS). The authors express their sincere gratitude to Prof. Yoshitaka Furukawa and Mr. Hiroshi Ibaragi of Kyushu Univ. for their assistance with the tank tests.

10 REFERENCES

Lee, Y-S., Toda, Y. and Sadakane, H., 2003. Hydrodynamic force acting on a ship hull under lateral low speed motion-IV - Shallow water calculation using CFD method-, J. Japan Institute of Navigation 108, 59-66. (in Japanese)

Okuda, R., Yasukawa, H., Yamashita, T. and Matsuda, A., 2023. Maneuvering simulations at large drift angles of a ship with a flapped rudder, Applied Ocean Research 135, 103567.

Okuda, R., Yasukawa, H., Hirata, N. and Matsuda, A., 2024. A study on berthing and unberthing of a single-shaft ship with a bow thruster, J. Marine Science and Technology 29(1), 53-74.

Sadakane, H. and Tsuruta, H., 1993. Transitional lateral drag acting on ship moving from rest -An experimental study by using a ship's model-, J. Japan Institute of Navigation 90, 273-279. (in Japanese)

Sadakane, H., 1996. A study on lateral drag coefficient for ship moving laterally from rest, J. Japan Institute of Navigation 95, 193-200. (in Japanese)

Shintani, S., Nishio, S. and Katsui, T., 2020. Behavior of hydrodynamic force acting on a berthing ship in extreme shallow water (2nd report: Analysis of response factors and the validation by means of measurement), Conf. Proc. of J. Japan Society of Naval Architects and Ocean Engineers 30, 589-592. (in Japanese)

Timman, R. and Newman, J. N., 1962. The coupling damping coefficients of a symmetric ship, J. Ship Res. 5, 1-7.

Yasukawa, H., Kawamura, S., Tanaka, S. and Sano, M., 2009. Evaluation of ship-bank and ship-ship interaction force using a 3D panel method, Proc. Int. Conf. on Ship Maneuvering in Shallow Water and Confined Water, Antwerp, Belgium, 127-133.

Yasukawa, H. and Yoshimura, Y, 2015. Introduction of MMG standard method for ship maneuvering predictions, J. Marine Science and Technology 20(1), 37-52.

Yasukawa, H. and Sano, M., 2024. On the hydrodynamic derivatives with respect to heading angle for ship maneuvering in a canal, J. Marine Science and Technology 29(3), 529-545.

Yoneda, S., Hashimoto, H. and Kobayashi, E., 2018. Experimental study on the wall effect on ship during emergency unberthing for tsunami evacuation, Transaction of Navigation 3(1), 15-24.

11 AUTHORS BIOGRAPHY

Ryusuke Okuda is a researcher at the Offshore Engineering System Research Group, Ocean Engineering Department, National Maritime Research Institute, Japan. He received a Ph. D. (Eng.) degree in 2024 from Hiroshima University. His main interest is ship maneuverability in low-speed maneuvering and ocean engineering.

Hironori Yasukawa is a professor at the Graduate School of Advanced Science and Engineering, Hiroshima University, Japan. His specialty is ship maneuverability. He was an ITTC member of the maneuverability committee (2005 to 2011), a member of the specialist committee on performance of ship in service (2014 to 2017), and the chairman of the specialist committee on maneuvering in waves (2017 to 2021).

COMPUTATION OF VESSEL MOTIONS IN WAVES USING FORWARD-SPEED FREE-SURFACE GREEN FUNCTION

Wim van der Molen, Baird, Australia

COMPUTATION OF VESSEL MOTIONS IN WAVES USING FORWARD-SPEED FREE-SURFACE GREEN FUNCTION

WIM VAN DER MOLEN, BAIRD, AUSTRALIA

SUMMARY

A new method for calculating ship response and wave drift forces on a ship sailing in coastal waters is introduced in this paper. The panel method uses the forward-speed free-surface Green function. This Green function is notoriously difficult to approximate, especially for finite water depth. In this work, the time-domain Green function is used for a moving source, and the Fourier Transform applied to obtain the corresponding Green function in frequency-domain. The same time-domain Green functions can be used for the full range of frequencies that are analysed, and many wave directions can be easily evaluated when the Green functions are obtained for a certain encounter frequency. This provides the required inputs for underkeel clearance models or manoeuvring simulations. The model was validated against benchmark model tests for squat, added resistance, sway drift forces and yaw drift moments.

NOMENCLATURE

Symbols:

$\mathbf{A}$	Added mass matrix (kg, kgm, kgm^2)
$\mathbf{C}$	Hydrostatic restoring matrix (N/m, N, Nm/rad)
c_G	Wave group speed (m/s)
$\vec{F}$	Force (N)
F_h	Depth-related Froude number (-)
g	Acceleration of gravity (m/s^2)
G^f	Frequency-domain Green function (m^{-1})
G^t	Time-domain Green function (m^{-1}s^{-1})
H_W	Wave height (m)
k	Wave number (rad/m)
h	Water depth (m)
$\mathbf{M}$	Inertia matrix (kg, kgm, kgm^2)
$\vec{n}$	Normal vector (-)
R	Horizontal distance (m)
r	Radial distance (m)
S_X	Motion spectrum (m^{2}rad/s, rad^3/s)
T_W	Wave period (s)
t	Time (s)
U	Ship forward speed (m/s)
$\vec{X}$	Displacement (m)
$\vec{x}$	Position of the field point (m)
p	Pressure (N/m^2)
ζ_A	Wave amplitude (m)
μ	Wave direction (going-to) (°)
$\vec{\xi}$	Position of the source point (m)
ρ	Density of water (kg/m^3)
σ	Source strength (m/s)
Φ	Total velocity potential (m^2/s)
$\overline{\phi}$	Steady velocity potential (m^2/s)
ϕ^I	Incident wave velocity potential (m^2/s)
ϕ^S	Scattered wave velocity potential (m^2/s)
χ	Radiated wave velocity potential (m)
ω	Encounter frequency (rad/s)
ω_0	Absolute frequency (rad/s)

Acronyms:

BEM	Boundary element method
DTC	Duisburg Test Case
EU	European Union
FHR	Flanders Hydraulics Research
FSGF	Forward-speed Green function
RANS	Reynolds-averaged Navier Stokes
RAO	Response amplitude operator
SHOPERA	– Energy Efficient Safe Ship Operation
UKC	Underkeel clearance
ZSGF	Zero-speed Green function

Subscripts denote partial derivatives.

1 INTRODUCTION

Calculation of the motions of a ship sailing in waves is relevant for ship design and for the design and operation of channels and fairways. Heave, roll and pitch affect the underkeel clearance, added resistance affects the required propulsion, and drift forces in sway and yaw affect the manoeuvring. Accurate calculation of the forces on and response of a ship sailing in waves is possible using RANS solvers (Shen et al., 2015; Sigmund and El Moctar, 2018) or Rankine panel models (Bunnik, 1999; Söding and Shigunov, 2015). However, for input to manoeuvring simulations and underkeel clearance models for

1999; Söding and Shigunov, 2015). However, for input to manoeuvring simulations and underkeel clearance models for channels, the calculation of response amplitude operators (RAO's) and drift forces usually rely on strip theory models or panel models that use the zero-speed free surface Green function (ZSGF; Papanikolaou and Schellin, 1992; Donatini et al, 2022). As such, many computations for different frequencies, wave directions and water depths can be completed fast. However, inaccuracies occur if the ship is sailing faster, since the propagation of diffracted waves along the vessel is not treated correctly. This is particularly the case for the drift forces, also at lower speeds (Shigunov et al., 2018).

A new 3D boundary element method (BEM) is introduced in this paper using the forward speed free-surface Green function (FSGF). This Green function is notoriously difficult to approximate, especially for finite water depth (Chen, 2000; Chen and Wu, 2001). In this work, the time-domain Green function is used for a moving source, and the Fourier Transform applied to obtain the corresponding Green function in frequency-domain. The same time-domain Green functions can be used for the full range of frequencies that are analysed, and many wave directions can be easily evaluated when the Green functions are obtained for a certain frequency. Time-domain Green functions are also used in time-domain panel methods (Korsmeyer and Bingham, 1998; Kara, 2011), but with the same disadvantage as the RANS and Rankine solvers that separate simulations are required for each wave frequency and direction.

The new method was implemented in the panel model *Wavescat*. The original model is based on the ZSGF with modifications for forward speed, including encounter frequency and interaction between the steady and wave-induced flows. The new method based on the FSGF is described in this paper together with validation against benchmark model test data for squat, vertical vessel motions, added resistance and drift forces. The original method based on the ZSGF also served as a reference in the validation.

2 MODEL DESCRIPTION

2.1 GENERAL

Consider a ship floating in a fluid that can be considered as incompressible, homogeneous and irrotational. The model domain $\mathcal{D}$ is bounded by the submerged hull surface $\mathcal{H}$, the fluid surface $\mathcal{F}$ and the seabed $\mathcal{B}$, see Figure 1. Γ is the intersection between the body and the fluid surface. The co-ordinate system Oxyz, with unit vectors $\vec{e}_x$, $\vec{e}_y$ and $\vec{e}_z$, is a right-handed system with the origin at the still water level and the *z*-axis positive upwards. The body is sailing with constant forward speed *U*, and is able to make any arbitrary motion, $\vec{X}$, in six degrees of freedom. The motions are assumed to be small, so that linear approximations are valid.

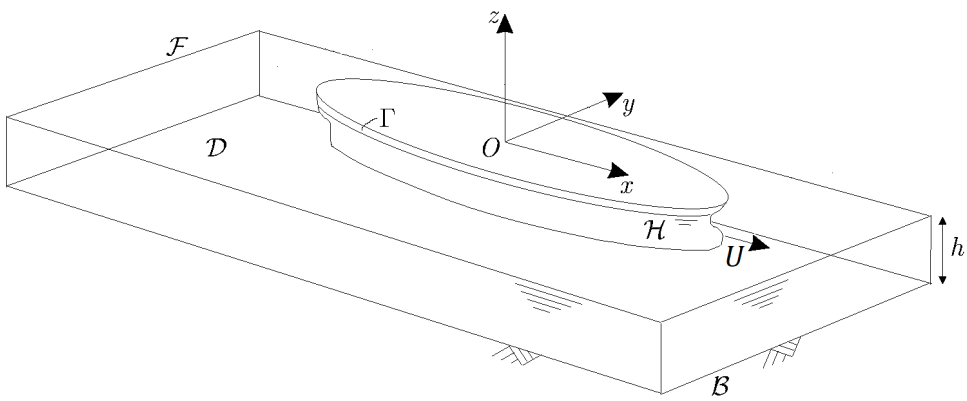

Figure 1. Definition sketch of the ship sailing in the computational domain.

The ship oscillates at the encounter frequency ω, while the wave number *k* is determined by the absolute wave frequency $\omega_0 = \sqrt{gk \tanh kh}$, with *g* the acceleration of gravity and *h* the water depth. These parameters are related by the modified dispersion relation

$$\omega = \omega_0 - kU \cos \mu \tag{1}$$

where μ is the wave direction (going-to) relative to the *x*-axis. The fluid flow around the floating body is described by means of a (complex) velocity potential Φ, which is defined such that its gradient is equal to the flow velocity, and oscillates according to $e^{i\omega t}$. The velocity potential in a regular wave with encounter frequency ω is decomposed into

$$\Phi = \phi^I + \phi^S + i\omega \sum_{j=1}^{6} \chi^j X^j \tag{2}$$

where ϕ^S is the scattered wave potential, describing the diffraction of the incident wave potential ϕ^I about the floating body. The radiation potentials are written as the product of the potentials χ^j and the ship motions $\vec{X}$ in six degrees of freedom. The sea floor $\mathcal{B}$ is assumed horizontal in the area surrounding the floating body, so that a constant water depth assumption can be applied for the calculation of the radiated and scattered waves. In addition, there is a steady potential $\bar{\Phi}$ due to the forward speed of the ship in still water.

The equation of motion of the floating body is

$$\{-\omega^2(\mathbf{M} + \mathbf{A}) + i\omega\mathbf{B} + \mathbf{C}\}\vec{X} = \vec{F} \tag{3}$$

where **M** is the inertia matrix and **C** is the matrix for the hydrostatic restoring. The wave force $\vec{F}$ due to a regular wave on the fixed body (due to the incident and scattered waves) is placed on the right-hand side of the equation, while the hydrodynamic forces due to the moving body, i.e. the added mass **A** and damping **B**, are placed on the left-hand side. Both the wave force $\vec{F}$ and the ship motion $\vec{X}$ are complex amplitudes.

2.2 STEADY POTENTIAL AND SQUAT

Squat is the steady sinkage of a ship sailing in a waterway. The steady flow and squat are modelled using the double-body flow assumption. This means that the free surface is assumed flat, so that the effect of free surface deformations on the flow pattern are ignored.

The flow is regarded relative to the ship. Thus, the ambient flow velocity is directed against the ship's sailing direction with speed U. The total steady flow velocity $\nabla\bar{\Phi}$ is decomposed on the ship hull surface as

$$\nabla\bar{\Phi} = -U\vec{e}_x + Un_x\vec{n} + \nabla\bar{\phi} \tag{4}$$

with

$$\bar{\phi} = \frac{U\psi}{\sqrt{1 - F_h^2}} \tag{5}$$

in which ψ follows from radiation integral equations (similar to the ones discussed for the wave diffraction in Section 2.3) for the surge motion with the zero-frequency Green function that assumes a (rigid) Neumann boundary conditions both at the seabed and the free surface ($\psi_z = 0$). This Green function is further discussed in Section 2.5. The term $1/\sqrt{1 - F_h^2}$ in Eq. 5, with $F_h = U/\sqrt{gh}$ the depth-related Froude number, is the Tuck factor that follows from slender-body theory in shallow water (Tuck, 1966). This factor accounts for nonlinear effects that are otherwise ignored due to the assumption that the free-surface deformations are equal to zero. The steady heave force on the ship can be determined from the pressure drop due to the velocity squared and subtracting the ambient pressure drop, which gives

$$\bar{F}_z = -\tfrac{1}{2}\rho \iint_{\mathcal{H}} (|\nabla\bar{\Phi}|^2 - U^2) n_z dS \tag{6}$$

The steady pitch moment $\bar{M}_y$ is determined in a similar way. The amidship squat $\bar{Z}$ and dynamic trim angle $\bar{\Theta}$ follow from

$$\begin{bmatrix} C_{33} & C_{35} \\ C_{53} & C_{55} \end{bmatrix} \begin{bmatrix} \bar{Z} \\ \bar{\Theta} \end{bmatrix} = \begin{bmatrix} \bar{F}_z \\ \bar{M}_y \end{bmatrix} \tag{7}$$

2.3 DIFFRACTION SOLUTION

The diffraction problem is solved for the scattering of waves around the ship hull $\mathcal{H}$. The scattered potential ϕ^S describes the scattering of the incident wave ϕ^I. The incident wave is defined as a regular wave with unit amplitude and direction β:

$$\phi^I = \frac{ig}{\omega_0}\frac{\cosh k(z+h)}{\cosh kh}e^{-ik(x\cos\mu + y\sin\mu)} \tag{8}$$

The scattered potential must meet the following boundary conditions:

$$\nabla^2\phi^S = 0 \quad \text{in } \mathcal{D} \tag{9}$$
$$-\omega^2\phi^S + g\phi_z^S = 0 \quad \text{on } z = 0 \tag{10}$$
$$\phi_z^S = 0 \quad \text{on } z = -h \tag{11}$$
$$\phi_n^S + \phi_n^I = 0 \quad \text{on } \mathcal{H} \tag{12}$$
$$\phi^S = 0 \quad \text{for } R \to \infty \tag{13}$$

where R is a horizontal distance and $\vec{n}$ is the unit normal vector directed out of the fluid domain; $n_{4,5,6} = (\vec{x} - \vec{x}_G) \times \vec{n}$ relative to the centre of gravity $\vec{x}_G$. For the determination of the potentials ϕ^S the indirect source potential method is applied. This is a common technique in potential theory with the advantage that the velocities in the fluid are easily obtained. The indirect formulation is reached after introducing a scalar potential ϕ' which describes the flow interior to the ship. The source strength σ is defined as the remaining difference between the normal velocities at the body surface

$$\sigma = \frac{1}{4\pi}(\phi_n^S - \phi') \tag{14}$$

The source strength is further defined such that $\phi' = \phi^S$ on the body surface. Substituting the formulations for σ in Green's theorem leads to the expression for ϕ^S

$$\phi^S(\vec{x}) = \iint_{\mathcal{H}} \sigma(\vec{\xi})G^f(\vec{x},\vec{\xi})dS + \frac{U^2}{g}\int_{\Gamma}\sigma(\vec{\xi})G^f(\vec{x},\vec{\xi})n'_x dl \tag{15}$$

G^f is the forward-speed frequency-domain Green function that is further discussed in Section 2.5. $n' = \vec{n}/|\cos\gamma|$, with γ the angle between $\vec{n}$ and the free surface, such that $[n'_x, n'_y, 0]$ forms the unit normal vector in the waterplane. The waterline contour integral arises as for a surface-piercing body the integral over the free surface is not equal to zero, but for convenience can be transformed to a contour integral over the intersection of the hull with the free surface (Guevel and Bougis, 1982). In ZSGF methods, this term is usually omitted to be consistent with the way the Green function is obtained. Calculations using the present FSGF method and results by Peng et al. (2015) using a time-domain method showed that, when included, its contribution is very small at low to moderate forward speed. At high speed, its effect is more significant due to the U^2 relationship, but improvement in accuracy and physical relevance are questionable. More dedicated validation at high speed is needed. To better highlight the difference between ZSGF and FSGF methods based on the formulation of the Green function alone, the contour integral is omitted here, and the expression for ϕ^S is reduced to

$$\phi^S(\vec{x}) = \iint_{\mathcal{H}} \sigma(\vec{\xi})G^f(\vec{x},\vec{\xi})dS \tag{16}$$

Accordingly, the unknown source strengths follow from the solution of a Fredholm integral equation of the second kind

$$2\pi\sigma(\vec{x}) + \iint_{\mathcal{H}} \sigma(\vec{\xi})G^f_{n(\vec{x})}(\vec{x},\vec{\xi}) = -\phi_n^I(\vec{x}) \tag{17}$$

2.4 WAVE AND HYDRODYNAMIC FORCES

The first order wave forces due to the incident and scattered wave are found by integration of first order pressures over the mean submerged hull, where the pressure p can be obtained using Bernoulli's equation

$$-(p - p_0)/\rho = gz + \Phi_t + \tfrac{1}{2}\nabla\Phi\cdot\nabla\Phi + \text{const} \tag{18}$$

where p_0 is the atmospheric pressure and ρ is the density of the fluid. The derivative of the potential to time Φ_t also contains forward speed terms

$$\Phi_t = i\omega\Phi - U\Phi_x + \nabla\bar{\phi}\cdot\nabla\Phi \tag{19}$$

The first order wave force and moment are obtained by integration of the first order incident and scattered potentials over the submerged hull

$$\vec{F}^{(1)} = \rho \iint_{\mathcal{H}} (-i\omega\phi^D + U\phi_x^D - \nabla\bar{\phi} \cdot \nabla\phi^D)\vec{n}\, dS \tag{20}$$

$$\vec{M}^{(1)} = \rho \iint_{\mathcal{H}} (-i\omega\phi^D + U\phi_x^D - \nabla\bar{\phi} \cdot \nabla\phi^D)\vec{x}^* \times \vec{n}\, dS \tag{21}$$

where ϕ^D is the total diffraction potential from the sum of the incident and scattered potentials, and $\vec{x}^* = \vec{x} - \vec{x}_G$.

The radiation problem for the radiation potentials χ^j for the body oscillating with unit velocity amplitude in the six modes *j* is solved analogously but for the boundary condition on the hull equal to

$$\chi_n^j = n_j + m_j/(i\omega)\,, \quad j = 1, 2, \dots 6 \tag{22}$$

where the *m*-terms are the modifications of the hull boundary condition due to forward speed

$$\vec{m}_{1,2,3} = -(\vec{n} \cdot \nabla)\nabla\bar{\phi} \tag{23}$$

$$\vec{m}_{4,5,6} = \vec{x}^* \times \vec{m}_{1,2,3} + \nabla\bar{\Phi} \times \vec{n} \tag{24}$$

This boundary condition forms the right-hand side in Eq. 17 for the radiation potentials. The second-order gradient of the steady potential along the hull is evaluated from the solution of an integral equation with Dirichlet boundary conditions on the hull surface (Wu, 1991; Chen and Malenica, 1996). This solution is robust, also for complex shapes with sharp angles in the hull surface. The added mass and damping coefficients are obtained from

$$i\omega A_{kj} + B_{kj} = \rho \iint_{\mathcal{H}} \left[\left(i\omega\chi^j - U\chi_x^j + \nabla\bar{\phi} \cdot \nabla\chi^j - P_3\right)n_k + P_4\right] dS\,, \quad k, j = 1,2, \dots 6 \tag{25}$$

The P_3 and P_4 terms contain minor contributions. $P_3 = \vec{X}' \cdot \nabla\bar{p}/\rho$ with $\bar{p}$ the steady pressure associated with the steady flow $\bar{\Phi}$, and $\vec{X}' = \vec{X} + \vec{\alpha} \times \vec{x}^* = (X', Y', Z')$ the local displacement due to the body translation $\vec{X}$ and rotation $\vec{\alpha}$ (only the *j*-mode is considered for the added mass and damping). P_4 is due to the cross product of steady pressure times first-order motion and the normal vector, and is non-zero only for rotations or moments. This term is not further elaborated here for brevity.

The mean wave drift force and moment in regular waves can be used for computation of added resistance and manoeuvring forces. The second-order wave drift force and moment are calculated with the near-field method by integration of second-order pressures, consisting of products of first-order quantities, over the submerged hull. The formulations derived by Ogilvie (1983) are used, with a modification such that the line integral also has a contribution to the vertical drift force and moment (Chen, 2007):

$$\vec{F}^{(2)} = \rho g \int_{\Gamma} \left(\tfrac{1}{2}\zeta^2 - Z'\zeta\right)\vec{n}'\, dl - \rho \iint_{\mathcal{H}} \left(\tfrac{1}{2}|\nabla\Phi|^2 + \vec{X}' \cdot \nabla\Phi_t + \Phi_t\vec{\alpha} \times\right)\vec{n}\, dS \tag{26}$$

$$\vec{M}^{(2)} = \rho g \int_{\Gamma} \left(\tfrac{1}{2}\zeta^2 - Z'\zeta\right)\vec{x}^* \times \vec{n}'\, dl - \rho \iint_{\mathcal{H}} \left[\left(\tfrac{1}{2}|\nabla\Phi|^2 + \vec{X}' \cdot \nabla\Phi_t + \Phi_t\vec{\alpha} \times\right)\vec{x}^* \times \vec{n} + \Phi_t\vec{X} \times \vec{n}\right] dS \tag{27}$$

where ζ is the water level.

2.5 GREEN FUNCTION

The forward speed, frequency-domain Green function is the solution of the potential due to an oscillatory source below a free surface and moving with a constant speed *U*. Efficient calculation is challenging since it depends on many variables. Nossen et al. (1991) and Huijsmans (1996) derived approximations, but these are only valid in deep water and for a low forward speed. The solution is written here in the form of a Fourier Transform of the time-domain Green function G^t

$$G^f\left(\vec{x}, \vec{\xi}, h, U, \omega\right) = \int_0^{\infty} G^t\left(\vec{x}, \vec{\xi}', h, t\right)e^{-i\omega t}dt \tag{28}$$

where $\vec{\xi}'$ is the position of the moving source $\vec{\xi}' = \vec{\xi} - Ut\vec{e}_x$. The time-domain Green function is the solution of the Cauchy-Poisson problem for a unit source below the free surface given by $\sigma^t(\vec{\xi}', t) = \delta(t)$. The solution

$$G^t(\vec{x}, \vec{\xi}', h, t) = \delta(t)G^{(0)}(\vec{x}, \vec{\xi}, h) + H(t)G^w(\vec{x}, \vec{\xi}', h, t) \tag{29}$$

consists of a Rankine part $G^{(0)}$ and a wave part G^w; $\delta(t)$ is the Dirac delta function and $H(t)$ is the Heaviside step function. The Rankine part is an immediate influence of the source on the field point and the wave part is a memory part that describes the influence due to a wave that has been formed at the free surface. The solution for the case of finite water depth is given by Wehausen and Laitone (1960, Eq. 13.53):

$$G^{(0)} = \frac{1}{r} + \frac{1}{r_2} - 2\int_0^\infty \frac{e^{-kh}}{\cosh k\,h} \cosh k(z+h) \cosh k(\zeta+h) J_0(kR)dk \tag{30}$$

$$G^w = 2\int_0^\infty \frac{\sqrt{gk \tanh kh}}{\cosh kh \sinh kh} \sin\left(t\sqrt{gk \tanh kh}\right) \cosh k(z+h) \cosh k(\zeta+h) J_0(kR)dk \tag{31}$$

where r and r_2 are the distances from the field point to the source and to the mirror source below the sea floor respectively, and R is the horizontal distance. z and ζ are the vertical coordinates of the field and source point, respectively. J_0 is the Bessel function of the first kind.

The variables are nondimensionalized with respect to the acceleration of gravity, g, and the water depth, h, thus defining the dimensionless variables $X = R/h$, $V_1 = 2+(z+\zeta)/h$, $V_2 = |z-\zeta|/h$ and $T = t\sqrt{g/h}$. After applying the addition theorem for the products of two hyperbolic cosines, the formulation of the the Green function expressed in the dimensionless variables takes the form

$$G^{(0)} = h^{-1}\left[F^{(0)}(X, V_1) + F^{(0)}(X, V_2)\right] \tag{32}$$

$$G^w = h^{-1}\sqrt{g/h}[F^w(X, V_1, T) + F^w(X, V_2, T)] \tag{33}$$

with

$$F^{(0)}(X, V) = \frac{1}{\sqrt{X^2+V^2}} - \int_0^\infty \frac{e^{-k}}{\cosh k} \cosh kV\, J_0(kX)dk \tag{34}$$

$$F^w(X, V, T) = 2\int_0^\infty \frac{\Omega}{\sinh 2k} \cosh kV \sin \Omega T\, J_0(kX)dk \tag{35}$$

where $\Omega = \sqrt{k \tanh k}$. $F^{(0)}$ can be expressed by the contribution of an array of Rankine image sources. The solution can be constructed from a pair of periodic source arrays or by Fourier series (Newman, 1992). A Chebyshev series approximation is used for $X \leq 1$ and the Fourier series for $X > 1$. It is noted that the contribution from the mirror source in the free surface is negative ($-1/r_1$), while this is positive for the zero-speed frequency-domain Green function (Wehausen & Laitone, 1960, Eq. 13.17).

The evaluation of the wave part of the Green function provides a more challenging problem. The kernel of the F^w integral in Eq. 35 is highly oscillatory, so that standard methods for numerical quadrature are inefficient. The evaluation of the infinite depth Green function can be simplified by making a change of variables, so that the Green function can be expressed by a function of only two variables. In case of finite depth however, this decomposition is not possible making an efficient computation much more complicated. Newman (1992) explored the asymptotic behaviour of the F^w integral, but an efficient algorithm to compute the Green function in this way was not possible. Van der Molen (2006) used an algorithm that is accurate but not efficient for a moving source. We apply a cruder way here to approximate the F^w integral, similar to Bratland et al. (1997), by dividing the (X,V,T) domain in segments of unit size. V can only have values between 0 and 2. The overall domain for X is truncated at 50 and for T at 100. This provides 10,000 3D segments for which Chebyshev coefficients were evaluated using the Van der Molen (2006) algorithm.

The value of F^w is approximated directly for $V \leq 1$. The infinite-depth Green function is subtracted for $V > 1$ and evaluated separately. For the infinite-depth Green function, a power series approximation is used for small non-dimensional time, and an asymptotic approximation is used for large time as provided by Newman (1992). This computation could be accelerated

by replacing the power series by Chebyshev expansions for several sub-domains, which is more efficient than an evaluation using a differential equation (Bingham, 2016).

In the integral for the frequency-domain Green function in Eq. 28, the Rankine part $G^{(0)}$ can be evaluated separately, and only contributes to the real part of G^f. The integration of the wave part G^w is done using Filon quadrature. The integral is truncated in the computation. For the remaining part beyond the truncation point, only the leading order asymptotic term of F^w equal to $1/\sqrt{T^2 - X'^2}$ is considered (Newman, 1992), where X' is the horizontal distance between $\vec{x}$ and $\vec{\xi}'$ relative to the water depth. The denominator is linearised with respect to T at the truncation point such that analytical integration is possible (Gradshteyn & Ryzhik, 2022, §2.641). The asymptotic behaviour of G^w in deep water involves several terms. Since the main intended purpose of the model is for manoeuvring in coastal waters, these terms are not integrated analytically.

The zero-frequency Green function that is used to determine the steady potential and squat is the zero-frequency limit of the zero-speed frequency-domain Green function:

$$G^f(\omega = 0) \;=\; \frac{1}{r} + \frac{1}{r_2} + 2\int_0^\infty \left[\frac{\cosh k\,(z+h)\cosh k\,(\zeta+h)}{\sinh kh} J_0(kR) - \frac{1}{kh}\right] e^{-kh}\,dk \;+\; \text{const} \tag{36}$$

The $e^{-kh}/(kh)$ term is subtracted to secure convergence, which is possible here since only vertical derivatives are prescribed as (Neumann) boundary conditions at the seabed and the free surface. Another effect is that the result for $R \to \infty$ is not equal to zero but equal to $-2/h \ln R/(2h)$. The constant is irrelevant for the calculation of the steady flow and squat, since it only involves gradients of the potential. The evaluation of this Green function is similar to the evaluation of the Rankine part of the time-domain Green function $G^{(0)}$. The solution can be constructed from four periodic source arrays or by Fourier series. Unlike the approximation of $G^{(0)}$, the contributions from all sources in the arrays are positive.

2.6 NUMERICAL CONSIDERATIONS

The integration of the integral equations 15 and 16 is carried using a linear panel method. The mean wetted surfaces of the body $\mathcal{H}$ is discretised by in total N flat quadrilateral elements at which the velocity potential is assumed constant. The collocation points for the unknown potentials are placed in the element centroids, thus leaving a system of N linear equations with N unknowns.

For the Green functions, a single evaluation is made between two panels based on the two collocation points. The integration of the Rankine part of the Green function ($1/r$ term) is performed analytically for the integration over the panel on which the collocation point lies. A multi-pole expansion is used for the integration of the $1/r$, $-1/r_1$ and $1/r_2$ terms over other panels.

In a run, the Rankine $G^{(0)}$ and wave part G^w of the time-domain Green functions are evaluated first, since they are independent of wave frequency, and saved to disc. Subsequently, for each encounter frequency, the frequency-domain Green functions G^f are computed by integration in Eq. 28, and the matrix $G^f_{n(x)}$ is inverted. This enables simple matrix multiplications to obtain the source strengths in Eq. 17 for all wave directions. This means that the vessel response results are given with respect to the encounter frequency, while the wave spectrum S_ζ is usually given with respect to the absolute frequency. For the computation of the response spectrum $\vec{S}_X$, the wave spectrum is transformed from the absolute frequency to the encounter frequency using the transformation factor $\partial\omega_0/\,\partial\omega$

$$\vec{S}_X(\omega,\beta) \;=\; \left|\vec{X}(\omega,\mu)\right|^2 S_\zeta(\omega_0,\mu)\,\frac{c_G}{c_G - U\cos\beta} \tag{37}$$

where $\left|\vec{X}\right|$ is the response amplitude operator (RAO) and c_G is the group speed of the waves corresponding to the absolute frequency ω_0

$$c_G \;=\; \frac{\omega_0}{2k}\left(1 + \frac{2kh}{\sinh 2kh}\right) \tag{38}$$

It is noted that the modified dispersion relation, Eq. 1, has two solutions for low frequencies in following seas, and does not have a solution for high frequencies, if the denominator in Eq. 37 is less than zero. In deep water the following relation applies: $\tau \equiv \omega U \cos\beta\,/g \leq \frac{1}{4}$.

Similar to computations using the ZSGF, the accuracy of the results may be affected near specific irregular frequencies. A common and convenient solution to eliminate irregular frequency effects in ZSGF models is to apply a free surface lid inside the vessel, and by this also solve the fictitious flow problem inside the vessel. However, due to the highly oscillatory nature of the time-domain Green function near the free surface, this solution is not practically feasible in the method used here. A lowered free surface lid would be feasible. Application of this is a topic of future work.

3 MODEL TESTS

The model tests used for the model validation in this paper for a ship sailing in waves were conducted using scale models of the DTC container ship in the towing tank at Flanders Hydraulics Research in Antwerp, Belgium (Van Zwijnsvoorde et al., 2019; Delefortrie, 2024) and in the deepwater basin at MARINTEK in Trondheim, Norway (Shigunov et al., 2018). Both model test programs were conducted as part of the EU funded SHOPERA project. The results of a selected seven tank tests were made available by FHR and the University of Ghent as part of open model test data for the 5th MASHCON in 2019. Set-up data and results from the deepwater basin tests were obtained from the Shigunov et al. (2018) paper.

The main particulars of the DTC container ship are given in Table 1. Different versions of the model ship were used at FHR and MARINTEK at a different model scale but the same hull shape. The tests at FHR that were used in this paper were captive tests, meaning that the vessel was towed under a carriage, free to move in heave, roll and pitch, while fixed in surge, sway and yaw. The tests at MARINTEK were free running using the propeller and rudder installed on the model ship.

Table 1. Dimensions and inertia properties of the of the DTC container at full scale

Parameter	Symbol	Unit	FHR	MARINTEK
Propulsion		-	Captive	Self-propelled
Scale		-	89.11	63.65
Length between Perpendiculars	L_{PP}	m	355	
Breadth	B	m	51	
Draft	T	m	14.5	
Block Coefficient	C_B	-	0.661	
Transverse Metacentric Height	$\overline{GM}$	m	5.2	5.1
Transverse Radius of Gyration	k_{xx}	m	19.8	20.3
Longitudinal Radius of Gyration	k_{yy}	m	84.9	87.3
Longitudinal Radius of Gyration	k_{zz}	m	86.6	87.4

The towing tank at FHR has a width of 7 m (624 m at full scale). This is wide compared to the vessel breadth. However, some confined channel flow effects occur at high speeds. The dimensions of the Ocean Basin at MARINTEK are 80 m x 50 m x 10 m. The depth is 636.5 m at full scale. The full scale tank width and basin depth are used in the BEM model set-up.

Tests for validation were selected for squat, wave response, added resistance (surge) and drift forces/moments (sway and yaw). The conditions of the selected tests are provided in Table 2. Note that the wave direction is going-to here; μ = 60° corresponds to 150° away from the bow. This direction was chosen as it contains the largest number of tested wave periods.

Table 2. Model test conditions at full scale

Test type	Laboratory	Test #	Speed (kts)	h (m)	μ (°)	T_W (s)	H_W (m)
Squat	FHR	C2	16	29.0	-	-	-
		C3	6	17.4	-	-	-
Wave Response	FHR	CW3	16	29.0	180	13.0	5.56
		CW5	6	17.4	180	15.7	1.90
Added Resistance	MARINTEK	4 Tests	6	636.5	180	13.9, 9, 8, 7	7.5, 10, 7.5, 5
		4 Tests	16	636.5	180	14.3, 9, 8, 7	7.5, 10, 7.5, 5
Drift Forces	MARINTEK	4 Tests	6	636.5	60	10, 9, 8, 7	6, 7.5, 7.5, 5

4 BEM MODEL SET-UP

The *Wavescat* model was set up for the DTC container ship for the model test conditions. The IGES file of the DTC hull was used to generate a hull mesh with 2160 panels. This mesh was used for the squat runs. However, this container ship hull poses a challenge for the calculation of FSGFs. The flared stern is almost parallel to the free surface and the panels on top of the bulbous bow are very close to the free surface. Due to the $1/r - 1/r_1$ singularities, the matrix for the source potentials

can become ill-defined, especially at high speed. To resolve this, the mesh was slightly adjusted for the runs that involve calculation of FSGFs. Some panels near the stern were lowered such that $n_z < 0.9$ for the waterline panels. The top of the bulbous bow was also slightly lowered. The adjusted hull mesh is shown in Figure 2. The vessel was considered free to move in three degrees of freedom for the captive towing tank tests, and in six degrees of freedom for the free-running basin tests.

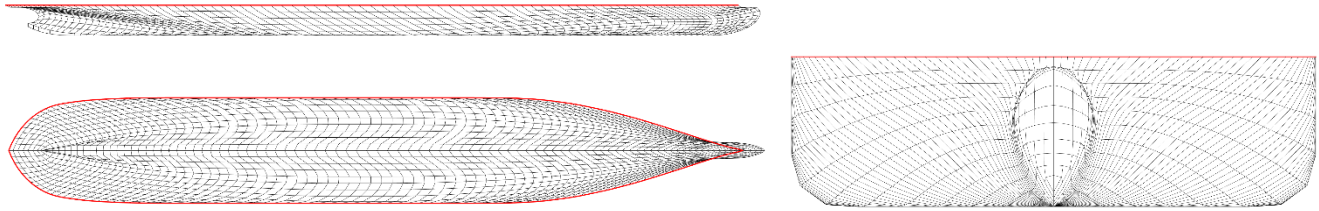

Figure 2. Hull mesh of the DTC container ship for the wave response, added resistance and drift force runs

The towing tank walls were ignored in the set-up for the wave response runs. A sensitivity run was added for the slow speed test (CW5) with the towing tank walls added as two arrays of panels. Two sets of runs were conducted for the squat runs, one for open water (as in the wave response runs) and one including the towing tank walls.

A sensitivity analysis was conducted upfront with respect to the time step and truncation time in the integration of the time-domain Green functions to determine the FSGF (Eq. 28). A time step of 0.4 s was chosen. The chosen truncation time is 120 s for the towing tank runs and the deepwater basin run at 6 knots. A longer time of 240 s was needed for the basin run at 16 knots to reach sufficient convergence of the results.

Comparative runs were also conducted with the model using the ZSGF. This method is based on the same formulations, including the difference between absolute and encounter frequency, and the interaction terms between the steady flow and first order wave in the formulations of the hydrodynamic coefficients, first order wave forces and drift forces. The same mesh used for the FSGF runs was also adopted for the ZSGF runs. A free-surface lid inside the vessel was added around and beyond the irregular frequencies.

5 RESULTS

5.1 SQUAT

The results of the squat runs are provided in Table 3 together with the measured data from the towing tank tests in still water. The raw model results with the towing tank walls added (canal) include the Tuck factor related to water depth, but do not include nonlinear effects related to confined flows. This effect is estimated based on formulations analogous to the method described by Lataire et al. (2012).

Table 3. Comparison of squat results for tests at FHR

Test #	Sinkage at Aft Perpendicular (m)				Sinkage at Forward Perpendicular (m)			
	Meas-ured	Sim., Open Water	Sim., Canal, Raw	Sim., Canal, Adjusted	Meas-ured	Sim., Open Water	Sim., Canal, Raw	Sim., Canal, Adjusted
C2	0.438	0.342	0.393	0.463	0.737	0.631	0.685	0.778
C3	0.110	0.083	0.096	0.100	0.132	0.137	0.152	0.157

Assuming uniform flow in the canal around the vessel's cross-section, the change in water level ζ due to the confined water flow speed U_c is

$$\zeta = -\frac{U_c^2 - U^2}{2g} \tag{39}$$

The part of the solution relative to U^2 would already be included in the model squat result. This linear part is

$$\zeta_{\text{lin}} = -\frac{U^2}{2g}(m_w^2 + 2m_w) \tag{40}$$

where $m_w = A_s/(A_c - A_s)$ is the blockage of the ship cross-sectional area relative to the wetted canal cross-section. $\zeta - \zeta_{lin}$ is calculated along the vessel using the body plan of the ship. The adjusted simulation result in Table 3 is the raw model result plus the resulting squat and dynamic trim due to the $\zeta - \zeta_{lin}$ water level change. The nonlinear confined flow effect is minimal for Test C3 at 6 knots, but is more significant for Test C2 at 16 knots. The critical speed for the towing tank at a (full scale) water depth of 29 m is 24.8 knots, so the vessel sails at 0.64 times the critical speed. After adding the adjustment, the modelled squat is slightly larger than the measured squat.

For test C3 with a small 20% underkeel clearance, the trim towards the bow is less pronounced in the measurements than in the simulations. This shift in trim is similar to comparison to full-scale measurements in a channel with limited UKC (Van der Molen et al., 2019). The full-scale measurements included propeller flows that cause a pressure drop near the stern, but may also have been influenced by viscous and turbulent flow effects observed here.

5.2 WAVE RESPONSE

Results of the heave and pitch RAO's are shown in Figure 3 for the two towing tank test conditions in head waves. The difference between the FSGF and zero-speed ZSGF results is small for test CW5 at 6 knots, but more pronounced for CW3 at 16 knots. Correspondence with the measured data for the FSGF results is close for the 16 knots condition. For the 6 knots condition at 20% underkeel clearance, the measured heave is significantly smaller. In the run with the tank walls added, it was found that resonant or off-resonant wave patterns are formed between the tank walls and the ship depending on the wave period. For the tested wave period, this caused a significant decrease of the heave motion. Similar effects were found in numerical modelling for the zero-speed tests (Gourlay et al., 2019). The effect of the basin walls appears to be much less at higher speed and higher encounter frequencies.

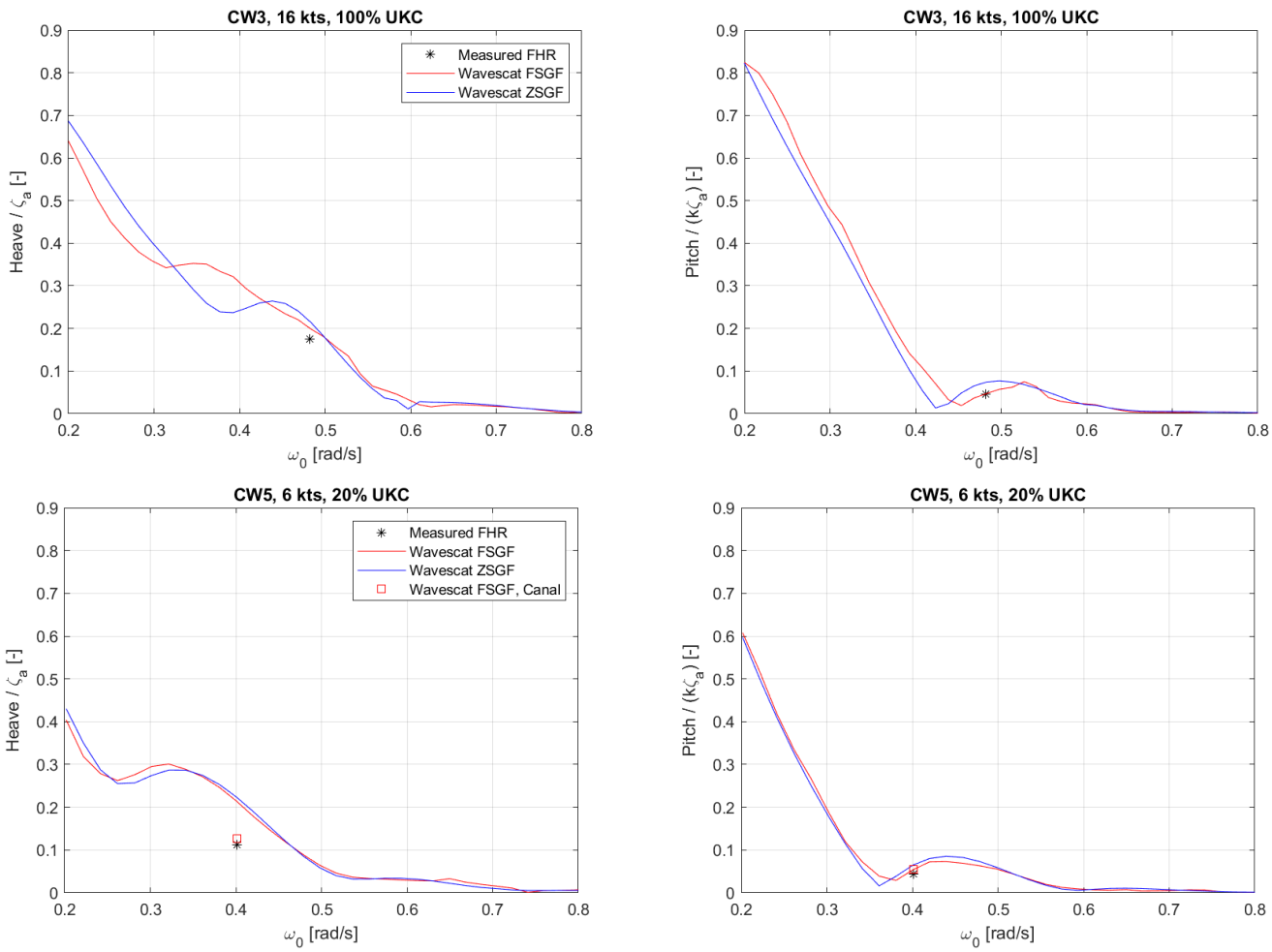

Figure 3. Comparison between measured and simulated heave (left) and pitch (right) RAO's for tests CW3 (top) and CW5 (bottom).

RAO's for the measured wave frequencies are also provided in Table 4 together with simulation results using *Fatima* (MARIN; Bunnik, 1999) and *HydroStar* (Bureau Veritas, 2011) taken from Gourlay et al. (2019). *Fatima* is a Rankine panel model, while *HydroStar* is a panel model based on the ZSGF. These models were also set up for open water, i.e. ignoring the towing tank walls. *Wavescat* FSGF generally agrees well with *Fatima*, both of which fully include forward speed effects. These models better predict the pitch motions for both tests compared to the two ZSGF models. *Wavescat* ZSGF corresponds well with *HydroStar* that is based on similar approximations.

Table 4. Comparison of heave and pitch RAO's for tests at FHR

Test #	Heave / ζ_a (-)					Pitch / ($k\zeta_a$) (-)				
	Measured	*Wavescat* FSGF	*Wavescat* ZSGF	*Fatima*	*Hydro-Star*	Meas-ured	*Wavescat* FSGF	*Wavescat* ZSGF	*Fatima*	*Hydro-Star*
CW3	0.175	0.199	0.214	0.194	0.214	0.045	0.048	0.075	0.053	0.079
CW5	0.113	0.215	0.224	0.214	0.220	0.043	0.054	0.065	0.043	0.063

5.3 ADDED RESISTANCE

Added resistance results are presented in Figure 4 for the deepwater basin tests in head waves. While the RAO results between the two calculation methods were close for the RAO's at 6 knots forward speed, there is significant difference for the added resistance. The FSGF method at low speed predicts a larger added resistance in swell. The FSGF results at 6 knots were significantly affected by erroneous irregular frequency effects beyond an absolute frequency of 0.67 rad/s. The sharp through near 0.57 rad/s in the FSGF curve at 16 knots is also an irregular frequency.

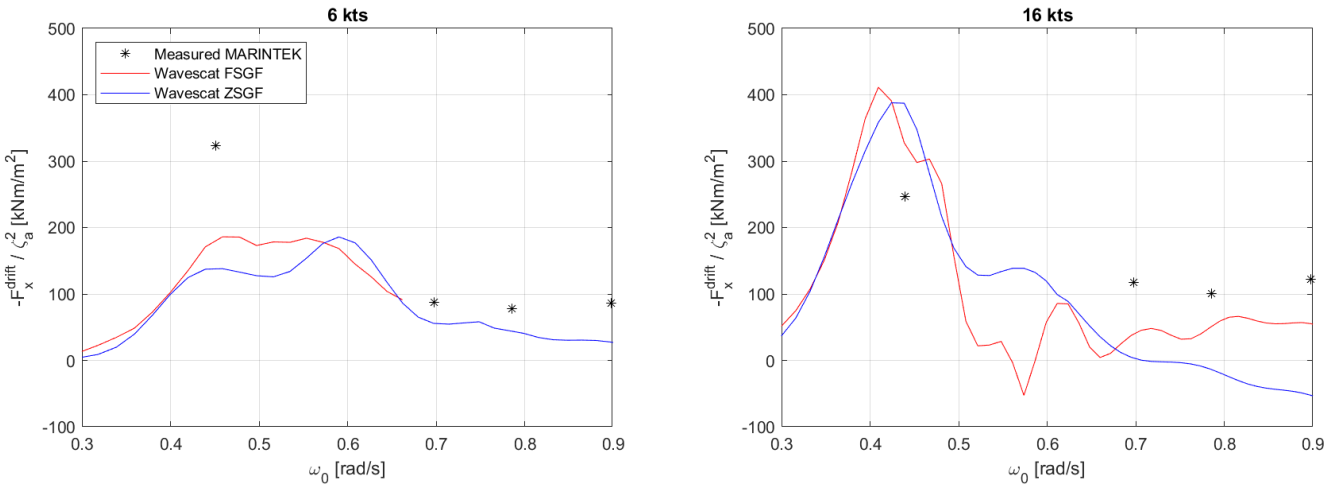

Figure 4. Comparison between measured and simulated added resistance in deep water for 6 knots (left) and 16 knots forward speed (right).

5.4 SWAY DRIFT FORCE AND YAW DRIFT MOMENT

Sway drift forces and yaw drift moments are provided in Figure 5 for the deepwater basin test at 6 knots in stern-quartering waves. Similar to the added resistance at 6 knots, there is a large difference between the two calculation methods. The FSGF method follows the trend of the sway drift forces well. For yaw, the FSGF method correctly predicts the negative moment, but is smaller than the measurements. However, as noted by Shigunov et al. (2018) there is also uncertainty in the measured yaw moments as these were challenging to acquire accurately.

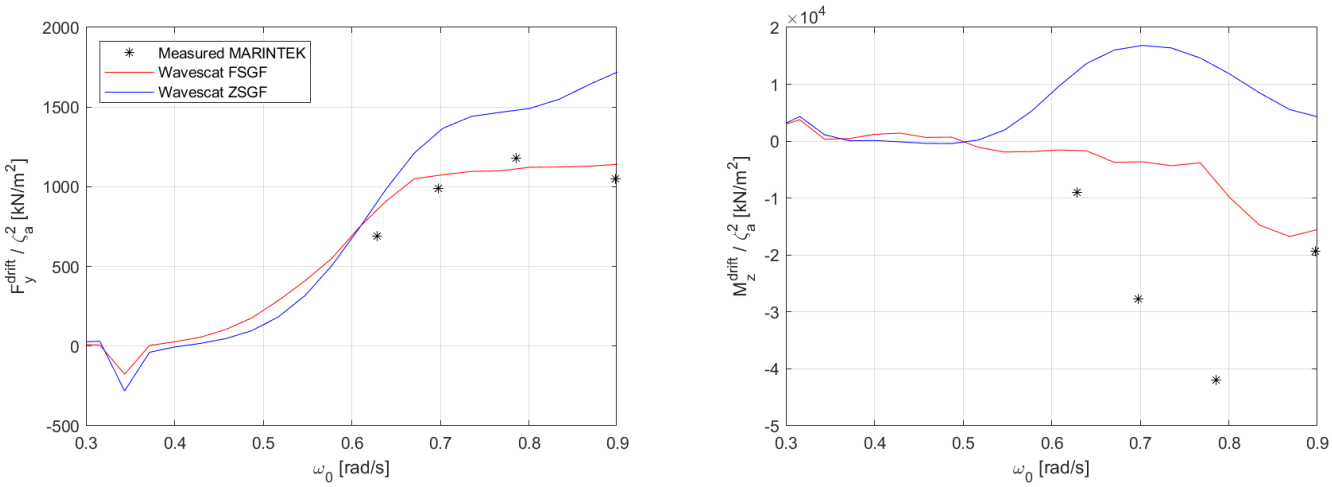

Figure 5. Comparison between measured and simulated sway drift forces (left) and yaw drift moments (right) in deep water for 6 knots forward speed and wave direction μ = 60°.

6 CONCLUSIONS

In this paper, a new boundary element method was introduced based on the forward-speed free-surface Green function, and computations presented for the DTC container ship. After calculating the time-domain Green functions upfront, first order wave forces, RAO's and drift forces can be obtained efficiently for a large matrix of encounter frequencies and wave directions. As such, it is especially suitable to provide input to underkeel clearance modelling or manoeuvring simulations. It was found that the new method provides more accurate results for the response of the vessel in long swell and at high speed compared to modelling using the ZSGF. Added resistance and drift forces in swells were improved, also at lower speeds. The ZSGF approximation may lead to an underestimation in the wave forces and vessel movements in these cases. However, the comparisons in this paper and based on a limited number of measured data points. It is recommended that more data are collected for comparison.

Particularly the added resistance results at higher frequencies were affected by irregular frequency effects. While these could be effectively eliminated using the ZSGF by applying a free-surface lid inside the vessel, this was not possible for the FSGF method due to the way that the Green function is evaluated using time-domain Green function. The application of a lowered lid inside the vessel will be the subject of further work. Alternatively, the vessel response and drift forces at higher encounter frequencies can be taken from the ZSGF results. The vessel generally moves less at these frequencies, and the ZFGF method provides more reliable RAO's at higher encounter frequencies.

REFERENCES

Bingham, H.B., 2016. A note on the relative efficiency of methods for computing the transient free-surface Green function. Ocean Eng. 120, 15-20. https://doi.org/10.1016/j.oceaneng.2016.05.020

Bratland, A.K., Korsmeyer, F.T., Newman, J.N., 1997. Time domain calculations in finite water depth. In: Proc. 12th IWWWFB, Carry-le-Rouet, France, pp. 13–17.

Bunnik, T.H.J., 1999. Seakeeping calculations for ships, taking into account the non-linear steady waves (PhD thesis). Delft University of Technology, The Netherlands.

Bureau Veritas, 2011. HYDROSTAR for experts user manual. Bureau Veritas, Paris, France.

Chen, X.B., 2000. Peculiar properties of ship-motion Green functions in water of finite depth. In: Proc. 15th IWWWFB, Caesarea, Israel.

Chen, X.B., 2007. Middle-field formulation for the computation of wave-drift loads. J. Eng. Math. 59, 61–82. https://doi.org/10.1007/s10665-006-9074-x

Chen, X.B. and Malenica, S., 1996. Uniformly valid solution of the wave-current-body interaction problem. In: Proc. 11th IWWWFB, Hamburg, Germany, pp. 17–20.

Chen, X.B., Wu, G.X., 2001. On singular and highly oscillatory properties of the Green function for ship motions. J. Fluid Mech. 445, 77–91. https://doi.org/10.1017/S0022112001005481

Delefortrie, G., 2024. Sailing in shallow water wave with the DTC container carrier: Open model test data for validation purposes – Addendum: Proposed post-processing for the captive tests. In: Proc. 5th MASHCON, Ostend, Belgium.

Donatini, L., Herdayanditya, I., Verao Fernandez, G., Pribadi, A.B.K., Lataire, E., Delefortrie, G., 2022. Implementation of forward speed effects on an open source seakeeping solver. In: Proc. 6th MASHCON, Glasgow, UK, pp. 20–33.

Gradshteyn, I.S., Ryzhik, I.M., 2022. Table of Integrals, series, and products (9th Ed.). D. Zwillinger & V.H. Moll (Eds.). San Diego: Academic Press.

Gourlay, T., Lataire, E., Delefortrie, G., Donatini, L., Tello Ruiz, M., Veen, D., Bunnik, T., Dallinga, R., 2019. Benchmarking of DIFFRAC, HYDROSTAR, MOSES, NEMOH, OCTOPUS, PDSTRIP, RAPID, SEAWAY, SLENDERFLOW and WAMIT against measured vertical motions of the Duisburg Test Case container ship in shallow water. Proc. 5th MASHCON, Ostend, Belgium, pp. 155–163.

Guevel, P, Bougis, J., 1982. Ship motions with forward speed in infinite depth. Int. Shipbuild. Progr. 29, 103–117.

Huijsmans, R.H.M., 1996. Mathematical Modelling of the Mean Wave Drift Force in Current (PhD thesis). Delft University of Technology, The Netherlands.

Kara, F., 2011. Time domain prediction of added resistance of ships. J. Ship Res. 55, 163–184. https://doi.org/10.5957/jsr.2011.55.3.163

Korsmeyer, F.T., Bingham, H.B., 1998. The forward speed diffraction problem. J. Ship Res., 42, 99–112.

Lataire, E., Vantorre, M., Delefortrie, 2012. A prediction method for squat in restricted and unrestricted rectangular fairways. Ocean Eng. 55, 71–80. http://dx.doi.org/10.1016/j.oceaneng.2012.07.009

Newman, J.N., 1992. The approximation of free-surface Green functions. In: Wave Asymptotics (P. A. Martin & G. R. Wickham, Eds.), pp. 107–135. Cambridge University Press.

Nossen, J., Grue, J., Palm, E., 1991. Wave forces on three-dimensional floating bodies with small forward speed. J. Fluid Mech. 227, 135–160.

Ogilvie, T.F., 1983. Second-order hydrodynamic effects on ocean platforms. In: Proc. Int. Workshop on Ship and Platform Motions, Berkeley, CA, USA, pp. 205–265.

Papanikolaou, A., Schellin, T.E., 1992. A Three-Dimensional Panel Method for Motions and Loads of Ships with Forward Speed. Ship Techn. Res. 39, 147–156.

Peng, H., Wang, J., Qiu, W., 2015. Effect of line integral on the computation of forward-speed ship motions. In: Proc. 34th Int. Conf. Ocean, Offshore, Arctic Eng., St. John's, NL, Canada. OMAE2015-41313.

Shen, Z., Wan, D., Carrica, P.M., 2015. Dynamic overset grids in OpenFOAM with application to KCS self-propulsion and maneuvering. Ocean Eng. 108, 287–306.

Sigmund, S., El Moctar, O., 2018. Numerical and experimental investigation of added resistance of different ship types in short and long waves. Ocean Eng. 147, 51–67.

Söding, H., Shigunov, V., Schellin, T.E., El Moctar, O., 2012. A Rankine panel method for added resistance of ships in waves. In: Proc. 31st Int. Conf. Ocean, Offshore and Arctic Eng., Rio de Janeiro, Brazil. OMAE2012-83457.

Tuck, E.O., 1966. Shallow water flows past slender bodies. J. Fluid Mech., 26, 81–95.

Van der Molen, W., 2006. Behaviour of moored ships in harbours (PhD thesis). Delft University of Technology, The Netherlands.

Van der Molen, W., Thomson, G., Nitkin, J., Taylor, D., Scott, D., 2019. Forecasting squat of Post Panamax ships in PortMiami's entrance channel. Proc. Ports 2019: Port Planning and Development, Pittsburgh, PA, USA (pp. 173–183). https://doi.org/10.1061/9780784482629

Van Zwijnsvoorde, T., Tello Ruiz, M., Delefortrie, G., Lataire, E., 2019. Sailing in shallow water waves with the DTC container carrier: Open model test data for validation purposes. Proc. 5th MASHCON, Ostend, Belgium, pp. 411–420.

Wehausen, J.V., Laitone, E.V., 1960. Surface waves. In: Handbuch der Physik (S. Flügge, Ed.), Vol. 9, pp. 446–778. Berlin: Springer.

Wu, G.X., 1991. A numerical scheme for calculating the m_j terms in wave-current-body interaction problem. Appl. Ocean Res., 13, 317–319.

AUTHOR'S BIOGRAPHY

Wim van der Molen, PhD, is a coastal and port engineer in the position of associate principal at Baird in Australia. He is responsible for the set-up and quality control of port operability and ship navigation projects. He has been the technical lead in the development of several port operational systems, such as forecasting systems for underkeel clearance in shipping channels and moored ship motions in coastal terminals.

COMPARISON OF WAMIT WITH MEASURED WAVE-INDUCED MOTIONS OF CONTAINER SHIPS AND BULK CARRIERS, USING AN ADJUSTMENT FOR SHIP SPEED

Tim Gourlay, Perth Hydro, Australia

COMPARISON OF WAMIT WITH MEASURED WAVE-INDUCED MOTIONS OF CONTAINER SHIPS AND BULK CARRIERS, USING AN ADJUSTMENT FOR SHIP SPEED

TIM GOURLAY, PERTH HYDRO, AUSTRALIA

SUMMARY

A computationally-efficient method is presented for approximating wave-induced motions of ships at low Froude number, using zero-speed Green functions as calculated using WAMIT software. The method is not new: other panel codes such as HydroSTAR and VERES3D offer a low-Froude-number approximation based on zero-speed Green functions. This article aims to set out mathematical equations for a speed-adjusted method, and validate the results against a range of available model test data. The method may be used in shallow or deep water.

NOMENCLATURE

SI units are used throughout.

AP	Aft perpendicular
CoG	Ship centre of gravity
DTC	Duisburg Test Case container ship
GM	Transverse metacentric height above CoG
FP	Forward perpendicular
KG	CoG height above keel
LBP	Length between perpendiculars
LCG	Longitudinal centre of gravity
LOA	Length overall
A_{jk}	Hydrodynamic added mass matrix
B_{jk}	Hydrodynamic damping matrix
C_{jk}	Hydrostatic restoring coefficient matrix
c_B	Block coefficient
k	Wave number $2\pi/\lambda$
k_{xx}	Roll gyradius
k_{yy}	Pitch gyradius
k_{zz}	Yaw gyradius
M_{jk}	Mass matrix
U	Ship speed
X_j	Wave load complex amplitude
z_a	Heave amplitude at aft perpendicular, defined as half of peak-to-peak heave
z_f	Heave amplitude at forward perpendicular, defined as half of peak-to-peak heave
ε_a	Heave phase at aft perpendicular (deg), ahead of wave elevation at CoG
ε_f	Heave phase at forward perpendicular (deg), ahead of wave elevation at CoG
ζ	Wave amplitude, defined as half of wave height
η	Wave elevation at ship CoG
λ	Wavelength
β	Wave heading, anticlockwise from stern-on
ω_0	Wave frequency (rad/s)
ω_e	Encounter frequency (rad/s)
ξ_k	Complex ship motion amplitude

1 INTRODUCTION

WAMIT is a panel method for calculating wave-induced loads and motions of ships and offshore structures (WAMIT 2023). WAMIT uses zero-speed Green functions and does not have an allowance for ship forward speed. A version called TIMIT using forward-speed Green functions was developed in the 1990s (Korsmeyer et al. 1999), but is not generally available.

2 ZERO-SPEED SHIP MOTIONS IN WAMIT

The ship origin, as used in WAMIT, is the ship centreline, waterline and LCG. The degrees of freedom are shown in Table 1.

Table 1. Ship motion degrees of freedom

x_1	Surge (positive forwards)
x_2	Sway (positive to port)
x_3	Heave (positive upwards)
x_4	Roll (positive to starboard)
x_5	Pitch (positive bow-down)
x_6	Yaw (positive bow-to-port)

We first consider a stationary ship in regular waves (long-crested waves with a single frequency). Wave phasing is defined such that, at the ship CoG,

$$\eta = \zeta \cos(\omega_0 t) \tag{1}$$

The equation of ship motion may be written (Salvesen et al. 1970, eq. 1) as

$$\sum_{k=1}^{6}\left[M_{jk} + A_{jk}\right]\ddot{x}_k + \sum_{k=1}^{6} B_{jk}\dot{x}_k + \sum_{k=1}^{6} C_{jk}x_k = Re\left\{X_j e^{i\omega_0 t}\right\} \; ; \; j = 1..6 \tag{2}$$

In WAMIT, the terms are calculated as follows:

- M_{jk} is the 6x6 generalized mass matrix, calculated as in WAMIT (2023, eq. 3.3)
- A_{jk}, B_{jk} are the 6x6 added mass and damping matrices. These depend on the *oscillation frequency*, which for a stationary ship is the same as the wave frequency. A_{jk}, B_{jk} are calculated by oscillating the ship in calm water and calculating the force in phase with the displacement (giving added mass) and the force in phase with the velocity (giving damping). This is the "radiation problem", as it concerns waves radiated from the ship due to its oscillations.
- C_{jk} is the 6x6 hydrostatic restoring matrix (WAMIT 2023, p3-3)
- $X_j e^{i\omega_0 t}$ are the wave exciting forces, with X_j the complex amplitude. These are a function of wave frequency and wave heading, and are solved by keeping the ship vertically and horizontally fixed in its calm-water position, and calculating the wave-induced pressures and forces on the ship. This is called the "diffraction problem", as it concerns waves diffracting around the hull.

Equation (2) is a typical spring-mass-damper equation, for which the motion oscillates at the same frequency as the forcing frequency. The motion can be written

$$x_k = Re\{\xi_k e^{i\omega_0 t}\} \tag{3}$$

Here ξ_k are the complex motion amplitudes. By substituting equation (3) into equation (2), we find that the complex motion amplitudes are the solution (WAMIT 2023, p3-5) of the matrix equation

$$\sum_{k=1}^{6}\left[-\omega_0^2\left(M_{jk} + A_{jk}\right) + i\omega B_{jk} + C_{jk}\right]\xi_k = X_j \; ; \; j = 1..6 \tag{4}$$

This gives the solution to the motion amplitudes and phases, for a ship at zero speed in regular waves at a given wave heading and frequency. For an irregular seaway, the motions may be linearly superposed for all headings and frequencies (St Denis and Pierson 1953).

3 USING WAMIT WITH A FORWARD-SPEED ADJUSTMENT

In this study, WAMIT will be used to approximate the wave-induced motions of a ship at forward speed. The method proceeds as follows.

Equation (2) as developed in Salvesen et al. (1970) is valid for ships at forward speed. In that case, the wave loading and the ship response both oscillate at the *encounter frequency* (Salvesen et al. 1970, eq. 22)

$$\omega_e = \omega_0 - kU\cos\beta \tag{5}$$

Thus, the encounter frequency may be calculated for any input ship speed, heading and wave frequency.

The added mass and damping are calculated with WAMIT at the correct *encounter frequency*, as this is the frequency at which the ship is oscillating.

The wave loads are calculated with WAMIT at the correct *wave frequency*. The primary component of wave loading is the Froude-Kriloff component, which is the hydrodynamic pressure integrated over the ship's hull, if the ship did not disturb the wave. This is very sensitive to the wavelength, as there are humps and hollows depending on the ratio of wavelength to ship length. Fig. 17 of Gourlay et al. (2015) shows that wave loads vary markedly with wave frequency, with only a small effect of ship speed. Therefore, to ensure the wavelength and Froude-Kriloff component are correct, we use the wave frequency for the wave load calculations.

A MATLAB program is written to take in the WAMIT-calculated coefficients and solve the matrix equation (4).

Some error is expected in the above approximations, as the added mass, damping and wave loads are calculated using zero-speed Green functions. However, as it is intended to apply the method to large ships at low Froude numbers, this effect may be small.

The following sections illustrate calculations using the proposed method, and comparison with model tests. In all plotted results, lines are numerical calculations and dots are experimental results. Different colours represent different speeds. In some cases, experimental results are available at different speeds; in other cases, numerical results are given at different speeds to show the effect of speed on the results. The "0 knots" results are calculated using the described method with $U = 0$; these results match the zero-speed RAOs output by WAMIT.

4 RESULTS FOR A 190 M BULK CARRIER

We consider the model test case of the Panamax bulk carrier "Ship G" which was tested at 8 and 10 knots in head seas at Flanders Hydraulics (Vantorre & Journée 2003). Test conditions are shown in Table 2.

Table 2. 190 m bulk carrier model test conditions

Parameter	Value	Source
LOA	190.00 m	Vantorre & Journée (2003, Table 1)
LBP	180.00 m	"
Beam	33.00 m	"
Maximum draft	13.00 m	"
c_B	0.85	"
Tested draft	11.6 m	Vantorre & Journée (2003, Table 3)
KG	11.6 m	"
Water depth	13.6 m	"
k_{yy}	25% LBP	"
k_{xx}	44.8% Beam	Gourlay et al. (2015)

A 4384-panel surface mesh for Ship G, up to the modelled waterline, was developed with OCTOPUS as shown in Gourlay et al. (2015, Fig. 6). This hull mesh was modelled with WAMIT v7.5, using the inputs shown in Table 2. Heave and pitch motions were calculated at 0, 8, 10 knots using the method described in Section 3. Results are shown in Figure 1.

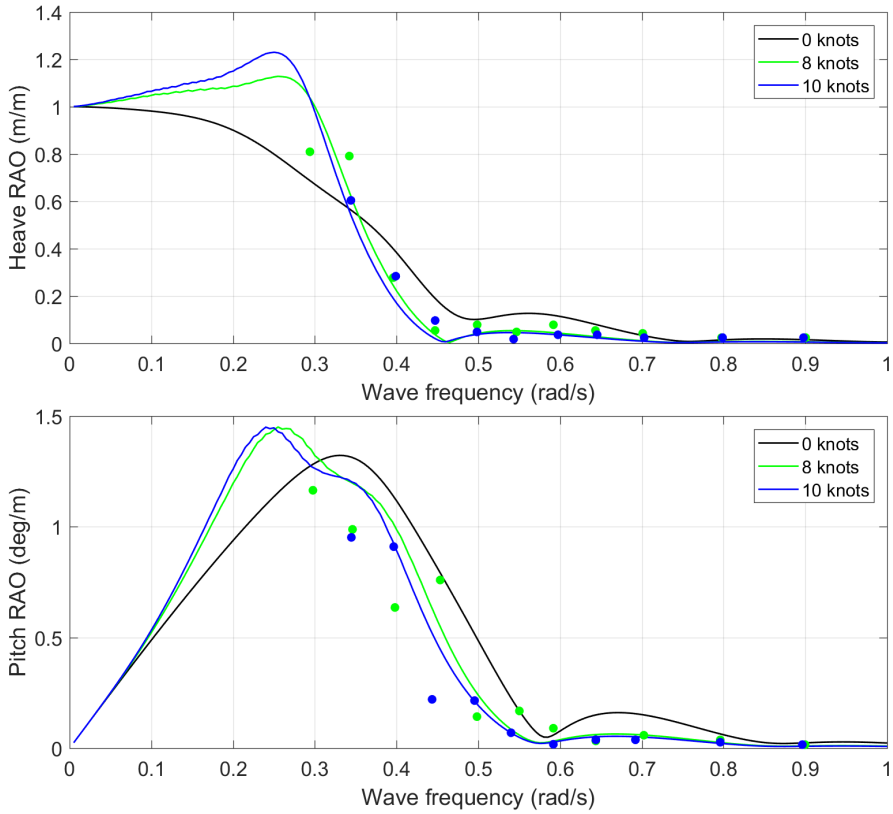

Figure 1. 190 m bulk carrier in head seas

We can compare the accuracy of the speed-adjusted panel method presented here, to the strip theory results (OCTOPUS and PDStrip) and Rankine-source panel method (GL Rankine) presented in Gourlay et al. (2015, Fig. 14). All numerical methods give fairly similar results for heave and pitch in head seas.

5 RESULTS FOR A 200 M CONTAINER SHIP

We consider the model test case of the Panamax container ship "Ship F" which was tested at 0, 8, 12 knots in head seas at Flanders Hydraulics (Vantorre & Journée 2003). Model test conditions are shown in Table 3.

Table 3. 200 m container ship model test conditions

Parameter	Value	Source
LOA	200.00 m	Vantorre & Journée (2003, Table 1)
LBP	190.00 m	"
Beam	32.00 m	"
Maximum draft	11.60 m	"
c_B	0.60	"
Tested draft	11.6 m	Vantorre & Journée (2003, Table 3)
KG	11.6 m	"
Water depth	13.6 m	"
k_{yy}	25% LBP	"
k_{xx}	36.6% Beam	Gourlay et al. (2015)

A 4320-panel surface mesh for Ship F, up to the modelled waterline, was developed with OCTOPUS as shown in Gourlay et al. (2015, Fig. 2). This hull mesh was modelled with WAMIT v7.5, using the inputs shown in Table 3. Heave and pitch motions were calculated at 0, 8, 12 knots using the method described in Section 3. Results are shown in Figure 2.

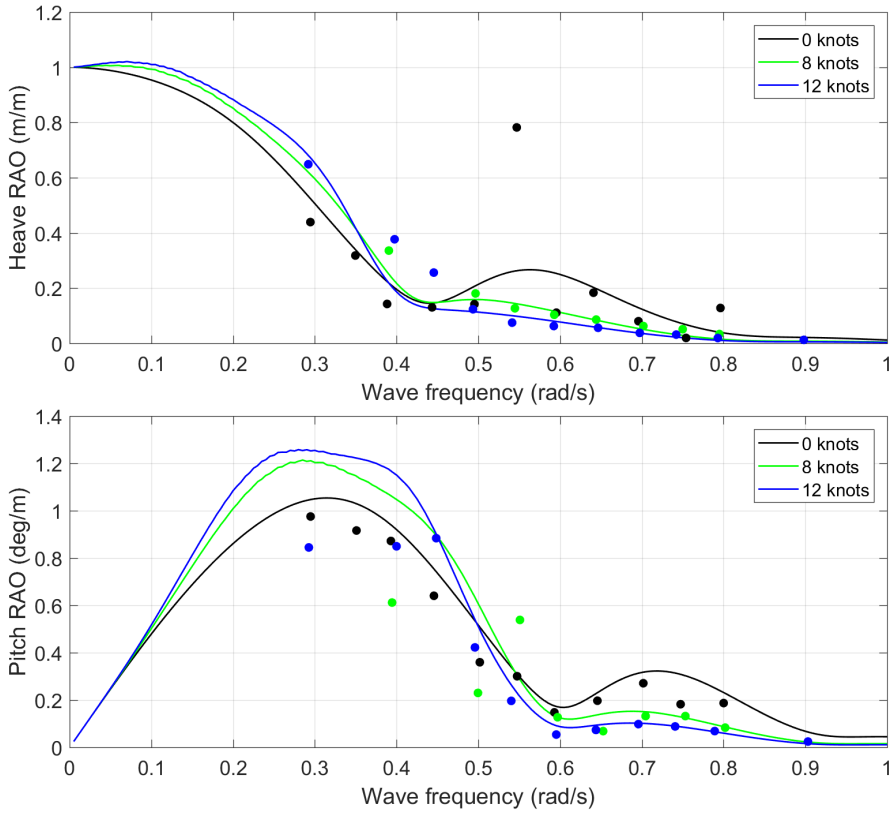

Figure 2. Comparison of speed-adjusted WAMIT (lines) with model test results (circles), for 200 m container ship in head seas

As discussed in Gourlay et al. (2015), the model-test zero-speed heave result at 0.55 rad/s is an anomaly, due to the finite width of the tank causing heave resonance at this frequency.

Comparing the accuracy of the speed-adjusted panel method presented here, to the strip theory results (OCTOPUS and PDStrip) and Rankine-source panel method (GL Rankine) presented in Gourlay et al. (2015, Fig. 11), we see that all numerical methods give fairly similar results for heave and pitch in head seas.

6 RESULTS FOR A 284 M CONTAINER SHIP

We consider the model test case of the Panamax container ship, which was tested in the Netherlands Ship Model Basin as described in Flokstra (1974), Wahab and Vink (1975) and Zhou et al. (1996). Some of these model test results are compared with numerical methods in Abdelwahab et al. (2023). Model test conditions are shown in Table 4.

Table 4. 284 m container ship model test conditions

Parameter	Value	Source
LOA	284.0 m	Zhou et al (1996, Table 1)
LBP	270.0 m	Flokstra (1974, Table 1)
Beam	32.2 m	"
Tested draft	10.85 m	"
c_B	0.60	"
KG	13.49 m	"
GM	1.15 m	"
Water depth	Deep	"
k_{yy}	24.8% LBP	"
k_{xx}	37.5% Beam	"

Heave, roll and pitch motions were calculated at 0, 10, 24.5 knots using the method described in Section 3. Results are shown in Figure 3 to Figure 5. The horizontal axis is (λ / LBP), and roll and pitch are plotted as a fraction of wave slope, to enable direct comparison with the numerical results in Flokstra (1974) and Abdelwahab et al. (2023).

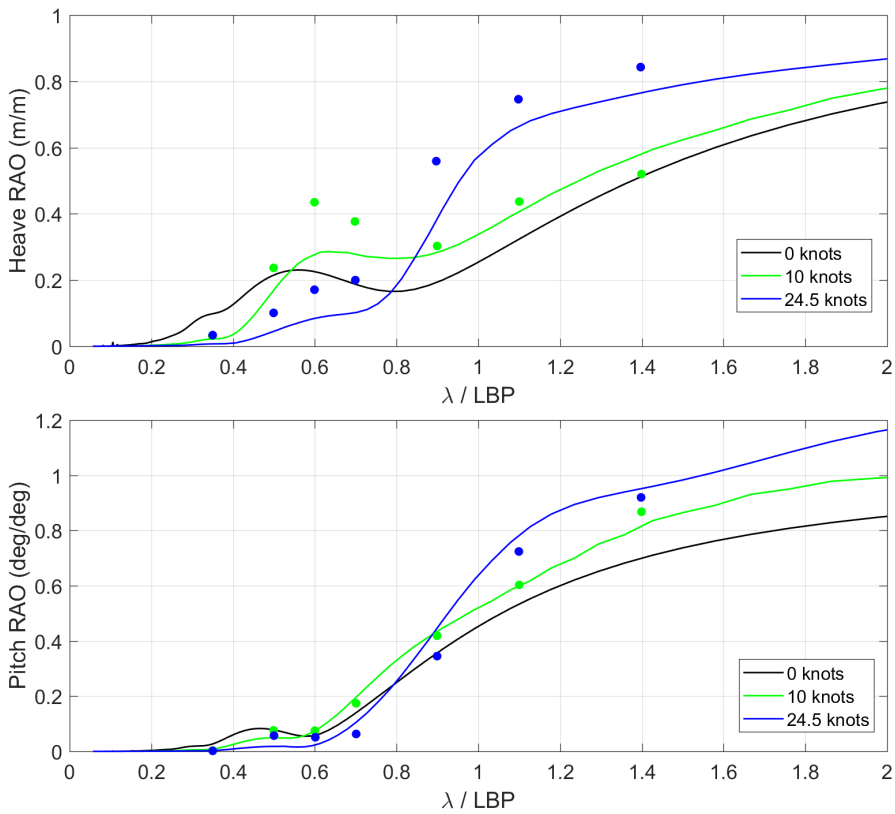

Figure 3. 284 m container ship in head seas

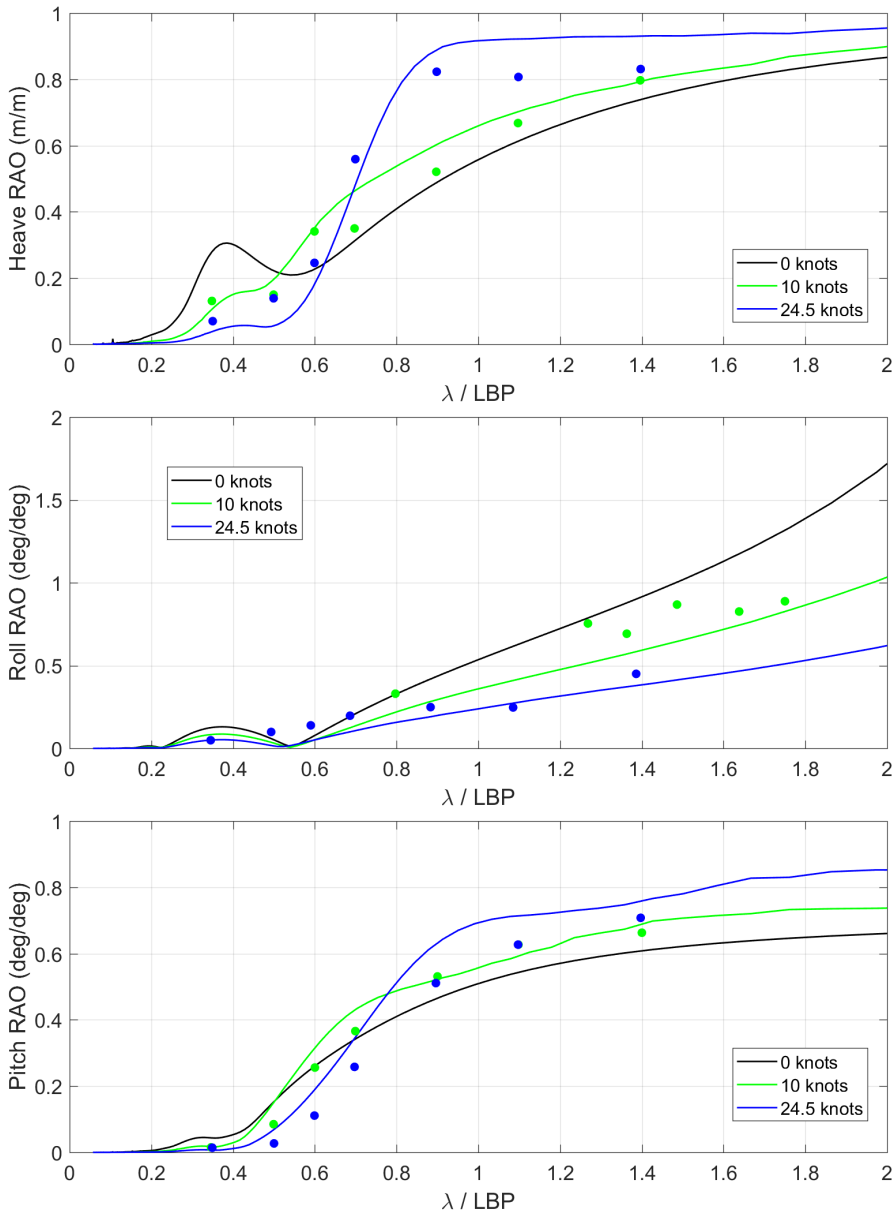

Figure 4. 284 m container ship in bow-quartering seas

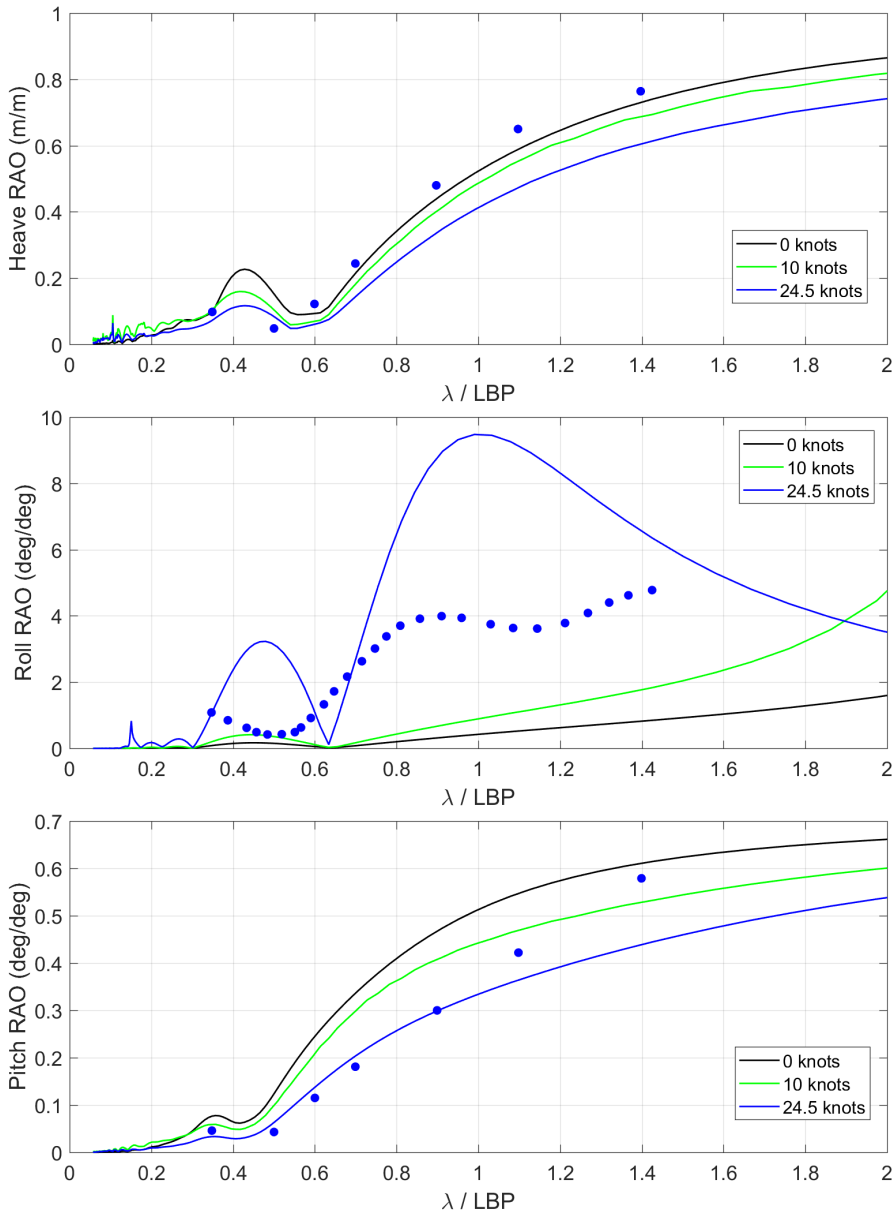

Figure 5. 284 m container ship in stern-quartering seas

We can compare the accuracy of the speed-adjusted panel method presented here, to the strip theory results presented in Flokstra (1974). As may be expected, because this Panamax container ship is a slender hull, the speed-adjusted panel method and strip theory method give fairly similar results for heave and pitch at all headings. The speed-adjusted panel method gives more accurate roll results in bow-quartering and stern-quartering seas.

Abdelwahab et al. (2023, Figs. 5,11) give results from the strip theory PDStrip for these same cases; these results are of similar accuracy to the speed-adjusted panel method presented here.

7 RESULTS FOR A 300 M CONTAINER SHIP

We consider the model test case of a 6,000-TEU container ship "Ship D" which was tested at Flanders Hydraulics (Vantorre & Journée 2003). We shall focus on the tests done at a full-scale speed of 12 knots, at wave headings of $\beta = 10°, 180°$, as studied in Gourlay et al. (2015). Model test conditions are shown in Table 5.

Table 5. 300 m container ship model test conditions

Parameter	Value	Source
LOA	300.00 m	Vantorre & Journée (2003, Table 1)
LBP	291.13 m	"
Beam	40.25 m	"
Maximum draft	15.00 m	"
c_B	0.60	"
Tested draft	15.00 m	Gourlay et al. (2015)
Water depth	18.0 m	"
k_{yy}	25% LBP	"
k_{xx}	33% Beam	"
KG	15.00 m	Vantorre & Journée (2003, Table 2)

A 1744-panel surface mesh for Ship D, up to the modelled waterline, was developed with OCTOPUS as described in Gourlay et al. (2015). This hull mesh was modelled with WAMIT v7.5, using the inputs shown in Table 5.

Heave, pitch and roll motions were calculated at 0 knots and 12 knots using the method described in Section 3. No viscous roll damping was included. Results are shown in Figure 6 and Figure 7.

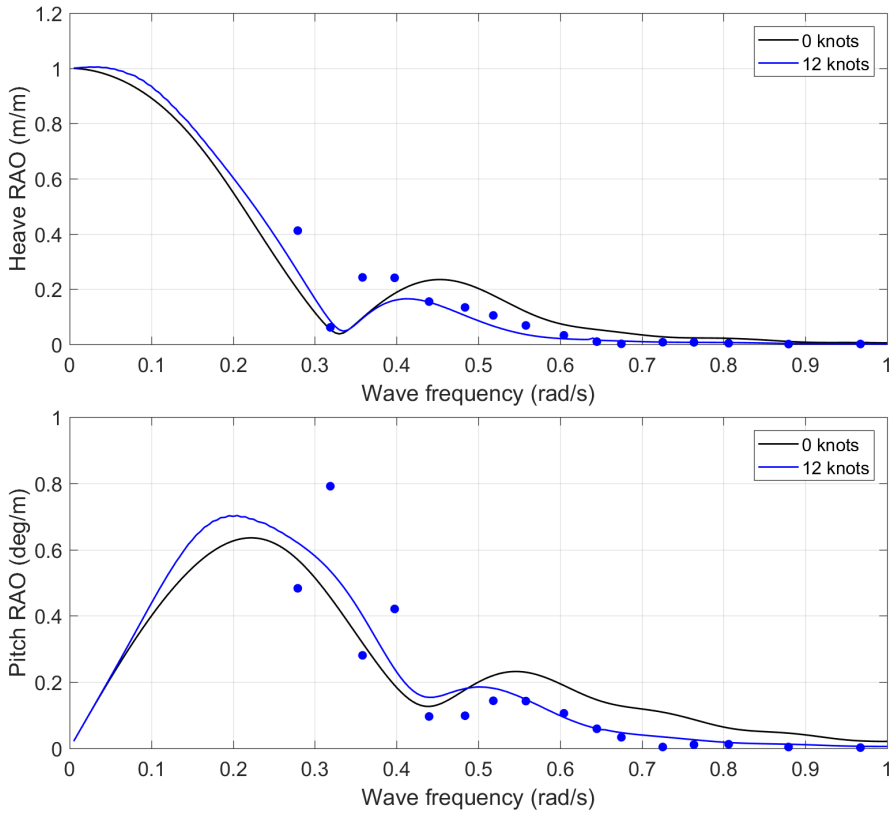

Figure 6. 300 m container ship in head seas

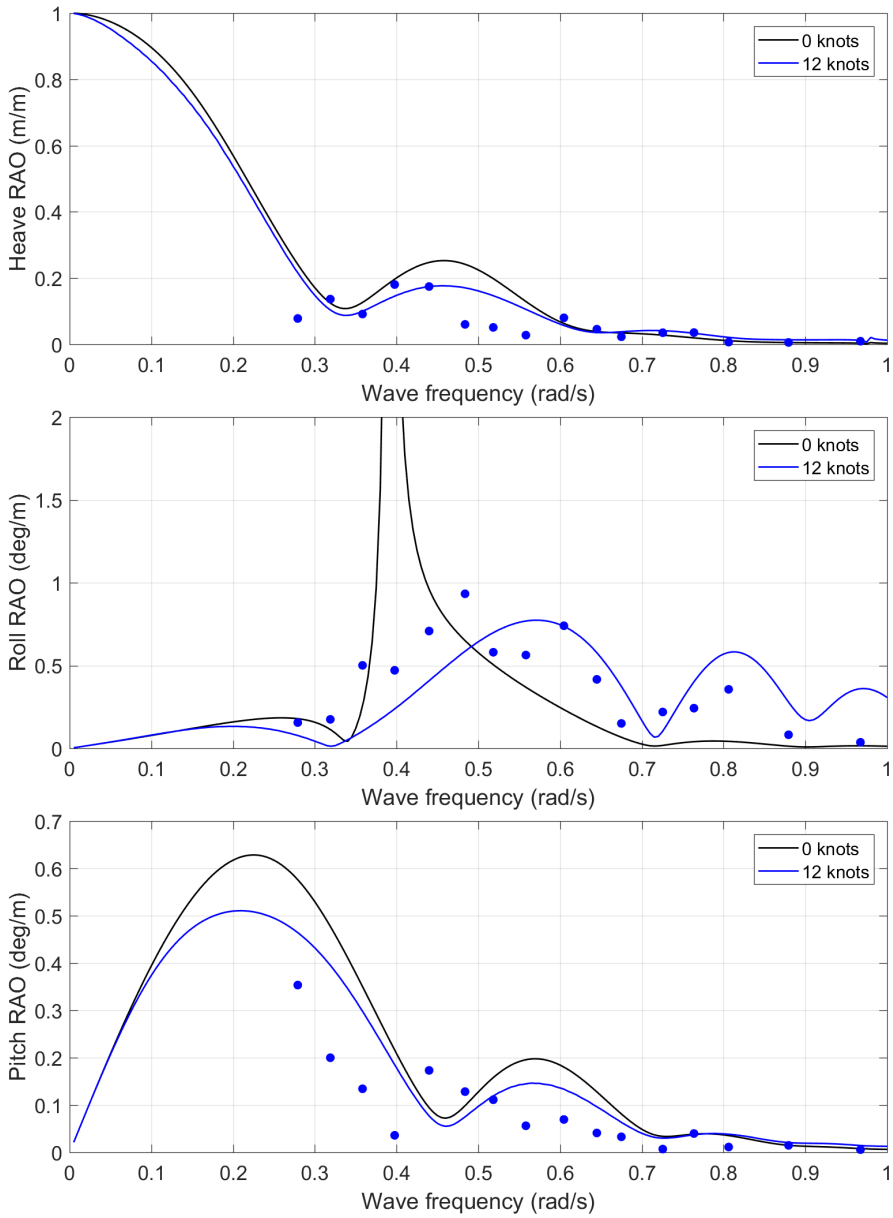

Figure 7. 300 m container ship in waves 10° off-stern

We can compare the accuracy of the speed-adjusted panel method presented here, to the strip theory results (OCTOPUS and PDStrip) and Rankine-source panel method (GL Rankine) presented in Gourlay et al. (2015, Fig. 16). All numerical methods give fairly similar results for this ship.

8 RESULTS FOR A 373 M CONTAINER SHIP

Here, we calculate results for the Duisburg Test Case container ship, for test cases CW1-CW5, as described in Van Zwijnsvoorde et al. (2019). The cases that were "blind" in that paper have since been kindly supplied by Ghent University and Flanders Hydraulics. Model test conditions are shown in Table 6.

Table 6. 373 m container ship model test conditions

Parameter	Value	Source
LOA	373.0 m	IGES file
LBP	355.0 m	Van Zwijnsvoorde et al. (2019)
Beam	51.00 m	"
Maximum draft	14.50 m	"
c_B	0.66	"
Tested draft	14.5 m	"
KG	19.8 m	"
k_{yy}	24% LBP	"
k_{xx}	38.9% Beam	"

Test cases CW1-CW5 are described in Table 7.

Table 7. 373 m container ship model test cases

Test case	Static UKC (% draft)	Speed (full-scale)	Wave height (full-scale)	Wave period (full-scale)
CW1	100%	0 knots	4.86 m	13.0 s
CW2	100%	6 knots	5.55 m	13.0 s
CW3	100%	16 knots	5.56 m	13.0 s
CW4	20%	0 knots	1.98 m	15.7 s
CW5	20%	6 knots	1.90 m	15.7 s

Motion calculations from various ship motion codes for these test cases are described in Gourlay et al. (2019). Table 8 and Table 9 show calculations for these model test cases, using the method described in Section 3.

Table 8. 373 m container ship vertical motion @AP

Test case	z_a/ζ model test	z_a/ζ WAMIT	ε_a model test	ε_a WAMIT
CW1	0.327	0.270	53	58
CW2	0.338	0.310	48	31
CW3	0.274	0.254	22	-20
CW4	0.270	0.348	36	59
CW5	0.276	0.340	34	24

Table 9. 373 m container ship vertical motion @FP

Test case	z_f/ζ model test	z_f/ζ WAMIT	ε_f model test	ε_f WAMIT
CW1	0.504	0.526	-174	179
CW2	0.363	0.565	180	151
CW3	0.346	0.387	134	106
CW4	0.401	0.440	174	158
CW5	0.268	0.352	165	136

We can compare the accuracy of the speed-adjusted panel method presented here, to the other numerical results in Gourlay et al. (2019). This comparison is shown in Figure 8.

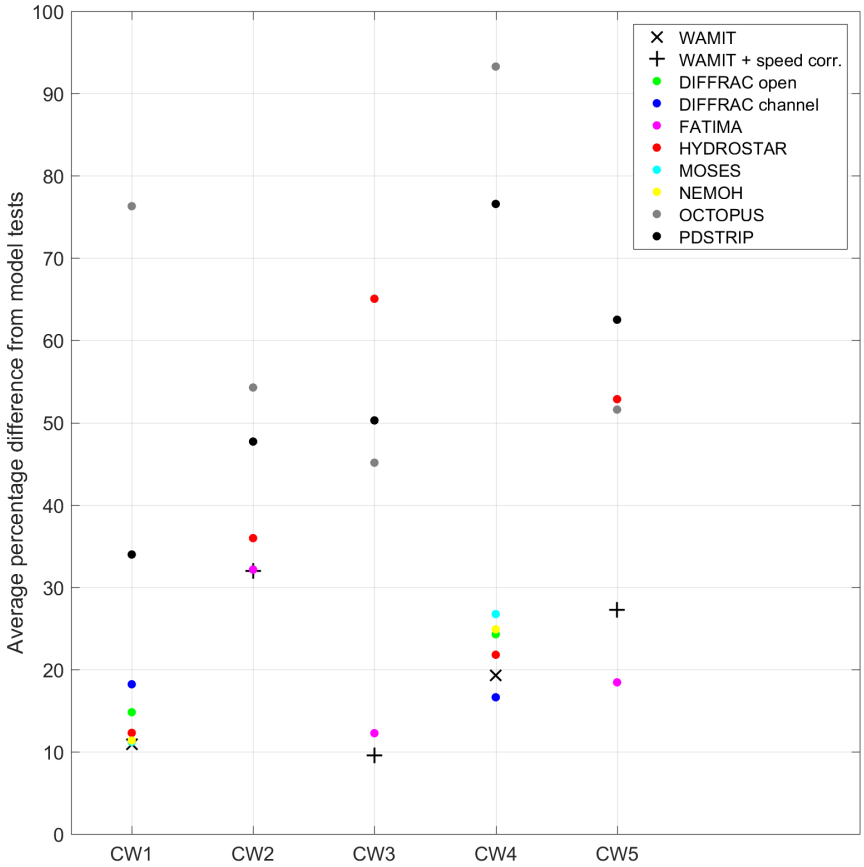

Figure 8. Percentage difference between numerical methods and model test results, averaged over bow and stern motion amplitudes

We see that WAMIT is amongst the most accurate methods for the zero-speed cases (CW1 and CW4), while the speed-adjusted WAMIT method is amongst the most accurate methods for the forward-speed cases (CW2, CW3 and CW5).

9 CONCLUSIONS

In conclusion, this study presents a computationally efficient method for approximating wave-induced motions of ships at low Froude numbers. By utilizing zero-speed Green functions from WAMIT and adjusting for ship speed, the method demonstrates comparable accuracy to established numerical methods such as strip theory and Rankine-source panel methods. The approach is validated against model test data for various ship types, including bulk carriers and container ships, under different speed and wave conditions. The speed-adjusted panel method can be used to predict ship motions in both shallow and deep water environments. While some error is expected due to the use of zero-speed Green functions, the method's simplicity and efficiency make it a valuable tool for preliminary ship design and performance assessment.

10 REFERENCES

Abdelwahab, H.S., Wang, S., Parunov, J., Guedes Soares, C. (2023) A new model uncertainty measure of wave-induced motions and loads on a container ship with forward speed. Journal of Marine Science and Engineering, Vol. 11.

Flokstra, C. (1974) Comparison of ship motion theories with experiments for a container ship. International Shipbuilding Progress, Vol. 21.

Gourlay, T.P., von Graefe, A., Shigunov, V., Lataire, E. (2015) Comparison of AQWA, GL RANKINE, MOSES, OCTOPUS, PDSTRIP and WAMIT with model test results for cargo ship wave-induced motions in shallow water. Proceedings, 34th International Conference on Ocean, Offshore and Arctic Engineering, St. John's, Canada.

Gourlay, T.P., Lataire, E., Delefortrie, G., Donatini, L., Tello Ruiz, M., Veen, D.J., Bunnik, T.H.J., Dallinga, R.P. (2019) Benchmarking of DIFFRAC, FATIMA, HydroSTAR, MOSES, NEMOH, OCTOPUS, PDStrip, RAPID, SEAWAY, SlenderFlow and WAMIT against measured vertical motions of the Duisburg Test Case container ship in shallow water. Proceedings, 5th International Conference on Ship Manoeuvring in Shallow and Confined Water, Ostend, Belgium.

Korsmeyer, F.T., Bingham, H.B., Newman, J.N. (1999) TIMIT – a panel-method program for transient wave-body interactions. MIT, May 1999.

Salvesen, N., Tuck, E.O., Faltinsen, O. (1970) Ship motions and sea loads. Presented at SNAME Annual Meeting, November 1970.

St Denis, M., Pierson, W.J. (1953) On the motions of ships in confused seas. Trans. SNAME, Vol. 61.

Van Zwijnsvoorde, T., Tello Ruiz, M., Delefortrie, G., Lataire, E. (2019) Sailing in shallow water waves with the DTC container carrier: open model test data for validation purposes. Proceedings, 5th International Conference on Ship Manoeuvring in Shallow and Confined Water, Ostend, Belgium.

Vantorre, M., Journée, J.M.J. (2003) Validation of the strip theory code SEAWAY by model tests in very shallow water. Numerical Modelling Colloquium, Flanders Hydraulics Research, Antwerp.

Vantorre, M., Laforce, E., Eloot, K., Richter, J., Verwilligen, J., Lataire, E. (2008) Ship motions in shallow water as the base for a probabilistic approach policy. Proc. ASME 27th Int. Conf. on Offshore Mechanics and Arctic Engineering OMAE 2008, Estoril, Portugal.

Wahab, R., Vink, J.H. (1975) Wave induced motions and loads on ships in oblique waves. International Shipbuilding Progress, Vol. 22.

WAMIT (2023) WAMIT v7.5 User Manual. WAMIT Inc.

Zhou, Z.-Q., Zhou, D.-C., Xie, N. (1996) A seakeeping experiment research on Flokstra container ship model. China Register of Shipping report, 20th July 1996.

11 AUTHOR BIOGRAPHY

Tim Gourlay, PhD, is principal consultant at Perth Hydro. He undertakes ship hydrodynamics computer modelling and full-scale measurements for industry and government in Australia and internationally. His previous contributions to MASHCON include a benchmarking study on DTC wave-induced motions for MASHCON 2019 and a benchmarking study on KCS dynamic sinkage for MASHCON 2016.

PREDICTIVE SIMULATION OF ONSHORE POWER SUPPLY REQUIREMENTS FOR PORTS

Lourdes Pecharromán, Siport21. Spain
Raul Redondo, Siport21. Spain
Raul Atienza, Siport21. Spain
Arturo Medio, Technical University of Madrid, Spain
Luis Ulla, Technical University of Madrid, Spain

PREDICTIVE SIMULATION OF ONSHORE POWER SUPPLY REQUIREMENTS FOR PORTS

RAUL REDONDO, SIPORT21. SPAIN
RAUL ATIENZA, SIPORT21. SPAIN
ARTURO MEDIO, TECHNICAL UNIVERSITY OF MADRID, SPAIN
LUIS ULLA, TECHNICAL UNIVERSITY OF MADRID, SPAIN
LOURDES PECHARROMÁN, SIPORT21. SPAIN

SUMMARY

Port infrastructure development projects require reliable data for the transition into "smart ports". The purpose of Onshore Power Supply (OPS) is to connect the ship to the electricity grid, reducing CO2 emissions and noises at port areas. In order to comply with governmental orders, ports have to be able to fulfill 90% of the electricity demand of container ships, passenger ships and ro-ro vessels by 2030. Nevertheless, there are still barriers to the development of this technology, as the installation requires a large investment, renewal of the fleets and available substations near ports. A methodology developed by Siport21 is described using a mathematical model of traffic forecast, based on statistical methods and simulation techniques. As a result, it helps ports in decision-making about the infrastructure required by the OPS technology. The tool considers the terminals of the port and traffic data based on AIS (Automatic Identification System) information to determine the power demand requirements by following the "4th IMO Greenhouse Gas Study" for ships power consumption

NOMENCLATURE

AIS	Automatic Identification System
GT	Gross Tonnage
OPS	Onshore Power Supply

1 INTRODUCTION

Cold ironing or Onshore Power Supply, OPS, is a new development and requirement for ports due to the present situation and legislative framework in maritime transport. This is currently undergoing a period of change due to regulations implemented by the International Maritime Organization (IMO) and other governmental organizations regarding CO2 emissions reduction. In 2021, the European Union launched 'Fit for 55', a package of measures with the aim of reducing greenhouse gas emissions by 55% compared to 1990 levels. One of these regulations states that European ports must ensure by January 1, 2030, sufficient shore-side electrical power to meet a high percentage of demand based on their average annual throughput of container ships, passenger ships and ro-ro vessels.

OPS provides significant benefits (emissions and carbon footprint reduction, elimination of noise and vibrations, less wear and tear on auxiliary engines, increased use of renewable energies in maritime transport, etc.). However, there are still barriers to the development of this technology. The main reasons are economic as these installations require a large investment.

Shipping companies should renew their fleets to connect the ships to the electricity grid, and ports should have available substations nearby with sufficient capacity to cover the demand. Therefore, there is a need for new reliable tools to help ports make sensible decisions on the OPS investment.

Siport21 has developed a methodology to define the sizing and optimization of OPS facilities in ports. It is based on statistical methods and Montecarlo simulation techniques, providing an estimate of hourly electricity demand over the course of a year associated with probability levels. This methodology will help ports have probability-based estimates and will therefore be essential for decision-making, evaluating the cost-benefit of the investment and the total power to be installed.

This paper will show the results of the analysis developed for a practical case, in which the sensitivity to the different hypotheses and variables involved in the problem can be appreciated and how a certain growth in the transformation of ships to be able to use OPS systems could affect the phased OPS investment in ports. Finally, the work will also show the results of the decrease of the carbon footprint in the port due to the OPS operation. A port which already defined its OPS capacity will be used as an example for calibration and comparison purposes with the methodology developed in Siport21.

2 METHODOLOGY

The methodology to address the required power demand for a specific port of terminal is based on a traffic flow simulation model which allows to understand the traffic movements per terminal in the port, and therefore their required power demands for connection to the local grid.

This study starts therefore with the AIS data analysis, allowing an accurate quantitative description of traffic movements in the port (type of vessels, number, size and draft, routes, speeds, scheduled calls, berth occupation, etc.). Given the enormous volume of data, the analysis is based on Big Data, Data Analytics and Data Viz techniques (algorithms used to identify space-time relationships between the different traffics and representation methods).
The AIS data analysis allows the definition of most of the inputs required for the accurate building of the traffic simulation model. Using probabilistic methods based on the terminals, time at berth, arrival frequency and sizes, allows a predictive simulation model in connection to the OPS.
Port infrastructure definition is the other input required in the model building. Each terminal is associated with a cargo type and has its infrastructure defined (length, draught, number of cranes, storage capacity, etc.).
Once all information is known the model is built, representing the digital movement so the port area, where port data definition represents the static element of the model and the ship movements the dynamic part.
Once the model is built, it is calibrated against real AIS data to check the model quality and its resemblance to the reality which intends to represent. Ultimately, future scenarios are described and quantified. Those scenarios represent the traffic evolution as well as the evolution of the port area and infrastructure based on port masterplan, therefore, the dimensions of the OPS are not done for current port and traffic, but for future requirements.

To follow the methodology, a base case to derive the power demand is presented. For comparison, the example relates to a real port which has already defined its OPS capacity and has a well-known infrastructure. A deep analysis of the type of vessels with arrival at the port and their facilities is important to check compliance with 'Fit for 55'.

2.1 AIS DATA ANALYSIS

The AIS system allows the identification and tracking of ships from other ships, or coast stations. This system is based on a device installed onboard that continuously and automatically transmits information. It allows other vessels in the area or onshore stations to identify their position, the state of the ship and movement parameters. The AIS emits messages with a variable period depending on the navigation status.
The AIS has been developed under the auspice of the International Maritime Organization (IMO) and its installation and use in ships is subjected to the SOLAS Convention (Safety of Life at Sea), compulsory since December 31, 2004. The vessels obligated to incorporate these devices are:

- All vessels on international voyages with a gross tonnage (GT) greater than or equal to 300.
- All vessels on non-international voyages with a gross tonnage (GT) greater than or equal to 500.
- All passenger ships regardless of size.

Once the quality and the reliability of the AIS data has been verified, different variables are analyzed to get to know the behavior of the vessels in the port. This will be used as input data in the simulation model.
The main study case is the analysis of ships at berth with some of the study variables listed below. The target vessels are container ships, passenger ships and ro-ro vessels. The variables considered are presented below with some figures with the results obtained from the AIS data:

- Type and size of vessels according to the cargo that access each terminal.

Figure 1 shows the number of vessels per year according to cargo and length for the vessels in the study case.

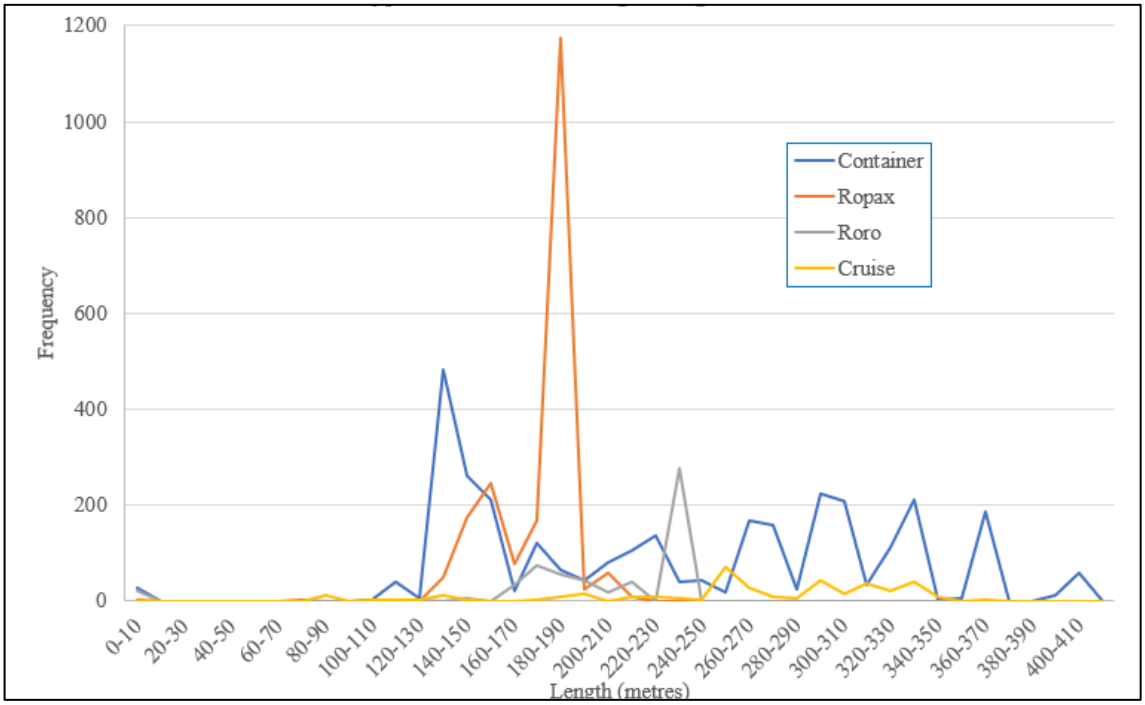

Figure 1 (Source: Siport21). Vessel size depending on cargo

- Occupation levels of the terminal studied.

Figure 2 shows the occupancy based on the length of the terminal studied. The level of occupancy is set close to 50% of the terminal and the values are quite regular during a year not depending at all in seasonality.

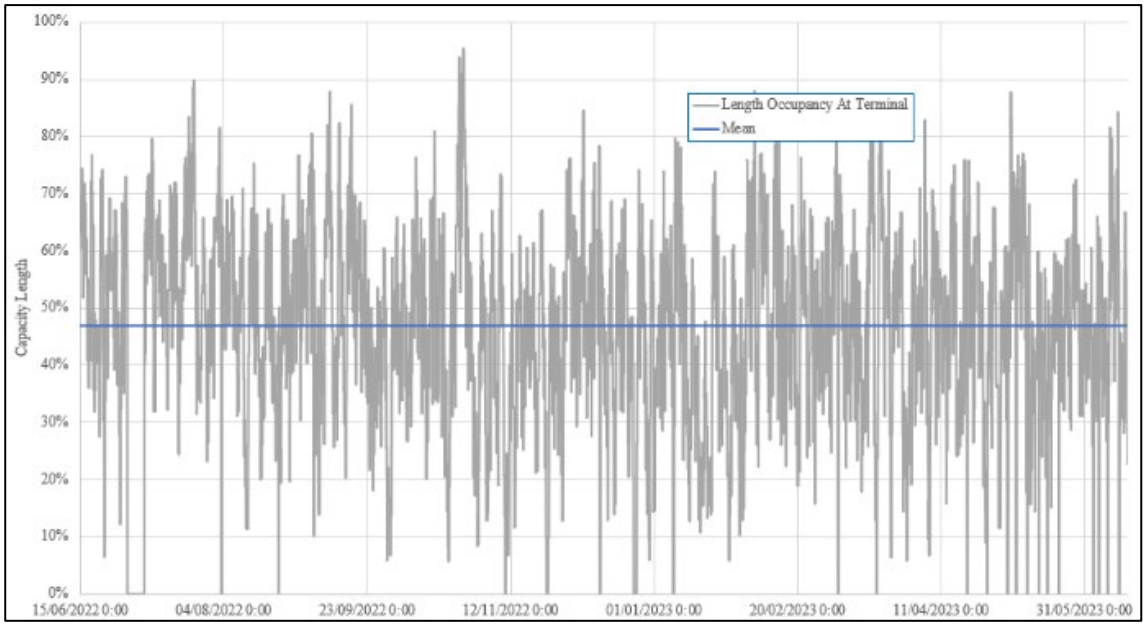

Figure 2 (Source: Siport21). Occupancy Level of the berth length for one of the Terminals considered

- Time spent at berth.

Figure 3 shows the time spent at berth depending on cargo and vessel size. As shown, most vessels spend less than 48 hours in port and there is no linear relationship between these variables.

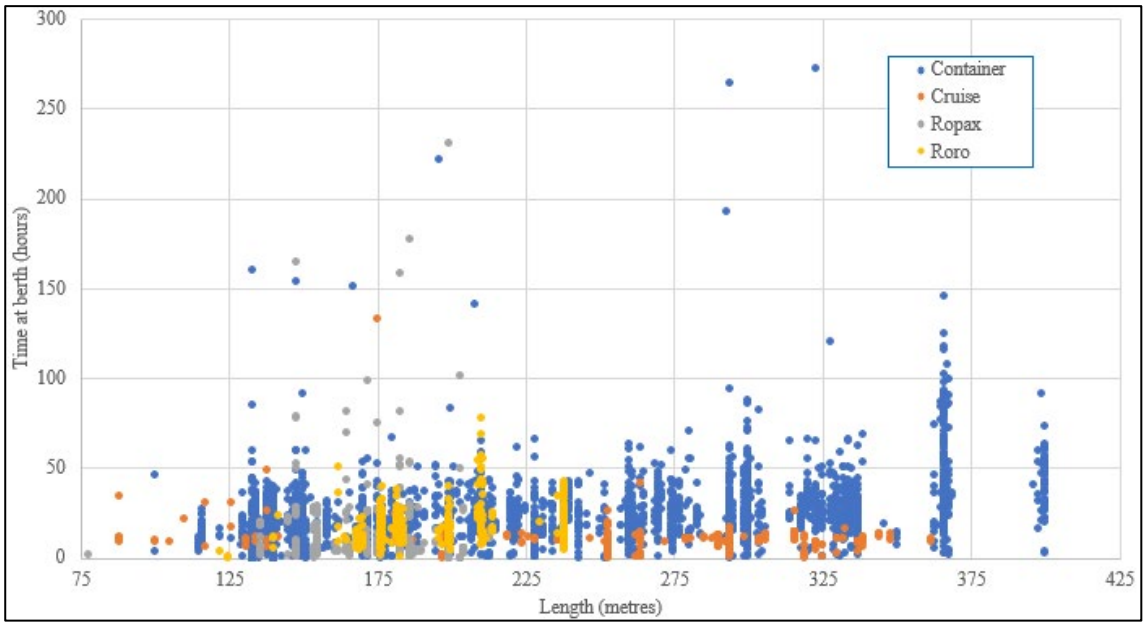

Figure 3 (Source: Siport21]). Time at berth depending on cargo and ship size

The result of the AIS data analysis can be collected in a wide variety of graphs depending on the purpose of the analysis. A series of KPIs (Key Performance Indicators) should be defined to facilitate decision making and understanding the results of the model.

For the particular case of the OPS definition, AIS data is basically used to derive the input data and the statistics of the dynamic part of the traffic model which will be built. Where ships data (type, size, frequency, distributions and time and berth) is the key to understand the power demand for each individual ship, and therefore, for the complete port area.

2.2 AUXILIARY ENGINE POWER

Based on AIS data and with a reliable database, a series of power demand values are obtained. Following the Fourth IMO Greenhouse Study allows the model to obtain the auxiliary power demand depending on the vessel type and its capacity (Cubic Meters for LNG Tankers, TEU for container ships, Gross Tonnage for passenger ships and Dead Weight for the rest). There are different power assignments depending on the operational mode. In this case study for power demand, vessels are berthed.

During its time at berth the vessels use their auxiliary engines instead of the main engine to supply the electricity demanded by the equipment, auxiliary engines are also used while loading/unloading cargo. When connected to the local grid, and the OPS; the power demand will be the one which is currently being provided by the auxiliary engines, and therefore, this power is addressed.

According to the Fourth IMO Greenhouse Study, the auxiliary engine and boiler power output follows a decision tree based on installed power given by the main engines:

- When the main engine power is between 0 and 150 kW the auxiliary engine and boiler are set to zero.
- When the main engine power is between 150 and 500 kW then the auxiliary engine is set to 5% of the main engine installed power while the boiler power output is based on tabulated values.
- When the main engine power is larger than 500 kW then the auxiliary engine and boiler values are tabulated.

The ‘Fourth IMO Greenhouse Study’ presents the auxiliary engine and boiler power outputs per ship class and operational mode.

Following these guidelines, an example of the power demand, for a year-period time, which would have been required for a specific terminal is shown below, in Figure 4:

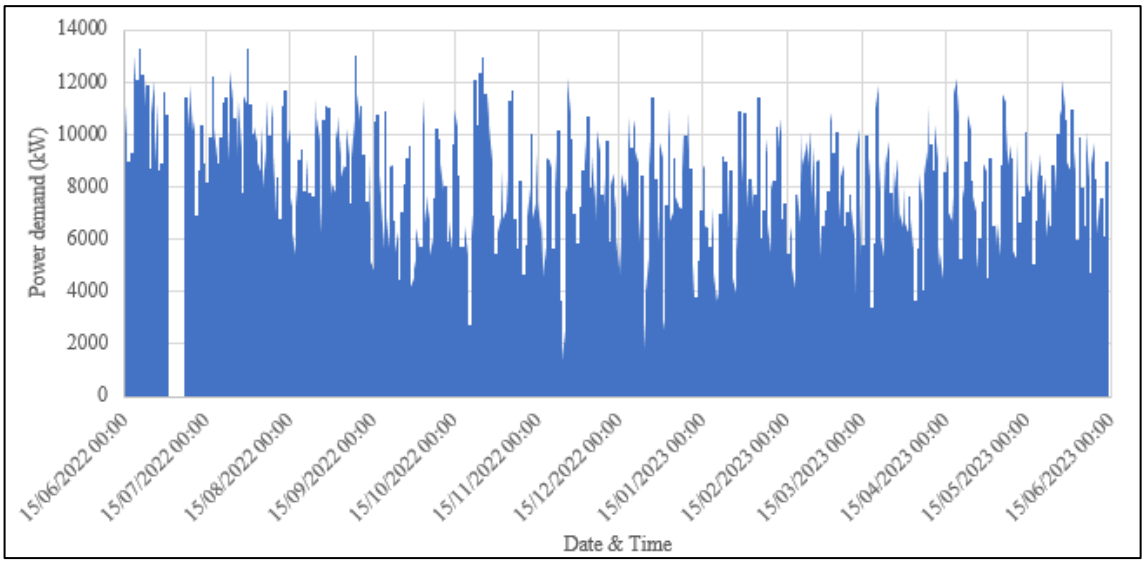

Figure 2 (Source: Siport21). Power Demand by container ships in a year-period time

2.3 DEFINITION OF KEY PERFORMANCE INDICATORS

In order to facilitate decision-making, a series of key indicators are defined which will allow different future scenarios to be compared with the current situation. KPIs must be aligned with the objectives and particularities of the project. In addition, the same indicators will serve as basis for the calibration process of the maritime traffic model.
In this study the indicators are those referred to the use of the terminals related to the efficiency of the port. Some examples are listed below:

- Related to the use of the terminals

The time ships are berthed and the gap between arrivals are indicators for the capacity and efficiency of the terminals. These KPIs, combined with the vessel occupancy at the dock, provide information for the capacity and efficiency of the terminals. Figure 5 provides number of vessels at the same time for 3 different container terminals in the port, while Figure 6 shows the gap of ship arrivals. Combining both figures, an estimation of the terminal occupancy can be provided, and an idea of traffic flow at the port can be made to introduce into the model.

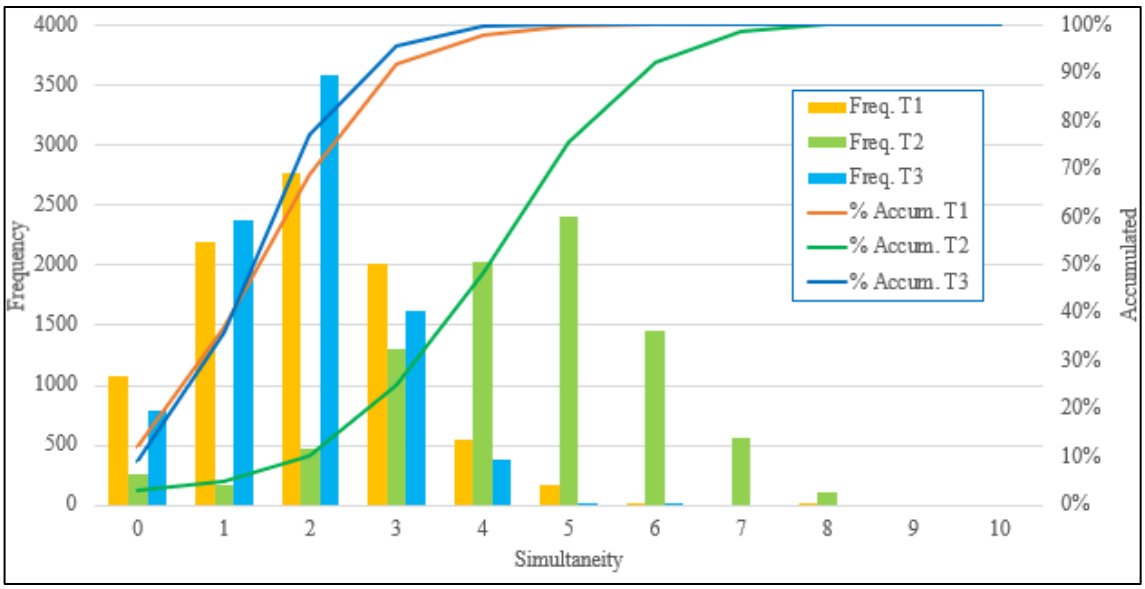

Figure 3 . (Source: Siport21). Simultaneity of vessel for the 3 container ship terminals

T1, T2 and T3 refer to each one of the three terminals assessed in this paper

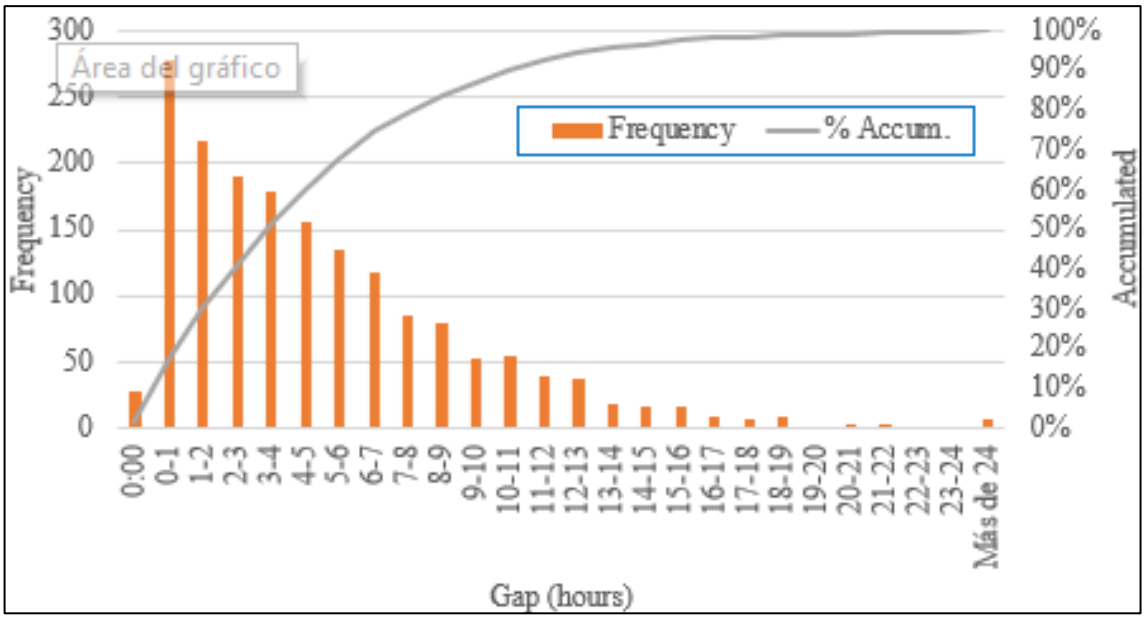

Figure 4 (Source: Siport21). Interarrival times for ships at the Terminal

- Related to the power demand.

Power demand depends on the vessel. It is a very important indicator for decision-making about the substations of the port. Next figure (Figure 7) shows an example of power demand for container vessels at 3 different terminals in the port.

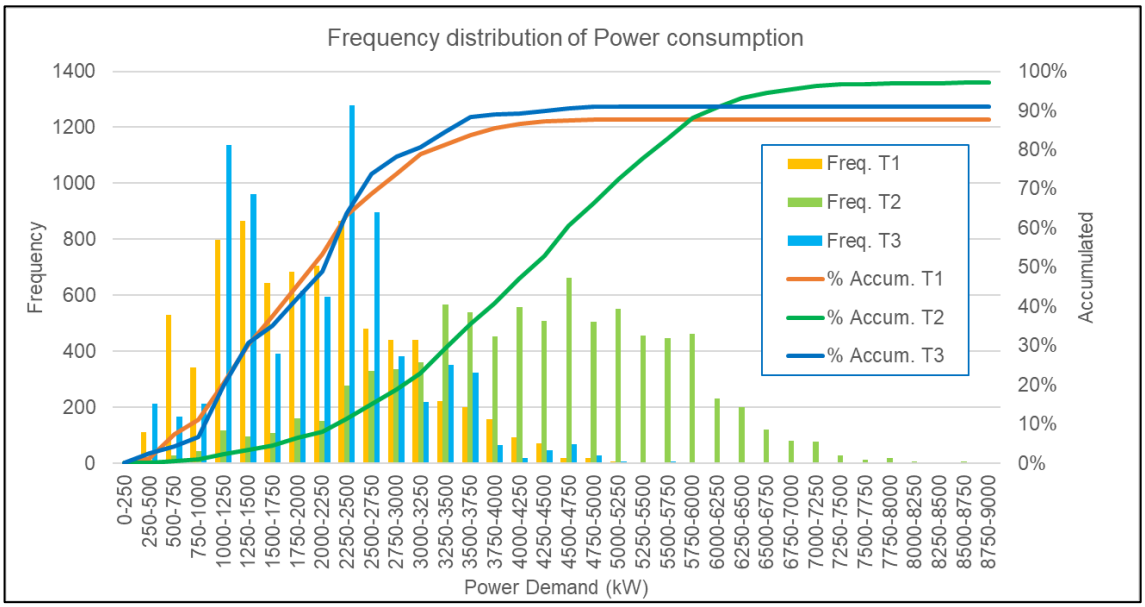

Figure 5 (Source: Siport21). Power demand for the 3 container ship terminals

- Related to the economic income

Given the time at berth, the electricity fare and adding the management of the technology by the operators, the economic income can be estimated.

- Related to the efficiency of the OPS technology

Less wear and tear on auxiliary engines, emissions and carbon footprint reduction (this can be estimated in the port area as well) and elimination of noise and vibrations.

2.4 MODEL BUILDING

The model building consists of defining the elements taking part in the connection to the OPS technology to the vessels at the port. The model consists of probabilistic distributions based on real AIS data to create random data close to reality. The list of elements is listed below:

- **Vessels**: for this study case, the model needs the length and the draught of the vessel to create a random sequence of arrivals to the dock, as well as a dock dwell time as close to reality as possible. The power demand is linked to the random vessel size and type.
- **Port area and Terminals**: areas where vessels remain for a determined time according to the operations of loading/unloading or refueling, before starting the departure maneuver. Terminals are limited by its length and draught. A maximum number of vessels can remain in terms of length. The gap between vessels must be considered.

2.5 SIMULATION

Once the elements of the model have been defined, the simulation process starts by generating a random vessel and keeps creating new vessels with a gap between arrivals to the port defined by statistical distributions. After the generation of each ship, a short simulation is done to recreate the channel navigation based on the speed of the vessel. Then, a series of questions in the following order are asked:

- Terminal according to the cargo of the vessel: depending on the cargo and the size of the vessel, a terminal with the appropriate infrastructure is assigned. The ship will go across the navigation channel belonging to the terminal.
- Terminal depending on the draught: terminals have a determined draught. The vessel must have a smaller draught than the terminal.
- Terminal depending on occupancy: depending on the size of the vessel, the occupancy level must be considered, terminals have a limited length. A maximum number of vessels can remain in the terminal. The total length is reduced due to the gaps between vessels for minimum safety distance.
- Docking available: the terminal can be distributed in different docks. The same question of the occupancy is set out for the docks. In case the docks are full, the vessels are directed to the anchorage area before arriving at the port.

Other restrictions can be considered by adding a waiting point (anchorage area) in the system where vessels can remain until the conditions come back to normality.
These series of questions are asked in the entrance of each vessel. Once the vessel finishes at its berth, the vessel waits at its dock until the exit channel is clear before leaving the port.
Once the process is built, the calibration is carried out by running the models in an iterative process of simulation (analysis of results) adjustment until reaching results close enough to reality. The calibration process is always carried out based on a real scenario, from which information on the behavior of ships berthed is available with an adequate level of detail and accuracy.
The level of detail required to achieve reliable results is based on the analysis of the AIS data. However, there is some information that cannot be extracted from its analysis, such as actual draft or the causes of waiting events.

2.6 ALTERNATIVE SCENARIOS ASSESSMENT

In general, the new alternative scenarios of interest will be those which have an impact on current traffic flow. These include an increase in traffic volume, new traffic demand which would require changes in port infrastructure (new terminals), new regulations (minimum safety distance between vessels, crossing in the channel, bunkering, …), larger vessels in terms of length or capacity with a new power demand, etc.
Once the model has been built and calibrated, the results are then compared to real AIS data. The results of the simulation are used in comparison with the KPIs previously defined of the alternative scenarios. In the model building phase, it is possible to adapt the model to the predicted forecast by adding various changes to assess their impact on the traffic behavior by adding new variables and correlations.
In order to find the best fit, each KPI is compared against real data using different distributions such as, gaussian, beta, gamma and erlang, with the purpose of minimizing the quadratic error. The density function is used for comparison, as it is more visual than the distribution function. An example is shown below, in Figure 8, for the gap between arrivals at the docks.

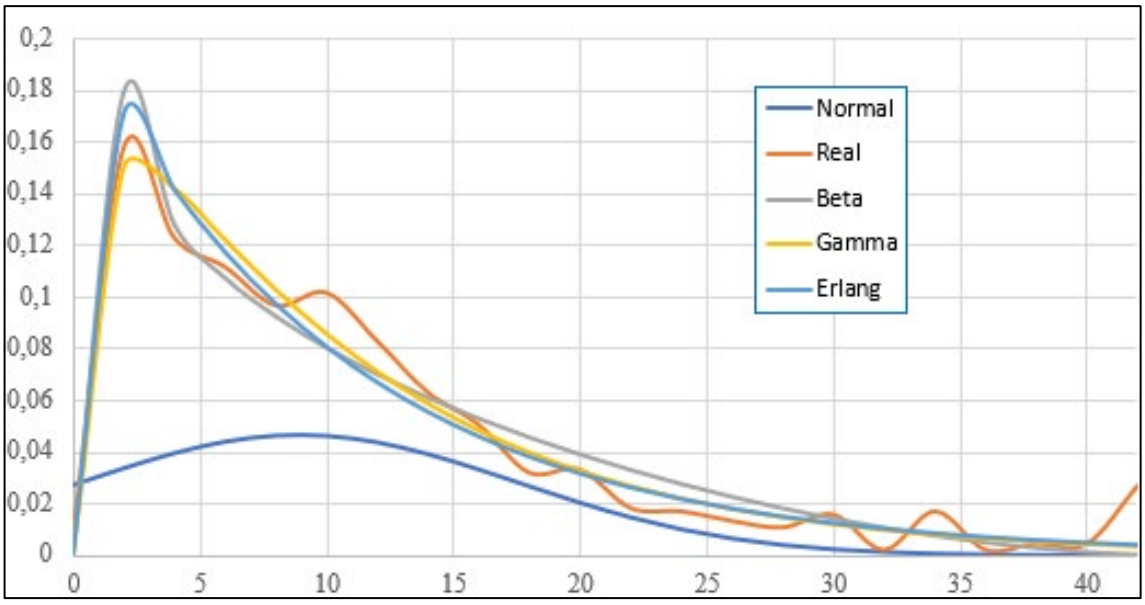

Figure 6 (Source: Siport21). Search of the Closest Fit Distribution

The objective is to achieve the closest fit to reality, which means different scenarios must be analyzed to check that the simulation is adapted to the KPIs and the predicted forecast. The traffic volume for the analysis of those future scenarios is defined through forecast studies of the cargo managed, port infrastructure plans and global market demand. Figure 9 shows an example of the power demand at the Port (orange bars) and power demand forecast (blue bars) for a period of 1 year.

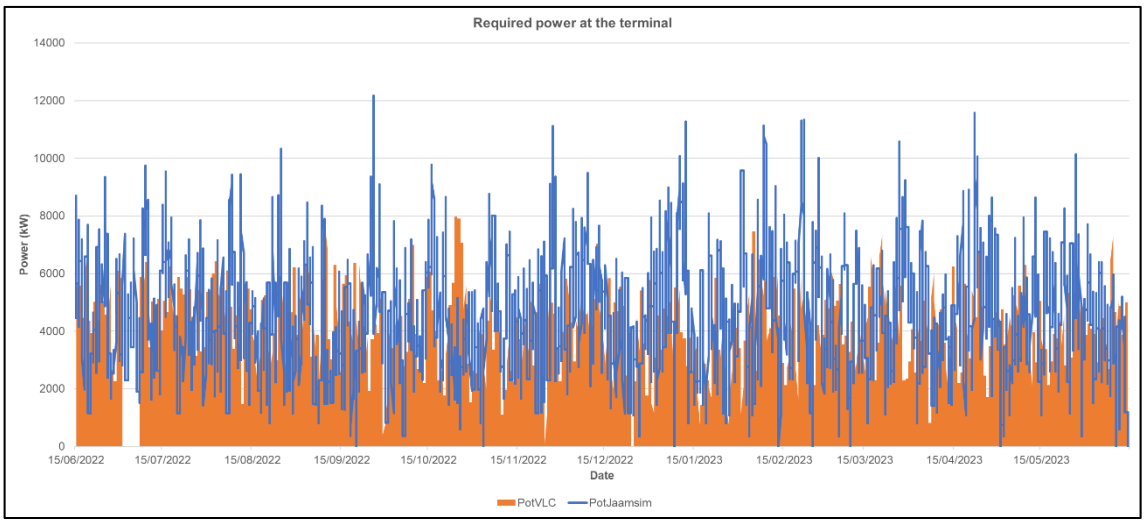

Figure 7 (Source: Siport21). Power Demand Forecast at Container Terminal based on Historical Data

In order to comply with governmental orders, ports have to be able to fulfill 90% of the electricity demand of container ships, passenger ships and ro-ro vessels. Using the mean value for a year-period of time and the deviation of the collected power demand values, the tool can predict the OPS capacity in order to fulfill the percentage required by the pack of measures launched in 'Fit for 55'.

Table 1. Predicted Power Demand to comply with Different Percentage in kW

	Mean Power	Standard Deviation	99%	95%	90%	85%
Port	4109	1553	7720	6662	6098	5718
Simulation	4497	1681	8407	7262	6651	6239

The analysis of several traffic volumes allows to determine the capacity of a given infrastructure scenario, such as maximum number of vessels that can access the system. For the purpose of this study is to estimate the power demanded by vessels to estimate the capacity of the OPS and the substation nearby that will cover this power demand.
Based on the Fourth IMO Greenhouse Study, the shortest power demand by a container ship is 610 kW and the largest 1400 kW. Based on the values of above table, the difference of the mean power at the port and the simulation, is the range between the minimum and the maximum range value set by the IMO Study.

3 CONCLUSIONS

This paper presents the methodology to assess the required power demand of port areas and terminals, and, based on the results, understand which requirements must be considered by the port and which percentage of the power demand they can accommodate. As designing for peaks, will lead for over-investments and over-designed systems, which will only be used fully few days per year, and it would be more likely to design and invest for a minor fulfilment of the power demand, understanding that in some cases, ships could be required to wait at anchorage before accessing the terminal due to the non-availability of OPS connection due to the limitations of the power infrastructure.

4 REFERENCES

Alzate Castro, Wilmar Alexander, y Erika Janeth Salazar Jiménez.

Simulación Monte Carlo: Análisis de una Herramienta para la Proyección del Estado de Resultados. Un estudio de Caso. s.f.

European Maritime Safety Agency (EMSA).

Shore-Side Electricity: Guidance to Port Authorities and Administrations. Part 1: Equipment and Technology. Lisbon, 2022

European Maritime Safety Agency (EMSA)

Shore-Side Electricity: Guidance to Port Authorities and Administrations. Part 2: Planning, Operations and Safety. Lisbon, 2022.

International Association of Marine Aids to Navigation and Lighthouse Authorities (IALA).

Establishment of AIS as an Aid to Navigation. Edition 1, December 2008: Guideline 1062.

International Association of Marine Aids to Navigation and Lighthouse Authorities (IALA).

Management and Monitoring of AIS Information. Edition 1, December 2005: Guideline 1050.

International Maritime Organization (IMO).

Fourth IMO Greenhouse Study. Study, London, 2020.

International Maritime Organization (IMO).

Third IMO Greenhouse Study. Study, London, 2014.

LLC, Starcrest Consulting Group.

Port of Los Angeles. Inventory of Air Emissions. Estudio, Los Ángeles, 2021.

Moreno-Gutiérrez, J.

Methodologies for Estimating Shipping Emissions and Energy Consupmtions: A Comparative Analysis of Current Methods. 2015.

Puertos del Estado

OPS Master Plan for Spanish Ports. Estudio, España, 2021.

Servizo Galego da Saude (SERGAS).

Epidat4. Ayuda de Distribuciones de Probabilidad. Capítulo 13. October 2014.

Tortosa Solvas, E. and Rebollo Lledó, J.

La Red AIS Portuaria. La Tecnología AIS Aplicada a la Explotación Portuaria y a las Ayudas a la Navegación. En Puertos nº 158, 9-21. 2010.

Trozzi, C.
Emission Estimate Technology for Maritime Navigation. US EPA 19th International Emission Inventory Conference. 2010.

5 AUTHORS BIOGRAPHY

Raul Redondo holds the current position of Director of Manoeuvring and Nautical Studies Area at Siport21. He coordinates and checks the technical projects. He specializes in ship manoeuvrability in port areas, both using numerical models and real-time simulation.

Raul Atienza holds the current position of Technical, Innovation and Quality Management Director at Siport21. He previously worked as Head of Manoeuvring and Nautical Studies Department at Siport21 and as a teacher in the Technical University of Madrid (Naval Architecture College).

Arturo Medio, is student at the Technical University of Madrid (Naval Architecture College). He collaborates with Siport21 through a collaboration grant associated to the Technical University of Madrid

Luis Ulla, is student at the Technical University of Madrid (Naval Architecture College). He collaborates with Siport21 through a collaboration grant associated to the Technical University of Madrid

Lourdes Pecharroman holds the current position of Project Manager of the Manoeuvring and Nautical Studies Area at Siport21. She is responsible for managing manoeuvring studies carried out with numerical tools (fast-time and real-time simulation). She is specialized on numerical models of vessels.

06105682
Battery
Hybrid
POA 2